Handbook of Coherent Domain Optical Methods

Biomedical Diagnostics, Environmental and Material Science, Volume 1 and 2

Edited by
Valery V. Tuchin

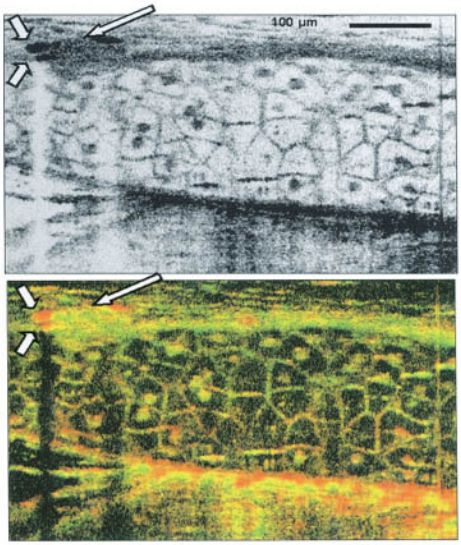

Kluwer Academic Publishers

How to go to your page

This eBook contains two volumes. Each volume has its own page numbering scheme, made up of a volume number and page numbers, separated by a colon.

For example, to go to page 35 of Volume 1, enter 1:35 in the “page #” box at the top of the screen and click “Go”. To go to page 35 of Volume 2, enter 2:35, and so on.

COHERENT-DOMAIN OPTICAL METHODS
Biomedical Diagnostics, Environmental and Material Science

Volume 1

This page intentionally left blank

COHERENT-DOMAIN OPTICAL METHODS
Biomedical Diagnostics, Environmental and Material Science

Volume 1

Edited by

VALERY V. TUCHIN
Saratov State University and Precision Mechanics and Control Institute of the Russian Academy of Sciences, Saratov, 410012 Russian Federation

KLUWER ACADEMIC PUBLISHERS
NEW YORK, BOSTON, DORDRECHT, LONDON, MOSCOW

eBook ISBN: 1-4020-7882-X
Print ISBN: 1-4020-7885-4

©2005 Springer Science + Business Media, Inc.

Print ©2004 Kluwer Academic Publishers
Boston

All rights reserved

No part of this eBook may be reproduced or transmitted in any form or by any means, electronic, mechanical, recording, or otherwise, without written consent from the Publisher

Created in the United States of America

Visit Springer's eBookstore at: http://ebooks.springerlink.com
and the Springer Global Website Online at: http://www.springeronline.com

Contents

Contributing Authors xi

Preface xv

Acknowledgments xxi

PART I: SPECKLE AND POLARIZATION TECHNOLOGIES

1. Light Correlation and Polarization in Multiply Scattering Media: Industrial and Biomedical Applications 3
Dmitry A. Zimnyakov

1.1 Introduction: Interference and Polarization Phenomena at Multiple Scattering 3
1.2 Temporal and Angular Correlations of Light Scattered by Disordered Media 5
1.3 Damping of Polarization of Light Propagating through the Disordered Media 9
1.4 Industrial and Biomedical Applications 25
1.5 Summary 38
References 38

2. Optical Correlation Diagnostics of Surface Roughness 43
Oleg V. Angelsky and Peter P. Maksimyak

2.1 Introduction 43
2.2 Theoretical Background 46
2.3 Computer Simulation 50
2.4 Dimensional Characteristics of Objects and Fields 58
2.5 Experimental Study 63
2.6 Singular Optics Concept 69
2.7 Zerogram Technique 75
2.8 Optical Correlation Technique 81
2.9 Conclusions 89
References 90

3. Laser Polarimetry of Biological Tissues: Principles and Applications 93
Alexander G. Ushenko and Vasilii P. Pishak

3.1 Introduction 93
3.2 Optical Models of Tissue Architechtonics 95
3.3 Polarization and Coherent Imaging 99
3.4 Stokes-Correlometry of Tissues 114
3.5 Wavelet-Analysis of Coherent Images 124
3.6 Summary 134
References 136

4. Diffusing Wave Spectroscopy: Application for Skin Blood Monitoring 139
Igor V. Meglinsky and Valery V. Tuchin

4.1 Introduction 139
4.2 Skin Structure and Sampling Volume 142
4.3 Principles of the Diffusing Wave Spectroscopy 144
4.4 DWS Experimental Approach and Data Analysis 148
4.5 Main Results and Discussion 150
4.6 Summary 158
References 159

5. Laser Speckle Imaging of Cerebral Blood Flow 165
Qingming Luo, Haiying Cheng, Zheng Wang, and Valery V. Tuchin

5.1 Introduction 165
5.2 Principles of Laser Speckle Imaging 166
5.3 Instrumentation and Performances 169
5.4 Applications 170
5.5 A Modified Laser Speckle Imaging Method with Improved Spatial Resolution 182
5.6 Conclusion 190
References 192

PART II: HOLOGRAPHY, INTERFEROMETRY, HETERODYNING

6. Low Coherence Holography 199
Paul French

6.1 Introduction to Low Coherence Holography 199
6.2 Phase-Stepping Interferometric Imaging 203
6.3 Off-Axis Holography 205
6.4 Photorefractive Holography 211
6.5 Conclusions and Outlook 226
References 229

7. Diffraction of Interference Fields on Random Phase Objects 235
Vladimir P. Ryabukho

7.1 Introduction 235
7.2 Collimated Interference Fields 237
7.3 Focused Spatially-Modulated Laser Beams 250
7.4 Interference Fringes in Imaging Systems 262
7.5 Interference Fringes Formed by Scattering Optical Elements 280
7.6 Industrial and Biomedical Applications 293
7.7 Summary 312
References 314

8. Heterodyne Techniques for Characterizing Light Fields 319
Frank Reil and John E. Thomas

8.1 Introduction to Heterodyne Detection 319
8.2 Optical Coherence Tomography (OCT) 323
8.3 Optical Phase-Space Measurements 326

8.4 Wigner Phase-Space Measurement 328
8.5 Applications 339
8.6 Summary 350
References 351

PART III: LIGHT SCATTERING METHODS

9. Light Scattering Spectroscopy: from Elastic to Inelastic 355
Lev T. Perelman, Mark D. Modell, Edward Vitkin, and Eugene B. Hanlon
9.1 Introduction 355
9.2 Principles of Light Scattering Spectroscopy 356
9.3 Applications of Light Scattering Spectroscopy 359
9.4 Principles of Raman Scattering Spectroscopy 373
9.5 Applications of Raman Spectroscopy 374
9.6 Near-infrared Raman Spectroscopy for *in vivo* disease diagnosis 380
9.7 Surface-Enhanced Raman Spectroscopy 386
References 392

10. Laser Doppler and Speckle Techniques for Bioflow Measurements 397
Ivan V. Fedosov, Sergey S. Ulyanov, Ekaterina I. Galanzha, Vladimir A. Galanzha, and Valery V. Tuchin

10.1 Introduction 397
10.2 Basic Principles of Laser Doppler and Speckle Techniques 398
10.3 Biomedical Applications of Laser Doppler and Speckle Techniques 413
10.4 Speckle-Correlation Measurements of Lymph Microcirculation in Rat Mesentery Vessels 423
10.5 Conclusion 431
References 432

11. Quasi-Elastic Light Scattering in Ophthalmology 437
Rafat R. Ansari

11.1 Introduction 437
11.2 QELS and Disease Detection 440
11.3 Early Detection of Ocular and Systemic Diseases 444
11.4 QELS Limitations 457
11.5 Future Outlook (Ophthalmic Tele-Health) 459

11.6 Conclusion 459
References 461

12. Monte-Carlo Simulations of Light Scattering in Turbid Media 465
Frits F. M. de Mul

12.1 Introduction 465
12.2 General Outline of the Program 467
12.3 Transport Algorithms 469
12.4 Scattering Functions 493
12.5 Light Sources 500
12.6 Detection 504
12.7 Special Features 509
12.8 Output Options 521
12.9 Conclusions 530
References 531

Index 533

This page intentionally left blank

Contributing Authors

Oleg V. Angelsky, Department of Correlation Optics, Chernivtsi National University, Chernivtsi, 58012 Ukraine,
e-mail: oleg@optical.chernovtsy.ua

Rafat R. Ansari, NASA Glenn Research Center at Lewis Field, Mail Stop 333-1, 21000 Brookpark Road, Cleveland, OH 44135 USA,
e-mail: Rafat.R.Ansari@grc.nasa.gov

Haiying Cheng, The Key Laboratory of Biomedical Photonics of Ministry of Education, Department of Biomedical Engineering, Huazhong University of Science and Technology, Wuhan, 430074 P.R. China,
e-mail: chhyibp@sina.com

Ivan V. Fedosov, Division of Optics, Department of Physics, Saratov State University, Saratov, 410012 Russian Federation,
e-mail: fedosov@optics.sgu.ru

Paul M. W. French, Imperial Collegeof Science, Technology and Medicine, London, SW7 2BZ, UK,
e-mail: paul.french@imperial.ac.uk

Ekateryna I. Galanzha, Division of Optics, Department of Physics, Saratov State University, Saratov, 410012 Russian Federation,
e-mail: galanzha@mail.ru

Vladimir A. Galanzha, Saratov State Medical University, Saratov, 410710 Russian Federation,

e-mail: galanzha@mail.ru

Eugene B. Hanlon, Department of Veterans Affairs, Medical Research Service, Bedford, MA 01730 USA,
e-mail: Eugene.Hanlon@med.va.gov

Qingming Luo, The Key Laboratory of Biomedical Photonics of Ministry of Education, Department of Biomedical Engineering, Huazhong University of Science and Technology, Wuhan, 430074 P.R. China,
e-mail: qluo@mail.hust.edu.cn

Peter P. Maksimyak, Department of Correlation Optics, Chernivtsi National University, Chernivtsi, 58012 Ukraine,
e-mail: maksimyak@itf.cv.ukrtel.net

Igor V. Meglinski, School of Engineering, Cranfield University, MK43 0AL, UK; Division of Optics, Department of Physics, Saratov State University, Saratov, 410012 Russian Federation,
e-mail: I.Meglinski@Cranfield.ac.uk

Mark D. Modell, Harvard Medical School, Beth Israel Deaconess Medical Center, Boston, MA 02215 USA,
e-mail: markmodell@erols.com

Frits F.M. de Mul, University of Twente, Department of Applied Physics, POBox 217, 7500 AE Enschede, the Netherlands,
e-mail: f.f.m.demul@tnw.utwente.nl

Lev T. Perelman, Harvard Medical School, Beth Israel Deaconess Medical Center, Boston, MA 02215 USA,
e-mail: lt.perel@verizon.net

Vasilii P. Pishak, Department of Medical Biology, Bucovinian State Medical Academy, Chernivtsi, 58000 Ukraine

Frank Reil, Physics Department, Duke University, Durham, NC 27708 USA,
e-mail: fr@phy.duke.edu

Vladimir V. Ryabukho, Division of Optics, Department of Physics, Saratov State University, Saratov, 410012; Precision Mechanics and Control Institute of the Russian Academy of Sciences, Saratov, 410028 Russian Federation
e-mail: rvp@sgu.ru

John E. Thomas, Physics Department, Duke University, Durham, NC 27708 USA,
e-mail: jet@phy.duke.edu

Valery V. Tuchin, Division of Optics, Department of Physics, Saratov State University, Saratov, 410012; Precision Mechanics and Control Institute of the Russian Academy of Sciences, Saratov, 410028 Russian Federation,
e-mail: tuchin@sgu.ru

Sergey S. Ulyanov, Division of Optics, Department of Physics, Saratov State University, Saratov, 410026 Russian Federation,
e-mail: ulianov@sgu.ru

Alexander G. Ushenko, Department of Correlation Optics, Chernivtsi National University, Chernivtsi, 58012 Ukraine,
e-mail: ushenko@itf.cv.ukrtel.net

Edward Vitkin, Harvard Medical School, Beth Israel Deaconess Medical Center, Boston, MA 02215 USA
e-mail: evitkin@bidmc.harvard.edu

Zheng Wang, The Key Laboratory of Biomedical Photonics of Ministry of Education, Department of Biomedical Engineering, Huazhong University of Science and Technology, Wuhan, 430074 P.R. China,
e-mail: nirvana_wz@sina.com

Dmitry A. Zimnyakov, Division of Optics, Department of Physics, Saratov State University, Saratov, 410026; Precision Mechanics and Control Institute of the Russian Academy of Sciences, Saratov, 410028 Russian Federation,
e-mail: zimnykov@sgu.ru

This page intentionally left blank

Preface

This book is about laser and coherent-domain methods designed for biomedical diagnostics, environmental monitoring and materials inspection. The appearance of the book was stimulated by a recent rapid progress in novel photonics technologies, on the basis of diode lasers, broadband femtosecond lasers (Ti:Sapphire or Cr:Försterite), light-emitting diodes (LEDs), and Superluminescence diodes (SLDs). Such technologies are applicable in many fields, in particular for biomedical, environmental and material diagnostics and monitoring. The main reason which has prompted me to edit the book is my many years co-chairing of the Conference on Coherent-Domain Optical Methods in Biomedical Science and Clinical Applications (SPIE Photonics West Symposia, San Jose, USA) together with Joseph Izatt and James Fujimoto and intensive work of my research group in collaboration with many leading research groups all over the world in the field of coherent optics of scattering objects in application to biomedicine and material inspection, and therefore, understanding that I can invite world-known experts to write the book.

The problem of light interaction with scattering media, including biological tissues, is of great interest for medicine, environmental studies and industry, and therefore is often discussed in monographic literature. Last ten years a number of books, handbooks, and tutorials were published (see, for example [1-15]). The present book is genetically linked with the mentioned literature. However, the book has some important specific features making it different from other books. In particular, for the first time in one book a variety of coherent-domain optical methods are discussed in the framework of various applications, which are characterized by a strong light scattering. A reader has an opportunity to learn fundamentals of light interaction with random media and to get an overview on basic research

containing the update results on coherent and polarization properties of light scattered by random media, including tissues and blood, on speckles formation in multiple scattering media and other non-destructive interactions of coherent light with rough surfaces and tissues, which allow a reader to understand principles of coherent diagnostics techniques presented in many other chapters of the book.

The book is divided in five parts entitled as Part 1: *Speckle and Polarization Technologies* (Chapters 1-5), Part 2: *Holography, Interferometry, Heterodyning* (Chapters 6-8), Part 3: *Light Scattering Methods* (Chapters 9-12), Part 4: *Optical Coherence Tomography* (Chapters 13-19), and Part 5: Microscopy (Chapters 20-22). The first volume of the book is comprised of first three parts (Chapters 1-12) and the second volume – of two other parts (Chapters 13-22). In the book recent the most prospective methods of coherent and polarization optical imaging, tomography, and spectroscopy, including polarization-sensitive optical coherent tomography, polarization diffusion wave spectroscopy, and elastic and quasi-elastic light scattering spectroscopy and imaging are presented. The holography, interferometry and optical heterodyning techniques in application to diagnostics of turbid materials are also discussed. Eleven chapters describe various aspects of optical coherence tomography (OCT) – very new and growing field of coherent optics, thus this is a good addition and updating of recent *Handbook of Optical Coherence Tomography* [13]. Reader will find two chapters on laser scanning confocal microscopy, which is characterized by recent extraordinary results on *in vivo* imaging. Raman and multiphoton microscopies as tools for tissues and various materials inspection are also analyzed in the book.

This book represents a valuable contribution by well-known experts in the field of coherent-domain light scattering technologies for diagnostics of random media and biological tissues. The contributors are drawn from Russia, USA, UK, the Netherlands, Ukraine, Austria, China, Denmark, and Switzerland.

Chapter 1 describes the approaches to multiply scattering media characterization on the basis of correlation and polarization analysis of scattered radiation, including fundamentals of diffusing-wave and polarization spectroscopies, results of basic research on speckle and polarization phenomena, industrial and biomedical applications of the speckle-correlation and polarization diagnostic techniques in the framework of their universality.

New feasibilities for optical correlation diagnostics of rough surfaces with various distributions of irregularities are considered in Chapter 2. In this chapter the possibilities for optical diagnostics of fractal surface structures are shown and the set of statistical and dimensional parameters of the scattered fields for surface roughness diagnostics is determined, a number of laser instruments for roughness inspection are described.

The Stokes-polarimetric method effective for diagnostics and imaging of phase-inhomogeneous objects and providing a high signal-to-noise ratio is presented in Chapter 3. In this chapter the 2-D polarization tomography of biological tissue architectonics and advantages of polarization-correlation and wavelet analyses of tissue orientation tomograms are discussed.

Chapter 4 describes the diffusing wave spectroscopy (DWS) methodology and its application to non-invasive quantitative monitoring of blood microcirculation important for diabetes studies, pharmacological intervention for failing surgical skin flaps or replants, assess burn depth, diagnose atherosclerotic disease, and investigation mechanisms of photodynamic therapy at cancer treatment.

In Chapter 5 authors introduce a laser speckle imaging method for dynamic, high-resolution monitoring of cerebral blood flow (CBF) which is crucial for studying the normal and pathophysiologic conditions of brain metabolism. By illuminating the cortex with laser light and imaging the resulting speckle pattern, relative CBF images with tens of microns spatial and millisecond temporal resolution were obtained.

Chapter 6 reviews wide-field coherence-gated imaging techniques for application through turbid media such as biological tissue, beginning with different approaches to coherence-gated imaging and then focusing on low coherence photorefractive holography. Fundamentals and optical schemes of photorefractive holography – a powerful coherent technique for material science and biological tissues – are described.

In Chapter 7 fundamentals and basic research on laser interferometry of random phase (light scattering) objects are discussed. Such discussion includes the random phase screen model as a basic model for describing of a spatially-modulated laser beam transportation through thin tissue layers or turbid thin films, results on collimated and focused spatially-modulated laser beams propagation in a scattering media, a novel spatially-resolved technique for a random object inspection, the interference methods of surface roughness measurements, and methods of retinal visual acuity determination at cataract and monitoring of scattering properties of blood during sedimentation and aggregation of erythrocytes.

In Chapter 8 authors give an overview of principles and techniques of optical heterodyne detection characterized by phase-sensitive measurements of light fields with a high signal-to-noise ratio and a large dynamic range and present basic applications such as OCT, OCM and CDOCT. Then authors analyze coherent light fields in multiple scattering media, demonstrate Wigner phase-space measurements in different modifications, and finally characterize a Gaussian-Schell beam, an enhanced-backscattered field and a single speckle, using the true Wigner functions.

Chapter 9 reviews light scattering spectroscopic techniques in which coherent effects are critical because they define the structure of the spectrum, in particular, in the case of elastic light scattering the targets

themselves, such as aerosol particles in environmental science or cells and sub-cellular organelles in biomedical applications, play the role of microscopic optical resonators; in the case of Raman spectroscopy, the spectrum is created due to light scattering from vibrations in molecules or optical phonons in solids. This chapter shows that light scattering spectroscopic techniques, both elastic and inelastic, are emerging as very useful tools in material and environmental science and in biomedicine.

Principles of speckle and Doppler measurements are considered in Chapter 10. Authors discuss the basic physics of speckle-microscopy, analyze the output characteristics of dynamic speckle-microscope for measurements of parameters of biological flows, provide *in vivo* measurements of velocity of blood and lymph flows in microvessels using speckle-microscopic and cross-correlation techniques, and show the difficulties of the absolute velocity measurements.

In Chapter 11 the possibility to diagnose ocular and systemic diseases through the eye is demonstrated. The recent progress of quasi-elastic light scattering (QELS) from a laboratory technique routinely used in the characterization of macromolecular dispersions to novel QELS instrumentation which has become compact, more sensitive, flexible, and easy to use. These developments have made QELS an important tool in ophthalmic research where diseases can be detected early and non-invasively before the clinical symptoms appear.

The Monte Carlo simulation program developed for modeling of light scattering in turbid media is described in Chapter 12. Such description includes various options for light transport and scattering, reflection and refraction at boundaries, light sources and detection, also some special features, like laser Doppler velocimetry, photoacoustics and frequency-modulation scattering.

The audience at which this book will be aimed are researchers, postgraduate and undergraduate students, laser engineers, biomedical engineers and physicians who are interested in designing and applications of laser and coherent optical methods and instruments for medical, material and environmental science, medicine and industry. Because of large amount of fundamental and basic research on coherent light interactions with inhomogeneous media presented in the book it should be useful for a broad audience including students and physicians. Investigators who are strongly involved in the field will find the update results in any direction discussed in the book. Physicians and biomedical engineers can be interested in clinical applications of designed techniques and instruments, which are described in a few chapters. Laser engineers could be interested in the book, because their acquaintance with new fields of laser applications can stimulate the new ideas of laser designing.

REFERENCES

1. E.P. Zege, A.P. Ivanov, and I.L. Katsev, *Image Transfer through a Scattering Medium* (Springer-Verlag, New York, 1991).
2. *Medical Optical Tomography: Functional Imaging and Monitoring* **IS11,** G. Müller, B. Chance, R. Alfano *et al.* eds. (SPIE Press, Bellingham, 1993).
3. A. Katzir, *Lasers and Optical Fibers in Medicine* (Academic Press, Inc., San Diego *et al.,* 1993).
4. D.H. Sliney and S.L. Trokel, *Medical Lasers and their Safe Use* (Academic Press, Inc., New York, *et al.* 1993).
5. *Laser–Induced Interstitial Thermotherapy,* G. Müller and A. Roggan eds. (SPIE Press, Bellingham, 1995).
6. *Optical–Thermal Response of Laser–Irradiated Tissue,* A.J. Welch and M.J.C. van Gemert eds. (Plenum Press, New York, 1995).
7. H. Niemz, *Laser-Tissue Interactions. Fundamentals and Applications* (Springer, Berlin *et al.* 1996).
8. O.V. Angelsky, S.G. Hanson, and P.P. Maksimyak, *Use of Optical Correlation Techniques for Characterizing Scattering Objects and Media* (SPIE Press, Bellingham, 1999).
9. V.V. Tuchin, *Tissue Optics: Light Scattering Methods and Instruments for Medical Diagnosis,* SPIE Tutorial Texts in Optical Engineering **TT38** (SPIE Press, Bellingham, 2000).
10. *Light Scattering by Nonspherical Particles,* M. I. Mishchenko, J. W. Hovenier, and L. D. Travis eds. (Academic, San Diego, 2000).
11. M.I. Mishchenko, L.D. Travis, A.A. Lacis, *Scattering, Absorption, and Emission of Light by Small Particles* (Cambridge Univ., Cambridge, 2002).
12. *Handbook of Optical Biomedical Diagnostics* **PM107,** V.V. Tuchin ed. (SPIE Press, Bellingham, 2002).
13. *Handbook of Optical Coherence Tomography,* B.E. Bouma and G.J. Tearney eds. (Marcel Dekker, New York, 2002).
14. *Lasers in Medicine,* D.R. Vij and K. Mahesh ed. (Kluwer Academic Publishers, Boston, Dordrecht, and London, 2002).
15. *Biomedical Photonics Handbook,* Tuan Vo-Dinh ed. (CRC Press, Boca Raton, 2003).

Valery V. Tuchin

Saratov, Russia

This page intentionally left blank

Acknowledgments

I greatly appreciate the cooperation and contribution of all authors of the book, who have done a great work on preparation of their chapters.

I would like to thank all those authors and publishers who freely granted permissions to reproduce their copyright works.

I am, grateful to Prof. D. R. Vij for his initiative in writing of this book and to Michael Hackett for his valuable suggestions and help on preparation of the manuscript.

It should be mentioned that this volume presents results of international collaboration and exchange of ideas between all research groups participating in the book project, in particular such collaboration of authors of Chapters 4 and 5 was supported by grant REC-006 of CRDF (U.S. Civilian Research and Development Foundation for the Independent States of the Former Soviet Union) and the Russian Ministry of Education; the Royal Society grant for a joint project between Cranfield University and Saratov State University; and grants of National Nature Science Foundation of China (NSFC).

I greatly appreciate the cooperation, contribution, and support of all my colleagues from Optics Division of Physics Department of Saratov State University.

Last, but not least, I express my gratitude to my wife, Natalia, and all my family, especially to daughter Nastya and grandkids Dasha, Zhenya, and Stepa, for their indispensable support, understanding, and patience during my writing and editing the book.

This page intentionally left blank

Part I:
SPECKLE AND POLARIZATION TECHNOLOGIES

This page intentionally left blank

Chapter 1

LIGHT CORRELATION AND POLARIZATION IN MULTIPLY SCATTERING MEDIA: INDUSTRIAL AND BIOMEDICAL APPLICATIONS

Dmitry A. Zimnyakov
Saratov State University, Saratov, 410012 Russian Federation

Abstract: This chapter describes the approaches to multiply scattering media characterization on the basis of correlation and polarization analysis of scattered probe radiation.

Key words: light scattering, correlation, polarization, random media

1.1 INTRODUCTION: INTERFERENCE AND POLARIZATION PHENOMENA AT MULTIPLE SCATTERING

This chapter is dedicated to the consideration of some important phenomena appearing as a result of the interaction of coherent light with optically dense disordered media. The situation when a coherent light propagating significant distances in a random medium scatters numerous times and finally loosing information about its initial propagating direction but nevertheless preserving its coherence in certain conditions is not obvious. However, there are a number of classical examples of coherence persisting despite multiple scattering by the random media. These examples are the existence of temporal, spatial, and angular correlations of the multiply scattered light revealing the information on the microscopic dynamic and structure properties of the scattering system. It should be noted that the abundance of theoretical and experimental papers related with

different manifestations of coherence in multiple scattering have been published during the last two decades, beginning from the classical works of Golubentsev [1], Stephen [2], John [3], etc. It is impossible to cite all of these works here and we will briefly review only the common aspects of coherence of light in multiple scattering that are important from the viewpoint of gaining a better understanding of the optics of condensed media and of practical applications in industrial and medical diagnostics. Statistical (correlation) properties of the multiply scattered light and methods of studying the optically dense disordered and weakly ordered systems by means of correlation spectroscopy are considered in this chapter. Also, we analyze some fundamental relations between correlation and polarization characteristics of the multiply scattered coherent light that can be interpreted as the existence of similarity in multiple scattering.

Among these phenomena the decay of polarization of multiply scattered light is one of the most important features of the radiative transfer in random media related to the vector nature of electromagnetic waves running through a scattering system. From the physical picture, it can be expected that the specific relaxation scale characterizing the rate of suppression of initial polarization of light propagating in a multiply scattering medium will be closely related to other relaxation scales which characterize an increase of uncertainty of other fundamental parameters of electromagnetic radiation. The obvious way is to establish the relations between the polarization relaxation parameters, which can be introduced as the characteristic spatial scales of decay of the polarization characteristics chosen to describe the scattered field [4-6], and relaxation parameter that characterizes the spatial scale in which the almost total loss of information about initial direction of light propagation occurs. In terms of the radiative transfer theory the latter parameter is defined as the mean transport free path (MTFP, [7]). The relations between the MTFP and the polarization decay parameters are controlled by the individual properties of each scattering medium and consequently, the given scattering system can be specified with the adequate reliability by measurements of the polarization decay rate for given scattering and detection conditions. Thus, the introduction of the additional polarization measurement channels in the systems traditionally used for optical diagnostics and visualization of optically dense scattering media provides a novel quality and spreads the functional ability of these systems.

The object of particular interest is the appearance of polarization effects in the case of stochastic interference of electromagnetic waves traversing random media. One of the most familiar examples of such appearance is the polarization dependence of temporal correlations of the electric field fluctuations induced by multiple scattering of coherent light by non-

stationary media. These phenomena indicate the vector character of electromagnetic radiation propagating in random media.

In this chapter, the correlation and polarization properties of multiply scattered light are considered from the viewpoint of their application for optical diagnostics of scattering systems with complex structure such as the biological tissue.

1.2 TEMPORAL AND ANGULAR CORRELATIONS OF LIGHT SCATTERED BY DISORDERED MEDIA

The existence of finite spatial and temporal correlation scales for amplitude and intensity fluctuations of coherent light propagating in optically dense random media is the direct manifestation of the coherence property of light multiply scattered by disordered and weakly ordered media. If coherent light is scattered by non-stationary disordered medium, then the statistical properties of a scattered field can be characterized by simultaneous analysis of the correlation of the complex amplitude values for two spatially separated observation points and for different moments of time. In this way, the spatial-temporal correlation function of scattered-field fluctuations is introduced as follows [8,9]:

$$G_1(\bar{r}_1, t_1, \bar{r}_2, t_2) = \langle E_1 E_2^* \rangle = \langle E(\bar{r}_1, t_1) E^*(\bar{r}_2, t_2) \rangle, \tag{1}$$

where the symbol * denotes complex conjugation. For many cases, the spatial-temporal fluctuations of scattered-field amplitude can be considered as the stationary random fields; this leads to the following form of the field correlation function:

$$G_1(\bar{r}_1, t_1, \bar{r}_2, t_2) = G_1(\bar{r}_1, \bar{r}_2, t_1 - t_2) = G_1(\bar{r}_1, \bar{r}_2, \tau). \tag{2}$$

In the similar manner, the spatial-temporal correlation function of scattered light intensity fluctuations can be introduced:

$$G_2(\bar{r}_1, \bar{r}_2, \tau) = \langle I_1 I_2 \rangle = \langle I(\bar{r}_1, t) I(\bar{r}_2, t + \Delta\tau) \rangle. \tag{3}$$

Moreover, for statistically homogeneous speckle patterns, the field and intensity correlation functions depend only on $\Delta\bar{r} = \bar{r}_2 - \bar{r}_1$:

$$G_1(\bar{r}_1,\bar{r}_2,\tau)=G_1(\Delta\bar{r},\tau);\ G_2(\bar{r}_1,\bar{r}_2,\tau)=G_2(\Delta\bar{r},\tau). \tag{4}$$

If a scattered optical field is characterized by the Gaussian statistics of complex amplitude that has zero mean value, then the normalized correlation functions of amplitude and intensity fluctuations:

$$g_1(\Delta\bar{r},\tau)=\langle E_1E_2^*\rangle\Big/\Big(\big\langle|E_1|^2\big\rangle\big\langle|E_2|^2\big\rangle\Big)^{1/2},$$

$$g_2(\Delta\bar{r},\tau)=\langle I_1I_2\rangle/\langle I_1\rangle\langle I_2\rangle$$

are related with each other as follows (the well-known Siegert relation) [8,9]:

$$g_2(\Delta\bar{r},\tau)=1+\beta\left|g_2(\Delta\bar{r},\tau)\right|^2, \tag{5}$$

where the factor β depends on the detection conditions and is equal to 1 under ideal circumstances.

Let us analyze only the temporal fluctuations of a multiple scattered coherent light in a fixed detection point. For simplicity, the scalar wave approach is frequently used to describe the statistics of a multiple scattered coherent light. It should be noted that, despite the obvious physical restrictions of this approach, it provides adequately valid results for the vast majority of scattering systems, provided appropriate scattering and detection conditions are chosen. Moreover, the scalar wave formalism can be appropriately modified to describe the propagation of polarized light in disordered media.

Propagation of coherent electromagnetic wave in random media can be considered as a sequence of statistically independent scattering events, taking place in the moment t at positions $\bar{r}_1(t)$, $\bar{r}_2(t)$,.... . Each scattering event is characterized by the wavevector $\bar{k}_i$. We will follow the physical picture first outlined by G. Maret and P. Wolf [10]. The scattered field interferes with itself but at time $t+\tau$. In this analysis we neglect the time delay of light propagation; correspondingly, we neglect displacements of scatterers during this propagation time.

In this case, each partial contribution to the scattered field is considered as the result of sequence of n scattering events:

$$E_k(t)=\exp(j\omega t)\prod_{i=1}^{N_k}E_i\exp\left(-j\bar{q}_i\bar{r}_i(t)\right), \tag{6}$$

and the total scattered field in the detection point is expressed as follows:

$$E(t)=\sum_k E_k(t).$$

In further analysis, the *single-path* correlation function of field fluctuations is introduced as

$$G_1^k(\tau)=\left\langle E_k(t)E_k^*(t+\tau)\right\rangle \approx exp(-j\omega\tau)\left\langle \prod_{i=1}^{N_k}|a_i|^2\, exp\{j\bar{q}_i\Delta\bar{r}_i(\tau)\}\right\rangle \approx$$

$$\approx exp(-j\omega\tau)\left\langle |a_i|^2\right\rangle exp\left\{-\left\langle \bar{q}^2\right\rangle\left\langle \Delta\bar{r}^2(\tau)\right\rangle N_k/6\right\} \quad .$$

For the discussed case, the mean value of $\bar{q}^2$ estimated for a sequence of scattering events can be expressed as:

$$\left\langle \bar{q}^2\right\rangle = 2k^2 l/l^* \ ,$$

where l is the scattering mean free path and l^* is the mean transport free path for the scattering medium [7]. The number of scattering events for each partial contribution can be expressed as: $N_k \approx s_k / l$, where s_k is the corresponding propagation path for k-th partial component inside a scattering medium. Thus, the single-path correlation function has the following form:

$$G_1^k(\tau)\approx \exp(-j\omega\tau)\left\langle |a|^2\right\rangle \exp\left\{-k^2\left\langle \Delta\bar{r}^2(\tau)\right\rangle s_k/3l^*\right\}. \qquad (7)$$

The total temporal correlation function of field fluctuations in the detection point can be obtained by the statistical summation of the single-path correlation functions over the ensemble of partial contributions:

$$G_1(\tau)\approx \sum_k P(k)G_1^k(\tau),$$

where $P(k)$ are the statistical weights characterizing contributions of partial components to formation of a scattered field in a detection point. This expression may be modified for multiple scattering systems characterized by the continuous distribution of optical paths s by integration over the range of all possible values of s :

$$G_1(\tau) \approx \int_0^\infty \exp\left(-\frac{k^2 \left\langle \Delta\bar{r}^2(\tau) \right\rangle s}{3l^*}\right) \tilde{\rho}(s) ds, \tag{8}$$

where $\tilde{\rho}(s)$ is the probability density of optical paths of scattered partial waves and the following normalization condition takes place:

$$\int_0^\infty \tilde{\rho}(s) ds = \langle I \rangle .$$

The normalized temporal correlation function can be introduced as

$$g_1(\tau) = \int_0^\infty \exp\left(-k^2 \left\langle \Delta\bar{r}^2(\tau) \right\rangle s / 3l^*\right) \rho(s) ds \tag{9}$$

by using the following normalization condition:

$$\rho(s) = \tilde{\rho}(s) \Big/ \int_0^\infty \tilde{\rho}(s) ds .$$

In particular, for Brownian scattering systems the argument of exponential kernel in the right-hand side of equation 9 has the well-known form:

$$2\pi s / \tau_0 l^* ,$$

where τ_0 is the so-called single-scattering correlation time defined as:

$$\tau_0 = \left(4\pi^2 D / \lambda^2\right)^{-1} = \left(k^2 D\right)^{-1},$$

where D is the diffusion coefficient of scattering sites and λ is the wavelength of the probe light.

Thus, analysis of the time-dependent correlation decay of the scattered light fluctuations allows us the characterization of non-stationary multiple scattering media through the reconstruction of the path length distribution function dependent on optical properties and geometry of the probed medium or through the reconstruction of the time-dependent variance of

scattering sites' displacements. The diagnostic approaches based on this principle will be discussed in section 1.4.

The existence of long-range spatial or angular correlations, a fundamental property of optical fields multiply scattered by random media, can be considered in terms of "angular memory" effect (Feng *et al.,* Ref. [11]). The possibility to use this effect as the physical basis for tomographic imaging of optically dense disordered media was discussed in Ref. [12]. The relations between angular correlations of multiply scattered coherent light and optical properties of scattering media for the transmittance mode of light propagation were studied theoretically and experimentally by Hoover with co-workers [13]. In this study, the potentiality to use the angular correlation analysis for disordered scattering media characterization was investigated. Also, an original approach to this problem, considered in Ref. [14] (see chapter 7), is based on the influence of angular correlation decay on an interference of optical fields induced by two illuminating coherent beams incoming in the scattering medium at different angles of incidence. In this case, the probed medium is illuminated by a spatially modulated laser beam formed by overlapping the two collimated beams. The spatial modulation of the resulting illuminating beam has the form of a regular interference pattern with the fringe spacing determined by the angle between the overlapping beams. In the absence of scattering, the angular spectra of incident beams have the δ-like forms; the appearance of scattering causes the broadening of these angular spectra and decay in the interference pattern contrast of the outgoing spatially modulated beam. Analysis of the interference pattern contrast for the outgoing beam and its dependence on the distance between the scatter and the observation plane and interference fringe period allows one to characterize the scattering properties of the probed medium.

1.3 DAMPING OF POLARIZATION OF LIGHT PROPAGATING THROUGH THE DISORDERED MEDIA

The relations between statistical properties of the path length distributions for partial waves propagating in random media, and statistical properties of multiply scattered vector optical fields manifest themselves in a number of theoretically predicted and experimentally observed effects [1–3,15–20], one of those is appearance of the similarity in multiple scattering. A group of relaxation phenomena in the case of coherent light propagation in the disordered systems can be considered as manifestations of the similarity in multiple scattering. This similarity is related to the same forms of dependences of certain statistical moments of scattered optical fields on the specific spatial scales which characterize the decay of the corresponding

moments in the course of the coherent light propagation in the disordered media. The following relaxation effects can be considered [21–23]:

- the existence of temporal correlations of amplitude and intensity fluctuations of scattered optical fields in the fixed detection point for non-stationary systems of scattering particles;
- the decay of polarization of light propagating in the disordered systems;
- the manifestation of Bougier's law in the case of multiple scattering with noticeable absorption.

The relaxation of the statistical moments of the scattered optical fields can be considered in terms of the path length distributions, i.e., by statistical analysis of ensembles of optical paths for partial waves, which propagate in the scattering medium and from which the observed scattered field can be constructed. For diffusion scattering mode, each partial component of the multiply scattered optical field is associated with a sequence of a great number N of statistically independent scattering events and is characterized by the path s. The statistical moments of scattered field can be considered as the integral transforms of the probability density function $\rho(s)$. In the weak scattering limit, when $l, l^* >> \lambda$, such second-order statistical moments as the average intensity of scattered light, the temporal correlation function of the field fluctuations and the degree of polarization of multiply scattered light in the arbitrarily chosen detection point can be expressed in the case of $N = s / l >> 1$ as the Laplace transforms of $\rho(s)$. In particular, the average intensity of the scattered light for multiply scattering medium with non-zero absorption can be written using the modified Bougier's law:

$$\langle I \rangle \cong \int_0^\infty \exp(-\mu_a s)\rho(s)ds = \int_0^\infty \exp(-s/l_a)\rho(s)ds, \qquad (10)$$

where the averaging is carried out over all possible configurations of the scattering sites. The normalization condition can be written in the following form:

$$\int_0^\infty \rho(s)\,ds = \langle I \rangle_0, \qquad (11)$$

where $\langle I \rangle_0$ is the average intensity in the absence of absorption.

For non-stationary disordered media consisting of moving scattering particles the normalized temporal autocorrelation function of the scattered field fluctuations is expressed as [10,24,25]:

$$g_1(\tau) \approx \frac{\int_0^{\infty} exp[-B(\tau)s/l]\,\rho(s)\,ds}{\int_0^{\infty} \rho(s)\,ds}, \tag{11}$$

where $B(\tau)$ is determined by the variance of the displacements of the scattering sites for the time delay τ. As considered above, in the particular case of Brownian systems the exponential kernel of the integral transform equation 11 is equal to $\exp(-2\tau s/\tau_0 l^*)$.

The relaxation of the initial polarization state of the coherent light propagating in the disordered multiply scattering medium is caused by the energy flux interchange between partial waves with different polarization states. In particular, for initial linear polarization of the propagating light linearly "co-polarized" and "cross-polarized" partial components of the scattered field can be considered; the first of them is characterized by the same direction of polarization azimuth as the incident illuminating beam and the other one - by the orthogonal direction, respectively. In a similar way the interrelation between the left circularly polarized component and right circularly polarized component can be analyzed if the illuminating light with the initial circular polarization is used. Propagation of linearly polarized light in a strongly scattering disordered medium can be considered with the use of a solution of the Bethe-Salpeter equation for the case of transfer of a linearly polarized partial, "single-path" contribution, which undergoes n scattering events in a disordered medium with isotropic scattering [17]. This consideration leads to the following expressions for intensities of the "single-path" cross-polarized and co-polarized components [5]:

$$\begin{aligned} I_{II}^s &= f_{II}^s(n) I^s(n), \\ I_{\perp}^s &= f_{\perp}^s(n) I^s(n), \end{aligned} \tag{12}$$

where the single-path "scalar" intensity $I^s(n)$ can be obtained by evaluating the photon density for a scalar wave propagating at the distance corresponding to n scattering events and the weighting functions $f_{II}^s(n), f_{\perp}^s(n)$ can be determined in the dependence on the number of scattering events as [5,17]:

$$f_{II}^{s}(n)=\left[\left(\frac{10}{15}\right)^{n-1}+2\left(\frac{7}{15}\right)^{n-1}\right]\Big/3,$$

$$f_{II}^{s}(n)=\left[\left(\frac{10}{15}\right)^{n-1}-\left(\frac{7}{15}\right)^{n-1}\right]\Big/3.$$

Thus, introducing a value of the polarization degree for the arbitrary single-path contribution of a scattered optical field with a propagation path equal to $s \approx nl$ as $P^{s}(n)=\left[I_{II}^{s}(n)-I_{\perp}^{s}(n)\right]/\left[I_{II}^{s}(n)+I_{\perp}^{s}(n)\right]$, we can obtain the following:

$$P^{s}(n)=\frac{f_{II}(n)-f_{\perp}(n)}{f_{II}(n)+f_{\perp}(n)}=\frac{3\left(\frac{7}{15}\right)^{n-1}}{2\left(\frac{10}{15}\right)^{n-1}+\left(\frac{7}{15}\right)^{n-1}}=$$

$$=3\left[2\exp\left\{(n-1)\ln\frac{10}{7}\right\}+1\right]^{-1}.$$

Correspondingly, the single-path polarization degree $P^{s}(n)$ for linearly polarized light obeys the exponential decay $P^{s}(n)\cong 1.5\exp\{(n-1)/n'\}$ with the decay parameter equal to $n_{L}' \approx 2.804$ for long propagation distances with a great number of scattering events $n >> 1$.

If a multiple scattering disordered medium is illuminated by circularly polarized light, then the single-path degree of circular polarization of multiple scattered light can be introduced as the ratio $P_{C}^{s}(n)=\left[I_{+}(n)-I_{-}(n)\right]/\left[I_{+}(n)+I_{-}(n)\right]$, where $I_{+}(n), I_{-}(n)$ are the intensities of circularly polarized partial contributions which undergo n scattering events and have the same helicity as an incident circularly polarized light (+) and the opposite helicity (-). Similar considerations for the case of multiple scattering of circularly polarized light also lead to the exponential decay of the single-path degree of circular polarization with the value of the decay parameter equal to $n_{C}' \approx \ln 2 \approx n_{L}'/2$ [5].

If polarized light propagates in the disordered medium characterized by the sufficiently non-zero value of the anisotropy parameter g (the case of anisotropic scattering) then the decay parameter $n_{L,C}'$ should be replaced by the effective value $\tilde{n}_{L,C}'$ determined by optical properties of scattering particles, which form a scattering system. Introducing the depolarization length $\xi_{L,C}=\tilde{n}_{L,C}'l$ as one of the dimension scales which characterize the

scattering system, we can find the relation between $\xi_{L,C}$ and another important scale – the mean transport free path l^*. This relation is strongly influenced by the optical properties of the scattering medium as well as by the illumination and detection conditions.

The degree of residual polarization of a scattered optical field in the arbitrarily chosen detection point can be determined by averaging the single-path polarization degree over the ensemble of partial components of a scattered optical field characterized by the path length density distribution $\rho(s)$:

$$P_{L,C} = \int_0^\infty P_{L,C}^s(s)\rho(s)ds \approx \frac{3}{2}\int_0^\infty \exp\left(-\frac{s}{\xi_{L,C}}\right)\rho(s)ds\,, \tag{13}$$

where the probability density function $\rho(s)$ is determined by the conditions of light propagation in a scattering medium between a source of polarized light and a detection system which allows the polarization discrimination of scattered light.

Theoretically predicted exponential decay of the single-path polarization degree with the increasing path length s was directly observed in the experiments with time-resolved intensity measurements for co-polarized and cross-polarized components of a backscattered light in the case of optically dense media illumination by a short pulse of linearly polarized laser light [26]. In these experiments the colloidal systems with volume fractions ranging from 5% to 54% and consisting of aqueous suspensions of 1-μm-diameter silica spheres with an ionic strength of 0.03 m/L $NaNO_3$ and pH = 9.5. Scattering samples were probed by laser pulses with a duration of 150 fs emitted by a dispersion-compensated, self-mode-locked Ti:sapphire laser pumped by a frequency-doubled Nd:YAG laser. The backscattered light pulses were analyzed with the use of a background-free cross-correlation technique. The Ti:sapphire laser, which had a repetition frequency of 76 MHz, was tuned to a wavelength of 800 nm, and its output was split into two beams by a 50:50 beam splitter. One beam passed through a delay stage and served as the gating pulse in the cross correlator. Data runs were typically recorded with a 3-mm (20-fs) step size. The other beam passed through a mechanical chopper, a second beam splitter, and a 15-cm-focal-length converging lens to a sample placed at the focus of the beam. The estimated value of the photon density corresponding to a single pulse of probe light was found equal to 5.3×10^{13} cm^{-2} /pulse.

The degree of polarization of the backscattered light was determined by use of a half-wave plate and a Glan-Tompson polarizer. Typical shapes of

the detected pulses for co-polarized and cross-polarized components of the backscattered light from two scattering samples with strongly differing values of the scattering coefficient are illustrated by Figure 1. The inset illustrates the tendencies in decay of the time-dependent degree of linear polarization of the backscattered light.

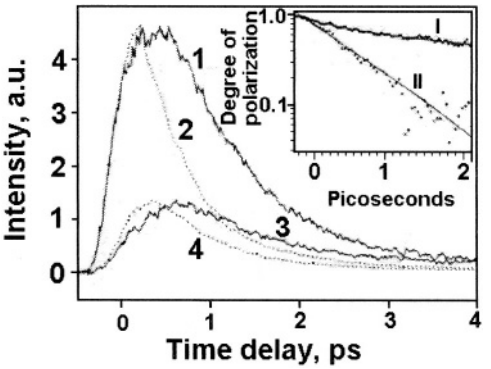

Figure 1. The pulse shapes for co-polarized and cross-polarized components of backscattered light. Solid lines – the scattering sample with 5% volume concentration of silica spheres; dotted lines – the scattering sample with 25% volume concentration of silica spheres. 1, 2 – intensity of the co-polarized component; 3, 4 – intensity of the cross-polarized component. Inset shows the evolution of the time-dependent degree of linear polarization of backscattered light for both samples (I – 5% volume concentration of the scattering sites; II – 25% concentration of the scattering sites) [26].

The analysis of obtained experimental results allows for the single-path degree of linear polarization to be expressed in the simple exponential form $P_L^s(n) \approx \exp(-n/n_L')$, where n_L' is regarded as the average number of scattering events needed to depolarize the optical wave. For an effective speed of light, v_{eff}, and the mean elastic scattering free path l, the time scale of the depolarization process can be estimated to be of the order of $\tau = n_L' l / v_{eff}$.

Also, the validity of the exponential decay model for the description of dissipation of the initial polarization state of light propagating in multiple scattering random media was confirmed by experimental studies of the depolarizing properties of optically thick random media with the slab geometry, which were probed in the transmittance mode [5,21,22]. Being calculated with the use of the diffusion approximation, the path length density distributions $\rho(s)$ for optically thick slabs in the transmittance mode are characterized by the single-sided Laplace transformation:

$$L_\rho(m) = \int_0^\infty \exp\left(-s/ml^*\right)\rho(s)ds\,,$$

which, analyzed for the fixed value of m, exponentially decays with the increasing dimensionless slab thickness L/l^*. This tendency is illustrated by Figure 2.

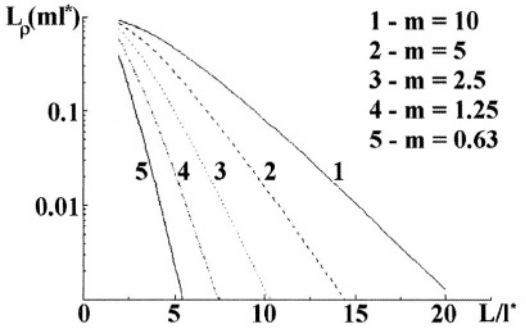

Figure 2. The Laplace transformations of the path length density distributions for probe light, which is transmitted through a scattering slab as depending on the normalized slab thickness [21,22]. The probability density functions $\rho(s)$ were calculated with the use of the diffusion approximation.

The above discussed exponential decay of the "single-path" degree of polarization should lead to the approximately exponential decay of the degree of polarization of light transmitted through optically thick slab ($L/l^* \geq 5$) with the increasing ratio L/l^*. Indeed, the dependences of the degree of polarization for linearly or circularly polarized light transmitted through the optically dense scattering slabs on the dimensionless slab thickness, which were obtained in the experiments with mono-disperse aqueous suspensions of polystyrene beads of various sizes, evidently show that $P_{L,C}$ falls as:

$$P_{L,C} \sim \exp\left(-KL/l^*\right)$$

with K depending on the size of scattering particles and the type of polarization of the incident light (Figure 3).

The principle of similarity in multiple scattering following from the exponential form of the "single-path" parameters of multiply scattered optical fields such as the "single-path" degree of polarization and the "single-path" temporal correlation function of scattered field fluctuations in the case of non-stationary scattering media is manifested as the equality of spatial scales which characterize the decay rate for corresponding parameter.

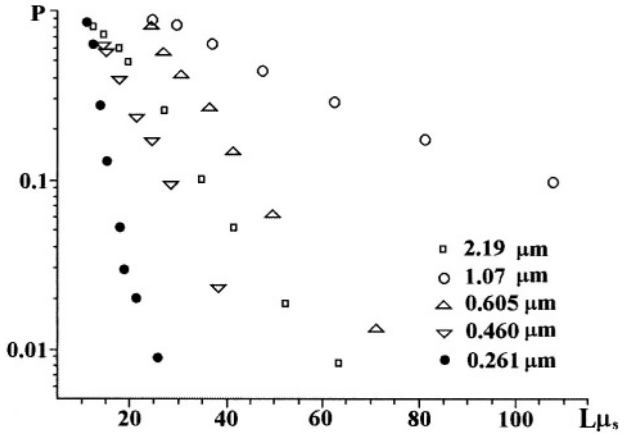

Figure 3. The measured values of the degree of linear polarization of light transmitted through the scattering slabs [21]. Scattering systems are the aqueous suspensions of polystyrene beads of various sizes. The values of the degree of polarization are plotted against the dimensionless scattering coefficient of corresponding scattering system. The used wavelength and cuvette thickness: 514 nm (Ar-ion laser) and 10 mm - for 0.460 μm and 1.07 μm particles; 532 nm (diode-pumped Nd-laser) and 20 mm – for 0.261 μm, 0.605 μm, and 2.19 μm particles.

In particular, such equality allows the specific parameter for non-stationary scattering media such as the characteristic correlation time [27,28] to be introduced. This parameter establishes the relation between the characteristic spatial scale of dissipation of optical field correlation due to multiple scattering in fluctuating random medium, the depolarization length, and the dynamic properties of Brownian scattering medium and can be written as follows:

$$\tau_{cd} \approx \frac{l^*}{2\xi_L D k_0^2},$$

where ξ_L is the depolarization length for linearly polarized radiation in scattering medium, D is the translation diffusion coefficient of scattering particles, and k_0 is the wave-number of probe light.

It is easy to conclude that the characteristic correlation time is independent on the concentration of scattering sites but is determined only by their optical and dynamic properties and thus can be considered as the universal parameter of multiple scattering dynamic media. Figure 4 illustrates the principle of evaluation of τ_{cd} with the use of results of simultaneous measurements of the temporal correlation function and the degree of polarization of multiply scattered light.

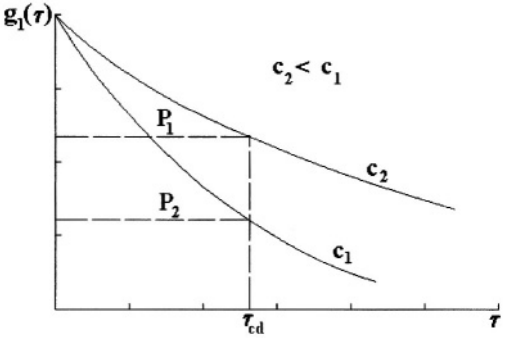

Figure 4. The method for determining the characteristic correlation time for multiply scattering Brownian medium.

The experiments with the aqueous suspensions of polystyrene spheres irradiated by linearly polarized light from Ar-ion laser evidently demonstrate the independence of the characteristic correlation time on the volume fraction of scattering particles (Figure 5). The values of τ_{cd} were determined by the method illustrated in Figure 4. Normalized values of module of the field correlation functions were obtained from experimentally measured intensity correlation functions by using the Siegert relation. Moreover, measurements of the "conventional" correlation time as the half-width of the normalized field correlation functions were performed. Figure 5 shows a logarithmic plot of the experimentally measured concentration dependences of τ_{cd} and $\Delta\tau_{0.5}$ ("conventional" correlation time estimated as the halfwidth of the correlation peak).

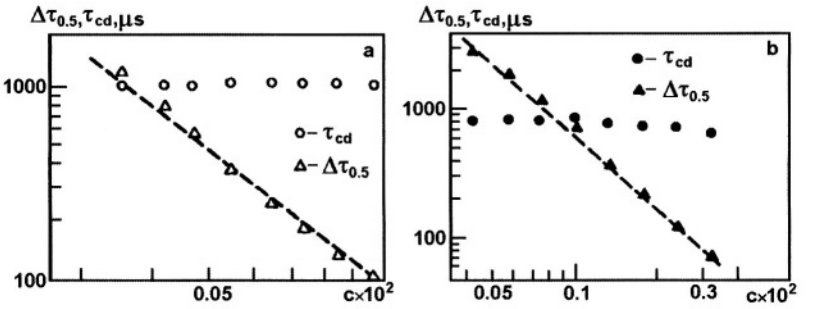

Figure 5. Concentration dependences of the characteristic correlation time and the half-width of the autocorrelation function of intensity fluctuations for aqueous suspensions of polystyrene beads (left - bead diameter 0.46 μm; right - bead diameter 1.07 μm) [27].

Analysis of the experimental data shows that in the experimental range of concentrations of the aqueous suspensions of polystyrene beads the concentration dependences $\Delta\tau_{0.5} = \varphi(c)$ are close to power-law functions $\Delta\tau_{0.5} \sim c^{-\alpha}$. The exponents α in the power-law functions approximating the experimental values of $\Delta\tau_{0.5}$ in Figure 5 are $\approx$ 2.21 and $\approx$ 1.96 for polystyrene beads of diameters 0.46 and 1.07 μm, respectively. These values are in satisfactory agreement with the value α = 2 given by the diffusion approach. Specifically, as was mentioned in Ref. [3], for an optically thick layer of thickness L consisting of Brownian scattering particles the normalized autocorrelation function of the amplitude fluctuations of the scattered coherent radiation allows the following approximation:

$$g_1(\tau) \approx \exp\left(-\sqrt{6\tau/\tau_0}\,\frac{L}{l^*}\right).$$

Thus, analysis of polarized light transfer on the basis of principle of similarity gives the additional possibilities for the description of scattering properties of probed media. In particular, the influence of the size parameter of scattering sites on the decay of polarization of propagated light can be studied with this approach, as it was shown in Ref. [27].

The consideration of influence of the size parameter of scattering centers on decay of the initial polarization state of coherent light backscattered by random media was pioneered by MacKintosh *et al.* [19]. On the basis of measurements of the intensity of backscattered light corresponding to opposite polarization channels (co-polarized and cross-polarized light in the case of linearly polarized probe light and components of scattered light with the opposite helicity in the case of circularly polarized light) they concluded

that backscattering of the linearly polarized light from random medium consisting of the large-sized dielectric particles (Mie scattering regime) is accompanied by the significant suppression of polarization of outgoing multiple scattered light (i.e., the backscattered light is almost totally depolarized). On the contrary, backscattering by random media consisting of the small-sized dielectric particles (Rayleigh scattering regime) is characterized by the significant degree of polarization of backscattered light. If the circularly polarized light is used to probe the scattering media in the backscattering mode, then scattering ensembles consisting of the small-sized particles are characterized by close values of the intensity of backscattered light in polarization channels with the opposite helicity. In contrast, the backscattering of circularly polarized light by media with the expressed scattering anisotropy exhibits a high degree of polarization memory, which is manifested as the noticeable difference between the values of intensity for helicity-preserving polarization channel and polarization channel with the opposite helicity: $\langle I_{+} \rangle / \langle I_{-} \rangle = 1.40$ for scattering system with $l^{*} = 10l$ [19].

The Monte Carlo simulation was used to analyze the influence of the size parameter of scattering dielectric spheres on the decay of linear polarization in the backscattering mode [29]. In the procedure followed, a transformation of the complex amplitude of partial waves, which form a backscattered optical field due to random sequences of scattering events, was simulated (Figure 6). Each partial wave was induced by an incident linearly polarized monochromatic plane wave propagating along the z-axis of the "fundamental" coordinate system (x,y,z). The electric field of an incident wave was directed along the x-axis. A scattering medium was considered as the disordered ensemble of non-absorbing dielectric particles with a given value of the size parameter. The relative refractive index of spheres was taken to be 1.2; this value is approximately equal to the refractive index for polystyrene beads in water. The direction of propagation of the incident linearly polarized plane monochromatic wave relative to the "fundamental" coordinate system was characterized by the normalized wave-vector:

$$\bar{k}_0 / \left| \bar{k}_0 \right| = (0,0,1),$$

where the z-axis was oriented normal to the scattering medium surface.

Transformation of the electric field of the propagating partial wave was analyzed for a sequence of n scattering events. For each i-th step, transformation of the complex amplitude for both orthogonally polarized components of the propagating wave was described by a (2×2) scattering matrix:

$$(S_{km}(\theta,\phi,i)) = (S''_{km}(\theta,i)) \times (S'_{km}(\phi,i)).$$

The complex elements of the scattering matrix were calculated for simulated random values of the scattering angle θ and azimuth angle ϕ by use of the current coordinates $(\tilde{x}_i, \tilde{y}_i, \tilde{z}_i)$ related to the i-th scattering event.

The $\tilde{z}_i$-axis is directed along the wavevector of the partial wave propagating after the i-th scattering event and the $\tilde{x}_i$-axis is directed normal to the scattering plane. The scattering angle distribution that corresponds to the Mie phase function for single scatter with a given value of the size parameter was used for simulation of the random value of θ for each scattering event. Random values of the azimuth angle ϕ were considered to be uniformly distributed within the range $(0,2\pi)$. The $(S'_{km}(\phi,i))$ matrix characterizes transformation of the $\tilde{x}$ and $\tilde{y}$ components of the electric field of the partial wave, which propagates after the $(i-1)$th scattering event, due to rotation by the angle ϕ during conversion of the $(\tilde{x}_{i-1}, \tilde{y}_{i-1}, \tilde{z}_{i-1})$ current coordinates to the $(\tilde{x}_i, \tilde{y}_i, \tilde{z}_i)$ ones (see Figure 6):

$$\left(E_{\tilde{x}}(i-1), E_{\tilde{y}}(i-1) \Rightarrow E'_{\tilde{x}}(i-1), E'_{\tilde{y}}(i-1)\right).$$

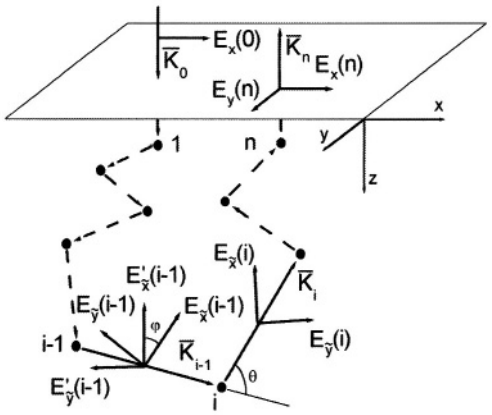

Figure 6. The scheme of transformation of polarization state of partial wave due to the random sequence of scattering events (Monte-Carlo simulation) [29].

During the simulation only the n-times scattered partial waves, which were characterized by a z component of the normalized wavevector with values between – 0.985 and –1 (relative to the "fundamental" coordinates),

were selected for further analysis. The magnitudes $I_x = |E_x|^2$ and $I_y = |E_y|^2$ were evaluated by calculating the x and y components of the electric field in the "fundamental" coordinates for each selected n-times scattered outgoing partial wave. After this, values $\langle I_{II} \rangle = \langle I_x \rangle$ and $\langle I_\perp \rangle = \langle I_y \rangle$ were calculated by averaging over the whole ensemble of the selected partial waves with:

$$-1 \le k_{zn} \Big/ \left|\hat{k}_n\right| \le -0.985$$

and a single-path value of P_L^s for a given number of scattering events was obtained as:

$$P_L^s = \left(\langle I_{II} \rangle - \langle I_\perp \rangle\right) \Big/ \left(\langle I_{II} \rangle + \langle I_\perp \rangle\right).$$

Figure 7 illustrates the typical dependences of the degree of single-path linear polarization on the number of scattering events as a result of the simulation procedure described above for two different scattering regimes [the Rayleigh scattering regime for small values of the anisotropy parameter, Figure 7(a), and the Mie scattering regime for large values of g, Figure 7(b)].

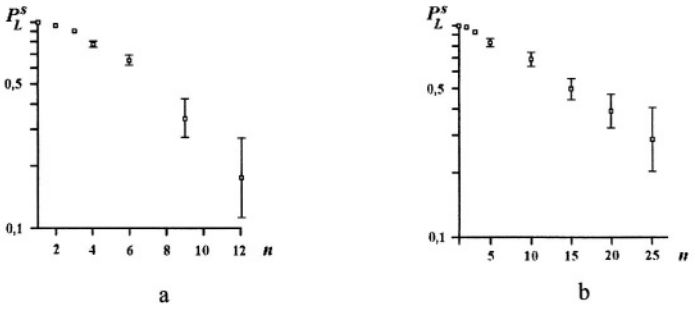

Figure 7. The dependences of the "single-path" degree of residual linear polarization in the backscattering mode on the number of scattering events (results of Monte-Carlo simulation). (a) – isotropic scattering ($ka = 1$, $g \approx 0.178$); (b) – anisotropic scattering ($ka = 6.5$, $g \approx 0.915$).

For a given number of scattering events, values of $\langle I_{II} \rangle, \langle I_\perp \rangle$ and $P_L^s(n)$ were calculated for a simulated scattering system, which was characterized by a given value of the size parameter, by averaging over the ensemble of

10,000 outgoing partial waves; after this, the obtained values of the single-path residual polarization were plotted in semi-logarithmic coordinates against the number of scattering events n. Bars show an increase in the deviation of the obtained $P_L^s(n)$ values with respect to the mean value of the single-path residual polarization with an increase in the number of scattering events. The value of the anisotropy parameter for each simulated scattering system was calculated as the mean cosine of the scattering angle by using Mie theory.

Typically, all curves obtained by the simulation procedure are characterized by the presence of two specific regions: a relatively small "low-step scattering" region with values of the single-path polarization degree which are close to 1, and a "diffusion scattering" region characterized by an approximately exponential decay of the single-path polarization degree $P_L^s(n)$. The location of the overlap between these regions, as well as the polarization decay rate for the diffusion scattering region, strongly depends on the anisotropy parameter of the scattering particles.

Values of the normalized depolarization length m_L, which were estimated as $m_L = (1-g)\overline{n}_L'$ by using the exponential approximation $P_L^s \propto \exp(-n/\overline{n}_L')$, are presented in Figure 8 by full circles as depending on the anisotropy parameter.

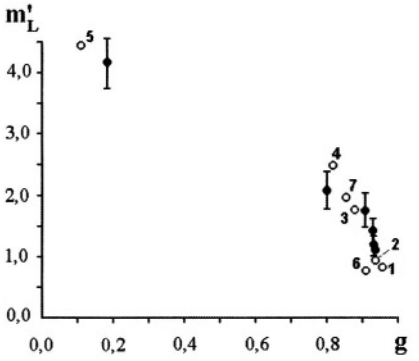

Figure 8. The normalized depolarization length for linearly polarized light in the backscattering mode versus the parameter of scattering anisotropy: full circles – results of Monte Carlo simulation; open circles – experimental data; 1 – 1.07 μm polystyrene beads in water, volume fraction is 10%, λ = 3 mm, λ = 488 nm; 2 – the same as 1, but λ = 633 nm; 3 – teflon, L = 30 mm, λ = 488 nm; 4 – the same as 3, but λ = 633 nm; 5 – 0.091 μm polystyrene beads in water, volume fraction is 5 %, λ = 488 nm [19]; 6 – 0.605 μm polystyrene beads in water, volume fraction is 2 %, λ = 488 nm [19]; 7 – 0.46 μm polystyrene beads in water, volume fraction is 10%, L = 3 mm, λ = 515 nm [30].

In order to obtain the dependence of the normalized depolarization length on g, the dependences of the single-path residual polarization on n, which are similar to those presented in Figure 8, were obtained by use of the above described Monte Carlo procedure for scattering systems characterized by given values of the size parameter and, correspondingly, the anisotropy parameter. After this, values of $\overline{n}_L'$ were determined versus g by evaluation of the slope of the corresponding dependences $\ln P_L^s = f(n)$ for the "diffusion scattering" region.

For small scatterers (the Rayleigh scattering regime), the value of m_L was obtained approximately equal to 4.2. This magnitude diverges from the above presented theoretical value $m_L \approx \overline{n}_L' \approx 2.8$ [5] by approximately 35%. With an increase in the anisotropy parameter up to values of the order of 0.6–0.8, m_L decreases insignificantly; for larger values of g the decay rate becomes large and m_L falls to values of the order of 1.0–1.2 in the vicinity of the first Mie resonance ($ka \approx 8, g \approx 0.93$).

In the case of "forward-scattering" mode (i.e., when the simulated partial waves are selected using the condition:

$$0.985 \le k_{zn} \Big/ \left|\hat{k}_n\right| \le 1)$$

the dependences of the single-path polarization degree on the number of scattering events obtained by Monte-Carlo simulation for the Rayleigh scattering system are similar to those obtained for backscattering mode (Figure 9).

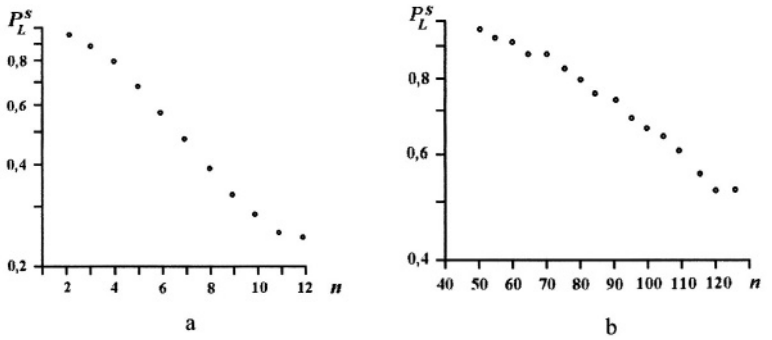

Figure 9. The dependences of the "single-path" degree of residual linear polarization in the forward scattering mode on the number of scattering events (results of Monte Carlo simulation). a – isotropic scattering ($ka = 1$, $g \approx 0.178$); b – anisotropic scattering ($ka = 6.5$, $g \approx 0.915$) [29].

Thus, it can be concluded that the estimates of the depolarization length for linearly polarized light in the case of scattering systems characterized by $ka << 1$ are insensitive to the regime of scattered light collection. On the contrary, the depolarization length for linearly polarized light estimated under similar condition for the forward scattering system consisting of large-sized particles significantly exceeds the value of the mean transport free path (Figure 9). The results of experimental studies of the polarization decay in the case of forward scattering of linearly polarized light by optically thick disordered layers of dielectric spheres [5,21], give the depolarization length ξ_L increasing with an increase in the size parameter ka of scattering sites.

For multiple scattering systems consisting of the optically soft dielectric spheres (e.g., aqueous suspensions of polystyrene spheres) the maximal value of ξ_L in the forward scattering mode was found in the vicinity of the first Mie resonance [5]. Theoretical analysis of the polarization decay for linearly polarized light multiply scattered in the forward direction by disordered media [31,32] also shows the better preservation of linear polarization of the forward scattered light in the case of random media with the expressed scattering anisotropy.

Being compared with the phantom scattering media, the propagation of polarized light in tissue is characterized by some features related to the rate of polarization dissipation. These features were studied by Jacques *et al.* [33–36], Sankaran *et al.* [37-39], L. Wang, J. Schmitt, and many other researchers (see, e.g., Refs. [40]-[42]) in experiments with various *in vivo* and *in vitro* tissues such as the human skin, the porcine adipose tissue, the whole blood, etc.

The difference between the values of the depolarization length for linearly or circularly polarized light estimated in the experiments with tissue layers and corresponding parameters of phantom scattering media (for instance, the aqueous suspensions of polystyrene beads) with the same optical properties (the mean transport free path and the parameter of scattering anisotropy) as the examined tissue samples can be considered as the main peculiarity of polarization decay in biological tissues. Figure 10 shows the values of the degree of linear and circular polarization for light transmitted through the porcine adipose layer in the dependence of the layer thickness.

As in the case of the phantom monodisperse scattering systems consisting of dielectric spheres of equal size, the dependencies of P_L and P_C (the degree of circular polarization) on the thickness of tissue layer demonstrates the presence of two characteristic regions: the region of non-diffuse scattering in the case of optically thin ($L \le l^*$) tissue samples, which is characterized by slow decay of the initial polarization, and the region in which the abrupt decrease of the degree of polarization takes place with the

increasing thickness of tissue layer. It is necessary to note that the decay rates for linear and circular polarization in the latter case are characterized by the close values and appear significantly smaller in comparison with scattering phantoms with the similar optical properties. In any case, in present time the peculiarities of the polarized light transfer in real tissues at cellular and subcellular levels of spatial scales are still far from complete understanding and thus require further theoretical and experimental investigations.

1.4 INDUSTRIAL AND BIOMEDICAL APPLICATIONS

Correlation analysis of temporal fluctuations of light propagated in optically dense weakly absorbing non-stationary media carried out in order to study the dynamic properties of the scattering system is the basis for a set of applied methods usually termed as *correlation spectroscopy,* or *diffusing-wave spectroscopy* (DWS). It is necessary to note that similar information about the scattering media can be obtained by using spectral analysis of the intensity fluctuations of multiply scattered dynamic speckles, but in the case of optically dense media characterized by a strong extinction of the probe light and very broad spectra of the speckle intensity fluctuations the DWS methods are more preferable because of the more developed instrumentation for the analysis of the detected intensity fluctuations (photon-counting, digital correlators, etc.).

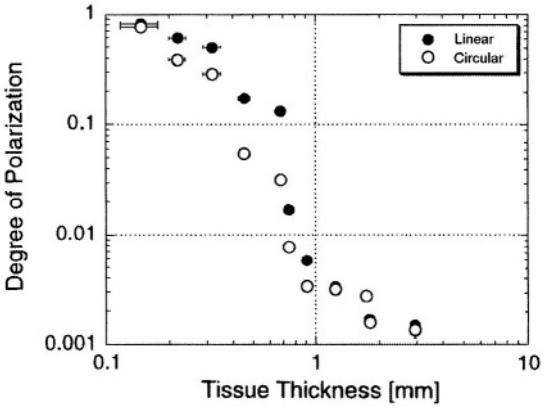

Figure 10. The degree of linear and circular polarization in sections of porcine adipose tissue as a function of tissue thickness [39].

A typical scheme for a DWS experiment is illustrated by Figure 11. Light emitted by a single-mode laser propagates through a multiply scattering dynamic medium (sample). As a result of superposition of the partial components of the scattered light, a random non-stationary interference pattern appears, which is associated with the spatial-temporal fluctuations of the scattered optical field. This interference pattern, or *dynamic speckle pattern,* contains the information about the dynamic properties of the scattering system. Part of the scattered light is selected by the collimator (collimating system can consist of two pinhole diaphragms, as in Figure 11) and falls onto the photosensitive area of photodetector.

Figure 11. Typical scheme of DWS experiment with use of the transmitted light detection.

The photomultiplier tube (PMT) operating in photon counting mode is usually necessary to obtain sufficient sensitivity to optically dense media. In this case, the output PMT signal is a random sequence of the amplified electron pulses which is then processed by a digital correlator. Commercially available digital correlators allow for analysis of temporal fluctuations of the scattered light with a bandwidth on the order of a hundred MHz, or, correspondingly, with a temporal resolution of 10 ns.

In order to perform the analysis at shorter time scales, different approaches are necessary. A good example of such an approach is the application of interferometers in order to induce the light beatings by mixing of the two identical optical signals with a controlled phase delay in one of channels of the interferometer (see, e.g., Ref. [43]). The principles of such *diffusing wave interferometry* are illustrated in Figure 12. This scheme, as applied to the analysis of the dynamics of multiply scattering media such as aqueous suspensions of polystyrene beads, enables a temporal resolution on the order of 1 ns, which is comparable with the time scale of hydrodynamic interactions for the scattering particles [44]. In this case, the time lag τ is determined by the optical path difference between two arms of the optical interferometer. The sample is illuminated by the single-mode laser beam just as in the case of conventional DWS experiments. The major difference is that the output dynamic speckle field, $E(t)$, is collected, collimated and directed into a Michelson interferometer. If the lengths of arms are equal,

respectively, to L_1 and L_2, then after the recombination the beams will be delayed by $\tau = 2(L_1 - L_2)/c$. If the intensities of both beams are equal to each other, then the intensity of light detected by PMT can be written as:

$$I(\tau) = \frac{1}{4}\left\langle |E(t)|^2 \right\rangle \left\{ 1 + \left[\left\langle E^*(t+\tau)E(t) \right\rangle \Big/ \left\langle |E(t)|^2 \right\rangle \right] \cos \omega\tau \right\}, \qquad (14)$$

where ω is the angular frequency of the probe light. The envelope multiplying the oscillating term is usually considered the visibility of the observed interference pattern. At the same time, this is the temporal correlation function of the scattered light evaluated for the given value of τ. Thus, analyzing the decay of the envelope with an increase of τ due to changing the position of mirror M_2, one can reconstruct the form of the normalized field correlation function for the required range of time scales.

Modification of the original DWS technique with a selection of partial contributions of the scattered optical field, characterized by the given value of the path length s, has been developed by D. Boas *et al.* [45]. This method is based on the usage of a low-coherence interferometer in order to discriminate the short-path and long-path components of the scattered field. The corresponding instrumentation is shown in Figure 13. In this case, the cut-on and cut-off values of the effective optical paths are determined by the optical path difference between two arms of the low-coherence interferometer as well as by the spectral bandwidth and the central wavelength of the light source. In this system, the single-mode fiber optic interferometer is illuminated with an 850-nm superluminescent diode (SLD). Interferometer adjustment is provided by changing the position of the retroreflector in the reference arm. Focusing lenses in the sample and reference arms of the interferometer are mounted on computer-controlled stages in order to provide the possibility of exact matching of the optical paths in both arms. It can be concluded that, in the case of probing Brownian multiply scattering media, the detected ac signal is characterized by the single-path temporal correlation function which has the typical exponential form:

$$G_1^s(\tau) \sim exp(-K\tau), \qquad (15)$$

and corresponding spectral density is the Lorentzian one.

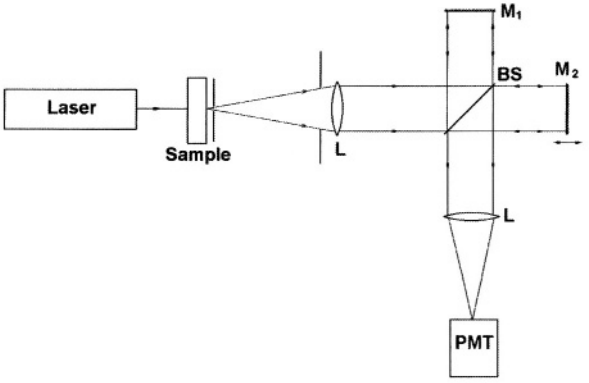

Figure 12. Optical scheme of the diffusing-wave interferometer for correlation analysis of scattered light with small time scales (Ref. [43]).

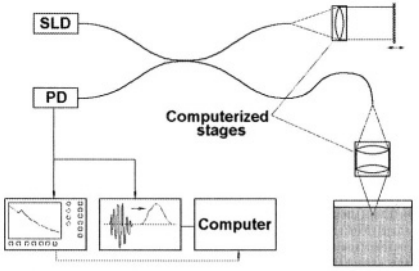

Figure 13. Schematic of the dynamic low-coherence interferometer system (Ref. [45]).

The value of K in the discussed case should strongly depend on scattering conditions: in the case of small sample depths (i.e., small path lengths), which are of the order of transport mean free path for scattering medium, only single- and low-order-scattered components of the diffuse retroreflected light will be selected by the low-coherence interferometer. In this case the single-path temporal correlation function has the typical "single-scattering" form and the parameter K which is related with the Lorentzian linewidth of the detected light beatings does not depend on the sample depth. But with increasing path length, when it becomes significantly larger than l^*, light beatings will be induced by the contributions that are scattered many times. In this case, the single-path temporal correlation function has the typical "multiple-scattering" form:

$$G_1^s(\tau) \sim exp\left[-\frac{2\tau s_{sel}(\Delta z)}{\tau_0 l^*}\right]. \tag{16}$$

Thus, dependence of the selected value s_{sel} of the path length of partial components, which induce the light beatings, on the sample depth Δz leads to the increase of the spectral width of the detected signal, when Δz increases. Such a physical picture is in qualitative agreement with experimental results obtained with a two-layer scattering system [45]. The first 580-μm-thick layer consists of 1.20 μm polystyrene (PS) beads (0.5% volume fraction) separated from the second layer (4% suspension of 0.22 μm PS beads) by a 150-μm-thick glass cover. Volume fractions for both layers were chosen to provide a mean scattering length equal to ≈ 100 μm. Due to anisotropic scattering in the first layer (mean cosine of the scattering angle is approximately equal to 0.89 at 830 nm), its thickness is less than the transport mean free path (≈ 1000 μm) and, consequently, single-scattered contributions strongly dominate in the formation of the detected light beating signal. On the contrary, the second layer, consisting of smaller particles, is characterized by a significantly smaller value of the anisotropy parameter ($g \approx 0.267$) and $l^* \approx 140$ μm for this scattering medium. Thus, if the sample depth exceeds this value, transition from the single- to the multiple-scattering mode of the formation for the detected optical signal takes place and the spectral width of the observed light beatings becomes dependent on the sample depth. In this experiment, such a transition was observed when the beam waist in the sample was embedded into the second layer at depths larger than 300 μm.

The effective approach in the diffusing-wave spectroscopy of non-stationary turbid media is the analysis of correlation transport viewed as a propagation of a correlation "wave" outwards from sources and its scattering by macroscopic inhomogeneities associated with spatial variations of dynamical or optical properties. It should be noted that evolution of the spatial-temporal correlation function of the optical field fluctuations due to the light propagation in free space has been analyzed in early works of E. Wolf. Later, it has been shown by Ackerson *et al.* [46] that certain analogies exist between the transport of correlation in disordered scattering media and transport of photons which can be described by the well-known radiative transport equation. The main feature of correlation transport relates with the accumulation of the decay of correlation function caused by each scattering event during the propagation of the correlation wave in the scattering system. In this case, considering the "stationary correlation transport" through the scattering medium (steady state) probed by continuous-wave

source, one can modify the radiative transfer equation in its usual form in order to obtain the corresponding correlation transport equation:

$$\begin{aligned}&\nabla G_1(\bar{r},\tilde{\Omega},\tau)+\mu_t G_1(\bar{r},\tilde{\Omega},\tau)=\\&=\mu_s\int G_1(\bar{r},\tilde{\Omega}',\tau)g_1^{\,s}f(\tilde{\Omega},\tilde{\Omega}')\,d\tilde{\Omega}'+S(\bar{r},\tilde{\Omega})\end{aligned}. \tag{17}$$

The temporal correlation function of the scattered field fluctuations $G_1(\bar{r},\tilde{\Omega},\tau)$ depends on the detection point position ($\bar{r}$) and direction in turbid medium ($\tilde{\Omega}$) chosen for correlation analysis; $\mu_t=\mu_s+\mu_a$. The term:

$$g_1'(\tau)=\exp\left(-\frac{1}{6}q^2\left\langle\Delta\bar{r}^2(\tau)\right\rangle\right),$$

which corresponds to single scattering, describes the accumulation of correlation decay due to sequences of scattering events; $f(\tilde{\Omega},\tilde{\Omega}')$ is the phase function of the scattering medium and $S(\bar{r},\tilde{\Omega})$ is the light source distribution.

In the case of validity of the standard diffusion approximation, the stationary correlation transport equation 17 can be rewritten in the following form [47]:

$$\left(D_\gamma\nabla^2-c\mu_a-\frac{1}{3}c\mu_s'k_0^{\,2}\left\langle\Delta\bar{r}^2(\tau)\right\rangle\right)G_1(\bar{r},\tau)=-cS(\bar{r}), \tag{18}$$

where $D_\gamma=cl^*/3$ is the photon diffusion coefficient, c is the light speed in the scattering medium and μ_s' is the reduced scattering coefficient. It should be noted that the term:

$$\frac{1}{3}v\mu_s'k_o^{\,2}\left\langle\Delta\bar{r}^2(\tau)\right\rangle$$

describes additional losses of correlation due to dynamic scattering in disordered media and can be interpreted as “correlation absorption” caused by the dynamic processes.

The presence of any kind of scattering medium dynamics is manifested as the appearance of the additional “absorbance” term in the correlation

diffusion equation. Thus, numerical solution of this equation for given source and detector positions with respect to embedded dynamic inhomogeneities can be used as the basis for an inverse problem solution (reconstruction of the inhomogeneity "image"). This technique has been applied by D. Boas *et al.* [48] and was verified in experiments with a multiply scattering "static" object (titanium dioxide-resin cylinder) containing a "dynamic" inhomogeneity (spherical space filled by a water solution of Intralipid). The sample was illuminated by an Ar-ion laser through fiber-optic light-guiding system; scattered light was collected by a single-mode fiber-optic light collector and detected by a photon-counting system. The scattered light intensity fluctuations as random sequences of photo-count pulses were processed by a digital autocorrelator to obtain $G_2(\tau)$ for given illumination and detection conditions. Apart from the geometry of the scattering system, angular scanning of the object was carried out; measurements were made every 30° at the surface of the cylinder with source-detector angular separations of 30° and 170°. Results of the inhomogeneity image reconstruction are shown in Figure 14.

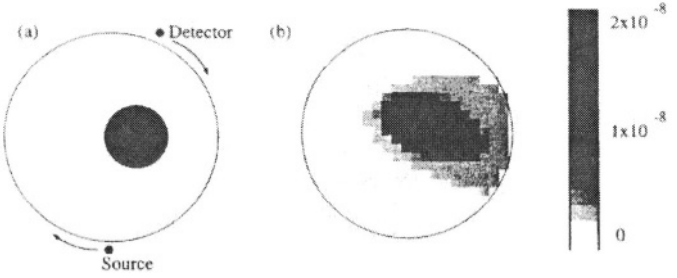

Figure 14. Imaging of the dynamic multiply scattering inhomogeneity embedded in the static scatterer, by means of the correlation diffusion analysis (Ref. [48]). Static scatterer is a 4.6 cm diameter cylinder with $l^* = 0.25$ cm and $\mu_a = 0.002$ cm^{-1}. Dynamic scatterer is a 1.3 cm diameter spherical cavity filled with a colloid with $l^* = 0.25$ cm, $\mu_a = 0.002$ cm^{-1} and $D_B = 1.5\times10^{-8}$ cm^{2}s^{-1}. A slice of the image is presented in (b). The values of the reconstructed particle diffusion coefficient are imaged by using the presented gray-level scale.

A typical example of the potential applications of the DWS technique in medicine is burn depth diagnostics. The main idea of this approach is based on the well-known dependence of the penetration of the light propagation paths on the source-detector separation in the case of backscattering (Figure 15).

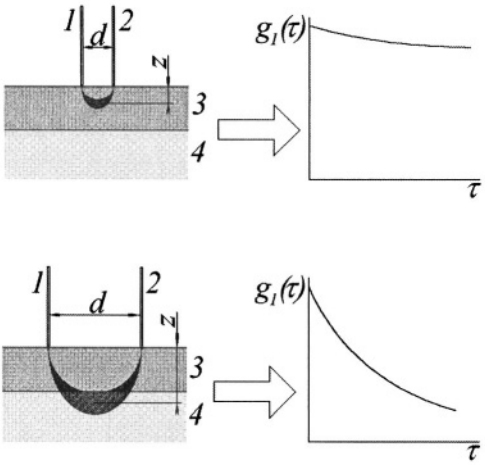

Figure 15. Burn depth diagnostics by means of speckle correlation measurements; 1 - source fiber; 2 - detector fiber; 3 - burned tissue; 4 - normal tissue.

For such a configuration, the regions of maximum density of light paths have a typical "banana-like" shape and the penetration depth for each "banana" can be expressed as [49]:

$$z \approx d / 2\sqrt{2}, \tag{19}$$

where d is the source-detector separation.

When the probe light propagates through the burnt layer, the lack of blood microcirculation means that the scattering is predominantly from stationary scatterers. As a result, there is only a slow decay of the correlation function of scattered light with increasing τ. Thus, in the case of surface burn diagnostics by a pair of closely adjacent light-emitting and light-collecting fibers (as shown in Figure 15) only the upper, necrotic layer of the burnt tissue will be probed and the DWS technique will show a slowly decaying $g_1(\tau)$. But with an increase in the distance between source and detector, the "banana-shaped" region of the maximum concentration of the photon paths will reach the underlying layers of tissue where there is blood flow. This will be manifested as an increase in the slope of the intensity correlation function and, correspondingly, $g_1(\tau)$. This promising possibility of DWS burn depth diagnostics was demonstrated by D. Boas and A. Yodh [50] using the pig burn model suggested by N. Nishioka and K. Schomacker at the Wellman Institute in Boston (Figure 16).

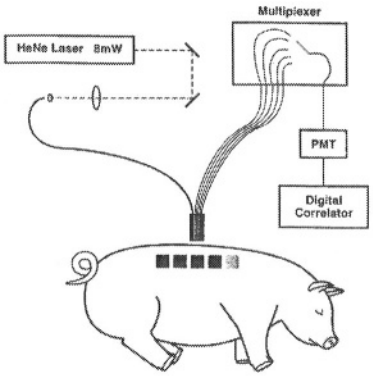

Figure 16. Schematic of the burn depth diagnostics (by Boas *et al,* [50]).

A He-Ne laser with an output power of 8 mW was used as the light source in their experiments. The laser light was coupled into a multi-mode optical fiber with a core diameter of 200 μm. This fiber delivered the probe light to the burn surface being diagnosed; after passing through the layer of burnt tissue, the backscattered laser light was collected by the light collecting system consisting of a single mode fiber assembly: several single mode fibers were positioned at different distances varying from 0.2 mm to 2.4 mm with respect to the source fiber. The light collecting fibers were connected to a photodetector (photon-counting photo-multiplier tube (PMT)) via an electronically controlled fiber-optical switch. The PMT output signal was processed by a digital autocorrelator to obtain the temporal correlation function for a given burn depth and source-detector separation. The burn depth was controlled by applying a hot metal block (100°C) to the surface of a pig skin for a given duration. In this experiment, five different durations of burn with consequently increasing depth (60-100 μm; 400-500 μm; 500-600 μm; 1500-2000 μm and 2100-2200 μm) were used. The strong dependence of the decay rate of the correlation function on the burn depth for a given source-detector separation allows the different grades of tissue burn to be distinguished (Figure 17).

To summarize the data for all source-detector separations and to produce the criteria for burn depth estimations, the following technique was suggested: decay rates of the field correlation functions were determined for $0 < \tau < 100$ μs by fitting a line to the data, and these values of decay rate were plotted against the source-detector separation. The tendencies of the decay rate behavior can be summarized as follows (Figure 18): for shallow burns, the decay rate increases linearly with the source-detector separation as observed for healthy tissue and as would be expected for a homogeneous system, i.e., the shallow burn does not perturb the correlation function.

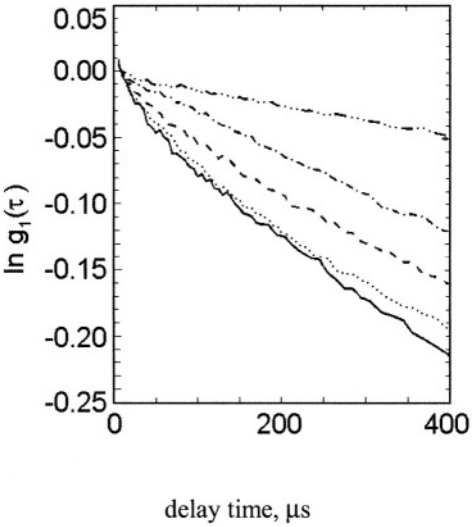

Figure 17. Temporal field correlation functions obtained from 48 hour old burns for a source-detector separation of 800 μm (by Boas *et al.,* taken from Ref. [50]); the correlation functions for burn duration times of 3s (solid line), 5 s (dotted line), 7s (dashed line), 12 s (dot-dash line) and 20 s (dot-dot-dot-dash line) are presented.

On the contrary, for deeper burns, the decay rate is smaller and no longer increases linearly with the source-detector separation. In recent years, the principle of polarization discrimination of multiply scattered light was fruitfully applied by many research groups for morphological analysis and visualization of the subsurface layers in strongly scattering tissues [35,51-57]. One of the most popular approaches to polarization imaging of heterogeneous tissues is based on use of linearly polarized light to irradiate an object (the chosen area of the tissue surface) and rejection of scattered light with the same polarization state (co-polarized radiation) by an imaging system. Typically, such kind of polarization discrimination is simply achieved by use of a polarizer between an imaging lens and the object. The optical axis of the polarizer is oriented perpendicular to the polarization plane of incident light. Thus, only cross-polarized component of scattered light contributes to formation of the object image. Despite its simplicity, this technique was demonstrated to be an adequately effective tool for functional diagnostics and imaging of the subcutaneous tissue layers.

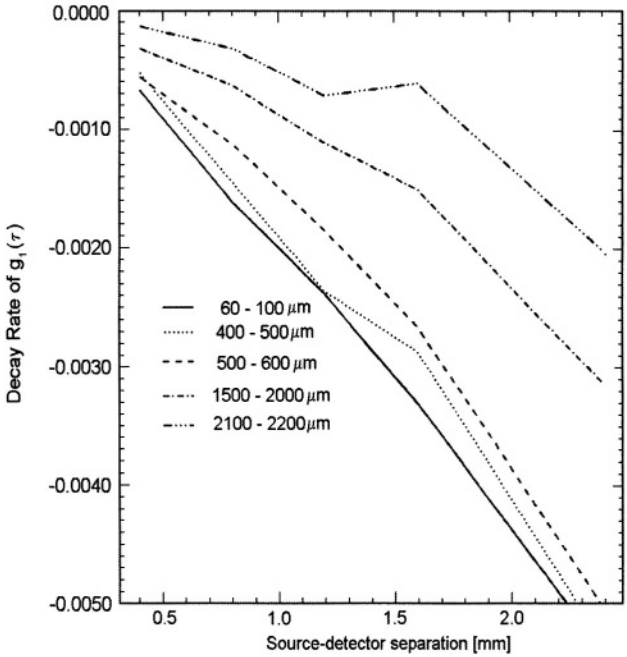

Figure 18. Dependence of the decay rates of the field correlation functions on the source-detector separations for different burn depths.

Moreover, the separate imaging of the object with co-polarized and cross-polarized light allows the separation of structural features of the shallow tissue layers (such as, e.g., the skin wrinkles, papillary net, etc.) and the deep layers (such as the capillaries in derma). Such elegant simplicity of this approach has stimulated its widespread application in laboratory and clinical medical diagnostics.

In the imaging system developed by Demos *et al.* [55], a dye laser with Nd:YAG laser pumping was used as an illumination source. The probe beam diameter is 10 cm and the average intensity was approximately equal to 5mW/cm^2. A cooled CCD camera with a 50 mm focal length lens is used to detect retroreflected light and to capture the image. A first polarizer placed after the beam expander is used to ensure illumination with linearly polarized light. A second polarizer is positioned in front of the CCD camera with its polarization orientation perpendicular or parallel to that of the illumination.

The similar camera system but with the incoherent white light source such as xenon lamp is described in Ref. [36], where the results of a pilot clinical study of various skin pathologies with use of polarized light are presented. The used image processing algorithm is based on evaluation of the degree of polarization $\left(I_{par} - I_{per}\right)/\left(I_{par} + I_{per}\right)$, which is then used as the

imaging parameter. The polarization images of pigmented skin sites (freckle, tattoo, pigmented nevi) and unpigmented skin sites (nonpigmented intradermal nevus, neurofibroma, actinic keratosis, malignant basal cell carcinoma, squamous cell carcinoma, vascular abnormality (venous lake), burn scar) were analyzed to find differences caused by various skin pathologies. Also, the point-spread function of backscattered polarized light was analyzed for images of a shadow cast from a razor blade onto a forearm skin site. This function describes the behavior of the degree of polarization as imaging parameter near the shadow edge. It was found that near the shadow edge, the degree of polarization approximately doubles in value because no I_{per} photons are superficially scattered into the shadow-edge pixels by the shadow region while I_{par} photons are directly backscattered from the superficial layer of these pixels. This result suggests that the point-spread function in skin for cross-talk between pixels of the polarization image has a half-width-half-max of about 390 μm.

The comparative analysis of the polarization images of normal and diseased human skin has shown the ability of the discussed approach to emphasize image contrast on the basis of light scattering in the superficial layers of the skin. The polarization images can visualize the disruption of the normal texture of the papillary and upper reticular layers by skin pathology. The polarization imaging has demonstrated itself as an adequately effective tool for identification of skin cancer margins and guidance of surgical excision of skin cancer.

Various modalities of the polarization imaging were also considered in Ref. [58]. In particular, the polarization-difference imaging technique was demonstrated to improve the detectability of target features that are embedded in scattering media. The improved detectability occurred for both passive imaging in moderately scattering media (<5 optical depths) and active imaging in more highly scattering media. These improvements are relative to what is possible with equivalent polarization-blind, polarization-sum imaging under the same conditions. In this study, the point-spread functions for passive polarization-sum and polarization imaging in single-scattering media were studied analytically, and Monte Carlo simulations were used to study the point-spread functions in single- and moderately multiple-scattering media. The obtained results indicated that the polarization-difference point-spread function can be significantly narrower than the corresponding polarization-sum point-spread function, implying that better images of target features with high-spatial-frequency information can be obtained by using differential polarimetry in scattering media. Although the analysis was performed for passive imaging at moderate optical depths, the results lend insight into experiments that have been performed in more highly scattering media with active imaging methods to help mitigate the effects of multiple scattering.

One of the promising approaches to early cancer diagnostics can be based on analysis of a single scattered component of light perturbed by tissue structure. Wavelength dependence of the intensity of radiation elastically scattered by tissue structure appears sensitive to changes in tissue morphology typical for pre-cancerous lesions. In particular, it was established that specific features of malignant cells such as the increased nuclear size, increased nuclear/cytoplasmic ratio, pleomorphism, etc. [59] are markedly manifested in the elastic light scattering spectra of the probed tissue [60]. A specific fine periodic structure in the wavelength of backscattered light was observed for mucosal tissue [61]. This oscillatory component of light scattering spectra are attributed to single scattering from surface epithelial cell nuclei and can be interpreted within the framework of Mie theory. Analysis of the amplitude and frequency of the fine structure allows one to estimate the density and size distributions of these nuclei. It should be noted, however, that the major problem is related to extraction of the single scattered component from the masking multiple scattering background. Also, absorption of the stroma caused by hemoglobin distorts the single scattering spectrum of the epithelial cells. Both these factors should be carefully taken into account in order to provide an adequate interpretation of the measured spectral dependencies of backscattered light.

The negative effect of the diffuse background and hemoglobin absorption can be significantly reduced by application of the polarization discrimination technique in the form of illumination of the probed tissue with linearly polarized light and separate detection of the elastic scattered light at parallel and perpendicular polarization (i.e., the co-polarized and cross-polarized components of backscattered light) [62,63]. This approach named as polarized elastic light scattering spectroscopy, or polarized reflectance spectroscopy (PRS), can potentially provide a quantitative estimate not only of the size distributions of cell nuclei but also the relative refractive index of the nucleus. These potentialities demonstrated in a series of experimental works with tissue phantoms and *in vivo* epithelial tissues allow one to classify PRS technique as a new step in the development of noninvasive optical devices for real-time diagnostics of tissue morphology and, consequently, for improved early detection of pre-cancers *in vivo.* An important point in further development of PRS method is the design of portable and flexible instrumentation applicable for *in situ* tissue diagnostics. In particular, use of fiber optic probes can “bridge the gap between benchtop studies and clinical applications of polarized reflectance spectroscopy” [64].

1.5 SUMMARY

Thus, the above considered approaches to characterization of strongly scattering media with complicated structure and dynamics exhibit the high sensitivity of the correlation and polarization characteristics of multiply scattered light to structural and dynamical features of probed objects. The relatively simple instrumentation and data processing algorithms necessary to provide the correlation or polarization diagnostics and visualization provide the opportunity for successful implementation of these techniques in industrial and clinical practice.

ACKNOWLEDGEMENT

The work on this chapter was partially supported by: grant N 04-02-16533 of Russian Foundation for Basic Research; grant REC-006/SA-006-00 "Nonlinear Dynamics and Biophysics" of CRDF and the Russian Ministry of Education; the Russian Federation President's grant N 25.2003.2 "Supporting of Scientific Schools" of the Russian Ministry for Industry, Science and Technologies; and grant "Leading Research-Educational Teams" N 2.11.03 of the Russian Ministry of Education.

REFERENCES

1. A.A. Golubentsev, "On the suppression of the interference effects under multiple scattering of light", *Zh. Eksp. Teor. Fiz.* **86**, 47-59 (1984).
2. M.J. Stephen, "Temporal fluctuations in wave propagation in random media", *Phys. Rev.B.* **37**, 1-5 (1988).
3. F.C. MacKintosh and S. John, "Diffusing-wave spectroscopy and multiple scattering of light in correlated random media", *Phys. Rev. B.* **40**, 2382-2406 (1989).
4. D. Bicout and C. Brosseau, "Multiply scattered waves through a spatially random medium: entropy production and depolarization," *J. Physique I* **2**, 2047-2063 (1992).
5. D. Bicout, C. Brosseau, A.S. Martinez and J.M. Schmitt, "Depolarization of multiply scattering waves by spherical diffusers: Influence of size parameter", *Phys. Rev. E* **49**, 1767-1770 (1994).
6. W. C. Brosseau, *Fundamentals of Polarized Light: a Statistical Optics Approach* (Wiley, New York, 1998).
7. A. Ishimaru, Wave Propagation and Scattering in Random Media (Academic, New York, 1978).
8. *Photon Correlation and Light-Beating Spectroscopy,* **3**, *NATO Advanced Study Institute Series B: Physics,* H.Z. Cummins and E.R. Pike eds. (Plenum, New York, 1974).
9. S.M. Rhytov, U.A. Kravtsov, and V.I. Tatarsky, *Introduction to Statistical Radiophysics, P.2. Pandom Fields* (Nauka Publishers, Moscow, 1978).
10. G. Maret and P.E. Wolf, "Multiple light scattering from disordered media. The effect of Brownian motions of scattterers," *Z. Phys. B* **65**, 409-413 (1987).

11. S. Feng, C. Kane, P.A. Lee, and A.D. Stone, "Correlations and fluctuations of coherent wave transmission through disordered media," *Phys. Rev. Lett.* **61**, 834 (1988).
12. R. Berkovits and S. Feng, "Theory of speckle-pattern tomography in multiple-scattering media," *Phys. Rev. Lett.* **65**, 3120 (1990).
13. B.G. Hoover, L. Deslauriers, S.M. Grannell *et al,* "Correlations among angular wave component amplitudes in elastic multiple-scattering random media," *Phys. Rev. E* **65**, 026614-1 (2002).
14. V.V. Tuchin, V.P. Ryabukho, D.A. Zimnyakov *et al.,* "Tissue structure and blood microcirculation monitoring by speckle interferometry and full-field correlometry,"*Proc SPIE* **4251**, 148-155 (2001).
15. S.John and M.Stephen, "Wave propagation and localization in a long-range correlated random potential," *Phys. Rev.B.* **28**, 6358-6380 (1983).
16. S. John, "Electromagnetic absorption in a disordered medium near a photon mobility edge," *Phys. Rev. Lett.* **53**, 2169-2172 (1984).
17. E. Akkermans, P.E. Wolf, R. Maynard, and G. Maret, "Theoretical study of the coherent backscattering of light by disordered media," *J. Phys. France* **49**, 77-98 (1988).
18. M.J. Stephen, G. Cwillich, "Rayleigh scattering and weak localization: effects of polarization,"*Phys. Rev. B* **34**, 7564-7572 (1986).
19. F.C. MacKintosh, J.X. Zhu, D.J. Pine and D.A. Weitz, "Polarization memory of multiply scattered light," *Phys. Rev. B* **40**, 9342 - 9345 (1989).
20. V.L. Kuz'min and V.P. Romanov, "Coherent phenomena in light scattering from disordered systems," *Soviet Phys. Usp.* **166**, 247-277 (1996).
21. D.A. Zimnyakov, "On some manifestations of similarity in multiple scattering of coherent light," *Waves Random Media* **10**, 417–434 (2000).
22. D.A. Zimnyakov, "Effects of similarity in the case of multiple scattering of coherent light: phenomenology and experiments," *Opt, Spectrosc.* **89**, 494-504 (2000).
23. D.A. Zimnyakov, "Coherence phenomena and statistical properties of multiply scattered light" in: *Handbook of Optical Biomedical Diagnostics,* V.V. Tuchin ed. (SPIE Press, Belligham, 2002), 265-310.
24. D.J. Pine, D.A. Weitz, P.M. Chaikin, and E. Herbolzheimer, "Diffusing wave spectroscopy," *Phys. Rev. Lett.* **60**, 1134-1137 (1988).
25. I. Freund, M. Kaveh, and M. Rosenbluh, "Dynamic light scattering: ballistic photons and the breakdown of the photon-diffusion approximation," *Phys. Rev. Lett.* **60**, 1130-1133(1988).
26. A. Dogariu, C. Kutsche, P. Likamwa, G. Boreman, and B. Moudgil, "Time-domain depolarization of waves retroreflected from dense colloidal media," *Opt. Lett.* **22**, 585-587(1997).
27. D.A. Zimnyakov and V.V. Tuchin, "About interrelations of distinctive scales of depolarization and decorrelation of optical fields in multiple scattering," *JETP Lett.* **67**, 455-460(1998).
28. D.A. Zimnyakov, V.V. Tuchin and A.G. Yodh, "Characteristic scales of optical field depolarization and decorrelation for multiple scattering media and tissues," *J. Biomed. Opt.* **4**, 157-163(1999).
29. D.A. Zimnyakov, Yu.P. Sinichkin, P.V. Zakharov, and D.N. Agafonov, "Residual polarization of non-coherently backscattered linearly polarized light: the influence of the anisotropy parameter of the scattering medium," *Waves Random Media* **11**, 395-412 (2001).
30. P. Wolf and G.Maret, "Weak localization and coherent backscattering of photons in disordered media," *Phys.Rev. Lett.* **55**, 2696-2699 (1985).

31. E.E. Gorodnichev, and D.B. Rogozkin, "Small-angle multiple scattering of light in a random medium," *JETP* **80**, 112-126 (1995).
32. E.E. Gorodnichev, A.I. Kuzovlev, and D.B. Rogozkin, "Depolarization of light in small-angle multiple scattering in random media," *Laser Physics* **9**, 1210-1227 (1999).
33. S.L. Jacques, M.R. Ostermeyer, L. Wang, and D. Stephens, "Polarized light transmission through skin using videoreflectometry: Toward optical tomography of superficial tissue layers," *Proc. SPIE* **2671**, 199-210 (1996).
34. S.L. Jacques and K. Lee, "Polarized video imaging of skin," *Proc. SPIE* **3245**, 356-362 (1998).
35. S.L. Jacques, R.J. Roman, and K. Lee, "Imaging superficial tissues with polarized light," *Lasers Surg. Med.* **26**, 119-129 (2000).
36. S.L. Jacques, J.C. Ramella-Roman, and K. Lee, "Imaging skin pathology with polarized light," *J. Biomed. Opt.* **7**, 329-340 (2002).
37. V. Sankaran, M.J. Everett, D.J. Maitland, and J.T. Walsh, "Comparison of polarized light propagation in biologic tissue and phantoms, " *Opt. Lett.* **24**, 1044-1046 (1999).
38. V. Sankaran, J.T. Walsh, and D.J. Maitland, "Polarized light propagation through tissue phantoms containing densely packed scatterers, " *Opt. Lett.* **25**, 239-241 (2000).
39. V. Sankaran, J.T. Walsh, and D.J. Maitland, "Comparative study of polarized light propagation in biologic tissues, *" J. Biomed. Opt.* **7**, 300-306 (2002).
40. A.H. Hielscher, J.R. Mourant, and I.J. Bigio, "Influence of particle size and concentration on the diffuse backscattering of polarized light from tissue phantoms and biological cell suspensions," *Appl. Opt.* **36**, 125-135 (1997).
41. R.C. Studinski and I.A. Vitkin, "Methodology for examining polarized light interactionwith tissues and tissue-like media in the exact backscattering direction," *J. Biomed. Opt.* **5**, 330-337 (2000).
42. G. Jarry, E. Steiner, V. Damaschini, M. Epifanie, M. Jurczak, and R. Kaizer, "Coherence and polarization of light propagating through scattering media and biological tissues," *Appl. Opt.* **37**, 7357-7367 (1998).
43. A.G. Yodh, N. Georgiades, and D.J. Pine, "Diffusing-wave interferometry," *Opt. Commun.* **83**, 56-59 (1991).
44. M.H. Kao, A.G. Yodh, and D.J. Pine, "Observation of Brownian motion on the time scale of hydrodynamic interactions," *Phys. Rev. Lett.* **70**, 242-245 (1993).
45. D.A. Boas, K.K. Bizheva, and A.M. Siegel, "Using dynamic low-coherence interferometry to image Brownian motion within highly scattering media," *Opt. Lett.* **23**, 319-321 (1998).
46. B.J. Ackerson, R.L. Dougherty, N.M. Reguigui, and U. Nobbman, "Correlation transfer: application of radiative transfer solution methods to photon correlation problems," *J. Thermophys. Heat Trans.* **6**, 577-588 (1992).
47. D.A. Boas and A.G. Yodh, "Spatially varying dynamical properties of turbid media probed with diffusing temporal light correlation," *JOSA A* **14**, 192-215 (1997).
48. D.A. Boas, L.E. Campbell, and A.G. Yodh, "Scattering and imaging with diffusing temporal field correlations," *Phys. Rev. Lett.* **75**, 1855-1858 (1995).
49. S. Feng, F. Zeng, and B. Chance, "Monte Carlo simulations of photon migration path distributions in multiple scattering media," *Proc. SPIE* **1888**, 78-89 (1993).
50. D.A. Boas and A.G. Yodh, "Spatially varying dynamical properties of turbid media probed with diffusing temporal light correlation," *JOSA A* **14**, 192-215 (1997).
51. R.R. Anderson, "Polarized light examination and photography of the skin," *Arch. Dermatol.* **127**, 1000-1005 (1991).
52. P.F. Bilden, S.B. Phillips, N. Kollias, J.A. Muccini, and L.A. Drake, "Polarized light photography of acne vulgaris," *J. Invest. Dermatol.* **98**, 606 (1992).

53. S.G. Demos, W.B. Wang, and R.R. Alfano, "Imaging objects hidden in scattering media with fluorescence polarization preservation of contrast agents," *Appl. Opt.* **37**, 792-797 (1998).
54. N. Kollias, "Polarized light photorgaphy of human skin" in *Bioengineering of the Skin: Skin Surface Imaging and Analysis,* K.-P. Wilhelm, P.Elsner, E. Berardesca, and H.I. Maibach eds. (CRC Press, New York, 1997), 95-106.
55. S.G. Demos, W.B. Wang, J. Ali, and R.R. Alfano, "New optical difference approaches for subsurface imaging of tissues" in *Advances in Optical Imaging and Photon Migration, OSA TOPS* **21**, J. G. Fujimoto and M. S. Patterson eds. (OSA, Washington, 1998), 405-410.
56. A. Muccini, N. Kollias, S.B. Phillips, R.R. Anderson, A.J. Sober, M.J. Stiller, and L.A. Drake, "Polarized light photography in the evaluation of photoaging," *J. Am. Acad. Dermatol.* **33**, 765-769 (1995).
57. O. Emile, F. Bretenaker, and A. LeFloch, "Rotating polarization imaging in turbid media," *Opt. Lett.* **21,** 1706-1709 (1996).
58. J.S. Tyo, "Enhancement of the point-spread function for imaging in scattering media by use of polarization-difference imaging," *J. Opt. Soc. Amer. A* **17**, 1-10 (2000).
59. G.A. Wagnieres, W.M. Star, and B.C. Wilson, *"In vivo* fluorescence spectroscopy and imaging for oncological applications," *Photochem Photobiol.* **68**(5), 603-632 (1998).
60. J.R. Mourant, T. Fuselier, J. Boyer, T.M. Johnson, and I.J. Bigio, "Predictions and measurements of scattering and absorption over broad wavelength ranges in tissue phantoms," *Appl. Opt.* **36**, 949-957 (1997).
61. L.T. Perelman, V. Backman, M. Wallace, G. Zonios, R. Manoharan, A. Nustar, S. Shields, M. Seiler, C. Lima, T. Hamano, I. Itzkan, J. Van Dam, J.M Crawford, and M.S Feld, "Observation of periodic fine structure in reflectance from biological tissue: A new technique for measuring nuclear size distribution," *Phys. Rev. Lett.* **80**, 627-630 (1998).
62. K. Sokolov, R. Drezek, K. Gossage, and R. Richards-Kortum, "Reflectance spectroscopy with polarized light: Is it sensitive to cellular and nuclear morphology," *Opt. Express* **5**, 302-317 (1999).
63. V. Backman, R. Gurjar, K. Badizadegan, I. Itzkan, R. Dasari, L.T. Perelman, and M.S. Feld, "Polarized light scattering spectroscopy for quantitative measurements of epithelial cellular structures *in situ," IEEE J. Sel. Top. Quantum Electron.* **5**, 1019-1026 (1999).
64. A. Myakov, L. Nieman, L. Wicky, U. Utzinger, R. Richards-Kortum, and K. Sokolov, "Fiber optic probe for polarized reflectance spectroscopy *in vivo:* Design and performance,"*J. Biomed. Opt.* **7**(3), 388-397 (2002).

This page intentionally left blank

Chapter 2

OPTICAL CORRELATION DIAGNOSTICS OF SURFACE ROUGHNESS

Oleg V. Angelsky and Peter P. Maksimyak
Chernivtsi National University, Chernivtsi, 58012 Ukraine

Abstract: New feasibilities are considered for optical correlation diagnostics of rough surfaces with various distributions of irregularities. The influence of deviations of the height surface roughness distribution from a Gaussian probability distribution on the accuracy of optical analysis is discussed. The possibilities for optical diagnostics of fractal surface structures are shown and the set of statistical and dimensional parameters of the scattered fields for surface roughness diagnostics is determined. Fast-operating optical correlation devices for roughness control are presented.

Key words: rough surface, fractal surface, optical correlation devices, singular and fractal optics.

2.1 INTRODUCTION

Rough interfaces of different media transform the amplitude, phase, and statistical moments of the spatial structure of an optical radiation field in a random way. Modeling of such spatial transforms of the field has been of interest for investigation of rough surfaces for a long time. On the other hand, rough interfaces are encountered in technologies ranging from microstructures to automobile manufacturing. The surface roughness of solids such as metals, plastics, and semiconductors can have an important effect on their physical performance. Another aspect showing the importance of surface roughness is the analysis of different kinds of devices or products made from raw materials. We may mention here several examples: laser-active crystals require very high surface quality to provide high gain of laser radiation; metal products are frequently subject to various finishing

processes to provide smooth contact surfaces (for instance, for car engines, and hydraulic pumps); interfaces of semiconductors must be smooth enough for proper electrical or laser function.

The quality of processing of many surfaces is characterized by the degree of roughness. Considerable progress in rough surface characterization has been achieved in last decades. Numerous techniques for surface roughness diagnostics have been developed as well as devices implementing such techniques. Noncontact, nondestructive diagnostic techniques undoubtedly possess well-known advantages. The possibility to use the low-power sources of coherent radiation has great advantages for optical surface roughness control [1-4]. All optical techniques may be divided into three large classes:

- profile interference and heterodyning techniques;
- techniques based on measuring of the angular distribution of scattered radiation;
- optical correlation techniques.

The profile interference and heterodyning techniques are implemented using the measuring devices such as WYKO TOPO-3D, Zygo NewView5000 Three-Dimensional Surface Profilers, and Talysurf (Talysurf Laser Interferometric Form/Surface Texture Measuring System) [1]. These devices, being rather complicated and expensive, provide rough surface mapping as well as a complete set of statistical parameters of the surface being studied in a range from 1Å to a few micrometers of the *rms* deviation of the profile from a mean surface line (*rms* roughness).

The second class includes techniques such as angle-resolved scattering [5,6], the total integrated scattering [7], and the bi-directional reflectance distribution [8]. These techniques do not facilitate estimation of the surface profile but merely permit assessing the *rms* roughness across the controlled area through measurement of the angular distribution of the scattered intensity. These techniques possess sensitivity down to a few angstroms, whereas the upper limit of the measured heights does not exceed tenth of a wavelength of the probing radiation [9].

Optical correlation techniques are based on the well-known model of a random phase screen (RPS) [10]. Using this model, one can obtain simple interrelations between the statistical moments of the object structure and similar parameters for the scattered field. The RPS model is applicable not only in connection with rough surface diagnostics but also in the characterization of inhomogeneous phase objects such as turbulence in liquid and gas and optical crystals with dislocations and others [11]. Thus, optical correlation techniques may be used for diagnoses a wide class of inhomogeneous phase objects, which may be described only by their statistical properties. At the same time the measuring devices implementing optical-correlation techniques can be designed as laboratory or portable

systems for on-line surface roughness control and for control of arbitrarily shaped surfaces [4]. Spatial averaging of the measured data over the illuminated area under study just in the optical channel provides a sensitivity threshold for these techniques of ~2 Å, and a measurement time of ~2 s.

However, optical correlation techniques based on the RPS model possess some limitations. So, the upper limit of the probed heights of the surface under investigation depends on the wavelength of the probing radiation, and the surface height deviation must obey Gaussian statistics. At the same time, any real surface has a finite number of irregularities whose statistics differs from Gaussian one. Besides, during the past decade, some papers were published confirming that surface roughness has fractal or fractal-like structure [12-15]. One of the many features of fractality is growth of the correlation length of inhomogeneities with the increase in the surface area under investigation [16]. This fact can be explained as a consequence of the surface structure self-similarity, when a part of the surface of a greater scale is of identical statistical structure as the parts of the surface with smaller scales. In this case the statistical approach based on the RPS model becomes insufficient. Fractals or self-similar objects must be considered within the framework of the theory of stochastic and chaotic oscillations [17]. Such objects are characterized by unconventional parameters such as fractal, correlation, mass, volume and other dimensions [18]. One of the possibilities for determining dimensional parameters is to characterize them on the basis of on the slope of the power spectrum of the scattered radiation in a logarithm scale [12,19]. But the techniques for measuring the dimensional parameters developed up to now also have some limitations [20]. Thus, the development of new approaches for diagnostics of fractal surfaces is urgent.

Generally, the problem of rough surface diagnostics must be considered as applied to specific practical task, whose set is rapidly extended. So, following to Whitehouse [21], there are two reasons for measuring surfaces. The first reason is to help in manufacture control, the second one is to help to ensure that the product perfumes well.

In manufacture there are two important areas: one is such manufacturing process as grinding and the other is the means applying the process, e.g., the path of the tool and machine tool characteristics. Surface assessment is used to control the first and to monitor the second.

The process control at a rudimentary level has been achieved by using simple surface parameter such as *rms* to detect changes in the process. This approach is acceptable for statistical process control because it can indicate that a process change has taken place: it cannot say what produced the change. For closed loop control the important process parameters have to be identified and measured.

In problems of this kind, the diagnostic parameters must be scale-dependent for unambiguous determination of the stage of surface processing to provide just the obtained magnitudes of the parameters and to correct the

processing process opportunely. It is doubtful in this situation, that such parameter as fractal dimension is applicable due to its scale-invariance, having the same magnitude at all scales of inhomogeneities [21]. At the same time, the fractal dimension can be regarded as one of the promising diagnostic parameters into the problem of classification of rough surfaces that are generated in processes, such as growth and etching of thin films. It is of the most importance, if the interface evolution obeys the model of dynamic scaling [22,23]. An attractive feature of optical technique is that it can be used for *in situ,* real-time monitoring of the growth process without interruption [24,25]. This argues the necessity of developing new measuring techniques. Thus, one strives to develop the measuring device providing *(a)* classification of surfaces into fractal and random ones, and *(b)* estimation of the parameters characterizing the structure of these surfaces, such as *rms,* R_a, R_z, and others.

The goal of this chapter is to study the effectiveness and potential of the usage of optical correlation techniques and fractal optics for the diagnostics of random and fractal surfaces, and of surface roughness with non-Gaussian statistics.

2.2 THEORETICAL BACKGROUND

2.2.1 The RPS Model

Within the framework of the RPS model, the surface roughness with a height distribution $h(\rho)$ (where ρ is the two-dimensional vector) is described by the surface phase correlation function [10]

$$\Psi_{\varphi_0}(\rho) = \sigma^2_{\varphi_0} K(\rho), \tag{1}$$

whose maximal magnitude is determined by the phase variance of the object $\sigma^2_{\varphi_0}$, with $K(\rho)$ the normalized phase correlation coefficient, while the half-width of the normalized correlation function determines the correlation length of the surface inhomogeneities l_{φ_0}. Using equation 1, one can obtain the height correlation function of the surface $\Psi_h(\rho) = \sigma_h^2 K(\rho)$, where $\sigma_h = \sigma_{\varphi_0} \lambda / [2\pi(n-1)]$ is the *rms* deviation of the profile from a mean surface line here given for a transmission configuration, where n_0 is the refractive index of the transmitting screen.

The model for an infinitely extended RPS is based on the following assumptions [10,26]: (1) All spatial frequency components associated with the phase structure of an object contribute to the formation of the radiation field resulting from the interaction of the probing beam with the object, presuming that the correlation length of the RPS inhomogeneities is larger than the wavelength, i.e., $l_{\varphi_0} > \lambda$; (2) The phase variance of the object is small, $\sigma^2_{\varphi_0} < 1$ (although equation 1 can still be valid if the surface is much rougher than a wavelength).

Using the RPS model one can obtain the following interrelations between the statistical parameters of the object structure and the scattering radiation in the far field (Fraunhofer zone). Hereinafter, we use the terms 'far field' and 'near field' in respect to isolated inhomogeneity rather than in respect to the object as a whole [10]. The phase variance, σ^2_{φ}, and the amplitude dispersion, σ^2_A, of the field in this zone is

$$\sigma^2_{\varphi} = \sigma^2_A = 0.5\sigma^2_{\varphi_0}, \tag{2}$$

and the scintillation index (normalized intensity dispersion) is

$$\beta^2_{\infty} = 2\sigma^2_{\varphi_0}. \tag{3}$$

Deriving equations 2 and 3, one assumes for convenience and unambiguity an average intensity of the boundary field and the field behind the screen to be equal unity [10]. In computer simulation and physical experiment, it presumes normalization of the field's intensity and amplitude on the average magnitudes of intensity and amplitude, respectively. Thus, the amplitude dispersion, σ^2_A, and the scintillation index, β^2, in equations 2 and 3 are dimensionless, as well as phase variance of the object, $\sigma^2_{\varphi_0}$, and the phase variance of the field, σ^2_{φ}, being determined in share of arc, i.e., radians.

The transverse coherence function of the field being equal to the transverse coherence function of the boundary field in any recording zone is defined as [10]

$$\Gamma_{\perp}(\rho) = \exp\left\{\sigma^2_{\varphi_0}\left[K(\rho) - 1\right]\right\} \tag{4}$$

The equations 1 to 4 are valid for surfaces whose inhomogeneities obey Gaussian statistics. If the number of inhomogeneities is limited or the height distribution function differs from a Gaussian distribution, one must consider the higher-order statistical moments both for the surface roughness and for the scattered radiation field. Knowing these parameters, one can reconstruct the height distribution function for the surface under study. So, the third- and the fourth-order statistical moments of the field determine in a unique and straightforward way, respectively, the skewness,

$$Sk = \frac{1}{\sigma_h^3}\frac{1}{N}\sum_{i=1}^{N} h_i^3 , \tag{5}$$

and the kurtosis,

$$Ku = \frac{1}{\sigma_h^4}\frac{1}{N}\sum_{i=1}^{N} h_i^4 , \tag{6}$$

of the height distribution function. Here, h_i is deviation of the profile from a mean surface line that is assumed to be zero, so that equations 5 and 6 are in terms of the third and fourth central moments, respectively.

2.2.2 Fractal Approach

The approach based on the theory of stochastic and chaotic oscillations essentially differs from the theory based on statistical models. This theory provides adequate description of various stochastic, chaotic, and fractal objects and processes [27]. According to this approach, surface roughness is characterized by the parameters of dimensionality, such as fractal and Hausdorff dimensions, spectrum of singularities, correlation exponent, and others [18].

Let us here consider one of the most common approaches for describing a fractal surface. Everyone has an intuitive understanding of roughness and correlation-length parameters, which appear to be easily measured. The mean-square roughness equals the value of the peak of the correlation function at the origin, and the correlation length is the width of this peak. However, as it was pointed out earlier, the surface finish of highly polished optical surfaces is frequently fractal-like in that their power spectra adhere to an inverse power law of the form

$$S(f_x) = K_n / f_x^n \quad \text{with} \quad 1 < n < 3. \tag{7}$$

The intrinsic surface parameters describing such surfaces are the spectral strengths, K_n, and spectral indices, n, rather than the *rms* roughness, σ_h, and the correlation length, l_{φ_0} [12,28]. The basis for this statement follows from the experiments presented in the cited papers, which show that changing the resolving power of the measuring tool (for example, the size of the scanning probe) results in a considerable change in the magnitude of the statistical parameters characterizing a slightly rough surface. Diminishing the scanning stylus leads to an increase in the evaluated phase variance of the boundary field [29]. This conclusion follows indirectly from discussions by T. Vorburger and K. O'Donnell that of the measured statistical parameters of a rough surface depend not only on the scanning region but also on the resolving power of the measuring tool used [9,30].

Generally, measurements of fractal surfaces are most naturally described in terms of the surface finish power spectrum rather than are based on its correlation function; in particular, they are described in terms of the quantities K_n and n appearing in the expression for the one-sided profile spectrum given by equation 7. This is sufficient for describing a 1-*D* or a corrugated surface. However, if the surface roughness is isotropic, the corresponding expression for the 2-*D* power spectrum is

$$S(f) = \frac{\Gamma[(n+1)/2]}{2\Gamma(1/2)\Gamma(n/2)} \cdot \frac{K_n}{f_x^{n+1}} \ . \tag{8}$$

This quantity appears in the analysis of the scattering from such surfaces [28]. Note that this expression falls off one power faster than the corresponding 1-*D* form.

The mathematical analysis of fractals makes use of two different parameters: the Hausdorff-Besicovitch dimension, *D*,

$$D = (5-n)/2 \ , \tag{9}$$

and a length parameter called the topothesy, *T*, where

$$T^{3-n} = -\frac{1}{2}\frac{(2\pi)^n}{\Gamma(n)\cos(n\pi/2)} K_n \ . \tag{10}$$

Physically, T is the average distance over which the chord between two arbitrary surface points has an *rms* slope of unity [31].

The case $n = 1$ ($D = 2$) is called the extreme fractal; $n = 2$ ($D = 1.5$) is the Brownian fractal and $n = 3$ ($D = 1$) is the marginal fractal; n must lie between 1 and 3, and D between 1 and 2.

The fact that such surfaces are most naturally described in terms of K_n and n instead of σ_h and l_{φ_0} does not mean that profile or scattering measurements of such surfaces cannot be analyzed in terms of the parameters σ_h and l_{φ_0}. But in this case the obtained parameters σ_h and l_{φ_0} are not the intrinsic parameters of the surface.

At the same time, the fractal approach has some limitations because the real surface roughness may be prefractal, i.e., fractal of finite level, or multifractal [32].

2.3 COMPUTER SIMULATION

2.3.1 Simulation of Rough Surfaces

We performed both a computer simulation and an experimental study for estimating the applicability of the optical correlation techniques to the problem of diagnostics of surface roughness with non-Gaussian statistics.

Let us consider the objects of two types: a non-fractal random surface (NRS) and a fractal random surface (FRS) [24]. The surface heights of the NRS within the area determined by $N \times N$ pixels were specified for each pixel by a random-number generator, following the normal law.

FRSs were simulated following the algorithm introduced in Ref. [33]. Here, the surface was represented by a square net of side length equal to unity, with the number of sampling points along each side equal to $2^n + 1$, where n is the number of iterations. The height values at the four corners of a square are specified as $h(0,0)=h(0,1)=h(1,0)=h(1,1)=0$. Then, a subroutine is used to generate independent Gaussian random numbers ξ with a mathematical expectation equal to zero and a decreasing dispersion as n increases:

$$\sigma_n^2 = (1/\sqrt{2})^{2nH} \sigma_0^2, \tag{11}$$

where σ_0^2 is the initial dispersion of random adding, and H is the Hurst's index, $0 < H < 1$[18].

In the first stage, a value for ξ is inserted, which is used as the level of a surface element at the center of the net (1/2,1/2). The heights at points

(0,1/2), (1/2,0), (1/2,1), (1,1/2), (1/4,1/4), (3/4,1/4), (1/4,3/4), and (3/4,3/4) are obtained by interpolation, as an arithmetic mean of the heights at the nearest diagonal points. Then, 13 independent values $\xi_{n=1}$ with dispersion σ_1^2 are added to the heights, earlier specified at the mentioned nodes of the net. Such a procedure is repeated n times. At each cycle the number of sampled points with specified heights is doubled, while spacing between these points is $2^{-1/2}$ times diminished.

The objects are formed by 900×900 pixels. Further, the NRS and the FRS ones undergo two-dimensional smoothing following either a Gaussian or an exponential law with various half-widths for the height distribution function. In such a way, quasi-smoothed micro irregularities of different transverse scale, reproduced by a distribution of pixel values are obtained. Now a surface relief (rather than deviation of the profile from a mean surface line) is computed that is essentially positive value. Next, the power non-linearities, $h^k(x,y)$ with k = 0.25, 0.5, 2, and 4, are inserted into the height distribution function for the surfaces. Some examples of the surfaces modeled in this way are shown in Figure 1 [24].

The height distribution functions for the surface irregularities are also represented in Figure 1 as well as the statistical parameters for the surfaces, including: arithmetic mean deviation of the profile from a mean surface line, R_a, *rms* deviation, R_q, the skewness, *Sk,* and the kurtosis coefficient, *Ku.* All the above-considered examples refer to the maximal span of the surface irregularity heights, $h_{\max} = 2\mu m$. In simulation, $h_{\max}$ was changed from $0.1\ \mu m$ to $10\ \mu m$, which corresponded to phase variation from 0.5 *rad* to 50 *rad*.

The following procedure was carried out for calculation of the field diffracted from the rough surface. Let us consider a transmitting object with a rough surface. This case is straightforwardly implemented. The approach for the case of reflecting rough surfaces is the same. So, for the transmitting object $\varphi(x,y) = k(n-1)h(x,y)$, while for the reflecting one $\varphi(x,y) = 2kh(x,y)$, where $h(x,y)$ is the relief height of a rough surface, n is the bulk index of refraction, $k = 2\pi/\lambda$ is the wave number, and λ is the wavelength. In our computations and experiments, $\lambda = 0.633\mu m$ (He:Ne laser), and n = 1.46 (fused quarts).

The amplitude and phase of the field resulting from diffraction of a plane wave at a rough surface can be calculated using the double Rayleigh-Sommerfeld diffraction integral [34],

$$U(\xi,\zeta)=\frac{z}{i\lambda}\int\int\frac{A(x,y)}{R^2(x,y,\xi,\zeta,z)}\exp\{-ik[R(x,y,\xi,\zeta,z)+(n-1)h(x,y)]\}dxdy; \quad (12)$$

where $A(x, y)$ is the aperture function that corresponds to the amplitude transmittance of a rough surface (see Figure 2),

$$R(x,y;\xi,\zeta,z)=\sqrt{z^2+(x-\xi)^2+(y-\zeta)^2}$$

is the distance between the surface point and the observation point, z is the distance between the plane of the object to the observation plane, and $x, y; \xi, \zeta$ are the rectangular Cartesian coordinates at the object plane and the observation plane, respectively, as shown in Figure 2.

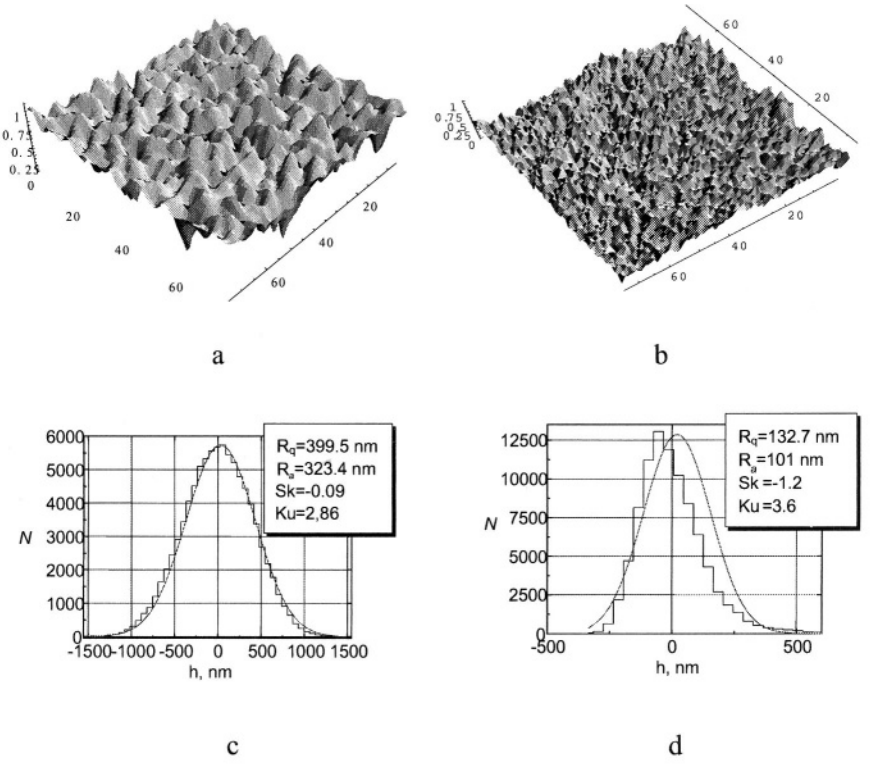

Figure 1. The relief maps (a, b) and the height distribution functions (c, d) for some modeled surfaces. The histogram shows the real surface height distribution, and the solid curve shows the Gaussian distribution with the same mean value and dispersion: (a, c) - non-smoothed fractal surface; (b, d)) - three-point smoothed non-fractal random surface obeying Gaussian law with a power non-linearity of 0.25.

In contrast to the Kirhhoff's diffraction integral [10], the integral, see equation 12, is applicable for the field calculations at arbitrary distances *z*. In this study we replace integration by summation dividing both the object and the field in the observation plane into elementary areas.

Knowing the real and imaginary parts of the complex amplitude $U(\xi,\zeta)$, one can compute the amplitude $A(\xi,\zeta)$, the phase $\varphi(\xi,\zeta)$, and the intensity $I(\xi,\zeta)$ as well as all statistical moments and correlation functions of the resulting field. The following statistical parameters of the field are of most importance for surface roughness diagnostics, i.e., phase variance, amplitude dispersion, scintillation index, skewness and kurtosis of the field's intensity distribution. It is known that kurtosis for a Gaussian distribution is equal to 3. Peculiarity of kurtosis for the field intensity is that it is equal or exceeds "three". To all appearance, this results from focusing properties of surface inhomogeneities. Bearing in the mind this circumstance, we will represent the parameter Ku^f connected with the field intensity kurtosis by equation $Ku^f = Ku - 3$, for the sake of convenience of data analysis.

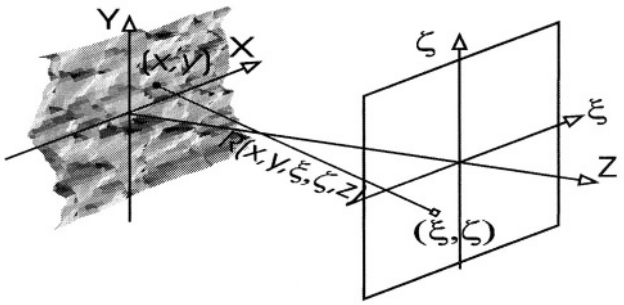

Figure 2. Formation of the field diffracted by a rough surface.

Let us first of all present the results of the computer simulation of optical diffraction at rough surfaces with average heights less than the wavelength. The behavior of the statistical moments of a field in the registration zone is shown in Figure 3 for the example of the NRS R3H02 (NRS smoothed over three pixels by applying the Gaussian law). Such a behavior is typical for all the studied random objects of this kind. The amplitude dispersion, σ_A^2, being of zero magnitude at the objects boundary field, grows monotonically as the distance *z* increases. The far-field magnitude of this parameter approach's one half of the phase variance of the boundary object field, $\sigma_{\varphi_0}^2$. At the same time, the phase variance of the field,

being equal to $\sigma^2_{\varphi_0}$ at the boundary object field, gradually decreases down to $0.5\sigma^2_{\varphi_0}$ in the far field. The scintillation index, β^2, exceeds the field's amplitude dispersion by approximately four times, being slightly fluctuating. Such a behavior of the mentioned statistical moments of a field correlates well with the basic relations of the RPS model [10]. However, one can see in Figure 3 that the far-field skewness and kurtosis prove to be different from zero (being very small but non-vanishing), while the corresponding coefficients for the boundary object field are of zero magnitude. This is obviously connected with the wave nature of the diffracting radiation. As the *rms* heights of the surface irregularities approach the wavelength, the far-field magnitudes of phase variance and amplitude dispersion increase proportionally. For the heights exceeding the wavelength, the far-field phase variance saturates at $\pi^2/3$. The far-field amplitude dispersion increases up to 0.5.

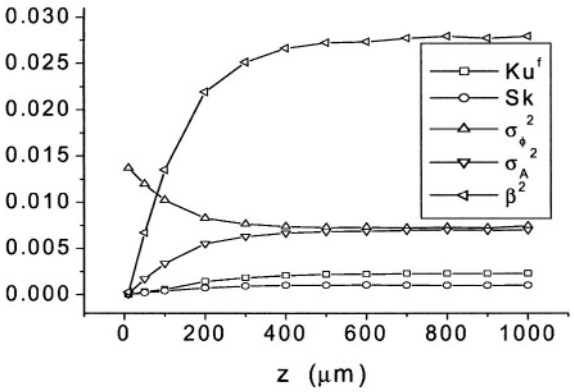

Figure 3. The typical behavior of the statistical moments as a function of the observation distance z for the surface R3H02 (three-point non-fractal random surface obeying Gaussian law with $h_{\max} = 200nm$): Ku^f - kurtosis coefficient of the field, *Sk* - asymmetry coefficient, σ^2_φ - phase variance of the field, σ^2_A - amplitude dispersion of the field, and β^2 - the scintillation index of the field [24] (Copyright @ OSA).

The scintillation index β^2 approaches unity in the far field, as the heights of the surface irregularities increase [10]. When $R_q > \lambda$, the magnitude of the scintillation index reaches a maximum in the focusing zone. The maximal magnitude of β^2 and its location on the z-axis depend on the phase variance of the boundary object field as well as on the correlation length of

this field [10]. However, these dependencies are only valid if the surface heights have a Gaussian distribution.

The kurtosis of the field intensity distribution turns out to be much more sensitive to the height span over the studied range. The behavior of the kurtosis with respect to the registration zone is shown in Figure 4 for various height spans of the rough surface (a surface map for various heights are the same in all cases).

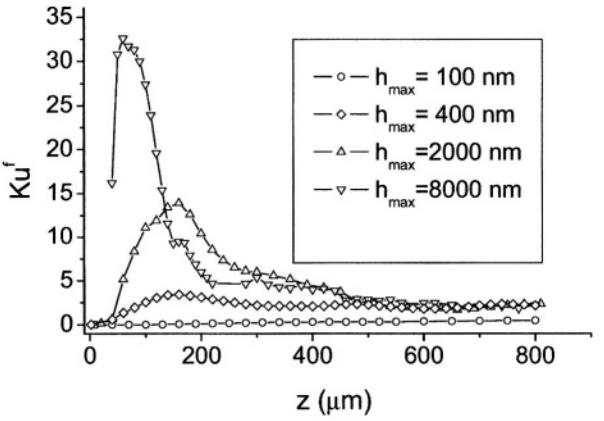

Figure 4. The kurtosis coefficient of the field, Ku^f, as a function of z for various height spans of the rough surface relief [24] (Copyright @ OSA).

This dependence has a sharp maximum whose position coincides with a focusing zone for surface irregularities. One can see in Figure 4 that the maximal magnitude of $Ku^f(z)$ grows considerably when the height span of the surface roughness increases. This fact may be explained by the following consideration. The diffraction field results from coherent summation of partial waves from each point of the surface, taking into account the actual amplitudes and phase delays of these waves. The most pronounced deviations of the field intensity distribution from a Gaussian one are observed in the caustic zone with respect to an isolated typical irregularity. For that, growing of the height of irregularities means that the slope of the irregularities increases for unchanged correlation length of them. It results in the forming of a wave front with considerable rate of change and, as a consequence, in sharper peaks in the caustic zone. Thus, it gives a hope that the established behavior of the field is promising for rough surface diagnostics.

Applying the power non-linearities to a Gaussian height distribution does not considerably alter the behavior of the statistical parameters of the field with respect to the registration zone. So, the phase variance and the amplitude dispersion of the field behave in the same manner, excluding a small shift of the maxima of the dependencies $\beta^2(z), \sigma_A^2(z)$, and $\sigma_\varphi^2(z)$.

The behavior of the statistical parameters of the field scattered at FRS differs considerably from the one pertinent to the radiation scattered by random surfaces. So, when the heights are less than the wavelength, the far-field phase variance and amplitude dispersion do not converge to each other as it is seen in Figure 5. One can see in Figure 5 the distinction (by several folds!) between the far-field phase variance and amplitude dispersion. For our opinion, this distinction may be used as a reliable criterion for surface classification, i.e., it reveals if the surface under study is a FRS or a NRS one. Other statistical moments of the field scattered by a fractal surface, such as $\beta^2(z), k_k(z), k_A(z)$, behave the same way as the statistical moments of the field scattered by a NRS, see Figure 5.

It is well known (see also equation 4) that the field's transverse coherence function, $\Gamma_\perp(\rho)$, is the important diagnostic characteristics of a RPS [4,10]. So, if the surface height distribution is Gaussian, one can obtain the correlation function of surface irregularities from $\Gamma_\perp(\rho)$. However, it is sufficient in most cases to know only the surface height dispersion, i.e., *rms* roughness. In this case, one measures the "tail" of the field's coherence function, namely for a transversal shift that exceeds the correlation length of the surface inhomogeneities:

$$\Gamma_\perp(\rho > l_{\varphi 0}) = \frac{I_{\max} - I_{\min}}{I_{\max} + I_{\min}} = \exp\left\{-\sigma_{\varphi 0}^2\right\} \tag{13}$$

Gaussian statistics does not suffice for description of all the objects of practical importance. It is quite obvious that $\Gamma_\perp(\rho)$ will be different for objects of different type. It is shown in Figures 6(a) and 6(b) where the behavior of $\Gamma_\perp(\rho)$ is different for the case of a FRS and for a NRS one. So, $\Gamma_\perp(\rho)$ is not saturated in the near zone of a fractal object. This results from increasing the correlation length of the irregularities of the fractal surface while simultaneously increasing the transverse scale of this surface. This conclusion is in agreement with the results represented in Ref. [16], when the correlation length of the irregularities approaches the object's cross-section.

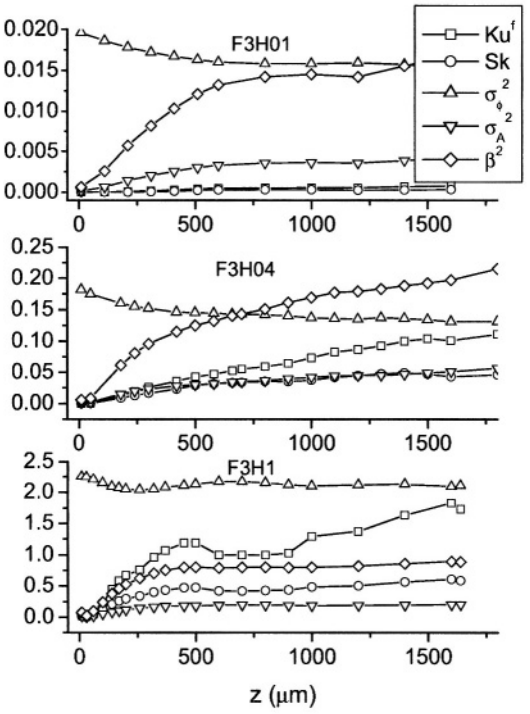

Figure 5. Behavior of the statistical parameters of the scattered field for a three-point smoothing by applying Gaussian law fractal surfaces: F3H01 - h_{max} = 100 nm, F3H04 - h_{max} = 400 nm, F3H1 - h_{max} = 1000 nm [24] (Copyright @ OSA).

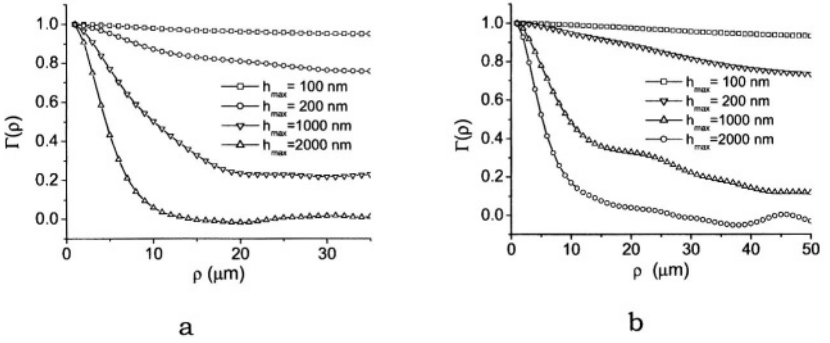

Figure 6. Transverse coherence function of the field, $\Gamma_{\perp}(\rho)$, for non-fractal (a) and fractal (b) objects with various values of h_{max} .

Introducing the power non-linearities into the height distribution of a NRS and a FRS gives rise to changes of the *rms* surface roughness for the same maximal height span. The magnitudes of the phase variance of such objects, $\sigma^2_{\varphi_0}$, found from the height distribution *(h)* and the measured far-field coherence function *(cf)* are represented in Table 1. For NRS this discrepancy does not exceed 10%. The magnitude of the phase variance found from the transverse coherence function for FSR is larger than 40%.

Table 1. Phase variance magnitudes, $\sigma^2{}_{\varphi_0}$, for fractal and non-fractal surfaces found from the height distributions (*h*) and from the measured far-field coherence function (*cf*) for various maximal height spans of surface irregularities and power nonlinearities: 0 - without nonlinearities, 1R - $k = 0.5$ (singly square rooted), 1S - $k = 2$ (singly squared), 2R - $k = 0.25$ (doubly square rooted), 2S - $k = 4$ (doubly squared).

		Fractal			Random				
h_{max} ,nm	σ_φ	0	1 R	1S	0	1R	2R	1S	2S
100	*h*	0.019	0.010	0.022	0.018	0.011	0.004	0.017	0.006
	cf	0.023	0.014	0.030	0.016	0.013	0.004	0.018	0.005
200	*h*	0.078	0.040	0.090	0.073	0.208	0.017	0.068	0.027
	cf	0.087	0.051	0.103	0.072	0.212	0.017	0.071	0.025
400	*h*	0.313	0.160	0.360	0.290	0.043	0.070	0.270	0.102
	cf	0.339	0.188	0.392	0.307	0.047	0.074	0.274	0.097

2.4 DIMENSIONAL CHARACTERISTICS OF OBJECTS AND FIELDS

The model used for the objects and the computed fields may be characterized using the parameters appearing in the theory of stochastic and chaotic oscillations [27]. These are: fractal dimension, D_f, singularity spectrum, $f(\alpha)$, and the correlation exponent, ν.

Fractal dimension may be obtained by several independent methods:

- directly from the analysis of surface relief using the method of triangular prism squares or cube volume [35];
- directly from the analysis of the surface profile length [18,36];
- from the slope of the power spectrum found through Fourier transformation of the correlation function of the surface relief $h(x,y)$[12,18];
- from the slope of the power spectrum in far-field of the scattered radiation [19,37].

The computed and measured fractal dimensions of the studied surface relief are found using the method of triangular prism squares (D_f^t), by the analysis of surface profile (D_f^p), and through Fourier transformation of the measured correlation function of the surface relief (D_f^c). The corresponding data are shown in Table 2. The magnitudes of fractal dimension D_f^t and D_f^p being within the interval from 2.26 to 2.50, the irregularities differ by 5%, while the magnitude D_f^c is larger by 15%. Obviously, this is explained by the considerable difference in procedures used for computation of the fractal dimension. Besides, one can observe a decrease of the magnitude of the fractal dimension that results from smoothing of the surface as well as from introducing non-linearities of arbitrary kind.

Table 2. The computed and measured fractal dimensions of the surface relief found through the triangular prism technique (D_f^t), through analysis of the surface profile (D_f^p), and through Fourier transformation of the measured correlation function of the relief (D_f^c).

Surface \ Dimension	D_f^t	D_f^p	D_f^c
R0	2.503	2.49	2.55
R1R	2.44	2.47	2.51
R1S	2.48	2.48	2.53
R2R	2.32	2.36	2.42
R2S	2.35	2.39	2.44
F0	2.44	2.45	2.42
F1R	2.36	2.38	2.44
F1S	2.45	2.43	2.48
F2R	2.26	2.31	2.36
F2S	2.38	2.36	2.39

Fractal properties of temporal and spatial fluctuations of intensity of the field scattered by moving FRS and NRS have been recently observed and discussed [38]. Here we study fractal dimension of the spatial intensity distribution for the field scattered by both FRS and NRS applying the model of RPS.

The procedure for computation of the fractal dimension of the object has been used for a two-dimensional intensity distribution. The dependences of the fractal dimension D_f^t on z are shown in Figure 7 for the NRS (a), (c)

and FRS (b) with various maximal height spans and with various power non-linearities.

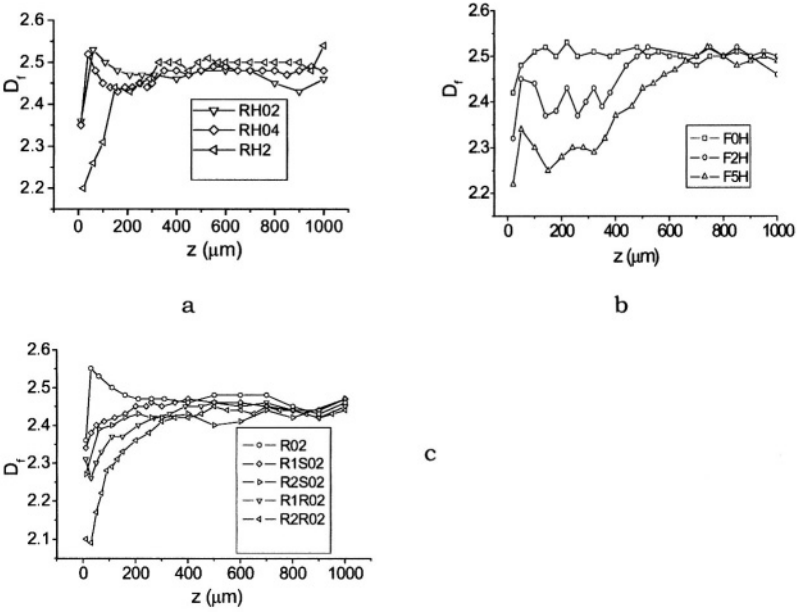

Figure 7. Behavior of the fractal dimension of the field, D_f', as a function of z for: (a) non-fractal surfaces - RH02 - h_{max} = 200 nm, RH04 - h_{max} = 400 nm, RH2 - h_{max} = 2000 nm; (b) fractal surfaces with h_{max} = 2000 nm - F0H2 - non-smoothed, F2H2 - two-point smoothed on Gaussian law, F5H2 - five-point smoothed on Gaussian law; (c) non-fractal surfaces with h_{max} = 200 nm with applied power nonlinearities: R02 - without nonlinearities, R1R02 - k = 0.5 (square rooted), R1S02 - k = 2 (squared), R2R02 - k = 0.25 (doubly square rooted), R2S02 - k = 4 (doubly squared).

The following peculiarities are observed in the behavior of the fractal dimension of the far-field intensity distribution:

- the degree of smoothing of surface irregularities (the number of pixels over which smoothing is carried out) does not considerably affect the magnitude of the fractal dimension;
- the fractal dimension does not depend on the maximal height span both for the FSR and for the NRS.

The fractal dimension of the intensity of radiation scattered by random surfaces possesses some peculiarities in the near field. The dependency of D_f' on z for random surfaces with a maximum height span of 0.2 μm and power non-linearities 0.4, 0.2, 2, and 4 is shown in Figure 7(c). One observes

a decrease of the magnitude of D_f' by 20% in the near field for $k > 1$ and by 10% for $k < 1$. Thus one can identify in a qualitative manner the presence of nonlinearities in the height distribution using the dependence of the fractal dimension on z in the near-field.

The estimation of the correlation exponent both for the surface height distribution and for the scattered radiation field proves to be of high efficiency. It has been shown in Refs. [40,41], that the correlation exponent v may be used for the characterization of the object complexity. As it follows from Ref. [32], the correlation exponent is connected with the number of harmonics of incommensurable periods representing the object structure. Such investigations were carried out for one-dimensional objects, as well as for temporal signals.

The correlation exponent, v, for a one-dimensional phase coordinate is computed using the Packard-Takens procedure [42,43]. In essence, this consists in the following. One constructs an m–dimensional vector

$$I_i^{(m)} = \{I_i, I_{i+1}, ..., I_{i+m-1}\}, \tag{14}$$

where I_i is the intensity of an optical field or phase distribution of the object at the coordinate x_i. Then, the correlation integral is computed

$$C_m(\varepsilon) = \lim_{N\to\infty} \frac{1}{N^2} \sum_{i=1}^{N} \sum_{j=1}^{N} \Theta\left(\varepsilon - \left|I_i^{(m)} - I_j^{(m)}\right|\right), \tag{15}$$

where Θ is the Heaviside function, N is the total number of points, m is the number of samplings or the vector measure. $C_m(\varepsilon)$ gives the portion of point pairs, the distance between which does not exceed ε. For small ε, the correlation integral approaches $C_m(\varepsilon) \cong \varepsilon^v$. As m increases, the magnitude

$$v = \lim_{\varepsilon\to 0} \left[\ln C_m(\varepsilon) / \ln \varepsilon\right] \tag{16}$$

also increases, while the slope of the dependence $\ln C_m(\varepsilon) = \ln \varepsilon$ increases.

The direct application of the Packard-Takens procedure to two-dimensional rough surfaces and other complex objects is difficult due to the rather large number of sampling points. It has been proposed to perform some operations of this procedure in the optical channel [41]. The computation of the correlation integral (see equation 15) includes the same procedure as the procedure for computation of the structure function for a random field [10],

$$D_I(\boldsymbol{r}_1,\boldsymbol{r}_2)=\left\langle\left|\Im(\boldsymbol{r}_1)-\Im(\boldsymbol{r}_2)\right|^2\right\rangle. \tag{17}$$

The structure function of locally uniform and isotropic objects and fields is connected with the correlation function,

$$D_I(\boldsymbol{r}_1,\boldsymbol{r}_2)=D_I(\rho)=2[\Psi_I(0)-\Psi_I(\rho)], \tag{18}$$

where $\Psi_i(\rho)$ and $\Psi_i(0)$ are the magnitudes of the transverse coherence function for $\rho=|\boldsymbol{r}_1-\boldsymbol{r}_2|$, and $\rho=0$, respectively.

Let us consider the correlation integral (equation 15) and determine the distance between two points in the *m*–dimensional space:

$$\left|I_i^{(m)}-I_j^{(m)}\right|=\left[\sum_{k=0}^{m-1}\left(I_{i+k}-I_{j+k}\right)^2\right]^{1/2}. \tag{19}$$

For large m equation 19 determines the square root of the structure function, $[D_I(\rho)]^{1/2}$. The scheme for computation of the correlation exponent v from the graph of the structure function $D_I(\rho)$ is shown in Figure 8.

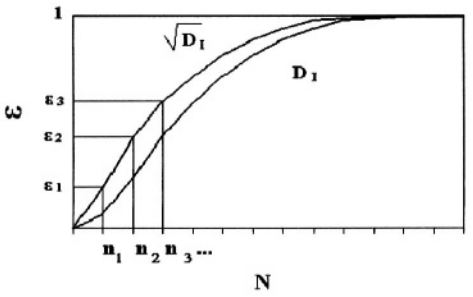

Figure 8. The scheme for calculation of the correlation exponent v from the structure function.

The typical behavior of the correlation exponent of the scattered radiation as a function of z is shown in Figure 9(a) for a random object with Gaussian statistics and a maximal height span h_{max} = 100, 400, 800, 1600, 3200, and 6400 nm smoothed over three points. One can see that the dependencies coincide for $h_{max} \le \lambda$. For $h_{max} \ge \lambda$ the magnitude of the correlation exponent grows as h_{max} increases. In comparison with NRS, FRS are characterized by a somewhat smaller magnitude of the correlation

exponent [Figure 9(b)]. Introduction of power non-linearities in the object height distribution results in a decrease of the field correlation exponent magnitude for objects with $k<1$ [Figure 9(c)].

The above-mentioned is promising for the usage of the correlation exponent as a diagnostic parameter for surface roughness characterization when $h_{max} \geq \lambda$.

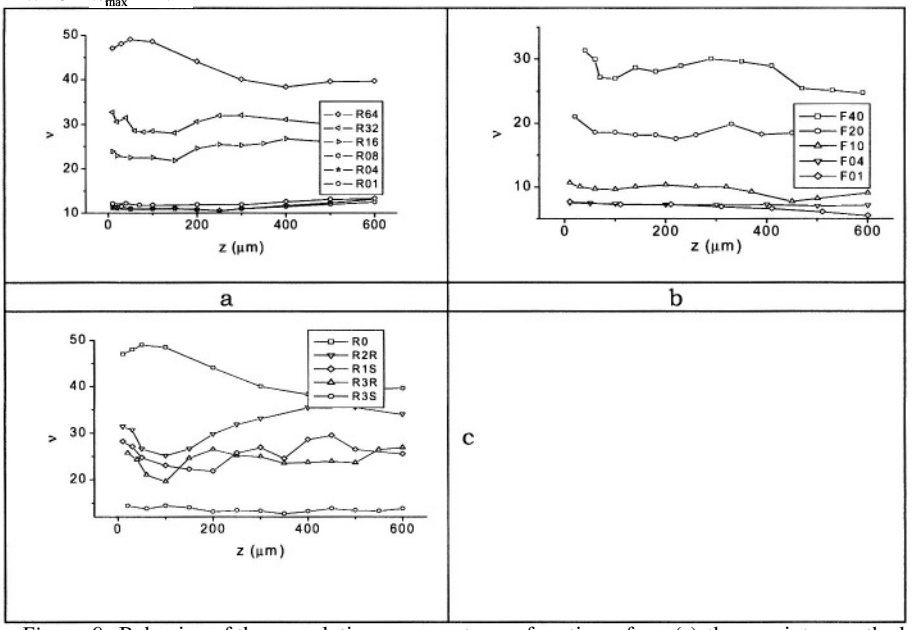

Figure 9. Behavior of the correlation exponent as a function of z : (a) three-point smoothed non-fractal random surface obeying Gaussian law with the maximal height span h_{max} = 100, 400, 800, 1600, 3200, and 6400 nm; (b) three-point smoothed fractal surface obeying Gaussian law with the maximal height span h_{max} = 100, 400, 1000, 2000, and 4000 nm; (c) three-point smoothed non-fractal random surface obeying Gaussian law with the maximal height span h_{max} = 2000 nm (R0 - without non-linearities, R2R - k = 0.25 , R1 S - k = 2 , R3R- k = 0.125, R3S- k = 8).

2.5 EXPERIMENTAL STUDY

The previous simulation results are necessary for developing a multifunctional system for the diagnostics of rough surfaces of various structures. Such diagnostic system could be based on measuring the field intensity distribution, a coaxial superposition of a reference wave (for obtaining the map of a surface profile and phase variance of the boundary object field), or be based on measuring the transverse coherence function of a field (for obtaining the correlation function, power spectrum, and *rms* of

the surface height distribution, as well as estimation of the correlation exponent of the field). All the mentioned operations may be performed using the set-up shown in Figure 10.

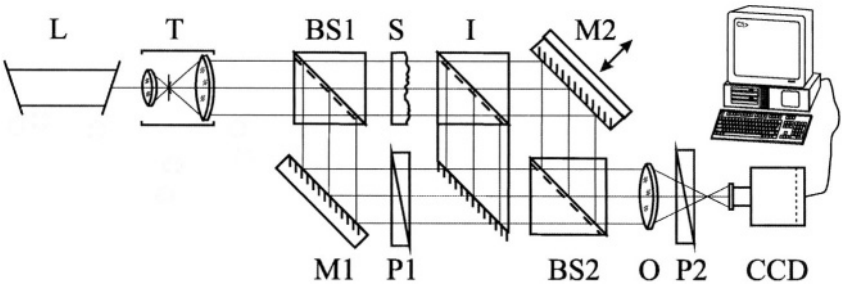

Figure 10. The experimental optical arrangement: *L* – He:Ne laser, *T*- inverse telescopic system, *BS1, BS2* - beamsplitters, *M1, M2* - mirrors, *S* - transmitting object with a rough surface, *P1, P2* - polarizers, *I* - interference block, *O* - objective, *CCD* - digital camera.

A single-mode He:Ne laser, *L,* is used as the source of optical radiation. The inverse telescopic system, *T,* forms a plane wave incident on the object. Beam splitters *BS1* and *BS2,* and the mirrors *M1* and *M2* make up the Mach-Zehnder interferometer. The transmitting object of interest with a rough surface *S* is placed in one of the interferometer arms. (The arrangement for test of a reflecting object is not considered here being in principle the same as the one for control of a transmitting object.) Polarizers *P1* and *P2* control the intensity of the wave in the reference arm of the interferometer. Introducing the interference block, *I,* one can perform amplitude splitting of the object beam and control the transverse shift between the two obtained beam components. The objective, *O,* projects an arbitrary transverse cross-section of the field scattered by a rough surface onto the *CCD* camera. The resulting image is fed to the computer for further processing.

Let us now consider the possibilities provided by this system.

1. The interference block is removed, and the reference wave is blocked.

In this case, one can record the two-dimensional field's intensity distribution in any registration zone by displacing the objective *O* together with the CCD camera along the beam axis. Subsequently, arbitrary statistical moments and correlation functions of the intensity distribution can be computed.

2. The interference block is removed, and the reference wave is superimposed on the object wave.

Such a technique is used for control of surfaces whose heights are less than the wavelength. It provides direct estimation of the *rms* deviation of the surface profile from the mean and deriving the two-dimensional surface

relief. The surface of interest is imaged onto the CCD camera by the objective, *O*.

Consider two interfering coaxial waves, one of which is a plane wave and the other is a phase-modulated wave. The resulting interference pattern can be written as

$$I_S(\xi,\varsigma) = A_0^2 + A^2(\xi,\varsigma) + 2A_0A(\xi,\varsigma)\cos\varphi(\xi,\varsigma), \qquad (20)$$

where $I_S(\xi,\varsigma)$ is the resulting intensity; $A(\xi,\varsigma)$ and A_0 are the amplitudes of the object and the reference waves, respectively, and $\varphi(\xi,\varsigma)$ is the phase difference between the reference and object waves. Assuming that $\langle A(\xi,\varsigma)\rangle = A_0, \langle\varphi(\xi,\varsigma)\rangle = \varphi_0 + \pi$, and assuming that the phase fluctuations are small, i.e., $\tilde{\varphi}(\xi,\varsigma) = \varphi(\xi,\zeta) - \langle\varphi(\xi,\zeta)\rangle < 20°$, then equation 14, after area averaging and some manipulation will take the form

$$\frac{\langle I_S(\xi,\varsigma)\rangle}{I_0} = \sigma_\varphi^2, \qquad (21)$$

where $\sigma_\varphi^2 = \langle\tilde{\varphi}^2(\xi,\varsigma)\rangle$ is the phase variance. Equation 21 thus provides the *rms* roughness.

The rough surface relief height distribution can be obtained if the mean phase of the object wave differs from the reference wave phase by $\pi/2$. If the reference wave and the object wave are of equal intensities, one directly obtains the two-dimensional surface relief, i.e.:

$$h(\xi,\zeta) = \frac{1}{k(n-1)}\left(\frac{I_S(\xi,\varsigma)}{2I_0} - 1\right). \qquad (22)$$

In both cases, precise control of the phase difference between the beams in the two arms of the interferometer is carried out using the mirror, *M2*, mounted on a piezoelectric translator.

3. Interference block is introduced.

The reference arm is blocked, and the transverse shift in the interferometer is varied in order to measure the transverse coherence function of the field. Mirror *M2* controls the transverse shift. If the heights of a rough surface are less than the optical beam wavelength, then the specular (coherent) component is present in the scattered field. This component will result in changes of the interference pattern contrast. For any specified

transverse shift, it is sufficient to measure the maximal and the minimal intensity magnitudes at the resulting pattern for strictly coaxial beams by summation of the pixel values, and to calculate the contrast of the interference pattern.

The unique feature of this interferometer is its ability to study fields scattered by a rough surfaces whose maximal height span exceeds the wavelength of the probing radiation. However, the data collection and processing in this case differ from the ones in the case when the height span is less than the wavelength of the probing radiation. For a specified transverse shift, one controls, using the mirror *M2,* the modulation with a path difference within a range comparable with the wavelength. This results in an intensity modulation between its minimal and its maximal magnitudes for each pixel of the CCD camera. Next, all maximal and all minimal intensity values ore summarized over the entire CCD camera elements, and computes the resulting contrast of the complex interference field is computed. Knowing the contrast of the interference pattern for various transverse shifts, one can reconstruct the transverse coherence function of the field.

Knowing the transverse coherence function of the field, it is possible to estimate:

- the *rms* roughness for slightly rough surfaces,
- the surface height correlation function whose Fourier transformation defines the power spectrum of the surface,
- the correlation exponent for the scattered field.

The described experimental arrangement provides verification of the results of the computer simulation. In order to accomplish this, we prepared a suite of NRSs and FRSs on photoresist by applying a photolithographic technique. An example of the modeled amplitude transmittance of a photo mask is shown in Figure 11. A phase profile of size $450 \times 450\ \mu m$ is obtained photolithographically from this mask. Non-linearities of the height distribution are introduced by changing of the developer concentration as well as through a change in the exposure time. The optical height of the irregularities is controlled using an immersion liquid. The relief of one of the studied surfaces prepared by the described technique is measured by applying the optical profilometry technique and is shown in Figure 12.

The computed and the measured dependences of the statistical moments of the field as a function of z are shown in Figure 13. This shows a good agreement between the simulated and the experimental results, though the experimental data are somewhat less than the computed ones. This discrepancy is believed to be caused by the finite averaging area of the optical elements in the experimental device.

The statistical parameters of the modeled object found by simulation and experimentally are shown in Figure 14. One can see from Figure 14 that

the discrepancy between the simulated and the experimentally obtained parameters is small. This illustrates the high sensitivity of the proposed arrangement as well as its wide metrological capability, as previously stated in Refs. [4,44-46].

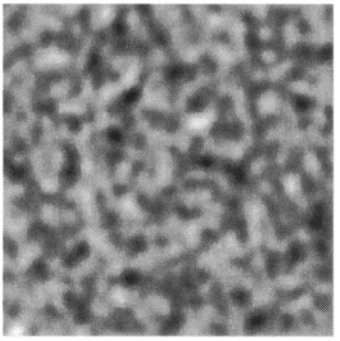

Figure 11. The conversion of an amplitude transmittance distribution of a photo mask into a transmission phase profile.

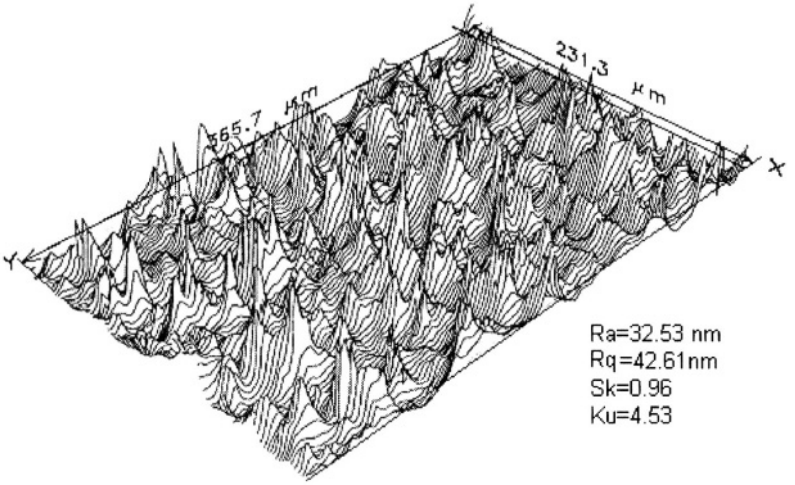

Figure 12. Profilometrically found surface relief structure.

Figure 15 shows the experimentally found power spectrum density function (PSDF) for a FRS represented in log-log scale. One can estimate the fractal dimension of a surface from the slope of the power spectrum, which

is found through Fourier transformation of the correlation function of the surface relief, *h(x,y)*. Its magnitude equals 2.42 for the fractal surfaces.

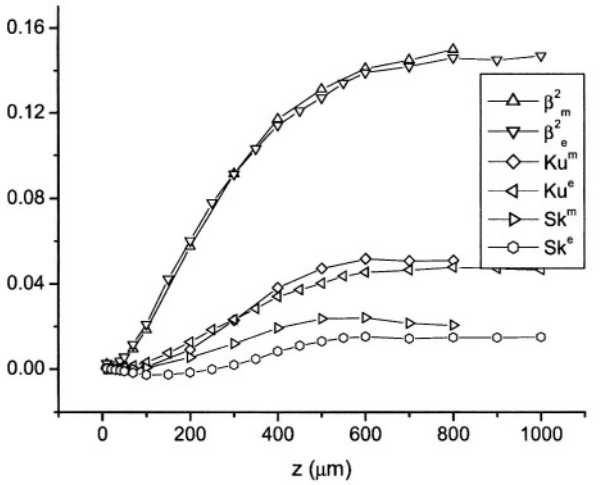

Figure 13. The calculated (index *m*) and the experimentally obtained (index *e*) statistical moments: the scintillation index, β^2, kurtosis coefficient, Ku^f, and asymmetry coefficient, *Sk,* of a field for a non-fractal random surface with $h_{max} = 200$ nm [24] (Copyright @ OSA).

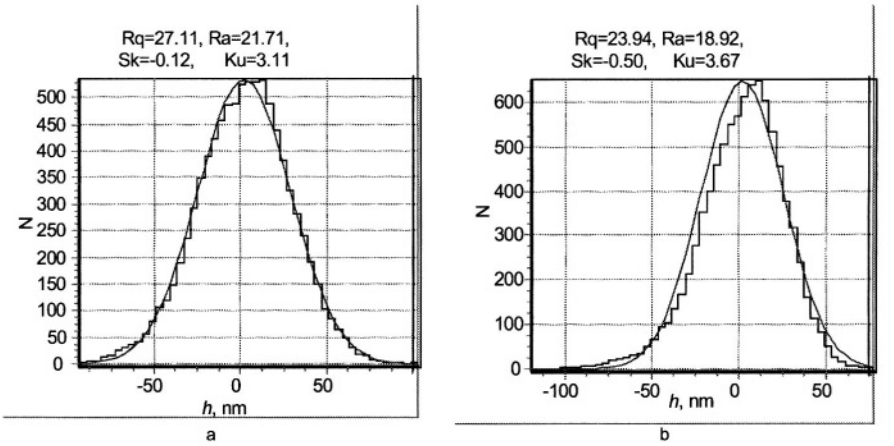

Figure 14. The height distribution for the modeled object (a) and the experimentally obtained height distribution (b). Histograms show the real height distribution, and the solid curve corresponds to a Gaussian distribution with the same mean value and dispersion [24] (Copyright @ OSA).

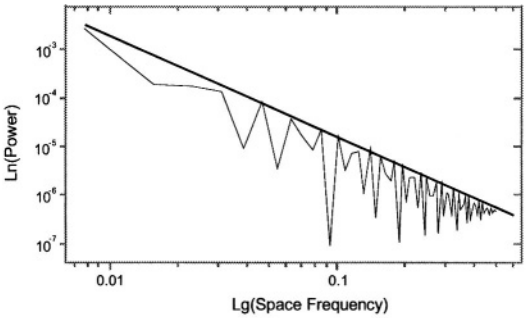

Figure 15. The experimentally found power spectrum density function for a FRS [24] (Copyright @ OSA).

2.6 SINGULAR OPTICS CONCEPT

2.6.1 Introduction

In the case of roughness with large-scale surface inhomogeneities with respect to the wavelength, $\sigma_{\varphi_0}^2 > 1$, unambiguous interconnection between the statistical parameters of the surface roughness, and the amplitude and the phase parameters of the scattered field is lost [4]. Of course, this obstructs the classification of a surface into a random or a fractal structure. The reason is that roughness with large-scale surface inhomogeneities is the main singularity-generating structure responsible for the singularities in the scattered radiation field, such as caustics in the zone of focusing of partial signals [47,48], and amplitude zeroes, which are singularities of the phase of the field [49,50]. It is expected that spatial distributions of both caustics and amplitude zeroes reflect structure irregularities of rough surfaces with large-scale inhomogeneities [51]. Therefore, the map of amplitude zeroes *(zerogram),* as a two-dimensional distribution of points in the observation plane, seems to provide a tool for the diagnostic problem. In fact, the study of the phase structure of a field in the vicinity of the amplitude zeroes shows that the behavior of a phase at a zero-crossing (the point, where the phase is undetermined) may be unambiguously predicted [51]. Furthermore, a convenient interference technique has recently been developed for

determination of the location, signs and topological charges of these amplitude zeroes [52], This provides new attractive feasibilities for non-contact optical classification and, perhaps, for quantitative characterization of rough surfaces with large-scale inhomogeneities [47-56].

Thus, the issue addressed here is looking for the means to obtain diagnostically important data by analyzing the field zerogram and, in part, in revealing statistical and fractal parameters appropriate to classify rough surfaces with large-scale inhomogeneities.

2.6.2 On the Structure of Scattered Radiation Field

Rough surfaces of two kinds (random and fractal) were simulated using procedure described in subsection 2.3.1.

A typical example of the associated plots of amplitude, intensity, and phase of the scattered field is shown in Figure 16.

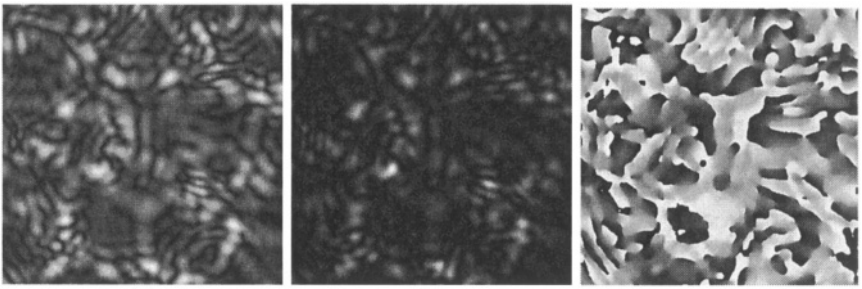

Figure 16. Distributions of the scattered field's amplitude (a), intensity (b), and phase (c) [56] (Copyright @ OSA).

To reveal the amplitude zeroes at the scattered field interferometrically, we developed a routine in *Delphy 6* that permitted us to impose a reference wave U_0 onto the scattered field of interest with a controlled amplitude and phase. The interference angle was specified to at least provide a few interference fringes for each speckle. Spatial distributions of amplitude, intensity, and phase of the scattered field with a superimposed reference wave are shown in Figure 17.

The data for a rough surface structure is in most details primarily reflected in the boundary object field, and in the near-field with respect to an isolated inhomogeneity. These data are easily interpreted, while the direct interconnection exists here between the structural parameters of the surface roughness, and the amplitude and phase parameters of the scattered field. The reasons are [4,10]: (*a*) there is no spatial-frequency filtering at this zone,

(b) the interference of partial scattered waves that accounts for redistribution of amplitude and phase of the field in the far zone, is not developed here.

Simulation for a surface with large-scale inhomogeneities (height span is $5\mu m$ for $\lambda = 0.633\mu m$) shows (see Figure 18) that a well-defined interferogram may be obtained at the boundary field undergoing superposition with a coherent reference wave. Such an interferogram reflects the phase structure of the surface and can be used to obtain conventional statistical parameters characterizing the structure of a rough surface.

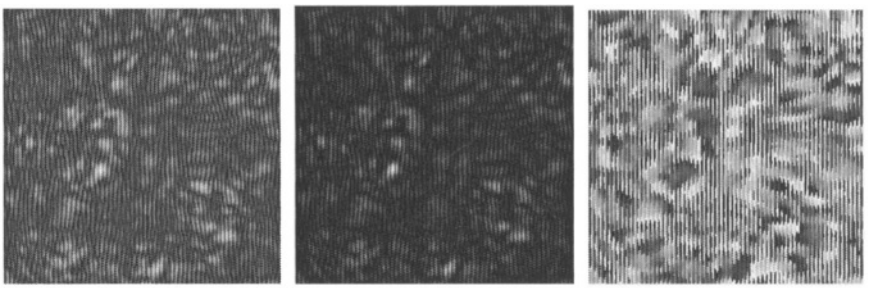

Figure 17. Distributions of the scattered field's amplitude (a), intensity (b), and phase (c) with a superimposed reference wave.

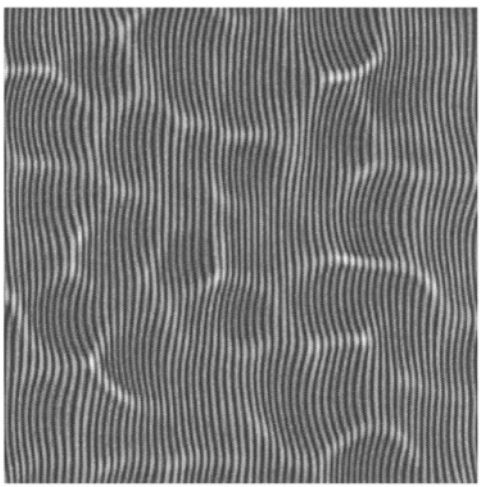

Figure 18. Simulated interferogram at the boundary field of a rough surface [56] (Copyright @ OSA).

Within the domain extending from the boundary object field to the caustics zone, energy redistribution at the scattered field is governed mainly by geometric-optical mechanisms [10]. At the caustics zone the intensity

distribution is only vaguely reflecting the surface properties, see Figure 19. The increased focusing of partial signals is mainly determined by the dispersion of height of the surface irregularities. Unfortunately, the interpretation of such distribution to obtain conventional statistical parameters for quantitative characterizing the roughness is rather difficult.

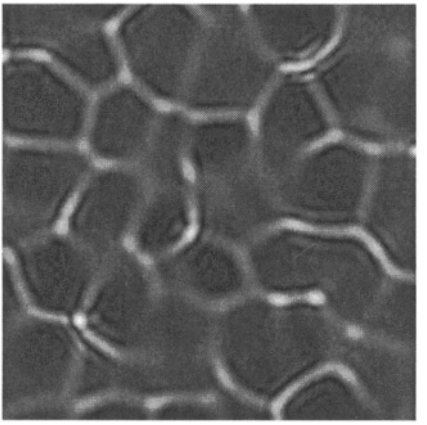

Figure 19. Intensity distribution at the caustics zone of a rough surface.

Concurrently, the caustics zone is the domain, where the phase singularities of a field known as 'optical vortices' nucleate [50,53]. Phase singularities correspond to amplitude zeroes of a field and are revealed using a coherent reference wave, as typical forklets (bifurcations of interference fringes) shown in Figure 20.

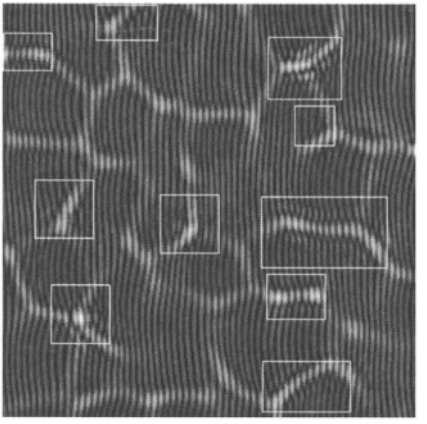

Figure 20. Interferogram of a field exhibiting phase singularities; the areas of most interest are indicated by squares.

One can see secondary diffraction maxima of lower intensity decorating the points of sharp focusing. Going from any caustics to the closest secondary diffraction maximum, one meets amplitude zeroes of the field revealed by bifurcation and shift of interference fringes. Such wave-front defect is classified as an *edge dislocation,* which in general is unstable [50].

The *screw-type* dislocations are the most widespread and spatially stable kind of wave-front defects. Any equi-phase surface of a field in the closest vicinity of an amplitude zero is helical, and the axis of the helicoid coincides with the line of the zero amplitude [54]. Interference of such a singular phase structure with a coherent reference wave results in a forklet. Alongside with conventional forklets corresponding to bifurcations of interference fringes associated with amplitude zeroes with a topological charge ± 1, one expects to observe more complicated interference patterns associated with higher-order topological charges of screw dislocations, when the circumference around the axis of a phase singularity leads to the change of the phase value an integer number of $2\pi n$, where n- is the integer numbers, see Figure 21 [53].

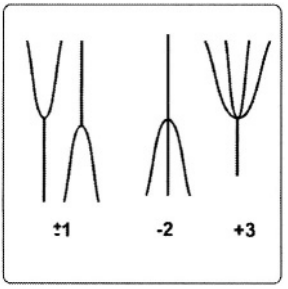

Figure 21. Examples of interference patterns corresponding to amplitude zeroes with various topological charges [53].

As the plane of observation is displaced from the caustics domain, the field structure increases in complexity due to interference of superimposed wavelets.

An interferometrically analyzed field structure shows a gradual increase of the number of amplitude zeroes. Thus, we checked a triple forklet at a distance of $35\mu m$, which would correspond to the amplitude zero with topological charge 2, see Figure 22*(b).* However, a detailed study conducted by altering of the interference angle (in both sagittal and meridional directions) shows, see Figures 22(*c*) and 22(*d*), that one deals with two isolated, however very closely spaced, one-charged vortices. Really, a little change of the interference angle, as well as a little change of the observation plane results in the decay of a triple forklet into two conventional ones, see Figure 22 *(e).* Thus, one can conclude that an observed triple forklet is only

caused by an accidental choice of the observation plane. The last conclusion is in agreement with well-known statement that higher-order amplitude zeroes are spatially unstable, and that they are decaying into isolated one-charged zeroes of the same sign [54]. Note that amplitude zeroes with high topological charges may be synthesized artificially using the technique of computer-generated holograms and studied in proper experimental arrangement [55].

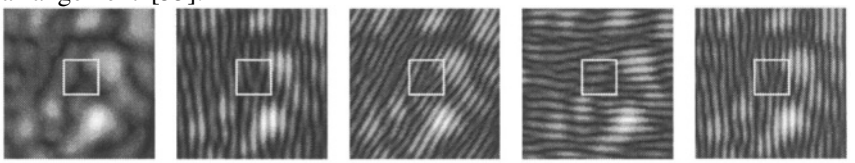

Figure 22. Spatial intensity distribution (a) and interferograms (b) to (e) of the scattered field for a rough surface at a distance of $35\mu m$ from the object for different interference angles. The area of interest demonstrating the field transformation is marked with squares [56] (Copyright @ OSA).

Let us now consider the key problem of interconnection between characteristics of surface roughness and phase singularities of the scattered field. Here we are looking for the parameters of the field of phase singularities, which reflect the parameters of the surface topography.

According to the conventional theory of singularities, the 'strength of a singularity' is defined by the rate of decrease of the absolute value of a function *vs* distance from the singular point. A scalar function *F(x)* is said to be Hölder of exponent $h_F(x_0)$ at a given point x_0 if, for any point y close enough to x_0, the following inequality holds: $|F(y)-F(x_0)| < A_0|y-x_0|^{h_F(x_0)}$, A_0 being a constant that depends on the point x_0; $h_F(x_0) < 1$ [32].

Thus, the physical interpretation of the 'strength of a singularity' is unambiguous. In the case of particular interest in this study, the 'strength of a singularity' is associated with the rate of change of the wave front, which is estimated by the number of forklets per unit of solid angle. This parameter is close in its physical meaning to the topological charge of the field's amplitude zeroes. In fact, high spatial density of isolated *elementary* (of topological charge ± 1) amplitude zeroes of the same sign may be considered as an indirect indication that the complex, higher-order amplitude zero existed in the vicinity.

2.7 ZEROGRAM TECHNIQUE

Scattered optical fields computed using the diffraction integral (see equation 12) are represented by two-dimensional matrices of complex amplitudes $A(x,y)$, 400×400 pixels, in our case. The areas of size $40\times40\mu m$ are analyzed at various distances from the surface. To determine the points of zero amplitude, we solve the equations:

$$\begin{cases} \mathrm{Re}\left[A(x,y)\right]=0, \\ \mathrm{Im}\left[A(x,y)\right]=0. \end{cases} \tag{23}$$

For each of the analyzed fields we obtain a set of coordinates of points where the amplitude vanishes. Using these data we obtain a zerogram of the field, see Figure 23.

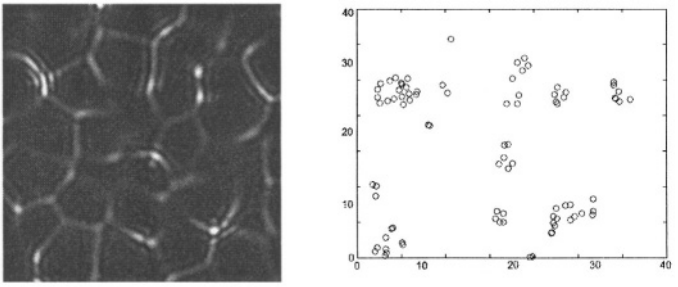

(a) (b)

Figure 23. Intensity distribution of the field scattered at a random rough surface at a distance of 10 μm (*a*); zerogram of this field *(b).*

This zerogram has been compared with the corresponding one obtained using a reference wave. In the last case, we estimate the number and location of amplitude zeroes by the number and location of interference forklets. The discrepancy of these data does not exceed 30%, and is caused by limitations of the interference technique, which relies on visual discrimination of the amplitude zeroes.

As it has been noted above, the amplitude zeroes are absent within the domain extending from the boundary field to the caustics zone. As the relation between the phase variance and the correlation length shortens, the distance of focusing and the domain of nucleation of amplitude zeroes moves toward the object.

We implement the following procedure to characterize the distribution of amplitude zeroes. We start by counting the amplitude zeroes per unit area of the field. A simulated area of the field, $S_0 = 40 \times 40 \mu m^2$, is divided into equally sized sub-areas $s(i,j)$, where $i,j = 1,2,...,\sqrt{K_0}$ are the indices of the sub-areas, $K_0 = S_0 / s(i,j)$ is the number of sub-areas, and $\sum_{i,j} s(i,j) = S_0$. To provide sufficient statistics for obtaining reliable results, we specify the size of sub-areas for various objects and for various observation zones proceeding from the proper average value of the local density of amplitude zeroes, $\bar{n}$, following the rule: $s(i,j) = \bar{n} S_0 / N_0$ with $\bar{n} = 5$. We then count the amplitude zeroes, $n(i,j)$ for each sub-area $s(i,j)$ and find the total number of amplitude zeroes over the area S_0, $\sum_{i,j} n(i,j) = N_0$. Next, we determine the local density of amplitude zeroes at each sub-area:

$$p(i,j) = \frac{n(i,j)}{s(i,j)}. \tag{24}$$

The obtained distribution of local density of amplitude zeroes is represented by histograms illustrating the dependence of the number of sub-areas with local density p, K_p, as a function of p.

A statistically homogeneous spatial distribution of amplitude zeroes is reflected in a narrow histogram with a half-width $\sim 0.07 \mu m^{-2}$, see Figure 24. Subsequently, the half-width of a histogram of the corresponding distribution serves as a useful parameter well suited for qualitatively comparison of the fields of different nature.

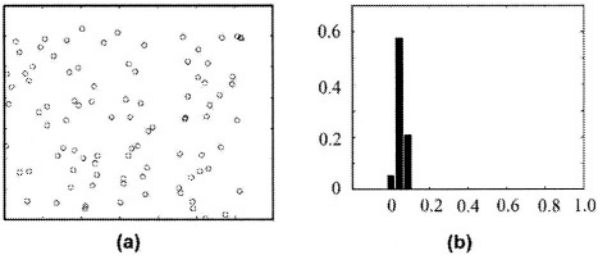

Figure 24. Zerogram of the field with statistically homogeneous, uniform spatial distribution of amplitude zeroes (a), and histogram of local density of amplitude zeroes, K_p/K_0 *vs* p, μm^{-2}, (b).

This is the key point of our consideration: any deviation of the distribution function for the amplitude zeroes from the uniform one, in part due to clustering of amplitude zeroes, is inevitably reflected into spreading

of the histogram. This accounts for zones (sub-areas) with higher local density of amplitude zeroes. This conclusion is illustrated in Figure 25.

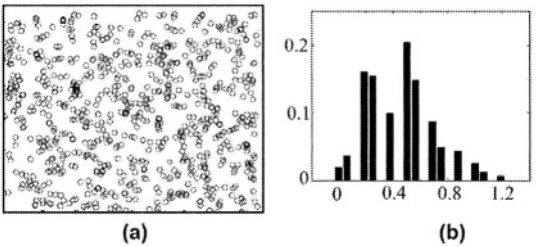

Figure 25. Zerogram of the field with non-uniform distribution of amplitude zeroes (a), and histogram of the local density of amplitude zeroes, K_p/K_0 *vs p,* μm^{-2}, (b).

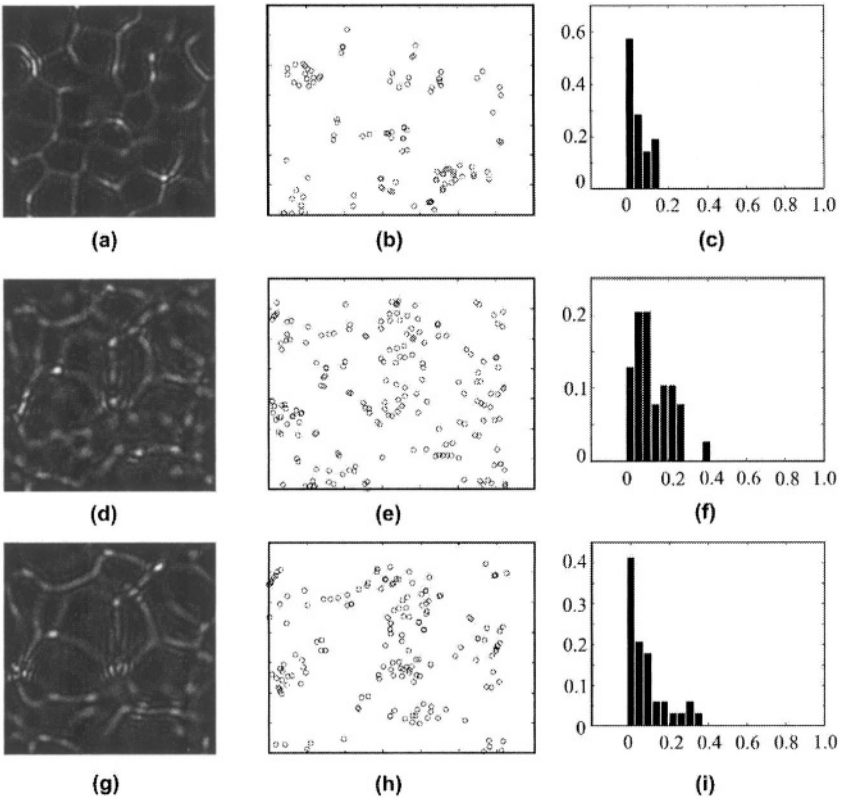

Figure 26. The set of intensity distributions, (a), (d), (g), zerograms, (b), (e), (h), and histograms of distributions of local density of amplitude zeroes, K_p/K_0 *vs p,* μm^{-2}, (c), (f), (i), at a distance of $10\mu m$ from the rough surfaces - random (a), (b), and (c); fractal surface, smoothed following a normal law over 3 pixels (d), (e), (f); fractal surface, smoothed following a normal law over 5 pixels (g), (h), (i) [56] (Copyright @ OSA).

Let us analyze zerograms of the fields produced by some test-objects, namely, by a random rough surface, and by two fractal rough surfaces with the same basic parameters (an area of the field simulated is $S_0 = 40 \times 40 \mu m^2$, the span of heights is $5 \mu m$, and the height dispersion is $1.25 \mu m$) *vs* spacing of the surface and the observation plane. Figure 26 shows the set of the field's intensity distributions, zerograms, and histograms of local density of amplitude zeroes, corresponding to the caustics zone.

One can see that a half-width of a histogram for a fractal surface exceeds the one for a random rough surface by approximately a factor of two, though the last also exhibits inhomogeneity of the spatial distribution of amplitude zeroes. The inhomogeneity of the distribution of amplitude zeroes is caused by the concentration of amplitude zeroes in the caustics zone, where the wave fronts change rapidly, which results in clustering of the amplitude zeroes. The steepness of the wave front determines the density of amplitude zeroes in some area. As a matter of fact, the field at the focus undergoes considerable diffraction spreading: one observes secondary diffraction maxima in the vicinity of the main one, and adjacent diffraction maxima are separated by amplitude zeroes.

As the observation plane is removed to a distance of $20 \mu m$ from the surface, one observes an increased width of the histograms due to both an increase in the number of amplitude zeroes and the associated clustering, see Figure 27.

Such behavior of a field is caused mainly by the diffraction spreading, which is most pronounced in the caustics zone, as well as due to engagement of additional focused wave fronts produced by the object's inhomogeneities of different phase variance (different inhomogeneity scales). Note that spreading of histograms is typical in the caustics zone for a random rough surface too. This can be explained by the effect of smoothing a surface and, thus, the focusing. This result becomes negligible at larger distances from the surface. Distinguishing feature of a random rough surface from fractal one is that a plane (or line) is the initiator for construction of random surface, which does not possess structural self-similarity (both in simulation and in physical experiment).

Clustering of amplitude zeroes observed for fractal rough surfaces is explained by the statistical self-similarity of the structure of such surfaces. In this case, multiple step-by-step changing of the size of the surface of interest is accompanied by a corresponding changing of the phase variance. This causes change of the location of the caustics zone. Thus, there is the possibility for tracking the distance-dependent changes of the caustics zones. It is founded on the cascade procedure for fractal surface construction.

The mentioned dependence of the phase variance on the size of the analyzed area is not revealed for random rough surfaces. As a consequence,

at a distance of $50\mu m$ amplitude zeroes produced by such a surface are uniformly distributed, as it is seen from Figure 28.

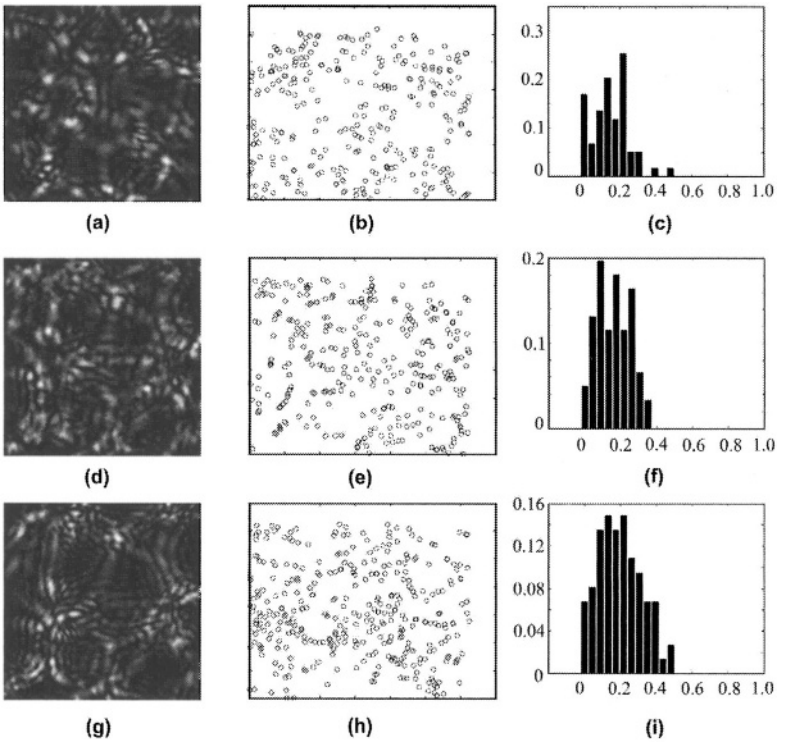

Figure 27. The set of intensity distributions, (a), (d), (g), zerograms, (b), (e), (h), and histograms of distributions of local density of amplitude zeroes, K_p/K_0 *vs* p, μm^{-2}, (c), (f), (i), at a distance of $20\mu m$ from the rough surfaces - random (a), (b), and (c); fractal surface, smoothed following a normal law over 3 pixels (d), (e), (f); fractal surface, smoothed following a normal law over 5 pixels (g), (h), (i) [56] (Copyright @ OSA).

Growing of clusters for the amplitude zeroes for fractal rough surfaces is explained by the above-mentioned reasons. The half-width of the associated histogram increases, being four-times larger than in case of a random rough surface.

Thus, a recurrent algorithm for construction of a fractal structure (either deterministic or statistical) presumes some scale-dependent self-similarity of the statistical phase structure of the surface. This initiates a pronounced tendency to cascade focusing of partial signals at various (but predictable) distances from the surface. This statement is indirectly confirmed by the fact that step-by-step diminishing of a fractal surface will make the height dispersion of surface irregularities decrease as well. As a consequence, the

phase variance of the radiation scattered by such a surface decreases correspondingly.

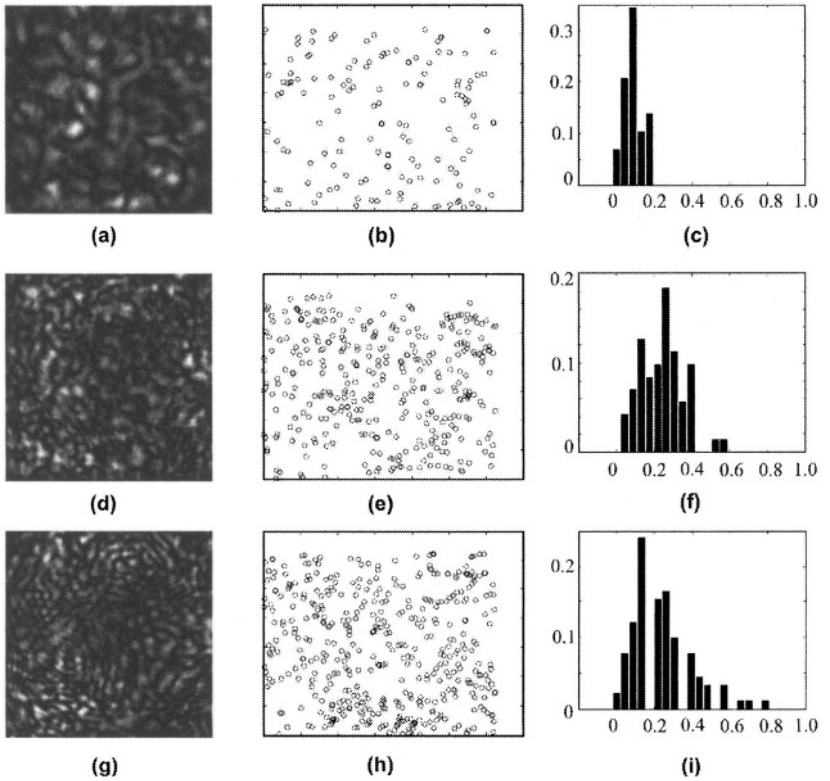

Figure 28. The set of intensity distributions, (a), (d), (g), zerograms, (b), (e), (h), and histograms of distributions of local density of amplitude zeroes, K_p/K_0 *vs* p, μm^{-2}, (c), (f), (i), at a distance of $50\mu m$ from the rough surfaces - random (a), (b), and (c); fractal surface, smoothed following a normal law over 3 pixels (d), (e), (f); fractal surface, smoothed following a normal law over 5 pixels (g), (h), (i) [56] (Copyright @ OSA).

Uniform spatial distribution of amplitude zeroes in the far zone corresponds to narrowing of histograms both for a random rough surface and for the fractal ones, cf. Figure 29. Therefore, the total number of amplitude zeroes per unit of area decreases due to diffraction spreading of the field.

Thus, one can conclude, that the domain from the caustics zone to the far field (where the statistics approaches the normal statistics and the density of spatial distribution of amplitude zeroes becomes uniform) is of most importance for the problem of rough surface classification and quantitative diagnostics.

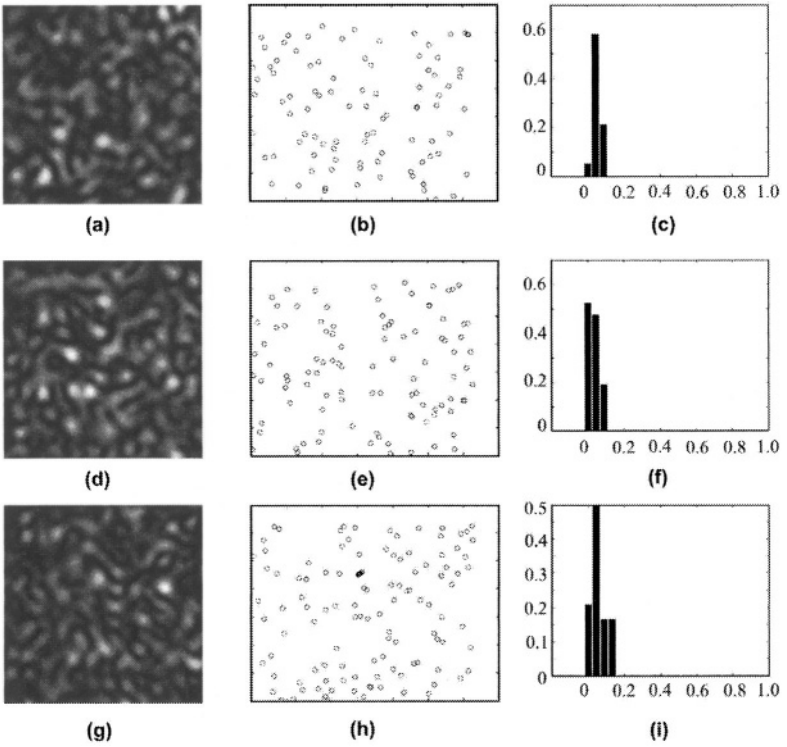

Figure 29. The set of intensity distributions, (a), (d), (g), zerograms, (b), (e), (h), and histograms of distributions of local density of amplitude zeroes, K_p/K_0 *vs* p, μm^{-2}, (c), (f), (i), at a distance of $500\mu m$ from the rough surfaces - random (a), (b), and (c); fractal surface, smoothed following a normal law over 3 pixels (d), (e), (f); fractal surface, smoothed following a normal law over 5 pixels (g), (h), (i).

2.8 OPTICAL CORRELATION TECHNIQUE

2.8.1 Introduction

Here we present novel optical correlation measuring devices, whose operation is based on the use of the RPS model considered in subsection 2.2.1 and whose efficiency is proved in subsection 2.3.1.

We propose two techniques for measuring of roughness, based on measurement of a phase variance of the boundary object field and on a transverse coherence function of a field, as well as the devices implementing these techniques [44,46].

2.8.2 Phase Variance Measuring Technique

Using an interrelation between the height parameters of surface roughness and the phase parameters of the boundary object field, one obtains according to the relation that follows from equation 21:

$$rms = \frac{\lambda}{4\pi}\sqrt{\frac{\langle I_S(x, y)\rangle}{I_0}} \tag{25}$$

The arrangement used for the measurement is shown in Figure 30 [44,46]. A telescope consisting of two objective lenses transforms a light beam from a single-mode laser source into a plane wave, which then undergoes amplitude splitting into a reference and an object wave using a beamsplitter. The object wave reflected by the beamsplitter is focused by an objective lens onto the rough surface of a sample. The reflected radiation is used to form the surface image in the plane of a 2×2 position-sensitive photodetector array. The radiation reflected by the mirror interferes with the object wave forming an interference pattern with fringes localized at infinity.

The zero-order interference fringe is automatically kept within the 2×2 position-sensitive photodetector array by means of a transverse displacement of the micro-objective in the reference arm using two electric motors, and a longitudinal displacement of the mirror using a piezoceramic modulator, which simultaneously accomplishes amplitude modulation of the resulting light beam. The output signal from the 2×2 position-sensitive photodetector array is fed into the phase comparators which generate control signals for the motors and the piezoceramic modulator. The net signal is transformed then into a R_q value using the analogue processing unit, and is displayed on the indicator.

In general case, when the reference-to-object intensity ratio is not equal to unity, we use the following equation derived from equation 25 [44]:

$$rms = \frac{\lambda}{4\pi}\sqrt{2 - \frac{I_{\max} - I_{\min}}{\sqrt{I_r}\sqrt{I_o}}}, \tag{26}$$

where $I_{\max}$ and $I_{\min}$ are the maximum and the minimum resulting intensities, respectively, and I_r and I_0 are the reference and the object beam intensities, respectively.

The distinguishing feature of both this and all devices discussed below consists in the modulation data transducing. It relieves of the necessity to provide protection of the measuring device against vibrations. As a result,

the sensitivity threshold for such devices approaches the level provided in heterodyne devices [4].

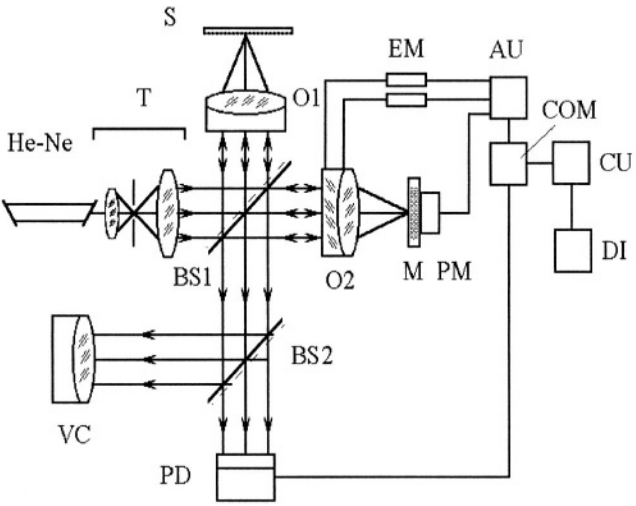

Figure 30. Experimental arrangement for measuring the degree of low-reflectance surface roughness: He:Ne - laser, T - telescope, BS1, BS2- beam-splitters, O1,O2 - objective lenses, S - sample, M - mirror, PM - piezoceramic modulator, PD-2×2 position-sensitive photodetector array, VC- visualization channel, EM - electric motors, AU - automatic zero fringe adjustment unit, COM - comparator, CU - analogue R_q calculation unit, DI - digital indicator.

The arrangement shown in Figure 30 can be custom-designed to meet specific requirements for measuring objects of different sizes under various conditions. The above arrangement permits measurements of low-reflectance surfaces since allowance has been made for the relative reflectance coefficient of the surface measured with respect to the reference mirror.

Usage of this technique at various technological stages of making microelectronic devices includes the quality control of finishing of silicon plate's surfaces, control of the aluminium-evaporated plates and the photoresist-evaporated ones, as well as control of the etched plates, etc. The inclusion of a visual channel in the device considered permits choosing the surface area of interest. Of course, usage of any contact profilometric technique for this purpose is prohibited.

It is interesting to note that moderate modification of the measuring technique permits to measure a height distribution function of surface microirregularities [46].

The laboratory version of the device for roughness control of plane and spherical surfaces is shown in Figure 31 (Device 1).

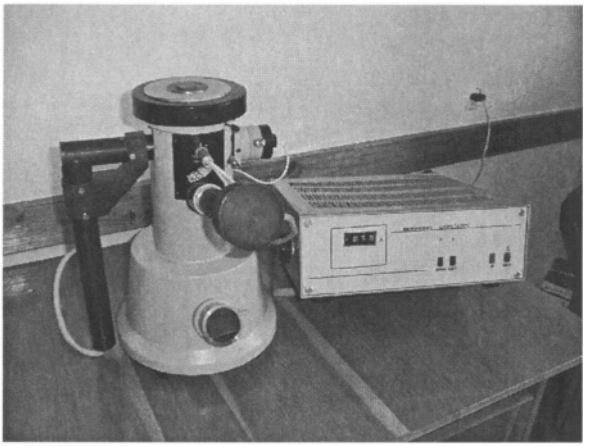

Figure 31. Device 1.

Technical parameters of Device 1:

- measured RMS range - 0,002 to 0.06 μm;
- measurement accuracy - 0.0005 μm;
- measurement scheme – microinterferometer;
- indication rate - one measurement per five second.

Fields of application of Device 1:

- plane and spherical surfaces with the radius of curvature larger than 0.1m;
- polishing machine tool, this device was used for the surface quality control during making of the detail;
- device can be made as a stationary instrument.

2.8.3 Transverse Coherence Function Measuring Technique

Another method for measuring the phase variance utilizes the relationship between the transverse coherence function $\Gamma_{\perp}(\rho)$ of the scattered field, on the one hand, and the statistical parameters of the object (equation 4). In deriving the equation 4, Gaussian statistics of the object is assumed. An important point is that, for objects with $\sigma_{\varphi_0}^2 < 1$, the transverse coherence function $\Gamma_{\perp}(\rho)$ is given by the transverse coherence function of the boundary field $\Gamma(\rho)$ in any recording zone. It is seen from equation 4 that, by taking the logarithms of both sides, one can obtain an expression for the object phase variance.

By making the transverse displacement ρ of optically mixed components larger than the inhomogeneity correlation length l_{φ_0} when measuring the $\Gamma_{\perp}(\rho)$ function, one gets $K_{\varphi_0}(\rho)=0$, that immediately gives the $\sigma^2_{\varphi_0}$ value [44].

The transverse coherence function $\Gamma_{\perp}(\rho)$ is known to be given by the boundary field coherence function $\Gamma_{\nu}(\rho)$, and can be defined as equation 4. Thus, by measuring $\Gamma_{\perp}(\rho)$ and making the relative displacement ρ of optically mixed components larger than the correlation length of the phase inhomogeneities l_{φ_0}, one can set $K_{\varphi_0}(\rho)=0$, and get [44]

$$\Gamma_{\perp}(\rho > l_{\varphi 0}) = \frac{I_{\max} - I_{\min}}{I_{\max} + I_{\min}} = \exp\left\{-\sigma^2_{\varphi 0}\right\} \tag{27}$$

This relation is commonly used in rough surface diagnostics.

The general schematic of the device that is intended for measuring the *rms* slightly rough surfaces is shown in Figure 32 [44].

A plane wave produced by the telescope T, consisting of a microscope objective, a pinhole and an objective lens, undergoes a total reflection in the polarizer cube PBS, and passes through the quarter-wave plate λ/4 after which it hits the surface S to be measured. The double-pass of the plane wave through the quarter-wave plate results in the rotation of the plane of polarization by 90°. Thus, all the reflected light with polarization equal to the polarization of the incident light passes through the polarizer cube. The cube, together with the two calcite wedges W, one of which is stationary, the other movable, and the analyzer A, make up a scanning polarization interferometer. The relative displacement of the interferometer beams is determined by the separation between the wedges. Finally, the displacement of the movable wedge results in the net intensity minima $I_{\min}$ and maxima $I_{\max}$, which are recorded by the photodetector PD. The height deviation *rms* that follows from equation 27, can be found from the relation

$$rms = \frac{\lambda}{4\pi}\sqrt{-\ln\frac{I_{\max} - I_{\min}}{I_{\max} + I_{\min}}}. \tag{28}$$

The information contained in the resulting interference pattern is extracted by transforming the optical signals into electric ones with subsequent processing in the analogue electronic unit CU.

The device can be made either as a measuring head, or as a stationary instrument, depending on the size and the position of the object to be controlled. The advantages of the device over those currently in use are its speed, its high precision, and the non-contact nature of the measurement

combined with the possibility of averaging over a large number of roughness elements.

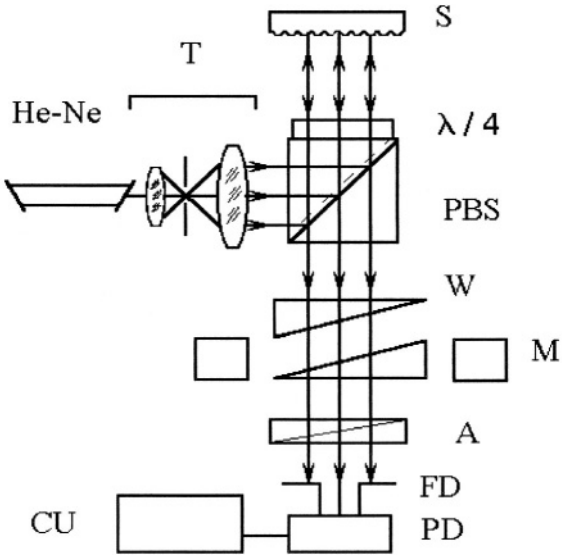

Figure 32. Experimental arrangement for measuring the degree of arbitrary surface roughness: He:Ne - laser, T - telescope, PBS- polarizing beamsplitter, S - sample, W- calcite wedges; M - electromechanical modulator, A - analyzer; FD - field-of-view diaphragm; PD - photodetector, CU - analogue R_q calculation unit.

Therefore, in a shearing interferometer, the object field interferes with itself, rather than with a reference field, thus making possible the measurements of arbitrarily shaped surfaces with radii of curvatures larger than 0.2 m. This is especially important, e.g., in the photochemical industry to monitor the quality of calander shafts, in the space industry to monitor the quality of mirrors fabricated by diamond micro-sharpening etc.

Being directly mounted at the polishing machine-tool, this device was used for surface quality control during processing. Calender shafts and spherical mirrors were monitored during fabrication by diamond micro-sharpening, and sensitivity of the *rms* height parameter down to 10Å was achieved.

We fabricated two versions of the device for a surface roughness control based on measuring of the field's transverse coherence function:

- stationary device which can be mounted on the processing tool (Figure 33, Device 2);
- portable device for control of large-area or small-area surfaces (Figure 34, Device 3).

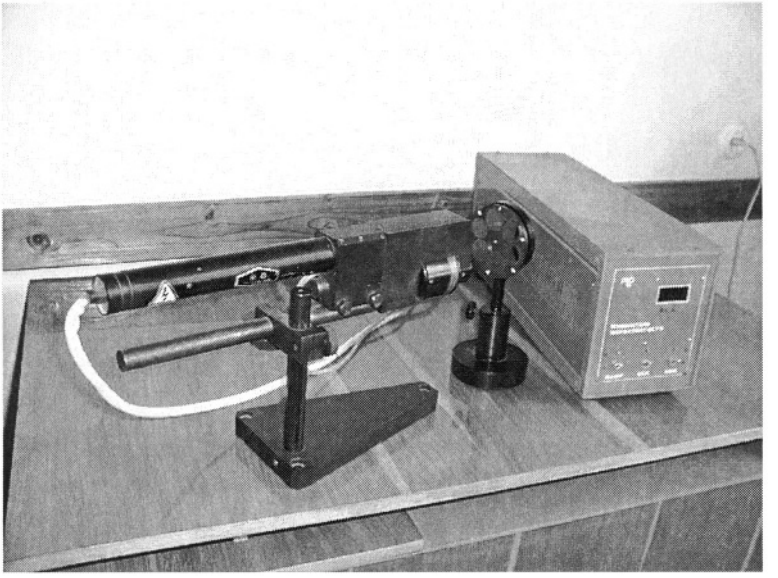

Figure 33. Stationary device which can be mounted on the processing tool (Device 2)

Technical parameters of Device 2:

- measured RMS range – 0,002 to 0.06 μm;
- measurement accuracy 0.001 μm;
- measurement scheme - polarization interferometer;
- indication rate – one measurement per second.

Fields of application of Device 2:

- arbitrarily shaped surfaces with the radius of curvature larger than 0.2m;
- the photochemical industry to monitor the quality of calender shafts;
- space industry to monitor the quality of mirrors fabricated by diamond micro sharpening;
- polishing machine tool, this device was used for the surface quality on-line control.

Technical parameters of Device 3:

- measured RMS range - 0,003 to 0.05 μm;
- measurement accuracy - 0.002 μm;
- measurement scheme - polarization interferometer;
- indication rate - one measurement per second.

Figure 34. Portable device for control of surfaces (Device 3).

Fields of application:

- polishing machine tool, this device was used for the surface quality control during making of the detail;
- device can be made either as a measuring head, or as a stationary instrument, depending on the size and the position of the object to be controlled.

2.8.4 Results of Testing

Measurements were performed on reflecting tool-steel samples (Table 3, samples NN 1-4) and surfaces of monocrystal germanium samples (Table 3, samples NN 5-8) whose parameters were in agreement with the model of infinitely extended RPS. Thus the phase correlation length, l_{φ_0} of the inhomogeneity, was in the range 18-26 μm, while the roughness phase variance, $\sigma^2{}_{\varphi_0}$, was always less than unity.

Table 3 compares the result on the *rms* parameter for eight samples obtained using a TALYSURF-5M120 profilometer to those obtained using Devices 1-3. The values are seen to agree to within 30%. The discrepancy, which is systematic, is probably due to a profilometric measurement error and a violation of the infinite extension condition. Reproducibility of the

interference measurements is about three times as high as that of the profilometric ones.

Table 3. RMS parameters for tool-steel samples (NN 1-4) and surfaces of monocrystal germanium samples (NN 5-8).

	rms (nm)			
N	TALYSURF	DEVICE 1	DEVICE 2	DEVICE 3
1	3	3.2	3.3	4
2	6	6.6	6.5	7
3	10	10.5	10.4	12
4	32	32.6	33.1	34
5	5	5.3	5.4	6
6	12	13.2	13.5	14
7	28	30.1	29.8	31
8	61	65.0	66.0	64

Roughness parameters obtained profilometrically are systematically less than the interference data. It can be explained by undertouching of the profile or by sharpening of a surface by the profilometer needle.

The lower limit of surface roughness measurements is 0.002 μm. The surfaces in question can be classified as optical surfaces such as optical element surfaces, crystal surfaces in microelectronics, machined surfaces, etc.

2.9 CONCLUSIONS

It has been established that if $\sigma_{\varphi_0}^2 < 1$, one can deduce the type of surface under study, i.e., if it is a FRS or a NRS one, by estimating the amplitude dispersion and the phase variance of the scattered radiation field.

It has been established that the kurtosis coefficient and the correlation exponent of the field are highly sensitive to changes of the surface irregularities. Thus, the kurtosis coefficient can be used as the diagnostic parameter within the height span from 0.1 to 20 μm, while the correlation exponent can be used as the diagnostic parameter within the height span from 0.8 to 20 μm (for $\lambda = 0.63$ μm).

The proposed measuring device has the following advantages: these are a high sensitivity, high operation speed, protection against vibrations, and an ability to probe surfaces whose maximal height span, $h_{\max}$, exceeds the

wavelength of the probing radiation. At the same time, this device possesses diverse functional characteristics. Namely, it facilitates measuring of the statistical moments and the dimensional parameters of NRS and FRS with various degrees of applied nonlinearities.

The spatial distribution of amplitude zeroes of the field scattered by a rough surface, from the caustics zone to the far zone, reflects the irregularities of the surface of interest. The half-width of histograms of local density of amplitude zeroes estimated at various distances from a surface differs considerably from random and fractal surfaces.

We also presented optical correlation device for diagnostics of slightly rough surfaces, which exhibited the advantages of them in fast on-line roughness control.

It is worth to note that the use of the considered approaches and techniques is not restricted by the evaluating of rough surfaces encountering in various branches of industry. As a matter of fact, the objects of different character whose transform the phase structure of a field in transmitting or reflecting radiation may be also described and evaluated within the framework of the proposed set of statistical and fractal parameters. The introduced diagnostic techniques may be applied to the investigations of biotissues, such as skin, eye cornea, finger-nail, hair, into study of tissue samples (biopsy) of cartilage, osseous tissues, growing cell structures, etc. Prospects of new applications of these techniques for monitoring of surroundings as laboratory techniques for control of various films, thin coatings, oxides arising at surfaces in atmosphere and aqueous medium are also imagined as very promising.

REFERENCES

1. J.M. Bennett and L. Mattson, *Introduction to Surface Roughness and Scattering* (Optical Society of America, Washington, D.C., 1989).
2. J.M. Bennett, "Surface Roughness Measurement," in *Optical Measurement Techniques and Applications,* P. K. Rastogi, ed. (Artech House Inc., Norwood,Mass., 1997), 341-367.
3. J.A. Ogilvy, *Theory of Wave Scattering from Random Rough Surfaces,* (Adam Hilger, Bristol, Philadelphia and New York, 1991).
4. O.V. Angelsky, P.P. Maksimyak, S. Hanson, *The Use of Optical-Correlation Techniques for Characterizing Scattering Object and Media,* **PM71** (SPIE Press, Bellingham, 1999).
5. P. Beckmann and A. Spizzichino, *The Scattering of Electromagnetic Waves from Rough Surfaces* (Pergamon Press, London, 1963).
6. H.E. Bennett and J.O. Porteus, "Relation between surface roughness and specular reflectance at normal incidence," *J. Opt. Soc. Am.* **51,** 123-129 (1961).
7. J.M. Elson and J.M. Bennett, "Vector scattering theory," *Opt. Eng.* **18**, 116-124 (1979).
8. F.E. Nicodemus, "Reflectance nomenclature and directional reflectance and emissivity," *Appl. Opt.* **9**, 1474-1475 (1970).

9. T.V. Vorburger, E. Marx, and T.R. Lettieri, "Regimes of surface roughness measurable with scattering," *Appl. Opt.* **32**, 3401-3408 (1993).
10. S.M. Rytov, Yu.A. Kravtsov, and V.I. Tatarsky, *Principles of Statistical Radiophysics,* (Springer, Berlin, 1989).
11. V.P. Ryabukho, "Interferometry of speckle-fields at zone of diffraction of the focused spatially modulated laser beam at random phase screen," *Opt. Spectrosc.* **94**, 513-520 (2002).
12. E.L. Church, "Fractal surface finish," *Appl. Opt.* **27**, 1518-1526 (1988).
13. J.C. Russ, *Fractal Surfaces* (Plenum Press, New York, 1994).
14. S. Davies and P. Hall, "Fractal analysis of surface roughness using spatial data," *J. Royal Statist. Soc.* **61**(1), 1-27 (1999).
15. I.A. Popov, L.A. Glushchenko, and J. Uozumi, "The study of fractal structure of ground glass surface by means of angle resolved scattering of light," *Opt. Comm.* **203**, 191-196 (2002).
16. E.L. Church, "Comments on the correlation length," *Proc. SPIE* **680**, 102-114 (1986).
17. B.B. Mandelbrot, *The Fractal Geometry of Nature* (Freeman, New York, 1982), Chapt.6., 37-57, and Chapt.39., 362-365.
18. E. Feder, *Fractals* (Plenum, New York, 1988).
19. K. Nakagawa, T. Yoshimura, and T. Minemoto, "Surface-roughness measurement using Fourier transformation of doubly scattered speckle pattern," *Appl. Opt.* **32**, 4898-4903 (1993).
20. A. Dogariu, J. Uozumi, and T. Asakura, "Sources of error in optical measurements of fractal dimension," *Pure. Appl. Opt.* **2**, 339-350 (1993).
21. D.J. Whitehouse, "Fractal or fiction," *Wear* **249**, 345-353 (2001).
22. Y.-P. Zhao, G.-C. Wang, and T.-M. Lu, "Diffraction from non-Gaussian rough surfaces," *Phys. Rev. B* **55**, 13938-13952 (1997).
23. Y.-P. Zhao, C.-F. Cheng, G.-C. Wang, and T.-M.Lu, "Power law behavior in diffraction from fractal surfaces," *Surface Science* **409**, L703-L708 (1998).
24. O.V. Angelsky, P.P. Maksimyak, V.V. Ryukhtin, and S.G. Hanson, "New feasibilities for characterizing rough surfaces by optical-correlation techniques," *Appl. Opt.* **40**, 5693-5707 (2001).
25. O.V. Angelsky, D.N. Burkovets, A.V. Kovalchuk, and S.G.Hanson "Fractal description of rough surfaces," *Appl. Opt.* **41**, 4620-4629 (2002).
26. O.V. Angelsky and P.P. Maksimyak, "Optical diagnostics of random phase objects," *Appl. Opt.* **29**, 2894-2898 (1990).
27. Yu.I. Neymark and P.S. Landa, *Stochastic and Chaotic Oscillations* (Nauka, Mascow, 1987).
28. E.L. Church, H.A. Jenkinson, and J.M. Zavada, "Relationship between surface scattering and microtopographic features," *Opt. Eng.* **18**, 125-136 (1979).
29. E.L. Church and P.Z. Takacs, "Effect of non-vanishing tip size in mechanical profile measurements," *Proc. SPIE* **1332**, 504-514 (1991).
30. K.A. O'Donnell, "Effect of finite stylus width in surface contact profilometry," *Appl. Opt.* **32**, 4922-4928 (1993).
31. R.S. Sayles and T.R. Thomas, "Surface topography as a nonstationary random process," *Nature* **271,** 431-442 (1978).
32. A. Arneodo, "Wavelet analysis of fractals" in *Wavelets,* G. Erlebacher, M. Y. Hussaini, L. M. Jameson eds. (Oxford University Press, Oxford, 1996), 352-497.
33. R.F. Voss, "Random fractal forgeries," in *Fundamental Algorithms in Computer Graphics,* R.A. Earnshaw ed. (Springer-Verlag, Berlin, 1985), 13-16, 805-835.
34. J.W. Goodman, *Introduction to Fourier Optics* (McGraw-Hill Book Company, San Francisco *et al.,* 1968).
35. K.S. Clarke, "Computtation of the fractal dimention of topographic surfaces using the triangular prism surface area method," *Comput. Geosciences* **12**, 113-122 (1986).

36. B. Dubuc, J.F. Quiniuo, C. Roques-Carmes, and C. Tricot, "Evaluation the fractal dimensions of profiles," *Phys. Rev.* **39,** 1500-1512 (1989).
37. A. Dogariu, J. Uozumi, and T. Asakura, "Angular power spectra of fractal structures," *J. Mod. Opt.* **41**, 729-738 (1994).
38. D.A. Zimnyakov and V. V. Tuchin "Fractality of speckle intensity fluctuations," *Appl. Opt.* **35**, 4325-4333 (1996).
39. D.A. Zimnyakov, "Binary fractal image quantification using probe coherent beam scanning," *Opt. Eng.* **36**, 1443-1451(1997).
40. O.V. Angelsky, P.P. Maksimyak, and T.O. Perun, "Optical correlation method for measuring spatial complexity in optical fields," *Opt. Lett.* **18**, 90-92 (1993).
41. O.V. Angelsky, P.P. Maksimyak, and T.O. Perun, "Dimensionality in optical fields and signals," *Appl. Opt.* **32**, 6066-6071 (1993).
42. N.H. Packard, J.P. Grutchfield, J.D. Farmer, and P.S. Shaw, "Geometry from a time series," *Opt. Lett.* **5,** 712-716 (1980).
43. F. Takens, "Detecting strange attractors in turbulence," *Lect. Notes in Math.* **898**, 366-381 (1981).
44. O.V. Angelsky and P.P. Maksimyak, "Optical diagnostics of slightly rough surfaces," *Appl.Opt.* **30**, 140-143 (1992).
45. O.V. Angelsky and P.P. Maksimyak, "Polarization-interference measurement of phase-inhomogeneous objects," *Appl. Opt.* **31**, 4417-4419 (1992).
46. O.V. Angelsky and P.P. Maksimyak, "Optical correlation measurements of the structure parameters of random and fractal objects," *Meas. Sci. Technol.* **9**, 1682-1693 (1998).
47. M. Berry, "Singularities in waves and rays," in *Physics of Defects, R. Bochan* ed. (North-Holland, Amsterdam, 1981).
48. G. Popescu and A. Dogariu, "Spectral anomalies at wave-front dislocations," *Phys. Rev. Lett.* **88**, 183902 (2002).
49. J.F. Nye and M. Berry, "Dislocations in wave trains," *Proc. R. Soc. London,* Ser. A **336**, 165-190 (1974).
50. J.F. Nye, *Natural Focusing and Fine Structure of Light* (Institute of Physics Publishing, Bristol and Philadelphia, 1999).
51. I. Freund, N. Shvartsman, and V. Freilikher, "Optical dislocation network in highly random media," *Opt. Comm.* **101**, 247-264 (1993).
52. M. Soskin and M. Vasnetsov, "Singular optics as new chapter of modern photonics: optical vortices fundamentals and applications," *Photonics Sci. News* **4**, 21-27 (1999).
53. M.S. Soskin, M. Vasnetsov and I. Bassistiy, "Optical wavefront dislocations," *Proc. SPIE* **2647**, 57-62 (1995).
54. N.R. Heckenberg, R. McDuff, C.P. Smith, and M.J. Wegener, "Optical Fourier transform recognition of phase singularities in optical fields" in *From Galileo's "Occhialino" to Optoelectronics,* Paolo Mazzoldi ed. (World Scientific, Singapore, 1992), 848-852.
55. N.R. Heckenberg, R. McDuff, C.P. Smith, and A.G. White, "Generation of optical phase singularities by computer-generated holograms," *Opt. Lett.* **17**, 221-223 (1992).
56. O.V. Angelsky, D.N. Burkovets, P.P. Maksimyak, and S.G. Hanson, "On applicability of the singular optics concept for diagnostics of random and fractal surfaces," *Appl. Opt.* **42**, 4529-4540 (2003).

Chapter 3

LASER POLARIMETRY OF BIOLOGICAL TISSUES: PRINCIPLES AND APPLICATIONS

Alexander G. Ushenko[1] and Vasilii P. Pishak[2]
1. Chernivtsi National University, Chernivtsi, 58012 Ukraine; 2. Bucovinian State Medical Academy, Chernivtsi, 58000 Ukraine

Abstract: The Stokes-polarimetric method of polarization information selection which is effective in phase-inhomogeneous layer (PIL) diagnostics and provides the 2-order level of increasing the signal-to-noise ratio (SNR) in their images has been presented. The mechanisms of forming the probability distribution of azimuths and ellipticities of the object field polarization of biological tissue as the set of optically uniaxial structures with crystalline and architectonic organization levels have been distinguished. The two-dimensional polarization tomography, which is effective for visualization and SNR increasing of the image of tissue architectonics, and the set of orientation tomograms has been elaborated. The possibilities of polarization-correlation and wavelet analyses of architectonics images and orientation tomograms of tissues have been studied. The interrelations between statistic parameters, correlation functions and coefficients of wavelet-transformation of polarization filtered images of architectonics and its orientation-phase structure in physiologically normal and pathologically changed states have been determined.

Key words: phase-inhomogeneous layer; polarization; Mueller matrix; signal-to-noise ratio; biotissue; architectonics; correlation function; tomography; wavelet analysis.

3.1 INTRODUCTION

Light based techniques are becoming an increasingly popular method of probing strongly scattering media such as body tissues [1-23]. For superficial

tissue layers or thin tissue samples it is possible to use the coherence or polarization properties of the light [3,4,6-18,20-23].

Early works in the field of tissue optics assumed a homogeneous scattering medium and measured the bulk scattering and absorption properties. More recently, attempts have been made to characterize the effect of different tissue layers. The problem using light to probe layered scattering media is that the scattered light propagates through many random paths through the different layers. It would be extremely useful to be able to characterize the optical properties and thickness of the different layers from measurements of the properties of the emerging light. For example, in studies of thick tissues models of the brain have been developed to include the effects of skin, bone, cerebrospinal fluid and white and gray matter.

Among the variety of directions of laser polarimetry (LP) of phase-inhomogeneous layers (PIL) the development of LP techniques in the optics of biological tissues is one of the most important.

It should be expected that the LP techniques will provide new information about the morphological and optical-anisotropic structure of BT on micro- and macro-levels of their arrangement, which is significant for optical diffuse and coherent tomography, directed to visualization and obtaining images of macroinhomogeneities in BT (tumors, hematomas, etc.).

That's why it can be stated that optical tomography demands further development both in determining the interrelation of orientation-phase structure of BT architectonics with their physiological state and in obtaining new types of tomograms and their processing. Therefore, it would be expedient the elaborate techniques of BT polarization tomography, based on polarization selection of BT architectonic images with obtaining the set of orientation and phase tomograms and further correlation and wavelet-analysis of them [24-48].

Thus, the importance of such a direction is stipulated by the necessity of more detailed investigation of the structure of different types of PIL; elaboration of new approaches of LP towards the analysis and measuring the properties of their object fields; the search of new techniques (as well as improving the traditional ones) of diagnostics of optical-geometric parameters of PIL with surface and volumetric inhomogeneous constituents; visualization and reconstruction of phase-orientation structure of tissue architectonics.

3.2 OPTICAL MODELS OF TISSUE ARCHITECTONICS

3.2.1 Tissue Organization

On the basis of information about tissue morphological structure [5,9,13,14,23] the following model scheme is suggested. A tissue generally consists of 2 phases: amorphous and optically anisotropic ones [31,33]. Optically anisotropic component of a tissue possesses two forms of organization – crystalline and architectonics ones.

Optically coaxial organic fibrils forming collagen, elastin, myosin fibers, mineralized (hydroxyapatite crystals) and organic fibers, etc can be included into crystalline form.

Architectonic nets of such tissues as skin derma (SD), muscle (MT) and bone tissues (BT) are, morphologically, the most typical ones. SD architectonics [21,27,35] is formed by statistically oriented bundles of collagen fibrils (Figure 1). The diameter of the fibrils is between 0.5 μm and 2 μm. Parallel bundles of fibrils form a fiber, the diameter of which is 5-7 μm (papillary layer [47]), and in the net layer it riches 30 μm. Collagen bundle, the average diameter of which changes from 100 μm to 200 μm, is considered to be the highest structural unit of optically active collagen [48] (birefringence value $\Delta n \approx 10^{-3}$).

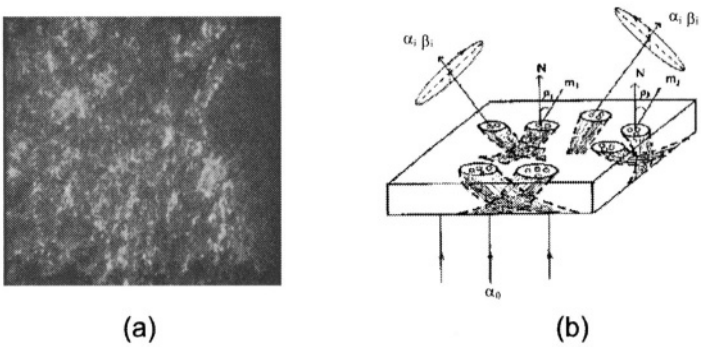

Figure 1. Model representation of skin derma architectonics.

BT represents a system [28,30,37,45,48], consisting of the trabeculae (A) layer and osteons (B) [Figure 2(1)]. Optically active matrix consists of hydroxyapatite crystals ($\Delta n \approx 10^{-1}$ [17]), long (optical) axes of which are oriented along the longitudinal axis of collagen fibers [Figure 2(2)]. They are located between microfibrils, fibrils and collagen fibers forming a separate

continuous mineral phase. Collagen fibers are spatially armored elements in mineral matrix. The bone trabeculae fibers orientation is ordered and parallel to their plane [Figure 2(3)]. For BT osteons the spatially spiral orientation of the armored collagen fibers is realized.

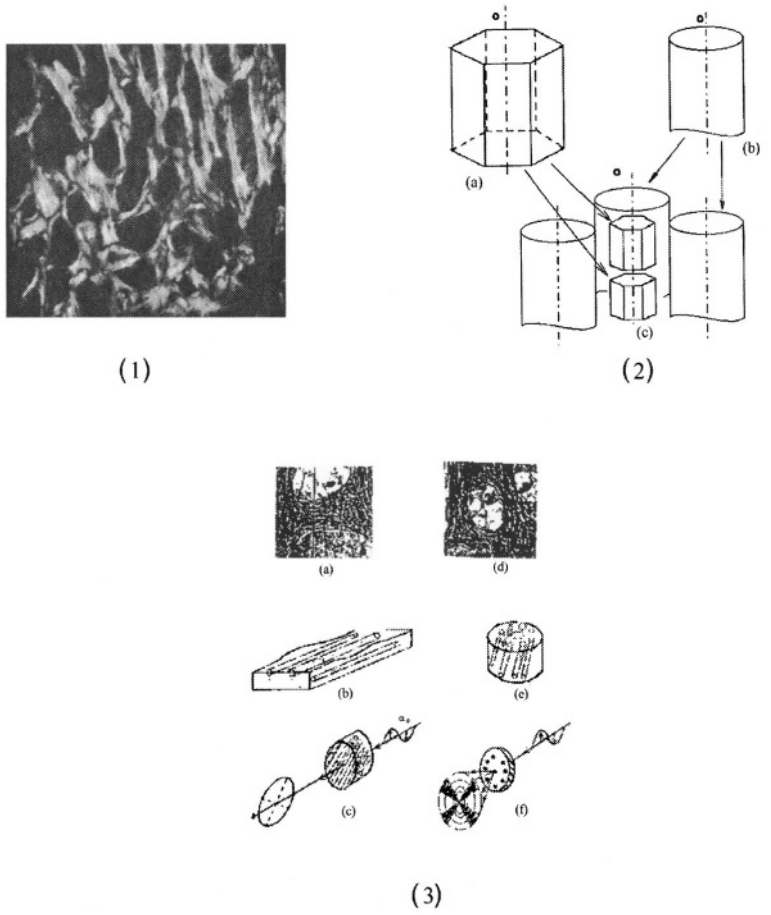

Figure 2. Model representation of bone tissue structure.

MT is a structuralized [29,48], spatially ordered system of protein bundles, consisting of optically isotropic actin and anisotropic myosin (Figure 3).

Optical properties of the primary (crystalline) form of tissue organization are characterized by Mueller operator of the following kind [32]:

$$\{Q\}=\begin{Vmatrix} 1; & 0; & 0; & 0; \\ 0; & \left(\sin^2\frac{\delta}{2}\cdot\cos 2\rho+\cos^2\frac{\delta}{2}\right); & \left(0{,}5\sin 4\rho\sin^2\frac{\delta}{2}\right); & \left(-\sin 2\rho\sin\delta\right); \\ 0; & \left(0{,}5\sin 4\rho\sin^2\frac{\delta}{2}\right); & \left(-\sin^2\frac{\delta}{2}\cdot\cos 2\rho+\cos^2\frac{\delta}{2}\right); & \left(\cos 2\rho\sin\delta\right); \\ 0; & \left(\sin 2\rho\sin\delta\right); & \left(-\cos 2\rho\sin\delta\right); & \left(2\cos^2\frac{\delta}{2}-1\right). \end{Vmatrix}. \quad (1)$$

Here ρ -orientation of optical axis, made by the direction of packing of anisotropic fibrils (collagen, myosin, elastin, hydroxyapatite, etc.), δ -value of phase shift, performed by their substance between ordinary and extraordinary waves.

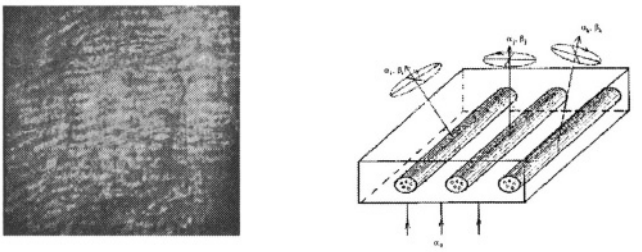

(a) (b)

Figure 3. Model representation of muscle tissue structure.

Within crystalline domain the orientation ρ and phase δ parameters are either typologically stationary ($\rho(x,y)$, $\delta(x,y)\approx \text{const}$) or determinedly distributed. In the first case, the polarization state of laser field (azimuth α and ellipticity β) is determined from the following matrix equation:

$$M=\begin{Vmatrix} 1 & 0 & 0 & 0 \\ 0 & \cos^2 2\rho+\sin^2 2\rho\cos\delta; & \sin 2\rho\cos 2\rho(1-\cos\delta); & -\sin 2\rho\sin\delta; \\ 0 & \sin^2\rho\cos^2\rho(1-\cos\delta); & \sin^2 2\rho+\cos^2 2\rho\cos\delta; & \cos 2\delta\sin\delta; \\ 0 & \sin 2\rho\sin\delta; & -\cos 2\rho\sin\delta; & \sin\delta. \end{Vmatrix}\cdot\begin{pmatrix} 1 \\ \cos 2\alpha_0 \\ \sin^2\alpha_0 \\ 0 \end{pmatrix}=$$

$$=\begin{pmatrix} 1 \\ (\cos^2 2\rho+\sin^2 2\rho\cos\delta)\cos 2\alpha_0+\sin 2\rho\cos 2\rho(1-\cos\delta)\sin 2\alpha_0 \\ \sin 2\rho\cos 2\rho(1-\cos\delta)\cos 2\alpha_0+(\sin^2 2\rho+\cos^2 2\rho\cos\delta)\sin 2\alpha_0 \\ \sin 2\rho\sin\delta\cos 2\alpha_0-\cos 2\rho\sin\delta\sin 2\alpha_0 \end{pmatrix}. \quad (2)$$

Here α_0 is the polarization azimuth of laser beam, which illuminates the tissue.

It follows from equation 2:

$$\alpha = \frac{1}{2} arctg \frac{\sin 2\rho \cos 2\rho (1 - \cos\delta)\cos 2\alpha_0 + (\sin^2 2\rho + \cos^2 2\rho \cos\delta)\sin 2\alpha_0}{(\cos^2 2\rho + \sin^2 2\rho \cos\delta)\cos 2\alpha_0 + \sin 2\rho \cos 2\rho (1 - \cos\delta)\sin 2\alpha_0}; \quad (3)$$

$$\beta = \frac{1}{2} \arcsin(\sin\delta \cdot \sin 2(\rho - \alpha_0)). \quad (4)$$

For flat-polarized wave with azimuth $\alpha_0 = 0^0$, equations 3 and 4 are transformed to:

$$\alpha = \frac{1}{2} arctg \left[\frac{\sin 2\rho \cos 2\rho (1 - \cos\delta)}{\cos^2 2\rho + \sin^2 2\rho \cos\delta} \right], \quad (5)$$

$$\beta = \frac{1}{2} \arcsin(\sin\delta \cdot \sin 2\rho). \quad (6)$$

In the second case (at curvilinear packing of fibrils described by the curve of the second order $(A_1x^2 + C_1y^2 + 2D_1x + 2E_1y + F_1 = 0)$) polarization characteristics of object field are continually changing in every point (x_i, y_i) and are determined by relations analogous to equations 3 to 6. The difference is in the fact that the angle ρ obtains the sense to angle $\omega = g(x,y)$ between the tangent to the curve in the point (x_i, y_i) and polarization azimuth of laser beam α_0.

Thus, for some modes of fibrils packing (circle, ellipse, parabola, hyperbola) it can be shown that in the direction x the functions g(x,y) obtain the following form [29]:

$$\omega = arctg \frac{\sqrt{r^2 - x^2}}{x}, \quad (7)$$

$$\varpi = arctg \frac{(a^2 - b^2) \cdot \sqrt{a^2 - x^2}}{a^3 b \cdot x}, \quad (8)$$

$$\varpi = arctg \frac{\sqrt{c^2 - x^2}\,(c^2 - 2d^2 x)}{cd^2 (c^2 + d^2 x^2)}, \quad (9)$$

$$\varpi = \frac{x^2}{k}. \quad (10)$$

Here r is the circle radius; a and b are the large and small half-axes of the ellipse; c, d, and k are coefficients of hyperbola and parabola, correspondingly.

For architectonic net of tissue vector structure of object field can be defined as a superposition of polarization states of crystallite (crystalline grains) part [31]:

$$\alpha^* = arctg\left(\frac{\sum_{m=1}^{N}\sum_{n=1}^{N} A_m \cos\alpha_n}{\sum_{m=1}^{N}\sum_{n=1}^{N} A_m \sin\alpha_n}\right), \tag{11}$$

$$\beta^* = arctg\left[\frac{\sum_{m=1}^{N}\sum_{n=1}^{N}\sum_{r=1}^{N} A_m(\cos\alpha_n + tg\beta_r \sin\alpha_n)}{\sum_{m=1}^{N}\sum_{n=1}^{N}\sum_{r=1}^{N} A_m(\sin\alpha_n + tg\beta_r \cos\alpha_n)}\right]. \tag{12}$$

Here N is the number of anisotropic structures, A_m are the amplitudes of light oscillations of partial object fields.

3.2.2 Architectonic Nets of Tissues

For the majority of tissues the substance of optically anisotropic architectonics is of the same type. That is why it can be considered that $\Delta n = const$. On the other hand, such an approximation is not always adequate. Thus, for anisotropic component of bone tissue non-organic crystals of hydroxyapatite and collagen fibrils are the main optically active structures. Spatial symmetry of crystallite structure of bone tissue non-organic and organic microcomponents is identical – this structure is originated by optically coaxial crystals [27-32]. Consequently, their joint effect on photometric and polarization characteristics of optical radiation can be expressed by superposition of matrix operators of {Q} type (equation 1)

$$\{Q\} = \{Q\}_1 + \{Q\}_2 \ . \tag{13}.$$

3.3 POLARIZATION AND COHERENT IMAGING

3.3.1 Introduction

This section is devoted to the analysis and experimental testing of the concept of laser polarization tissue probing. The methods of increasing the signal-to-noise ratio (SNR) in coherent images of the optically anisotropic architectonics of the morphological tissue structure are considered. The

possibilities of polarization selection and contrasting of a target tissue layer image screened by other tissue layers are examined. The influence of the depolarization degree of the scattering background on the SNR is investigated. The possibilities of polarization correction of the probing beam for contrasting tissue images are analyzed.

Let a light field, described by Stokes vector $S^{(0)}$, propagate within two-layer optically heterogeneous medium (Figure 4) [38,40-42,46]. Due to light scattering by heterogeneities of the first layer the tissue layer under study is irradiated by a beam with another Stokes vector $S^{(1)} = \{Y\}S^{(0)}$, where $\{Y\}$ is a matrix of radiation light scattering made by screening tissue layer.

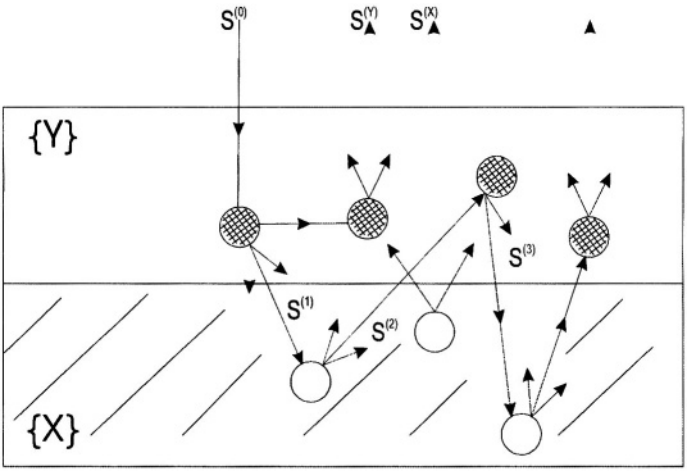

Figure 4. Model scheme.

At interaction of radiation with the subsurface layer there is formed an object field, the polarization characteristic features of which can be described by the vector $S^{(2)} = \{X\}\{Y\}S^{(0)}$. Here $\{X\}$ is the matrix of light scattered by the target tissue layer.

The radiation detector measures the light field, Stokes vector of which takes the following form: $S^{(X)} = \{Y\}\{X\}\{Y\}S^{(0)}$ and $S^{(Y)} = \{Y\}\ S^{(0)}$.

If one takes into account the multiple acts of object re-irradiation ($S^{(3)}$) and the further outlet of the component of luminous flux into external medium ($S^{(*)}$), it is possible to write it down as follows: $S^{(*)} = \{Y\}\{X\}\{Y\}\{X\}\{Y\}S^{(0)}$.

Proceeding basing on the assumption about the independence of statistical structure of tissue layers the resulting light field can be presented by the partial vector sum [38]:

$$S^{(Z)} = S^{(Y)} + S^{(X)} + S^{(*)} . \qquad (14)$$

It takes the following matrix form:

$$\{Z\} = \{Y\} + \{YXY\} + \{YXYXY\}\,, \tag{15}$$

where $\{Z\}$ is the resulting matrix of light scattered by an object: "rough layer – turbid medium" [46].

First let us consider the first two constituent parts, i.e., let us assume:

$$\{Y\} + \{YXY\} >> \{YXYXY\}. \tag{16}$$

From the analysis of the equation 15 one can conclude that under determined conditions – having the information on matrices $\{Z\}$ and $\{Y\}$ – it is possible to define statistically $\{X\}$-matrix structure:

$$\{X\} = \{Z - Y\}\{Y\}^{-1}\{Y\}^{-1}. \tag{17}$$

Here $\{Y\}^{-1}$ is an inverse matrix to that of $\{Y\}$.

3.3.2 Transformation of Laser Field Polarization

3.3.2.1 General Description

Let us consider the possibilities of determining polarization structure of laser radiation scattered by tissue layers. In a general case Stokes vector of a radiating (probing) field is defined as follows [26]:

$$S^{(0)} = \{1; \cos 2\alpha_0 \cos 2\beta_0; \sin 2\alpha_0 \cos 2\beta_0; \sin 2\beta_0\}\,, \tag{18}$$

where α_0, β_0 are polarization azimuths and ellipticity of a probing laser beam. It is successively possible to demonstrate the determination of polarization characteristic features of partial scattered fluxes $(\alpha_x, \beta_x; \alpha_y, \beta_y)$ from the following equations [40]:

$$\alpha_{x,y} = 0.5 arctg\left(\frac{f_{32}\cos 2\alpha_0 \cos 2\beta_0 + f_{33}\sin 2\alpha_0 \cos 2\beta_0 + f_{34}\sin 2\beta_0}{f_{22}\cos 2\alpha_0 \cos 2\beta_0 + f_{23}\sin 2\alpha_0 \cos 2\beta_0 + f_{24}\sin 2\beta}\right), \tag{19}$$

$$\beta_{x,y} = 0.5 \arcsin(f_{42}\cos 2\alpha_0 \cos 2\beta_0 + f_{43}\sin 2\alpha_0 \cos 2\beta_0 + f_{44}\sin 2\beta_0), \tag{20}$$

where f_{ik} are the elements of partial matrices of light-scattering.

Thus, having the information on matrices {Z}, {Y}, one can "construct" matrix {X}, i.e., one is able to find polarization structure of a signal (α_x, β_x), reflected by the object under probing.

3.3.2.2 Polarization-Phase Technique

The idea of the technique of polarization-phase extraction of object image against a background of impediments is based on determining polarization structure (α_x, β_x; α_y, β_y) of the resulting light field $S^{(Z)}$ by using the measured matrices {Y}, {Z} with the further polarization compensation of a background signal component $S^{(Y)}$.

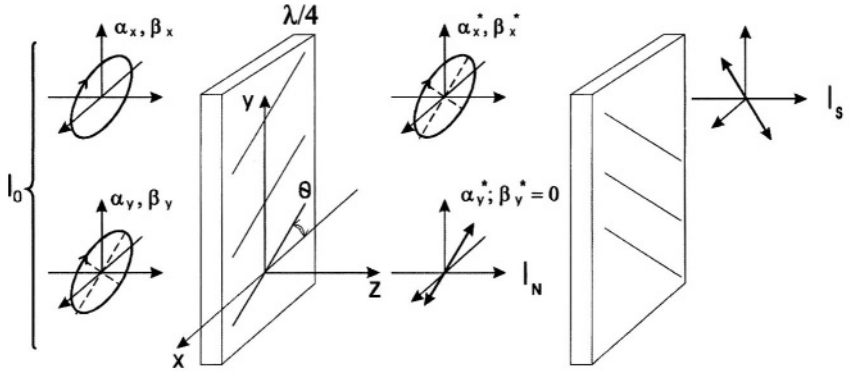

Figure 5. The scheme of polarization-phase extraction of informative signal: I_0 is the intensity of the resulting laser beam; I_S - is the output intensity of informative signal.

One can essentially decrease the value of intensity of scattered background polarization component while the intensity of object signal remains considerable. The latter is possible when placing a polarization filter before a photodetector. The filter consists of an analyzer and quarter-wave plate. Figure 5 demonstrates the mechanism of increasing the SNR being determined as follows:

$$\eta = 10^3 \left\{1 - \cos\left[\alpha_y^* - \alpha_x^*\right] \cos 2\beta_x^*\right\}. \qquad (21)$$

Here α_y^* is the azimuth of background signal polarization after passing through the phase plate "$\lambda/4$"; α_x^*, β_x^* are informative signal azimuth and ellipticity after passing through the quarter-wave plate. The axis of the latter is oriented in a special way, thus, the ellipticity of background signal polarization $\beta_y^* = 0$; the constant 10^3 characterizes the linearity of polarizer – analyzer.

The functioning of the phase-shifting plate "$\lambda/4$" can be described by the following matrix operator:

$$\{\Phi\}=\begin{Vmatrix} 1 & 0 & 0 & 0 \\ 0 & 0.5(1+\cos 2\Omega) & 0.25\sin 4\Omega & -\sin 2\Omega \\ 0 & 0.25\sin 4\Omega & 0.5(1-\cos 2\Omega) & \cos 2\Omega \\ 0 & \sin 2\Omega & -\cos 2\Omega & 0 \end{Vmatrix}, \quad (22)$$

where Ω is the rotation angle of the greatest speed axis of the quarter-wave plate with respect to incidence plane.

By orienting the greatest speed axis at the angle $\Omega = \alpha_y^*$ one can obtain the following polarization characteristic features of informative and background signals:

$$\beta_x^* = 0.5\arcsin\{\cos 2\beta_x \sin[2(\theta-\alpha_x)]\}, \quad (23)$$

$$\alpha_x^* = 0.5\arccos\left\{\frac{0.5\cos 2\beta_x[\cos(4\theta-2\alpha_x)+\cos 2\alpha_x]\sin 2\beta_x \sin 2\theta}{\cos 2\beta_x^*}\right\}, \quad (24)$$

$$\alpha_y^* = 0.5\arccos\{0.5\cos 2\beta_y[\cos(4\theta-2\alpha_y)-\sin 2\beta_y \sin 2\theta]\}, \quad (25)$$

$$\beta_y^* = 0. \quad (26)$$

Thus, SNR within the optical field under registration is described by:

$$\eta_0 = \frac{I_S}{I_N} = \frac{P_S I_S + \Delta_S I_S}{P_N I_N + \Delta_N I_N}, \quad (27)$$

where I_S and I_N are intensities of informative and background signals, respectively (Figure 5); P_S, Δ_S and P_N, Δ_N are respectively polarization and depolarization components of the scattered radiation field.

By orienting the greatest speed axis of the phase element at the angle $\pi/2 + \alpha_x^*$, it is possible to increase SNR:

$$\eta_s = \frac{P_S I_S \cos^2 \varsigma + 0.5\Delta_S I_S}{kP_N I_N + 0.5\Delta_N I_N}, \quad (28)$$

where $k = 10^{-3}$ is the relative intensity of a completely polarized signal component passed through the analyzer; ς is the angle between the fluctuation plane of electrical intensity vector of a completely polarized

constituent part of informative signal and analyzer axis direction A (Figure 5). Besides, through the analyzer it is passed 50% intensity of completely depolarized constituent parts. Thus, the relative increase of SNR is given by:

$$\eta = \frac{\eta_s}{\eta_0} = \frac{P_S \cos^2 \varsigma + 0.5\Delta_S}{kP_N + 0.5\Delta_N}, \tag{29}$$

where

$$\cos^2 \varsigma = \frac{\sin^2\left(\alpha_y^* - \alpha_x^*\right) + \cos^2\left(\alpha_y^* - \alpha_x^*\right) tg^2 \beta_x^*}{1 + tg^2 \beta_x^*}. \tag{30}$$

The analysis of equations 29 and 30 shows that maximal level of the SNR is achieved if the following conditions are fulfilled:

$$\begin{aligned} &\varsigma \to \frac{\pi}{2}; \\ &\beta_y^* \to 0 \end{aligned}. \tag{31}$$

3.3.3 Computer Modeling, Analysis, and Discussion

3.3.3.1 Single Scattering

Figure 6 presents the results of computer modeling of the distributions of the coefficient $\eta(\alpha_0, \Theta)$ for an object with the following parameters of birefringence: $\Delta n_x = 0.1$; $\Delta n_y = 0.03$ [Figure 6(a)] and 0.08 [Figure 6(b)], and the directions of preferable orientations of tissue architectonics fibers, $\Delta\rho = \rho_x - \rho_y = 20^0$.

The results of these calculations allow us to make the following conclusions:

1. The efficiency of polarization selection of the informative signal is highly sensitive to the azimuthal geometry of probing beam. The coefficient $\eta(\alpha_0, \Theta)$ has a rather complicated topological distribution, and the value of this coefficient ranges from 0 to $\eta = \mu = 10^3$;
2. The maximum of $\eta(\alpha_0, \Theta)$ for all the angular arrangements is localized around the azimuthal angle of polarization of the probing beam $\alpha_0 = \Delta\rho$;

3. The decrease in the difference of anisotropy (Δn_x and Δn_y) in tissues is accompanied by the formation of additional maximum $\{\eta(\alpha_0, \Theta)\}\big|_{\Theta i=\text{const}}$ for all the values of azimuthal angles α_0.

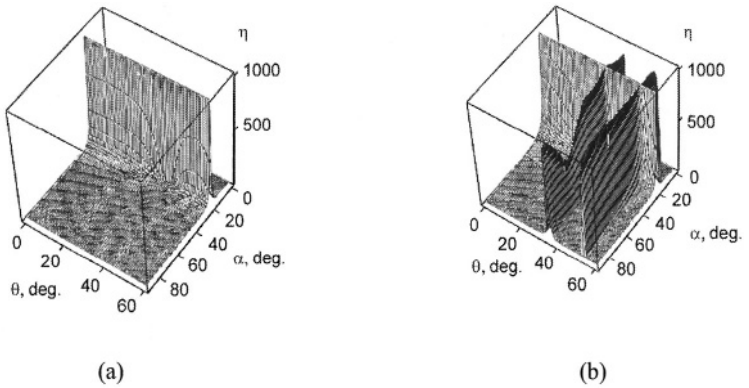

Figure 6. Dependences of the SNR improvement factor, Θ is the scattering angle.

As it follows from boundary conditions (equation 31), the SNR maximum is achieved when the background signal is linearly polarized. In this case, the intensity of the background signal can be reduced to $\mu^{-1}I_N$. Such background suppression is achieved when the azimuth α_0 coincides with the anisotropy direction ρ_y of screening tissue (this direction is measured from ρ_x), i.e., $\alpha_0 = \Delta\rho$. Thus, a maximum line should exist in the distribution $\eta(\alpha_0, \Theta)$ for all the scattering angles Θ.

On the other hand, equations 23-26 show that the background and informative signals considerably depends on the relations between the partial matrix elements $\{x_{ik}\}$ and $\{y_{ik}\}$. The values of these elements fluctuate in different ways, depending on Δn_x, Δn_y, and Θ [32]. Therefore, a linearly polarized background and the relevant extreme lines $\eta(\alpha_0, \Theta)\big|_{\Theta i=\text{const}}$ may be observed within a broad range of α_0 [Figures 6(b) and 6(d)].

Figure 7 displays the dependences characterizing the transformation of the polarization structure of the background (I_N) and informative (I_S) signals in response to variations in the azimuth α_0 of the probing beam. These results were obtained for the following scattering angles: $\Theta = 0^0$ [Figures 7(a) and 7(d)], $\Theta = 35^0$ [Figures 7(b) and 7(e)], and $\Theta = 55^0$ [Figures 7(c) and 7(f)]. The left-hand column corresponds to anisotropy parameters $\Delta n_x = 0.1$ and $\Delta n_y = 0.03$, while the right-hand column corresponds to anisotropy parameters $\Delta n_x = 0.1$ and $\Delta n_y = 0.08$.

The analysis of these data reveals a correlation between zero values of the ellipticity of the background signal $\beta_y(\alpha_0 = \Delta\rho)$ (curves 3) and the maximal value of the SNR improvement factor $\eta(\alpha_0, \Theta) \to \mu$, which is observed for arbitrary values of polarization parameters of the informative signal $\alpha_x - \alpha_y = \Delta\alpha$ and β_x^* (curves 1 and 2).

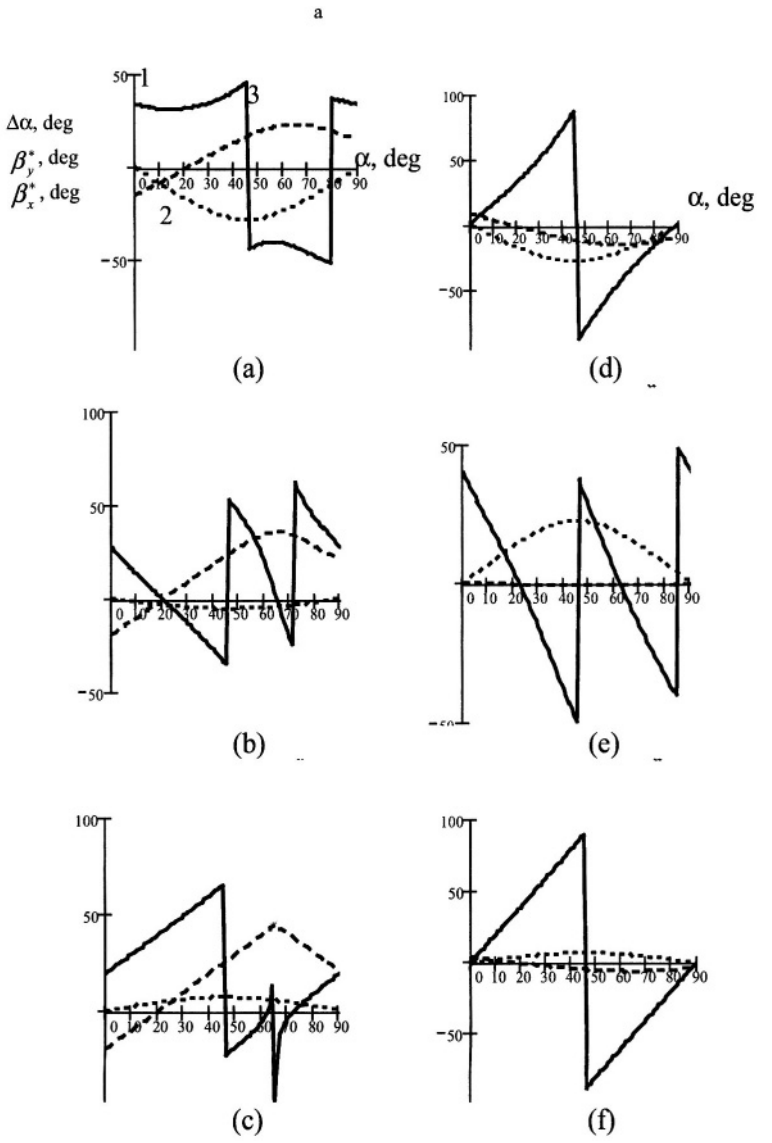

Figure 7. Polarization structure of the background and informative signals.

For other azimuthal angles of polarization of the probing beam, α_0, two field components of scattered laser radiation are generally elliptically polarized. Therefore, the coefficient $\eta(\alpha_0, \Theta)$ becomes much lower, vanishing around $\beta_x^* \approx \beta_y^*$.

The choice of the optimal scattering angle Θ (with $\alpha_0 = \Delta\rho$) and the optimal polarization plane for scattering angles corresponding to the

maximum, $\{\eta(\alpha_0, \Theta)\}\big|_{\Theta=\text{const}}$, is important for the photometry of the informative signal I_S. This is due to the fact that, when the maximum $\eta(\alpha_0, \Theta) = \mu$ is achieved, the polarization structure of the informative signal differs for different α_0 and Θ.

Figure 8 displays a series of dependences of I_S calculated for the directions $\alpha_0 = 20^0$. [Figure 8(a)] and $\Theta = 35^0$ [Figure 8(b)], $\Theta = 55^0$. [Figure 8(c)] of maximal of the coefficient $\eta(\alpha_0, \Theta)$.

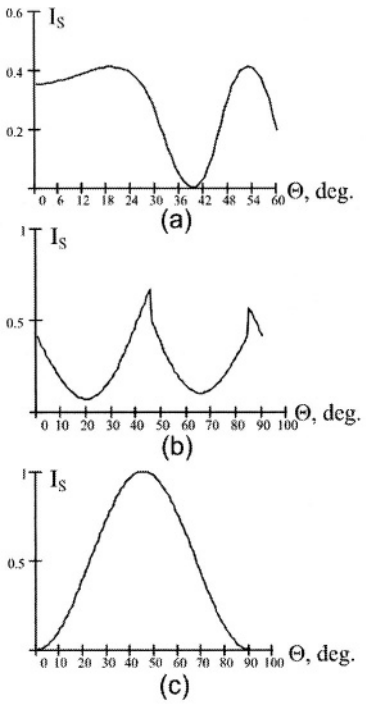

Figure 8. The transfer function of the informative signal.

Analysis of these results shows that, when the minimum of background ($\mu^{-1}I_N$) is achieved, the informative signal may vary within a broad dynamic range of three orders of magnitude (from 10^{-3} up to 1). An optimal photometric situation is achieved when the boundary conditions for the polarization state of the object signal produced by a tissue (equations 31) are satisfied.

3.3.3.2 Multiple Scattering

In accordance with equations 29 and 30 the dependency of η on polarization angle characteristics of the probing beam (α_0, β_0) makes the possibility to optimize polarization probing, i.e., to select the optimal

probing beam parameters when η has a maximum. We will consider first the linearly polarized scattering fields. Study function $\eta(\alpha_0)$ for its maximum:

$$\frac{d\eta}{d\alpha} = \frac{\partial\eta}{\partial\xi}\frac{\partial\xi}{\partial\alpha_0} + \frac{\partial\eta}{\partial\beta_x^*}\frac{\partial\beta_x^*}{\partial\alpha_0} = 0 \tag{32}$$

gives that for polarization probing of a two-layer scattering medium the optimal conditions are described by equations 31.

The relations described by equations 31 are realized when polarization azimuth of the probing laser beam satisfies the following relation:

$$\begin{aligned}
&\alpha_0^* = 0.5\,arctan\frac{q_1 + \sqrt{q_1^2 - 4q_2q_3}}{2q_3};\\
&q_1 = -\left[y_{32}(x_{33} + x_{22}) + x_{32}(y_{33} + y_{22})\right];\\
&q_2 = x_{32}y_{23} + x_{22}y_{22};\\
&q_3 = x_{23}y_{32} + x_{33}y_{33}.
\end{aligned} \tag{33}$$

The analogous results can be gained for polarization ellipticities of the probing beam at the constant value of polarization azimuth (α_0=const) [41]. The optimal value for polarization ellipticity (Figure 9) is defined by solution of the following equation:

$$\frac{d\eta}{d\beta} = \frac{\partial\eta}{\partial\xi}\frac{\partial\xi}{\partial\beta_0} + \frac{\partial\eta}{\partial\beta_x^*}\frac{\partial\beta_x^*}{\partial\beta_0} = 0 \tag{34}$$

$$\beta_0^* = -0.5\,arctan\left[\frac{(x_{32} + x_{22})cos\,2\alpha_0^* + (x_{33} + x_{23})sin\,2\alpha_0^*}{x_{34} + x_{24}}\right]. \tag{35}$$

As can be seen from equation 29, the depolarization parameter Δ noticeably lowers the improvement factor of the SNR for multiply scattering objects. This tendency is shown in Figure 9, which illustrates the decay of the improvement factor of the SNR with a decrease in the polarization degree.

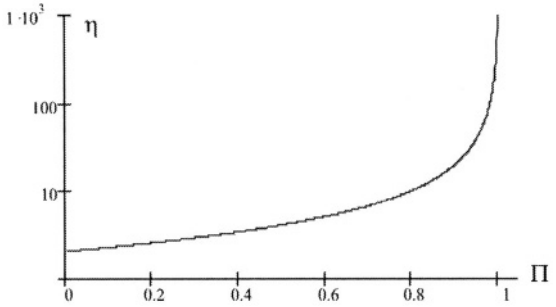

Figure 9. The SNR as a function of the depolarization degree of the background signal.

As can be seen from Figure 9, for polarization degree $\Pi = (1 - \Delta) = 0.9$, the coefficient η is reduced by two orders of magnitude, while for $\Pi = 0.1$, the factor η decreases further virtually by another order of magnitude. On the other hand, the analysis of equation 29 shows that the SNR improvement factor reaches its maximum when both conditions of equation 31 are satisfied.

3.3.3.3 Computer Modeling

Figure 10 presents the results of computer modeling for the "spatial" and "topological" distributions of the SNR η obtained in the cases of single (Figures 10(a) and 10(b), $\Pi = 1.0$) and multiple (Figures 10(c) and 10(d), $\Pi = 0.12$) scattering and in the regime of polarization correction of the probing beam [Figures 10(e) and 10(f)]. The object model is a sequence of layers of cancellous bony and fibrillar muscular tissues with $\Delta n_x = 0.1$, $\Delta n_y = 0.03$, and $\Delta\rho = \rho_x - \rho_y = 0^0$.

The results of modeling allow us to make the following conclusions:

- In the regime of single scattering, the SNR improvement factor reaches its maximal value,. $\eta \rightarrow 10^3$) for the polarization azimuthal angles α_0 and scattering angles Θ corresponding to a background signal whose vector structure tends to the structure of linearly polarized radiation ($\beta_y^* \rightarrow \min$), [Figures 11(b) and 11(c)]. Conversely, in the case when the informative and background signals are elliptically polarized ($\beta_y^* \rightarrow \max$, $\beta_x^* \rightarrow \max$), the coefficient $\eta(\alpha_0, \Theta) \rightarrow \min$) tends to its minimum, vanishing in the limiting case, regardless of the difference of polarization azimuthal angles $\Delta\alpha$ [Figure 11 (a)].
- In the case of a multiply scattering muscular tissue, η decreases by virtually three orders of magnitude within the entire range of azimuthal and scattering angles α_0 and Θ. This is due to the fact that the polarization states of the informative and background signals are

virtually indistinguishable in this case, $\Delta\alpha \rightarrow \min$; $\beta_y^* \approx \beta_x^*$ [Figures 11(d)–11(f)].

- Polarization correction of the polarization state of a laser beam probing a multiply scattering object increases the SNR improvement factor by an order of magnitude for any scattering angle Θ.

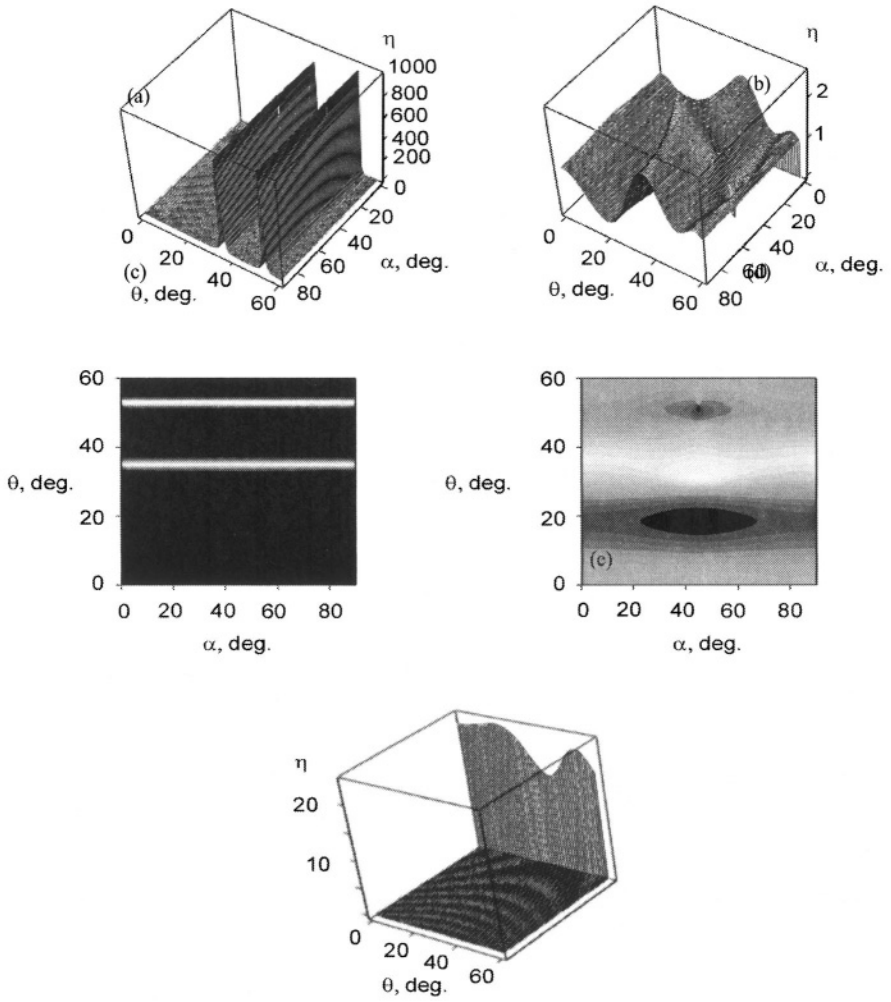

Figure 10. Spatial–azimuthal and topological dependences of the SNR improvement factor for singly and multiply scattering biostructures and in the regime of polarization correction of the probing beam.

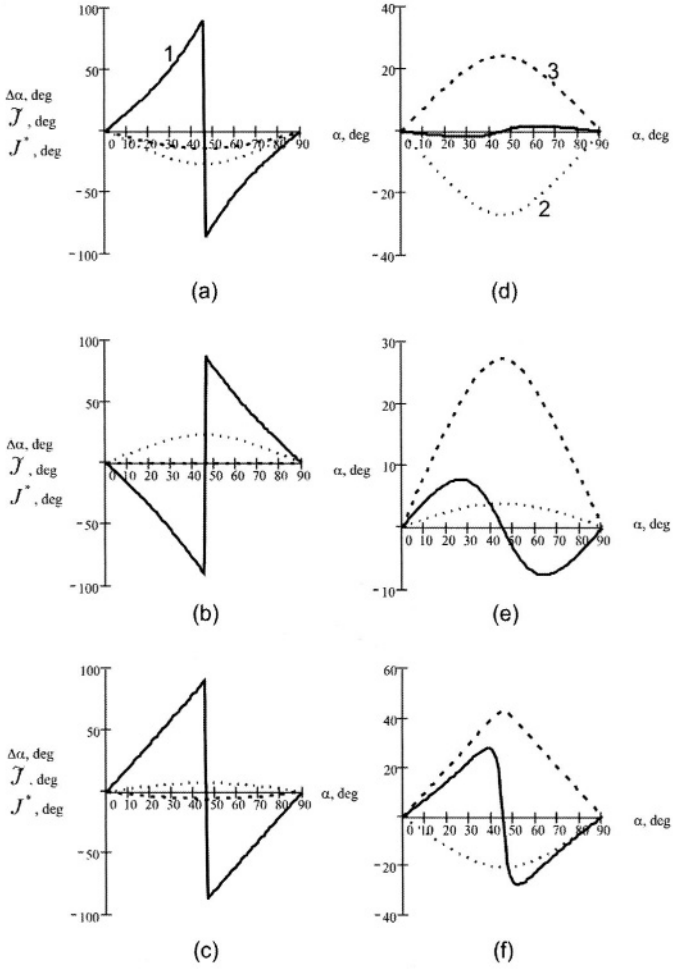

Figure 11. Polarization structure of the background and informative signals.

3.3.3.4 Automatic Polarimeter Design

The overall layout of the instrument is shown in Figure 12. The main optical elements of the polarimeter are the He:Ne laser (λ = 0.633 μm, 10 mW), the polarizer P, two quartz-made quarter-wave ($\lambda/4$) plates (4th order) and the analyzer A. By setting the polarization plane of P in parallel to the optical axis of the first quarter-wave plate the object under test O (a tissue sample) was illuminated by a linearly polarized light beam. The analyzer was similarly coupled to the second quarter-wave plate.

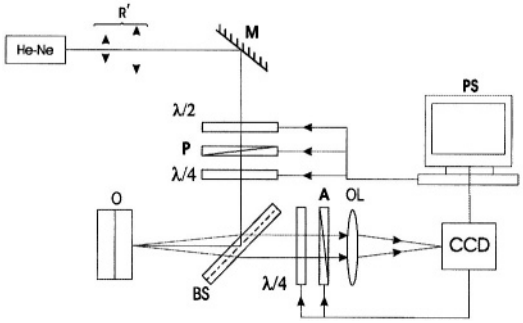

Figure 12. Optical scheme.

The He:Ne laser beam was expanded by the afocal system R up to the diameter of 3 mm. The pinhole located in the expansion optics removed secondary reflections in the optical system. The role of the half-wave plate $\lambda/2$ was to match the laser beam polarization plane to the polarizer transmittance direction and, at the same time, to control the light intensity at the CCD to avoid its saturation.

The tissue sample was placed on the microscope slide. The slide with tissue was fixed in a mount providing transverse translations in two mutually perpendicular directions in the range of 5 mm to enable choosing various fragments of the sample.

The sample image was formed on the CCD by the optical system composed of two microscope objectives OL. The overall dimensions of the quarter-wave and analyzer driving systems did not allow one to place the imaging optics closer than 200 mm to the sample. The images registered by the CCD and the frame grabber transferred it in a digital form to the computer.

The half-wave plate, the quarter-wave plates, the polarizer and analyzer were rotated by means of step motors. One step was corresponded to 22.5 minutes of arc of the rotation of an optical element.

Before making measurements the automatic system calibration was performed in the following order:

- the optical axes of quarter-wave plates were set in parallel to transmittance directions of polarizer and analyzer;
- the transmittance planes of polarizer and analyzer were set in parallel;
- the half-wave plate was rotated to obtain the maximum signal registered by the CCD (without saturation);
- both the analyzer and the second quarter-wave plate were rotated into the crossed position to the polarizer.

Figure 13 presents the results of experimental testing of the method.

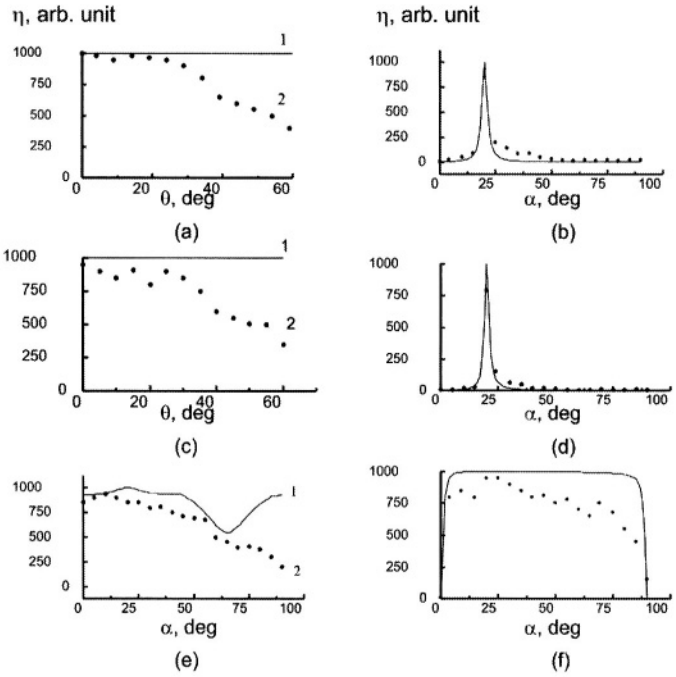

Figure 13. Experimental dependences $\eta(\Theta)$ at single scattering.

Histological slices of biostructures placed in a sequence were employed as objects of studies. The following types of tissue sections were used:
- cancellous bone tissue (the absorption coefficient μ_a = 2.6 cm^{-1}, the scattering coefficient μ_s = 60 cm^{-1}, the anisotropy parameter g = 0.88, the birefringence Δn = 0.1, the thickness $z = 40$ μm);
- skin derma (μ_a = 2.2 cm^{-1}, μ_s = 185 cm^{-1}, g = 0.82, Δn = 0,01, $z = 30$ μm);
muscular tissue (μ_a = 2 cm^{-1}, μ_s = 215 cm^{-1}, g = 0.96, Δn=0,03, z = 30 μm).
Experiments were performed for the following objects:

- "skin derma - cancellous bony tissue" for the following parameters $\Delta\rho \approx 20^0$, and $\alpha_0 = 20^0$. [Figure 13(a)] and $\Theta = 0^0$ [Figure13(b)];
- "muscular tissue–skin derma" with $\Delta\rho \approx 20^0$, $\alpha_0 = 20^0$ [Figure 13(c)], $\Theta = 0^0$ [Figure 13(d)], $\Theta = 35^0$. [Figure 13(e)], and $\Theta = 55^0$ [Figure 13(f)].

The results of measurements of the coefficient $\eta(\alpha_0, \Theta)$ demonstrate the efficiency of polarization probing of tissues within a sufficiently broad range of scattering angles, $\Theta < 20^0$. The discrepancy between the results of computer modeling (solid lines) and experimental data (points) does not exceed 10–20% within this range. As the observation angle Θ increases, the coefficient $\eta(\alpha_0, \Theta)$ noticeably decreases, while the discrepancy between theoretical predictions and experimental data may reach 50–80%. This effect

is apparently due to the increase in the multiplicity of light scattering and the growth in the depolarization of the background signal, which is not included in theoretical modeling. However, even in this regime, the SNR improvement factor remains sufficiently high [$\eta(\alpha_0, \Theta) \sim 10$–$100$].

The results of experimental testing of the method of laser probing with a fixed polarization state and correction of the azimuth and ellipticity of polarization are presented in Figure 14.

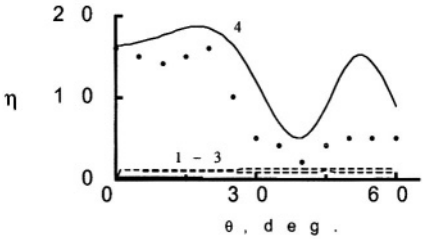

Figure 14. Experimental dependences $\eta(\Theta)$, at multiple scattering.

Curves 1–3 obtained for the scattering angles $\Theta = 0^0$, $\Theta = 20^0$, and $\Theta = 20^0$, respectively, illustrate the efficiency of polarization probing of tissues with a strong depolarized background signal. The thickness of shading tissue (skin derma) was $z = 250\ \mu m$. The results of laser probing with polarization correction are presented by curve 4.

The comparative analysis of the experimental data reveals the growth in the SNR improvement factor by virtually an order of magnitude for any angle Θ.

Comparison with the results of analytical modeling shows a satisfactory agreement between theoretical predictions and experimental data. The discrepancy varies from 10 to 30%. Lower SNR obtained in experiments may be due to some variance of orientations of optically active elements in bony and muscular tissues, which may increase the ellipticity of the object field [29, 33], and a variance of the optical anisotropy of tissues.

3.4 STOKES – CORRELOMETRY OF TISSUES

The analysis of the processes of pathological changes in tissues allows us to classify such structural changes as the following:

- tumor formation of soft tissues of woman reproductive sphere (WRS) with forming of collagen multifractal nets [33,34,36,48];

- excrescence of skin collagen structure (collagen diseases, psoriasis) [33,35,38,48].

As a result of laser radiation passing through tissue the coordinately-distributed optical signal S(X, Y) is formed:

$$S(X,Y) = I(X,Y) + U(X,Y), \tag{36}$$

where $U(X,Y)$, $I(X,Y)$ are the random and "anisotropic" (informative) components of object field. Their structure in the general case, can be represented by the superposition of random and stochastic (quasi-regular) components:

$$\mathrm{I}(X,Y) = \mathrm{I}^{*}(X,Y) + \mathrm{I}^{\otimes}(X,Y). \tag{37}$$

Using autocorrelation concept we will consider the possibility of detection and analysis of multifractal component of tissue coherent image on the background of interference, made by its amorphous component. To make it simpler as a first step a one-dimensional case will be analyzed. The corresponding autocorrelation function (ACF) is determined by the expression [33,43]:

$$G_{xx}(\Delta x) = \lim_{x\to\infty} \frac{1}{X_0} \int_0^x [\mathrm{I}(X) + U(X)][\mathrm{I}(X-\Delta X) + U(X-\Delta X)]dx \,. \tag{38}$$

According to correlation operator distribution, we have the following:

$$G_{xx}(\Delta x) = G_{ii}(\Delta x) + G_{uu}(\Delta x) + G_{iu}(\Delta x) + G_{ui}(\Delta x). \tag{39}$$

We suggested that the noise $U(x)$ and the signal $I(x)$ are independent. Therefore, correlation functions $G_{iu}(\Delta x)$ and $G_{ui}(\Delta x)$ are equal to zero (to the errors of estimations, stipulated by the finite interval of integration). That is why equation 39 will be rewritten as follows:

$$G_{xx}(\Delta x) = G^{*}{}_{ii}(\Delta x) + G^{*}{}_{uu}(\Delta x) + G^{\otimes}{}_{ii}(\Delta x) + G^{\otimes}{}_{uu}(\Delta x). \tag{40}$$

Noise ACFs $G^{\otimes}{}_{ii}(\Delta x); G^{\otimes}{}_{uu}(\Delta x)$ tend to zero with the increasing of the interval Δx [33]. So, in the expression for ACF of multifractal component of tissue coherent image, only two items remain:

$$G_{xx}(\Delta x) = G^{*}{}_{ii}(\Delta x) + G^{*}{}_{uu}(\Delta x). \tag{41}$$

The component $G^*_{uu}(\Delta x)$ plays the role of an error in the determination of $G_{xx}(\Delta x)$. Generally speaking, $G^*_{ii}(\Delta x) \approx G^*_{uu}(\Delta x)$. That is why the diagnostic ability of ACF $G^*_{ii}(\Delta x)$ appears to be not quite effective.

The solution of this problem can be achieved by polarization selection of the tissue coherent image. It can be said that image contrast of the given fractal fragment against the background of the amorphous substance will be determined by the equation [38]:

$$V(\sigma_\rho, \Theta) = \frac{I_* - I}{I_* + I} = \frac{A - \Delta I \cdot B}{A + \Delta I \cdot B}, \tag{42}$$

in which

$$\Delta I = \frac{I_0}{a^2}, \tag{43}$$

$$A = \cos^2(\alpha - \Theta) + \tan^2 \beta \sin^2(\alpha - \Theta), \tag{44}$$

$$B = \cos^2 \Theta. \tag{45}$$

Here, I, I_* are the intensities of background and object signals, through-passed by the amorphous and crystalline components of tissue for random value of the rotation angle of the polarization axis of polarizer-analyzer Θ; I_0, a^2 – corresponding intensities for $\Theta = 0^0$.

Multifractal collagen structure of tissue in the plane of histological section possesses a wide array of random values of orientation ρ and optical anisotropy δ, and, consequently, spatially distributed parameters of polarization $\alpha(X, Y)$; $\beta(X, Y)$ of boundary field. That is why the image contrast (visualization parameter) of such a multifractal net in the coherent image will be determined as follows:

$$V_\Sigma(\Theta) = \sum_{\alpha=0}^{\pi} \sum_{\beta=0}^{\frac{\pi}{2}} V(Q_\alpha, W_\beta, \alpha, \beta). \tag{46}$$

Here, Q_α and W_β are the distribution functions of the azimuths α and ellipticities β of object field polarization, determined by the statistics of orientations and values of fractal fibers birefringence.

It appears from the analysis equations 42 and 46, that V depends on the parameters of anisotropy of fractal domains ρ and δ, the probability distributions Ψ_ρ, Ω_δ and on polarization structure of the probing laser beam.

Figure 15 presents the results of computer modeling of the visualization parameter for tissue multifractal collagen net at different values of ordering, σ_ρ.

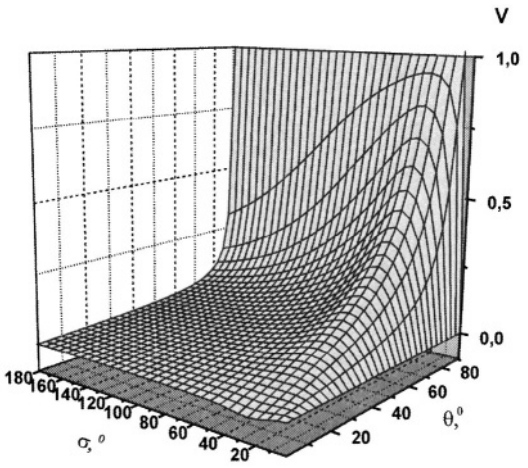

Figure 15. The distribution of the visualization parameter of tissue multifractal net.

To simplify it, the following suppositions (without reducing the analysis generality) are used:

$$\Delta L=1; \quad \delta(X,Y)=const;$$

$$\Psi_\rho = \frac{1}{\sigma\sqrt{2\pi}} e^{\frac{-(x-a)^2}{2\sigma^2}}. \tag{47}$$

Here $\sigma=\sigma_\rho$ is the dispersion of fractal domain orientations; x and a are random and mean values of orientations.

The results obtained show that $V(\sigma_\rho, \Theta)$ experiences a wide range of changes in its value. The highest value is achieved at the rotation angle of the analyzer $\Theta = 90°$. In the given case, the object signal (see equation 36) is as follows:

$$S^*(X) = \mathrm{I}^*(X) + \mathrm{I}^{\otimes}(X), \tag{48}$$

and the ACF is:

$$G^*(\Delta x) = \lim_{x\to\infty} \frac{1}{X_0} \int_0^x Q_\alpha(\Delta x) W_\beta(\Delta x) \left\{ \begin{array}{l} \left[\sin^2\alpha(x) + \tan^2\beta(x)\cos^2\alpha(x)\right] \times \\ \left[\sin^2\alpha(x-\Delta x) + \tan^2\beta(x-\Delta x)\cos^2\alpha(x-\Delta x)dx\right] \end{array} \right\} \tag{49}$$

Thus, the equation 49 illustrates the possibilities of autocorrelation analysis of multifractal component in the tissue coherent image. According to Wiener-Khintchine [39] theorem, for estimating such a component, it is convenient to make use of the algorithm of its spectral density:

$$J_{xx}(\nu_p) = \int_{-\infty}^{\infty} G^*_{xx}(\Delta x)\cos 2\pi\nu_p x dx \cdot \qquad (50)$$

Here ν_ρ is a spatial frequency.

The analysis of equations 49 and 50 proves that the appearance of pathological changes, leading to the formation of tissue multifractal collagen structure (tumor forming processes) is connected with the appearance of the function $G^*_{xx}(\Delta x)$ oscillations and of quasi-linear spectrum $S_{xx}(\nu_\rho)$, corresponding to them. On the contrary, the overgrowth and off-orientation of the architectonic collagen net (psoriasis) will show off in smoothing $G^*_{xx}(\Delta x)$ and forming the continuous spectrum $S_{xx}(\nu_\rho)$.

Figure 16 represents the tendencies of changing the ACF $G^*_{xx}(\Delta x)$ and corresponding spectral densities $S_{xx}(\nu_\rho)$, obtained from the algorithms of equations 49 and 50 for the following orientation parameters of multifractal net, containing the harmonious component ν_ρ:

- ρ_0=45°, σ_ρ=5° - Figure 16(a);
- ρ_0=45°, σ_ρ=45° - Figure 16(b);
- ρ_0=45°, σ_ρ=90° - Figure 16(c).

It can be seen that the efficiency of the appearance of the harmonic component in the coherent image intensity distribution is the highest for σ_ρ=5° and, on the contrary, the lowest for σ_ρ=90°.

The following groups of tissue samples were investigated experimentally:

- histological sections of myometrium (the WRS tissue) – group A;
- histological sections of skin derma – group B.

The thickness of the samples was 10 μm that corresponds to the condition of a single scattering.

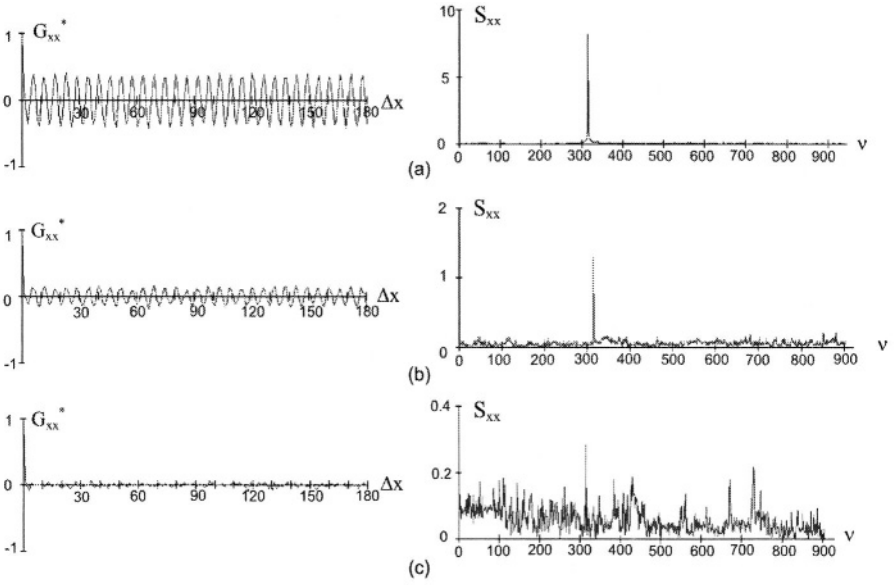

Figure 16. Analytical ACFs and spectral densities of coherent images of tissue multifractal structure.

Figure 17 presents a number of microphotographs of such sections, obtained in the crossed (⇑⇒) polarizer and analyzer. On the fragments [Figures 17(a) and 17(d)] the normal structure of tissues "A" and "B" are shown, respectively, while the fragments [Figures 17(b), 17(c), 17(e), and 17(f)] present the pathologically changed ones.

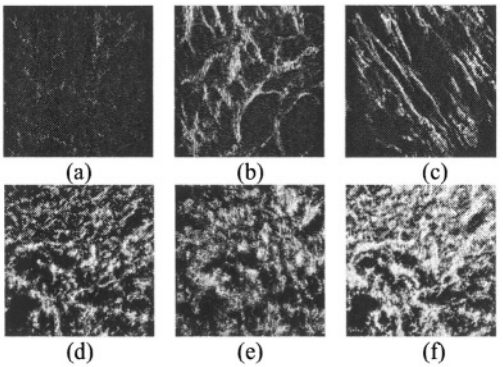

Figure 17. Coherent images of WRS (Woman Reproductive Sphere) myometrium [(a)–(c)] and skin derma [(d)–(f)]. (a) and (d) – the normal structure of tissues "A" and "B" are shown; (b), (c), (e), and (f) present the pathologically changed ones.

From the data obtained one can see, that the coherent images of myometrium tissue sample with the probable forming of fibromyoma node

[36] [Figures 17(b) and 17(c)] possess optically anisotropic collagen net, if compared with the physiologically normal tissue [Figure 17(a)].

The psoriasis process [Figures 17(e) and 17(f)] is accompanied by the sufficient enlargement and disorientation of human skin derma collagen net in comparison with its physiologically normal polarization image [Figure 17(d)].

Figure 18 presents the scheme of experimental arrangement. The He:Ne laser radiation 1 (λ=0.6328 μm) is collimated by the system objectives 2 and passes through the polarization illuminator ($\lambda/4$ plate 3 and polarizer 4) illuminating the sample 5, placed into the cuvette with physiological solution 7. The objective 8 projects the coherent image of histological section through the analyzer 9 into the plane of CCD-camera, connected with PC 11. The detected polarization images are digitized according to their intensity (256 levels) and represent a set of pixels (800×600).

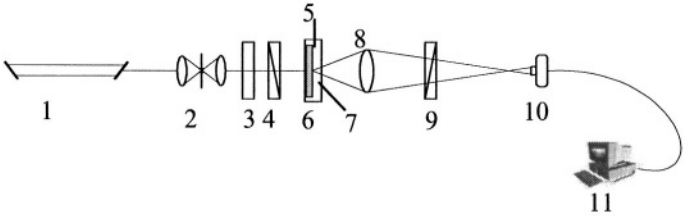

Figure 18. Optical scheme of experimental setup.

Figure 19 illustrates the series of ACF of myometrium tissue coherent images with the probable forming of fibromyoma germ, obtained for the analyzer passing axis orientations 0°, 45° and 90° [Figures 19(a), 19(b), and 19(c)]. The corresponding spectral densities are given in Figures 19(d), 19(e), and 19(f).

In all the ACF graphs one can see the peak (at the beginning of the coordinates) that corresponds to the white noise, connected with random fluctuations of tissue coherent image intensities. In the ACF tails one can observe the oscillations, the amplitudes of which are connected with the presence of quasi-harmonics in the structure of multifractal net polarization images. It is seen, that for crossed polarizer and analyzer the quasi-harmonic components of the coherent images observed in the spectral densities $S_{xx}(\nu_\rho)$ can be determined.

Figure 20 presents the results of the comparative polarization-correlation analysis of coherent images of physiologically normal [Figure 20(a) and 20(b)] and pathologically changed myometrium tissue [Figure 20(c) and 20(d)]. It can be seen that the correlation structure of polarization images of physiologically normal myometrium does not contain any sufficiently marked fluctuation component. The fibromyoma germ shows the growth of

fluctuation amplitudes (1.8-2 times) in the ACF tail and the maximum of quasi-linear spectrum $S_{xx}(\nu_\rho)$ of the image.

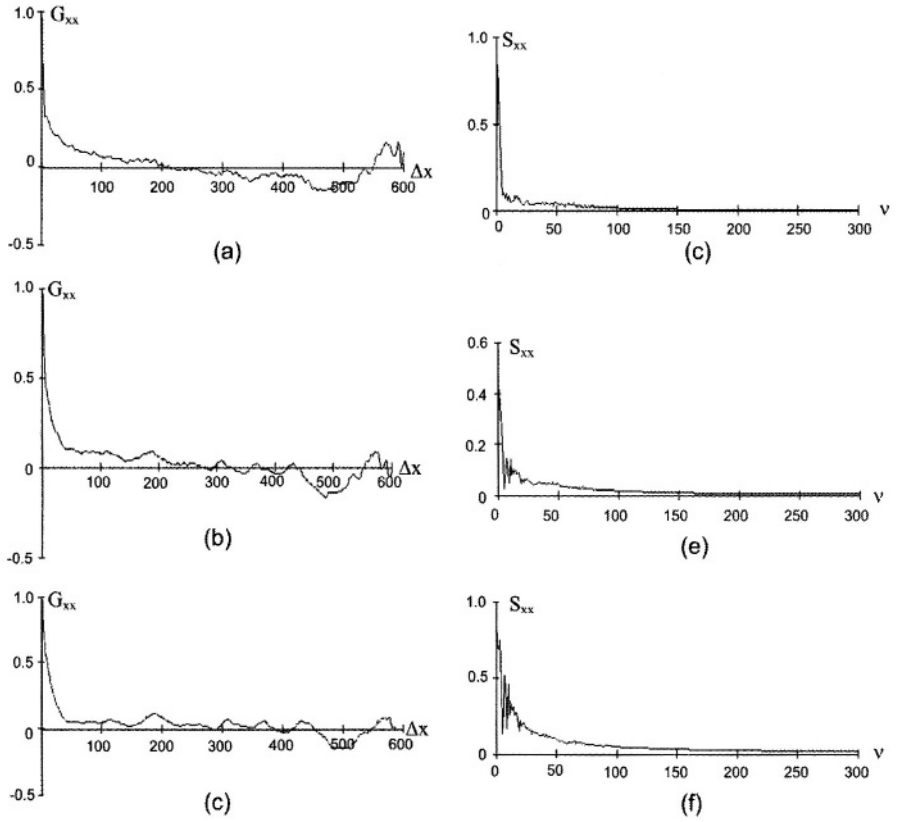

Figure 19. The dynamics of polarization response of the ACF and spectral densities of coherent image of myometrium with the probable fibromyoma germ.

Polarization dynamics of changes in ACF and $S_{xx}(\nu_\rho)$ spatial intensity distributions of skin derma coherent images is shown in Figure 21. The data obtained point to the sufficient difference of ACF half-width G_{xx}^{*} - Δx_0 [Figures 21(a), 21(b), and 21(c)] and spectrum power $S_{xx}(\nu_\rho=0)$ [Figures 21(d), 21(e), and 21(f)] of the dermal layer coherent images. Such tendencies are, obviously, connected with the expansion of mean-statistic size of collagen structures, that leads to the increase of correlation interval Δx_0 [33] of the ACF and diffraction concentration of the intensity of collagen structures polarization images in the vicinity of the spatial frequency ν_ρ=0.

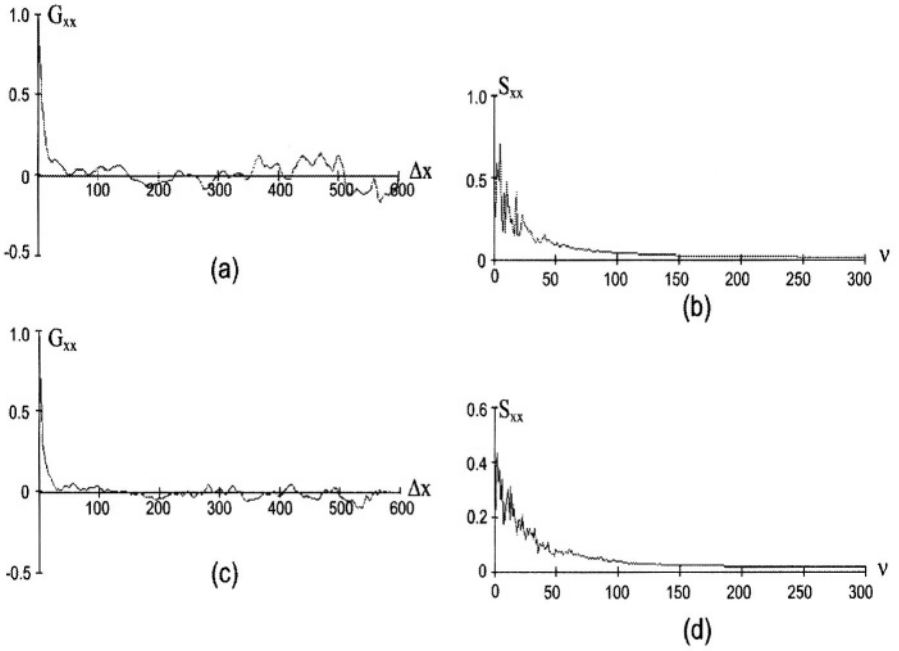

Figure 20. Polarization-correlation structure of myometrium coherent images in the normal and pathological states.

In the Figure 22 one can see the histograms of distribution of parameters Δx_0 and $S_{xx}(\nu_\rho=0)$ for coherent images of 38 samples of physiologically normal derma and 41 samples of derma changed by psoriasis. The data obtained prove the effectiveness of the technique of polarization correlometry of the skin tissue in the diagnostics of pathological changes of their collagen structures.

Thus, the investigation of polarization-correlation structure of tissue object fields gives the possibility:

1. To determine the stochastic quasi-periodic component in the coordinate distribution of the sample coherent image intensity, which is identically connected with the orientation structure of tissue multifractal net.

2. To define the spatial-frequency structure of optically anisotropic fractal component of tissue.

3. To diagnose the appearance and dynamics of the progress of pathological changes of morphological structure of tissue collagen net.

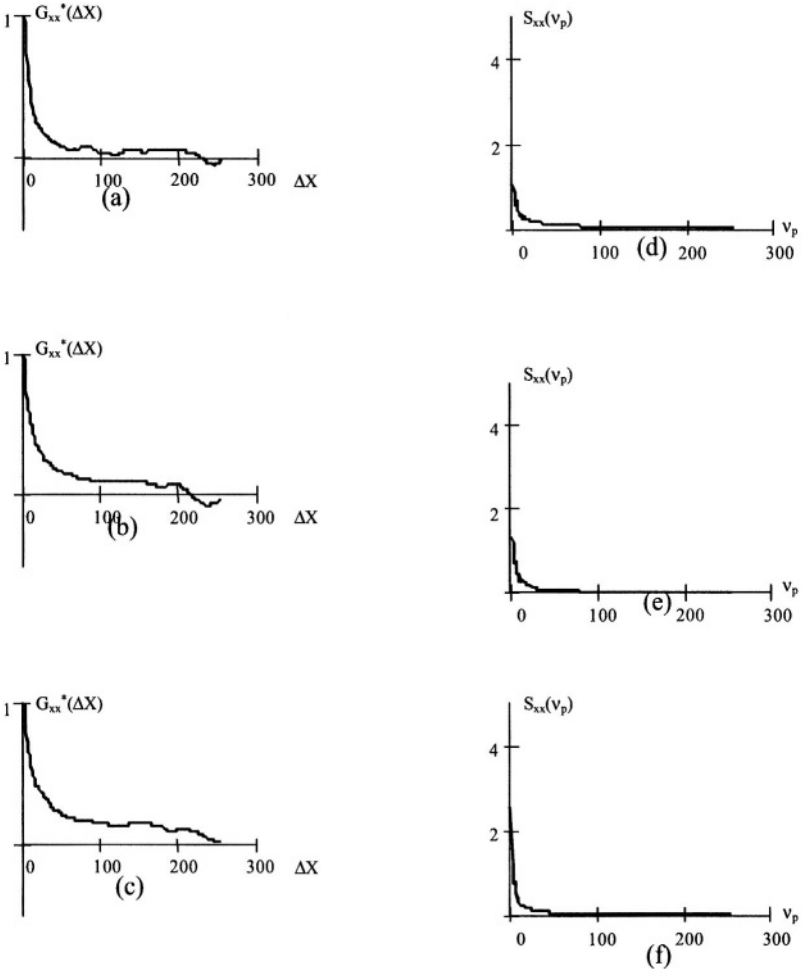

Figure 21. Polarization-correlation structure of dermal coherent images in the normal and pathological states.

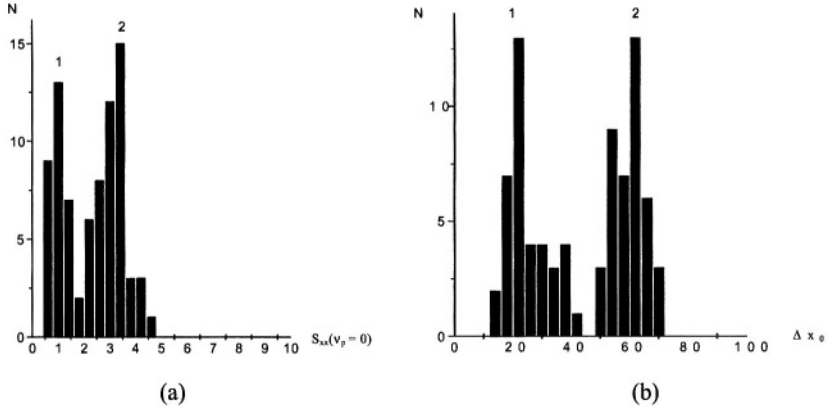

(a) (b)

Figure 22. The probability structure of the ACF (a) and spectral densities (b) of skin derma coherent images. 1 – the histograms of physiologically normal tissue; 2 – the histograms for pathologically changed tissue.

3.5 WAVELET-ANALYSIS OF COHERENT IMAGES

3.5.1 Computer Modeling

This section is aimed for studying the vector structure of object laser fields, formed by structured biological tissues and the subsequent development of optical diagnostics of their physiological state based on correlation processing and wavelet analysis of corresponding polarization images.

Histological sections of physiologically normal muscular tissue (MT) (group A) and necrotically changed (myocardium infarct) tissue (group B) of a rat heart were studied.

Let's consider the mechanisms of forming polarization structure of object field on the example of MT architectonics. Muscular tissue is known to be a structured system of protein fascicles consisting of optically isotropic actin and anisotropic myosin [28,48].

Optical properties of this system can be described by a superposition of matrix operators of amorphous and crystalline components

$$\{M\}=\{A\}+\{K\}=\begin{Vmatrix} a_{11}+k_{11} & a_{12} & 0 & 0 \\ a_{21} & a_{22}+k_{22} & k_{23} & k_{24} \\ 0 & k_{32} & a_{33}+k_{33} & k_{34} \\ 0 & k_{42} & k_{43} & a_{44}+k_{44} \end{Vmatrix}, \qquad (51)$$

where a_{ik} and k_{mn} are elements of partial Mueller matrices of the components of actin and myosin of biological tissue [32,39].

As a laser beam polarized with an azimuth α_0 passes though this structure, an object field with the following polarization state is formed:

$$\alpha = 0.5 \arctan\left[\frac{\cos 2\alpha_0 k_{32} + \sin 2\alpha_0 (a_{33} + k_{33})}{a_{21} + \cos 2\alpha_0 (a_{22} + k_{22}) + \sin 2\alpha_0 k_{23}}\right], \tag{52}$$

$$\beta = 0.5 \arcsin(\cos 2\alpha_0 + \sin 2\alpha_0 k_{43}). \tag{53}$$

The spatial intensity distribution of this field, observed through an analyzer oriented at an angle Ω relative to the plane of incidence, can be written as

$$I(X,Y) = I_0\{\cos^2(\alpha - \Omega) + \sin^2(\alpha - \Omega)\tan^2\beta\}. \tag{54}$$

On the other hand, this field is formed by the superposition of two components

$$I(x, y) = \Psi(x, y) + T(x, y), \tag{55}$$

were $\Psi(x,y)$ and $T(x,y)$ are the field components formed by the myosin and the actin components of muscular tissue, respectively.

It follows from the analysis of equations 51 to 53 that the vector structures of images of these components are fundamentally different. The object field of the actin component is linearly polarized. Therefore, the intensity of the $T(x,y)$ component can be practically reduced to zero by using an analyzer oriented at the angle

$$\Omega^* = \frac{\pi}{2} + 0.5 \arctan\left(\frac{\sin 2\alpha_0 a_{33}}{a_{21} + \cos 2\alpha_0 a_{22}}\right). \tag{56}$$

In this case, a system of polarizophots (zero intensity lines) is formed. The corresponding intensity distribution in a coherent image of the actin component of muscular tissue varies to the level determined by the relation

$$\Psi^*(X,Y) = 0.25\Psi(X,Y) \times \left\{ \begin{array}{l} \cos^2\left[\dfrac{\sin 2\alpha_0 k_{33} + \cos 2\alpha_0 k_{32}}{\sin 2\alpha_0 k_{33} + \cos 2\alpha_0 k_{22}}\right] + \\ \sin^2\left[\dfrac{\sin 2\alpha_0 k_{33} + \cos 2\alpha_0 k_{32}}{\sin 2\alpha_0 k_{32} + \cos 2\alpha_0 k_{22}}\right] \end{array} \right\}. \tag{57}$$

The relation between the concentrations of myosin and actin protein components and their biochemical exchange play a major role in the mobility and contraction of muscular tissue, which is one of the decisive factors in its vital activity. Pathological changes in this biological tissue are accompanied by a reduction or disappearance of actin proteins, which leads to the dystrophy or necrosis (myocardium infarct) of muscles [39].

Early optical diagnostics of these processes can be represented by the following stages: formation of noncoherent image of muscular tissue, polarization selection of this image with subsequent visualization of the myosin and actin components, correlation processing of the corresponding polarization images, and wavelet analysis of their structures.

A wavelet transformation of the object field consists in its expansion by a certain basis, which is constructed of a solution-like (wavelet) function by way of its scaling and translation. Each function of this basis characterizes a certain spatial frequency as well as its spatial localization in the coherent image of biological tissue [24,25,39]. Thus, the following new possibilities in addition to correlation analysis appear:

- Revealing the spatial-distributed properties of the object field of the investigated tissue.
- The differentiation of alternation and dissipation areas.
- Obtaining the local high-frequency and global large-scale information on tissue structure.

That is why the wavelet-analysis can be regarded as "Mathematical microscope." The ability of such a "microscope" to detect the inner structure of sufficiently inhomogeneous object and to study the local scaling properties is shown by many examples: Weierstraße fractal function, probabilistic measures of Cantor sets, multifractal measures of several well-known dynamic systems, modeling the process of transfer to chaos, observed in dissipative systems [24,25].

Thus, the intensity distribution of the object field can be represented as the series

$$\Psi(X) = \sum_{j,k=-\infty}^{\infty} c_{jk}\xi_{jk}(X). \tag{58}$$

The distribution $\Psi(X)$ belongs to the space $L^2(R)$, where it is defined over the entire real axis $R(-\infty,+\infty)$ and is determined by the finite energy (norm)

$$E_f = \int_{-\infty}^{\infty} \left| \Psi(X)^2 \right| dx < \infty. \tag{59}$$

The waves forming the space $L^2(R)$ can be constructed by using scaling and translation of the wavelet $\xi(X)$ with arbitrary values of basis parameters, namely, the scaling coefficient a and the translation parameter b

$$\xi_{ab}(X) = \left| a^{-1/2} \right| \xi\left(\frac{X-b}{a} \right); a, b \in R; \ \xi \in L^2(R). \tag{60}$$

Based on this, the integral wavelet transformation takes the form

$$[W_\xi W](ab) = |a|^{-1/2} \int_{-\infty}^{\infty} \Psi(X) \xi^*\left(\frac{X-b}{a} \right) dx = \int_{-\infty}^{\infty} \Psi(X) \xi_{ab}^*(X) dx. \tag{61}$$

The coefficients $c_{ik}=\langle \Psi, \xi_{jk} \rangle$ of expansion of the function Ψ in series in wavelets (see equation 58) can be defined through the integral wavelet transformation:

$$c_{jk} = [W_\xi \Psi]\left(\frac{1}{2^j}, \frac{k}{2^j} \right). \tag{62}$$

If we follow the above mentioned analogy with the "Mathematical microscope," then the shift parameter b fixes the focusing point of the microscope, the scale coefficient a – magnification, and finally, by choosing the basic wavelet ψ - the optical properties of the microscope are determined.

Basic wavelets are often constructed on the basis of the Gaussian function. Among them the complex (Morlett) wavelets and real bases (MHAT) can be observed. The first ones are well suited to the analysis of the complex signals or fields. As a result of the wavelet transform the two-dimensional arrays of absolute values and phase are received. The application of the MHAT-wavelet for analyzing the distribution of the tissues coherent images is preferable. It has a narrow energy spectrum and two moments (zero and the first ones) equal zero, and is well suited to the analysis of scale-coordinate structure of optical fields [39].

It should be pointed out that this choice is not an exclusive one. There exists a wide class of wavelets, the choice of which is determined by the type of information one needs to extract from 1D or 2D signals. Optimization of the wavelet-function choice represents a separate problem, which is not considered in this chapter.

In order to determine diagnostic possibilities of wavelet analysis of revealing such image anomalies on the first stage, computer modeling of the corresponding cases has been performed.

Figure 23 presents the series of images of wavelet-coefficients c_{ik}, given in the axes "coordinate (b) – scale parameter (a)." The following harmonic was used as analyzed signal $I(x)$:

$$I(X) = \begin{cases} I_0 \sin 2\pi\nu x; x_1 < x < x_2 \\ I_0^* \sin 2\pi\nu x; x \le x_1, x \ge x_2 \end{cases}. \qquad (63)$$

For tissue architectonics pathology $I_0 < I_0^*$; for degenerative-dystrophic changes $I_0 > I_0^*$.

From the data obtained it can be seen [Figure 23(a) and 23(c)] that coefficients c_{jk} are harmonically distributed in the interval $x_1 < x < x_2$ and they possess: localized maximum, corresponding to the coefficient a_0, determined by frequency ν, and the maximum in the field of large scales, given rise to the size b_0, corresponding to "multifrequent" parts of $I(x)$ distribution (fragments 1 and 2 in Figure 23). For the part of "anomalies" there is a change of the wavelet-coefficient value, linearly connected with the change of I_0^* amplitude. That is why, we shall use the correlation of the wavelet-coefficients for the different values of a and b parameters as a criterion for determining the areas of localization of maxima of the intensity of tissue image.

For the frequency-modulated signal $I(x)$ the wavelet-coefficients transformation is observed. It consists in redistribution of their amplitudes and increase of the corresponding interval of scale coefficient a_i [Figures 23(c) and 23(d)]. However, the parts of the image of model anomaly of pathological type are characterized by big amplitudes c_{jk} and interval a_i. For the model of defect of degenerative-dystrophic change of tissue there is the decrease of c_{jk} values in the field of small a_i and, *vice versa,* their increase in the field of large scales. Thus, the wavelet-coefficients dispersion for corresponding scales has maximal values. It can be regarded as an additional criterion for determining the localization of the anomalies of image intensities.

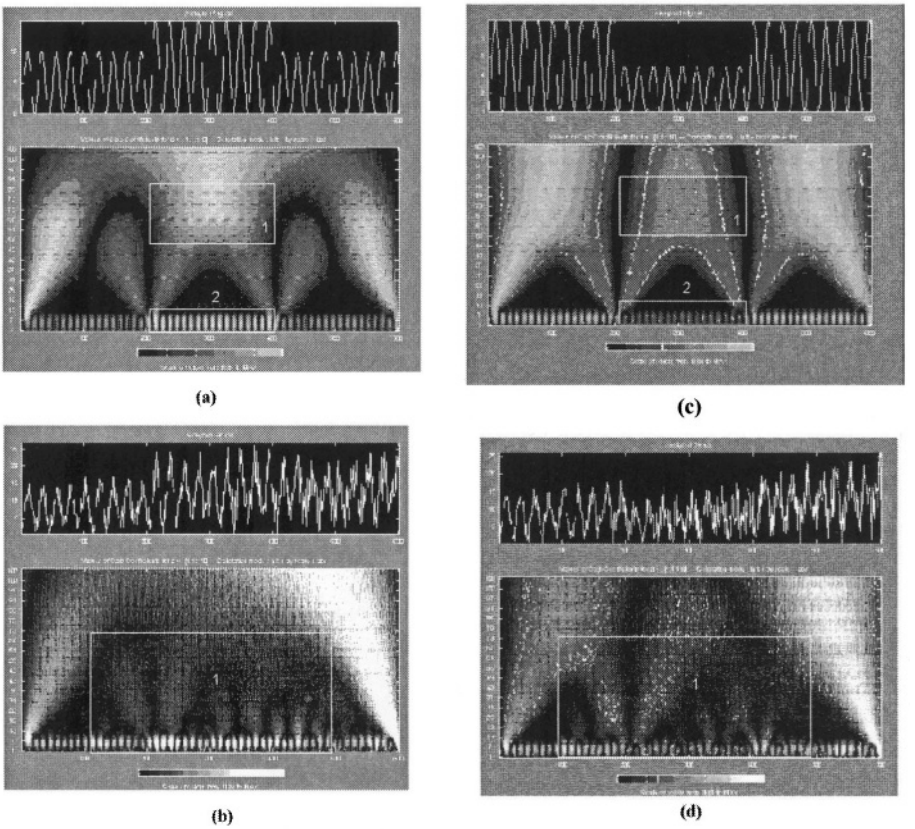

Figure 23. Diagnostic possibilities of wavelet analysis of image anomalies.

Thus, computer modeling proved the effectiveness of diagnostic use of wavelet-transform for the anomalies of harmonic and quasi-harmonic structure images.

3.5.2 Experimental Study and Discussion

Figure 24 presents coherent images of physiologically normal muscular tissue of the heart of a rat (the upper row) and necrotically (myocardium infarct) changed tissue (the lower row) obtained with a parallel [Figure 24(a) and 24(c)] and crossed [Figure 24(b) and 24(d)] polarizer and analyzer.

The morphological structure of tissue of both types is seen to represent systems of spatially ordered muscular fibers. This structure (its optically anisotropic component) is observed with the highest contrast using a crossed polarizer.

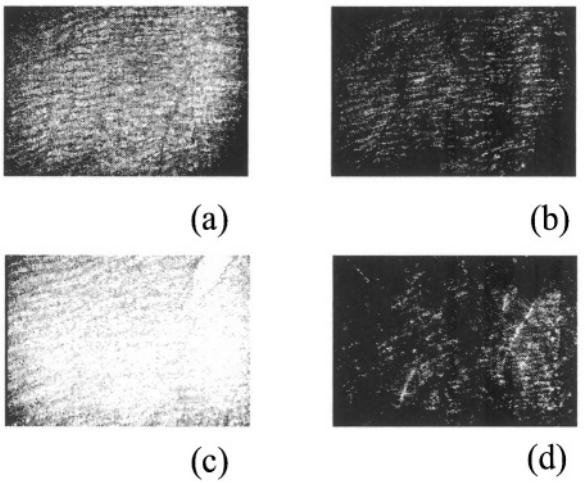

Figure 24. The coherent images of muscle tissues.

Figure 25 presents a series of dependences of the autocorrelation functions (ACF) $G(\psi\psi)$ of the coherent images.

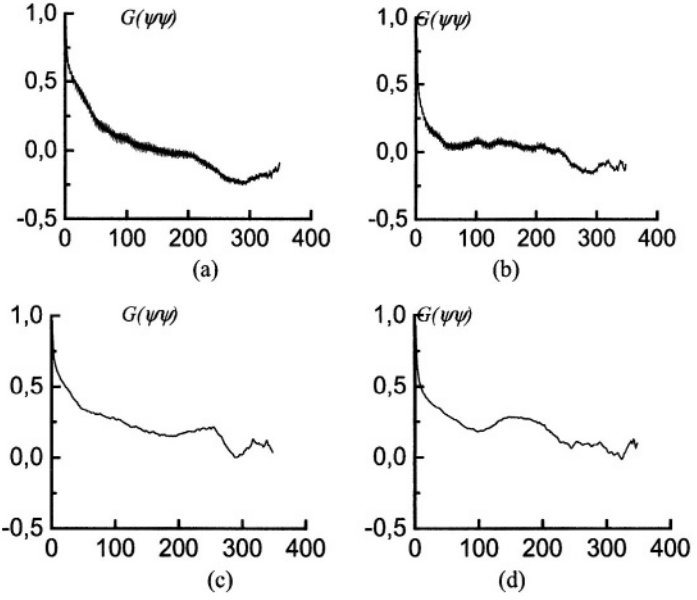

Figure 25. ACFs of the muscle tissue images.

The obtained autocorrelation functions set possess general properties:

- All ACF's in the beginning of the coordinate system possess the maximum, which corresponds to complete coincidence of coordinate distribution of intensities of the MT architectonics image.
- When the shift coordinates (m,n) of coherent image along predominating direction of MT bundles packing increases, the functions $G(\psi\psi)$ monotonously decrease. This points to coordinate decorrelation of intensities distribution of the corresponding image.
- Correlation length, which is determined for the $G(\psi\psi)/e$ value, in parallel analyzer-polarizer is 70-80 μm for all types of samples, and becomes smaller for the crossed analyzer-polarizer and comes to 40-50 μm.

The data obtained caused by specific architectonic muscle tissue morphological structure. The average size of MT bundles is of 50 μm.

The coherent images of such samples obtained in parallel polarizer-analyzer [Figure 25(a) and 25(c)] contain polarization non-filtered component – speckle noise. That is why correlation length of corresponding ACF appears to be somewhat larger. In the crossed polarizer-analyzer the contrast of MT architectonics image increases owing to the speckle-noise compensation. Thus, the ACF correlation length corresponds to average statistical size of muscle bundles.

The comparative analysis of the ACF series of images of tissue of group A and B revealed the presence of a high-frequency quasi-harmonic component modulating the function $G(\psi\psi)$ of physiologically normal muscular tissue of the heart [Figures 25(a) and 25(b)]. The modulation frequency corresponds to the characteristic morphological size of the dark region (~2 μm) in the coherent image. This ACF component is absent for necrotically changed tissue [Figures 25(c) and 25(d)].

The special feature revealed can be associated with polarization visualization of the actin component in the image of fibers of muscular tissue. It is known that a periodic (equidistant) spatial distribution of this protein in the form of transverse disks with a mean statistic thickness of 1-3 μm is typical of physiologically normal fibers. Therefore, in the case of a crossed polarizer and analyzer this image component represents a system of equidistant bands of zero intensity (polarizophots) perpendicular to the direction of stacking of myosin fibers. Thus, the ACFs of such images turn out to be periodically modulated.

On the contrary, processes of degenerative-dystrophic changes in muscular tissue are accompanied by the degradation of the structure of actin proteins, which is manifested optically by an increase in the intensity of images of the corresponding polarizophots and in the violation of their

equidistance. Therefore, the modulation amplitude of the ACF of these images decreases and practically disappears in case of muscular tissue necrosis (myocardium infarct) [Figures 25(c) and 25(d)].

These processes are highlighted in greater detail by determining the power spectrum $J(\psi, \psi)$ [33] of a series of the ACF of polarization patterns of coherent images of tissues. The spectra $J(\psi, \psi)$ of muscular tissue of groups A and B are presented in Figure 26, notations are the same as in Figure 25.

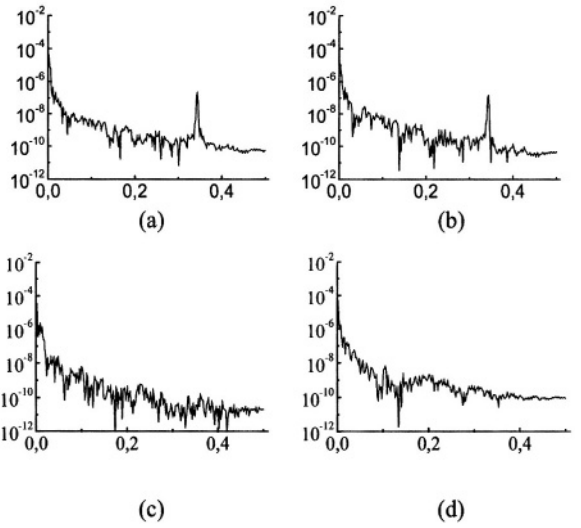

Figure 26. Spectral densities of images of the muscular tissue. Notations are the same as in Figure *25.*

The most pronounced distinctions between them are observed in the high-frequency spectral region in the case of crossed polarizer and analyzer. A clearly localized spectral maximum corresponds to the quasi-harmonic structure of the image of the actin component in the coherent image of physiologically normal tissue [Figure 26(b)]. A virtually smooth spectrum $J(\psi, \psi)$ is typical for muscular tissue samples with necrotic changes. This indicates the practically complete degradation of actin proteins.

On the other hand, processes of degenerative-dystrophic changes of biological tissue turn out to be spatially localized. Thus, the diagnostic efficiency of correlation processing of the corresponding images turns out to be insufficient. This is caused by the integral nature of averaging over the entire intensity array in the image plane, which considerably decreases the sensitivity of detecting anomalies in the structure of the corresponding ACFs and their power spectra.

Figure 27 presents results illustrating the diagnostic potentialities of the wavelet analysis of coherent images of physiologically normal muscular tissue obtained with a parallel [Figure 27(a)] and crossed [Figure 27(b)] polarizer and analyzer. Figures 27(c) and 27(d) show identical data for necrotically changed tissue.

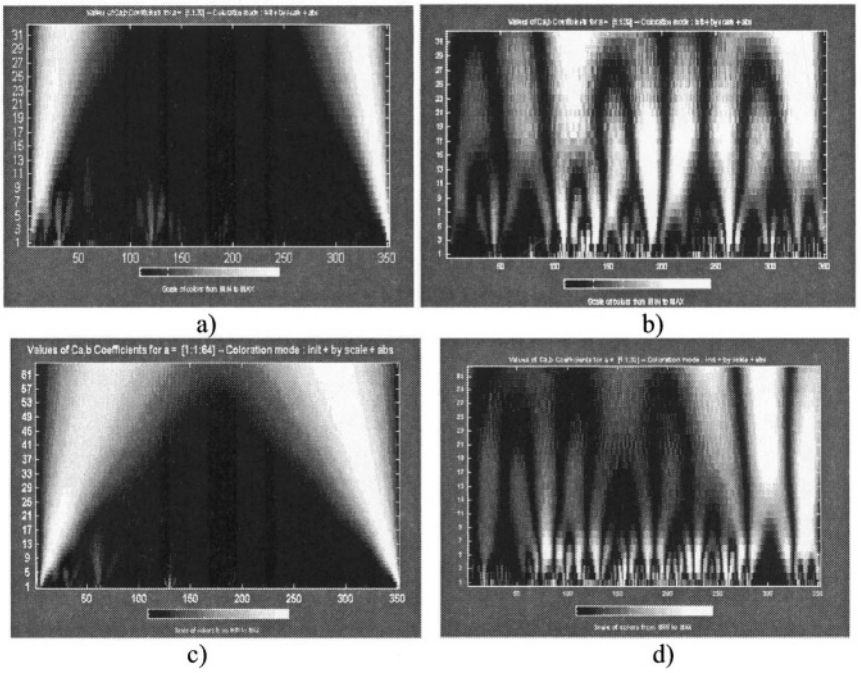

Figure 27. Wavelet analysis of coherent images of the muscular tissue (see explanations in the text).

The results obtained allow the following conclusions to be made.

In the case of a parallel polarizer and analyzer, the spatial distribution of maximal values of the coefficients c_{jk} of the wavelet expansion of the intensities $\Psi(X)$ of coherent images of muscular tissues of both groups is concentrated in the region of small scales a and turns out to be sufficiently smooth and weakly fluctuating for large scales of "windows" of the analysis.

In the case of a crossed polarizer and analyzer, maxima of coefficients of the wavelet-decomposition of images of physiologically normal muscular tissue are observed for almost all scales of the function $\xi_{jk}(X)$. The pattern is different for pathologically damaged biological tissue. If the analysis is carried out within a low-frequency window, a spatially localized maximum of the coefficients c_{jk} is observed. Their values are 2-3 times higher than the average values of the coefficients determined for the given wavelet-function

scales. They practically equal to zero for low scales of the analysis of a coherent image.

The results obtained can be related to special features of the morphological structure of muscular tissue. Samples of both groups are characterized by fiber stacking, which is uniform enough over the space. This is manifested in a smooth distribution of spatial frequencies of the corresponding coherent images. However, a strong light scattering background in images obtained with a parallel polarizer and analyzer masks their low-frequency component. As a result, the wavelet analysis diagnoses only the spatial distribution of the high-frequency structure of the corresponding images. Their polarization filtering allows the maximum contrast of an image of a collection of muscular fibers to be achieved. This determines the increase in the sensitivity if wavelet analysis and the increase in fluctuations of its coefficients.

In muscular tissue with necrotic changes, the region of myocardium infarct (the region where the structure of its fibers is destroyed) is present. From the optical point if view, this is a low-frequency pattern with almost zero intensity in the case of a crossed polarizer and analyzer, which results from the loss of anisotropic properties in proteins. Therefore, the corresponding wavelet expansion is characterized by a maximum of large-scale coefficients precisely in this spatial domain of a polarization-filtered image. Conversely, the high-frequency structure of a coherent image of the necrotic region is absent, which is represented by a set of zero values of the small-scale coefficients c_{jk}.

3.6 SUMMARY

Here are the most important results, presented in the chapter:

- The universal technique of polarization selection of information in random laser fields, based on the synthesis of experimentally measured Mueller matrix of the object by partial matrices of reflecting and transmitting the light through the turbid medium has been elaborated;

- The mechanisms of transforming the states of object field polarization as a result of manifestation of optical anisotropy of crystalline and architectonic of biological tissue structure has been analyzed. The interrelation between the values of the azimuths and ellipticities of object field polarization with the orientation direction and birefringence of the fibrillar substance (collagen, elastin, myosin, hydroxyapathite, etc.) of crystalline structures of tissue of different physiological origin has been determined. The reconstruction of orientation and optically active tissue structure, which is the basis of the new techniques of polarization-phase reconstruction, has been performed by measuring the spatial distribution of polarization states of the object fields.

- It has been found that the processes, connected with reduction of architectonics substance birefringence determine the 2-3 times reduction of the average values of statistical parameters in comparison with the corresponding parameters obtained for the physiologically normal structures. On the contrary, under the pathological changes (tumor-forming processes) the statistic parameters of the corresponding images have the opposite tendency, connected with increasing of birefringence of architectonic substance.

- It was determined that forming the directions of pathological growth of tissue architectonics is accompanied by forming the stochastic component of autocorrelation function of the polarization filtered images. The degenerative-dystrophic processes (disorientation of crystalline domains) are accompanied by smoothing the oscillations of autocorrelation function. It is shown that the dispersion of the autocorrelation function can be used as a diagnostic feature of the architectonics state of tissues of different physiological origin. The ranges of this parameter variation for different types of physiologically normal and pathologically changed tissue have been determined.

- Optical defects of crystallite phase (decalcification and degradation of architectonics substance) of tissue are determined by local decrease of wavelet-decomposition coefficients; the formation of the directions of tumor-growth is accompanied by local increase of wavelet-decomposition coefficients. Maximal values of wavelet coefficients, obtained for correspondingly minimal and maximal windows of the analysis (wavelet-functions) determine micro- and macro-sizes of the architectonics optical defect, which corresponds to the appearance of the processes of its morphological changes.

- The determined interrelations of statistic, correlation, and wavelet properties of polarization filtered images of tissue architechtonics with its orientation-phase structure make the basis of the elaborated technique of 2D polarization tomography of biological tissues.

REFERENCES

1. W.-F. Cheong, S.A. Prahl, and A.J. Welch, "A review of the optical properties of biological tissues," *IEEE J. Quantum Electr.* **26**, 2166-2185 (1989).
2. R.R. Anderson, J.A. Parrish, "Optical properties of human skin," in *The Science of Photomedicine,* J.D. Regan and J.A. Parrish eds. (Plenum Press, N.Y., 1982), 147-194.
3. J.M. Schmitt, A.H. Gandjbakhche, and R.F. Bonnar, "Use of polarized light to discriminate short-photons in a multiply scattering medium," *Appl. Opt.* **31**, 6535-6546 (1992).
4. H. Rinneberg, "Scattering of laser light in turbid media, optical tomography for medical diagnostics," in *The Inverse Problem,* H. Lubbig, ed. (Akademie Verlag, Berlin, 1995) 107-141.
5. V.V. Tuchin, "Coherence-domain methods in tissue and cell optics," *Laser Physics* **8**, 1-43 (1998).
6. J.M. Schmitt, A.H. Gandjbakhche, and R.F. Bonnar, "Use of polarized light to discriminate short-photons in a multiply scattering medium," *Appl. Opt.* **31**, 6535-6546 (1992).
7. D.A. Zimnyakov, V.V. Tuchin, and A.A. Mishin, "Spatial speckle correlometry in applications to tissue structure monitoring,"*Appl.Opt.* **36**, 5594-5607 (1997).
8. S.P. Morgan, M.P. Khong, and M.G. Somekh, "Effects of polarization state and scatterer concentration optical imaging through scattering media," *Appl. Opt.* **36**, 1560-1565(1997).
9. H. Horinaka, K. Hashimoto, K. Wada, and Y. Cho, "Extraction of quasi-straightforward-propagating photons from diffused light transmitting through a scattering medium by polarization modulation," *Opt. Lett.* **20**, 1501-1503 (1995).
10. M.R. Ostermeyer, D.V. Stephens, L. Wang, and S.L. Jacques, "Nearfield polarization effects on light propagation in random media," *OSA TOPS on Biomedical Optics Spectroscopy and Diagnostics* **3**, 20-25 (1996).
11. A.M. Hielscher, J.R. Mourant, and I.J. Bigio, "Influence of particle size and concentration on the diffuse backscattering of polarized light," *OSA TOPS on Biomedical Optics Spectroscopy and Diagnostics* **3**, 26-31 (1996).
12. D. Bicout, C. Brosseau, A.S. Martinez, and J.M. Schmitt, "Depolarization of multiply scattering waves by spherical diffusers: influence of the size parameter," *Phys. Rev. E.* **49**, 1767-1770(1994).
13. J.R. de Boer, T.E. Milner, M.J.C. van Gemert, and J.S. Nelson, "Two-dimensional birefringence imaging in biological tissue by polarization-sensitive optical coherence tomography," *Opt. Lett.* **22**, 934-936 (1997).
14. V.V. Tuchin, "Coherent and polarimetric optical technologies for the analysis of tissue structure (overview)," *Proc. SPIE* **2981**, 120-159 (1997).
15. D.A. Zimnyakov, V.V. Tuchin, and K.V. Larin, "Speckle patterns polarization analysis as on approach to turbid tissues structure monitoring," *Proc. SPIE* **2981**, 172-180 (1997).
16. P. Bruscaglioni, G. Zaccanti, and Q. Wci, "Transmission of a pulsed polarized light beam through thick turbid media: numerical results," *Appl. Opt.* **32**, 6142-6150 (1993).

17. I. Freund, M. Kaveh, R. Berkovits, and M. Rosenbluh, "Universal polarization correlations and microstatistics of optical waves in random media," *Phys.Rev.B.* **42**, 2613-2616(1990).
18. M.R. Hee, D. Huang, E.A. Swanson, and J.G. Fujimoto, "Polarization-sensitive low-coherence reflectometer for birefringence characterization and ranging," *J. Opt. Soc. Am. B.* **9**, 903-908 (1992).
19. J.T. Bruulsema, J.E. Hayward, and T.J. Farrell, "Correlation between blood glucose concentration in diabetics and noninvasively measured tissue optical scattering coefficient," *Opt. Lett.* **22**, 190-192 (1997).
20. H.-J. Schnorrenberg, R. Haβner, M. Hengstebeck, K. Schlinkmeier, and W. Zinth, "Polarization modulation can improve resolutionin diaphanography," *Proc. SPIE* **2326**, 459-464 (1995).
21. N. Kollias, "Polarized Light Photography of Human Skin," in *Bioengineering of the Skin: Skin Surface Imaging and Analysis,* K.-P.Wilhelm, P.Elsner, E.Berardesca, and H.I.Maibach eds. (CRC Press, Boca Raton *et al.,* 1997), 95-106.
22. Special section on Tissue Polarimetry, L. V. Wang, G. L. Cote', and S. L. Jacques eds. *J. Biomed. Opt.* **7** (3), 278–397 (2002).
23. S.G. Demos, W.B. Wang, and R.R. Alfano, "Imaging objects hidden in scattering media with fluorescence polarization preservation of contrast agents," *Appl. Opt.* **37**, 792-797 (1998).
24. F. Yang, W. Liao, "Modeling and decomposition of HRV signals with wavelet transforms," *IEEE Eng. Med. Biol.* **16**, 17-22 (1997).
25. M. Antonini, M. Barlaud, P. Mathieu, and I. Daubechies, "Image coding using wavelet transform," *IEEE Trans. Image Processing* **1**, 205-220 (1992).
26. A.G. Ushenko, "Polarization structure of scattering laser fields," *Opt. Eng.* **34**, 1088-1093 (1995).
27. A.G. Ushenko and V.P. Pishak, "Vectorial structure of skin biospeckles," *Proc. SPIE* **3317**, 418-425 (1997).
28. A.G. Ushenko and V.P. Pishak, "Crystal optic properties of the transverse and longitudinal sections of the bone," *Proc. SPIE* **3317**, 425-434 (1997).
29. O.V. Angelsky, A.G. Ushenko, A.D. Arkhelyuk, and S.B. Yermolenko, "Investigation of polarized radiation diffraction on the systems of oriented biofractal fibers," *Proc. SPIE* **3573**, 616-619(1998).
30. A.G. Ushenko, S.B. Ermolenko, D.N. Burcovets, and Yu.A. Ushenko, "Microstructure of laser radiation scattered by optically active biotissues," *Opt. Spectrosc.* **87**, 434-438 (1999).
31. A.G. Ushenko, "Laser diagnostics of biofractals," *Quant. Electron.* **29**, 1078-1084 (1999).
32. O.V. Angelsky, A.G. Ushenko, S.B. Ermolenko, and D.N. Burcovets, "Structure of matrices for the transmission of laser radiation by biofractals," *Quant. Electron.* **29**, 1074-1077(1999).
33. A.G. Ushenko, "Stokes-correlometry of biotissues," *Laser Physics* **10**, 1 – 7 (2000).
34. O.V. Angelsky, A.G. Ushenko, D.N. Burkovets, V.P. Pishak, Yu.A. Ushenko, and O.V. Pishak, "Polarization-correlation investigations of biotissue multifractal structures and their pathological changes diagnostics," *Laser Physics* **10**, 1136-1142 (2000).
35. A.G. Ushenko, "Laser biospeckles' fields vector structure and polarization diagnostics of skin collagen structure," *Laser Physics* **10**, 1143-1149 (2000).
36. O.V. Angelsky, A.G. Ushenko, S.B. Ermolenko, D.N. Burcovets, and Yu.A. Ushenko, "Laser polarimetry of pathological changes in biotissues," *Opt. Spectrosc.* **89**, 973-978 (2000).
37. A.G. Ushenko, "Polarization structure of biospeckles and the depolarization of laser radiation," *Opt. Spectrosc.* **89**, 597-600 (2000).

38. O.V. Angelsky, A.G. Ushenko, S.B. Ermolenko, D.N. Burcovets, V.P. Pishak, and Yu.A. Ushenko, "Polarization-based visualization of multifractal structures for the diagnostics of pathological changes in biological tissues," *Opt. Spectrosc.* **89**, 799-804 (2000).
39. A.G. Ushenko, "Correlation processing and wavelet Analysis of polarization images of biological tissues," *Opt. Spectrosc.* **91**, 773-778 (2001).
40. A.G. Ushenko, "Laser probing of biological tissues and the polarization selection of their images," *Opt. Spectrosc.* **91**, 932-936 (2001).
41. A.G. Ushenko, "Polarization contrast enhancement of images of biological tissues under the conditions of multiple scattering," *Opt. Spectrosc.* **91**, 937-940 (2001).
42. A.G. Ushenko, "Laser polarimetry of polarization-phase statistical moments of the object field of optically anisotropic scattering layers," *Opt. Spectrosc.* **91**, 313-316 (2001).
43. A.G. Ushenko, "Correlation processing and wavelet analysis of polarization images of biological tissues," *Opt. Spectrosc.* **91**, 773-778 (2001).
44. A.G. Ushenko, D.N. Burcovets, and Yu.A. Ushenko, "Laser polarization visualization and selection of biotissue images," *Laser Physics* **11**, 624-631 (2001).
45. O.V. Angelsky, A.G. Ushenko, D.N. Burcovets, and Yu.A. Ushenko, "Polarization-correlation analysis of anisotropic structures in bone tissue," *Opt. Spectrosc.* **90**, 458-462(2001).
46. A.G. Ushenko, "Polarization correlometry of angular structure in the microrelief of rough surfaces," *Opt. Spectrosc.* **92**, 227-229 (2002).
47. Yu.A. Ushenko, "Skin as a transformer of the polarization structure of laser radiation," *Opt. Spectrosc.* **93**, 321-325 (2002).
48. A.G. Ushenko, D.N. Burcovets, and Yu.A. Ushenko, "Polarization-phase mapping and reconstruction of biological tissue architectonics during diagnosis of pathological lesions," *Opt. Spectrosc.* **93**, 449-456 (2002).

Chapter 4

DIFFUSING WAVE SPECTROSCOPY: APPLICATION FOR SKIN BLOOD MONITORING

Igor V. Meglinski[1,2] and Valery V. Tuchin[1]
1. Saratov State University, Saratov, 410012 Russian Federation; 2. School of Engineering, Cranfield University, MK43 0AL, UK

Abstract: This chapter describes the developing and validation of the diffusing wave spectroscopy (DWS) methodology further to the point that DWS skin blood flow measurements can be routinely and accurately obtained in a separate skin vascular bed on normal skin, and to estimate changes before, during and after medical and/or cosmetic procedures. This is likely lead to non-invasive quantitative monitoring of the effectiveness of general diagnostics, diabetes studies, pharmacological intervention for failing surgical skin flaps or replants, blood microcirculation monitoring during sepsis, assess burn depth, diagnose atherosclerotic disease, and investigate mechanisms of photodynamic therapy for cancer treatment.

Key words: diffusing wave spectroscopy, skin blood microcirculation

4.1 INTRODUCTION

The development and the use of non-invasive optical diagnostic techniques for diagnoses, studies and control in biology and medicine are one of the important trends in modern optics [1,2]. The non-invasive probing of skin tissues at the cells scale and mapping of the blood flow in the micro-vascular network are common objectives for physicians, biologists, physiologists and pharmacists.

Typically, the vascular circulation disturbances are due to malformation structure of the capillary loops and the red blood cells (RBC) aggregation changes. The disturbances in the most peripheral blood circulation are a

frequent complication of various common diseases including diabetes [3], arteriosclerosis [4], venous leg ulceration [5], anemia [6], ischemia [7], *etc.* The *World Health Organization* has recently reported that these diseases are now more prevalent than cancer [8]. To diagnose and treat the diseases effectively, clinically applicable methods that allow high-resolution quantitative non-invasive monitoring of micro-vascular flows are required. The optical diagnostic techniques offer unique opportunities for the researchers working in various branches of biology, medicine, cosmetics and health care industry.

Nevertheless, the problem of implementing these techniques in clinical practice in order to solve a wide range of actual diagnostic tasks remains unresolved. The difficulties in application are due to strong anisotropic scattering and absorption of the sounding radiation in most biological tissues in the visible and near-infrared spectrum (400-1500 *nm)* [2]. As a result, diffraction and scattering by the structural elements of biological tissues produce phase shifts in optical waves, causing multiple interference phenomena. Furthermore, complex inhomogeneous variations of the optical properties of skin tissues, for example, act like a screen, which keeps stray optical radiation from penetrating deeply into the human body. An analytical mathematical expression for the propagation of optical radiation describing these conditions is complex. Practically, it is extremely difficult to distinguish regular waves corresponding to internal structure of the medium or individual characteristics of the scattering particles. Whereas, the analysis of these wave groups enables one to retrieve the most significant characteristics of the probed media.

The problems involving the multiple scattering of laser radiation in various complex highly scattering media have been attracting a great deal of attention in the past years [9]. This is due to both the diversity of beautiful physical effects observed under multiple scattering conditions (i.e., enhancement of coherent back-scattering, angular, and temporal correlation of the scattered radiation, waves localization, *etc*.) and the extensive use of optical diagnostic techniques in many practical industrial and medical applications.

During the last decade a number of emerging technologies have become available for the non-invasive studies of blood flow and micro-circulation, including Doppler ultrasound [10], conventional and magneto resonance angiography [11], laser Doppler flowmetry (LDF) [12, 13], capillaroscopy [14], laser-scanning confocal imaging [15], optical Doppler tomography (ODT) [16] and color Doppler optical coherence tomography (CDOCT) [17]. However, the high-resolution non-invasive techniques for *in vivo* quantitative blood flow measurements are not currently available as a diagnostic tool in medicine, as each of these methods has a limitation.

Doppler ultrasound provides a means to resolve flow velocities at different locations in a tissue, but a long acoustic wavelength required for deep tissue penetration limits spatial resolution to 200 μm. Application of the capillaroscopy technique requires the tissues to be thin enough (less than 400 μm) to be transilluminated. Images obtained using laser-scanning confocal microscopy can only be collected at a fraction of the normal video rate. Conventional and magneto resonance angiography provides the information mainly about large blood vessels, such as coronary artery.

LDF techniques are very useful for measuring fluid velocities, including blood flow at the secluded topical capillary/vein, but suffer from the limitation that they measure the velocity only at a single point [13]. To observe a map of blood flow velocity distribution a scanning is required. However, strong optical scattering in biological tissue limits spatially resolved flow measurements by LDF techniques. As a result LDF can provide only an average characteristic of blood flow in a unit of tissue per unit of time, so-called perfusion. Whereas, to distinguish blood flow in different compartments of vascular network LDF measurements require a precise understanding of which vascular bed is primarily responsible for the detected signal.

The disadvantages of recently developed ODT and CDOCT are a high sensitivity to movement of the measured object, and an inability to quantify flow value in the vascular bed at the required resolution, i.e., 50 μm or less, for small diameter vessels, where the blood flow is less than ~100 $\mu m/s$.

In contrast, Diffusing Wave Spectroscopy (DWS) is sensitive to fluctuations of the media on the length-scales much smaller than the wavelength of sounding laser radiation (often as small as several Angstroms, Å [18]. This technique allows providing information on the average size of particles and their motion within highly scattering tissues avoiding mentioned above limitations.

The present chapter describes the developing and validation of the DWS methodology further to the point that DWS skin blood flow measurements can be routinely and accurately obtained in a separate skin vascular bed on normal skin, and to estimate changes before, during and after medical procedures. This is likely lead to non-invasive quantitative monitoring of the effectiveness of general diagnostics, diabetes studies, pharmacological intervention for failing surgical skin flaps or replants, blood micro-circulation monitoring during sepsis, assess burn depth, diagnose atherosclerotic disease, and investigate mechanisms of photo-dynamic therapy for cancer treatment.

It should be noted, that authors do not try including the references for all significant and interesting reviews, research papers, reports, and monographs in the discussed area. We are given references to basic monographs and

reviews, which offer the most systematic and fundamental consideration of various aspects of DWS and blood microcirculation, both at highly qualified and comprehensive levels. We refer to the original papers only to gain an insight into those questions, attention to which are evaded in monographs, but are essential for understanding the operation principles of the experimental setup and some theoretical aspects.

4.2 SKIN STRUCTURE AND SAMPLING VOLUME

As an object of investigation by optical techniques the skin represents a complex heterogeneous medium consisting of different visible layers [19-21]: 1- epidermis, 2- dermis and 3- subcutaneous fat (Figure 1).

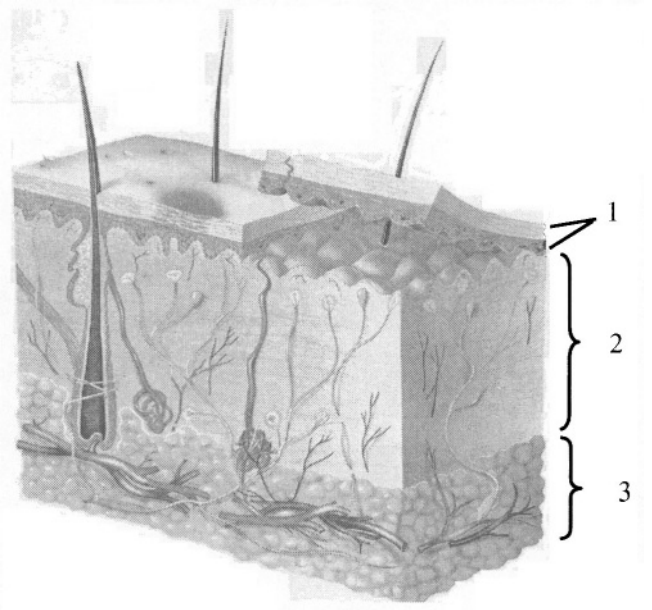

Figure 1. Skin structure.

These layers contain the chromophores including DNA, urocanic acid (UCA), amino acids, elastin, collagen, keratin, NADH, melanin and their precursors and metabolites, whereas the major contribution to light absorption in visible (400-770 *nm*) and near-infrared (NIR) (770-1400 *nm*) spectral regions arises from oxy- and deoxy- hemoglobin, contained in blood, melanin and water [2, 22, 23]. Thereby, the non-invasive monitoring of blood from the collected reflectance spectra of the skin is complicated by

the fact that the pigments and blood content of the skin tissues can vary both in the spatial distribution and in the amount [19-21, 24-27].

Corresponding to the blood vessels distribution within the skin it is possible to sub-divide skin into layers in agreement with the geometry and sort of the vessels: capillary loops, venules, arterioles, venues and so on. Thus, in our model the first dermal layer, named *Papillary dermis* (approximately 150 μm thick) included capillary loops generally orientated perpendicularly to the surface of the skin capillary loops [24-27]. These superficial capillary loops with the inner diameter about 2-40 μm perfuse by slow-speed red blood cells that supply the tissue with oxygen and nutritive substances and remove waste metabolites. The behavior of the blood flow in the capillaries is non-Newtonian [28,29] that presents difficulties for the phantom modeling and computer simulation of it. Deeper in the *Upper blood net dermis* (80 μm thick) lie arterioles, venules and arterio-venous anastomoses with inner diameter of 10-40 μm which take an active part in body temperature regulation. *Reticular dermis* (1500 μm thick) includes small arteries and veins (20-60 μm inner diameter) mainly orientated perpendicularly to the surface of the skin. These small vessels constitute routes for blood supply and drainage to veins and arteries (50-100 μm inner diameter) from the *Deep blood net dermis* (170 μm thick) and *Subcutaneous fat* (can be as much as 5-6 *mm* thick).

Regarding this blood vessel distribution, the measurements require an understanding of which vascular bed is primarily responsible for the detected signal. This problem is well known as the related field of Laser Doppler Flowmetry [30,31]. Knowing the sampling volume makes it possible to find the best range of different probe geometry for the measurements of signal from the required zones and groups of vessels within the skin.

However, due to the multiple scattering, the radiation inside the skin becomes distributed within an area, determined by the structural/geometrical and optical properties of the tissues and conditions of its illumination [1,2]. From the practical viewpoint, this area of radiation distribution is mainly of interest for optical dosimetry problems, whereas for diagnostics the detected-signal localization, or so-called 'sampling volume', is of greatest interest. The direct measurements of the sampling volume can apparently be performed only *in vitro* [32], and only if it coincides with the distribution of incident radiation. However, the profile of the detected-signal localization within the tissues can be determined by using Monte Carlo modeling [33], by analyzing the photon measurement density function (PMDF), which characterizes the mean time of localization of the photons detected by the detector within a certain elementary volume of the medium.

Recently, the area of the sounding radiation localization within the skin at the small (200-800 μm) fiber-optics probe spacing has been estimated using Monte Carlo technique [34,35]. In this study the computational model of

skin is represented as a complex inhomogeneous multi-layered highly scattering and absorbing medium, with the randomly rough boundaries of skin layers corresponding to their cells structure [19-21]. The volume fraction of derma occupied by blood vessels is usually in the 1-20% range, and varies in apparent blood content ranging from 2-12% [24-27]. On the other hand, the skin is quite fibrous and the apparent average blood content is quite low. If one assumed that the blood was uniformly distributed in skin, that average blood content would be about 0.2%. However, the reality is that the blood is located in the venous plexus and is probably in the 2-10% range within a 50-100 μm thickness. This is one of particular reason that we subdivide the derma into four different layers: *Papillary dermis, Upper blood net dermis, Reticular dermis, Deep blood net dermis.* Indeed, these layers are approximate, but illustrate that blood spatial distribution in a heterogeneous tissue is an important factor influencing the optics, that were discussed widely [2,36-38]. The details of skin optics modeling, high accuracy of the technique and its validation are presented in [34,35,39]. It is also demonstrated that when the computational model of skin is supplied with the reasonable physical and structural parameters typical for skin tissues [2,19-27,36,40-42], the results of skin diffuse reflectance spectra simulation agree reasonably well with the results of *in vivo* skin spectra measurements [43, 44].

4.3 PRINCIPLES OF THE DIFFUSING WAVE SPECTROSCOPY

DWS is a novel modern technique uniquely suited for the measurements of the average size of particles and their motion within the turbid macroscopically homogeneous highly scattering media, like sprays, aerosols or liquid suspensions. This technique is an extension of conventional Dynamic Light Scattering (DLS) [45] to the regime of multiple scattering. Introduced in 1987 [46], DWS has rapidly evolved in recent years and is currently applied to study various types of turbid media in Brownian motion, for example, colloidal suspensions, particle gels, aerosols, foams, emulsions, and biological media [18,47,48].

Despite the define similarity between the experiments on DWS and conventional experimental schemes of correlation spectroscopy of optical mixing [45,49] the DWS theory is based on a qualitatively different interpretation of radiation propagation in strongly scattering media. Here, propagation of coherent radiation through a randomly inhomogeneous highly scattering medium describes in terms of diffusion approximation [48, 50] and coherent scattering channels theory [51]. It is assumed thereby that due

to multiple scattering in a randomly inhomogeneous highly scattering medium the each photon, that has reached given observation point of the detector, experiences a great number of scattering events *N*. The successive scattering acts taking place at the instant of time t at the scattering particles located in points $r_1(t)$, $r_2(t)$, $\ldots r_i(t), \ldots r_N(t)$ in medium with wave vectors k_1, $k_2, \ldots k_i, \ldots k_N$, result in formation of the field $E(t)$, whose total phase change $\Delta\phi(t)$ is determined as [52]:

$$\Delta\phi(t) = \sum_{i=0}^{N} k_i(t)\left[r_{i+1}(t) - r_i(t)\right], \tag{1}$$

$\Delta\phi(t)$ is dependent on the total path length s of each photon migrated from the source r_0 to the detector r_{N+1} points (Figure 2):

$$s = \sum_{i=0}^{N}\left|r_{i+1}(t) - r_i(t)\right| = \sum_{i=0}^{N}\left(\frac{k_i}{|k_i|}\right)\left(r_{i+1}(t) - r_i(t)\right). \tag{2}$$

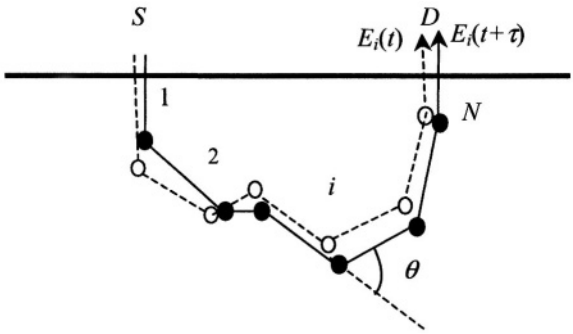

Figure 2. Schematic diagram of coherent radiation propagation through a randomly inhomogeneous semi-infinite medium with strong scattering, in which light passes from the radiation source (*S*) towards the detector (*D*): (•) shows the location of scattering particles at the instant of time $(t + \tau)$ and (o) indicates the location of scattering particles at the instant of time τ.

The quantity s is related to the number of scattering acts by the obvious relation $s = Nl^*$, where l^* is the mean free path of a photon (the reciprocal of the medium scattering coefficient μ_s, i.e., $l^* = (\mu_s)^{-1}$). In highly scattering media (e.g., human skin, where typical values of μ_s at the visible/near-infrared region of spectra are 10-100 mm^{-1}) s can be considered as a statistically independent random walk. The distribution function of photon

migration paths $P(s)$ in the medium is determined as the probability that light will cover the optical paths s, moving from the point r_0 to the point r_{N+1} [52]:

$$P(s) = \left(\frac{\upsilon}{4\pi s D}\right)^{3/2} \exp\left(\frac{\upsilon |r_0 - r_{N+1}|^2}{4sD}\right). \quad (3)$$

Here, $D = \upsilon l / 3$ is the photon diffusion coefficient, υ is the speed of light in the medium, and l is the transport length of free path $l^* = (\mu'_s)^{-1}$, where μ'_s is the reduced scattering coefficient determined as: $\mu'_s = \mu_s(1 - \langle\cos\theta\rangle)$, and $\langle\cos\theta\rangle$ is the mean cosine of scattering angle.

The field $E(t)$ interferes with the field $E^*(t+\tau)$ scattered slightly later at the same series of the scattering particles at the instant of time $t+\tau$ (see Figure 2). The time it takes the photons to travel the entire optical path in the medium is much shorter than the characteristic time of changing the position of scattering particles in the medium. Thus, in result of motion of the particles the phase between fields $E(t)$ and $E^*(t+\tau)$ will be different at different instants of time or fluctuate. This predetermines temporal fluctuations of the scattered radiation intensity recorded in the far zone. The patterns of the intensity fluctuations, called speckles, can be visualized on a screen, or sensed by a homodyne detector [53].

Quantitatively these fluctuations are better to examine by the comparative analysis of temporal field correlation function

$$G_1(\tau) = \langle E(t) E^*(t+\tau)\rangle, \quad (4)$$

determined as:

$$G_1(\tau) = I_0 \sum_{j=0,\infty} P(s_j) \exp\left(-\frac{N}{6}\langle q^2\rangle\langle \Delta r^2(\tau)\rangle\right), \quad (5)$$

where $I_0 = \langle |E(t)|^2\rangle$, $\langle \ldots \rangle$ denotes an ensemble average, q is the change in the wave vectors k_i and k_{i+1}:

$$q = |k_i - k_{i+1}| = 2k_0 \sin\frac{\theta}{2}. \quad (6)$$

Respectively,

$$\left\langle q^2 \right\rangle = \left\langle 4k_0^2 (1-\cos\theta) \right\rangle = 2k_0 \left(1 - \left\langle \cos\theta \right\rangle\right) = 2k_0 \frac{l^*}{l}, \tag{7}$$

where $k_0 = |k_i| = |k_{i+1}|$, and θ is the angle between the directions $k_i = k_{i+1}$ (i.e., angle of the i-th scattering act). Substituting equation 7 in equation 5, we obtain that normalized temporal field autocorrelation function $g_1(\tau) = G_1(\tau) / \langle |E(t)|^2 \rangle$, has the form:

$$g_1(\tau) = \int_0^\infty P(s) \exp\left(-\frac{1}{3} k_0^2 < \Delta r^2(\tau) > \frac{s}{l} \right) ds. \tag{8}$$

It is seen, that similar to the conventional DLS technique [45], the change in $g_1(\tau)$ is determined in terms of their mean-square displacements $\langle \Delta r^2(\tau) \rangle$, with the difference that slope of $g_1(\tau)$ increases in proportion to the average number of scattering particles. This has been verified directly by Yodh *et al,* using a pulsed laser and gating the broadened response to select photon path lengths of a specific length [54]. For the continuous wave illumination equation 8 is valid given the assumption that the laser coherence length is much longer than the width of the photon path length distribution [55].

For a system that multiply scatters laser radiation, the transport of temporal field correlation function is accurately modeled by the correlation diffusion equation [56,57], i.e.:

$$\left(D\nabla^2 - \upsilon\mu_a - 2\upsilon\mu'_s D_B k_0^2 \tau \right) \cdot G_1(\mathbf{r}, \tau) = -\upsilon S(\mathbf{r}). \tag{9}$$

Here, $G_1(\mathbf{r}, \tau)$ is determined by equation 4, and is a function of position $\mathbf{r}$, and correlation time τ; it has units of intensity, energy per area per second. D is the photon diffusion coefficient, k_0 is the wavenumber of the light in the medium, υ is the speed of light in the medium and S($\mathbf{r}$) is the distribution of light sources with units of photons per volume per second. Note that similar to μ_a, describing losses due to photon absorption, $\left(2\mu'_s D_B k_0^2 \tau\right)$ is a loss term representing the 'absorption' of correlation due to dynamic processes. The correlation diffusion equation (see equation 9) is valid for turbid samples with the dynamics of scattering particles governed by Brownian motion. When $\tau = 0$ there is no 'dynamical absorption' and equation 9 reduces to the steady-state photon diffusion equation [58].

The correlation diffusion equation can be modified to account for other dynamic processes. In the cases of random flow and shear flow the correlation diffusion equation becomes:

$$\left(D\nabla^2 - \upsilon\mu_a - \frac{1}{3}\upsilon\mu'_s k_0^2 < \Delta r^2(\tau) > - \frac{1}{3}\upsilon\mu'_s < \Delta V^2 > k_0^2 \tau - \right.$$
$$\left. - \frac{1}{15}\upsilon\mu'^{-1}_s \Gamma^2_{eff} k_0^2 \tau^2 \right) G_1(\mathrm{r}, \tau) = -\upsilon S(\mathrm{r}) \quad . \quad (10)$$

Here, the forth and fifth terms on the left-hand side arise from random and shear flows respectively. $<V^2>$ is the second moment of the particle velocity distribution (assuming the velocity distribution is isotropic and Gaussian) [59,60] and Γ_{eff} is the effective shear rate [61]. Notice that the 'dynamical absorption' for flow in equation 10 increases as τ^2 compared to the τ increase for Brownian motion because particles in flow fields travel ballistically; also D_B, $<V^2>$ and Γ_{eff} appear separately because the different dynamical processes are uncorrelated. The form of the 'dynamical absorption' term for random flow is related to that for Brownian motion. Both are of the form $\frac{1}{3}\upsilon\mu'_s k_0^2 < \Delta r^2(\tau) >$, where $<\Delta r^2(\tau)>$ is the mean square displacement of a scattering particle. For Brownian motion $<\Delta r^2(\tau)> = D_B$ and for random flow $<\Delta r^2(\tau)> = <V^2>\tau^2$. For a complete discussion of the shear flow term the reader is referred to Wu *et al.* [61].

Flow in turbid media is an interesting problem that has received some attention. In these measurements experimenters typically determine a correlation function that may be a compound of many decays representing a weighted average of flow within the sample.

4.4 DWS EXPERIMENTAL APPROACH AND DATA ANALYSIS

Typical DWS experimental set-up (Figure 3) consists of a small numerical aperture multi-mode optical fiber ('source'), which transports a laser beam on the sample surface (4). In our case, coherent laser radiation at wavelength $\lambda = 514$ *nm* and power 1 *W,* generated in the TEM_{00} mode by an argon ion laser (1) with a Fabry–Perot etalon placed inside the laser cavity, is injected by means of a system of mirrors and a lens into a multimode fiber-optic waveguide (~ core diameter 100 μm, numerical aperture 0.16). The Fabry–Perot etalon inside the laser cavity gives an adequate radiation coherence length (~ about 3 *m*), which is necessary in experiments on multiple scattering of light [55].

Passing along the fiber-optic waveguide ('source') the light is incident on the surface of the sample. Diffusely scattered within the sample laser

radiation is then collected by means of a single-mode optical fiber ('detector', ~ diameter 3.1 μm, numerical aperture 0.13), which allows the fluctuations of the light intensity within the coherence area of the scattered radiation to be recorded. Passing along the single mode fiber, combined with the 'source' fiber in the probe (2), the scattered radiation enters the detecting system (3), included photo-multiplier tube (PMT) or avalanche photodiode (APD), operated in the photon counting mode and connected with a digital multichannel autocorrelator. The use of fiber-optics to deliver the laser radiation to the sample and to record the scattered light and the use of a digital correlator make it possible to obtain a high signal-to-noise ratio in the measurement process. The 'detector' separated from the 'source' at the small range of centre-to-centre distances (from 100 μm to 3 *mm).* The small 'source-detector' separation precedes shallow detecting depth discrimination in the medium [34, 35].

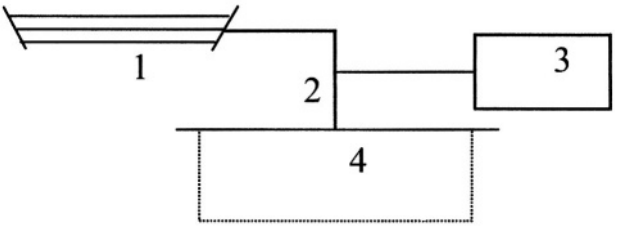

Figure 3. Schematic diagram of the diagnostic experimental set-up: 1 - source of laser radiation; 2 - fiber-optic probe; 3 - detecting system & computer; 4 - sample of investigation.

The output signal is then processed with an autocorrelator to the temporal intensity correlation function $g_2(\tau) = \langle I(\tau)I(t+\tau)\rangle / \langle I\rangle^2$, that is related to the normalized temporal field autocorrelation function $g_1(\tau)$ by the Siegert relation [45]:

$$g_2(\tau) = 1 - \beta |g_1(\tau)|^2 . \tag{11}$$

Here, $\langle I\rangle$ is the ensemble-averaged intensity, β is the some dimensionless parameter ($0 \le \beta \le 1$), which depends on the number of speckles detected and the coherence length, so called aperture function or correlation function 'interception' [62]. In ideal experimental set-up $\beta = 1$. The Siegert relation is valid for the Gaussian random optical fields only, when the scattering field's phase and amplitude variations are statistically independent of each other.

Further subsequent analysis of measured temporal field autocorrelation functions can be performed similar to the conventional DLS approach [45],

when the autocorrelation functions measured in single scattering regime can be evaluated by their representation in a semi-logarithmic plot [63]:

$$Y(\tau) = -\frac{1}{\tau}\ln\left(g_2(\tau) - 1\right) = D_B q^2 + v^2/2\omega^2 \,. \qquad (12)$$

Plotting $Y(\tau)$ versus τ gives a straight line with slope equal to the inverse beam transit time squared and intercept equal to the inverse correlation time. The data analysis for the conventional DLS becomes relatively easy because the intersection with the ordinate, by the Stokes-Einstein relation $D_B = \frac{k_B T}{6\pi\eta r}$, is a measure of the particle size, whereas the slope of correlator data is proportional to the convection velocity of scattering particles $v^2/2\omega^2$ [63]. Here, k_B denotes the Boltzmann constant, T the absolute temperature, η the shear velocity, and r the radius of the particles. Similar approach can be applied in case of the multiple scattering.

This opens the possibility of imaging an object consisting of scattering particles undergoing a motion which differs from the particle's motion outside the object even if there is no static scattering contrast between the object and its environment.

4.5 MAIN RESULTS AND DISCUSSION

The described above principles are applied systematically in strongly multiple scattering regime for measuring of velocity gradients of laminar shear flow [61], Poiseuille flow and Brownian motion of particles inside the particles in Brownian motion with different size [65,66], and to Brownian motion and Poiseuille, random and turbulent flows inside a stationary scattering environment ($D_B = 0$) [67,68]. These studies clearly demonstrate the validity of correlation diffusion equation for systems with Brownian motion, Poiseuille and shear flows.

Figure 4 presents an example of typical measured temporal field autocorrelation functions [64,68,69], measured in remission from a highly scattering solid slab of TiO_2 suspended in resin ($\Gamma_{eff} = 0$). The slab contains a single cylindrical vein containing a highly scattering liquid (0.5% solution of Intralipid - polydisperse suspension of fat particles ranging in diameter from 0.1 μm to 1.1 μm [70]) under Poiseuille flow. Liquid flow is pumped through the cylindrical vein in the slab with pump speeds of 0.08 cm s^{-1}, 0.62 cm s^{-1} and 3.22 cm s^{-1}.

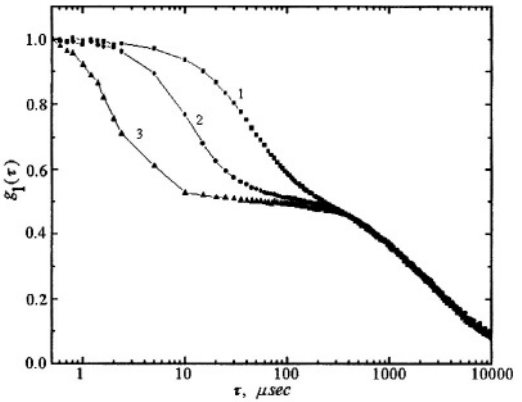

Figure 4. An example of measured temporal field autocorrelation functions for three different values of flow hidden within highly scattering medium: 0.08 (1), 0.62 (2) and 3.22 (3) cm/s [64].

The early τ (1-300 μsec) decay corresponds to the flow dynamics while the long τ (1000-10000 μsec) decay results from the ensemble averaging. The three curves come from three different flow speeds 0.08 (1), 0.62 (2) and 3.22 (3) *cm/s.* The early τ decay rate increases with the flow speed. The longer τ decay depends only on the rate of ensemble averaging, which is held constant.

Figure 5 presents an example of the results of the phantom measurements [64] and results predicted by the DWS theory, i.e., autocorrelation functions are calculated for the same amounts of flow embedded in a semi-infinite highly scattering random medium.

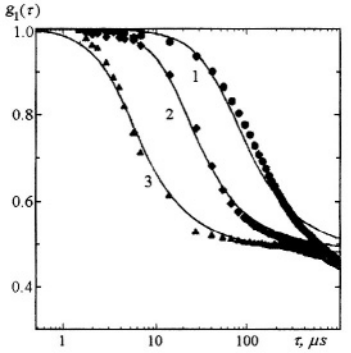

Figure 5. Fragments of the normalized temporal field autocorrelation functions measured (see Figure 4) and calculated by the DWS theoretical approach: lines – the results of DWS theory, and symbols - the results of experimental measurements for three different values of flow in highly scattering phantom medium: 0.08 (1), 0.62 (2) and 3.22 (3) cm/sec. In all cases, *a priori* knowledge of the flow is used in the calculation.

The comparison between experiment (symbols) and theory (solid lines) shown in Figure 5 indicates a good agreement. The parameters used in the calculation except for Γ_{eff}, were the known parameters. The effective shear rate, Γ_{eff}, was determined by fitting the analytic solution to the data with the constraint that Γ_{eff} had to scale linearly with the flow speed. The best fit to the data indicates that Γ_{eff} is approximately 6.8 cm^{-1} times the flow speed. Since the shear rate is given by the change in speed per unit length in the direction perpendicular to the flow, one might expect that the effective shear rate would be the flow speed divided by the radius of the vein. This simple calculation gives an effective shear rate that is a factor of two smaller than the measured Γ_{eff}. This difference results from the mismatches in optical indices of refraction and sensitivity to the semi-infinite boundary condition.

As one can see from these figures, the section of the correlation function in the bounded range of delay times τ ($1 < \tau < 400$ μs) under the conditions of the experiment [64,68] is most sensitive to a change in the velocity of the fluid flow inside the dynamic region; this agrees with the results obtained in Ref. [65]. For $\tau < 1$ μs the behavior of the correlation function is determined mainly by small but non-zero absorption of radiation in the medium, the absorption being the same both inside and outside the capillary. While for τ < 50–300 μs $g_1(\tau)$ tends to saturate at a constant level ('plateu') that is independent of the flow velocity (see Figures 4 and 5). This fact was predicted theoretically [71] and can be easily explained qualitatively on the basis of the correspondence between the short trajectories of photons in the medium and the long delay times τ [46]. For large τ the rate of decrease of $g_1(\tau)$ is determined mainly by photons with relatively short trajectories, since photons with long trajectories are now completely decorrelated. Photons with short trajectories consist mainly of photons which do not reach the capillary, and since the particles in the medium surrounding the capillary are immobile, the theoretically computed function $g_1(\tau)$ approaches a constant different from zero as $\tau \to \infty$. The value of this constant is determined solely by the depth at which the capillary is located. In other words, the intermediate 'plateau' (see Figures 4 and 5) shows fraction of the detected photons sampled in the dynamic region.

A number of phantom studies and development of the theoretical model carried out in terms of temporal field correlation functions based on the DWS approach show a good agreement between the experimental and theoretical results [48,57,60,61,64-69]. The correlation diffusion approach is more general, and we expect that the application of correlation diffusion imaging will further clarify information about heterogeneous flows in turbid media. Moreover, there are a number of systems now where DWS micro-rheology measurements well agree quantitatively with the traditional

macroscopic mechanical rheometry over time scales at which these techniques overlap [18,72,73].

Having carrying out the evaluation tests of the technique via the various theoretical and phantom studies [57,61-69], we made an attempt to monitor the dynamics of time variations in the skin blood microcirculation [64,74,75]. Measurements were made on the arm (back-side) of a healthy man with the experimental system described above (see Figure 3), where CW light generated by the He-Ne laser at wavelength λ=632.8 nm, coherence length of about 4 *cm,* and incident power 10 μW. The measurements of skin blood flow clearly demonstrate a reproducible drop of $g_1(\tau)$ in blood perfusion changes with the cuff pressure (Figure 6).

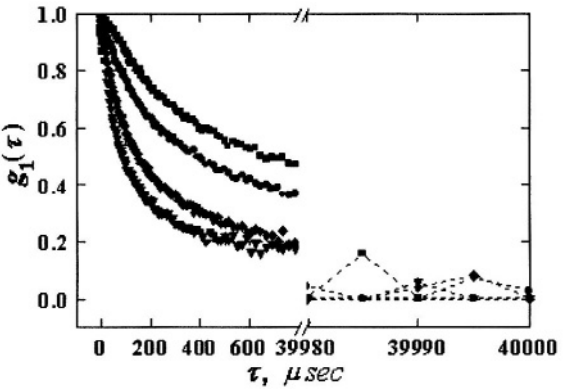

Figure 6. Typical temporal field autocorrelation functions $g_1(\tau)$ measured with the different dynamics of blood (i.e., arm suppression).

For the different dynamic of scattering particles within the multiple scattering medium $g_1(\tau)$ consists of different independent time scales (Figure 4), as, for example, τ_B and τ_S for Brownian motion and convective shear flow [61]:

$$g_1(\tau) = \int_0^\infty P(s) \exp\left(-2\left[\tau/\tau_B + \left(\tau/\tau_S \right)^2 \right] \frac{s}{l^*} \right) ds. \qquad (13)$$

When shear flow significantly dominate under the Brownian motion, taken into account equation 10, we consider semi-logarithmic plot of $g_1(\tau)$ versus $\tau^{1/2}$ that gives a straight line (Figure 7) with a slope proportional to the velocity of the scattering particles flow (Figure 8). As we discussed above this method of the analysis is not new and is implicit in various applications of the linear least-squares equation to an exponential such as equation 8.

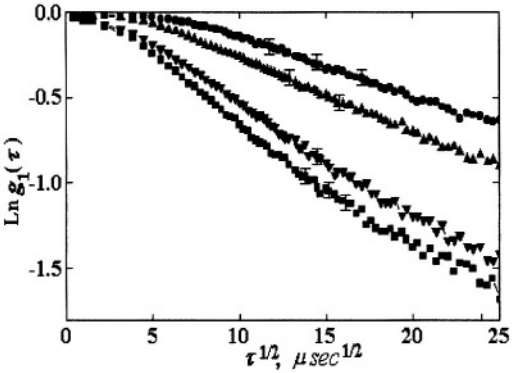

Figure 7. Example of typical semi-logarithmic plot of temporal field autocorrelation functions, presented in Figure 6, versus $\tau^{1/2}$.

The changes of flow relative slope of the autocorrelation functions (Figure 7) are due to different blood flow produced by the arm suppression. The decay rate of the correlation function decreases as the cuff pressure is increased. There is a small decrease when the cuff pressure is increased to 50 *mm Hg,* a large decrease when the arm suppression is increased to 100 *mm Hg,* and then a small decrease when cuff pressure is increased to 150 *mm Hg.* The large change in the slopes of autocorrelation functions (see Figure 7) results from venous occlusion.

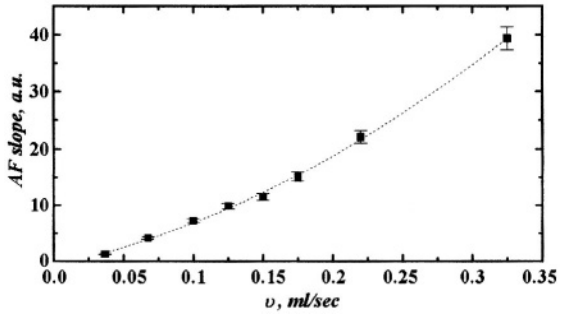

Figure 8. The measured slopes of the temporal field autocorrelation functions versus average velocity of flows (phantom measurements see Figures 4 and 5).

To determine the accuracy of the technique we performed the physiological reproducibility studies in respect to the recommendations of the Standardization group of the *European Society of Contact Dermatitis* [76,77]. These studies also included: consideration of signal processing limitations, choice of processing bandwidth, instrument calibration, the effect of probe pressure on the skin surface, motion artefacts, alterations in patient posture, skin temperature, *etc.*

Figure 9 represents the changes of flow relative slope with the arm suppression changes in real time of experiment. Cuff ischemia refers to the use of a pressure cuff to occlude blood flow in a limb thus preventing the delivery of oxygen to the limb. Initial baseline (un-cuffed) measurements, when blood flow, blood volume, and deoxygenation are constant, was measured for the first 20 minutes. Then the arm suppression was quickly raised to 230 *mm Hg* to simultaneously occlude venous and arterial flow. The response was measured for 12 minutes. Average blood volume and oxygenation (Figure 10) was measured simultaneously using a Runman device (NIM Inc. Philadelphia, PA) to measure photon absorption at 760 nm and 850 nm [78]. Each correlation measurement was integrated for 2 minutes while blood volume and oxygenation measurements were gathered continuously. Finally, the cuff pressure was released in intervals over the next 20 minutes and measurements made until the blood flow, volume, and oxygenation returned to normal.

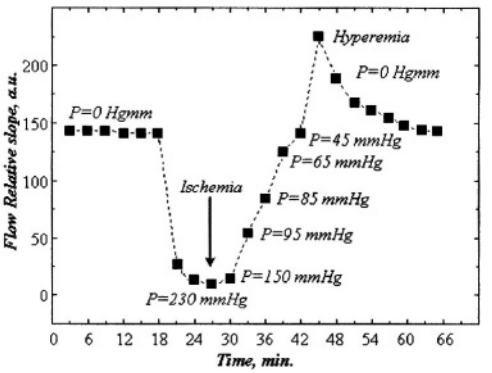

Figure 9. The relative slope of temporal field autocorrelation functions measured for the arm suppression changes in real time.

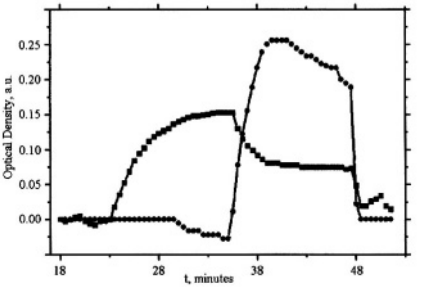

Figure 10. The blood volume and deoxygenation measured simultaneously with the measurements of slope of temporal field autocorrelation functions changes (see Figure 9).

The results clearly demonstrate change in the relative slopes of autocorrelation functions, including the post-occlusive reactive hyperemic overshoot after the cuff release (see Figure 9). Compare these results to the results of blood volume and oxygenation measurements (see Figure 10) it is easy to see, that during venous and arterial occlusion, the volume did not change, but the deoxygenation increased while the flow rapidly decreased. No change in blood volume occurs because blood flow has been abruptly halted, as indicated by the change in flow. The deoxygenation of the blood increases, corresponding to a decrease in oxygenation, because of oxygen delivery to and metabolism by the surrounding cells. When the arteries are opened by dropping the pressure below 150 *mm Hg,* a significant increase in the blood volume is observed, as well as drop in blood deoxygenation. This is because the arteries are able to deliver more blood to the arm, but at the same time the blood cannot leave because the venous pathways are still occluded. As the pressure is dropped further the blood volume drops a little because of incomplete venous occlusion allowing blood to leak back to the heart. This notion of leakage is supported by the measured flow increasing as the pressure is decreased. Under normal circumstances the veins remain occluded and the blood volume and flow rate remain fixed until the pressure drops below 80 *mm Hg.* When the pressure is dropped to zero the blood volume and oxygenation is seen to return to normal but the blood flow first increases above the baseline because of a hyperemic response.

In the later case, DWS and an alternative technique, so-called *Diffuse Laser Doppler Velocimetry* (DLDV) [79] are used to determine the perfusion flow rate of various human tissues [64,79-82], and to characterize RBC and their aggregation [82-85]. DWS and DLDV are related to each other according to the Wiener-Kintchine theorem [86]:

$$S(\omega) = \frac{\langle I \rangle^2}{2\pi} \int_{-\infty}^{+\infty} [g_1(\tau)]^2 \cos(i\omega_0 \tau) d\tau . \qquad (14)$$

The DWS and DLDV techniques may seem identical, and the main distinction between them is technical requirements and convenience rather than anything fundamental. However, for the weak optical signals (at the photon counting rate) photon correlation approach is more preferable. Recent high-technology breakthroughs and development of digital multi-channel autocorrelators based on the high-speed processors lifted many technical restrictions from the correlation method, and now medium fluctuations may be probed over an extraordinarily wide range of time-scales, from 10^{-8} to 10^{5} sec [18].

In the results of the studies (see Figures 6, 7, and 9) the uncertainty of the sampling depth leads to ambiguities in the interpretation of what fraction of

the recorded signal is generated by capillary blood flow and by flow through arterioles, venues and arterio-venous anastomosis, *etc.* However, due to a small distance (0.3 mm) between source-detector fibers, we assumed that detected laser radiation is predominantly localized in the *Pappilary dermis, Upper blood net dermis,* and topical *Reticular dermis* [34,35]. This assumption permitted us to state that we observed changes in the cutaneous blood flow rate. On the other hand, the analysis of the area of the detected signal localization makes it possible to obtain the fragments of autocorrelation functions related to the flow rates in different vessels or groups of vessels within the medium. To convert measured DWS data to the flow parameters an analysis of autocorrelation function as a function of the path length for the various flows in the medium and their contribution to the detected signal is the current/future target. This will allow us to reliably decompose the detected correlation function into the components corresponding to contribution of different compartments of blood vascular net.

Instead of traditional fiber-optic DWS system developed during our studies, analyzed intensity fluctuations at a single point (one-speckle spot), a large area of the intensity pattern (hence multi-speckle) of the scattered light in future can be analyzed using a CCD camera [87,88].

The main advantage of this set-up is the significantly reduced data acquisition time, since a large number of DWS-scattering experiments are performed simultaneously, and the measured autocorrelation function never suffers the problems of non-ergodicity. The instrument should be capable of measuring with high precision and accuracy the values of flow parameters in medium. However, this approach requires the spatially resolved analysis and developing an algorithm to convert measured autocorrelation function to the flow values.

The development of such non-trivial conversion algorithm is an ultimate aim being to obtain the fragments of autocorrelation function related to the flow rates in different groups of vessels. To convert measured DWS data to the flow parameters an analysis of autocorrelation function as a function of the path length for the various flow dynamics in different compartments of medium vascular network and its contribution to the detected signal will be established. This could be done by comparing the phantom DWS fiber-optics/CCD measured flow with the one calculated by MC simulation for the actual dynamics of particles in the phantom. Analysis of the region of the detected-signal localization, makes it possible to reliably determine the optimal configuration of an optical system intended to the medium probing [34,35], as well as to decompose the detected signal into the components corresponding to contribution of different compartments of blood vascular net.

4.6 SUMMARY

DWS is a novel modern technique uniquely suited for the measurements of the average size of particles and their motion within the randomly inhomogeneous highly scattering and absorbing media, including bio-tissues. The technique is based on the illuminating of the medium with a coherent laser light, and analyzing the loss of coherence of the scattered field arises from motion of the scattering particles with respect to each other.

Current chapter reviews the experimental DWS approach for the express non-invasive quantitative monitoring and functional diagnostics of skin blood flow and skin blood microcirculation *in vivo.* The presented technique encourages developing and validation of the methodology further to the point that skin blood microcirculation measurements can be routinely and accurately obtained in a normal skin, and to estimate its changes before, during and after medical procedures. We also seek to demonstrate the variations of the skin blood microcirculation caused by cosmetic/health care and some safe chemical agents acting of the skin. This is likely lead to non-invasive quantitative monitoring of the effectiveness of general diagnostics [89], diabetes studies [90], pharmacological intervention for failing surgical skin flaps or replants [91], blood microcirculation monitoring during sepsis, assess burn depth [92], diagnose atherosclerotic disease, and investigate mechanisms of photodynamic therapy for cancer treatment [93]. Apart from that, this method is effectively applied in both colloid chemistry and material science [18,72,73].

ACKNOWLEDGMENTS

This work was made possible only by our close collaboration with Professor Britton Chance and Professor Arjun Yodh at the University of Pennsylvania (USA), Professor David Boas at the Harvard Medical School (USA), Dr. Steve Matcher at the Exeter University (UK), Professor Angela Shore and Professor Jon Tooke at the Peninsula Medical School (UK), Dr. Sergey Skipetrov at the CNRS Grenoble (France). We also thank Professor Dmitry Zimnyakov, Dr. Yury Sinichkin at the Saratov State University (Russia) and Dr. Alexander Priezzhev at the Moscow State University (Russia) for their interest in this work and useful discussions. This work was partially supported by: grant N RB1-230 of the U.S. Civilian Research and Development Foundation for the Independent States of the Former Soviet Union (CRDF); grant REC-006/SA-006-00 “Nonlinear Dynamics and Biophysics” of CRDF and the Russian Ministry of Education; the Russian Federation President’s grant N 25.2003.2 “Supporting of Scientific Schools” of the Russian Ministry for Industry, Science and Technologies; and grant

"Leading Research-Educational Teams" N 2.11.03 of the Russian Ministry of Education.

REFERENCES

1. *Handbook on Optical Biomedical Diagnostics* **PM107**, V.V. Tuchin ed. (SPIE Press, Bellingham, 2002).
2. V.V. Tuchin, *Tissue Optics: Light Scattering Methods and Instruments for Medical Diagnosis,* SPIE Tutorial Texts in Optical Engineering, **TT38** (SPIE Press, Bellingham, 2000).
3. A.A. Rossini and W.L. Chick, "Microvascular pathology in diabetes mellitus" in *Microcirculation,* **III**, G. Kaley and B.M. Altura eds. (University Park Press, Baltimore, 1980), 245-271.
4. E. Davis, "Hypertension and peripheral vascular diseases" in *Microcirculation,* **III**, G. Kaley and B.M. Altura eds. (University Park Press, Baltimore, 1980), 223-234.
5. P.D. Coleridge-Smith, P.R.S. Thomas, J.D. Scurr, and J.A. Dormandy, "The etiology of venous ulceration - a new hypothesis," *Br. Med. J.* **296**, 1726-1727 (1988).
6. P.C. Hübert, L. Qun Hu, G.P. Biro, "Review of physiologic mechanisms in response to anemia," *CMAJ* **156**, S27-40 (1997).
7. B. Fagrell, "Microcirculatory methods for the clinical assessment of hypertension, hypotension, and ischemia," *Annal. Biomed. Eng.* **14** (2), 163-73 (1986).
8. *2001 Heart and Stroke Statistical Update* (American Heart Association, Dallas, 2000) URL: www.americanheart.org/statistics/index.html.
9. *Waves and Imaging through Complex Media,* P. Sebbah ed. (Kluwer Academic Publishers, Dordrecht, 2001).
10. J.V. Chapman and G.R. Sutherland, "The Noninvasive Evaluation of Hemodynamics" in *Congenital Heart Disease. Doppler Ultrasound Applications in the Adult and Pediatric Patient with Congenital Heart Disease. Developments in Cardiovascular Medicine Series* **114** (Kluwer Academic Publishers, Dordrecht, 1990).
11. W.J. Manning, W. Li, R.R. Edelman, "A preliminary-report comparing magnetic-resonance coronary angiography with conventional angiography," *New England J. Med.* **328**, 828-832(1993).
12. R.F. Bonner and R. Nossal, "Principles of Laser-Doppler Flowmetry" in *Laser-Doppler Blood Flowmetry,* A.P. Shepherd and P.A. Oberg eds. (Kluwer, Dordrecht, 1990), 17-45.
13. J.D. Briers, "Laser Doppler, speckle and related techniques for blood perfusion mapping and imaging," *Physiol. Meas.* **22**, R35-R66 (2001).
14. B. Fagrell and A. Bollinger, "Application of microcirculation research to clinical disease (Chapter 11)" in *Clinically Applied Microcirculation Research,* J.H. Barker, G.L. Anderson, and M.D. Menger eds. (CRC Press, Inc., Boca Raton, 1995), 149-160.
15. M. Rajadhyaksha, M. Grossman, D. Esterowitz, R.H. Webb, and R.R. Anderson, "*In vivo* confocal scanning laser microscopy of human skin: Melanin provides strong contrast," *J. Invest. Dermatol.* **104**, 946-952 (1995).
16. Z. Chen, Y. Zhao, S.M. Srinivas, J.S. Nelson, N. Prakash, and R.D. Frostig, "Optical Doppler tomography," *IEEE J. Sel. Tops Quant. Electr.* **5** 1134-1142 (1999).
17. J.A. Izatt, M.D. Kulkarni, S. Yazdanfar, J.K. Barton, and A.J. Welch, "*In vivo* bidirectional color Doppler flow imaging of picoliter blood volumes using optical coherence tomography," *Opt. Lett.* **22** (18), 1439-1441 (1997).

18. J.L. Harden and V. Viasnoff, "Recent advances in DWS-based micro-rheology," *Curr. Opin. Colloid In.* **6** (5-6), 438-445 (2001).
19. K.S. Stenn, "The skin" in *Cell and Tissue Biology,* L. Weiss ed., (Urban & Shwarzenberg, Baltimore, 1988), 541-572.
20. G.F. Odland, "Structure of the skin" in *Physiology, Biochemistry, and Molecular Biology of the Skin* **1**, L.A. Goldsmith ed. (Oxford University Press, Oxford, 1991), 3–62.
21. J. Serup and G.B.E. Jemec, *Non-invasive Methods and the Skin* (CRC Press, Inc., Boca Raton, 1995), 83-131.
22. J.W. Feather, J.B. Dawson, D.J. Barker, and J.A. Cotterill, "A theoretical and experimental study of optical properties of *in vivo* skin" in *Bioengineering and the Skin,* R. Marks and P.A. Payne eds. (MTP, Lancaster, 1981), 275-281.
23. A.R. Young, "Chromophores in human skin," *Phys. Med. Biol.* **42** (5), 789-802 (1997).
24. E.M. Renkin, C.C. Michel, S.R. Geiger, *Handbook of Physiology. Section 2: The Cardiovascular System. Microcirculation Part 1,* **IV** (American Physiological Society, Bethesda, Maryland, 1984).
25. G.I. Mchedlashvilli, *Capillar Circulation of the Blood* (Izv. AN Gruzinskoi SSR, Tbilisi, 1958).
26. G.I. Mchedlashvilli, *Microcirculation of Blood: General Conformity to Natural Laws of the regulation and violation* (Nauka, Leningrad, 1989).
27. T.J. Ryan, "Cutaneous Circulation" in *Physiology, Biochemestry and Molecular Biology of the Skin* **II**, L.A. Goldsmith ed. (Oxford University Press, Oxford, 1991), 1019-1084.
28. S. Chen, "Biophysical behavior of red blood cells in suspensions" in *The Red Blood Cell* **II**, D. MacN. Sargenor ed. (Academic Press, New York, 1975), 1031-1133.
29. T.J. Pedley, *The Fluid Mechanics of Large Blood Vessels* (Cambridge Univ. Press, Cambridge, 1980).
30. A. Jakobsson, G.E. Nilsson, "Prediction of sampling depth and photon pathlength in laser Doppler flowmetry," *Med. Biol. Eng. Comp.* **31**, 301-307 (1993).
31. F.F. de Mul, M.H. Koelink, M.L. Kok, P.J. Harmsma, J. Greve, R. Graaff, and J.G. Aarnoudse, "Laser Doppler velocimetry and Monte Carlo simulation on models for blood perfusion in tissue," *Appl. Opt.* **34** (28), 6595-6611 (1995).
32. C.L. Tsai, Y.-F.Yang, C.-C. Han, J.-H. Hsieh, and M. Chang, "Measurement and simulation of light distribution in biological tissues," *Appl. Opt.* **40** (31), 5770-5777 (2001).
33. D.T. Delpy and M. Cope, "Quantification in tissue near-infrared spectroscopy," *Phil. Trans. R. Soc. Lond.* B **352**, 649-659 (1997).
34. I.V. Meglinsky and SJ. Matcher, "Modelling the sampling volume for skin blood oxygenation measurements," *Med. Biol. Eng. Comp.* **39** (1), 44-50 (2001).
35. I.V. Meglinskii and SJ. Matcher, "The analysis of spatial distribution of the detector depth sensitivity in multi-layered inhomogeneous highly scattering and absorbing medium by the Monte Carlo technique," *Opt. Spectrosc.* **91** (4), 654-659 (2001).
36. S.L. Jacques, "Origins of tissue optical properties in the UVA, visible, and NIR regions" in *OSA TOPS on Advances in Optical Imaging and Photon Migration* **2**, R.R. Alfano and J.G. Fujimoto eds. (Optical Society of America, Washington, 1996), 364-369.
37. W. Verkruysse, G.W. Lucassen, and M.J.C. van Gemert, "Simulation of color of port wine stain skin and its dependence on skin variables," *Laser Surg. Med.* **25**, 131-139 (1999).

38. Yu.P. Sinichkin, N. Kollias, G.I. Zonios, S. R. Utz, and V. V. Tuchin, "Reflectance and fluorescence spectroscopy of human skin *in vivo*" in *Handbook of Optical Biomedical Diagnostics,* V.V. Tuchin (ed.) (SPIE Press, Washington, 2002), 727-785.
39. D.Y. Churmakov, I.V. Meglinski and D.A. Greenhalgh, "Influence of refractive index matching on the photon diffuse reflectance," *Phys. Med. Biol.,* **47** (23), 4271-4285 (2002).
40. R.M.P. Doornbos, R. Lang, M.C. Aalders, F.M. Cross, and H.J.C.M. Sterenborg, "The determination of *in vivo* human tissue optical properties and absolute chromophore concentrations using spatially resolved steady-state diffuse reflectance spectroscopy," *Phys. Med. Biol.* **44**, 967-981 (1999).
41. C.R. Simpson, M. Kohl, M. Essenpreis, and M. Cope, "Near-infrared optical properties of *ex vivo* human skin and subcutaneous tissues measured using the Monte Carlo inversion technique," *Phys. Med. Biol.* **43**, 2465-2478 (1998).
42. R. Marchesini, C. Clemente, E. Pignoli, and M. Brambilla, "Optical properties of *in vivo* epidermis and their possible relationship with optical properties of *in vivo* skin," *J. Photochem. Photobiol. B: Biol.* **16**, 127-140 (1992).
43. I.V. Meglinski and S. J. Matcher, "Quantitative assessment of skin layers absorption and skin reflectance spectra simulation in visible and near-infrared spectral region," *Physiol. Meas.* **23** (4), 741-753 (2002).
44. I.V. Meglinski and S.J. Matcher, "Computer simulation of the skin reflectance spectra," *Comput. Meth. Prog. Biol.* **70** (2), 179-186 (2003).
45. H.Z. Cummins and E.R. Pike, *Photon correlation and light beating spectroscopy* (Plenum Press, New York, 1973).
46. G. Maret and E. Wolf, "Multiple light scattering from disordered media. The effect of Brownian motion of scatterers," *Z. Physik B – Condens. Matter* **65**, 409-413 (1987).
47. Special issue on Photon Correlation and Scattering, *Appl. Opt.* **40** (24), 3965-4242 (2001).
48. *Dynamic Light Scattering. The Method and Some Applications,* W. Brown ed. (Oxford University Press, New York, 1993).
49. R. Pecora, *Dynamic Light Scattering: Applications of Photon Correlation Spectroscopy.* (Plenum Press, New York, 1985).
50. D.J. Pine, D.A. Weitz, G. Maret, P.E. Wolf, E. Herbolzheimer, and P.M. Chaikin, "Dynamical correlations of multiply scattered light" in *Scattering and Localization of Classical Waves in Random Media. World Scientific Series on Direction in Condensed Matter physics* **8**, P. Sheng ed. (World Scientific Publishing Co. 1990), 312-372.
51. K.M. Watson, "Multiple scattering of electromagnetic waves in an underdense plasma," *J. Math. Phys.* **10**, 688-702 (1969).
52. D.A. Weitz and D.J. Pine, "Diffusing-wave spectroscopy (Chapter 16)" in *Dynamic Light Scattering. The Method and Some Applications,* W. Brown ed. (Oxford University Press, New York, 1993), 652-720.
53. N.A. Fomin, *Speckle Photography for Fluid Mechanic Measurements: Experimental Fluid Mechanics* (Springer-Verlag Berlin and Heidelberg GmbH & Co., Berlin, 1998).
54. A.G. Yodh, P.D. Kaplan, and D.J. Pine, "Pulsed diffusing-wave spectroscopy: High resolution through nonlinear optical gaiting," *Phys. Rev. B* **42**, 4744-4747 (1990).
55. T. Bellini, M.A. Glaser, N.A. Clark, and V. Degiorgio, "Effects of finite laser coherence in quasi-elastic multiple-scattering," *Phys. Rev. A* **44** (8), 5215-5223 (1991).
56. D.A. Boas, L.E. Campbell, and A.G. Yodh, "Scattering and imaging with diffusing temporal field correlations," *Phys. Rev. Lett.* **75** (9), 1855-1858 (1995).

57. D.A. Boas, *Diffuse Photon Probes of Structural and Dynamical Properties of Turbid Media: Theory and Biomedical Applications* (PhD dissertation in physics, University of Pennsylvania, USA, 1996).
58. A. Isimaru, *Wave Propagation and Scattering in Random Media* (John Wiley & Sons Inc, New York, 1999).
59. R. Nossal, S.H. Chen, and C.C. Lai, "Use of laser scattering for quantitative determinations of bacterial motility," *Opt. Commun.* **4** (1), 35-39 (1971).
60. D.J. Pine, D.A. Weitz, J.X. Zhu, and E. Hebolzheimer, "Diffusing-wave spectroscopy: dynamic light scattering in the multiple scattering limit," *J. Phys. France* **51,** 2101-2127 (1990).
61. X.-L. Wu, D.J. Pine, P.M. Chaikin, J.S. Huang, and D.A. Weitz, "Diffusing-wave spectroscopy in shear flow," *J. Opt. Soc. Am. B* **7**(1), 15-20 (1990).
62. E. Overbeck and C. Sinn, "Three-dimensional dynamic light scattering," *J. Mod. Opt.* **46** (2), 303-326(1999).
63. D.P. Chowdhury, C.M. Sorensen, T.W. Taylor, J.F. Merklin, and T.W. Lester, "Application of photon-correlation spectroscopy to flowing Brownian-motion systems," *Appl. Opt.* **23** (22), 4149-4154 (1984).
64. I.V. Meglinski, *Experimental Substantiation of Application of the Laser Correlation Spectroscopy for the In Vivo Investigations of Bio-Tissues* (PhD dissertation in biophysics, Saratov State University, Russia, 1997).
65. M. Heckmeier, S.E. Skipetrov, G. Maret, and R. Maynard, "Imaging of dynamic heterogeneities in multiple-scattering media," *J. Opt. Soc. Am. A,* **14** (1), 185-191 (1997).
66. M. Heckmeier and G. Maret, "Visualization of flow in multiple-scattering liquids," *Europhys. Lett.* **34** (4), 257-262 (1996).
67. D.A. Boas, I.V. Meglinsky, L. Zemany, L.E. Campbell, B. Chance, and A.G. Yodh, "Diffusion of temporal field correlation with selected applications" in *CIS Selected Papers: Coherence-Domain Methods in Biomedical Optics, Proc. SPIE* **2732**, V.V. Tuchin ed. (SPIE Press, Bellingham, 1996), 34-46.
68. S.E. Skipetrov and I.V. Meglinskii, "Diffusing-wave spectroscopy in random inhomogeneous media with spatially localized scatterer flow," *J. Exp. Theor. Phys.* **86** (4), 661-665(1998).
69. D.A. Boas, I.V. Meglinsky, L. Zemany, L.E. Campbell, B. Chance, and A.G. Yodh "Flow properties of heterogeneous turbid media probed by diffusing temporal correlation" in *Advances in Optics Imaging and Photon Migration* **2**, R.R. Alfano and J.G. Fujimoto eds. (Optical Society of America, Washington, 1996), 175-178.
70. H.J. van Staveren, C.J.M. Moes, J. van Marle, S.A. Prahll, and M.J.C. van Gemert, "Light scattering in Intralipid - 10% in the wavelength range of 400-1100 nm," *Appl. Opt.* **30** (31), 4507-4514 (1991).
71. S.E. Skipetrov and R. Maynard, "Dynamic multiple scattering of light in multilayer turbid media," *Phys. Lett. A* **217** (2-3) 181-185 (1996).
72. M.J. Solomon and Q. Lu, "Rheology and dynamics of particles in viscoelastic media," *Curr. Opin. Colloid In.* **6** (5-6), 430-437 (2001).
73. F.C. MacKintosh and C.F. Schmidt, "Microrheology," *Curr. Opin. Colloid In.* **4**, 300-307(1999).
74. I.V. Meglinski, D.A. Boas, A.G. Yodh, and B. Chance, *"In vivo* measuring of blood flow changes using diffusing wave correlation techniques" in *Advances in Optical Imaging and Photon Migration* **2,** R.R. Alfano and J.G. Fujimoto eds. (Optical Society of America, Washington, 1996), 195-197.

75. I.V. Meglinsky, D.A. Boas, A.G. Yodh, B. Chance, and V.V. Tuchin, "The development of correlation of intensity fluctuations technique for the non-invasive monitoring and measurements of the blood flow parameters," *Izv. VUZ. Appl. Nonlinear Dynamics* **4** (6), 72-81 (1996).
76. A. Bircher, E.M. de Boer, T. Agner, J.E. Wahlberg, and J. Serup, "Guidelines for measurement of cutaneous blood flow by laser Doppler flowmetry," *Contact Dermatitis,* **30**, 65-72 (1994).
77. A. Fullerton, M. Stücker, K.-P. Wilhelm, K. Wårdell, C. Anderson, T. Fischer, G.E. Nilsson, and J. Serup, "Guidelines for visualization of cutaneous blood flow by laser Doppler perfusion imaging: A report from the Standardization Group of the European Society of Contact Dermatitis based upon the HIRELADO European community project," *Contact Dermatitis,* **46** (3), 129-140 (2002).
78. A. Chance, M. Dait, C. Zhang, T. Hamaoka, and F. Hagerman, "Recovery from exercise-induced desaturation in the quadriceps muscles of elite competitive rowers," *Am. J. Physiol.* **262**, C766-C775 (1992).
79. P. Snabre, J. Dufaux, and L. Brunel, "Diffuse laser Doppler velocimetry from multiple scattering media and flowing suspensions" in *Waves and Imaging through Complex Media,* P. Sebbah ed. (Kluwer Academic Publishers, New York, 2001), 369-382.
80. D.A. Boas and A.G. Yodh, "Spatially varying dynamical properties of turbid media probed with diffusing temporal light correlation," *J. Opt. Soc. Am. A* **14**, 192-215 (1997).
81. K. Jurski, J. Dufaux, L. Brunei, and P. Snabre, "Optical flow detection and imaging," *Comptes Rendus de L'Academie des Science, Serie IV* **2**(8), 1179-1192 (2001).
82. I.V. Meglinskii, A.N. Korolevich, and V.V. Tuchin, "Investigation of blood flow microcirculation by diffusing wave Spectroscopy," *Crit. Rev. Biomed. Eng.* **29** (3), 535-548 (2001).
83. I.V. Meglinski, A.N. Korolevich, and D.A. Greenhalgh, "Application of low scattering photon correlation Spectroscopy for blood monitoring" in *Diagnostic Optical Spectroscopy in Biomedicine, Proc. SPIE* **4432**, T.G. Papazoglou and G.A. Wagnieres eds. (SPIE Press, Bellingham, 2001), 24-28.
84. A.N. Korolevich and I.V. Meglinsky, "The experimental study of the potentialities of diffusing wave Spectroscopy for the investigating of the structural characteristics of blood under multiple scattering," *Bioelectrochemistry* **52**, 223-227 (2000).
85. A.V. Priezzhev, *Optics of Blood and New Optical Sensing and Diagnostic Technique and Instrumentation,* Munich European Biomedical Optics, Short Course 101 (SPIE Press, Bellingham, 2001).
86. S.M. Rytov, Yu.A. Kravtzov, and V.I. Tatarskii, *Introduction to Statistical Radiophysics. I. Random Processes* (Nauka, Moscow, 1978).
87. L. Cipelletti and D.A. Weitz, "Ultralow-angle dynamic light scattering with a charge coupled device camera based multispeckle, multitau correlator," *Rev. Sci. Instrum.* **70**, 3214-3221 (1999).
88. V. Viasnoff, F. Lequeux, and D.J. Pine, "Multi-speckle diffusing-wave Spectroscopy: A tool to study slow relaxation and time-dependent dynamics," *Rev. Sci. Instrum.* **73** (6), 2336-2344 (2002).
89. J.E. Tooke and L.H. Smaje, "The microcirculation and clinical disease" in *Clinically Applied Microcirculation Research,* J.H. Barker, G.L. Anderson, and M.D. Menger eds. (CRC Press, Inc., Boca Raton, 1995), 3-15.
90. A.J. Jaap and J.E. Tooke, "Diabetes and the microcirculation" in *Clinically Applied Microcirculation Research,* J.H. Barker, G.L. Anderson, and M.D. Menger eds. (CRC Press, Inc., Boca Raton, 1995), 31-44.

91. P.C. Neligan, "Monitoring techniques for the detection of flow failure in the postoperative period," *Microsurgery* **14**, 162-164 (1993).
92. Z.B.M. Niazi, T.J.H. Essex, R. Papini, D. Scott, N.R. Mclean, and M.J.M. Black, "New laser-Doppler scanner, a valuable adjunct in burn depth assessment," *Burns* **19**, 485-489 (1993).
93. M. Korbelik and G. Krosl, "Cellular-levels of photosensitizers in tumors - the role of proximity to the blood-supply," *Brit. J. Cancer* **70**, 604-610 (1994).

Chapter 5

LASER SPECKLE IMAGING OF CEREBRAL BLOOD FLOW

Qingming Luo,[1] Haiying Cheng,[1] Zheng Wang,[1] and Valery V. Tuchin[2]
1. Huazhong University of Science and Technology, Wuhan, 430074 P.R. China; 2. Saratov State University, Saratov, 410012 Russian Federation

Abstract: Monitoring the spatio-temporal characteristics of cerebral blood flow (CBF) is crucial for studying the normal and pathophysiologic conditions of brain metabolism. By illuminating the cortex with laser light and imaging the resulting speckle pattern, relative CBF images with tens of microns spatial and millisecond temporal resolution could be obtained. In this chapter, a laser speckle imaging (LSI) method for monitoring dynamic, high-resolution CBF is introduced. Its applications on detecting the change in local CBF induced by sensory stimulation and the influence of a chemical agent to CBF are given. To improve the spatial resolution of current LSI, a modified LSI method is proposed. Dynamic of CBF under different temperatures is investigated by both methods and their results are compared with each other.

Key words: laser speckle imaging, cerebral blood flow, spatio-temporal characteristics

5.1 INTRODUCTION

Monitoring the spatio-temporal characteristics of cerebral blood flow (CBF) is crucial for studying the normal and pathophysiologic conditions of brain metabolism. At present there are several techniques for velocity measurement. One of these is laser-Doppler flowmetry (LDF), which provide information about CBF from a limited number of isolated points in the brain (approximately 1 mm^3) [1,2]. Scanning laser-Doppler can be used to obtain spatially resolved relative CBF images by moving a beam across the field of interest, but the temporal and spatial resolution of this technique is limited by the need to mechanically scan the probe or the beam [3,4], such

as Laser Doppler Perfusion Imaging (LDPI). Another method is time-varying laser speckle [5-7], which suffered from the same problems as LDF. Single photon emission computed tomography (SPECT) uses the tracer 99mTC-HMPAO to obtain quantitative CBF values (ml/100 g/min). However, it suffers from the injection of exogenous substances [8,9]. Positron emission tomography (PET) scanning is currently the most versatile and widely used functional imaging modality both in health and disease. The spatial resolution is quite limited, being about 0.5 cm^3 [10,11]. The recently developed thermal diffusion technique is based on the thermal conductivity of cortical tissue, allowing continuous recordings of CBF in a small region of the cortex. The spatial resolution is determined by the placement of the sensor [12,13]. Although autoradiographic methods provide three-dimensional spatial information, they contain no information about the temporal evolution of CBF changes [14]. Method based on magnetic resonance imaging, such as functional Magnetic Resonance Imaging (fMRI) provides spatial maps of CBF but are limited in their temporal and spatial resolution [15,16]. Therefore, a noninvasive simple method removing the need for scanning and providing full-field dynamic CBF images would be helpful in experimental investigations of functional cerebral activation and cerebral pathophysiology.

One such technique is laser speckle imaging technique (LSI) using the first-order spatial statistics of time-integrated speckle, which is firstly proposed by the group of A.F. Fercher and J.D. Briers [17,18]. The speckle method has been used to image blood flow in the retina [19] and skin [20]. Lately, the group in Harvard medical school applied this method to image blood flows during focal ischemia and cortical spreading depression (CSD) [21,22]. In this chapter, we will first introduce the principle of laser speckle imaging method, then give some experimental results on various animal models for dynamic, high-resolution cerebral blood flows (CBF) monitoring.

5.2 PRINCIPLES OF LASER SPECKLE IMAGING

Laser speckle is an interference pattern produced by the light reflected or scattered from different parts of the illuminated rough (i.e., nonspecular) surface. When the area illuminated by laser light is imaged onto a camera, there produced a granular or speckle pattern. If the scattered particles are moving, a time-varying speckle pattern is generated at each pixel in the image. The spatial intensity variations of this pattern contained information of the scattered particles. In areas of increased blood flow, the intensity fluctuations of the speckle pattern are more rapid and the speckle pattern

integrated over the CCD camera exposure time becomes blurred in these areas.

To quantity the blurring of the speckles, the local speckle contrast [17,18] is defined as the ratio of the standard deviation to the mean intensity in a small region of the image: $k = \sigma_s/\langle I\rangle$. Here k, σ_s, and $\langle I\rangle$ stand for speckle contrast, the standard variation and the mean value of light intensity, respectively. The higher the velocity, the smaller the contrast is. For Gaussian statistics of intensity fluctuations the speckle contrast lies between the values of 0 and 1. A speckle contrast of 1 demonstrated there is no blurring of speckle, therefore, no motion, whereas a speckle contrast of 0 indicates the scatterers are moving fast enough to average out all of the speckles.

The speckle contrast is a function of the exposure time, T, of the camera and is related to the autocovariance of the intensity temporal fluctuations in a single speckle [23], $C_t^{(2)}(\tau)$, by

$$\sigma_s^2(T) = \frac{1}{T}\int_0^T C_t^{(2)}(\tau)d\tau . \tag{1}$$

$C_t^{(2)}(\tau)$ is defined as follows:

$$C_t^{(2)}(\tau) = \langle (I(t) - \langle I\rangle_t)(I(t+\tau) - \langle I\rangle_t)\rangle_t ,$$

where $I(t)$ is the intensity at time t, τ is the "lag", $\langle\rangle_t$ is the time average.

The normalized autocorrelation function of a field can often be approximated by a negative exponential function (for the case of a Lorentzian spectrum, for example, it is exactly negative exponential [17]):

$$g_t^{(1)}(\tau) = \exp(-\frac{|\tau|}{\tau_c}) \tag{2}$$

where τ_c is the "correlation time"; $g_t^{(1)}(\tau)$ is defined as follows [15]:

$$g_t^{(1)}(\tau) \equiv \frac{\langle E^+(t)E^-(t+\tau)\rangle_t}{\langle I\rangle_t},$$

where $E(t) = E^+(t) + E^-(t)$ is the field at time t and $I(t) = E^+(t)E^-(t)$ is the intensity.

The Siegert relationship [17] is valid for the speckle fluctuations (strictly true only for Gaussian statistics):

$$g_t^{(2)}(\tau) = 1 + \left|g_t^{(1)}(\tau)\right|^2 . \tag{3}$$

$g_t^{(2)}(\tau)$ is the normalized second-order autocorrelation function, i.e., the autocorrelation of the intensity, and is defined as follows:

$$g_t^{(2)}(\tau) \equiv \frac{\langle I(t)I(t+\tau)\rangle_t}{\langle I\rangle_t^2}.$$

From the definition of the various correlation functions we have, assuming stationarity:

$$g_t^{(2)}(\tau) = 1 + c_t^{(2)}(\tau), \tag{4}$$

where $c_t^{(2)}(\tau)$ is the normalized autocovariance,

$$c_t^{(2)}(\tau) = C_t^{(2)}(\tau) / < I >_t^2 . \tag{5}$$

Combining equations 3 to 5 we get:

$$C_t^{(2)}(\tau) = < I >_t^2 \left| g_t^{(1)}(\tau) \right|^2 . \tag{6}$$

Assuming our negative exponential approximation for the normalized autocorrelation function, we combine equations 2 and 6 to get:

$$C_t^{(2)}(\tau) = < I >_t^2 \exp(-2\tau/\tau_c) d\tau . \tag{7}$$

Substituting this expression in equation 1 we obtain the following expression for the spatial variance in the time-averaged speckle pattern:

$$\sigma_s^2(T) = (< I >_t^2 \tau_c / 2T)[1 - \exp(-2T/\tau_c)]. \tag{8}$$

Assuming ergodicity, we can replace the time average by the ensemble average to obtain:

$$k = \frac{\sigma}{\langle I\rangle} = \{\frac{\tau_c}{2T}[1 - \exp(-\frac{2T}{\tau_c})]\}^{\frac{1}{2}}. \tag{9}$$

Equation 9 gives us an expression for the speckle contrast in the time-averaged speckle pattern as a function of the exposure time T and the correlation time $\tau_c = 1/(ak_0 v)$, where v is the mean velocity of scatterers, k_0 is the light wavenumber, and a is a factor that depends on the Lorentzian width and scattering properties of the tissue [24]. As in laser-Doppler measurements, it is theoretically possible to relate the correlation times, τ_c, to the absolute velocities of the red blood cells, but this is difficult to do in practice, inasmuch as the number of moving particles that light interacted with and their orientations are unknown [24], However, relative spatial and temporal measurements of velocity can be obtained from the ratios of $2T/\tau_c$ that is proportional to the velocity and defined as measured velocity in present chapter.

5.3 INSTRUMENTATION AND PERFORMANCES

5.3.1 LSI System

The schematic diagram of the experimental set-up is shown in Figure 1. A He:Ne laser beam (λ=632.8 nm, 3 mW) was coupled into an 8 mm diameter fiber bundle, which was adjusted to illuminate the area of interest evenly. The illuminated area was imaged through a zoom stereo microscope (SZ6045TR, Olympus, Japan) onto a CCD camera (PIXELFLY, PCO Computer Optics, Germany) with 480×640 pixels yielding an image of 0.8 mm to 7 mm depending on the magnification. And the exposure time T of CCD was 20 ms. Images were acquired through the easy-control software (PCO Computer Optics, Germany) at 40 Hz.

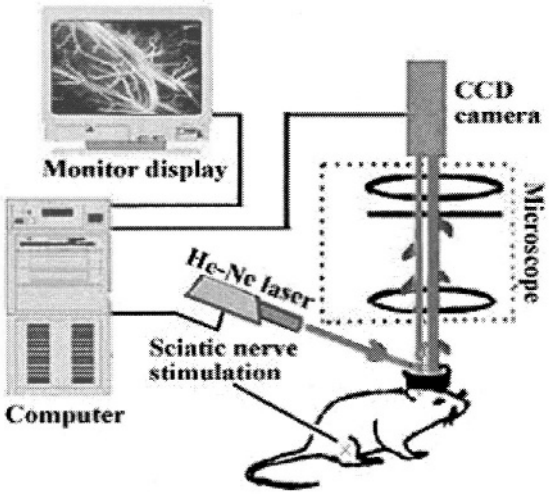

Figure 1. Schematic of system for laser speckle imaging. A He:Ne laser (λ=632.8 nm, 3 mW) beam is expanded to illuminate the interest area of brain, which is imaged onto a CCD camera. The computer acquires raw speckle images and computes relative blood flow maps [25].

5.3.2 Data Analysis

The raw speckle images were acquired to compute the speckle contrast image. The number of pixels used to compute the local speckle contrast can be selected by the user: lower numbers reduce the validity of the statistics, whereas higher numbers limit the spatial resolution of the technique. To ensure proper sampling of the speckle pattern, the size of a single speckle should be approximately equal to the size of a single pixel in the image,

which is equal to the width of the diffraction-limited spot size and is given by 2.44 $\lambda f/D$, where λ is the wavelength and f/D is the f number of the system. In our system, the pixel size was 9.9 μm. With a magnification of unity the required f/D is 6.4 at a wavelength of 632.8 nm. Squares of 5×5 pixels were used according the theoretical studies [17,18]. The software calculated the speckle contrast (k) for any given square of 5 × 5 pixels and assigned this value to the central pixel of the square. This process was then repeated to obtain a speckle contrast map. To each pixel in the speckle contrast map, the measured velocity $(2T/\tau_c)$ was obtained through equation 9 that describes the relationship between the correlation time and velocity, therefore measures velocity map.

To compute the relative blood flows in interest vessels, first a threshold was set in a region of interest from the measured velocity image and then the interest vessels were identified by the pixels with values above this threshold. The mean values of the measured velocity in those pixels were computed at each time-point. The relative velocity in interest vessel was expressed as the ratio of the measured velocity in the condition of stimuli to that of control condition.

5.4 APPLICATIONS

LSI is a noninvasive full-field optical imaging method with high spatial and temporal resolution, which is a convenient technique in measuring dynamic of CBF [21,22]. In this chapter, we tried to use LSI method to monitor the dynamics of CBF in several animal models.

5.4.1 Speckle Imaging of CBF Dynamics During Sciatic Nerve Stimulation [25]

The postulation by Roy and Sherrington in 1890 that the brain possesses an intrinsic mechanism by which its vascular supply can be varied locally in correspondence with locally variation of functional activity provided a principal basis of neurophysiology and neuroenergetics for modern functional neuroimaging techniques [26]. The change in local cerebral blood flow (CBF) induced by sensory stimulation is considered as an index to investigate the effects of activated neural activity based on the above hypothesis. The response of evoked regional CBF to somatosensory stimulation in rats has been studied using some techniques such as Laser-Doppler flowmetry (LDF) and functional MRI (fMRI) [27,28]. In addition, quantitative and temporal relationship between regional CBF and neuronal activation has also been reported which combined electrophysiological and LDF techniques [29]. It is well-documented that CBF at the level of

individual capillaries and the coupling of neuronal activity to flow in capillaries are fundamental aspects of homeostasis in the normal and the diseased brain [30]. However, it is hard for most present techniques to probe the dynamics of blood flow at this level due to their limitations of temporal or spatial resolution. Therefore, a new alternative approach is needed to assess the intrinsic hemodynamic response in the corresponding cortical areas and elucidate the role of CBF in circulatory and metabolic correlates of functional activation in the brain [31]. Here we apply the laser speckle imaging method to image the CBF dynamics during sciatic stimulation.

5.4.1.1 Animal Preparation

Male adult Sprage-Dawley rats weighing from 350 to 400 g (n=16) were anesthetized with an intraperitoneal injection of 2% α-chloralose and 10% urethane (50 and 600 mg/kg, respectively) to execute craniotomy. And atropine (0.4 ml/kg per hour) was administered to reduce mucous secretion during surgery. A closed cranial window (4×6 mm) over the parietal cortex was created as the following: a midline incision was made to expose the surface of the skull, then the skull overlying the hindlimb sensory cortex was bored to translucency with a dental drill under constant cooling with saline. The thinned skull preparation has the advantage over a full craniotomy since it keeps the dura mater intact and allows a long-term investigation into the changes in a somatosensory cortex within a single animal while preserving the integrity of the brain surface environment. The cranial window fully exposed the hindlimb sensory cortex in an area of 2.46×3.28 mm^2, centered at 2 mm caudal and 1.5 mm lateral to the bregma.

The animals were mounted in a stereotaxic frame, and body temperature was maintained at (37.0±0.5)°C with a thermostatic heating blanket. A tracheotomy was performed to enable mechanical ventilation using a ventilator (TKR-200C, Animal Mechanical Respirator, China) with a mixture of air and oxygen (20% O_2, 80% N_2) to achieve physiological arterial blood levels of O_2 and CO_2 tension. The right femoral artery and vein were cannulated for measurement of blood pressure (PcLab Instruments, China) and intravenous administration of drugs. Periodically, a small volume of blood was drawn from the femoral artery, and the blood gas pressure (pO_2, pCO_2) and pH value were analyzed (JBP-607, Dissolved Oxygen Analyzer, China). After surgery, the animals were left for at least half an hour before the experiment began and supplemental doses of anesthetic (one-fifth initial dose/h) were also needed.

Stimulation of the sciatic nerve was similar to that used in conventional physiological studies. The contralateral sciatic nerve was dissected free and cut proximal to the bifurcation into the tibial and peroneal nerves. Then the proximal end was placed on a pair of silver electrodes and bathed in a pool

of warm mineral oil in order to keep wettish. We stimulated the single sciatic nerve on the left with a rectangular pulse of 350 mV intensity, 0.5 ms duration, and at a rate of 5 Hz frequency for a train duration of 2 s (Multi Channel Systems, Germany). These parameters were chosen to optimize vessel response without affecting systemic blood pressure and kept constant during each experiment. The single sciatic nerve on the left was stimulated 2 s with rectangular pulses of 0.5 ms duration, 350 mV amplitude, and 5 Hz frequency (Multi Channel Systems, Germany). In all animals, a single-trial procedure was repeated 15 to 20 times and separated by an interval of at least 4 min. 400 frames of raw images were obtained in one 10 s single-trial while the electrical stimuli started at 2 s while the images in the first two seconds were recorded as baseline. Images were acquired through the Easy-control software (PCO computer optics, Germany) at 40 Hz and synchronized with Multi Channel Systems. Notably, here data acquisition was synchronized with the electrical signal via an appropriate trigger circuit, and therefore the procedures of data analysis described below could improve the reproducibility of our results and enhance the signal-to-noise ratio. All recorded data were finished within 3 to 4 h after the beginning of chloralose-urethane anesthesia.

5.4.1.2 Results

With LSI technique we monitored blood flow in somatosensory cortex in a total of 16 rats under electrical stimulation of sciatic nerve, and obtained the activated blood flow distribution at different levels of arteries/veins and the change of activated areas. Although there existed slight differences in individual anatomic features in the rat cortex, we could eliminate this influence since the imaged area was much bigger than the scope demarcated by Hall *et al.* [32]. One example of our results is shown in Figure 2, in which the brighter areas correspond to the area of increased blood flow. In comparison with LDF, an area of 1 mm^2 ROI in Figure 2(a) was chosen to evaluate its mean velocity (Figure 3): the evoked CBF started to increase (0.7±0.1) s, peaked at (3.1±0.2) s and then returned to the baseline level. It is coherent with the conclusions obtained from LDF technique [27,29]. In order to differentiate the response patterns of artery/vein under the same stimulus, we labeled six distinct levels of vessels in Figure 2(a) and displayed their changes of blood flow. The results clearly showed that the response patterns of arteries and veins in the somatosensory cortex were totally different: vein 1 (V-1, ~140 μm in diameter) almost remained unaffected, and arteriole 1 (A-1, ~35 μm in diameter) responded slowly; arteriole 2 (A-2, ~35 μm in diameter) peaked at (3.5±0.5) s after the onset of stimulation and then reached the steady-state plateau, and vein 2 (V-2, ~70 μm in diameter) presented a delay and mild response; blood flow in the

capillaries (A-3 and V-3, ~10 μm in diameter) surged readily and increased significantly. We also measured the changes in arteries and veins with different diameters and the results are shown in Figure 4. The statistical results exhibited that arterioles (A-II, ~35 μm in diameter) dilated abruptly ($p<0.05$) but arteriole 1 (A-I) did not change and dilated slightly at 5 to 6 s after the end of stimulation ($p<0.05$). No alterations in vein with diameter of >70 μm were observed during sciatic nerve stimulation ($p>0.05$). We found that the blood flow in capillaries in hindlimb sensory cortex was firstly activated to increase at (0.5 ± 0.2) s; then arterioles with diameter of >70 μm began to respond at (2.5 ± 0.5) s, dilated up to maximum at (3.5 ± 0.5) s and came back to the prestimulus level; and finally the activation propagated to the entire scope of somatosensory cortex. Blood flow in arteriole 1 did not increase until after 5 to 6 s end of stimulation since it was situated farther from the hindlimb cortex. The activation pattern of cerebral blood flow is discrete in spatial distribution and highly localized in the evoked cortex with the temporal evolution. This is consistent with the hypothesis of Roy and Sherrington and the conclusions drawn by other research groups [27-29,33].

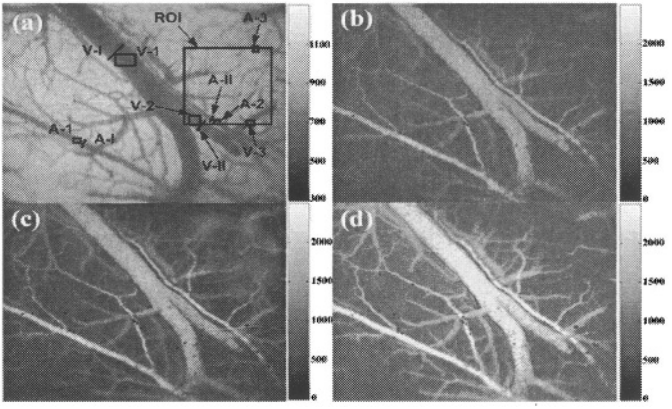

Figure 2. Blood flow change in contralateral somatosensory cortex of rats under unilateral sciatic nerve stimulation. (a) A vascular topography illuminated with green light (540±20 nm); (b)–(d) blood activation map at prestimulus, 1 s and 3 s after the onset of stimulation (the relative blood-flow images are shown and converted from the speckle-contrast images, in which the brighter areas correspond to the area of increased blood flow.), respectively. A-1, 2, 3 and V-1, 2, 3 represent the arbitrarily selected regions-of-interest for monitoring changes in blood flow. A-I,II and V-I,II represent the selected loci on the vessel whose diameters are measured in the experiment [25].

5.4.1.3 Discussion

The present study is influenced by various kinds of experimental conditions due to the complicacy of biological experiments. The first factor is stimulation parameters that should reach the threshold of response, and not

affect systemic blood pressure and evoke the maximal magnitude of vascular response. The optimal parameters (350 mV, 0.5 ms, and 5 Hz) were adopted in our experiments. The second is anaesthesia condition of animals. It was proved by the former investigations that chloralose-urethane is most suitable for the study on neurovascular coupling since it induces minimal cardiovascular effects [29,33]. In order to minimize spontaneous oscillations (also known as "vasomotion"), it is important to maintain an adequate anesthesia and keep blood pressure above 80 mmHg. Anesthesia would exert direct influence on the animals' respiration and probably cause CBF fluctuating in nearly synchrony with the respiratory cycle. Thirdly, tissue pH and blood composition also influence regional CBF. Acids and bases cause cerebral vasodilation and vasoconstriction, respectively. When functional activity in blood-perfused tissue is activated, the rate of energy metabolism is increased and the gas tension of CO_2 is elevated to cause cerebral vasodilation and increase local CBF. Electrical stimulation of unilateral sciatic nerve is a classical biological model that was used to probe effects of increased functional activity in somatosensory cortex [27,33,34].

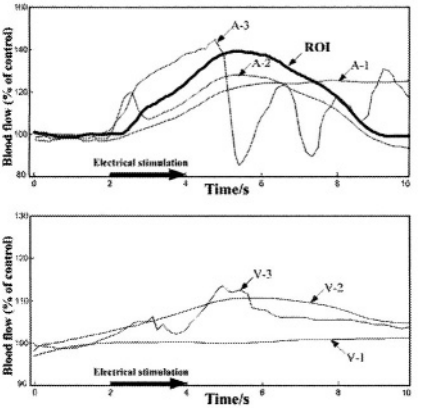

Figure 3. The relative change of blood flow in 6 areas indicated in Figure 2(a) (divided by the values of prestimulus) [25].

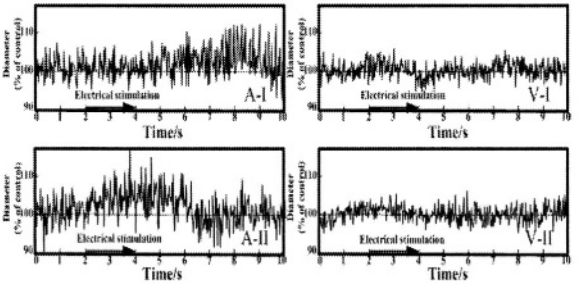

Figure 4. Relative alterations in vessel diameter during sciatic nerve stimulation (divided by the values of prestimulus) [25].

In our experiments, several physiological parameters (including body temperature, femoral blood pressure, pO_2, pCO_2 and pH) were monitored for keeping a normal physiological status during the experiment. Thus it improved the reliability and reproducibility of our results.

Until now the response of evoked CBF to somatosensory stimulation in rats has been studied using some techniques such as laser-Doppler flowmetry (LDF) [27] and functional magnetic resonance imaging (fMRI) [28] under laboratory or clinical conditions. However, those conventional methods have their own limitations like lower temporal/spatial resolutions in fMRI, or radioactive effects in positron emission tomography (PET), or limited information from isolated points in LDF. It is difficult to apprehend comprehensively behaviors of CBF during brain functional activity. It is almost certain that the dynamic regulation of the cerebral circulation is not mediated by a single exclusive mechanism but is achieved by numerous factors acting in concert. Most of the effects of these neural vasomotor pathways were observed in pial arteries and might not apply to the small parenchymal resistance vessels that regulate the blood flow, which is also known as the "spatial heterogeneity of microcirculation" [26]. The sample tissue volume of conventional LDF technique is approximately 1 mm^3 [27, 29,35], as exerted great limitations on its application [36].

5.4.2 Speckle Imaging of CBF Dynamics under the Effect of a Hyper-Osmotic Chemical Agent

Optical clearing of tissue technique alters the optical properties of normally turbid tissues, offering many potential advantages in laser surgery and phototherapy [37-39]. The idea is that by reducing the scattering effect of the tissue by means of physical or chemical manipulation, among which are compression, coagulation, dehydration and immersion into osmotically active chemical agents [40-42], imaging and surgical techniques can probe deeper into the tissue than is normally possible. This effectively opens a window into the tissue for more effective treatment, aiding diagnosis of deeper-lying tumors, for example.

In the application of light-based cerebral surgery and diagnostics, one of the problems deals with transport of the laser beam through the *dura mater* tissue. As *dura mater,* a typical fibrous tissue, is turbid due to the random scattering within tissue caused by variations in refractive index, depth penetration of optical methods is limited [38,39]. Through application of hyper-osmotic chemical agents, the scattering effect of tissue can be temporarily modified, which is demonstrated in many studies [43,44], and imaging modalities would benefit from an increased penetration depth [45,46]. As tissue clearing is a reversible process, usually after a short time,

interstitial liquid is reabsorbed into the tissue and the scattering returns to normal, the clearing effects and period of time of the chemical agents action are the focuses in these studies. The influence of chemical agents to tissue normal physiological function is investigated rarely. In present chapter, optical properties of *in vitro* and *in vivo* rabbit *dura mater* with the application of a hyper-osmotic chemical agent, glycerol, were measured, and the influence of epidurally applied hyper-osmotic glycerol on *in vivo* resting cerebral blood flow (CBF) was investigated by laser speckle imaging method based on our previous studies [25,47-49].

5.4.2.1 Materials and Methods. Animal Preparation

Healthy rabbits, weighting 4÷5kg, were used for the experiments. Before experiments, the animals were housed in individual cages in a specialized animal department where they were allowed free access to food and water. The experimental design has been approved by the local ethics committee. Rabbits were narcotized by 20% urethane (0.5 ml/kg). Animals were divided into three groups for *in vitro* transmittance spectra, *in vivo* reflectance spectra and *in vivo* CBF measurement separately. In *in vitro* experiment, *dura mater* was removed from anesthetic rabbits. In *in vivo* experiments, rabbits were fixed on a stereotaxic apparatus. Body temperature was kept constant at 37°C with a thermostablizing stage during experiments. The left femoral artery was cannulated for continuous blood pressure monitoring. Animals were ventilated and breathed room air supplemented with oxygen. The skull was removed and intact *dura mater* was exposed. The reflectance spectra were measured to investigate the optical clearing effect of glycerol on *in vivo* rabbit *dura mater.* The photographs were taken through digital video camera (Panasonic, Japan) in above two cases. To study the influence of glycerol to *in vivo* CBF, a small area of *dura mater* was removed. Warm dehydration glycerol was administrated near the exposed area. CBF in the exposed area was monitoring by laser speckle imaging method.

Transmission and Diffuse Reflectance Measurements

Optical property measurements were performed on *in vitro* and *in vivo* samples of rabbit *dura mater* with a computer-controlled PC 1000 spectrometer (Fiber Optic Spectrometer, Ocean Optics Inc., U.S.A.) of scanning wavelengths of 370÷2,000 nm. Native *dura mater,* which had not been treated with any chemical agents, and samples immerging into dehydration glycerol placed between two glass-slides were measured separately. Transmission spectra were obtained. To assess the optical

property change of *in vivo dura mater* under the action of glycerol, glycerol was directly applied on the intact *dura mater* of the rabbits and reflectance spectra were measured.

Speckle Imaging Measurement

The instrument for speckle imaging measurement is shown in Figure 1. As described above, images were acquired through the easy-control software (PCO Computer Optics, Germany) at 40 Hz. Conversion of the raw speckle image to blood flow maps controlled by our written software that computed the speckle contrast and correlation time values at each pixel according to the principle of LSI [18].

5.4.2.2 Results

Figure 5 illustrates the dynamic changes in *in vitro dura mater* turbidity after application of glycerol. A resolution target was placed under a dura mater sample. After the treatment of glycerol for 1min, the target, which was not visible under the native *dura mater* [Figure 5(a)], was seen through the dura mater specimen [Figure 5(b)]. Optical property measurement results [Figure 5(c)] confirmed the visually observed reduction in scattering. Figure 5(c) shows the increase in transmittance within the wavelength range of 400-750 nm as a function of time the *dura mater* was soaked in glycerol. The hemoglobin absorption became so much more prominent after application of glycerol due to the blood on the *dura mater* [Figure 5(b)].

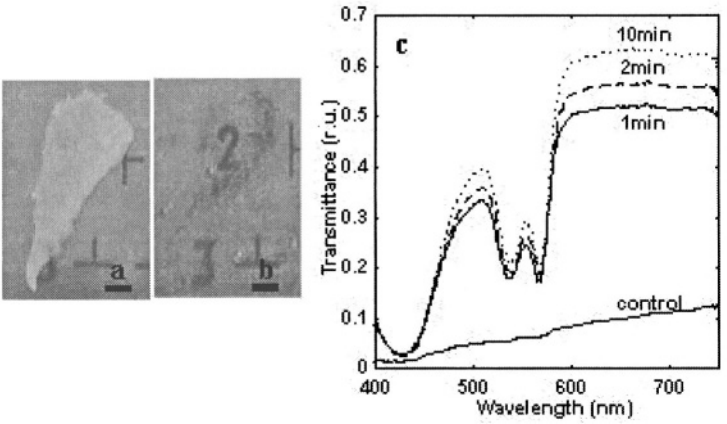

Figure 5. Visual changes in the *in vitro* turbid rabbit dura mater and the measured optical changes before and after application of glycerol. (a) Native *dura mater* placed over the resolution target, bar=1mm. (b) One-minute application of glycerol, bar=1mm. (c) Transmittance spectra for native *dura mater* measured at application of glycerol for 1, 2, and 10 min.

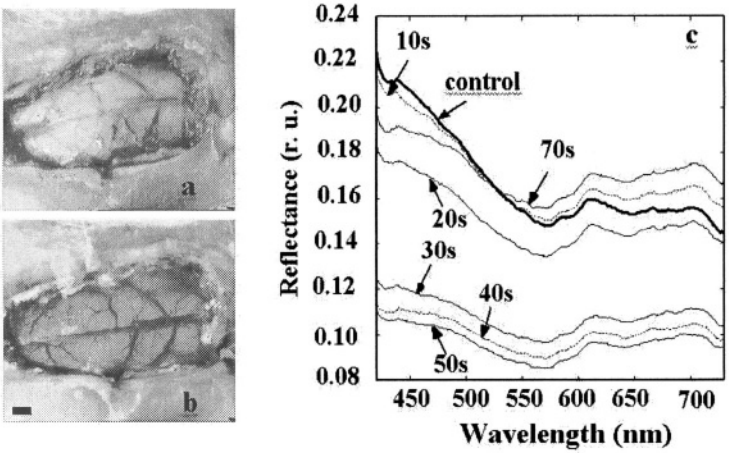

Figure 6. Visual changes and the measured optical changes for *in vivo* rabbit *dura mater* before and after treatment with glycerol epidurally. (a) Native *in vivo* turbid dura mater, bar=1mm. (b) Fifty-second application of glycerol, bar=1mm. (c) Reflectance spectra for native *dura mater,* application of glycerol epidurally for 10, 20, 30, 40, 50 and 70 seconds.

In vivo experiment results were demonstrated in Figure 6. Epidurally applying glycerol changed the turbidity of *dura mater.* The vasculature under the dura mater became visible after the treatment of glycerol [Figures 6(a) and 6(b)]. The reflectance decreased as a function of time glycerol action, which proved the visually observation. In Figure 6(c), it was seen that, the *dura mater* nearly recovered to native condition after 1 min.

Velocity images of *in vivo* CBF under the effect of glycerol are shown in Figure 7. Glycerol was applied around the exposed area. When glycerol diffused in brain tissue and influenced CBF under the *dura mater,* CBF in exposed area would also change. Figure 7 illustrates the spatio-temporal characteristics of CBF changes under the treatment of glycerol. Under the action of glycerol, blood flow first decreased while the blood vessels underneath the *dura mater* became increasingly visible. Then blood flow increased to near baseline, at the same time the turbidity of the *dura mater* returned.

Figure 8 gave the time course of changes in four different vessels, which was expressed as the ratio of the measured velocity in the conditions of treatment with glycerol to that of control condition. Vessel 2 was an arteriole. Vessel 1, 3 and 4 were veinules. Blood flow in vessel 2 (arteriole) began to decrease after twenty-second application of glycerol, while that in other vessels (veinules) decreased immediately after application with glycerol. The blood flow in vessel 1 decreased slower than that in other vessels, which suggested that blood flow in the arteriole had different response from that in the veinules. Blood flow in all vessels decreased to 70% to 80% of baseline after treatment with glycerol.

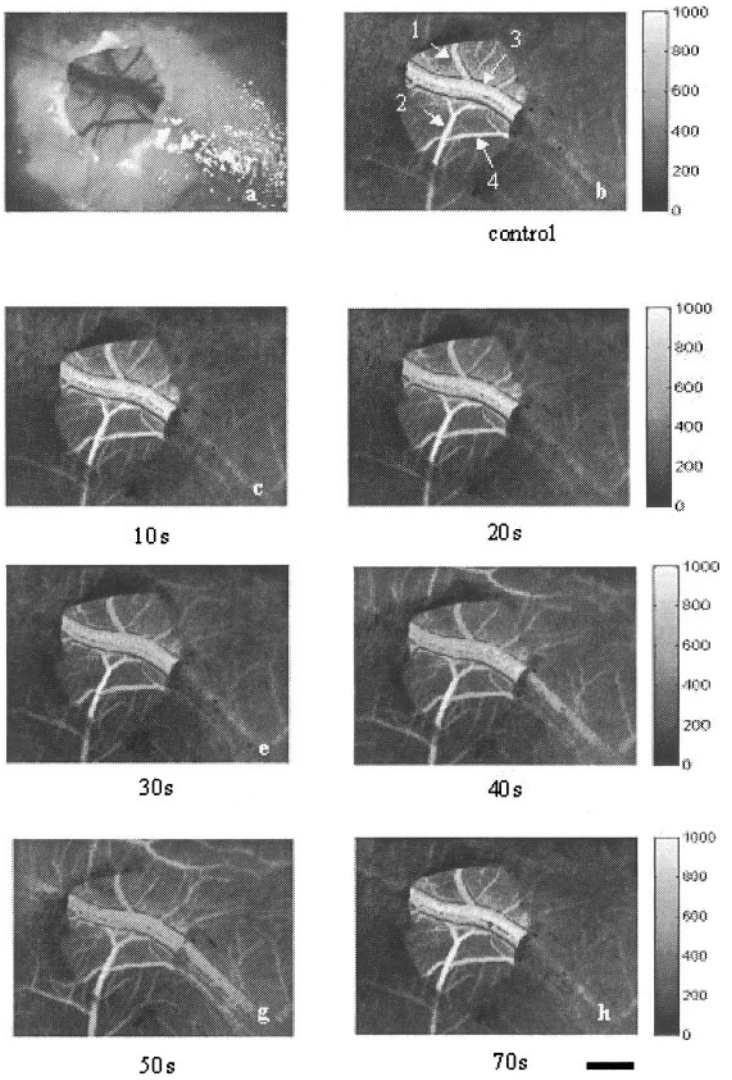

Figure 7. Blood–flow images following the epidurally applied with glycerol around the exposed area of *in vivo dura mater.* (a) The white light picture of the interest area. Four vessels are indicated (b) (b)–(h) Blood flow maps expressed as measured velocity, which is proportional to the blood flow velocity, during the treatment with glycerol and represented by images at the time-points shown in Figure 8. (b) Imaged blood flow before the application with glycerol (control). (c) Ten-second application of glycerol. No obvious change in blood flow was observed. (d) Twenty-second application of glycerol. Blood flow began to decrease. (e) Thirty-second application of glycerol. The blood vessels underneath *dura mater* began to be clear. (f) Forty-second application of glycerol. Blood flow decreased and the transparency of surround *dura mater* increased. (g) Fifty-second application of glycerol. More blood vessels could be seen through *dura mater* and the blood flow decreased significantly. (h) Seventy-second application of glycerol. Blood flow increased and *dura mater* became to be turbid again. Bar=1mm.

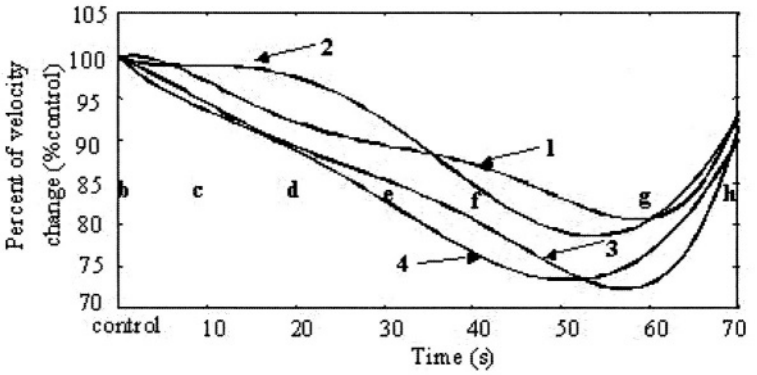

Figure. 8. The time course of change in relative blood flow in vessel 1, 2, 3, and 4, which are indicated in Figure 7(b), before and after the application of glycerol epidurally. After twenty seconds, the blood flow in vessel 2 (arteriole) began to decrease, while blood flow in other vessels (veinules) decreased immediately after application with glycerol. Decreases of blood flow in these vessels were 20% to 30% of baseline. b, c, d, e ,f, g, and h denote the time points of corresponding images in Figures 7(b), (c), (d), (e), (f), (g), and (h).

5.4.2.3 Discussion

Optical Clearing Effects on In Vitro and In Vivo Dura Mater

After treatment with glycerol, the *in vitro dura mater* specimen became increasingly transparent, which lasted for a long period of time. However, *in vivo dura mater* became transparent and then recovered to be turbidity within very short period of time. This may be due to different interactions between tissue and the agent under *in vitro* and *in vivo* conditions.

The optical effect caused by glycerol is a time-dependent process in that it occurs as a consequence of the transport of chemical agent and water in and out of the tissue, respectively. The mass transport occurs when experiencing an osmotic stress. Interstitial water travels from areas of high water potential and a lower osmotic potential to a lower water potential and higher osmotic potential. This indicates water leaves interstitial (extrafibrillar) spaces in the case of topical application of a hyper-osmotic agent and leaves the bulk tissue when the agent surrounds it. Due to a high affinity glycerol to water and its much higher viscosity in comparison with water, local tissue dehydration takes place, collagen fibrils may become more closely packed. This will reduce multiple scattering if the packed fibers act as a single scatterer. In *in vivo* studies at the point when equilibrium is reached, water will begin reentering the extrafibrillar space over the treated

area, while glycerol is washed out. The change in optical properties of tissue with variations in fiber and/or cell size, refractive index mismatch between the extrafibrillar or extracellular and intrafibrillar or intracellular spaces, and fibrillar and/or cellular volume fraction are still under investigation [40–43, 50]. In spite of high viscosity of glycerol it cannot be assumed that in the *in vivo* setup it only acts on *dura mater* tissue as a dehydration agent. Diffusion into brain tissue has to be considered. In addition, glycerol was applied epidurally at high concentrations due to no protection in its surface and a high tension in present study, not like studies [45] of using glycerol to reduce scattering in skin, in which glycerol was needed to inject subdermally because the penetration of glycerol through the epidermis was quite limited due to the protective (cellular) nature of the stratum corneum.

Influence of Glycerol to Resting CBF

In our study, glycerol was applied on the *dura mater* surface around the exposed area. When it diffused into brain tissue and influenced the CBF, the blood flow of exposed area also changed. LSI was a noninvasive full-field optical imaging method for the measurement of blood flow, which provided high resolution maps of spatial and temporal evolution of CBF changes. The dynamic change of CBF in exposed area monitored by LSI reflected the effect of glycerol. From our results (Figure 7), the CBF perfusion decreased as the transparence of *dura mater* increased, which was also proved by the *in vivo* optical measurement (Figure 6). The increase of tissue transmittance may be due to the index matching between the ground substance and the collagen fibrils, caused mostly by tissue dehydration induced by glycerol [45]. From the other hand the release of neurotransmitters or vasoactive substances during glycerol application [51], although glycerol is biologically inert and is widely used in cosmetics and medicine [52,53], may affect CBF. The mechanism of glycerol's influence to *in vivo* CBF needed further research in future.

LSI

LSI is a noninvasive full-field optical imaging method with high spatial and temporal resolution, which was found to be a convenient technique in measuring dynamic of CBF [20,21]. As other optical imaging methods, LSI could only provide the velocity information on the surface of the turbid tissues due to the high scattering properties of the light in the biological tissue. In brain studies, as *dura mater* on the surface of the brain cortex was a typical fibrous tissue and turbid for the light between visible and NIR spectra range, which limited the depth penetration of optical methods, it was

usually removed [54,55]. This destroyed the normal physiological condition of CBF and caused the need of a complex method to maintain the normal encephalic pressure. Our study can be viewed as an attempt to find a suitable agent to improve optical properties while measuring cerebral blood flow *in vivo.*

Existed studies showed that the technique of reduced tissue scattering by optical clearing agents could be of benefit to a number of optical diagnostic or therapeutic applications. For example, the potential of the method to enhance penetration depth in imaging had been shown for the specific case of OCT, which demonstrated that the glycerol reduced excessive scattering in the tissue enough to image an underlying area that was previously not visible [45]. This method was also used to study the effects of transient tissue scattering on the remitted fluorescence emission intensity from a target placed under a tissue sample. The detected fluorescent signal was found to increase as the scattering in tissue samples was substantially reduced. Although the increase was different between different chemical agents, it was not statistically different between *in vivo* skin and *in vitro* skin [46]. In our study, LSI method was used to image the regional blood flow. After application with glycerol, the blood flow in blood vessels underneath *in vivo dura mater* became clearly visible, which suggested that the light penetration increased. The optical immersion technique could increase the light penetration of LSI. However, administration with glycerol decreased 20% to 30% of control cerebral blood flow at the same time. This indicated that glycerol was not suitable to be used for our purpose. In our experiment, as glucose (40%) and mannitol (156 mg/ml) solutions have no significant clearing effect by epidurally application on *in vivo dura mater* (data not shown), only glycerol's effect was studied in present chapter.

5.5 A MODIFIED LASER SPECKLE IMAGING METHOD WITH IMPROVED SPATIAL RESOLUTION [56]

As described above, laser speckle imaging (LSI) was based on the first order spatial statistics of time-integrated speckle. The main disadvantage of LASCA is the loss of resolution caused by the need to average over a block of pixels to produce the spatial statistics used in the analysis, although it actually has higher resolution than other techniques such as scanning laser Doppler. In this chapter, we presented a modified laser speckle imaging (LSI) method utilizing the temporal statistics of the time-integrated speckle based on our previous studies [47,48,57]. First a model experiment was designed to validate this method, and then imaging of the rat cerebral blood

flow distribution was performed. Also the influences of temperature to the rat cerebral blood flow (CBF) were investigated by this method compared with LSI.

5.5.1 Materials and Methods

5.5.1.1 Model Experiment

A porcelain plane, which was pushed by a stepping motor (SC3, Sinoptek, China), moved with the velocity that ranged from 0.018 to 2.3 mm/s. The laser beam illuminated evenly on the surface of the plane and the imaged area was about 2.46×3.28 mm^2. Three measurements were performed under each velocity condition.

5.5.1.2 *In Vivo* CBF Measurement

The experiment was performed on Sprague-Dawley rats (350÷450 g), which were anesthetized with α-chloralose and urethane (50 and 600 mg/kg, respectively). The right femoral artery was cannulated for measurement of mean arterial blood pressure (Pclab Instruments, China) and blood sampling. A tracheotomy was executed to enable mechanical ventilation with a mixture of air and oxygen (20% O_2, 80% N_2, TKR-200C, China). Periodically blood gases analysis was performed to ensure that noemoxia was maintained at normal physiological levels (pO_2, pCO_2 and pH) (JBP-607, Dissolved Oxygen Analyzer, China). The animals were mounted in a stereotaxic frame, and rectal temperature was maintained at 37.0±0.5°C with a thermostatic heating blanket. The skull was thinned to translucency using a dental drill under constant cooling with saline. Following surgical preparation the animals were left for at least 30 min before the experiment began. In all animals, the physiologic parameters were kept within normal range throughout the experiments. The temperature of the rat cortex was changed locally by constant application of warm saline solution to the cortex for ten minutes under each temperature condition: 35°C, 45°C, and 50°C. The raw speckle images were acquired firstly under control condition (38°C), then under other temperatures to obtain the CBF map.

5.5.1.3 Speckle Imaging Processing

Laser speckle is an interference pattern produced by the light reflected or scattered from different parts of the illuminated rough (i.e., nonspecular) surface. When the area illuminated by laser light is imaged onto a camera,

there produced a granular or speckle pattern. If the scattered particles are moving, a time-varying speckle pattern is generated at each pixel in the image. The intensity variations of this pattern containes information of the scattered particles.

Analysis of LASCA (Laser Speckle Contrast Analysis)

In the current version of LSI [18], to quantify the blurring of the speckles, the local speckle contrast was defined as the ratio of the standard deviation to the mean intensity in a small region of the image:

$$k = \frac{\sigma_s}{< I >}. \tag{10}$$

Here k, σ_s and $<I>$ represent speckle contrast, the standard deviation and the mean value of light intensity respectively. This method uses the spatial intensity variations in speckle pattern to obtain the relative blood flow map. In practice, a 5×5 or 7×7 region of pixels is used: lower numbers reduce the validity of the statistics, whereas higher numbers limit the spatial resolution of the technique. In this section, squares of 5×5 pixels were used. The software computes the speckle contrast k for any given square and assigns this value to the central pixel of the square. The process is then repeated for 5×5 squares centered on each pixel in turn. This results in a smoothing of the contrast map, but the spatial resolution is lost for the averaging over a block of pixels.

Theory and Analysis of Modified LSI

The first-order temporal statistics of time-integrated speckle patterns can be used to provide velocity information, which were described in detail in Ref. [58]. In the previous research works, only the velocity of a single point area (a single speckle size in detected plane) is measured by this method.

$$N_t = \frac{< I^2 > - < I >^2}{< I >^2}, \tag{11}$$

where $<I>$ and $<I^2>$ are the mean and square-mean values of time-integrated speckle intensity variations during the time interval t, N_t is inversely proportional to the velocity of scattering particles [58].

Here we utilized the first-order temporal statistics of time-integrated speckle to obtain the 2-D blood flow distribution. Each pixel in the speckle image can be viewed as the single point area in the previous study. Then the signal processing consists of calculation the temporal statistics of the intensity of each pixel in the image:

$$N_{i,j} = [\langle I_{i,j,t}^2 \rangle_t - \langle I_{i,j,t} \rangle_t^2] / \langle I_{i,j,t} \rangle_t^2$$

$$i = 1 \div 480, j = 1 \div 640, t = 1 \div m, \quad (12)$$

where $I_{i,j,t}$ is the instantaneous intensity of the *i*- and *j*-th pixels at the *t*-th frame of raw speckle images, and $\langle I_{i,j,t} \rangle_t$ is the average intensity of the *i*- and *j*-th pixels over the consecutive *m* frames. $N_{i,j}$ is inversely proportional to the velocity of scattering particles. The value $N_{i,j}$ of each pixel in the consecutive *m* frames $(I_{i,j,t})$ of raw speckle pattern is computed according to equation 12. The process is then repeated for the next group of *m* frames. The results are given as 2-D gray-scale (65536 shades) or false-color (65536 colors) coded maps that describe the spatial variation of the velocity distribution in the area examined.

5.5.2 Results and Discussion

5.5.2.1 Validation of the Modified LSI Method

In the model experiment, the *N* values of the center pixel of the interest area under the conditions of different velocities were computed according to equation 12. Figure 9 shows the value of the reciprocal of *N(1/N)* computed from different number of frames *(m)* of consecutive images under different velocity conditions *(V)*.

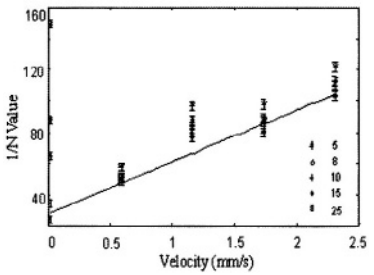

Figure 9. The value of 1/*N* under different velocity *(V)* conditions calculated through different frames. The solid line was a least squares fit between 1/*N* and *V* when *m* equaled 25 [56].

The correlation value (R^2) between *V* and *1/N* are given in Figure 10. It is obvious to see that the correlation value (R^2) increased with *m.* When *m* is larger than fifteen, the high correlation $(R^2=0.96)$ is obtained. This can be explained as that for small number of integrated speckles the experimental results of the probability density function are slightly different from the theoretical ones (gamma distribution), which may be due to the statistical

uncertainty associated with the experiments [58], and therefore the linear is only for high *m.* The linearity is not as good as that of LDPI, for equation 12 is obtained under an ideal condition of fully developed speckle pattern [17,58], and actual experiment conditions are usually contiguous to the ideal one, which does not influence much in measuring the relative velocity change.

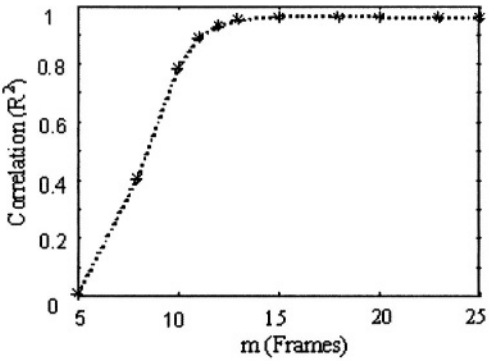

Figure 10. The correlations (R^2) between the actual velocity and the 1/*N*. R^2 increases with *m* [56].

In Figure 9, the high 1/*N* values obtained for the lower *m* may be due to that for small number of integrated speckles, the fluctuation of the moving porcelain plane becomes significant and its effect cannot be neglected [58], i.e., for lower *m,* the value of $[\langle I^2\rangle - \langle I\rangle^2]^{1/2}/\langle I\rangle$ (between 0 and 1, reflecting the fluctuation) would be larger and *N* would be smaller, and thus the corresponding 1/*N* value became larger. To insure the temporal resolution, we could choose *m* larger than fifteen. Assuming ergodicity, the principle of modified LSI method was similar to that of LASCA. In theory, to obtain the same the signal to noise ratio (SNR) as LASCA, 25 temporal samplings used, i.e., *m* equaled 25. In present section, we would compare the blood flow map obtained when *m* equaled 25 with that obtained by LASCA. The least squares fit between *V* and 1/*N* is displayed when *m* equaled 25 (Figure 9), which suggests that the change of 1/*N* value could be used to reflect the velocity change of scatterers effectively in the illuminated area. The same problem of being difficult to measure the absolute velocity of scatterers from the time-integrated speckle pattern was met, which was the problem shared with all time-varying speckle techniques, as well as with laser Doppler [18,24,59].

As stated in previous studies about image speckle [59,60], each point in image plane is the superposed result of the points near the corresponding

point in object plane, i.e., the size of single speckle is approximately equal to the size of a single pixel in the image acquired by CCD and the captured image from different speckles do not interact with others, which was different from that in case of laser Doppler. Each $1/N_{i,j}$ value reflected the velocity change of one pixel *(i,j)* in imaged area. If velocities of the imaged plan were diversiform just like the inhomogeneities in CBF model, the N value of each pixel would be different, forming the velocity map of CBF. We choose a moving porcelain plane as the model for the convenience of controlling the speed by computer. Of course, a tube model using a layer of static scatter above with different velocities and concentrations of Intralipid (or blood) would be better than this model for its close propinquity to a real CBF model.

Further research is needed to clarify the relationship between the signal and the velocity and concentration by a tube model.

5.5.2.2 The CBF Maps Obtained by Modified LSI

The white light image of the vasculature is shown in Figure 11 (a). By illuminating the expanded laser beam on the interest areas (2.46×3.28 mm^2), the raw speckle images were captured. The CBF maps obtained by the modified LSI method are represented in Figures 11(b), (c), (d), and (e), which are the blood flow maps obtained by 5, 8, 15, and 25 frames *(m),* respectively. It is easy to see that as m increases, the signal to noise ratio (SNR) of blood flow map increases.

5.5.2.3 The Spatial Resolution of Modified LSI

In the *in vivo* CBF experiment, the field of view was approximately 2.46×3.28mm^2. The size of each raw speckle image was 480×640 pixels. According to the principle of modified LSI, the resolution of the map was 5 μm (246/480). In another hand, the resolution of the map obtained by LASCA was effectively reduced by the use of 5×5 squares of pixels from 480×640 (pixels) to approximately 96×128 (pixel blocks). Hence the spatial resolution was approximately 25 μm, which was low as one fifth as that of modified LSI in theory. Comparing with the work by Linden *et al.* [61], in which an enhanced high-resolution laser Doppler imaging (EHR-LDI) technique intended for visualization of separate microvessels was evaluated by use of *in vitro* flow models, the resolution of the modified LSI is much higher than that of EHR-LDI (about 40μm). The modified LSI and LASCA were utilized to measure the CBF respectively under the same conditions. According to equation 12, the maps of flows represented by N values under control condition (38°C) were achieved (Figure 11(e), m=25). Comparing with the map obtained by LSI [Figure 11(f)], we could see that the spatial

resolution of the modified method was much higher, more small blood vessels appeared clearly in the case of modified LSI, although both methods could well resolve the statically and dynamically scattering regions in the map of flow.

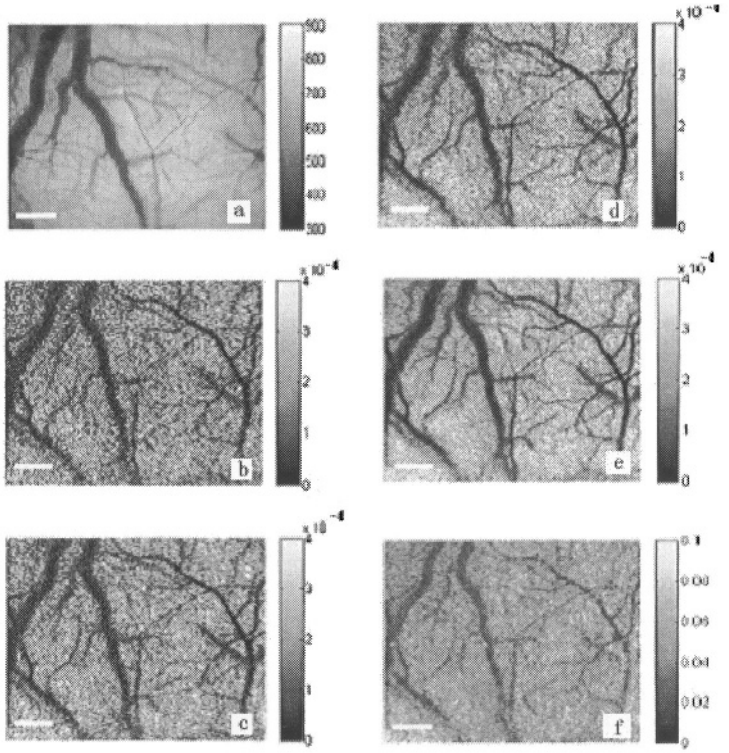

Figure 11. The blood flow maps obtained by the methods of modified LSI and LASCA under control condition, (a) Vascular image of the interest area of rat brain under control condition. (b), (c), (d), and (e) – The blood flow maps obtained by the modified method when *m* chosen as 5, 8, 15, and 25, respectively (gray bar indicated as *N* value on the right side of the picture), (f) The blood flow map obtained by LASCA (gray bar indicated as *k* value on the right side of the picture). Bar=500 μm. Figure (a) is a white light picture, and b – e the scale is $0\text{-}4\times10^{-4}$, which is the value of *N*. Figure (f) is indicated by value of *k*, the scale is 0-0.1 [56].

5.5.2.4 Influence of Temperature to CBF

The CBF distributions of the rats under different temperatures (35°C 45°C, 50°C were examined in this study. The results are illustrated in Figure 12. When the temperature increased from 35°C to 50°C the map of flow gained by the modified LSI became darker [Figure 12(a), (b), (c)], indicating *N* value became smaller, therefore the increased blood perfusion. In some small blood vessels, indicated by panes in Figure 12(a), the blood perfusion increased obviously. However, these vessels could not be clearly seen in the

map obtained by LSI [Figure 12(d), (e), (f)] due to the lower spatial resolution, although these two methods showed the same tendency of the thermal influence to CBF. Hence, in the physiological studies, the modified LSI could provide more information about small blood vessels. As in brain studies, brain homeostasis depended on adequate levels of blood flow to ensure the delivery of nutrients and to facilitate the removal of metabolites and excess heat, the exchange of material between constituents in the blood and neurons and glia occurred at the level of individual capillaries [62]. Our modified LSI with improved spatial resolution would be helpful for these brain researches.

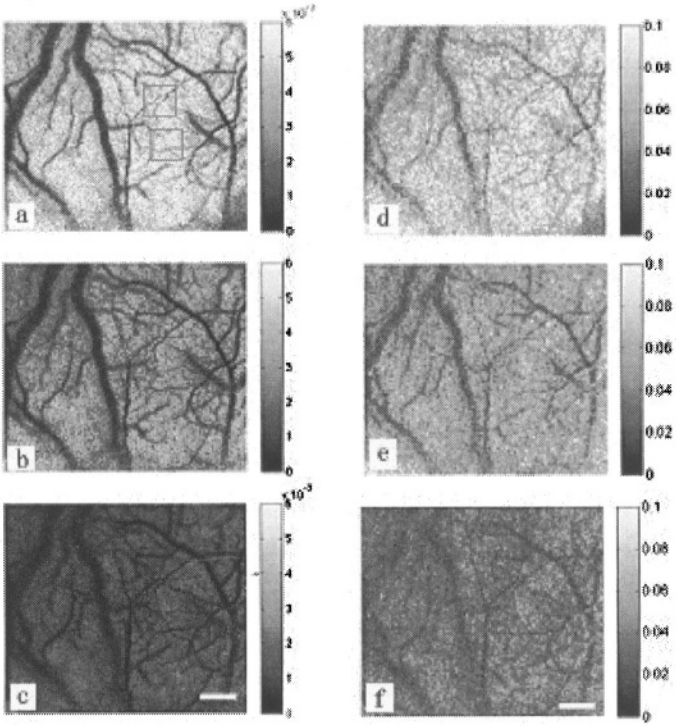

Figure12. The blood flow maps obtained by two methods. (a), (b), and (c) – The blood flow distributions obtained by the modified LSI when *m* equaled 25 under the temperatures of 35ºC, 45°C and 50°C, respectively (the indicated as *N* values). (d), (e), and (f) – The blood flow distributions obtained by LASCA under the temperatures of 35°C, 45°C 50°C, respectively (the indicated as *k* values). The pane areas in (a) were used to notice the blood perfusion change of small blood vessels under the thermal influence. Darker areas in the maps obtained by two methods both represented increased cerebral blood flow. Bar=500 μm [56].

5.5.2.5 The Temporal Resolution of Modified LSI

The sampling frame of our CCD was 40 Hz. From the principle of modified LSI method, the temporal resolution was about 0.4 to 0.6 s (15/40,

25/40), which was determined by the sampling frequency of CCD camera and the value of *m.* As described in above, the temporal resolution of LSI was only determined by the sampling frequency (1/40 s), which was higher than that of modified LSI. In many cases of physiological studies, the CBF response was a slow change [21,62], and the temporal resolution of second was enough for the measurement. On the other hand, the data processing time of this method was reduced a lot, which was advantage to a real-time operation.

5.6 CONCLUSION

In this chapter, we present a LSI technique, which is a new alternative approach in measurement of blood flow. It develops the spatial statistical characteristics of time-varying image speckle, extracts the velocity information from speckle signals within an area of 5×5 pixels and obtains the velocity distribution in the whole region. Its spatial resolution is equal to the area in the image plane corresponding to 5×5 pixels, far better than LDF. LSI is capable of accurately imaging the cortical blood flow response over an area ranging from a few millimeters to a centimeter over time scales of milliseconds to hours. For its higher temporal and spatial resolution (here 25 ms and 27 μm, respectively), we can choose small regions-of-interest in two-dimensional maps of blood vessels so as to analyze the spatial patterns of different vessels response to sciatic nerve stimulation and also show their evolution along the time axis, as can furnish more information to characterize the regulation mechanism of microcirculation associated with cerebral functional events. The finding of this study is that spatial response of CBF is highly localized in cortical anatomic distribution and discretely coupled to the microvasculature in the targeted cortex. Different levels of arteries, veins and capillaries are activated successively with the time varying. Compared with the former conclusions, we found more elaborated details besides those accordant results and offered a new proof to the hypothesis proposed by Roy and Sherrington more than 100 years ago.

As other optical imaging methods, LSI could only provide the velocity information on the surface of the turbid tissues due to the high scattering properties of the light in the biological tissue. Optical immersion method is a technique using chemical agents to alter the optical properties, established on that immersion into index-matching fluids greatly reduced the amount of specular scattering of a dispersive system. Our present study tried to combine the optical immersion and LSI method to obtain deeper CBF information through intake *dura mater.* Before this we should investigate the chemical agents' influence on CBF. Here we demonstrated a hyperosmotic agent of glycerol causing a reduction in scattering in the *dura mater* and its

influence on *in vivo* CBF revealed by LSI. Optical property changes are given for *in vitro* and *in vivo* clearing of *dura mater.* The differences between the *in vivo* and *in vitro* cases indicate that the processes of reduction in scattering might be different for the two conditions. Clearly, the agent drastically increases the optical depth of the tissue in the case of LSI. At the same time, it decreased 20% to 30% blood flow of baseline. These suggest that although glycerol is biocompatible, it does irritate tissue and is not the agent of choice for *in vivo* procedure. It is not a suitable agent for *in vivo* CBF imaging. Further experiments of the mechanism about the chemical agent's influence to CBF are required. Not only the optical clearing effects and period of time of the chemical agents action but also the influence to tissue normal physiological function are the challenges in optical clearing technique.

To improve the spatial resolution of current LSI, we proposed a modified LSI based on the temporal resolution of time-integrated speckle. Compared with other laser Doppler perfusion imaging (LDPI), this modified LSI method did not need the moving scanning components, and the spatial resolution was highly improved to five times of that of LSI thus being able to discriminate the small blood vessels and providing more spatial information under the same condition. The temporal resolution of this method was much lower than that of LSI and the laser Doppler perfusion imaging with a complimentary metal oxide semiconductor sensor proposed by Serov *et al.* recently [63] for the limitation of the frame rate of CCD camera. However, this method could be used to measure the relative slow change of blood flow. By use of a CCD camera with high sampling frame rate, the temporal resolution would increase. Also our system was an easy-to-use instrument for the whole field blood flow imaging.

ACKNOWLEDGEMENTS

This work was supported by National Nature Science Foundation of China (NSFC) (Grants No. 59836240, 30070215, 30170306, 60178028), and NSFC for distinguished young scholars (Grant No. 60025514). It was also partly supported by grant REC-006/SA-006-00 "Nonlinear Dynamics and Biophysics" of CRDF (U.S. Civilian Research and Development Foundation for the Independent States of the Former Soviet Union) and the Russian Ministry of Education; the Russian Federation President's grant N 25.2003.2 "Supporting of Scientific Schools" of the Russian Ministry for Industry, Science and Technologies; and grant "Leading Research-Educational Teams" N 2.11.03 of the Russian Ministry of Education.

REFERENCES

1. K.U. Frerichs and G.Z. Feuerstein, "Laser Doppler flowmetry: a review of its application for measuring cerebral and spinal cord blood flow," *Mol. Chem. Neuropathology* **12**, 55 – 61(1990).
2. U. Dirnagl, B. Kaplan, M. Jacewicz, and W. Pulsinelli, " Continuous measurement of cerebral cortical blood flow by laser-Doppler flowmetry in a rat stroke model, *"J. Cereb. Blood Flow Metab.* **9**, 589–596(1989).
3. B.M. Ances, J.H. Greenberg, and J.A. Detre, "Laser Doppler imaging of activation-flow coupling in the rat somatosensory cortex," *Neuroimage* **10**, 716–723(1999).
4. M. Lauritzen and M. Fabricius, "Real time laser-Doppler perfusion imaging of cortical spreading depression in rat neocortex," *Neuroreport* **6**, 1271–1273(1995).
5. D.A. Zimnyakov, J.D. Briers, and V.V. Tuchin, "Speckle technologies for monitoring and imaging of tissues and tissuelike phantoms" in *Handbook of Optical Biomedical Diagnostics,* **PM107**, V.V. Tuchin ed. (SPIE Press, Bellingham, 2002), 987–1036.
6. D.A. Zimnyakov and V.V. Tuchin, "Laser tomography" in: *Medical Applications of Lasers,* D.R. Vij and K. Mahesh eds. (Kluwer Academic Publishers, Boston, 2002), 147–194.
7. E.I. Galanzha, G.E. Brill, Y. Aizu, S.S. Ulyanov, and V.V. Tuchin, "Speckle and Doppler methods of blood and lymph flow monitoring" in *Handbook of Optical Biomedical Diagnostics,* **PM107**, V.V. Tuchin ed. (SPIE Press, Bellingham, 2002), 881–937.
8. R. Bullock, P. Statham, J. Patterson, D. Wyper, D. Hadley, and E. Teasdale, " The time course of vasogenic oedema after focal human head injury-evidence from SPECT mapping of blood brain barrier defects," *Ada Neurochirurgica* (Supplement) **51**,286–288(1990).
9. M. Schröder, J.P. Muizelaar, R. Bullock, J.B. Salvant, and J.T. Povlishock, "Focal ischemia due to traumatic contusions, documented by SPECT, stable Xenon CT, and ultrastructural studies," *J Neurosurg.* **82**, 966-971(1995).
10. A. Alavi, R. Dann, J. Chawluk, *et al.,* " Positron emission tomography imaging of regional cerebral glucose metabolism," *Seminars in Nuclear Medicine* **16**, 2–34 (1996).
11. W.D. Heiss, O. Pawlik, K. Herholz *et al.,* "Regional kinetic constants and cerebral metabolic rate for glucose in normal human volunteers determined by dynamic positron emission tomography of [18F]-2-fluoro-2-deoxy-D-glucose," *J. Cereb. Blood Flow Metab.* **3**,250–253(1984).
12. L.P. Carter, "Surface monitoring of cerebral cortical blood flow," *Cerebrovasc. Brain Metab. Rev.* **3**, 246–261(1991).
13. C.A. Dickman, L.P. Carter, H.Z. Baldwin *et al.,* "Technical report. Continuous regional cerebral blood flow monitoring in acute craniocerebral trauma," *Neurosurgery* **28**, 467–472(1991).
14. O. Sakurada, C. Kennedy, J. Jehle, J.D. Brown, G.L. Carbin, "Sokoloff measurement of local cerebral blood flow with iodo [14C] antipyrine," *Am. J. Physiol.* **234**, H59–66 (1978).
15. D.S. Williams, J.A. Detre, J.S. Leigh *et al.,* "Magnetic resonance imaging of perfusion using spin inversion of arterial water," *Proc. Natl. Acad. Sci. USA* **89**, 212–216 (1992).
16. F. Calamante, D.L. Thomas, G.S. Pell, J. Wiersma, and R. Turner, "Measuring cerebral blood flow using magnetic resonance imaging techniques," *J. Cereb. Blood Flow Metab.* **19**, 701–735(1999).
17. A.F. Fercher and J.D. Briers, "Flow visualization by means of single-exposure speckle photography," *Opt. Commun.* **37**, 326-329 (1981).
18. J.D. Briers and S. Webster, "Laser speckle contrast analysis (LASCA): A nonscanning, full-field technique for monitoring capillary blood flow," *J. Biomed. Opt.* **1**, 174-179 (1996).

19. K. Yaoeda, M. Shirakashi, S. Funaki, H. Funaki, T. Nakatsue, and H. Abe, "Measurement of microcirculation in the optic nerve head by laser speckle flowgraphy and scanning laser Doppler flowmetry," *Am. J. Ophthalmol.* **129**, 734-739 (2000).
20. B. Ruth, "Measuring the steady-state value and the dynamics of the skin blood flow using the non-contact laser speckle method," *Med. Eng. Phys.* **16**, 105-111 (1994).
21. A.K. Dunn, H. Bolay, M.A. Moskowitz, and D.A. Boas, "Dynamic imaging of cerebral blood flow using laser speckle," *J. Cereb. Blood Flow Metab.* **21**, 195-201 (2001).
22. H. Bolay, U. Reuter, A.K. Dunn, Z. Huang, D.A. Boas, and A.M. Moskowitz, "Intrinsic brain activity triggers trigeminal meningeal afferernts in a migraine model," *Nat. Med.* **8**,136-142(2002).
23. J.W. Goodman, "Some effects of target-induced scintillation on optical radar performance,"*Proc. IEEE* **53**, 1688 – 1700(1965).
24. R. Bonner and R. Nossal, "Model for laser Doppler measurements of blood flow in *tissue" Appl. Opt.* **20**, 2097–2107(1981).
25. Z. Wang, Q.M. Luo, H.Y. Cheng, W.H. Luo, H. Gong, and Q. Lu, "Blood flow activation in rat somatosensory cortex under sciatic nerve stimulation revealed by laser speckle imaging," *Prog. Nat. Sci.* (accepted).
26. R. Greger and U. Windhorst, *Comprehensive Human Physiology* (Springer-Verlag, Berlin, 1996), 561-578.
27. A.C. Ngai, J.R. Meno, and H.R.Winn, "Simultaneous measurements of pial arteriolar diameter and Laser-Doppler Flow during somatosensory stimulation," *J. Cereb. Blood Flow Metab.* **15**, 124-127(1995).
28. A.C. Silva, S. Lee, G. Yang, C. Iadecola, and S. Kim, "Simultaneous blood oxygenation level-dependent and cerebral blood flow function magnetic resonance imaging during forepaw stimulation in the rat,"*J. Cereb. Blood Flow Metab.,* **19**, 871-879 (1999).
29. T. Matsuura and I. Kanno, " Quantitative and temporal relationship between local cerebral blood flow and neuronal activation induced by somatosensory stimulation in rats," *Neurosci. Res.* **40**, 281-290 (2001).
30. D. Kleinfeld, P.P.Mitra, F. Helmchen, and W. Denk, "Fluctuations and stimulus-induced changes in blood flow observed in individual capillaries in layers 2 through 4 of rat neocortex,"Proc. *Natl. Acad. Sci. USA* **95**, 15741-15746 (1998).
31. M.E. Raichle, "Neuroenergetics: relevance for functional brain imaging" in *Human Frontier Science Program* (Strasbourg, Bureaux Europe, 2001), 65-68.
32. R.D. Hall and E.P. Lindholm, "Organization of motor and somatosensory neocortex in the albino rat," *Brain Res.* **66**, 23-28 (1974).
33. A.C. Ngai, K.R. Ko, S. Morii, and H. R.Winn, "Effects of sciatic nerve stimulation on pial arterioles in *rats," Am. J. Physiol.* **269**, H133-H139 (1988).
34. A.C. Ngai, M.A. Jolley, R. D'Ambrosio J.R. Meno, and H.R. Winn, "Frequency-dependent changes in cerebral blood flow and evoked by potentials during somatosensory stimulation in the rat," *Brain Res.* **837**, 221-228 (1999).
35. J.A. Detre, B.M. Ances, K. Takahashi, and J.H. Greenberg, "Signal averaged Laser Doppler measurements of activation-flow coupling in the rat forepaw somatosensory cortex," *Brain Res.* **796**, 91-98 (1998).
36. R. Steinmeier, I. Bondar, C. Bauhuf, and R. Fahlbusch, "Laser Doppler flowmetry mapping of cerebrocortical microflow characteristics and limitations," *Neurolmage* **15**, 107-119(2002).
37. G. Taubes, "Play of light opens a new window into the body," *Science* **27**, 1991-1993 (1997).
38. A.N. Bashkatov, E.A. Genina, V.I. Kochubey, Y.P. Sinichkin, A.A. Korobov, N. A. Lakodina, and V. V. Tuchin, *"In vitro* study of control of human dura mater optical properties by acting of osmotical liquids," *Proc SPIE* **4162**, 182-188 (2000).

39. A.N. Bashkatov, E.A. Genina, Yu.P. Sinichkin, V.I. Kochubey, N.A. Lakodina, and V.V. Tuchin, "Glucose and mannitol diffusion in human dura mater," *Biophys. J.* **85**, 3310–3318(2003).
40. E. Chan, B. Sorg, D. Protsenko, M. O'Neil, M. Motamedi, and A.J. Welch, "Effects of compression on soft tissue optical properties," *IEEE J. Select. Topics* Quant. Electr. **2**, 943-950(1997).
41. I.F. Cilesiz and A.J. Welch, "Light dosimetry: effects of dehydration and thermal damage on the optical properties of the human aorta," *Appl. Opt.* **32**, 477-487 (1993).
42. V.V. Tuchin, I.L. Maksimova, D.A. Zimnyakov, I.L. Kon, A.K. Mavlutov, and A.A. Mishin, "Light propagation in tissues with controlled optical properties," *J. Biomed. Opt.* **2**, 401-417(1997).
43. V.V. Bakutkin, I.L. Maksimova, T.N. Semyonova, V.V. Tuchin, and I.L. Kon, "Controlling of optical properties of sclera," Proc. *SPIE* **2393**, 137-141 (1995).
44. B. Nemati, A. Dunn, A.J. Welch, and H.G. Rylander, "Optical model for light distribution during transscleral cyclophotocoagulation," *App. Opt.* **37**, 764-771 (1998).
45. G. Vargas, E.K. Chan, J.K. Barton, H.G. Rylander, and A.J. Welch, "Use of an agent to reduce scattering in skin," *Lasers Surg. Med.* **24**, 133-141 (1999).
46. G. Vargas, K.F. Chan, S.L. Thomsen, and A. J. Welch, "Use of osmotically active agents to alter optical properties of tissue: effects on the detected fluorescence signal measured through skin," *Lasers Surg Med.* **29**, 213-220 (2001).
47. H.Y. Cheng, Q.M. Luo, S.Q. Zeng, J. Cen, and W.X. Liang, "Optical dynamic imaging of the regional blood flow in the rat mesentery under the effect of noradrenalin," *Prog. Nat.Sci.***13**,198-201(2003).
48. H.Y. Cheng, Q.M. Luo, Z. Wang, and S.Q. Zeng, "Laser speckle imaging system of monitoring the regional velocity distribution," *Chinese J. Sci. Instr.* (accepted).
49. E.I. Galanzha, V.V. Tuchin, A.V. Solovieva, T.V. Stepanova, Q.M. Luo, and H.Y. Cheng, "Skin backreflectance and microvascular system functioning at the action of osmotic agents," *J. Phys. D: Appl. Phys.* **36**, 1739-1746 (2003).
50. H. Liu, B. Beauvoit, M. Kimura, and B. Chance, "Dependence of tissue optical properties on solute-induced changes in refractive index and osmolarity," *J. Biomed. Opt.* **1**, 200-211(1996).
51. Y.R. Tran Dinh, C. Thurel, A. Serrie, G. Cunin, and J. Seylaz, "Glycerol injection into the trigeminal ganglion provokes a selective increase in human cerebral blood flow," *Pain* **46**, 13-16 (1991).
52. E. Jungermann and N.O.V. Sonntag, *Glycerine: a Key Cosmetic Ingredient* (New York, Marcel Dekker, 1991).
53. J.B. Segur, "Uses of glycerine" in *Glycerol,* C.S. Miner and N.N. Dalton eds. (Reinhold Publishing, New York, 1953), 238-330.
54. A. Grinvald, R.D. Frostig, R.M. Siegel, and E. Bartfeld, "High-resolution optical imaging of functional brain architecture in the awake monkey," *Proc. Natl. Acad. Sci. USA* **88**, 11559–11563 (1991).
55. L.M. Chen, B. Heider, G.V. Williams, F.L. Healy, B.M. Ramsden, and A.W. Roe, "A chamber and artificial dura method for long-term optical imaging in the monkey," *J. Neurosci. Meth.* **113**, 41-49 (2002).
56. H.Y. Cheng, Q.M. Luo, S.Q. Zeng, S.B.Chen, J. Cen, and H. Gong, "A modified laser speckle imaging method with improved spatial resolution,"*J. Biomed. Opt.* (accepted).
57. H.Y. Cheng, D. Zhu, Q.M. Luo, S.Q Zeng, Z. Wang, and S.S. Ul'yanov, "Optical monitoring of the dynamic change of blood perfusion," *Chinese J. Lasers* **30**, 668-672 (2003) (in Chinese).
58. J. Ohtsubo and T. Asakura, "Velocity measurement of a diffuse object by using time-varying speckles," *Opt. Quant. Electron.* **8**, 523-529 (1976).
59. J.D. Briers, "Laser Doppler and time-varying speckle: reconciliation," *J. Opt. Soc. Am. A.* **13**, 345-350 (1996).

60. P.S. Liu, The optical bases of speckle statistic (Science Press, Beijing, 1987) (in Chinese)
61. M. Linden, H. Golstcr, S. Bertuglia, A. Colantuoni, F. Sjoberg, and G. Nilsson, "Evaluation of enhanced high-resolution laser Doppler imaging in an *in vitro* tube model with the aim of assessing blood flow in separate microvessel," *Microvasc. Res.* **56**, 261-270 (1998).
62. D. Kleinfeld, P.P. Mitra, F. Helmchen and W. Denk. "Fluctuations and stimulus-induced changes in blood flow observed in individual capillaries in layers 2 through 4 of rat neocortex," *Proc. Natl. Acad. Sci. USA* **95**, 15741-15746 (1998).
63. A. Serov, W. Steenbergen, and F.D. Mul, "Laser Doppler perfusion with a complimentary metal oxide semiconductor image sensor," *Opt. Lett.* **27**, 300-302 (2002).

This page intentionally left blank

Part II:
HOLOGRAPHY, INTERFEROMETRY, HETERODYNING

This page intentionally left blank

Chapter 6

LOW COHERENCE HOLOGRAPHY

Paul M. W. French
Imperial Collegeof Science, Technology and Medicine, London, SW7 2BZ, UK

Abstract: This chapter reviews wide-field coherence-gated imaging techniques for application through turbid media such as biological tissue, beginning with different approaches to coherence-gated imaging and then focusing on low coherence photorefractive holography.

Key words: holography; interferometry, coherence, photorefractive, 3D imaging

6.1 INTRODUCTION TO LOW COHERENCE HOLOGRAPHY

This chapter aims to describe the background and state-of-the-art of low coherence photorefractive holography, which is a technique to provide real-time high resolution 3-D imaging, including through turbid media, providing rapid whole-field image acquisition. Potential applications include biomedical imaging, high-speed 3-D profiling, and imaging through the atmosphere and seawater. The investigation of optical techniques for the study of biomedical systems is a rapidly developing field that has seen a dramatic expansion in recent years. Medical diagnostic imaging, often described as “optical biopsy”, inevitably requires image acquisition through significant depths of biological tissue. Its realization presents a major scientific challenge since tissue is extremely heterogeneous and interacts very strongly with optical radiation. While it is this interaction that provides the opportunity for functional biomedical imaging, the strong absorption and scattering of the various tissue components have historically restricted optical imaging to thin histological tissue sections or to superficial tissues.

The development of near infrared diode and ultrafast solid-state laser technology with emission spectra matching the absorption window for biological tissue lying between ~ 650 - 1.400 nm has prompted many researchers to address the remaining challenges associated with imaging through significant depths of scattering media. In order to form high (~ diffraction-limited) resolution images, or to make accurate quantitative intensity measurements, it is highly desirable to use light that has not been scattered. For this reason there is a wealth of techniques that aim to form images with ballistic (i.e. unscattered) light. There is a recent review in [1]. Coherence-gated techniques are of particular interest because ballistic photons retain coherence with their source, while randomly scattered photons, in principle, do not. In particular, low coherence interferometry provides a means to preferentially detect ballistic photons and to realize 3-D imaging since the interferometric detection requires the signal and reference arms to be matched to within the coherence length of the light source.

6.1.1 Single Channel Coherence-Gated imaging: OCT

Coherence-gated imaging may be conveniently divided into single channel techniques, such as optical coherence tomography (OCT) [2,3], that build up an image by sequential pixel scanning and wide-field multiple channel techniques that interrogate a 2D pixel array simultaneously. OCT is particularly powerful since it combines the ballistic light selection of coherent detection with the powerful spatial filtering associated with confocal microscopy. As a single channel technique, it does not suffer from interpixel cross-talk, e.g. due to scattering, it can utilize all the available power from a laser source for each pixel and it can take advantage of high dynamic range detectors and complex signal processing electronics. It is also readily implemented in fibre-optic technology, making it both robust and compact for clinical applications. This approach is possibly the most successful biomedical optical imaging modality demonstrated to date. It has been used to image a range of biological tissues, both *in vitro* and *in vivo,* from the retina to the gastro-intestinal tract. OCT has also been extended to include polarization sensitive detection, e.g. [4], measurements of sample velocity through the induced Doppler shift, e.g. [5], and spectrally resolved detection, e.g. [6]. It continues to be widely developed for a range of applications, many of which are discussed in this book.

There are, perhaps two drawbacks to OCT and other single channel coherence-gated imaging techniques. The first is that the serial pixel acquisition and the requirement for scanning mean that the ultimate imaging speed is limited – although video rate OCT has been demonstrated [7]. Rapid scanning of the reference arm is essential for high-speed OCT. This

has been addressed using a piezo-electric fibre stretcher capable of scanning over 3 mm at 600 Hz [8] but is more recently realized using rapid depth-scanning delay lines utilizing a scanning mirror in the Fourier plane of a lens imaging a diffraction grating to provide phase and/or group delay [9]. This approach can provide a scan velocity of 6 m/s at 2 kHz over a range of 3 mm in an OCT set up.

The second drawback is that OCT requires light sources of low temporal coherence and high spatial coherence – ideally with high average power. Low temporal coherence is important for improved depth resolution and also for improved rejection of scattered light, since scattered photons tend to exhibit longer path trajectories. High spatial coherence is important since it is desirable to couple as much light as possible into the interferometric and confocal detection channel. High average power is important when imaging through scattering media since the number of ballistic photons detected will clearly depend on the input signal. It is also important when working to increase the imaging rate of OCT, since it is necessary to use a higher power source when scanning faster if the same information per pixel is to be acquired. These source requirements are difficult to realize in practice since lasers, although usually providing output beams of high spatially coherence, tend to exhibit gain-narrowing, such that the spectral width decreases as the output power is increased. The most common source used – and the cheapest – is a superluminescent diode (SLD), which provides spatially coherent amplified spontaneous emission with spectral widths of ~ 20-40 nm, sufficient to provide a depth resolution of ~ 10 - 20 μm, with up to a few mW average power coupled into a single mode fibre, e.g. [10]. This is the approach often taken in commercial OCT systems used for retinal imaging. For OCT applications requiring higher power and/or higher depth resolution, it is usually necessary to employ mode-locked lasers. Mode-locking is one way to circumvent gain-narrowing and typically a mode-locked femtosecond solid-state laser (Ti:Sapphire or Cr:Försterite) is employed to provide average powers of 100's mW and spectral widths of 50-100's nm, yielding depth resolutions as low as ~ 2 μm. Such femtosecond lasers have only recently become commercially available and are relatively large, complex and expensive. For the ultimate resolution, the femtosecond pulses may be used to generate supercontinua in microstructured optical fibres, thereby achieving sub micron coherence lengths [11]. Near-micron level axial resolution has also been demonstrated using this method at the more deeply penetrating centre wavelength of ~1.1 μm [12,13]. In general the high average power, broadband (low temporal coherence) radiation sources used in high performance OCT systems are all derived from mode-locked solid-state lasers and these are too complex and expensive for many real-world applications. While there have been some attempts at developing simpler

broadband lasers, e.g. a grating-tuned external cavity semiconductor laser, delivering a linewidth of 25 nm with 35 mW average power in 100 ms [14] and a broadband c.w. diode-pumped solid-state laser delivering 10's nm spectral width with up to 100 mW average power [15], none have yet provided a promising low-cost alternative and this remains one of the most significant challenges for the widespread deployment of OCT.

6.1.2 Wide-Field Coherence Gated Imaging

Wide-field coherence-gated imaging offers the potential to remove the requirement to acquire the pixels (or voxels) in series and to exploit relatively low-cost high power broadband sources of low spatial coherence such as LED's or thermal light sources. Currently this usually entails using 2-D electronic imaging detectors such as CCD cameras, although there has been significant work towards developing arrays of "smart detectors" that are essentially multiple OCT systems performing heterodyne envelope detection in parallel [16]. Currently, an array of 58×58 pixels has been achieved and this technique has also demonstrated video-rate volumetric imaging [17]. Wide-field coherence-gated (interferometric) detection, however, is usually implemented using CCD cameras to record the interference signal, with the use of low coherence light in a reflection geometry providing depth-resolved imaging. The desired wide-field coherent signal may be extracted from the acquired "coherent signal + incoherent background" images using appropriate post processing.

Unfortunately the lack of the confocal spatial filter in wide-field coherence-gated imaging means that much more scattered light will reach the detector and contribute to a background on the acquired signal. Also, the dynamic range of CCD cameras (< ~ 50 dB) is significantly lower than that of the photodiodes (>> 100 dB) usually employed for OCT. Another consideration is that CCD detectors cannot adequately sample rapidly changing signals, so they are not able to provide synchronous detection at kHz and higher frequencies to reduce 1/f noise. These factors limit the signal-to-noise ratio of detection and mean that wide-field coherence gated imaging systems generally can penetrate to significantly lower depths of scattering media than OCT. This is compounded by the observation that, while OCT uses all of its radiation in a single channel, wide-field detection necessarily divides the available power between each pixel and so the imaging depth is reduced accordingly - unless higher power sources are used to provide an equivalent photon flux per pixel.

A further limitation of wide-field coherent detection compared to OCT is inter-pixel cross-talk, resulting from photons being scattered from one transverse pixel to another. This can be particularly challenging for coherent

imaging because these inter-pixel scattered photons will have an arbitrary phase and this leads to speckle noise on the coherent image. When imaging through liquid scattering media, however, the Brownian motion of the scatterers tends to randomize the phase of the scattered photons and so they merely contribute to the incoherent scattered light background. It is much more of a challenge when imaging through static turbid media for which stable speckle noise may be observed superimposed on the ballistic light image. Many of the coherent imaging experiments reported in the literature report experiments imaging through liquid scattering media and so one should be cautious when evaluating their success.

One way to eliminate inter-pixel cross-talk in coherent imaging systems is to use spatially incoherent light –arranging for all the transverse pixels in the coherent imaging "beams" to be mutually incoherent such that all transversely scattered photons are uncorrelated with the ballistic light and so do not contribute to the interferometric signal but simply average to a uniform background. This additional d.c. signal will be detected by the CCD camera, however, and reduce the effective dynamic range. Generally it is prohibitively expensive to use CCD cameras with a bit depth greater than 16 and any unwanted background is a significant issue. Spatial filtering can provide some rejection of scattered light in wide-field systems, e.g. [18], [19], however, and should be exploited whenever possible – although this will inevitably compromise transverse resolution. Of course averaging maybe used to increase the signal to noise ratio but this will be at the expense of image acquisition time.

Wide-field interferometric imaging may be described as holography and the various approaches may be conveniently separated into techniques that utilize interference in the temporal or spatial domain. The former approach, which may be considered as a wide-field version of OCT, is sometimes described as optical coherent heterodyne imaging or "phase-stepping interferometric imaging", in which the object and image beams are collinear at the detector and the interferometric fringe pattern is observed in time as the pathlength between the object and reference arms is scanned. The latter may be described as "off-axis holography", in which non-collinear object and reference beams interfere at the detector plane to produce a transverse spatial fringe pattern.

6.2 PHASE-STEPPING INTERFEROMETRIC IMAGING

Chiang *et al.* [20] demonstrated sub-mm depth resolved wide-field imaging through a liquid scattering medium of 17 (roundtrip) scattering

MFP using "c.w. broadband interferomctry" with a superluminescent diode of 8 nm bandwidth. The image-processing algorithm involved subtracting the incoherent background from each (coherent + incoherent) acquired image acquired and then averaging the "coherent" images. The use of a spatially coherent SLD resulted in some speckle noise on the acquired images. The speckle was somewhat reduced by averaging over multiple frames and over adjacent pixels.

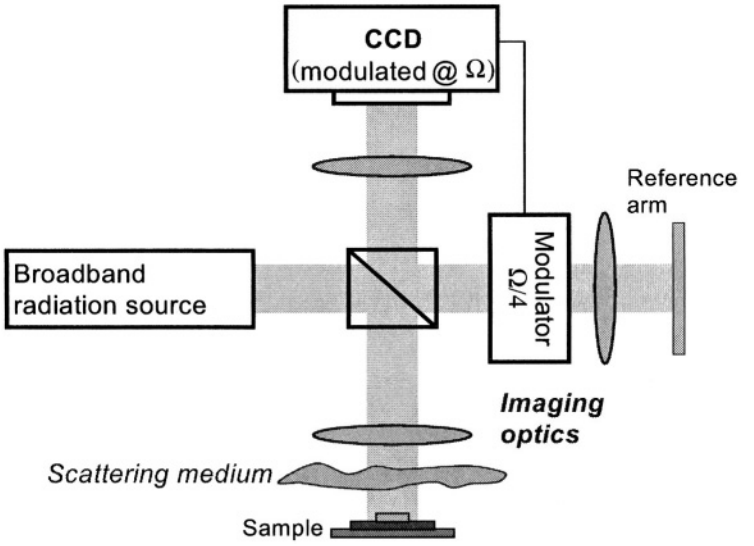

Figure 1. Phase-stepping interferometric imaging for wide-field coherence-gated imaging (from Ref. [1]).

A more sophisticated wide-field coherence-gated imaging system using optical heterodyne detection was reported by Beaurepaire *et al.* [21]. Figure 1 shows a generic schematic of this approach, which involves recording four wide-field interferometric images with different phase delays (ϕ_1-ϕ_2) between the object and reference beams and processing them to recover both the coherent amplitude and phase images. This technique was originally implemented using an LED source and a photoelastic modulator in a Michelson/Linnik interferometer set-up, in which the reference and object beams are orthogonally polarized. It has recently been modified to utilize a thermal broadband light source of ~ 10's W average power, to provide sub-micron depth resolution with a simple piezo-actuator being used at the reference mirror to provide the required phase differences between the two arms [22]. This simple but powerful technique can exploit considerable averaging to achieve a sensitivity of ~ 90 dB for an image acquisition time

of 4 s. Images have been acquired through both liquid and solid scattering media, including biological samples, with the use of broadband light sources of low spatial coherence eliminating the problem of speckle noise. A particularly powerful feature is the ability to calculate the phase of the coherent image, as well as the amplitude [23]. This can provide depth information at sub-wavelength precision (i.e. a few nm).

A potential disadvantage of this technique for biological imaging is that this approach requires the sample to be interferometrically stable during the acquisition of the four phase-stepped interferometric images. Although the system can acquire images at 100's Hz using a high speed CCD camera, the interferometric stability requirement still implies that the sample is effectively stationary on a millisecond timescale. An approach to overcome this limitation has recently been demonstrated that acquires all four phase-stepped interferometric images in a single shot [24]. This is done by using appropriate polarizing optics and beamsplitters to project the four phase-stepped images simultaneously on a single CCD camera and has been used to acquire depth-resolved images of moving objects at video rate.

6.3 OFF-AXIS HOLOGRAPHY

Off-axis holography may be considered as wide-field coherence-gated imaging exploiting spatial heterodyne detection, making it a potentially "single-shot" technique. Thus it is an obvious choice for high-speed imaging through turbid media. It was with holography that Stetson first showed the principle of coherence gating for imaging through a fog-like medium [25]. In 1989 light-in-flight (LIF) holography was demonstrated with short temporal coherence radiation to facilitate depth resolved imaging of three-dimensional objects [26], including through optical diffusers. However, photographic film was used as the holographic recording medium and so each image acquisition had to be chemically developed before being reconstructed. Subsequent research has concentrated on using real-time methods to perform the holographic recording and reconstruction, focusing mainly on two techniques: "electronic" or "digital" holography and photorefractive holography. (Note that the terms "digital holography" and "electronic holography" are synonymous for the purposes of this review.)

A schematic of off-axis holography applied to imaging through scattering media is shown in Figure 2. During the holographic recording process, the image information is modulated onto a spatial carrier, producing a fringe pattern. There is "heterodyne gain"in the process since a powerful reference beam can interfere with a weak signal beam to overcome any dark noise in the recording medium. This may be a conventional photographic film or it

may be a photorefractive medium. Alternatively the recording medium may a CCD camera, as in the case of "electronic" or "digital" holography and the reconstruction may be undertaken computationally in post-processing.

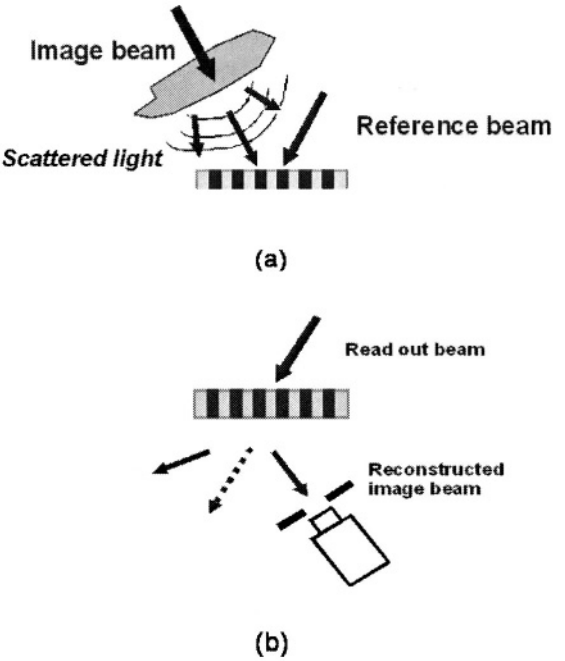

Figure 2. Off-axis holographic imaging through turbid media: (a) recording and (b) reconstructing the hologram (from Ref. [1]).

In principle, if there is no inter-pixel cross-talk, only the ballistic image will be coherent with the reference beam and contribute to the hologram – although the diffuse scattered light may saturate the recording medium. In the case of the film or the photorefractive medium, there is an additional mechanism for gain when the (potentially weak) hologram may be reconstructed using a powerful read-out beam for subsequent acquisition by a CCD camera. Furthermore, the read-out beam may be a different wavelength from the writing beams and so all light scattered by the object can be excluded by a spectral filter. For the case of digital holography, in which the reconstruction is done numerically, the CCD camera will record any incident scattered light along with the hologram, as is the case with phase-stepping interferometric imaging, and this will compromise the dynamic range of detection and the ability to reconstruct the ballistic light image. The relative performance of optically versus numerically reconstructed holography will depend on the respective dynamic ranges of

the photosensitive holographic recoding media and the electronic detection. As will be seen later, photorefractive holography offers an intrinsic insensitivity to a d.c. light background.

Like phase-stepping interferometric imaging, off-axis holography may be implemented with light sources of low spatial coherence – in fact Leith has shown that holography with spatially incoherent light is formally equivalent to confocal imaging [27]. It is also intrinsically a single-shot technique and so may be applied to high-speed 2-D and 3-D imaging of dynamic objects. This significant advantage is, however, somewhat offset by issues associated with the necessarily noncollinear interference geometry. These include optical aberrations arising from the off-axis image propagation through the optical system, the issue of "beam walk-off, encountered at the intersection of interfering beams whose coherence length is comparable or less than the beam diameter, and the issue of spatial resolution.

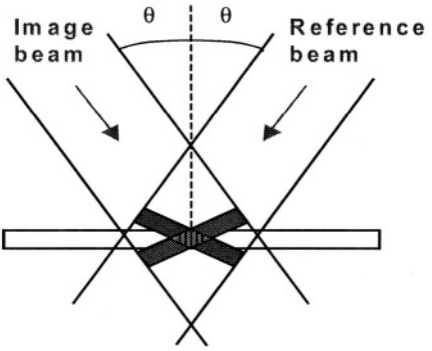

Figure 3. Beam walk-off during off-axis holography with broadband radiation (from Ref. [1]).

For digital holography, aberrations in the imaging system may be corrected at the image processing stage but for optical holography, including photorefractive holography, they can only be minimized by using appropriate optical systems. The problem of beam walk-off, which arises when using broadband radiation to provide depth resolution and/or rejection of scattered light, is illustrated in Figure 3. This presents a significant problem for angles of incidence much greater than a few degrees with broadband radiation of > ~10 nm [28]. By adjusting the group delay with respect to the phase delay (wavefront) as a function of lateral position across the beams, e.g. using prisms, it is possible of overcome this walk-off and recover the whole field of view [29]. The issue of transverse spatial resolution is a function of the number of resolution elements in the holographic recording medium. For electronic holography the pixel size of

the CCD camera is generally of the order of 5 μm (or greater for CCD sensors with large well capacity and high dynamic range). To ensure adequate sampling of he holographic interference pattern, the fringe period must be at least twice this and the corresponding spatial frequency must be more than three times the highest spatial frequency in the image to avoid aliasing in the holographic reconstruction. In practice, micron resolution is achievable in systems with optical magnification but this consideration does place constraints on the optical system that are not present for collinear wide-field phase-stepping interferometric imaging. For photorefractive holography, the diffraction efficiency is a function of the fringe period, according to the photorefractive medium used. For electro-optic crystals, the highest diffraction efficiencies are obtained for fringe periods around 1 μm, which is desirable for high spatial resolution but a problem with respect to beam walk-off. For photorefractive MQW devices, the diffraction efficiency is maximized at fringe periods greater than ~ 20 μm and this presents similar spatial resolution considerations as large CCD pixels do for electronic holography.

6.3.1 Low Coherence Digital or Electronic Holography

Electronic holography was demonstrated as a means to coherence-gate the early arriving light when imaging through a scattering medium by Chen *et al.* [30] in 1991. By spatially filtering the transmitted beam before it was incident on the CCD camera and using a broadband source, a resolution of < 1 mm has been achieved through a scattering solution equivalent to ~ 4 mm of tissue [31]. As with wide-field phase-stepping interferometric imaging, the chief limitation of this technique is the scattered light background, from which the coherent holographic image must be extracted.

The principal advantage of electronic or digital holography is that, because the holographic reconstruction is done in software, there is great flexibility in the processing that may be carried out. For instance, it is possible to use a tunable narrowband laser and compute the coherence-gated hologram that would have been obtained using a broadband source by combining a series of holograms recorded using the narrowband source tuned over the equivalent spectral range. This has been described as Fourier synthesis holography [32]. An elegant extension to this approach is that of "spectral holography", [33,34]. This combines the ideas of Fourier synthesis holography, sweeping a tunable dye laser over 15 nm, with spectral interferometry. It has the very significant practical advantage that it is not necessary to accurately match the arm lengths of the interferometer to acquire depth-resolved image information. This is because each spectral component has a long coherence length and the short coherence information

can be extracted when a series of spectrally resolved interferograms are combined. A similar spectral interferometry technique utilizing a broadband SLD source was shown to achieve 38 μm depth resolution with a depth range of 7.5 mm in air [35].

Digital holography also has the advantage that post processing may also be applied to compensate for aberrations in the imaging system, as long as they are characterised [36], and one can filter out zero order and twin images [37]. In some situations, aberrations may be reduced by locating the recording (CCD) plane away from an image plane. With today's computers, the computation required to reconstruct the holograms takes only a few ms and real-time imaging is practical. As with phase-stepping interferometric imaging, it is possible to obtain both the amplitude and the phase of the coherent image and so achieve axial resolution for surface profiling [38].

6.3.2 Low Coherence Photorefractive Holography

In 1993 Mamaev *et al.* [39] showed that a photorefractive crystal called strontium barium niobate (SBN) could be used to image through a suspension of milk in real time with no chemical developing. This demonstrated the efficacy of photorefractive holography, although narrowband c.w. radiation in the green was used and the imaging configuration was in transmission. In 1995 Hyde *et al.* demonstrated, for the first time, real-time 2-D and 3-D imaging through a scattering medium using both c.w. and ultrashort pulsed broadband near infra-red radiation with rhodium-doped barium titanate (Rh-Ba:TiO_3) as the recording medium [40]. This work highlighted the observation that photorefractive holography is insensitive to a uniform background of e.g. multiply-scattered diffuse light. This reflects the *unique* properties of photorefractive media that make them sensitive, not to the incident intensity but to the *spatial derivative of the incident intensity distribution* - in contrast to all other wide-field imaging detectors for which the uniform scattered photons are detected and can saturate the detector, compromising its dynamic range (apart from arrays of smart pixels as discussed earlier).

Figure 4 shows a typical set-up for low coherence photorefractive holography for 3-D imaging through turbid media. The set-up is essentially the same as for electronic holography except that the CCD in the holographic recording plane is replaced by a photorefractive medium, from which the reconstructed image is read out using a convenient c.w. laser that may be at a different wavelength from the broadband source. Thus all scattered photons may be blocked at the CCD camera using a color filter. The read-out aperture located after the hologram plane is necessary to block light from the zero order undiffracted read-out beam that is scattered by

inhomogeneities inside the photorefractive medium. As discussed below, this parasitic scattering of the read-out beam is the main factor that limits the performance of low coherence photorefractive holography. This aperture is conveniently located at a Fourier plane of the lens used to relay the read out holographic image to the CCD sensor. When imaging through turbid media using high power beams to overcome the ballistic attenuation, a second spatial filter is sometimes deployed in a Fourier plane before the detection (hologram) plane, to reduce the amount of (scattered) light reaching the photorefractive medium.

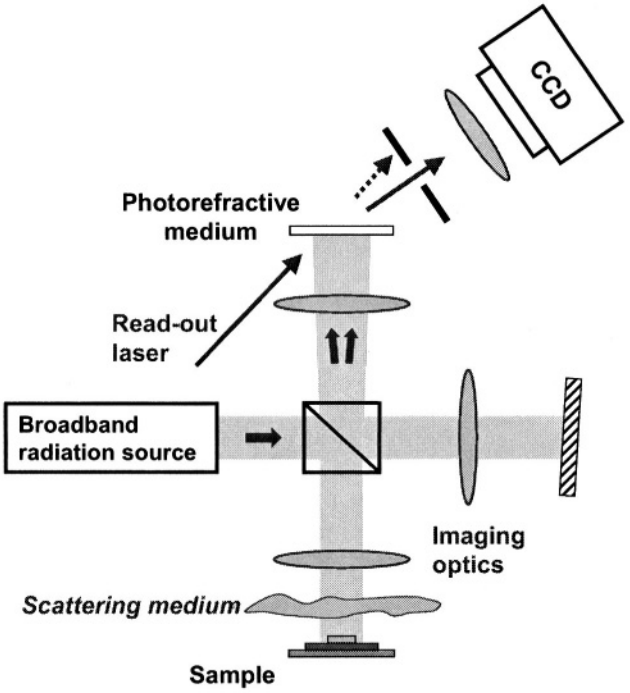

Figure 4. Low coherence photorefractive holography (from Ref. [1]).

Using Rh-Ba:TiO_3 as the photorefractive medium, the detection of a weak coherent image in the presence of a 10^6 x greater incoherent background was demonstrated using a low-cost video camera with a bit depth of ~ 6 [41]. 3-D imaging through scattering media of up to 16 MFP (roundtrip) thickness was demonstrated for the first time with sub-100 μm depth and transverse spatial resolution [42], albeit with a long (~ 300 s) integration time owing to the relatively slow response of Rh-Ba:TiO_3 as a photorefractive recording medium for such weak intensities. Rh-Ba:TiO_3 was investigated for this application because it offers the highest diffraction

efficiency of the electro-optic photorefractive crystals in the optical "window" of transmission of biological tissue around 800 nm. Its slow response, however, makes it impractical for most real-world applications. To obtain both high speed and near infra-red sensitivity, the most promising candidates are semiconductor media. To date, the highest sensitivities and fastest responses have been obtained from semi-insulating photorefractive MQW devices (PRQW) exploiting the transverse Franz Keldysh effect [43], which is discussed in the next section.

The application of photorefractive MQW devices to rapid 3-D imaging through turbid media with near infrared radiation was demonstrated to permit depth-resolved image acquisition with integration shorter than 0.4 ms [44]. Later 3-D imaging was demonstrated with image acquisition direct to a video-cassette recorder, without recourse to a digital frame-grabber [45]; [46]. Recently the technique has been adapted to the use of spatially incoherent light from LED's, providing sub-10 μm depth resolution [47] and demonstrating speckle free images through static turbid media including sandstone and chicken tissue [48]. Using a high-speed CCD camera, this approach has realized depth-resolved imaging at 476 frames/s [49] and , more recently at 830 frames/s [50].

The chief appeal of this approach is that photorefractive holography does have the potential to detect a weak coherent image in the presence of a uniform background of scattered light and so offers an opportunity to increase the effective dynamic range of wide-field coherence-gated imaging, compared to the limitations of direct detection with a CCD camera. To date, however, the major drawback of low coherence photorefractive holography has been the scattering of the read-out beam by inhomogeneities in the photorefractive media. This parasitic scattering introduces a source of additional background noise at the CCD camera that can degrade the reconstructed holographic image. This is a significant issue for current PRQW devices (and for bulk semi-conductor crystals) – as discussed in the following section.

6.4 PHOTOREFRACTIVE HOLOGRAPHY

The photorefractive effect allows the recording and reconstruction of holograms in real-time or over an extended integration period, capturing whole-field 2-D images in a single acquisition. It provides a unique optical detector in that it is sensitive to the spatial derivative of an incident intensity distribution, rather than to the intensity itself. This means that it is a natural recording medium for off-axis holography, in which an image is spatially modulated onto a carrier fringe pattern. Furthermore it may be used to detect

weak spatially modulated signals (e.g., interference fringe patterns) in the presence of spatially uniform backgrounds (e.g., of diffuse light) that could saturate a conventional detector. This observation would suggest that it is well suited to the application of coherent imaging through turbid media.

6.4.1 The Photorefractive Effect

The photorefractive effect is often defined as a non-linear optical effect where the optical properties of a photorefractive medium are altered by a spatially varying intensity pattern. This effect was first noticed as 'optical damage' in lithium niobate ($LiNbO_3$) in 1966 where it degraded the performance of the crystal as a second harmonic generator [51]. Its main difference compared to other non-linear optical effects is that it responds to intensity gradients rather than absolute intensity, resulting in the written hologram being phase-shifted with respect to the incident intensity. This non-local response is caused by charge migration, which also underlies the ability of photorefractive materials to integrate over time. The ability to integrate weak signals results in photorefractive media being sensitive to very low light levels - photorefractive materials typically operate in the range of $\mu W/cm^2$ - mW/cm^2, whereas conventional intensity dependent nonlinear effects typically require kW/cm^2 of incident light. Of course there is a trade-off to be made between sensitivity and integration time for any particular application. There is, however, a wide range in the properties of different photorefractive materials, with response times ranging from ps - 10's hours, and this diversity has resulted in photorefractive media being applied to a wide variety of different applications, from long term holographic memories [52], to fast ultrasonic detectors [53].

The dynamics of the recoding of photorefractive gratings are rather complex and only a simple discussion will be presented here, pertaining specifically to the two photorefractive media most commonly used for coherence-gated imaging by our group at Imperial College London. The first of these was bulk Rhodium-doped barium titanate ($Rh:BaTiO_3$), which is a single photo-carrier type (electrons) crystal medium with no externally applied electric field. The holographic recording process is depicted schematically in Figure 5.

When a spatially varying intensity pattern (such as the sinusoidal pattern produced by two interfering beams) is incident upon a photorefractive crystal, photocarriers are preferentially generated in the high intensity regions (bright fringes). These photocarriers are then free to either diffuse due to carrier density gradients, or to drift under the influence of any applied fields. We use $Rh:BaTiO_3$ with no applied field and so it operates in the purely diffusive regime, in which the high density of photocarriers in the

high intensity regions causes carriers to diffuse into the low intensity regions where they are trapped by defects in the crystal. A carrier distribution is therefore built up in anti-phase to the initial intensity distribution. The resulting space charge field is dependent upon the gradient of the carrier distribution and so is 90 ° out of phase with both the carrier distribution and the initial intensity distribution. This space charge field then acts via the linear Pockels' effect to produce a change in the refractive index of the photorefractive material. In the purely diffusive regime the recorded refractive index grating is thus 90 ° out of phase with the incident intensity grating. When an external field is applied to the crystal, drift of photocarriers also becomes important and this phase shift can be anywhere in the region 0-180°.

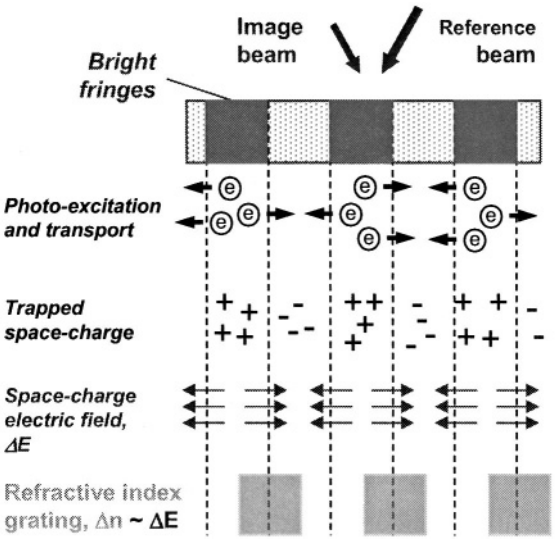

Figure 5. Holographic recording in an electro-optic medium such as Rhodium-doped Barium titanate.

This simplified description indicates why the photorefractive effect is dependent only upon the gradient of intensity. If a uniform intensity is incident upon a photorefractive crystal, no carrier density gradients are formed within the crystal, therefore no space charge fields are set up and no refractive index grating is written. This is an advantage when using photorefractive crystals to image through turbid media, because a *uniform* diffuse, background is not recorded and does not saturate the detector. For this application a variety of different photorefractive media have been examined. An ideal material would be highly sensitive in order to write holograms with very low intensities, as well as having a fast response time to

allow imaging in real time. Unfortunately these two properties cannot be usually obtained together as high sensitivity usually implies long integration times. The next section looks at the main classes of photorefractive media and their suitability for ballistic light imaging applications.

6.4.2 Photorefractive Media

The following attributes are required for materials to exhibit the photorefractive effect:

- *photo-conductive,* i.e. they can yield photocarriers
- *semi-insulating,* i.e. photocarriers are trapped
- *electric field-dependent refractive index,* i.e. their optical properties will be locally modified by the space-charge distribution, e.g. through the linear Pockels effect
- *low dark conductivity,* i.e. the desired space charge must not be swamped or erased by thermally excited carriers

Photo-conductivity is necessary because the photorefractive effect relies on the photoexcitation of defect levels within the crystal. The media should be semi-insulating such that they have an appropriate density of charge defects that can trap photocarriers to build up a space-charge. The linear Pockels' effect is desirable because the recorded refractive index profile should have the same period as the intensity grating, although other mechanisms may also be exploited. Low dark conductivity is important as it means the written hologram is resistant to erasure by carrier leakage and that that weak optical signals can induce sufficient photocarriers to compete with background level of thermally excited charge carriers.

Photorefractive media may be conveniently divided into three classes: bulk photorefractive crystals, MQW semiconductor devices and organic polymer devices. Bulk crystals are by far the most commonly used photorefractive media. They tend to exhibit relatively slow response times at the power levels typically encountered in biomedical imaging, however, and so have received less attention than the photorefractive MQW devices for this application. Bulk photorefractive crystals operate in the Bragg diffraction regime, recording volume holograms that require carefully aligned Bragg-matched read-out beams for real-time imaging. In contrast, photorefractive MQW devices are essentially thin films and conveniently operate in the Raman-Nath regime.

6.4.3 Bulk Photorefractive Crystals

6.4.3.1 Ferroelectric Oxides

The ferroelectric group contains some of the more common photorefractive media, which were the first materials experimentally demonstrated to be photorefractive. The term ferroelectric is analogous to ferromagnetic and means that the material contains electric dipoles. During growth there is generally a short-range order to the crystals such that domains of similarly orientated dipoles are formed. For a bulk photorefractive effect to be observed in these crystals they must be poled, i.e. all the separate, randomly orientated domains in the crystal need to be aligned. This may be done by applying an electric field when the crystal is raised to the correct temperature [54]. Like other photorefractive media, the photocarriers in ferroelectrics are provided by defects in the crystal. These defects can be caused by unavoidable dopants during the crystal growth or by intentional doping that may increase the response in a particular wavelength region. Ferroelectrics can be classed in three main categories: ilmenites, perovskites and tungsten bronzes.

The ilmenites contain lithium niobate, the first material in which photorefractive behavior was observed, and lithium tantalate. Although both are extensively used for non-linear frequency conversion and large samples with high optical quality are available, they are not suitable for real-time imaging applications since they exhibit a low dark current and slow response time. These features make them more suitable for optical storage applications [55].

The perovskite family includes the crystals potassium niobate and barium titanate - one of the most commonly used photorefractive materials owing to its having the largest (r_{42}) electro-optic coefficient found in inorganic crystals. Initially the main dopant thought to be responsible for the photorefractive behavior in $BaTiO_3$ was iron [56], although more recent experiments have shown photorefractive behavior in samples grown from ultra-pure sources [57]. This behavior is thought to be due to barium vacancies [58]. Doping with other transition metals, in particular cobalt and rhodium, has enhanced the response of the crystal in the near infra-red [59] and $Rh{:}BaTiO_3$ provides a photorefractive response in the biological tissue window of absorption. The main disadvantage associated with barium titanate is its relatively slow response time. At an incident intensity of $1 W/cm^2$ the typical response time is in the region 0.1-1 s, although experiments using reduced crystals [60], or crystals at high temperatures

have shown the potential for this to be improved by at least two orders of magnitude [61].

The tungsten bronze family includes strontium barium niobate (SBN) and barium sodium niobate (BNN). SBN has a high electro-optic coefficient although, like barium titanate, this is coupled with a slow response time. Application of an external electric field can enhance the response time [62].

6.4.3.2 Cubic Oxides

The cubic oxides, or sillenites include $Bi_{12}SiO_{20}$ (BSO), $Bi_{12}GeO_{20}$ (BGO) and $Bi_{12}TiO_{20}$ (BTO). These crystals are renowned for their relatively large photoconductivity and hence fast response time, which has lead to their use in real-time holography [63]. Sillenites are mainly sensitive in the visible spectrum (500-650 nm), however, and exhibit birefringence (BSO has a rotatory power of 21°/mm at 633 nm) which can reduce their diffraction efficiency [64]. The sillenites possess only one non-zero electro-optic tensor, which has a small magnitude in the visible region ranging from 4-6 pm/V. Applying an external AC electric field, or using DC fields with moving gratings, has enhanced the magnitude of the space charge field while keeping the relative phase shift optimized to 90° [65]. The identity of the species responsible for the photorefractivity in sillenites is still not clear.

6.4.3.3 Organic Crystals

Organic crystals are much easier to grow than their inorganic counterparts and have shown non-linear coefficients comparable to $LiNbO_3$ [66]. One drawback of these crystals, however, is that they have not been optimized for speed, and typical response times are ~ 30 minutes for an incident intensity of 3 W/cm^2 [67].

6.4.3.4 Bulk Compound Semiconductors

Non-centro symmetric bulk semiconductors e.g. GaAs, InP, GaP and CdTe have many advantages over other photorefractive media. Firstly the maturity of semiconductor growth technology allows large samples to be grown. Secondly the high carrier mobility's of semiconductors result in very fast response times, several orders of magnitude higher then those in the oxides. Their high dark current means that hologram persistence in these crystals is very short so they are unsuitable for holographic storage but may be used for real-time applications. The wavelength coverage is from the red (e.g., CdS [68]) to the infra-red (e.g., CdTe:V has shown photorefractivity at 1.55 μm [69]). Like the sillenites the small electro-optic coefficients of these

crystals result in low diffraction efficiencies, but this may be enhanced by external electric fields. Bulk semiconductors also show a resonant enhancement of their diffraction efficiencies near their band-edge. This is attributed to the Franz-Keldysh effect [70], which occurs because the space charge field distorts the band-edge leading to electroabsorption and electrorefraction. This effect can be large, especially at wavelengths slightly larger then the band-gap where the background absorption is low.

6.4.4 Multiple Quantum Well Semiconductor Devices

The photorefractive effect may be enhanced using semi-insulating multiple quantum well (MQW) devices, e.g., in GaAs/AlGaAs. Considering the first of four main stages of the photorefractive effect, as indicated in Figure 5, the large resonant excitonic transition of the MQW increases the absorption compared to bulk semiconductors and so enhances photo-excitation. The resulting carriers (electrons and holes) exhibit excellent carrier mobility's in the plane of the quantum wells. MQW structures typically do not contain the defects necessary for trapping the photocarriers and so these must be introduced into the MQW devices either by growing them at low temperature, by including suitable dopants such as Cr, or by bombarding the MQW wafers with protons after growth. The increased absorption experienced when working near the exciton peak also yields much faster build-up of the space charge when compared to bulk crystals [71] (2 μs for writing intensities of 280 mW/cm^2) and results in very sensitive devices with fast response times, which have exhibited diffraction efficiencies of up to 3 % for a 2 μm thick device [72]. As noted above, these are essentially thin film devices and so are read out in the Raman-Nath regime, which means that the diffraction efficiency is not critically dependant on the angle of incidence and this leads to much simpler optical set-ups than for volume holograms, which require the read-out beam to be "Bragg-matched" to the recording beams.

The conversion of the space charge field into a refractive index grating in photorefractive MQW devices is not realized by the linear Pockels effect – instead the desired refractive index gratings are produced through either the Franz-Keldysh effect [43] or the Quantum Confined Stark Effect (QCSE) [73]. This involves applying an external field either parallel or perpendicular to the plane of the quantum wells. The external electric field adds to the space charge field and the resulting spatially modulated electric field produces an absorption or refractive index grating with the same period as the incident light intensity distribution, leading the MQW devices to act like photorefractive materials. The high absorption and electron mobility of

photorefractive MQW devices means that they can operate with low incident intensities (~ 20 μW cm^{-2} [43]) and exhibit fast response times (<10 μs [74]).

For PRQW devices based on the Franz-Keldysh effect [43], the electric field is applied in the plane of the quantum wells. This leads to many excitons becoming ionized, which results in a broadening of the optical exciton absorption spectrum, with a concomitant decrease in the peak absorption, due to the decreased excitonic lifetime. This is described as transverse quantum-confined exciton electroabsorption [75] and is considered a quadratic effect that does not depend on the polarity of the electric field. The parallel applied electric field geometry means that the magnitude of the field must increase with one dimension of the Franz-Keldysh PRQW device area. In practice the applied field is of the order of 10 kV/cm and a typical device has an imaging aperture of ~ 3 mm parallel to the applied field. Given that the spatial resolution of these PRQW (see 6.4.3.2) is of the order of 10 μm, this corresponds to ~ 300 resolution elements. Note that there is no such limit to the imaging aperture in the other lateral dimension.

The QSCE occurs for an electric field applied perpendicular to the plane of the quantum wells [73]. In this geometry the applied field does not ionize the excitons; instead the applied potential is superimposed on the quantum well and this reduces the quantum well confinement potential, thereby decreasing the exciton binding energy and thus producing a "Stark shift" in the optical exciton absorption peak. This QCSE also has a quadratic dependence on the electric field. Unlike the devices based on the Franz-Keldysh geometry, QCSE devices do not behave like conventional photorefractives in that they do respond to a uniform illumination signal since all incident photons can excite photocarriers that will shield the applied field. Rabinovich *et al.* have shown, however, that by applying an appropriately alternating external field, it is possible to cancel out the contribution due to the d.c. component of the incident light field while integrating the spatially modulated component [76]. Since the QCSE geometry implies an electric field applied perpendicular to the quantum well layers, there is no compromise with the imaging aperture size - an applied field of only a few volts is sufficient since the PRQW devices are only a few microns thick.

To date, most coherence-gated imaging research has used PRQW devices in the Franz Keldysh geometry to minimize experimental complexity. For an extensive discussion of PRQW devices, see the review by Nolte and Melloch [77].

6.4.5 Organic Photorefractive Polymers

Organic polymer films are easier to prepare than bulk organic crystals and offer improved optical quality and scaling to large areas. The composition of polymer films can be altered in order to optimize each part of the photorefractive cycle (i.e. the charge donation, transport and trapping). The polymer bisphenol-A-diglycidylether 4-nitro-l,2-phenylenediamine doped with diethylamino-benzaldehyde diphenylhydrazone has shown photorefractive behavior. A 500 μm thick sample showed diffraction efficiency of $2x10^{-5}$ at 647 nm [78] with an optimized grating build-up time of 1 s at an intensity of 1 W/cm^2 [79]. Polymers are currently in an early stage of development but this is a very fast-moving field and the versatility possible in their growth and composition may mean that they may one day compete with inorganic photorefractive media. Organic polymer films have already been applied to photorefractive imaging through turbid media [80] and image amplification [81] although the slow response time has limited their application to date. Recent advances in this technology, however, have realized video-rate holographic recording in photorefractive polymers [82], [83] and this approach looks promising for the future since it should be possible to make photorefractive polymer devices with large areas of high optical quality.

6.4.6 Issues for Biomedical Photorefractive Holography

While low coherence photorefractive holography, with its intrinsic wide-field rejection of a uniform background of e.g. diffuse light, appears to be a promising technique for high-speed imaging through turbid media, its uptake has been restricted to a few groups whose efforts have focused more on solving technical and material issues than imaging biological samples. This is partly a consequence of the limited availability of suitable photorefractive media and is partly due to the continuing improvement of CCD (and now CMOS) cameras – and the concomitant decrease in cost - that may be directly applied to wide-field coherence-gated imaging. This section aims to review the relevant properties of the main photorefractive media investigated for imaging through turbid media.

Ideally a photorefractive imaging device should be of high optical quality with an appropriate spectral response, i.e. sensitive in the near infrared for biomedical imaging, and an appropriate spatial response, i.e. offer a uniform response with respect to spatial frequency and provide a reasonable number of resolution elements. It also needs to offer a suitably fast response time and a high dynamic range for recording holograms in the presence of scattered

light. The photorefractive medium must be robust and able to handle the power levels associated with its application.

6.4.7 Spectral Response

For biomedical imaging, the wavelength criteria tends to discount the cubic oxides and polymers as their response is mainly in the visible, while the slow response times of ilmenites and tungsten bronzes makes them unsuitable for real-time applications. For these reasons the main thrust of research to date has been investigating barium titanate doped with rhodium (for infra-red sensitivity) and semiconductors. The semiconductors investigated are CdTe and GaAs/AlGaAs PRQW devices. These crystals have all shown reasonable optical quality and, when an external electric field is applied, give a useable, though not ideal response with spatial frequency, as is discussed further in the next section. We note that the media usually favored for work in the visible, e.g. the cubic oxides and polymers, tend to be relatively slow (i.e. ms – seconds response time). The use of interband transitions in thin crystals with u.v. radiation, however, has facilitated high speed imaging with sub-ms response times [84].

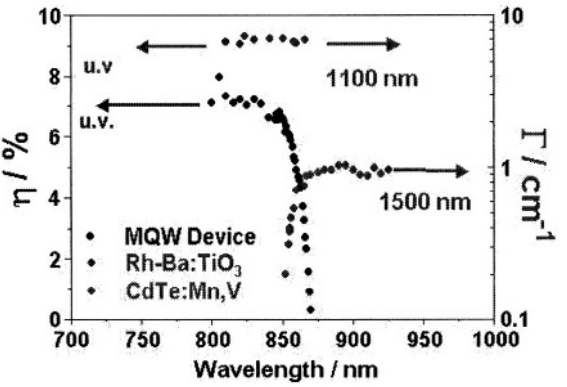

Figure 6. Spectral response of photorefractive media.

Figure 6 shows the measured spectral response of the photorefractive media we have investigated at Imperial College. (The limited range of data points reflects our ability to tune our laser radiation, rather than the material properties of the samples.) For the bulk photorefractive crystals, we characterized the two beam-coupling coefficient as a function of wavelength. Rh-$BaTiO_3$ exhibited a reasonably flat response out to 1100 nm and there have been reports of photorefractivity at 1.55 μm in the telecommunications

window, as there have been for Cadmium telluride doped with Manganese and Vanadium (CdTe:Mn,V). Owing to its relatively small band gap, CdTe exhibits extremely low absorption in the visible spectrum below 850 nm and therefore very weak photorefractivity. Rh-$BaTiO_3$ extends in response below 800 nm through the visible to the u.v. and we have applied it to depth resolved imaging through a scattering media in the blue spectral region [28]. For the PRQW devices, we directly measured the diffraction efficiency as a function of wavelength. Owing to the high absorption, the GaAs/AlGaAs MQW devices exhibit a strong response at wavelengths below their bandgap at ~ 850 nm. They may therefore be used to record holograms with visible radiation and it is feasible to develop a colour 3-D imaging system based on this technology. PRQW devices have also been demonstrated to operate at longer wavelengths such as ~ 1.064 μm using InGaAs/GaAs [85] and at 1.55 μm using Fe-doped InGaAs/InGaAsP [86].

6.4.8 Spatial Response

The spatial response of a photorefractive medium is extremely important in determining its performance in an imaging system. Essentially the properties of a photorefractive material, particularly the charge carrier mobility, determine how efficiently a spatially modulated light field will be recorded. If the grating period is too short, the migrating charge carriers will tend to overshoot and the grating will be washed out. If the period is too large, then the carriers will not migrate far enough to set up the desired space-charge field. For ferroelectric crystals, in which the photocarrier mobility is relatively low, the optimum grating period is on the order of a micron. For semiconductor materials, it is considerably longer. It should be noted that the spatial response of a photorefractive medium may be somewhat modified by applying an external electric field that will increase the length scale over which the charge carriers migrate.

Figure 7 shows the spatial response of Rh-Ba:TiO_3 and the photorefractive MQW devices. For the former, material considerations imply a grating period, Λ, of 1 μm but at 800 nm this corresponds to an angle, θ, of 47° between the writing beams, according to the formula $\Lambda = \lambda/[\sin(\theta_{1/2})]$. This presents a serious problem for low coherence holography, for which the coherence length is typically less than the diameter of the writing beams. As illustrated in Figure 3, the overlap between the object and reference beams for radiation with the same path lengths for large angles of incidence may be restricted to just the central portion of the field of view. If one increases the coherence length to recover a full field of view, then of course the depth resolution is correspondingly degraded.

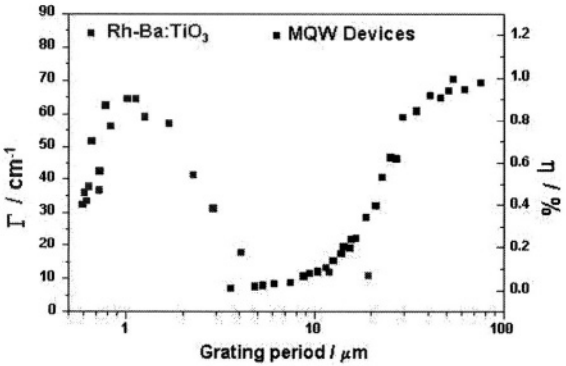

Figure 7. Spatial response of photorefractive media.

Working with radiation from a commercially available femtosecond Ti:Sapphire laser at 790 nm with a spectral width of 8 nm, corresponding to a coherence length of ~ 20 μm, we found that a full angle of 6° between the beams resulted in a compromised depth resolution of 100 μm [87]. This corresponded to a grating period of ~ 5 μm. This was judged to be a reasonable compromise between resolution and sensitivity – it will be seen from Figure 7 that, nevertheless, we were accepting a substantial penalty in photorefractive sensitivity.

For the PRQW devices, the high carrier mobility favors grating periods longer than ~ 20 μm and so the beams can approach a collinear geometry. In practice one requires a minimum grating period in order to be able to spatially separate the diffracted image beam from the zero order of the readout beam. We typically compromise on 30 μm and walk-off is not a problem when using radiation of 10 nm spectral width. If, however, we use radiation with spectral widths exceeding ~ 30 nm, such as is available from sources of low spatial coherence, such as LED's or thermal sources, we do experience problems with walk off. As discussed above, this issue may be partly addressed incorporating special prisms in each arm of the interferometer that cause the group delay across the beam to vary such that all the light with the same phase delay across the writing beams arrives at the recording medium at the same time [29].

The transverse spatial resolution is impacted by the material properties of the photorefractive material, which limits the grating period that can be used, but for off-axis holography, the practical limit is usually imposed by any spatial filter that is deployed before the detection (holographic recording) plane or by the read-out aperture used to block the scattered zero order read-out light when reconstructing the hologram.

For Rh-Ba:TiO_3 crystals the spatial fringe period can be less than 1 μm and the crystal aperture can be ~ 5 – 10 mm. The maximum number of lateral resolution elements is therefore ~ 5000 in each dimension, which is normally more than is available from the CCD camera. As discussed above, to limit the problems associated with walk-off, a fringe period of ~ 5 μm was employed and this, combined with the aperture used to block light scattered from the zero order undiffracted read-out beam, limited the transverse spatial resolution to ~ 15 μm in a 1:1 imaging system.

For the PRQW devices, the material properties imposed a minimum fringe period of ~ 10 - 20 μm, depending on the PRQW device used. Our PRQW devices, which were designed and manufactured by Nolte and colleagues at Purdue University, were typically fabricated with an aperture of ~ 3 mm between the electrodes. This aperture is practically limited by the breakdown voltage of the devices and so the number of resolution elements in this direction is limited to ~ 100. In the orthogonal direction, parallel to the electrodes and perpendicular to the applied field, there is no such restriction on the aperture of the device and so the number of resolution elements may be increased. When imaging through turbid media using PRQW devices, a spatial filter was implemented by placing an aperture in a Fourier plane in front of the detector plane in order to keep the total incident light below the Joule heating limit by blocking some of the scattered light. This, together with the read-out aperture used to block the zero order read-out light scattered by inhomogeneities in the PRQW device, also effectively limit the transverse spatial resolution to ~ 30 μm.

6.4.9 Temporal Response, Sensitivity, Dynamic Range and Optical Quality

The temporal response and sensitivity of photorefractive media are coupled and, in general, the response time depends partly on the intensity of the writing beams. Thus any statement of minimum intensity required to record a hologram must also specify the integration time and vice versa. For any photorefractive medium, there will be an upper limit to the total incident intensity during the hologram recording (and read-out) process. In bulk photorefractive crystals, this limit is set by the onset of parasitic gratings and beam fanning, which arise from the recording beams being scattered from inhomogeneities in the photorefractive medium. For Rh-Ba:TiO_3 this limit is the order of ~ 5W/cm^2. In today's PRQW devices, the upper limit to the incident intensity is the Joule heating limit, which is ~ 30 mW/cm^2.

For all photorefractive media, the parasitic scattering of the undiffracted zero order read-out beam by inhomogeneities in the photorefractive medium results in an unwanted background signal that is detected by the read-out

CCD camera. This background signal may be electronically subtracted from the acquired image to prevent it being degraded, but it does compromise the dynamic range of the detection. As an example, Figure 8 [88] shows read-out images from a typical PRQW device before and after background subtraction. The relatively large scattering inhomogeneities are due to bubbles of epoxy and trapped dust particles that are introduced during fabrication of the devices. These are particularly problematic since they scatter significant light compared to the hologram and, if the read-out intensity or the image integration time is too large, this parasitic scattered read-out light will saturate the read-out CCD camera. There are also smaller scattering inhomogeneities, known as oval defects, which contribute to the scattered read-out light background. Thus the diffraction from recorded hologram competes with parasitic scattering from these "defects" in the photorefractive medium and so the "optical quality" is the primary limitation to the system's ability to record weak holograms – and therefore to the dynamic range of the system. As discussed above, the read-out aperture can reduce this background signal – at the expense of spatial resolution – but it cannot block it completely.

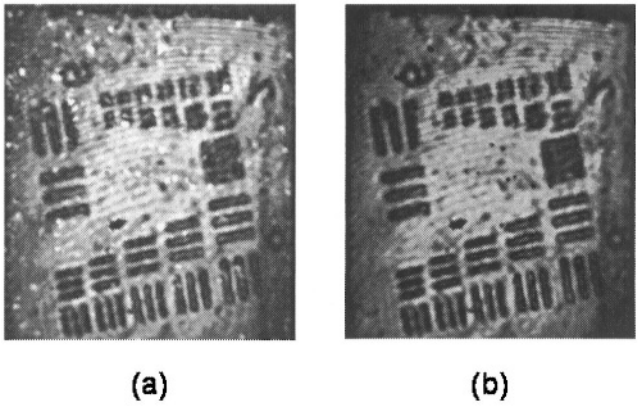

Figure 8. (a) Typical read-out holographic image of USAF test chart from PRQW device, showing scattering defects and (b) read-out image after background subtraction (from Ref [88], Copyright @ SPIE).

After optimizing the ratio of the writing beams and the read-out beam intensities for photorefractive holography using Rh-Ba:TiO_3 [87], we experimentally determined that, for a low-cost video CCD read-out camera, the minimum object beam intensity level to record usable holograms in Rh-Ba:TiO_3 was ~ 10 nW/cm^2 for an image recording time of ~ 300 s. Longer holographic recording times were not possible because of the build up of

parasitic light signals due to scattering of the high power (100's mW) read-out beam by defects in the Rh-Ba:TiO_3 crystal. Similarly we observed a minimum object beam recording intensity level of 2.2 $\mu W/cm^2$ for a GaAs/AlGaAs PRQW device using the same video read-out camera. In this case the integration time was limited by the parasitic scattering of the read-out beam (limited to ~1 mW by Joule heating considerations) from defects in the PRQW device that saturated the readout CCD camera.

Although the bulk Rh-Ba:TiO_3 crystal appeared to be more sensitive than the PRQW device, the 300 second image recording time is impractical for biomedical imaging. At significantly higher power levels its response is fast enough to permit real-time read-out and viewing of depth-resolved images, which may find free space 3D imaging applications. As discussed above, PRQW devices typically reach their steady-state modulation depth in less than one millisecond and may be much faster for higher intensities. As well as offering the possibility of high-speed 3-D imaging at frame rates approaching 1000/s, this fast response permits significant scope for averaging and thereby increasing the sensitivity. Of course the same is true for electronic holography with direct detection by a CCD camera. In order to try to understand the future potential of low coherence photorefractive holography using PRQW, we have undertaken a theoretical study of its performance relative to direct CCD detection.

This study [89] first considered the ability of electronic or digital holography to record a weak interferometric signal (hologram) in the presence of an incoherent scattered background signal. When directly measuring such small variations in intensity using a CCD camera, it is primarily the full-well capacity that determines the dynamic range and therefore the smallest change in incident intensity that can be detected. Ideally the CCD camera should be operated near to the full-well capacity of the pixels, such that the detection is a reasonable approximation to being shot noise limited - the number of electrons stored in the well being typically much greater than the readout, digitization and other noise sources. The smallest detectable change in signal is then proportional to the square root of the number of electrons stored in the pixel-well, which typically ~10^4 or greater. If spatial averaging (pixel binning) or temporal averaging is employed then the effective number of electrons in the pixel-well is increased by a factor equal to the number of pixels and/or frames averaged. For a typical scientific grade 12-bit cooled CCD camera with a full well capacity of 1.8×10^4 electrons that is operating near to saturation with 4×4 binning, the estimated dynamic range is ~ 49 dB.

To estimate the performance of photorefractive holography using a PRQW device, it is necessary to determine the input diffraction efficiency, which is typically 4×10^{-3} for a Franz-Keldysh geometry PRQW device and

the parasitic scattering coefficient, η_s, which has been measured to be 4×10^{-5}, for a typical device. By considering typical operating parameters with the same typical scientific grade 12-bit cooled CCD camera for the read-out, an estimated dynamic range of 44 dB is obtained, with a corresponding minimum detectable object beam intensity of $20\ \mathrm{nW/cm^2}$ for a read-out intensity of $0.5\ \mathrm{mW/cm^2}$ and an integration time of ~1.5 s. As the read-out beam intensity is increased, the maximum integration time decreases and the minimum detectable object beam intensity increases due to the increase in scattered read-out light.

It is instructive to consider how this performance would change if the optical quality of the PRQW device could be improved. A decrease in η_s by a factor of 10 would increase the systems dynamic range to 52 dB for a 900 ms integration time. If the optical defects could be effectively eliminated, i.e. $\eta_s > 0$, then the dynamic range would be as high as 60 dB for an exposure time of one second.

6.5 CONCLUSIONS AND OUTLOOK

In conclusion, this chapter has reviewed techniques for wide-field coherence-gated imaging, with particular emphasis on low coherence photorefractive holography. It has discussed the principle techniques for achieving wide-field low-coherence-gated imaging together with the advantages that these confer in terms of speed and the ability to exploit low-cost, high power broadband sources of low spatial coherence such as LED's and thermal light sources. The reader is referred to the publications cited for details of specific implementations and application to biomedical imaging. In general these wide-field techniques have received much less attention to date than OCT and it is expected that their range of application will increase over the next few years. One of the chief drawbacks of wide-field coherence-gated imaging through turbid media is that the lack of a confocal spatial filter, which degrades the dynamic range of the system in the presence of scattered light and also means that that transverse speckle due to interpixel crosstalk can degrade the image if spatially coherent illumination is used. Direct detection by a CCD camera is attractive because of its simplicity and because of the decreasing cost of high performance CCD cameras. It also lends itself to phase-sensitive imaging and this has been demonstrated with both phase-stepping interferometric imaging and off-axis digital holography. Unfortunately the limited dynamic range of CCD cameras, compounded by the presence of interpixel scattered light, does preclude them from achieving the same imaging depths through turbid media as OCT, although, OCT images are degraded by "axial speckle" before reaching the depth that is

limited only by the dynamic range of this technique, e.g. [90]. To improve the dynamic range of direct CCD detection techniques, it is necessary to increase the well capacity of the CCD sensors, which will decrease their acquisition rate, or to engineer arrays of smart pixels that can remove the d.c. component on-chip.

At first sight, low coherence photorefractive holography offers several significant advantages compared to low coherence digital holography (phase-stepping or off-axis holography). The observation that the photorefractive effect is insensitive to a uniform d.c. spatial component in the incident signal offers the potential to immediately remove a d.c. background signal, such as diffuse scattered light or the interpixel scattered light signal that arises from coherent interpixel cross-talk with illumination sources of low spatial coherence. This "photorefractive advantage" is unfortunately mitigated by several factors: Firstly the effective "quantum efficiency" of the photorefractive media, which is a function of its absorption coefficient, maximum permissible incident intensity and the corresponding achievable holographic diffraction efficiency, is much lower than that of a CCD camera or photodiode. For the PRQW devices operating in the Franz-Keldysh geometry, we have estimated it to be ~ 0.002 [89]. Modern CCD cameras, particularly those incorporating microlens arrays to improve the optical fill factor, or back-thinned sensors, can reach a quantum efficiency exceeding ~ 0.8. The imaging aperture size is also an issue, although much larger imaging areas are possible, albeit with an unconventional aspect ratio. In addition, the scattering of the holographic read-out beam by inhomogeneities in the photorefractive medium also degrades the effective dynamic range of the system, as discussed in the previous section. With the current state-of-the-art devices, the achievable dynamic range – in terms of the detection of a coherent (ballistic) image signal against an incoherent (scattered) light background – is slightly less than that of a CCD camera. If the optical quality of the PRQW devices can be improved, or if an alternative photorefractive medium can be developed with lower scattering properties, such as a photorefractive polymer device, then the dynamic range of low coherence photorefractive holography should exceed that of current CCD cameras. It remains to be seen whether improving the optical quality of photorefractive media is a greater technological challenge than increasing the well capacity of affordable CCD cameras. I note that the current state-of-the-art PRQW devices were fabricated by graduate students at Purdue University and, while they represent a significant and creditable achievement in the development of new photorefractive technology, they are very much "proof-of-principle" devices. From a technological viewpoint, the PRQW devices are relatively simple, compared to e.g. a CCD chip, and any commercial growth and clean-

room fabrication is expected to produce significantly superior devices in terms of optical quality. In the meantime, David Nolte's group at Purdue University continues to refine their own fabrication techniques, outsourcing growth and fabrication steps wherever possible, and this is expected to provide significantly improved "proof-of-principle" devices.

A particularly promising application of low coherence photorefractive holography is high-speed depth-resolved imaging. The fast response time of the PRQW devices means that holograms can be recorded and red-out in less than a millisecond, permitting depth-resolved imaging at frame rates approaching or even exceeding 1000 frames/second – the limitation is currently the speed of the read-out camera. Currently the fastest such system has realized coherence-gated depth-resolved imaging at 830 frames/second and this rate was limited by the data rate of the frame-grabber [50]. Being based on off-axis holography, it is a single-shot technique, and so is faster than phase-stepping interferometric imaging, for which the sample must be interferometrically stable over the required four acquisitions. It also proves a depth-resolved image with no computer processing required (apart from a background subtraction if necessary), unlike digital holography. Like phase stepping and digital holography, photorefractive holography can also make use of averaging to improve the dynamic range of detection. In this situation the fast response of the PRQW devices is particularly convenient because there is no stringent requirement for interferometric stability between the individual acquisitions – as there is for both off-axis and phase-stepping interferometric imaging. The PRQW device serves as an "adaptive detector", with the optical read-out leading to the reconstructed images being averaged, rather than the interferometric fringe patterns.

Future developments in wide-field coherence-gated imaging will be driven by the demands of specific applications. These are likely to be applications for which image acquisition rate is a priority. Off-axis digital holography has been employed in the study of neuron activity and phase-stepping interferometric imaging has been applied to in vivo imaging of live organisms. Low coherence photorefractive holography has been applied to image tumor spheroids in living tissue cultures for which the ability to follow the dynamics of living, moving tissue has permitted real-time contrast between living and necrotic tissue [91]. This latter work presents intriguing possibilities to use low coherence photorefractive holography to image with partially scattered light, increasing the imaging depth and extracting information from the dynamic speckle patterns. Other applications for high-speed wide-field coherence-gated imaging could include imaging and characterizing MEMS devices, rapid scanning for biometrics applications, imaging of fluid flow, e.g. in lab-on-a-chip technology and morphologically-based assay and cytometry applications. The list of potential applications

will grow with the number of researchers in the area and with the progress in imaging technology – particularly in the area of smart pixels.

ACKNOWLEDGEMENTS

I would like to thank the many colleagues who have contributed to the coherence-gated imaging programme at Imperial College London, particularly those PhD students and post-doctoral researchers whose hard work has led to whatever insights I have been able to present here. I would particularly like to thank Christopher Dunsby for his critical reading of this chapter. I should also acknowledge the financial support of the UK Engineering and Physical Research Council (EPSRC) who, together with the Imperial College Challenge Fund, have provided most of the support for our programme on photorefractive holography.

REFERENCES

1. C. Dunsby and P.M.W. French, "Techniques for depth-resolved imaging through turbid media including coherence-gated imaging," *J. Phys. D: Appl. Phys.* **36** R207-R227 (2003).
2. D. Huang, E.A. Swanson, C.P. Lin, J.S. Schuman, W. G. Stinson, W. Chang, M.R. Hee, T. Flotte, K. Gregory, C.A. Puliafito, and J.G. Fujimoto, "Optical Coherence Tomography", *Science* **254**, 1178-1181 (1991).
3. *Handbook of Optical Coherence Tomography,* B.E. Bouma and G.J. Tearney eds. (Marcel Dekker, New York, 2002).
4. J.F. de Boer, T.E. Milner, M.J.C. van Gemert, and J.S. Nelson, "Two-dimensional birefringence imaging in biological tissue by polarization-sensitive optical coherence tomography," *Opt. Lett.* **22**, 934-936 (1997).
5. Z.P. Chen, T.E. Milner, S. Srinivas, X.J. Wang, A. Malekafzali, M.J.C. van Gemert, and J.S. Nelson, "Noninvasive imaging of *in vivo* blood flow velocity using optical Doppler tomography," *Opt. Lett.* **22**, 1119-1121 (1997).
6. U. Morgner, W. Drexler, F.X. Kartner, X.D. Li, C. Pitris, E.P. Ippen, and J.G. Fujimoto, "Spectroscopic optical coherence tomography", *Opt. Lett.* **25**, 111-113 (2000).
7. A.M. Rollins, M.D. Kulkarni, S. Yazdanfar, R. Ung-arunyawee, and J. A. Izatt, *"In vivo* video rate optical coherence tomography", *Opt. Express* **3**, 219-229 (1998).
8. G.J. Tearney, B.E. Bouma, S.A. Boppart, B. Golubovic, E.A. Swanson, and J.G. Fujimoto, "Rapid acquisition of *in vivo* biological images by use of optical coherence tomography", *Opt. Lett.* **21,** 1408-1410 (1996).
9. G.J. Tearney, B.E. Bouma, and J.G. Fujimoto, "High-speed phase- and group-delay scanning with a grating-based phase control delay line", *Opt. Lett.* **22**, 1811-1813 (1997).

10. G. A. Alphonse, in *Test and Measurement Applications of Optoelectronic Devices* **4648**, 125-138 (2002).
11. B. Povazay, K. Bizheva, A. Unterhuber, B. Hermann, H. Sattmann, A.F. Fercher, W. Drexler, A. Apolonski, W. J. Wadsworth, J. C. Knight, P. S. J. Russell, M. Vetterlein, and E. Scherzer, "Submicrometer axial resolution optical coherence tomography", *Opt. Lett.* **27**, 1800-1802 (2002).
12. Y.M. Wang, Y.H. Zhao, J.S. Nelson, Z.P. Chen, and R.S. Windeler, "Ultrahigh-resolution optical coherence tomography by broadband continuum generation from a photonic crystal fiber", *Opt. Lett.* **28**, 182-184 (2003).
13. I. Hartl, X.D. Li, C. Chudoba, R.K. Ghanta, T.H. Ko, J.G. Fujimoto, J.K. Ranka, and R.S. Windeler, "Ultrahigh-resolution optical coherence tomography using continuum generation in an air-silica microstructure optical fiber", *Opt. Lett.* **26**, 608-610 (2001).
14. S.R. Chinn, E.A. Swanson, and J. G. Fujimoto, "Optical coherence tomography using a frequency-tunable optical source", *Opt. Lett.* **22**, 340-342 (1997).
15. D. Parsons-Karavassilis, Y. Gu, Z. Ansari, P.M.W. French, and J.R. Taylor, "Diode-pumped spatially dispersed broadband Cr : LiSGAF and Cr : LiSAF c.w. laser sources applied to short-coherence photorefractive holography", *Opt. Commun.* **181**, 361-367 (2000).
16. M. Ducros, M. Laubscher, B. Karamata, S. Bourquin, T. Lasser, and R.P. Salathe, "Parallel optical coherence tomography in scattering samples using a two-dimensional smart-pixel detector array", *Opt. Commun.* **202**, 29-35 (2002).
17. M. Laubscher, M. Ducros, B. Karamata, T. Lasser, and R. Salathe, "Video-rate three-dimensional optical coherence tomography", *Opt. Express* **10**, 429-435 (2002).
18. G. Indebetouw, "Distortion-free imaging through inhomogeneities by selective spatial-filtering", *Appl. Opt.* **29**, 5262-5267 (1990).
19. G.E. Anderson, F. Liu, and R.R. Alfano, "Microscope imaging through highly scattering media", *Opt. Lett.* **19**, 981-983 (1994).
20. H.P. Chiang, W.S. Chang, and J. P. Wang, "Imaging through random scattering media by using c.w.-broad-band interferometry", *Opt. Lett.* **18**, 546-548 (1993).
21. E. Beaurepaire, A. C. Boccara, M. Lebec, L. Blanchot, and H. Saint-Jalmes, "Full-field optical coherence microscopy", *Opt. Lett.* **23**, 244-246 (1998).
22. L. Vabre, A. Dubois, and A.C. Boccara, "Thermal-light full-field optical coherence tomography", *Opt. Lett.* **27**, 530-532 (2002).
23. A. Dubois, L. Vabre, and A.C. Boccara, "Sinusoidally phase-modulated interference microscope for high- speed high-resolution topographic imagery", *Opt. Lett.* **26**, 1873-1875 (2001).
24. C.W. Dunsby, Y. Gu, and P.M.W. French, "Single-shot phase-stepped wide-field coherence-gated imaging", *Opt. Express* **11**, 105 - 115 (2003).
25. K.A. Stetson, "Holographic fog penetration", *J. Opt. Soc. Am.* **57**, 1060-1061 (1967).
26. K.G. Spears, J. Serafin, N.H. Abramson, X.M. Zhu, and H. Bjelkhagen, "Chrono-coherent imaging for medicine", *IEEE Trans. Biomed. Eng.* **36**, 1210-1231 (1989).
27. P.C. Sun and E.N. Leith, "Broad-source image plane holography as a confocal imaging process", *Appl. Opt.* **33**, 597-602 (1994).
28. S.C.W. Hyde, N.P. Barry, R. Jones, J.C. Dainty, and P.M.W. French, "High resolution depth resolved imaging through scattering media using time resolved holography", *Opt. Commun.* **122**, 111-116 (1996).

29. Z. Ansari, Y. Gu, M. Tziraki, R. Jones, P.M.W. French, D.D. Nolte, and M. Melloch, "Elimination of beam walk-off in low coherence, off-axis, photorefractive holography", *Opt. Lett.* **26**, 334-336 (2000).
30. H. Chen, Y. Chen, D. Dilworth, E. Leith, J. Lopez, and J. Valdmanis, "2-Dimensional imaging through diffusing media using 150-Fs gated electronic holography techniques", *Opt. Lett.* **16**, 487-489 (1991).
31. E. Leith, P. Naulleau, and D. Dilworth, "Ensemble-averaged imaging through highly scattering media", *Opt. Lett.* **21**, 1691-1693 (1996).
32. E. Arons and D. Dilworth, "Analysis of Fourier synthesis holography for imaging through scattering materials", *Appl. Opt.* **34**, 1841-1847 (1995).
33. M.P. Shih, H.S. Chen, and E.N. Leith, "Spectral holography for coherence-gated imaging", *Opt. Lett.* **24**, 52-54 (1999).
34. I. Iglesias, H.S. Chen, K.D. Mills, D.S. Dilworth, and E.N. Leith, "Electronic channel fringe holography for depth and delay measurements", *Appl. Opt.* **38**, 2196-2203 (1999).
35. A.F. Zuluaga and R. Richards-Kortum, "Spatially resolved spectral interferometry for determination of subsurface structure", *Opt. Lett.* **24**, 519-521 (1999).
36. E. Cuche, P. Marquet, and C. Depeursinge, "Simultaneous amplitude-contrast and quantitative phase-contrast microscopy by numerical reconstruction of Fresnel off-axis holograms", *Appl. Opt.* **38**, 6994-7001 (1999).
37. E. Cuche, P. Marquet, and C. Depeursinge, "Spatial filtering for zero-order and twin-image elimination in digital off-axis holography", *Appl. Opt.* **39**, 4070-4075 (2000).
38. E. Cuche, F. Bevilacqua, and C. Depeursinge, "Digital holography for quantitative phase-contrast imaging", *Opt. Lett.* **24**, 291-293 (1999).
39. A.V. Mamaev, L.L. Ivleva, N.M. Polozkov, and V.V. Shkunov, in *Conference on Lasers and Electro-Optics* **11**(OSA, 1993), 632-633.
40. S.C. W. Hyde, N.P. Barry, R. Jones, J.C. Dainty, P.M. W. French, M.B. Klein, and B.A. Wechsler, "Depth-resolved holographic imaging through scattering media by photorefraction", *Opt. Lett.* **20**, 1331-1333 (1995).
41. N.P. Barry, R. Jones, S.C.W. Hyde, J.C. Dainty, and P.M.W. French, "High background holographic imaging using photorefractive barium titanate", *Electron. Lett.* **33**, 1732-1733(1997).
42. S.C. W. Hyde, N.P. Barry, R. Jones, J.C. Dainty, and P.M.W. French, "Sub 100 μm depth-resolved holographic imaging through scattering media in the near-Infrared", *Opt. Lett.* **20**, 2330-2332 (1995).
43. Q. Wang, R.M. Brubaker, D.D. Nolte, and M.R. Melloch, "Photorefractive quantum-wells - transverse Franz-Keldysh geometry", *J. Opt. Soc. Am. B-Opt. Phys.* **9**, 1626-1641 (1992).
44. R. Jones, S.C.W. Hyde, M.J. Lynn, N.P. Barry, J.C. Dainty, P.M.W. French, K.M. Kwolek, D.D. Nolte, and M.R. Melloch, "Holographic storage and high background imaging using photorefractive multiple quantum wells", *Appl. Phys. Lett.* **69**, 1837-1839 (1996).
45. R. Jones, M. Tziraki, P.M.W. French, K.M. Kwolek, D.D. Nolte, and M.R. Melloch, "Direct-to-video holographic 3-D imaging using photorefractive multiple quantum well devices", *Opt. Express* **2**, 439-448 (1998).

46. R. Jones, N.P. Barry, S.C.W. Hyde, P.M.W. French, K.W. Kwolek, D.D. Nolte, and M.R. Melloch, "Direct-to-video holographic readout in quantum wells for three-dimensional imaging through turbid media", *Opt. Lett.* **23**, 103-105 (1998).
47. M. Tziraki, R. Jones, P.M.W. French, D.D. Nolte, and M.R. Melloch, "Short-coherence photorefractive holography in multiple-quantum-well devices using light-emitting diodes", *Appl. Phys. Lett.* **75**, 1363-1365 (1999).
48. M. Tziraki, R. Jones, P. M. W. French, M. R. Melloch, and D. D. Nolte, "Photorefractive holography for imaging through turbid media using low coherence light", *Appl. Phys. B-Lasers Opt.* **70**, 151-154 (2000).
49. Z. Ansari, Y. Gu, J. Siegel, D. Parsons-Karavassilis, C. W. Dunsby, M. Itoh, M. Tziraki, R. Jones, P. M. W. French, D. D. Nolte, W. Headley, and M. R. Melloch, "High frame-rate, 3-D photorefractive holography through turbid media with arbitrary sources, and photorefractive structured illumination", *IEEE J. Sel. Top. Quant. Electron.* **7**, 878-886 (2001).
50. C. Dunsby, D. Mayorga-Cruz, I. Munro, Y. Gu, P. M. W. French, D. D. Nolte, and M. M. R., "High-speed wide-field coherence-gated imaging via photorefractive holography with photorefractive multiple quantum well devices", *J. Opt. A: Pure Appl. Opt.* (2003 - in press).
51. A. Ashkin, G. D. Boyd, J. M. Dziedzic, R. G. Smith, A. A. Ballman, J. J. Levinstein, and K. Nassau, "Optically induced refractive index inhomogeneities in LiNbO3 and LiTaO3", *Appl. Phys. Lett.* **9**, 72-73 (1966).
52. J. F. Heanue, M. C. Bashaw, and L. Hesselink, "Volume Holographic Storage and Retrieval of Digital Data", *Science* **265**, 749-752 (1994).
53. P. Delaye, J. M. C. Jonathon, G. Pauliat, and G. Roosen, "Photorefractive materials : specifications relevant to applications", *Appl. Opt.* **5**, 541-559 (1996).
54. M. H. Garrett, J. Y. Chang, H. P. Jenssen, and C. Warde, "A method for poling barium-titanate, BaTiO3", *Ferroelectrics* **120**, 167-173 (1991).
55. Y. S. Bau and R. Kachru, "Nonvolatile holographic storage with two-step recording in lithium niobate using cw lasers", *Phys. Rev. Lett.* **78**, 2944-2947 (1997).
56. M. B. Klein, "Optimization of the Photorefractive Properties of Bati03", *J. Opt. Soc. Am. A-Opt. Image Sci. Vis.* **3**, P10-P10 (1986).
57. P. G. Schunemann, T. M. Pollack, Y. Yang, Y. Y. Teng, and C. Wong, "Effects of feed material and annealing atmosphere on the properties of photorefractive barium-titanate crystals", *J. Opt. Soc. Am.* **B 5**, 1702-1710 (1988).
58. B. A. Wechsler and M. B. Klein, "Thermodynamic Point-Defect Model of Barium-Titanate and Application to the Photorefractive Effect", *J. Opt. Soc. Am. B-Opt. Phys.* **5**, 1711-1723 (1988).
59. B. A. Wechsler, M. B. Klein, C. C. Nelson, and R. N. Schwartz, "Spectroscopic and Photorefractive Properties of Infrared- Sensitive Rhodium-Doped Barium-Titanate", *Opt. Lett.* **19**, 536-538 (1994).
60. S. Ducharme and J. Feinberg, "Altering the photorefractive properties of BaTiO3 by reduction and oxidation at 650 °C", *J. Opt. Soc. Am.* **B 3**, 283-292 (1986).
61. D. Rytz, M. B. Klein, R. A. Mullen, R. N. Schwartz, G. C. Valley, and B. A. Wechsler, "High-Efficiency Fast Response in Photorefractive Batio3 at 120- Degrees-C", *Appl. Phys. Lett.* **52**, 1759-1761 (1988).

62. K. Sayano, A. Yariv, and R. R. Neurgaonkar, "Order-of-magnitude reduction of the photorefractive response-time in rhodium-doped Sr0.6Ba0.4Nb2O6 with a dc electric-field", *Opt. Lett.* **15,** 9-11 (1990).
63. J. P. Huignard, H. Rajbenbach, R. P. H., and L. Solmar, "Wave mixing and in photorefractive bismuth silicon oxide crystals and its applications", *Opt. Eng.* **24**, 586-592 (1985).
64. A. Marrakchi, R. V. Johnson, and A. R. Tanguay, "Polarisation properties of photorefractive diffraction in electroopic and optically active sillenite crystals (Bragg regime)", *J. Opt. Soc. Am.* **B 3**, 321-336 (1986).
65. B. Imbert, H. Rajbenbach, S. Mallick, J. P. Herriau, and J. P. Huignard, "High photorefractive gain in 2-beam coupling with moving fringes in GaAs-Cr crystals", *Opt. Lett.* **12**, 327-329 (1988).
66. Y. Zhang, R. Burzynski, S. Ghosal, and M. K. Casstevens, "Photorefractive polymers and composites", *Advanced Materials* **8**, 111-125 (1996).
67. K. Sutter and P. Gunter, "Photorefractive gratings in the organic-crystal 2-cyclooctylamino-5-nitropyridine doped with 7,7,8,8-tetracyanoquinodimethan", *J. Opt. Soc. Am.* **B 7**, 2274-2278 (1990).
68. P. Tayebati, J. Kumar, and S. Scott, "Photorefractive effect at 633-nm in semiinsulating cadmium-sulfide"," *Appl. Phys. Lett.* **59,** 3366-2668 (1991).
69. Y. Belaud, P. Delaye, J. C. Launay, and G. Roosen, "Photorefractive response of CdTe-v under ac electric-field from 1 to 1.5 μm", *Opt. Commun.* **105,** 204-208 (1994).
70. A. Partovi and E. M. Garmire, "Band-Edge Photorefractivity in Semiconductors - Theory and Experiment", *J. Appl. Phys.* **69,** 6885-6898 (1991).
71. A. Partovi, A. M. Glass, T. H. Chiu, and D. T. H. Liu, "High-Speed Joint-Transform Optical-Image Correlator Using Gaas/Algaas Semiinsulating Multiple-Quantum Wells and Diode- Lasers", *Opt. Lett.* **18,** 906-908 (1993).
72. A. Partovi, A. M. Glass, D. H. Olson, G. J. Zydzik, H. M. Obryan, T. H. Chiu, and W. H. Knox, "Cr-Doped Gaas/Algaas Semiinsulating Multiple Quantum-Well Photorefractive Devices", *Appl. Phys. Lett.* **62,** 464-466 (1993).
73. D. A. B. Miller, D. S. Chemla, T. C. Damen, A. C. Gossard, W. Wiegmann, T. H. Wood, and C. A. Burrus, "Band-edge electroabsorption in quantum well structures: the quantum confined stark effect", *Phys. Rev. Lett.* **53,** 2173-2176 (1984).
74. S. Balasubramanian, I. Lahiri, Y. Ding, M. R. Melloch, and D. D. Nolte, "Two-wave-mixing dynamics and nonlinear hot-electron transport in transverse-geometry photorefractive quantum wells studied by moving gratings", *Appl. Phys. B-Lasers Opt.* **68,** 863-869 (1999).
75. F. L. Lederman and J. D. Dow, "Theroy of electoabsorption by anisotropic and layered semiconductors. I. Two-dimensional excitons in a uniform electric field", *Phys. Rev. B.* **13**, 1633-1642 (1976).
76. W. S. Rabinovich, R. Mahon, S. R. Bowman, D. S. Katzer, and K. Ikossi-Anastasiou, "Lock-in holography using optically addressed multiple-quantum- well spatial light modulators", *Opt. Lett.* **24**, 1109-1111 (1999).
77. D. D. Nolte and M. R. Melloch, in *Photorefractive Effects and Materials,* D.D. Nolte ed. (Kluwer Academic Publishers, Dordrecht, 1995), 373-452.
78. S. Ducharme, J.C. Scott, R.J. Tweig, and W.E. Moerner, "Observation of the photorefractive effect in a polymer", *Phys. Rev. Lett.* **66,** 1846-1849 (1991).

79. S. M. Silence, C. A. Walsh, J. C. Scott, J. Matray, R. J. Tweig, F. Hache, G. C. Bjorklund, and W. E. Moerner, "Subsecond grating growth in a photorefractive polymer", *Opt. Lett.* **17**, 1107-1109 (1992).
80. D. D. Steele, B. L. Volodin, O. Savina, B. Kippelen, N. Peyghambarian, H. Rockel, and S. R. Marder, "Transillumination imaging through scattering media by use of photorefractive polymers", *Opt. Lett.* **23**, 153-155 (1998).
81. A. Goonesekera, D. Wright, and W. E. Moerner, "Image amplification and novelty filtering with a photorefractive polymer", *Appl. Phys. Lett.* **76**, 3358-3360 (2000).
82. D. Wright, M. A. Diaz-Garcia, J. D. Casperson, M. DeClue, W. E. Moerner, and R. J. Twieg, "High-speed photorefractive polymer composites", *Appl. Phys. Lett.* **73**, 1490-1492 (1998).
83. E. Mecher, F. Gallego-Gomez, H. Tillmann, H. H. Horhold, J. C. Hummelen, and K. Meerholz, "Near-infrared sensitivity enhancement of photorefractive polymer composites by pre-illumination", *Nature* **418,** 959-964 (2002).
84. P. Bernasconi, G. Montemezzani, M. Wintermantel, I. Biaggio, and P. Gunter, "High-resolution, high-speed photorefractive incoherent-to- coherent optical converter", *Opt. Lett.* **24**, 199-201 (1999).
85. S. Iwamoto, S. Taketomi, H. Kageshima, M. Nishioka, T. Someya, Y. Arakawa, K. Fukutani, T. Shimura, and K. Kuroda, "Photorefractive multiple quantum wells at 1064 nm", *Opt. Lett.* **26**, 22-24 (2001).
86. C. De Matos, H. L'Haridon, J. C. Keromnes, G. Ropars, A. Le Corre, P. Gravey, and M. Pugnet, "Multiple quantum well optically addressed spatial light modulators operating at 1.55 mu m with high diffraction efficiency and high sensitivity", *J. Opt. A-Pure Appl. Opt.* **1**, 286-289 (1999).
87. S. C. W. Hyde, R. Jones, N. P. Barry, J. C. Dainty, P. M. W. French, K. M. Kwolek, D. D. Nolte, and M. R. Melloch, "Depth-resolved holography through turbid media using photorefraction", *IEEE J. Sel. Top. Quant. Electron.* **2**, 965-975 (1996).
88. C. Dunsby, Y. Gu, D. D. Nolte, M. R. Melloch, and P. M. W. French, "Wide-field coherence gated imaging: photorefractive holography and wide-field coherent heterodyne imaging" in *Coherence Domain Optical Methods and Optical Coherence Tomography in Biomedicine VII,* **4956,** V.V. Tuchin, J.A. Izzat, and J. G. Fujimoto eds. (SPIE, San Jose, 2003), 26-33.
89. C. Dunsby, Y. Gu, Z. Ansari, P. M. W. French, L. Peng, P. Yu, M. R. Melloch, and D. D. Nolte, "High-speed depth-sectioned wide-field imaging using low-coherence photorefractive holographic microscopy", *Opt. Commun.* **219**, 87-99 (2003).
90. N. Iftimia, B. E. Bouma, and G. J. Tearney, "Speckle reduction in optical coherence tomography by "path length encoded" angular compounding", *J. Biomed. Opt.* **8**, 260-263 (2003).
91. P. Yu, L. L. Peng, M. Mustata, D. D. Nolte, J. J. Turek, M. R. Melloch, C. Dunsby, Y. Gu, and P. M. W. French, "Imaging of tumor necroses usingfull-frame optical coherence imaging" in *Coherence Domain Optical Methods and Optical Coherence Tomography in Biomedicine VII,* **4956,** V.V. Tuchin, J.A. Izzat, and J. G. Fujimoto eds. (SPIE, San Jose, 2003), 34-41.

Chapter 7

DIFFRACTION OF INTERFERENCE FIELDS ON RANDOM PHASE OBJECTS

Vladimir V. Ryabukho
Saratov State University, Saratov, 410012; Precision Mechanics and Control Institute of the Russian Academy of Sciences, Saratov, 410028 Russian Federation

Abstract: In the chapter the interference pattern formation are studied at diffraction on an inhomogeneous object of a light interference field – light beam with regular interference fringes (spatially-modulated light beam). The feasibilities of determination of statistical parameters of optical inhomogeneities of thin scattering objects satisfying the "random phase screen" model are discussed; also the processes of image formation of a scattering object are considered. The interference methods of surface roughness measurements, diagnostics of retinal acuity of vision at cataract of an eye, and methods of diagnostics of changes of scattering properties of blood during sedimentation and aggregation of erythrocytes with use of the probing spatially-modulated laser beams are discussed.

Key words: Interferometry, diffraction, scattering, inhomogeneous objects, correlation of optical fields, speckles, imaging, diffractive optics, roughness measurements, laser retinometry, blood erythrocytes diagnostics

7.1 INTRODUCTION

The optical interference methods in material and biomedical applications are used for determination of the form of objects, optical parameters of their structure, parameters of movement, vibrations, and deformations. In these methods an output signal of the interference device is read-out as the temporal or spatial oscillations of intensity of an interference field and corresponding oscillations of a photoelectric signal. Temporal or spatial period of these oscillations is determined by length of a light wave, which serves as a measure and determines accuracy of measurements.

In the other class of interference measurements an information signal is the envelop of interference oscillations (contrast of interference fringes or modulation factor of a temporal signal). These methods [1-18] are used for the study of parameters of scattering microstructure of optically inhomogeneous objects. When light diffracts on randomly inhomogeneous objects, the scattered field contains information on the statistical parameters of the optical inhomogeneities of these objects. Optical interferometry, within the framework of which the parameters of inhomogeneities of scattering objects are determined from the contrast of interference fringes or temporal oscillations observed with the help of interferometers, should be assigned to the most informative and sensitive methods for determining these parameters. The set of methods and means of interference measurements of parameters of microstructure of scattering objects are called optical interferometry of randomly inhomogeneous media.

Three approaches used in optical interferometry of randomly inhomogeneous media can be distinguished. Within the first of them, the classic approach, an object under study is placed in an arm of the interferometer, and the interference of the object field with a reference wave is observed at the output of the interferometer [1–5]. High sensitivity to external perturbations and the influence of the object macroshape on the form and spatial frequency of the interference fringes should be considered as the main disadvantage of such interferometers. Within the second approach, interferometers with wavefront division [6–9], or shearing interferometers [1,5,10,11] are used. The light field scattered by an object is directed into the interferometer, and the interference of two scattered object waves is observed at the output of the device. Within the third approach, the interferometer itself serves as an illuminating system: an object under study is placed at the interferometer output and probed by an interference field—a light beam with regular interference fringes (spatially modulated laser beam (SMLB)) and fringes contrast is observed in diffraction field [12–20]. The two last approaches are more efficient than the first one because the object under test is placed outside the interferometer. In turn, the third approach is significantly simpler than the second one because the interferometer–illuminator can have an extremely simple design, in particular, in the form of a diffractive (holographic) optical element, and can be highly vibration-proof.

The probing of randomly inhomogeneous object by SMLB can be accomplished in several ways. If the object has the large enough sizes and simple form, the collimated beam is used and interference pattern is registered in the near area of diffraction (see section 7.2). In Refs. [19] and [20], wide-aperture collimated SMLB was used to probe scattering 3D media and determine the correlation of angular components of the diffraction field. The small sizes of testing object, essential curvature of a surface, statistical heterogeneity of its scattering properties and other reasons cause use focused

SMLB at observing interference fringes in the far area of diffraction (section 7.3). The third way of probing is based on formation of the image of an interference pattern in optical system with inhomogeneous object in spatial frequency plane (section 7.4). Finally, the fourth way of SMLB probing is based on the use of a special diffractive optical element (DOE) with double identical light diffractive microstructures (section 7.5).

The methods of SMLB diffraction on a random inhomogeneous object have found the most effective application in surface roughness measurements, in diagnostic ophthalmology – in laser interferential retinometry at cataract, and in determination of changes of scattering properties of blood in processes of sedimentation and aggregation of erythrocytes (section 7.6).

7.2 COLLIMATED INTERFERENCE FIELDS

Spatially-modulated laser beams as beams with regular interference fringes are extensively used in coherent optical measurements to determine the microprofile [21] and shape [22] of a surface by the so-called methods of fringe projection. In speckle interferometry, illumination of this kind is used to measure microshifts and deformations of rough surfaces [22,23], and in laser anemometry [24], to count and measure the velocity of particle motion. In these methods, the spatial period of interference fringes in an illuminating beam is small and comparable with average sizes of inhomogeneities. It was found [25] that probing beams with a modulation fringe period greatly exceeding size of inhomogeneities may be used to determine statistical parameters of a certain class of scattering objects – random phase objects (RPO) satisfying the "random phase screen" model (RPS) [26-28]. In this case, average-intensity interference fringes are observed in the diffraction field. Their contrast varies with the distance z from a scattering object. The character of this variation is determined by correlation properties of the scattered light field, which are determined, in turn, by statistical parameters of optical inhomogeneities, namely, by the variance σ_ϕ^2, the correlation radius l_ϕ, and the form of the correlation function of the phase inhomogeneities.

In this item of the chapter, we present the results of theoretical, numerical, and experimental investigations of the evolution of the contrast of average-intensity fringes resulting from the diffraction of a collimated SMLB by optically inhomogeneous objects satisfying the RPS model. The transformation of correlation properties of the scattered speckle-field, which was caused by the finite size of the aperture of an illuminating beam, was taken into account within the framework of the Fresnel diffraction.

7.2.1 Contrast of Average Intensity Fringes in the Diffraction Zone

The effect of variation of the contrast of average-intensity fringes in a scattered beam can be explained in the context of regularities of interference of identical speckle fields [5,29,30]. If the spatial modulation of an illuminating beam is produced by the interference of two waves propagating at a small angle θ to each other, the diffraction field can be represented in the form of a superposition of coherent mutually transverse displaced identical speckle fields formed by scattering each of the waves of the illuminating beam. The mutual shift of speckle fields $|\Delta\zeta|$ depends on the angle θ and the distance z from the object: $|\Delta\zeta| = \theta z$. Because of this, the cross correlation of interfering speckle fields and, consequently, the fringe contrast decrease with increasing distance z. Figure 1 presents interferograms illustrating the effect of fringe contrast variation.

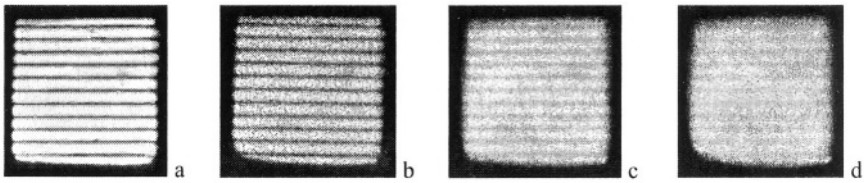

Figure 1. Interference fringes in (a) the illuminating spatially-modulated beam and (b-d) the diffraction field at various distances z from a RPS for a beam aperture of $17\times17\ mm^2$, fringe period $\Lambda = 1.5\,mm$, and RPS parameters $\sigma_\phi \approx 1.9$, $l_\phi \approx 43\,\mu m$: z = (b) 20, (c) 40, and (d) 400 *mm*.

Let us consider an illuminating laser beam with parallel fringes formed by the interference of two identical waves propagating at a small angle θ to each other (Figure 2). The complex amplitude of this field in the plane $(\vec{\rho}, z = 0)$ can be represented in the form

$$U_i(\vec{\rho},0) = A(\vec{\rho})\left[A_1 \exp(ik\vec{\chi}\vec{\rho}) + A_2 \exp(-ik\vec{\chi}\vec{\rho} - \phi_0)\right], \qquad (1)$$

where A_1 and A_2 are constants, $A(\vec{\rho})$ is the complex wave amplitude, $\pm\vec{\chi}(\theta/2,0)$ are the components of unit vectors of directions of wave propagation determined in the plane $\vec{\rho}(x,y)$, ϕ_0 is the initial phase shift, and k is the wave number. In view of equation 1, the intensity distribution in the illuminating beam has the form

$$I_i(\vec{\rho}) = |A(\vec{\rho})|^2\left[A_1^2 + A_2^2 + 2A_1A_2\cos(2k\vec{\chi}\vec{\rho} - \phi_0)\right], \qquad (2)$$

i.e., straight fringes [Figure 1(a)] are observed. They are parallel to the y-axis and have a period $\Lambda = \lambda / \theta$ and a contrast $V_0 = 2A_1A_2 / \left(A_1^2 + A_2^2\right)$. Let us show that interference fringes with contrast V varying in the longitudinal direction as a function of parameters of optical inhomogeneities of an object are present in the spatial distribution of the average intensity of the scattered speckle-modulated field [Figures 1(b)-(d)].

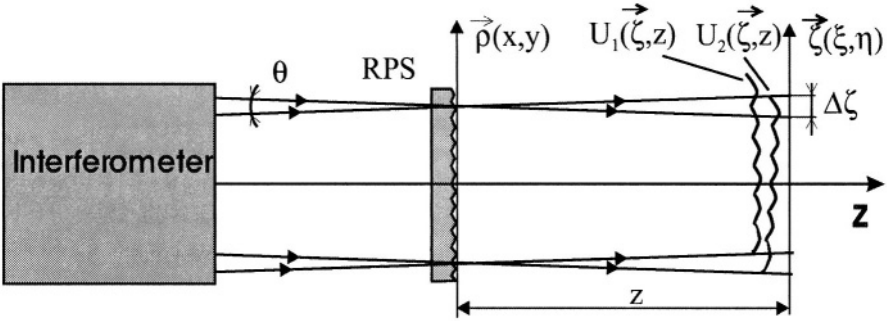

Figure 2. An optical configuration illustrating the theoretical analysis of the average intensity of the scattered field formation.

Let us assume that an object has smooth inhomogeneities; that is, their correlation radius l_ϕ is much larger than the wavelength λ and the mean-square deviation of path difference $\sigma_\Delta = (\lambda / 2\pi)\sigma_\phi$: $l_\phi >> \lambda$ and $l_\phi >> \sigma_\Delta$, where σ_ϕ^2 is the variance of phase fluctuations of the field. This object may be considered as RPS with a transmission function of the form [26, 28]

$$t(\vec{\rho}) = t_0 \, exp\left(i\phi(\vec{\rho})\right), \tag{3}$$

where $\phi(\vec{\rho})$ are the spatial phase fluctuations. Let us also assume that the transmission function is constant within small angles of incidence θ of an illuminating beam. Then, the complex amplitude of the boundary field, that is, the field in the plane $\vec{\rho}, z = 0$ positioned in the immediate vicinity behind a RPS, can be represented in the form

$$U(\vec{\rho},0) = U_i(\vec{\rho},0)t(\vec{\rho}). \tag{4}$$

One can show, using equations 1 and 4, and the approximation of Fresnel diffraction, that the scattering field in the near paraxial region represents the superposition of two mutually displaced speckle fields with complex amplitudes of the form

$$U_1(\vec{\zeta},z)=a_1U_0\left(\vec{\zeta}-\frac{\Delta\vec{\zeta}}{2},z\right)exp\left(ik\vec{\chi}\vec{\zeta}\right)exp\left(-\frac{ik}{2}z\vec{\chi}^2\right), \quad (5)$$

$$U_2(\vec{\zeta},z)=a_2U_0\left(\vec{\zeta}+\frac{\Delta\vec{\zeta}}{2},z\right)exp\left(-ik\vec{\chi}\vec{\zeta}-i\phi_0\right)exp\left(-\frac{ik}{2}z\vec{\chi}^2\right). \quad (6)$$

Here, $\vec{\zeta}(\xi,\eta)$ is a coordinate in the observation plane, $\left|\Delta\vec{\zeta}\right|=\left|2\chi z\right|=\theta z$ is the mutual shift of the fields, and $U_0(\vec{\zeta},z)$ is the complex amplitude of the scattered field in the case where the RPS is illuminated at normal incidence $(\chi=0)$ by one of the waves forming the spatially-modulated beam

$$U_0(\vec{\zeta},z)=Ct_0\int_{-\infty}^{\infty}\int A(\vec{\rho})exp(i\phi(\vec{\rho}))exp\left(\frac{ik}{2z}(\vec{\rho}-\vec{\zeta})^2\right)d^2\vec{\rho}, \quad (7)$$

where $C=\frac{k}{2\pi iz}exp(ikz)$.

Let us consider the average intensity of the total scattered field. This averaging is needed to smooth out speckle modulation and separate out the determinate component in the spatial intensity distribution. In view of equations 5 and 6, the total-field intensity averaged over the ensemble of realizations is determined by the following expression in the form of the classical equation of interference

$$\begin{aligned}\left\langle I(\vec{\zeta},z)\right\rangle &= A_1^2\left\langle I_1(\vec{\zeta},z)\right\rangle+A_2^2\left\langle I_2(\vec{\zeta},z)\right\rangle+2A_1A_2\left[\left\langle I_1(\vec{\zeta},z)\right\rangle\left\langle I_2(\vec{\zeta},z)\right\rangle\right]^{1/2}\\ &\times\left|\mu(\vec{\zeta},\Delta\vec{\zeta},z)\right|cos(\alpha+2\vec{\chi}\vec{\zeta}+\phi_0),\end{aligned} \quad (8)$$

where $\alpha=arg(\mu)$ and

$$\mu(\vec{\zeta},\Delta\vec{\zeta},z)=\frac{\left\langle U_0\left(\vec{\zeta}-\frac{\Delta\vec{\zeta}}{2},z\right)U_0^*\left(\vec{\zeta}+\frac{\Delta\vec{\zeta}}{2},z\right)\right\rangle}{\left[\left\langle I_1(\vec{\zeta},z)\right\rangle\left\langle I_2(\vec{\zeta},z)\right\rangle\right]^{1/2}}=\frac{B(\vec{\zeta},\Delta\vec{\zeta},z)}{\left[B\left(\vec{\zeta}-\frac{\Delta\vec{\zeta}}{2},0,z\right)B\left(\vec{\zeta}+\frac{\Delta\vec{\zeta}}{2},0,z\right)\right]^{1/2}} \quad (9)$$

is the coefficient of transverse correlation of the complex amplitude of the scattered field in the case where the RPS is illuminated at normal incidence by one wave only with complex amplitude $A(\vec{\rho})$. In equations 8 and 9, we

also used the notations: $\left\langle I_1\left(\vec{\zeta},z\right)\right\rangle = \left\langle I_0\left(\vec{\zeta}-\frac{\Delta\vec{\zeta}}{2},z\right)\right\rangle = B\left(\vec{\zeta}-\frac{\vec{\zeta}}{2},0,z\right)$ and $\left\langle I_2\left(\vec{\zeta},z\right)\right\rangle = \left\langle I_0\left(\vec{\zeta}+\frac{\Delta\vec{\zeta}}{2},z\right)\right\rangle = B\left(\vec{\zeta}+\frac{\Delta\vec{\zeta}}{2},0,z\right)$ are average intensities of the diffraction field at two points $\left(\vec{\zeta}\pm\frac{\Delta\vec{\zeta}}{2},z\right)$ of the observation plane in the case of illuminating the RPS by one wave, and $B\left(\vec{\zeta},\Delta\vec{\zeta},z\right)=\left\langle U_0\left(\vec{\zeta}-\frac{\Delta\vec{\zeta}}{2},z\right)U_0^*\left(\vec{\zeta}+\frac{\Delta\vec{\zeta}}{2},z\right)\right\rangle$ is the transverse correlation function of the complex amplitude of the scattered field.

It follows from equation 8 that the scattered field exhibits average-intensity fringes with a period $\Lambda=\lambda/\theta$ and a contrast V determined by the value of $\left|\mu\left(\vec{\zeta},\Delta\vec{\zeta},z\right)\right|$ and the ratio of average intensities $A_1^2\left\langle I_1\left(\vec{\zeta},z\right)\right\rangle$ and $A_2^2\left\langle I_2\left(\vec{\zeta},z\right)\right\rangle$. In the case of a non-planar illuminating beam with $A(\vec{\rho})\neq const$, the scattered field is statistically non-uniform [26]; that is, the average intensity $\left\langle I_0\left(\vec{\zeta},z\right)\right\rangle$ and the coefficient of correlation $\mu\left(\vec{\zeta},\Delta\vec{\zeta},z\right)$ depend on the transverse coordinate $\vec{\zeta}$. However, equation 8 can be simplified if we consider the average intensity of the total field on the optical axis $\vec{\zeta}=0$ for an even distribution of complex field amplitude in the illuminating beam. In this case, $\left\langle I_0\left(+\frac{\Delta\vec{\zeta}}{2},z\right)\right\rangle=\left\langle I_0\left(-\frac{\Delta\vec{\zeta}}{2},z\right)\right\rangle=B\left(\pm\frac{\Delta\vec{\zeta}}{2},0,z\right)$ and the fringe contrast on the optical axis is determined by the expression

$$V=\frac{2A_1A_2}{A_1^2+A_2^2}\left|\mu\left(0,\Delta\vec{\zeta},z\right)\right|=V_0\frac{B\left(\vec{\zeta},\Delta\vec{\zeta},z\right)}{B\left(\vec{\zeta}\pm\Delta\vec{\zeta}/2,0,z\right)}, \qquad (10)$$

where V_0 is the fringe contrast in the illuminating spatially-modulated beam. Because of the mutual field shift $\left|\Delta\vec{\zeta}\right|=\theta z=\lambda z/\Lambda$, the correlation coefficient $\left|\mu\left(\vec{\zeta},\Delta\vec{\zeta},z\right)\right|$ decreases, which is accompanied by a decrease in fringe contrast with distance from the screen. RPSs with different values of σ_ϕ^2 and l_ϕ are characterized by different variations of contrast. This fact is supported by experimental data. Recall that the dependence of μ on z is

determined by two competing processes, the mutual shift of speckle fields $\Delta\zeta(z)$ and the transformation of the scattered field along the longitudinal coordinate z caused by a finite aperture of the illuminating beam and a decrease in the average intensity of the scattered component of the field. We will show below that, in the near field, the first process dominates because the autocorrelation function in the numerator of equation 10 decreases faster than the denominator, the average field intensity. The effect of the second process becomes prominent for small apertures of the illuminating beam comparable in size with the fringe period or at sufficiently large distances from a RPS.

7.2.2 The Coefficient of Transverse Correlation of the Complex Amplitude of the Scattered Field

Let us determine the relation between $|\mu(z)|$ for each section of the scattered field z and the parameters σ_ϕ^2, l_ϕ. In view of equation 7, the correlation function $B(\vec{\zeta},\Delta\vec{\zeta},z)$ is given by the expression [26-28, 31]

$$B(\vec{\zeta},\Delta\vec{\zeta},z)=|C|^2 t_0^2 \int_{-\infty}^{\infty}\int_{-\infty}^{\infty} A(\vec{\rho})A^*(\vec{\rho}')\mu_t(\vec{\rho},\vec{\rho}',0)$$
$$\times exp\left[\frac{ik}{2z}\left(\vec{\rho}-\left(\vec{\zeta}+\frac{\Delta\vec{\zeta}}{2}\right)\right)^2-\frac{ik}{2z}\left(\vec{\rho}'-\left(\vec{\zeta}-\frac{\Delta\vec{\zeta}}{2}\right)\right)^2\right]d^2\vec{\rho}\,d^2\vec{\rho}', \tag{11}$$

where $\mu_t(\vec{\rho},\vec{\rho}',0)=\langle exp(i\phi(\vec{\rho})-i\phi(\vec{\rho}'))\rangle$ is the coefficient of correlation of the boundary field for an RPS illuminated by a plane wave of unity amplitude for $t_0=1$. If $\phi(\vec{\rho})$ is a statistically stationary Gaussian process with a zero mean value, $\mu_t(\vec{\rho},\vec{\rho}',0)$ is expressible in the form [26,27]

$$\mu_t(\vec{\rho},\vec{\rho}',0)=\mu_t(\vec{\rho}-\vec{\rho}',0)=exp\left[-\sigma_\phi^2\left(1-K_\phi(\vec{\rho}-\vec{\rho}')\right)\right], \tag{12}$$

where $K_\phi(\vec{\rho}')$ is the coefficient of correlation of the boundary-field phase. Following Refs. [26] to [28], let us change the variables: $R(x,y)=(\vec{\rho}+\vec{\rho}')/2$ and $\Delta\vec{\rho}(\Delta x,\Delta y)=\vec{\rho}-\vec{\rho}'$. Then equation 11 changes to the form

$$B(\vec{\zeta},\Delta\vec{\zeta},z)=|C|^2 exp\left(\frac{ik}{z}\Delta\vec{\zeta},\vec{\zeta}\right)t_0^2\int_{-\infty}^{\infty}\int_{-\infty}^{\infty}A\left(\vec{R}+\frac{\Delta\vec{\rho}}{2}\right)A^*\left(\vec{R}-\frac{\Delta\vec{\rho}}{2}\right)$$
$$\times\mu_t(\Delta\vec{\rho},0)exp\left(\frac{ik}{z}\vec{R}\left(\Delta\vec{\rho}-\Delta\vec{\zeta}\right)\right)exp\left(-\frac{ik}{z}\Delta\vec{\rho}\vec{\zeta}\right)d^2\vec{R}d^2\Delta\vec{\rho}, \tag{13}$$

which is more suitable for analysis.

If an illuminating beam has a reasonably wide aperture and is collimated, $A\left(\vec{R}+\frac{\Delta\vec{\rho}}{2}\right)A^*\left(\vec{R}-\frac{\Delta\vec{\rho}}{2}\right)\approx\left|A\left(\vec{R}\right)\right|^2=const$ and integration $\vec{R}$ in equation 13 gives the δ-function. Then, for $\mu\left(\vec{\zeta},\Delta\vec{\zeta},z\right)$ we have an expression

$$\mu\left(\vec{\zeta},\Delta\vec{\zeta},z\right)=\mu_t\left(\Delta\vec{\zeta},0\right)=exp\left[-\sigma_\phi^2\left(1-K_\phi\left(\Delta\vec{\zeta}\right)\right)\right] \tag{14}$$

similar to the expression for the coefficient of correlation of the boundary field [26].

Thus, we obtained an important result: correlation properties of the scattered field are conserved behind a screen, even though speckle modulation is developed in this field. The length of this region behind a screen z_0 is determined by the width of an illuminating beam $2w$ and the correlation radius of the boundary field ρ_c. It is estimated by the relation [26]

$$z_0\approx\frac{w\rho_c}{\lambda}, \tag{15}$$

where ρ_c is determined, in turn, by the parameters σ_ϕ^2 and l_ϕ of inhomogeneities. Hence, the evolution of the fringe contrast V in the near field diffraction may be described within a certain approximation using the coefficient of correlation of the scattered field in the form of equation 14 (curve 1 in Figure 3), provided the width of the illuminating beam $2w$ is chosen appropriately.

To take into account the effect of a finite aperture of the illuminating beam on the variation of the coefficient of correlation of the scattered field, we considered a collimated beam with a Gaussian amplitude profile $A(\vec{\rho})=exp\left(-\vec{\rho}^2/w^2\right)$. In this case, equation 13 can be integrated analytically over $\vec{R}$ and

$$\begin{aligned}B\left(\vec{\zeta},\Delta\vec{\zeta},z\right)=&\left|C\right|^2\left(\frac{\pi w^2}{2}\right)exp\left(\frac{ik}{z}\Delta\vec{\zeta}\vec{\zeta}\right)t_0^2\int_{-\infty}^{\infty}\int exp\left(-\frac{\Delta\vec{\rho}^2}{2w^2}\right)\mu_t\left(\Delta\vec{\rho},0\right)\\&\times exp\left[-\frac{1}{2}\left(\frac{kw}{2z}\left(\Delta\vec{\rho}-\Delta\vec{\zeta}\right)\right)^2\right]exp\left(-\frac{ik}{z}\vec{\zeta}\Delta\vec{\rho}\right)d^2\Delta\vec{\rho}.\end{aligned} \tag{16}$$

For simplicity, subsequent calculations are made for a one-dimensional RPS with a large phase correlation radius along the y-axis satisfying the condition $l_{\phi y}>>2w$. In this case, we can perform-analytical integration over Δy in equation 16. The integration over Δx was performed numerically

within the paraxial approximation $\zeta(\xi,\eta)=0$ using a standard calculation procedure. Values of $|\mu(z)|$ were calculated using the relation

$$\mu(0,\Delta\xi,z)=\frac{B^1(0,\Delta\xi,z)}{B^1\left(\pm\frac{\Delta\xi}{2},0,z\right)}, \tag{17}$$

where

$$B^1(\xi,\Delta\xi,z)=\int_{-\infty}^{\infty} exp\left(-\frac{\Delta x^2}{2w^2}\right)exp\left[-\sigma_\phi^2\left(1-K_\phi(\Delta x)\right)\right]$$
$$\times exp\left[-\frac{1}{2}\left(\frac{kw}{2z}(\Delta x-\Delta\xi)\right)^2\right]cos\left(\frac{k\xi\Delta x}{z}\right)d\Delta x \tag{18}$$

and $\Delta\xi=\left|\Delta\vec{\zeta}\right|$. Moreover, in equation 18, we took into account the evenness of the function that was Fourier-transformed. The coefficient of phase correlation $K_\phi(\Delta x)$ was approximated by the function

$$K_\phi(\Delta x)=exp\left[-\left(\frac{|\Delta x|}{l_\phi}\right)^a\right]. \tag{19}$$

Figure 3 illustrates the results of numerical calculations of coefficient $|\mu(z)|$ for an unbounded illuminating beam ($w=\infty$, equation 14) and Gaussian illuminating beams with finite width (equation 17) for a Gaussian ($a=2$) coefficient of phase correlation K_ϕ. They were performed for the following values of parameters: $\lambda=0.63\mu m$, $\Lambda=0.83mm$, $\sigma_\phi=1.5$, and $l_\phi=20\mu m$. In the case of an unbounded illuminating beam, the curve $|\mu(z)|$ reaches a steady-state level $\mu_0=exp\left(-\sigma_\phi^2\right)$ at $K(\Delta\xi(z))=K(\lambda z/\Lambda)\approx 0$. In the case of a finite beam width, a local minimum $\mu_m(z_m)>\mu_0$, a subsequent extended peak (curve 5 in Figure 3, values of z are given in the upper scale), and a reduction to zero in the far field of diffraction are observed. In the region $z<z_m$, rather good agreement between the values of $|\mu|$ for beams with finite and infinite apertures is observed. A noticeable difference in this region appears only for those beams whose aperture $2w$ approaches the fringe period Λ.

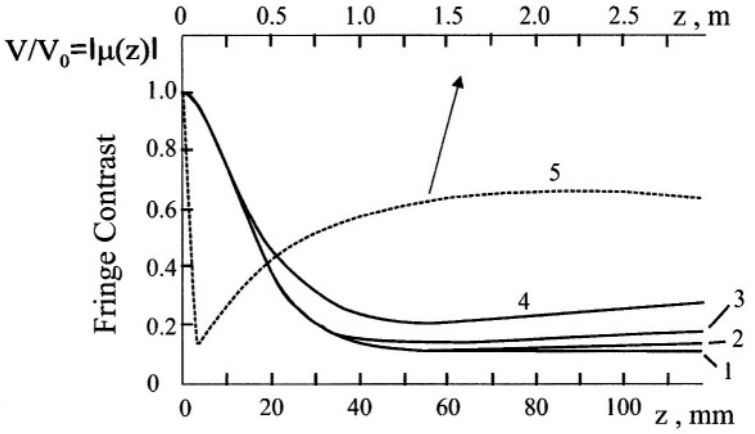

Figure 3. The variation in the contrast of average-intensity fringes in the field of diffraction of (1) unbounded and (2-5) bounded spatially modulated beams with different aperture radii w by a RPS. w = (1) ∞, (2) 4, (3) 1.66, (4)0,83, and (5) 1.66 mm (values of z are given on the upper scale).

We can make the following estimate for the beam radius w. The variation in fringe contrast will be determined by the coefficient of correlation of the boundary field in the case where the mutual shift of interfering speckle fields in the region $z < z_0$ reaches at least two radii of field correlation; that is, $\Delta\xi = (\lambda z/\Lambda) = 2\rho_c$. In view of equation 15, we have $w > 2\Lambda$. For such beam apertures, we have the difference $\mu_m - \mu_0 \le 0.05$ with a maximum for $\sigma_\phi \approx 1$. The position of the minimum z_m is determined mainly by the radius of phase correlation l_ϕ and the fringe period Λ, but is virtually independent of σ_ϕ, for $w > 2\Lambda$. It can be estimated by the expression

$$z_m \approx \frac{\Lambda l_\phi}{\lambda}\left[2 ln\left(\frac{\pi w}{\Lambda}\right)\right]^{1/2}. \qquad (20)$$

The increase in $|\mu(z)|$ and therefore, in fringe contrast is caused by filtering properties of free space [32], the relative growth or the nonscattered component of the field on the background of the scattered component whose intensity decreases rapidly with distance z. Therefore, fringes are observed only within the boundaries of the nonscattered beam. The subsequent decrease in fringe contrast is caused by a rapid decrease in field intensity in the region of overlap of nonscattered components of an illuminating beam.

7.2.3 Experimental Results

The schematic diagram of the experimental setup is presented in Figure 4. It contains a photodetector with a slit aperture to average speckle modulation and obtain a photoelectric signal proportional to the average field intensity. In the case of a statistically quasi-uniform field, this averaging is similar, to some extent, to averaging over the ensemble of realizations of speckle fields that was introduced in equations 8 and 9, provided the area of aperture considerably exceeds the area of spatial field correlation ρ_c^2.

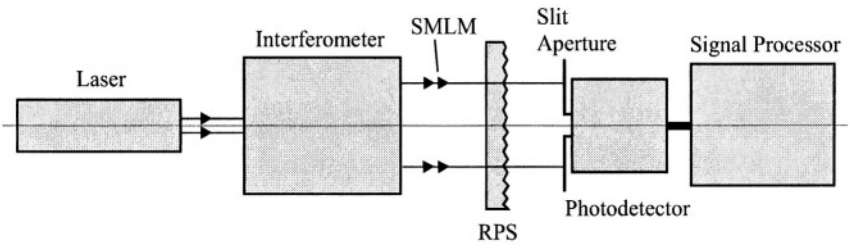

Figure 4. Schematic diagram of the experimental setup.

A spatially-modulated laser beam was formed using either a special holographic element [33] or a thin glass plate illuminated by a focused beam [34]. To form movable interference fringes suitable for measuring fringe contrast, we used a piezoelectric deflector providing beam oscillations with small amplitude of $l_0 \le \Lambda/2$. In this case, we have an alternating photoelectric signal from a motionless photodetector and the modulation factor β obtained is proportional to the contrast V of the average intensity of the detected field: $\beta = MV$. Measuring the modulation factor of a photoelectric signal, produced by an illuminating beam (without a sample), which is given by $\beta_0 = MV_0$, where V_0 is the fringe contrast in this beam, we can find the ratio $V/V_0 = \beta/\beta_0$. Hence, according to equation 10, the desired value of the modulus of the coefficient of field correlation is determined by the simple relation $|\mu| = \beta/\beta_0$. In this way, we realize measurements of $|\mu|$ at one point, specifically, on the axis of an illuminating beam, as was expected in the theoretical analysis.

As RPSs, we used phase (bleached) specklegrams [12, 25]. The phase of a beam was modulated by smooth spatial fluctuations of thickness and the refractive index of an emulsion layer. The statistical parameters σ_ϕ^2 and l_ϕ of such RPSs can be changed over rather wide ranges by varying the exposure and size of recorded speckles. Moreover, using non-linearity of photoresponse or a complex aperture of a scatterer in the process of

specklegram recording, one can obtain RPSs with a multi-scale or strongly oscillating coefficient of phase correlation of the boundary field $K_\phi(\Delta\vec{\rho})$.

Figure 5 illustrates experimental data and theoretical plots of the dependence $|\mu(z)|$. Numerical calculations are performed using equations 17 and 18 for a bounded (Gaussian) illuminating beam ($w = 5.6mm$, $\Lambda = 0.83mm$) and RPS parameters determined from experimental data in the approximation of an unbounded illuminating beam, i.e., using equation 14. The variance σ_ϕ^2 was determined, as in Ref. [14], from the minimum level of experimental values of $|\mu|$ given by $\mu_m \approx \mu_0 = exp(-\sigma_\phi^2)$. The correlation radius l_ϕ was determined using equation $l_\phi = z_c\,\lambda/\Lambda$, where the value z_c corresponds to the level μ_c giving a decrease in coefficient K_ϕ by a factor of e. The form of the coefficient of phase correlation K_ϕ and the exponent a in approximating function (equation 19) can easily be determined from equation 14 as well, using experimental data on $|\mu|$ and z (specifically, interferograms in Figures 1 are obtained for RPSs with an exponent $a = 1.5$)

$$K_\phi(\Delta x) = K_\phi\left(\frac{\lambda z}{\Lambda}\right) = 1 - \frac{ln|\mu(z)|}{ln(\mu_0)}. \qquad (21)$$

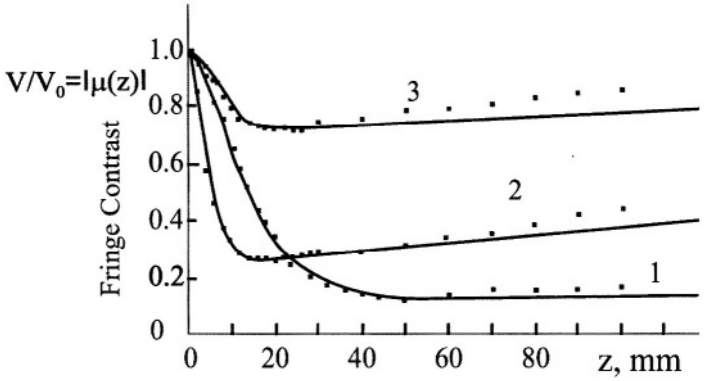

Figure 5. Experimental (points) and theoretical (solid lines) curves illustrating the dependence of the modulus of coefficient of correlation of the scattered field for RPSs (specklegrams) with different parameters of inhomogeneities: (1) $\sigma_\phi = 1.5$, $l_\phi = 19.5\mu m$, $a = 1.6$; (2) $\sigma_\phi = 1.16$, $l_\phi = 5\mu m$, $a = 1.8$; and (3) $\sigma_\phi = 0.57$, $l_\phi = 7\mu m$, $a = 2$.

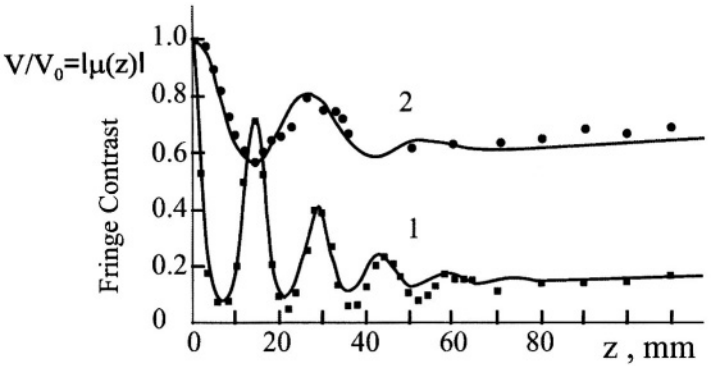

Figure 6. Experimental (points) and theoretical (solid lines) curves illustrating the dependence of the modulus of coefficient of correlation of the scattered field for RPSs with the oscillating coefficient of phase correlation K_ϕ: (1) $\sigma_\phi = 1.64$, $l_\phi = 35\mu m$, $l_0 = 5.5\,\mu m$, $a = 1.8$; (2) $\sigma_\phi = 0.75$, $l_\phi = 35\mu m$, $l_0 = 10.5\mu m$, $a = 2$.

Figure 6 presents experimental data and theoretical plots of the dependence $|\mu(z)|$ for RPSs with an oscillating coefficient of phase correlation

$$K_\phi(\Delta x) = exp\left[-\left(\frac{|\Delta x|}{l_\phi}\right)^a\right] cos^2\left(\frac{\pi\Delta x}{2l_0}\right), \qquad (22)$$

where $2l_0$ is the oscillation period. The oscillating character of the dependence $|\mu(z)|$ and, hence, of the fringe contrast $V(z)$ can be qualitatively attributed to the overlap of interference fringes in mutually shifted diffraction orders by a quasi-periodic structure of such RPSs.

7.2.4 Conclusion

In the case of a sufficiently wide illuminating beam $(w > 2\Lambda)$ the variation in contrast of average-intensity fringes in the near field behind an RPS is determined by the coefficient of correlation of the complex amplitude of the boundary field μ_t. This is provided by a relatively rapid increase in mutual shift of interfering speckle fields $|\Delta\vec{\zeta}| = \lambda z/\Lambda$ upon a minor transformation of correlation properties of the field in this region. In view of the fact that the mutual shift increases linearly with distance z, the form of the curve describing the fringe contrast $V(z)$ coincides with the profile of modulus of μ_t, within an argument scale factor of $\lambda/\Lambda \approx 10^{-3}$. This dependence, being consistent with the principles of shear interferometry [1-

3,10,11], can be used as the basis for determining statistical parameters of objects satisfying the RPS model.

In the region $z > z_m$ of full decorrelation of speckle fields with respect to the fluctuation (scattered) component where the mutual shift $|\Delta\bar{\zeta}|$ exceeds minimum speckle size, the correlation of speckle fields is realized by the nonscattered component. An increase in fringe contrast in this region is caused by a rapid decrease in the intensity of the scattered field component relative to the nonscattered one.

A decrease in fringe contrast observed after a local but quite extended peak is caused by a decrease in intensity (relative to the scattered field component) of overlapping areas of nonscattered beams where interference fringes are observed. In this region, the mutual shift is comparable with the beam radius *w*.

As for the interrelation between the fringe contrast and statistical characteristics of a screen, the near field is the most informative region. The distinctions observed between experimental and theoretical values in the far field are caused, in addition to instrumental errors, mainly by the fact that the profile of the coefficient of phase correlation K_ϕ, of an actual screen has a more complex form than the profiles specified by functions described by equations 19 and 22. Moreover, the form of K_ϕ affects the ascending part of the dependence $|\mu(z)|$ in the far field. However, it seems likely that a systematic excess of experimental values over theoretical is caused by two-dimensionality of an actual screen, inaccuracy in determining the radius of an illuminating beam *w,* and instrumental errors associated with measurements of rather low intensities in this region.

Note in conclusion that the results obtained correlate with concepts of Ref. [33], where the manifestation of spatial coherence of an extended thermal light source at diffraction by a hologram (a shift interferometer) is considered. A similar approach is used also in holographic methods of image recording through a scattering medium making phase distortions [36, 37].

The method of a collimated probing SMLB can be used for determination of statistical parameters of inhomogeneities of objects of technical or biological origin. In subsection 7.6.2 the method and experimental system for study of scattering properties of blood suspension is considered. Another example of biomedical diagnostics, where the probing SMLB is used, is laser interferential retinometry [38], when the pattern of fringes of different period is formed on a retina with the purpose of determination of a retinal acuity of vision. At turbidity of a crystalline lens the laser system of the retinometer is similar to the considered above interferential system, as two mutually coordinated laser beams pass through scattering area of a lens (see subsection 7.6.3). However, in retinometry the beams focused on scattering

media are used. In the following section the physical background of focused SMLB diffraction on random phase objects is considered.

7.3 FOCUSED SPATIALLY-MODULATED LASER BEAMS

In a number of practically important problems of optical technological and biomedical diagnostics, it is necessary to use probing beams with a sufficiently small aperture – focused laser beams. In this case, the use of an interferometer as a source of probing beam assumes the focusing of the SMLB onto the surface or into the bulk of the randomly inhomogeneous object to be controlled [13-15]. The diffraction of the focused SMLB on random phase object (RPO) differs in a number of essential physical features caused by a rather small area of illumination of object and the large divergence of a light beam. These features are considered below in detail and the dependence of contrast of observable interference fringes on statistical parameters of the object and parameters of the illuminating beam is established.

7.3.1 Interference of Speckle Fields in the Diffraction Zone

Let two laser beams with equal divergences, being combined by an interferometer with a small angle θ_0 between their optical axes, propagate together after leaving the interferometer. Interference of such beams leads to the formation of a laser beam with a system of rectilinear equidistant fringes having the period $\Lambda_0 \approx \lambda/\theta_0$. We will consider the focusing of such an SMLB on the surface of a randomly inhomogeneous phase object and analyze, on the qualitative level, specific features of the diffraction pattern formed (Figure 7).

In the focal plane, two diffraction spots are formed with the diameter $2w_0 \approx 2\lambda f/D$ and the separation between their centers $\rho_0 \approx \lambda f/\Lambda_0$, where f is the focal length of the objective and D is the diameter of its aperture (Figure 7). If an RPO is placed in the focal plane, the spatial structure of the diffraction field will change significantly and will be determined by the relation between the parameters of the probing laser beam $2w_0$, ρ_0 and the average transverse size l_ϕ (the correlation radius) of the object inhomogeneities (see Figure 8). Three characteristic regimes of probing an RPO can be distinguished.

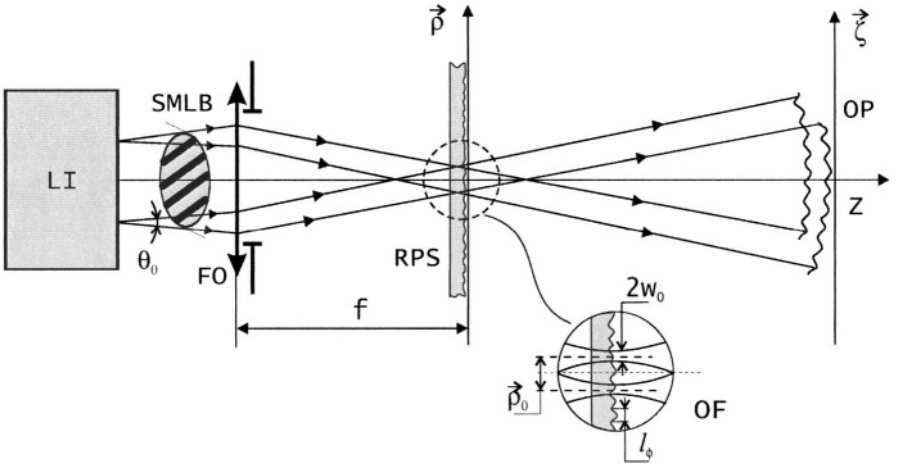

Figure 7. Optical scheme for observation the diffraction of a focused spatially-modulated laser beam (SMLB) by a random phase object: LI, laser interferometer; FO, focusing objective; RPS, random phase screen; OF, magnified fragment of the region of focusing of the laser beams; OP, plane of observation.

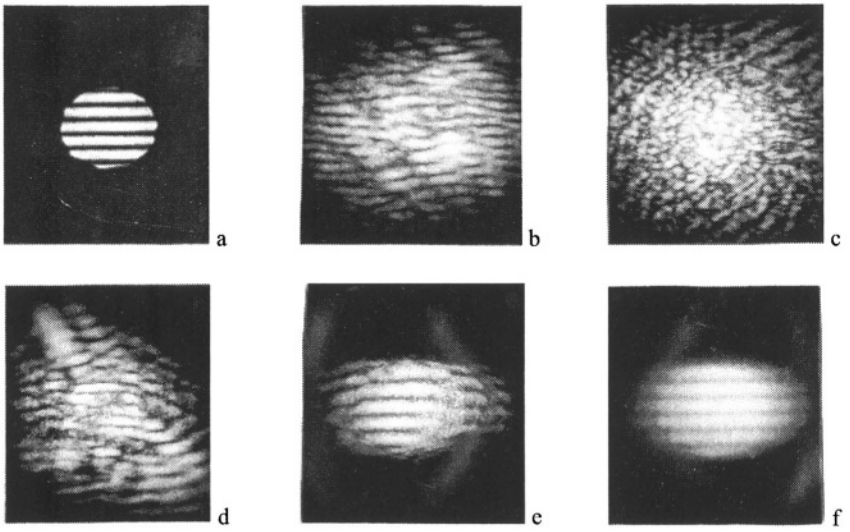

Figure 8. Interference patterns in the far diffraction field of a spatially-modulated laser beam focused onto a random phase object: (a) fringes in the absence of the object; (b, c) diffraction by a great number of inhomogeneities ((b) – $\Lambda < \varepsilon_\perp$; (c) – $\Lambda > \varepsilon_\perp$); (d) diffraction by a small number of inhomogeneities; (e) the regime of deflection of the fringes ($2w_0 < l_\phi$); and (f) average-intensity fringes.

A. ***Diffraction by a Great Number of Inhomogeneities*** **[15]**

When $2w_0 > l_\phi$, a rather great number of inhomogeneities are located within the waists of the focused laser beams. Diffraction of light by them leads to the formation of speckle fields. Interference of these fields determines the form of the resulting diffraction field. If the beam waists do not overlap on the surface of the RPO $\rho_0 > 2w_0$, which is equivalent to $2\Lambda_0 < D$, uncorrelated fields are formed. Within the limits of individual speckles of these fields, fringes with the period $\Lambda = \lambda z / \rho_0$ are formed [Figure 2(b)]; the transverse size of the speckles $\varepsilon_\perp \approx \lambda z / \sqrt{2} w_0$ [39]. The contrast of these interference fringes is governed by the ratio of the intensities of the interfering fields in each individual speckle and does not depend directly on the parameters of the inhomogeneities of the probed object. When $\rho_0 < 2w_0$, the focused beams partially overlap and partially correlated fields are formed in the diffraction field; the fringes within the limits of speckles disappear, because their period Λ exceeds the speckle size: $\Lambda > \varepsilon_\perp$ [Figure 2(c)]. The transverse displacement of the RPO is accompanied by fluctuations of the speckle fields, by a change in their realizations, and by the formation of the pattern of average-intensity fringes.

B. ***Diffraction by a Small Number of Inhomogeneities***

When $2w_0 \approx l_\varphi$, a small number of inhomogeneities turns out to be within the limits of the waists of the focused laser beams; the transverse size of the speckles in the diffraction field are comparable with the transverse size of the diffraction halo itself [40]. If $\rho_0 > 2w_0$, strongly curved interference fringes are observed [Figure 2(d)]; when $\rho_0 < 2w_0$, the fringes disappear. The form of the diffraction field essentially depends on the position of the RPO, whose displacement in the transverse direction leads to a change in realizations of the speckle fields and to the formation of the pattern of average-intensity fringes.

C. ***Regime ofDeflection ofInterference Fringes*** **[16]**

If $2w_0 < l_\phi$, the speckle modulation in the diffraction field is almost absent; both interfering beams have small distortions of the wavefronts, and one can see almost the same interference pattern in the diffraction field as in the absence of an RPO [Figure 2(e)]. Passing through different parts of the inhomogeneous object, the focused laser beams undergo different phase shifts, which determine the position of interference fringes in the diffraction field. In the case of a transverse displacement of the object, these phase shifts change and the fringes undergo a random transverse displacement. When $\rho_0 > l_\phi$, the deflection of the interference fringes inside the

diffraction field is observed, and when $\rho_0 < l_\phi$, the deflection of the beam as a whole together with the interference fringes takes place. Therefore, if the time constant of the photodetector is large enough, a pattern of average-intensity fringes is observed [Figure 2(f)].

In all three regimes, a transverse displacement of the scattering object results in fluctuations of the complex amplitude of the diffraction fields and, as a consequence, in the formation of an averaged diffraction pattern, which can be observed with the use of a sufficiently inertial photodetector. In this averaged field, interference fringes are formed whose contrast is governed by the SMLB parameters $2w_0$ and ρ_0 and by the parameters of the phase inhomogeneities of the object - by the correlation radius of the inhomogeneities l_ϕ and the root-mean-square deviation of the phase σ_ϕ of the wave passing through the optical inhomogeneities of the object [13-16].

Let us establish the analytical dependence of the contrast of the average-intensity fringes being observed on the parameters of the object inhomogeneities and on the parameters of the probing SMLB.

7.3.2 Contrast of the Average-Intensity Interference Fringes

In the optical scheme under consideration (Figure 7), the object is simultaneously illuminated by two mutually coherent laser beams. Consequently, a diffraction field is formed as the result of interference of two fields with the complex amplitudes $U_1(\vec{\zeta},z)$ and $U_2(\vec{\zeta},z)$. In the scalar approximation, for the intensity of the resulting diffraction field averaged over the ensemble of realizations of the fields U_1 and U_2, we can write the classic expression for interference [27,41]

$$\left\langle I(\vec{\zeta},z)\right\rangle = \left\langle I_1(\vec{\zeta},z)\right\rangle + \left\langle I_2(\vec{\zeta},z)\right\rangle + 2\,Re\left\{B_{12}(\vec{\zeta},z)\right\}, \tag{23}$$

where $B_{12}(\vec{\zeta},z) = \left\langle U_1(\vec{\zeta},z)U_2^*(\vec{\zeta},z)\right\rangle$ is the cross-correlation function, $\left\langle I_1(\vec{\zeta},z)\right\rangle = B_{11}(\vec{\zeta},z)$ and $\left\langle I_2(\vec{\zeta},z)\right\rangle = B_{22}(\vec{\zeta},z)$ are the average intensities of the fields, and the angle brackets denote averaging over the ensemble of field realizations. In experiment, this averaging is realized if object inhomogeneities are mobile or the object itself moves in a transverse direction and the photodetector being used is inertial enough.

The contrast of the interference pattern defined by equation 23 is represented by the relationship

$$V\left(\vec{\zeta}\right) = \frac{\left|B_{12}(\vec{\zeta},z)\right|}{\left[B_{11}(\vec{\zeta},z)B_{22}(\vec{\zeta},z)\right]^{1/2}}\,. \tag{24}$$

In this case, the experimental possibility of determining the fringe contrast at a specified observation point $(\vec{\zeta}, z)$ by displacing the interference fringes by one half-period $\Lambda/2$, changing the phase difference $\Delta\Phi_{12}$ between the interfering waves in the illuminating SMLB by π, is taken into account.

To establish the explicit form of equation 24, let us take advantage of the approximation of far-field diffraction, assuming that the sizes of the illuminated area on the RPO surface are small enough compared to the distance z to the plane of observation of the interference pattern (Figure 7). By using this approximation [32, 41, 42], let us write the complex amplitude of one of the diffraction fields in the following form:

$$U_1(\vec{\zeta}, z, \vec{\rho}_0) = C \int_{-\infty}^{+\infty} A_1 U_0(\vec{\rho} + \vec{\rho}_0/2) t(\vec{\rho}) \exp\left(-\frac{ik}{z}\vec{\rho}\vec{\zeta}\right) d\vec{\rho} = \\ CA_1 \exp\left(i\frac{k}{2z}\vec{\rho}_0\vec{\zeta}\right) \int_{-\infty}^{+\infty} U_0(\vec{\rho}) t(\vec{\rho} - \vec{\rho}_0/2) \exp\left(-\frac{ik}{z}\vec{\rho}\vec{\zeta}\right) d\vec{\rho}, \tag{25}$$

where C is a complex factor, $A_1 U_0(\vec{\rho} + \vec{\rho}_0/2)$ is the complex amplitude of the field of one of the focused laser beams on the RPO surface, and $t(\vec{\rho}) = t_0 \exp[i\varphi(\vec{\rho})]$ is the complex transmittance of the RPO. When writing the expression for the boundary field in the form $U(\vec{\rho}) = A_1 U_0(\vec{\rho}) t(\vec{\rho})$, we assumed that the RPO satisfies the random phase screen model [26, 27].

The expression for the complex amplitude of the second diffraction field $U_2(\vec{\zeta}, z)$ has an analogous form with the replacement of the complex amplitude of the illuminating field by $A_2 U_0(\vec{\rho} - \vec{\rho}_0/2) \exp(-i\Delta\Phi_{12})$ and, correspondingly, with the replacement of $\vec{\rho}_0$ by $-\vec{\rho}_0$ in equation 25.

By using equation 25 for $U_1(\vec{\zeta}, z; \rho_0)$ and $U_2(\vec{\zeta}, z; \rho_0)$, we can write the following expression for the cross-correlation function of the interfering fields:

$$B_{12}(\vec{\zeta}, z; \rho_0) = \left\langle U_1(\vec{\zeta}, z; \rho_0) U_2^*(\vec{\zeta}, z; \rho_0) \right\rangle |C|^2 A_1 A_2 \exp\left(i\frac{k}{z}\vec{\rho}_0\vec{\zeta} + i\Delta\Phi_{12}\right) \\ \times \int_{-\infty}^{+\infty}\int U_0(\vec{\rho}) U_0^*(\vec{\rho}') \left\langle t(\vec{\rho} - \vec{\rho}_0/2)\, t^*(\vec{\rho}' + \vec{\rho}_0/2) \right\rangle \exp\left(-\frac{ik}{z}(\vec{\rho} - \vec{\rho}')\vec{\zeta}\right) d\vec{\rho}\, d\vec{\rho}', \tag{26}$$

where the order of performing the integration and averaging was changed and the function $\left\langle t(\vec{\rho} - \vec{\rho}_0/2)\, t^*(\vec{\rho}' + \vec{\rho}_0/2) \right\rangle = t_0^2 \mu_t(\vec{\rho}, \vec{\rho}', \vec{\rho}_0)$ has the meaning of the correlation function of the RPS complex transmittance.

Let us make the following change of variables $\vec{R} = (\vec{\rho} + \vec{\rho}')/2$, $\Delta\vec{\rho} = \vec{\rho} - \vec{\rho}'$ in equation 26; correspondingly, $\vec{\rho} = \vec{R} + \Delta\vec{\rho}/2$, $\vec{\rho}' = \vec{R} - \Delta\vec{\rho}/2$ [26-28]. Then, equation 26 takes a form more convenient for subsequent transformations.

$$B_{12}(\vec{\zeta}, z; \rho_0) = |C|^2 A_1 A_2 t_0^2 \exp\left(i\frac{k}{z}\vec{\rho}_0\vec{\zeta} + i\Delta\Phi_{12}\right) \times \int_{-\infty}^{+\infty}\int U_0(\vec{R} + \frac{\Delta\vec{\rho}}{2}) U_0^*(\vec{R} - \frac{\Delta\vec{\rho}}{2}) \mu_t(\Delta\vec{\rho} - \vec{\rho}_0) \exp\left(-\frac{ik}{z}\Delta\vec{\rho}\vec{\zeta}\right) d\vec{R}d\vec{\rho}\,, \tag{27}$$

where the assumption of the statistical homogeneity of the RPS was used:

$$\left\langle t\left(\vec{R} + (\Delta\vec{\rho} - \vec{\rho}_0)/2\right) t^*\left(\vec{R} - (\Delta\vec{\rho} - \vec{\rho}_0)/2\right)\right\rangle = t_0^2\, \mu_t(\Delta\vec{\rho} - \vec{\rho}_0)\,.$$

We can obtain the expressions for the average intensities of the interfering fields, setting $\vec{\rho}_0 = 0$; in equation 27: $\left\langle I_1(\vec{\xi}, z)\right\rangle = B_{11}(\vec{\zeta}, z; \vec{\rho}_0 = 0)$ and

$$\left\langle I_2(\vec{\xi}, z)\right\rangle = B_{22}(\vec{\zeta}, z; \vec{\rho}_0 = 0)\,.$$

To simplify further transformations, assume that the SMLB was obtained by way of interference of two Gaussian laser beams, so that, for the amplitudes of the beams in the focal plane, we can write $U_0(\vec{\rho}) = \exp\left(-\vec{\rho}^2/w_0^2\right)$. Then, in equation 27,

$$U_0(\vec{R} + \frac{\Delta\vec{\rho}}{2}) U_0^*(\vec{R} - \frac{\Delta\vec{\rho}}{2}) = \exp\left(-2\frac{\vec{R}^2}{w_0^2}\right)\exp\left(-2\frac{\Delta\vec{\rho}^2}{w_0^2}\right). \tag{28}$$

Let us substitute equation 28 into equation 27 and introduce the notation

$$B(\vec{\zeta}, z; \rho_0) = \int_{-\infty}^{\infty} \exp\left(-\frac{\Delta\rho^2}{2w_0^2}\right) \mu_t(\Delta\vec{\rho} - \vec{\rho}_0) \exp\left(-i\frac{k}{z}\Delta\vec{\rho}\vec{\zeta}\right) d\vec{\rho}\,. \tag{29}$$

By using equations 27, 24, and 29, we can write the expression for the contrast of the average-intensity fringes in the diffraction field in the form

$$V = V_0 \frac{\left|B(\vec{\zeta}, z; \rho_0\right|}{B(\vec{\zeta}, z; \rho_0 = 0)}, \tag{30}$$

where $V_0 = A_1 A_2 / (A_1^2 + A_2^2)$ is the contrast of the interference fringes in the diffraction field in the absence of an RPO ($\mu_t(\Delta\vec{\rho}) \equiv 1$).

The expression for $B(\vec{\zeta}, z; \rho_0)$ and, correspondingly, for the contrast of the fringes V allows a substantial simplification if we assume that the

diameter of the focused laser beams $2w_0$ is noticeably smaller than the correlation radius of the phase inhomogeneities of the RPS l_ϕ, $2w_0 << l_\phi$ and that the probing focused beams "resolve" the structure of the RPS inhomogeneities. In this case, we can assume that the width of the Gaussian function $exp\left(-\Delta\vec{\rho}^2/2w_0^2\right)$ in equation 29 is considerably smaller than the width of the correlation function $\mu_t(\Delta\vec{\rho})$ and this width can be formally replaced by the δ-function, $exp\left(-\Delta\vec{\rho}^2/2w_0^2\right) \approx \delta(\Delta\vec{\rho})$. Then, we obtain the simple expression for the fringe contrast

$$V(\vec{\rho}_0) = V_0\,\mu_t(\vec{\rho}_0), \tag{31}$$

which, it is important to note, is valid for any statistics of the phase inhomogeneities of the RPS. Assuming Gaussian statistics of the phase inhomogeneities of the RPS, we have for $\mu_t(\vec{\rho}_0)$ as in equation 12

$$\mu_t(\vec{\rho}_0) = \exp\left\{-\sigma_\phi^2\left[1 - K_\phi(\vec{\rho}_0)\right]\right\}, \tag{32}$$

where σ_ϕ^2 is the variance of spatial fluctuations of the phase function $\varphi(\vec{\rho})$ of the RPS transmittance $t(\vec{\rho})$ and $K_\phi(\vec{\rho}_0)$ is the normalized correlation function of spatial fluctuations of the phase $\varphi(\vec{\rho})$, which is often approximated by an exponential function: $K_\phi(\vec{\rho}_0) = exp\left\{-\left|\vec{\rho}_0/l_\phi\right|^a\right\}$, where l_ϕ is the correlation radius of the phase inhomogeneities of the RPS. For statistically anisotropic RPSs, the contrast of average-intensity fringes depends on both the magnitude and the direction of the vector $\vec{\rho}_0$ (on the period Λ and the orientation of the interference fringes in the probing SMLB).

In the regime of deflection of the interference fringes, by determining the value of the relative contrast $V(\vec{\rho}_0)/V_0$ for different $\vec{\rho}_0$ (different periods of the fringes Λ) it is sufficiently easy (by using equations 9 and 10), as in Ref. [12], to realize the possibility of solving the inverse problem, i.e., the determination of the statistical parameters of the RPS σ_ϕ, l_ϕ, and a from the data of an interference experiment.

For an arbitrary relation between the radius of the probing beam w_0 and the radius of correlation of the RPS inhomogeneities l_ϕ, the explicit dependence of the fringe contrast on the RPS parameters can be obtained under the assumption of Gaussian statistics of screen inhomogeneities for the Gaussian form of the correlation coefficient of the inhomogeneities

$K_\phi(\Delta\vec{\rho}) = exp(-\Delta\vec{\rho}^2 / l_\phi^2)$. In this case, for $\mu_t(\Delta\vec{\rho})$ in form of equation 32, we can use the rather correct approximation [15]

$$\mu_t(\Delta\vec{\rho}) = exp(-\sigma_\phi^2) + \left[1 - exp(-\sigma_\phi^2)\right] exp\left(-\frac{\Delta\vec{\rho}^2}{\rho_\perp^2}\right), \tag{33}$$

where $\rho_\perp = l_\phi \left\{-ln\left[\sigma_\phi^{-2} ln\left(1 + exp(\sigma_\phi^2 - 1) exp(1)\right)\right]\right\}^{1/2}$ is the correlation radius of the function of the RPS complex transmittance $t(\vec{\rho})$. The use of equations 11 and 29 leads to the following expression for $B(\vec{\zeta}, z; \vec{\rho}_0)$:

$$\begin{aligned} B(\vec{\zeta}, z; \vec{\rho}_0) &= 2\pi w_0^2 \, exp(-\sigma_\phi^2) exp\left(-\frac{2\pi^2 w_0^2}{\lambda^2 z^2}\vec{\zeta}^2\right) \\ &+ \frac{2\pi w_0^2}{(\rho_\perp^2 + 2w_0^2)} \rho_\perp^2 \left(1 - exp(-\sigma_\phi^2)\right) exp\left[-\frac{\vec{\rho}_0^2}{(\rho_\perp^2 + 2w_0^2)}\right] \\ &\times exp\left(-\frac{2\pi^2 w_0^2 \rho_\perp^2 \vec{\zeta}^2}{\lambda^2 z^2 (\rho_\perp^2 + 2w_0^2)}\right) exp\left[-i\frac{2\pi}{\lambda z}\frac{2w_0^2 \vec{\rho}_0 \vec{\zeta}}{(\rho_\perp^2 + 2w_0^2)}\right], \end{aligned} \tag{34}$$

In the paraxial region $\vec{\zeta} \approx 0$, for the contrast of the average-intensity fringes in the diffraction field, we obtain

$$V = V_0 \frac{\mu_0 + (1-\mu_0)\, \rho_\perp^2 (\rho_\perp^2 + 2w_0^2)^{-1} exp\left(-\vec{\rho}_0^2 / (\rho_\perp^2 + 2w_0^2)\right)}{\mu_0 + (1-\mu_0)\, \rho_\perp^2 (\rho_\perp^2 + 2w_0^2)^{-1}}, \tag{35}$$

where the notation $\mu_0 = exp(-\sigma_\phi^2)$ is used.

When $2w_0^2 << \rho_\perp^2$, equation 35 takes the form $V \approx V_0 \mu_t(\vec{\rho}_0)$ and, hence, the regime of deflection of interference fringes is realized.

The curves and the experimental data presented in Figure 9, obtained for different values of w_0, illustrate the effect of the radius of the waists w_0 of the laser beam on the function $V(\rho_0)/V_0$. In the experiments, as an RPS bleached specklegrams were used, whose parameters σ_ϕ and l_ϕ were previously determined by the collimated probing SMLB method (see section 7.2).

In the regime of diffraction by a great number of inhomogeneities, $2w_0^2 >> \rho_\perp^2$ and equation 35 can be written in the form

$$V \approx V_0 \frac{\mu_0 + (1-\mu_0)(\rho_\perp^2 / 2w_0^2) exp\left(-\vec{\rho}_0^2 / 2w_0^2\right)}{\mu_0 + (1-\mu_0)(\rho_\perp^2 / 2w_0^2)}. \tag{36}$$

The further simplification of equations 35 and 36 can be realized under the assumption of small $\sigma_\phi < 1$ and relatively large $\sigma_\phi > 1$ phase perturbations; in these cases, respectively, $\rho_\perp \approx l_\phi$ and $\rho_\perp \approx l_\phi / \sigma_\phi$.

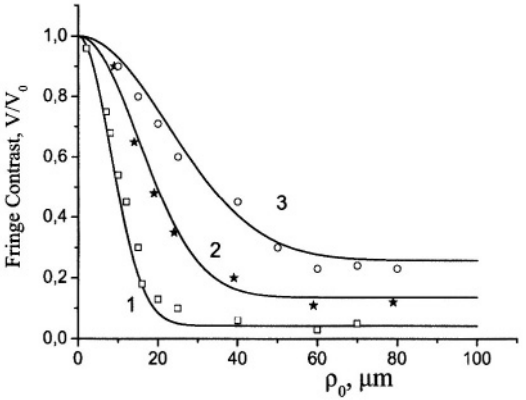

Figure 9. Contrast of the average-intensity fringes (theoretical curves and experimental data) depending on the magnitude of the transverse shift ρ_0 of the waists of the probing laser beam ($\sigma_\phi \approx 1.8$, $l_\phi \approx 18\,\mu m$): $w_0 \approx$ (1) 2.8; (2) 12, and (3) 20 μm.

Note important specific features of the obtained dependences of the fringe contrast on the parameters of the RPS and the probing SMLB in various regimes. The change in the fringe contrast V in dependence on the correlation radius of the RPS inhomogeneities l_ϕ has a nonmonotonic character with a local minimum corresponding to the regime of diffraction by a small number of scatterers (Figure 10). In the regime of diffraction by a great number of inhomogeneities, an increase in the sizes of the inhomogeneities l_ϕ is accompanied by a decrease in the fringe contrast, whereas in the regime of deflection of the fringes, with increasing l_ϕ, an increase in the contrast of the average-intensity fringes is observed. We can propose the following explanation for this specific feature. In the case of diffraction by a great number of inhomogeneities, the contrast of the average-intensity fringes is governed by the relation between the intensities of the unscattered components $\bar{I}_1$, $\bar{I}_2$ and the average intensities of the scattered components $\langle \tilde{I}_1 \rangle, \langle \tilde{I}_2 \rangle$ of the diffraction field [5, 12, 15]: $V = 2\sqrt{\bar{I}_1 \bar{I}_2} \Big/ \left[\left(\bar{I}_1 + \bar{I}_2 \right) + \left(\langle \tilde{I}_1 \rangle + \langle \tilde{I}_2 \rangle \right) \right]$. With increasing l_ϕ, the divergence of the scattered field components decreases and, correspondingly, their average intensity in small angles $\left(\vec{\zeta} \approx 0 \right)$ increases, at constant intensities of the

unscattered components $\bar{I}_1 + \bar{I}_1 \approx \left(A_1^2 + A_2^2\right) exp(-2\sigma_\phi^2)$, and the fringe contrast V decreases with increasing l_ϕ.

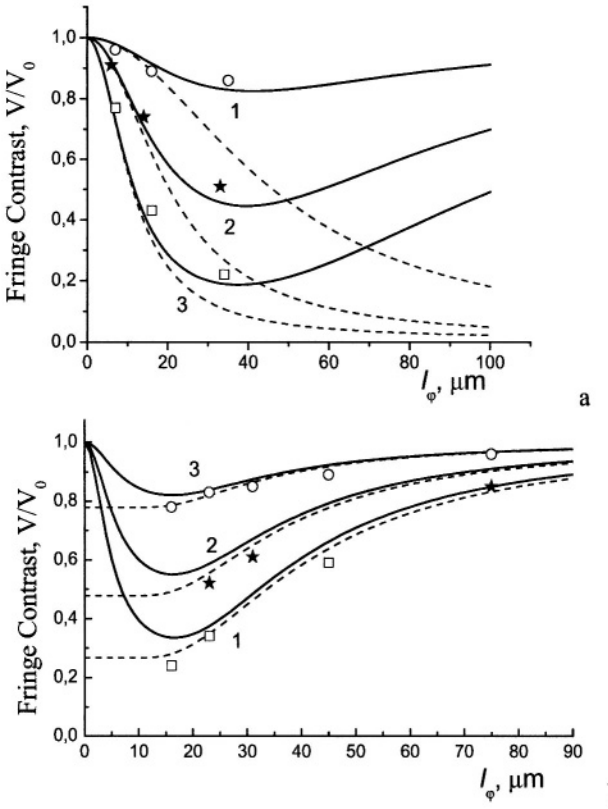

Figure 10. Contrast of the average-intensity fringes in dependence on the correlation radius l_ϕ of inhomogeneities of a random phase screen (the solid curves were obtained with the use of equation 35; the dashed curves, with approximate equations 36 and 31): (a) experimental data obtained under the conditions of diffraction by a great and small number of inhomogeneities for $w_0 \approx 20\,\mu m$ and $\rho_0 \approx 60\,\mu m$: $\sigma_\phi \approx$ (1) 0.6, (2) 1.2, and (3) 1.7; (b) experimental data obtained in the regime of deflection of the interference fringes for $w_0 \approx 5\,\mu m$ and $\rho_0 \approx 29\,\mu m$: $\sigma_\phi \approx$ (1) 0.5, (2) 0.86, and (3) 1.15.

Qualitatively different processes take place for $l_\phi > 2w_0$, when the averaging of the diffraction field occurs in the regime of deflection of the interference fringes, whose displacement amplitude is governed by the "steepness" of inhomogeneities σ_ϕ / l_ϕ. With increasing l_ϕ, the amplitude of deflection of the fringes decreases and the contrast of the average-

intensity fringes increases. These dependences are verified by experiments (Figure 10) in which statistically anisotropic RPSs (bleached specklegrams) with a correlation radius l_ϕ varying with direction at a constant σ_ϕ were used.

In the regime of diffraction by a great number of inhomogeneities at a sufficiently large ratio $2w_0/l_\phi$, one can observe an almost stepwise change in the fringe contrast in dependence on σ_ϕ in the region of $\sigma_\phi > 2$ (see Figure 3 in Ref. [15]. In this case, the virtually constant value of the fringe contrast $V(\sigma_\phi) \approx V_0$ in the range $0 < \sigma_\phi < 2$ is caused by the competition of two processes with increasing σ_ϕ: by a decrease in the intensities of the unscattered components $\bar{I}_1$, $\bar{I}_2$ and a corresponding decrease in the average intensities of the scattered field components $\langle \tilde{I}_1 \rangle$ and $\langle \tilde{I}_2 \rangle$ because of the decrease in the correlation radius of the screen transmission $\rho_\perp$. This threshold effect of variation in the contrast of the fringes of a strongly scattering object can be used in diagnostics of biological media, in the laser interference method for determining the retinal acuity of vision in the presence of cataract, and for controlling comparatively rough surfaces (see section 7.6).

An almost jump-like increase in the fringe contrast was also found in the dependence of the fringe contrast on the radius of the probing beam w_0 in the region $0 < w_0 < 20\ \mu m$ at comparatively small values of $\sigma_\varphi \le 1{,}5$ and small sizes of the inhomogeneities $l_\phi \approx 5\ \mu m$. This effect can be used, in particular, in laser interference retinometry, in the case of cataract, for the enhancement of the contrast of the average-intensity fringes being observed and for the early detection of cataract by the eye retinal acuity estimations using laser beams with different divergences (section 7.6).

Let us turn our attention to another consequence following from equation 36, which is valid for the regime of diffraction by a great number of RPS inhomogeneities. For $\sigma_\phi > \pi$ (a strong scatterer), $\mu_0 = exp(-\sigma_\phi^2) \approx 0$ and the contrast of the average-intensity fringes is virtually independent of the parameters of the RPS inhomogeneities, but is governed by the normalized correlation function of the amplitude of the field of the focused probing laser beams:

$$V(\vec{\rho}_0)/V_0 \approx exp\left(-\vec{\rho}_0^2/2w_0^2\right). \qquad (37)$$

In this case, unscattered components are virtually absent in the diffraction field and the interference fringes are observed only under the condition of partial correlation of the scattered components, which takes place in the case

of a partial overlap of the probing beams on the RPS surface, i.e., when $\rho_0 \le \sqrt{2} w_0$.

7.3.3 Discussion and Conclusions

Approximate expression in equation 33 for the RPO transmittance correlation function $\mu_t(\Delta\vec{\rho})$ allowed us to obtain an analytical expression for the contrast of interference fringes of average intensity as a function of the parameters of the RPO and the probing SMLB. The accuracy of this approximation is analyzed in Ref.[15]. The difference between the theoretical values for the fringe contrast that were obtained with the use of equation 33 and those obtained with the help of the numerical calculations using equation 32 for $\mu_t(\Delta\vec{\rho})$ does not exceed 10%. The maximum discrepancy is observed for the dependence of V on σ_ϕ for $\sigma_\phi \approx 2$. However, the tendencies and specific features of all the dependences of V on σ_ϕ, l_ϕ, ρ_0, and w_0 are retained. Thus, the expression for $V(\sigma_\phi, l_\phi, \rho_0, w_0)$ obtained in analytical form allows one to analyze in detail the dependence of V on the parameters of the RPS and the probing SMLB.

For solving the inverse problem, i.e., for determining the average statistical parameters of inhomogeneities of random phase objects, the regime of deflection of interference fringes is most efficient. In this regime, the relation between the fringe contrast and the object parameters has the simplest form of equation 31. However, to realize this regime, sharp focusing of the laser beam is necessary, under which the diameters $2w_0$ of the focused beams are considerably smaller than the transverse sizes l_ϕ of the inhomogeneities of the RPO.

Note an important practical specific feature of the processes under consideration. When displacing the RPO along the optical axis out of the plane of focusing of the SMLB, the contrast of the average-intensity fringes, as experiment shows, remains unchanged for all three regimes. In the regime of deflection of the fringes, the defocusing results in qualitative changes in the diffraction field: A great number of object inhomogeneities fall into the illuminated region on the object surface, and the sizes of speckles in the diffraction field become smaller than the period of the interference fringes. Thus, the invariability of the fringe contrast is determined by the constancy of the ratio $l_\phi / 2w_0 >> 1$ and, hence, by the invariable relation between the divergences of the unscattered and scattered components of the diffraction field. Apparently, the relation between the divergences of the scattered and unscattered components of the diffraction field, which, in their turn, are determined respectively by the correlation radius of the RPO transmittance

$\rho_\perp$ and the radius of the focused laser beam w_0, serves as a governing factor in different regimes. Therefore, the absence of stringent requirements for the focusing onto the scattering surface provides the possibility of using the method being discussed for diagnostics of three-dimensional scattering media.

When displacing the scattering surface out of the plane of focusing of the laser beams, in addition to an increase in the illuminated region itself, the overlap of the laser beams on the object surface also increases. The scattered fields of each beam acquire a larger degree of identity, which, it would seem, must be accompanied by an increase in the contrast of the average-intensity fringes. However, since in the out-of-focus zone in the region of crossing of the beams, interference fringes are formed, the diffracted fields acquire a transverse mutual shift (see section 7.2), which in the far zone exceeds the transverse sizes of speckles, and the scattered components of the interfering fields prove to be mutually uncorrelated at each point of the space.

The optical averaging necessary for observation of average intensity interference fringes using of focused SMLB can be realized by movement of the object or its inhomogeneities, or by scanning object by an illuminating beam. The special way of averaging consists of simultaneous illumination of an object by a set of the focused SMLB obtained, or with the help of additional scatterer, being an irregular diffractive grating [17] or with the help of a special diffractive optical element with double identical diffractive microstrucrure [18]. The optical systems based on these principles of probing of random phase objects are considered in the following sections of the chapter.

7.4 INTERFERENCE FRINGES IN IMAGING SYSTEMS

In the previous section it was established that the parameters of the phase inhomogeneities of an object satisfying the "random phase screen" model can be determined using a spatially modulated laser probe beam focused onto the surface of the screen. In order to observe the average inteneity interference fringes which carry the information on the inhomogencity parameters it is necessary to move the object or the inhomogeneities relative to the probe beam. Equivalent averaging is performed by scanning the laser beam over the object. In the present section we consider an alternative method of obtaining average-intensity fringes with both the object and the probe beam fixed. This method involves simultaneous probing the object with ensemble of the focused SMLBs obtained using a primary diffuser functioning as an irregular diffraction grating. The method is based on the use of a telescope imaging system with an illuminating SMLB, a diffuser in

the entry plane and a random phase object in the spatial-frequency plane. It is shown that the system can operate as a shift interferometer where the contrast of the fringes in the image plane is independent on the primary diffuser characteristics. Analytic expressions are obtained for the contrast of the fringes as a function of the parameters of the object and the illuminating SMLB. The dependence of the optical transfer function of the system under study on spatial coherence of the light in the pupil of the system with the random phase screen is established

In shearing interferometers the fringe contrast is determined by the modulus of the transverse spatial coherence function of the light field in the plane of mutual shift of the fields and by the shift magnitude and direction [33,42,43]. When interferometers of this kind are used for a scattered coherent light, e.g., in the problems of controling statistical parameters of randomly inhomogeneous objects, the contrast of the averaged intensity fringes is determined by the normalized correlation function of complex amplitudes of the fields and, in particular, of the boundary fields, if the interference pattern is detected in close proximity to the surface of the object [1,3,5,10]. The statistical averaging of intensity of the coherent scattered fields makes the interference systems equivalent in partially coherent light or totally coherent scattered light [27,33].

At the same time, the image contrast of an object with sinusoidal amplitude transmission in an incoherent optical system is known to be determined by modulus of the optical transfer function (OTF) [32, 45-47], which, in the presence of a thin scattering screen in the pupil of the system, equals the normalized correlation function of complex transmittance of the screen [27, 46]. In the coherent analogue of such a system, where the image of the sinusoidal fringes is formed through a scattering screen placed in the pupil of the system, the fringe contrast of the image upon statistical averaging of the light intensity, is also determined by the correlation function of the screen transmittance [48]. In this section, we successively analyze the processes of the interference-pattern image formation in a coherent imaging system with a thin scattering medium, satisfying the "random phase screen" model in the pupil of the system.

7.4.1 Fringe Contrast in the Image of the Interference Pattern. Localization of Interference Fringes

To simplify the formal analysis, we will consider, following Ref. [27], an imaging optical system with a double Fourier transform (Figure 11). The scatterer S_1 placed in the front focal plane of the Fourier-transforming lens L_1 is exposed simultaneously to two quasi-plane waves, which produce

rectilinear equidistant interference fringes in the irradiating laser beam, with the field distribution in this plane given by equation 38

$$I(\vec{r}) = 2I_0(\vec{r})\left\{1 + V_0 \cos\left(\Delta\vec{k}_{12}\vec{r}\right)\right\}, \tag{38}$$

where $I_0(\vec{r})$ is the distribution of the laser-beam average intensity. $\left|\Delta\vec{k}_{12}\right| = \left|\vec{k}_1 - \vec{k}_2\right| = k2\sin(\theta/2) \approx k\theta$, $\Delta\vec{k}_{12}$ and θ are, respectively, the difference between the wave vectors and the angle between the wave propagation directions in the irradiating beam, and V_0 is the contrast of the pattern with periodic fringes spaced by $\Lambda = 2\pi/\left|\Delta\vec{k}_{12}\right|$.

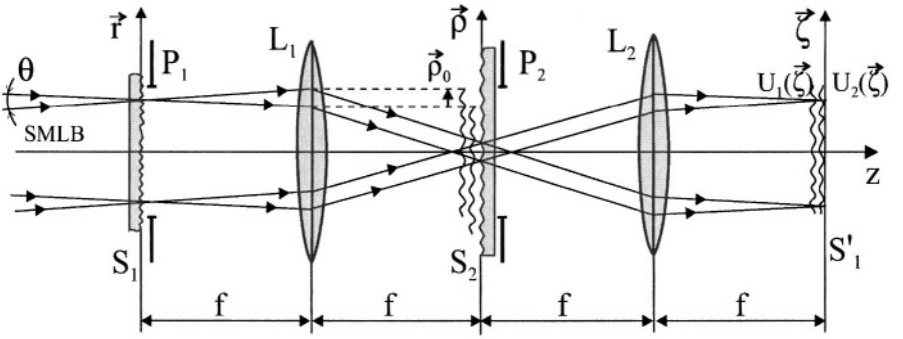

Figure 11. Optical system of the interference pattern imaging in the presence of a random phase screen in the spatial–frequency plane of the system: SMLB is illuminating laser beam with parallel interference fringes; L_1 and L_2 are collecting lenses; S_1 is a scatterer in the focal plane of the lens L_1; S_2 is a random phase screen in the rear focal plane of the lens L_1; P_1 and P_2 are diaphragm of the field of view and aperture diaphragm of the system; S_1' is an image of the scatterer S_1; and $U_1(\vec{\zeta})$ and $U_2(\vec{\zeta})$ are interfering fields in the image plane.

In this way, the interference field localized on the scatterer S_1 is formed. The image contrast of this field is analyzed in the exit plane of the system, i.e., in the rear focal plane of the second Fourier-transforming lens L_2. The RPS S_2 is arranged in the spatial-frequency plane of the system, i.e., in the rear focal plane of the Fourier-transforming lens L_1.

Without RPS in the system, the localized interference pattern is formed in the image space with the maximum contrast in the plane of the image. The effect of spatial localization of the fringes can be explained as follows. Since the rectilinear interference fringes are produced by exposing the scatterer S_1 simultaneously to two quasi-plane waves with the propagation directions

differing by the angle θ, two identical speckle-fields are formed behind the scatterer and propagate at the same angle θ to each other (see section 7.2). Therefore, there arises a transverse spatial shift $\Delta r = \theta z = \lambda z / \Lambda$ between these fields, increasing linearly with the distance z from the scatterer S_1. In the rear focal plane of the lens L_1, the mutual shift between the fields is $\Delta\rho = \rho_0 = \lambda f / \Lambda$, where f is the focal length of the lens. In the image space of the scatterer S_1, the mutual shift between identical speckle fields, under unit magnification of the optical system, is $\Delta\zeta(l) = \lambda l / \Lambda$, where l is the distance from the image plane. Thus, in the image space, we observe the interference pattern of the identical speckle-fields $U_1(\vec{\zeta}, z)$ and $U_2(\vec{\zeta}, z) = U_1(\vec{\zeta} - \Delta\vec{\zeta}(l), z)$ with the mutual spatial shift $\Delta\vec{\zeta}$ varying along the z axis. The average intensity fringe contrast in this pattern, $V(\Delta\vec{\zeta})$, is proportional to the modulus of the normalized transverse correlation function of the speckle-fields $B_{11}(\Delta\vec{\zeta})$, and, in conformity with the Van Cittert–Zernicke theorem [27, 31, 41], is determined, for a circular pupil in the system under study, by the expression

$$V(\Delta\zeta)/V_0 = |B_{11}(\Delta\zeta)| / B_{11}(0) = 2|J_1(\pi D_2 \Delta\zeta / \lambda f)/(\pi D_2 \Delta\zeta / \lambda f)|, \quad (39)$$

where $J_1(u)$ is the first-order Bessel function and D_2 is the diameter of the pupil P_2. The fringes vanish wherever the transverse shift between the fields becomes equal to the correlation radius of the fields ($\Delta\zeta = \rho_c$ or $\lambda l / \Lambda = 1.22 \lambda f / D_2$). Hence, the length of the fringe localization region is $2l \approx 2f\Lambda / D_2$.

The presence of the RPS in the spatial–frequency plane of the system leads to decorrelation of the identical speckle fields $U_1(\vec{\zeta}, z)$ and $U_2(\vec{\zeta}, z)$ and to a decrease in the contrast of the average intensity fringcs in the image plane. Indeed, since the identical speckle fields in the rear focal plane of the lens L_1 have the mutual transverse shift $\rho_0 = f|\Delta\vec{k}_{12}|/k = \theta f = \lambda f / \Lambda$, they pass through the RPS in spatially and structurally different regions. For this reason, the identical speckle fields acquire additional random phase modulation. The degree of statistical variation of this modulation is determined by the ratio of the shift ρ_0 to the correlation radius of the RPS inhomogeneities l_ϕ and depends also on the modulation depth, i.e., on the variance of the spatial phase fluctuations σ_ϕ^2.

In the image plane, where the mutual shift between the speckle fields is zero, the average intensity fringe contrast decreases due to correlation

between the fringes in the RPS plane. For this reason, the fringe contrast in the image plane should be determined by the modulus of the normalized cross-correlation function $B_{12}(\vec{\zeta},\vec{\rho}_0)$ of the light fields $U_1(\vec{\zeta})$ and $U_2(\vec{\zeta})$ in this plane; i.e.,

$$\frac{V(l=0)}{V_0}=\left|\frac{B_{12}(\vec{\zeta},\vec{\rho}_0)}{B_{12}(\vec{\zeta},\vec{\rho}_0=0)}\right|, \quad B_{12}(\vec{\zeta},\vec{\rho}_0)=\left\langle U_1(\vec{\zeta})U_2^*(\vec{\zeta})\right\rangle , \qquad (40)$$

where the angle brackets denote statistical averaging.

Outside the image plane, this decorrelation is complemented by that related to the mutual shift $\Delta\vec{\zeta}(l)$ of the fields. Therefore, in view of equation 29, the general expression for the fringe contrast can be written as

$$\frac{V}{V_0}=\left|\frac{B_{12}(\vec{\zeta},\vec{\rho}_0)}{B_{12}(\vec{\zeta},\vec{\rho}_0=0)}\right|\cdot\left|\frac{2J_1(\pi D_2\Delta\zeta/\lambda f)}{\pi D_2\Delta\zeta/\lambda f}\right| . \qquad (41)$$

This expression determines the longitudinal variations of the fringe contrast in the interference-pattern localization region, with the RPS in the spatial–frequency plane of the optical system.

The theoretical dependences plotted according to equation 41 and the experimental points for the relative fringe contrast are shown in Figure 12. In these experiments, bleached specklegrams were used as RPSs [12].

7.4.2 Cross-Correlation Function of the Interfering Fields

Let the scatterer S_1 and the RPS S_2 be characterized by the complex transmittances $t_1(\vec{r})$ and $t_2(\vec{\rho})$, respectively. Then, using two successive Fourier-transforms and assuming that all the scattered light enters the apertures of the lenses L_1 and L_2, we can write the following equation (valid to within factors unessential here) for the complex amplitude of the field $U_1(\vec{\zeta})$:

$$U_1(\vec{\zeta})=\int_{-\infty}^{+\infty}\int_{-\infty}^{+\infty}U_0(\vec{r})\exp(i\vec{k}_1\vec{r})t_1(\vec{r})P_1(\vec{r})\exp\left(i\frac{k}{f}\vec{r}\vec{\rho}\right)t_2(\vec{\rho})P_2(\vec{\rho}) \times\exp\left(i\frac{k}{f}\vec{\zeta}\vec{\rho}\right)d^2\vec{r}\,d^2\vec{\rho} . \qquad (42)$$

Here, $U_0(\vec{r})$ is the complex amplitude of one of the quasi-plane waves in the laser beam illuminating the scatterer S_1, $\vec{k}_1$ is the wave vector of this wave, and $P_1(\vec{r})$ and $P_2(\vec{\rho})$ are the transmission functions of the field and aperture diaphragms of the system. The equation for the field $U_2(\vec{\zeta})$ has a similar form with the vector $\vec{k}_1$ replaced by $\vec{k}_2$.

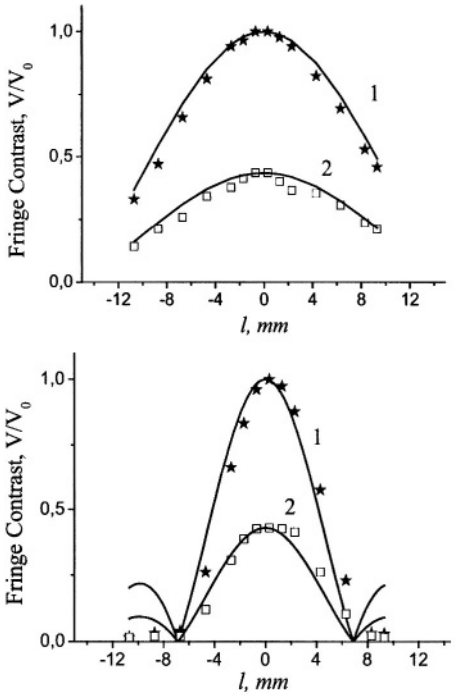

Figure 12. Longitudinal distribution of the fringe contrast (theoretical curves and experimental points) in the region of localization of the image (1) in the absence and (2) in the presence of the RPS in the pupil of the system for $D/\Lambda =$ (a) 11.25 and (b) 25.

By substituting equations 42 for $U_1(\vec{\zeta})$ and $U_2(\vec{\zeta})$ into equation 40, by changing the order of integration and averaging, and by taking into account the mutual independence of the random functions $t_1(\vec{r})$ and $t_2(\vec{\rho})$, we arrive at the following expression for the cross-correlation function of the complex amplitudes of the fields in the image plane:

$$B_{12}(\vec{\zeta},\Delta\vec{k}_{12})=\int_{-\infty}^{+\infty}\int_{-\infty}^{+\infty}\left\langle I_f(\vec{\rho})\right\rangle P_2\left(\vec{\rho}+\frac{\Delta\vec{\rho}}{2}\right)P_2^*\left(\vec{\rho}-\frac{\Delta\vec{\rho}}{2}\right)$$
$$\times B_f\left(\Delta\vec{\rho}+\frac{f}{k}\Delta\vec{k}_{12}\right)\mu_{t_2}(\Delta\vec{\rho})\,exp\left(i\frac{k}{f}\vec{\zeta}\Delta\vec{\rho}\right)d^2\vec{\rho}\,d^2\Delta\vec{\rho}\,, \tag{43}$$

Here, $\left\langle I_f(\vec{\rho})\right\rangle=\int_{-\infty}^{+\infty}\int\mu_{t_1}(\Delta\vec{r})exp\left(i\frac{k}{f}\Delta\vec{r}\vec{\rho}\right)d^2\Delta\vec{r}$ is the distribution of the average intensity in the rear focal plane of the lens L_1 (the spatial spectrum of the scatterer S_1); the function $B_f\left(\Delta\vec{\rho}+\frac{f}{k}\Delta\vec{k}_{12}\right)=\int_{-\infty}^{+\infty}\int I_0(\vec{r})\left|P_1(\vec{r})\right|^2 exp\left(i\frac{k}{f}\Delta\vec{\rho}+\frac{f}{k}\Delta\vec{k}_{12}\right)d^2\vec{r}$ has the meaning of the autocorrelation function of the field illuminating the RPS; $\mu_{t_1}(\Delta\vec{r})$ and $\mu_{t_2}(\Delta\vec{\rho})$ are the normalized autocorrelation functions of the complex transmittances of the scatterer S_1 and the RPS S_2, respectively.

Equation 43 was derived based on the following assumptions:
(i) the complex field amplitude $U_0(\vec{r})$ and the aperture function $P_1(\vec{r})$ depend more weakly on $\vec{r}$ compared to $t_1(\vec{r})$ within the scale of variation of the function $\mu_{t_1}(\Delta\vec{r})$, so that
$U_0(\vec{r}+\Delta\vec{r}/2)U_0^*(\vec{r}-\Delta\vec{r}/2)\approx U_0(\vec{r})U_0^*(\vec{r})=I_0(\vec{r})$ and
$P_1(\vec{r}+\Delta\vec{r}/2)P_1^*(\vec{r}-\Delta\vec{r}/2)\approx\left|P_1(\vec{r})\right|^2$; this means that dimensions of spatial structure of the illuminating field $U_0(\vec{r})$ and the size of the field aperture P_1 are much larger than the individual inhomogeneities of the scatterer S_1;
(ii) the wave propagation direction in the illuminating beam is symmetric with respect to the longitudinal coordinate z, so that $(\vec{k}_1+\vec{k}_2)\vec{r}=0$; and
(iii) the scatterer S_1 and the RPS S_2 are statistically uniform, so that $\mu_{t_1}(\vec{r},\Delta\vec{r})=\mu_{t_1}(\Delta\vec{r})$, and $\mu_{t_2}(\vec{\rho},\Delta\vec{\rho})=\mu_{t_2}(\Delta\vec{\rho})$.

An Optical System without RPS

Let us assume that there is no RPS S_2 in the system. Then, we have to set $\mu_{t_2}(\Delta\vec{\rho})=1$ in equation 43. If the function $B_f(\Delta\vec{\rho})$ is substantially narrower than $P_2(\vec{\rho}+\Delta\vec{\rho}/2)P_2^*(\vec{\rho}-\Delta\vec{\rho}/2)$, which in fact means that the field correlation radius ρ_f in the pupil P_2 is much smaller than the pupil diameter, then this field may be regarded as δ-correlated and we may set in equation 6 $B_f(\Delta\vec{\rho}+f\Delta\vec{k}_{12}/k)=\delta(\Delta\vec{\rho}+\vec{\rho}_0)$, where $\vec{\rho}_0=f\Delta\vec{k}_{12}/k$ is the

vector of spatial shift of the fields in the spatial–frequency plane of the system. In this case, equation 43 can be rearranged to the form

$$B_{12}\left(\vec{\zeta},\vec{\rho}_0\right)=exp\left(i\frac{k}{f}\vec{\zeta}\vec{\rho}_0\right)\int_{-\infty}^{+\infty}\left\langle I_f(\vec{\rho})\right\rangle P_2(\vec{\rho}+\vec{\rho}_0/2)P_2^*(\vec{\rho}-\vec{\rho}_0/2)d^2\vec{\rho} \quad . \quad (44)$$

If the scatterer S_1 is δ-correlated, then $\left\langle I_f(\vec{\rho})\right\rangle = const$, and equation 44 acquires the form of an autocorrelation function of transmittance of the optical system pupil, which is the classical expression for the OTF of the system [8, 10]. Thus, the fringe contrast is determined, according to equation 40, by the OTF modulus, similar to the process for a completely spatially incoherent system. A partial coherence of the illuminating light should result in taking into account, in equation 44, the finite extent of the function $\left\langle I_f(\vec{\rho})\right\rangle$ in the spatial-frequency plane. This dependence will be most pronounced for comparable widths of the functions $\left\langle I_f(\vec{\rho})\right\rangle$ and $P_2(\vec{\rho})$.

If the aperture of the diaphragm P_1 is not large enough, the function $B_f(\Delta\vec{\rho})$ may appear to be comparable in its width to the function $P_2(\vec{\rho}+\Delta\vec{\rho}/2)P_2^*(\vec{\rho}-\Delta\vec{\rho}/2)$. In this case, $B_f(\Delta\vec{\rho})$ in equation 43 cannot be approximated by δ-function. Therefore, the correlation function $B_{12}\left(\vec{\zeta},\vec{\rho}_0\right)$ and, hence, the fringe contrast V in the image appear to depend on the field-of-view aperture P_1 or, similarly, on the transverse size of the object. If we consider an incoherent optical system (the field is δ-correlated in the object plane), a decrease in the object aperture is accompanied by an increase in the spatial coherence radius ρ_f of the field in the spatial-frequency plane of the system. For this reason, the dependence of the image fringe contrast on the object aperture should be interpreted, from the physical point of view, as the effect of the degree of spatial coherence of the field in the pupil of the imaging system on the contrast of the image to be formed. This effect is most noticeable when the spatial coherence radius ρ_f is comparable to the diameter of the pupil aperture. If, however, the optical system shows considerable aberrations and, hence, the transmission function of the pupil $P_2(\vec{\rho})$ shows a high frequency spatial structure, the effect of the aperture of the object on the contrast of its image should manifest itself at comparatively large apertures of the object, when the correlation radius ρ_f appears to be comparable to the characteristic dimensions of structural elements of $P_2(\vec{\rho})$. A prominent example of such a situation is the case when there is a scattering medium, in the pupil of the optical system, with the dimensions of its inhomogeneities being comparable to, or even smaller than, the spatial

correlation radius of the field in the pupil. Let us consider such a system in more detail.

The RPS in the Spatial-Frequency Plane

Let a thin scattering screen be placed in the pupil P_2 of the optical system shown in Figure 11. Structural elements of the screen are supposed to be much smaller than dimensions of the pupil. Then we can set in equation 6 $P_2(\vec{\rho}+\Delta\vec{\rho}/2)P_2^*(\vec{\rho}-\Delta\vec{\rho}/2)\approx|P_2(\vec{\rho})|^2$ in comparison with $\mu_{t_2}(\Delta\vec{\rho})$, and, for the cross-correlation function $B_{12}(\vec{\zeta},\vec{\rho}_0)$ we obtain

$$B_{12}(\vec{\zeta},\vec{\rho}_0)=\int_{-\infty}^{+\infty}\int\langle I_f(\vec{\rho})\rangle|P_2(\vec{\rho})|^2\,d^2\vec{\rho}$$
$$\times\int_{-\infty}^{+\infty}\int B_f(\Delta\vec{\rho}+\vec{\rho}_0)\,\mu_{t_2}(\Delta\vec{\rho})\,exp\left(i\frac{k}{f}\vec{\zeta}\Delta\vec{\rho}\right)d^2\Delta\vec{\rho} \quad . \qquad (45)$$

By substituting equation 45 into equation 40, we can see that contrast of the interference fringes in the image is independent of $\langle I_f(\vec{\rho})\rangle$ and, hence, of $\mu_{t_1}(\Delta\vec{r})$; i.e., it is independent of the scattering properties of the first scatterer. For this reason, this scatterer, in general, may be absent in the system.

For sufficiently large field-of-view aperture P_1, at which the width of the function $B_f(\Delta\vec{\rho})$ is substantially smaller than the width of the function $\mu_{t_2}(\Delta\vec{\rho})$, so that $B_f(\Delta\vec{\rho})$ may be approximated by the δ-function, the formula for the fringe contrast becomes extremely simple as equation 31 in section 7.3, i.e.,

$$V=V_0\,\mu_{t_2}(\Delta\vec{\rho}=\vec{\rho}_0)\,. \qquad (46)$$

The contrast of the interference fringes in the image is governed only by the normalized correlation function of the RPS complex transmittance as a function of the magnitude and direction of the mutual shift $\vec{\rho}_0$, i.e., of the period Λ and orientation of the fringes in the illuminating laser beam, $|\vec{\rho}_0|=\lambda f/\Lambda$. A similar dependence of the interference pattern contrast on the transmission correlation function of a random phase object is characteristic of the transverse shearing interferometers [1-3, 5, 10, 12]. For this reason, the optical system of the interference pattern image formation under study may be considered as a shearing interferometer, provided that the correlation radius ρ_f of the field in the spatial-frequency plane is

substantially smaller than the correlation radius of the RPS transmittance $\rho_\perp$, $\rho_f << \rho_\perp$.

Let us make some estimates. Using the Van Cittert–Zernicke theorem, we can write $\rho_f \approx \lambda f / D_1$, where D_1 is the diameter of the field diaphragm P_1 [27]. For the RPS with the Gaussian distribution of inhomogeneities, the correlation function of its transmittance $\mu_{t_2}(\Delta\vec{\rho})$ can be presented in the explicit form [26, 27] as

$$\mu_{t_2}(\Delta\vec{\rho}) = \exp\left\{-\sigma_\phi^2\left[1 - K_\phi(\Delta\vec{\rho})\right]\right\}, \tag{47}$$

where σ_ϕ^2 is the variance of the phase fluctuations acquired by the illuminating field on the RPS; $K_\phi(\Delta\vec{\rho})$ is the screen inhomogeneity correlation factor, which is often approximated by a Gaussian; $K_\phi(\Delta\vec{\rho}) = exp\left(-\Delta\vec{\rho}^2 / l_\phi^2\right)$; and l_ϕ is the correlation radius (mean correlation size) of the screen inhomogeneities. At $\sigma_\phi < 1$, the correlation radius of the screen transmittance is $\rho_\perp \approx l_\phi$, and at $\sigma_\phi > 1$, $\rho_\perp \approx l_\phi / \sigma_\phi$ [15]. Using these estimates, we can determine the conditions for operation of the imaging optical system under study in the mode of a shearing interferometer.

Note also that the direct dependence of contrast in interference fringes of average intensity on the RPS transmittance correlation function, similar to equation 46, takes place upon probing of the screen with a sharply focused spatially-modulated laser beam in the interference fringe deflection regime [16], when the probe-beam waist radius in the plane of the screen w_0 is substantially smaller than the transverse dimensions of the screen inhomogeneities l_ϕ, $w_0 << l_\phi$.

A decrease in diameter D_1 of the field diaphragm P_1 gives rise to an increase in the correlation radius ρ_f of the field illuminating the RPS S_2 and leads to increasing contrast of the interference fringes in the image plane [see Figures 13 and 14(b)].

To obtain an analytical expression for the fringe contrast at an arbitrary field of view of the optical system, we assume that the diaphragm P_1 is infinitely large, and the field of view is limited by the aperture $D_1 = 2w$ of the illuminating laser beam with a Gaussian profile of the mean intensity $I_0(\vec{r}) = I_0\, exp\left(-2\vec{r}^2 / w^2\right)$. Let us assume also that the RPS inhomogeneities have a normal distribution, and their correlation coefficient $K_\phi(\Delta\vec{\rho})$ is of Gaussian shape. Then, for $\mu_{t_2}(\Delta\vec{\rho})$, instead of equation 47, we can use the approximate equation 33 convenient for integration:

$$\mu_{t_2}(\Delta\vec{\rho}) \approx \left[1 - exp\left(-\sigma_\phi^2\right)\right] exp\left(-\frac{\Delta\vec{\rho}^{\,2}}{\rho_\perp^2}\right) + exp\left(-\sigma_\phi^2\right). \qquad (48)$$

Here, $\rho_\perp = l_\phi \left\{-ln\left[\sigma_\phi^{-2} \cdot ln\left[1 + \left(exp\left(\sigma_\phi^2\right) - 1\right) exp(-1)\right]\right]\right\}^{1/2}$ is the correlation radius of the RPS transmission function at any values of σ_ϕ.

Using these approximations in equation 45, we can obtain the following expression for the fringe contrast in the paraxial region of the image $\vec{\zeta} = 0$ (see for comparison the equation 36):

$$V = V_0 \frac{\mu_0 + (1-\mu_0)\rho_\perp^2\left(\rho_\perp^2 + \rho_f^2\right)^{-1} exp\left[-\rho_0^2/\left(\rho_\perp^2 + \rho_f^2\right)\right]}{\mu_0 + (1-\mu_0)\rho_\perp^2\left(\rho_\perp^2 + \rho_f^2\right)^{-1}}. \qquad (49)$$

Here, $\mu_0 = exp\left(-\sigma_\phi^2\right)$ and $\rho_f = \sqrt{2}\,\lambda f/\pi w$ is the correlation radius of the field illuminating the RPS S_2. Figure 14 shows theoretical plots, obtained using equation 49, and experimental points for the relative fringe contrast V/V_0 in the interference-pattern image as a function of the parameters of the object-illuminating field ρ_0, Λ, and ρ_f, as well as the RPS parameters l_ϕ and σ_ϕ. One can distinctly see that the fringe contrast is enhanced with increasing correlation radius of the field ρ_f (with decreasing aperture of the field of view $2W$).

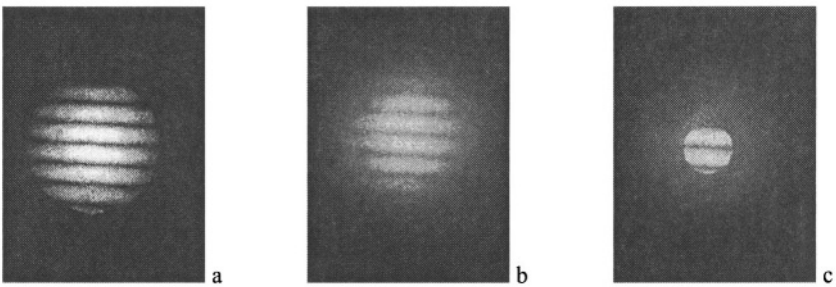

Figure 13. The patterns of interference fringes in the image (a) with and (b, c) without the random phase screen in the spatial-frequency plane of the optical system for different diameters of the field-of-view diaphragm.

The dependence of the fringe contrast on the correlation radius l_ϕ, of the RPS inhomogeneities, as follows from equation 49, shows an interesting feature consisting in the presence of a local minimum (Figure 15). At $l_\phi < \rho_f$, when many scattering centers of the RPS are within the correlation

area, the fringe contrast increases with l_ϕ. The local minimum is formed at $\rho_f \approx l_\phi$ and shifts toward larger l_ϕ with increasing ρ_0. This enhances the decorrelation of the speckle fields passed through the RPS. The enhancement of the fringe contrast with increasing l_ϕ is observed at $l_\phi > \rho_f$, when the correlation structure of the speckle fields probing the screen is found to be finer than that of the RPS. In this case, we can state that the probe field, in a certain sense, resolves the screen structure, and the fringe contrast of the image obeys equation 46.

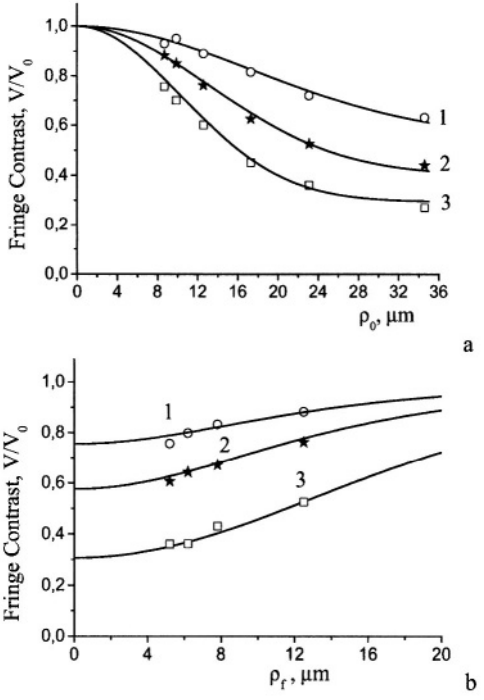

Figure 14. Contrast of the interference fringes in the image: (a) as a function of the parameter $\rho_0 = \lambda f / \Lambda$ (of the fringe period Λ) for the RPS with $\sigma_\phi = 1.15$ and $l_\phi = 17\,\mu m$ for different values of the illuminating laser-beam apertures $2w$ and, respectively, for different values of the correlation radius of the field probing the RPS at $f = 110\,mm$: (1) for $2W$ = 3*mm* and $\rho_f = 20.8\,\mu m$; (2) for $2W$ = 5*mm* and $\rho_f = 12.5\,\mu m$; and (3) for $2W$ = 12*mm* and $\rho_f = 5.2\,\mu m$. (b) As a function of the field correlation radius ρ_f (of the aperture of the beam $2w$) for different values of the fringe pattern period: for Λ = (1) 8, (2) 5.5, and (3) 3 *mm.*

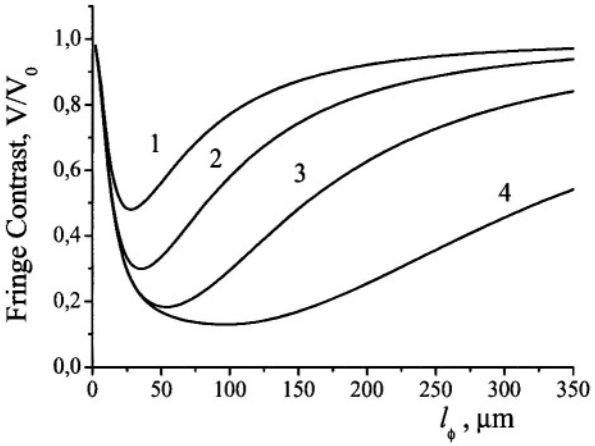

Figure 15. Contrast of the interference fringes of the image as a function of the correlation radius of inhomogeneities of the RPS for different periods of the fringe patterns and, correspondingly, for different values of mutual shift of the speckle fields ρ_0 probing the RPS ($\sigma_\phi = 1.5$, $\rho_f = 28\,\mu m$): for p_0 = (1) 40, (2) 60, (3) 100, and (4) 200 μm.

Optical System in the Absence of the Scatterer S_1

If there is no scatterer S_1 in the optical system under study, the RPS is illuminated by focused fields, i.e., by two focused laser beams. In order to observe in such a system the pattern of fringes of average intensity in the rear focal plane of the lens L_2, one has either to transversely shift the RPS or to scan the laser beam itself over the screen (see section 7.3). This operation of the intensity averaging is physically equivalent to statistical averaging. Therefore, the contrast of fringes with average intensity is determined, in this case, by the cross-correlation function of the light fields $U_1(\vec{\zeta})$ and $U_2(\vec{\zeta})$ formed due to diffraction of each of the beams on the RPS. In this case, the interference fringes are not localized, as in the presence of the scatterer S_1 in the system, and their contrast is given by equation 40.

If the interference pattern is formed in the illuminating beam by a superposition of two Gaussian beams with the amplitude distributions $U_0(\vec{r}) = A_0 \exp(-\vec{r}^2/w^2)$, and the beam aperture is assumed to be much smaller than the diameter of the field aperture P_1 $(2w << D_1)$, then, by setting in equation 42 $P_1(\vec{r}) = 1$ and $t_1(\vec{r}) = 1$, we can obtain for the cross-correlation function $B_{12}(\vec{\zeta}, \vec{\rho}_0)$ the expression similar to equation 45:

$$B_{12}(\vec{\zeta},\vec{\rho}_0)=\int_{-\infty}^{+\infty}\int I_f(\vec{\rho})|P_2(\vec{\rho})|^2 d^2\vec{\rho}\int_{-\infty}^{+\infty}\int B_f(\Delta\vec{\rho}+\vec{\rho}_0)\mu_{t_2}(\Delta\vec{\rho})exp\left(i\frac{k}{f}\vec{\zeta}\Delta\vec{\rho}\right)d^2\Delta\vec{\rho} \quad , \quad (50)$$

where $|\vec{\rho}_0|=\lambda f/\Lambda$ is the distance between the waist centers of the focused laser beams in the RPS plane,

$$B_f(\Delta\vec{\rho}+\vec{\rho}_0)=\int_{-\infty}^{+\infty}\int exp\left(-2\vec{r}^2/w^2\right)exp(ik(\Delta\vec{\rho}+\vec{\rho}_0)/f)d^2\vec{r}\ ,$$

and

$$I_f(\vec{\rho})=\int_{-\infty}^{+\infty}\int A_0^2\ exp\left(-\Delta\vec{r}^2/w^2\right)exp(ik\,\vec{\rho}\Delta\vec{\rho}/f)d^2\Delta\vec{\rho}\ .$$

By using approximate equation 48 for $\mu_{t_2}(\Delta\vec{\rho})$, we obtain for the fringe contrast, in accordance with equation 40, an expression coinciding with equation 49 by substituting $\sqrt{2}w_0$ for ρ_f, where $w_0=\lambda f/\pi w$ is the waist radius of the laser beams on the surface of the RPS.

The coincidence of the expressions for the fringe contrast in the optical system with and without the scatterer S_1 is not accidental. Indeed, as shown in Ref. [48], diffraction of the laser beam by the scatterer S_1 gives rise to many similar beams, which probe simultaneously the RPS and form a pattern of regular fringes in the far field of the diffraction upon averaging of the speckle modulation.

7.4.3 An Incoherent Optical System

The operation of averaging the scattered coherent light intensity accomplished by one means or another leads, in fact, to the spatially partially coherent or completely incoherent formation of the image in the optical system. For this reason, one may expect that when, e.g., an object with sinusoidal amplitude transmission is illuminated incoherently, one will observe similar effects of dependence of the image fringe contrast on the parameters of the system and RPS located in the spatial-frequency plane. In particular, one can experimentally observe the effect of enhancing the contrast in the image of sinusoidal fringes with decreasing field-of-view aperture, i.e., with increasing radius of spatial coherence ρ_f of the field illuminating the RPS.

The dependence of the image fringe contrast on the field-of-view aperture also means the dependence of the OTF of the system under study on parameters of the object. This feature of the imaging systems is not treated in

the framework of classical analysis of the linear optical systems [27, 32, 45, 47].

Thus, the considered above optical system becomes an incoherent system when averaging on ensemble of realizations of scatterer S_1 is introduced, and radius of correlation of inhomogeneities S_1 is much less than the diameter of a circle of the resolution of optical system. In this case the spatial-frequency response of the system is defined by its optical transfer function (OTF) which is equal to the normalized autocorrelation function of complex transmission of a pupil of the optical system [27].

For imaging system with the scattered screens OTF is actually equal to the normalized transmission function of the screen, if the size of inhomogeneities of the screen is much less than the sizes of a pupil of the system [27]. When forming the images of patterns with sine wave distribution of intensity transmission the relative fringe contrast in the image is equal to the modulus of OTF [32]. Hence we can write down

$$V / V_0 = \left|\mu_{12}(\Delta\vec{\rho})\right|. \tag{51}$$

Thus, the contrast of the image of sine wave fringes of intensity in incoherent optical system is defined by the modulus of the normalized correlation function of transmittance of the screen when the system contains scattered screen with relatively fine grained structure of inhomogeneities. This dependence can be basically used for measurement of statistical parameters of scattering object using such optical system.

We have stated that when using coherent illumination of scatterer S_1 by a laser beam with regular interference fringes, the contrast of fringes in the image depends not only on $\mu_{t_1}(\lambda f / \Lambda)$, but also on the sizes of the covered area of the first scatterer. It means that the contrast of fringes depends on the size of radius of correlation ρ_f of a field illuminating random phase screen S_2.

This dependence is best manifested when correlation radius of field illuminating of RPS S_2 becomes comparable with the radius of correlation of inhomogeneities l_ϕ of RPS S_2, $\rho_f \approx l_\phi$. From the point of view of spatially frequency response of the incoherent systems, OTF of the system depends on a ratio between radius of spatial coherence of a field illuminating the RPS S_2 and sizes of screen inhomogeneities.

To verify this conclusion we have used optical system, whose scheme is given in Figure 15. Quasi-monochromatic or polychromatic extended light source was used as an illuminating source. The sine-wave distribution of light exposure on scatterer S_1 was created by a thin transparence with sine-wave intensity transmission. The cross sizes of the transparent were limited

with the help of field aperture with a variable diameter. Radius of spatial coherence of light is defined according to the Van-Cittert-Zernike theorem [27,41] and for the spatial-frequency plane it is equal to $\rho_{cf} \approx \lambda f / 2w$. Hence, the change $2w$ is accompanied by change ρ_{cf}.

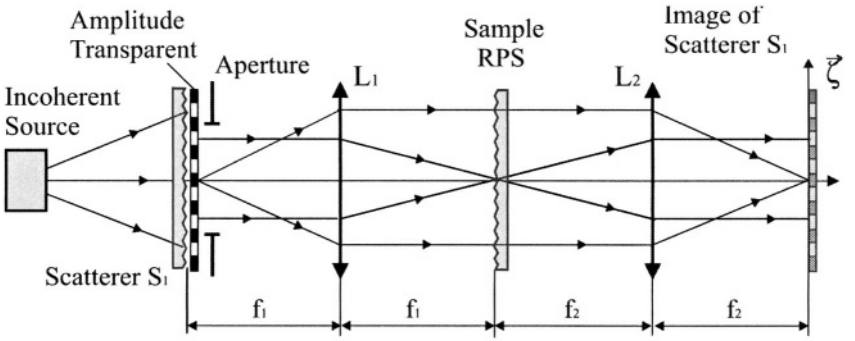

Figure 16. Optical system with a random phase screen in spatial-frequency plane for image formation in incoherent light.

Figure 17 presents the images of sine-wave fringes observed in white light at the various apertures $2w$ at the absence of RPS and at the presence RPS with fine structure inhomogeneities in the spatial-frequency plane are given. The increase of fringe contrast with reduction of the field aperture size of optical system is clearly observed.

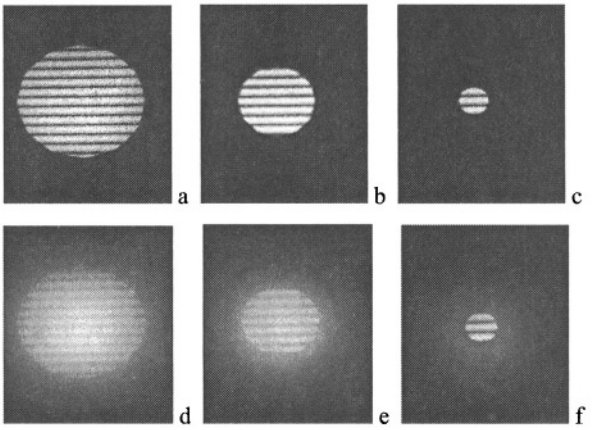

Figure 17. The images of a sine-wave pattern in incoherent light obtained at various sizes of field aperture in optical system without the scattering screen (a, b, c) and with the scattering random phase screen (d, e, f) in spatial-frequency plane.

In Figure 18 the experimental data for contrast of the image of sine-wave fringes are given as function of diameter of field aperture of optical system. In experiment red light-emitted diode HLMP-8103 with $\bar{\lambda} = 0.6354\,\mu m$ and $\Delta\lambda \approx 0.02\,\mu m$ was used as the incoherent light source.

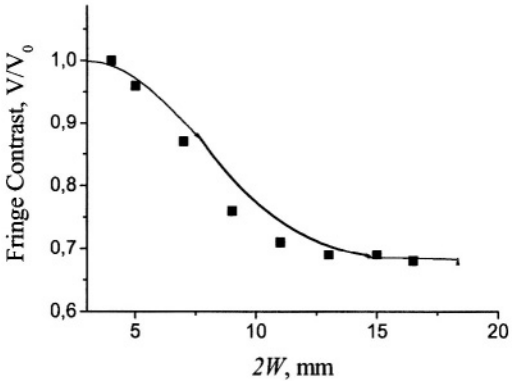

Figure 18. Relative contrast of fringes of the image of a sine-wave pattern in incoherent optical system with the random phase screen ($\sigma_\phi = 1.3$, $l_\phi = 6.5\,\mu m$) as a function of diameter 2*w* of a field aperture at $\Lambda = 5\,mm$.

The effect of increase of contrast of the image when reducing the aperture of a field of sight implies, in particular, a simple way to improve image quality transferred through a scattering medium by successive formation of separate small fragments of the image. We have tested this method experimentally by selecting fragments of words upon formation of the text image through a thin scattering medium. The illustration of this way of increase of quality of the image is shown in Figure 19.

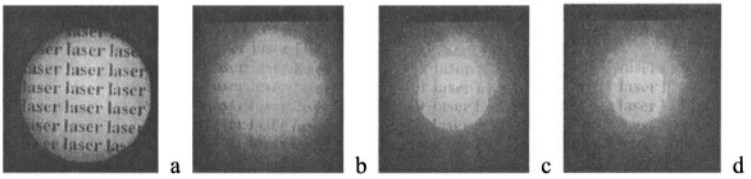

Figure 19. Increase of contrast (clearness) of the image of the text when reducing a field of sight in optical system with the scattering screen in spatial frequency plane, (a) Image without scattering screen, (b), (c), (d) images obtained when a screen is present in the optical system.

The effect of decrease of contrast of the image of fringes when increasing of diameter of a field aperture has a simple physical interpretation. Using geometrical constructions of light rays in optical system, it is easy to see, that the rays from certain points of object scattering on the random phase

screen get to other points of the image of object and create additive noise decreasing contrast of the image.

However, the concepts, used in this work have independent physical meaning enrich our knowledge of processes of image formation in coherent and incoherent light. Within the concept spatial coherence degree of light illuminating the scattering screen in spatial-frequency plane influences fringe contrast of the image.

The obtained analytical expressions for contrast of fringes allow to study image formation process quantitatively and to predict changes of fringe contrast depending on certain parameters of optical system or parameters of scatterer in a pupil of this system.

7.4.4 Conclusions

Upon formation of the interference pattern image in the optical system with a random phase screen (RPS), the image fringe contrast in the pupil is determined by a combination of parameters of the illuminating light, optical system, and RPS. If the optical system provides conditions for δ-correlated illumination of the RPS, when the correlation radius of the illuminating field is much smaller than the correlation radius of the screen inhomogeneities, then the fringe contrast is determined virtually only by the RPS parameters expressed in terms of the correlation function of the screen complex transmittance. The imaging system, in such a mode operates, in fact, as a shearing interferometer with dependence of the shift magnitude and direction on the period and orientation of the pattern of interference fringes in the object field. This mode of operation of the optical system is interesting from the standpoint of measuring statistical parameters of inhomogeneous scattering of both technical and biological nature.

Note that the processes of imaging the interference patterns in the optical system with a RPS in the spatial-frequency plane have much in common with the processes of formation of the interference patterns in the field of diffraction upon probing of the RPS with a focused spatially-modulated laser beam (section 7.3).

The dependence of the image fringe contrast on the degree of spatial correlation (coherence) of the light field probing the RPS in the pupil of the system is of great methodological and practical importance. This means, in fact, that the OTF of the system depends not only on the degree of coherence of the light field illuminating the object [45], but also on the degree of spatial coherence of the field in the pupil of the optical system. This dependence is most pronounced in the presence of a thin scattering medium in the system with the size of inhomogeneities being comparable to the illuminating-field correlation radius. The effect of enhancement of the image contrast with decreasing aperture of the field of view (upon fragmentation of the object)

can find use in solving problems of transfer of optical images through scattering media. This effect can be used in biomedical applications, e.g., in ophthalmology for determination of retinal acuity of vision in case of cataract both by means of laser interference retinometry and incoherent optical systems (see section 7.6).

7.5 INTERFERENCE FRINGES FORMED BY SCATTERING OPTICAL ELEMENTS

In the previous section the optical system has been considered, in which the controllable object is illuminated by ensemble of the scattered focused SMLB. In other words, it is possible to realize that the object is illuminated by a pair of identical speckle fields with the given mutual cross shift. Such pair of fields can be created with the help of a special diffractive optical element (DOE) with a double identical stochastic microstructure and thus to simplify substantially the optical interference system.

In a simplest way, a DOE with a double identical microstructure represents a plane opaque screen containing two identical ensembles (with a certain shift relative to each other) of a great number of point holes located in a random fashion. These holes form pairs and play the role of quasi-point secondary light sources. The same result is achieved in using a transparency with a system of pairs of identical opaque spots on a transparent background or with a system of pairs of identical phase inhomogeneities. Such a DOE can be rather easily fabricated by the photolithographic method, but the simplest technological method consists of recording of a double-exposure shift specklegram [22, 31, 39].

The basis of the method being proposed for determining statistical parameters of scattering objects is a modified Young scheme in which, instead of a screen with two holes, a DOE with a double identical microstructure is used. Behind the DOE, three light fields are formed: the field of the zero-order diffraction and two identical speckle-modulated fields having a mutual transverse shift [49]. In the plane of Fourier transformation of the DOE, the mutual shift of the speckle fields is transformed into their mutual tilt, which causes the occurence in the spatial transmission spectrum of the DOE of average-intensity fringes with a spacing that is inversely proportional to the mutual shift of the DOE structures [22, 49].

If a scattering object is placed behind the DOE, a decrease in the fringe contrast in the plane of the DOE Fourier transformation is observed, which is connected with the scattering properties of the object. When passing through the object, each light field propagating trough the DOE forms two fields: scattered and unscattered. Two scattered fields having a mutual transverse shift and a certain degree of decorrelation have special importance because

they pass through different areas of the object. Thus, the distribution of the average light intensity in the plane where the spatial spectrum of the DOE is formed proves to be dependent on the autocorrelation function of transmission of the thin scattering object and, as a consequence, on statistical parameters of its inhomogeneities.

7.5.1 Spatial Transmission Spectrum of the DOE Combined with Thin Scattering Object

Consider the most general case: a partially coherent optical system (Figure 20). Let an extended quasi-monochromatic light source with a mean wavelength of light $\bar{\lambda}$ be positioned at the distance z_0 from a DOE 2 having a transverse shift of identical structures $\Delta\vec{r}$. The DOE and a thin scattering object 3 are placed immediately adjacent to a converging lens 5 so that the separation Δz between the elements 2 and 5 as compared to the separation z between the lens and the observation plane 6 can be neglected. A circular aperture diaphragm 4 of radius R limits the illuminated region to the DOE and the scattering object.

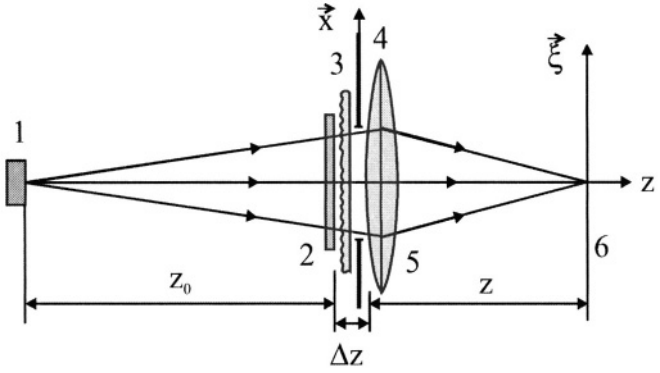

Figure 20. Scheme for observing the average-intensity interference fringes in the Fourier transform plane of transmission of a DOE with a double identical microstructure.

Let us obtain the distribution of the average light intensity in the plane of the spatial spectrum of the DOE + thin scattering object system. The complex amplitude of the illuminating field in the DOE plane can be specified by the expression $U_0(\vec{x},t)exp\left(i\pi\vec{x}^2/\bar{\lambda}z_0\right)$, where $U_0(\vec{x},t)$ describes random space-time fluctuations of the illuminating field and the factor $exp\left(i\pi\vec{x}^2/\bar{\lambda}z_0\right)$ is the deterministic phase distribution in the Fresnel diffraction approximation. Let the DOE and the object be thin transparencies with the complex transmission functions $t(\vec{x})$ and $t_s(\vec{x})$, respectively. Then,

the complex amplitude of the field in the spatial-frequency plane coincident with the plane of the real image of the light source (Figure 20) is defined by the Fourier integral [32, 42]

$$U(\vec{\xi},t)=\frac{C}{\lambda z}\cdot\int_{-\infty}^{+\infty}U_0(\vec{x},t)t(\vec{x})t_S(\vec{x})P(\vec{x})exp\left(-i\frac{2\pi}{\lambda z}\vec{\xi}\vec{x}\right)d^2\vec{x}, \qquad (52)$$

where $\vec{\xi}$ is the radius vector of a point (ξ,η) in the Fourier plane, $\vec{x}$ is the radius vector of a point *(x,y)* in the DOE plane, $P(\vec{x})$ is the transmission function of the aperture diaphragm, and *C* is a complex factor.

The light intensity $I(\vec{\xi})$ in the plane under consideration is defined in the following manner:

$$I(\vec{\xi})=\left\langle U(\vec{\xi},t)U^*(\vec{\xi},t)\right\rangle=\frac{|C|^2}{\lambda^2z^2}\cdot\int_{-\infty-\infty}^{+\infty+\infty}\Gamma_{12}(\vec{x}_1,\vec{x}_2)t(\vec{x}_1)t^*(\vec{x}_2)t_S(\vec{x}_1)$$
$$\times t_S^*(\vec{x}_2)P(\vec{x}_1)P^*(\vec{x}_2)exp\left(-i\frac{2\pi}{\lambda z}(\vec{x}_1-\vec{x}_2)\vec{\xi}\right)d^2\vec{x}_1d^2\vec{x}_2, \qquad (53)$$

where the angle brackets denote averaging over the ensemble of realizations in the observation time and $\Gamma_{12}(\vec{x}_1,\vec{x}_2)=\left\langle U_0(\vec{x}_1,t)U_0^*(\vec{x}_2,t)\right\rangle$ is the function of the transverse spatial coherence of the illuminating field [27, 41].

Since both the DOE and the object have a scattering structure ($t(\vec{x})$ and $t_S(\vec{x})$) are random functions), the spatial spectrum of the DOE + object system, in the general case, turns out to be speckle-modulated. To smooth this random modulation and reveal the deterministic modulation, it is necessary to introduce, in equation 53, the averaging over the ensemble of realizations of $t(\vec{x})$ and $t_S(\vec{x})$. In practice, such averaging is realized if a statistically homogeneous DOE and a statistically homogeneous object are continuously shifted in front of a limited aperture diaphragm of an optical system and the observation is carried out with a sufficiently inertial photodetector. If the DOE and the object are fixed, averaging over a single realization of the light field can prove to be equivalent to the statistical averaging under the condition that deterministic variations in the field over the area of averaging are negligible and, simultaneously, there are a sufficient number of random field fluctuations. In other words, the photodetector aperture should be smaller than the spacing of the interference fringes being determined and, at the same time, it should considerably exceed the speckle size.

Under these assumptions and the condition of the statistical independence of the functions $t(\vec{x})$ and $t_s(\vec{x})$, the expression for the average intensity $\langle I(\vec{\xi})\rangle$ in the spatial-frequency plane can be written in the form

$$\langle I(\vec{\xi})\rangle = \frac{|C|^2}{\lambda^2 z^2}\cdot\int_{-\infty}^{+\infty}\int_{-\infty}^{+\infty}\Gamma_{12}(\vec{x}_1,\vec{x}_2)M(\vec{x}_1,\vec{x}_2)M_s(\vec{x}_1,\vec{x}_2)\times \\ \times P(\vec{x}_1)P^*(\vec{x}_2)exp\left(-i\frac{2\pi}{\lambda z}(\vec{x}_1-\vec{x}_2)\vec{\xi}\right)d^2\vec{x}_1 d^2\vec{x}_2, \tag{54}$$

where $M(\vec{x}_1,\vec{x}_2)=\langle t(\vec{x}_1)t^*(\vec{x}_2)\rangle$ and $M_S(\vec{x}_1,\vec{x}_2)=\langle t_s(\vec{x}_1)t_s^*(\vec{x}_2)\rangle$ are the autocorrelation functions of the transmission of the DOE and of the object, respectively.

Let us make in equation 54 the change of variables $\vec{x}_1=\vec{x}+\Delta\vec{x}/2$ and $\vec{x}_2=\vec{x}-\Delta\vec{x}/2$ and assume that the illuminating field, the DOE, and the object are statistically homogeneous: $\Gamma_{12}(\vec{x}_1,\vec{x}_2)=\Gamma_{12}(\Delta\vec{x})$, $M(\vec{x}_1,\vec{x}_2)=M(\Delta\vec{x})$, and $M_s(\vec{x}_1,\vec{x}_2)=M_s(\Delta\vec{x})$.

We will represent the complex transmittance of the DOE with the double identical microstructure $t(\vec{x})$ as the sum of two terms:

$$t(\vec{x})=t_d(\vec{x}+\Delta\vec{r}/2)+t_d(\vec{x}-\Delta\vec{r}/2). \tag{55}$$

Then,

$$M(\Delta\vec{x})=2M_d(\Delta\vec{x})+M_d(\Delta\vec{x}+\Delta\vec{r})+M_d(\Delta\vec{x}-\Delta\vec{r}), \tag{56}$$

where $M_d(\Delta\vec{x})=\langle t_d(\vec{x}+\Delta\vec{x}/2)t_d^*(\vec{x}-\Delta\vec{x}/2)\rangle$ is the autocorrelation function of transmission of the individual microstructure of the DOE.

Now, equation 54 for the average intensity takes the form

$$\langle I(\vec{\xi})\rangle = \frac{\pi R^2|C|^2}{\lambda^2 z^2}\cdot\int_{-\infty}^{+\infty}\Gamma_{12}(\Delta\vec{x})[2M_d(\Delta\vec{x})+M_d(\Delta\vec{x}+\Delta\vec{r})+M_d(\Delta\vec{x}-\Delta\vec{r})] \\ \times M_s(\Delta\vec{x})exp\left(-i\frac{2\pi}{\lambda z}\Delta\vec{x}\vec{\xi}\right)d^2\Delta\vec{x}, \tag{57}$$

where it was taken into account that the aperture diaphragm is considerably larger than the coherence radius ρ_c of the illuminating field and the sizes of individual inhomogeneities of the DOE and of the object:

$$P(\vec{x}+\Delta\vec{x}/2)P^*(\vec{x}-\Delta\vec{x}/2)=|P(\vec{x})|^2$$

and

$$\int_{-\infty}^{+\infty}\int |P(\vec{x})|^2 d^2\vec{x} = \pi R^2 .$$

It follows from equation 6 that the average intensity distribution $\left\langle I(\vec{\xi})\right\rangle$ in the spatial-frequency plane is governed by the statistical properties of the illuminating field in the DOE plane, of the DOE itself, and of the scattering object.

Consider limiting cases. Let there be no thin scattering object in the optical system and let the illumination be completely coherent, i.e., $M_s(\Delta\vec{x}) = const$ and $\Gamma_{12}(\Delta\vec{x}) = I_0 = const$. Then we obtain the following expression from equation 57:

$$\left\langle I(\vec{\xi})\right\rangle \sim 2I_d(\vec{\xi})\cdot\left[1+cos\left(\frac{2\pi}{\bar{\lambda}z}\Delta\vec{r}\,\vec{\xi}\right)\right], \tag{58}$$

where $I_d(\vec{\xi}) = F\{M_d(\Delta\vec{x})\}$ and $F\{\ \}$ is the Fourier transform symbol. Thus, the DOE spatial spectrum $I_d(\vec{\xi})$ is modulated by average-intensity fringes of unit contrast with the spacing $\Lambda = \bar{\lambda}z/|\Delta\vec{r}|$.

Let us now assume that there is no scattering object in the optical system and that the DOE is illuminated by spatially partially coherent radiation. Let also the sizes of the DOE inhomogeneities be considerably smaller than the radius of light coherence ρ_c, so that, in equation 57, the function $\Gamma_{12}(\Delta\vec{x})$ can be considered to be comparatively weakly dependent on $\Delta\vec{x}$. Then, the distribution of the average light intensity in the plane of the DOE spatial spectrum can be written as

$$\left\langle I(\vec{\xi})\right\rangle \sim 2\Gamma_{12}(0)F\{M_d(\Delta\vec{x})\} + \Gamma_{12}(\Delta\vec{r})F\{M_d(\Delta\vec{x}+\Delta\vec{r})\}$$
$$+\Gamma_{12}(-\Delta\vec{r})F\{M_d(\Delta\vec{x}-\Delta\vec{r})\} = I_d(\vec{\xi})\cdot\left[1+|\gamma_{12}(\Delta\vec{r})|\cdot cos\left(\frac{2\pi}{\bar{\lambda}z}\Delta\vec{r}\,\vec{\xi}\right)\right], \tag{59}$$

where $\gamma_{12}(\Delta\vec{r}) = \Gamma_{12}(\Delta\vec{r})/\Gamma_{12}(0)$ is the degree of spatial coherence of the light in the DOE plane. In this case, the contrast of the interference fringes $V(\Delta\vec{r})$ can be determined by the expression $V(\Delta\vec{r}) = |\gamma_{12}(\Delta\vec{r})|$.

Note that the method for determining the degree of spatial coherence of an extended light source by the contrast of the interference fringes observed in the Fourier plane of the shift specklegram with the δ-correlated transmission was considered in Refs. [49] and [51].

Let a thin scattering object be present in the optical system and the DOE be illuminated by partially coherent radiation. If the sizes of the DOE

inhomogeneities are much smaller than the sizes of object inhomogeneities and the radius of coherence of the incident radiation, then, by analogy with equation 59, for the DOE + object system, we have

$$\left\langle I\left(\vec{\xi}\right)\right\rangle \sim I_d\left(\vec{\xi}\right)\cdot\left[1+\left|\gamma_{12}\left(\Delta\vec{r}\right)\right|\cdot\left|\mu_s\left(\Delta\vec{r}\right)\right|cos\left(\frac{2\pi}{\bar{\lambda}z}\Delta\vec{r}\vec{\xi}\right)\right], \qquad (60)$$

where $\mu_s\left(\Delta\vec{r}\right)=M_s\left(\Delta\vec{r}\right)/M_s\left(0\right)$ is the normalized autocorrelation function of the object transmission and the contrast of the fringes $V\left(\Delta\vec{r}\right)=\left|\gamma_{12}\left(\Delta\vec{r}\right)\right|\cdot\left|\mu_s\left(\Delta\vec{r}\right)\right|$. However, this rather simple expression does not reflect in full measure the real pattern of the field formed in the plane of the DOE spatial spectrum, namely, the effect of the diffraction halo of the scattering object, which occupies a certain area inside the DOE diffraction halo, on the fringe contrast. A part of the interference fringes always falls in this area. The diffraction halo of the object blurs the interference pattern, and the fringe contrast inside this area proves to be lower than beyond its boundaries. The condition under which equation 60 was obtained in practice means the following: The sizes of the object inhomogeneities are so large and, hence, the diffraction halo formed by it has such a small diameter that all interference fringes are located beyond its boundaries. Thus, equation 60 is valid only beyond the boundaries of the object diffraction halo.

7.5.2 Determination of Spatial Coherence of an Extended Light Source and the Autocorrelation Function of Complex Transmission of a Thin Scattering Object

The optical system under consideration can be applied for solving two problems: determining the function of spatial coherence of an extended light source and determining the autocorrelation function of complex transmission of a thin scattering object. To determine the autocorrelation function of transmission of a thin scattering object from the change in the distribution of the average light intensity in the DOE Fourier plane, it is necessary either to use an extended light source with a known function of transverse spatial coherence $\gamma_{12}\left(\Delta\vec{x}\right)$ or to form a coherent illumination of the DOE and the scattering object, which is the most convenient for analysis and processing of experimental results.

Let us return to equation 57. We will consider the case when the DOE and the scattering object have comparable sizes of inhomogeneities and obtain in explicit form an expression that determines the dependence of the interference fringe contrast on the statistical parameters of the object. Let a random phase object (RPO) satisfying the “random phase screen” model be used as a thin scattering object.

The RPS complex transmittance has the form

$$t(\vec{x}) = t_0 \cdot exp\left(i\varphi(\vec{x})\right), \tag{61}$$

where $\varphi(\vec{x})$ is a random function with a zero mean value, the variance σ_ϕ^2, and the correlation factor $K(\Delta\vec{x})$, which is often approximated by the Gaussian function $K(\Delta\vec{x}) = exp\left(-\Delta\vec{x}^2 / l_\phi^2\right)$, where l_ϕ is the correlation radius (the average size) of the inhomogeneities. Then, the autocorrelation function of the RPS transmission in the approximation of Gaussian statistics $\varphi(\vec{x})$ is determined by the expression [26, 27]

$$M(\Delta\vec{x}) = |t_0|^2 \cdot exp\left\{-\sigma^2\left[1 - K(\Delta\vec{x})\right]\right\}, \tag{62}$$

which can be written in the approximated form of equation 33

$$M(\Delta\vec{x}) \approx |t_0|^2 \cdot \left[\left(1 - exp\left(-\sigma_\phi^2\right)\right) \cdot exp\left(-\frac{\Delta\vec{x}^2}{\rho_\perp^2}\right) + exp\left(-\sigma_\phi^2\right)\right], \tag{12}$$

where $\rho_\perp = l\left[-ln\left\{\sigma_\phi^{-2} \cdot ln\left[1 + \left(exp\left(\sigma_\phi^2\right) - 1\right) \cdot exp(-1)\right]\right\}\right]^{1/2}$ is the correlation radius of the RPS transmission function $t(\vec{x})$ at any value of σ_ϕ.

Assume that the DOE with a double identical microstructure with the shift $\Delta\vec{r}$ between the identical microstructures and the microstructure itself are also random phase screens; i.e., the transmission functions $t_s(\vec{x})$ and $t_d(\vec{x})$ satisfy equation 61.

Let us make use of approximate equation 63 to write the autocorrelation functions of the DOE $M_d(\Delta\vec{x})$ and of the object $M_s(\Delta\vec{x})$ in explicit form in diffraction integral shown by equation 57. In doing so, we will assume that the average sizes of the phase inhomogeneities of the DOE, l_d, and of the RPO, l_ϕ, are considerably smaller than the radius of coherence of the illuminating radiation ρ_c, $l_d << \rho_c$ and $l_\phi << \rho_c$, and that $|\Delta\vec{r}| << \rho_c$ (coherent illumination). Then, for the average intensity in the plane of the spatial spectrum of the DOE + RPS system, we can write

$$\left\langle I(\vec{\xi})\right\rangle = I_1(\vec{\xi}) + I_2(\vec{\xi}) + I_3(\vec{\xi}) + I_4(\vec{\xi}), \tag{64}$$

$$I_1(\vec{\xi}) = \frac{2K}{w_c^2(z)} exp\left(-\sigma_d^2\right) exp\left(-\sigma_s^2\right) exp\left(-\frac{\vec{\xi}^2}{w_c^2(z)}\right), \tag{65}$$

where σ_d^2 is the variance of phase fluctuations created by scatterer S_1, and we used the representation of the spatial coherence function in the form of a Gaussian function: $\Gamma_{12}(\Delta\vec{x}) = I_0 \cdot exp\left(-\Delta\vec{x}^2/\rho_c^2\right)$, $I_0 = \Gamma_{12}(0)$,

$$I_2(\vec{\xi}) = \frac{2K}{w_s^2(z)} exp\left(-\sigma_d^2\right)\left(1 - exp\left(-\sigma_s^2\right)\right) exp\left(-\frac{\vec{\xi}^2}{w_s^2(z)}\right), \tag{66}$$

$$I_3(\vec{\xi}) = \frac{K}{w_d^2(z)}\left(1 - exp\left(-\sigma_d^2\right)\right) exp\left(-\sigma_s^2\right) exp\left(-\frac{\vec{\xi}^2}{w_d^2(z)}\right) \cdot \left[1 + cos\left(\frac{2\pi}{\bar{\lambda}z}\Delta\vec{r}\,\vec{\xi}\right)\right], \tag{67}$$

$$I_4(\vec{\xi}) = \frac{K}{w_d^2(z)} \cdot \frac{\rho_s^2}{\rho_d^2 + \rho_s^2}\left(1 - exp\left(-\sigma_d^2\right)\right)\left(1 - exp\left(-\sigma_s^2\right)\right)$$
$$\times exp\left(-\frac{\rho_s^2}{\rho_d^2 + \rho_s^2} \cdot \frac{\vec{\xi}^2}{w_d^2(z)}\right)\left[1 + exp\left(-\frac{\Delta\vec{r}^2}{\rho_d^2 + \rho_s^2}\right) cos\left(\frac{2\pi\rho_s^2}{\bar{\lambda}z\left(\rho_d^2 + \rho_s^2\right)}\Delta\vec{r}\,\vec{\xi}\right)\right], \tag{68}$$

where $K = 2I_0|C|^2 R^2 |t_0|^2$, $w_{d,s}(z) = \bar{\lambda}z/\pi\rho_{d,s}$, is the radius of the diffraction halo of the DOE or the RPO, and $w_c(z) = \bar{\lambda}z/\pi\rho_c$ is the radius of the light source image.

The analysis of equations 64 to 68 shows that four groups of light fields propagate behind the RPO:

(1) One light field that is scattered neither by the DOE nor by the RPO (unscattered radiation). It forms the light source image (see equation 14). In a real optical system, the light intensity in the image is determined by the function $F\{\Gamma_{12}(\Delta\vec{x})\}$, if $\rho_c << R$, or by $|F\{P(\vec{x})\}|^2$, if $\rho_c >> R$.

(2) One light field that is not scattered by the DOE but is scattered by the RPO. It forms the RPO diffraction halo with the intensity distribution determined by equation 66.

(3) Two identical light fields scattered by the DOE and unscattered by the RPO, which have a mutual transverse shift $\Delta\vec{r}$. They form the DOE diffraction halo, modulated by average-intensity fringes with unit contrast and the spacing $\Lambda_1 = \bar{\lambda}z/|\Delta\vec{r}|$ (see equation 67).

(4) Two light fields scattered by both the DOE and the RPO. They are already not identical, because they passed through different parts of the RPO and turned out to be, to a certain extent, decorrelated. These fields form the diffraction halo (see equation 68) that represents the convolution of the DOE and RPO diffraction halos modulated by average-intensity fringes with the contrast $V_2 = exp\left(-\Delta\vec{r}^2/\left(\rho_d^2 + \rho_s^2\right)\right)$ and the spacing

$\Lambda_2 = \bar{\lambda} z \left(\rho_d^2 + \rho_s^2\right) \Big/ \left|\Delta\vec{r}\right| \rho_s^2$; when $\rho_s^2 >> \rho_d^2$, Λ_1 and Λ_2 coincide. With increasing $\left|\Delta\vec{r}\right|$, the degree of decorrelation of these light fields increases and the fringe contrast V_2 decreases. At large values of $\left|\Delta\vec{r}\right|$, only the fringes with the spacing Λ_1 are observed in practice.

As a consequence of the incoherent superposition of all the groups of fields participating in the formation of the spatial spectrum of transmission of the DOE + thin scattering object system, a decrease in the interference fringe contrast occurs in the whole pattern (Figure 21).

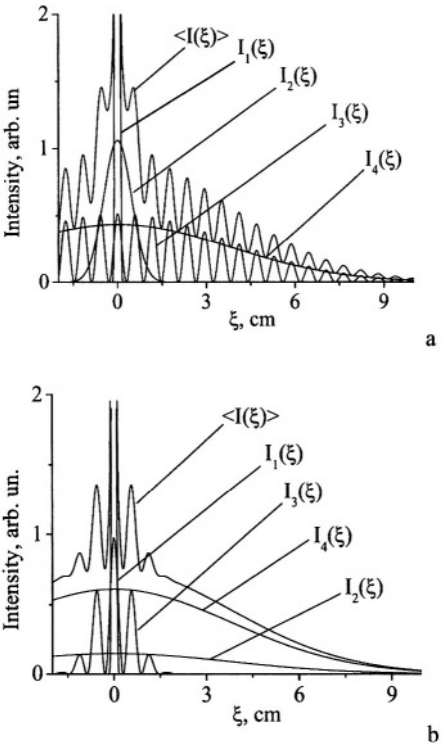

Figure 21. Distributions of the average intensity and its components in the plane of the spatial spectrum of the DOE + thin scattering object system. (a) $l_d = 2\ \mu m$, $\sigma_d = 2$, $l_\phi = 10\ \mu m$, and $\sigma_\phi = 1$; (b) $l_d = 10\,\mu m$, $\sigma_d = 1.5$, $l_\phi = 2\,\mu m$, and $\sigma_\phi = 2$. $\left|\Delta\vec{r}\right| = 30\,\mu m$, $R = 4.5\ cm$, $z = 28\ cm$, and $\bar{\lambda} = 0.63\ \mu m$.

In the resulting diffraction pattern, the contrast of each n^{th} interference fringe depends on the coordinates of its maximum $\vec{\xi}_{1n}$ and minimum $\vec{\xi}_{2n}$

intensity (the expression is not presented in explicit form because it is too cumbersome).

If the average size of the DOE inhomogeneities is much smaller than the average size of the RPO inhomogeneities, $l_d << l_\phi$, then, correspondingly, the RPO diffraction halo proves to be considerably narrower than the DOE diffraction halo. Let $w_1(z) >> \left|\vec{\xi}_{1n} - \vec{\xi}_{2n}\right|$. Then, we can set $\vec{\xi}_{1n} \approx \vec{\xi}_{2n} = \vec{\xi}_{av}$ and write the expression for the fringe contrast in the form

$$V\left(\vec{\xi}_{cp}, \Delta\vec{r}\right) = \mu_s(\Delta\vec{r}) \cdot \left[1 + 2\frac{exp\left(-\sigma_d^2\right)}{1 - exp\left(-\sigma_d^2\right)}\left\{exp\left(-\sigma_s^2\right)\frac{w_d^2(z)}{w_c^2(z)} \times \right.\right.$$

$$\left.\left. \times exp\left(-\frac{\vec{\xi}_{av}^{\,2}}{w_c^2(z)}\right) + \left(1 - exp\left(-\sigma_s^2\right)\right)\frac{w_d^2(z)}{w_s^2(z)} exp\left(-\frac{\vec{\xi}_{cp}^{\,2}}{w_s^2(z)}\right)\right\}\right]^{-1}. \quad (69)$$

Consider the part of the plane of the spatial spectrum of the DOE + RPO system where the individual spatial spectra of the RPO and the DOE do not overlap (i.e., $\vec{\xi}_{\text{cp}}$ is chosen so that $exp\left(-\vec{\xi}_{cp}^{\,2}/w_s^2(z)\right) \approx 0$ and, all the more, $exp\left(-\vec{\xi}_{av}^{\,2}/w_c^2(z)\right) \approx 0$. Then equation 69 is substantially simplified:

$$V(\Delta\vec{r}) \approx \mu_s(\Delta\vec{r}). \quad (70)$$

A similar result can be obtained if in equation 63 we set $\sigma_d >> 1$ (i.e., all of the incident radiation is scattered by the DOE and an unscattered component of the field is absent): $V(\Delta\vec{r}) = \mu_s(\Delta\vec{r})$ within the limits of the whole diffraction halo of the DOE.

One can see from Figure 22 that, inside the RPO diffraction halo, a substantial decrease in the contrast of the interference fringes takes place, but, beyond its boundaries, the value of the fringe contrast is constant and equal to the value of the normalized autocorrelation function of the RPO transmission for the corresponding shift of the DOE identical structures. Within the limits of the diffraction halo of the object, the fringe contrast is determined by the statistical parameters of both the DOE and the RPO.

Thus, measuring the contrast of the average-intensity fringes in the plane of the spatial spectrum of the DOE + RPO system in that part where the individual spectra of the RPO and the DOE do not overlap, one can obtain the value of the autocorrelation function of the RPO transmission at the point corresponding to the shift of the identical structures recorded on the DOE.

To construct the whole autocorrelation function, a collection of DOEs with different shifts is required.

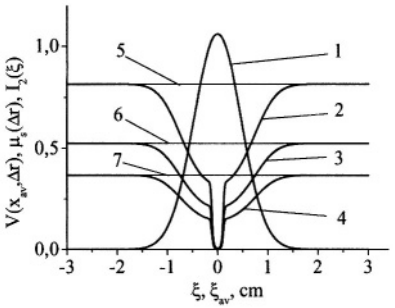

Figure 22. Change in the visibility of the average-intensity fringes in the plane of the spatial spectrum of the DOE + thin scattering object system depending on the magnitude of the shift $|\Delta\vec{r}|$ for different coordinates ξ_{av}. (1) $I_2(\xi)$; (2) $V(\xi_{av},5)$; (3) $V(\xi_{av},10)$; (4) $V(\xi_{av},30)$; (5) $\mu_s(5)$; (6) $\mu_s(10)$; (7) $\mu_s(30)$.

Consider a situation when the average size of the DOE inhomogeneities is considerably larger than the average size of the RPO inhomogeneities, $l_d >> l_\phi$. Then, the diffraction halo of the object under study proves to be considerably wider than the DOE diffraction halo. In this case, the contrast of the average-intensity fringes in the Fourier plane of the DOE + RPO system depends on the statistical parameters of both the DOE and the RPO. For the area where the light source image and the DOE diffraction halo do not overlap, the following expression is valid:

$$V\left(\vec{\xi}_{av},\Delta\vec{r}\right)= \\ =\frac{1+\dfrac{\rho_s^2}{\rho_d^2}\cdot\dfrac{1-exp\left(-\sigma_s^2\right)}{exp\left(-\sigma_s^2\right)}exp\left(-\dfrac{\Delta\vec{r}^{\,2}}{\rho_d^2}\right)exp\left(\dfrac{\vec{\xi}_{av}^{\,2}}{w_d^2(z)}\right)}{1+\left[2\dfrac{exp\left(-\sigma_d^2\right)}{1-exp\left(-\sigma_d^2\right)}\cdot\dfrac{w_d^2(z)}{w_s^2(z)}+\dfrac{\rho_s^2}{\rho_d^2}\right]\cdot\dfrac{1-exp\left(-\sigma_s^2\right)}{exp\left(-\sigma_s^2\right)}exp\left(\dfrac{\vec{\xi}_{av}^{\,2}}{w_d^2(z)}\right)}. \quad (71)$$

It should be noted that, to observe the interference pattern inside the relatively narrow angular spectrum of the DOE transmission, it is necessary that the interference fringe spacing Λ be smaller than the diameter of the DOE diffraction halo $2w_d(z)$. This circumstance imposes a restriction on the value of the shift of the DOE identical microstructures: $|\Delta\vec{r}| > \pi\rho_d/2$;

i.e., $|\Delta\vec{r}|$ should be large enough. In the limiting case, when the RPO is δ-correlated $(l_\phi \to 0)$, unit-contrast fringes are observed.

Figure 4 demonstrates the intensity distributions in the Fourier plane of the optical system that are created by (a) a single DOE with a double identical microstructure, (b) a single RPO, and (c) by the DOE and the RPO jointly with $|\Delta\vec{r}| \approx 24\mu m$.

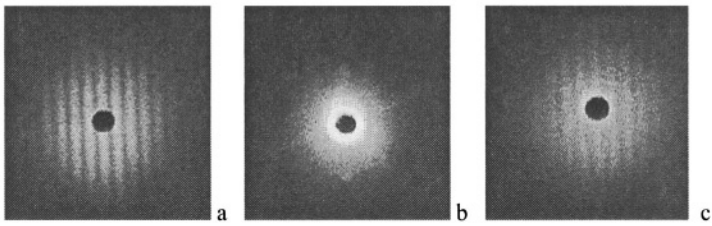

Figure 23. Intensity distributions in the Fourier plane of the optical system created by (a) a DOE with the double identical microstructure, (b) an RPS, and (c) the DOE and the RPS jointly when $|\Delta\vec{r}| \approx 24\ \mu m$.

The RPO parameters l_ϕ and σ_ϕ can be determined from the experimental plot $\mu_s(\Delta\vec{r})$ in the same manner as in section 7.2. For $|\Delta\vec{r}| >> \rho_s$, $K(\Delta\vec{r}) = 0$ and $\mu_s(\Delta\vec{r}) \approx exp(-\sigma_\phi^2)$. The value of l_ϕ is determined from the experimental plot $\mu_s(|\Delta\vec{r}|)$ with the use of the relationship $\mu_s(|\Delta\vec{r}| = l_\phi) \approx \exp\{(-\sigma_\phi^2)(1-\exp(-1))\}$.

7.5.3 Discussion and Conclusions

In the presence of a thin scattering object in the optical channel of an imaging system containing a DOE with a double identical microstructure, average-intensity fringes are formed in the plane of the DOE spatial spectrum. Their contrast is governed by the statistical parameters of the illuminating radiation in the DOE plane, of the DOE itself, and of the scattering object. If the sizes of the DOE inhomogeneities are considerably smaller than the radius of spatial coherence of the illuminating radiation in the DOE plane and the sizes of inhomogeneities of the scattering object, then an area is created in the spatial spectrum of the DOE transmission in which the broad diffraction halo of the DOE does not overlap with the relatively narrow diffraction halo of the scattering object. In this area, the contrast of the average-intensity fringes – the fringes of modulation of the DOE spatial spectrum – proves to be proportional to the modulus of the normalized

autocorrelation function of the RPO complex transmission. A similar result is obtained if the unscattered light beam is virtually absent behind the DOE. In this case, the image of the light source and the diffraction halo of the object are absent and the fringe contrast turns out to be proportional to the modulus of the normalized autocorrelation function of the object complex transmission in the whole plane of the spatial spectrum. This dependence is fundamental for the new method of measuring the autocorrelation function of the RPO complex transmission, which is based on the analysis of changes in the contrast of the interference fringes created in the Fourier plane of the DOE transmission when an RPO is introduced in the optical channel.

The decrease in the fringe contrast connected with the scattering properties of the object also occurs in the case when the average size of the DOE inhomogeneities is comparable with, or larger than, the average size of inhomogeneities of the scattering object. In this case, the DOE diffraction halo is formed inside the comparatively broad diffraction halo of the scattering object and the contrast of the interference fringes is governed by the statistical parameters of both the object and the DOE. However, in this case, the dependence of the fringe contrast on the object parameters has a complicated form and, in practice, there is no way to solve the inverse problem.

As the correlation radius of transmission of the DOE increases, its diffraction halo becomes narrower and enhancement of the fringe contrast is observed at the same parameters of the scattering object. This effect of enhancement of the fringe contrast was used by us in modified interference systems for retinometry with the application of a DOE with a double microstructure to increase the contrast of the fringes on the retina of the eye at initial stages of cataract.

The use of radiation of extended light sources leads to complication of the analytical expressions for the average intensity and the contrast of interference fringes in the Fourier plane of the DOE, as well as to a decrease in the measured values of the interference fringe contrast. In particular, when the average size of the DOE inhomogeneities is considerably smaller than the radius of spatial coherence of the illuminating radiation in the DOE plane and the average size of inhomogeneities of the scattering object, the fringe contrast in the part of the spatial spectrum where the individual spectra of the DOE and the RPO do not overlap is determined by the product of the degree of spatial coherence of the light in the DOE plane and the normalized autocorrelation function of complex transmission of the thin scattering object. Without the object, the fringe contrast proves to be proportional to the modulus of the degree of spatial coherence, and this dependence can be used for determining the spatial coherent properties of the light field. Estimates show that the use of a DOE with a double identical microstructure increases the light-gathering power of the method by 10^5 times as compared to that of the classic Young scheme [52].

The results of this study can be used in technical and biomedical investigations, in particular, in ophthalmology, for determining the statistical parameters of inhomogeneities of scattering media or for optimizing parameters of optical systems forming images of interference patterns through scattering media.

7.6 INDUSTRIAL AND BIOMEDICAL APPLICATIONS

7.6.1 Testing of Scattering Objects

The light field reflected or passed through an object carries the information about macro- and microstructure of the object. In optical interferometry the form of an object determines the form and spatial frequency of interference fringes. The microstructure of an object if it is not resolved by optical system influences the contrast of the average intensity fringes. In laser interferometry of random media values of the contrast of interference fringes it is possible to determine parameters of inhomogeneities of testing object. For these purposes various interference methods and instruments are used. The object can be placed in one of the interferometer branches, thus the interference fringes due to object and reference waves interference are observed at the output. It is possible to apply shift interferometers to which the input of an object field is directed. Interferometer can serve as an illuminating system, and a testing object in this case is probed by an interference field generated at an output of the interferometer - a spatially-modulated laser beam (SMLB). In this case the average intensity interference fringes with the contrast determined by the object inhomogeneities are observed in the object scattered field. Two last approaches are more preferable than the first one, as the testing object is located outside the interferometer and such measurement systems have good vibration protection. Moreover, as the interference of two object waves is observed in these methods, the macroshape of object practically does not influence the form and spatial frequency of interference fringes, which are determined by parameters of the interferometer. In the first approach small distinctions in the forms of object and reference surfaces, comparable to wavelength complicate significantly the structure of an interference pattern. Frequently for real objects of a technical or biological origin there is no chance to observe the average intensity fringes pattern because of certain distinctions in phase distributions of object and reference waves. In turn, measuring systems with interference probing beams differ by technical

simplicity and wider functional ability in comparison with systems of the second group, where rather complex shift interferometer is used.

As it is shown in section 7.2, the measuring systems with collimated SMLB allow to determine basic statistical parameters of inhomogeneities of transparent and reflecting objects satisfying the model "the random phase screen" in which scattering heterogeneity is concentrated in a rather thin layer. These parameters are variance of phase fluctuations of a light field on scattering surface σ_ϕ^2, the average size inhomogeneities - radius of correlation l_ϕ, parameter of the average form of the inhomogeneities a, being an exponent at approximate equation $K_\phi(\Delta\vec{\rho}) = exp\left[-\left|\Delta\vec{\rho}/l_\phi\right|^a\right]$ for correlation function of phase fluctuation, where $\Delta\vec{\rho}$ is a vector of a difference of the coordinates on a scattering surface. If inhomogeneities represent a roughness of a surface, then $\sigma_\phi = 2\pi(n-n_0)\sigma_h/\lambda$ at normal incident light beam for transparent objects, and $\sigma_\phi = 4\pi n_0\sigma_h/\lambda$ for reflecting objects, where n and n_0 are the indices of refraction of an object and environment, correspondingly, λ is the wavelength, σ_h^2 is the variance of heights of a surface.

The scheme of the experimental setup for testing the transparent random phase objects is shown in Figure 24. With the help of special interferometer, or optical wedge, or holographic optical element the laser beam with interference fringes in its cross section is generated. This beam is used to probe the testing object. In the scattered light field in the region near to scattering surface the pattern of the average intensity fringes is formed. The contrast of the fringes V taking into account Gaussian statistics of inhomogeneities is determined by the expression

$$V = V_0\, exp\left\{-\sigma_\phi^2\left(1 - K_\phi\left(\frac{\lambda z}{\Lambda_0}\right)\right)\right\}, \qquad (72)$$

where V_0 and Λ_0 are the contrast and period of fringes in probing SMLB, z is the distance from a scattering surface up to a plane of registration of an interference pattern. As samples of testing objects we used bleached phase specklegrams with smooth spatial inhomogeneities satisfying model "the random phase screen." Besides, we have applied the method for definition of roughness parameters of an internal surface of TV and computer monitor screens.

For definition of contrast of interference fringes we use SMLB with temporal modulation. With the help of special beam deflector the vibrating fringes pattern with amplitude of oscillation $l_0 < \Lambda/4$ was formed. It

allowed us to register a quasi-sine-wave signal, which factor of modulation β is proportional to contrast of the average intensity fringes in an interference pattern.

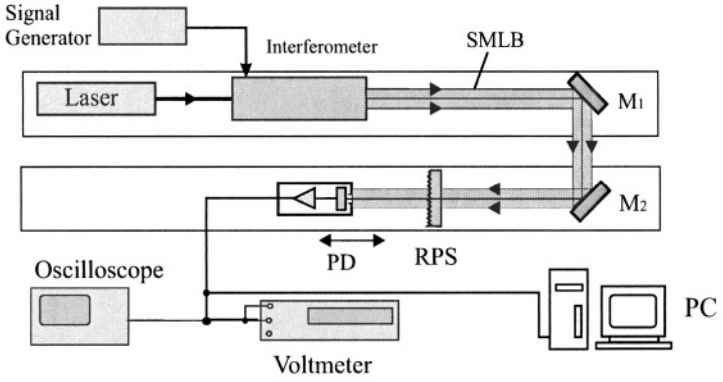

Figure 24. The set up of experimental installation for the testing of transparent random phase objects with use of the probing spatially-modulated laser beam.

Figure 25 gives the example of the experimental data and theoretical curves *V(z),* constructed with use of equation 1 and experimentally determined parameters σ_ϕ, l_ϕ and a. The technique of determination of these parameters is described in section 7.2.

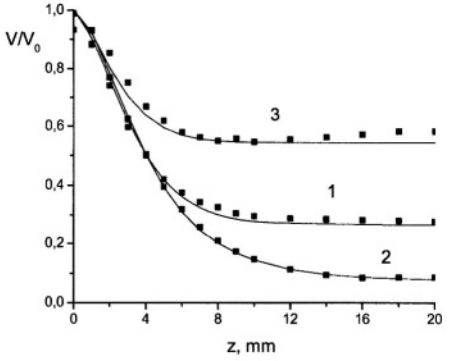

Figure 25. Relative contrast of interference fringes V/V_0 as a function of distance z from a scattering surface for samples with various parameters of inhomogeneities σ_ϕ, l_ϕ and a: 1 - $\sigma_\phi = 1.35$, $l_\phi = 2.9\,\mu m$, $a = 1.6$; 2 - $\sigma_\phi = 1.65$, $l_\phi = 5.1\,\mu m$, $a = 1.6$; 3 - $\sigma_\phi = 0.78$, $l_\phi = 2.7\,\mu m$, $a = 1.6$.

It is worth noting, that a rather large linear aperture 2*w* of probing SMLB is necessary (see section 7.2) for realization in experiment of equation 72 with an error not exceeding 10%. The period of fringes in the beam accounts for speed of change *V(z).* The considered method allows us to determine the form $K_\phi(\Delta\rho)$ with the micrometer spatial resolution, i.e., to determine the average form of scattering inhomogeneities (Figures 26 and 27), as l_ϕ is determined by the relation $l_\phi = \lambda z_c / \Lambda_0$, where z_c is distance, at which $K_\phi(\lambda z_c / \Lambda_0) = exp(-1)$, and in experiment $\lambda / \Lambda_0 < 10^{-3}$, respectively.

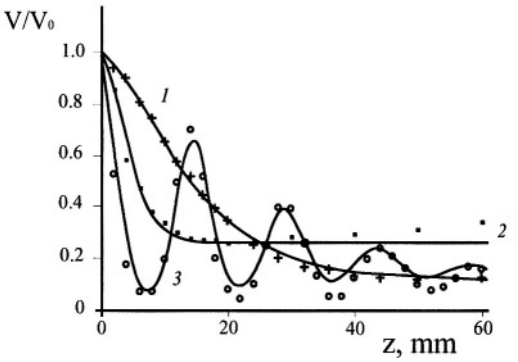

Figure 26. Relative contrast of fringes (experimental data and theoretical curves) vs distance *z* object - plane of registration received for transparent scattering objects with various statistical parameters of inhomogeneities: 1 - $\sigma_\phi = 1.5$, $l_\phi = 20\mu m$, *a* = 1.6; 2 - $\sigma_\phi = 1.21$, $l_\phi = 5\mu m$, a = 1.8; 3 - $\sigma_\phi = 1.64$, $l_\phi = 35\mu m$, $l_0 = 5.5\mu m$, *a* = 1.8.

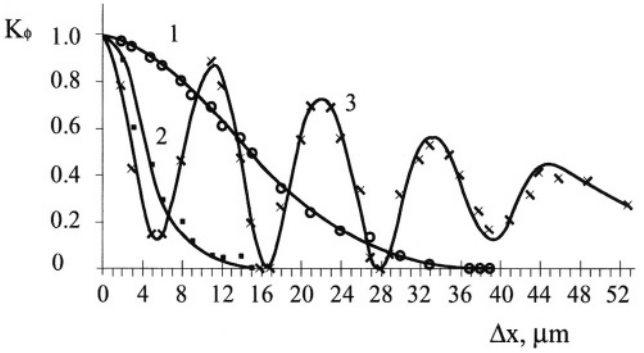

Figure 27. Factors of correlation phase inhomogeneities obtained from experimental data 1, 2 and 3 in Figure 26.

The range of measurements l_ϕ extends from units up to a few hundreds microns. The measurement range of values σ_ϕ is narrow enough $\sigma_\phi = 0.1 - 2.5$, which means, that $\sigma_h = 0.02 - 0.5\,\mu m$ for a wavy surface of transparent object, and $\sigma_h = 0.05 - 0.13\,\mu m$ for reflecting object, at $\lambda = 0.63\,\mu m$, where σ_h is the variance of heights of surface inhomogeneities.

To determine parameters of object inhomogeneities it is also possible to use experimental dependence $V(\Lambda_0)$. Laser beams with the varied period of interference fringes Λ_0 are necessary for this purpose. In particular, effective laser beams with linearly varied spatial frequency of fringes $1/\Lambda_0$ can be employed in cross section of the beam.

The change of interference fringe orientation in SMLB allows to determine $K_\phi(\Delta\vec{\rho})$ in various directions and to estimate parameters of inhomogeneities of statistically anisotropic scattering object. For the same purposes the beam with ring fringes and linearly varied spatial frequency of fringes (Newton rings) can be used. In this case parameters σ_ϕ, $l_{\phi x}$, $l_{\phi y}$, a can be determined according to the variance of fringe contrast in one cross section of the diffraction field.

Measuring systems based on definition in experiment of dependence $V(\Lambda_0)$ assume the use of CCD for frame recording of the interference patterns and the subsequent computer processing of the digital images.

The optical systems with collimated SMLB can also be applied for testing bulk scattering media, including media with statistical parameters varied in time. In subsection 7.6.2 the application of such measuring system to study the dynamics of scattering properties of blood solution in processes of erythrocyte aggregation and sedimentation is considered.

In a number of applications it is necessary to use spatially-modulated laser beams focused on a testing surface (section 7.3). In this case additional operation of averaging on ensemble of realizations of speckle-fields is necessary for observing a fringe pattern of the average intensity. It is caused by the presence of a few inhomogeneities in the illuminated area, and the period of fringes in diffraction field is comparable or even less than cross size of speckles in this field. The operation of speckle averaging is carried out with use of rather inertial photodetector in cases of motility of an object itself, or its separate inhomogeneities, or probing beam scanning relative to the object surface.

For the focused SMLB the dependence of contrast of the average intensity fringes on parameters of object inhomogeneities and beam parameters has more complex view than when the collimated beam (see section 7.3) is used

$$V = V_0 \frac{\mu_0 + (1-\mu_0)\,\rho_\perp^2(\rho_\perp^2 + 2w_0^2)^{-1}\exp\left(-\vec{\rho}_0^2/(\rho_\perp^2 + 2w_0^2)\right)}{\mu_0 + (1-\mu_0)\,\rho_\perp^2(\rho_\perp^2 + 2w_0^2)^{-1}}, \quad (73)$$

where $\rho_\perp \approx l_\phi$ at $\sigma_\phi < 1$ and $\rho_\perp \approx l_\phi / \sigma_\phi$ at $\sigma_\phi > 1$, $2w_0$ is waist diameter of the focused laser beam, $\rho_0 = \lambda f / \Lambda_0$ is distance from center to center of waists in the focused SMLB, f is focal length of a focusing lens.

The equation 73 practically does not suppose the solving of an inverse problem – estimation of σ_ϕ and l_ϕ based on values of fringe contrast $V(w_0, \rho_0)$. However this expression can be used for the solution of a direct problem of formation of interference fringes with the given contrast with scattering media in optical system. The laser retinometer belongs to such systems. The laser beam with rectilinear interference fringes focused in a nodal plane of an eye lens is directed on a retina with the help of the retinometer. In case of cataract – scattering media, the fringes on a retina collapses and there is a problem of formation of a fringe pattern with high enough contrast through scattering media of an eye lens. Various ways of the solving the problem are considered in subsection 7.6.3.

Using the focused SMLB we have dependence $V(\sigma_\phi)$ with almost constant value of contrast of fringes V in a range $0 \le \sigma_\phi < 2$ at a rather large beam waist diameter $2w_0$ and abrupt fall of contrast up to 0 in the area of a rather large values σ_ϕ (Figure 28). This abrupt "enlightenment" of scattering media can have certain significance in solving problem of diagnostics of technical and biological inhomogeneous objects.

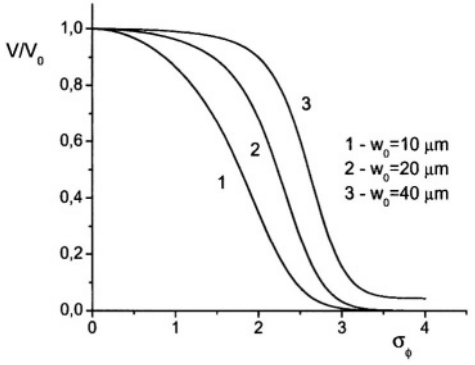

Figure 28. Abrupt change of the average intensity fringe contrast as a function of the parameter of inhomogeneity σ_ϕ of scattering object ($l_\phi = 5\,\mu m$, $\rho_0 = 100\,\mu m$).

The dependence of the average intensity fringes contrast on parameters of object inhomogeneities can have much simpler form, if the diameter of a laser focused beam waist $2w_0$ will be much less than inhomogeneities size, $2w_0 << l_\phi$. In this case laser beam "resolves" inhomogeneities of the object and contrast of fringes is determined by a simple expression

$$V(\rho_0) = V_0 \left| \mu_t(\vec{\rho}_0) \right| , \tag{74}$$

where $\left|\vec{\rho}_0\right| = \lambda f / \Lambda_0$ determines the value and direction of mutual shift of waists in the focused SMLB, and $\mu_t(\vec{\rho}_0)$ is the normalized correlation function of object phase inhomogeneities which in a case of Gaussian statistics of these inhomogeneities is determined by expression $\mu_t(\vec{\rho}_0) = exp\left\{-\sigma_\phi^2\left(1 - K_\phi(\vec{\rho}_0)\right)\right\}$. In this probing mode of an object, as well as in a case of collimated SMLB the inverse problem of estimation of object parameters σ_ϕ, l_ϕ, and a is solved in a simple way. The experimental data and theoretical curves for contrast of fringes are given in Figure 29(a). In Figure 29(b) theoretical curves and experimental data for contrast of fringes obtained by this probing mode are also shown.

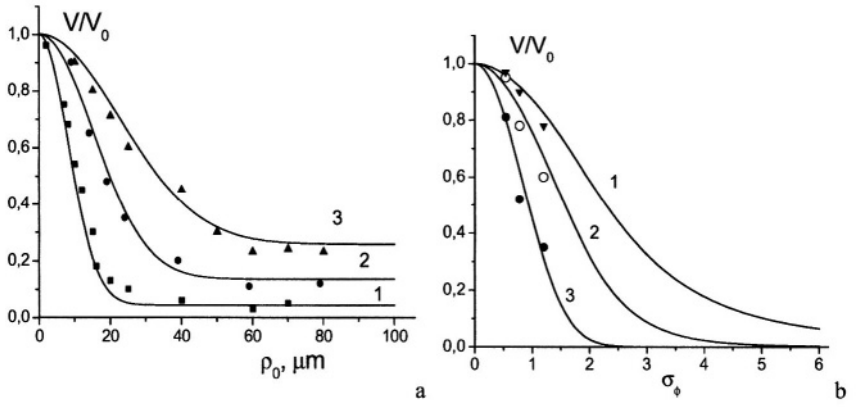

Figure 29. Contrast of the average-intensity fringes as functions of the beam parameter ρ_0 and the variance of the phase fluctuations σ_ϕ, showing both theoretical curves and experimental data: (a) $\sigma_\phi \approx 1.8$, $l_\phi \approx 18\,\mu m$: 1 - $w_0 \approx 2.8\ \mu m$, 2 - $w_0 \approx 12\ \mu m$, 3 - $w_0 \approx 20\ \mu m$; (b) $l_\phi = 23\,\mu m$, $w_0 = 3\,\mu m$: 1 – $\rho_0 = 9.4\,\mu m$, 2 – $\rho_0 = 14\,\mu m$, 3 – $\rho_0 = 29\,\mu m$.

If the testing object is motionless and inhomogeneities are also fixed, then for formation of average intensity fringe pattern it is necessary to scan focused SMLB on the object surface. However the fringe pattern observable

in the far field of diffraction should be motionless. Such procedure of speckle averaging is accomplished with the use of imaging optical system with double Fourier-transformation when arranging a deflecting mirror in a front focal plane, and testing object in a back focal plane of first Fourier-transforming lens. The system of fringe registration should be placed in a back focal plane of the second lens. This measuring system was successfully used for testing both transparent and reflecting random phase non-uniform objects of technical and biological origin.

The optical scanning system of an object with double Fourier-transformation has stationary analogue, in which an object is probed simultaneously by a set of focused SMLB. These beams form conterminous interference patterns in the far field of diffraction. For this purpose a thin scatterer is put in a front focal plane and illuminated by collimated SMLB of the first lens (see section 7.4). The light field behind the object represents a set of SMLB diffracted at various angles with different amplitudes and phase. These beams are simultaneously focused on the object by the first lens. The field scattered by the object is transformed by the second lens. In a back focal plane of the lens the image of scatterer with the average intensity fringes and contrast that depend on parameters of object is observed. This system is similar to the incoherent optical one, as the structure of scatterer is not resolved by the system. Hence, in such system instead of a laser beam incoherent illumination of a transparent object can be used with sine wave distribution in an input plane.

The set of probing focused SMLB can be generated with the use of a special diffractive optical element (DOE), having double chaotic microstructure (see section 7.5). When illuminating the DOE by laser beam two mutually displaced speckle-modulated fields are formed behind it. These fields can be considered as a system of identical pairs of focused beams, which simultaneously probe a testing object that is placed just behind DOE. The average intensity fringe pattern is recorded in the far field of diffraction – interference fringes modulate a spatial frequency spectrum of DOE. Thus, the system with DOE is analogous to optical system with double Fourier-transformation, but differs significantly in simplicity and compactness. Optical systems with the DOE can be used for determination of inhomogeneities parameters of transparent scattering media. Another application of the DOE is optical systems with inhomogeneous media for formation of interference images.

Thus, the optical systems with probing SMLB can find practical use for the testing of wide class of inhomogeneous objects of both technical and biological origin. Besides, such systems in various modifications can be used for solving of number of problems of formation of interference image transmitted through scattering media. As an example of such system the ophthalmology device for determination of retinal acuity of vision will be considered in the next subsection.

7.6.2 Testing of Scattering Properties of a Blood Solution

The erythrocyte sedimentation rate (ESR) determination is a simple and inexpensive laboratory test that is frequently ordered in clinical medicine [53-55]. The test is used to measure the distance that erythrocytes have fallen after one hour in a vertical column of anticoagulated blood under the influence of gravity. The basic factors influencing the ESR have been found since the early part of past century; the amount of fibrinogen in the blood correlates directly with the ESR. Although there is a large literature on ESR, its clinical effectiveness is still hampered by the poor understanding of the phenomena of blood sedimentation [56-58].

Under physiological norm erythrocytes sedimentation rate is low, that is caused by blood plasma albumins predominance over other protein fractions. Albumins are lyophilic colloids, frame around erythrocytes hydrant environment and keep them in a suspension.

The test remains helpful in the specific diagnosis of a few cases, including diabetes mellitus and myocardial infarction, temporal arteritis, rheumatic polymyalgia, rheumatoid arthritis and others. It may predict relapse in patients with Hodgkin's disease. The erythrocyte sedimentation rate emerged as a strong predictor of coronary heart disease mortality.

The rate of spontaneous sedimentation depends significantly on erythrocytes aggregation ability. According to bridge theory of aggregation a bridge of fibrinogen and other macromolecular proteins are absorbed on the surface of an erythrocyte [59]. The degree of erythrocyte aggregation is determined by difference between attractive force in bridges of fibrin and macromolecular proteins and electrostatic repulsion force of negatively charged erythrocytes.

Red blood cells (RBC) sedimentation rate is a complicated process defined by: (1) shape and weight of cells; (2) their amount in blood – hematocrit; (3) many endogenous or exogenous macromolecules influence on the cell membrane potential, its fluidity and deformability, transmembrane transport, aggregation bridges forming, plasma density and so on [53,57,50,61]. For example, improved nutrition causes the decreasing of ESR, elevation of the blood urea accelerates the ESR, cholesterol increases ESR, whereas lecithin decreases it. Dextrans have been extensively used in aggregation studies, and some of them are used in clinic as plasma expanders. They are also known to have a biphasic effect on RBC aggregation - induce aggregation at low concentrations and disaggregation at high concentrations. Dextran efficiency to produce aggregation increases with molecular weight. Both size and shape of RBC aggregates define the role of aggregation in the blood microcirculation. Parameters of sedimentation process are mostly defined by RBC aggregation ability that is why simple measurements of ESR and other parameters of sedimentation *in vitro* should be useful for diagnostic purpose.

To study blood sedimentation a few optical techniques have been suggested recently [62-67]. Some of them are based on the precise dynamic vertical photometry of RBC/blood plasma interface or concurrent photometry monitoring of two interfaces – RBC/blood plasma and RBC/RBC aggregates, another methods use light scattering or coherent phenomena like optical coherent tomography (OCT) or speckle dynamics in scattered coherent light.

We have studied the human blood sedimentation by the technique, which is newly applied for blood sedimentation study and based on measuring of scattering properties of blood suspension by its illumination by a spatially-modulated laser beam (see section 7.2). This method was used to study a highly diluted blood, i.e., to study the sedimentation of individual and weakly-interacting erythrocytes and was tested in clinical research. The clinical protocol included men aged from 42 to 54 with stable angina pectoris of II and III functional classes by Canadian classification and men in comparative age range with acute coronary syndrome. Control group included practically healthy men aged from 28 to 45. Patients with arterial hypertension, disorders in carbohydrate metabolism were excluded from the study.

Blood samples were withdrawn from cubital vein under standard conditions and were stabilized with 3.8% citrate sodium. The picked out erythrocytes were washed with saline and then diluted by saline or poor plasma and 20% glucose solution in proportion 1 to 200. Prepared suspension after mechanical disaggregation (mixing with a stirrer) was put in siliconized glass vessel and placed in the experimental setup.

The experimental setup is presented in Figure 30. The He:Ne laser beam was expanded to diameter of 10 mm, the special interferometer created the parallel fringes in the laser beam. The piezodeflector was used to make dynamic fringes. Such a spatially-modulated beam was put to incident vertically on horizontally placed glass vessel with blood under study. To provide a harmonic form of the detecting signal the scanning amplitude l_0 of the laser beam and fringes at the photodetector aperture was not higher then a quarter of fringe spacing, $l_0 < \Lambda/4$, where Λ is the fringe period. The mean value of the photodetector signal U and the amplitude of its variable component $\tilde{U}$ were measured. The $\tilde{U}$ changes in a process of blood sedimentation leading to transition of the scattering media from a multiple scattering to a single scattering one due to a high degree of packing of the fallen down erythrocytes.

The purpose of the experiments was to register dependence of fringe contrast changing in the course of time. The increase of a fringe contrast (see Figures 31-33) is the result of changing of blood suspension scattering properties in the course of sedimentation.

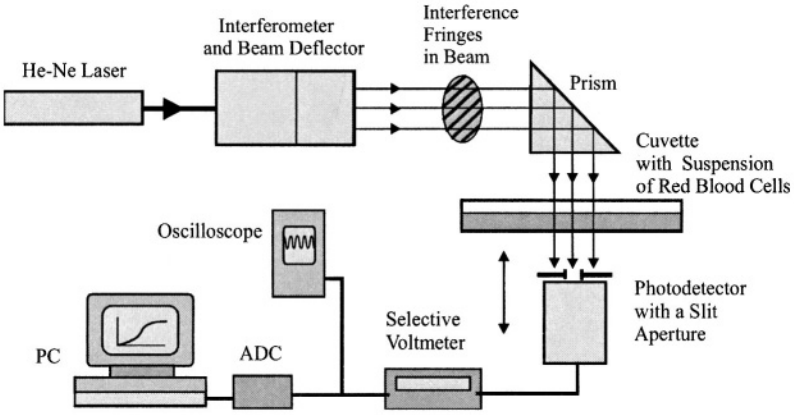

Figure 30. Laser system with a spatially-modulated laser beam for study of dynamic scattering properties of the suspension of red blood sells during spontaneous aggregation and sedimentation of cells.

The stationary value of contrast increases with increasing of the particle size. Before aggregation erythrocytes have the size approximately 7 microns. Thus, in process of aggregates formation the scattering particles size is constantly increased and consequently the contrast of fringes is improved.

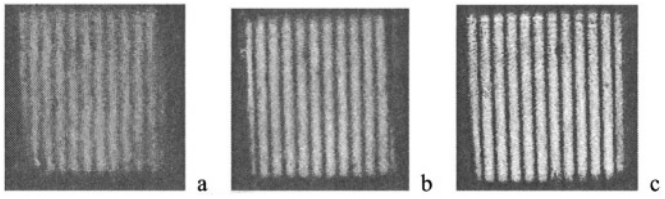

Figure 31. Interference fringes in the diffraction field in the course of blood suspension sedimentation: (a) at the initial moment, after (b) 20 min, and (c) 30 min passed.

After achievement of the certain conditions the scattering properties of blood suspension stop to change, and the fringe contrast leaves on a stationary level. The character of change of fringe contrast can be seen on the diagrams shown in the Figure 32. The increase of a fringe contrast is the result of changing of blood suspension optical properties during processes of spontaneous aggregation and sedimentation of the erythrocytes.

For saline diluted samples (1:200) precise stages of sedimentation process, reflecting the contribution of a denseness and magnitude of an electrical charge on the erythrocyte membrane surface were established. The latent stage, low rate sedimentation stage, “incisor,” a stage of a high-rate sedimentation and an exit on a plateau were selected.

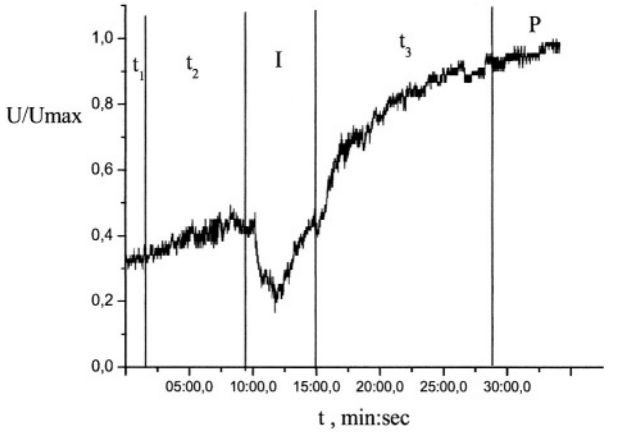

Figure 32. Erythrocyte sedimentation stages (saline suspension 1:200) t_1 is the latent time, t_2 is the low rate contrast changing, I is the"incisor," t_3 is the high rate contrast changing, P is the plateau.

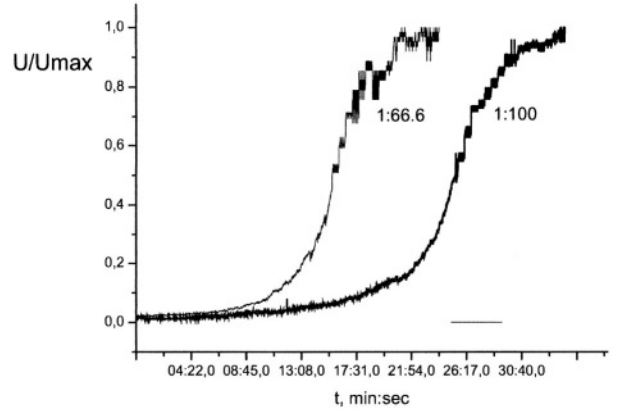

Figure 33. Influence of blood hematocrit on the erythrocyte sedimentation in saline.

The evidence of the influence of the increase of blood suspension hematocrit on sedimentation rate follows from experimental curves presented in Figure 33.

As it is clear from Figure 34 time and rate characteristics of sedimentation of RBC of patients with stable angina pectoris and acute coronary syndrome differs significantly. It concerns duration of a stage of latency, time of appearance and duration of "incisor." However common time of sedimentation varied a little bit. That underlines a diagnostic significance of the indicated method.

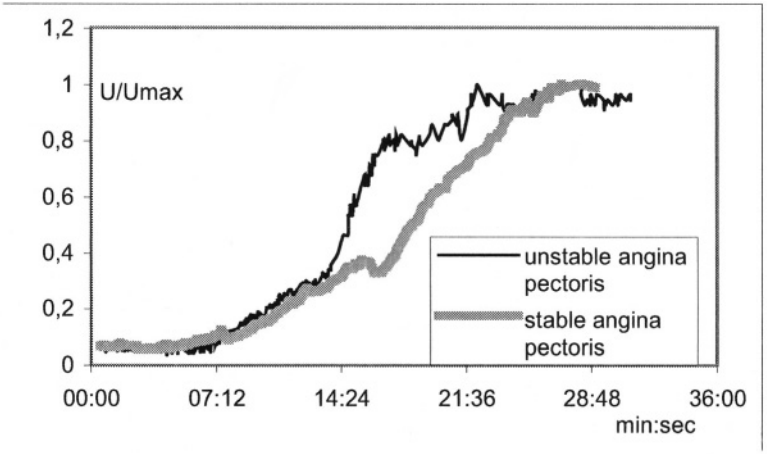

Figure 34. The dynamic of scattering characteristics of erythrocyte suspension for the patients with stable and unstable angina pectoris.

For the testing of change of scattering properties of a blood solution during erythrocyte aggregation and sedimentation the effective application can find the method of a focused spatially-modulated laser beam. As shown in section 7.3 with change of the scatterer sizes the curve of fringes contrast evolution has nonmonotonous character with a local minimum in the range of values approximately equal to the diameter $2w_0$ of laser beam waists.

7.6.3 Interference Retinometry

7.6.3.1 Laser Interference Retinometers

Coherent retinometers used for investigation of human retinal visual acuity consist of a laser, an optical dual-beam interferometer which forms two coherent beams and a focusing lens (Figure 35) [38, 68, 69]. At the output of the interferometer two laser beams form a spatially-modulated laser beam (SMLB) with parallel fringes. The SMLB goes through the focusing lens, and after that through human lens and forms interference fringe pattern on the retina (Figure 36).

Period of fringes and their orientation depend on corresponding parameters of the incident spatially-modulated laser beam. Decreasing of the fringe spacing of the incident beam leads to decreasing of the spacing of fringe pattern at the retina. It is necessary to note that the fringe pattern contrast at human retina is very high, practically it equals to unity because of high degree of mutual coherence of the laser beams.

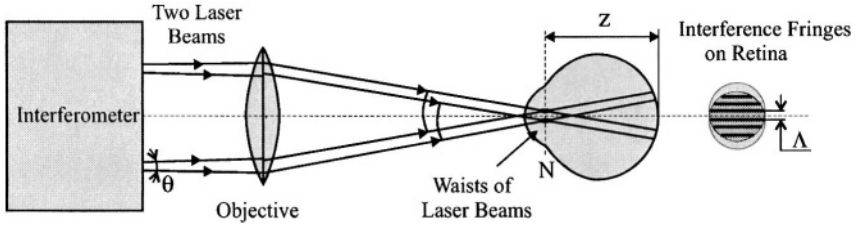

Figure 35. Scheme of a laser interference retinometer.

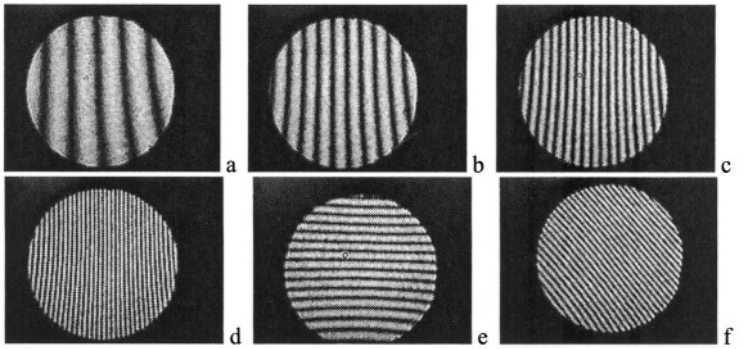

Figure 36. Interference fringes of various spacing and orientation on a retina.

The procedure of estimation of retinal visual acuity is simple. At first a fringe pattern with a large period at patient's retina is formed. Patient let the doctor know that he/she is able to see a fringe pattern. Then period of the fringes is decreased and the patient must indicate ability to see the pattern. Such procedure is repeated until patient is unable to see the pattern. According to the previous period of fringe pattern which patient had observed it is possible to conclude about retinal visual acuity.

7.6.3.2 Fringes Formed on the Retina for the Turbid Eye Lens

For patients with cataractous (turbid) lens, the usage of interferential retinometer described above becomes hindered. Scattering of spatially-modulated laser beam by turbid eye lens leads to disappearance of the fringe pattern [69-70]. Figure 37(a) presents interference fringe pattern formed at retina with normal eye lens, and Figure 37(b) shows that fringe pattern at human with turbid eye lens is destroyed.

The problem of interference diagnostics of human retina when eye lens is turbid is to find out the ways of forming high contrast fringe pattern on human retina. This problem seems to be solved in several ways. Each of them has advantages and disadvantages.

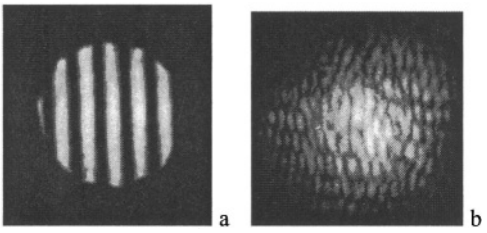

Figure 37. (a) Fringe pattern which is formed at human retina for the normal eye lens and (b) speckle modulated fringe pattern when eye lens is turbid.

We will model a turbid eye lens as a lens with a thin layer of phase inhomogeneities at the rear lens surface. Theoretical analysis was done in framework of random phase screen ideology (sections 7.2-7.5). Such approach is valid for some types of cataract.

Observation of Fringe Pattern Inside the Speckles

This is the simplest way [71]. Spatially-modulated laser beam scattered by the eye lens irregularities that induce speckle modulation which decreases the fringe pattern contrast. The speckle size is defined by the following expression [39]

$$\varepsilon_{\perp} \approx \frac{\lambda z}{2w_0}, \tag{75}$$

where z is the distance between eye lens and retina, $2w_0$ is the light spots diameter at the eye lens.

The period of interference fringe pattern is

$$\Lambda = \frac{\lambda z}{\rho_0}, \tag{76}$$

where ρ_0 is the distance between the centers of light spots at eye lens.

If spacing of fringes is less than speckle size, $\Lambda < \varepsilon_{\perp}$, then fringes are observed inside each speckle (Figure 38).

With the help of this method the determination of the maximal acuity of vision is possible, as maximal distance ρ_0 between laser spots is equal to a diameter of a pupil of an eye.

The method requires small light spots $2w_0$ to produce sufficiently large size speckles. Patient sees speckles with interference fringes which are inside them. High contrast of the fringes may be considered as an advantage. Disadvantage is in the difficulties that some patients may have in describing complicated image that they see.

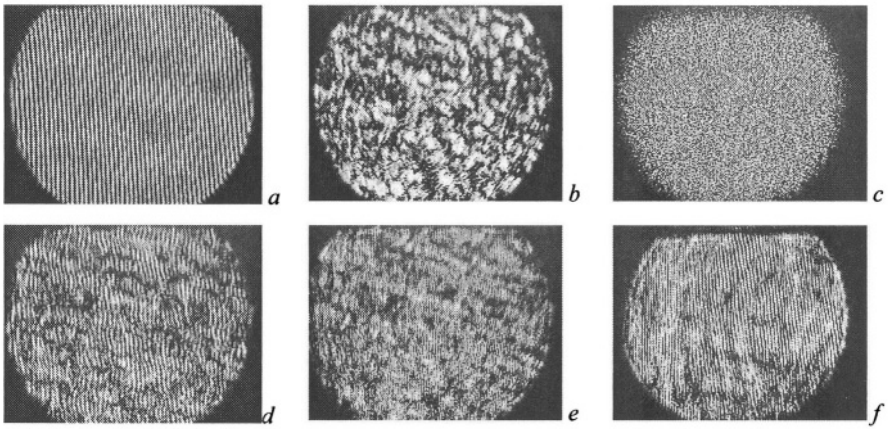

Figure 38. Speckle-modulated interference patterns observable when scattering media is present in a laser beam at the output of retinometer: (a) interference pattern formed without scattering media; (b), (c) patterns with the various speckle sizes in scattered laser beam; (d), (e), (f) speckle-modulated interference patterns observable under condition when the spacing of interference fringes is less than the cross sizes of speckles $\Lambda < \varepsilon_{\perp}$.

Observation of the Average Intensity Fringes by Scanning the Spatially-Modulated Laser Beam

This method helps to "repair" fringe pattern on human retina but its contrast is less than unity and depends on eye lens irregularities parameters. The idea of the method is to produce averaging of decayed pattern at retina. It is reached by using spatially-modulated laser beam moving in scattering region of eye lens. As a result a patient will see a regular fringe pattern with spacing defined by interferometer adjusting. It is important to construct optical scheme so that the image of the fringe pattern is immovable on the retina. It is achieved by scheme in Figure 39(a). Spatially-modulated laser beam used for testing of retina is moved by mirror of deflector. All focal length of the lenses and distances is specially selected to form immovable fringes on retina.

Fringe contrast is supposed to be low for the severe stage of cataract and high for initial stages. That is a problem because it is possible to create the average intensity fringes on retina but the contrast may be not high enough for a patient to see fringes. They exist on retina but patient's retina cannot detect them.

The theoretical analysis presented in section 7.3 shows, that the contrast of the average intensity fringes is increased with increasing of a waist diameter of laser beams, $2w_0$, in a plane of scattering media. This effect can be used in the retinometry for increase of contrast of fringes on a retina.

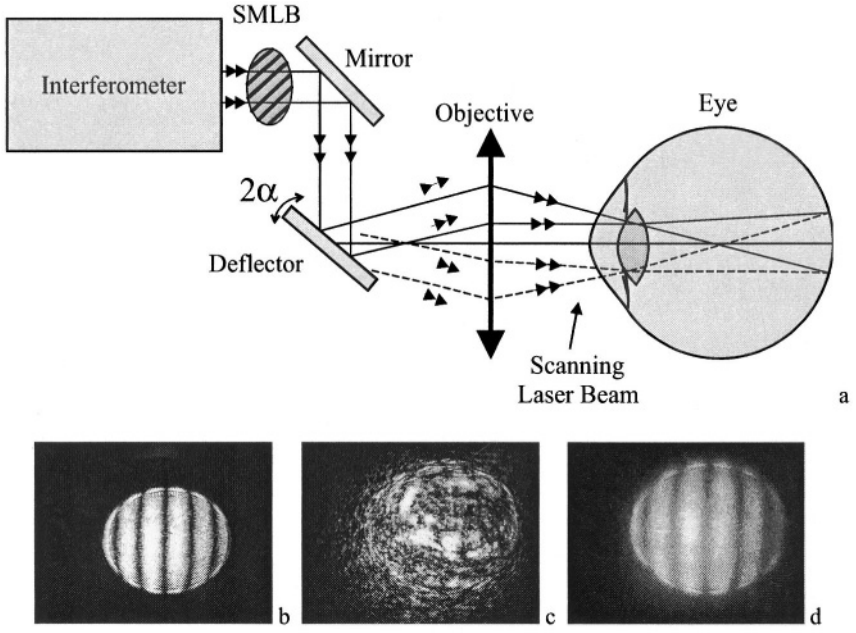

Figure 39. Observation of average intensity fringes on a retina: (a) scheme for forming average intensity fringes on retina; (b) fringes without scattering media; (c) pattern in presence of the scattering media; (c) average intensity fringes.

In Figure 40 the curves of fringe contrast V as a function of waist radius w_0 are shown. The curves are constructed with the help of equation 35 in section 7.3.

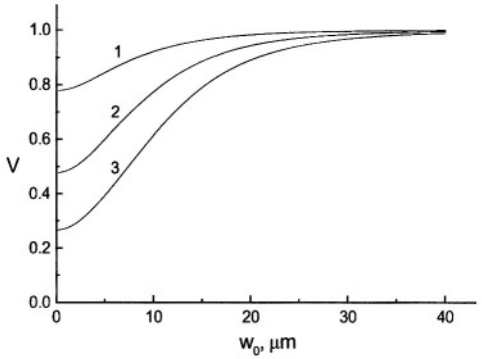

Figure 40. Dependence of fringe contrast V on a beam parameter w_0 at different parameters of scattering inhomogeneities: (1) $\sigma_\phi = 0.5$, $l_\phi = 10\mu m$; (2) $\sigma_\phi = 0.86$, $l_\phi = 10\mu m$; (3) $\sigma_\phi = 1.15$, $l_\phi = 10\mu m$, $\rho_0 = 30\mu m$.

The increase of a diameter of the laser beam waist, $2w_0$, with the diffractive point of view means the decrease of the angular aperture of the focused laser beams and, consequently, reduction of a field of view. For example, for $w_0 \approx 20\,\mu m$ angular aperture of a view field is equal to $2\lambda/\pi w_0 \approx 1.8^o$. Such increase of interference fringes contrast on a retina was verified experimentally.

Imaging System with the Scattered Spatially-Modulated Laser Beam

In section 7.4 the theoretical and experimental principles of interference fringes formation in imaging optical systems with the scattering screen in an optical tract of the system are considered. The similar optical system is in the eye at cataract. In this case the image of a primary scatterer with interference fringes is formed on a retina (see Figure 41).

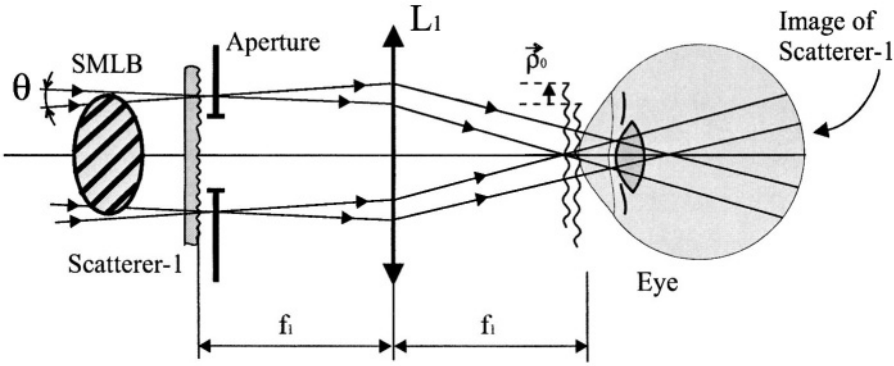

Figure 41. Scheme of a retinometer with a spatially-modulated laser beam diffracted by a primary scatterer.

It is shown that the contrast of average intensity fringes in a plane of the image depends essentially on the size of the field view. Contrast of fringes is increased at reduction of a diameter of the field view [see curves in Figure 14(b)]. This effect can be used for interference retinometry at cataract.

Application of Special Diffractive Optical Elements

Diffractive optical elements with double identical microstructure allow one to create the system of interference fringes in a plane of the image of a light source (section 7.5). Such optical elements, actually, replace the interferometer, which forms a system of fringes in a probing beam of light. With the help of DOE one can just observe an interference pattern in partially coherent light. For this purpose, for example, light-emitting diodes

of various colors can be used. Therefore DOE can be applied in retinometry to construct simple optical devices. The scheme of an optical retinometer with DOE is given in Figure 42.

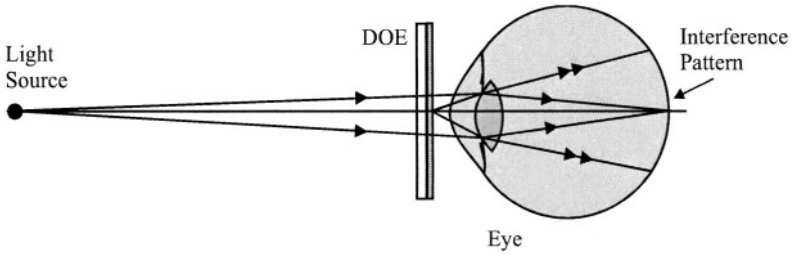

Figure 42. The principle scheme of interferential retinometer on the basis of the special diffractive optical element with double identical microstructure.

Dependence of contrast of observable fringes on parameters of DOE, the degree of spatial coherence of light and parameters of inhomogeneities of scattering media can be found in section 7.5.

The basic drawback of such retinometer is practical impossibility to create interference fringes on a retina with the small period. In this case spatial coherence of light can also be manifested, when the extended enough incoherent source of light is used. It limits a range of determination of acuity of vision. Another drawback of the retinometer is dependence on refraction of an eye, as it is necessary to observe the focused image of a light source.

Use of a Converging Spatially-Modulated Laser Beam

There is some complicated theoretical analysis developed in this method that was verified by experimental observations. As theoretical analysis and experiments show if converging spatially-modulated laser beam is used for probing of the random phase screen, then evolution of average intensity contrast along an optical axis demonstrates a very interesting behavior. There is a special region where contrast reaches local maximum close to unity.

The evolution of the average intensity fringe contrast in diffraction region is presented in Figure 43. It is necessary to find the appropriate parameters of spatially-modulated laser beam to coincide plane of high contrast with human retina.

The effect of local increase of interference fringes contrast using the converging spatially modulated laser beam was observed experimentally on a retina directly.

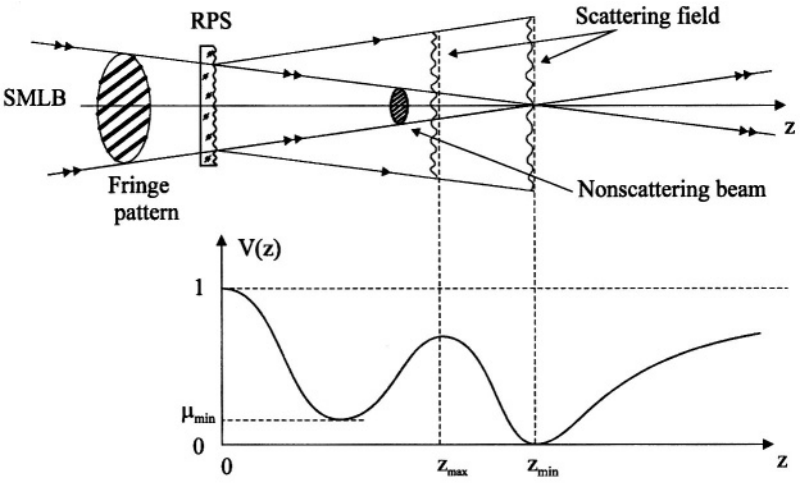

Figure 43. The evolution of the average intensity fringe contrast in diffraction field: (SMLB) spatially-modulated laser beam, (RPS) random phase screen.

Thus, it was shown theoretically and experimentally that retinal visual acuity can be estimated not only for clear eye lens but also for turbid (cataractous) lens. All suggested methods can be used in practice within the discussed limitations. It is difficult to say which method is preferable. It seems to us that only combination of all methods may give satisfactory results.

7.7 SUMMARY

Methods of optical interferometry allow one to estimate parameters of inhomogeneities of scattering objects with high precision. High precision is conditioned by short light wavelength that is the measure of comparison to the parameters under discussion. Methods of optical interferometry considered in the chapter are based on the application of light interference beams as the object probing ones. They present a number of advantages against traditional methods in testing of scattering objects of technical and biological origin. These advantages are due to the use of an interferometer as an illuminating device. In this case the problem of matching of interference light fields is out of question. Vibro-proof of an interferometer is significantly higher for an object is beyond the area of the device.

As a rule, inverse problems are often ambiguous and difficult to solve in optical interferometry. The same disadvantages take place in interferometry of random media. The methods considered in the chapter are not free from these disadvantages, either. In a number of cases the dependence of the average intensity fringe contrast on object parameters is so complicated that

the estimation of these parameters on the basis of the observed interference patterns becomes impossible.

Methods of random media interferometry have a limited range of measurement of optical inhomogeneity dispersion, σ_ϕ^2. The limitation is defined by the light wavelength of the source used. Exceeding of mean square variance σ_ϕ of phase fluctuations of π radians leads to the "saturation" of fluctuations of a scattered field. The lower boundary of the range is defined by the small dependence of the fringe contrast on small phase fluctuations of a field. However, the moving of lower range boundary to small values σ_ϕ up to $\sigma_\phi \approx \pi/100$ becomes possible using the familiar technique in interferometry – by providing the initial phase shift $\Delta\varphi_0 = \pi/2$ between interfering waves. This technique is readily realized in methods of interferometry of random media using classical interferometers. However, for interference-modulated beam method the analogue of the technique failed to be found. Nevertheless, for collimated probing SMLB at temporal modulation the average intensity fringe contrast of 10^{-3} can be measured.

An important practical merit of the considered methods is a rather wide range of measurement of transverse sizes of object inhomogeneities, l_ϕ. They range from a unity to several hundreds micrometers. When testing the object with inhomogeneities of large sizes, one has a real possibility to solve this kind of problem. The intensity of light scattered at small angles can be defined on the basis of measuring of contrast of interference fringe with a rather small period.

Another problem discussed in the chapter concerns image formation through a scattering media. In our case we considered the problem of image formation of interference pattern both in coherent and in partially coherent light. Such problems occur in technology as well as in biomedical optics. In particular, the estimation of surface roughness is related to the problem by observing the distinctness of the object image reflected by the surface. A good example of solving a biomedical problem is laser interference retinometry for a cataractous lens. This problem is discussed in details in the chapter.

Further development of the methods of probing of scattering objects by interference light beams described in the chapter will concern solving the problems of scattering in a bulk media with multiple scattering and amplitude-phase modulation of a light wave.

ACKNOWLEDGEMENTS

The author gratefully acknowledges Yu.A. Avetisyan, A.V. Chausskii, O.A. Perpeletsina, A.E. Grinevich, D.V. Lyakin, L.I. Malinova for their assistance in theoretical work and experiments, Prof. V.V. Tuchin for useful discussion of many results presented in this chapter, Prof. V.V. Bakutkin and M.V. Orekhov for help in the research on laser retinimetry.

The work was supported by grant REC-006/SA-006-00 "Nonlinear Dynamics and Biophysics" of CRDF and the Russian Ministry of Education; the Russian Federation President's grant N 25.2003.2 "Supporting of Scientific Schools" of the Russian Ministry for Industry, Science and Technologies; and grant "Leading Research-Educational Teams" N 2.11.03 of the Russian Ministry of Education.

REFERENCES

1. O.V. Angelsky, P.P. Maksimyak, and S. Hanson, *The Use of Optical-Correlation Techniques for Characterizing Scattering Object and Media* **PM71** (SPIE Press, Bellingham, WA, 1999).
2. O.V. Angelsky and P.P. Maksimyak. "Optical diagnostics of random phase objects," *Appl. Opt.* **29**, 2894-2898 (1990).
3. O.V. Angelsky, I.I. Magun, and P.P. Maksimyak, "Optical correlation methods in statistical studies of random phase objects," *Opt.Commun.* **72**, 153-156 (1990).
4. E. Lorincz, P. Richter, and F. Engard, "Interferometric statistical measurment of surface roughness," *Appl. Opt.* **25**, 27-28 (1986).
5. V.P. Ryabukho, "Interference of partially developed speckle fields," *Opt. Spectrosc.* **78**, 970-977(1995).
6. G.M. Gorodinsky, and V.N. Galkina, "Disturbance of light coherence by frosted glass surfaces," *Zh. Prikl. Spektrosk.* **5**, 451-455 (1966).
7. O.K. Taganov and A.S. Toporets, "Coherence degree of radiation ordered scattered by rough surface," *Opt. Mekh. Prom.* N12, 70-71 (1975).
8. O.K. Taganov and A.S. Toporets, "Study of coherence degree of radiation passed through rough surface," *Opt. Spectrosc.* **40**, 878-882 (1976).
9. B. Grzegorzewski, "Young's interference experimental in the study of partially developed speckle," *Optik (Stuttgart)* **82** (3), 75-81 (1989).
10. S.I. Kromin, V.V. Lyubimov, and V.N. Shekhtman, "Measurement of scattered component of light wave," *Quant. Electr.* **13**, 962-966 (1986).
11. M. Ohlidal, I. Ohlial, M. Druckmuller, and D. Franta, "A method of shearing interferometry for determining the statistical quantities of randomly rough surfaces for solids," *Pure and Appl. Opt. A.* **5**, 599-616 (1995).
12. V.P. Ryabukho, Yu.A. Avetisyan, and A.B. Sumanova, "Diffraction of a spatially modulated laser beam on a random phase screen," *Opt. Spectrosc.* **79**(2), 275-281 (1995).

13. V.P. Ryabukho and A.A. Chausskii, "Interference of speckle fields in zone of diffraction of a focused spatially-modulated laser beam on a random phase screen," *Tech. Phys. Lett.* **21**, 658-663(1995).
14. V.P. Ryabukho, A.A. Chaussky, and V.V. Tuchin, "Interferometric testing of the random phase objects by focused spatially-modulated laser beam," *Photonics Optoelectr.* **3**(2), 77-85(1995).
15. V.P. Ryabukho and A.A. Chausskii, "Probing of a random phase object by a focused spatially modulated laser beam. Diffraction at a large number of inhomogeneities," *Tech. Phys. Lett.* **23**,755-757(1997).
16. V.P. Ryabukho and A.A. Chausskii, "Probing of a random phase object by a focused spatially modulated laser beam: deflection of interference fringes," *Tech. Phys. Lett.* **25**, 23-25(1999).
17. V.P. Ryabukho, A.A. Chausskii, and O.A. Perepelitsyna, "Interference-pattern image formation in an optical system with a random phase screen in the space–frequency plane," *Opt. Spectrosc.* **92**, 191-198 (2002).
18. O.A. Perepelitsina, V.P. Ryabukho, and B.B. Gorbatenko, "Diffractive optical elements with a double identical microstructure for determination of statistical parameters of random phase objects," *Opt. Spectrosc.* **95** (2), 303–310 (2003).
19. B.G. Hoover, "Optical determination of field angular correlation for transmission through three-dimensional turbid media," *J. Opt. Soc. Am. A* **16**, 1040-1048 (1999).
20. B.G. Hoover, L. Deslauriers, S.M. Grannell, R.E.Ahmed, D.S. Dilworth, B.D. Athey, and E.N. Leith, "Correlations among angular wave component amplitudes in elastic multiple-scattering random media," *Phys. Rev. E* **65**(2), 026614-(1-8) (2001).
21. R.W. Wygant, S.P. Almeida, and O.D.D. Scares, "Surface inspection via projection interferomery," *Appl. Opt.* **27**, 4626 – 4630 (1988).
22. R. Jones and C. Wykes, *Holographic and Speckle Interferometry* (Cambridge Univ., Cambridge, 1983).
23. G.R. Lokshin, S.M. Kozel, I.S. Klimenko, and V.E. Belonuchkin, "Modulation methods in holographic interferometry," *Opt. Spectrosc.* **72**(6), 1444-1450 (1992).
24. B.S. Rinkevichus, *Laser Diagnostics of Flows* (MEI, Moscow, 1990).
25. V.P. Ryabukho, Yu.A. Avetisyan, A.E. Grinevich, D.A. Zimnyakov, and L.I. Golubentseva, "Effects of speckle-fields correlation at diffraction of spatially-modulated laser beam on a random phase screen," *Pis'ma Zh. Tekh. Fiz.* **20**(11), 74–78 (1994).
26. S.M. Rytov, Yu.A. Kravtsov, and B.I. Tatarskii, *Introduction to Statistical Radiophysics. II: Stochastic Fields* (Nauka, Moscow, 1978).
27. J.W. Goodman, *Statistical Optics* (Wiley-Interscience, New York, 1985).
28. S.A. Akhmanov, Yu.E. D'yakov, and A.S. Chirkin, *Introduction to Statistical Radio Physics and Optics* (Nauka, Moscow, 1981).
29. I.S. Klimenko, V.P. Ryabukho, and B.V. Freduleev, "Manifestation of fine amplitude-phase structure of the speckle-fields at its coherent superposition," *J. Techn. Phys.* **55**(7), 1338–1347(1985).

30. *Holographic Interferometry. Principles and Methods: Springer Series in Optical Sciences,* **68**, P. K. Rastogi ed. (Springer-Verlag, Berlin, 1995).
31. J.W. Goodman "Statistical properties of speckle patterns" in *Laser Speckle and Related Phenomena,* J. C. Dainty ed. (Springer, Berlin, 1975), 9–75.
32. J.W. Goodman, *Introduction to Fourier Optics* (McGraw-Hill, New York, 1968).
33. N.G. Vlasov, G.V. Skrotskiy, and E.G. Solov'ev, "Coherence study by a diffraction shire interferometer," *Kvantovaya Elektron (Moscow)* N3, 84-86 (1972).
34. P.W. Kiedron, "Angle-scanning laser interferomer for film thickness measurement," *Proc. SPIE* **621**, 103-114(1986).
35. V.N. Lakshin, R.Yu. Orlov, A.S. Chirkin, and V.M. Yusubov, "Coherence of light scattered by random phase screen," *Opt. Spectrosc.* **53**(3), 493-497 (1982).
36. J.W. Goodman, W.H. Huntley, D.W. Jackson, and M. Lehmann, "Imaging through inhomogeneous media by reconstruction of wave front," *Appl. Phys. Lett.* **8**(12), 311-315 (1966).
37. R. Collier, C. Burckhardt, and L. Lin, *Optical Holography* (Academic, New York, 1971).
38. A.V. Priezzhev, V.V. Tuchin, and L.P. Shubochkin, *Laser Diagnostics in Biology and Medicine* (Nauka, Moscow, 1989).
39. M. Francon, *Laser Specle and Application in Optics,* (Masson, Paris, 1977).
40. E. Jakeman and R.J.A. Tough, "Non-Gaussian models for the statistics of scattered waves," *Adv. Phys.* **37**,471 (1988).
41. M. Born and E. Wolf, *Principles of Optics,* 4th ed. (Pergamon Press, Oxford, 1969).
42. A. Papoulis, *Systems and Transforms with Applications in Optics* (McGraw-Hill, New York, 1968).
43. P. Hariharan and D. Sen, "Effect of partial coherence in two-beam interference," *J. Opt. Soc. Am.* **51**, 1307 (1961).
44. *Optical Shop Testing,* D. Malacara ed. (Wiley, New York, 1978).
45. B.J. Tomson, "Image formation in partially coherent light" in *Progress in Optics* **7** (North-Holland, Amsterdam, 1969), 169–230.
46. É.P. Zege, A.P. Ivanov, and I.L. Katsev, *Image Transfer in Scattering Medium* (Nauka i Tekhnika, Minsk, 1985).
47. C. S. Williams and O. A. Becklund, *Introduction to the Optical Transfer Function* (Wiley-Interscience, New York, 1989).
48. V.P. Ryabukho, A.A. Chausskii, and A.E. Grinevich, "Probing of a random phase object by a focused spatially modulated laser beam. Integral scanning method," *Tech. Phys. Lett.* **25**(12), 971-973 (1999).
49. I.S. Klimenko, *Holography of Focused Images and Speckle interferometry* (Nauka, Moscow, 1985).
50. I.S. Klimenko, B.B. Gorbatenko, V.P. Ryabukho, and B.V. Feduleev, "Localisation and visibility of fringes in holographic and speckle-interferometry," *Sov. Phys. Tech. Phys.* **33**, 1180-1185 (1988).
51. N. Takai, H. Amber, and T. Asakura, "Spatial coherence measurements of quasimonochromatic thermal light using double-exposure specklegrams," *Opt. Commun.* **60** (3), 123-127 (1986).

52. V. P. Ryabukho, O. A. Perepelitsyna, and A. A. Chausskii, "Manifestation of spatial coherence of light in Young interference scheme in demonstration and laboratory experiments". *Fiz. Obraz. Vyssh. Uchebn. Zaved.(Moscow)* **7**(4), 99-111 (2001).
53. C. Saadeh. "The erythrocyte sedimentation rate: old and new clinical applications," *South Med. J.* **3**, 220-225 (1998).
54. M. Brigden. "The erythrocyte sedimentation rate: still a helpful test when used judiciously," *Postgrad. Med.* **103**, 257-274 (1998).
55. H.C. Sox Jr., M.H. Liang. "The erythrocyte sedimentation rate: guidelines for rational use," *Ann. Intern. Med.* **104**, 515-523 (1986).
56. T.L. Fabry, "Mechanism of erythrocyte aggregation and sedimentation," *Blood.* **70**(5), 1572-1576(1987).
57. V.A. Levtov, S.A. Regirer, and N.Kh.Shadrina, *Rheology of Blood* (Meditsina, Moscow, 1982).
58. A.V. Priezzhev, O.M. Ryaboshapka, N.N. Firsov, and I.V. Sirko, "Aggregation and disaggregation of erythrocytes in whole blood: study by backscattering technique," *J. Biomed. Opt.* **4** (1), 76 - 84 (1999).
59. P.H. Chien, S. Chien, and R. Scalak, "Effect of hematocrit and rouliaux on apparent viscosity in capillaries," *Biorheology* **24**(1), 14-56 (1987).
60. E.S. Losev, N.V. Netrebko, and I.V. Orlova, "Gravitational sedimentation of aggregating particles in shear flow," *Fluid Dynamics (USSR)* **24**, 242-245 (1989).
61. E.S. Losev, N.V. Netrebko, S.A. Regirer, A.S. Stepanyan, and N.N. Firsov, "Interaction between gravitational sedimentation and shear diffusion in suspension moving in rotation viscosimeter gap," *Fluid Dynamics (USSR)* **25**, 685-691 (1990).
62. Y. Aizu and T. Asakura, "Coherent optical techniques for diagnostics of retinal blood flow," *J. Biomed. Opt.* **4**, 61-75 (1999).
63. V.L. Voeikov, Yu.S. Bulargina, E.V. Buravleva, and S.E. Kondakov, "Non-equilibrium and coherent properties of whole blood revealed by analysis of its sedimentation behavior," Chapter 6 in *Biophotonics and Coherent Systems* (Moscow Univ. Press, Moscow, 2000).
64. I. Fine, B. Fikhte, and L. D. Shvartsman, "RBC aggregation assisted light transmission through blood and occlusion oximetry," *Proc SPIE* **4162**, 130-139 (2000).
65. V.V. Tuchin, X. Xu, and R.K. Wang, "Dynamic optical coherence tomography in optical clearing, sedimentation and aggregation study of immersed blood," *Appl. Opt.* **41**, 258–271 (2002).
66. A.H. Gandjbakhche, P. Mills, and P. Snabre, "Light-scattering technique for the study of orientation and deformation of red blood cells in a concentrated suspension," *Appl. Opt.* **33**, 1070-1078 (1994).
67. V.L. Voeikov, C.N. Novikov, and N.D. Vilenskaya, "Low-level chemiluminescent analysis of nondiluted human blood reveals its dynamic system properties," *J. Biomed. Opt.* **4**, 54-60(1999).
68. B.E.A. Saleh, "Optic treatment of information and vision of man" in *Applications of Fourier-Optics Methods*, G. Stark ed. (Academic Press, New York, 1982), 412-439.

69. J. M. Enoch, M. J. Giraldez, D. Huang, H. Hirose, R. Knowles, P. Namperumalsamy, L. LaBree, and S. P. Azen, "Hyperacuity test to evaluate vision through dense cataracts: research preliminary to a clinical study in India," *Opt. Eng*. **34**(3), 765-771 (1995)
70. S. Jutamila and G. Green, "Diffraction pattern on retina of eye testing," *Opt. Eng*. **34**, N.3, 780-784(1995).
71. E.Yu. Radchenko, G.G. Akchurin, V.V. Bakutkin, V.V. Tuchin, and A.G. Akchurin, "Measurement of vetinal visual acuity in human eyes," *Proc. SPIE* **4001**, 228-237 (1999).

Chapter 8

HETERODYNE TECHNIQUES FOR CHARACTERIZING LIGHT FIELDS

Frank Reil and John E.Thomas
Physics Department, Duke University, Durham, NC 27708 USA

Abstract: We give an overview of optical heterodyne techniques, which provide phase-sensitive methods to characterize light fields with a high signal-to-noise ratio and a large dynamic range. We present basic applications such as OCT, OCM and CDOCT. We then introduce Wigner functions, which fully characterize a light field including its coherence properties, and demonstrate two techniques which enable the measurement of smoothed (One-Window method) and true Wigner functions (Two-Window technique). We conclude this chapter with the characterization of a Gaussian-Schell beam, an enhanced-backscattered field and a single speckle, using the Two-Window technique.

Key words: heterodyne, beat signal, OCT, Wigner, Gaussian-Schell, enhanced backscattering

8.1 INTRODUCTION TO HETERODYNE DETECTION

The heterodyne technique is a phase-sensitive method to measure a light field. It is based on the superposition of the signal field to be measured with a reference beam from the same light source, referred to as the "local-oscillator" beam. At least one of the fields is frequency-shifted by a few MHz, which causes the resulting interference pattern to oscillate at the beat frequency of both beams. The superposed field is collected by a detector and the interference terms are selectively detected by band-pass filtering of the beat frequency.

The beat intensity is proportional to the amplitude of the signal field and not the intensity, as opposed to direct intensity-measurements without a local

oscillator beam. Because the amplitude of an electric field is proportional to the square root of the intensity, the measured range in the heterodyne technique contains twice as many orders of magnitude.

The beat intensity also depends on the phase of the signal field relative to the local oscillator beam, by way of their constructive or destructive interference. Therefore the measured intensity contains information on the phase of the signal field- unlike direct intensity measurements.

The signal measurement occurs at a non-zero frequency - as opposed to direct intensity measurements and homodyne methods - where the noise level is reduced due to the $1/f$-dependence of common background noise. This technique also allows the discrimination between interference terms stemming from different fields which have different beat frequencies.

A frequency shift of one or more beams can be accomplished by reflecting its light off a moving mirror, which introduces a Doppler shift to the reflected light. Another way to shift the frequency is by means of acousto-optic modulators, where a beam passes through a standing ultrasonic soundwave within a crystal. The soundwave transfers momentum to the light field by modulating the crystal's index of refraction.

In the following we will start off by explaining signal detection methods in the heterodyne technique, followed by the presentation of "Optical Coherence Tomography" or "OCT", where the principles of heterodyne detection are applied in the most basic way (section 8.2). After that we turn our attention to the measurement of phase-space measurements (section 8.3) and in particular Wigner functions (section 8.4), which provide a convenient way to fully describe a light field in position and momentum, and obey rigorous transport laws. With broadband light, the presented techniques allow time-resolved measurements, exploiting the finite coherence length of this type of light.

In section 8.5 we present three applications of the techniques described in section 8.4; the time-resolved characterization of Gaussian-Shell beams (subsection 8.5.1), light fields in multiple scattering media (subsection 8.5.2) and a single speckle (subsection 8.5.3).

The chapter concludes with the Summary in section 8.6.

8.1.1 Signal Detection Methods

In order to take full advantage of the low noise level the heterodyne technique provides by shifting the signal in frequency as described above, a detection technique which suppresses classical noise in the light source itself is required. Also, all intensity contributions, which are not part of the interference and consequently the beat signal, should be suppressed before they enter the electronics of the detection. All this can be accomplished by a

balanced detector, as will be shown in subsection 8.1.2. In order to suppress electronic noise, i.e., noise introduced after the field is collected by the detector, a real-time noise suppression system is introduced into the system, which will be explained in subsection 8.1.3.

8.1.2 Balanced Detector

A balanced detector allows the detection of a signal field down to the shot-noise level by subtracting classical noise which does not contribute to the beat signal. Figure 1 shows how the scheme works.

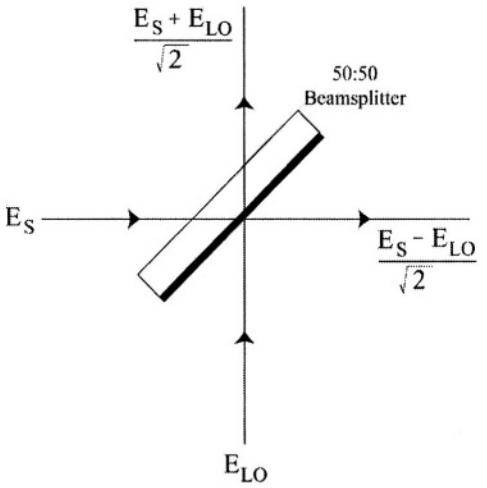

Figure 1. E_S and E_{LO} are incident on a 50:50 beamsplitter and add with different signs due to a 180 degree phase-shift for the LO at the reflecting surface.

The signal (S) and local oscillator (LO) fields are superposed by a 50:50 beam splitter. The reflected fraction of one of the beams experiences a 180-degree phase-shift, while the corresponding fraction of the other beam and both transmitted components do not. This phase shift is due to the reflection off a medium with higher index of refraction. Assuming for the moment perfect matching of S and LO transversely and longitudinally, the resulting intensities I_1 and I_2 at the outputs of the beam splitter are:

$$I_1 = \left(\frac{E_S}{\sqrt{2}}\right)^2 + \left(\frac{E_{LO}}{\sqrt{2}}\right)^2 + E_S E_{LO}, \tag{1}$$

$$I_2 = \left(\frac{E_S}{\sqrt{2}}\right)^2 + \left(\frac{E_{LO}}{\sqrt{2}}\right)^2 - E_S E_{LO}, \tag{2}$$

where the suffices S and LO denote the respective beams.

I_1 and I_2 are incident onto two photodiodes in the balanced detector, which are connected in parallel (see Figure 2). This way the currents generated in each diode are subtracted from each other: the intensities of each beam cancel, while the intensity contribution generated by the interference of S and LO add, due to their opposite sign. The resulting total photo current is therefore

$$J \propto E_S E_{LO} \propto \sqrt{I_S I_{LO}} \quad , \tag{3}$$

where I denotes the intensity of the respective beams. Hence, this method suppresses the classical noise, which contains not only intensity fluctuations but also the frequency shifts of all beams. For an ideal balanced detection system, the signal to noise ratio up to the detection by the photodiodes is limited by shot-noise.

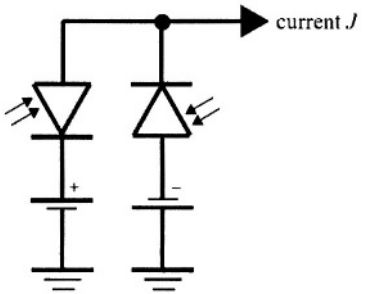

Figure 2. The two photodiodes of a balanced detector are connected in parallel with opposite polarity so that their photocurrents subtract.

In experiments, the beat signal is usually detected by a spectrum analyzer, which provides a root mean square voltage V_{RMS} proportional to the beat signal measured at the beat frequency.

In the next section we are going to describe a method to suppress the noise that enters the system after the detection by the photo diodes and which is part of V_{RMS}.

8.1.3 Real-Time Noise Suppression

While the balanced detection scheme enables the suppression of optical noise, the following scheme allows the subtraction of noise entering the system *after* the detection by the photodiodes, i.e., electronic noise.

The root mean square voltage which is usually provided by a spectrum analyzer set to the beat frequency is proportional to the beat intensity of the Signal- and LO field, but also contains noise from various sources. Because

the noise and the signal are uncorrelated, their mean square voltages, rather than their voltages itself, add. Including the remaining noise, this voltage is

$$V_{RMS} = \sqrt{V^2_{Signal} + V^2_{Noise}}\ , \tag{4}$$

where $V^2_{Noise} = V^2_{Noise,1} + V^2_{Noise,2} + \ldots$ contains all noise sources. V_{RMS} is now squared by a low-noise multiplier, so that the resulting V^2_{RMS} is a sum of the squared voltages from the signal and all noise sources. By chopping the Signal- or the LO beam, and detecting V^2_{RMS} by means of a lock-in-amplifier with the chopping frequency as a reference, V^2_{Signal} can be extracted, while the noise terms are subtracted. This is because V^2_{Signal} is the only square voltage which is always in phase with the chopping frequency among the terms contributing to V^2_{RMS}.

Having described the basic signal detection techniques used in heterodyne measurements, we are now going to present methods were these techniques are employed.

8.2 OPTICAL COHERENCE TOMOGRAPHY (OCT)

Optical coherence tomography (OCT) is the most basic optical detection method using the principles of the heterodyne technique. Figure 3 shows setup: two beams are generated from a broadband source – superluminescence diode (SLD) which we will again refer to as *signal-* and *local oscillator* beam. The signal beam is incident on the sample; the transmitted or scattered light is then superposed with the local oscillator beam in the balanced detector.

Due to the broad spectrum of the light, its longitudinal coherence length is small; typically on the order of tens of micrometers. The light coming from the sample and the local oscillator beam only interfere if their path-length is matched within the coherence length of the light. By increasing the path length of the local oscillator beam Δl with the reference mirror M_R the local oscillator beam will interfere only with those parts of the signal field that have traveled the same distance Δl in the medium. Therefore, signal field contributions from different photon path lengths in the sample can be selected. For skin tissues, a map of tissue reflectivity versus depth can be obtained this way ("*vertical*" scan).

In practice, the reference mirror is moved at a fixed speed, and the heterodyne beat signal resulting from the Doppler-shift of the local oscillator beam reflected from the moving mirror is recorded at the same time. By moving the laser beam in a two-dimensional raster and taking vertical scans for each point, a three-dimensional image can be obtained.

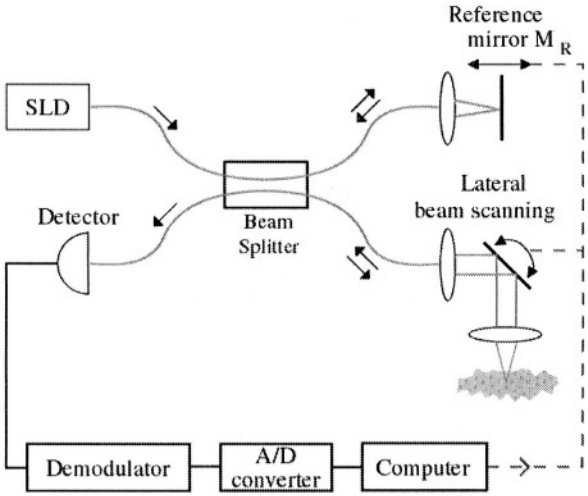

Figure 3. Setup for optical coherence tomography (OCT). Light from the SLD is split up by a beam splitter into a local oscillator beam and a signal beam which is incident on to the medium under investigation. The reflected field is superposed with the LO beam reflected from the reference mirror; the superposed field is measured by a detector.

Optical coherence *microscopy* (OCM) directly combines OCT and confocal microscopy [1]. While its general principle is the same as that of OCT, it adds a high NA objective in order to increase lateral and axial resolution due to the smaller focal spot size and Rayleigh length.[1] In addition, the high NA objective provides enhanced rejection of out-of-focus or multiply scattered light. OCM can be used in case where there are no physical constraints with respect to the distance between the sample and the objective. Figure 4 demonstrates the differences between OCT and OCM [1].

In the Figure shown, the OCM objective is immersed in water where the wavelength is smaller, thereby enhancing the resolution. Since the small Rayleigh length and the strong rejection of out-of-focus light in OCM determine the axial location of the examined plane, a vertical scan can not be performed as easily as for OCT, using the Doppler-shift introduced by the reference mirror, unless the focal plane of the objective is changed at the same rate.[2] This problem also arises when the reference mirror is moved stepwise and the heterodyne signal is generated by the beat frequency of the

[1] The Rayleigh length is the distance after which a beam passing through its beamwaist grows to twice its area. It is inversely proportional to the size of the beamwaist.

[2] This is non-trivial since the depth-dependent refractive index in the sample influences the depth of the focal plane, which has to be taken into account when adjusting the relative path delay between the signal- and local oscillator beam.

signal- and local oscillator beams frequency-shifted by means of acousto-optic modulators.

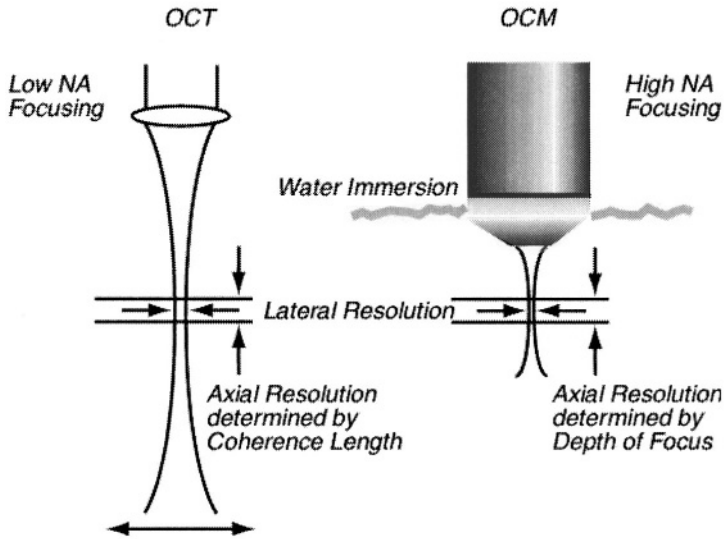

Figure 4. Optical coherence tomography (OCT, left) compared to optical coherence microscopy (OCM, right).

Compared to confocal microscopy alone, the short coherence of the broadband light in OCM helps rejecting light coming from above and beneath the objective focal plane, where its point-spread function is broad.

Figure 5 shows an OCT image of *in vivo* hamster skin (Courtesy of Joseph A. Izatt). It shows various layers of the skin, with the epidermis (skin surface) at the top.

Color Doppler optical coherence tomography measures the flow of objects in a sample by taking advantage of the additional Doppler-shift they introduce. This way, reflections from objects moving away and towards the incident signal beam cause frequency components in the heterodyne signal below and above the Doppler-frequency generated by the reference mirror. Several groups have used this technique for quantitative measurements of blood flow in tissue with micron-scale resolution [2,3]. The spatial resolution in [2] is better than 45 μm in depth and 10 μm laterally, the velocity resolution on the order of 0.5 mm/s, the latter being easily adjustable by varying the speed of the reference mirror. Figure 6 (Courtesy of Joseph A. Izatt) shows the same *in vivo* hamster skin as in Figure 5 by looking at the spectrum of the returned signal. Three blood vessels are seen in this image as a result of the Doppler shift caused by the flowing blood.

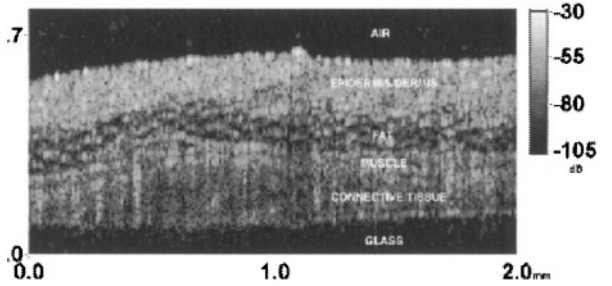

Figure 5. OCT scan of *in vivo* hamster skin (Courtesy of Joseph A. Izatt).

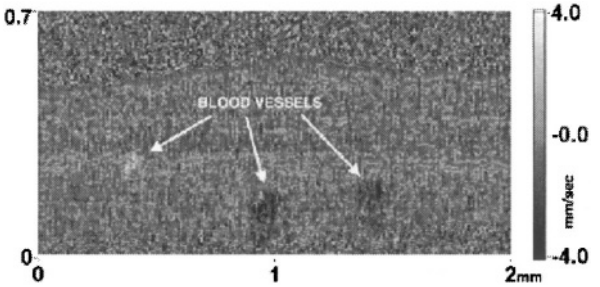

Figure 6. CDOCT scan of the same *in vivo* hamster skin as in Figure 5. The white and dark areas represent blood vessels (Courtesy of Joseph A. Izatt).

8.3 OPTICAL PHASE-SPACE MEASUREMENTS

In OCT and OCM, the signal field is measured as a function of transverse position only, no information about the transverse momentum, i.e., its direction is recorded. For coherent fields, the transverse momentum distribution of the field can be calculated by Fourier transforming, its transverse position distribution.

For partially coherent fields, this method does not work since the correlation between two different positions in the signal field, which influences the transverse momentum as well, is unknown: the information provided by OCT and OCM is incomplete. A way to solve that problem is to record the transverse momentum distribution directly for each position as described in the following. This way, a phase-space profile of the signal field is generated.

Due to diffraction, the product of the width of the transverse momentum distribution times the width of the position distribution cannot be arbitrarily small. Therefore we will get an uncertainty in both position and momentum which depends on the method of measurement. The most straight-forward

way of measuring a phase-space distribution of the field's intensity is by means of two apertures, as shown in Figure 7:

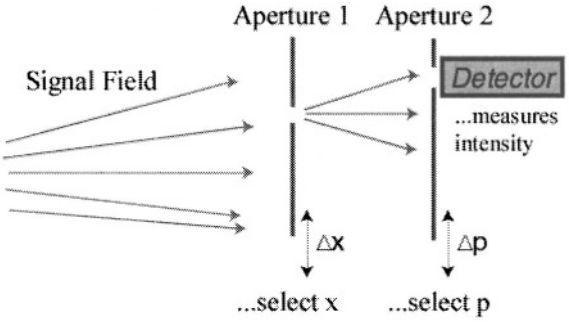

Figure 7. Two-aperture method to record the phase-space distribution of a signal field.

A signal field is incident from the left. The field's transverse position x to be measured is selected by aperture 1. The field behind that aperture still contains the full transverse momentum distribution at that position. A second aperture (2) at a certain distance from the first, then selects the parts of the field with a given transverse momentum p, i.e., the wavenumber k times the angle defined by both apertures. The intensity of the light passing through aperture 2 is measured by a detector. By recording the intensity for a range of transverse positions and momenta, the phase-space profile of the field can be determined.

This method's resolution is again determined by the size of the apertures. The disadvantage is that the transmission function of the apertures is a step-function, thereby introducing additional diffraction which decreases the resolution in both x and p. The maximal attainable resolution in this method would be obtained by using apertures with a Gaussian transmission function, since a Gaussian beam has the smallest size in phase-space.

A way to achieve this resolution without the need for apertures is by means of the heterodyne technique, where the signal field is superposed with a Gaussian local oscillator beam whose transverse position x and momentum p relative to the signal field is changed while the mean square beat signal is recorded simultaneously. Due to the finite size of the LO both in position and momentum, the measured phase-space profiles do not contain the entire information contained in the field. The phase-space profiles obtained this way correspond to smoothed Wigner functions which we will introduce in section 8.4. In that section, we will present the basic properties of Wigner functions which fully describe an optical field, and demonstrate their usefulness in the description and of optical fields and their propagation. We

are going to show an experimental method to measure smoothed Wigner functions according to the scheme already outlined above, and a new "Two-Window"-technique that allows the acquisition of *true,* i.e., non-smoothed Wigner functions.

8.4 WIGNER PHASE-SPACE MEASUREMENTS

A convenient way to describe a light field is by means of the Wigner function [4,5]. Wigner functions characterize the spatial and angular distribution of a field at the same time as well as its coherence properties. They obey simple transport equations in first-order systems such as thin lenses, magnifiers and free space [6] which are analogous to those in ray-optics.

8.4.3 Definition of Wigner Phase-Space Distribution (WPSD)

A Wigner phase-space distribution, or Wigner function, is a real function, which simultaneously describes a distribution in two conjugate variables, like time and frequency or space and momentum. In the first case it can be compared to a musical score, which tells a musician the frequencies of a song as a function of time. In the second case it can be considered the local spatial frequency spectrum of a signal. The Wigner function for a Gaussian beam closely resembles its ray-optical equivalent in geometrical optics [6]. For all other types of fields Wigner functions exhibit interference terms and negative features. Wigner functions belong to the group of so-called *quasi-probabilities.*

The Wigner function for a light field $E(x)$ is

$$W(x,p) = \frac{1}{2\pi}\int d\varepsilon \exp(i\varepsilon p)\left\langle E^*(x+\frac{\varepsilon}{2})E(x-\frac{\varepsilon}{2})\right\rangle \qquad (5)$$

$$= \int d\varepsilon \exp(i\varepsilon p)\Gamma(x+\frac{\varepsilon}{2}, x-\frac{\varepsilon}{2}) \quad ,$$

where x and p are again the transverse position and the transverse wave-vector of the light field. The angled brackets signify temporal averaging for partially coherent light fields. For a given transverse position x, $W(x,p)$ is the Fourier transform integral of the mutual coherence functions $\Gamma(x + \varepsilon/2, x - \varepsilon/2)$ centered around x. Similarly, for a given transverse momentum p,

$W(x,p)$ is the Fourier transform integral of the *angular* mutual coherence functions $\Gamma(p + q/2, p - q/2)$ centered around p.

Wigner functions contain the complete phase information about a light field, which can easily be seen from its Fourier transform relationship to the mutual coherence function. Therefore, they offer an attractive framework in which to study the propagation of optical coherence through random media [7].

The light sources suitable for OCT and related methods usually belong to the group of Gaussian-Schell sources. Those sources are characterized by a transverse mutual coherence function, which depends only on the distance between two points in a plane perpendicular to the direction of propagation [8]. The mutual coherence function for such a Gaussian-Schell beam can be written as

$$\Gamma(x_1, x_2) = \exp\left[-\frac{x_1^2 + x_2^2}{4\sigma_s^2} - \frac{(x_1 - x_2)^2}{2\sigma_g^2} - \frac{ik}{2R}(x_1^2 - x_2^2)\right], \quad (6)$$

where $2\sigma_s$ is the beam e^{-2} intensity beam radius, σ_g is its transverse coherence length and R its radius of curvature.

Most laser- and SLD beams can be viewed as transverse coherent, where $\sigma_g >> \sigma_s$. In that case the exponential term in the middle of equation 6 is approximately unity. The mutual coherence function then becomes separable and is proportional to the product of the fields at positions x_1 and x_2.

For the mutual coherence function in equation 6, the corresponding Wigner function is, according to equation 5,

$$W(x, p) = \frac{\pi}{a}\exp\left[-\frac{x^2}{2\sigma_s^2} - \frac{\left(\frac{kx}{R} + p\right)^2}{4\alpha}\right], \quad (7)$$

where $a = 1/(8\sigma_s^2) + 1/(2\sigma_g^2)$. The momentum spread of a light field in phase-space becomes larger with decreasing transverse coherence length σ_g. The momentum peaks at $p = -kx/R$.

For transversely coherent light, the resulting Wigner function reduces to

$$W^{coh}(x, p) = 8\pi\sigma_s^2 \exp\left[\frac{x^2}{2\sigma_s^2} - 2\sigma_s^2\left(\frac{kx}{R} + p\right)^2\right]. \quad (8)$$

For the collimated beam $R = \infty$ on the left, σ_s is both in the denominator of the x-prefactor and the enumerator of the p-prefactor, which confirms the inverse relationship between the size of the beam and its angular spread.

Figure 8 shows ray-diagrams (top) and their corresponding Wigner functions (bottom) for a Gaussian beam waist (left), a divergent (middle) and convergent (right) Gaussian beam.

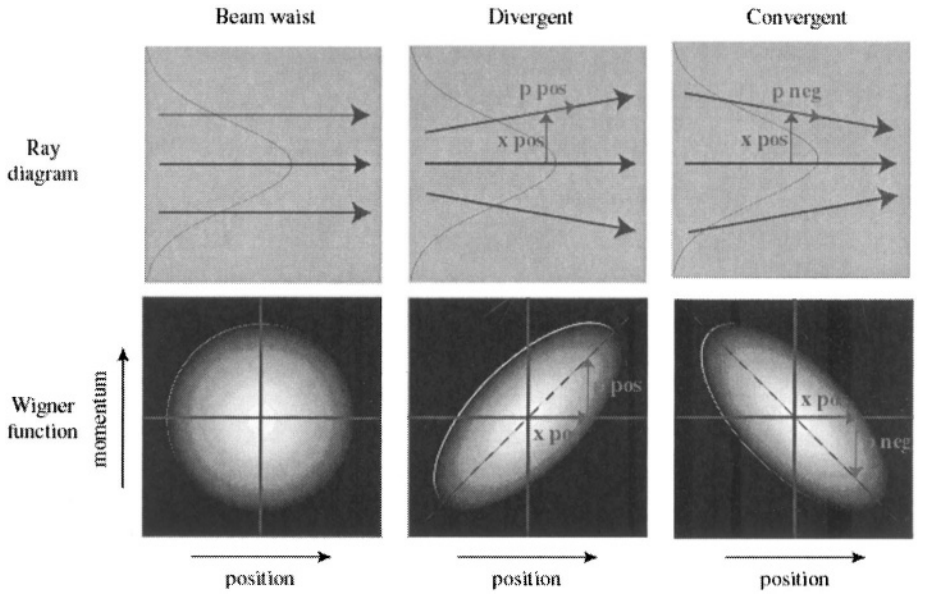

Figure 8. Ray-diagrams and their corresponding Wigner function for a collimated, divergent and convergent Gaussian beam.

For a beam waist, there is no correlation between transverse position and transverse momentum; the corresponding Wigner function is a circle or upright ellipse. For a divergent beam (R positive), the momentum distribution is centered around positive values for positive x and around negative values for negative x. This is consistent with the physical picture of off-axis parts of a divergent beam moving away from the center. An opposite relationship between x and p exists for a convergent beam, seen on the right, as can easily be seen.

A Gaussian beam is the only field for which the Wigner distribution is positive throughout phase-space. Even the combination of two Gaussian beams separated by a distance displays negative features as part of an additional oscillatory term in momentum [5].

8.4.2 Propagation of Wigner Functions

From the point-spread functions of mutual coherence functions, the laws of propagation for a Wigner function can easily be derived [6]. Along a direction z, a Wigner functions propagates according to

$$W_o(x,p) = W_i(x - \frac{zp}{k}, p) \quad . \tag{9}$$

For the transmission through a lens of focal length f, the Wigner functions transforms according to

$$W_o(x,p) = W_i(x, p + \frac{kx}{f}) \quad . \tag{10}$$

In both cases, the phase-space coordinates x and p transform as in the ray-picture. This convenient property also holds for other Luneburg's first-order systems.

8.4.3 Single-Window Heterodyne Technique for Measuring Smoothed WPSD's

In this section we will explain the experimental setup for the single-window technique that we have used in the past to measure *smoothed* Wigner phase-space distributions (WPSD's). The basic concept is the heterodyne measurement of a signal field by means of a single local oscillator (LO) beam as already described in subsection 8.1.2. The signal- and LO fields are frequency-shifted by different amounts and superposed on a detector. The detector measures a beat note, which corresponds to the difference in frequencies of signal- and LO fields. Its amplitude is proportional to the overlap integral of both fields at the area of coincidence. By stepwise changing the relative transverse position x and transverse momentum p of the LO with respect to the signal field and recording the beat signal, the phase-space distribution of the signal field can be determined. For maximum resolution, the LO itself must be as small as possible in phase-space, that means its diameter and angular spread must be minimal. The trade-off between small size and angular spread can best be met by using a Gaussian beam. A Gaussian beam of 'diameter' a has an angular spread of about λ/a. Therefore, the smallest features in the signal field that can be measured arc on the order of a in size and $1/a$ in transverse momentum. The finite x- and p resolution leads to a smoothing effect of the measured signal. Therefore, we refer to the single-LO technique as a technique for measuring *'smoothed'* Wigner functions, which will be explained in the following.

Figure 9 shows the basic setup for the measurement of stationary smooth Wigner functions. The light source in this setup is a *superluminescent diode* (SLD), which produces broadband-light usually centered in the red to infrared and with a spectral width of about 10 nm. The longitudinal coherence length is on the order of tens of microns then.

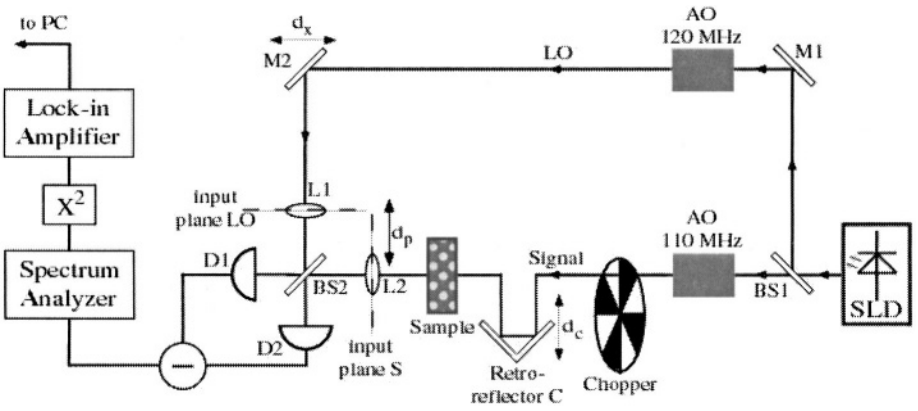

Figure 9. Experimental setup for measuring stationary smoothed Wigner functions using a superluminescent diode (SLD) as a light source.

The SLD beam is split at beam splitter BS_1 in a *signal* arm S and a *local oscillator* arm LO. Each beam is sent through an acousto-optic modulator crystal (AO); the signal beam is shifted by 110 MHz and the LO beam by 120 MHz. This results in a frequency difference of 10 MHz, which will enable the detection of a beat signal. The signal beam then passes through a chopper and a retro-reflector, which for now we will assume to be adjusted so that the path lengths of signal and local oscillator beam are identical. Afterwards, the signal beam passes through the cell containing the sample under investigation and reaches the input plane at the location of lens L_2. The LO passes a translating mirror M_2 and reaches the second input plane at lens L_1. The input planes are defined as the reference planes at which the incident signal field and the LO beam are compared to each other and where the Wigner function is measured. After passing the input planes, the signal and the LO fields are superposed in beam splitter BS_2 and the 10 MHz beat signal is detected by a balanced detector, the workings of which are described in section 8.1.2. Lenses L_1 and L_2 are at a distance of their focal length f=6 cm from the detector for three reasons. Firstly, the incident fields are usually rather more collimated than focused; by passing them through a lens and placing the detector in the focal plane, all light can be collected into the detector. Secondly, the translation of one of the lenses, in our case L_2, can be used to change the relative angle between the signal- and the LO field, which is how the momentum distribution of the signal field is scanned. Finally, when mirror M_2 is translated in order to change the transverse position of the LO relative to the signal field, the detector input lens keeps the focal point of the LO on the detector.

The light of the superposed signal and LO field generate - among other terms - a 10 MHz beat note current in the photodiodes, which is proportional

to the spatial overlap of their electric fields in the detector planes. The total photodiode current is transformed into a voltage and fed into a spectrum analyzer, which provides a root mean square voltage at its output which is proportional to the beat signal. The output voltage of the spectrum analyzer is then squared using a low noise multiplier and fed into a lock-in amplifier, which detects the squared beat signal using the chopper frequency as a reference. The squaring of the beat signal allows direct measurement of smoothed Wigner function and real time noise suppression, as explained in subsection 8.1.3.

In order to generate smoothed Wigner function plots of the signal field, we scan the LO relative to it in position and momentum and simultaneously record the mean square beat signal. The relative position of the LO to the signal field S can be changed by an amount d_x via translation of mirror M_2. The relative angle between S and LO is modified via translation of lens L_2 by an amount d_p. These translations are performed by linear actuators holding M_2 and L_2 on their moving table, respectively. These actuators are controlled by a LabView program on a PC. The scanning process is performed line by line in phase-space: for each momentum, the signal is measured for a recurring set of positions.

It is apparent that a translation of M_2 by d_x corresponds to a translation of the LO with respect to the signal beam by the same amount. The translation of lens L_2 by an amount d_p on the other hand changes the angle of the transmitting field in its focal plane by $\theta_p = -d_p/f$ as depicted in Figure 10. This corresponds to a change in transverse momentum of $k\theta_p$, where $k=2\pi/\lambda$ is the wavevector of the field.

The usage of broadband light in our experiment enables the time-resolved measurement of Wigner functions. This is because in order for S and LO to interfere, their path lengths must match within a coherence length l_c of the light used. This path difference requirement translates into a time-difference requirement with $t_c = l_c/c$, where c is the speed of light in the sample. In our experiments, we are mainly interested in the selection of path-lengths, in particular in the experiments involving random media.

The implementation of time-resolution requires the addition of a retro-reflector into the signal arm to equalize the path lengths of S and LO during the adjustment process (see Figure 9). Later on it enables the selection of a path delay offset Δl to selectively measure parts of the signal field that have traveled a path length Δl in the medium. The retro-reflector also counterbalances changes in the relative path-delay between S and LO due to the movement of M_2 and L_2 during the scanning process. The total path-delay of the retro-reflector is

$$2d_c + d_x + \frac{d_p^{\,2}}{2f} - \frac{d_x d_p}{2f} \quad , \tag{11}$$

where d_c is the translation of the reflector; the factor accounts for twice that distance the light travels on its way to and from the reflector. The second term is the correction term for the translation of mirror M_2 when scanning the position of the signal field; the last two terms are the corrections for the translation of lens L_2 when scanning the momentum. For a derivation we refer to [9,10].

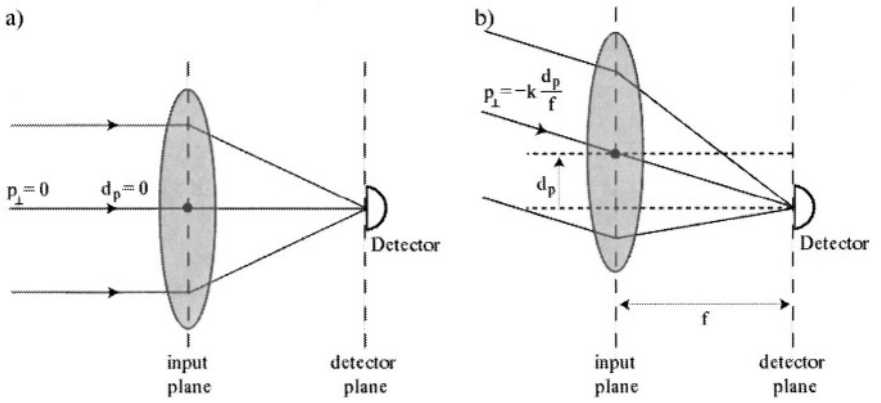

Figure 10. Selection of transverse momenta of a detected signal field. a) lens is centered with respect to detector; field contributions with p=0 are detected at the focus. b) lens is off center by d_p; field contributions with $p = -kd_p/f$ are detected at the focus.

The beat voltage is proportional to the integral of the beat intensity of the electric fields incident onto the detector:

$$V_B \sim \int dx \left\langle E_S^*(x) E_{LO}(x) \right\rangle \quad . \tag{12}$$

Using well-known laws for the propagation of fields and mutual coherence functions [8], the beat voltage can be expressed in terms of the fields incident on to the *input plane* in our experiment (see Figures 9 and 10). The mean square beat signal then follows directly:

$$|V_B(d_x, d_p)|^2 \sim \left| \int d\eta \left\langle E_{LO}^*(\eta - d_x) E_S(\eta) \right\rangle \exp\left(\frac{ik\eta d_p}{f} \right) \right|^2 \quad , \tag{13}$$

where the angled brackets denote averaging over the rapidly fluctuating broadband light.

For sufficiently transverse coherent light, i.e., for $\sigma_g >> \sigma_s$, the electric fields of signal and LO field interfere over their full beam width, provided their path length is equal to within the coherence length. In that case, no averaging is necessary and equation 13 can be further simplified. After a few lines of transformation we get:

$$|V_B(d_x, d_p)|^2 \sim \int dx dp W_{LO}(x - d_x, p - p_x) W_S(x, p) \; . \qquad (14)$$

This is a convolution in both x and p of the Wigner functions of the signal- and the LO field, which shows that the measured distribution is indeed a smoothed Wigner function. For identical signal- and LO beams, such a convolution broadens the phase-space profile by a factor $\sqrt{2}$.

The degree of smoothing and therefore the resolution of the measured signal field is determined by the size of the LO in phase-space, namely its spatial width and its angular spread. For a Gaussian beam with a diameter of $4\sigma_s$ the angular spread is about $\lambda/(4\sigma_s)$, i.e., $\Delta k = 1/(4\sigma_s)$, so that $\Delta x \Delta k \approx 1$.

There is obviously a trade-off between good position- and momentum resolution: a small size of the LO provides good position resolution, but its resulting high momentum spread decreases the momentum resolution. The opposite relationship holds for a wide collimated beam. This uncertainty relation associated with Fourier transform pairs can be surpassed by using a combination of a focused and a collimated LO, as will be described in the next section.

8.4.4 Two-Window Heterodyne Measurement of True Wigner Functions

The previous section, which treated the experimental setup for the single-window technique showed that there is a trade-off between position and momentum resolution if a single LO is used. Therefore, the measured signal is a smoothed Wigner function rather then a true Wigner function. In the following, we present a *two-window* technique, which employs a combination of two phase-coupled LOs, which enables the measurement of non-smoothed Wigner functions [11]. The set of phase-coupled LOs consists of an LO which is narrowly focused to allow high spatial resolution (*small* LO or SLO), and a second LO which is highly collimated and which provides high angular resolution (*big* LO or BLO). The LOs are frequency-shifted by 120 and 120.003 MHz, respectively; their frequency-difference of 3 kHz is locked to an external oscillator by means of a phase-locked loop. The signal field S, which is frequency-shifted by 110 MHz as in the single-window experimental setup, is superposed with the dual-LO in the detector plane.

This time, the beat note contains two frequency components, one from the superposition of S and BLO at 10 MHz, the other from S and SLO at 10.003 MHz. The beat-signals are detected by a spectrum analyzer and squared as in the single-window case. The signal exiting the squarer oscillates at the frequency difference of SLO and BLO of 3 kHz and is detected in the lock-in amplifier, which uses the 3 kHz external oscillator as a reference. The quadrature outputs of the lock-in amplifier contain all the information about the true Wigner function, as we will see below.

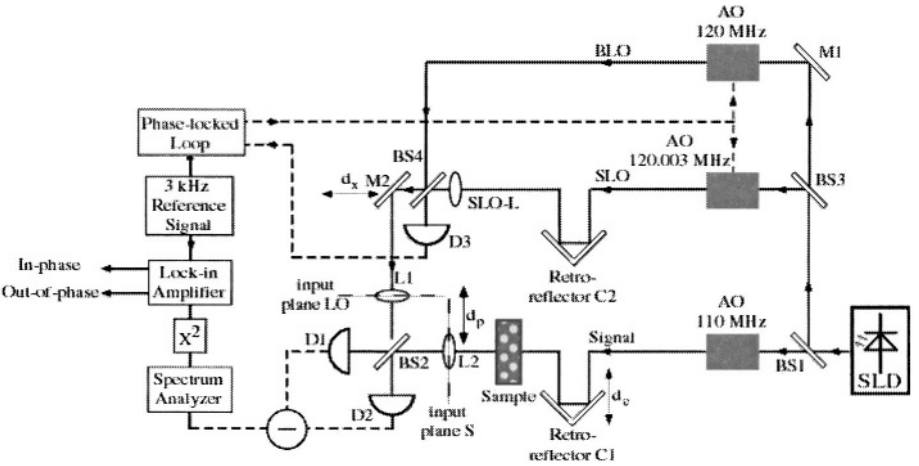

Figure 11. Two-window technique experimental setup for measuring true Wigner functions.

As already mentioned, the two-window technique employs a pair of phase-coupled LO's instead of a single LO as in the single-window case. This pair consists of a large collimated beam ('Big LO' or 'BLO',) providing high momentum resolution and a small focused beam ('Small LO' or 'SLO') providing high spatial resolution. Figure 11 shows the experimental setup. Again, several optical components, which are not crucial for grasping the concept of this technique, were omitted in the Figure. Electronic connections are displayed as dashed lines, optical pathways as solid lines. While the signal arm has lost the chopper, the LO arm is split up by beam splitter BS_3. The SLO beam is shifted by 120.003 MHz and reaches the lens SLO-L (f=25 cm), which focuses the beam onto the LO-input plane. The BLO is shifted by 120 MHz and superposed with the SLO at beamsplitter BS_4. In order to match the path length of BLO and SLO, a second retro-reflector is introduced in the BLO. The 3 kHz frequency difference between the SLO and the BLO is kept constant by means of a phase-locked loop (PLL) and detector D_3: The PLL compares a 3 kHz reference signal with the beat signal of SLO and BLO at detector D_3, and multiplies both signals and adjusts the

voltage controlled SLO-AO by an error voltage in order to keep the averaged product zero, which is *only* the case when reference- and beat-frequency are equal and out of phase by 90 degrees. The phase-coupled LO-pair is, as in the single-LO setup, mixed with the signal field and detected by a balanced detector. The beat notes of 10 and 10.003 MHz are detected by a spectrum analyzer, squared, and fed into a lock-in amplifier which uses the 3 kHz reference signal as a reference as opposed to the chopper used in the single-window setup. The lock-in amplifier produces two quadrature voltages: an *in-phase* signal which is proportional to the signal component which is in phase with respect to the reference signal, and an *out-of-phase* signal which is proportional to the component which is 90 degrees shifted to it. In combination they contain the complete amplitude- and phase information of the detected signal field. In the following we show how the true Wigner function of a signal field can be measured using this setup.

As described above, the LO in the dual-LO scheme is a phase-coupled pair of a SLO and the BLO. Its electric field can be written as:

$$E_{LO}(x) \propto \exp\left(-\frac{x^2}{2a^2}\right) + \beta e^{i\omega t} \exp\left(-\frac{x^2}{2A^2}\right), \qquad (15)$$

where $e^{i\omega t}$ denotes the relative phase of the BLO with respect to the SLO determined by the phase-locking at $\omega = 2\pi \times 3$ kHz and β its relative amplitude. a and A are the beam intensity e^{-2} radii for the SLO and BLO, respectively. The Wigner function of this dual-LO can be calculated using equation 5, but keeping only the cross-terms, because we detect the beat signal at frequency ω. For $A >> a$, we obtain

$$W_{LO}(x,p) \propto \exp\left(-\frac{2x^2}{A^2} - 2a^2p^2\right)\cos(2xp - \omega t) \ . \qquad (16)$$

When we choose the diameters of BLO and SLO so that A is much bigger than the position range of the signal field and $1/a$ much bigger than the momentum range of the signal field we measure, the exponential terms in equation 16 reduce to unity and we get:

$$W_{LO}(x,p) \propto \cos(2xp - \omega t) \qquad (17)$$

The *in-phase* beat signal then follows directly from equation 14, where we change the notation from $|V_B|^2$ to S_B for the two-window case:

$$S_B^{in}(d_x, p_x) \propto \int dx dp \cos[2(x - d_x)(p - p_x)] \ W_S(x,p) \ . \qquad (18)$$

The second quadrature of the lock-in amplifier, which is referred to as *out-of-phase* signal, measures the signal field component that is 90 degrees out of phase with respect to the reference signal and can be found by subtracting a phase of 90 degrees from ωt in equation 17. This manipulation just changes cosine into sine:

$$S_B^{out}(d_x, p_x) \propto \int dx dp \sin[2(x-d_x)(p-p_x)]\, W_S(x,p)\ . \quad (19)$$

The combined *in-phase* and *out-of-phase* signals can be written more elegantly using complex notation:

$$S_B(d_x, p_x) \propto \int dx dp \exp[i2(x-d_x)(p-p_x)]\, W_S(x,p)\ . \quad (20)$$

This expression shows that $S_B(x,p)$ is a *Margenau-Hill* transformation of the *true* Wigner function $W_S(x,p)$ of the field. We will refer to $S_B(d_x,p_x)$ as the *complex beat signal.*

In order to retrieve the Wigner function $W_S(x,p)$ of the signal field, the expression in equation 20 must be inverted. It can easily be verified that the inverse *Margenau-Hill* transformation is

$$W_S(x,p) \propto \frac{1}{\pi} \int dx' dp' \exp[-i2(x-x')(p-p')] S_B(x',p')\ . \quad (21)$$

Equation 21 shows that the two-window technique enables the retrieval of the *true* Wigner function without the smoothing effect of a convolution with the Wigner function of a single-LO. The spatial and momentum resolution with which the Wigner function is measured is limited by the size of the small LO and the degree of collimation of the big LO. In practice, we use a C++ program to perform this inverse *Margenau-Hill* transformation for the data we measure.

Another interesting relationship connects the complex beat signal directly with the electric field of the signal field and can be derived from the product integral of the two LO beat notes which itself cause the 3 kHz beat note:

$$S_B(x,p) \propto \int dx\ V_{SLO}^*(x) V_{BLO}(x) \quad (22)$$

$$= \langle E^*(x) E(p) \rangle \exp(ixp). \quad (23)$$

The last line follows from the first line for an ideal dual-LO, i.e., perfectly collimated BLO and focused SLO. In this case, the measured signal $S_B(x,p)$ is the averaged correlation of the signal field at a given position $E(x)$ and the signal field at given $E(p)$, times a phase-factor which is due to an additional relative path difference between BLO and S. In applications

where the signal field is sufficiently broad in space and in momentum, equation 23 is very accurate. This is the case in all our experiments involving turbid media. In our experiments involving the characterization of the signal beam itself on the other hand, we have to take into account the finite size of the BLO and the non-zero size of the SLO we use. Depending on the beam parameters, there are various approximations, which can easily be calculated using equations 12 and 23. We will mention only one important case here, where BLO and S are flat and have the same size (i.e., $A=B$). In that case, the complex beat signal is

$$S_B(x,p) \propto \left\langle E^*\left(\frac{x}{\sqrt{2/3}}\right) E\left(\frac{p}{\sqrt{2}}\right)\right\rangle \exp\left(i\frac{xp}{2}\right) \quad . \qquad (24)$$

This corresponds to a narrowing of the beat voltage profile in position and a broadening in momentum.

8.5 APPLICATIONS

In this section, we will present three applications of our two-window technique. We demonstrate the characterization of Gaussian-Schell beams (subsection 8.5.1), of light fields in multiply scattering media (subsection 8.5.2), and of a speckle field (subsection 8.5.3).

8.5.1 Characterizing Gaussian-Schell Beams

A Gaussian-Schell beam is a Gaussian beam where the spectral degree of coherence depends only on the difference between two points in a plane perpendicular to the direction of propagation [8].

The spatial- and coherence properties of such a signal beam S can easily be determined using the two-window technique [10]: the complex beat signal $S_B(d_x,p_x)$ and the longitudinal profile $S_B(z)$ of the signal beam itself are measured, which then determine all beam parameters of interest for our experiment. For general Gaussian-Schell beams, the resulting expressions for $S_B(d_x,p_x)$ are very complicated. For special cases, i.e., beam waists, very small/big R or transversely coherent beams, those relations simplify considerably.

In the following section, we first show how to extract the beam size and *transverse* coherence length of the signal beam from a transverse scan at the beams waist, which yield the global coherence for the beam everywhere. We also demonstrate how to derive beam size and radius of curvature of a transversely coherent Gaussian beam.

For a Gaussian-Schell signal beam at its waist, the measured complex beat signal is of the form

$$S_B(x,p) \propto \exp\left[-\frac{d_x^2}{(d_x^e)^2}-\frac{p_x^2}{(p_x^e)^2}-i\frac{d_x p_x}{2}\right], \qquad (25)$$

d_x^e and p_x^e then determine the beam parameters σ_s and σ_g. Figure 12 shows the quadrature signals for this case; a) is the in-phase signal, that is, the real part of $S_B(x,p)$, b) is the out-of-phase signal, which is the imaginary part of $S_B(x,p)$.

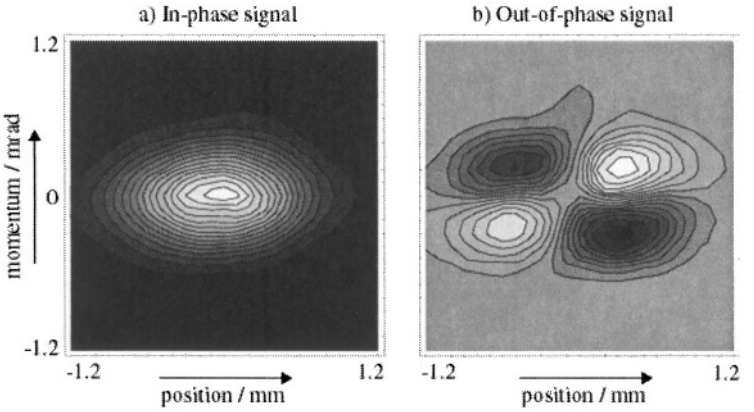

Figure 12. In-phase- (a) and out-of-phase (b) quadrature signal of a Gaussian-Schell beam waist.

d_x^e and p_x^e are:

$$\frac{1}{\left(d_x^e\right)^2}=\frac{3}{8\sigma_s^2}+\frac{1}{4\sigma_s^2+2\sigma_g^2} \qquad (26)$$

$$\frac{1}{\left(p_x^e\right)^2}=\frac{1}{2\left(\frac{1}{\sigma_s^2}+\frac{4}{\sigma_g^2}\right)}. \qquad (27)$$

Solving for σ_s and σ_g and yields:

$$\sigma_s^2=-\frac{\frac{8}{(d_x^e)^2}-\frac{5}{2}(p_x^e)^2+\sqrt{\frac{64}{(d_x^e)^4}-24\frac{(p_x^e)^2}{(d_x^e)^2}+\frac{25}{4}(p_x^e)^4}}{8p_x^e/d_x^e}, \qquad (28)$$

$$\sigma_g^2 = -\frac{\frac{8}{(d_x^e)^2} - \frac{7}{2}(p_x^e)^2 + \sqrt{\frac{64}{(d_x^e)^4} - 24\frac{(p_x^e)^2}{(d_x^e)^2} + \frac{25}{4}(p_x^e)^4}}{4(p_x^e)^2/(d_x^e)^2 - \frac{3}{4}(p_x^e)^4} \quad . \quad (29)$$

The beam parameters can be derived from both quadrature signals. The easiest way is to derive them from the phase-space distance between the peaks in the out-of-phase signal as opposed to the in-phase part, which requires fitting a Gaussian to a curve to measure its width. Figure 13 shows a general out-of-phase signal; the distance between the peaks is $2x_m$ in position and $2p_m$ in momentum.

The parameter d_x and p_x of the complex beat signal in equation 25 can then be expressed in terms of the half-distances x_m and p_m:

$$d_x^e = \sqrt{\frac{4x_m}{p_m}\tan\left(\frac{x_m p_m}{2}\right)} \quad , \quad (30)$$

$$p_x^e = \sqrt{\frac{4p_m}{x_m}\tan\left(\frac{x_m p_m}{2}\right)} \quad , \quad (31)$$

σ_s and σ_g then follow directly when we insert the values obtained in equations 30 and 31 into equations 28 and 29.

A similarly simple way of retrieving σ_s and R applies in the case for a transversely coherent beam. Figure 14 shows the quadrature signals in that case. The complex beat signal in this case reads [10]:

$$S_B(d_x, p_x) = \exp\left[-\frac{1}{4\sigma_x^2}\left(d_x^2 - p_x^2\frac{R^2}{k^2}\right) + \frac{ik}{2R}\left(d_x - p_x\frac{R}{k}\right)^2\right] . \quad (32)$$

Here it is more convenient to use the points of intersection between one of the quadrature signal contours with the position- and momentum axes that vanish for a flat wavefront. In the following, we choose again the out-of-phase part. Figure 15 shows the position- and momentum distribution along the axes.

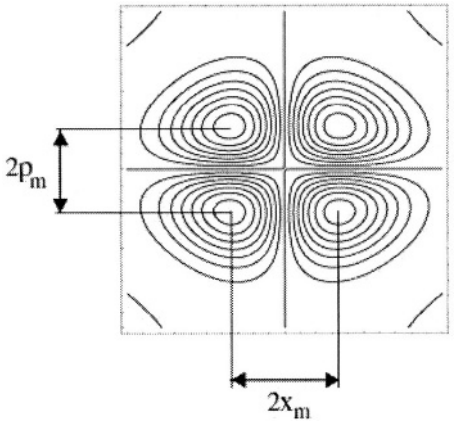

Figure 13. The distances in position and momentum between the peaks of the out-of-phase signal yield x_m and p_m for the calculation of d_x^e and p_x^e.

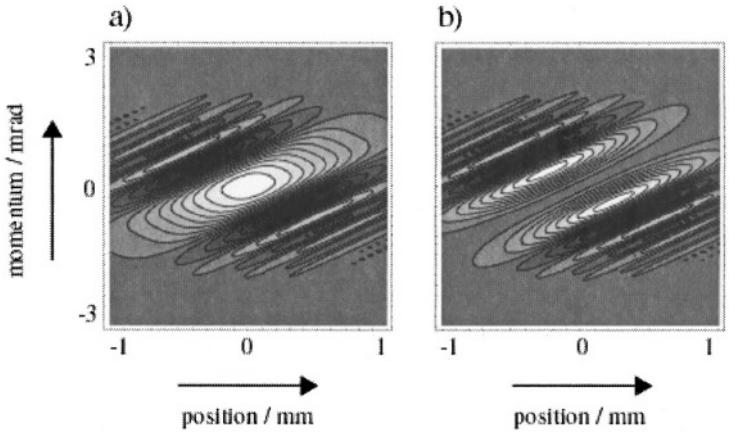

Figure 14. In-phase- (a) and out-of-phase quadrature signal (b) of $S_B(d_x, p_x)$ for a divergent Gaussian beam.

The intersection of the peaks with the axes can be calculated by setting position or momentum to zero and requiring the first derivative with respect to the other variable to vanish. After a few lines of calculation, we get

$$R = \pm \frac{d_x^m}{p_x^m} k \tag{33}$$

and

$$\sigma_s = \sqrt{\frac{1}{2}\frac{d_x^m}{p_x^m}\tan\left(\frac{d_x^m p_x^m}{2}\right)} \quad . \tag{34}$$

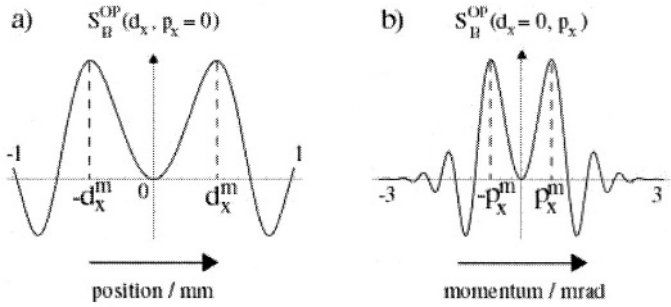

Figure 15. The position distribution for zero momentum (a) and the momentum distribution at the beam center (b) of the out-of-phase quadrature part of $S_B(d_x, p_x)$ in Figure 14(b) are used to extract σ_s and R.

8.5.2 Light Fields in Multiple Scattering Media

Scattering in random media is of great interest in biophysics, where many optical techniques exist to characterize biological tissue, in particular *in vivo*. In some cases, scattering by cells is an unwelcome byproduct that can be suppressed by certain techniques. In other cases the scattered light is detected and analyzed in order to gain information about the scatterers themselves. In particular, the spatial and angular distribution of a field scattered from a skin layer can provide useful information about an architectural atypia of its skin cells, which is an indicator for or, for mild abnormalities, a potential precursor to skin cancer.

This provides the grounds for a new diagnostic tool, which might potentially replace the time-consuming and invasive biopsy of today. Scattering theory is a vast and complex field and there exists no unique theory to describe and model all scenarios. Depending on the density and physical and geometrical properties of the scatterers and the surrounding medium, several approximations exist that provide exact results in many practical cases. Due to the advance of sufficiently fast computers, most of today's modeling in scattering theory has shifted to numerical calculations, in particular Monte Carlo computations.

For sufficiently dense distributions of scatterers and a scattering coefficient with low angular dependence, the propagation of photons can be approximated by a Markovian random-walk which means the intensity distribution is described by the isotropic *diffusion equation*. Most practical examples in the diffusion-approximation regime display an incoherent light field emerging from the random medium, due to the rapid randomization of

the fields' phase and amplitude. There are some interesting coherent phenomena though, which have gained increasing attention since their realization in optical experiments in the beginning of the 1980s. They are based on interference of waves counter-propagating through identical paths in the medium. The most important examples of this kind are *Anderson localization* and *enhanced backscattering,* the latter of which we will observe by means of our two-window technique [10].

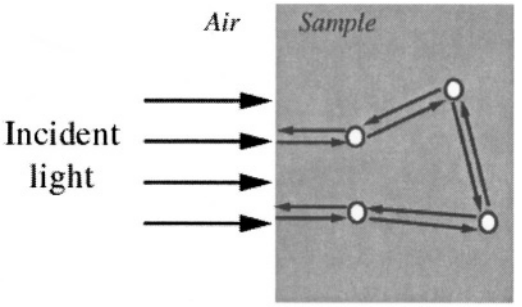

Figure 16. Principle of enhanced backscattering: a light field is on to a turbid medium. Two wavelets are traveling in opposite directions and are scattered by the same sequence of scatterers. Their fields add coherently, leading to twice the intensity opposite to the direction of incidence.

Enhanced backscatter is a precursor to Anderson localization and is often called 'weak localization' [12,13]. It can be observed for much less dense random media though. Figure 16 illustrates the enhanced backscattering effect: a light beam is incident on a highly scattering random medium. As in the case of Anderson localization, two wavelets traveling the same path in the medium, but from opposite directions, interfere constructively, resulting in an reflective intensity in the opposite direction of the incoming beam twice as high as in other directions. This is due to the fact that the amplitudes of the counter-propagating wavelets add up rather than the intensities.

With our time-resolved two-window technique we are able to study the contributions to enhanced backscattering from various path lengths in the medium. In order to study the propagation and backscattering of arbitrary incident fields, it is convenient to switch to the Wigner function notation. We assume the diffusion equation to be valid, so that the probability density for a photon entering the random medium at position $\boldsymbol{r}$ and time t=0 to leave the medium at position $\boldsymbol{r'}$ and time t is

$$P(r,r',t) = \frac{z_0^2}{(4\pi)^{3/2}(Dt)^{5/2}} \exp\left(-\frac{(r-r')^2}{4Dt}\right) , \qquad (35)$$

where z_0 is about 2/3 of the mean free scattering path in the medium and D the diffusion constant. The derivation for the backscattered Wigner function

as a function of the Wigner function of an incident field is rather lengthy (see [10]), so we will just mention the results. The resulting Wigner functions consists of the sum of two contributions, an incoherent and coherent part:

$$W_{Back}^{Incoh}(x,p) \propto \frac{z_0^2}{(4\pi)^{3/2}(Dt)^{5/2}} \iint d^2x' d^2p' \exp\left[-\frac{(x-x')^2}{4Dt}\right] W_0(x',p') \,, \quad (36)$$

$$W_{Back}^{Coh}(x,p) \propto \frac{z_0^2}{Dt} \int d^2p' \exp\left[-Dt(p+p')^2\right] W_0(x,p'), \quad (37)$$

W_{Back}^{Incoh} describes the incoherent background, i.e., the light which backscatters without interference effects. W_{Back}^{Coh} describes the light that undergoes enhanced backscattering. W_0 is the Wigner function of the. incident field.

W_{Back}^{Incoh} is the convolution of the incident Wigner function and a Gaussian broadening term. It becomes broader with time as diffusion progresses. For the hypothetical case of $W_0=\delta(x)$, W_{Back}^{Incoh} would be proportional to the probability density in equation 35. It shows no directional preference.

For the coherent part W_{Back}^{Coh}, the incident Wigner function is convolved with a Gaussian term, which, unlike its counterpart in the incoherent term, becomes narrower with time, thereby causing the momentum distribution of the enhanced backscatter Wigner function also to narrow with time. This Gaussian term is maximal for $\boldsymbol{p} = \boldsymbol{p}'$, which agrees with the physical picture that enhanced backscattering is most intense in the direction exactly opposite of the incident field.

In order to detect enhanced backscattering, we modify the signal arm close to the detector as shown in Figure 17. The signal beam is deflected onto the sample by a beam splitter and projected onto the detector input plane by a 4*f*-system. The 4*f*-system is necessary to collect the light immediately at the sample surface, which would otherwise change its wavefront while propagating to the detection input plane.

The turbid medium we use in our backscatter experiments consists of polystyrene spheres with a diameter of 0.5 μm (1.9% variance) suspended in a neutral buoyancy solution of water (80%) and glycerol (20%). The mixture has a refractive index of n_0=1.36, the spheres n_{sph}=1.59, resulting in a relative refractive index of the spheres of 1.17. These spheres are a little

smaller than the wavelength of our SLD, which means their angular scattering distribution is relatively large.

Figure 18 shows the experimental data and the theoretical predictions for the Wigner functions of the enhanced backscatter peak for two different path delays in the medium. In the top row the path delay is 150 μm, which results in a path delay in the medium of 150 μm/n_0=150 μm/1.36 = 110 μm. In the bottom row the path delay is 250 μm resulting in a path delay in the medium of 185 μm. From left to right, the quadrature signals comprising the complex beat signal and the resulting Wigner function are shown; on the right is the theoretical prediction of the Wigner function. The concentration of the sample is 1.2×10^{12} spheres/cm^3, which yields a scattering mean free path of 8.3 μm and a transport mean free path of l^*=42.3 μm, according to Mie theory. The half-radius σ_s for the BLO and the incident beam are 343 μm, and for the SLO 25 μm.

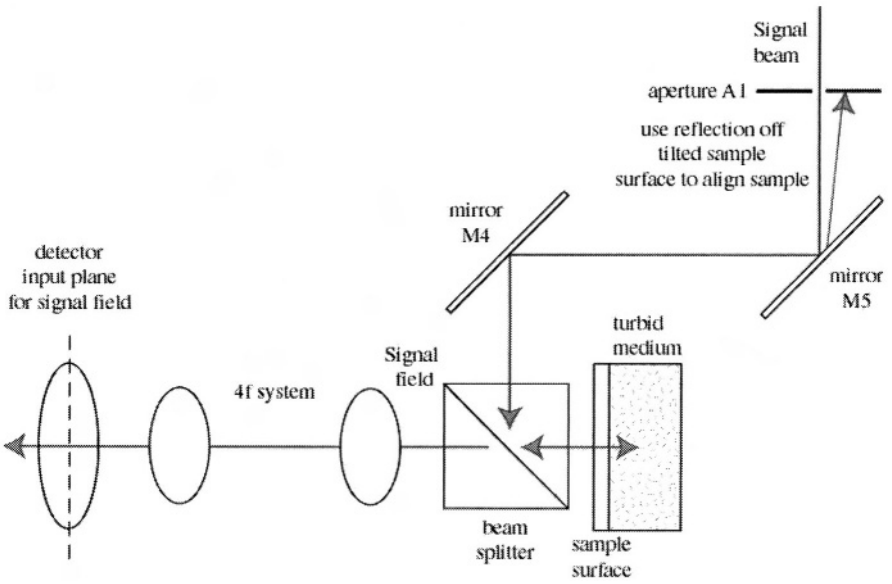

Figure 17. Modifications of signal arm for the detection of enhanced backscattering.

W_{Back}^{Incoh} is seen as the band-like structure, which is localized in position but very broad in momentum, while W_{Back}^{Coh} is the peak that is localized both in position and momentum. As can clearly be seen, the enhanced backscatter peak is narrowing in momentum with increasing path delay. The position distribution remains unaffected.

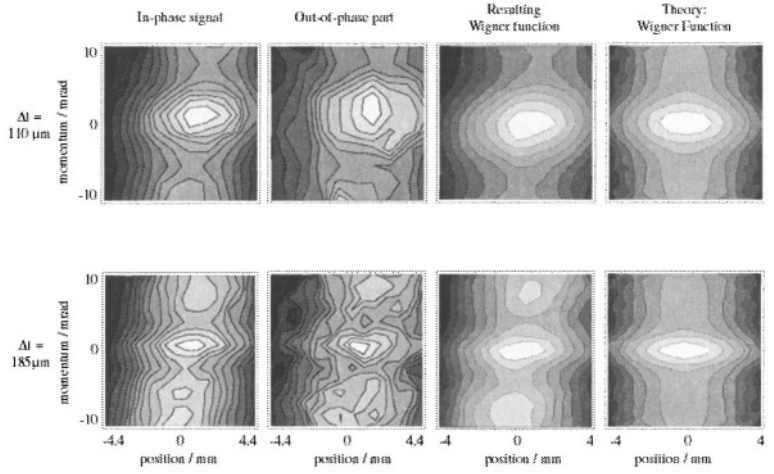

Figure 18. From left to right: measured in-phase and out-of-phase quadrature signals, and resulting Wigner function. Right: theory. Top row: path-delay of 150 μm, bottom: 250 μm.

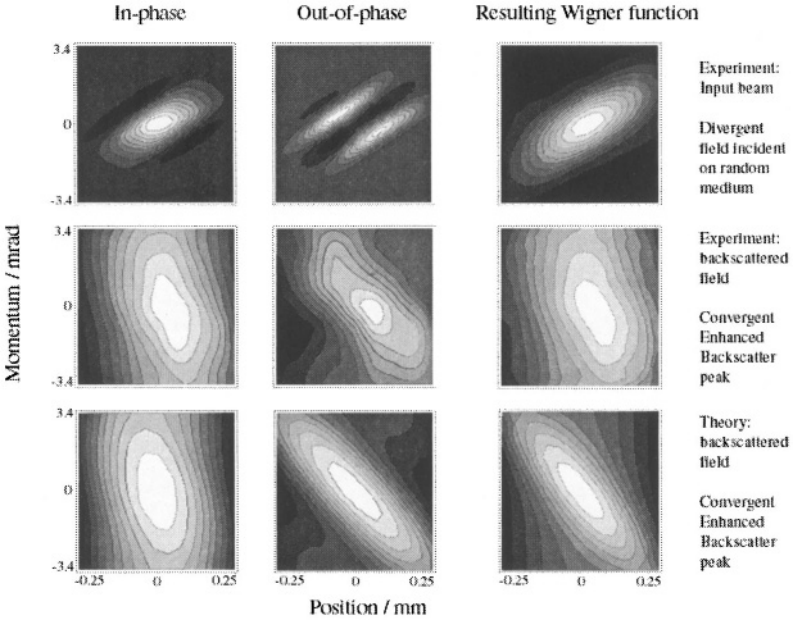

Figure 19. Top row: measured complex beat signal and resulting Wigner function of field incident on random medium. Middle row: enhanced backscatter cone of field shown in top row at a path delay of 300 μm. Bottom row: numerical simulation of backscattered field, using field parameters retrieved from incident field. The reversal of the tilt in the ellipses signifies the reversal of the curvature between the incident and backscattered field.

In the next experiment, we study the backscattered field for a divergent incident beam. The top row in Figure 19 shows the signal beam incident on the sample, measured as the beam reflected off the polished surface of the sample container. From left to right: the in-phase and out-of-phase quadrature signals at 3 kHz, scanned over +/-0.25 mm and +/-3.4 mrad. On the right is the corresponding Wigner function that is obtained from an inverse Margenau-Hill transformation of the in- and out-of-phase parts as described above. The divergence of the incident beam manifests itself in the tilted elliptic shape of the depicted Wigner function (compare Figure 8). The second row shows the enhanced backscattered field at a path-delay in the medium of 300 μm. The slope of the phase-space ellipse has changed its sign: The enhanced backscatter cone is convergent. The bottom row shows the theoretical prediction for the backscattered field, using the parameters of the incident field and the local oscillators beams used in the experiment. Theory correctly predicts the changing sign of the radius of curvature.

The out-of-phase signal seems to be more sensitive to the coherent part than the in-phase signal. This comes from the fact that the out-of-phase for the incoherent part is zero everywhere, at least theoretically. While the superposed incoherent background in the in-phase part seems to stretch the enhanced backscatter peak vertically, this influence is missing in the out-of-phase part.

8.5.3 Speckle Field

Speckle is an irregular interference pattern that can be seen when transversely coherent light is randomly scattered by a surface with fine irregularities. Figure 20 shows the in-phase signal (left column) and out-of-phase signal (right column) for a scan of a speckle field, which was generated by shining a Gaussian SLD beam on to a glass containing tiny air bubbles [10]. From top to bottom, the same speckle field is measured with increasing magnification.

The smallest range (bottom row) presents a view inside a speckle; the product of position- and momentum range is

$$0.5\,\mathrm{mm} \times 1.3\,\mathrm{mrad} = 650\,\mathrm{nm} \quad , \tag{38}$$

which is smaller than the wavelength of 678.3 nm we use.

The same phase-space is scanned by only the BLO and only the SLO is shown in Figure 21. Clearly, the resolution provided by a single LO is not sufficient to resolve the speckle. The Wigner function retrieved from the quadrature signals in Figure 20 is shown in Figure 22.

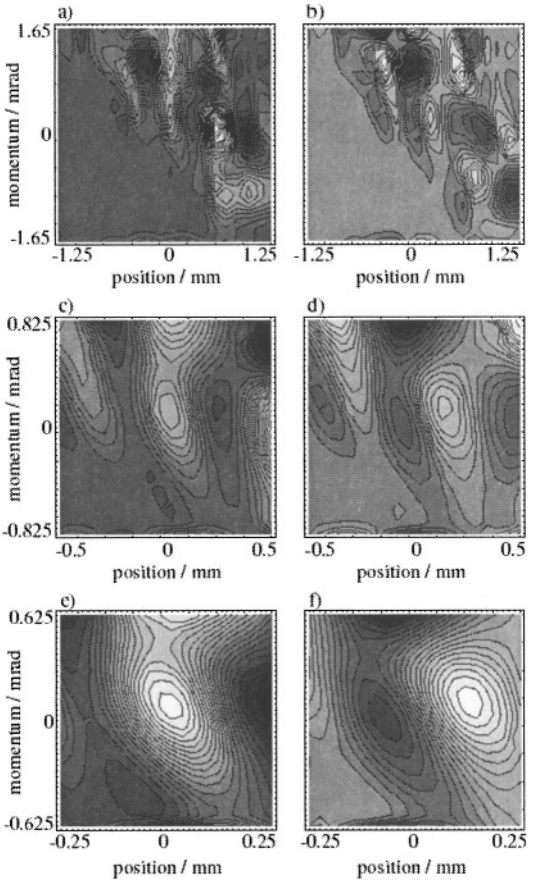

Figure 20. Quadrature signal phase-space profiles of a speckle field generated by a SLD beam incident on a piece of glass containing air bubbles. Left columns: in-phase signal, right columns: out-of-phase signal; increasing magnification from top to bottom.

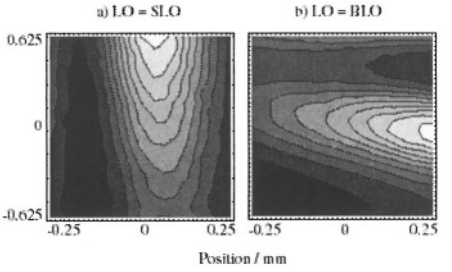

Figure 21. Single LO-scans of the speckle field shown in Figure 20(e) and (f). a) SLO only and b) BLO only.

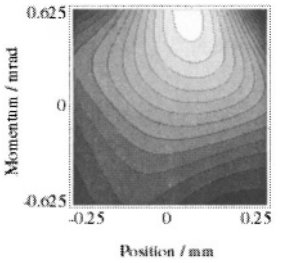

Figure 22. Wigner function of speckle field shown in Figure 20(e) and (f).

8.6 SUMMARY

Optical heterodyne techniques present a powerful tool to measure light fields. In this technique, the signal field to be measured is superposed with a local oscillator field, which is frequency-shifted relative to the signal field, and the beat note is measured. The dynamic range of this technique is very high compared to direct intensity measurements of the signal field. Its noise level is also comparably low because the signal is measured at a non-zero frequency where the noise background is weaker, and a balanced detection system enables the subtraction of classical noise.

The most basic technique employing optical heterodyne detection is optical coherence tomography (OCT). In that technique, the heterodyne beat note is measured as a function of the position of a local oscillator beam. The short coherence length of a broadband light source adds path-length resolution to the measurements, enabling depth-resolved scans of samples like *in vivo* skin tissue. In color Doppler OCT (CDOCT), the flow of objects in a sample can be measured by taking advantage of the Doppler-shift they induce in the scattered light and therefore in the heterodyne beat note.

A further development of OCT is the measurement of Wigner functions, which fully describe a light field. Wigner functions obey rigorous transport equations and are therefore a convenient way to describe the propagation of light fields.

Smoothed Wigner functions can be measured using a one-window technique by recording the mean square beat signal as a function of position and momentum. In the two-window technique, true Wigner function are obtained by recording the correlation of two beat signals, one of which depends only on the relative transverse momentum and the other one only on the relative transverse position of the dual-LO with respect to the signal field. This way, full phase- and amplitude information about the signal field, including first-order coherence properties, is obtained.

We demonstrated three applications of the two-window method; the characterization of a Gaussian-Schell signal beam, the time-resolved detection of enhanced backscattering in a turbid medium, and the examination of the field of a single speckle.

REFERENCES

1. J.A. Izatt, M.D. Kulkarni, K. Kobayashi, M.V. Sivak, J.K. Barton, and A.J. Welsh, "Optical coherence tomography for biodiagnostics," *Optics & Photonics News* 41–47 (May 1997).
2. J. A. Izatt and M. D. Kulkarni, "Doppler flow imaging using optical coherence tomography," *OSA Conference on Lasers and Electro-Optics, Anaheim,* CA, 1006, post-deadline paper CPD3-1 (1996).
3. Z. Chen, T.E. Milner, D. Dave, and J.S. Nelson, "Optical Doppler tomographic imaging of fluid flow velocity in highly scattering media," *Opt. Lett.* **22**, 64–66 (1997).
4. A. Wax, S. Bali, G.A. Alphonse, and J.E. Thomas, "Characterizing the coherence of broadband sources using optical phase space contours," *J. Biomed. Opt.* **4**, 482–489 (1999).
5. A. Wax, S. Bali, and J.E. Thomas, "Optical phase space distributions for low-coherence light," *Opt. Lett.* **24**, 1188–1190 (1999).
6. M.J. Bastiaans, "Application of the Wigner distribution function to partially coherent light," *J. Opt. Soc. Am. A* **3**, 1227–1238 (1986).
7. C.-C. Cheng and M.G. Raymer, "Long-range saturation of spatial decoherence in wave-field transport in random multiple-scattering media," *Phys. Rev. Lett.* **82**, 4807–4810 (1999).
8. L. Mandel and E. Wolf, *Optical Coherence and Quantum Optics* (Cambridge University Press, Cambridge, 1995).
9. A. Wax, "Optical phase space distributions for coherence tomography," Ph.D. Dissertation (Duke University, Durham, 1999).
10. F. Reil, "Two-window heterodyne methods to characterize light fields," Ph.D. Dissertation (Duke University, Durham, 2003).
11. K.F. Lee, F. Reil, S. Bali, A. Wax, and J.E. Thomas, "Heterodyne measurement of Wigner distributions for classical optical fields," *Opt. Lett.* **24**, 1370–1372 (1999).
12. M. van Albada and A. Lagendijk, "Observation of weak localization of light in a random medium," *Phys. Rev. Lett.* **55** 2692–2695 (1985).
13. P.E. Wolf and G. Maret, "Weak localization and coherent backscattering of photons in disordered media," *Phys. Rev. Lett.* **55** 2696–2699 (1985).

This page intentionally left blank

Part III:
LIGHT SCATTERING METHODS

This page intentionally left blank

Chapter 9

LIGHT SCATTERING SPECTROSCOPY: FROM ELASTIC TO INELASTIC

Lev T. Perelman,[1] Mark D. Modell,[1] Edward Vitkin,[1] and Eugene B. Hanlon[2]
1. Harvard Medical School, Beth Israel Deaconess Medical Center, Boston, MA 02215 USA
2. Department of Veterans Affairs, Medical Research Service, Bedford, MA 01730 USA

Abstract: This chapter reviews light scattering spectroscopic techniques in which coherent effects are critical because they define the structure of the spectrum. In the case of elastic light scattering spectroscopy the targets themselves, such as aerosol particles in environmental science or cells and sub-cellular organelles in biomedical applications, play the role of microscopic optical resonators. In the case of inelastic light scattering spectroscopy or Raman spectroscopy, the spectrum is created due to light scattering from vibrations in molecules or optical phonons in solids. We will show that light scattering spectroscopic techniques, both elastic and inelastic, are emerging as very useful tools in material and environmental science and in biomedicine.

Key words: light scattering spectroscopy (LSS), Raman spectroscopy, cells, organelles, elastic scattering, inelastic scattering, cancer, dysplasia

9.1 INTRODUCTION

Optical spectroscopy is an important tool for understanding matter by means of its interaction with electromagnetic radiation. There are important spectroscopic methods where coherence of light does not play the essential role. At the same time in light scattering spectroscopy (LSS) coherent effects are critical since they define the structure of the spectrum. In the case of elastic LSS, the targets themselves, such as aerosol particles in environmental science or cells and sub-cellular organelles in biomedical applications, play the role of microscopic optical resonators. Thus, the LSS spectrum depends on their size, shape, and optical properties, such as refractive indices and absorption coefficients. In case of inelastic light

scattering spectroscopy or Raman spectroscopy, the spectrum is created due to light scattering from vibrations in molecules or optical phonons in solids. We will show that light scattering spectroscopic techniques, both elastic and inelastic, are emerging as very useful tools in material and environmental science and in biomedicine.

9.2 PRINCIPLES OF LIGHT SCATTERING SPECTROSCOPY

9.2.1 Light Scattering Spectroscopy

Not only does light scattered by cell nuclei have a characteristic angular distribution peaked in the near-backward directions but it also exhibits spectral variations typical for large particles. This information has been used to study the size and shape of small particles such as colloids, water droplets, and cells [1]. The technique which utilizes the fact that the scattering matrix, a fundamental property describing the scattering event, depends not only on the scatterer's size, shape, and relative refractive index, but also on the wavelength of the incident light is called Light Scattering Spectroscopy or LSS. LSS can be useful in biology and medicine as well.

Bigio *et al.* [2] and Mourant *et al.* [3] demonstrated that spectroscopic features of elastically scattered light could be used to detect the transitional carcinoma of the urinary bladder and adenoma and adenocarcinoma of the colon and rectum with good accuracy. In 1997 Perelman *et al.* observed characteristic LSS spectral behavior in the light backscattered from the nuclei of human intestinal cells [4]. The cells, approximately 15 μm long, affixed to glass slides in buffer solution, formed a monolayer of contiguous cells similar to the epithelial lining of the colon mucosa. In the experiments, an optical fiber probe (NA=0.22) was used to deliver white light from a xenon arc lamp onto the sample and to collect the reflected signal. After the measurement was performed, the cells were fixed and stained with H&E, a dye that renders otherwise transparent cell nuclei visible under microscope examination and is widely used in biology and medicine to examine tissue morphology. Microphotographs of the monolayer were obtained, and the size distribution of the nuclei was measured. It centered at about 6 μm and had a standard deviation of approximately 0.5 μm. Comparison of the experimentally measured wavelength varying component of light backscattered by the cells with the values calculated using the Mie theory and the size distribution of the cell nuclei determined by microscopy, demonstrated that both spectra exhibit similar oscillatory behavior. The fact that light scattered by a cell nucleus exhibits oscillatory behavior with

frequency depending on its size was used to develop a method of obtaining the size distribution of the nuclei from the spectral variation of light backscattered by biological tissues. This method was then successfully applied to diagnose precancerous epithelia in several human organs *in vivo* [5,6].

One very important aspect of LSS is its ability to detect and characterize particles, which are well beyond the diffraction limit. Detection and characterization of particles beyond the diffraction limit by LSS, specifically 260 nm particles, has been recently demonstrated experimentally by Fang *et al.* [7] and Backman *et al.* [8,9]. As explained in Perelman and Backman [10] particles much larger than the wavelength of light give rise to a prominent backscattering peak and the larger the particle, the sharper the peak. On the other hand, particles with sizes smaller than the wavelength give rise to very different scattering behavior. The small particle contribution dominates for large angles. It is important to note that this conclusion does not require an assumption that the particles are spherical or homogenous.

9.2.2 Interaction of Light with Cells

Studies of light scattering by cells have a long history. The first publications in this area investigated the angular dependence of the scattered light. Most of the experiments were performed at a single wavelength and the angular distribution of the scattered light was measured either with an array of photodetectors, fiber optics, or CCD. Brunsting *et al.* initiated a series of experiments aiming to relate the internal structure of living cells with the scattering pattern by measuring forward and near forward scattering by cell suspensions [11]. This turned out to be one of the first attempts to explain light scattering by cells using rigorous quantitative approaches.

The cell has complex structure with a very broad range of scatterer sizes: from a few nanometers, the size of a macromolecule, to 7-10 μm, the size of a nucleus, and to 20 μm, the size of the cell itself. Most cell organelles and inclusions are themselves complex objects with spatially varying refractive index. On the other hand, several studies have confirmed that many organelles such as mitochondria, lysosomes, and nuclei do posses an average refractive index substantially different from that of their surrounding and, therefore, viewing a cell as an object with continuously or randomly varying refractive index is not accurate either. A more accurate model acknowledges sub-cellular compartments of various sizes with refractive index, though not constant over the compartment's volume, but different from that of the surrounding.

Despite this diversity (more than 200 different cell types have been identified), cells have many common features [10]. A cell is bounded by a

membrane, a phospholipid bilayer approximately 10 nm in thickness with integral and peripheral proteins embedded in it. Two major cell compartments are the nucleus and the surrounding cytoplasm. The cytoplasm contains organelles, which are metabolically active subcellular organs, and inclusions, which are metabolically inactive. Mitochondria typically have the shape of a prolate spheroid. Their size varies greatly even within a single cell. The large dimension of a mitochondrion may range from 1 μm to 5 μm. The larger diameter typically varies between 0.2 μm to 0.8 μm. The mitochondria are quite flexible and may easily change their shape. The numbers of mitochondria differ depending on the cell size and its energy needs.

Endoplasmic reticulum is composed of tubules and flat sheets of membranes distributed over the intracellular space. The outer diameter of these tubules ranges from 30 to 100 nm. Their wall thickness is about 10 nm. There are two types of endoplasmic reticulum: rough endoplasmic reticulum and smooth endoplasmic reticulum. The rough endoplasmic reticulum differs from the smooth endoplasmic reticulum in that it bears 20-25 nm spherical or sometimes spheroidal particles called ribosomes.

Golgi apparatus is composed of a group of 4 to 10 flattened parallel membrane-bounded cisternae and functions in the modification and packaging of the macromolecules. The overall thickness of this organelle can range from 100 to 400 nm.

Lysosomes are 250 to 800 nm organelles of various shapes. The numbers of lysosomes are highly variant for different cells as well: the cells of membranous epithelial lining of cervix, for example, contain just a few lysosomes, while hepatocytes may possess a few hundred ones.

Peroxisomes are 200 nm to 1.0 μm spheroidal bodies of lower densities than lysosomes that are more abandoned in the metabolically active cells such as hepatocytes where they are counted in hundreds.

Cytoskeleton is composed of filamentous arrays of proteins. Its three major components are microtubules, which are about 25 nm in diameter with a wall 9 nm thick and a 15 nm lumen, 10 nm in diameter intermediate filaments, and 7 nm in diameter microfilaments.

Various cytoplasmic inclusions, such as lipids, glycogen, secretory granules, and pigments, come in all different sizes ranging from 20 to 500 nm. They might be of various shapes but usually appear to be near spherical. The surface roughness of an inclusion can range from 2 to 40 nm.

Extensive studies of angular dependence of light scattering by cells using a goniometer were carried out by Mourant *et al.* [12]. Measurements of light scattering from cells and cell organelles were performed from 2° to 171° and from 9° to 168° respectively. In both cases, the unpolarized light was delivered by a He-Ne laser at 632.8 nm. The angular resolution was about 0.5° and most of the data was taken for every 2°. The concentration of

the cells was 10^5 cells/ml. This concentration was chosen so that multiple scattering events would be rare. The researchers used two types of cells in their experiments: immortalized rat embryo fibroblast cells and a ras-transfected clone, which is highly tumorigenic. The cells were suspended in phosphate-buffered saline and kept on ice. Nuclei and mitochondria were isolated from MR1 cells by standard methods and resuspended mannitol sucrose buffer.

Not only organelles themselves but their components also can scatter light. Finite-difference time-domain (FDTD) simulations provide means to study spectral and angular features of light scattering by arbitrary particles of complex shape and density. Using FDTD and choosing proper models, one can learn a great deal about origins of light scattering.

Drezek *et al.* investigated the influence of cell morphology on the scattering pattern [13] and found that the internal structure of an organelle does affect the scattering at large angles but not in the forward or backward directions. In fact, this finding is not paradoxical and should be expected: light scattered in the forward or backward directions depends more on the larger structures within an organelle, for example the organelle itself. It samples average properties of the organelle, which were kept constant in the simulations. On the other hand, smaller structures within the organelle scatter strongly in the intermediate angles. Thus, light scattering at these angles is influenced by its internal structure.

9.3 APPLICATIONS OF LIGHT SCATTERING SPECTROSCOPY

9.3.1 Measuring Size Distribution of Epithelial Cell Nuclei with Light Scattering Spectroscopy

Enlarged nuclei are primary indicators of cancer, dysplasia and cell regeneration in most human tissues, and recent studies demonstrate that LSS can accurately detect dysplasia clinically in the esophagus, colon and bladder [4,5,6,9].

The hollow organs of the body are lined with a thin, highly cellular surface layer of epithelial tissue, which is supported by underlying, relatively acellular connective tissue. In healthy tissues, the epithelium often consists of a single, well-organized layer of cells with en–face diameter of 10–20 μm and height of 25 μm. In dysplastic epithelium, cells proliferate and their nuclei enlarge and appear darker (hyperchromatic) when stained.

LSS can be used to measure these changes. Consider a beam of light incident on an epithelial layer of tissue. A portion of this light is backscattered from the epithelial nuclei, while the remainder is transmitted to deeper tissue layers, where it undergoes multiple scattering and becomes randomized before returning to the surface.

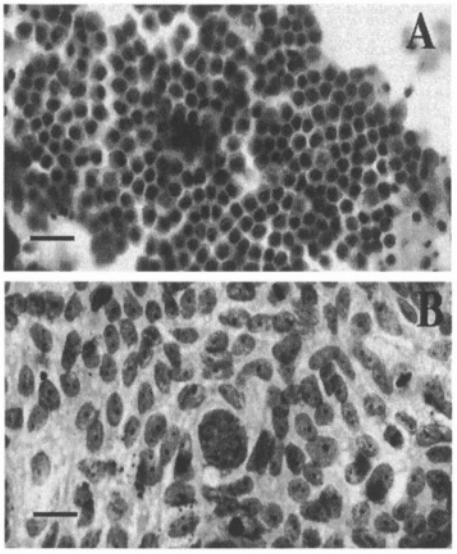

Figure 1. Microphotograph of the isolated normal intestinal epithelial cells (panel A) and intestinal malignant cell line T84 (Panel B). Note the uniform nuclear size distribution of the normal epithelial cell (A) in contrast to the T84 malignant cell line, which at the same magnification shows larger nuclei and more variation in nuclear size (B). Solid bars equal 20μm in each panel. The cells were stained after the LSS experiments were performed (from Ref. [16]).

Epithelial nuclei can be treated as spheroidal Mie scatters with refractive index, n_n, which is higher than that of the surrounding cytoplasm, n_c. Normal nuclei have a characteristic diameter l = 4–7 μm. In contrast, dysplastic nuclei can be as large as 20 μm, occupying almost the entire cell volume. In the visible range, where the wavelength $\lambda << l$, the Van de Hulst approximation can be used to describe the elastic scattering cross section of the nuclei:

$$\sigma_s(\lambda,l)=\frac{1}{2}\pi d^2\left(1-\frac{\sin(2\delta/\lambda)}{\delta/\lambda}+\left(\frac{\sin(\delta/\lambda)}{\delta/\lambda}\right)^2\right), \qquad (1)$$

with $\delta = \pi l\,(n_n - n_c)$. Equation 1 reveals a component of the scattering cross section, which varies periodically with inverse wavelength. This, in turn, gives rise to a periodic component in the tissue reflectance. Since the

frequency of this variation (in inverse wavelength space) is proportional to particle size, the nuclear size distribution can be obtained from the Fourier transform of the periodic component.

To test this, Perelman *et al.* [4] studied elastic light scattering from densely packed layers of normal and T84 tumor human intestinal cells, affixed to glass slides in buffer solution (Figure 1). The diameters of the normal cell nuclei ranged from 5 to 7 μm, and those of the tumor cells from 7 to 16 μm. The reflectance from the samples exhibits distinct spectral features. The predictions of the Mie theory were fit to the observed spectra. The fitting procedure used three parameters, average size of the nucleus, standard deviation in size (a Gaussian size distribution was assumed), and relative refractive index.

The solid line of Figure 2 is the distribution extracted from the data, and the dashed line shows the corresponding size distributions measured morphometrically *via* light microscopy. The extracted and measured distributions for both normal and T84 cell samples were in good agreement, indicating the validity of the above physical picture and the accuracy of the method of extracting information.

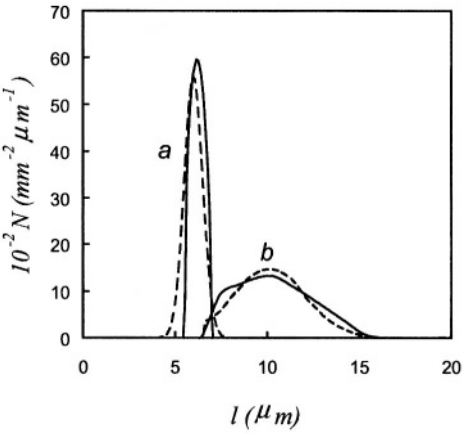

Figure 2. Nuclear size distributions. (a) Normal intestinal cells; (b) T84 cells. In each case, the solid line is the distribution extracted from the data, and the dashed line is the distribution measured using light microscopy (from Ref. [4]).

9.3.2 Non-invasive Diagnostic Technology for Early Cancer Detection

It is a well-known fact that often, when cancer is found, it is too late to treat it. Thus, the most effective method of fighting cancer might be its prevention at an early stage when pre-cancerous changes are often confined

to the superficial cellular layer called the epithelium. The question is what non-invasive diagnostic technology can be used to detect those early lesions, as they are microscopic, flat and not readily observable. Over the last decades substantial progress has been made in medical diagnostic technologies that target anatomic changes at the organ level. Such techniques as magnetic resonance imaging (MRI) and spectroscopy (MRS), X-ray computed tomography (X-ray CT), and ultrasound made it possible to "see through the human body". At the same time, there is clearly a need for the development of diagnostic techniques that use our current knowledge of the cellular and sub-cellular basis of disease. The diagnostic techniques applicable *in situ* (inside human body) that can provide structural and functional information about the tissue at the cellular and sub-cellular level - the kind of information that is currently obtainable only by using methods requiring tissue removal - will have great implications on the detection and prevention of disease as well as enabling targeted therapy.

9.3.3 Application of Light Scattering Spectroscopy to Barrett's Esophagus

Recently Perelman *et al.* [6] observed periodic fine structure in diffuse reflectance from Barrett's Esophagus (BE) of human subjects undergoing gastroenterological endoscopy procedures. A schematic diagram of the proof-of-principle system used to perform LSS is shown in Figure 3.

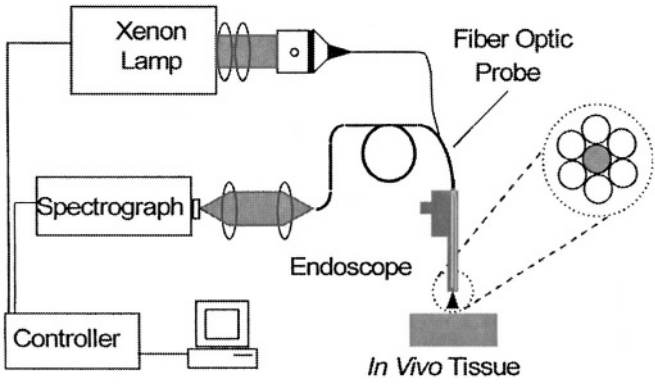

Figure 3. Schematic diagram of the proof-of-principle LSS system (from Ref [6]).

Immediately before biopsy, the reflectance spectrum from that site was collected using an optical fiber probe. The probe was inserted into the accessory channel of the endoscope and brought into gentle contact with the mucosal surface of the esophagus. It delivered a weak pulse of white light to

the tissue and collected the diffusely reflected light. The probe tip sampled tissue over a circular spot approximately 1 mm^2 in area. The pulse duration was 50 milliseconds, and the wavelength range was 350-650 nm. The optical probe caused a slight indentation at the tissue surface that remained for 30-60 seconds. Using this indentation as a target, the site was then carefully biopsied, and the sample was submitted for histologic examination. This insured that the site studied spectroscopically matched the site evaluated histologically.

The reflected light was spectrally analyzed, and the spectra were stored in a computer. The spectra consist of a large background from submucosal tissue, on which is superimposed a small (2-3%) component that is oscillatory in wavelength because of scattering by cell nuclei in the mucosal layer. The amplitude of this component is related to the surface density of epithelial nuclei (number of nuclei per unit area). Because the area of tissue probed is fixed at 1 mm^2, this parameter is a measure of nuclear crowding. The shape of the spectrum over the wavelength range is related to nuclear size. The difference in nuclear size distributions extracted from the small oscillatory components for non-dysplastic and dysplastic BE sites is pronounced. The distribution of nuclei from the dysplastic site is much broader than that from the non–dysplastic site, and the peak diameter is shifted from ~7 μm to about ~10 μm. In addition, both the relative number of large cell nuclei (>10 μm) and the total number of nuclei are significantly increased.

However, single scattering events cannot be measured directly in biological tissue. Because of multiple scattering, information about tissue scatterers is randomized as light propagates into the tissue, typically over one effective scattering length (0.5-1 mm, depending on the wavelength). Nevertheless, the light in the thin layer at the tissue surface is not completely randomized. In this thin region the details of the elastic scattering process can be preserved. Therefore, the total signal reflected from a tissue can be divided into two parts: single backscattering from the uppermost tissue structures such as cell nuclei, and the background of diffusely scattered light. To analyze the single scattering component of the reflected light, the diffusive background must be removed. This can be achieved either by modeling using diffuse reflectance spectroscopy [4,14,15] or by polarization background subtraction [16].

Polarization background subtraction has the advantage of being less sensitive to tissue variability. However, the diffuse reflectance spectroscopy has its own advantages since it can provide valuable information about biochemical and morphological organization of submucosa and degree of angiogenesis.

9.3.4 Diffuse Reflectance Spectroscopy of Colon Polyps and Barrett's Esophagus

A technique for modeling clinical tissue reflectance in terms of the underlying tissue scatterers and absorbers, which is called diffuse reflectance Spectroscopy, was developed by Zonios *et al.* [14] in studies of colon polyps and applied by Georgakoudi *et al.* [15] to Barrett's Esophagus. This method provides both direct physical insight and quantitative information about the tissue constituents that give rise to the reflectance spectra.

The method described in Zonios *et al.* [14] is based on the diffusion approximation. It describes the tissue reflectance spectrum collected by a finite sized probe with an effective probe radius r_c. Biological tissue is treated as a homogeneous medium with wavelength–dependent absorption coefficient μ_a and reduced scattering coefficient μ_s'. Incident photons are absorbed and scattered in the tissue, with the survivors eventually escaping from the tissue surface. A fraction of the escaping diffusely reflected light is collected by a probe of finite size.

Starting with an expression derived by Farrell, Patterson and Wilson [19], Zonios *et al.* [14] obtains analytical expression for the diffuse reflectance collected by the probe:

$$R_p(\lambda) = \frac{\mu_s'}{\mu_s' + \mu_a}\left\{e^{-\mu z_0} + e^{-(1+\frac{4}{3}A)\mu z_0} - z_0\frac{e^{-\mu r_1'}}{r_1'} - (1+\frac{4}{3}A)z_0\frac{e^{-\mu r_2'}}{r_2'}\right\}, \qquad (2)$$

with $\mu = \left(3\mu_a(\mu_a + \mu_s')\right)^{1/2}$, $z_0 = \dfrac{1}{\mu_s' + \mu_a}$, $r_1' = \left(z_0^2 + r_c'^2\right)^{1/2}$, and $r_2' = \left(z_0^2(1+\dfrac{4}{3}A)^2 + r_c'^2\right)^{1/2}$. The paramater A depends in the known way on the refractive index n of the medium. For a given probe geometry there is an optimal value the effective probe radius r_c, which can be determined by calibrating equation 2 using the reflectance measurement of a tissue phantom with known optical properties.

For the visible tissue reflectance spectra collected in colon [14] and BE [15], researchers found hemoglobin (Hb) to be the only significant light absorber. To account for both oxygenated and deoxygenated forms of Hb, the total absorption coefficient, $\mu_a(\lambda)$ is given by

$$\mu_a(\lambda) = \ln\left(c_{Hb}\left[\alpha\,\varepsilon_{HbO_2}(\lambda) + (1-\alpha)\,\varepsilon_{Hb}(\lambda)\right]\right), \qquad (3)$$

where α is the Hb oxygen saturation parameter and c_{Hb} the total hemoglobin concentration. The wavelength dependent extinction coefficients (*i.e.,* the ε's) of both forms of hemoglobin are well documented [17].

To test the model Zonios *et al.* [14] measured the reflectance spectra of a series of tissue phantoms with known absorption and scattering properties. The phantom reflectance spectra were accurately modeled by equation 2, using the known absorption and scattering coefficients. By fitting equation 2 to the experimental phantom data obtained using various values of Hb concentration, oxygen saturation, scatterer size, and scatterer density, the authors found that the values of these parameters could be recovered with accuracy of better than 10% over the full range of the four parameters. This established that the experimental spectra are adequately described by the diffusion model, and that the model could be used in an inverse manner to extract the parameters from the spectra with reasonable accuracy.

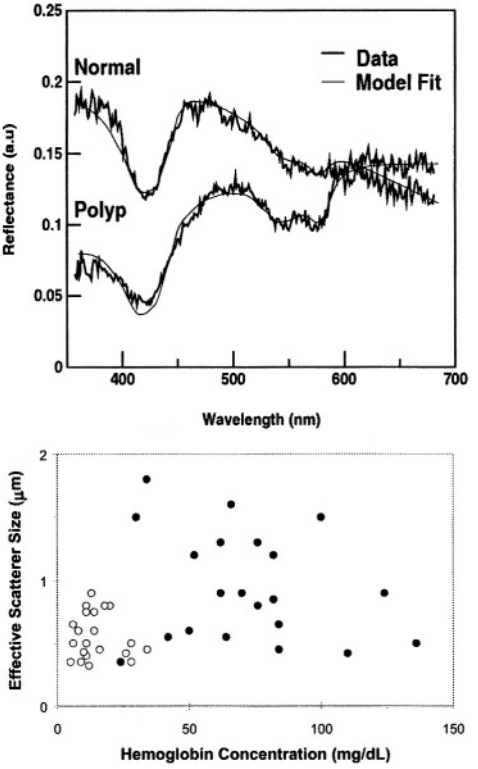

Figure 4. Diffuse reflectance analysis. (a). Top: reflectance spectra (thick lines), and modeled fits (thin lines). (b). Bottom: binary plot. Open circle: normal. Filled circle: polyp (from Ref. [14]).

Diffuse reflectance spectra were then collected from adenomatous polyps in 13 patients undergoing routine colonoscopy. The clinical data were analyzed using the model and the known spectra of oxy- and deoxy-hemoglobin to extract values of Hb concentration and saturation, and $\mu_s'(\lambda)$. For biological tissue, the reduced scattering coefficient $\mu_s'(\lambda)$ is the sum of contributions from the various tissue scatterers. Detailed information about these individual scatterers is not presently known. Therefore, the reduced scattering coefficient can be presented in the form $\mu_s'(\lambda) = \rho_s \sigma_s'(\lambda)$, with ρ_s the *effective* scattering density and $\sigma_s'(\lambda)$ the *effective* reduced scattering cross section. With this, tissue scattering properties were modeled in an average way, as if tissue contained a single well–defined type of scatterer. In general, $\sigma_s'(\lambda)$ depends on the refractive index, shape and size of the scatterer, as well as on the refractive index of the surrounding medium. Mie scattering theory was applied to evaluate $\sigma_s'(\lambda)$ [17], assuming the scatterers to be homogeneous spheres of diameter d_s and relative refractive index *n*, $\sigma_s'(\lambda)$.

Figure 4(a) shows typical diffuse reflectance spectra from one adenomatous polyp site and one normal mucosa site. The model fits, also shown, are excellent. Both the absorption dips and scattering slopes are sensitive functions of the fit parameters, providing an inverse algorithm, which is sensitive to such features. The inverse algorithm was applied to the clinical spectra and values of the four parameters for each site probed were obtained. These parameters provide valuable information about the tissue properties.

Figure 4(b) shows a binary plot of effective scatter size vs. Hb concentration. Adenomatous colon polyps were characterized by increased Hb concentration, in agreement with the published results that precancerous tissues such as adenomatous polyps exhibit increased microvascular volume [20,21]. The Hb oxygen saturation was found to be approximately 60%, on average, for both normal mucosa and adenomatous polyps. This result is reasonable, inasmuch as the measurements were essentially performed in the capillary network of the mucosa, where oxygen is transferred from Hb to tissue. The authors also observed an intrinsic differentiation in the scattering properties between the two tissue types studied. For adenomatous polyps, the average effective scattering size was larger, and the average effective scatterer density was smaller, as compared to normal mucosa. The range of effective scattering sizes was in good agreement with that reported for average scatterer sizes of biological cell suspensions [12].

Figure 5 shows typical diffuse reflectance spectra from one nondysplastic BE site [15]. The analysis showed that the reduced scattering coefficient, μ_s', of Barrett's esophagus tissue changes gradually during the

progression from nondysplastic, to low-grade, to high-grade dysplasia. Additionally, the wavelength dependence of μ_s' changes during the development of dysplasia. To describe these changes, the authors [15] fit a straight line to $\mu_s'(\lambda)$and used the intercept at 0 nm and slope of this line as additional to LSS diagnostic parameters [Figure 6(b)].

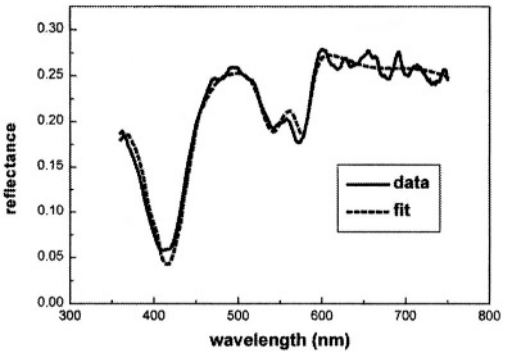

Figure 5. Reflectance spectrum of a nondysplastic BE site. *Solid line,* experimental data; *dashed line,* model fit (from Ref. [15]).

Georgakoudi *et al.* [15] found that the scattering coefficient of tissue decreases significantly during the development of dysplasia, suggesting that changes that are not observed histopathologically are taking place within the lamina propria and submucosa before the onset of invasion. The change in the slope of μ_s' as a function of wavelength suggests that the mean size of the tissue scattering particles is changing. Crowding of the cells and nuclei of the epithelial layer may be responsible for this change.

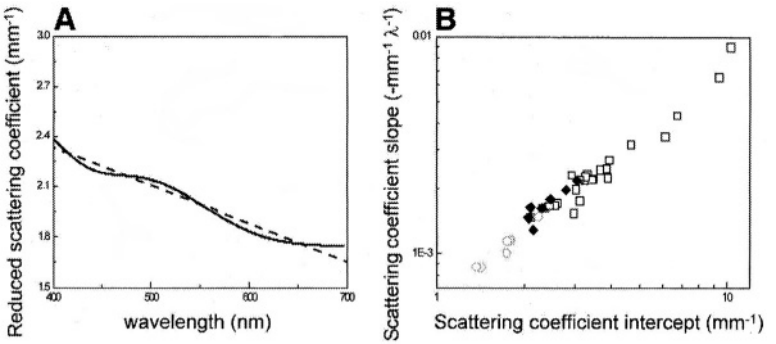

Figure 6. (A) Reduced scattering coefficient as a function of wavelength for a representative nondysplastic BE site *(solid line)* and corresponding linear fit *(dashed line). (B)* Slopes and intercepts of linear fit to the wavelength-dependent tissue reduced scattering coefficient, μ_s', for nondysplastic (□), low-grade (◆), and high-grade (○) dysplastic BE sites. A log-log scale is used to facilitate visualization of all the data points (from Ref. [15]).

9.3.5 Polarization Background Subtraction

To study the spectrum of polarized back-scattered light, Backman *et al.* [16] employed an instrument that delivers collimated polarized light on tissue and separates two orthogonal polarizations of back-scattered light. In the system described in [16] (Figure 7), light from a broadband source (250 W CW tungsten lamp) is collimated and then refocused with a small solid angle onto the sample, using lenses and an aperture. A broadband polarizer linearly polarizes the incident beam. In order to avoid specular reflectance, the incident beam is oriented at an angle of~15° to the normal to the surface of the sample. The sample is illuminated by a circular spot of light of 2 mm in diameter. The reflected light is collected in a narrow cone (~0.015 radian), and two polarizations are separated by means of a broadband polarizing beam splitter cube, which also serves as the analyzer. The output from this analyzer is delivered through 200 μm core diameter optical fibers into two channels of a multichannel spectroscope. This enables the spectra of both components to be measured simultaneously in the range from 400 to 900 nm. The studies have shown that the unpolarized component of the reflected light can be canceled by subtracting $I_{\perp}$ from $I_{\parallel}$ allowing the single scattering signal to be extracted.

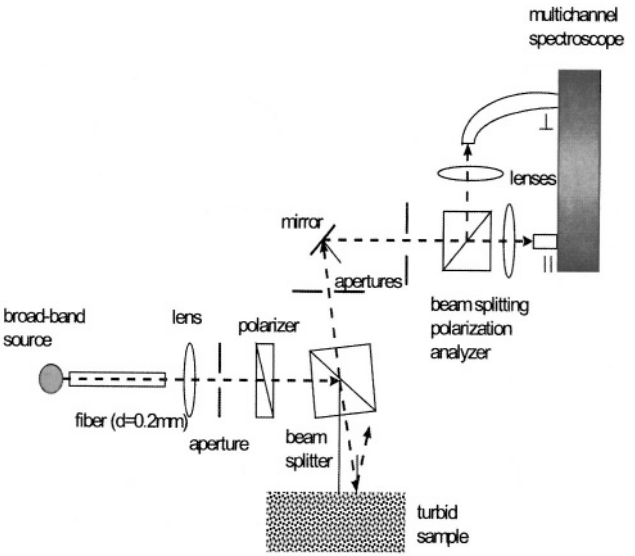

Figure 7. Schematic diagram of the experiment with polarized light (from Ref. [16]).

Backman *et al.* [16] performed experiments with cell monolayers. A thick layer of gel containing $BaSO_4$ and blood was placed underneath the

cell monolayer to simulate underlying tissue. The predictions of Mie theory were fit to the observed residual spectra. The fitting procedure used three parameters, average size of the nucleus, standard deviation in size (a Gaussian size distribution was assumed), and relative refractive index. For normal intestinal epithelial cells, the best fit was obtained using d=5.0 μm, Δd=0.5 μm, and n=1.035 [Figure 8(a)].

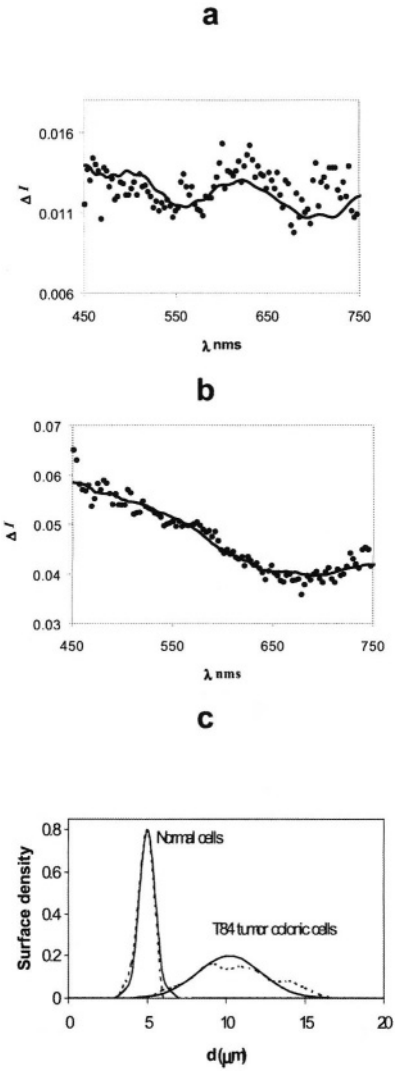

Figure 8. Spectrum of polarized component of backscattered light from (a) normal intestinal cells, (b) T84 intestinal malignant cells, and (c) correspondent nuclear size distributions. In each case, the solid line is the distribution extracted from the data, and the dashed line is the distribution measured using light microscopy.

For T84 intestinal malignant cells the corresponding values were d= 9.8 μm, Δd=1.5 μm, and n=1.04 [Figure 8(b)]. In order to check these results, the distribution of the average size of the cell nuclei was measured by morphometry on identical cell preparations that were processed in parallel for light microscopy. The nuclear sizes and their standard deviations were found to be in very good agreement with the parameters extracted from Mie theory. A histogram showing the size distributions obtained for the normal intestinal epithelial cells and T84 cells are shown in Figure 8(c). The accuracy of the average size is estimated to be 0.1μm, and the accuracy in n as 0.001. Note the larger value of n obtained for T84 intestinal malignant cells, which is in agreement with the hyperchromaticity of cancer cell nuclei observed in conventional histopathology of stained tissue sections.

The experiments [16] show that polarized light scattering spectroscopy is able to distinguish between single backscattering from uppermost cells and the diffusive background. It provides valuable information about the macroscopic properties of the tissue. On the other hand, the single scattering component provides morphological information about living cells, which potentially has valuable biomedical applications.

9.3.6 Clinical Detection of Dysplasia in Four Organs Using Light Scattering Spectroscopy

The ability of LSS to diagnose dysplasia and CIS was tested in *in vivo* human studies in four different organs and in three different types of epithelium: columnar epithelia of the colon and Barrett's esophagus, transitional epithelium of the urinary bladder, and stratified squamous epithelium of the oral cavity [5,22]. All clinical studies were performed during routine endoscopic screening or surveillance procedures. In all of the studies an optical fiber probe delivered white light from a xenon arc lamp to the tissue surface and collected the returned light. The probe tip was brought into gentle contact with the tissue to be studied. Immediately after the measurement, a biopsy was taken from the same tissue site. The biopsied tissue was prepared and examined histologically by an experienced pathologist in the conventional manner. The spectrum of the reflected light was analyzed and the nuclear size distribution determined. The majority of distributions of dysplastic cell nuclei extended to larger size.

These size distributions were then used to obtain the percentage of nuclei larger than 10 micron, and the total number of nuclei per unit area (population density). As noted above, these parameters quantitatively characterize the degree of nuclear enlargement and crowding, respectively.

Figure 9 displays these LSS parameters in binary plots to show the degree of correlation with histological diagnoses. In all four organs, there is

a clear distinction between dysplastic and non-dysplastic epithelium. Both dysplasia and CIS have a higher percentage of enlarged nuclei and, on average, a higher population density, which can be used as the basis for spectroscopic tissue diagnosis.

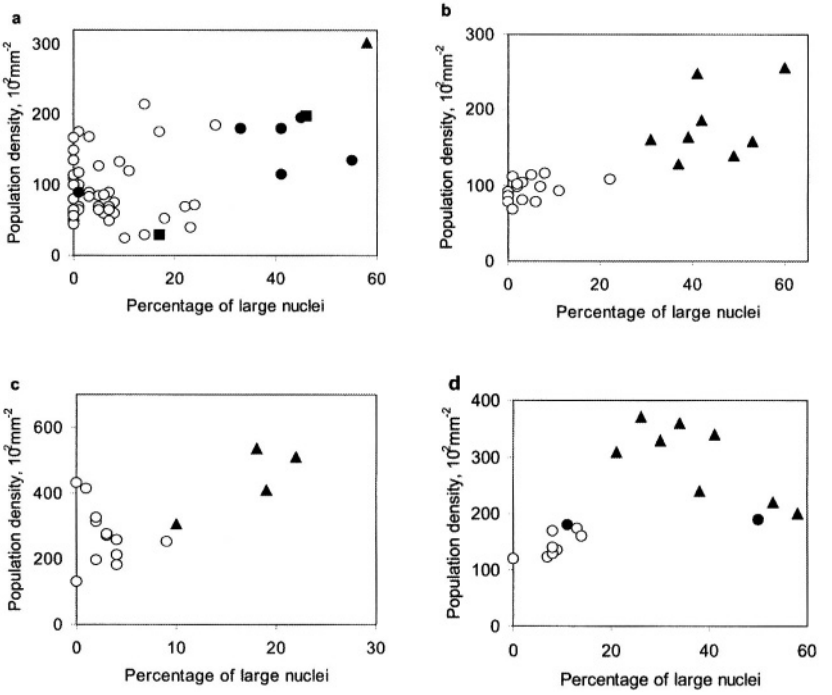

Figure 9. Dysplasia/CIS classifications for four types of tissue obtained clinically with LSS, compared with histologic diagnosis. In each case the ordenate indicates the percentage of enlarged nuclei and the abscissa indicates the population density of the nuclei, which parametrizes nuclear crowding. (a) Barrett's esophagus: non-dysplastic Barrett's mucosa (○), indefinite for dysplasia (■), low grade dysplasia (●), high grade dysplasia (▲); (b) colon: normal colonic mucosa (○), adenomatous polyp (▲); (c) urinary bladder: benign bladder mucosa (○), transitional cell carcinoma *in situ* (▲); (d) oral cavity: normal (○), low grade dysplasia (■), squamous cell carcinoma *in situ* (▲) (from Ref. [5]).

These results show the promise of LSS as a real–time, minimally invasive clinical tool for accurately and reliably classifying invisible dysplasia. Although the presented data sets are limited in size, the effectiveness of LSS in diagnosing early cancerous lesions is again clearly demonstrated, and this suggests the general applicability of the technique.

9.3.7 Clinical Detection of Dysplasia in Barrett's Esophagus Using Light Scattering Spectroscopy

The studies in BE described in Perelman *et al.* [4], Backman *et al.* [5] and Wallace *et al.* [6], were conducted at the Brigham and Women's Hospital and the West Roxbury Veterans Administration Medical Center. Patients undergoing surveillance endoscopy for a diagnosis of Barrett's esophagus or suspected carcinoma of the esophagus were evaluated by systematic biopsy. In surveillance patients, biopsy specimens were taken in 4 quadrants, every 2 cm of endoscopically visible Barrett's mucosa. In patients with suspected adenocarcinoma, biopsy specimens for this study were taken from the Barrett's mucosa adjacent to the tumor.

Spectra were collected by means of an optical fiber probe, inserted in the biopsy channel of the gastroscope and brought into gentle contact with the tissue. Each site was biopsied immediately after the spectrum was taken. Because of the known large interobserver variation [23] the histology slides were examined independently by four expert GI pathologists. Sites were classified as NDB, IND, LGD or HGD. Based on the average diagnosis [24, 25] of the four pathologists, 4 sites were diagnosed as HGD, 8 as LGD, 12 as IND and 52 as NDB.

To establish diagnostic criteria, 8 samples were selected as a "modeling set", and the extracted nuclear size distributions were compared to the corresponding histology findings. From this, the authors decided to classify a site as dysplasia if more than 30% of the nuclei were enlarged, with "enlarged" defined as exceeding a 10 μm threshold diameter, and classified as non–dysplasia otherwise. The remaining 68 samples were analyzed using this criterion. Averaging the diagnoses of the four pathologists [23], the sensitivity and specificity of detecting dysplasia were both 90%, with dysplasia defined as LGD or HGD, and non–dysplasia defined as NDB or IND, an excellent result, given the limitations of interobserver agreement among pathologists.

To further study the diagnostic potential of LSS, the entire data set was then evaluated adding a second criterion, the population density of surface nuclei (number per unit area), as a measure of crowding. The resulting binary plot (Figure 10) reveals a progressively increasing population of enlarged and crowded nuclei with increasing histological grade of dysplasia, with the NDB samples grouped near the lower left corner and the HGD samples at the upper right. Using logistic regression [26], the samples were then classified by histologic grade as a function of the two diagnostic criteria. The percentage agreements between LSS and the average and consensus diagnoses (at least 3 pathologists in agreement) were 80% and 90%, respectively. This is much higher than that between the individual pathologists and the average diagnoses of their 3 colleagues, which ranged

from 62 to 66%, and this was also reflected in the kappa statistic values [27].

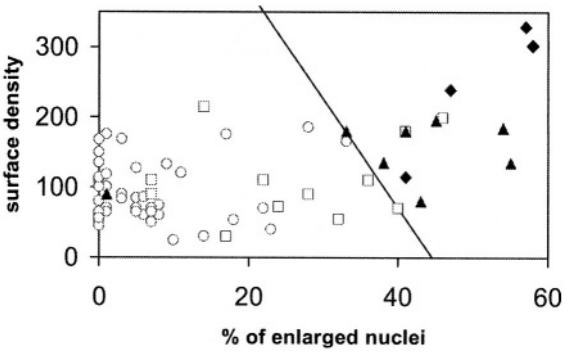

Figure 10. LSS diagnostic plots of Barrett's esophagus data. NDB–circles; IND–squares; LGD–triangles; HGD–diamonds. The decision threshold for dysplasia is indicated (from Ref. [6]).

9.4 PRINCIPLES OF RAMAN SCATTERING SPECTROSCOPY

The Raman effect, known since the early 1920s, is an inelastic light scattering process. Energy is exchanged between the incident field and the scattering medium, leaving each in a different state as a result of the scattering event. Typically, the quanta exchanged are on the order of molecular vibrational energies. The frequency of the scattered light may be lower than (Stokes scattering) or higher than (anti-Stokes scattering) that of the incident light, and the scattering molecules will be left in higher or lower vibrational states, respectively.

The change in frequency in the scattered light corresponds to the energy difference between the initial and final vibrational states of the scattering molecule and is independent of the incident light wavelength. Hence the typical Raman scattering spectrum represents the ground state vibrational spectrum of molecules in the scattering medium and is therefore unique to each molecular species. The Raman spectrum displays the intensity of scattered light as a function of the difference in frequency between the scattered and the incident light. Since each molecular species has its own unique set of molecular vibrations, the Raman spectrum of a particular species will consist of a series of peaks or bands of scattered light, each shifted from the incident light frequency by one of the characteristic vibrational frequencies of that molecule.

Though the effect has been known for almost a century, it is only within the last few decades that Raman spectroscopy has flourished as a powerful

molecular spectroscopy technique. Widespread use had to await the advent of lasers and more recently high quantum efficiency detectors to compensate for the extremely low efficiency of Raman scattering. The intensity of Stokes Raman scattered light is typically 10^{-7} to 10^{-15} the intensity of the excitation light, and for Anti-Stokes Raman it is even less. Thus, real-time monitoring or detection of Raman scattering spectra was not practical until the commercial development of lasers and subsequent advances in detector technology, which in turn facilitated an enormous number of applications and growth in the related Raman literature (see, for example, Ref. [39] and its citations, Refs. [33], [34], and [41]).

In this chapter we will limit the discussion of Raman spectroscopy to two of the most exciting developments of the past decade: biomedical near-infrared Raman spectroscopy (NIRRS), for *in vivo* medical diagnosis and Surface-Enhanced Raman spectroscopy (SERS) for biological, biomedical and nanotechnology related material science.

9.5 APPLICATIONS OF RAMAN SPECTROSCOPY

9.5.1 Near-infrared Raman Spectroscopy for *In Vivo* Biomedical Applications

Technological advances in excitation sources, spectrographs, detectors and optical fibers, as well as realization that Raman spectroscopy can provide chemical composition, molecular structure, and molecular interactions in cells and tissues, brought substantial interest to the medical applications of near-infrared Raman spectroscopy. These applications and corresponding instrumentation have been most recently reviewed by several authors [28,32,38,41,42,43]. We will summarize major issues and successes of Near-infrared Raman Spectroscopy (NIRRS) using material from these reviews and adding results reported later.

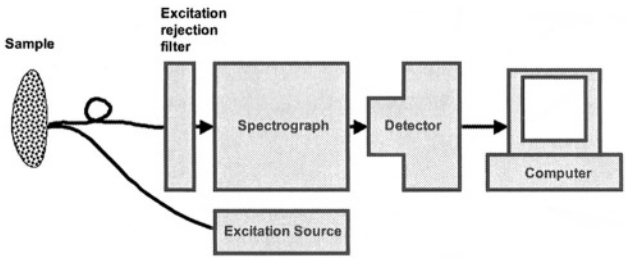

Figure 11. Block diagram for generic Raman system.

Figure 11 is a depiction of a generic Raman system. The excitation source sends light to the sample. The collector directs the scattered light through the excitation rejection filter into the spectrograph. The excitation rejection filter blocks light at the excitation wavelength from reaching the spectrograph. The spectrograph disperses the scattered light so that light intensity at each wavelength can be measured. The detector transforms the light exiting the spectrograph into electrical signals so that the radiation at each wavelength is still distinguishable. The signals are then digitized and sent to a computer, where all signal processing and spectrum extraction is produced. Each component of the system has been dramatically improved in the last 5-10 years, to enable successful *in vivo* biomedical applications. First we will discuss the spectral range for the system.

9.5.2 Why Near-Infrared Excitation?

Most biological tissues fluoresce when excited by visible or near UV wavelengths (within 300-700 nm) and the fluorescence is usually a broadband signal within the same spectral range as the Stokes Raman spectrum. In most tissues, the fluorescence cross section is about 6 orders of magnitude stronger than the Stokes Raman cross section, thus the fluorescence signal can overwhelm the tissue Raman spectrum. Two strategies for reducing fluorescence interference are to use near-infrared (NIR) excitation or UV resonance excitation (Figure 12, modified from Ref. [32]).

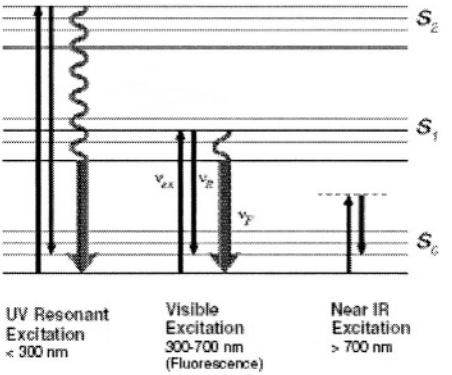

Figure 12. Raman effect: UV, visible and NIR excitation strategies. S_0, ground electronic state; S_1 and S_2, excited electronic states. The horizontal lines indicate vibrational energy levels. The diagram shows how a molecule in the ground state, S_0, can make a transition from the lowest vibrational level to the first excited vibrational level by means of Raman scattering. Thin upper arrows indicate the frequency of the laser excitation light; thin down-arrows indicate frequency of the Raman scattered light. The difference in length between thin up- and down-arrows indicates molecular vibration frequency. Thick arrows indicate frequency of the fluorescence light.

As one can see from Figure 12, Raman scattering at different excitation wavelengths, UV, visible and NIR, produces the same change in vibrational energy; therefore the excitation wavelength can be chosen to avoid spectral interference by fluorescence. For visible excitation, the fluorescence light frequency and Raman scattered light frequency are similar. This leads to intense fluorescence background in visible excitation Raman spectra. NIR light has too low frequency to excite fluorescence, while for UV excitation, the fluorescence light frequency is much lower than the Raman scattered light frequency. Hence, using UV or NIR excitation can reduce fluorescence background in the Raman spectrum.

Most materials, including tissue, exhibit reduced fluorescence emission as the excitation wavelength increases into the NIR region. Thus, fluorescence interference in tissue Raman spectra can be greatly reduced by using NIR excitation. Another approach would be to use excitation wavelengths in the ultraviolet (UV) range. Background fluorescence is suppressed in tissue Raman spectra for excitation wavelengths below about 270 nm. However, the tissue penetration of the UV excitation is limited (10s of microns) and, in addition, it has a risk of causing tissue damage through mutagenesis.

9.5.3 Near-infrared Raman Spectroscopy System

Currently, the two most commonly used instrument design approaches for acquiring Raman spectra in the NIR spectral range are the Fourier Transform (FT) spectrometer and the dispersive imaging spectrograph. The FT-Raman spectrometer was introduced earlier (in the 1980s). Usually a Nd:YAG laser (a flash lamp or diode pumped solid state laser emitting at 1064 nm) is used to excite the sample and the resulting Raman signal is detected using an interferometer with a single element detector. Nd:YAG lasers have excellent beam quality and a range of available power. When diode lasers replace the lamp as a source of optical pumping for these lasers, it reduces thermal effects and improves pumping stability, thus increasing the overall S/N by reducing flicker noise.

High throughput and averaging rate makes FT Raman systems attractive for biomedical applications. In addition, the introduction of high quality solid-state lasers and laser diodes at different wavelengths and detectors with high sensitivity, S/N and broad dynamic range for these wavelengths provides the FT–based Raman spectrometer with flexibility unsurpassed by dispersive systems, especially, for *in vitro* applications. However, for *in vivo* applications, FT-based systems are much too bulky and vibration sensitive. There are some attempts to make the scanning interferometer for the Fourier Transform without mechanically moving parts. So far they have not reached an acceptable level of performance or cost effectiveness.

The present state of the art NIRRS instrument for *in vivo* applications capable of rapid collection of spectra in a mobile and physician friendly setup is based on the dispersive system. This system consists of a NIR semiconductor laser, a suitable fiber-optic probe that illuminates the tissue with laser light and collects scattered light, and a high numerical aperture imaging spectrograph equipped with a cooled CCD camera that are both optimized for the NIR region. This system has a limitation of how far into the NIR spectral range the excitation can be moved to suppress fluorescence of tissue. Most CCD detectors in use today are silicon based. Their sensitivity rolls off sharply at 1000 nm. There are specially developed silicon CCD arrays sensitive to 1100 nm, with low quantum efficiency after 1000 nm. Thus excitation wavelengths longer than ~800 nm would not be useful with this detector for observing vibrational transitions above about $2500 cm^{-1}$, although tissue fluorescence still can be substantial with this 800 nm excitation. Hanlon *et al.* [32] discussed several experimental and mathematical methods, which can be used for reducing the fluorescence component of biological Raman spectra. However, the fluorescence signal decreases the useful dynamic range of the CCD detector and that can be a critical issue for measurements of trace chemical species in the tissue or when high resolution of measurements are required.

Despite these limitations, cooled CCD-based systems with compact high quality imaging spectrographs and semiconductor lasers are the preferred configuration for clinical NIRRS systems.

Recently, the advances in the integrated circuits development led to development of InGaAs photodiode array detectors hybridized with a CMOS readout multiplexer (for example, Sensor Unlimited, Inc. Princeton, NJ) that should provide improved noise characteristics. The InGaAs photodiode has a spectral response from 900 to 1700 nm with quantum efficiency greater than 70% from 1000 nm to 1600 nm. Use of this type of detector should allow using semiconductor lasers with wavelengths well above 1000 nm, further diminishing the tissue fluorescence background and broadening the range of biomedical applications for NIRRS.

In NIRRS, the two most widely used dispersive spectrograph configurations are the off-axis reflective and the axial transmissive [49], [50]. The off-axis reflective configuration is the Czerny-Turner design with off-axis mirrors as collimators and reflective gratings in the collimated space. The off-axis configuration suffers from strong astigmatism, which can be greatly reduced by using torroidal mirrors for collimation (see for example, SpectraPro series from Acton Research Corporation, Acton, MA). The spectrographs with this configuration are generally available with f-number not less than 4. As a result, the numerical aperture of the entering beam has to be limited to reduce the stray light in the spectrograph. This is

especially important for fiber probe collection since the numerical aperture of the entering beam is limited by the probe fiber numerical aperture [47].

Relatively few design options are available on the market for the dispersive spectrograph with axial transmissive configuration (see for example HoloSpec series from Kaiser Optical Systems, Inc., Ann Arbor, MI). This transmissive configuration uses lenses to collimate the beam and places them very close to a volume holographic trasnmissive diffraction grating. This permits f-numbers < 4 without compromising on resolution and provides a very compact commercial package. As a result, this configuration allows for efficient coupling with fiber-optic probes. It was shown that this configuration has an advantage of about 2 or more over the off-axis reflective design [51]. Usually multi-element lenses are required to provide adequate chromatic correction for Raman spectra and have good quality over the image plane [48].

The main disadvantage of the axial transmissive configuration is wavelength inflexibility. Fixed gratings may need to be changed for different excitation wavelengths or detection ranges. The low f-number lenses can be chromatically corrected only for a limited wavelength range, thus requiring refocusing or changing lenses for different excitation wavelengths as well.

9.5.4 Rejection Filter

Another critical component is the excitation rejection filter. The intensity of the Raman scattered signal in NIR is about 10^{-10} times that of the excitation intensity, thus the backscattered excitation light should be rejected from getting into the spectrograph and, if possible, into the collection fiber. The current choice for achieving this rejection is a notch rejection filter. This filter usually transmits about 10^{-4} - 10^{-8} in a narrow band at the wavelength of the excitation laser and about 80% for the wavelength regions of the Stokes and anti-Stokes Raman spectra. The most popular choice for excitation rejection filters in Raman spectroscopy is the holographic filters. Holographic notch filters are excellent filters for removing the laser line and are available in a variety of wavelengths (see for example, holographic notch filters from Kaiser Optical Systems, Inc., Ann Arbor, MI, www.kosi.com). They have practically replaced the second and third stages of traditional Raman spectrometers [40]. The holographic notch filters are widely used in a variety of NIRRS applications and provide excellent performance. It should be mentioned that another choice for the rejection notch filter could be a multilayer dielectric interference filter (see for example Omega Optical Inc., Brattleboro, VT, www.omegafilters.com). These filters can provide rejection on the laser wavelength greater than 5 orders with the Raman spectra ~70%. The advantage of these filters is that they are relatively inexpensive. The major drawback is that there is filter ringing at the Raman scattered wavelengths caused by the multilayer structure of these filters.

Also, the spectral width of the rejection notch is greater than that of the holographic notch filter. However, these filters offer reasonable alternatives that would be worth considering when the cost of the system is important.

9.5.5 Fiber Optics

The fiber probe can easily measure exposed areas of the body, such as skin, hair, nails, and areas of the mouth. Fiber probes can also be miniaturized and incorporated into endoscopic probes or biopsy needles or internal analysis. This is the most critical component of the NIRRS system. First of all, this component couples the system with the sample to be examined. Thus, it has to be implemented so as to maximize the system performance, requiring customization for the specifics of the measurement objective. Secondly, it is the component that brings the excitation light into the tissue and collects the emitted light from the tissue. Thus, this is the place in the system where both signals are present. The relative intensity of the Raman scattered signal in NIR is about 10 orders of magnitude lower than the excitation intensity, thus any interference of the excitation light with the optical and photoelectrical path of the Raman signal may create a background effectively completely obstructing the Raman signal. For example, the back reflection of the fiber end, even if antireflection coated, 1% of the excitation light reflected through the fiber is still 8 orders of magnitude greater than Raman signal. Though the reflected excitation light can be rejected with a notch filter, the fluorescence and Raman scattering induced by the excitation light traveling back through the fiber may be at about the same wavelength as the tissue Raman. There are processing methods to separate fast changing Raman spectra from slow changing fluorescence spectra, but these methods do not help against fiber Raman scattering. Again, these background signals due to the fiber itself use the available dynamic range of the detector and induce shot noise which may decrease the signal-to-noise ratio for the tissue Raman signal to an unusable level. New fiber materials have reduced these effects, although very weak tissue Raman signals may still be obscured. Also, a beveled fiber exit surface has been explored and showed to decrease this reflection. The most common arrangement currently used in the NIRRS system is a probe using two separate paths for the excitation and scattered light. Also, some designs incorporate the rejection filter up front before the collection fiber to eliminate any backscattered excitation light from getting into the collection fiber. Utzinger *et al.* [47] presented a comprehensive analysis of fiber probe designs in the recent review.

NIRRS applications have been reported by a number of researchers for the *in vivo* cancer and precancerous conditions for various tissues (brain, breast, cervix, bladder), for other disease diagnosis (skin studies,

Alzheimer's disease, atherosclerotic plagues) and blood analysis. We have cited earlier several recent reviews [28,32,38,41,42,43], where there are comprehensive discussions and citations of these reports. Here we will review the three latest reports of NIRRS applications for *in vivo* precancerous conditions of polyps [37], *in vivo* cervical precancers [46] and analysis of whole blood *ex vivo* [30].

9.6 NEAR-INFRARED RAMAN SPECTROSCOPY FOR *IN VIVO* DISEASE DIAGNOSIS

During the last decade NIRRS has been applied for *in vivo* diagnosis of various diseases. To illustrate diagnostic potential of NIRRS we will review three applications of this technique for detection of colon and cervical cancer and also blood analysis.

Recently Molckovsky *et al.* [37] demonstrated that NIRSS can be used for *in vivo* classification of adenomatous and hyperplastic polyps in the GI tract. To achieve that researchers used an in-house built NIRRS endoscopic system [45] comprised of a tunable laser diode emitting at 785 nm, a high throughput holographic spectrograph and a liquid nitrogen-cooled CCD detector. The schematic diagram of this system is presented in Figure 13.

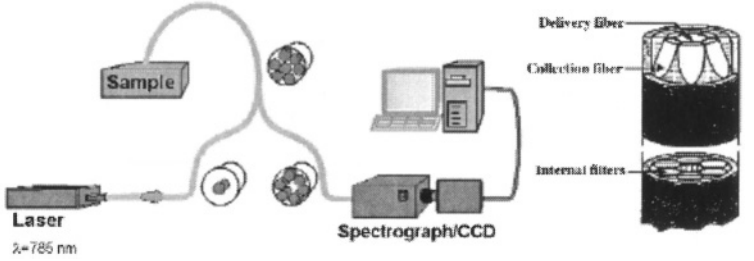

Figure 13. Schematic diagram of Raman spectroscopic system and filtered fiberoptic probe (from Ref. [37]).

Researchers used custom-made fiber-optic Raman probes (Enviva Raman probes, Visionex, Inc., Atlanta, Ga.). The probes consisted of a central 400 μm core diameter excitation fiber surrounded by 7 collection fibers 300 μm core diameter each. The probes employed internal filters, which significantly reduced interfering fluorescence and Raman background signals generated in the fiber-optics.

An *ex vivo* study used for analysis a total of 33 polyps from 8 patients. When the large polyps were retrieved in multiple fragments, *ex vivo* Raman spectra were collected from individual polypectomy specimens. Thus, a total

of 54 spectra were available for analysis (20 hyperplastic, 34 adenomatous). A preliminary *in vivo* study was carried out whereby a total of 19 spectra, each corresponding to a different measurement site, were collected from 9 polyps (5-30 mm in size) in 3 patients. The polyps were histologically classified as hyperplastic (9 spectra/specimens, 5 polyps, 2 patients) or adenomatous (10 spectra/specimens, 4 polyps, 3 patients).

The average *ex vivo* Raman spectrum of adenomatous polyps versus that of hyperplastic polyps is shown in Figure 14(A) (from Ref. [37]). Similarly, Figure 14(B) contrasts the average *in vivo* Raman spectra of these 2 polyp types. In both *ex vivo* and *in vivo* settings, typical tissue Raman peaks were identified at 1645 to 1660, 1450 to 1453, 1310, 1260, and 1003 cm^{-1}, which correspond, respectively, to the protein amide I band, CH_2 bending mode, CH_2 twisting mode, protein amide III band and the phenyl ring breathing mode [31,45].

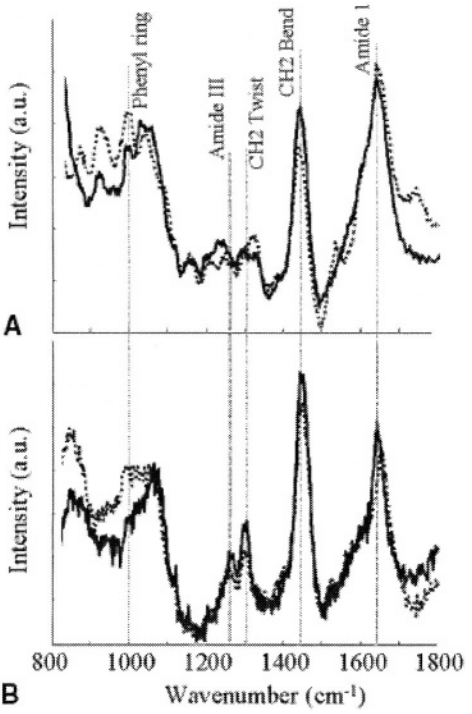

Figure 14. **A,** Average Raman spectra of hyperplastic (*n*=20; *solid line*) and adenomatous *(n* = 34; *broken line)* colon polyps collected *ex vivo* (power=200 mW; 30-second collection time). **B,** Average Raman spectra of hyperplastic (*n*=9; *solid line*) and adenomatous *(n*= 10; *broken line)* colon polyps collected *in vivo* (power=100 mW; 5-second collection time). The spectra have been intensity-corrected, wavelength-calibrated and fluorescence background-subtracted (from Ref. [37]).

The diagnostically important spectral differences found in the Molckovsky *et al.* [37] study were used to develop PCA/LDA-based diagnostic algorithm. With the limited number of samples, the predictive accuracy of the classification algorithm developed was estimated by using a leave-one-out cross validation technique. Using this technique the classification of colon polyps *ex vivo* identified adenomatous polyps with a sensitivity of 91%, a specificity of 95%, and an overall accuracy of 93%. For the *in vivo* data set, the algorithm identified adenomas with a sensitivity of 100%, a specificity of 89%, and an accuracy of 95%.

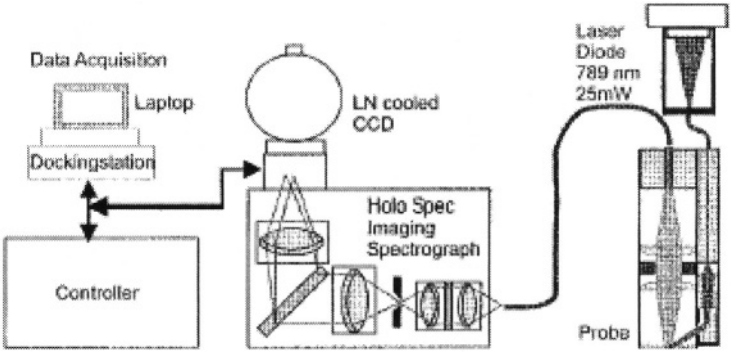

Figure 15. Block diagram of system used to measure Raman spectra *in vivo* (from Ref. [46]).

We believe the larger NIRRS studies in the GI tract should be very important. The reward of these studies (both *in vivo* and *ex vivo*) would be a step toward understanding what NIRRS is really measuring and how it relates to disease progression since it may establish the connection between the NIRRS extracted biochemical changes and the bimolecular chemistry and cell biology of the disease. Further development along these lines may advance our understanding of the connection between cancerous processes at the single cell level and various levels of neoplastic conditions and invasive tumors.

Detection of cervical precancer using NIRRS was recently reported by Utzinger *et al.* [46] in the *in vivo* pilot study where histopathologic biopsy was used as the gold standard. The block diagram of the system [35] for collection the spectra from the cervical epithelium *in vivo* is shown in Figure 15 (from Ref. [46]).

It includes a diode laser at 789 nm coupled to a fiber optics delivery and collection probe. The probe guides the illumination light onto the cervix and collects the resulting Raman scattered light onto a holographic spectrograph coupled to a liquid nitrogen cooled, back-illuminated, deep depletion, CCD camera. The probe was optimized to measure epithelial tissue layers.

The probe was advanced through the speculum and placed in contact with a colposcopically normal and abnormal site on the cervix. Following the spectral measurement, each site was biopsied. During the cervical colposcopy, normal and abnormal areas were identified by the colposcopist, and Raman spectra were measured from one normal and one abnormal area of the cervix. Each of these sites was then colposcopically biopsied. Biopsies were submitted for routine histologic analysis by a gynecologic pathologist. The pathologic categories were normal cervix, inflammation, squamous metaplasia, low-grade squamous dysplasia (HPV and CIN 1) and high grade squamous dysplasia (CIN 2, CIN 3) and cancer. The pathologist was blinded to the Raman spectroscopic study.

Raman spectra were grouped according to histopathologic findings and average spectra were calculated. These average spectra were examined visually to identify a set of Raman peaks common to most spectra.

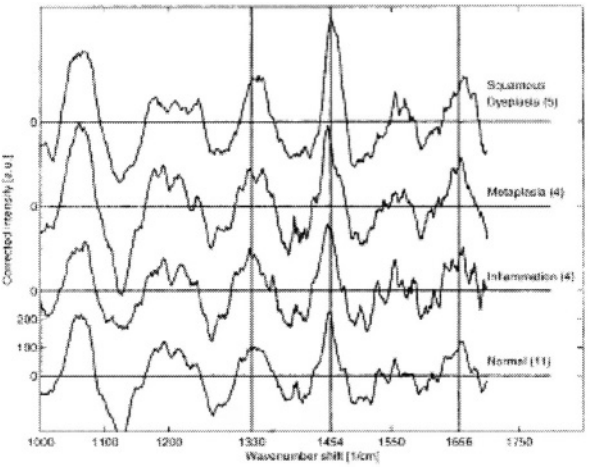

Figure 16. Average Raman spectra of each diagnostic category: normal, inflammation, metaplasia, and squamous dysplasia (from Ref. [46]).

In the study 24 measurements were made in 13 patients. Figure 16 (from Ref. [46]) shows average Raman spectra of each diagnostic category, normal, inflammation, metaplasia, and squamous dysplasia. The scatter plot presented in Figure 17 (from Ref. [46]) shows performance of the diagnostic algorithms derived from the data.

The report [46] demonstrates the potential to measure near-infrared Raman spectra *in vivo* and extract potentially useful information. Spectra measured *in vivo* resemble those measured *in vitro* [35].

There are obvious visual differences in the spectra of normal cervix and high-grade squamous dysplasia in the same patient. Average spectra reveal a

consistent increase in the Raman intensity at 1330, 1454, and 1650 cm^{-1} as tissue progresses from normal to high-grade squamous dysplasia. These peaks are consistent with contributions from collagen, phospho-lipids, and DNA. However, because tissue is a complex, heterogeneous structure, definitive assignment is difficult.

The limitations of this study are that it is a pilot study with a small number of patients. The authors' experience shows that pilot studies are very useful in the development of emerging technologies; however, larger clinical trials are required to confirm these results. Improvements in hardware, measurement conditions, and training clinical staff to optimally participate in data collection are necessary and possible to allow these larger trials. Thus, NIRRS offers an attractive tool for surveying the biochemical changes that accompany the development of dysplasia.

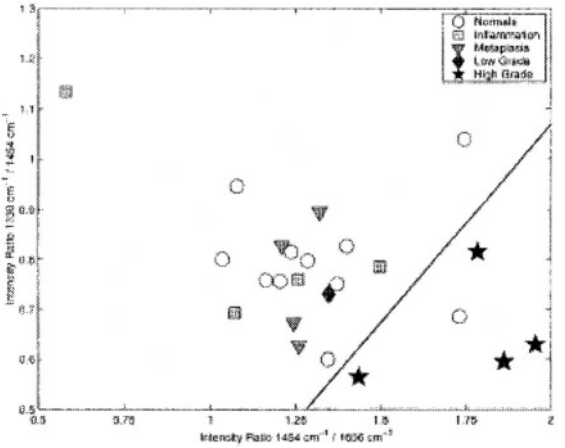

Figure 17. This scatter plot indicates the intensity of each of the 24 sites measured by diagnostic category at three frequencies; the intensity ratio at 1330/1454 cm^{-1} is plotted against the ratio of intensities at 1454/1656 cm^{-1}. The straight-line algorithm separates high-grade squamous dysplasia from all others, misclassifying one normal sample (from Ref. [46]).

We would add to the author's comments that perhaps a greater data base of Raman spectra may allow to apply one of the statistical methods discussed in the previous report to identify differentiation criteria so that all six diagnostic categories (normal cervix, inflammation, squamous metaplasia, low-grade squamous dysplasia (HPV and CIN 1) and high grade squamous dysplasia (CIN 2, CIN 3) and cancer) discussed in the report would be possible to differentiate. Also, it seems that even a simple model of the NIR Raman spectra including the Raman effective components in the tissue and the excitation and Raman radiation propagation in the tissue may provide useful improvement. Other comments made regarding the colon polyp differentiation apply here as well.

Near-infrared Raman spectroscopy has also been recently used for blood analysis. The major challenge in such analysis, even in a whole blood, lies in the presence of numerous low-concentration components, all with weak signals that are further distorted by the strong light absorption and scattering caused by the red blood cells. Enejder *et al.* [30] reported the application of NIRRS to analysis of whole blood with quantitative determination of multiple analytes in whole blood at clinically relevant precision. The analytes quantified are glucose, urea, cholesterol, albumin, total protein, triglycerides, hematocrit (hct), hemoglobin, and bilirubin, all of which are frequently ordered diagnostic tests used in connection with common medical conditions.

A block diagram of the NIRRS system for the whole blood measurements reported in [30] is shown in Figure 18. A beam of 830-nm light from a diode laser is passed through a bandpass filter, directed toward a parabolic mirror by means of a small prism, and focused onto a quartz cuvette containing a whole blood sample. Raman-scattered light emitted from the whole blood surface (1-mm^2 area) is collected by the mirror, passed through a notch filter to reject backreflected 830-nm light, and coupled into an optical fiber bundle, which converts the circular shape of the collected light to rectangular to match the entrance slit of the spectrograph. The spectra were collected by a cooled CCD array detector.

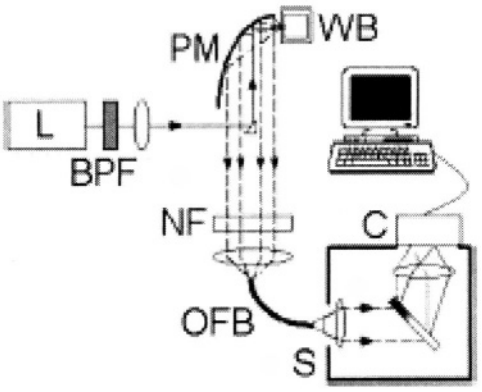

Figure 18. Schematic diagram of the Raman instrument (from Ref. [30]).

The background subtracted Raman spectra from whole blood samples collected from 31 patients shown in Figure 19 (from Ref. [30]). For each sample, 30 consecutive 10-s spectra were collected over a 5-min period. Conventional clinical laboratory methods, including absorbance spectrophotometry and automated cell counting, were used to assess the nine

analytes concentration. These reference concentrations were correlated with the recorded NIR-Raman spectra and used for multivariate calibration and validation.

The accuracy of the technique was established using the cross validation method. It was demonstrated that NIRRS could be used to extract quantitative information about bimolecular contents in whole blood at clinically relevant precision. The authors state that further improvement in prediction accuracy may be obtained by correction for variations in scattering and absorption. It is worth noting that for *in vivo* measurements the tissue fluorescence may provide a very strong background. Although, by subtracting the background fluorescence the effect of the background associated noise can be significantly reduced, the tissue fluorescence intensity may be high relative to the NIRRS signal from the blood. As a result, the dynamic range of the detector and the fluorescence-induced noise can complicate meaningful measurements. Further *in vivo* studies are required to demonstrate the applicability of the NIRRS for blood analyte measurements.

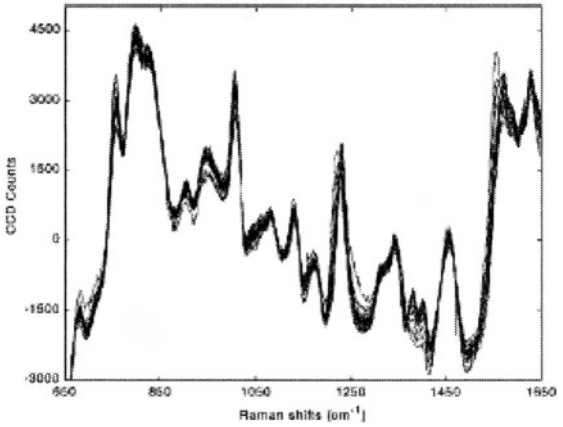

Figure 19. Raman spectra of 31 whole blood samples after polynomial background subtraction (from Ref. [30]).

9.7 SURFACE-ENHANCED RAMAN SPECTROSCOPY

Surface-enhanced Raman scattering (SERS) is an intriguing technique based on a strong increase in Raman signals from molecules if those molecules are attached to submicron metallic structures. Two effects are believed to contribute to the SERS enhancement mechanisms: electromagnetic effects and chemical effects [56].

When electromagnetic wave interacts with a smooth metal surface, there is a small enhancement of Raman intensities compared with that in the absence of the surface (on the order of 10 or less for metals like Ag) arising primarily from coherent superposition of the incident and reflected fields at the position of the molecule doing the scattering [58].

If the surface is rough, then enhanced local electromagnetic fields at the place of the molecule nearby the metal surface occur due to excitation of electromagnetic resonances by the incident radiation [57]. These resonances appear due to collective excitation of conduction electrons in the small metallic structures and also called surface plasmon resonances. Both the excitation and Raman scattered fields contribute to this enhancement, thus the SERS signal is proportional to the fourth power of the field enhancement factor [59].

The surface roughening effect can be achieved by isolated metal particle, by gratings, by assemblies of particles on surfaces, and randomly roughened surfaces. All these structures provide enhancement if the metal involved has narrow plasmon resonances at convenient frequencies for Raman measurements [58]. The chemical effects or "chemical mechanism" of enhancement is commonly defined to include any part of the surface enhancement that is not accounted for using the electromagnetic mechanism [58]. The "chemical mechanisms" include enhancements that arise from interactions between molecule and metal. The most commonly considered interaction that require overlap between molecular and metal wavenumbers occurs when charge transfer between the surface and molecule leads to the formation of excited states that serve as resonant intermediates in Raman scattering [58]. Interactions that do not require overlap between molecular and metal wavenumbers arise from electromagnetic coupling between the vibrating molecule and the metal. These interactions can occur either at the vibrational frequency or at optical frequencies. The combined enhancement factors can be as high as 10^{14}, which is enough to observe SERS spectra from single molecules.

9.7.1 Single Molecule Detection Using Surface-Enhanced Raman Scattering

By exploiting this very high enhancement factor from surface-enhanced Raman scattering (SERS), Kneipp *et al.* [52] observed Raman scattering of a single crystal violet molecule in aqueous colloidal silver solution.

The excitation source was an argon-ion laser pumped cw Ti:sapphire laser operating at 830 nm with a power of about 200 mW at the sample. Dispersion was achieved using a Chromex spectrograph with a deep depletion CCD detector. A water immersion microscope objective (363, NA 0.9) was brought into direct contact with a 30 ml droplet of the sample

solution for both excitation and collection of the scattered light. Scattering volume was estimated to be approximately 30 pl.

Using one second excitation time and $2 \cdot 10^5$ W/cm^2 nonresonant near-infrared excitation researchers observed clear fingerprint of its Raman features between 700 and 1700 cm^{-1}. Spectra observed in a time sequence for an average of 0.6 dye molecule in the probed volume exhibited the expected Poisson distribution for actually measuring 0, 1, 2, or 3 molecules (see Figure 20).

The relatively well "quantized" signals for 1, 2, or 3 molecules suggest relatively uniform enhancement mechanism(s) despite the nonuniform shape and size of the silver particles forming the clusters. The large SERS enhancement can be understood by favorable superposition of a very strong electromagnetic enhancement due to silver clusters, which is particularly effective at NIR excitation coupled with a strong chemical enhancement.

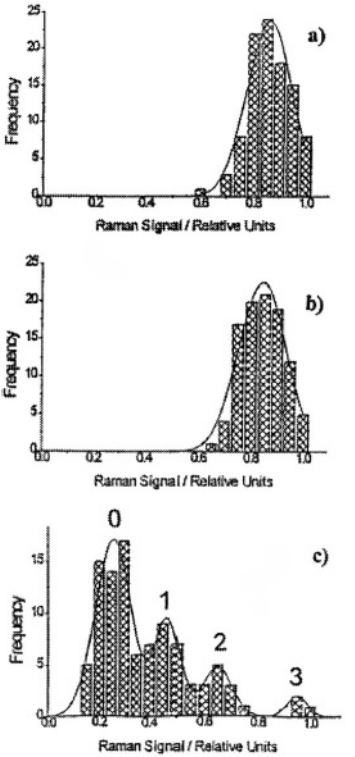

Figure 20. (a) Statistical analysis of 100 "normal" Raman measurements at 1030 cm^{-1} of 1014 methanol molecules. (b) Statistical analysis of 100 SERS measurements (1174 cm^{-1} Raman line) of six crystal violet molecules in the probed volume. The solid lines are Gaussian fits to the data. (c) Statistical analysis of 100 SERS measurements (1174 cm^{-1} Raman line) for an average of 0.6 crystal violet molecules in the probed volume. The peaks reflect the probability to find just 0, 1, 2, or 3 molecules in the scattering volume (from Ref. [52]).

9.7.2 Surface-Enhanced Raman Spectroscopy of Carbon Nanotubes

Carbon nanotubes are macromolecules whose structure is honeycomb lattices rolled into the cylinders [53]. They also possess unique mechanical, electronic, and chemical properties. Raman scattering spectroscopy can be a very valuable tool in probing carbon nanotubes phonon spectra and also their electronic density of states. And since SERS is very sensitive and also it can provide information about high energy anti-Stokes side of the excitation laser it should be a perfect tool to study carbon nanotubes.

Recently Kneipp *et al.* [54,55] used SERS to measure narrow Raman bands corresponding to the homogeneous linewidth of the tangential C–C stretching mode in semiconducting nanotubes. Normal and surface-enhanced Stokes and anti-Stokes Raman spectra were discussed in the framework of selective resonant Raman contributions of semiconducting or metallic nanotubes to the Stokes or anti-Stokes spectra, respectively, of the population of vibrational levels due to the extremely strong surface-enhanced Raman process, and of phonon-phonon interactions.

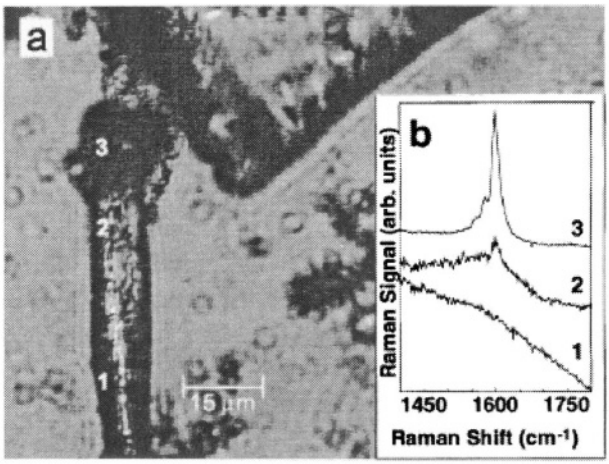

Figure 21. Microscope view of (a) a section of a nanotube bundle touching a colloidal Ag cluster, and (b) SERS spectra collected along various points (1, 2, 3) on the bundle, using 830 nm cw Ti:sapphire laser excitation with a 1 mm spot size. The black spots in (a) are colloidal silver particles of different sizes that are aggregated by addition of NaCl (from Ref. [54]).

Kneipp *et al.* [54] found that a very small number of tubes or perhaps even a single nanotube might be detected using SERS technique (Figure 21). The strong enhancement and confinement of the electromagnetic field on a silver cluster, within domains that can be as small as 20 nm, may provide an

additional high lateral resolution tool for selectively probing a small numbers of nanotubes that are adjacent to the interface just in such a domain. Kneipp *et al.* [54] expects that even stronger SERS enhancement could be observed at low Raman frequency shifts. Thus, it may be possible for SERS to reveal the radial breathing mode band for individual carbon nanotubes free from the inhomogeneous broadening effects observed for this mode in normal resonant Raman spectra.

9.7.3 Example of Biomedical Application of Surface-Enhanced Raman Spectroscopy: Glucose Biosensor

It was shown [30] (see section 9.6) that NIR Raman spectroscopy could be used for whole blood analysis. In this section we show that surface-enhanced Raman spectroscopy can potentially be utilized for measuring glucose *in vivo.* Shafer-Peltier *et al.* [60] reported detection of glucose using SERS.

The researchers prepared a novel SERS medium by using a self-assembled alkanethiol monolayer adsorbed on a silver film over nanosphere (AgFON) surface as a partition layer to concentrate glucose from solution within the ~4 nm SERS activation distance of the silver. The SERS surface was fabricated by drop coating undiluted white carboxyl-substituted latex nanospheres (diameter 390 ± 19.5 nm) on glass substrates that had been cleaned and made hydrophilic. These were allowed to dry in ambient conditions then vapor deposited with Ag to a mass thickness of 200 nm. Since glucose SERS on this surface could not be observed, the authors used the alkanethiol monolayer assembled over the AgFON to concentrate glucose and increase its SERS interaction with AgFON. This is analogous to creating a stationary phase in high performance liquid chromatography. The SERS substrate thus prepared should be stable electochemically and thermally. A confocal microscope, a modified Nikon Optiphot (Frier Company, Huntley, IL) with a 20X objective in backscattering geometry, was used to measure spatially resolved SERS spectra. The laser light at 532 nm or 632.8 nm was coupled into a 200 μm diameter fiber. The collected backscattered light was coupled by another fiber into a VM-505 monochromator (Acton Research Corporation, Acton MA) with entrance slit set at 250 μm and Spec-10-400B liquid nitrogen-cooled CCD camera (Roper Scientific, Trenton NJ).

Figure 22 (from Ref. [60]) shows example spectra from the different stages of glucose/1-decanethiol/AgFON surface. Figure 22(A) shows the SERS spectrum of 1-decanethiol on AgFON surface. In Figure 22(B) the SERS spectrum of the superposition of the SERS spectra of 1-decanethiol layer and glucose with features from glucose (1123 and 1064 cm^{-1}) and 1-decanethiol (1099, 864 and 681 cm^{-1}) is shown.

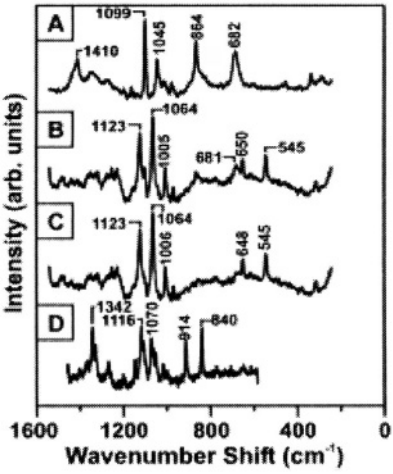

Figure 22. Spectra used in quantitative analysis. (A) - 1-DT monolayer on AgFON substrate, λ_{ex} = 532 nm, *P* = 1.25 mW, acquisition time = 30 s. (B) Mixture of 1-DT monolayer and glucose partitioned from a 100 mM solution, λ_{ex} = 532 nm, *P* = 1.25 mW, acquisition time = 30 s. (C) Residual glucose spectrum produced by subtracting (A) from (B). (D) Normal Raman spectrum of crystalline glucose for comparison, λ_{ex} = 632.8 nm, *P* = 5 mW, acquisition time = 30 s (from Ref. [60]).

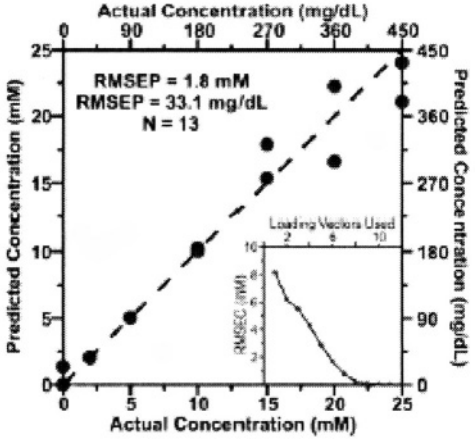

Figure 23. Plot of PLS predicted physiologically relevant glucose concentrations versus actual glucose concentrations using leave-one-out cross-validation (10 loading vectors). AgFON samples were made, incubated for 19 h in 1 mM 1-DT solution, and dosed in glucose solution (range: 0-25 mM) for 1 h. Each micro-SERS measurement was made, whereas samples were in an environmental control cell filled with glucose solution, using λ_{ex} = 632.8 nm (3.25 mW, 30 s). Dashed line is not a fit, but rather represents perfect prediction. Inset shows the root-mean-squared error of calibration as a function of number of loading vectors used in the PLS algorithm (from Ref. [60]).

The SERS spectra with the excitation laser at 632 nm were measured for 36 samples with glucose concentration from 0 to 250 mM. This data set was processed using partial-least squares analysis with leave-one-out cross validation. The resulting error of prediction was 3.3 mM. The results were repeated with multiple, similar data sets.

Similar measurements were carried out with the concentration within the clinically relevant range. Thirteen samples were measured. Performing partial-least squares analysis with leave-one-out cross validation rendered a corresponding prediction error of 1.8 mM (see Figure 23, from Ref. [60]).

The authors concluded that the reported results demonstrate the feasibility of a SERS based glucose sensor. They also observed that the expensive bulky equipment they used is already possible to down size to much smaller and less expansive instruments utilizing a linear array based spectrometer. In the future they suggest that micro- and nanophotonics approaches would produce a hand size apparatus for SERS measurement. They also projected that the SERS substrate can be miniaturized to become an implantable device not only for glucose but also for other analytes in the human body fluids. We would add to the author's comments that it is reasonable to assume that the nanophotonics will be able to implement the entire device including a substrate as well as a SERS measurement apparatus in the scale amenable for implanting in the body. This could allow new levels for treating physiological conditions using implantable devices dispersing therapeutic agents with the real-time feedback and/or auto-adaptation, for example, an insulin-dispersing device, which could regulate the dose based on the glucose level continuously measured in the body by a nano-SERS device.

ACKNOWLEDGEMENTS

This work was supported by NSF Grant No. BES-0116833, CIMIT New Concepts Award, OBGYN Foundation and Department of Veterans Affairs Merit Review Grant.

REFERENCES

1. R.G. Newton, *Scattering Theory of Waves and Particles* (McGraw-Hill Book Company, New York, 1969).
2. I.J. Bigio and J.R. Mourant, "Ultraviolet and visible spectroscopies for tissue diagnostics: fluorescence spectroscopy and elastic-scattering spectroscopy," *Phys. Med. Biol.* **42,** 803-814(1997).

3. J.R. Mourant, J. Boyer, T. Johnson, J. Lacey and I.J. Bigio, "Detection of gastrointestinal cancer by elastic scattering and absorption spectroscopies with the Los Alamos Optical Biopsy System," *Proc. SPIE* **2387**, 210-217 (1995).
4. L.T. Perelman, V. Backman, M. Wallace, G. Zonios, R. Manoharan, A. Nusrat, S. Shields, M. Seiler, C. Lima, T. Hamano, I. Itzkan, J. Van Dam, J.M. Crawford, M.S. Feld, "Observation of periodic fine structure in reflectance from biological tissue: a new technique for measuring nuclear size distribution," *Phys. Rev. Lett.* **80**, 627-630, (1998).
5. V. Backman, M. Wallace, L.T. Perelman, R. Gurjar, G. Zonios, M.G.Müller, Q. Zhang, T. Valdez, J.T. Arendt, H.S. Levin, T. McGillican, K. Badizadegan, M. Seiler, S. Kabani, I. Itzkan, M. Fitzmaurice, R.R. Dasari, J.M. Crawford, J. Van Dam, M.S. Feld, "Detection of preinvasive cancer cells. Early-warning changes in precancerous epithelial cells can be spotted *in situ," Nature* **406** (6791), 35-36 (2000).
6. M. Wallace, L.T. Perelman, V. Backman, J.M. Crawford, M. Fitzmaurice, M. Seiler, K. Badizadegan, S. Shields, I. Itzkan, R.R. Dasari, J. Van Dam, M.S. Feld, "Endoscopic detection of dysplasia in patients with Barrrett's esophagus using light scattering spectroscopy," *Gastroentorolgy* **119**, 677-682 (2000).
7. H. Fang, M. Ollero, E. Vitkin, L.M. Kimerer, P.B. Cipolloni, M.M. Zaman, S.D. Freedman, I.J. Bigio, I. Itzkan, E.B. Hanlon, and L.T. Perelman, "Noninvasive sizing of subcellular organelles with light scattering spectroscopy," *IEEE J. Sel. Top. Quant. Elect.* **9**(2) (2003).
8. V. Backman, V. Gopal, M. Kalashnikov, K. Badizadegan, R. Gurjar, A. Wax, I. Georgakoudi, M. Mueller, C.W. Boone, R.R. Dasari, and M.S. Feld, "Measuring cellular structure at submicrometer scale with light scattering spectroscopy," *IEEE J. Sel. Top. Quant. Eectl.* **7,** 887-893 (2001).
9. V. Backman, R. Gurjar, L.T. Perelman, V. Gopal, M. Kalashnikov, K. Badizadegan, A. Wax, I. Georgakoudi, M. Mueller, C.W. Boone, I. Itzkan, R.R. Dasari, M.S. Feld, "Imaging and measurement of cell organization with submicron accuracy using light scattering spectroscopy" in *Optical Biopsy IV, Proc. SPIE* **4613**, R.R. Alfano ed. (SPIE Press, Bellingham, 2002), 101-110.
10. L.T. Perelman and V. Backman, "Light scattering spectroscopy of epithelial tissues: Principles and applications" in *Handbook on Optical Biomedical Diagnostics* **PM107**, V.V. Tuchin ed. (SPIE Press, Bellingham, 2002), 675-724.
11. A. Brunsting and F. Mullaney, "Differential light scattering from spherical mammalian cells," *Biophys. J.* **14,** 439-453 (1974).
12. J.R. Mourant, J.P. Freyer, A.H. Hielscher, A.A. Eick, D. Shen, and T.M. Johnson, "Mechanisms of light scattering from biological cells relevant to noninvasive optical-tissue diagnosis," *Appl. Opt.* **37**, 3586-3593 (1998).
13. R. Drezek, A. Dunn, and R. Richards-Kortum, "Light scattering from cells: finite-difference time-domain simulations and goniometric measurements," *Appl. Opt.* **38**, 3651-3661 (1999).
14. G. Zonios, L.T. Perelman, V. Backman, R. Manoharan, M. Fitzmaurice, and M.S. Feld. "Diffuse Reflectance Spectroscopy of Human Adenomatous Colon Polyps In Vivo," *Appl. Opt.* **38**, 6628-6637 (1999).
15. I. Georgakoudi, B.C. Jacobson, J. Van Dam, V. Backman, M.B. Wallace, M.G. Muller, Q. Zhang, K. Badizadegan, D. Sun, G.A. Thomas, L.T. Perelman, and M.S. Feld, "Fluorescence, reflectance and light scattering spectroscopies for evaluating dysplasia in patients with Barrett's esophagus," *Gastroentorolgy* **120**, 1620-1629 (2001).
16. V. Backman, R. Gurjar, K. Badizadegan, R. Dasari, I. Itzkan, L.T. Perelman, and M.S. Feld, "Polarized light scattering spectroscopy for quantitative measurement of epithelial cellular structures *in situ," IEEE J. Sel. Top. Quant. Elect.* **5**, 1019-1027(1999).
17. O.W. van Assendelft, *Spectrophotometry of Haemoglobin Derivatives* (C.C. Thomas, Springfield, 1970).

18. A. Ishimaru, *Wave propagation and scattering in random media* (Academic Press, Orlando, 1978).
19. T.J. Farrell, M.S. Patterson, and B.C. Wilson, "A diffusion theory model of spatially resolved, steady-state diffuse reflectance for the non-invasive determination of tissue optical properties," *Med. Phy.s* **19**, 879-888 (1992).
20. G.L. Tipoe and F.H. White, "Blood vessel morphometry in human colorectal lesions," *Histol Histopathol.* **10**, 589-596(1995).
21. S.A. Skinner, G.M. Frydman, and P.E. O'Brien, "Microvascular structure of benign and malignant tumors of the colon in humans," *Digest Dis. Sci.* **40**, 373-384 (1995).
22. V. Backman, L.T. Perelman, J.T. Arendt, R. Gurjar, M.G. Muller, Q. Zhang, G. Zonios, E. Kline, T. McGillican, T. Valdez, J. Van Dam, M. Wallace, K. Badizadegan, J.M. Crawford, M. Fitzmaurice, S. Kabani, H.S. Levin, M. Seiler, R.R.Dasari, I. Itzkan, and M. S. Feld, "Light scattering spectroscopy: A new technique for clinical diagnosis of precancerous and cancerous changes in human epithelia", *Lasers Life Sci.* **9**, 255-263 (2001).
23. B.J. Reid, R.C. Haggitt, C.E. Rubin, G. Roth, C.M. Surawicz, G. Vanbelle, K. Lewin, W.M. Weinstein, D.A. Antonioli, H. Goldman, W. Macdonald, and D. Owen, "Observer variation in the diagnosis of dysplasia in Barrett's esophagus," *Hum. Pathol.* **19**, 166-178(1988).
24. R.H. Riddell, H. Goldman, D.F. Ransohoff, H.D. Appelman, C.M. Fenoglio, R.C. Haggitt, C. Ahren, P. Correa, S.R. Hamilton, B.C. Morson, S.C. Sommers, J.H. Yardley, "Dysplasia in inflammatory bowel disease: Standardized classification with provisional clinical applications," *Hum. Pathol.* **14**, 931-986 (1983).
25. R.C. Haggitt, "Barrett's esophagus, dysplasia, and adenocarcinoma," *Hum. Pathol.* **25**, 982-993 (1994).
26. M. Pagano and K. Gauvreau, *Principles of Biostatistics.* (Duxbury Press, Belmon, 1993).
27. J. Landis and G. Koch, "The measurement of observer agreement for categorical data," *Biometrics* **33**, 159-174(01977).
28. L.P. Choo-Smith, H.G.M. Edwards, H.P. Endtz, J.M. Kroz, F. Heule, H. Barr, J.S. Robinson Jr., H.A. Bruining, and G.J. Puppels, "Medical applications of raman spectroscopy: From proof of principle to clinical implementation," *Biopolymers (Biospectroscopy)* **67**, 1-9 (2002)
29. N.B. Colthup, L.H. Daly, S.E. Wiberley, *Introduction to Infrared and Raman Spectroscopy* (3d edition, Academic Press, Boston, 1990)
30. A.K.M. Enejder, T.-W. Koo, J. Oh, M. Hunter, S. Sasic, and M. Feld, "Blood analysis by Raman spectroscopy," *Opt. Lett.* **27**, 2004-2006, (2002).
31. Y. Guan, E.N. Lewis, and I.W. Levin, "Biomedical applications of Raman spectroscopy: tissue differentiation and potential clinical usage" in *Analytical applications of Raman spectroscopy,* M.J. Pelletier, Ed., (Blackwell Science Ltd, Oxford, 1999), 276-327.
32. E.D. Hanlon, R. Manoharan, T.-W. Koo, K.E. Shafer, J.T. Motz, M. Fitzmaurice, J.R. Kramer, I. Itzkan, R.R. Dasari, and M.S. Feld, "Prospects for in vivo Raman spectroscopy," *Phys.Med. Biol.* **45**, R1-R59 (2000).
33. *Handbook of Vibrational Spectroscopy,* J.M. Chalmers and P.R. Grifiths eds. (John Wiley & Sons Ltd, Chichester, 2002).
34. *Handbook of Raman Spectroscopy,* L.R. Lewis and H.G.M. Edwards, eds (Marcel Dekker, New York, 2001).
35. A. Mahadevan-Jansen, M. Follen Mitchell, N. Ramanujam, U. Utzinger, and R. Richard Kortum; "Development of a fiber optic probe to measure NIR Raman spectra of cervical tissue *in vivo," Photochem. Photobiol,* **68**, 427-431 (1998).
36. H. Martens and T. Naes, *Multivariate Calibration* (John Wiley & Sons Ltd, New York, 1989).

37. A. Molckovsky, L.-M. Wong Kee Song, M.G. Shim, N.E. Marcon, and B.C. Wilson, "Diagnostic potential of near-infrared Raman spectroscopy of colon: differentiating adenomatous from hyperplastic polyps," *Gastrointest. Endosc.* **57**, 396-402 (2003).
38. A. Mahavedan-Jensen and R. Richards-Kortum, "Raman spectroscopy for the detection of cancers and precancers," *J. Biomed. Opt.* **1**, 31-70 (1996).
39. S.P. Mulvaney and C.D. Keating, "Raman Spectroscopy," *Anal. Chem.* **72**, 145R-157R (2000).
40. H. Owens, "Holographic optical components for laser spectroscopy applications," *Proc. SPIE* **1732**, 324–332 (1993).
41. D. Pappas, B.W. Smith, J.D. Winefordner, "Raman spectroscopy in bioanalysis," *Talanta* **51**, 121-144(2000).
42. R. Petry, M. Schmitt, and J. Popp, "Raman spectroscopy--a prospective tool in the life sciences," *Chemphyschem.* **4**, 14-30 (2003).
43. R.K. Dukor, "Vibrational spectroscopy in the detection of cancer," in *Handbook of Vibrational Spectroscopy,* J.M. Chalmers and P.R. Grifiths eds. (John Wiley & Sons Ltd, Chichester, 2002).
44. *Analytical Applications of Raman Spectroscopy,* M.J. Pelletier ed. (Blackwall Science Ltd, Oxford, 1999).
45. M. G. Shim, L.-M. Wong Kee Song, N.N. Marcon, and B.C. Wilson, *"In vivo* near-infrared Raman spectroscopy: demonstration of feasibility during clinical gastrointestinal endoscopy," *Photochem Photobiol* **72**, 146-50 (2000).
46. U. Utzinger, D.L. Heintselman, A. Mahadevan-Jansen, A. Malpica, M. Follen, and R. Richards-Kortum, "Near-infrared Raman spectroscopy for *in vivo* detection of cervical precancers," *Appl. Spectrosc.* **55**, 955-959 (2001).
47. U. Utzinger and R. Richards-Kortum, "Fiber-optic probes for biomedical optical spectroscopy," *J. Biomed. Opt.* **8**, 121-147 (2003).
48. D.E. Bettey, J.B. Slater, R. Wludyka, H. Owen, D.M. Pallister, and M.D. Morris, "Axial transmissive f/1.8 imaging Raman spectrograph with volume-phase holographic filter and grating," *Apll Spectrosc* **47**, 1913-1919 (1993).
49. M.J. Pelletier, "Raman instrumentation" in *Analytical Applications of Raman Spectroscopy,* M.J. Pelletier ed. (Blackwall Science Ltd, Oxford, 1999), 53-105.
50. J.B. Slater, J.M. Tedesco, R.C. Fairchild, and I.R. Lewis, "Raman spectrometry and its adaptation to the industrial environment," in *Handbook of Raman Spectroscopy,* I.R. Lewis and H.G.M. Edwards eds. (Marcel Dekker, New York, 2001), 41-144.
51. J.B. Tedesco and K.L. Davis, "Calibration of Raman process analyzers," *Proc SPIE* **3537**, 200-212(1998).
52. K. Kneipp , Y. Wang, H. Kneipp, L.T. Pereleman, I. Itzkan, R.R. Dasari, and M.S. Feld, "Single molecule detection using surface-enhanced Raman scattering (SERS)," *Phys. Rev. Lett.* **78**, 1667-70(1997).
53. R. Saito, G. Dresselhaus, and M.S. Dresselhaus, *Physical Properties of Carbon Nanotubes* (Imperial College Press, London, 1998).
54. K. Kneipp, H. Kneipp, P. Corio, D.M. Brown, K. Shafer, J. Motz, L.T. Perelman, E.B. Hanlon, A. Marucci, G. Dresselhaus, and M.S. Dresselhaus, "Surface-enchanced and normal Stokes and anti-Stokes Raman spectroscopy of single-walled carbon nanotubes," *Phys. Rev. Lett.* **84**, 3470-3 (2000).
55. K. Kneipp, L.T. Perelman, H. Kneipp, V. Backman, A. Jorio, G. Dresselhaus, and M.S. Dresselhaus, "Coupling and intensity exchange between phonon modes observed in strongly enhanced Raman spectra of single-wall carbon nanotubes on silver colloidal clusters," *Phys. Rev. B* **63**, 6319 (2001)
56. A. Otto, "Surface-enhanced Raman scattering: 'classical' and 'chemical' origins" in *Light Scattering in Solids IV,* **1984,** M. Cardona and G. Guntherodt eds. (Springer-Verlag, Berlin, Germany, 1984), 289.
57. M. Moskovits, "Surface-enhanced spectroscopy," *Rev. Mod. Phys.* **57**, 783-826 (1985).

58. C.S. Schatz and R.P. Van Duyne, "Electromagnetic mechanism of surface-enhanced spectroscopy," in *Handbook of Vibrational Spectroscopy,* J.M. Chalmers and P.R. Grifiths eds. (John Wiley & Sons Ltd, Chichester, 2002).
59. K. Kneipp, H. Kneipp, I. Itzkan, R. Dasari, and M.S. Feld, "Ultrasensitive chemical analysis by Raman spectroscopy," *Chem. Rev* **99,** 2957-2975 (1999).
60. K.E. Shafer-Peltier, C.L. Haynes, M.R. Glucksberg, and R.P. Van Duyne, "Toward a glucose biosensor based on surface-enhanced Raman scattering," *J. Am. Chem. Soc.* **125,** 588-593 (2003).

Chapter 10

LASER DOPPLER AND SPECKLE TECHNIQUES FOR BIOFLOW MEASUREMENTS

Ivan V. Fedosov,[1] Sergey S. Ulyanov,[1] Ekateryna I. Galanzha,[1] Vladimir A. Galanzha,[2] and Valery V. Tuchin[1]

1. Saratov State University, Saratov, 410012; 2. Saratov State Medical University, Saratov, 410710 Russian Federation

Abstract: Principles of speckle and Doppler measurements are considered in this chapter. Special attention is paid to the basic physics of speckle-microscopy. Output characteristics of speckle-microscope for measurement of the spatial structure of random bioflow are analyzed. Speckle-microscopic and cross-correlation techniques are adapted to the problems of measurements of velocity of blood and lymph flows in microvessels *in vivo*. Difficulties of measurements of absolute velocity of bioflows are demonstrated. It is shown that utilizing of laser measuring systems for study of microflow requires the preliminary calibration.

Key words: laser beam, scattering, Doppler effect, speckle, correlation, speckle-microscopy

10.1 INTRODUCTION

Blood and lymph microvessel system carries many very important functions in organism [1]. Mechanisms of different pathological processes (inflammation, intoxication, stress, shock, cancer, edema and etc.) include microvascular disturbances [2-6]. Therefore detail knowledge of blood and lymph microcirculation function is important for diagnosis, treatment and prevention of diseases.

For example, blindness is caused very often by disorders of blood microcirculation in the nutrient vessels of the optic nerve or retina. Thus, analysis of retinal blood flow may be useful in ophthalmologic diagnostics.

Such analysis also allows one to evaluate the pathologies of brain microvessels. Intravascular aggregation of red blood cells also arises at several cardiovascular diseases. This pathology may be found through the studying of blood flow in a single vessel of bulbar conjunctiva or nail bed. Essential change of the character of blood and lymph motion in the capillaries may arise at the applications of drugs. Investigation of such disorders, for instance in the vessels of rat mesentery, may serve the basis of the screening of medical preparations or studying of the influence of toxins.

At present time, two main techniques of laser measurements of bioflow velocity have been developed: Doppler and speckle-interferometric ones [7-17]. In Refs. [16] and [18] D. Briers shown that these techniques are practically identical. Interrelation of the Doppler and speckle techniques and their differences have also been discussed thoroughly in papers by T. Asakura *et al.,* see Ref. [19].

In this chapter basic physics and practical biomedical applications of Doppler and speckle techniques will be discussed and compared.

10.2 BASIC PRINCIPLES OF LASER DOPPLER AND SPECKLE TECHNIQUES

10.2.1 Doppler Technique

In 1842 Christian Doppler in his paper "On the Colored Light of Double Stars and Some Other Heavenly Bodies" was formulated principle that frequency of registered radiation depends on the velocity of relative motion of radiation source and detector [20-22]. This effect takes place in all wave processes including propagation of acoustical and electromagnetic waves. Doppler effect was experimentally confirmed by W. Huggins in 1868 in astronomy. In optics, Russian scientist A. Belopolsky first observed Doppler effect in 1900 using the system of rotating mirrors [22].

One of most important application of Doppler effect is the measurements of moving object velocity based on registering of frequency changes of scattered laser radiation. At present this technique, named Laser Doppler Velocimetry (LDV), is used in different branches of science and engineering ranging from studies of blood microcirculation to investigation of hypersonic gas flows [7,19-24].

Let us consider the basic principle of LDV [21,22]. Schematic diagram of laser light scattering on moving particle is shown in Figure 1. Coherent light from laser source 1 illuminates particle 2, which is moving with velocity **u;** ω_0 and $\mathbf{k}_0$ are respectively frequency and wave vector of the incident light

and ω_s and $\mathbf{k}_s$ are the same parameters of the scattered light. Since scattering particle moves relative the laser light source, the frequency of incident laser radiation ω' is changed due to Doppler effect.

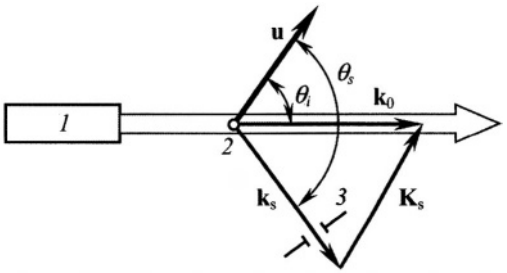

Figure 1. Laser light scattering on a moving particle: 1- laser light source; 2 – moving particle, 3 – detector.

In the case of non-relativistic particle ($u<<c$, where $u = |\mathbf{u}|$ and c is the light velocity in vacuum) ω' can be determined using the well known formula for Doppler effect:

$$\omega' = \omega_0\left[1-(u/c)\cos(\theta_i)\right], \tag{1}$$

where θ_i is the angle between the incident light wave vector $\mathbf{k}_0$ and particle velocity vector **u.** On the second step we may consider this particle like moving light source. Then this particle emits light with frequency ω' in direction toward the detector. Particle moves relative detector and frequency of light received by fixed detector is determined as:

$$\omega_s = \frac{\omega'}{\left[1-(u/c)\cos(\theta_s)\right]}, \tag{2}$$

where θ_s is the direction between the scattered light wave vector $\mathbf{k}_s$ and particle velocity vector **u.** We can calculate scattered light frequency ω_s substituting equation 1 in equation 2:

$$\omega_s = \omega_0 \frac{\left[1-(u/c)\cos(\theta_i)\right]}{\left[1-(u/c)\cos(\theta_s)\right]}. \tag{3}$$

Since assumption $u/c<<1$ is valid for practical situations of non-relativistic objects velocity measurement, we may approximate the difference between

the frequencies of incident and scattered light $\omega_D=\omega_s - \omega_0$, named Doppler frequency shift, see Ref. [22]:

$$\omega_D = \omega_0 \frac{u}{c}\left[\cos(\theta_i) - \cos(\theta_s)\right] = (\mathbf{k}_s - \mathbf{k}_0)\mathbf{u}, \tag{4}$$

It can be seen that Doppler frequency shift is proportional to the particle velocity. Particle velocity could be easily calculated using equation 4 if the incident light frequency ω_0, Doppler frequency shift ω_D and the angles θ_i and θ_s are determined. This is the basic idea of laser Doppler velocimetry.

In practice, Doppler frequency shift could not be measured directly because it is small in comparison with the carrier frequency of light wave. For example, for particle velocity 1 cm/s (it is typical value for blood microcirculation) Doppler frequency shift will not exceed one hundred of kilohertz. It is impossible to measure such small frequency changes using traditional light spectroscopy techniques. But it can be easily done with optical heterodyning (or beating) technique. The main idea of optical heterodyning is to use the interference of two coherent light waves with different frequencies. The resulting intensity will beat with frequency equal to the difference of frequencies of interfering light waves. Measuring of Doppler frequency shift using the optical heterodyning technique is the second basic principle of LDV [22].

Since 1970 LDV is very intense developing technique for flow investigation. At present time, a number of laser Doppler velocimeters have been proposed for different applications. One of universal and often used scheme of LDV is the differential one. This scheme is utilizing two illuminating laser beams and one photodetector that allows perform the optical heterodyning (Figure 2), see Ref. [22].

Let us consider the operating of such scheme. If ω_1, $\mathbf{k}_1$, ω_2, $\mathbf{k}_2$, are the frequencies and wave vectors of first and second beam respectively, then the frequencies of scattered waves are:

$$\omega_{s1} = \omega_1 - (\mathbf{k}_{s1} - \mathbf{k}_1)\mathbf{u}, \tag{5a}$$

$$\omega_{s2} = \omega_2 - (\mathbf{k}_{s2} - \mathbf{k}_2)\mathbf{u}, \tag{5b}$$

where $\mathbf{k}_{s1}$, $\mathbf{k}_{s2}$ are the wave vectors of scattered light of first and second beams. Since scattered light is registered with one detector and Doppler frequency shift is small in comparison with optical frequency we can calculate the frequency difference of scattered waves:

$$\omega_{d12} = \omega_{s1} - \omega_{s2} = \Omega_{12} - \mathbf{Ku}, \tag{6}$$

where $\Omega_{12} = \omega_1 - \omega_2$ is the frequency difference of incident beams, $\mathbf{K} = \mathbf{k}_1 - \mathbf{k}_2$ is the difference of wave vectors of incident beams and $\mathbf{u}$ is the particle velocity.

As it is clearly seen from equation 6 resulting Doppler frequency shift does not depend on the scattered light detector position [21-23].

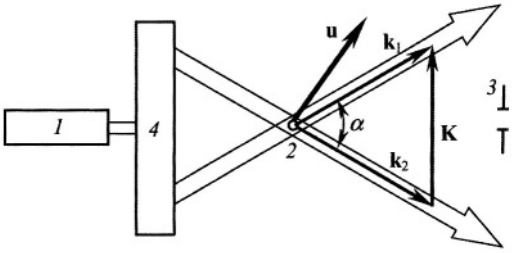

Figure 2. Differential scheme of laser Doppler velocimeter: 1 – laser; 2 – scattering particle; 3 – detector; 4 – beam splitter.

In this paragraph only the most common principles of laser Doppler anemometry are overviewed. Some specific schemes of laser Doppler velocimeters that have been developed for biomedical applications are described in this chapter below.

10.2.2 Laser Speckle-Correlation Technique

Laser speckle-correlation technique is based on the space-time correlation properties of dynamic speckle field. It allows one to measure the vector of scattering object velocity [25-29]. When random object is irradiated by coherent light speckle-pattern is formed. This means that phase and intensity of scattered light have pure stochastic nature.

The statistical properties of speckle fields have been investigated over the past 40 years from the points of view of temporal and spatial coherence. If the scatterers are in random motion, e.g., in Brownian motion, optical speckles obey to the Gaussian statistics. The spatial-temporal correlation function of complex amplitude of scattered light can be factorized and presented as a product of spatial and temporal correlation functions. In other hand, if the scattering medium is modeled as a moving deep random phase screen (RPS) the spatial and temporal intensity fluctuations are not statistically independent of each other, therefore optical field does not satisfy the conditions of cross-spectral purity [26-29]. Since spatial correlation

properties of such fields cannot be analyzed independently from the temporal properties a spatial-temporal correlation function was introduced for description of dynamic speckles. A useful review of statistical properties of dynamic speckles was given by T. Yoshimura [25].

Let us consider the spatial-temporal correlation properties of dynamic speckles, which are formed at the scattering of Gaussian beam by moving RPS [25]. Diffuse object, which contains a large number of randomly distributed scattering centers, moves in-plane with velocity **v** (Figure 3).

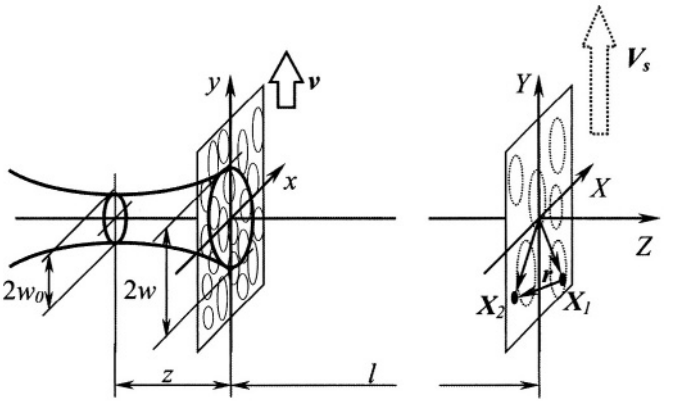

Figure 3. Scattering by a random moving phase screen.

Let us assume that phase fluctuations obey to the Gaussian statistics and the phase variation of scattered light is large in comparison with a wavelength:

$$\langle \phi^2 \rangle >> \lambda^2, \tag{7}$$

Usually the following variations are introduced:

$$\mathbf{r} = \mathbf{X_1} - \mathbf{X_2}\,,\ \tau = t_1 - t_2\,. \tag{8}$$

Then the normalized spatial-temporal correlation function of stationary process may be written as [25]:

$$g^{(2)}(\mathbf{r},\tau) = \frac{\langle I_1 I_2 \rangle}{\langle I_1 \rangle \langle I_2 \rangle} = 1 + \left| g^{(1)}(\mathbf{r},\tau) \right|^2. \tag{9}$$

In equation 9,

$$g^{(1)}(\mathbf{r},\tau)=\frac{\left\langle E_1E_2^*\right\rangle}{\left(\left\langle E_1E_1^*\right\rangle\left\langle E_2E_2^*\right\rangle\right)^{1/2}} \tag{10}$$

is the spatial-temporal correlation function of the complex amplitude of scattered field.

Consider now the specific case, when RPS is illuminated by Gaussian laser beam. Beam axis is normal and beam waist is apart at a distance z from the object plane (see Figure 3). Beam spot radius w and radius of wavefront curvature ρ in object plane are determined by the following formulae:

$$w=w_0\left[1+\left(\frac{z}{a}\right)^2\right]^{1/2}, \tag{11}$$

$$\rho=z\left[1-\left(\frac{a}{z}\right)^2\right], \tag{12}$$

where $a=\pi w_0^2/\lambda$.

In the considering case, the normalized spatial-temporal correlation function of intensity of scattered light in observation plane, which is apart at the distance l from the object plane, is denoted as [25]:

$$g_I(\mathbf{r},\tau)-1=\exp\left(-\frac{|\mathbf{v}|^2}{w^2}\tau^2\right)\exp\left(-\frac{1}{r_s^2}\left|\mathbf{r}-\left(1+\frac{l}{\rho}\right)\mathbf{v}\tau\right|^2\right), \tag{13}$$

where $\mathbf{r}$, τ are defined by equation 8, $r_s=2l/(k_0w)$ is the mean speckle size in the observation plane. Again, $\mathbf{v}$ is the RPS translation velocity. As can be seen from equation 13, speckles translate in the observation plane with velocity [25]:

$$\mathbf{V}_s=\frac{\mathbf{r}}{\tau}=\left(1+\frac{l}{\rho}\right)\mathbf{v}. \tag{14}$$

It is well known, that the motion of dynamic speckles may arise in two different modes, namely, speckles moving without changing the structure, called *"speckle translation"* and the speckle changing only the structure in time without translation, called *"speckle boiling"*. Evidently, the time, which

is required to change the realization of scatterers under the illuminating beam, is equaled:

$$\tau_T = \frac{w}{|\mathbf{v}|}. \tag{15}$$

Taking into account equation 14 the translation distance can be estimated as:

$$r_T = \left(1 + \frac{l}{\rho}\right) w. \tag{16}$$

The described dependence of speckle dynamics on velocity of the object is the basis of speckle-correlation technique of velocity measurement. The main idea of this technique (see for details Ref. [25]) is to measure speckle translation velocity in the observation plane and then recalculate the object velocity using equation 14. There are also a lot of methods for measurements of displacement of speckle-field translation, ranging from the photographic registration to high-speed video recording [25]. One of simplest way to measure the velocity of speckle translation is to record the intensity fluctuation at two spatially separated points in the observation plane. If distance between observation points is shorter than r_T two similar records delayed to the time τ_d one relative another will be obtained. Value τ_d exactly corresponds to the time, which is required for speckle motion from one point to another. It could be easily measured using cross-correlation technique, see section 10.3.

10.2.3 Speckle-Microscopy

Often, the size of investigated object may be very small. For example, diameter of smallest blood microvessel is about a value of few sizes of red blood cell. So, laser irradiation should be strongly focused into such vessel (for the vessel to be resolved by the optical system). By now focused laser beam are widely used in different high-resolution measuring devices for biomedical applications, such as confocal, Doppler or scanning microscopes. The problem of utilizing of sharply focused coherent irradiation in medical diagnostics has very long history, see review [7]. Nevertheless, speckle phenomena in laser microscopes need to be treated more thoughtfully.

10.2.3.1 Optical Model for Speckle-Microscopy

The optical scheme of typical speckle-microscope for investigations of random flows or rough surface is presented in Figure 4. A beam of He-Ne

laser (λ=633 nm) is focused into a spot of a small radius (w_0=1.5 μm) in the investigated microvessel. A conventional optical microscope combined with a TV camera and a videorecorder enables visual observation of the lymph or blood flow in a microvessel. The computer image analyzer processes consequence of video images (frame-by-frame analysis). As blood or lymph flows through the vessel, the strongly focused laser beam is modulated in the waist plane. This leads to the formation of the dynamic speckle pattern in the far zone of diffraction. Speckles of a large size are formed in the case of small number of scatterers [30]. The diameter of the photodetector aperture is essentially smaller than the average speckle size. The temporal fluctuations of scattered intensity are detected by the photoreceiver.

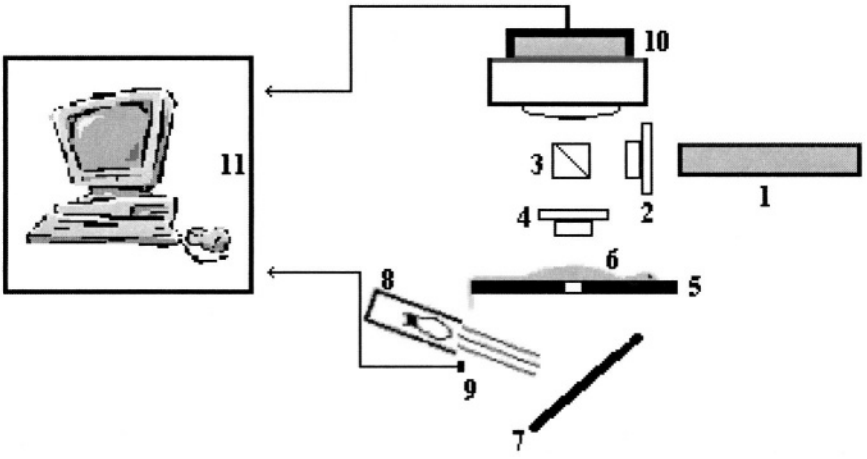

Figure 4. Optical scheme of speckle-microscope: 1 – laser, 2 – microobjective with 10^x magnification, 3 – beamsplitter, 4 –microobjective with 8^x magnification, 5 - stage, 6 – biological object (mesentery of white rat), 7 - mirror, 8 - lamp, 9 - photoreceiver with a pinhole, 10 - TV camera, 11 - image-analyzer.

The output signal of speckle-microscope amplified, recorded on the audiotape and processed by the computer, see Figure 5.

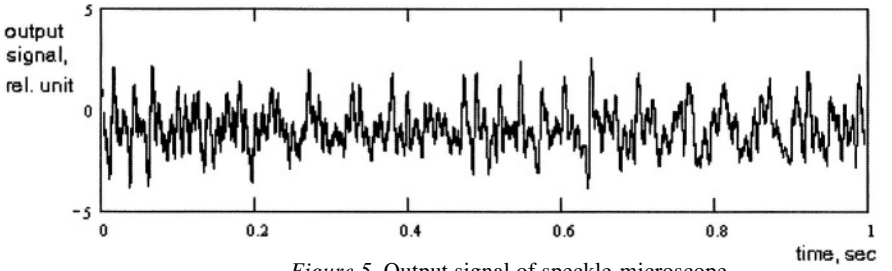

Figure 5. Output signal of speckle-microscope.

Results of a more detailed experimental investigation of bioflows with a speckle-microscope were presented earlier in Refs. [30-33].

10.2.3.2 Principles of Speckle-Microscopy

In a number of papers [30-32], the blood flow was considered as a moving random phase screen. In the present chapter, the bioflow is also considered as moving surface-like scatterers, but the screen imitating the flow has a complicated multi-frequency periodic relief. In other words, the profile of this screen contains a number of spatial harmonics.

Of course, such a screen cannot be considered as a precise optical model of a real microflow. But this simplified model allows analyzing the general output characteristics of the speckle-microscope. Such type of microscopes may be effectively used for the measurements of refractive index oscillations of bioflow (i.e., spatial structure of microflow).

When a focused Gaussian beam is diffracted by the moving periodic screen, the scattered field is also presented by a set of Gaussian beams. Evidently (see Ref.[34]), the angle of diffraction ϕ_d is determined by:

$$\sin\phi_d = \frac{\lambda}{d}, \tag{17}$$

where d is the fundamental period of the screen relief, λ, again, is the wavelength of the incident light. Let us assume the laser beam is precisely focused on the screen. Then, diffraction lobes overlap in space, if

$$\frac{2\lambda}{\pi \cdot w_o} > \frac{\lambda}{d}, \tag{18}$$

where w_0 is the waist radius of the beam, see Figure 6.

The left part of inequality 18 is the value of angle divergence of the incident Gaussian beam. The right part is the diffraction angle denoted by period d of the screen. When condition 18 is fulfilled (clearly, this happens when the waist beam radius w_0 is less than $(2/3)d$), the central area of the diffraction pattern is formed as a result of interference of the specular

component and a few first orders of diffraction. The phase of each diffraction order depends on the coordinate of the screen point, which is illuminated by a laser beam. If the screen moves under the beam, the phases vary in time. As the diffraction orders interfere, this leads to the appearance of temporal fluctuations of intensity in the observation plane, i.e., to the speckle dynamics.

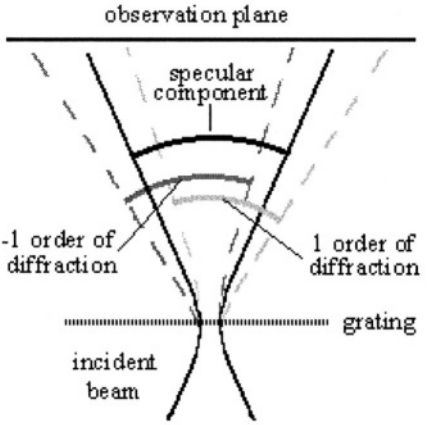

Figure 6. Illustration for the process of scattering of strongly focused Gaussian beam by the screen with periodic relief (grating).

10.2.3.3 Amplitude-Frequency Characteristics of the Speckle-Microscope

It should be noted, the function that describes the relief of a moving phase screen (or fluctuations of the refractive index of the flow) is considered here as the input of the speckle-microscope. Temporal fluctuations in intensity of scattered light are considered as the output of the measuring system. The study of the output signal of the speckle-microscope (at the analysis of such a simplest test object as a moving phase screen with a cosine relief) allows for investigating the general output characteristics of the measuring system.

We will consider now the amplitude-frequency characteristics of the speckle-microscope. This characteristic is expressed by the dependence of the amplitude of the output signal on the value of w_0/d at the fixed value of the screen roughness.

Let us analyze diffraction of the focused Gaussian beam from a moving phase grating. Grating moves with a constant velocity v. Amplitudes of diffraction orders (see Ref. [34]) are expressed as:

$$C_n = J_n(2\pi\frac{A}{\lambda})\cdot\exp(in\phi)\,, \tag{19}$$

where A is the amplitude of the grating relief, $\phi=(2\pi vt/d)+\phi_0$ is the time-dependent phase, ϕ_0 is the initial phase, J_n is the Bessel function of order n. Then, the temporal fluctuations of the complex amplitude of the total field in the observation plane are given by

$$U(t) = const \cdot \left\{ -J_1(2\pi\frac{A}{\lambda}) \cdot \exp(-2\pi i \cdot \frac{v \cdot t}{d} - \phi_o) \cdot K_{-1} + J_o(2\pi\frac{A}{\lambda}) \cdot K_0 + \right. \tag{20}$$

$$\left. J_1(2\pi\frac{A}{\lambda}) \cdot \exp(2\pi i \cdot \frac{v \cdot t}{d} + \phi_o) \cdot K_1 \right\},$$

where *const* is some unimportant constant, which will further be ignored and

$$K_n\left(\frac{w_o}{\lambda}, \frac{w_o}{d}, \frac{x^o}{z}\right) = \frac{\exp\left[-\left[\pi \cdot \frac{w_o}{\lambda} \cdot \frac{x^o}{z} - n \cdot \frac{\pi w_o}{d}\right]^2\right]}{\exp\left[-\left[\pi \cdot \frac{w_o}{\lambda} \cdot \frac{x^o}{z}\right]^2\right]}, \tag{21}$$

is the form-factor, that takes into account the mutual overlapping of diffraction orders; z is the distance between the scattering and observation planes, x^0 is the observation point coordinate, n is the number of diffraction order. As already mentioned the interaction of only first orders of diffraction with the specular component was taken into account in equation 20.

Clearly, the temporal fluctuations of scattered intensity are given by

$$I(t) = U(t) \cdot U^*(t), \tag{22}$$

where symbol $*$ denotes the complex conjugation. Equations 20, 21 and 22 can then be applied to yield the ***speckle contrast*** (the ratio of the square root of the variance of the speckle intensity fluctuations to the time-averaged intensity). If the period of inhomogeneities is large in comparison with the waist beam radius, then the speckle contrast equals to:

$$Contrast = \frac{2J_o(2\pi\frac{A}{\lambda}) \cdot J_1(2\pi\frac{A}{\lambda}) \cdot \left[\pi \cdot \frac{w_o}{\lambda} \cdot \frac{x^o}{z}\right] \cdot \left[\frac{\pi w_o}{d}\right]}{J_o^2(2\pi\frac{A}{\lambda}) + 2J_1^2(2\pi\frac{A}{\lambda})}. \tag{23}$$

For the case of diffraction of a focused beam by the phase grating, whose period is smaller than the waist beam radius, the expression for the contrast takes the following form:

$$Contrast = \frac{J_o(2\pi\frac{A}{\lambda}) \cdot J_1(2\pi\frac{A}{\lambda}) \cdot K_1\left(\frac{w_o}{\lambda}, \frac{w_o}{d}, \frac{x^o}{z}\right)}{J_o^2(2\pi\frac{A}{\lambda}) + J_1^2(2\pi\frac{A}{\lambda}) \cdot K_1^2\left(\frac{w_o}{\lambda}, \frac{w_o}{d}, \frac{x^o}{z}\right)}, \tag{24}$$

where $K_1(w_0/\lambda;\ w_0/d;\ x^0/z)$ is again denoted by equation 5.

As it follows from equation 24, in the case of small values of $(A/\lambda)<<1$ the contrast of scattered field is proportional to the function of $K_1(w_0/\lambda;\ w_0/d;\ x^0/z)$. This function, after some rearrangement, may be written in the following form:

$$K_1\left(\frac{w_o}{\lambda},\frac{w_o}{d},\frac{x^o}{z}\right)=2\left[\pi\frac{w_o}{\lambda}\frac{x^o}{z}\right]\cdot\left[\frac{\pi w_o}{d}\right] \tag{25a}$$

and

$$K_1\left(\frac{w_o}{\lambda},\frac{w_o}{d},\frac{x^o}{z}\right)=\exp\left[-\left[\left[\frac{\pi w_o}{d}\right]^2-2\pi^2\frac{w_o}{\lambda}\frac{x^o}{z}\frac{w_o}{d}\right]\right]. \tag{25b}$$

Equation 25(a) is valid for the case of scattering from the periodic screen with large-scale inhomogeneities. Equation 25(b) corresponds to the case of diffraction by the screen whose period is small in comparison with the waist beam radius. Function $K_1(w_0/d)$, which is normalized to its maximal value, may be interpreted as amplitude-frequency characteristics of the considered measuring system, see Figure 7.

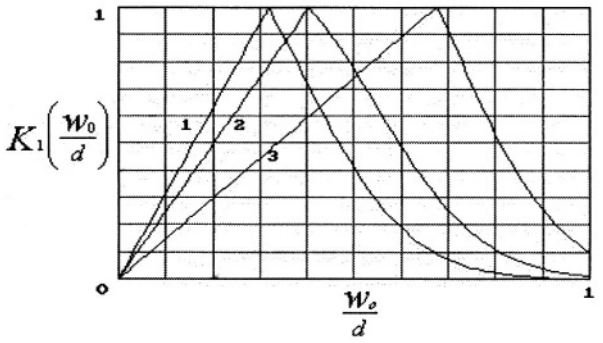

Figure 7. Normalized amplitude-frequency characteristics of a speckle-microscope: curve 1 – $\pi(w_0/\lambda)(x^0/z)=0.5$; curve 2 – $\pi(w_0/\lambda)(x^0/z)=1$; curve 3 – $\pi(w_0/\lambda)(x^0/z)=2$ [33].

The high frequency peak appears in these characteristics when the observation angle is different from zero. The position of the spectral maximum shifts to the higher frequencies at the observation angle increases.

10.2.3.4 Amplitude Characteristics of the Speckle Microscope

Amplitude characteristics of the speckle-microscope are expressed by the dependence of the output signal magnitude on the value of A (at the fixed value of parameter w_0/d). As it follows from equations 23 and 24, the

amplitude characteristic of the considered system is defined by the factor of

$$I\left(\frac{A}{\lambda}\right) = J_o\left(2\pi\frac{A}{\lambda}\right)\cdot J_1\left(2\pi\frac{A}{\lambda}\right). \tag{26}$$

The amplitude characteristic is close to the linear one in the range of $0<(A/\lambda)<0.075$. If parameter $(A/\lambda) > 0.2$, then the amplitude characteristic begins to oscillate in an intricate way, see Figure 8. It transforms to zero, when the first order of diffraction is destructed.

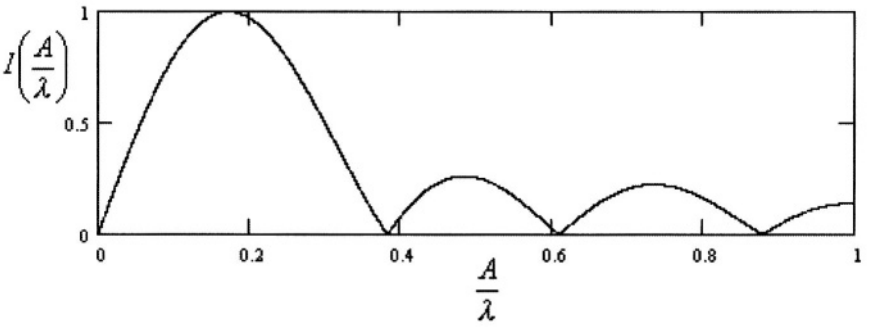

Figure 8. Normalized amplitude characteristics of the speckle-microscope [33].

10.2.3.5 Phase Characteristics

Phase characteristics of the speckle-microscope are expressed by the dependence of the output signal phase of the measuring system on the values of A/λ and w_0/d. As it follows from equations 20 and 22, the phase of the output signal of the speckle-microscope is linearly proportional to the phase of the scattering screen relief at the incision point of the laser beam. So, phase characteristics do not depend on the values of A/λ, w_0/d or x^0/w, (where w is the radius of a laser non-disturbed beam in the observation plane). Figuratively speaking, "the ideal" phase characteristics are inherent for the speckle-microscope.

10.2.3.6 Nonlinear Distortions in the Speckle-Microscope

When $(A/\lambda)<0.1$, the amplitude of the second or higher order harmonics in the output signal is essentially lower than the amplitude of the harmonic at the fundamental frequency. This means the nonlinear distortions of the signal are negligible. The ratio RT between the amplitude values of the

second and first harmonics is presented in Figure 9.

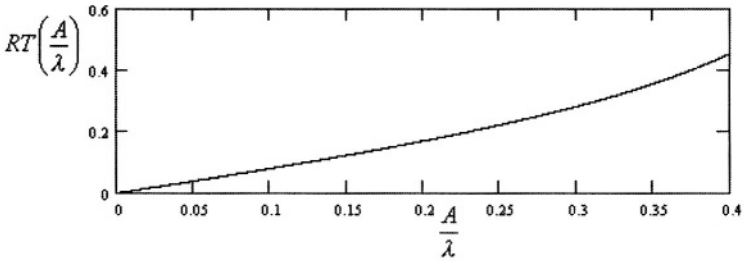

Figure 9. Nonlinear distortion of the signal in the speckle-microscope [33].

10.2.3.7 Formation of the Output Signal in the Speckle-Microscope in the Case of Multi-Frequency Relief of the Screen

Now, we consider the general case of scattering by the screen with non-small phase fluctuations. When the Gaussian beam is scattered by a complex periodic relief, the amplitudes of the diffraction orders are described by [35]

$$S_k = F\left[\prod_m\left[\sum_n\left[i^n J_n\left(2\pi\frac{A_m}{\lambda}\right)\cdot\exp\left(\frac{2\pi i\cdot m\cdot n\cdot v\cdot t}{d}+n\cdot\Psi_m\right)\right]\right]\right], \tag{27}$$

where F denotes the Fourier transforms, A_m and Ψ_m are the amplitude and phase of the m^{th} harmonic of the phase screen relief.

Again, the intensity fluctuations of the scattered light may be expressed in the form of equation 22, namely:

$$I(t) = U_{sp}(t)\cdot U^*_{sp}(t), \tag{28}$$

where the complex amplitude of the field $U_{sp}(t)$ is described by

$$U_{sp}(t) = \sum_k\left(S_k\cdot\exp\left(-\left(\frac{k\pi w_o}{d}-\frac{x^o}{w}\right)^2\right)\cdot\exp\left(\frac{2\pi i\cdot k\cdot v\cdot t}{d}\right)\right). \tag{29}$$

10.2.3.8 Distortions of the Signal of the Speckle-Microscope in the Multi-Frequency Mode

Equations 28 and 29 allow (see Ref. [35]) scrutinizing the operation of the speckle-microscope in the multi-frequency mode.

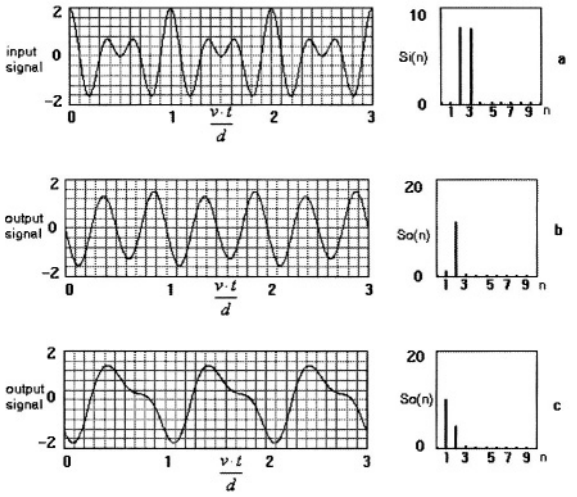

Figure 10. Input and output signals of the speckle-microscope and their spectra [33].

The best way to analyze nonlinear and frequency distortions is to consider the propagation of the two-frequency signal through the measuring system. Let us suppose that the screen profile with a two-frequency relief contains only the second and third harmonics of the fundamental frequency with equal amplitudes [see Figure 10(a)]. For relatively small values of the standard deviation σ=0.001 of the screen relief, the third harmonic practically disappears in the output signal, see Figure 10(b). This phenomenon is caused by the restricted frequency bandwidth of the system considered. If the $\sigma > 0.1$, the first harmonic dominates in the output signal [Figure 10(c)]. This harmonic was absent in the input signal [Figure 10(a)]. Its appearance in the output signal is caused only by the inter-mode interaction of the second and third harmonics of the fundamental frequency.

10.2.3.9 Resolution of Speckle-Microscope for Study of the Spatial Microstructure of a Random Bioflow

Analysis of output characteristics of speckle-microscope has shown that spatial resolution of the microscope is determined by the waist radius of a focused beam. The minimal size of flow inhomogeneities that can be resolved by the speckle-microscope is about 0.25 of the waist beam diameter. The output signal of the speckle-microscope carry the information about fluctuations in the refractive index of moving medium without nonlinear distortion only at the measurement of weakly scattering flows. The considered device operates in the linear mode when fluctuations in the optical path of the investigated object are less than 0.01λ. So, measurement of the spatial structure of bioflow is possible only over a very limited range.

10.3 BIOMEDICAL APPLICATIONS OF LASER DOPPLER AND SPECKLE TECHNIQUES

10.3.1 Blood Microcirculation Studies: Sites and Approaches

As was mentioned two different approaches of blood microcirculation studies using optical methods have been developed. The first one named laser Doppler flowmetry (LDF) is useful for assessment of blood microcirculation statement in certain volume of tissue containing large number of blood capillaries. Originally, it was developed by M.D. Stern in 1975 [29]. LDF technique is based on the illumination of tissue volume with coherent light. Since tissue contains blood cells moving in capillaries with different velocities and directions, scattered light spectra becomes broader because of the Doppler effect. Width and shape of scattered light intensity fluctuations spectra are related with the blood perfusion in the sampling volume of tissue. Theoretical principles of LDF have been developed by Bonner and Nossal [36]. LDF allows extracting the information about the root mean square velocity of blood cells in tissue volume. LDF system could be used for *in vivo* microscopic, endoscopic and intraoperational monitoring of local blood microcirculation.

The principal disadvantage of LDF technique is strong dependence of the LDF output signal on the structure of the tissue site under investigation. It makes difficult any measurements of blood perfusion or absolute blood flow velocity [7, 37].

Another approach in blood microcirculation diagnostics is based on the investigation of blood flow in single microvessel [19, 24, 38-44]. Analysis of isolated vessel provides the detailed information about the blood flow, but there are not too much human organs where such measurements could be performed with the purposes of medical diagnostics. Only nail bed, ocular fundus and conjunctiva are available for non-invasive investigation of capillary blood flow. In this section the application of laser Doppler technique for examination of blood microcirculation in human eye conjunctiva is described.

10.3.2 Capillaries of Human Eye Conjunctiva

From the medical point of view one of the most important sites for blood microcirculation assessment is the human eye. Eye conjunctiva contains single layer of blood vessels that are available for observation. Early diagnostics of disorders of retinal blood flow, caused by several diseases like

diabetic retinopathy, hypertonic retinal angiopathy or glaucoma, allows for blindness prevention.

Blood vessels of different diameter are available for blood flow monitoring with LDF at two parts of the eye. The first one is the retina, the light sensitive inner side of ocular fundus, and the second one is the connective tissue layer covering frontal surface of eyeball (except cornea) and the inner surface of eyelids named eye conjunctiva. Blood vessels of retina could be inspected through the optical system of eye using the conventional technique of ophthalmoscopy. Vessels are situated directly on the surface of light sensitive layer of retina. Diagnostics of blood flow in these vessels is very important because they deliver blood directly to retina. Now a number of commercial lasers Doppler instruments are available for retinal blood flow assessment. But laser Doppler diagnostics of retinal blood flow is still the art procedure: the level of retinal irradiation is closed to the maximal permissible limit [19], so measurements require the unique manipulation with patient. It is convenient to investigate single vessel on the part of conjunctiva that covers the frontal surface of eye bulb named bulbar conjunctiva (Figure 11) [45].

Bulbar conjunctiva has the main attractive feature from viewpoint of laser diagnostics: the single layer of blood vessels is situated on the surface of homogeneous scattering sclera, which does not contain other blood vessels. This is a unique condition for blood vessels investigation because blood vessels of nail bed or retina are placed in the tissues, which are containing other blood vessels. The presence of a large number of microvessels makes it difficult the separation of single vessel for microcirculation monitoring. Blood vessels of conjunctiva are connected in general with vasculatory of eyelid and just several vessels are related with that of inner structures of eye trough the sclera [45]. Vascular pathology that can be observed in eye conjunctiva corresponds with the similar pathology in other parts of the eye (such as retinal and choroidal vessels) and other parts of human organism as a whole. For example, it is very important for cardiovascular diseases diagnostics because conjunctiva is the single site where vessels of different diameter could be investigated in details. Moreover, *in vivo* measurements of blood flow in conjunctiva vessels are safer in comparison with the same measurements on retinal vessels.

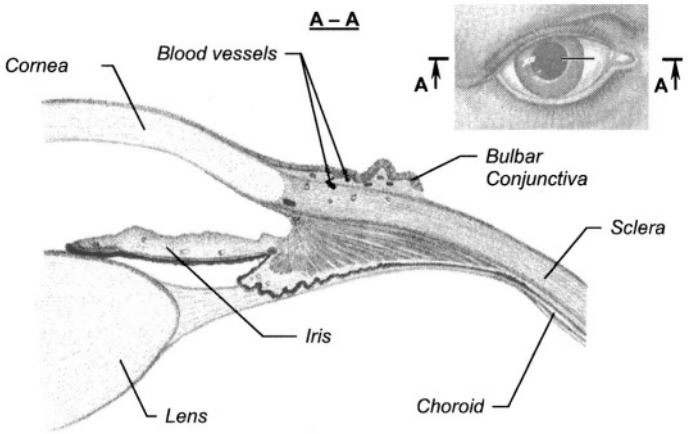

Figure11. Bulbar conjunctiva of the human eye.

10.3.3 Coherent Light Scattering by a Blood Vessel

Laser Doppler velocimetry was the first laser method applied for blood flow velocity in retinal vessels. The use of optical heterodyne technique for Doppler frequency shift of laser radiation scattering by particles moving in laminar flow was proposed in 1964, just several years later after the invention of lasers. Ten years later, in 1974 the first successful *in vivo* measurements of blood flow velocity in vessels of human retina was described in Ref. [46].

There are some specific problems in laser Doppler measurements of blood flow in human ocular fundus [19, 47]. First one is the strong limitation of maximal permissible level of the retinal irradiation. It requires using low power laser radiation for eye safety reason. In the other hand the limitation of incident laser power makes very difficult the registration of scattered light with sufficient signal-to-noise ratio. The second problem is the patient's head and eye movements. To eliminate blood vessel shifting during measurements the sampling volume have to be larger than vessel cross-section. But it makes impossible the investigation of the blood flow velocity profile. If vessel cross section is uniformly illuminated the Doppler frequency shift power spectrum have a complicated structure due to the superposition of light fraction, scattered by blood cells moving with different velocities. The third problem concerns the influence of multiple light scattering effects on the frequency bandwidth of Doppler spectra. At some conditions multiple scattering may cause failure of absolute flow velocity measurements [47].

To solve problems listed above a special kind of LDV arrangement was proposed by C.E. Riva that differs from the classical LDV schemes. It should be noted that classical schemes, overviewed in the first section of this chapter [40, 41], have been developed for technical applications.

The scheme for laser Doppler velocimetry of blood flow in the vessels of ocular fundus is shown in Figure 12.

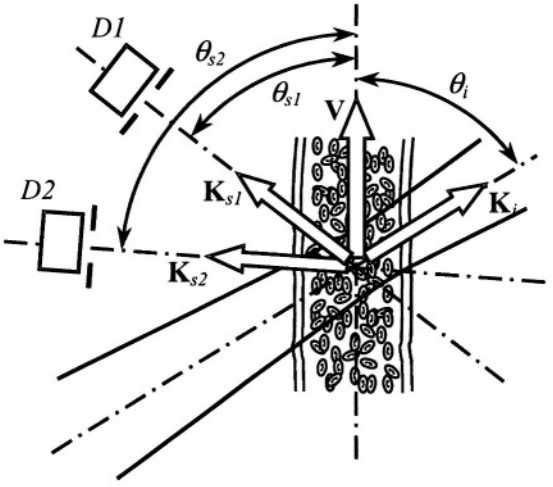

Figure 12. Arrangement for Laser Doppler measurements of ocular blood flow.

Blood vessel is illuminated by a laser beam. Laser light is scattered from a vessel wall and by moving blood cells. Scattered light is registered by two detectors: *D1* and *D2*. The resulting Doppler frequency shift could be calculated for each detector using equation 4 in the case of single scattering of light:

$$\omega_{D1} = (\mathbf{k}_{s1} - \mathbf{k}_i)\mathbf{v}, \quad \omega_{D2} = (\mathbf{k}_{s2} - \mathbf{k}_i)\mathbf{v}, \tag{30}$$

again, $\mathbf{k}_i$ is the wave vector of the incident laser radiation, $\mathbf{k}_{s1}$, $\mathbf{k}_{s2}$ are the wave vectors of light scattered toward the first and the second detectors respectively and $\mathbf{v}$ is the cell velocity vector. The magnitude of cell velocity vector in real flow changes with distance from center of flow to the vessel's wall. In other words, velocity profile of laminar flow of Newtonian liquid in cylindrical tube has a parabolic shape:

$$V(r) = V_{max}\left[1 - \left(\frac{r_v}{r_0}\right)^2\right], \tag{31}$$

where r_v is the distance from center of flow, r_0 is the vessel radius, and V_{max} is the maximal flow velocity at the center of the vessel. Maximal value of frequency shift corresponds to the centerline flow velocity V_{max} according to equation 31. Light, scattered by vessel wall and surrounding tissue is used for heterodyning to measure Doppler frequency shift. Light, scattered by motionless structures, allows to eliminate eye movements and to measure velocity of blood cells relative vessel wall. As a result, the spectral density of scattered intensity fluctuations, which are caused by the interference of dynamic speckles scattered by moving cells and light fraction, scattered from vessel wall, has the constant value in the frequency range from zero to ω_{max} and then rapidly drops to the noise level for frequencies higher than ω_{max}. Such shape allows one to provide easy measurements of ω_{max}.

To calculate flow velocity, angles θ_i and θ_s have to be precisely measured. But in real *in vivo* experiment it is no easy to do. To exclude these angles from formula for flow velocity, two detectors were separated by a constant angle $\alpha = \theta_{s1} - \theta_{s2}$. Maximal flow velocity may be calculated using the formula derived from equation 30:

$$V_{\max} = \frac{\lambda[\omega_{\max 1} - \omega_{\max 2}]}{2\pi n \sin(\alpha)}, \tag{32}$$

where ω_{max1}, ω_{max2} are the maximal Doppler frequency shifts evaluated from measured spectra of the first and the second detector signals respectively; λ is laser light wavelength in vacuum; and n is the refractive index of medium, which is surrounding the blood cells. Described principle serves the basis of special technique named bi-directional laser Doppler velocimetry.

Now bi-directional LDV is a conventional technique for retinal blood flow monitoring, but it has some limitations. At first, blood is not a Newtonian liquid since it contains cells in high volume concentration (up to 45%). It is not dramatic because in practice it just causes some flattening of velocity profile in vessel that does not sufficiently affect spectrum of scattered light intensity fluctuations and ω_{max} is clearly measurable as a cutoff frequency. Much more serious limitation concerns to the scattering properties of blood and surrounding tissues. LDV works well only in single scattering mode when each photon reaches the detector after only one single scattering on moving cell. But most of biological tissues are the high scattering structures and usually multiple light scattering is dominant. In multiple scattering mode light changes its direction in tissue two or more times interacting with moving or motionless scattering centers. As a result the angles of incidence and scattering of light by moving cell are defined by random trajectory of light in tissue rather than light source and detector position. In this case absolute flow velocity measurement using bi-directional LDV is impossible

because scattered light intensity fluctuations spectra are distorted and cutoff frequencies are not clearly seen. As it was shown in literature, bi-directional LDV allows for successful measurements of blood flow velocity only in vessels larger than 40 μm in diameter due to reasons described above [19, 48,49].

In opposite to retinal vessels multiple scattering is dominant when vessels of conjunctiva are illuminated (Figure 11). Sclera consists of thin collagen molecules that looks like fibers with refractive index $n_c = 1.47$ surrounded with base substance $(n_b = 1.345)$. Sclera is highly scattering medium with averaged thickness about 1 mm [50].

Light scattering by a vessel of eye conjunctiva is schematically shown in Figure 13.

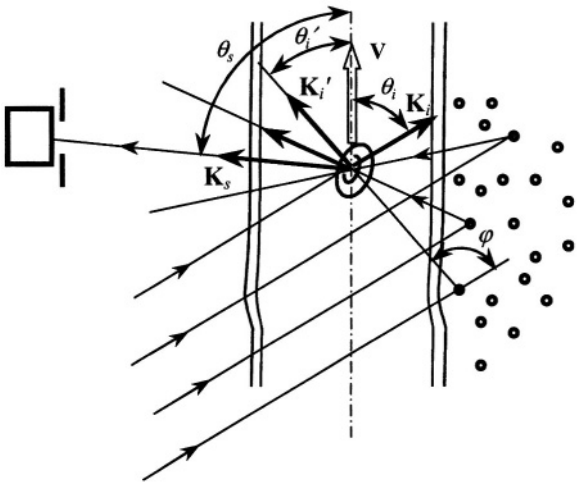

Figure 13. Scattering of laser radiation by a blood vessel of eye conjunctiva.

There are several ways for light to be scattered. These are single back scattering by moving cells and multiple scattering by fixed scattering centers, and by moving cells. In Figure 13 single scattering by a blood cell is depicted with wave vectors $\mathbf{K}_i$ and $\mathbf{K}_s$. We can see that in the case of double scattering, wavevector $\mathbf{K}_i'$ is not determined by the direction of the incident laser radiation, but by the background scattering. Since direction of incident light wave vector θ_i' varies randomly in wide range in case of multiple scattering, then the resulting Doppler frequency shifts of light scattered by the cells are also random. So, the shape of Doppler spectrum is close to negative exponent and cutoff frequency could not be measured.

It makes impossible to carry out the measurements of absolute flow velocity in blood vessel of eye conjunctiva using bi-directional LDV in spite of retinal vessels. But width of spectra depends on flow velocity. As it was

shown by several authors the zero- and first-order spectral moments could be used for characterization of blood flow in case of multiple light scattering in a tissue [7, 36, 39]:

$$M_0 = \int P(\omega) d\omega, \tag{33}$$

$$M_1 = \int \omega P(\omega) d\omega, \tag{34}$$

where ω is spectral frequency and $P(\omega)$ is Doppler shift power spectrum. Zero-order spectral moment is directly proportional to average number of blood cells in the illuminated area and first moment is proportional to the product of root mean square of blood cell velocity and average number of cells. So, first normalized spectral moment:

$$M_1^{'} = \frac{M_1}{M_0} \tag{35}$$

is directly proportional to root mean square of blood cell velocity. All coefficients of proportionality are usually unknown since they are determined by huge number of different factors like scattering geometry; structure and optical properties of tissue; number and diameter of blood vessel in illuminated area, etc. But human eye conjunctiva is a unique site for Doppler measurements, because it has very simple structure. This is an ideal situation for interpretation of LDF measurements: single blood vessel located on surface of homogeneous scattering layer of sclera. Moreover scattering properties of sclera are well known and vessel diameter could be precisely measured using microscopic imaging technique [39].

10.3.4 Experimental Setup

Laser Doppler measuring system for investigation of blood flow in blood microvessels of bulbar conjunctiva on frontal surface of human eye has been developed on the basis of standard slit-lamp microscope (Figure 14) [39].

Laser beam delivering module was mounted on the top of the microscope (it is not shown in Figure 14). And two photodetectors of bi-directional detecting system was placed at the left side of the microscope. The linearly polarized incident beam was provided by a red laser diode (λ=650 nm). The incident laser power was attenuated with a rotating polarizer to 30-50 μW to provide laser eye safety [51]. The incident beam has been focused by laser beam delivering optics and directed to the object plane of the microscope

with mirror (5, Figure 14). Laser spot size in the object plane was 30 μm in diameter.

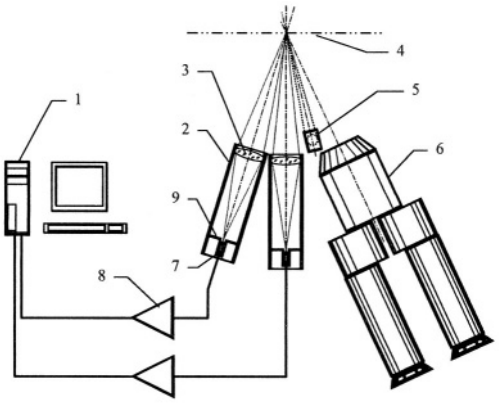

Figure14. Laser Doppler measuring system for blood flow measurements: 1 – computer and data acquisition board; 2 – photodetector module; 3 – objective; 4 – object plane; 5 – mirror of laser beam delivering module; 6 – microscope; 7 – photodiode detector; 8 – amplifier; 9 – field diaphragm.

Two similar photodiode modules were used to detect the light scattered in two different directions. The photodetector modules are separated by the angle of 17° The scattered light passed through the aperture is collected by the FD256 photodiode detector. The linear field of each of photodetector modules in the object plane was 100 μm. The output photocurrent signals from both photodiodes were amplified by the high sensitivity current-to-voltage amplifiers ($5 \cdot 10^{10}$ V/A within the frequency range [0.5–20 kHz]). The resulting photocurrent signal was digitized by Creative Labs Sound Blaster with 16-bit resolution at sampling frequency of 44.1 kHz. Non-overlapping modified periodograms with cosine time window were calculated using Fast Fourier transform with time period of 23 ms. from 5 to 130 periodograms were averaged to obtain smooth power spectrum estimation. The microscope was used for visual guidance of laser beam and measurement of the vessel diameter [39].

A series of experiments were performed with the model of blood vessel to test the sensitivity of the instrument and to investigate the influence of the multiple light scattering on the Doppler frequency shift power spectra forming. The plastic tube with an internal diameter of 30 μm has been used as a model of blood vessel. The 10% suspension of erythrocytes in Ringer solution was flowing through this capillary tube at a constant rate. In our experiments the scattering geometry was close to that in real bulbar

conjunctiva of the human eye. The plastic capillary tube had been placed on the background of 0.5 mm Teflon plate to reproduce the scattering from the sclera and the space between the capillary tube and background was filled up by an immersion oil (n = 1.51) to reduce the Fresnel reflection from the back side of the tube. These experiments described in Ref. [39] had shown that the multiple scattering by the background eliminates the angular dependence of scattered light fluctuations spectra shape and makes impossible the use of bi-directional laser Doppler technique for blood flow velocity in capillaries of conjunctiva. Also it was shown that the first normalized spectral moment of Doppler frequency shift power spectra is directly proportional to the flow velocity.

10.3.5 *In Vivo* Results

After testing of the measuring system using the models of blood vessels *in vivo* measurements on human volunteer eye conjunctiva were performed. A spectrogram of Doppler frequency shift recorded when laser light is scattered by the human eye conjunctiva blood microvessels is shown in Figure 15. Spectrogram is recorded during investigation of two vessels of 9 μm and 30 μm in diameter and part of conjunctiva containing no vessels.

Doppler spectra, which are corresponded to the light scattering by vessel of 30 μm in diameter, by vessel of 9 μm in diameter by site of conjunctiva containing no vessels, are shown in Figure 16 (curves 1, 2 and 3 respectively). Spectra have negative exponential shape. They are not dependent on the angle of detection (left and right channels are separated by the angle of 17° as it described in previous section).

As it already mentioned, first normalized spectral moment is informative parameter to characterize flow velocity in capillaries. The plot of dependence of first normalized spectral moment on time is presented in Figure 17. This plot corresponds to the spectrogram presented in Figure 15. We can see that first normalized spectral moment depends on the vessel diameter and flow velocity. Since vessel diameter could be easily measured we can perform empirical calibration of dependence of spectral moment on vessel diameter in norm and for patients with different pathologies. This technique could be effectively used for cardiovascular diagnostics.

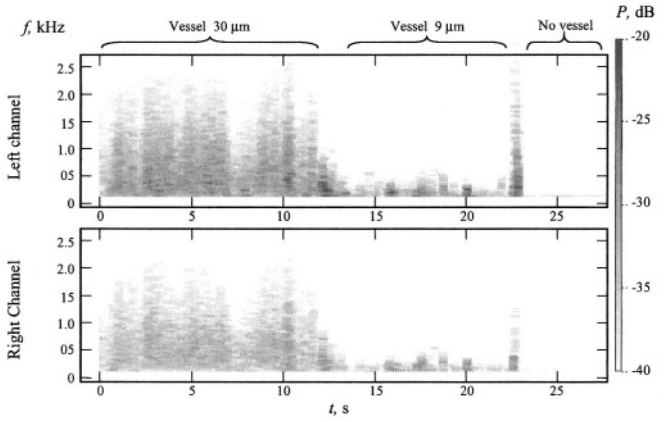

Figure 15. Spectrogram of Doppler frequency shift.

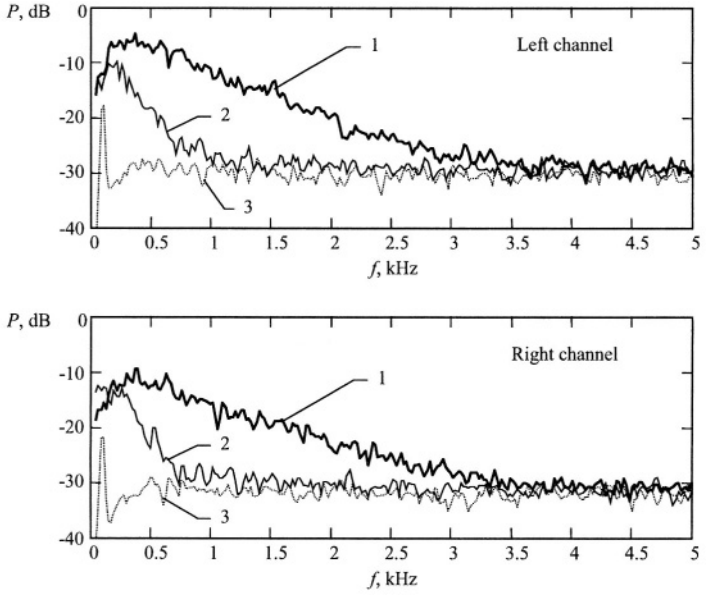

Figure 16. Spectra of Doppler frequency shift of laser light scattered by blood vessels of human eye conjunctiva: 1 – vessel of 30 μm diameter; 2 – vessel of 9 μm diameter; 3 – site without vessels.

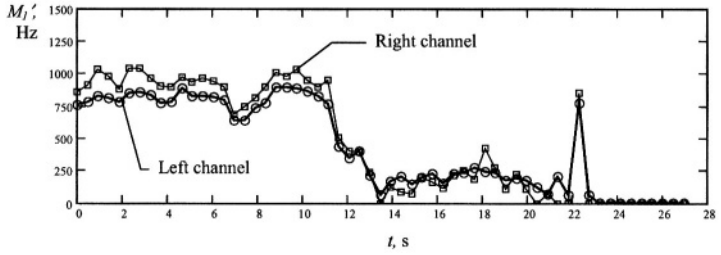

Figure 17. First normalized spectral moment.

10.4 SPECKLE-CORRELATION MEASUREMENTS OF LYMPH MICROCIRCULATION IN RAT MESENTERY VESSELS

10.4.1 Peculiarities of Lymph Microcirculation

Microlymphatic system is a part of microcirculation. It constantly drains tissue and preserves the content and volume of extracellular liquid, participates in the constant removal of proteins, cells, and fluid from tissue and their return to the bloodstream. Small lymphatics consist from segments (lymphangion), which isolated by valves from each other. As a result lymphatic acts as small pumps with alternating pressure and suction mechanisms [52]. Lymph flow and, correspondingly, effective lymph drainage are provided by a combination of passive (in response to muscle contractions, respiratory movements, intestinal peristalsis, etc.) and active driving forces (gradient of transmural pressure, phasic contractions, valve function) [52-55]. At present, important role of the lymphatics in pathogenesis of many diseases has been proved [2-4, 56]. Especially the importance of lymph drainage is increased compensatory and significantly at the different disturbances of blood microcirculation including the increase in blood capillary pressure, the decrease of plasma colloid-osmotic pressure, lesion of blood capillaries and etc. [57]. Some authors indicate that the efficacy of drug injection to the lymph and not to the blood has been demonstrated [58-60].

The lymph flow in microvessels has some specific features because of specificity of structure and function of microlymphatic. The basic scattering element in lymphatic vessel is lymphocyte (white blood cell). Its size is about 3-5 μm [60]. As a rule, lymph flow differed from blood flow in its periodic oscillations, relatively lower velocity, markedly low cell

concentration, transparent of lymph and etc. [52,61-63]. Thus, lymph flow dynamics essentially differs from the well-known blood flow dynamics [64-66].

10.4.2 Methods for Lymph Flow Monitoring

Structure and optical properties of lymphatic of rat mesentery determine the choice of instrumentation for lymph flow monitoring. The most common technique for lymph microcirculation studies is the light microscopy. Rat mesentery anatomy provides the unique conditions for microscopic imaging in transillumination geometry. In this case high contrast microscopic images of mesentery allows not only for precise measurement of lymph vessel geometry but even for tracking of single lymphocytes by means of videorecording. Dynamics parameters of lymphatic, such as valve activities, vessel diameter, cell velocity, concentration and flow direction could be determined from frame to frame analysis of video records [38, 43, 61, 63].

But there are some limitations in this technique application to the microcirculation studies. The first one is the possibility of cell velocity measurement only when single cell could be tracked in several frames of video record. It means, that each cell has to cross over the eyesight of microscope relatively slow to be recorded at least two times. Since frame rate and field of view are limited by the video camera construction and the microscope magnification respectively, some cells can be "lost" because they are moving too fast. Moreover, if cell concentration is high, the tracking of single cell is impossible because flow looks like smoothed moiré fringes. Another principal drawback of video microscopy is a time consuming and elaborate image processing required for flow dynamics monitoring [38].

The laser measuring techniques could be used in addition to the light microscopy. The laser instrumentation have to be able to: 1) measure flow velocity in a wide range in real time; 2) measure flow velocity in the vessels even in case of high cell concentration; 3) determine flow direction. Optical measurements of the lymph flow velocity taking into account the direction of flow for a single scattering of light can be performed at present by Doppler laser microscopy technique [7, 22, 42]. Laser Doppler microscopy is a well-developed way to obtain the flow parameters including absolute flow velocity and flow direction. It is successfully applied to estimating lymph flow and sometimes to diagnosing lymph node changes.

Specialized laser Doppler microscopes have been developed for research of biological flows in microvessels. But there are problems in the application of such technique to monitoring bioflows which velocity is low and direction changes like in lymphatic vessels. The use of the comprehensive frequency shifting devices in laser Doppler microscope is necessary to overcome the

mentioned problem but requires quite complex and expensive equipment [22,42].

Another approach in the laser measurements of lymph flow is the laser speckle technique. The speckle field of a laser beam scattered by a lymph vessel is the result of interference of light waves scattered by lymph cells moving at different velocities in the flow, and those scattered by immobile tissues surrounding a vessel [25-28], The fluctuations of the speckle field intensity have a quite complicated form in this case. The properties of such a speckle field differ considerably from the properties of speckle fields that are formed, for example, upon a single scattering of laser radiation by a moving screen with a rough surface, and have been studied extensively. A special term "biospeckles" was introduced to emphasize the peculiar nature of this speckle field. Because of the extreme complexity of biospeckles, a theoretical explanation of this effect has not been obtained so far [11, 67-69], Even an exact relation between speckle field intensity fluctuations and the velocity of lymph flow has not been established. However, numerous experiments using microvessel models indicate that the width of the autocorrelation function or of the power spectrum of the speckle field intensity fluctuations is linearly connected with the mean velocity of flow of the cells [7,19]. In the blood or lymph flow studies, the speckle field intensity fluctuations are detected at one point, and the flow velocity is estimated from the width of power spectrum of these fluctuations or from the width of their autocorrelation function. Measurements of this type described in previous section cannot be used to determine the direction of flow in lymph vessels because the speckle field fluctuations recorded at a point do not depend on the direction of motion of the scattering object. Another method of measurement the velocity of motion of an object is based on the recording of intensity fluctuations of the speckle field at two points separated in space and on an analysis of their mutual correlation. The principle of this technique is overviewed in section 10.3. This method makes it possible to determine the velocity as well as direction of motion of an object and is used in various technical applications. However, the possibility of using this method for measurement the lymph flow velocity has not been investigated so far. It was experimentally shown earlier that analysis of spatial-temporal cross-correlation function of intensity fluctuations of single scattered dynamic speckles allow us to determine the velocity of the flow and its direction [38, 62, 70-72].

10.4.3 Experimental Setup for Lymph Flow Diagnostics

The optical scheme of setup is shown in Figure 18. Radiation from a LG-207 633-nm He-Ne laser is delivered through the illuminator channel and

focused by the objective of the microscope (2) into a spot of diameter about 2 μm in a plane situated at a distance z = 100 μm above the axis of the microvessel (13) [38]. The radius of curvature of the wavefront of the beam illuminating the microvessel is quite small to ensure the acceptable translation length of biospeckles (3). The measuring volume is formed by the intersection of the diverging laser beam with the microvessel and has the shape of a truncated cone (whose elements have a slope 10° and a mean diameter of the order of 30 μm). The laser radiation scattered by the lymph flow is directed with the help of the beamsplitter (4) to the photodetector (5) placed at a distance of 300 mm from the objective plane of the microscope. The diameter of each photodetector is 3 mm, which corresponds to the mean speckle diameter in the observation plane. The distance between the centers of the photodetectors is about 7 mm. Signals from the photodetectors are amplified by the photocurrent transducers (7) and digitized with the help of a two-channel 16-bit analogue-to-digital converter with a sampling frequency 44.1 kHz. A PC is used to determine the cross-correlation function of the photodetector signals as well as the position of its peak.

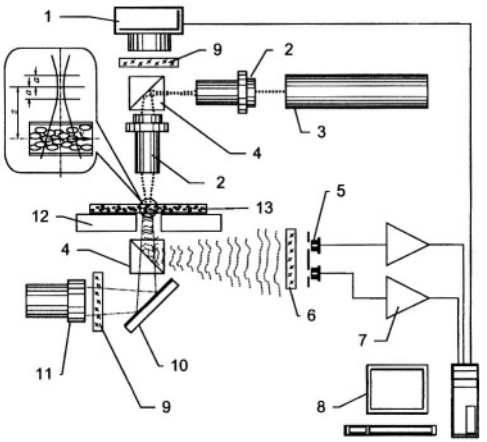

Figure 18. Scheme of the experimental setup: 1 - digital video camera; 2 - micro-objective; 3 - He-Ne laser; 4 - beamsplitter; 5 - photodiodes; 6 - red light filter; 7 – photocurrent converters; 8 - PC; 9 - green light filters; 10 - mirror; 11 - illuminator; 12 - thermally stabilized table; 13 - lymph microvessel of mesentery. The inset shows illumination of a lymphatic vessel by a focused Gaussian laser beam (a is the length of the laser beam waist and z is the separation between the flow axis and the waist plane of the laser beam) [38].

Depending on the time resolution, the processing of realization of photodetector signals of duration 60 s takes between 90 and 300 s. The setup makes it possible to detect the changes of direction of motion of cells and to measure the lymph flow velocity within the velocity range from 10 μm/s to

10 mm/s with a time resolution up to 50 ms. A digital video camera (1) combined with transmission microscope is used for analysis of lymph microvessel function *in vivo* in real time: estimate the mean flow velocity and its direction, measure the diameter of microvessel, register the appearance of phasic contraction in the investigated lymphatic. Digital video images are processed with specially developed software. The cell velocity is determined as the ratio of the difference in cell coordinates in two consecutive frames to the time interval between two frames. The mean flow velocity is calculated by averaging the velocities of four to six cells. This method allows us to record the lymph flow velocity in the range from 25 μm/s to 2-2.5 mm/s with a time resolution of 40 ms. The processing of a video recording of duration 15 s (375 frames) takes about 10 h, and involves the tracking of the motion of about 2000 cells.

10.4.4 Experiments Based on the Lymph Vessel Model

The efficiency of the system was verified in a series of experiments using the lymph vessel model. A thin-walled plastic tube of diameter 200 μm is served as such a model. Water, containing the suspension of particles of red pigment with an average diameter 3 μm, flows through the tube. The concentration of particles was about 1%. Figure 19 shows the time dependence of the mean flow velocity (measured by a LDV) on the variation of the pressure difference at the ends of the capillary.

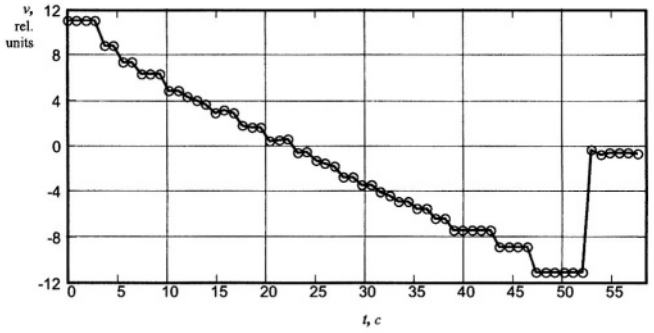

Figure 19. Time dependence of the mean flow velocity in the lymph microvessel model [38].

The sensitivity of the speckle-correlation method to the flow direction is illustrated because the mean flow velocity in the experiments is directly proportional to the difference in pressures at the ends of the capillary. The velocity measured by the velocimeter is expressed in relative units because the velocimeter described above does not allow measurement of velocity

without a preliminary calibration. This is due to the fact that the radius of curvature r of the wave front of the laser beam in the plane of the microvessel, determined by the distance z between the axis of the vessel and the plane of the beam waist, cannot be determined quite accurately during *in vivo* measurements. In Figure 20 typical time series of speckle intensity fluctuations are shown.

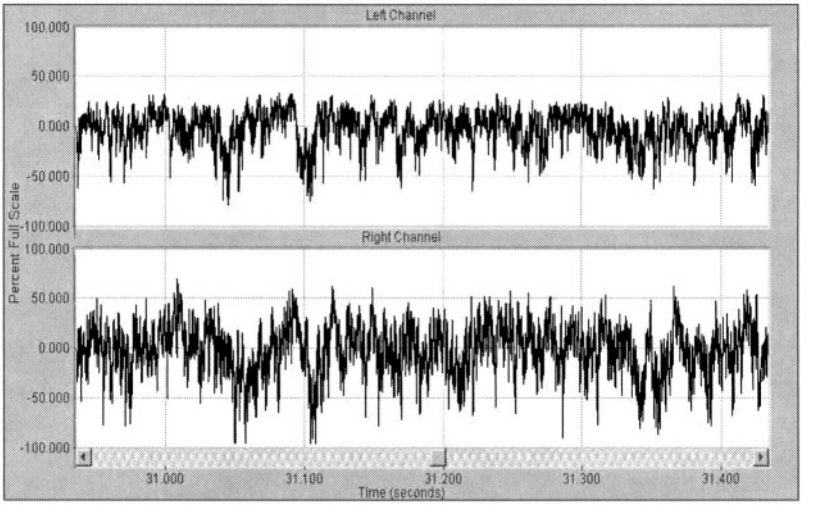

Figure 20. Typical time series of speckle field intensity measured by left and right channel photodetectors are shown. Series are partially similar but one is delayed relative another due to speckle field translation.

Cross-correlation functions of scattered intensity fluctuations, corresponding to the 7^{th} and 24^{th} seconds of recording is presented in Figure 21. Test measurements confirmed the linear dependence between the measured flow velocity and the difference in pressures at the ends of the capillary. The dependence (regression line) of the relative flow velocity on the difference in pressures at the ends of capillary is shown in Figure 22(a). Correlation coefficient equals to 0.996, which confirms the validity of the model.

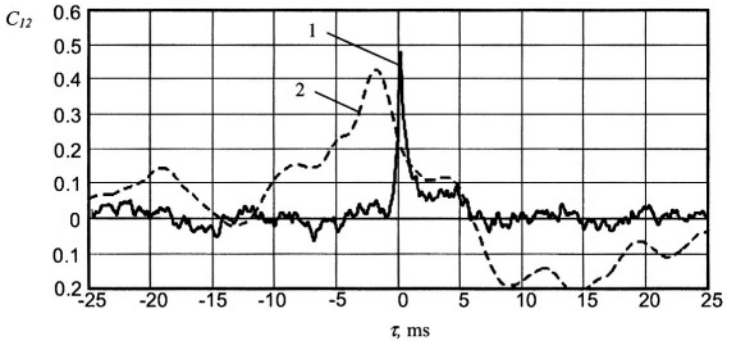

Figure 21. Cross-correlation functions of signals corresponding to 7th (curve 1) and 24th (curve 2) seconds of the recording shown in Figure 20, for delays 0.15 ms (curve 1) and -1.9 ms (curve 2) corresponding to the maxima of correlation functions [38].

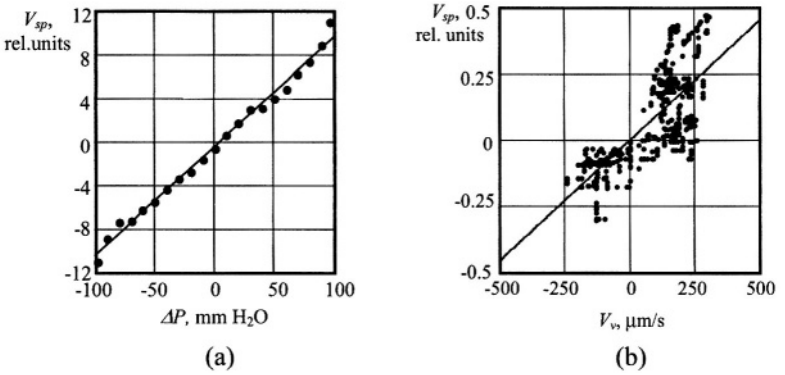

Figure 22. Dependencies of the flow velocity determined by a laser velocimeter on the difference in pressures at the ends of a capillary (a), and on the lymph flow velocity in the lymphatic of rat mesentery, measured by the method of functional videomicroscopy (b). The solid line corresponds to linear regression, the correlation coefficient of linear regression being 0.996 (a) and 0.723 (b) respectively [38].

10.4.5 Measurement of the Lymph Flow Velocity in the Lymphatic of the Rat Mesentery

The described setup is also tested for *in vivo* measurements of lymph flow velocity in the mesentery vessel of narcotized white rat. Animals were placed on a termostabilized stage (37.7° C) (12) of the microscope (see Figure 18) and the mesentery and intestine was kept moist with Ringer's solution at 37° C (pH ~7.4). The images of microvessels were evaluated by transmission microscopy and laser velocimeter simultaneously.

Figure 23 shows the time dependence of the flow velocity in investigated microlymphatic of mean diameter 170 ±5 μm and mean lymph flow velocity 169±4.6 μm/s. This dependence was obtained by laser velocimeter and by processing of the video images as well. As it was mentioned, laser velocimeter allows one to measure the lymphocyte velocity in relative units only. The proportionality coefficient between the data of laser velocimetry and the mean flow velocity, measured by the video microscope was determined from the slope of the regression line [Figure 22(b)]. The correlation coefficient of linear regression between the velocities (measured by these two methods) is relatively high and equals to 0.72.

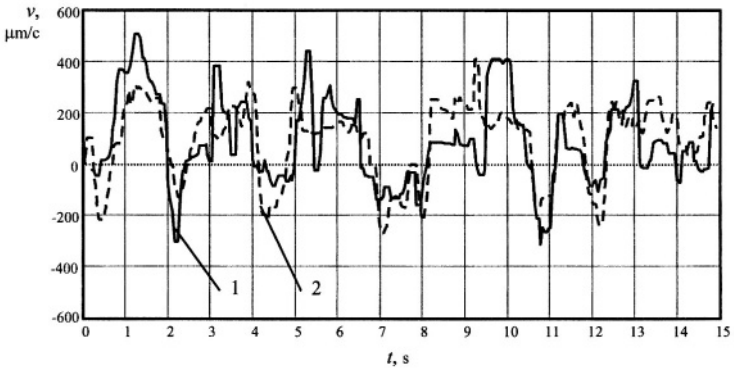

Figure 23. Time dependence of the lymph flow velocity in the lymphatic vessel of mean diameter 170 ±5 μm of a white rat mesentery, recorded with a velocimeter (curve 1) and by processing of video recording (curve 2) [38].

10.4.6 Discussion of Advantages of Laser Diagnostics of Lymph Flow

Experiments on scattering of focused beams of coherent radiation from lymph microvessel models as well as native lymph microvessels *in vivo* revealed that a correlation exists between the speckle field intensity fluctuations recorded at two spatially separated points. This correlation indicates the manifestation of translation dynamics of the speckles. Moreover, a linear dependence is established between the flow velocity, radius of curvature of the laser beam wave front, and the speckle field translational velocity. The linear dependence between the mean flow velocity and the peak of the cross-correlation function of the intensities is confirmed, in particular, by the experimental results based on the lymphatic model presented in this work [see Figure 22(a)]. However, the cells in a lymphatic move with different velocities depending on their position relative

to the flow axis. Therefore, further investigations must be carried out in order to find the relation between the flow velocity calculated in the moving random phase screen approximation and the mean flow velocity.

The velocity of the cell crossing the measuring volume may differ significantly from the mean velocity of the cells moving within a field of characteristic size of 150 μm. However, the results of measurements of velocities, made by two entirely independent methods are quite convincing since the correlation coefficient between the results of velocity measurements is quit large.

The advantages of proposed method is also supported by the fact that the time dependencies of the lymph flow velocity shown in Figure 23 required an operator time of 10 h (videorecording of duration 15 s was processed), while the processing of the signals registered by photodetectors over the same period of time was completed in just 30 s.

Thus, we have studied experimentally the space-time correlation properties of the dynamic speckle fields formed upon a single scattering of a focused beam of coherent radiation by liquid flows containing scattering particles, and considered the possibility of their application for measurement of flow velocity. Optical measurements of the blood or lymph flow velocity taking into account the direction of flow for a single scattering of light can be performed at present only by functional microscopy or Doppler laser microscopy technique. It was mentioned above that functional microscopy requires a prolonged and cumbersome processing of images, while Doppler laser microscopy requires quite complex and expensive equipment. Of course, the method described here for measurement the lymph and blood flow velocities in biological and medical experiments requires a more detailed analysis of the properties of speckle fields formed as a result of scattering of coherent radiation beams from blood and lymph vessels of various diameters, and also a modification of the existing experimental equipment. However, even the experimental results presented in this work indicate that the changes in the velocity as well as the direction of lymph microflow can be recorded quite expediently by using relatively simple equipment.

10.5 CONCLUSION

In this chapter principles of Doppler and speckle diagnostics of different types of microvessels have been presented. It has been demonstrated that measurement of absolute velocity of bioflow is a complicated problem. Measuring signal depends not only on the velocity of bioflow, but also on it's scattering characteristics. It was demonstrated that it is possible to carry

out the direct measurements of bioflow velocity in the case of single scattering.

Speckle or Doppler methods can be effectively applied for the relative measurement of bioflow velocity. But it also requires the great caution because the bandwidth of spectrum of scattered intensity fluctuations may vary not only as a result of relative changes of flow velocity. The same effect may be caused by the changes of scattering properties of the flow, which may be due to the influence of drugs and medical preparations.

ACKNOWLEDGMENT

Investigations have been supported by the following grants: MD-358.2003.04 of President of Russian Federation, N01-04-49023 and N03-02-17359 of Russian Foundation of Basic Research, E02-6.0-159 of Ministry of Education of Russian Federation, N25.2003.2 of President of Russian Federation "Supporting of Scientific Schools", N2.11.03 "Leading Research-Educational Teams" of the Russian Ministry of Education, and REC-006 of CRDF (U.S. Civilian Research and Development Foundation for the Independent States of the Former Soviet Union) and the Russian Ministry of Education.

REFERENCES

1. A.M. Chernukh, P.M. Aleksandrov, and O.V. Alexeyev, *Microcirculation* (Medicine Press, Moscow, 1984).
2. L. Richard and M.D. McCann, "Disorders of the lymphatic system. Chapter 47" in *Textbook of Surgery* (W.B. Saunders com., London, 2000), 1573-1577.
3. D. Saito, M. Hasui, T. Shiraki, and H. Kono, "Effects of coronary blood flow, myocardial contractility, and heart rate on cardiac lymph circulation in open-chest dogs. Use of a direct cannulation method for subepicardial lymph vessel," *Arzneimittelforschung* **47**(2), 119-124 (1997).
4. J.B. Smith, N.C. Pederson, and M. Dede, "The role of the lymphatic system in inflammatory responses," *Ser. Haematol.* **3**, 2-7 (1970).
5. A. Bollinger, I. Herrig, M. Fisher, U. Hoffmann, and U.K. Franzeck, "Intravital capillaroscopy in patients with chronic venous insufficiency and lymphedema," *Int. J. Microcirc.* **15**,41-44(1995).
6. C.L. Witte, M.H. Witte, E.C. Unger, W.H. Williams, M.J. Bernas, J.C. McNeill, and A.M. Stazzone, "Advance in imaging of lymph flow disorder," *Radio Graphics* **20,** 1697-1719(2000).
7. *Laser Doppler Blood Flowmetry,* A.P. Shepherd and P.A. Oberg eds. (Kluwer Academic Publishers, Boston, Dordrecht, London, 1989).
8. *Bioengineering of the Skin: Cutaneous Blood Flow and Erythema,* E. Berardesca, P. Elsner, and H. Maibach eds. (CRC Press, New York, 1995).

9. B. Ruth, "Non-contact blood flow determination using a laser speckle method," *Opt. Laser Technol.* **20** (6), 309-316 (1988).
10. B. Ruth, "Superposition of two dynamic speckle," *J. Mod. Opt.* **39**(12), 2421-2436 (1992).
11. Y. Aizu and T. Asakura, "Bio-speckle phenomena and their application to the evaluation of blood flow," *Opt. Laser Technol.* **23**(4), 205-219 (1991).
12. A. Jakobsson and G. E. Nilsson, "Prediction of sampling depth and photon pathlength in laser Doppler flowmetry," *Med. & Biol. Eng. & Comput.* **31**, 301-307 (1993).
13. K. Wardell, A. Jakobsson, and G. E. Nilsson, "Laser Doppler perfusion imaging by dynamic light scattering," *IEEE Trans. Biomed. Eng.* **40**(4), 309-316 (1993).
14. K. Wardell, I.M. Braverman, D.G. Silverman, and G.E. Nilsson, "Spatial heterogeneity in normal skin perfusion with laser Doppler imaging and flowmetry," *Microvascular Res.* **48**(1), 26-38(1994).
15. M.H. Koelink, F.F. de Mul, J. Greve, R. Graaff, A.C.M. Dassel, and J.G. Aarnoudse, "Laser Doppler blood flowmetry using two wavelength: Monte Carlo simulations and measurements," *Appl. Opt.* **33**(16), 3549-3558 (1994).
16. J.D. Briers and S. Webster, "Laser speckle contrast analysis (LASCA): a nonscanning, full field technique for monitoring of capillary blood flow," *J. Biomed. Opt.* **1**(2), 174-179(1996).
17. A. Kienle, M.S. Patterson, L. Ott, and R. Steiner, "Determination of the scattering coefficient and the anisotropy factor from laser Doppler spectra of liquids including blood, *"Appl. Opt.* **35**(19), 3404-3412 (1996).
18. J.D. Briers, "Laser Doppler and time-varying speckle: A reconciliation," *J. Opt. Soc. Am. A* **13**,345-350(1996).
19. Y. Aizu and T. Asakura, "Coherent optical techniques for diagnostics of retinal blood flow," *J. Biomed. Opt.* **4**(1), 61-75 (1999).
20. T. Gill, *The Doppler Effect. An Introduction to the Theory of the Effect* (Academic Press, London, 1965).
21. L.E. Drain, *The Laser Doppler Technique* (John Wiley & Sons, New York, 1980).
22. B.S. Rinkevichus, *Laser Techniques of Flow Diagnostics* (MPEI Publishers, Moscow, 1990).
23. C. Tropea, "Laser Doppler anemometry: recent developments and future challenges," *Meas. Sci. Technol.* **6**, 605-619 (1995).
24. *Handbook of Optical Biomedical Diagnostics,* **PM107**, V.V. Tuchin ed. (SPIE Press, Bellingham, 2002).
25. T. Yoshimura, "Statistical properties of dynamic speckles," *J. Opt. Soc. Am. A* **3**(7), 1032-1054(1986).
26. M. Francon, *Laser Speckle and Applications in Optics* (Academic Press, New York, 1979).
27. J. Goodman, *Statistical Optics* (Wiley-Interscience, New York 1985).
28. R. Jones and C. Wykes, *Holographic and Speckle Interferometry* (Cambridge Univ. Press, Cambridge, 1983).
29. M.D. Stern, "*In vivo* evaluation of microcirculation by coherent light scattering," *Nature* **254**, 56-58 (1975).
30. S.S. Ulyanov, "New type of manifestation of the Doppler effect: an applications to blood and lymph flow measurements," *Opt. Eng.* **34**(10), 2850-2855 (1995).
31. S.S. Ulyanov, V.V. Tuchin, A.A. Bednov, G.E. Brill, and E.I. Zakharova, "The applications of speckle interferometry for the monitoring of blood and lymph flow in microvessels," *Laser Med. Sci.* **12**, 31-41 (1997).

32. A.A. Bednov, S.S. Ulyanov, V.V. Tuchin, G.E. Brill, and E.I. Zakharova, "*In vivo* laser measurements of blood and lymph flow with a small number of scatterers," *Appl. Nonlinear Dynamics* **4**(3), 42-51 (1996).
33. S.S. Ulyanov, "High-resolution speckle-microscopy: study of the spatial structure of a bioflow," *Physiol. Meas.* **22**, 681-691 (2001).
34. J.W. Goodman, *Introduction to Fourier Optics* (McGrow-Hill Book Company, San Francisco, New York, St. Louis, Toronto, London, Sydney, 1968).
35. S.S. Ulyanov, "Analysis of surfaces with a complex periodic relief," *Opt. Eng. Bulletin* **1**(5), 20-23(1995).
36. R. Bonner and R. Nossal, "Model for laser measurements of blood flow in tissue," *Appl. Opt.* **20**(12), 2097-2107 (1981).
37. A. Liebert, P. Lukasiewicz, D. Bogget, and R. Maniewski, "Optoelectronic standardization for laser Doppler perfusion monitors," *Rev. Sci. Instrum.* **70**, 1352-1354 (1999).
38. I.V. Fedosov, V.V. Tuchin, E.I. Galanzha, A.V. Solov'eva, and T.V. Stepanova, "Recording of lymph flow in microvessels using correlation properties of scattered coherent radiation," *Quant. Electron.* **32**(11), 970-974 (2002).
39. I.V. Fedosov, V.A. Galanzha, and V.V. Tuchin, "Blood flow assessment in capillaries of human eye conjunctiva using laser Doppler technique," *Proc. SPIE* **4427**, 104-108 (2001).
40. C.E. Riva, B.L. Petrig, and G.E. Grunwald, "Retinal blood flow" in: *Laser Doppler Blood Flowmetry,* A.P. Shepherd, and P.A. Oberg eds. (Kluwer Academic Publishers, Boston, Dordrecht, London, 1989), 339-383.
41. E. Logean, M.H. Geiser, B.L. Petrig, and C.E. Riva, "Portable ocular laser Doppler red blood cell velocimeter," *Rev. Sci. Instrum.* **68**(7), 2878-2882 (1997).
42. T. Eiju, M. Nagai, K. Matsuda, J. Ohtsubo, K. Homma, and K. Shimizu, "Microscopic laser Doppler velocimeter for blood velocity measurement," *Opt. Eng.* **32**(1), 15-20 (1993).
43. E.I. Galanzha, G.E. Brill, Y. Aizu, S.S. Ulyanov, and V.V. Tuchin, "Speckle and Doppler methods of blood and lymph flow monitoring," in *Handbook on Optical Biomedical Diagnostics,* **PM107,** V.V. Tuchin ed. (SPIE Press, Bellingham, 2002), 881-937.
44. S.S. Ulyanov, "Speckled speckle statistics with a small number of scatterers: implication for blood flow measurement,"*J. Biomed. Opt.* **3**(3), 227-236 (1998).
45. R.D. Sinelnikov and Ya.R. Sinelnikov, *Atlas of Human Anatomy,* **Issue 4** (Medicine Publishers, Moscow, 1994).
46. G.T. Feke and C.E. Riva, "Laser Doppler measurement of blood velocity in human retinal vessels,"*J. Opt. Soc. Am.* **68**(4), 526-531 (1978).
47. G.T. Feke, A. Yoshida, and C.L. Schepens, "Laser based instruments for ocular blood flow assessment,"*J. Biomed. Opt.* **3**(4), 415-422 (1998).
48. C.E. Riva, J.E. Grunvald, and B.L. Petrig, "Laser Doppler measurements of retinal blood velocity: Validity of the single scattering model," *Appl. Opt.* **24**, 605-607 (1985).
49. C.E. Riva, B.L. Petrig, R.D. Shonat, and C.J. Pouranas, "Scattering process in LDV from retinal vessels," *Appl. Opt.* **28**, 1078-1083 (1989).
50. *Tissue Optics,* A.J. Welch and M.C.J. van Gemert eds. (Academic Press, New York, 1992).
51. D.H. Sliney and S.L. Torkel, *Medical Lasers and Their Safe Use* (Academic Press, New York, 1993).
52. K. Aukland, and R.K. Reed, "Interstitial-lymphatic mechanisms in the control of extracellular fluid volume," *Physiol. Rev.* **73**, 1-78 (1993).

53. W.L. Olszwski, "Contractility patterns of normal and pathologically changed human lymphatics," *Ann. N Y Acad. Sci.* **979**, 52-63 (2002).
54. G.M. Johnston, "The intrinsic lymph pump: progress and problems," *Lymphology* **22**, 116-122(1989).
55. A.A. Gashev, "Physiologic aspects of lymphatic contractile function: current perspectives," *Ann N Y Acad Sci.* **979**, 178-187 (2002).
56. C.L. Witte and M.H. Witte, "Disorders of lymph flow," *Acad. Radial.* **2**, 324-334 (1995).
57. E. Foldi, M. Foldi, and L. Clodius, "The lymphedema chaos: A lancet," *Ann. Plast. Surg.* **22**, 505-515 (1989).
58. C.J.H. Porter and W.N. Charman, "Uptake of drugs into the intestinal lymphatics after oral administration," *Adv. Drug Delivery Rev.* **25,** 71-89 (1997).
59. A.A. Ramelet, "Pharmacologic aspects of a phlebotropic drug in CVI-associated edema," *Angiology* **51**, 19-23 (2000).
60. *Human Physiology,* R.F. Schmidt and G. Thews eds. (Springer-Verlag, Berlin, Heidelberg, 1989).
61. E.I. Galanzha, V.V. Tuchin, A.V. Solov'eva, and V.P. Zharov, "Development of optical diagnostics of microlymphatics at the experimental lymphedema: comparative analysis," *J. X-Ray Sci. and Technol.* **10**, 215-223 (2002).
62. I.V. Fedosov, E.I. Galanzha, A.V. Solov'eva, T.V. Stepanova, G.E. Brill, and V.V. Tuchin, "Laser speckle flow velocity sensor for functional biomicroscopy," *Proc. SPIE* **4707**, 206-209 (2002).
63. E.I. Galanzha, V.V. Tuchin, A.V. Solov'eva, T.V. Stepanova, G.E. Brill, and V.P. Zharov, "The diagnosis of lymph microcirculation on rat mesentery *in vivo," Proc. SPIE* **4965**, 325-333 (2003).
64. M.J. Lighthill, "Pressure-forcing of tightly fitting pellets along fluid-filled elastic tubes," *J. Fluid. Mech.* **34**(1), 113-143 (1968).
65. J.M. Fitz-Gerald, "Mechanics of red-cell motion through very narrow capillaries," *Proc. Royal Soc.* **B174**, 193-227 (1969).
66. A. Perlin and Tin-Kan Hung, "Flow development of a train of particles in capillaries," *J. Eng. Mechanics Div.* **EM1**, 49-66 (1978).
67. Y. Aizu, K. Ogino, T. Sugita, T. Yamamoto, N. Takai, and T. Asakura, "Evaluation of blood flow at ocular fundus by using laser speckle," *Appl. Opt.* **31**(16), 3020-3029 (1992).
68. Y. Aizu, H. Ambar, T. Yamamoto, and T. Asakura, "Measurements of flow velocity in microscopic region using dynamic laser speckles based on the photon correlation," *Opt. Commun.* **72**(5), 269-273 (1989).
69. Y. Aizu, T. Asakura, K. Ogino, T. Sugita, Y. Suzuki, and K. Masuda, "Measurements of retinal blood flow using biospeckles: experiments with glass capillary and in the normal human retina," *Proc. SPIE* **2678**, 360-371 (1996).
70. I.V. Fedosov and V.V. Tuchin, "The spatial-time correlation of the intensity of a speckle field formed as a result of scattering of focused coherent radiation by a capillary liquid flow containing scattering particles," *Opt. Spectrosc.* **93**(3), 473-477 (2002).
71. I.V. Fedosov, V.V. Tuchin, E.I. Galanzha, and A.V. Solov'eva, "Laser monitoring of the flow velocity in lymphatic microvessels based on a spatial-temporal correlation of the dynamic speckle fields," *Tech. Phys. Lett.* **28**(8), 690-692 (2002).
72. I.V. Fedosov and V.V. Tuchin, "Use of dynamic speckle field space-time correlation function estimates for the direction and velocity determination of blood flow," Proc. SPIE 4434, 192-196(2001).

This page intentionally left blank

Chapter 11

QUASI-ELASTIC LIGHT SCATTERING IN OPHTHALMOLOGY

Rafat R. Ansari
NASA Glenn Research Center at Lewis Field, Mail Stop 333-1, 21000 Brookpark Road, Cleveland, OH 44135 USA

Abstract: The eye is not just a "window to the soul", it can be considered a "window to the body" as well. The eye is built much like a camera. Light which travels from the cornea to the retina traverses through tissues that are representative of nearly every tissue type in the body. It is possible to diagnose ocular and systemic diseases through the eye. Quasi-elastic light scattering (QELS) is a laboratory technique routinely used in the characterization of macromolecular dispersions. In the past few years, QELS instrumentation has become compact, more sensitive, flexible, and easy to use. These developments have made QELS an important tool in ophthalmic research where diseases can be detected early and non-invasively before the clinical symptoms appear.

Key words: quasi-elastic light scattering (QELS), dynamic light scattering (DLS), ophthalmology, non-invasive detection of diseases, ophthalmic diagnostics, ocular research, optical technologies, cataract, vitreopathy, diabetes, glaucoma, LASIK, Alzheimer's

11.1 INTRODUCTION

The technique of quasi-elastic light scattering (QELS) was originally developed to study fluid dispersions of colloidal (size ≤ 1 μm) particles [1]. This is also known as dynamic light scattering (DLS) and photon correlation spectroscopy (PCS). It was first used in the eye by Tanaka and Benedek to study the onset of cataract in the ocular lens nearly three decades ago [2, 3]. However, its use remained limited to few research laboratories and it did not find wide-scale commercial acceptance in ophthalmology. Thanks to the innovations in the field of optoelectronics, QELS is now emerging as a potential ophthalmic tool making the study of virtually every tissue and fluid comprising the eye possible, pushing the envelope for broader applications

in ophthalmology. The ability of QELS in the early detection of the molecular morphology has the potential to help develop new drugs to combat not just the diseases of the eye such as cataract but to diagnose and study those of the body such as diabetes and possibly Alzheimer's. Recently Ansari gave an overview of this field and its current state of development [4].

11.1.1 Need for Non-invasive Diagnostics in Ophthalmology

Blindness is a global problem. According to the World Health Organization (WHO), 90 % of all blind people live in developing countries. In the United States alone, one person goes blind every 11 minutes. The current economic cost of blindness in India and the U.S. is estimated at 4.6 and 4.1 US$ billion per year respectively and is rising. These are alarming figures since half of all blindness can be prevented if detected and treated early [5].

Ophthalmology is a specialized branch of medicine which deals with the study, detection, and treatment of eye diseases. Normal aging is the leading cause for ocular problems and refractive disorders such as cataract, age-related macular degeneration (AMD), vitreous liquefaction, glaucoma, and hyperopia. Certain systemic diseases can also lead to eye diseases early. For example, diabetes contributes to early formation of cataract and retinopathy and hypertension can lead to glaucoma.

The visual function and ocular health is evaluated everyday by ophthalmologists with subjective (e.g., patient history) and objective methods that can include visual acuity charts, direct and indirect ophthalmoscopy, retinoscopy, keratometry, and applanation tonometry. The classical principles of light scattering (Rayleigh, Mie, etc.) are employed virtually in every ophthalmic instrument in one form or another. The slit-lamp biomicroscope, based upon the optical principles of compound microscopy, is the most widely used ophthalmic instrument for examination from the cornea to the retina. This instrument, except for some mechanical designs and illumination techniques, has not changed in principle in the past 140 years [6]. The modern instruments employ direct illumination for the examination of lesions in conjunctiva, retro-illumination for corneal opacities, cataract, and iris atrophy in glaucoma, sclerotic scatter for corneal edema, and specular reflection for making the epithelium and endothelium cells in the cornea visible. A principle known as Scheimpflug [6] is employed in slit-lamp biomicroscopes to generate stereoscopic images of the lens to study cataract. The fundus cameras are often mounted on these instruments to capture abnormalities of the retina (e.g., diabetic retinopathy, and macular degeneration). Beyond these conventional methods, the modern

techniques of optical coherence tomography (OCT), scanning laser ophthalmoscope (SLO), confocal microscopy, and quasi-elastic light scattering (QELS), are some of the emerging tools that are showing potential in the early diagnosis of ocular disease.

11.1.2 Principles of QELS

In a QELS experiment, a constant fluctuating speckle pattern is seen in the far field when light passes through an ensemble of small particles suspended in a fluid [1]. This speckle pattern is a result of the interference in the light paths and it fluctuates as the particles in the scattering medium perform random walks on a time scale of ≥ 1 μsec due to the collisions between themselves and the fluid molecules (Brownian motion).

In the absence of particle-particle interactions (dilute dispersions) light scattered from small particles fluctuates rapidly while light scattered from large particles fluctuates more slowly. During a simple homodyne experiment, only scattered light is collected (absence of local oscillator) at a photodetector, assuming the particles are uniformly sized and spherically shaped, and an intensity-intensity temporal autocorrelation function (TCF) is measured

$$g^2(\tau) = A\left[1 + \beta \exp(-2\Gamma\tau)\right], \tag{1}$$

where $A = < i >^2$ is the average d.c. photocurrent or the baseline of the autocorrelation function, and β $(0<\beta<1)$ is an empirical experimental constant and is a measure of the spatial coherence of the scattering geometry of the collection optics which can be related to signal-to-noise (S/N). Γ is a decay constant due to diffusing motion of the particles in the scattering volume and τ is the delay time.

$$\Gamma = D_T \cdot q^2, \tag{2}$$

where D_T is the translational diffusion coefficient and q is the magnitude of the scattering wave vector,

$$q = \frac{4\pi n}{\lambda} \sin\left(\frac{\theta}{2}\right), \tag{3}$$

where n is the refractive index of the solvent, λ is the wavelength of the incident light in vacuum, and θ is the scattering angle. Using the Stokes-

Einstein relationship for spherical particles, D_T can be related to the hydrodynamic radius *(R)* of the particle,

$$D_T = \frac{KT}{6\pi\eta R}, \tag{4}$$

where K is Boltzmann's constant (1.38×10^{-23} J K^{-1}), T is the absolute temperature of the scattering medium, and η is the solvent viscosity. In clinical ophthalmic applications, for n and η, value of water can be used at a body temperature of 37 °C. Equation 4 then can be used to extract average size of the particles in the transparent aqueous, lens, and vitreous. The lens and vitreous are polydisperse in nature and exhibit bi-modal behavior. Today, commercial software packages are available to analyze equation 1 in terms of bi-modal and multi-modal size distributions based upon the schemes reviewed by Stock and Ray [7].

Thus a QELS experiment provides dynamic information such as diffusion, size, shape, and molecular interactions [1]. The most attractive features of QELS are that it is non-invasive and quantitative, works effectively for particle size ranging from few nm to few μm, requires small sample volume, and works reasonably well for polydisperse or multiple size (up to 2-3 component) dispersions. The new ocular QELS instrumentation is several orders of magnitude more sensitive than current ophthalmic instruments based on imaging and photographic techniques of slit-lamp biomicroscopy, retro-illumination, and Scheimpflug systems. These instruments are being used in clinical settings with better alignment and reproducibility to characterize the cornea, aqueous, lens, vitreous, and retina. Although still in experimental realm, many new applications have been realized to detect a diverse range of diseases early, non-invasively, and quantitatively. These include corneal evaluation of wound healing after refractive surgery, e.g., laser *in situ* keratomileusis (LASIK), pigmentary glaucoma, cataract, vitreopathy, diabetic retinopathy, and possibly Alzheimer's.

11.2 QELS AND DISEASE DETECTION

Until recently, QELS instruments were physically bulky, required vibration isolation, index-matching (for flare control), tedious optical alignment, and were difficult to use. The new generation systems are compact and efficient due to new solid-state laser sources, sensitive photo-detectors, and by using mono-mode optical fibers for launching and detecting low levels of laser light into the eye. The fiber-optic based QELS

design developments for studies of cataractogenesis are covered by Dhadwal *et al.* [8], Rovati *et al.* [9], Ansari *et al.* [10], and the references contained in their papers. The fiber-optic QELS probe, shown in Figure 1, combines the unique attributes of small size, low laser power, and high sensitivity (β values in equation 1). The probe was originally developed at NASA to conduct fluid physics experiments in the absence of gravity onboard a space shuttle or space station orbiter. The system is easy to use because it does not require sensitive optical alignment nor vibration isolation devices. Currently, the probe has been successfully employed in many ocular experiments to monitor the early symptoms of various eye diseases. A low power (50-100 μW) light from a semi-conductor laser, interfaced with a mono-mode optical fiber is tightly focused in a 20 μm diameter focal point in the tissue of interest via a GRIN (gradient index) lens. On the detection side, the scattered light is collected through another GRIN lens and guided onto an avalanche photodiode (APD) detector built into a photon-counting module. APD processed signals are then passed on to a digital correlator for analysis. The probe provides quantitative measurements of the pathologies of cornea, aqueous, lens, vitreous, and the retina. The device is modular in design. If needed, by suitable choice of optical filters, it can be converted into a device for spectral measurements (autofluoresence and Raman spectroscopy) and laser-Doppler flowmetry/velocimetry providing measurements of oxidative stress and blood flow in the ocular tissues. The device can easily be mounted onto many conventional ophthalmic instruments to significantly increase their diagnostic power. These instruments, presently in clinical use, include slit-lamps (Figure 2), Scheimpflug cameras (Figure 3), videokeratoscopy (Figure 4), and fluorometry (Figure 5).

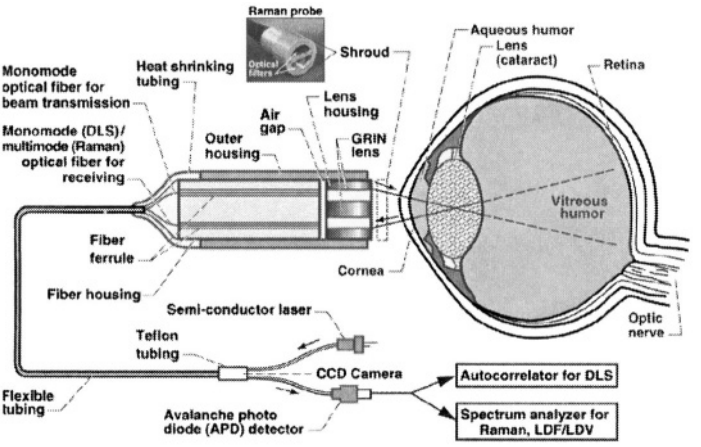

Figure 1. QELS fiber-optic probe schematic diagram.

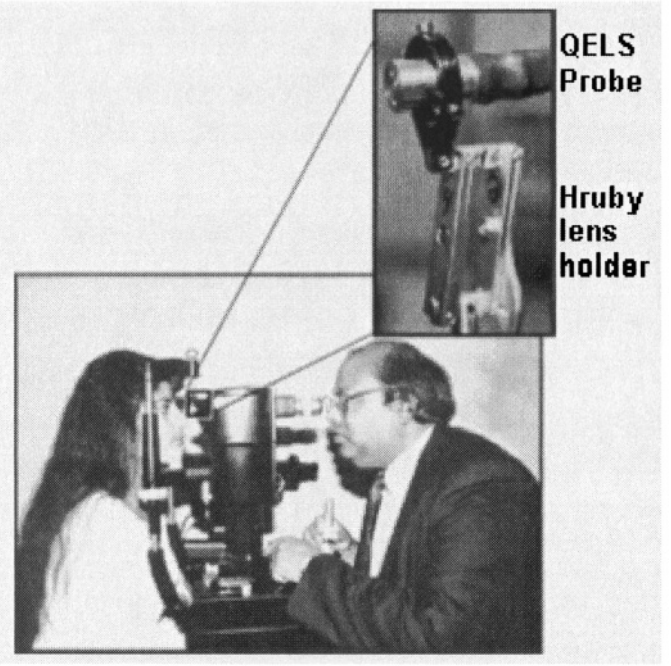

Figure 2. Modified slit-lamp apparatus (the person on right is the author and the person on left is Rahila Ansari, School of Medicine, Case Western Reserve University).

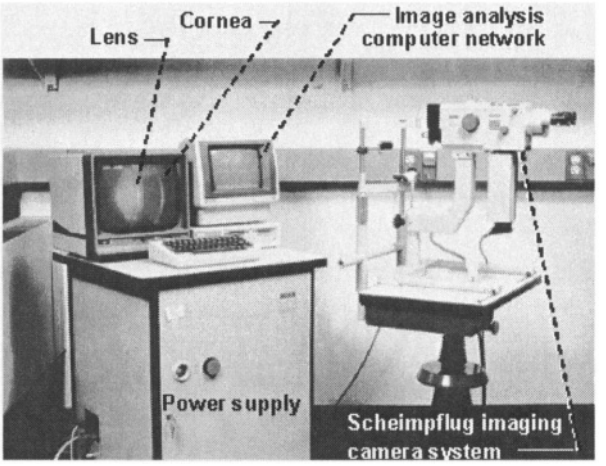

Figure 3. Zeiss Scheimpflug imaging set-up with QELS at NEI/NIH (photo courtesy of Manuel B. Datiles III, MD, NEI/NIH).

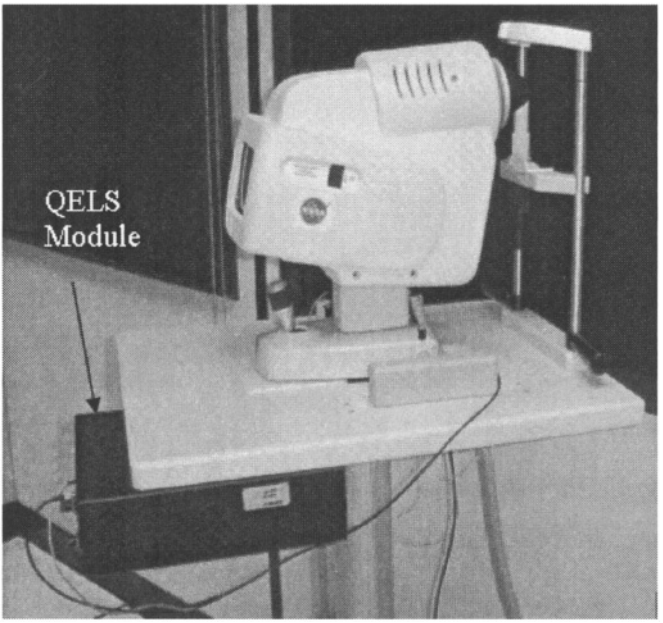

Figure 4. Modified corneal analyzer (Keratron videokeratoscope) with QELS probe.

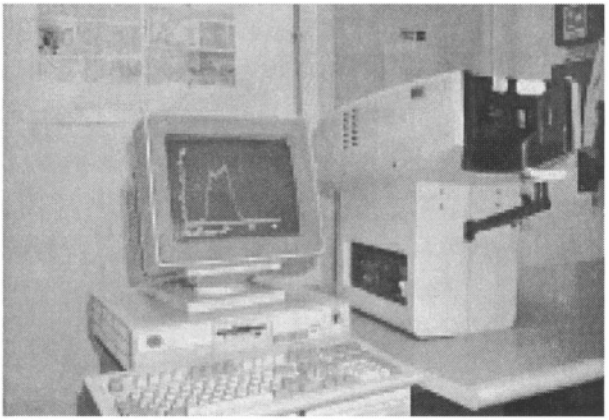

Figure 5. QELS probe intergrated with fluorometry in a Fluorotron Master (photo courtesy of Luigi Rovati, Ph.D., University of Modena).

11.3 EARLY DETECTION OF OCULAR AND SYSTEMIC DISEASES

Table 1 represents various diseases and the respective ocular component of interest in a QELS experiment.

Table 1. Diseases and the Ocular Fluid/Tissue components as measured by QELS

Disease	Cornea	Aqueous	Lens	Vitreous
Uveitis		Albumins		
Glaucoma		Pigments		
Cataract			Crystallins	
Diabetes			Crystallins	Hyaluronan and Collagen
Diabetic Retinopathy	Nucleotides Pyridines			Hyaluronan and Collagen
Wound Healing (after refractive surgery)	Glycoproteins and collagen			
Oxidative Stress (radiation, aging, etc)	Nucleotides Pyridines		Crystallins	
Alzheimer's		Amyloids	Amyloid-induced crystallin aggregation	

11.3.1 Uveitis

Aqueous humor can be considered an ultra-filtrate of blood since it contains most of the molecules found in the serum at concentrations that are reflective of serum levels. For example, certain metabolites (glucose) and proteins (human serum albumin or HSA) are present in the aqueous. Since glucose molecules are much smaller (~0.6 nm in diameter) than the visible wavelength (λ) region they do not contribute significantly to scattered light especially at the low laser power levels and at the normal physiological glucose concentration (~100 mg/dL). The HSA particles can scatter light appreciably since they are spherical in shape and their size (~7.0 nm in diameter) is comparable to λ frequently applied in QELS experiments.

Uveitis is an inflammatory disease of the anterior chamber. It can produce high numbers of protein particles in the aqueous humor. This increase in protein concentration gives rise to increased scattered light intensity or "flare". Clinically, flare and therefore the severity of uveitis can be easily detected and quantified by QELS. Similarly, cholesterol levels in the body can also be evaluated through the aqueous as suggested by Bursell *et al.* [3]. But this important application has not been pursued thoroughly either in laboratory or clinical settings.

11.3.2 Pigmentary Glaucoma

Glaucoma is a disease of the anterior chamber in which the intra-ocular pressure (IOP) increases. If IOP increase is not treated it can lead to degeneration of the optic nerve and eventually loss of vision. Recently QELS was applied to study one specific type of glaucoma known as pigmentary dispersion glaucoma (PDG). The posterior layer of the iris epithelium contains high number of melanin granules. These granules are released into the aqueous as a consequence of natural epithelium cell death, infection, or trauma. The melanin granules can be trapped in the trabecular meshwork over time and block the aqueous outflow. This can cause an increase in IOP finally leading to PDG. Pollonini *et al.* [11] used QELS to detect and quantify melanin granules in a clinical study of normal and PDG volunteer patients. The results (Figure 6) indicated presence of small (1-10 nm) and large (up to 1 μm) particles in the aqueous of normal and the PDG patients respectively and therefore showed the potential of QELS in monitoring this type of glaucoma non-invasively.

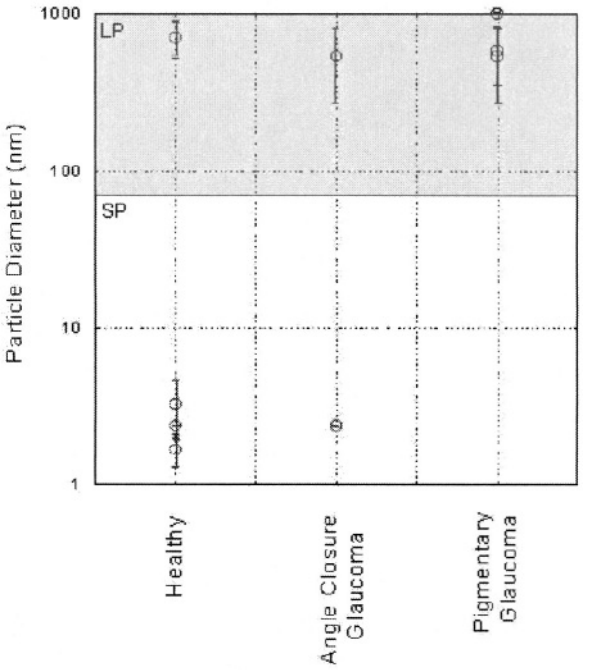

Figure 6. Glaucoma detection with QELS.

11.3.3 Cataract

Cataract (lens opacification), its clinical evaluation, and classification is discussed in detail elsewhere by Datiles and Ansari [12].

Cataract is the major cause of blindness worldwide. At the present time clinical methods of classifying cataracts are based mainly upon visual acuity (Snellen charts) and photographic means (slit-lamps). The inside of the eye is illuminated either directly or indirectly (retro-illumination) by a slit from an incandescent source of light. These approaches, however, are subjective because they cannot be accurately quantified. Furthermore, they do not have the ability to capture a growing cataract in its incipient stage. Therefore, by the time a cataract is diagnosed by these methodologies it is too late to alter its course non-invasively or medically. QELS holds promise in detecting cataract much earlier than the photographic techniques currently in use.

The normal lens in a human eye, situated behind the cornea, is a transparent tissue. It contains 35% (by weight) protein and 65% (by weight) water. Aging, disease (e.g., diabetes), smoking, dehydration, malnutrition, and exposure to UV and ionizing radiation can cause agglomeration of the lens proteins. Protein aggregation can take place anywhere in the lens causing lens opacity. The aggregation and opacification could produce nuclear (central portion of the lens) or cortical (peripheral) cataracts. Nuclear and posterior sub-capsular (the membrane capsule surrounds the whole lens) cataracts, being on the visual optical axis of the eye, cause visual impairment, which can finally lead to blindness. The lens proteins, in their native state, are small in size. As cataract develops this size grows from a few nm (transparent) to several microns (cloudy). Ansari and Datiles have shown that QELS can detect cataracts at least two-three orders of magnitude earlier (non-invasively and quantitatively) than the best imaging (Scheimpflug) techniques in clinical use today [13].

Animal models are usually helpful in the validation of new instruments and testing of therapies prior to clinical use. Until recently, it was difficult to use QELS in small animals models due to instrument limitations e.g., physical size, power requirements, and alignment problems. Compact probes described in Figure 1 are proving to be very useful in this area of research. A generic experimental set up is shown in Figure 7. Cataractogenesis is monitored *in vivo* by following TCF profiles (equation 1) at different time lines. As an example, Philly mice were monitored. This animal develops cataract spontaneously between day 26 and 33 after birth.

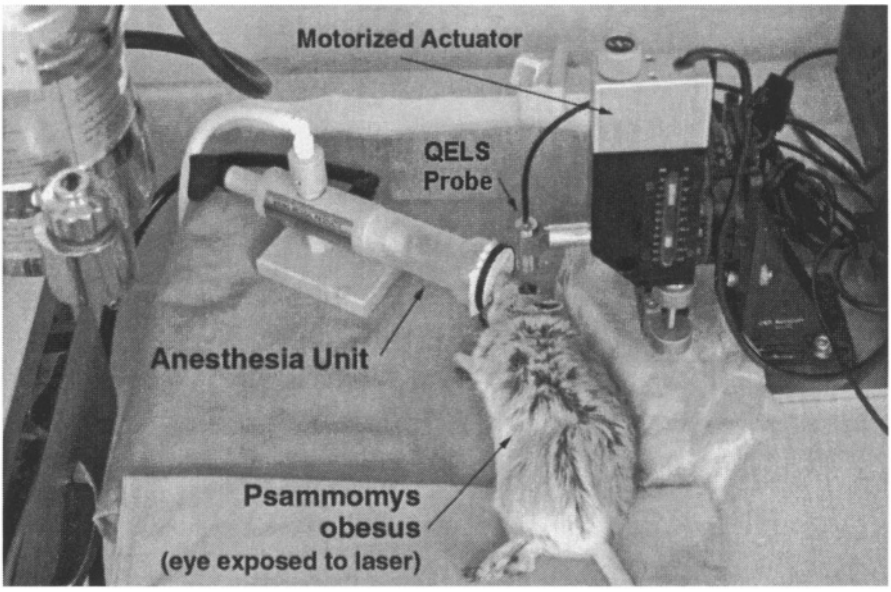

Figure 7. QELS scanning set up for laboratory animals.

The data includes a 45 days old normal mouse of the control FVB/N strain which does not develop a cataract and two Philly mice roughly 26-29 days old. The eye examinations of these mice with a slit-lamp biomicroscope concluded a normal (transparent) and two other eyes having trace to mild cataracts. Each measurement took 5 seconds at a laser power of 100 μW. The changing TCF slope is an indication of cataractogenesis as the lens crystallins aggregate to form high molecular weight clumps and complexes. The QELS autocorrelation data is converted into particle size distribution using an exponential sampling program and is shown in Figure 8. Although, conversion of the QELS data into particle size distributions requires certain assumptions regarding the viscosity of the lens fluid, these size values do indicate a trend as the cataract progress. These measurements suggest that a developing cataract can be monitored quantitatively with reasonable reliability, reproducibility (5%-10%), and accuracy.

11.3.3.1 Drug Screening for Cataract

In the absence of a non-surgical treatment, 50% of all blindness is due to cataracts. At the present time, 34 million Americans over the age of 65 have cataracts. Foster predicts this figure to rise to 70 million by year 2030 [14]. According to Kupfer, “A delay in cataract formation of about 10 years would reduce the prevalence of visually disabling cataracts by about 45%” [15].

QELS can help achieve this goal by detecting cataracts at the very early stages and by screening potential anti-cataract drugs for their efficacy.

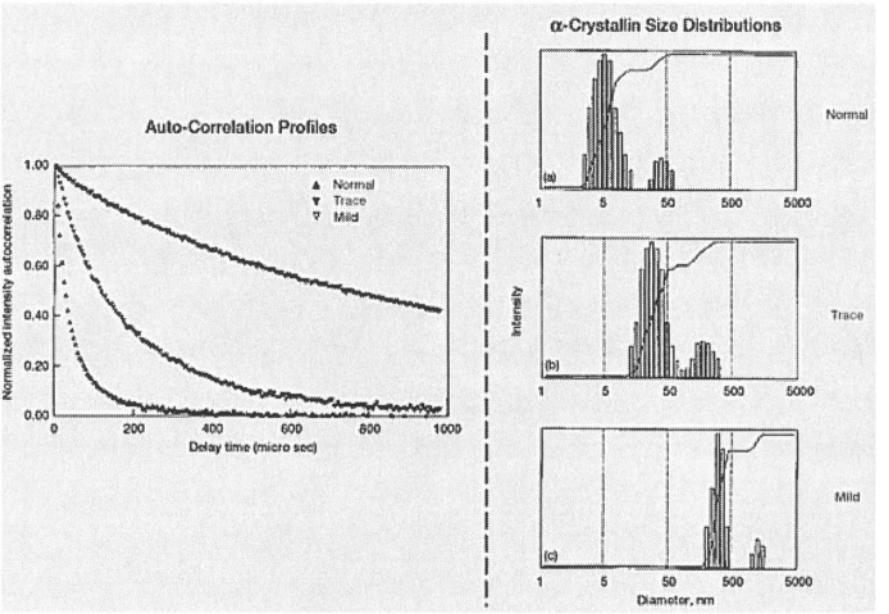

Figure 8. In vivo cataract measurements in mice.

Pantethine is a metabolically active stable disulfide form of pantetheine and a derivative of pantothenic acid (Vitamin B5). It can be used as an anti-cataract drug but the clinical trial of pantethine was inconclusive with respect to effectiveness [16, 17]. The results of both preclinical and clinical tests of potential therapeutic agents indicate the need for more sensitive measures of protein aggregation and opacification *in vivo.* Studies in humans predicted that QELS will be useful in testing of anti-cataract drugs to inhibit or reverse the progression of cataract formation during longitudinal clinical trials [11-12, 18-19].

Recently Ansari *et al.* [20], using QELS demonstrated the efficacy of pantethine in very early stages (few hours to few days) of selenite-induced lens damage, well before formation of a mature cataract in the selenite model [21]. In this study, QELS measurements were made on 33 animals (rats) aged 12-14 days at the time of selenite or pantethine injection. Pantethine treatment resulted in a substantial decrease in dimensions of scattering centers in lens *in vivo* during the early stages of opacification prior to their detection with conventional ophthalmic instruments. An obvious opacity was not observed using a slit-lamp bio-microscope. Typical representative

size distribution data is presented in Figure 9 for control, Se-treated (12 and 60 hours post treatment), and Se-pantethine-treated animal (42 hours post treatment) at a distance of ~2 mm from the lens anterior surface. The size distribution of scatterers in the control animal ranges from 60-80 nm in diameter. In the Se-treated animals, the TCF shows bi-modal behavior with aggregates ranging in size from 400 to 800 nm and 3000 to 10,000 nm in diameter. The Se-pantethine-treated animal shows an aggregate size averaging around 200 nm. The experimental results indicated clearly that QELS was able to discern subtle molecular changes very early in cataract formation. The results suggested that pantethine inhibits the initial aggregation process.

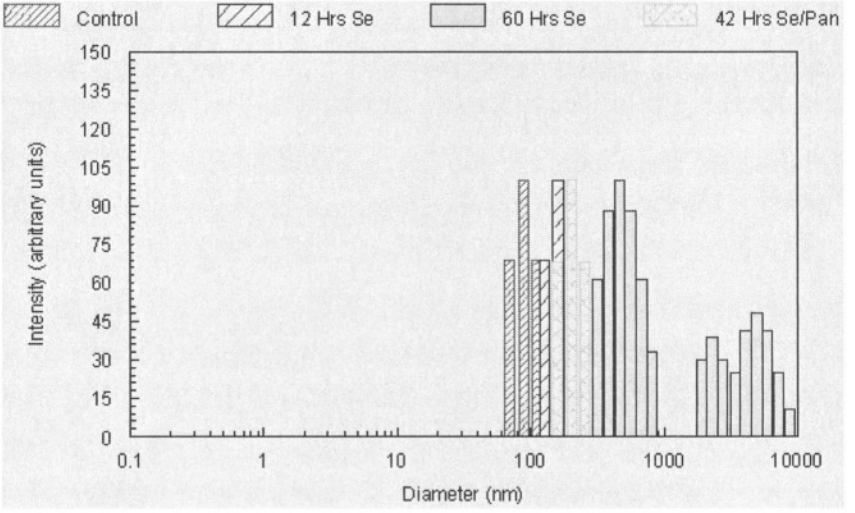

Figure 9. Cataract treatment in rats. Exponential sampling particle size distribution analysis.

In conclusion, the results are encouraging. The future outlook for finding a medical cure for cataract seems optimistic when combined with advances in the detection technology, understanding of fundamental processes, and the efforts in designing new anti-cataract drug formulations. This work is picking up momentum at Zigler's laboratory at the NEI/NIH [22-24]. At the time of this writing the author's laboratory is starting a study using QELS on the efficacy of isoflavones found in soy-based diets for their anticipated anti-cataract properties in non-human primates.

11.3.4 Diabetes

QELS can be applied to detect early onset of diabetes through the transparent ocular lens. Chenault *et al.* have indicated that cataracts are 1.6 times more common in diabetic patients than non-diabetics [25]. The Food and Drug Administration (FDA) in the U.S. has a unique animal model to study type-II diabetes. Psammomys obesus (sand rat) is a wild rodent found in the desert areas of the Middle East and Africa. It develops mild to moderate obesity, hyperglycemia and the complications of diabetes such as cataracts and vision loss when it consumes a high caloric diet. In a recent study [25], blood glucose levels, insulin, and glycohemoglobin values in this animal were correlated with histopathology, traditional ophthalmology assessments, and QELS measurements toward developing a non-invasive means to detect early stages of eye damage due to diabetes mellitus. The control animal demonstrated no significant change in crystallin size distributions. Study animals exhibited significant increases in the sizes of crystallin scattering centers and substantial shifts in the size distributions. No discernable difference was observed by ophthalmic examination or by histology between the control and study animals. The results demonstrated evidence of subtle changes in the lens of the diabetic sand rats after only two months on the diabetogenic diet using QELS (see Figure 10 top graphs) Conventional ophthalmic instrumentation did not detect these changes (see Figure 10 bottom photographs). At the time of this writing, sand rat experiments on the screening of some conventional and non-conventional drugs to control diabetes (hyperglycemia) and lens damage are underway at FDA using QELS.

11.3.5 Diabetic Vitreopathy

The vitreous body is the largest structure within the eye. Ansari *et al.* and Rovati *et al.* were the first to characterize vitreous structure with QELS and applied it to the study of diabetic vitreopathy [26,27]. In a QELS measurement, the vitreous body truly exhibits a two exponential behavior consistent with its gel like properties due to hyaluronan (HA) and collagen found respectively in the vitreous gel. A typical measurement is shown in Figure 11. QELS can be a powerful tool to study the effects of diabetes on vitreous morphology due to the glycosylation of HA and collagen.

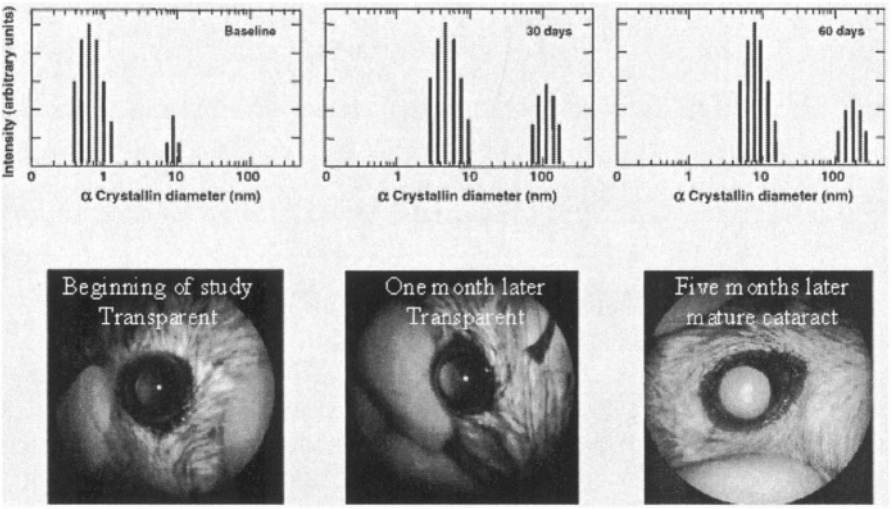

Figure 10. Cataract formation due to diabetes in sand rats: top) QELS particle size distribution. bottom) Slit lamp photographs (photo courtesy of Michelle Chenault, PhD., FDA).

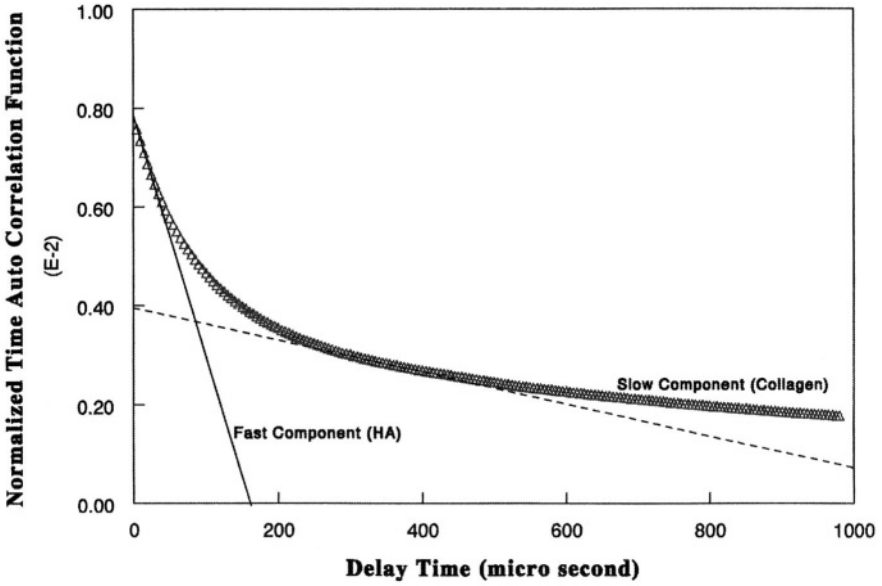

Figure 11. Time relaxation of human vitreous gel.

The effect of diabetes on the retina (diabetic retinopathy) is a leading cause of blindness in Americans between 20 and 74 years of age [28]. There

has been little progress to diagnose this condition during early stages. Elevated levels of glucose affect tissues throughout the body by altering protein through the phenomenon of nonenzymatic glycation [29]. One of the most ubiquitous and important proteins altered by this process is collagen. Hyperglycemic effects on collagen underlie the basement membrane pathology in blood vessels throughout the body, including the retina. At present there are no methods by which to evaluate glycation effects on collagen in the retinal vasculature. An alternative approach that could provide insight into this process would be to evaluate glycation effects upon collagen in ocular tissue, e.g., vitreous. In recent years, the vitreous has come to be recognized as an important contributor to advanced diabetic retinopathy. Studies have determined that there are elevated levels of glucose in the vitreous of diabetic patients. It is believed that these effects underlie the structural abnormalities in diabetic vitreopathy [30,31], similar to the effects of hyperglycemia on collagen elsewhere in the body [29]. Interestingly, these alterations appear to the quite similar to those observed in the vitreous during aging [30,32,33], consistent with the concept that diabetes induces accelerated aging in target tissues and organs [29]. Considering that the aforementioned effects of diabetes on vitreous collagen induce cross-linking and aggregation of fibrils into larger than normal fibers, it has been of interest to apply the methodology of QELS to assess the particle sizes found in diabetic vitreous and compare those to non-diabetic controls (see Figure 12). Furthermore, in studies [34] of excised human eyes, QELS detected the structural changes [30] resulting from diabetic vitreopathy [35]. Interestingly, these QELS findings appear to corroborate the finding of dark-field slit microscopy where glycation of vitreous proteins resulted in cross-linking of collagen fibrils and aggregation into large bundles of fibrils. It is plausible that these are detected by QELS as particles of larger size with more variability than that seen in non-diabetic control in this preliminary study. Future studies in humans will determine if this phenomenon can be detected in a clinical setting, confirming these preliminary *in vitro* results.

11.3.6 Evaluation of Corneal Surgery Outcomes

Corneal tissue is avascular composed primarily of collagen. The human cornea is about 500 μm thick at the apex and about 700 μm at the periphery (check corneal thickness values at center and edge) or limbus [36]. Clearly, transparency is the most important corneal property to maintain good quality vision. Slight loss of transparency can cause problems such as haze and glare. A change in corneal shape can lead to myopic, astigmatic, and hyperopic vision.

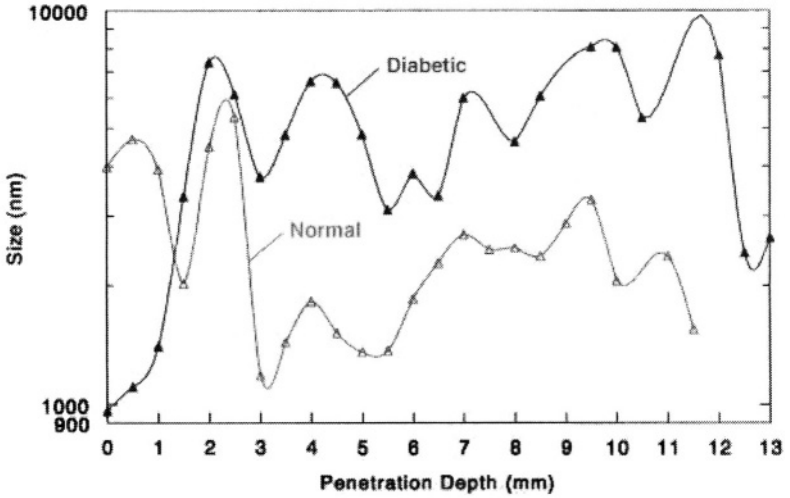

Figure 12. Measurement of diabetic vitreopathy.

Modern photo refractive surgeries, such as LASIK (laser-assisted *in situ* keratomileusis), have become popular to treat corneal refractive errors. The goal of refractive surgery is to sculpt the corneal surface, changing its physical shape. If successful, it will result in the elimination of refractive errors. In ~5% post-LASIK cases patients experience a variety of effects such as haze, glare, star bursts, dry-eye syndrome, and tissue healing issues. At present, no objective methods are available to evaluate quantitatively and non-invasively underlying molecular changes resulting in these corneal abnormalities after a LASIK procedure. McLeod [37], in his editorial, stressed the need for new diagnostic capabilities to better evaluate current refractive surgery outcomes.

Recently QELS concepts discussed above were applied by Ansari *et al.* to the study of cornea as a molecular measure of clarity [38]. In a preliminary study [39], excised but intact bovine eyes were treated with chemicals, cotton swabs, and radial and photo-refractive surgeries. QELS measurements were performed as a function of the penetration depth into the corneal tissue. Topographical maps of corneal refractive power from untreated and treated corneas were also obtained using videokeratoscopy and the results compared.

The findings suggested the potential of QELS in measuring changes in the pre- and post-refractive surgeries. However, the ultimate aim for developing the technique using QELS for clinical applications in early evaluation of corneal complications after LASIK surgeries as well as other

corneal abnormalities has yet to be proven. At the time of this writing, this validation work is being conducted at NEI/NIH.

11.3.7 Environmental Ocular Toxicity

It is a well-known fact that the cornea offers the first line of defense against external stresses. It can, however, be opacified and degenerated (like an onion peel) if exposed to toxic chemicals and biological agents (e.g., mustard gas). Exposure to X-ray and treatment under hyperbaric oxygen can lead to the formation of cataract in the lens. We will discuss these two examples and the ability of QELS to study the oxidative stresses early.

11.3.7.1 Exposure to X-ray

Figure 13 summarizes the effects of X-ray exposure in rabbit eyes as a function of time. Up until three weeks after the initial damage to the lens epithelium cells, few biochemical changes are expected to take place. However these anticipated changes cannot be measured at the present time with conventional methods. From week 3 to 8, some biochemical changes can be measured post-mortem by chemical assay. Matured nuclear cataract is visible at week 9 by photographing the lens. QELS is able to discern subtle differences very early.

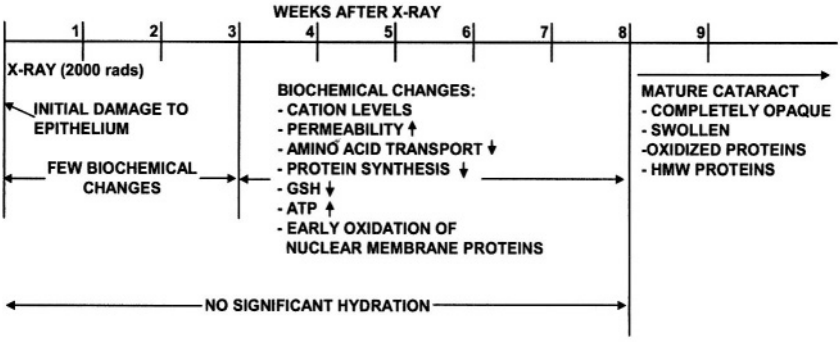

Figure 13. Biochemical effects of X-ray in rabbit eyes (courtesy of Frank Giblin, Ph.D., Oakland University).

The study animals were exposed to X-ray (one time only) at a radiation level of 2000 rads for 15 minutes. The animals were anesthetized with an injection of xylazine (30 mg/Kg) and ketamine (7 mg/Kg). Their eyes were dilated using a 0.5% solution of tropicamide. A laser power of 50 microwatts at a wavelength of 638 nm was used. Each TCF was collected for 5 seconds.

The experiments were conducted at Oakland University under the NIH guidelines on handling and safety of animals.

The QELS experiments were concluded on day 54 after the irradiation. The relative change in the average protein crystallin size is plotted for one normal and one irradiated animal (see Figure 14). Figure 14 is obtained by dividing each measured particle size, using the cumulant analysis method [8], by the mean value calculated from the average of all the values in the control or non-irradiated animal from day 1–54. The size remains constant (within 10 to 15%) in the lens of the control animal (no radiation exposure). However, a significant increase in size can be noted in the experimental (irradiated) animal lens. Between day 1 and day 17 the protein aggregation seems to occur linearly. After a period of 2 to 2.5 weeks, the size increases almost exponentially. The average protein size in the lens of the animal exposed to ionizing X-ray radiation, compared with the control animal, increases by a factor of 2 by day 19, more than factor of 3 by day 31, more than factor of 4 on day 40, and almost by a factor of 7 by day 54. Slit-lamp imaging did not show any evidence of nuclear opacity until day 60.

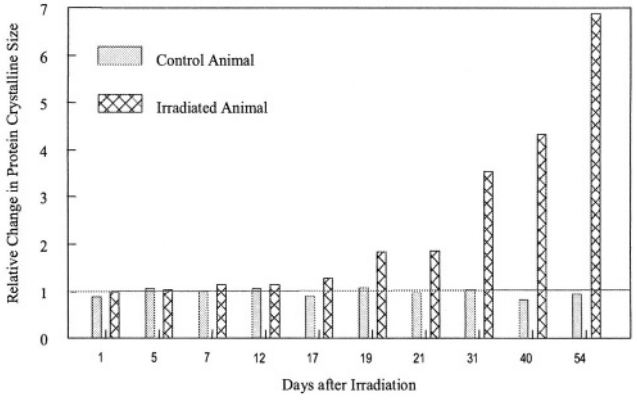

Figure 14. Changes in rabbit lenses post X-ray irradiation measured by QELS.

11.3.7.2 Hyperbaric Oxygen (HBO) Treatment

HBO is commonly used in major hospitals for treating diabetic complications such as poor wound healing due to impaired blood circulation. Palmquist *et al.* have shown that HBO therapy can cause myopia and nuclear cataract [40]. Giblin's group at Oakland University showed HBO to accelerate the insolubilization of crystallins and the loss of cytoskeletal proteins in guinea pig lens nucleus [41]. The qualitative nature of slit-lamp photography does not allow early detection of subtle changes in the lens.

QELS is applied here to study the effects of HBO treatment in guinea pig lenses *in vivo.*

Guinea pigs, initially 18 months old, were treated for up to 86 times with HBO (2.5 atm 100% O_2, 2.5 h, 3x per week). Aged-matched untreated animals were used as controls. The eyes of the animals were analyzed *in vivo* using an integrated static and QELS fiber optic probe at 34, 67, and 83 HBO treatments (3-7 months of treatment). *In vivo* static light scattering (QELS) scans were made at 0.01 mm/sec to obtain the level of scatter along the optical axis of the eye. QELS measurements were made at intervals of 0.1 mm along the 5 mm visual axis from the anterior to the posterior capsules. Each measurement was completed in 5 seconds at a laser (λ= 670 nm) power of 100 μW. Other complementary methods employed in this study include periodic monitoring of the animals with slit-lamp biomicroscopy.

The QELS scans were able to clearly indicate the anatomy and the structure (Figure 15) within the guinea pig eye including the cornea, aqueous, the different regions of the lens, and the vitreous. Lenses from control animals typically showed a low level of scatter throughout the lens. Lenses from experimental animals typically showed an increased level of scatter throughout the lens, particularly in the nucleus. Control lenses showed a single group of proteins with a mean diameter of 50 to 60 nm. Experimental lenses showed two groups of proteins having mean diameters of 400 and 10,000 nm depending upon their location.

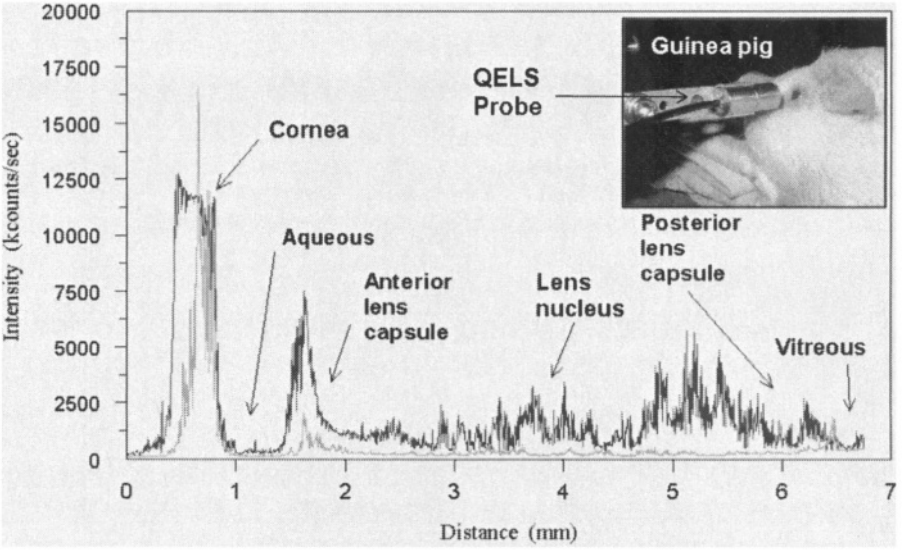

Figure 15. QELS intensity scan showing enhanced light scattering in a guinea pig with HBO exposure (dark line: 67 treatments) compared with no HBO exposure (light line: no treatment) control animal.

11.3.8 Alzheimer's

Frederikse *et al.* [42] at NEI/NIH were the first to give a demonstration of Alzheimer's biology occurring in the lens. Alzheimer's disease (AD) sufferers loose cognitive abilities and thus serious deterioration in the quality of life. In simplistic terms, amyloid proteins forming plaques on the brain tissue leads to development of AD. Currently, these amyloid plaques or deposits can only be studied under a microscope by looking at the brain tissue at autopsy. Frederikse provided evidence of amyloid protein structure in the lens and its association with cataractogenesis [43]. Recently it was suggested by Goldstein *et al.* [44] that amyloid proteins may promote the aggregation of ocular proteins linking the formation of supra nuclear cataract in human lenses to AD. A proof-of-concept experiment was conducted *in vivo* by measuring protein aggregation in the lenses of transgenic mice using NASA's QELS setup. The preliminary results indicated enhanced aggregation in study animals as opposed to controls [4]. This opens up an opportunity for QELS to be tried non-invasively in detailed studies of AD detection and treatments.

11.4 QELS LIMITATIONS

Several things can go wrong in a QELS experiment. A few experimental tips are outlined below to avoid disappointments and artifacts.

11.4.1 Precise Control of Sample Volume

The lens and vitreous being transparent do not have any visible markers. Therefore, in longitudinal studies, reproducibility in repeat patient visits remains a big concern. QELS instrumentation must have the ability to precisely control and sample the same location inside the tissue of interest. The eye movements must be controlled and the subject should remain well fixated during the QELS measurement cycle. In animal experiments, it is not much of a concern because animals can be sedated. However, they should be closely watched since some animals roll their eyes while sedated.

11.4.2 Laser Safety

In QELS ophthalmic applications, the major safety concern is the amount of light exposure to the retina. To minimize the risk of exposure the power levels must be low and the exposure time must be short to satisfy the safety requirements set by ANSI (American National Safety Institute). Current

ophthalmic QELS instruments typically use a laser power of roughly 50-100 microwatts with exposure duration of 5-10 seconds. This makes it several orders of magnitude lower and therefore safer for use in animals and humans. However, every QELS instrument has its own unique optical arrangement for launching and receiving light signals, alignment procedures, and to maintain coherence conditions inside the scattering volume. Therefore extra caution and care must be exercised in calculations for maximum possible exposure (MPE) limits set by ANSI and double checked by FDA to ensure patient safety.

11.4.3 Measurement of Visible Abnormalities

It is tempting to compare the QELS data, especially in clinical practice, with obvious ocular abnormalities. But one should bear in mind that QELS is only suitable for studies of very early ocular abnormalities. It is not suitable to measure visible or mature lens or corneal opacities. Such measurements will introduce artifacts due to multiple scattering of light.

QELS can be used effectively in the determination of accurate particle size in water-based dispersions from transparent to extremely turbid (~7 orders of magnitude higher than the turbidity of water) samples ranging in size from few nanometers to almost a micron [10]. However, such analysis should be avoided in a cataractous eye because of unknown factors such as the changing viscosity. Therefore, it is acceptable to exploit the good dynamic range of QELS to follow a systematic trend as a marker for monitoring early ocular pathology, but due caution must be exercised in data interpretation when dealing with mild to mature pathologies.

11.4.4 Eye Irrigation and Anesthesia in Animal Models

The drying of cornea and appearance of cold cataract, especially in animal measurements, produces artifacts. The corneas should be constantly irrigated (see Figure 16) with saline solutions in between the QELS measurements to avoid corneal dehydration. In general, the body temperature drops in animals under anesthesia. This can cause cold-induced cataract especially in mice and rats. This can be avoided by using a heating pad and keeping the body temperature constant around 37 °C during the QELS experiments.

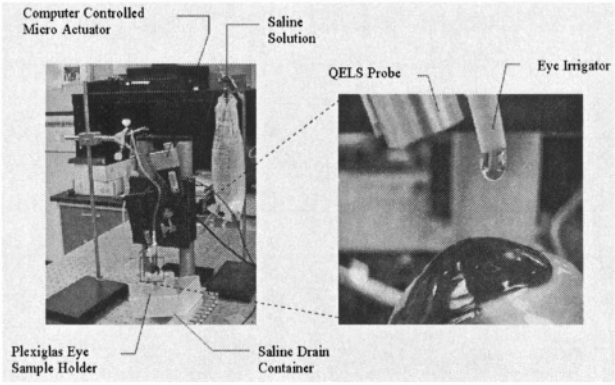

Figure 16. Corneal irrigation system for QELS measurements.

11.5 FUTURE OUTLOOK (OPHTHALMIC TELE-HEALTH)

The effects of space travel on the human body are similar to those of aging here on earth, e.g., osteoporosis and cataract. The absence of gravity in space affects human physiology and the development of cataract in astronauts is linked to the radiation exposure even in low earth orbit missions, e.g., on-board the space shuttle and space station orbiters [45, 46]. This risk can be substantial if humans plan to travel to Mars [47]. A head-mounted goggles-like device with a suite of non-invasive optical technologies to ensure the mission safety and the health of astronauts is being developed in the author's laboratory at NASA. QELS is one technique among several others to be integrated in this device that may play an important role in monitoring ocular health remotely and non-invasively [48]. A prototype head-mounted QELS system is shown in Figure 17 for this purpose.

11.6 CONCLUSION

In the present economic climate, preventive medicine seems to be the direction of the future. Thus the early detection of ocular diseases long before the appearance of clinical symptoms to help find medical cures is the most desired goal. The new developments in QELS ophthalmic research seem promising and indicate good potential to help achieve this goal.

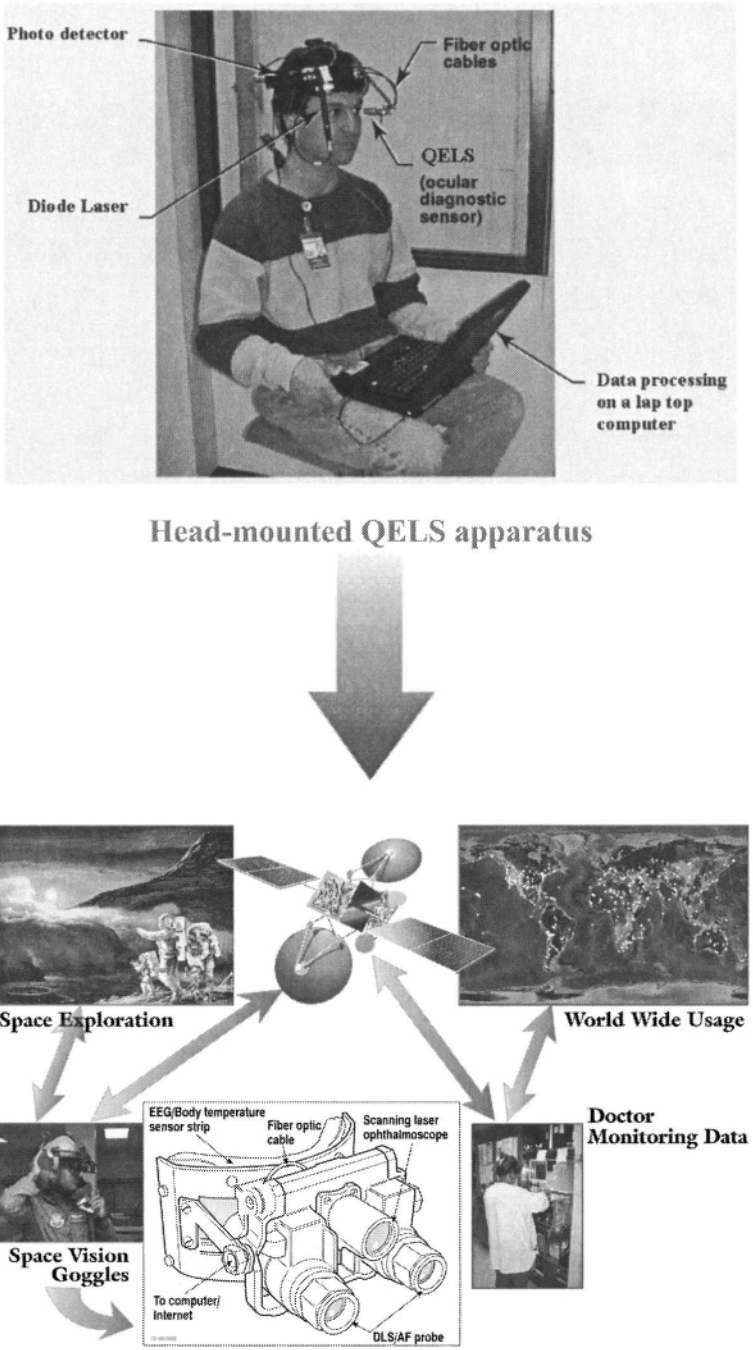

Figure 17. Present and future: Celestial and terrestrial ophthalmic tele-health monitoring (the person pictured on top is James F. King of the author's laboratory).

ACKNOWLEDGEMENTS

The author would like to thank Dr. Valery Tuchin for inviting him to write this chapter. He is also indebted to many colleagues and collaborators with whom experiments reported in this chapter were conducted. These include Sam Zigler and Manuel Datiles of NEI/NIH in Bethesda, MD for animal and clinical cataract studies, Luigi Rovati of the University of Modena in Italy for glaucoma studies, John Clark of the University of Washington in Seattle for pantethine treatment, Frank Giblin of the Oakland University in MI for guinea pig HBO and rabbit X-ray studies, Michelle Chenault of FDA, Rockville Pike in MD for studies on diabetic sand rats, Jerry Sebag of Doheny Eye Institute in Los Angeles, CA for vitreopathy studies, Leo Chylack and Lee Goldstein of Harvard University in Boston for proof-of-concept Alzheimer's experiments, and Kwang Suh and Jim King of the author's laboratory for new instrument development. The support under NASA-NIH and NASA-FDA Interagency Agreements on the development and use of QELS in ophthalmology and funding from the John H. Glenn Biomedical Engineering Consortium for the bio-astronautics research is greatly appreciated.

DISCLAIMER

The views and opinions expressed in this article are those of the author's and not those of the National Aeronautics and Space Administration (NASA) or the United States Government.

REFERENCES

1. B. Chu, *Laser Light Scattering: Basic Principles and Practice* (Academic Press, New York, 1991).
2. T. Tanaka and G.B. Benedek, "Observation of protein diffusivity in intact human and bovine lenses with application to cataract," *Invest. Ophthal. Vis. Sci.* **14** (6), 449–456 (1975).
3. S.E. Bursell, P.C. Magnante, and L.T. Chylack, *"In vivo* uses of quasi-elastic light scattering spectroscopy as a molecular probe in the anterior segment of the eye," *Noninvasive Diagnostic Techniques in Ophthalmology,* B.R. Masters ed. (Springer-Verlag, New York, 1990) 342-365.
4. R.R. Ansari, "Ocular static and dynamic light scattering: A non-invasive diagnostic tool for eye research and clinical practice," *J. Biomed. Opt.* **9**(1) (2004).
5. Vision Problems in the U.S.: Prevalence of Adult Vision and Age-Related Eye Disease in America, National Eye Institute (National Institutes of Health) and Prevent Blindness America (2002). Also available at www.usvisionproblems.org.

6. G.W. Tate and A. Safiz, "The slit lamp, history, principle, and practice," *Duane's Clinical Ophthalmology* **1** (59), W. Tasman and E.A. Jaeger ed. (J.B. Lippincott Co, Philadelphia, PA, 1992).
7. R.H. Stock and W.H. Ray, "Interpretation of photon correlation data: A comparison of analysis methods,*"J. Polym. Sci.* **23**, 1393-1147 (1985).
8. H.S. Dhadwal, R.R. Ansari , and M.A. Dellavecchia, "Coherent fiber optic sensor for early detection of cataractogenesis in a human eye lens," *Opt. Eng.* **32** (2), 233-238 (1993).
9. L. Rovati, F. Fankhauser II, and J. Rick, "Design and performance of a new ophthalmic instrument for dynamic light scattering in the human eye," *Rev. Sci. Instrum.* **67** (7) 2620 (1996).
10. R.R. Ansari, K.I. Suh, A. Arabshahi, W.W. Wilson, T.L. Bray, and L.J. DeLucas, "A fiber optic probe for monitoring protein aggregation, nucleation and crystallization," *J. Crystal Growth* **168**, 216-226 (1996).
11. L. Pollonini, L. Rovati, R.R. Ansari, "Dynamic light scattering and natural fluorescence measurements in healthy and pathological ocular tissues," *SPIE Proc.* **4611,** 213-219 (2002).
12. M.B.Datiles III and R.R. Ansari, "Clinical evaluation of cataracts," *Duane 's Clinical Ophthal.* **73B**, W. Tasman, and E. Jaeger eds. (Lippincott Co. Inc., Philadelphia, PA, 2003).
13. M.B. Datiles III, R.R. Ansari, and G.F. Reed, "A Clinical study of the human lens with a dynamic light scattering device," *Exp. Eye Res.* **74** (1), 93-102 (2002).
14. A. Foster, "Cataract- A global perspective: output, outcome and outlay," *Eye* **3**, 449-53 (1999).
15. C. Kupfer, "Bowman lecture. The Conquest of Cataract: A Global Challenge," *Trans. Ophthal. Soc.* **104** (1), 1-10 (1984).
16. J.J. Harding, "Drugs," *Aging* **18** (7), 473-86 (2001).
17. G.B. Benedek, J. Pande, G.M. Thurston, and J.L. Clark, "Theoretical and experimental basis for the inhibition of cataract," *Prog. Retin. Eye Res.* **18**, 391-402 (1999).
18. G.M. Thurston, D.L. Hayden, P. Burrows, J.I. Clark, V.G. Taret, J. Kandel, M. Courogen, J.A. Peetermans, M.S. Bowen, D. Miller, K.M. Sullivan, R. Storb, H. Stern, and G.B. Benedek, "Quasielastic light scattering study of the living human lens as a function of age," *Curr. Eye Res.* **16** (3), 197–207 (1997).
19. H. Dhadwal and J. Wittpen, *"In vivo* dynamic light scattering characterization of the human lens: cataract index," *Curr. Eye Res.* **20** (6), 502-510 (2000).
20. R.R. Ansari, J.I. Clark, J.F. King, and T. Seeberger, "Early detection of cataracts and response to therapy with non-invasive static and dynamic light scattering," *Proc. SPIE* **4951**,168-176(2003).
21. J.I. Clark, J.C. Livesey, and J.E. Steele, "Delay or inhibition of rat lens opacification using pantethine and WR-77913," *Exp. Eye Res.* **62**, 75-85 (1996).
22. F.A. Bettelheim, R.R. Ansari, Q-F. Cheng, and J.S. Zigler Jr., "The mode of chaperoning of dithiothreitol-denatured alpha lactalbumin by alpha crystallin," *Biochem. Biophys. Res. Commun.* **261**, 292-297 (1999).
23. J.S. Zigler Jr., P. Russel, S. Tumminia, C. Qin, and C.M. Krishna, "Hydroxylamine compositions for the prevention or retardation of cataracts," U.S. Patent 6,001,853 (Dec. 14, 1999).
24. J.S. Zigler Jr., C. Qin, T. Kamiya, M.C. Krishna, Q. Cheng, S. Tumminia, and P. Russell, "Tempol-H inhibits opacification of lenses in organ culture," *Free Radical Biol. Med.,* in press (2003).

25. V.M. Chenault, M.N. Ediger, and R.R. Ansari, *"In vivo* assessment of diabetic lenses using dynamic light scattering," *Diab Tech & Ther.* **4** (5), 651-659 (2002).
26. R.R. Ansari, K.I. Suh, S. Dunker, N. Kitaya, and J. Sebag, "Quantitative molecular characterization of bovine vitreous and lens with non-invasive dynamic light scattering," *Exp. Eye Res.* **73**, 859-866 (2001).
27. L. Rovati, F. Fankhauser II, F. Docchio, and J. Van Best, "Diabetic retinopathy assessed by dynamic light scattering and corneal autofluorescence," *J. Biomed. Opt.* **3** (3), 357-363 (1998).
28. R. Klein, B.E.K. Klein, and S.E. Moss, "Visual impairment in diabetes," *Ophthalmol.* **91**, 1-9 (1984).
29. M. Brownlee, "The role of nonenzymatic glycosylation in the pathogenesis of diabetic angiopathy," *Complications of Diabetes Mellitus,* B. Drazin, S. Melmed, and LeRioth eds. (Alan R. Liss, New York, 1989), 9-17.
30. J. Sebag, "Abnormalities of human vitreous structure in diabetes," *Graef. Arch. Clin. Exp. Ophthalmol.* **231**, 257-260 (1993).
31. J. Sebag "Diabetic vitreopathy [guest editorial]," *Ophthalmol.* **103**, 205-206 (1996).
32. J. Sebag, *The Vitreous – Structure, Function, and Pathobiology* (Springer-Verlag, New York, 1989).
33. J. Sebag, "Age-related changes in human vitreous structure," *Graef. Arch. Clin. Exp. Ophthalmol.* **225**, 89-93 (1987).
34. J. Sebag, R.R. Ansari, S. Dunker, and K.I. Suh, "Dynamic light scattering of diabetic vitreopathy," *Diabetes Technology & Therapeutics* **1** (2), 169-176 (1999).
35. J. Aguayo, B. Glaser, A. Mildvan, H.M. Cheng, R.G. Gonzalez, and T. Brady, "Study of the vitreous liquefaction by NMR spectroscopy and imaging," *Invest. Ophthal. Vis. Sci.* **26**, 692-697 (1985).
36. C.W. Oyster, *The Human Eye Structure and Function* (Sinauer Associates, Inc., Sunderland, MA, 1999).
37. S.D. McLeod, "Beyond Snellen acuity: The assessment of visual function after refractive surgery," *Arch. Ophthalmol.* **119**, 1371-1373 (2001).
38. L.B. Sabbagh, "Dynamic light scattering focuses on the cornea," *Rev. Ref. Surgery.* (5) 28-31 (2002).
39. R.R. Ansari, A. K. Misra, A.B. Leung, J.F. King, and M.B. Datiles III, "Noninvasive evaluation of corneal abnormalities using static and dynamic light scattering," *Proc. SPIE* **4611**, 220-229 (2002).
40. B.M. Palmquist, B. Philipson, and P.O. Barr, "Nuclear cataract and myopia during hyperbaric oxygen therapy," *British J. Ophthalmol.* **68**, 113-117 (1984).
41. V.A. Padgaonkar, L.R. Lin, V.R. Leverenz, A. Rinke, V.N. Reddy, and F. J. Goblin, "Hyperbaric oxygen *in vivo* accelerates the loss of cytoskeletal proteins and MIP26 in guinea pig lens nucleus," *Exp. Eye. Res.* **68**, 493-504 (1999).
42. P.H. Frederikse, D. Garland, J.S. Zigler, and J. Piatigorsky, "Oxidative stress increases production of beta-amyloid precursor protein and beta-amyloid (A beta) in mammalian lenses, and A beta has toxic effects on lens epithelial cells, *J. Biol. Chem.* **271** (17), 10169-10174(1996).
43. P.H. Frederikse, "Amyloid-like protein structure in mammalian ocular lenses," *Curr. Eye Res.* **20** (6), 462-468 (2000).
44. L. Goldstein, J. Muffat, R. Cherny, K. Faget, J. Coccia, F. Fraser, C. Masters, R. Tanzi, L. Chylack Jr., and A. Bush, "αBeta peptides in human and amyloyd-bering transgenic mouse lenses: implications for alzheimer's disease and cataracts," *Invest. Ophthalmol. Vis. Sci.* **42** (4) ARVO abstract 1614 (2001).

45. F.A Cucinotta, F.K. Manuel, J. Jones, G. Izard, J Murrey, B. Djojonegro, and M. Wear, "Space radiation and cataracts in astronauts." *Radiation Research* **156** (5), 460-466 (2001)
46. Z.N. Rastegar, P. Eckart, and M. Mertz, "Radiation-induced cataract in astronauts and cosmonauts," *Graef. Arch. Clinl Exp. Ophthalmol.* **240** (7), 543-7 (2002).
47. R.R. Ansari, L. Rovati, and J. Sebag, "Non-invasive and remote detection of cataracts during space exploration with dynamic light scattering," *Ophthalmic Technologies XI* **4245,** F. Manns, P.G. Soderberg, and A. Ho, eds. (SPIE, Bellingham, 2001) 129-134.
48. R.R. Ansari, L. Rovati, and J. Sebag, "Celestial and terrestrial tele-ophthalmology: A health monitoring helmet for astronauts/cosmonauts and general public use," *Ophthalmic Technologies XI* **4245,** F. Manns, P.G. Soderberg, and A. Ho, eds. (SPIE, Bellingham, 2001), 177-185.

Chapter 12

MONTE-CARLO SIMULATIONS OF LIGHT SCATTERING IN TURBID MEDIA

Frits F.M. de Mul
University of Twente, Department of Applied Physics, POBox 217, 7500 AE Enschede, the Netherlands

Abstract: The physics behind the simulation program developed in our group is explained. The various options for light transport and scattering, reflection and refraction at boundaries, light sources and detection, and output are described. In addition. some special features, like laser Doppler velocimetry, photoacoustics and frequency-modulation scattering, are described.

Key words: light scattering, light transport, absorption, refraction, polarization, detection, layers, photoacoustics, frequency modulation scattering

12.1 INTRODUCTION

In the past decade, much effort has been devoted to the elucidation of the optical properties of turbid media, especially tissue, from human and animal origin. This is worthwhile since these properties can reveal data and conclusions about the physiological condition of the tissue. These optical properties are the scattering and absorption characteristics, both as a function of position in the tissue and as a function of time, *e.g.,* after administration of drugs, hydrogenation or temperature treatment. In addition, the spectroscopic response of the tissue (*e.g.,* Raman-spectroscopy, induced or auto-fluorescence, absorption spectroscopy) can be of interest to obtain useful information.

Typical experiments to extract values for the optical properties of tissue are: measuring the response of the tissue upon a stimulus from the outside. In the optical case, this mostly corresponds with measuring the properties of

light (*e.g.,* intensity) or of another suitable variable (*e.g.,* sound, with photoacoustics) that will emerge from the tissue, as a function of the distance from the point of entrance of the light, or will pass through the tissue and eventually will appear at the backside of the sample.

In the case of "light in – light out" several interesting methods have been developed in addition to simple intensity measurements. Among those are "frequency-modulation" of the light, enabling to measure the phase delay upon passage through the sample, or "optical coherence tomography," where single-scattered light is detected interferometrically.

In order to extract the optical properties from the measured data, it is necessary to have suitable analytical models relating those properties with general ideas about the physics of the light transport in tissue. The best models for this purpose rely on the radiative transfer equation (RTE; also known from disciplines as neutron physics) and the diffusion approximation (DA) derived from it [1,2,3]. The RTE describes the light transport in turbid media in the form of an integro-differential equation of the (place-time-dependent) radiance, arising from well-defined sources and subject to scattering and absorption. The DA takes into account that in tissue most scattering is predominantly in forward direction. Then the light fluence is divided into two contributions: an isotropic term and a term describing the forward contribution. Several authors [4-10] have published sophisticated models for two- and even three-layered samples. For inhomogeneous samples, the models soon become very complex and difficult to apply, and the number of variables to be used in fitting to the experimental data will soon grow beyond manageability.

Therefore, it turns out to be very difficult to produce tractable analytical models of the transport of light in those media, necessary to extract values for the optical properties from experimental data, especially when those media are more complex than homogeneous semi-infinite layers. This is the case with two- or three layered samples, or when deviant structures, like vessels or plates, are present in those layers. Especially in those cases, Monte-Carlo simulations of the light transport will be of help.

In Monte-Carlo simulations, a completely different approach is followed. The light transport in tissue is described in the form of separate photons traveling through the sample. On its way, the photon might be scattered at (or in) particles, by which the direction of the photon is changed, or the photon is absorbed. The scattering phenomenon will be determined by suitable angle-dependent scattering functions. When a boundary between two layers, or between the sample and the surrounding medium, or between an internal structure and the surrounding layer, is encountered, the photon might be reflected or refracted. This is determined by the well-known Fresnel relations. In between these events, the photon will propagate, and the

optical mean free path in that part of the sample will determine the length of the propagation path. The actual length of the contributions to the path, the angles of scattering, the choice between scattering and absorption, and between reflection and refraction, are determined by random number-based decisions.

Some extra features can be applied to the photons. For instance, photons can be thought of as scattering at particles at rest or at moving particles. This effect will cause a Doppler shift in the frequency of the photons, which can be registered. Afterwards from the Doppler shift distribution of all suitably detected photons the frequency power distribution can be derived. Several models are present for this velocity shift: unidirectional or random flow, various flow profiles and so on. Another option is to use as the light source not a beam impinging from the outside world, but a photon absorption distribution inside the sample. In this way, fluorescence or Raman scattering can be mimicked.

When recording the path of the photons through the sample, one might deduce the path length distribution, and from that the time-of-flight distribution. The latter can be used to predict the distributions of phase delays and modulation depths encountered when performing frequency-modulation experiments.

Further, the distribution of positions where photons were absorbed can be used as the distribution of sources for calculating the photoacoustic response, to be detected using suitable detector elements (or groups of elements, to take interference effects into account) at the surface of the sample.

With these applications in mind, we developed [11,12] our Monte-Carlo light simulation package.

12.2 GENERAL OUTLINE OF THE PROGRAM

We decided to build the package in a modular and self-explaining form, in the sense that all necessary input to run the simulations can be produced within the program itself. In addition, the output – in the form of parameter plots and other visualisations – can be obtained using the same program.

In overview, the program package consists of following parts:

- Calculation of angle-dependent scattering functions for all types of particles;
- Definition of the light source, either a pencil beam or a broad divergent beam or an internal source;
- The sample system, consisting or one or more layers with different contents, with different optical characteristics and velocity profiles;

- The contents may consist of (arrays of) cylinders, spheres, cones, rectangular blocks, and mirrors, see Figure 1;
- Definition of the detection system, consisting of a poly-element detection window, and of its numerical aperture;
- Definition of the calculation mode, *e.g.,* reflection or transmission, or absorption, or a combination of those;
- The simulation part, in which a preset amount of photons is injected in the sample and followed along their paths, until either detection or absorption;
- The analysing part, in which parameter plots can be produced and statistics can be calculated;
- Extra features, like laser Doppler flowmetry, photoacoustics and frequency modulation.

These parts will be detailed in following sections.

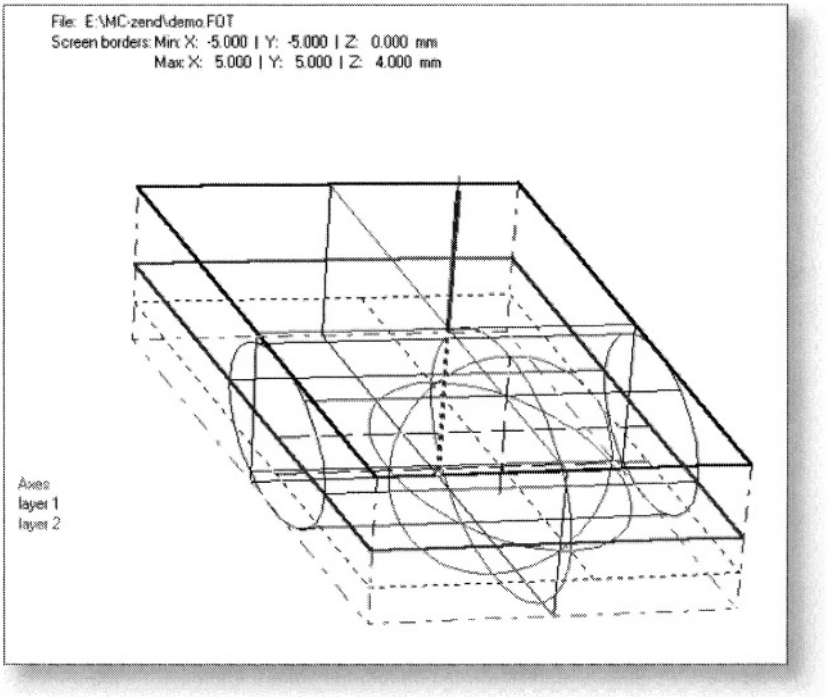

Figure 1. Structure plot of a two-layer system with a horizontal cylindrical tube and a sphere (see section 12.2), filled with various concentrations of scattering/absorbing particles. Laser light (here diverging beam) injected around Z-axis.

12.3 TRANSPORT ALGORITHMS

In order to describe the transport of photons through the sample, one needs algorithms for the various events that the photon may encounter. Those are: scattering or absorption, reflection or refraction at boundaries, and detection. In addition, a mechanism accounting for the destruction of irrelevant photons *(e.g.* photons that have travelled extremely far from the detection window) should be available.

We start with defining the basic optical properties relevant for this problem:

- σ_{sv} : scattering cross section [μm^2] of particle type v ;
- σ_{av} : absorption cross section [μm^2] of particle type v ;
- σ_{tv} : total cross section = $\sigma_{sv} + \sigma_{av}$ [μm^2] of particle type v ;
- a_v : albedo (= $\sigma_{sv} / \sigma_{tv}$) of particle type v ;
- c_{lv} : concentration [particles/mm^{-3}] of particle type v in layer l (or "block" l);
- μ_{sl} : scattering coefficient [mm^{-1}] of layer l (or "block" l);
- μ_{al} : absorption coefficient [mm^{-1}] of layer l (or "block" l);

All internal structures in a layer (vessels, tubes, blocks, mirrors, spheres, cones...) will further be denoted as "blocks".

So the probability f_{lv} to find a particle of type v in layer (or block) l is

$$f_{lv} = \frac{c_{lv}\sigma_{tv}}{\sum_{v} c_{lv}\sigma_{tv}} \tag{1}$$

There are two basic algorithms for handling non-zero absorption in layers or particles. Frequently the probability of absorption (given by $1 - a_v$) is taken into account as a "weight factor" for the photon. The cumulative effect of applying these subsequent factors at each scattering event will reduce its overall weight in calculating averages of relevant variables (such as intensity) over a set of emerged photons. An example is the work of Wang and Jacques [13]. An advantage is that no photons will be lost by absorption, which can be of importance when the absorption is relatively strong.

Another algorithm does not make use of weight factors, but applies a "sudden death"-method: the photon is considered to be completely absorbed at once, and will thus be removed from the calculation process. This method might be a bit more time consuming, especially when absorption is not very low in a relative sense, but it offers the advantage to study the positions where the photons actually are absorbed. In this way extra features like photoacoustics or fluorescence response can be studied.

In view of this option, we have chosen for the second method. The general laboratory coordinate system is chosen as shown in Figure 2.

12.3.1 Propagation

Here we will describe the algorithm used for propagation. Also the correction to be made upon crossing an interface (between different layers, or between a layer and a "block", or between a layer or block and the outside world) will be handled.

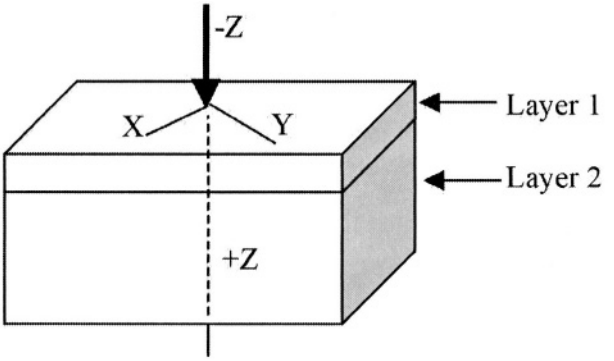

Figure 2. The laboratory coordinate system. The +Z-axis is chosen as pointing inward. The arrow indicates the default direction of a pencil laser beam.

We may write down the average translation distance for a photon in a layer or block l with scattering particles of varying type, in the case of no absorption by that layer or block itself, as

$$L_l = \frac{1}{\sum_v c_{lv}\sigma_{tv}}. \tag{2}$$

From this we deduce the expression for calculating the actual path length Δp:

$$\Delta p = -L_l . \ln(1 - R), \tag{3}$$

where R is a random number ($0 \leq R < 1$) and we have used for the probability f_{sl} to arrive at a path length Δp:

$$f_{sl} = 1 - \exp(-\Delta p / L_l). \tag{4}$$

The expression with 1n (1-*R*) is chosen to avoid the singularity in case *R* should equal 0. However, this path might end prematurely when a boundary at an interface is met. In this case we can geometrically calculate a path fraction f_p, using the distance between the previous event point and the intersection point of the path with the interface, and define the "effective path" Δp_{eff}, by

$$\Delta p_{eff} = f_p . \Delta p \,. \tag{5}$$

In case $f_p < 1$, the path will partially stretch out into the medium at the other side of the interface. When dealing with this part of the path, it should be kept in mind that it has to be corrected in length according to the mean free path for the photons in the two media. See below for a full account.

Now we can define the probability f_{al} for absorption by the medium l (layer or block) before the photon has reached the end of path Δp_{eff}:

$$f_{al} = 1 - \exp(-\mu_{al} . \Delta p_{eff}) \,. \tag{6}$$

This probability will lie between 0 and 1. Now we choose a fresh random number *R*. There are two possibilities:

- If this *R* is smaller than f_{al}, then absorption has occurred during path Δp_{eff}.
- It this is not the case, then absorption will occur within the particle at the end of path Δp_{eff} when

$$R < 1 - a_{vl} \,, \tag{7}$$

where *R* again is a fresh random number. If equation 7 is not fulfilled, then the photon will be scattered.

Since we handle the absorption by the particles in the medium as taking place within the particles themselves, and the absorption by the medium itself separately, we can define the "average translation length" $L_{trans,l}$ for medium l:

$$L_{trans,l} = \left[\mu_{al} + \sum_v c_{lv} \sigma_{sv} \right]^{-1} , \tag{8}$$

and the "average absorption length" $L_{abs,l}$ caused by the medium and the scatterers in that medium:

$$L_{abs,l} = \left[\mu_{al} + \sum_v c_{lv} \sigma_{av} \right]^{-1} \,. \tag{9}$$

Now we can correct equation 3 and subsequent expressions for absorption, and find for the path with length Δp:

$$\Delta p = -L_{trans,1}.\ln(1-R)\,. \tag{10}$$

In a previous paper [14] we discussed two equivalent algorithms to determine the remaining path length after crossing an interface. In Figure 3 we present a view of a running simulation in a sample with two layers and two "blocks".

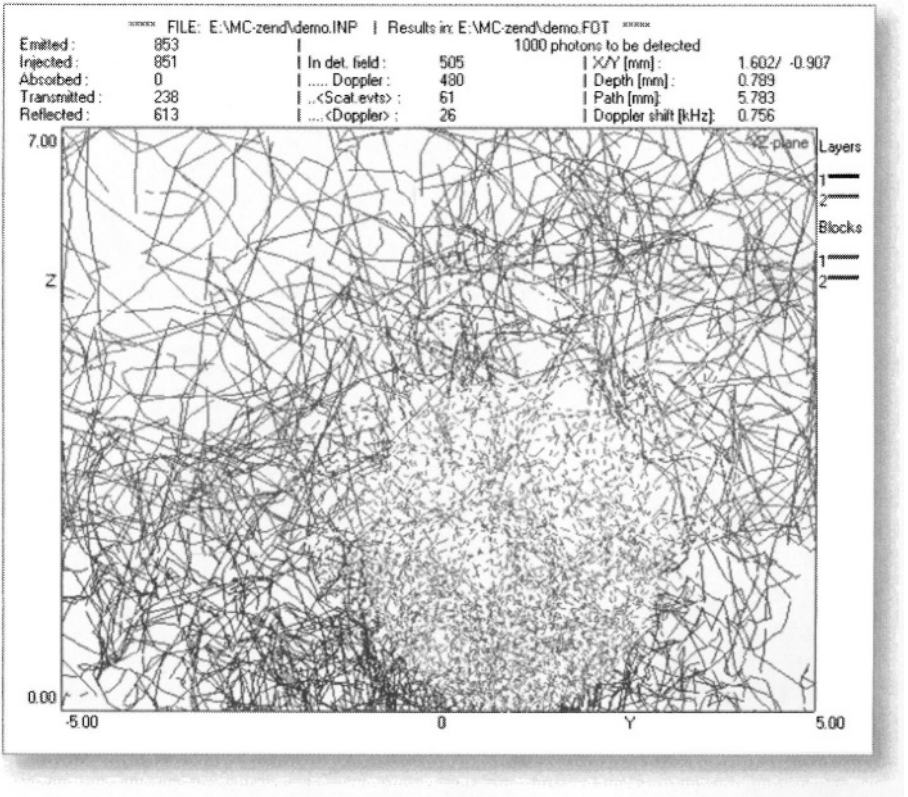

Figure 3. Running graphics of the simulation process of the structure of figure 1. View in YZ-plane. Photons entering around pos (0,0,0). The tube (X-direction) and sphere can be seen.

12.3.2 Scattering

In case the photon is not absorbed during or at the end of a translation step, the photon will be scattered. We define the angle θ as the polar angle of scattering, with the direction of the previous translation step as the Z-axis of the local coordinate system. For natural (unpolarized) light, the X-axis can be chosen at random in the plane perpendicular to the Z-axis (see Figure 4). For polarized light, the directions of the X- and Y-axes are determined by the polarization state of the incoming photon.

The probability of scattering to the direction given by the angles θ and φ is described by the *scattering function* $p(\theta,\varphi)$. This function is normalized in such a way that the total scattering over the whole 4π solid angle is unity:

$$\int_0^{2\pi} d\varphi \int_0^{\pi} d\theta . p(\theta,\varphi)\sin\theta = 1 . \tag{11}$$

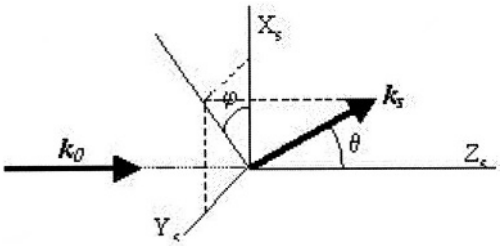

Figure 4. Basic scattering geometry in the "scattering system" (subscript *s*). The incoming and scattered wavevectors are denoted by k_0 and k_s, respectively. $|k| = 2\pi/\lambda$, with $\lambda = \lambda_{\text{vacuum}} / n$ (n = refractive index of the medium).

For the scattering function, several models are available: Dipole- or Rayleigh-scattering, Rayleigh-Gans scattering, Mie scattering, isotropic or peaked-forward scattering. These scattering functions have been described in many textbooks. We refer here to the standard books of Van de Hulst [15]. They will be dealt with in detail in section 12.4.

The standard method of determining the scattering angles θ and φ is as follows:

- The azimuthal angle φ is given by :

$$\varphi = R.2\pi \tag{12}$$

- For the polar angle θ a normalised cumulative function $C(\theta,\varphi)$ is constructed:

$$C(\theta,\varphi)=\frac{C'(\theta,\varphi)}{C'(\pi,\varphi)} \text{ with } C'(\theta,\varphi)=\int_0^{\theta} p(\theta',\varphi).\sin\theta'.d\theta', \qquad (13)$$

and the angle θ is obtained by taking a fresh random number R and determining the angle for which

$$C(\theta,\varphi)=R\,. \qquad (14)$$

The determination of θ can be done by interpolation procedures or by constructing the inverse cumulative function, *e.g.,* using a polynomial approximation. However, as we will see in section 12.4, most relevant scattering functions decrease sharply for small angles, and then a simple polynomial approximation will not suffice. Since these small angles will occur frequently, an interpolation procedure will be more accurate (in the program, we have adopted this option).

In case polarization effects have to be taken into account, the choice of the angles θ and φ is coupled to the polarization state of the photon. We will deal with polarization in subsection 12.3.5.

In order to connect the local "scattering coordinate frame" with the "laboratory coordinate frame", we use Figure 5.

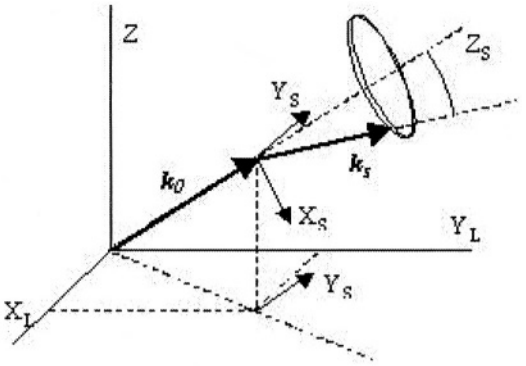

Figure 5. Relation between the laboratory frame (subscript L) and the local scattering frame (subscript S). The circle indicates the set of possible vector directions for fixed θ and random φ.

The connection between the S-system and the L-system is constructed in three steps:

$$(1)\ z_S = \frac{k_0}{|k_0|} \quad ; \quad (2)\ y_S = \frac{z_L \times z_S}{|z_L \times z_S|} \quad ; \quad (3)\ x_S = \frac{y_S \times z_S}{|y_S \times z_S|} \tag{15}$$

This means that

$$k_S = |k_S| \left[x_S \cos\varphi . \sin\theta + y_S \sin\varphi . \sin\theta + z_S \cos\theta \right]. \tag{16}$$

The length of k_S is determined by the local wavelength, as $2\pi/\lambda_{local}$. With this, the scattered wavevector is fixed in the laboratory frame. In the program the unit vector, along the scattered wave vector, and expressed in the laboratory frame vectors, is updated at each event in which the photon direction is changed.

12.3.3 Boundaries

Since the program allows for insertion of special structures, like tubes, spheres, mirrors and cones in the layer system, we have to deal with boundaries at flat surfaces (like those between layers) and at curved surfaces.

(a) Flat Surfaces Perpendicular to the Z-axis

In this situation, the calculation of reflection or refraction angles is relatively simple: according to Snell's Law:

$$\frac{\sin\theta_2}{\sin\theta_1} = \frac{n_1}{n_2} \quad , \tag{17}$$

where θ and n denote the angles with the surface normal and the refractive indices in the two media 1 and 2 respectively. See Figure 6.

The fraction of reflected light is given by the Fresnel relations:

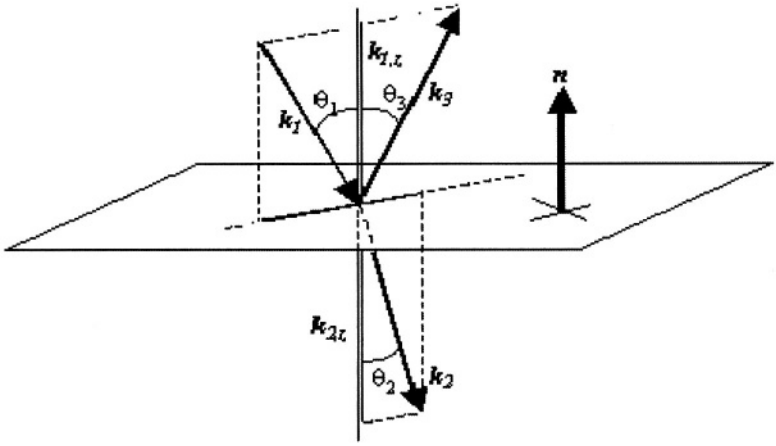

Figure 6. Reflection or refraction at interfaces. Here the k-vectors denote unit vectors, and n is the unit vector perpendicular to the surface. $\theta_3 = \theta_1$.

$$
\begin{aligned}
R_F(\theta_1) &= \left(\frac{n_1 - n_2}{n_1 + n_2}\right)^2 \quad if \quad \theta = 0 \\
&= \tfrac{1}{2}\left[\frac{\sin^2(\theta_1 - \theta_2)}{\sin^2(\theta_1 + \theta_2)} + \frac{\tan^2(\theta_1 - \theta_2)}{\tan^2(\theta_1 + \theta_2)}\right] \quad if \quad 0 < \theta_1 < \theta_c \\
&= 1 \quad if \quad \theta_1 > \theta_c; \quad with \quad \theta_c = \arcsin\left(n_2 / n_1\right)
\end{aligned}
\tag{18}
$$

Reflection takes place if a fresh random number $R < R_F(\theta_1)$, and refraction otherwise.

New unit vectors are calculated according to (see Figure 4):

$$
\begin{aligned}
\boldsymbol{k}_{1,z} &= \cos\theta_1\,(-\boldsymbol{n})\,; & \boldsymbol{k}_{1,\perp} &= \boldsymbol{k}_1 - \boldsymbol{k}_{1,z}\,; \\
\boldsymbol{k}_{2,z} &= \cos\theta_2\,(-\boldsymbol{n})\,; & \boldsymbol{k}_{2,\perp} &= (n_1/n_2)\,\boldsymbol{k}_{1,\perp}\,; \\
\boldsymbol{k}_{3,z} &= -\,\boldsymbol{k}_{1,z}\,; & \boldsymbol{k}_{3,\perp} &= \boldsymbol{k}_{1,\perp}\,.
\end{aligned}
\tag{19}
$$

Here the symbol $\perp$ stands for the vector component parallel to the surface.

(b) Curved Surfaces, or Flat Surfaces not Perpendicular to the Z-axis

For the general case of interfaces with a curved surface, at first a new coordinate frame is constructed as follows (see Figures 6 and 7):

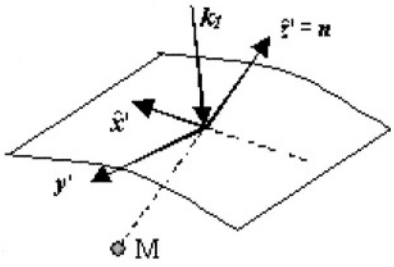

Figure 7. Coordinate frame at curved surfaces. Vectors x' and y' are directed along the surface. M is the center point (or the point where the normal vector n intersects the symmetry axis) of the structure (tube, sphere, etc…).

$$\hat{z}' = \boldsymbol{n}$$

$$\hat{\boldsymbol{y}}' = (\boldsymbol{k}_1 \times \boldsymbol{n}) / |\boldsymbol{k}_1 \times \boldsymbol{n}| \quad . \tag{20}$$

$$\hat{\boldsymbol{x}}' = \hat{\boldsymbol{y}}' \times \hat{\boldsymbol{z}}'$$

Then the new vectors for refraction and reflection are found to be

$$\begin{aligned} &\boldsymbol{k}_2 = k_{1,x}\hat{\boldsymbol{x}}' - k_{1,z}\hat{\boldsymbol{z}}' \quad ; \quad \boldsymbol{k}_3 = k_{2,x}\hat{\boldsymbol{x}}' + k_{2,z}\hat{\boldsymbol{z}}' \\ &\text{with} \quad k_{1,z} = -k_1 . \sin\theta_1 \quad ; \quad k_{1,z} = -k_1 . \cos\theta_1 \quad ; \\ &\qquad k_{2,x} = -k_1 \sin\theta_2 \quad ; \quad k_{2,z} = \sqrt{k_1^{\,2} - k_{2,x}} \quad ; \end{aligned} \tag{21}$$

and θ_1 and θ_2 are given by Snell's relation (equation 17).

We will now deal with the geometry of how to determine the intersection points and normal vectors with special cases of curved surfaces.

(c) An Oblique Cylinder

See Figure 8. The point O' represents a point on the symmetry axis. Vector $\boldsymbol{b}$ is the direction vector (unit vector) and vector $\boldsymbol{r}$ points to the surface points.

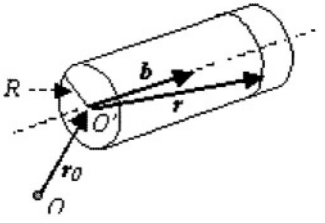

Figure 8. Vectors for an oblique cylinder. R is the radius and $\boldsymbol{b}$ is the direction vector, $\boldsymbol{r}$ directs to a point at the surface.

The general equation for such a cylinder is

$$\left| \boldsymbol{r} - (\boldsymbol{r} \bullet \boldsymbol{b})\, \boldsymbol{b} \right| = R\,, \tag{22a}$$

which in fact is a quadratic equation in the coordinates of the cylinder wall points:

$$\left(x^2 + y^2 + z^2\right) - \left(x b_x + y b_y + z b_z\right)^2 = R^2\,. \tag{22b}$$

The vector expression between the absolute bars represents the direction of the normal vector on the surface at point $\boldsymbol{r}$.

Let vectors $\boldsymbol{p_0}$, $\boldsymbol{p}$ and $\boldsymbol{\Delta p}$ denote the "old", "new" position of the photon, $\boldsymbol{\Delta p} = \boldsymbol{p} - \boldsymbol{p_0}$ the path length vector, as determined in subsection 12.2.2, respectively, and $\boldsymbol{p_0}'$ and $\boldsymbol{p}'$ the same vectors in the internal frame of the cylinder ($\boldsymbol{p_0}' = \boldsymbol{p_0} - \boldsymbol{r_0}$ and $\boldsymbol{p}' = \boldsymbol{p} - \boldsymbol{r_0}$). Then the crossing point $\boldsymbol{p_S}$ with the interface is given by insertion of

$$\boldsymbol{p}' = \boldsymbol{p_0}' + \lambda . \boldsymbol{\Delta p} \tag{23}$$

as the vector $\boldsymbol{r}$ into equation 22. Of the two resulting values of λ only those between 0 and 1 are acceptable. The smallest of those λ-value(s) determines the intersection point $\boldsymbol{p_S}$.

In the following, we will use those primed vectors to indicate positions relative to the internal origin point of the block (tube, sphere, cone....).

(d) Cylinders parallel to the Surface

As an example, we will discuss here the case of a straight cylinder parallel to the Y-axis. Insertion of equation 23 into equation 22 leads to

$$\left[(\Delta x)^2 + (\Delta z)^2\right] \lambda^2 + 2\left[p_0'_{,x} . \Delta x + p_0'_{,z} . \Delta z\right] \lambda + \left[(p_0'_{,x})^2 + (p_0'_{,z})^2\right] = R^2, \tag{24}$$

where Δx, Δy and Δz are the components of $\boldsymbol{\Delta p}$.

In general this equation will have two λ-roots, with in order to be valid intersection points should be real numbers between 0 and 1. Let us denote these with λ_m and λ_M, with $\lambda_m < \lambda_M$. The λ-value for the intersection point will be equal to λ_m if $0 < \lambda_m < 1$ and $\boldsymbol{p_0}$ is outside the cylinder, and to λ_M if $0 < \lambda_M < 1$ and $\boldsymbol{p_0}$ is inside the cylinder (in that case $\lambda_m < 0$) respectively. See Figure 9 for a clarification.

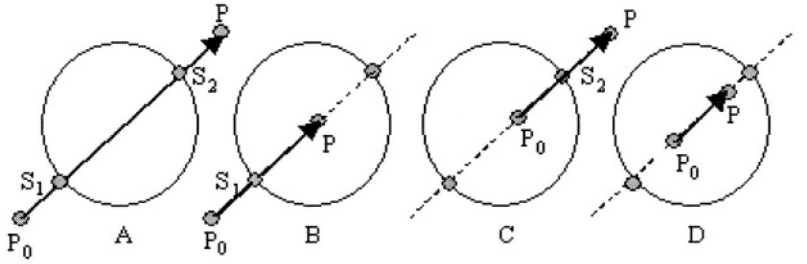

Figure 9. Intersection points with a cylinder. P_0 and P are the begin- and ends of the path. In case A the intersection point is S_1 (at $\lambda=\lambda_m<\lambda_M$), B: S_1 (at $\lambda=\lambda_m<\lambda_M$), C: S_2 (at $\lambda=\lambda_M$; $\lambda_m<0$), D: no intersection ($\lambda_m<0$ and $\lambda_M>1$).

The direction of the normal vector $\boldsymbol{n_S}$ on the cylinder surface at the intersection point is given by

$$\boldsymbol{n}_S \,//\, \left(p_{S,x} - r_{0,x}, 0, p_{S,z} - r_{0,z}\right) \quad . \tag{25}$$

Similar expressions can be formulated for cylinders parallel to the X-axis. In the program both X- and Y-cylinders have infinite length. For cylinders parallel to the Z-axis one also has to take into account that those cylinders may have cover lids and bottom at an interface between layers or with the surface. We will deal with that shortly.

Now we will discuss the option of more than one cylinder, in the form of linear arrays of those cylinders. This means that the program can handle an infinite number of cylinders, arranged next to each other, with constant spacing distance, as is shown in Figure 10.

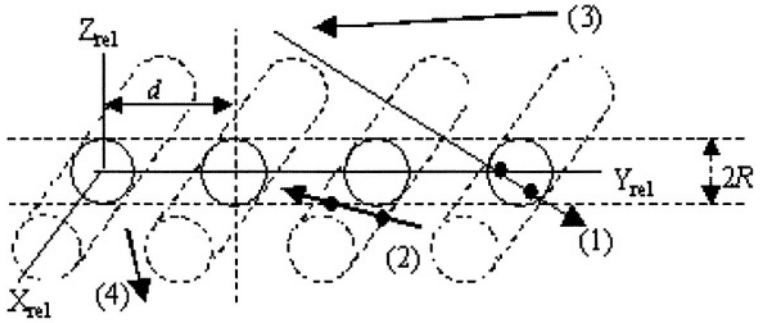

Figure 10. An array of cylinders parallel to the X-axis. The dots indicate intersection points. With the subscript "rel" we denote relative coordinates with respect to the generating cylinder of the set. R = radius; d = repetition distance. For paths (1)...(4): see text.

We denote the position vectors $\boldsymbol{p_0'}$ and $\boldsymbol{p'}$ with respect to the internal frame of the generating cylinder (located at the origin of the "rel"-frame). The repetition distance is d and the radius is R. The generating cylinder has tube number $t_n = 0$; the adjacent tubes have numbers $t_n = +1, +2 \ldots$ and $-1, -2 \ldots$ for tubes at the right and left sides respectively.

For the determination of intersections points we take following reasoning:

- Will the path contain points with $-R < z_{rel} < +R$? In that case

$$\left(p_0{}'_{,z} - R\right)\frac{dp_y}{dp_z} < 0 \quad or \quad \left(p_0{}'_{,z} + R\right)\frac{dp_y}{dp_z} < 0 \qquad , \tag{26}$$

and the path will cross one of the planes $z_{rel} = \pm R$, like path (1) or (2) in Figure 8. If not, no intersection will take place (*e.g.* path (3) or (4) in Figure 8).

- If equation 26 holds, does the path start inside the volume with boundaries $z_{rel} = \pm R$, or:

$$\left|p_0{}'_{,z}\right| < R \; ? \tag{27}$$

- If equation 27 holds, does the path start inside one of the tubes? If so, following expression must hold:

$$\left|\boldsymbol{p}_0' - t_n \; d \; \hat{\boldsymbol{y}}_{rel}\right| < R$$

with

$$t_n = round\left(\frac{p_0{}'_{,y}}{d}\right). \tag{28}$$

The operator "round" takes that integer value which is nearest to the argument between the brackets. Now we can solve the analogous equation 24 for cylinders parallel to the X-axis:

$$\left[(\Delta y)^2 + (\Delta z)^2\right]\lambda^2 + 2\left[p_0{}''_{,y}.\Delta y + p_0{}''_{,z}.\Delta z\right]\lambda + \left[(p_0{}''_{,y})^2 + (p_0{}''_{,z})^2\right] = R^2 \tag{29}$$

with $\boldsymbol{p_0''} = \boldsymbol{p_0'} - t_n \, d \; \hat{\boldsymbol{y}}_{rel}$.

- In case equation 28 does not hold, then the path starts outside all tubes.

In that case we solve equation 29 while taking for t_n the value

$$t_n = trunc\left(\frac{p_{0,y}'}{d}\right), \tag{30}$$

where the operator "trunc" removes the fraction from its argument. However, since according to equation 27 the starting point is inside the volume where $z_{rel} < \pm R$, the only tubes that can be intersected are those with tube numbers t_n and $t_n + 1$, we have to solve equation 29 for those two tubes only.

- However, in case equation 27 does not hold, the path will start outside the volume where $z_{rel} < \pm R$.
  Then first the intersection point with the nearest of the two planes $z_{rel} = \pm R$ is calculated, and from there the procedure is followed as in the case of a valid equation 27.
- Finally, the intersection point is corrected for the coordinate shifts due to the tube number being $\neq 0$ and the relative position of the generating tube (at tube number $t_n = 0$).

(e). Cylinders Parallel to the Z-axis

In the case of cylinders parallel to the Z-axis, the program offers the opportunity to insert two-dimensional arrays of cylinders, with equal repetition distance for the X- and Y-pitch. In addition, the cylinders do not have infinite length, as was the case for cylinders parallel to the surface, but will have a coverlid and a bottom lid. This will enlarge the intersection possibilities to be considered. See Figure 11.

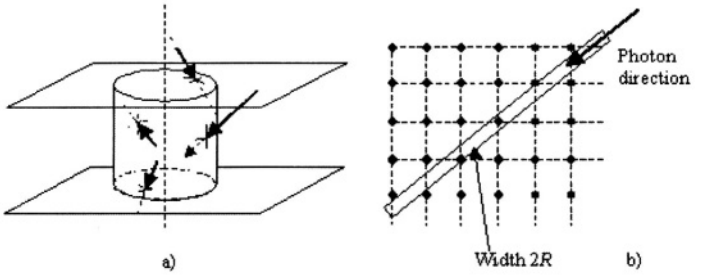

Figure 11. Cylinders parallel to the Z-axis. a) Several possibilities for intersections. b) Two-dimensional array of cylinders; the dots indicate the symmetry axes, pointing into the plane of drawing. The photon will intersect with the nearest cylinder that is positioned within 2R distance of the photon propagation vector.

Now we have to define two tube numbers, one for X-tubes and one for Y-tubes: t_{nx} and t_{ny}. In this case, the reasoning is as follows:

- Is the start position of the path in between the planes of the top and bottom lids of the tubes? If not, the nearest intersection, if any, will occur at the top or bottom lid of one of the tubes. See below.
- Is the start position of the path inside one of the tubes? This is equivalent with:

$$\left| \boldsymbol{p}_0' - t_{ny}\, d\, \hat{\boldsymbol{y}}_{rel} \right| < R \qquad \text{with} \qquad t_{ny} = round\left(\frac{p_{0,y}'}{d} \right) , \tag{31}$$

and simultaneously a similar question for the X-coordinate.

If so, we can calculate the intersection points with the curved wall and with the two lids of that tube, and take that intersection point (if any) that is reached first. For the curved wall we use a similar expression as equation 29:

$$\left[(\Delta x)^2 + (\Delta y)^2\right]\lambda^2 + 2\left[p_0''_{,x}.\Delta x + p_0''_{,y}.\Delta y\right]\lambda + \left[(p_0''_{,x})^2 + (p_0''_{,y})^2\right] = R^2, \tag{32a}$$

$$\boldsymbol{p_0}'' = \boldsymbol{p_0}' - t_{nx}\, d\, \hat{\boldsymbol{x}}_{rel} - t_{ny}\, d\, \hat{\boldsymbol{y}}_{rel} . \tag{32b}$$

In case an intersection with the curved wall exists, we check whether an intersection with one of the lids will occur earlier in the path. For the lids we first calculate the intersection points of the (relative) photon vector with the planes $z = z_{top}$ and $z = z_{bottom}$, given by

$$x_S = p_0''_{,x} + \frac{\Delta x}{\Delta z}.(z_{top} - p_0''_{,z}) \quad ; \quad y_S = p_0''_{,y} + \frac{\Delta y}{\Delta z}.(z_{top} - p_0''_{,z}) \tag{33}$$

(and similarly for the bottom lid) and check whether these points will lye on the lid of one of the tubes, *i.e.,* have a distance to the axis of the nearest tube that is smaller than *R.* This procedure is also followed when a photon is approaching a layer with Z-tubes from another layer.

If equation 31 is not valid for one of the X or Y coordinates, the photon starts outside any tube. Now the firstly encountered tube, with axis within *2R* distance from the propagation vector of the photon, has to be determined. The tube number of the nearest tube will depend on the sign of $s_x = \Delta x / |\Delta x|$ and $s_y = \Delta y / |\Delta y|$, as is the number sequence of tubes to investigate for the existence of intersection points (going to higher or lower numbers). Following the photon path $\Delta \boldsymbol{p}$ the subsequent tubes most adjacent to the path are interrogated about intersection points by solving a similar equation as equation 32, until that equation has an acceptable solution (between 0 and 1) or the path has been completed (*i.e.,* no intersection found). This procedure is illustrated in Figure 12.

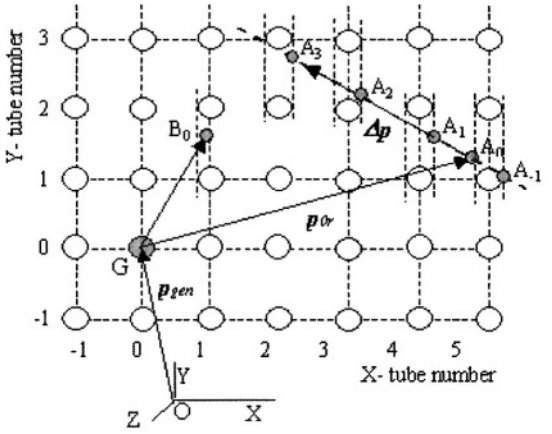

Figure 12. The procedure for intersection points with Z-tubes. O is the origin of the layer system. G is the generating tube (position p_{gen}). A_0 is the starting point (at p_{0r}) of the actual photon path D_p. Subsequently the existence of intersections is investigated with adjacent tubes. This is done by shifting point A_0 to A_{-1}, A_1, …A_3…respectively, and solving a similar equation as equation 32 for both adjacent tubes along the Y-axis. In this case points A_1 and A_2 will not lead to intersection points, and A_{-1} and A_3 would have led to intersection points, but outside vector D_p (λ<0 and λ>1 respectively). In case the starting point lies within a distance R from the axis (point B_0), that point is not shitted to B_{-1} (analogous to A_{-1}).

(f). Spheres

As with tubes parallel to the Z-axis, one might define sets of identical spheres arranged in a plane perpendicular to the Z-axis, with equidistant spacing. For those spheres, a similar procedure as for Z-tubes can be followed. Equation 32 is replaced by (see Figure 13):

$$\left|\boldsymbol{p}-\boldsymbol{p_0}\right|^2\lambda^2+2(\boldsymbol{p_0}-\boldsymbol{m})\bullet(\boldsymbol{p}-\boldsymbol{p_0})\lambda+\left|\boldsymbol{p_0}-\boldsymbol{m}\right|^2=R^2, \tag{34}$$

which can be written as:

$$\begin{aligned}&\left[(\Delta x)^2+(\Delta y)^2+(\Delta z)^2\right]\lambda^2+2\left[p_0''_{,x}.\Delta x+p_0''_{,y}.\Delta y+p_0''_{,z}.\Delta z\right]\lambda+\\&\quad\left[(p_0''_{,x})^2+(p_0''_{,y})^2+(p_0''_{,z})^2\right]=R^2\end{aligned} \tag{35}$$

with $\boldsymbol{p_0''}$ defined as above (see equation 32). With these equations the intersection point S can be calculated (if present). For calculating refraction and reflection, one needs the normal vector $\boldsymbol{n_S}$ and the angle of incidence θ_i of $\boldsymbol{\Delta p}$ with $\boldsymbol{n_S}$ at the sphere surface:

$$\cos\theta_i = \frac{\Delta\mathbf{p} \bullet \mathbf{n}_S}{|\Delta\mathbf{p} \bullet \mathbf{n}_S|} \quad ; \quad \mathbf{n}_S // \mathbf{s} - \mathbf{m}. \tag{36}$$

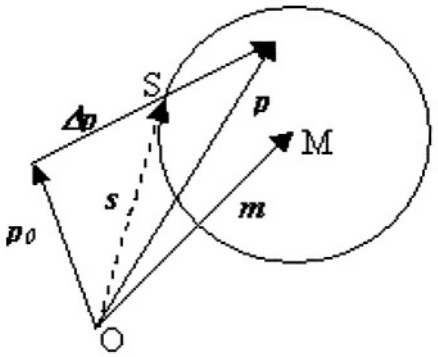

Figure 13. Determination of the intersection point S with a sphere. $\boldsymbol{p_0}$, $\boldsymbol{p}$ and $\boldsymbol{D_p}$ are the photon vectors, $\boldsymbol{m}$ is the center point vector and $\boldsymbol{s}$ points at the (first encountered) intersection point.

The direction of the normal vector depends on the way the surface is crossed, with the photon arriving from the inside or outside. The other axes ($\boldsymbol{l_S}$ and $\boldsymbol{m_S}$) of the coordinate system at point S can be found using

$$\boldsymbol{n_S} \times \Delta\boldsymbol{p} = \boldsymbol{m}_S \quad ; \quad \boldsymbol{n_S} \times \boldsymbol{m_S} = \boldsymbol{l}_S, \tag{37}$$

with $\boldsymbol{m}_S$ perpendicular to the plane of reflection or refraction and $\boldsymbol{l}_S$ lying in that plane, along the sphere surface.

(g). Rectangular Blocks

Rectangular blocks, as used in the program, always have their side planes parallel to the laboratory coordinate axes. The position and dimensions are defined using maximum and minimum values for the coordinates of the side planes, *e.g.,* x_{max} and x_{min}, and similarly for y and z. All six sides have to be interrogated for the presence of intersection points. For instance, for the block side at $z = z_{max}$, we calculate a ratio $f_{z,max}$ as

$$f_{z,\max} = \frac{z_{\max} - p_{0,z}}{\Delta z} \tag{38}$$

and similarly for all other sides. The smallest value of those six *f*-values, provided between 0 and 1, will determine the side where the first intersection will take place. If no such *f*-value can be found, no intersection point is present.

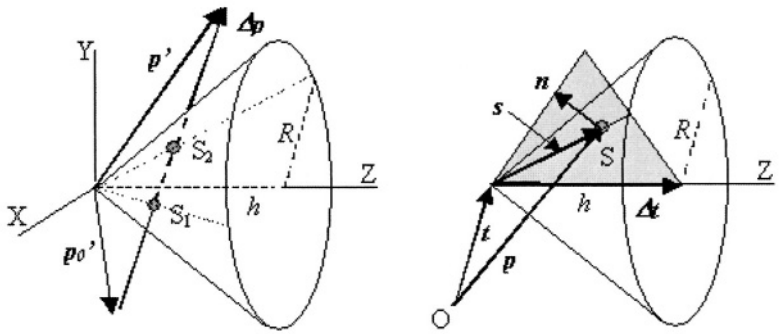

Figure 14. Intersection with a cone (example: directed along the +Z-axis). The cone is characterized by its direction vector (along the axis) and its opening angle, or its radius *R* at height h. Right: construction of the normal vector.

(h). Cones

The equation for cones is:

$$(x-x_O)^2 + (y-y_O)^2 - \alpha(z-z_O)^2 = 0 \quad ; \quad \alpha = (R/h)^2 \tag{39a}$$

for a cone directed along the Z-axis, as shown in Figure 14. The relevant intersection points are given by

$$(p_0{}'_{,x} + \lambda.\Delta x)^2 + (p_0{}'_{,y} + \lambda.\Delta y)^2 - \alpha(p_0{}'_{,z} + \lambda.\Delta z)^2 = 0\,. \tag{39b}$$

The smallest value of λ, if between 0 and 1, determines the valid intersection point S, provided the z-component of *S* is smaller than *h.* However, equation 38 also describes the other half of the cone, and therefore, for the intersection point to be accepted, this point should lie between top and

bottom of the cone, which defines an additional condition for point *S* to exist.

For reflection and refraction, we have to construct the normal vector $\boldsymbol{n}$ on the surface in point S:

$$\boldsymbol{s} = \boldsymbol{p} - \boldsymbol{t} \quad ; \quad \boldsymbol{v} = (\Delta\boldsymbol{t} \times \boldsymbol{s}) \times \boldsymbol{s} \quad ; \quad \boldsymbol{n} = \boldsymbol{v}/|\boldsymbol{v}| \quad , \tag{40}$$

with $\boldsymbol{t}$ and $\Delta\boldsymbol{t}$ as the position and direction vectors of the cone, and $\boldsymbol{v}$ as a vector in *S* parallel to the cone surface and perpendicular to the plane spanned by $\Delta\boldsymbol{t}$ and $\boldsymbol{s}$. The direction of $\boldsymbol{n}$ depends on the way the surface is crossed: arriving from the inside or outside. The determination of the angle of incidence is similar to the case of tubes and spheres.

With cones, also an intersection with the bottom is possible. In the coordinate frame of Figure 12, we have two conditions to be fulfilled:

$$\begin{aligned} &p_0{}'_{,z} + \lambda.\Delta z = h \qquad \text{with} \quad 0 < \lambda < 1, \\ &\left(p_0{}'_{,x} + \lambda.\Delta x\right)^2 + \left(p_0{}'_{,y} + \lambda.\Delta y\right)^2 \le R^2 \end{aligned} \tag{41}$$

In all cases the smallest of the λ-values of all possible intersections, if between 0 and 1, should be taken for the intersection point.

In the program the available cones are those with the axis parallel to the ±X, ±Y or ±Z-axis.

(i). Mirrors

The normal equation of a mirror plane is given, using the normal vector $\boldsymbol{a} = (a_1, a_2, a_3)$, by

$$a_1.x + a_2.y + a_3.z + d = 0, \tag{42}$$

where *d* is a constant. Vector $\boldsymbol{a}$ should point to the half plane where the starting point of the photon path is situated.

We can calculate the vector $\boldsymbol{p}_S$ to the intersection point *S* by insertion of the photon path $(\boldsymbol{p}_S = \boldsymbol{p}_0 + \lambda.\Delta\boldsymbol{p})$ into equation 42, which will render the λ-value corresponding to *S*. The direction vector $\boldsymbol{l}$ after reflection is given by

$$\boldsymbol{l} // \Delta\boldsymbol{p} - 2(\Delta\boldsymbol{p} \bullet \boldsymbol{a}).\boldsymbol{a} \quad ; \quad |\boldsymbol{l}| = (1 - \lambda).|\Delta\boldsymbol{p}| \tag{43}$$

(j). Entrance in a "Block"

When a photon enters a new layer, it is possible that it immediately will enter a "block" in that layer rather than first the material of the layer itself. An example is the entrance in a layer where a single Z-tube or a set of those tubes is present. This has to be checked separately. Therefore, the photon,

after reaching that interface, is temporarily propagated further along its path over a very small distance, to ensure that it is placed inside. The next step is to check whether the following condition C is true (with $\boldsymbol{p_c}$ as the temporary position vector, $\boldsymbol{p_c'}$ as that vector relative to the block or to the generating block in case of an array, and d as the repetition distance):

- Rectangular block:

$$C = (p_{cx} > x_{\min}) \wedge (p_{cx} < x_{\max}) \wedge (p_{cy} > y_{\min}) \wedge (p_{cy} < y_{\max}) \wedge (p_{cz} > z_{\min}) \wedge (p_{cz} < z_{\max}) \tag{44a}$$

- Cylindrical tube(s) parallel to the X-axis:

$$C = \left[(p_c{}'_{,y} - q_y)^2 + (p_c{}'_{,z})^2 < R^2\right] \quad \text{with}$$
$$q_y = 0 \quad \text{if} \quad d = 0\,; \text{otherwise} \quad q_y = round\left(p_c{}'_{,y} / d\right).d \tag{44b}$$

- Cylindrical tube(s) parallel to the Y-axis :

$$C = \left[(p_c{}'_{,x} - q_x)^2 + (p_c{}'_{,z})^2 < R^2\right] \quad \text{with}$$
$$q_x = 0 \quad \text{if} \quad d = 0\,; \text{otherwise} \quad q_x = round\left(p_c{}'_{,x} / d\right).d \tag{44c}$$

- Cylindrical tube(s) parallel to the Z-axis :

$$C = \left[(p_c{}'_{,x} - q_x)^2 + (p_c{}'_{,y} - q_y)^2 < R^2\right] \wedge \left[p_{c,z} > z_{top}\right] \wedge \left[p_{c,z} < z_{bottom}\right] \tag{44d}$$

with z_{top} and z_{bottom} as the z-coordinates of the top and bottom lids of the tube(s),

- Spheres :

$$C = \left[(p_c{}'_{,x} - q_x)^2 + (p_c{}'_{,y} - q_y)^2 + (p_c{}'_{,z})^2 < R^2\right] \tag{45}$$

- Cones (*e.g.,* with symmetry axis (bottom $\rightarrow$ top) pointing to +Z-axis):

$$C = (p_c{}'_{,z} > 0) \wedge (h > 0) \wedge (0 < p_c{}'_{,z} / h < 1) \wedge \left[(p_c{}'_{,x})^2 + (p_c{}'_{,y})^2 < (p_c{}'_{,z}.R / h)^2\right] \tag{46}$$

and analogously for the five other directions.

- Oblique cylinders (using $\boldsymbol{b}$ as the directional unit vector along the symmetry axis):

$$C = \left[(p_c{}'_{,x})^2 + (p_c{}'_{,y})^2 + (p_c{}'_{,z})^2 - (\mathbf{p_c}' \bullet \mathbf{b})^2 < R^2\right] \wedge \left[p_{c,z} > z_{top}\right] \wedge \left[p_{c,z} < z_{bottom}\right] \tag{47}$$

- Mirrors (with $\boldsymbol{b}$ as the normal vector on the mirror surface):

$$C = (\mathbf{p}' \bullet \mathbf{b} = 0). \tag{48}$$

12.3.4 Absorption

Normally the position of the photon, together with its directional angles, is stored upon reflection or transmission. However, when in absorption mode, the position of absorption will be stored, together with the directional angles of the previous (last) photon path. These angles are stored using the normal convention for the polar angle θ and azimuthal angle φ:

$$\Delta \boldsymbol{p} = |\Delta \boldsymbol{p}| \, . \, (\sin\theta . \cos\varphi, \sin\theta . \sin\varphi, \cos\theta), \tag{49}$$

with $\theta = 0$, if the direction is pointing along the +Z-axis, inside the sample, and φ in the XY-plane, as the angle with the X-axis.

12.3.5 Polarization

(1). Polarization in Scattering Events

To handle polarization effects in scattering events we use Van de Hulst 's scattering matrix [15], with $\boldsymbol{E_0}$ and $\boldsymbol{E}$ as the incoming and scattered electric field vectors:

$$\begin{pmatrix} E_l \\ E_r \end{pmatrix} = \frac{\exp(-ikr - i\omega t)}{i.4\pi\varepsilon_m kr} \begin{pmatrix} S_2 & S_3 \\ S_4 & S_1 \end{pmatrix} \begin{pmatrix} E_{l0} \\ E_{r0} \end{pmatrix}, \tag{50}$$

where the subscript l and r denote parallel and perpendicular polarization, respectively. In the following we will limit ourselves to spherical particles, where S_3 and S_4 are = 0. The other parameters S_1 and S_2 are functions of the polar scattering angle θ. The factor $(4\pi\varepsilon_m)$ can be inserted in the S-functions as well. Note that Van de Hulst uses Gaussian units instead of SI-units, which means that he does not take the factor $(4\pi\varepsilon_m)$ into account.

The Stokes vector $\boldsymbol{S}^T = (I,Q,U,V)$ can be constructed from this matrix:

$$\begin{aligned} I &= E_l E_l^* + E_r E_r^* \\ Q &= E_l E_l^* - E_r E_r^* \\ U &= E_l E_r^* + E_r E_l^* \\ V &= i(E_l E_r^* - E_r E_l^*). \end{aligned} \tag{51}$$

With

$$\begin{aligned} E_l &= a_l \exp(-ik_z - i\omega t - i\varepsilon_l) \\ E_r &= a_r \exp(-ik_z - i\omega t - i\varepsilon_r), \end{aligned} \tag{52}$$

it follows:

$$\begin{aligned} I &= a_l^2 + a_r^2 & U &= 2a_l a_r \cos\delta & \delta &= \varepsilon_l - \varepsilon_r \\ Q &= a_l^2 - a_r^2 & V &= 2a_l a_r \sin\delta \end{aligned} \tag{53}$$

For normal (non-birefringent) materials $\varepsilon_l = \varepsilon_r$. The degree of polarization is defined as

$$\Phi_P = \frac{1}{I}\sqrt{Q^2 + U^2 + V^2}, \tag{54}$$

Transformation of the Stokes vector upon scattering (for spherical particles) is given by

$$\boldsymbol{S}^T{}_n = \overline{\overline{\boldsymbol{F}}} \,.\, \boldsymbol{S}^T \tag{55}$$

with

$$\overline{\overline{\boldsymbol{F}}} = \begin{pmatrix} \frac{1}{2}(M_2 + M_1) & \frac{1}{2}(M_2 - M_1) & 0 & 0 \\ \frac{1}{2}(M_2 - M_1) & \frac{1}{2}(M_2 + M_1) & 0 & 0 \\ 0 & 0 & S_{21} & -D_{21} \\ 0 & 0 & D_{21} & S_{21} \end{pmatrix} \tag{56}$$

and

$$\begin{aligned} M_k &= S_k S_k^* = |S_k|^2 \,;\, k = 1,2 \\ S_{21} &= \tfrac{1}{2}(S_1 S_2^* + S_2 S_1^*) \\ D_{21} &= \tfrac{1}{2} i (S_1 S_2^* - S_2 S_1^*), \end{aligned} \tag{57}$$

and so we arrive at the Mueller matrix $\overline{\overline{\boldsymbol{M}}}$ replacing $\overline{\overline{\boldsymbol{F}}}$:

$$\overline{\overline{\mathbf{M}}} = \begin{pmatrix} m_{11} & m_{12} & 0 & 0 \\ m_{12} & m_{11} & 0 & 0 \\ 0 & 0 & m_{33} & m_{34} \\ 0 & 0 & -m_{34} & m_{44} \end{pmatrix}, \tag{58}$$

where the parameters $m_{11} \ldots m_{44}$ depend on the particular scattering function and the scattering angles θ and φ. We will deal with those parameters in the next section.

Transformation of the Stokes vector upon scattering has to be preceded by a rotation from the actual coordinate system (given by the unit vectors $\boldsymbol{e}_l$, $\boldsymbol{e}_r$, $\boldsymbol{e}_p$, with directions parallel and perpendicular to the actual polarization direction, and parallel to the direction of propagation respectively) to that in the scattering plane ($\boldsymbol{e}_l'$, $\boldsymbol{e}_r'$, $\boldsymbol{e}_p'$, with $\boldsymbol{e}_p' = \boldsymbol{e}_p$). This rotation is determined by the rotation matrix $\boldsymbol{R}$:

$$\overline{\overline{\mathbf{R}}} = \begin{pmatrix} 1 & 0 & 0 & 0 \\ 0 & \cos 2\varphi & -\sin 2\varphi & 0 \\ 0 & \sin 2\varphi & \cos 2\varphi & 0 \\ 0 & 0 & 0 & 1 \end{pmatrix}, \tag{59}$$

with φ as the azimuthal scattering angle (see Figure 15).

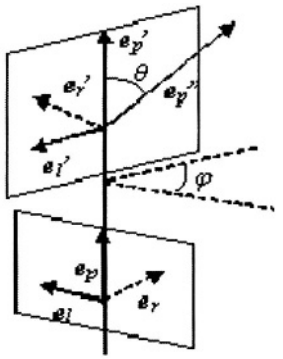

Figure 15. Coordinate frames of subsequent scattering events. The propagation vector $\boldsymbol{e}_p$ is first transformed into $\boldsymbol{e}_p'$ (by rotation over φ) and then to $\boldsymbol{e}_p''$ (by rotation over θ). The vectors $\boldsymbol{e}_l$, $\boldsymbol{e}_r$ and $\boldsymbol{e}_l'$, $\boldsymbol{e}_r'$ are frame vectors parallel and perpendicular to the scattering planes.

Subsequent multiplication with the Mueller matrix produces the new Stokes vector in the coordinate frame ($\boldsymbol{e}_l''$, $\boldsymbol{e}_r''$, $\boldsymbol{e}_p''$) connected to the new propagation direction $\boldsymbol{e}_p''$ (with $\boldsymbol{e}_p'' \bullet \boldsymbol{e}_p' = \cos\theta$):

$$e_r" = \begin{pmatrix} \cos\varphi \\ \sin\varphi \\ 0 \end{pmatrix} \quad ; \quad e_l" = \begin{pmatrix} -\cos\theta.\sin\varphi \\ \cos\theta.\cos\varphi \\ \sin\theta. \end{pmatrix} \quad ; \quad e_p" = \begin{pmatrix} \sin\theta.\sin\varphi \\ -\sin\theta.\cos\varphi \\ \cos\theta. \end{pmatrix} \quad . \tag{60}$$

Subsequent scattering events (θ_i, φ_i, with i=*1...n*) will result in

$$\mathbf{S}^T{}_{result} = \left[\prod_{i=1}^{n} \overline{\overline{\mathbf{M}}}(\theta_i) \overline{\overline{\mathbf{R}}}(\varphi_i) \right] . \mathbf{S}^T{}_0, \tag{61}$$

and this determines the polarization state of the emerging photon. Here the vector $\boldsymbol{S}^T{}_0$ is the Stokes vector of the incoming photon, given by equation 47 after determination of the parallel and perpendicular directions corresponding to $E_{//}$ and $E_{\perp}$.

In the non-polarized case (natural light), the scattering angles can be determined using two subsequent random numbers. In the polarized state that is not the case any more. When determining an angle φ using a random number, the angle θ is determined by the joint probability:

$$p(\theta,\varphi) = m_{11}(\theta) + m_{12}(\theta).\,(Q.\cos 2\varphi + U.\sin 2\varphi) / I\,. \tag{62}$$

Yao and Wang's approach [16] calculates θ with m_{11} (as in fact is done with natural light) and subsequently φ with equation 62. Several authors have dealt with polarization of light in turbid media [16-21].

(2). Polarization at Interfaces

Changing of polarization direction may also occur at interfaces, where reflection or refraction takes place. With α_1, α_2 and α_3 as the angles of the electric vector $\boldsymbol{E}$ with the plane of incidence (formed by the incident propagation direction and the normal on the surface at the point of intersection) for the incident (1), refracted (2) and reflected (3) vector respectively (see Figure 4), and A as the field amplitude it can be shown (see, *e.g.,* Born and Wolf [22]) that

$$A_{1,l} = A_1.\cos\alpha_1 \quad ; \quad A_{1,r} = A_1.\sin\alpha_1 \quad , \tag{63}$$

where α_1 can be derived from the components of the incident Stokes vector using

$$A_{1,l} = \tfrac{1}{2}(I + Q) \quad ; \quad A_{1,r} = \tfrac{1}{2}(I - Q). \tag{64}$$

Now we calculate the amplitudes of the reflected and transmitted (refracted) wave

$$A_{3,l} = \frac{\tan(\theta_1 - \theta_2)}{\tan(\theta_1 + \theta_2)} A_{1,l} \quad ; \quad A_{3,r} = -\frac{\sin(\theta_1 - \theta_2)}{\sin(\theta_1 + \theta_2)} A_{1,r} \quad \text{with} \quad \frac{\sin\theta_1}{\sin\theta_2} = \frac{n_2}{n_1}$$

$$A_{2,l} = \frac{2\sin\theta_2.\cos\theta_1}{\sin(\theta_1 + \theta_2).\cos(\theta_1 - \theta_2)} A_{1,l} \quad ; \quad A_{2,r} = \frac{2\sin\theta_2.\cos\theta_1}{\sin(\theta_1 + \theta_2)} A_{1,r}$$

$$\tan\alpha_3 = -\frac{\cos(\theta_1 - \theta_2)}{\cos(\theta_1 + \theta_2)} \tan\alpha_1 \quad ; \quad \tan\alpha_2 = \cos(\theta_1 - \theta_2).\tan\alpha_1. \tag{65}$$

From these we can derive the corresponding Stokes vector coefficients and Mueller matrices $\underline{\underline{M}}_R$ and $\underline{\underline{M}}_T$, where the subscripts R and T stand for reflection and transmission (refraction). However, to construct the new Stokes vector it is easier by using the amplitudes directly.

To find out whether reflection or refraction (transmission) will take place, we have to look at the reflectivity R and transmittivity T of the energy instead of those of the amplitude:

$$R = \frac{|A_{3,l}|^2}{|A_{1,l}|^2}\cos^2\alpha_1 + \frac{|A_{3,r}|^2}{|A_{1,r}|^2}\sin^2\alpha_1 \quad ;$$

$$T = \frac{n_2\cos\theta_2}{n_1\cos\theta_1}\left[\frac{|A_{2,l}|^2}{|A_{1,l}|^2}\cos^2\alpha_1 + \frac{|A_{2,r}|^2}{|A_{1,r}|^2}\sin^2\alpha_1\right], \tag{66}$$

where we can verify that

$$R + T = 1 \tag{67}$$

The procedure for handling reflection and refraction at interfaces is as follows:

- Rotate the coordinate frame of the incoming photon to the coordinates of the plane of reflection, using a rotation matrix as in equation 55;
- Determine whether reflection or refraction will take place, using equation 67 and a fresh random number R_N. Reflection will take place if $R_N \leq R$, and refraction otherwise.

- Construct the new coordinate frame for the photon and the new Stokes vector, using equation 65.

12.4 SCATTERING FUNCTIONS

Now we introduce various scattering functions that are frequently used in light scattering simulations. In most cases, we will follow the treatment of Van de Hulst [15] and of Ishimaru [2,3]. Further references can be found there.

In matters of light scattering by particles two parameters are important: the aspect ratio x and the relative refractive index n_{rel}. The aspect ratio is given by

$$x = \frac{2\pi a}{\lambda_{med}} = ka \quad ; \quad \lambda_{med} = \frac{\lambda_{vac}}{n_{med}}, \tag{68}$$

where a denotes the radius of the particle, λ the wavelength of the light and k the modulus of the wavevector. The subscripts *med* and *vac* denote "medium" and "vacuum" respectively. The relative index n_{rel} is the index of the particles with respect to the surrounding medium.

We start with very small particles (small compared to the wavelength: $x<<1$), giving rise to "dipolar" or "Rayleigh" scattering. When gradually increasing the radius we encounter "Rayleigh-Gans" or "Debije"-scattering and finally scattering by large particles ($x<<1$). Generally valid expressions were developed by Mie ("Mie"-scattering). Finally we have expressions of a more phenomenological nature, like "Henyey-Greenstein"-scattering or "peaked-forward"-scattering.

We will use the *geometrical* and *scattering cross sections* σ_g and σ_s [m^2], being the real and the apparent shadow of the particle, and the efficiency factor $Q_{sca} = \sigma_s / \sigma_g$, with $\sigma_g = \pi a^2$.

The ultimate way of treating scattering in numerical simulation is to use the *scattering coefficient* μ_s (in m^{-1}), defined as

$$\mu_s = n_s \sigma_s \tag{69}$$

with n_s as the particle concentration (in m^{-3}). The scattering coefficient is a measure for the average number of scattering events per unit of length. Normally in tissue the scattering is predominantly in forward direction, which means that randomization of the photon direction only will occur after a relatively large number of scattering events. Therefore, in those cases it is worth while to use the *reduced scattering coefficient* μ_s', defined as

$$\mu_s' = \mu_s(1-g), \tag{70}$$

where g stands for the averaged cosine of the polar scattering angles during those events. This value will be 1 for perfectly forward scattering and 0 for isotropic scattering. For tissue $g \approx$ 0.8-0.9 and for blood $g \approx$0.95-0.99.

Standard electromagnetic theory for light scattered by dipoles leads to the expression:

$$\boldsymbol{E}_s(\boldsymbol{R},t) = -\frac{1}{4\pi\varepsilon_0 R}\iiint_V d^3\boldsymbol{r} \quad \boldsymbol{k}_s \times \boldsymbol{k}_s \times \left[\overline{\overline{\varepsilon}}(\boldsymbol{r},t') \bullet \boldsymbol{E}_0(\boldsymbol{r},t')\right] \tag{71}$$

with $\boldsymbol{E_s}$ and $\boldsymbol{E_0}$ as the scattered and the incoming electric field respectively; $\boldsymbol{R}$ is the vector from the scattering volume V to the point of detection, $\boldsymbol{k_s}$ is the scattered wave vector in that direction, and $\boldsymbol{\varepsilon}$ is the dielectric tensor (which frequently reduces to a scalar). The time t' is the reduced time, given by

$$t' = t - \frac{|\boldsymbol{R}-\boldsymbol{r}|}{c} \tag{72}$$

with c as the light velocity in the media. In equation 71 the dimensions of the scattering volume V are assumed to be small compared to R. The significance of the double vector product is illustrated in Figure 16.

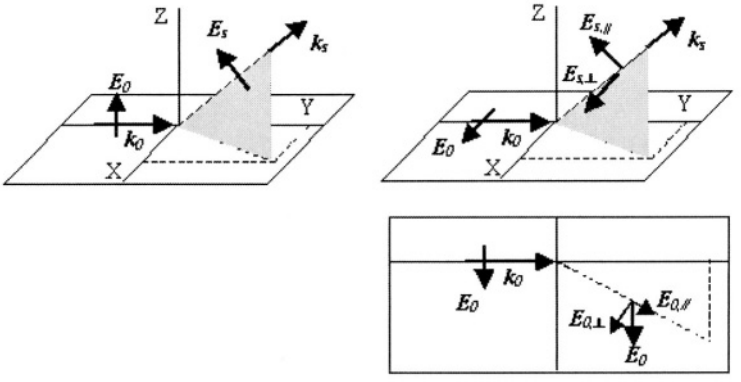

Figure 16. The meaning of the double vectorial product in determining the direction of scattering and polarization, for two cases: polarization perpendicular to the XY-plane (left) and parallel to that plane (right). Here ε is taken as a scalar.

12.4.1 Dipolar (Rayleigh)

With dipolar scattering, the particles are assumed to be so small that light scattered from different oscillating electrical dipoles in the particles will not lead to phase differences upon arrival at the point of detection. Using standard electromagnetic dipole radiation theory, or a standard Green's functions approach, we may derive for the radiative term $\boldsymbol{E_{rad}}$ of the scattered electric field strength (Figure 17):

$$\mathbf{E_{rad}} = -\frac{p_m k^2}{4\pi\varepsilon r} \sin\gamma . \exp(i\omega t') . \mathbf{e}_\theta \quad ; \quad t' = t - \frac{r}{c}, \tag{73}$$

where p_m is the amplitude of the oscillating dipole $\boldsymbol{p}(t) = \boldsymbol{p_m} \exp(i\omega t)$, with ω as the frequency ($\omega = c / k$, with c the local light velocity). The parameter t' accounts for the time retardation upon arrival at detection, which generally could be the origin of phase differences. For clarity: Van de Hulst uses Gaussian rather than S.I.-units, which means that the factor $(4\pi\varepsilon_m)$ is set to unity.

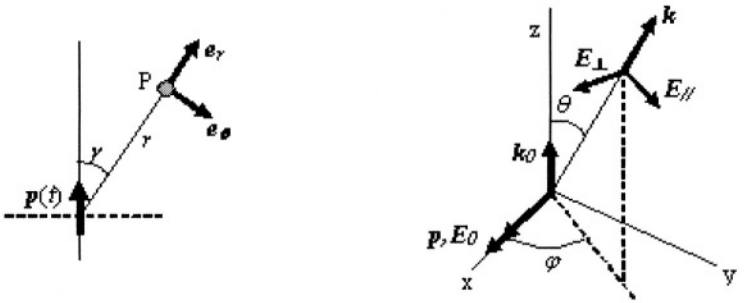

Figure 17. a) Electric dipole, radiating towards detection point P at distance r and with polar scattering angle γ. The vectors $\boldsymbol{e_r}$ and $\boldsymbol{e_\theta}$ are unit vectors. Due to symmetry, the azimuthal angle does not play a role.

Frequently $\boldsymbol{p_m}$ can be considered as being related to the incoming electric field $\boldsymbol{E_0}$, through the polarisability tensor $\overline{\overline{\alpha}}$ of the particle. In a number of cases this tensor reduces to a mere constant α, with

$$\alpha = 4\pi\varepsilon_m \alpha_H \quad ; \quad \alpha_H = a^3(\varepsilon_p - \varepsilon_m) f_p \quad ; \quad f_p = \frac{3\varepsilon_m}{\varepsilon_p + 2\varepsilon_m}, \tag{74}$$

where ε_p and ε_m are the dielectric constants of the particle and the medium, α_H is the polarizability as used by Van de Hulst (assuming $4\pi\varepsilon_m$ = unity) and f_p denotes the correction for the internal enhancement of the incoming field

(see standard EM text books). Note the dependence on the particle volume, through a^3.

We find for the two electric field components:

$$|E_{//}| = \frac{\alpha k^2}{4\pi\varepsilon_m r}\cos\theta.|E_{0,//}| = \frac{\alpha k^2}{4\pi\varepsilon_m r}\cos\theta.\cos\varphi.|E_0| = \frac{\alpha k^2}{4\pi\varepsilon_m r}\cos\theta.|E_{0,//}| \qquad (75)$$

$$|E_{\perp}| = \frac{\alpha k^2}{4\pi\varepsilon_m r}|E_{0,\perp}| = \frac{\alpha k^2}{4\pi\varepsilon_m r}\sin\varphi.|E_0| = \frac{\alpha k^2}{4\pi\varepsilon_m r}.|E_{0,\perp}|$$

The intensities $I_{//}$ and $I_{\perp}$ are proportional to the squares of the field strengths ($I = \frac{1}{2}c\varepsilon_m E^2$), thus

$$I_{//} = \frac{\alpha^2 k^4}{(4\pi\varepsilon_m)^2 r^2}\cos^2\theta.\cos^2\varphi.\, I_0,$$

$$I_{\perp} = \frac{\alpha^2 k^4}{(4\pi\varepsilon_m)^2 r^2}\sin^2\varphi.\, I_0. \qquad (76)$$

Due to the dependence on α^2 and k^4, the intensities are proportional to a^6 and $1/\lambda^4$.

The components of Van de Hulst's scattering matrix, equation 73, will read

$$S_2(\theta) = \alpha k^3\cos\theta \quad ; \quad S_1(\theta) = \alpha k^3 \quad ; \quad S_3 = S_4 = 0. \qquad (77)$$

This means that the component perpendicular to the scattering plane shows uniform scattering, but the parallel component has a cosine behavior: when viewing the scattering particle along a direction parallel to the polarization, no scattering will be observed.

For natural light the total intensity will be proportional to $\frac{1}{2}(S_1^2+S_2^2)$, and thus

$$I_{nat}(\theta) = \frac{\alpha^2 k^4 I_0}{(4\pi\varepsilon_m)^2 r^2}\frac{1+\cos^2\theta}{2}. \qquad (78)$$

Spatial integration of equation 74 over θ and φ leads to the total scattered intensity I_{tot} (now expressed in W/sr instead of W/m^2):

$$I_{tot} = \frac{8\pi}{3}\frac{\alpha^2 k^4 I_0}{(4\pi\varepsilon_m)^2}. \qquad (79)$$

The scattering cross section σ_s is defined with (using Ω as the scattering solid angle and $F(\Omega)$ as the angle-dependent scattering function, but normalized to unity upon Ω-integration over 4π):

$$I(\Omega) = \sigma_s . F(\Omega) . I_0, \tag{80}$$

with $I(\Omega)$ expressed in W/sr and I_0 in W/m^2. This leads to

$$\sigma_s = \frac{8\pi}{3} \frac{\alpha^2 k^4}{(4\pi\varepsilon_m)^2} = \frac{8\pi}{3} {\alpha_H}^2 k^4. \tag{81}$$

The ratio Q_{sca} is given by

$$Q_{sca} = \frac{\sigma_s}{\sigma_g} = \frac{8}{3} a^4 (\varepsilon_p - \varepsilon_m)^2 \left(\frac{3\varepsilon_m}{\varepsilon_p + 2\varepsilon_m} \right)^2 k^4 \approx \frac{8}{3} x^4 \left(\frac{m^2 - 1}{m^2 + 2} \right)^2, \tag{82}$$

where m^2 is the relative refractive index of the particles in the surrounding medium: $m^2 = \varepsilon_p / \varepsilon_m$.

12.4.2 Rayleigh-Gans

When particles grow larger, the phase differences of scattered waves arriving at the detection point from different source points in the scattering medium, cannot be neglected any more.

Here we will follow Van de Hulst, using the approximation $|\varepsilon_p - \varepsilon_m| << \varepsilon_m$. Also the value of $x|\varepsilon_p - \varepsilon_m|/\varepsilon_m$ should be << 1. With these assumptions we may write for a volume element *dV:*

$$d\alpha_H = \frac{m^2 - 1}{4\pi} dV \approx \frac{m - 1}{2\pi} dV \tag{83}$$

with m is the relative refractive index of the particles in the medium: $m^2 = \varepsilon_p / \varepsilon_m$. The non-zero components of the scattering matrix will read:

$$S_2 = 4\pi\varepsilon_m \frac{m-1}{2\pi} V . R(\theta, \varphi) \; ; \; S_1 = 4\pi\varepsilon_m \frac{m-1}{2\pi} V . R(\theta, \varphi) . \cos\theta \tag{84}$$

with $R(\theta, \varphi)$ obtained by integration over the volume V using a phase-dependent factor $i\delta$:

$$R(\theta, \varphi) = \frac{1}{V} \iiint \exp(i\delta) . dV. \tag{85}$$

The phase-difference δ is given by $\boldsymbol{k}\bullet(\boldsymbol{r}-\boldsymbol{r_O})$, where $\boldsymbol{r}$ and $\boldsymbol{r_O}$ are the position vectors from the scattering volume element under consideration and the origin in the sample. The scattering cross section will be (for natural incoming light):

$$\sigma_s = \frac{1+\cos^2\theta}{2} k^4 V^2 \frac{(m-1)^2}{(2\pi)^2} \left|R(\theta,\varphi)\right|^2. \tag{86}$$

For special particles the function $R(\theta,\varphi)$ can be expressed analytically:

$$R(\theta,\varphi) = \sqrt{\frac{9\pi}{2u^3}} J_{3/2}(u) = \frac{3}{u^2}(\sin u - u\cos u) \quad \text{with} \quad u = 2x.\sin\tfrac{1}{2}\theta \tag{87}$$

The factor Q_{sca} for spherical particles is given by:

$$Q_{sca} = \frac{32}{27}(m-1)^2 x^4 \quad (x<<1) \quad \text{and} \quad Q_{sca} = 2(m-1)^2 x^2 \quad (x>>1) \tag{88}$$

For other shapes, see Van de Hulst.

12.4.3 Mie

In principle, the rigorous scattering theory, as developed by Mie (see refs. in Ref. [15]), presents analytical expressions for all kind of particles. It departs from the Maxwell equations and solves the scalar part of the wave equation, taking boundary conditions into account. This leads to complicated expressions for the components of Van de Hulst's scattering matrix, which are only tractable when treated numerically.

In the Montcarl-program we use a procedure developed by Zijp and Ten Bosch [23], which renders S_2 and S_1. Again, for natural light the total intensity will be proportional to $\frac{1}{2}(S_1^2+S_2^2)$. See Figure 18 for an example.

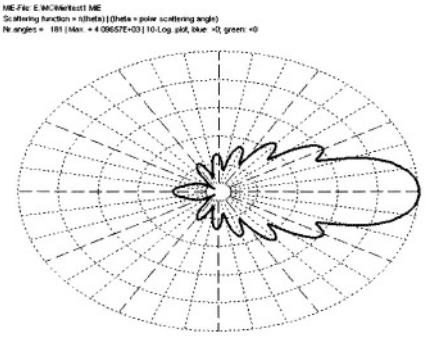

Figure 18. Example of a MIE-file. Scattering function according to the Mie-formalism.

12.4.4 Henyey-Greenstein

The Henyey-Greenstein scattering function [24] originates from the astronomical field, to calculate the scattering by cosmic particle clouds. Since it can be written in a closed analytical form, it can be used as a fast replacement for the Mie-functions. The function reads:

$$p_{HG}(\theta,\varphi) = \frac{1}{4\pi}\frac{1-g^2}{(1+g^2-2g.\cos\theta)^{3/2}}, \tag{89}$$

where g is the averaged cosine of the polar angle θ of the scattering events. This function is normalised to unity upon integration over 4π solid angle.

A drawback of this expression is that the function only describes the angle-dependent behavior of the scattering. The calculation of the scattering cross section has to be done by other means. One option is to insert the total scattering cross section as obtained by Mie-scattering (or another approach, if applicable) as a separate factor in the Henyey-Greenstein expression.

12.4.5 Isotropic

Isotropic scattering can be described using the (normalized) function

$$p_{iso}(\theta,\varphi) = \frac{1}{4\pi}. \tag{90}$$

The normalised cumulative function $C(\theta)$ will read

$$C(\theta) = \tfrac{1}{2}(1 - \cos\theta). \tag{91}$$

and thus θ can be found from $\theta = \arccos(1 - 2R_N)$, with R_N as a fresh random number $(0<R_N<1)$. The value of g will be zero.

12.4.6 Peaked Forward

A peaked-forward scattering function is completely artificial. It can be useful for special applications. A possible functional form (not normalized) is

$$p_{PF} = \exp(-\theta^2/\theta_0^{\,2}). \tag{92}$$

12.5 LIGHT SOURCES

For the injection of photons, one can imagine various mechanisms. Most general is the pencil beam, entering from the top. However, other beam profiles can be used as well. Here we offer a broad spectrum of those profiles.

12.5.1 Pencil Beams

Pencil beams are the simplest way to inject photons into the sample. The only programmatic requisite is to define the point of injection at the sample surface. With those beams, one still has to take care for a proper handling of the transport through the upper interface of the sample with the air, to take reflection losses into account.

Pencil beams can be tilted in two directions, which can be described using the tilting polar and azimuthal angles θ and φ. See subsection 12.5.2.

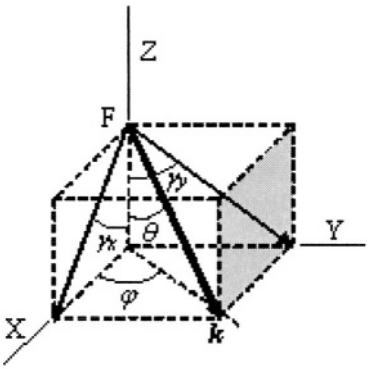

Figure 19. Entrance of the beam. The surface of the sample is the XY-plane. F is the focus, and θ and φ are tilting angles of the symmetry axis of the beam.

12.5.2 Broad Beams

Broad beams come in two forms: divergent beams and parallel beams. For divergent beams we have adopted following procedure (see Figure 19):

We define the divergence angles of the beam projection on the XZ- and YZ-planes respectively, as α_x and α_y, and the tilting angles of the symmetry axis of the beam with the Z-axis and the X-axis in the XY-plane, as θ and φ respectively;

Then we may write (*k* is the length of $\boldsymbol{k}$):

$$k_x = k\ \sin\theta\ \cos\varphi\,; \quad k_y = k\ \sin\theta\ \sin\varphi\,; \quad k_z = k\ \cos\theta \tag{93}$$

and for the tilting angles:

$$\tan\gamma_x = \frac{k_x}{k_z} = \tan\theta.\cos\varphi \quad ; \quad \tan\gamma_y = \frac{k_y}{k_z} = \tan\theta.\sin\varphi \tag{94}$$

With adaptation for divergence:

$$\begin{aligned} \gamma_x' &= \gamma_x + \alpha_x = \arctan(\tan\theta.\cos\varphi) + \alpha_x\ , \\ \gamma_y' &= \gamma_y + \alpha_x = \arctan(\tan\theta.\sin\varphi) + \alpha_y\ . \end{aligned} \tag{95}$$

The new direction vector $\boldsymbol{k}'$ will be given by

$$k'_x = \tan\gamma_x'.\,k'_z \quad ; \quad k'_y = \tan\gamma_y'.\,k'_z \quad ; \quad |k'| = k\,. \tag{96}$$

This approach offers the opportunity to define divergent beams with different opening angles in X- and Y-directions, and with different profiles (Gaussian or uniform).

For parallel beams an ideal thin positive lens with focal point in F (see Figure 19) is thought to be positioned horizontally on the surface.

12.5.3 Ring-Shaped Beams

Here we only apply ring-shaped beams with uniform filling, which means that the light intensity will be equal at all point in the ring. Then the amount of photons passing through a ring at distance r from the center and with width dr will be proportional to rdr. To define the actual distance of the photon we need to construct the cumulative function $C(r)$:

$$C(r) = \int_{R_1}^{r} c.r'.dr', \tag{97}$$

where c is a proportionality constant and $R_1 \le r \le R_2$ (R_1 and R_2 being the inner and outer ring radii), and normalize $C(R_2)$ to unity. This results in the cumulative function $C(r)$:

$$C(r) = \frac{r^2 - R_1^{\,2}}{R_2^{\,2} - R_1^{\,2}}. \tag{98}$$

By equaling this function to a fresh random number between 0 and 1, the value of r is set. Subsequently the φ-value is chosen randomly between 0 and 2π.

The ring-shaped beam can be combined with divergence and tilting as mentioned before.

12.5.4 Isotropic Injection

We can adopt several models for isotropic injection. The simplest model is:

$$I(\theta) = c \quad ; \quad c = \text{constant.} \tag{99}$$

Then we can construct the normalized cumulative function

$$C(\theta) = \frac{C'(\theta)}{C'(\pi)} = \tfrac{1}{2}(1-\cos\theta) \quad \text{with} \quad C'(\theta) = \int_0^{\theta} I(\theta').\sin\theta'.d\theta', \tag{100}$$

and by equaling this function to a fresh random number R_N, the value of θ can be derived, as $\theta = \arccos(1\text{-}2R_N)$. Again, the value of φ is obtained from a random number between 0 and 2π.

Another model uses isotropic radiances. See Figure 20.

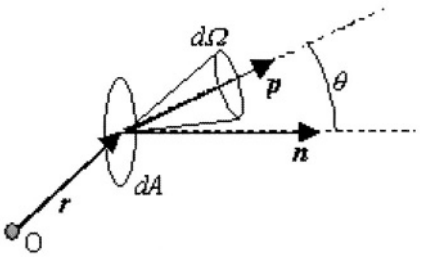

Figure 20. Radiance and power are supposed to be emitted through area dA in direction $\boldsymbol{p}$ in solid angle $d\Omega$.

Using the radiance $L(\mathbf{p},\mathbf{r})$, expressed in $\mathrm{W.m^{-2}sr^{-1}}$, we find for the emitted power contribution and the flux vector $\mathbf{F}$:

$$\begin{aligned} dP &= L(\mathbf{p},\mathbf{r}).\cos\theta.dA.d\Omega \\ \mathbf{F}(\mathbf{r}) &= \int_{\Omega} \mathbf{p}.L(\mathbf{p},\mathbf{r}).d\Omega \end{aligned} \tag{101}$$

In the case of isotropic radiance, $L(\boldsymbol{p},\boldsymbol{r})$ will be a function of $\boldsymbol{r}$ only, and thus

$$\mathbf{F}(\mathbf{r}) = L(\mathbf{r}).\int_{\Omega} \mathbf{p}.d\Omega, \tag{102}$$

and for the component along the normal vector (Z-component):

$$F_z(\mathbf{r}) = L(\mathbf{r})\int_{\Omega} \cos\theta.d\Omega = \pi.L(\mathbf{r}). \tag{103}$$

The other components will render zero, because of a zero result of the φ-integration of the function sin φ and cos φ over 2π. And so, using a constant value L_0 for $L(\mathbf{r})$, we find for the normalized cumulative function:

$$C(\theta) = \frac{C'(\theta)}{C'(\pi)} = \sin^2\theta \quad \text{with} \quad C'(\theta) = \int_0^{\theta} L_0.\cos\theta'.\sin\theta'.d\theta'.$$

By equalling a fresh random number (between 0 and 1) to $C(\theta)$, we find the corresponding value for θ (between 0 and π).

12.5.5 Internal Point Sources

For internal point sources, we may follow the same lines as with pencil beams or broad, divergent beams, if wanted combined with a tilting angle. In this way, we are able to construct a layered sample with internal structures like spheres and cylinders, and to direct a beam either from the side or upwards, from the backside of the sample. It is also possible to combine this option with the option of internal detection, as will be described below.

12.5.6 Distributed Sources

Distributed sources will originate from points in a certain well-defined volume within the sample. These points will emit in random directions, and the light will not have a beam-like character. This type of photon source will be encountered, for instance when calculating Raman or fluorescence scattering from within a scattering and absorbing volume. In those cases the calculations will consist of two steps:

- Absorption of light with wavelength λ_1 at relevant positions inside the medium,
- Scattering to the surface of the sample, using photons originating from the absorption positions of the previous step, but now with wavelength λ_2.

For fluorescence and Raman-Stokes emission λ_1 should be smaller than λ_2. This means that in general the optical characteristics of the sample and its internal structure will be different in the two steps.

Due to the absorption step that precedes the fluorescence or Raman emission the direction of emission of the photon will be at random. Then the procedure of isotropic scattering can be used, see subsection 12.4.5. This means that the polar angle θ can be found from $\cos\theta = 1 - 2R_N$, where R_N is a fresh random number. Now $\cos\theta$ is identical to the Z-component of the direction unit vector, and from that the other components can be found, using a random number between 0 and 2π to find φ.

The polarization direction will be randomized as well, which will randomise the components of the Stokes vector. The Stokes vector $\boldsymbol{S}^T_0$, which starts the polarization procedure in equation 61, will now be defined on a local coordinate frame, with its Z-axis along the propagation vector of the photon and its X- and Y-axes perpendicular to that direction and to each other. Then the two components $E_{//}$ and $E_\perp$ might be chosen at random, as long as they satisfy $E_{//}^2 \cos^2\theta + E_\perp^2 \sin^2\theta = E_0^2$, where θ is the angle of the electric vector in the XY-plane with the X-axis.

12.6 DETECTION

Normally the detection of emerging photons will take place at the surface, either at the top or at the bottom of the sample. We will denote these external detection options as "reflection" and "transmission" respectively. Another way of detection is to make use of "internal" detectors. Here the photons are supposed to end their path at a certain position inside the sample.

A general property for both options is the presence of a limited Numerical Aperture (*NA*), with $NA = \sin\theta_D$, where θ_D is the (half) opening angle of the detection cone. *NA* ranges from 0 (pure pencil beam) to 1 (all incoming angles accepted). Its value can be set in the program.

The program stores the place of detection of the photon (*x,y,z*-coordinates) and the direction angles (θ and φ) with respect to the external laboratory coordinate frame. It also stores the number of scattering events and the percentage of Doppler scattering events. It also stores the resulting Doppler frequency and the path length, either geometrical or optical. The latter is corrected for wavelength changes due to changes in the refractive index, by multiplication of the local contribution to the path with the refractive index of the local medium.

12.6.1 External Detection

In the case of external detection, either reflection or transmission, the photon is assumed to be detected if

- It passed the detection plane in the proper direction. This implies that the photon indeed has crossed the final interface between the sample and the

medium where the detector is. This is to be decided using the proper Fresnel relations (see above);

- It passed that plane within the borders of the "detection window". This window can be chosen rectangular, circular or ring-shaped.

Contrary to what is mentioned above with external detection the program does not store the z-coordinate of detection, but the average depth of all scattering events along the path, or (as desired) the maximum depth along the path.

12.6.2 Internal Detection

With internal detection two options are present, one at the interface between two layers, and one at the internal interface of a structure (or "block"), like a sphere or cylinder.

- The first option is handled in the same way as with external detection, using "reflection" and "transmission" to denote the interface crossing direction necessary for detection.
- The second option is more complicated. This is elucidated in Figure 21, where the situation is sketched for a sphere, as an example. A cylinder can be described analogously.

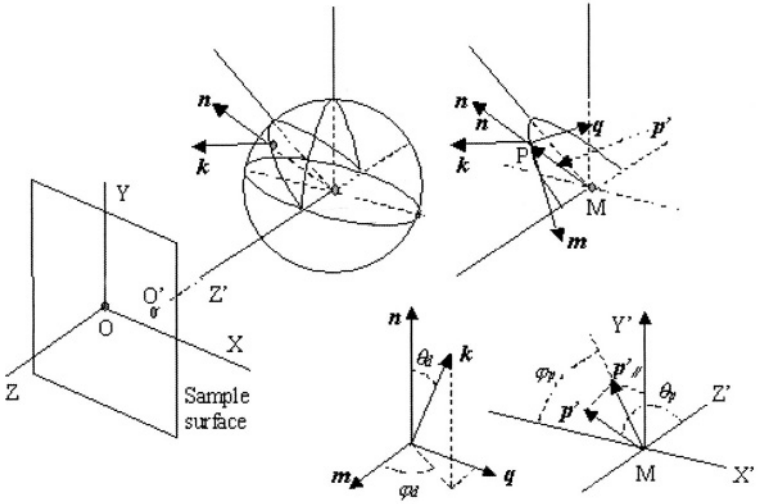

Figure 21. Internal detection at the inside of a spherical surface. The vectors ***p'***, ***k*** and ***n*** denote the position vector (relative to the origin of the sphere), the direction vector and the normal on the surface respectively. The vectors ***n***, ***m*** and ***q*** represent the local coordinate frame at the detection point P, with ***m*** in the plane spanned by ***n*** and the Z'-axis, and ***q*** // ***n*×*m***. All vectors except ***p'*** are here considered to be unit vectors. The subscripts p and d denote"position"and"direction"respectively.

With the definitions as in Figure 21 the calculation of the position and direction angles proceeds as follows:

$$
\begin{aligned}
&(1).\ \boldsymbol{q} = \boldsymbol{n} \times \boldsymbol{e}_z\,,\\
&(2).\ \boldsymbol{m} = \boldsymbol{q} \times \boldsymbol{n}\,,\\
&(3).\ \theta_d = \arccos\,(\boldsymbol{n} \bullet \boldsymbol{k}),\\
&(4).\ \boldsymbol{k}_{/\!/} = \boldsymbol{k} - \boldsymbol{n}\,.\cos\,\theta_d = \boldsymbol{k} - \boldsymbol{n}.(\boldsymbol{n} \bullet \boldsymbol{k})\,,\\
&(5).\ \varphi_d = (1/|\boldsymbol{k}_{/\!/}|).\ \arccos\,(\boldsymbol{m} \bullet \boldsymbol{k}_{/\!/})\,,\\
&(6).\ \boldsymbol{p}' = \boldsymbol{p} - \boldsymbol{r}_M = R\,.\,\boldsymbol{n}\,,\\
&(7).\ \theta_p = \arccos\,(\boldsymbol{p}' \bullet \boldsymbol{e}_z)\,,\\
&(8).\ \boldsymbol{p}'_{/\!/} = \boldsymbol{p} - \boldsymbol{e}_z\,.\,\cos\,\theta_p\,,\\
&(9).\ \varphi_p = (1/|\boldsymbol{p}'_{/\!/}|).\ \arccos\,(\boldsymbol{p}'_{/\!/} \bullet \boldsymbol{e}_x)\,.
\end{aligned}
\tag{104}
$$

Expressing $\boldsymbol{k}$ from the (X',Y',Z')-frame into the (X,Y,Z)-frame is as follows (Figure 22):

$$
\begin{aligned}
&\boldsymbol{k} = \sin\theta'.\cos\varphi'.\boldsymbol{e}_x' + \sin\theta'.\sin\varphi'.\boldsymbol{e}_y' + \cos\theta'.\boldsymbol{e}_z',\\
&\boldsymbol{e}_x' = \cos\theta_0.\cos\varphi_0.\boldsymbol{e}_x + \cos\theta_0.\sin\varphi_0.\boldsymbol{e}_y - \sin\theta_0.\boldsymbol{e}_z\\
&\boldsymbol{e}_y' = -\sin\varphi_0.\boldsymbol{e}_x + \cos\varphi_0.\boldsymbol{e}_y\\
&\boldsymbol{e}_z' = \sin\theta_0.\cos\varphi_0.\boldsymbol{e}_x + \sin\theta_0.\sin\varphi_0.\boldsymbol{e}_y + \cos\theta_0.\boldsymbol{e}_z
\end{aligned}
\tag{105}
$$

The program offers the options to record internally detected photons in "reflection" mode *(i.e.,* with direction angles $\theta > \pi/2$) or in "transmission" mode ($\theta < \pi/2$). It also allows calculating the direction angles at the point of detection in both coordinate frames (laboratory frame and local frame). See Figure 23.

12.6.3 Sampling of Photons

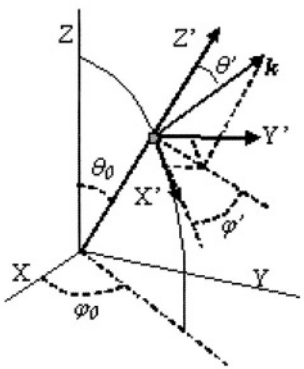

Figure 22. Expressing *k* from the (X',Y',Z')-frame into the (X,Y,Z)-frame.

For the sampling of photons some options for the maximum number of photons can be set:

- Emitted photons,
- Injected photons,
- Detected photons.

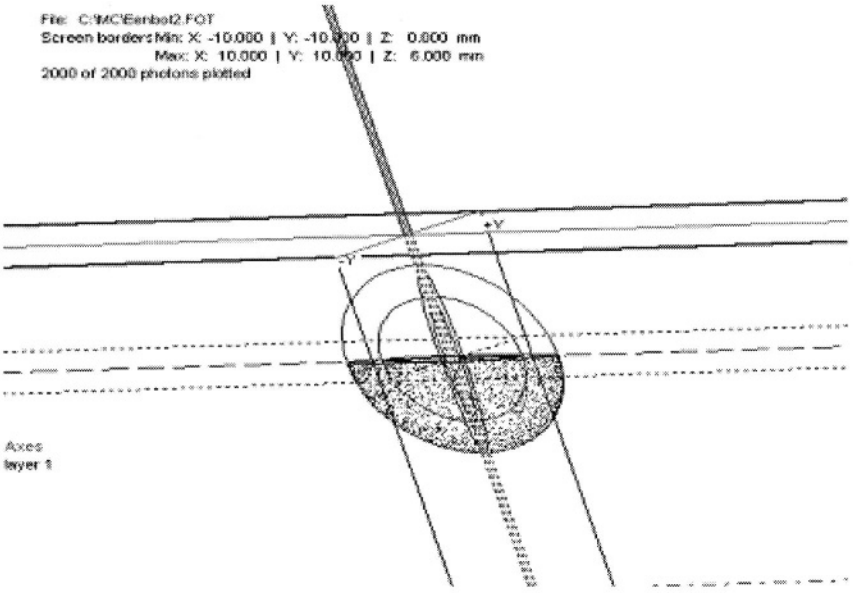

Figure 23. Internal detection at the inside of a sphere. Settings: detection of photons arriving at the transmission side of the sphere only.

In all cases we consider photons to be detected only when arriving at the plane of detection within the detection window (rectangular, circular or ring-shaped). The difference between the options “emitted” and “injected” is due to the chance of reflection of the incoming beam at the surface of the sample and will be determined by the Fresnel relations.

Besides the recording of all properly detected photons, there exists also the option of recording the position of the photons during their paths, thus performing time-of-flight tracking. This can be done at a number of presettable time points, and the photons are stored in files similar to the files with detected photons.

12.6.4 Photon Path Tracking

The tracking of the path of the photon, *i.e.,* recording the coordinates of the scattering events and of the intersections with interfaces, can easily result

in enormous files. Consider a typical case of scattering in tissue, with a scattering coefficient μ_s of about 10-20 mm^{-1} and a *g*-factor (average of the cosines of the polar scattering angles) of about 0.80 – 0.90. Then in each mm of the path about $1/\mu_s \approx 10$ scattering events will take place. However, due to the large *g*-factor the scattering will be predominantly in forward direction and it will only be after about $1/\mu_s' \approx 1$ mm that the direction of the photon can be considered as randomized. When detecting "reflected" photons, the path length of the photons will depend on the distance *d* between the point of injection of the light in the sample and the point of detection. For homogeneous samples the average depth in the middle of that distance is about ½*d,* and the average smoothed path length for perpendicular entrance and exit will be ½π*d*. However, the actual paths are very irregular and the actual path lengths can range from about that value to tens or hundreds times as large. This means that in most cases the number of scattering events will be very large. As an example, for a thick homogeneous medium with $\mu_s' = 1$ mm^{-1} and without absorption the average path length will be about 6*d,* which for $d = 2$ mm means about 120 scattering events, thus per photon at least 120 × 3 × 4 bytes = 1440 bytes. A typical simulation needs at least 10^4 photons, and thus in total 1440 Mbytes. Therefore, in those case it is better to register only part of the events, namely those at intervals of $1/\mu_s' = 1$ mm, which will decrease the storage space to 144 Mbytes per simulation.

Therefore, the program offers the options of recording the paths at intervals of $1/\mu_s$ or $1/\mu_s'$.

Photons originating from a pencil beam and emerging at equal distances *d* from the point of injection but at different positions on that ring are equivalent. However, visualization of those tracks will end up in a bunch that cannot be unraveled. Therefore, to clarify viewing we may rotate the whole paths around the axis of the pencil beam to such an orientation as if the photons all emerged at the same position on the ring, *e.g.,* the crossing point with the X-axis. This particular rotation is given by

$$\begin{pmatrix} x' \\ y' \\ z' \end{pmatrix} = \begin{pmatrix} \cos\varphi & \sin\varphi & 0 \\ -\sin\varphi & \cos\varphi & 0 \\ 0 & 0 & 1 \end{pmatrix} \begin{pmatrix} x \\ y \\ z \end{pmatrix}. \tag{106}$$

See Figure 24 for an example of the path tracking method.

12.7 SPECIAL FEATURES

We now will describe some special features that are incorporated in the program. Laser-Doppler Flowmetry is the oldest feature, built in from the beginning of the development of the program, and meant to support measurements of Laser-Doppler Perfusion Flowmetry in tissue. Photoacoustics has been added to simulate the acoustic response to pulsed light. Frequency modulation is a modality adding extra information using path length-dependent phase delay information.

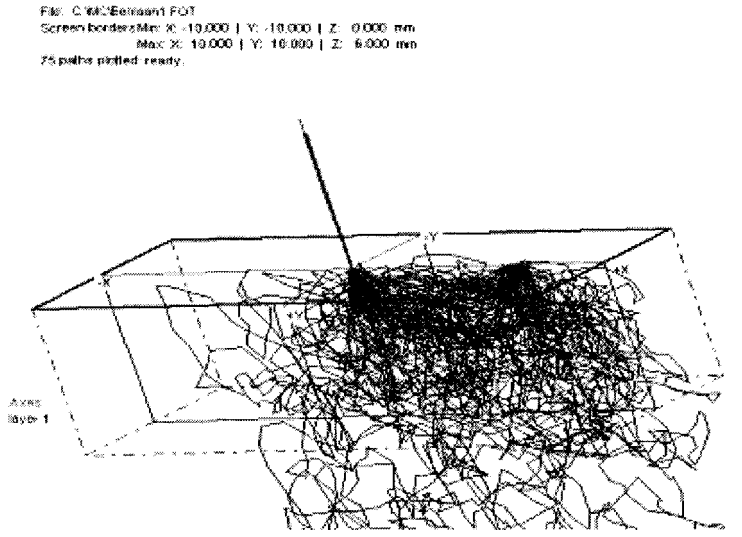

Figure 24. Photon path tracking: Photon "bananas" arising by scattering from beam entrance point to exit area (between 5 and 6 mm). For clarity, all photon paths were rotated afterwards as if the photons had emerged on the +X-axis.

12.7.1 Laser-Doppler Velocimetry

(1). Introduction

Laser-Doppler Flowmetry (LDF) makes use of the Doppler effect encountered with scattering of photons in particles when those particles are moving. In Figure 25 the principles are shown. Using the definitions of the variables given in that Figure, the Doppler frequency is given by

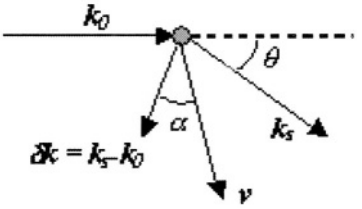

Figure 25. Principles of Laser-Doppler Flowmetry. The particle has a velocity v. Vectors $\boldsymbol{k_0}$ and $\boldsymbol{k_s}$ denote the incoming and scattered light wave vectors, and $\boldsymbol{dk}$ is the difference vector.

$$\omega_D = (\boldsymbol{k}_s - \boldsymbol{k}_0) \bullet \boldsymbol{v} \tag{107}$$

and with

$$|\delta \mathbf{k}| = 2k.\sin\tfrac{1}{2}\theta, \tag{108}$$

we find

$$f_D = \frac{kv}{\pi}\sin\tfrac{1}{2}\theta.\cos\alpha. \tag{109}$$

When applied to tissue, frequently the angles θ and α might be considered randomized. This is due to three reasons:

- Preceding scattering by non-moving particles might cause the direction of the photons to be randomized upon encountering moving particles;
- Most important moving particles are blood cells in capillaries. Due to the (more or less) random orientation of the capillaries the velocities will have random directions;
- Traveling from injection point to detection point, in general the photons will encounter many Doppler scattering effects, with random velocities and orientations.

All three effects will broaden the Doppler frequency distribution, which ideally would consist of one single peak, to a smooth distribution as in Figure 26. This means that it is not possible to measure the local velocity, but we only may extract information about the averaged velocity over the measuring volume. The averaging concerns the three effects mentioned above.

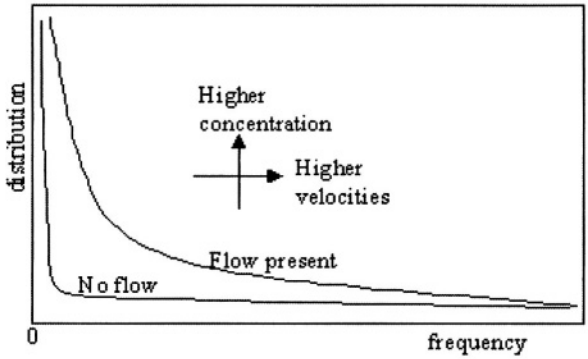

Figure 26. A typical Doppler frequency spectrum as measured with LDF tissue perfusion (positive frequencies shown).

There are two options to record these LDF-spectra: homodyne and heterodyne, depending on the relative amount of non-shifted light impinging on the detector. The first is the mutual electronic mixing of the Doppler-shifted signals, and the second is the mixing of those signals including mixing with non-shifted light, which can be overwhelmingly present. The resulting frequency and power spectra (which is the autocorrelation function of the frequency spectrum) will look as sketched in Figure 27.

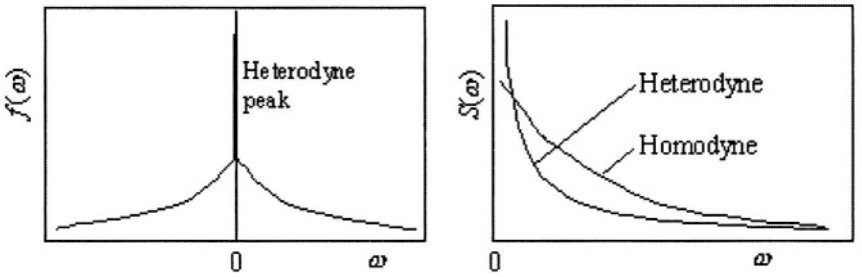

Figure 27. Homodyne and heterodyne frequency spectra $f(\omega)$ and power spectra $S(\omega)$. Normally the heterodyne peak is much higher than the signals at non-zero frequencies.

To characterize the frequency spectra use is made of moments of the power spectrum, defined as

$$M_n = \int_0^\infty \omega^n . S(\omega) . d\omega, \tag{110a}$$

and the reduced moments

$$M_n' = \frac{M_n}{M_0{}^n}. \tag{110b}$$

The zeroth moment is the area under the power spectrum itself, and can be considered as proportional to the concentration of moving particles in the measuring volume. Bonner *et al.* [5] showed that the first moment M_1 is proportional to the averaged flow, while the ratio of the reduced moment $M_1' = M_1 / M_0$ will be proportional to the averaged velocity. Analogously, the reduced moment $M_2' = M_2 / M_0{}^2$ will be proportional to the average of the velocity-squared.

All three moments may be calculated within the package.

(2). Construction of the Doppler Power Spectrum

For the construction [11] of the Doppler power spectrum from the frequency distribution all photons detected within the detection window will be sorted into a discrete frequency distribution $N(\omega_i)$. Suppose we recorded a_i photons in the i-th spectral interval (width $\Delta\omega = 2\pi\Delta f$). This number is proportional to $I(f_i).\Delta f$, where I is the intensity, which is proportional to $|E^2|$, E being the electric field amplitude.

$$E(t) = \sum_{j=0}^{N} \sqrt{a_j}\, \exp\left[i(j\Delta\omega.t + \phi_j)\right], \tag{111}$$

where $N+1$ is the number of intervals, and ϕ_j is the phase of the jth component. Since in the experiment we assume all photons to arrive at the same time, coherence between photons in the same frequency interval cannot be excluded. Therefore, ideally $\Delta\omega$ should be so small that the only values for a_j would be 0 and 1. However, to be able to work with tractable summations, a_j is to be read as the probability of the photon to arrive in that interval.

A square-law detector will at time $n\Delta t$ measure a current I proportional to E^*E:

$$i(n\Delta t) = c\sum_{v=0}^{N}\sum_{w=0}^{N} \beta_{vw}\sqrt{a_v a_w}\, \exp\{\, i[(w-v)\Delta\omega.n\Delta t + \phi_w - \phi_v]\} + cc, \tag{112}$$

where c is a proportionality constant, cc stands for "complex conjugate" (to ensure that i is real) and β is a constant related to the degree of coherence of the signals in the frequency intervals ($\beta = 1$ for perfect coherence, but $\beta < 1$ when the detector area is larger than a single coherence area). Assuming that β is not frequency dependent, one can write

$$I(n\Delta t) = c\beta \sum_{v=0}^{N} \sum_{w=0}^{N} \sqrt{a_v a_w}\ \exp\{\, i[(w-v)\Delta\omega.n\Delta t + \phi_w - \phi_v]\} + cc. \tag{113}$$

Now we rename v = *p,* and define $k = w - v$ and the factor f_{pk} as

$$f_{pk} = c\beta\sqrt{a_p a_{p+k}}\ \exp\left[i\left(\phi_{p+k} - \phi_p\right)\right] \tag{114}$$

and find

$$I(n\Delta t) = \sum_{p=0}^{N} \sum_{k=0}^{N-p} f_{pk}\ \exp(i\Delta\omega.n\Delta t) + cc. \tag{115}$$

The Fourier transform $S(t)$ of the power spectrum $S(\omega)$, defined as

$$S(t) = < i^*(0).i(t) >, \tag{116}$$

can be written as

$$S(m\Delta t) = \frac{\Delta t}{N-m+1} \sum_{n=0}^{N-m} I(n\Delta t)\ I((n+m)\Delta t), \tag{117}$$

with $\Delta\omega = 2\pi/[(N+1).\Delta t]$. We construct the power spectrum $S(j\Delta\omega)$ using

$$S(j\Delta\omega) = \sum_{m=0}^{N} S(m\Delta t)\ \exp(-ij\Delta\omega.\Delta t), \tag{118}$$

and find

$$S(j\Delta\omega) = \sum_{m=0}^{N} \sum_{n=0}^{N-m} \sum_{p=0}^{N} \sum_{k=0}^{N-p} \sum_{p'=0}^{N} \sum_{k'=0}^{N-p} \frac{\Delta t}{N-m+1} \times \tag{119}$$

$$\left[\begin{array}{l} f_{pk}.f_{p'k'}.\exp\{i\Delta\omega\Delta t[kn + k'(n+m) - mj]\} + \\ f_{pk}^*.f_{p'k'}^*.\exp\{-i\Delta\omega\Delta t[kn + k'(n+m) + mj]\} + \\ f_{pk}.f_{p'k'}^*.\exp\{i\Delta\omega\Delta t[kn - k'(n+m) - mj]\} + \\ f_{pk}^*.f_{p'k'}.\exp\{-i\Delta\omega\Delta t[kn - k'(n+m) + mj]\} \end{array}\right].$$

Now, in the limit of $N \to \infty$, the phase factors will average out, except when their exponentials equal zero. Since the sum $n + m$ appears in each exponential, in order to have the exponential equal zero for each

combination of n and m the variables n and m must not be present in the exponentials. This is possible in the last term only, under the condition that $k = k'=j$:

$$S(j\Delta\omega)=\sum_{m=0}^{N}\sum_{n=0}^{N-m}\sum_{p=0}^{N}\sum_{k=0}^{N-p}\sum_{p'=0}^{N}\sum_{k'=0}^{N-p'}\frac{\Delta t}{N-m+1}f_{pk}*.f_{p'k'}\,\delta(k-k')\,\delta(k-j). \tag{120}$$

Since $0 \le k \le N - p$, with $k = j$, it follows that $N - p \ge j$ or $p \le N - j$. Then

$$S(j\Delta\omega)=\sum_{m=0}^{N}\sum_{n=0}^{N-m}\sum_{p=0}^{N-j}\sum_{p'=0}^{N-j}\frac{\Delta t}{N-m+1}f_{pj}*.f_{p'j}=\sum_{p=0}^{N-j}\sum_{p'=0}^{N-j}2\pi\frac{f_{pj}*.f_{p'j}}{\Delta\omega} \tag{121}$$

and

$$S(j\Delta\omega)=2\pi\frac{c^2\beta^2}{\Delta\omega}\sum_{p=0}^{N-j}\sum_{p'=0}^{N-j}\sqrt{a_pa_{p'}a_{p+j}a_{p'+j}}\,\exp\left[i\left(\phi_p-\phi_{p'}+\phi_{p'+j}-\phi_{p+j}\right)\right]. \tag{122}$$

Now, suppose that all photons arrive at the detector with equal phases. Then the exponential in equation (122) becomes zero, and

$$S(j\Delta\omega)=2\pi\frac{c^2\beta^2}{\Delta\omega}\left[\sum_{p=0}^{N-j}\sqrt{a_pa_{p'}}\right]^2. \tag{123}$$

However, in general the photons will have different phases due to their different path lengths. The measured power will be the expectation value of equation 122 averaged over all phases. Thus for the term in equation 122 with p and p', the expectation value will be zero unless $p=p'$. This leads to

$$S(j\Delta\omega)=2\pi\frac{c^2\beta^2}{\Delta\omega}\sum_{p=0}^{N-j}\sqrt{a_pa_{p+j}a_pa_{p+j}}=2\pi\frac{c^2\beta^2}{\Delta\omega}\sum_{p=0}^{N-j}a_pa_{p+j}. \tag{124}$$

This is the general expression for the calculation of the power spectrum from the simulated frequency distribution.

In the case of heterodyne detection, where one of the spectral components (normally that at zero frequency, set $p = 0$ for that frequency) is much more intense than all others, equations 123 and 124 will lead to the same result:

$$S(j\Delta\omega)_{het}=2\pi\frac{c^2\beta^2}{\Delta\omega}a_0a_j. \tag{125}$$

(3). Implementation of Velocity Profiles

For the velocity profiles of the scattering particles following options are available:

- Velocity direction along X-, Y- or Z-axis, or (in case of oblique blocks) along the block axis.
- Velocity direction randomized for each scattering event, with all particles equal velocities. The direction is determined with a similar procedure as with isotropic injection of light (see subsection 12.5.4).
- Profiles can be uniform (equal velocity for all particles), or parabolic (in tubes and rectangular blocks only), or they can have a Gaussian distribution.

  With the parabolic distribution the actual velocity is calculated according to

$$v = 2v_0(1 - \frac{r^2}{R^2}) \tag{126}$$

with v_0 as the average velocity value over the profile, r as the position of the particle with respect to the symmetry axis of the tube or block, or the mid plane of the layer when relevant, and R as the radius of the tube, or the distance between the adjacent interfaces .

The Gaussian profile is handled using a cumulative function for the Gaussian profile. Here the standard deviation is expressed in a percentage of v_0, being the maximum velocity in the profile. The actual value of the velocity is determined by equaling a fresh random number to that cumulative function.

12.7.2 Photoacoustics

With photoacoustics (PA) short light pulses are injected in the sample. At positions where absorbing particles are present, part of the light will be absorbed. Due to the short duration of the pulse, the particle will heat up adiabatically. Normally this would result in volume dilatation, but since the surrounding medium is not heated, this dilatation will be prevented and a pressure shock wave will result. Some authors have investigated this mechanism. A review and some new theoretical aspects can be found in Hoelen's thesis and papers [25-28].

Typical values for the duration (FWHM) of the light pulses and the amount of energy to be injected are: 15 ns and 1 mJ/cm^2. With this values a safety factor of 20 from the European maxima for human tissue irradiation

with this type of light pulses is maintained. Using a sound velocity of 1500 m/s this corresponds to a distance of 22.5 μm.

The PA-response of a spherical source on a short laser pulse is given by:

$$P(r,t) = C\frac{v^2}{r}\left(t-\frac{r}{v}\right)\exp\left\{-\left[\frac{v}{r_0}\left(t-\frac{r}{v}\right)\right]^2\right\}, \tag{127}$$

with r as the distance from PA-source to the detector, r_0 as the source radius, t as the time after the pulse and v as the acoustic velocity. Since for the calculations in this program we only have to deal with relative values, we have incorporated variables describing the dilatation, the heat capacity and the heat conduction of the source, and the laser pulse energy in the constant C.

This function is a bipolar function, as in Figure 28.

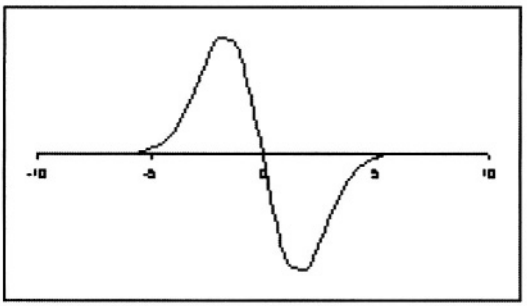

Figure 28. Bipolar PA-pulse response: function $P = x\cdot\exp(-x_2/x_0)$, with $-10 < x < 10$ and $x_0 = 5$.

We suppose that the sample can be subdivided into many 3D-voxels, which may serve as elementary PA-sources, provided light absorbing material is present. The voxels are supposed to be cubical, with sides *da.* It can be shown that the peak-peak time, *i.e.,* the time τ_{pp} between the positive and negative peak of the bipolar pulse, is given by

$$\tau_{pp}^{\ 2} = (2\sigma)^2 = (2\sigma_l)^2 + (2\sigma_s)^2 = 2\tau_e^{\ 2}, \tag{128}$$

where σ_l is the standard deviation of the laser pulse, σ_s is that of the source voxel, σ is that of the bipolar pulse and τ_e is the effective pulse length. The value of σ_l is given by $FWHM/[2\sqrt{(2.\ln 2)}]$, with $FWHM$ as the full width at half maximum of the (Gaussian) laser pulse. For a cubical voxel, σ_s is given by $\sigma_s = da/(2\sqrt{2}.v)$, with $da/\sqrt{2}$ as the effective diameter of the heat source element.

The expression for the pressure given by equation 127 has to be adapted for ultrasound attenuation during the time-of-flight to the detector. This will result in the corrected pressure pulse *P'(r,t):*

$$P(r,t) = C\frac{v^2}{r}\left(t-\frac{r}{v}\right)\exp\left\{-\left(\frac{t-r/v}{\tau_e}\right)^2\right\}.\exp(-\mu_{US}.r), \tag{129}$$

where μ_{US} is the ultrasonic attenuation coefficient. This coefficient is slightly dependent on the ultrasound frequency. Here we take it as a constant, in view of the broad frequency bandwidth of the PA-pulse.

This function has been implemented in the program, with C =1. The pressure pulse is calculated as originating from the center of the source voxel and arriving at the centers of the elements of the detector array. Therefore, the resulting pressure signal has to be multiplied with the area of the detector element, and normalized to the volume of the voxel. However, in reality with elements that are not "small", due to phase differences upon arrival of the pressure pulse at different positions on a detector element, some destructive interference might be present, which will decrease the multiplication factor. We may correct for this effect in two ways:

- The detector elements are at first chosen very small (*i.e.,* much smaller than the wavelength of the sound) and are afterwards grouped to larger detector elements, taking into account the phase differences between the center points of the constituting elements in the group, for each voxel;
- The contribution from individual PA-sources to individual detector elements is corrected using the Directivity, or the Numerical Aperture function, of the detector element. Normally this is a Gaussian function, centered along the symmetry axis perpendicular to the element, with a certain opening angle given by the dimensions of the element and the characteristics of the laser pulse.

In the program both methods are implemented. For the Directivity a Gaussian, uniform or triangular function can be chosen. The groups are built from rectangles of single elements. See Figure 29.

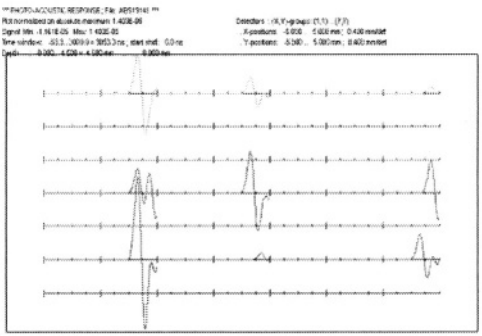

Figure 29. Photoacoustic response at a 7 × 7 - detector array of a sample consisting of several absorbing objects in a scattering (but not absorbing) medium.

12.7.3 Time-of-Flight Spectroscopy and Frequency Modulation

A relatively new branch of the art of light scattering in tissue is time-of flight resolved scattering. The general idea is to distinguish between photons on the basis of their paths in tissue. This can be of help to elucidate the distribution of the optical properties, for instance when dealing with samples consisting of various layers.

There are two main methods:

- Time-of-flight spectroscopy, in which the photon paths are registered using time-resolved detection, *e.g.,* with ps- or fs-lasers and an ultrafast camera like a streak camera, or by using ultrafast time-windowing using Kerr's cells. A typical time is 3 ps for 1 mm resolution (light velocity = 3×10^8 m/s).
- Frequency Modulation spectroscopy, where the light source is modulated at very high frequencies, and the phase differences are recorded between photons arriving at the same detection point but after having traveling over different paths. The frequency range in use starts at 100 MHz and stops nowadays at about 1-2 GHz. For 100 MHz a path length difference of 1 mm will result in a phase difference of about 0.1 degree.

The first option of *Time-of-flight spectroscopy* has been taken care of in two ways:

- By implementing the possibility to register the positions of the photons at certain presentable time points during the scattering process;
- Using the option of analyzing the registered time-of-flight distributions, that can be calculated form the simulated paths lengths (geometrical or optical) of the detected photons.

The second option of *Frequency Modulation spectroscopy* uses simple Fourier transformation of the path length distribution. For this purpose the path length distribution is translated into a time-of-flight distribution, using the local light velocities. The Fourier transform of this distribution will result in the frequency response. When denoting that Fourier transform with $F_j(\omega)$, we can deduce for the phase delay $\varphi_j(\omega)$ and the AC/DC modulation depth $m_j(\omega)$:

$$\varphi_j(\omega) = \arctan\frac{\mathrm{Im}\,F_j(\omega)}{\mathrm{Re}\,F_j(\omega)} \quad \text{and} \quad m_j(\omega) = \sqrt{\frac{\mathrm{Im}^2 F_j(\omega) + \mathrm{Re}^2 F_j(\omega)}{\mathrm{Re}^2 F_j(0)}}. \tag{130}$$

For the actual transform we may use the possibility of enlarging the number of points n in the time-of-flight distribution to an integer power of 2, named N, by filling the new points with zeros. Then Fast-Fourier transform algorithms will become possible. In doing this, the step size in the frequency spectrum will be smaller. When the time step in the time-of-flight distribution is given by Δt, then the maximum frequency is $f_{max} = 1 / (2\Delta t)$ and the frequency step is $\Delta f = f_{max} / (\frac{1}{2}N) = 1 / (N.\Delta t)$. This factor 2 is included due to the aliasing effect of this type of Fourier transform, by which the frequency spectrum ($f = 0..f_{max}$) is folded out and copied to $f = f_{max}..2f_{max}$.

The program also offers facilities to calculate frequency modulation spectra using literature models, based on the diffusion approximation of the Radiative Transfer Equation, from Haskell *et al.* [8] for one-layer samples and Kienle *et al.* [9,10] for two-layer samples. Here we only list their results as far as implemented in the program.

We will use the notation (μ_a and μ_t are the absorption and total scattering coefficients: $\mu_t = \mu_a + \mu_s'$, and ω is the frequency):

$$k_R = \mathrm{Re}(k) = K(1) \quad ; \quad k_I = \mathrm{Im}(k) = K(-1), \tag{131}$$
$$K(p) = \sqrt{\tfrac{3}{2}\mu_a\mu_t}\sqrt{\sqrt{1+\omega^2\tau^2}+p}$$

For small frequencies these functions can be approximated by

$$k_R = \sqrt{3\mu_a\mu_t}\left[1+\tfrac{1}{8}\omega^2\tau^2\right] \quad ; \quad k_I = \tfrac{1}{2}\sqrt{3\mu_a\mu_t}\,\omega\tau \quad ; \quad \tau = \frac{1}{\mu_a c/n}$$

Haskell *et al.* calculated five models, (a) through (e), for the one-layer case, and Kienle *et al.* added a general model (f) for the two-layer case. These models are implemented in the program.

(a). Infinite medium.

$$\Delta\varphi = k_I r \quad ; \quad m = \exp\left[-\left(k_R - \sqrt{2}q\right)r\right], \tag{132a}$$

where r is the source-detector distance and $q = \sqrt{(3\mu_a \mu_t/2)}$.

Using equation 131b we may see that for small frequencies $\Delta\varphi$ will start linear with ω and m will start as a (slowly decreasing) constant. When ω increases, the slope of $\Delta\varphi$ will decrease gradually and the value of m will decrease as well.

(b). Semi-infinite medium, taking refractive index differences at the interface into account:

$$\Delta\varphi = k_I r - \arctan(I/R) \quad ; \quad m = (1/D)\sqrt{I^2 + R^2} \tag{132b}$$

with D, I and R complicated functions of r, μ_a, μ_t and of the refractive indices and the refraction angles.

(c). Semi-infinite medium, without interface correction.

$$\Delta\varphi = k_I r - \arctan\frac{k_I}{k_R + 1/r_0} \quad ;$$
$$m = \frac{\sqrt{(k_R + 1/r_0)^2 + k_I^2}}{\sqrt{2}q + 1/r_0} \exp\left[-\left(k_R - \sqrt{2}q\right)r_0\right] \tag{132c}$$

with $r_0^2 = r^2 + (1/\mu_t)^2$.

(d). Extrapolated boundary condition, where the interface has been shifted over a distance dependent of the refractive indices at the interface (see Haskell *et al.* [8] for this and following models).

(e). Partial Current and Extrapolated Boundary Unification.

(f). Two-layer model (Kienle *et al.* [9,10]).

12.8 OUTPUT OPTIONS

The program offers several possibilities for output of the data. Apart from various ways to write photon data and corresponding statistics to file, we have several plot options. They will be described below. All plots can be exported in the form of *.BMP-files.

12.8.1 Parameter Plots

The fastest way of plotting data is using parameter plots of photon distributions, in which the number of photons is plotted as a function of one out of a set of variables. These variables are:

(a) X- , Y-, or R- position at detection or at plane-crossings (see below; R is the radius of the circle around central Z-axis),
(b) (R-position)^2 (as above),
(c) Path length or Time-of-flight distribution, followed by Phase and Modulation depth spectra using Frequency Modulation Spectroscopy,
(d) Polar angle θ or azimuthal angle φ of the photon direction at the detection point,
(e) Z-position: several options (the averaging <..> is performed over all detected photons):
- Depth (in absorption mode or with photons-in-flight at plane-crossing points),
- <Scattering depth> (in reflection or transmission mode),
- Maximum scatter depth,
- <Doppler scattering depth> (Doppler-scattering events only),

(f) Number of scatter events (or number of plane crossing),
(g) Number of Doppler scatter events,
(h) Doppler frequency,
(i) With Internal detection: Polar and azimuthal angles θ and φ,
(j) Paths: crossings with X=c planes
(k) Paths: crossings with Y=c planes
(l) Paths: crossings with Z=c planes
(m) Paths: crossings with R=c (cylindrical) planes.

Intensity Plots

Normally we may choose for plotting of photon distributions, as a function of one of the variables. However, in case the variable is R or R^2 we have the option for plotting the intensity instead, thus dividing distribution function by $2\pi R.dR$, with dR as the interval width of the horizontal variable.

We also have the option for comparing simulated intensity plots with theoretical ones. Several models are available for that purpose. See subsection 12.8.4 (1) and Figure 30.

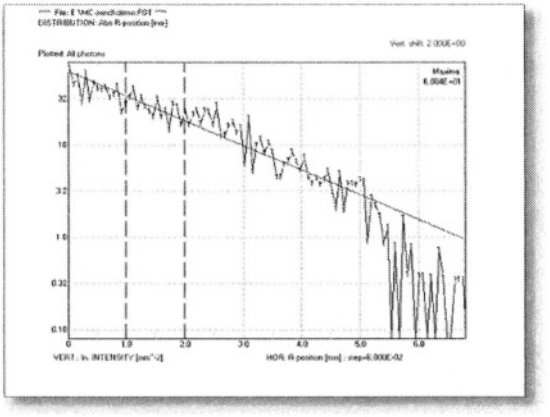

Figure 30. Example of output plots. Here ln (Intensity) vs. R-position from the Z-axis. Also included: a model approximation (solid line).

Parameters

In addition to their role as horizontal variables in the distribution plots, all variables may also be used as parameters in the plots. For instance, suppose we divide the value region of a parameter into n intervals. This will result into n lines in the plot.

There are two layers of parameters, the first offers the option of shifting the lines horizontally over a certain value, the second vertically. We also may choose the option "Compare Files", by which different files (simulations) can be compared directly, as the second parameter.

Plane-Crossing Intersections

With the options "path tracking" the intersection points of the photon paths on their travel from source to detection point, with a set of planes perpendicular to the direction of the photons as seen at the surface, are recorded. The average coordinates of those intersections are calculated.

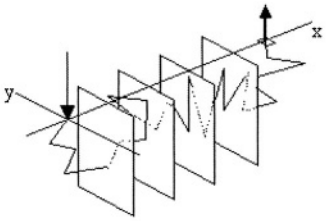

Figure 31. Example of recording of path tracking of the photons, in which the photons are meant to emerge through a small window at the X-axis. The arrows indicate the injection and detection points. For analysis, we define a set of planes perpendicular to the X-axis and record the Y- and Z-coordinates of the intersections. Since photons can take steps in all directions, they might cross some planes more than once.

For instance, when photons are tracked, for which the detection point lies at the surface on the X-axis, the crossing planes are defined parallel to the X-axis, ranging from the injection point to the detection point, and the Y- and Z-coordinates of those intersection points are recorded and (afterwards) averaged. This might be clarified with Figure 31. Results are presented in Figure 32.

In order to enhance the efficiency of the simulation process, photons emerging at positions with equal radii to the injection point, might be taken together by rotating the whole path until an orientation as if the photon were emerging at that radius on the X-axis. See subsection 12.6.4.

The options for crossing planes are: flat planes perpendicular to the X- and Y-axis, and cylindrical planes around the central Z-axis at the injection point. All plots can be made on a linear or logarithmic scale, and in the form of lines or symbols or both. We may choose for the option of *n*-points quadratic smoothing.

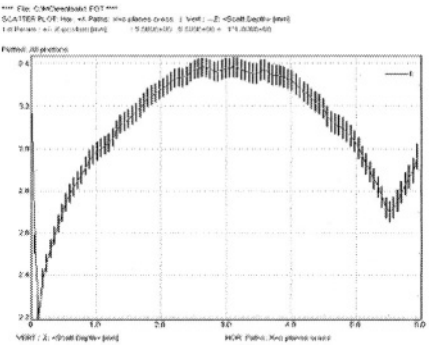

Figure 32. Paths tracking: Averaged depths of photons, emerging between 5 and 6 mm from source origin, with standard deviation in the average. Settings: reduced scattering coefficient = 1 /mm; absorption = 0. Plot for distance > 5.5 mm is due to spurious photons.

Normalization

The plots may be normalised on their own maximum, or on the highest maximum of the set, or on the maximum of the first curve. We also may normalise on the number of detected, or injected or emitted, photons.

Doppler Frequency Handling

The distributions as a function of the Doppler frequency, the "frequency distribution" may be converted into "power spectra" using the formalism described in subsection 12.7.1 (2). From those spectra we may have the program calculate the moments of the power spectrum, as discussed in subsection 12.7.1 (1).

12.8.2 Scatter Plots

In addition to the distribution and intensity plots as described above, an option of producing "scatter plots" is present, in which the values of a second variable are on the vertical axis. The individual photons can be plotted as points, or their average values (per X-axis interval) as symbols or lines.

Again we have the opportunity to divide the set of points in subsets corresponding with different values of (two) parameters. The points belonging to different parameters are presented as two spatially separated clusters. We also may choose for horizontal or vertical shifting per parameter value. See Figure 33.

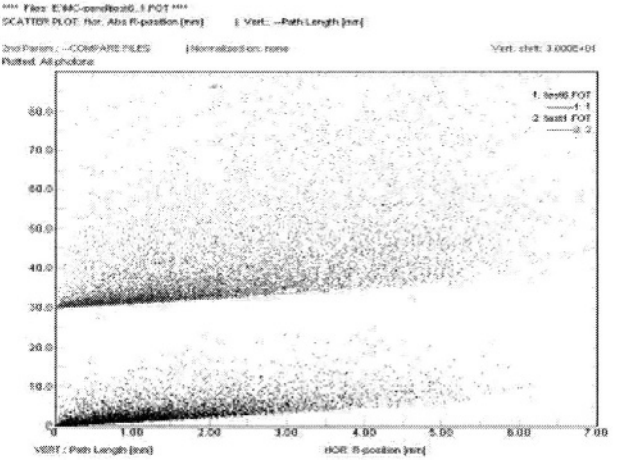

Figure 33. Scatter plots of two samples, consisting of 1 layer with μ_s' =1 mm^{-1}; μ_a = 0 (upper) and 0.1 (lower) mm^{-1} respectively. Plotted: Path length vs. detection position. In both cases 10000 photons recorded. Higher absorption results in a broader path length distribution.

12.8.3 2D/3D-plots

Another plot option is to produce 2D- or 3D-plots, based on the border values (See Figures 34 and 35).

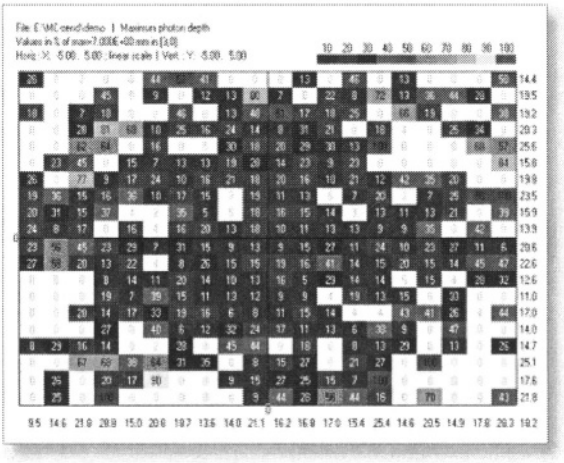

Figure 34. Example of 2D-plot: Here the maximum photon depth plotted as function of *(x,y)*-position.

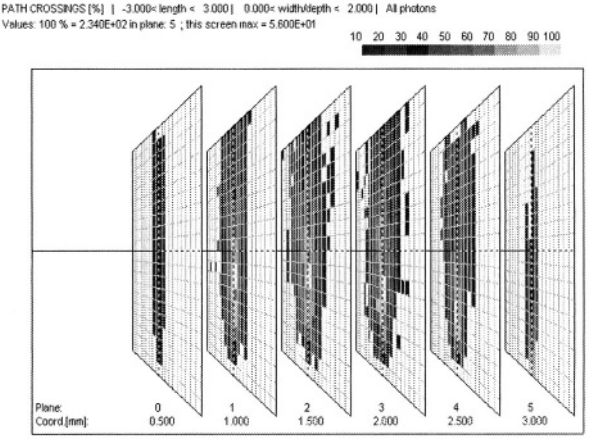

Figure 35. 3D-plot of Path tracking: photon "bananas": average depths of photon paths. Entrance at position 0; photons emerging between positions 5 and 6 mm from entrance. Normalization per frame.

12.8.4 Approximations

As a final step in the simulations one may want to compare the simulated results with theoretical curves. For this purpose we included several options in the program. The first option is to compare intensity data with published results of theoretical models based on the Diffusion Approximation. The second is to fit Doppler power spectra with exponential curves.

(1). Intensity Approximations

In literature several approximate curves for the intensity as a function of the source-detector distance were investigated. Most important are those of Groenhuis and Ten Bosch [4], Bonner *et al.* [5], Patterson *et al.* [6], and Farrell *et al.* [7]. Here we will deal with those models and give their results.

Ishimaru [2,3] notes for the light output as a function of the source-detector distance *r:*

$$I(r) = \frac{P\mu_{eff}^{\ 2}}{4\pi\mu_a r^n} \exp(-\mu_{eff}.r), \tag{133}$$

where $I(r)$ is the energy fluence rate (in W/m^2) or the photon fluence rate (in $m^{-2}s^{-1}$), depending on the definition of P, being the injected power (in W) or the number of injected photons (in s^{-1}) , n is an exponential depending on the underlying physical model, and μ_{eff} is a characteristic "effective" attenuation coefficient, given by

$$\mu_{eff} = \sqrt{3\mu_a(\mu_a + \mu_s')}\,. \tag{134}$$

There is some dispute about the value of the variable n. According to the Diffusion Approximation n should be unity. However, Groenhuis *et al.* [4] arrive at n = ½, on the basis of a simple scattering model consisting of a combination of an isotropic scattering term and a forward scattering term. Bonner *et al.* [5] use a probabilistic lattice model and derive an expression with n=2. Using an expression for the time-of-flight intensity for homogeneous slab samples, Patterson *et al.* published a model containing effective light sources at depths $z_0 + k.d$ (d = sample thickness; k= 1,2...) together with negative image sources at $-(z_0 + k.d)$ to ensure zero light flux at the surface:

$$I(r) = c\left[\sqrt{\frac{\pi}{a_+}}\exp(-2\sqrt{\mu_a a_+}) + \sqrt{\frac{\pi}{a_-}}\exp(-2\sqrt{\mu_a a_-})\right], \tag{135a}$$

where

$$a_{\pm} = \frac{(z \pm z_0)^2 + r^2}{4D} \quad , \quad D = \frac{\mu_a}{\mu_{eff}^{\ 2}}, \tag{135b}$$

with D being a diffusion constant, and $z_0 = 1/\mu_s'$.

However, when integrating this function over volume, two singularities arise, at $z = \pm z_0$. This problem was tackled by Rinzema and Graaff [29] who included non-scattered photons. This leads to a change:

$$I(r) = \frac{P}{4\pi D r}\exp(-\mu_{eff} r) \quad \rightarrow \quad \frac{P}{4\pi}\left[\frac{a'}{D_a r}\exp(-\kappa_0 r) + \frac{1}{r^2}\exp(-\mu_t r)\right], \tag{136a}$$

and it is seen that, as in Bonner's model, a term with n =2 is present. In equation 136a $\mu_t = \mu_s + \mu_a$, $a' = \mu_s / \mu_t$ (albedo) and $D_a = \mu_a / \kappa_0$, with κ_0 is the positive root of

$$a'.\arctan(\kappa_0 / \mu_t) = \kappa_0 / \mu_t. \tag{136b}$$

The model of Patterson *et al.* was extended by Farrell *et al.* [7] who starting from assuming an effective source at $z=z_0 = 1/ (\mu_a + \mu_s')$ (with corresponding negative image source at $-z_0$), calculated the photon current leaving the tissue as the gradient of the fluence rate at the surface times D, and arrive at

$$I(r) = \frac{1}{4\pi}\sum_{k=1,2} z_{0k}\left(\mu_{eff} + \frac{1}{r_k}\right)\frac{\exp(-\mu_{eff} r_k)}{r_k^{\ 2}} \tag{137a}$$

with

$$r_1 = \left[(z - z_0)^2 + r^2\right]^{1/2} \quad ; \quad r_2 = \left[(z + z_0 + 2z_b)^2 + r^2\right]^{1/2} \tag{137b}$$

The depth correction z_b arises from taking refractive index mismatch at the surface interface into account [4, 30]

$$z_b = 2AD \quad ; \quad A = \frac{1 + r_d}{1 - r_d} \tag{137c}$$

and

$$r_d = -1.440\, n_{rel}^{-2} + 0.710\, n_{rel}^{-1} + 0.668 + 0.0636\, n_{rel}. \tag{137d}$$

An example of the Farrell model is given in Figure 36, in which a Monte-Carlo simulation for a typical situation is compared.

This model is implemented in the program, together with the simple model given in equation 133, for different values for *n*.

Farrell *et al.* also extended the model given above by assuming that the effective source extends along the Z-axis, obeying a Lambert-Beer-like attenuation law with $\mu_a + \mu_s'$ as the attenuation coefficient, but this results in expressions that are not very tractable.

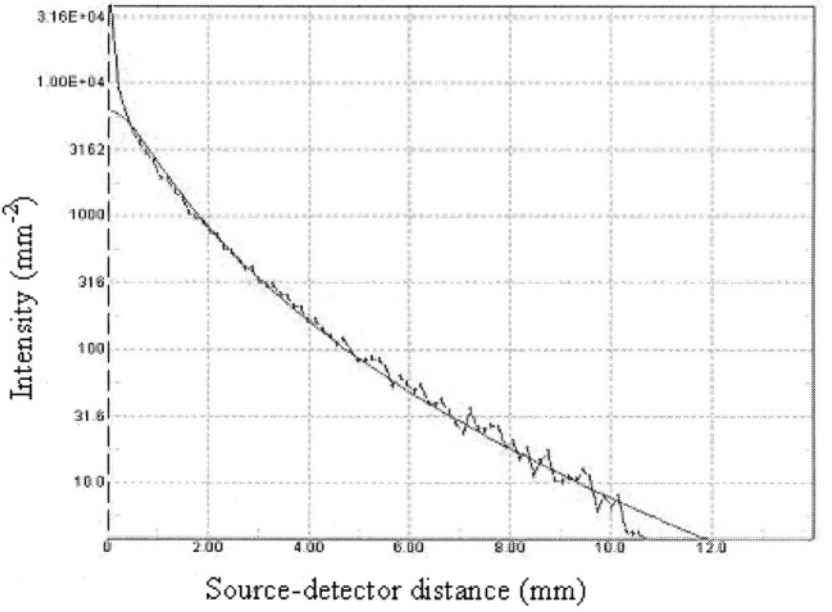

Figure 36. Comparison of the Farrell-model with simulations, for a one-layer semi-infinite sample with $\mu_s' = 1$ mm^{-1} and $\mu_a = 0.01$ mm^{-1}. In simulations: Henyey-Greenstein scattering function, $g = 0.90$. Detected photons: 50000. Detection window radius: 0-12 mm. Ratio of reflected vs. injected photons: in the simulation: 0.748, in the model: 0.749. At small r-values deviations occur due to the limited applicability of the Diffusion Approximation in that region.

Total Reflection

The approximations given above can be integrated over the surface, using

$$I_{total} = \int_0^\infty I(r).2\pi r.dr \tag{138}$$

and this will lead to

$$I_{total} = c\left(\pi/\mu_{eff}\right)^{3/2}; \quad = c\,2\pi/\mu_{eff}; \quad = \infty \quad \text{for } b = 1/2; 1; 2 \tag{139a}$$

and for the Farrell-model

$$I_{total} = \tfrac{1}{2} Pa' \exp(-\mu_{eff} z_0)\left[1 + \exp\left\{-\tfrac{4}{3} A\, \mu_{eff} z_0\right\}\right] \tag{139b}$$

with *a'* as the reduced albedo: $a' = \mu_s'/(\mu_a+\mu_s')$. It turns out that the correspondence of the Farrell model with simulated data, for values of the optical constants typical for tissue, is rather satisfactory. This is reflected in Figure 37, where the ratios of reflected and injected photons in the simulation and in the model are compared.

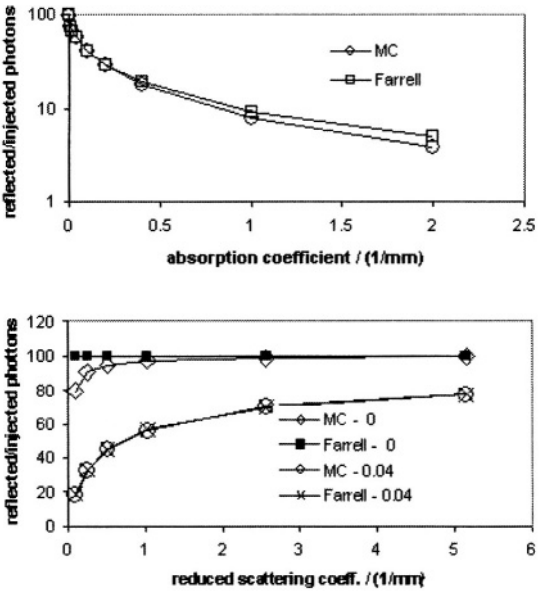

Figure 37. Comparison of the ratio of reflected vs. injected photon numbers, calculated with the Farrell model and with Monte-Carlo simulations. Upper panel: varying absorption coefficient μ_a; μ_s = 10.4 mm^{-1}; g = 0.90; μ_s'=1.04 mm^{-1}. Lower panel: varying reduced scattering coefficient μ_s'; g = 0.90; parameter: μ_a [mm^{-1}]. Here the difference for zero absorption and low scattering may be caused by the limited thickness of the sample (65 mm).

(2). Doppler Power Spectrum Approximations

In subsection 12.7.1 the option of including particle velocities, leading to Doppler frequency spectra, was treated. In subsection 12.8.1 the possibility for calculating the moments of the Doppler power spectra was mentioned.

The program offers the option of fitting those spectra with pre-defined functions, since Bonner *et al.* [5] showed that sometimes these spectra might correspond to simple Lorentzian or Gaussian time functions.

For a Gaussian function, suppose the frequency distribution $f(\omega)$ looks like

$$f(\omega) = \exp(-\omega^2 / s^2)\,, \tag{140a}$$

as is known with interval $\Delta\omega$, then the homodyne power spectrum (for $\omega \geq 0$ only!) will have the form

$$S(\omega) = \sqrt{\tfrac{1}{2}\pi}.s.\exp(-\omega^2/(2s^2))\,\Delta\omega\,, \tag{140b}$$

and so the maximum (at ω=0) and the width of $S(\omega)$ will be $\sqrt{(\pi/2)}.s.\Delta\omega$, and $\sqrt{2}$ (= 1.414) times the maximum and the width of $f(\omega)$, respectively.

The moments are listed below, in Table 1.

For a Lorentzian function, suppose the frequency distribution $f(\omega)$ is given by

$$f(\omega) = \exp(-|\omega|/s)\,, \tag{141a}$$

then

$$S(\omega) = (\omega + s)\exp(-\omega/s)\,\Delta\omega, \tag{141b}$$

and the maximum and the width of $S(\omega)$ will now be $s.\Delta\omega$ and 1.67835 s respectively, while those of $f(\omega)$ are: 1 and s.ln2 (=0.69315 s) respectively, a broadening with a factor of 2.4213.

Table 1. Moments of Lorentzian and Gaussian Power Spectra (after integration over ω from 0 to ∞)

model	M_0	M_1	M_2	M_1/M_0	$\sqrt{(M_2/2M_0)}$
Gaussian	$\frac{1}{2}\, s\sqrt{\pi}$	$\frac{1}{2}\, s^2$	$\frac{1}{4}\, s^3\sqrt{\pi}$	$s / \sqrt{\pi}$	$\frac{1}{2}\, s$
Lorentzian	s	s^2	$2\, s^3$	s	s

12.9 CONCLUSIONS

We have described the physics and mathematics behind the Monte-Carlo light scattering simulation program as developed in our group. It offers a large number of options and extra features. Among the options are: to include various structures, like tubes and spheres, in the layer system, to work with different concentrations of particles with different optical characteristics, to investigate reflection, transmission and absorption, to

study path-length and time-of-flight distributions, to include frequency-modulation spectra and ultrafast transillumination phenomena, to handle Doppler frequency shifts upon scattering at moving particles, to calculate photoacoustic response from sources of absorbing particles, to perform Raman- and fluorescence spectroscopy. The light source might be a pencil beam, a broad parallel beam or a divergent beam, from an external or an internal focus, or photons produced at the positions were (in previous simulations) photons were absorbed.

The output options include: distribution plots of a number of variables, like the position of detection, the angles at detection, the number of scattering events, the path length (either optical or geometrical), the Doppler frequency shift. Detection might occur in reflection and transmission, *i.e.,* at the surface or at the bottom of the sample, or internally, *e.g.,* at the inner surface of an embedded sphere.

In addition to the simulations, a number of approximations is present, namely for the Doppler power spectra, the intensity curves and the frequency-modulation distributions of the phase and the modulation depth.

REFERENCES

1. K.M. Case and P.F. Zweifel, *Linear Transport Theory* (Addison-Wesley, Reading, Ma, USA, 1967).
2. A. Ishimaru, "Diffusion of light in turbid material," *Appl. Opt.* **28,** 2210-2215 (1989).
3. A. Ishimaru, *Wave Propagation and Scattering in Random Media,* **1, 2** (Academic Press, San Diego, USA, 1978).
4. R.A.J. Groenhuis, H.A. Ferwerda, and J.J. ten Bosch, "Scattering and absorption of turbid materials determined from reflection measurements, 1: Theory," *Appl. Opt.* **22,,** 2456-2462 (1983); 2: Measuring method and calibration," *Appl. Opt.* **22,** 2463-2467 (1983).
5. R.F. Bonner, R. Nossal, S. Havlin, and G.H. Weiss, "Model for photon migration in turbid biological media," *J. Opt. Soc. Am. A* **4,** 423-432 (1987).
6. M.S. Patterson, B. Chance, and B.C. Wilson, "Time resolved reflectance and transmittance for the non-invasive measurement of tissue optical properties," *Appl. Opt.* **28**,2331-2336(1989).
7. T.J. Farrell, M.S. Patterson, and B.C. Wilson, "A diffusion theory model of spatially resolved, steady-state diffuse reflectance for the noninvasive determination of tissue optical properties *in vivo," Med. Phys.* **19,** 879-888 (1992).
8. R.C. Haskell, L.O. Svaasand, T.T. Tsay, T.C. Feng, M.S.McAdams, and B.J. Tromberg, "Boundary conditions for the diffusion equation in radiative transfer," *J. Opt. Soc. Am. A* **11,**2727-2741 (1994).
9. A. Kienle, M.S. Patterson, N. Dögnitz, R. Bays, G. Wagnières, and H. van den Bergh, "Noninvasive determination of the optical properties of two-layered media," *Appl. Opt.* **37,** 779-791 (1998).
10. A. Kienle and T. Glanzmann, *"In vivo* determination of the optical properties of muscle with time-resolved reflecntance using a layered model," *Phys. Med. Biol.* **44,** 2689-2702 (1999).

11. F.F.M. de Mul, M.H. Koelink, M.L. Kok, P.J. Harmsma, J. Greve, R. Graaff, and J.G. Aarnoudse, "Laser Doppler velocimetry and Monte Carlo simulations on models for blood perfusion in tissue," *Appl. Opt.* **34,** 6595-6611 (1995).
12. For further information: see http://bmo.tn.utwente.nl/montecarlo or the general site of the University Twente, click to "Faculties" or "Departments", then to "Applied Physics", "Research", "Biophysics", "Biomedical Optics", "courses".
13. L. Wang and S.L. Jacques, "Hybrid model of Monte-Carlo simulation and diffusion theory for light reflectance by turbid media," *J.Opt.Soc.Am. A* **10,** 1746-1752 (1993).
14. V.G.Kolinko, F.F.M. de Mul, J. Greve, and A.V. Priezzhev, "On refraction in Monte-Carlo simulations of light transport through biological tissues," *Med. Biol. Eng. Comp.* **35,**287-288(1997).
15. H.C. van de Hulst, *Light Scattering by Small Particles* (Dover Publications, New York, USA, 1957, 1981).
16. G. Yao and L.V. Wang, "Propagation of polarized light in turbbid media: simulated animation sequences," *Opt. Express* **7**, 198-203 (2000).
17. M.J. Rakovic and G.W. Kattawar, "Theoretical analysis of polarization patterns from incoherent backscattering of light," *Appl. Opt.* **37,** 3333-3338 (1998).
18. M.J. Rakovic, G.W. Kattawar, M. Mehrubeoglu, B.D. Cameron, L.V. Wang, S. Rastegar, and G.L. Coté, "Light backscattering polarization patterns from turbid media: theory and experiment," *Appl.Opt.* **38,** 3399-3408 (1999).
19. W.S. Bickel and W.M. Bailey, "Stokes vectors, Mueller matrices and polarized light," *Am. J. Phys.* **53**, 468-478 (1985).
20. S. Bartel and A.H. Hielscher, "Monte-Carlo simulations of diffuse backscattering Mueller matrix for highly scattering media," *Appl.Opt.* **39,** 1580-1588 (2000).
21. X. Wang, G. Yao, and L.V. Wang, "Monte Carlo model and single-scattering approximation of the propagation of polarized light in turbid media containing *glucose," Appl.Opt.* **41,** 792-801 (2002).
22. M. Born and E. Wolf, *Principles of Optics* (Cambridge University Press, 6th ed. 1980-1993).
23. J.R. Zijp and J.J. ten Bosch, "Pascal program to perform Mie calculations," *Opt. Eng.* **32,** 1691-1695(1993).
24. L.G. Henyey and J.L. Greenstein, "Diffuse radiation in the galaxy," *Astrophys. J.* **93,** 70-83(1941).
25. C.G.A. Hoelen, F.F.M. de Mul, R. Pongers, and A. Dekker, "Three-dimensional photoacoustic imaging of blood vessels in tissue," *Opt. Lett.* **23**, 648-650 (1998).
26. C.G.A. Hoelen and F.F.M. de Mul, "A new theoretical approach to photoacoustic signal generation," *J.Acoust.Soc.Am.* **106,** 695-706 (1999).
27. C.G.A. Hoelen, A. Dekker, and F.F.M. de Mul, "Detection of photoacoustic transients originating from microstructures in optically diffuse media such as biological tissue," *IEEE – UFFC* **48,** 37-47 (2001).
28. C.G.A. Hoelen and F.F.M. de Mul, "Image reconstruction for photoacoustic scanning of tissue structures,"*Appl. Opt.* **39,** 5872-5883 (2000).
29. R. Graaff and K. Rinzema, "Practical improvements on photon diffusion theory: application to isotropic scattering," *Phys. Med. Biol.* **46,** 3043-3050 (2001).
30. M. Keijser, W.M. Star, and P.R. Storchi, "Optical diffusion in layered media," *Appl. Opt.* **27**, 1820-1824 (1988).

Index

A

Absorption, 140; 199; 465
  coefficient, 113; 364
  window for biological tissue, 200
Actin, 125
Acousto-optic modulator, 320
Additive noise, 279
Adenoma, 356
Adenocarcinoma, 356
Aerosols, 144
Aerosol particles, 353
Aggregation
  lens crystallins, 447
  proteins, 446
  collagen fibrils, 452
Albumins, 301
Alzheimer's disease (AD), 379; 438; 457
American National Safety Institute (ANSI), 457
Amplitude
  complex, 5; 53; 237; 403
  dispersion, 47
  fluctuations, 5
  -frequency characteristics, 409
Amyloid protein, 457
Anderson (weak) localization, 346
Anemia, 140
Angiogenesis, 364
"Angular memory" effect, 9
Angular spectrum, 9
Anti-cataract drugs, 448
Architectonics, 94
Area of spatial field correlation, 246
Arteriole, 178
Artery, 172
  femoral, 176
Arteritis, 301
Arteriosclerosis, 140
Asymmetry, 4
Atherosclerotic plagues, 379
Autocorrelation function, 10; 115; 146;167; 439
Autofluoresence, 441; 465
Avalanche photodiode (APD), 149;441

B

Backscattered light, 14
Balanced detector, 320

Beam spot radius, 403
Beat frequency, 324
Bethe-Salpeter equation, 11
Biological tissue (biotissue), 5; 90; 93; 140
Biopsy, 362
Bifurcations of interference fringes (forklets), 72
Birefringence, 95
Bladder
 urinary, 254
Blood
 analysis, 379
 analytes
  albumin, 384
  bilirubin, 384
  cholesterol, 384
  glucose, 384
  hemoglobin, 384
  total protein, 384
  triglycerides, 384
  urea, 384
 deoxygenation, 156
 flow
  cerebral (CBF), 165; 187
  retinal, 414
 microcirculation, 32; 140; 397
 oxygenation, 155
 perfusion, 141; 153; 413
 pressure, 176
  capillary, 423
  plasma colloid-osmotic, 423
 sedimentation, 301
 volume, 155
Brain, 165; 379
 microvessels, 396
Brownian
 scattering system, 8; 16
 motion, 144; 401; 439
Burn depth diagnostics, 33; 141

C

Cancer diagnostics, 37; 359; 379; 397
Cancerous lesions, 371
Capillaroscopy, 140
Carbon nanotubes, 388
Carcinoma, 356
 squamous cell *in situ,* 371
 transitional cell *in situ,* 371
Cardiovascular diseases, 371
Cataract, 237; 437
 cortical, 446
 nuclear, 446
  matured, 454
 posterior sub-capsular, 446
Caustic zone, 55
CCD camera, 35; 64; 112; 166; 202
 cooled, 377
Cell
 cytoplasm, 358
 cytoplasmic
  glycogen, 358
  lipids, 358
  pigments, 358
  secretory granules, 358
 cytoskeleton, 358
 endoplasmic reticulum, 358
 epithelial, 37
 fibroblast, 359
 Golgi apparatus, 358
 lysosomes, 357
 malignant, 37; 360
 membrane, 358
 mitochondria, 357
 morphology, 359
 nuclear size distribution, 361
 nucleus, 37; 356
  hyperchromatic, 360
 organelles, 355
 peroxisomes, 356
 regeneration, 359
Cerebral
 blood flow (CBF), 165
  maps, 187

vasodilation, 174
vasoconstriction, 174
Chemical agents
glycerol, 176
hyper-osmotic, 175
osmotically active, 175
Cholesterol level detection, 444
Clinical trials, 384
Coherence
function
angular mutual, 329
transverse, 47
-gated techniques, 200
length, 200
longitudinal, 323
transverse, 339
partial (low), 328
spatial, 201; 249; 284; 401; 439
temporal, 201; 401
Coherent
back-scattering, 140
image, 99; 119; 130; 203
light, 3; 396
optical measurements, 237
radiation propagation, 144
Collagen, 95; 142; 282; 450
bundle, 95
cross-linking, 452
fibrils, 180
diseases, 115
multifractal net, 114
Colloids, 13; 356
Colloidal particles, 437
Confocal microscopy, 325
Conjunctiva, 398; 438
bulbar, 414
Co-polarized component, 11
Correlation
angular, 3; 140
coefficient, 242
decay, 30
diffusion equation, 147
exponent, 58
function, 5; 237
spatial, 401
spatial-temporal, 402
temporal, 401
transverse, 241; 265
integral, 61
length, 47; 131
radius, 237
spectroscopy, 4; 25; 144
spatial, 3;
temporal, 3; 140
time, 17, 147; 167
transport equation, 30
Correlator
auto-, 33
auto- digital multichannel, 149
cross-, 13
digital, 26; 441
Cortex
hindlimb sensory, 171
somatosensory, 172
Cortical spreading depression (CSD), 166
Cross-correlation function, 254
spatial-temporal, 425
Cross-polarized component, 11
Cross-talk
inter-pixel, 202
Crystalline, 95
lens, 249
size distributions, 450
Crystallite (crystalline grains), 99
Cumulant analysis, 455
Cutoff frequency, 417
Cytoskeletal proteins, 455

D

Decorrelation, 131; 266
Deflection of the
beams, 253
interference fringes, 260
Dehydration, 446
Depolarization
component, 103
length, 12; 24

Deviation, 51
Dextrans, 301
Diabetes, 140; 301; 437
Diabetic retinopathy, 414
Diffraction, 51; 236
  angle, 406
  Bragg, 214
  efficiency, 208
  far-field, 254; 405
  field, 238
  Fresnel, 237
  -limited spot size, 169
  halo, 252; 285
  order, 407
  Raman-Nath, 214
  Rayleigh-Sommerfeld integral, 51
Diffractive
  grating (irregular), 262
  optical element (DOE), 237; 280
    with double identical microstructure, 262
Diffuse laser Doppler velocimetry (DLDV), 156
Diffusing-wave spectroscopy (DWS), 25; 141
Diffusion
  approximation (equation), 14; 30; 144; 343; 466
  coefficient
    translational, 439
Dimension
  correlation, 45
  fractal, 45
  Hausdorff, 48
  Hausdorff-Besicovitch, 49
  mass, 45
  volume, 45
Dislocation
  edge, 73
  screw-type, 73
Disordered medium, 5
DNA, 142
Doppler
  anemometry, 401
  effect, 398
  frequency shift, 323; 400; 467
  spectrum, 419
Droplets, 356
Dynamic
  light scattering (DLS), 144
  media, 17
Dysplasia, 359

E

Edema, 397
Elastin, 95; 142
Emulsions, 144
Encephalic pressure, 182
Endoscopy
  gastroenterological, 362
Enhanced backscattering, 346
Environmental science, 356
Ergodicity, 186
Erythrocytes (red blood cells), 421
  aggregation, 237; 301; 398
  sedimentation, 237; 301
    rate, 301
Extinction coefficient, 365
Extracellular
  liquid, 423
  space, 181
Extrafibrillar space, 181
Eye
  acuity
    retinal 260; 305
    visual, 446
  anterior chamber, 444
  conjunctiva, 418
  cornea, 452
  disease
    age-related macular degeneration (AMD), 438
    astigmatism, 452
    cataract, 237; 437
    corneal abnormalities

dry-eye syndrome, 453
edema, 438
glare, 453
haze, 453
star bursts, 453
diabetic vitreopathy, 450
glaucoma, 414; 438
hyperopia, 438; 452
iris atrophy, 438
myopia, 452
rctinopathy, 438
uveitis, 444
vitreous liquefaction, 438
lens, 306; 445
limbus, 452
sclera, 418
trabecular meshwork, 445

F

Fabry-Perot etalon, 148
Far field (Fraunhofer zone), 47; 146
Ferroelectric, 215
Fibril packing mode, 98
Fibrinogen, 301
Fibromyoma, 119
Field
boundary, 47; 239
correlation function, 5
enhanced-backscattered, 319
fluctuations, 4
object, 94
of view, 187; 272
phase fluctuations, 239
scattered, 243
speckle, 348
stationary random, 5
statistically quasi-uniform, 246
Finite-difference time-domain (FDTD) simulations, 359
Flow
laminar, 150; 416
Poiseuille, 150
random, 147; 467
shear, 147
turbulent, 150
Fluctuations
intensity, 5; 146; 166
spatial, 401
temporal, 401
phase, 65
Fluid physics experiments, 441
Foams, 144
Focused laser beam, 254
Fog-like medium, 205
Food and Drug Administration (FDA), 450
Fourier transform (FT), 66; 329; 361;411
double, 264
fast (FFT), 420
spectrometer, 376
Fractal (self-similar)
approach, 48
Brownian, 50
dimension, 45
extreme, 50
marginal, 50
multifractal, 50
object, 44
optics, 46
prefractal, 50
random surface (FRS), 50
surface, 48
Franz Keldysh effect, 218
Frequency-modulation experiments, 467
Fresnel relations, 466
Fringe projection methods, 237
Functional
magnetic resonance imaging (fMRI), 166
neuroimaging techniques, 170
Fundus camera, 438

G

Gaussian

amplitude profile, 243
beam, 330; 402
waist, 330
height distribution, 56
laser beam, 255; 327
process, 242
random optical field, 149
-Schell beam, 319
transmission function, 327
size distribution, 369
Glaucoma, 414, 438
pigmentary dispersion (PDG), 445
Glycohemoglobin, 450
Glycosylation (glycation), 450
nonenzymatic, 452
Glucose detection, 390; 444
Gradient index (GRIN) lens, 441
Gravity, 441

H

Half-wave plate, 112
Hemoglobin, 142; 364
oxy-, 142; 364
deoxy-, 142; 364
Hepatocytes, 358
Heterodyne
frequency spectrum, 511
technique, 44
High-speed 3-D profiling, 199
Histological sections, 118; 362
Hodgkin's disease, 301
Holographic filter, 378
Holography, 199
electronic (digital), 205
Fourier synthesis, 208
light-in-flight (LIF), 205
low coherence, 199
off-axis, 203
photorefractive, 199
spectral, 208
Homodyne
detection, 146; 320; 439
frequency spectrum, 511
Human serum albumin (HAS), 444
Hurst's index, 50
Hyaluronan (HA), 450
Hydrodynamic radius, 440
Hydroxyapatite crystal, 95
Hyperbaric oxygen (HBO), 455
Hyperglycemia, 450
Hypertonic retinal angiopathy, 414

I

Image contrast, 116
Imaging
biomedical, 199
magnetic resonance (MRI), 362
through the
atmosphere, 199
scattering medium, 305
seawater, 199
Implantable devices, 392
Inflammation, 383; 398
Inflammatory disease, 444
Insulin, 450
Intensity
average, 240
beat, 319
correlation function, 5
fluctuations, 5; 146
-intensity temporal autocorrelation function (TCF), 439
spatial distribution, 240
Interference
classical equation, 240
fringe
contrast, 236
period, 245
fringes, 236
pattern, 66; 235; 321
contrast, 9; 66; 235
retinometer, 306

Interferential retinometry, 237
Interferometer
  low-coherence, 27
  Mach-Zehnder, 64
  Michelson, 26
  Michelson/Linnik, 204
  polarization, 87
  shearing, 236
  with wavefront division, 236
Interferometry
  diffusing wave, 26
  low-coherence, 200
Interstitial (extrafibrillar) space, 180
Intoxication, 397
Intracellular, 181
Intrafibrillar, 181
Intra-ocular pressure (IOP), 445
Inverse problem, 261
Ionizing radiation, 445
Ischemia, 140

K

Keratin, 142
Kurtosis, 48

L

Laser
  anemometry, 237
  Ar-ion, 31
  beam, 400
    waist, 257
  coherence length, 147
  Cr:Forsterite, 201
  diode, 382; 420
  Doppler
    enhanced high-resolution imaging (EHR-LDI), 187
    flowmetry (LDF), 140; 165; 413;509
    perfusion imaging (LDPI), 166
    velocimetry (LDV), 398
    bi-directional, 417
  femtosecond, 201
  focused beam, 404
  He-Ne, 33; 51; 64; 111; 153; 168;302;405
  in situ keratomileusis (LASIK), 440
  maximum possible exposure (MPE), 458
  mode-locked, 201
  Nd:YAG, 13; 35; 376
  polarimetry (LP), 94
  safety, 457
  scanning
    confocal imaging, 140
    ophthalmoscope (SLO), 441
  speckle
    contrast analysis (LASCA), 184
    correlation technique of velocity measurement, 401
    imaging technique (LSI), 166
  surgery, 175
  technology
    infrared diode, 200
    ultrafast solid-state, 200
  Ti:sapphire, 13; 201; 387
  tunable dye, 208
Light
  emitting diode (LED), 202; 310
  microscopy, 361
  partially (low) coherent, 263
  path ("banana-shaped"), 32
  polychromatic, 276
  quasi-monochromatic, 276
  scattering, 3; 43; 93; 139; 165; 199;235;321;465
    dynamic (DLS), 437
    elastic, 356
    inelastic, 356
    quasi-elastic (QELS), 437
    spectroscopy (LSS), 355
      elastic, 356
      inelastic, 356

quasi-elastic(QELS), 437
limitations, 457
Lipids
phospho-, 384
Local-oscillator, 319
Long-range correlations
angular, 9
spatial, 9
Luneburg's first-order systems, 331
Lymph, 397
drainage, 423
flow, 423
microcirculation, 397
microvessel system, 397
transmural pressure, 423
valve, 423
vessel phasic contraction, 423
Lymphangion, 423
Lymphatics, 423
Lymphocyte (white blood cell), 423

M

Malnutrition, 445
Mannitol, 359
Margenau-Hill transformation, 338
Markovian random-walk, 343
Mass transport, 180
Mean free path (MFP), 145; 210
Mean-square displacement, 147
Mean transport free path (MTFP), 4
Melanin, 142
granules, 445
Microinterferometer, 84
Microscope
confocal, 405; 439
digital video, 424
Doppler, 404
laser, 404
scanning, 404
slit-lamp, 419; 438
speckle, 405
resolution, 412
Microscopic optical resonators, 355
Microprofile, 237
Modified Bougier's law, 10
Molecular vibrational energies, 373
Monitoring ocular health, 459
Monte Carlo simulation, 19; 143; 343;466
Moving scattering particles, 10
Mueller
matrix, 125; 490
operator, 96
Multiple quantum well (MQW) device, 208
Muscle, 95
Mustard gas, 454
Myocardium infarct, 124; 301
Myosin fibers, 95

N

NADH, 142
Nanophotonics, 392
Nanotechnology, 374
NASA, 441
Necrotic layer, 32
Neoplastic conditions, 382
Neurophysiology, 170
Neurotransmitters, 181
Newtonian liquid, 416
Noise, 417
background, 322
electronic, 323
shot, 323
suppression, 324
Non-fractal random surface (NRS), 50
Non-stationary disordered medium, 5
Nuclear/cytoplasmic ratio, 37

Numerical aperture, 377

O

Ocular fundus, 416
Ophthalmic
 instruments
  corneal analyzer (Keratron videokeratoscope) with QELS probe, 443
  QELS probe intergrated with fluorometry, 443
  Scheimpflug camera with QELS probe, 442
  slit-lamp apparatus, 442
 tele-health, 459
Ophthalmology, 237; 397; 437
Optic nerve, 397
Optical
 biopsy, 199
 coherence
  microscopy (OCM), 319
  tomography (OCT), 182; 200; 319;466
   color Doppler (CDOCT), 140; 319
   video rate, 200
 coherent heterodyne imaging, 203
 correlation
  measuring devices, 81
  technique, 44
 diagnostics, 4;
 Doppler tomography (ODT), 140
 fiber
  bundle, 169; 385
  multi-mode, 33, 148
  probe, 362
  QELS probe, 441
  single mode, 33, 149
 heterodyne detection (technique), 204; 319; 400
 imaging
  full-field, 170
  mixing, 144
  path, 7
  phase-space measurements, 326
  profilometry, 66
  system pupil, 265
  transfer function (OTF), 263
  visualization, 4
  vortices, 72
Optically
 dense disordered media, 3
 thick slabs, 14
Osmotic stress, 180
Osteon, 95
Osteoporosis, 459
Oxidative stress, 441; 454

P

Packard-Takens procedure, 61
Paraxial approximation, 244
Particle
 distribution
  size
   bi-modal, 440
   multi-modal, 440
  velocity, 148
 gels, 144
 protein, 444
Path
 delay, 348
 length, 4
  density distribution, 13; 467
Phase
 correlation radius, 243
 function
  Mie, 20
 -inhomogeneous layer (PIL), 94
 grating, 408
 object, 44
 -sensitive method, 319
 singularities, 72
 -stepped interferometric images, 203
 variance, 47
Photoacoustics, 466

Photochemical industry, 86
Photo-conductivity, 214
Photodynamic therapy (PDT), 141
Photolithographic technique, 66; 280
Photo-multiplier tube (PMT), 149
Photon
  ballistic, 200
  density, 11
  diffusion coefficient, 8; 17; 145
  -counting module, 149; 441
  measurement density function (PMDF), 143
  path length distribution, 147
  random walk, 146
  total path length, 145
  transport length, 145
Photorefractive
  crystal, 209
    strontium barium niobate (SBN), 209
    rhodium-doped barium titanate (Rh-Ba: TiO_3), 209
  effect, 212
  grating, 212
  materials, 212
  MQW devices (PRQW), 211
Phototherapy, 175
Piezoelectric deflector, 246
Pixel, 169
Plane
  observation, 9
  scatter, 9
Pleomorphism, 37
Pockels' effect, 213
Point-spread function, 36
Polarization
  azimuth, 11; 98
  background subtraction, 368
  circular, 11
  characteristics, 4
  decay parameter, 4
  degree, 10
  effects, 474
  ellipticity, 101
  helicity, 12
  imaging, 36
  interferometer,
  linear, 11
  memory, 19
  pattern, 132
  structure, 99
  visualization, 131
Polarized reflectance spectroscopy (PRS), 37
Polarizer, 420
  broadband, 368
  Glan-Tompson, 13
Polarizophots (zero intensity lines), 125
Porcelain plane, 183
Power
  -law function, 18
  nonlinearities, 51
  spectrum density function (PSDF), 67
Pre-cancer, 37
Profile interference technique, 44
Psoriasis, 115

Q

Quantum confined Stark effect (QCSE), 217
Quarter-wave plate, 103
Quasi-plane wave, 264

R

Radiative transfer
  theory (RTT), 4;
  equation (RTE), 29; 466
Raman
  peak
    CH_2 bending mode, 381
    CH_2 twisting mode, 381

phenyl ring breathing mode, 381
protein amide I band, 381
protein amide III band, 381
spectroscopy, 356
Random
flow, 405
medium, 3; 236; 329
phase object (RPO), 237
phase screen (RPS), 44; 237; 401
statistically anisotropic, 260
Rat mesentery, 398
Rayleigh length, 324
Red blood cell (RBC), 156; 168
Reflection, 476
Fresnel, 421
Refraction, 476
Refractive index, 364
mismatch, 180
Refractive surgery, 440
Relaxation
scale, 4
parameters, 4
Retina, 249; 397
Retinal vessels, 419
Ringer solution, 421
Rotation matrix, 492
Rough surface, 43
Roughness diagnostics, 44

S

Sampling volume, 143
Scalar wave approach, 6
Scattered field, 3; 5
Scattering
angle, 20; 467
anisotropic, 12, 140
anisotropy parameter, 21; 113
anti-Stokes, 373
coefficient, 113; 469
reduced, 362; 492
"diffusion", 22
elastic, 356
"forward", 23
function, 473
Henyey-Greenstein, 493
inelastic, 355
isotropic, 11
"low-step",22
matrix, 20; 356; 488
mean free path, 7
medium, 144, 200; 373; 439
Mie, 21; 356; 438; 473
multiple, 3;108;140; 180; 323; 360;418;465
object, 236; 401
particle, 145; 399
plane, 20
Rayleigh, 19; 438; 473
Rayleigh-Gans (Debije), 473; 492
single, 104; 416
Stokes, 373
system, 4
Scheimpflug principle, 438
Scintillation index, 47
Sepsis, 141
Shock, 397
Siegert relation, 6; 149; 167
Signal
beat, 321
complex beat, 340
in-phase, 340
nonlinear distortions, 411
out-of-phase, 340
quadrature , 343
-to-noise ratio (SNR), 99; 149; 172;202;439
Silicon plate's surface, 83
Sillenites,216
Silver
clusters, 387
particles, 387
Similarity in multiple scattering, 9
Single-path correlation function, 7
Single scattering correlation time, 8; 17

Single-shot technique, 207
Singular optics, 69
Singularity spectrum, 58
Skewness, 48
Skin
 actinic keratosis, 36
 arterioles, 143
 arterio-venous anastomoses, 143
 blood flow, 139, 153
 burn scar, 36
 capillary loops, 143
 deep blood net dermis, 143
 derma, 95; 142
  capillaries, 35; 142
  upper blood net, 143
 epidermis, 142; 325
 freckle, 36
 layers, 325
 malignant basal cell carcinoma, 36
 neurofibroma, 36
 nevus (pigmented and nonpigmented), 36
 papillary
  dermis, 143
  net, 35
 replants, 141
 reticular dermis, 143
 squamous cell carcinoma, 36
 structure, 142
 subcutaneous fat, 142
 tattoo, 36
 vascular abnormality (venous lake), 36
 venues, 143
 venules, 143
 wrinkles, 35
Skull, 176
Source-detector separation, 31
Space
 -charge, 214
 industry, 86
 shuttle, 441
 station orbiter, 441
 travel, 459
Spatial
 filtering, 203
 frequency, 118, 236
 modulation, 238
 spectrum, 288
 -temporal
  correlation function, 5
  fluctuations, 5
Spatially modulated laser beam (SMLB), 9; 236
Speckle
 blurring, 184
 boiling, 402
 contrast, 167; 184; 408
  map, 169
 field, 245
  decorrelation, 249
  dynamic, 401
  fluctuations, 167; 439
  identical, 238
 intensity fluctuations
  time series, 428
 interferometry, 237
 microscopy, 404
 noise, 131; 203
 pattern, 166; 401
  dynamic, 26
  statistically homogeneous, 5
  time-averaged (integrated), 168;184
 size, 249
 translation, 403
Specklegrams, 246
 double-exposure shift, 280
Speckles, 146
 fully developed, 186
Spectral moments, 419
Spectrograph
 dispersive
  axial transmissive, 377
  off-axis reflective (Czerny-Turner), 377
 holographic, 380

Spectroscope
multichannel, 368
Spectroscopy
absorption, 465
auto-fluorescence, 465
diffuse reflectance, 363
magnetic resonance (MRS), 362
photon correlation (PCS), 437
Raman, 441; 465
near-infrared (NIRRS), 374
surface-enhanced (SERS), 374
Spectrum
Raman, 373
reflectance, 176; 362
transmittance, 176
vibrational of molecules, 373
Specular
component, 406
reflectance, 368; 438
Sprage-Dawley rats, 171
Sprays, 144
Stimulation
sciatic nerve, 171
somatosensory, 170
Statistical moments, 10; 43
Statistics
Gaussian, 6; 45; 167; 257; 401
non-Gaussian, 50
Stochastic interference, 4
Stokes-Einstein relation, 150; 439
Stokes vector, 100; 488
'Strength of a singularity', 74
Stress, 397
Structure function, 61
Surface
relief, 58; 411
rough, 405
roughness, 43
plasmon resonance, 386
spectral
index, 49
strength, 49
profiling, 209
Superluminescent diode (SLD), 27;201;333
Suspensions
colloidal, 144
liquid, 144
mono-disperse aqueous, 15
polydisperse of fat particles (Intralipid), 150

T

Telescope imaging system, 263
Temporal
correlation function, 17
field, 146
intensity, 149
Time-of-flight distribution, 467
Tissue
absorbers, 364
adipose, 25
bladder, 359
bone, 95
breast, 379
bulk, 180
cervical, 358
coagulation, 175
colon, 356
compression, 175
connective, 359; 414
dehydration, 175
dura mater, 175
epithelium, 37; 359
columnar, 370
stratified squamous, 370
transitional, 370
epithelial squamous
dysplasia (high grade), 383
dysplasia (low-grade) (HPV and CIN 1), 383
metaplasia, 383
esophagus, 359
Barrett's, 362
eye
aqueous humor, 440

cornea, 440
lens, 306; 249; 440
retina, 249; 397; 440
sclera, 418
vitreous, 440
fibrous, 175
fluorescence, 375
immersion, 175
lamina propria, 367
mucosal, 37
muscular, 126
optical clearing, 175
organization
biochemical, 364
morphological, 364
phantom, 24; 151; 364
polyps
adenomatous, 364; 380
hyperplastic, 380
precancerous, 366
rectal, 356
scatterers, 364
soft, 114
stroma, 37
subcutaneous, 34
submucosal, 363
turbid, 181
Tomograms
orientation, 94
phase, 94
Tomographic imaging, 9
Tomography,
polarization, 94
positron emission (PET), 166
single photon emission computed (SPECT), 166
X-ray computed tomography (X-ray CT), 362
Topothesy, 49
Trabeculae, 95
Transmission function, 239
Tumor, 114
invasive, 382
Turbid medium, 101; 144; 206; 466

U

Urocanic acid (UCA), 142
UV exposure, 445

V

Van Cittert–Zernicke theorem, 265
Van de Hulst approximation, 360
Vasoactive substances, 181
Veins, 172
Veinule, 178
Venous leg ulceration, 140
Vibrational frequencies, 373
Visual acuity, 446
Volume fraction, 17

W

Waist beam radius, 408
Wavefront, 343
curvature radius, 403
Wavelet
analysis, 124
coefficients, 128
complex (Morlett), 127
MHAT, 127
Weakly ordered medium, 5
Whole-field image, 199
Wiener-Khintchine theorem, 118; 156
Wide-field
coherence-gated (interferometric) detection, 202
multiple channel techniques, 200
Wigner function (phase-space distribution), 319; 328
smoothed, 331
true, 336

Woman reproductive sphere (myometrium), 114
World Health Organization (WHO), 440
Wound healing, 440

X

X-ray exposure, 454

Z

Zerogram, 69

COHERENT-DOMAIN OPTICAL METHODS
Biomedical Diagnostics, Environmental and Material Science

Volume 2

This page intentionally left blank

COHERENT-DOMAIN OPTICAL METHODS
Biomedical Diagnostics, Environmental and Material Science

Volume 2

Edited by

VALERY V. TUCHIN
Saratov State University and Precision Mechanics and Control Institute of the Russian Academy of Sciences, Saratov, 410012 Russian Federation

KLUWER ACADEMIC PUBLISHERS
NEW YORK, BOSTON, DORDRECHT, LONDON, MOSCOW

eBook ISBN: 1-4020-7882-X
Print ISBN: 1-4020-7886-2

©2005 Springer Science + Business Media, Inc.

Print ©2004 Kluwer Academic Publishers
Boston

All rights reserved

No part of this eBook may be reproduced or transmitted in any form or by any means, electronic, mechanical, recording, or otherwise, without written consent from the Publisher

Created in the United States of America

Visit Springer's eBookstore at: http://ebooks.springerlink.com
and the Springer Global Website Online at: http://www.springeronline.com

Contents

Contributing Authors ix

Preface xv

Acknowledgments xix

PART IV: OPTICAL COHERENCE TOMOGRAPHY

13. Optical Coherence Tomography – Light Scattering and Imaging Enhancement 3
Ruikang K. Wang and Valery V. Tuchin

13.1 Introduction 3
13.2 Optical Coherence Tomography: The Techniques 5
13.3 OCT in Imaging 13
13.4 Effects of Light Scattering on OCT 21
13.5 New Technique to Enhance OCT Imaging Capabilities 32
13.6 Summary 50
References 52

14. Optical Coherence Tomography: Advanced Modeling 61
Peter E. Andersen, Lars Thrane, Harold T. Yura, Andreas Tycho, and Thomas M. Jørgensen

14.1 Introduction 61
14.2 Analytical OCT Model Based on the Extended Huygens-Fresnel Principle 63
14.3 Advanced Monte Carlo Simulation of OCT Systems 83
14.4 True-Reflection OCT Imaging 95
14.5 Wigner Phase-Space Distribution Function for the OCT Geometry 102
Appendix 111
References 115

15. Absorption and Dispersion in OCT 119
Christoph K. Hitzenberger

15.1 Introduction 119
15.2 Theoretical Aspects 121
15.3 Absorption in OCT 126
15.4 Dispersion in OCT 142
References 158

16. *En-Face* OCT Imaging 163
Adrian Podoleanu

16.1 Different Scanning Procedures 163
16.2 Simultaneous *En-Face* OCT and Confocal Imaging 178
16.3 Parallel OCT 181
16.4 *En-Face* OCT Imaging with Adjustable Depth Resolution 189
16.5 *En-Face* OCT and 3D Imaging of Tissue 191
16.6 Particularities of En-Face OCT 198
16.7 En-Face Non-Scanning Systems 203
References 206

17. Fundamentals of OCT and Clinical Applications of Endoscopic OCT 211

Lev S. Dolin, Felix I. Feldchtein, Grigory V. Gelikonov, Valentin M. Gelikonov, Natalia D. Gladkova, Rashid R. Iksanov, Vladislav A. Kamensky, Roman V. Kuranov, Alexander M. Sergeev, Natalia M. Shakhova, and Ilya V. Turchin

17.1 Introduction 211
17.2 Theoretical Models for OCT Imaging 212
17.3 Methods and Element Basis for PM Fiber Optical Interferometry 222
17.4 Experimental OCT Systems 233
17.5 Clinical Applications of OCT 242
17.6 Discussion and Future Directions 266
References 267

18. Polarization OCT 271
Johannes F. de Boer

18.1 Introduction 271
18.2 Theory 273
18.3 Determination of the Sample Polarization Properties 281
18.4 Fiber Based PS-OCT systems 286
18.5 Multi-Functional OCT 296
18.6 PS-OCT in Ophthalmology 301
18.7 Future Directions in PS-OCT 310
References 311

19. Optical Doppler Tomography 315
Zhongping Chen

19.1 Introduction 315
19.2 Principle and Technology of ODT 318
19.3 Applications of ODT 331
19.4 Conclusions 339
References 340

PART V: MICROSCOPY

20. Compact Optical Coherence Microscope 345
Grigory V. Gelikonov, Valentin M. Gelikonov, Sergey U. Ksenofontov, Andrey N. Morosov, Alexey V. Myakov, Yury P. Potapov, Veronika V. Saposhnikova, Ekaterina A. Sergeeva, Dmitry V. Shabanov, Natalia M. Shakhova, and Elena V. Zagainova

20.1 Overview of main approaches to OCM design 345
20.2 Interferometer for compact OCM 348
20.3 Development of broadband light source and interferometer elements 350
20.4 Influence of light scattering on OCM spatial resolution 352
20.5 Electro-mechanical system for dynamic focus 354

20.6 Digital signal processing as a tool to improve OCM resolution 357
20.7 Experimental OCM prototype 358
20.8 Biomedical applications 359
20.9 Summary 360
References 361

21. Confocal Laser Scanning Microscopy 363

Barry R. Masters

21.1 Introduction 363
21.2 Optical Principles of Confocal Microscopy 364
21.3 Types of Confocal Microscopes 375
21.4 Applications to Material Sciences 390
21.5 Biomedical Applications 391
21.6 Comparison Between Confocal Microscopy and Mutiphoton Excitation Microscopy 403
References 410

22. Comparison of Confocal Laser Scanning Microscopy and Optical Coherence Tomography 417

Sieglinde Neerken, Gerald W. Lucassen, Tom (A.M.) Nuijs, Egbert Lenderink, and Rob F.M. Hendriks

22.1 Introduction 417
22.2 Techniques 419
22.3 Application of OCT and CLSM 424
22.4 Discussion 436
References 437

Index 441

Contributing Authors

Peter E. Andersen, Optics and Fluid Dynamics Department, Risø National Laboratory, P.O. Box 49, DK-4000 Roskilde, Denmark,
e-mail: peter.andersen@risoe.dk

Johannes F. de Boer, Wellman Center of Photomedicine, Massachusetts General Hospital, Harvard Medical School, Boston, MA 02114 USA,
e-mail: deboer@helix.mgh.harvard.edu

Zhongping Chen, Beckman Laser Institute, University of California, Irvine, CA 92612 USA,
e-mail: zchen@bli.uci.edu

Lev S. Dolin, Hydrophysics and Hydroacoustics Division, Institute of Applied Physics of Russian Academy of Sciences, Nizhny Novgorod, 603950 Russian Federation,
e-mail: Lev.Dolin@hydro.appl.sci-nnov.ru

Felix I. Feldchtein, Imalux Corporation, 1771 E 30 str., Cleveland, OH 44114 USA,
e-mail: felixfel@imalux.com

Grigory V. Gelikonov, Division of Nonlinear Dynamics and Optics, Institute of Applied Physics of Russian Academy of Sciences, Nizhny Novgorod, 603950 Russian Federation,
e-mail: grig@ufp.appl.sci-nnov.ru

Valentin M. Gelikonov, Division of Nonlinear Dynamics and Optics, Institute of Applied Physics of Russian Academy of Sciences, Nizhny Novgorod, 603950 Russian Federation,
e-mail: gelikon@ufp.appl.sci-nnov.ru

Natalia D. Gladkova, Medical Academy, Nizhny Novgorod, 603005 Russian Federation,
e-mail: ngladkova@imalux.com

Rob F.M. Hendriks, Philips Research, Personal Care Institute and Optics and Mechanics, Professor Holstlaan 4, (WB 32), 5656 AA Eindhoven, the Netherlands,
e-mail: r.f.m.hendriks@philips.com

Christoph K. Hitzenberger, Department of Medical Physis, University of Vienna, Waehringerstr.13, A-1090 Vienna, Austria,
e-mail: Christoph.Hitzenberger@univie.ac.at

Rashid R. Iksanov, Division of Nonlinear Dynamics and Optics, Institute of Applied Physics of Russian Academy of Sciences, Nizhny Novgorod, 603950 Russian Federation,
e-mail: rir@ufp.appl.sci-nnov.ru

Thomas M. Jørgensen, Optics and Fluid Dynamics Department, Risø National Laboratory, P.O. Box 49, DK-4000 Roskilde, Denmark,
e-mail: thomas.martini@risoe.dk

Vladislav A. Kamensky, Division of Nonlinear Dynamics and Optics, Institute of Applied Physics of Russian Academy of Sciences, Nizhny Novgorod, 603950 Russian Federation,
e-mail: vlad@ufp.appl.sci-nnov.ru

Sergey U. Ksenofontov, Division of Nonlinear Dynamics and Optics, Institute of Applied Physics of Russian Academy of Sciences, Nizhny Novgorod, 603950 Russian Federation,
e-mail: xen@appl.sci-nnov.ru

Roman V. Kuranov, Division of Nonlinear Dynamics and Optics, Institute of Applied Physics of Russian Academy of Sciences, Nizhny Novgorod, 603950 Russian Federation,
e-mail: roman@ufp.appl.sci-nnov.ru

Egbert Lenderink, Philips Research, Personal Care Institute and Optics and Mechanics, Professor Holstlaan 4, (WB 32), 5656 AA Eindhoven, the Netherlands,
e-mail: egbert.lenderink@philips.com

Gerald W. Lucassen, Philips Research, Personal Care Institute and Optics and Mechanics, Professor Holstlaan 4, (WB 32), 5656 AA Eindhoven, the Netherlands,
e-mail: gerald.lucassen@philips.com

Barry R. Masters, Department of Ophthalmology, University of Bern, Bern, Switzerland,
e-mail: brmail2001@yahoo.com

Andrey N. Morosov, Division of Nonlinear Dynamics and Optics, Institute of Applied Physics of Russian Academy of Sciences, Nizhny Novgorod, 603950 Russian Federation,
e-mail: morozov_a_n@mail.ru

Alexey V. Myakov, Division of Nonlinear Dynamics and Optics, Institute of Applied Physics of Russian Academy of Sciences, Nizhny Novgorod, 603950 Russian Federation,
e-mail: myakov@ece.utexas.edu

Sieglinde Neerken, Philips Research, Personal Care Institute and Optics and Mechanics, Professor Holstlaan 4, (WB 32), 5656 AA Eindhoven, the Netherlands,
e-mail: Sieglinde.Neerken@philips.com

Tom (A.M.) Nuijs, Philips Research, Personal Care Institute and Optics and Mechanics, Professor Holstlaan 4, (WB 32), 5656 AA Eindhoven, the Netherlands,
e-mail: tom.nuijs@philips.com

Adrian Podoleanu, School of Physical Sciences, University of Kent at Canterbury, Canterbury CT2 7NR, UK,
e-mail: A.G.H.Podoleanu@ukc.ac.uk

Yury P. Potapov, Division of Nonlinear Dynamics and Optics, Institute of Applied Physics of Russian Academy of Sciences, Nizhny Novgorod, 603950 Russian Federation,
e-mail: pyp@ufp.appl.sci-nnov.ru

Veronika V. Saposhnikova, Division of Nonlinear Dynamics and Optics, Institute of Applied Physics of Russian Academy of Sciences, Nizhny Novgorod, 603950 Russian Federation,
e-mail: sapozhnikova@ufp.appl.sci-nnov.ru

Alexander M. Sergeev, Division of Nonlinear Dynamics and Optics, Institute of Applied Physics of Russian Academy of Sciences, Nizhny Novgorod, 603950 Russian Federation,
e-mail: ams@ufp.appl.sci-nnov.ru

Ekaterina A. Sergeeva, Hydrophysics and Hydroacoustics Division, Institute of Applied Physics of Russian Academy of Sciences, Nizhny Novgorod, 603950 Russian Federation,
e-mail: sea@ufp.appl.sci-nnov.ru

Dmitry V. Shabanov, Division of Nonlinear Dynamics and Optics, Institute of Applied Physics of Russian Academy of Sciences, Nizhny Novgorod, 603950 Russian Federation,
e-mail: dvshab@ufp.appl.sci-nnov.ru

Natalia M. Shakhova, Division of Nonlinear Dynamics and Optics, Institute of Applied Physics of Russian Academy of Sciences, 603950, Nizhny Novgorod; Medical Academy, Nizhny Novgorod, 603005 Russian Federation,
e-mail: shakh@ufp.appl.sci-nnov.ru

Lars Thrane, Optics and Fluid Dynamics Department, Risø National Laboratory, P.O. Box 49, DK-4000 Roskilde, Denmark,
e-mail: lars.thrane@risoe.dk

Valery V. Tuchin, Division of Optics, Department of Physics, Saratov State University, Saratov, 410012; Precision Mechanics and Control Institute of the Russian Academy of Sciences, Saratov, 410028 Russian Federation,
e-mail: tuchin@sgu.ru

Ilya V. Turchin, Division of Nonlinear Dynamics and Optics, Institute of Applied Physics of Russian Academy of Sciences, Nizhny Novgorod, 603950 Russian Federation,
e-mail: ilya@ufp.appl.sci-nnov.ru

Andreas Tycho, Optics and Fluid Dynamics Department, Risø National Laboratory, P.O. Box 49, DK-4000 Roskilde, Denmark,
e-mail: andreas.tycho@risoe.dk

Ruikang K. Wang, Cranfield Biomedical Centre, Institute of BioScience and Technology, Cranfield University at Silsoe, Bedfordshire MK45 4DT, UK,
e-mail: r.k.wang@cranfield.ac.uk

Harold T. Yura, The Aerospace Corporation, Electronics and Photonics Laboratory, P.O. Box 92957, Los Angeles, CA 90009 USA
e-mail: hal.t.yura@aero.org

Elena V. Zagainova, Medical Academy, Nizhny Novgorod, 603005 Russian Federation
e-mail: ezag@mailru.com

This page intentionally left blank

Preface

This is Volume 2 of the book *Coherent-Domain Optical Methods: Biomedical Diagnostics, Environmental and Material Science,* which represents a valuable contribution by well-known experts in the field of coherent-domain light scattering technologies for diagnostics of random media and biological tissues. The contributors are drawn from Russia, USA, UK, the Netherlands, Ukraine, Austria, China, Denmark, and Switzerland.

The book is divided in five parts entitled as Part 1: *Speckle and Polarization Technologies* (Chapers 1-5), Part 2: *Holography, Interferometry, Heterodyning* (Chapters 6-8), Part 3: *Light Scattering Methods* (Chapters 9-12), Part 4: *Optical Coherence Tomography* (Chapters 13-19), and Part 5: Microscopy (Chapters 20-22). The first volume of the book is comprised of first three parts (Chapters 1-12) and the second volume – of two other parts (Chapters 13-22).

In Volume 1 recent the most prospective methods of coherent and polarization optical imaging, tomography, and spectroscopy, polarization diffusion wave spectroscopy, elastic, quasi-elastic and inelastic light scattering spectroscopy and imaging are presented. The holography, interferometry and optical heterodyning techniques in application to diagnostics of turbid materials and tissues are also discussed. In two chapters some aspects of low coherence holography and interferometry are described.

Volume 2 presents very new and growing field of coherent optics: optical coherence tomography (OCT). Various aspects of OCT techniques and applications, preferably in biomedicine, are discussed. Reader also will find description of laser scanning confocal microscopy, which is characterized by recent extraordinary results on *in vivo* imaging. Multiphoton microscopy as a tool for tissue and material inspection is also analyzed in the volume.

The fundamentals of OCT and brief description of its applications in medicine, biology and material study are presented in Chapter 13. The impact of multiple scattering in tissues on the OCT imaging performances is analyzed. The developments and mechanisms of reduction the overwhelming multiple scattering effects and improving imaging capabilities by the use of optical immersion technique are discussed. A novel technique based on the use of biocompatible and osmotically active chemical agents to impregnate the tissue and to enhance the OCT images is described.

Analytical and numerical models for describing the light propagation in scattering samples imaged by OCT systems are given in Chapter 14. Analytical and numerical models based on the extended Huygens-Fresnel principle and advanced Monte Carlo technique are derived and used for calculating the OCT signal. For improvement of OCT images the so-called true-reflection algorithm in which the OCT signal may be corrected for the attenuation caused by scattering is developed and verified experimentally and by Monte Carlo modeling. A novel method of OCT imaging is proposed on the basis of derived Wigner phase-space distribution function.

Advanced OCT techniques, in particular spectral OCT, based on measuring of spectral intensity and spectral phase as a function of depth and giving information on sample absorption and dispersion are presented in the book. Chapter 15 discusses spectral OCT techniques and their physical limits, dispersion induced image degradation and possible solutions, and provides a review of literature on absorption and dispersion related phenomena in OCT.

The so-called *en-face* OCT, which delivers slices in the tissue of coherence length thickness with an orientation similar to that of confocal microscopy is presented in Chapter 16. The versatile operation in A, B, C scanning regimes, simultaneous OCT and confocal imaging and simultaneous OCT imaging at different depths are considered. B-scan and C-scan images from different types of tissue are presented.

Chapter 17 discusses the theoretical issues of OCT imaging on the basis of the wave and energy approaches, presents the development of polarization maintaining fiber optical elements for the OCT Michelson interferometer and various modifications of OCT such as “two-color”, 3D, cross-polarized and endoscopic OCT modalities. It also overviews clinical applications of OCT, discusses criteria of norm and pathology, diagnostic value and clinical indications in OCT. Compression of tissues and their impregnation by chemical agents are used for improvement of OCT images. An effective mathematical algorithm for post-processing of OCT images accounting for tissue scattering is demonstrated.

The implementation of a real time fiber based polarization-sensitive OCT (PS-OCT) system, the associated behavior of polarization states in single

mode fibers, and optimal polarization modulation schemes are described in Chapter 18. The principle of Stokes parameters determination in OCT, processing of PS-OCT signals to extract polarization properties of tissue, such as birefringence, optical axis orientation, and diattenuation, and results of *in vivo* determination of skin birefringence and birefringence of the retinal nerve fiber layer for glaucoma detection are discussed.

Chapter 19 describes a non-invasive optical method for tomographic imaging of *in vivo* tissue structure and hemodynamics with high spatial resolution. The principle of ODT, system design and implementation, and clinical application are described. The recent advances in imaging speed, spatial resolution, and velocity sensitivity as well as potential applications of ODT for mapping 3-D microvasculature for tumor diagnosis and angiogenesis studies are discussed.

Chapter 20 discusses development of a compact optical coherence microscope (OCM) with ultrahigh axial (3.4 μm) and lateral (3.9 μm) resolution for imaging internal structures of biological tissues at the cellular level. Such resolution is achieved due to combined broadband radiation of two spectrally shifted SLDs and implementation the dynamic focus concept which allows for in-depth scanning of a coherence gate and beam waist synchronously. Results of theoretical investigation of OCM axial and lateral resolution degradation caused by light scattering in tissues are also presented. The first OCM images of plant and human tissue *ex vivo* are demonstrated.

Principles and instrumentation of laser scanning confocal microscopy are described in Chapter 21. Current results on *in vivo* imaging of skin, eye tissues, and cells are demonstrated. Applications to materials inspection are also discussed. The principles of optical sectioning in confocal and multiphoton excitation microscopies are compared.

In Chapter 22 a comparison of OCT and confocal laser scanning microscopy (CLSM) at studies of human skin *in vivo* is presented. These techniques deliver different information on the skin structure, mainly due to differences in penetration depth into the skin, resolution and field of view. The OCT system described produces images of 2×2 mm^2 perpendicular to the skin surface, at one frame per second, with 14 μm axial resolution and 1 to 2 mm penetration depth. Used video rate CLSM with a modified Vivascope1000 (Lucid Inc., USA) provides images of 0.5×0.5 mm^2 parallel to the skin surface with 1×5 μm (lateral x axial) resolution, but with a limited penetration depth into the skin of 0.25 mm. Some examples on the application of the OCT and CLSM systems to study changes in skin due to UV irradiation and ageing are presented.

This page intentionally left blank

Acknowledgments

I greatly appreciate the cooperation and contribution of all authors of the book, who have done a great work on preparation of their chapters.

I would like to thank all those authors and publishers who freely granted permissions to reproduce their copyright works.

I am grateful to Prof. D. R. Vij for his initiative in writing of this book and to Michael Hackett for his valuable suggestions and help on preparation of the manuscript.

It should be mentioned that this volume presents results of international collaboration and exchange of ideas between all research groups participating in the book project, in particular such collaboration of authors of Chapter 13 was supported by grant REC-006 of CRDF (U.S. Civilian Research and Development Foundation for the Independent States of the Former Soviet Union) and the Russian Ministry of Education and the Royal Society grant for a joint project between Cranfield University and Saratov State University.

I greatly appreciate the cooperation, contribution, and support of all my colleagues from Optics Division of Physics Department of Saratov State University.

Last, but not least, I express my gratitude to my wife, Natalia, and all my family, especially to daughter Nastya and grandkids Dasha, Zhenya, and Stepa, for their indispensable support, understanding, and patience during my writing and editing the book.

This page intentionally left blank

Part IV:
OPTICAL COHERENCE TOMOGRAPHY

This page intentionally left blank

Chapter 13

OPTICAL COHERENCE TOMOGRAPHY

Light Scattering and Imaging Enhancement

Ruikang K. Wang[1] and Valery V. Tuchin[2]

1.Cranfield University at Silsoe, Bedfordshire MK45 4DT, UK; 2. Saratov State University, Saratov, 410012 Russian Federation

Abstract: The fundamental aspects of optical coherence tomography and brief description of its applications in medicine and biology are presented. The impact of multiple scattering in tissues on the OCT imaging performances, and the developments in reducing the overwhelming multiple scattering effects and improving imaging capabilities by the use of immersion technique are discussed. A novel technique based on the use of biocompatible and osmotically active chemical agents to impregnate the tissue and to enhance the OCT images is described. The mechanisms for improvements of imaging depth and contrast are discussed, primarily through the experimental examples.

Key words: optical coherence tomography, multiple scattering, osmotically active agents, refractive index matching, skin, mucosa, colon, tooth, ceramics

13.1 INTRODUCTION

Over the last decade, non-invasive or minimally invasive spectroscopy and imaging have been witnessed widespread and exciting applications in biomedical diagnostics. Optical techniques that use the intrinsic optical properties of biological tissues, such as light scattering, absorption, polarization and fluorescence, have many advantages over the conventional *x*-ray computed tomography, MRI and ultrasound imaging in terms of safety, costs, contrast and resolution features. Time-resolved and phase-resolved optical techniques are capable of deep-imaging of the tissues that could provide information of tissue oxygenation states and detect brain and breast tumors [1,2], whereas confocal microscopy and multi-photon excitation imaging have been used to show cellular and sub-cellular details of superficial living tissues [3,4]. However, most biological tissues strongly

scatter the probing light within the visible and near infrared range, i.e., the therapeutic and/or diagnostic optical window. The multiple scattering of light is severely detrimental to imaging contrast and resolution, which limits the effective probing depth to several hundred micrometers for the confocal microscopy and multi-photon excitation imaging techniques. However, some clinical applications, such as early cancer diagnosis, require the visualization of intermediate depth range of the localized anatomical structures with micron-scale resolution.

Optical coherence tomography (OCT) fills a nice niche in this regard. It uses low coherence interferometry to image internal tissue structures to the depth up to 2 millimeters with micron-scale resolution [5,6]. Its first applications in medicine were reported less than a decade ago [7-11], but its root lie in early work on white-light interferometry that led to the development of optical coherence-domain reflectometry (OCDR), a one-dimensional optical ranging technique [12]. Although OCDR was developed originally for finding faults in fiber-optic cables and network components [13], its ability to probe the eye [14-16] and other biological tissues [17] was soon realized. The superb axial resolution is achieved by exploiting the short temporal coherence of a broadband light source. Borrowing the concept of confocal microscopy, OCDR was quickly extended to section the biological tissues [7] through the point-by-point scan, so called optical coherence tomography. OCT enables microscopic structures in biological tissue to be visualized at a depth beyond the reach of conventional confocal microscopes. Probing depth exceeding 2 cm has been reported for transparent tissues, including the eye [18] and frog embryo [19]. To date, successful stories of *in vitro* and *in vivo* OCT applications in medicine have been delivered in a wide branch of areas, for example ophthalmology [20], gastrointestinal tract [21-25], dental [26], dermatology [27-29] etc. OCT will shortly become viable as a clinical diagnostic tool with the recent advent of high-power, low coherence sources and near real time image scanning technology [30]. The high resolution ($< 20\ \mu m$) and high dynamic range (>100 dB) of OCT would allow for *in situ* tissue imaging approaching the resolution of excisional biopsy. An advantage that OCT has over high-frequency ultrasonic imaging, a competing technology that achieves greater imaging depths but with low resolution [31], is the relative simplicity and cost-effectiveness of the hardware on which OCT systems are based.

This chapter is designed to introduce the fundamental aspects of optical coherence tomography and briefly its applications in medicine and biology. In the later parts of chapter, we will discuss how multiple scattering of tissue would impact on the OCT imaging performances, and the developments in reducing the overwhelming multiple scattering effects and improving imaging capabilities by the use of immersion techniques.

13.2 OPTICAL COHERENCE TOMOGRAPHY: THE TECHNIQUES

13.2.1 Introduction

OCT is analogous to ultrasonic imaging that measures the intensity of reflected infrared light rather than reflected sound waves from the sample. Time gating is employed so that the time for the light to be reflected back, or echo delay time, is used to assess the intensity of backreflection as a function of depth. Unlike ultrasound, the echo time delay of an order of femtosecond cannot be measured electronically due to the high speed associated with the propagation of light. Therefore, time-of-flight technique has to be engaged to measure such ultra-short time delay of light backreflected from the different depth of sample. OCT uses an optical interferometer to solve this problem. Central to OCT is a low-coherence optical reflectometry (LCR) that can be realized by a Michelson or a Mach-Zehnder interferometer illuminated by a low coherent light source.

13.2.2 Low Coherence Reflectometry

LCR, or "white light interference" has been used for centuries in industrial metrology, e.g., to measure the thickness of thin film [32], as a position sensor [33], and with other measurements that can be converted to a displacement [34]. At present, all OCT techniques use LCR to obtain the depth resolved information of a sample as shown in Figure 1.

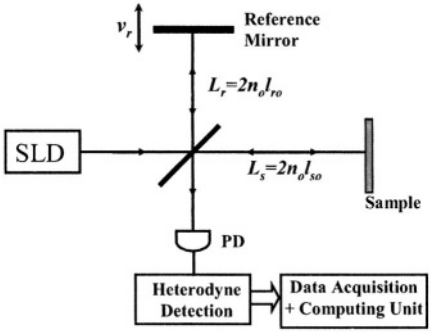

Figure 1. Schematic of low coherence interferometer.

One arm of the interferometer is replaced by the sample under measurement. The reference mirror is translated with a constant velocity v_r to produce interference modulation with Doppler frequency $f_D=2v_r/\lambda_o$ for optical heterodyne detection, where λ_o is the central wavelength of low-

coherence light source. Then the interference can occur only when the optical path lengths of light in both the sample arm and reference arm are matched to within the coherence length of light source.

The principle of LCR can be analyzed in terms of the theory of two-beam interference for partially coherent light. Assuming that the polarization effects of light are neglected, $E_s(t - L_s/c)$ and $E_r(t - L_r/c)$ are scalar complex functions that represent the light fields from the sample and reference arms of a Michelson interferometer, respectively. L_s and L_r are the corresponding optical path lengths. Given assumption that the photodetector captures all of the light from the reference and sample arms, due to time invariance of the light field, the resultant intensity at detector PD is then:

$$I_d(\tau) = \left\langle [E_s(t) + E_r(t+\tau)][E_s(t) + E_r(t+\tau)]^* \right\rangle, \tag{1}$$

where the angular brackets denote the time average over the integration time at the detector. $\tau = \Delta L/c$ is the time delay corresponding to the round-trip optical path length difference between the two beams, i.e., $\Delta L = L_s - L_r = 2n_0(l_{s0} - l_{r0})$. $n_0 \cong 1$, is the refractive index of air, and l_{s0} and l_{r0} are the geometric lengths of two arms, as indicated in Figure 1. Because $I_s = \left\langle E_s(t)E_s^*(t) \right\rangle$ and $I_r = \left\langle E_r(t+\tau)E_r^*(t+\tau) \right\rangle$, equation 1 can then be written as:

$$I_d(\tau) = I_s + I_r + 2\,\mathrm{Re}\{< E_s(t)E_r^*(t+\tau) >\}. \tag{2}$$

The last term in the above equation, which depends on the optical time delay τ set by the position of reference mirror, represents the amplitude of interference fringes that carry information about the structures in sample. The nature of the interference fringes, or whether any fringes form at all, depends on the degree to which the temporal and spatial characteristics of E_s and E_r match. Thus the interference functions as a cross-correlator and the amplitude of interference signal generated after integration on the surface of the detector provides a measure of the cross-correlation amplitude. The first two terms in equation 1 contribute to the dc signal only in the interference signal detected by photodetector. To facilitate the separation of cross-correlation amplitude from the dc component of detected intensity, various techniques have been realized to modulate the optical time delay, i.e., τ. A few of these techniques will be discussed later.

Under the assumption that the sample behaves as a perfect mirror that leaves the sample beam unchanged, the correlation amplitude depends on the temporal-coherence characteristics of the source, according to

$$\mathrm{Re}\{< E_s(t)E_r^*(t+\tau) >\} = |G(\tau)| \cos[2\pi f_0 \tau + \phi(\tau)], \tag{3}$$

where $f_0 = c/\lambda_0$ is the central frequency of the source with c the speed of light, and $G(\tau)$ is its complex temporal coherence function with argument of

$\phi(\tau)$. According to the Wiener-Khintchine theorem, $G(\tau)$ is related to the power spectral density of the source, $S(f)$, as [35,36]

$$G(\tau) = \int_0^\infty S(f)\exp(-j2\pi\tau)\mathrm{d}f \,. \tag{4}$$

It follows from this relationship that the shape and width of the emission spectrum of the light source are important variables in the low-coherence interferometry, thereby OCT because of their influence on the sensitivity of the interferometer to the optical path length difference between the sampling and reference arms. Light sources with broad bandwidth are desirable because they produce interference signals of short temporal extent. The relationship between $S(f)$ and $G(\tau)$ can be seen clearly when both are represented by Gaussian functions:

$$S(f) \leftrightarrow G(\tau) \tag{5}$$

with

$$S(f) = \frac{2\sqrt{\ln 2/\pi}}{\Delta f}\exp\left[-4\ln 2\left(\frac{f-f_0}{\Delta f}\right)^2\right], \tag{6}$$

and

$$G(\tau) = \exp\left[-\left(\frac{\pi\Delta f\tau}{2\sqrt{\ln 2}}\right)^2\right]\exp(-j2\pi f_0\tau)\,. \tag{7}$$

In these equations, the full-width-half-maximum bandwidth Δf represents the spectral width of the source in the optical frequency domain. The corresponding measure of the correlation width, derived from equation 7, is the correlation length (in free space), given by

$$l_c = \frac{2c\ln 2}{\pi}\cdot\frac{1}{\Delta f} \approx 0.44\frac{\lambda_0^2}{\Delta\lambda}\,, \tag{8}$$

where $\Delta\lambda$ is the full-width of the coherence function at half-maximum measured in wavelength units. Other definitions of the coherence length yield similar expressions, but with a different constant factor. For example, defined as the speed of light in medium times the area under the squared amplitude of the normalized temporal coherence function, $l_c \approx 0.66\lambda_0^2/\Delta\lambda$ [35]. In the OCT community, equation 8 is often used.

13.2.3 Noise

One of the main noise sources in LCR is mechanical $1/f$ noise. To achieve shot-noise-limited detection, a heterodyne technique can be used. The most straightforward and simplest technique in optics is to use the Doppler effect, e.g. simply moving the reference mirror with constant speed v. Thus, the time delay will be

$$\tau = \frac{2vt}{c} \quad . \tag{9}$$

Then we have the ac term of detected interference signal time-modulated by

$$\mathrm{Re}\{< E_s(t)E_r^*(t+\tau) >\} = \mid G(\tau) \mid \cos[4\pi f_0 vt / c + \phi(\tau)] \quad . \tag{10}$$

From here, the central Doppler frequency will be

$$f = \frac{2f_0 v}{c} = \frac{2v}{\lambda_0} . \tag{11}$$

Figure 2(a) shows an example of a time-modulated interference signal detected by the photodetector. If the detected ac signal is bandpass filtered with respect to the central Doppler frequency as the center frequency, then rectified and low-pass filtered. The output of the low-pass filter is the envelope of the time-modulated ac interference signal, which is equivalent to the cross-correlation amplitude mentioned above. Figure 2(b) gives an example of the detected envelope corresponding to Figure 2(a).

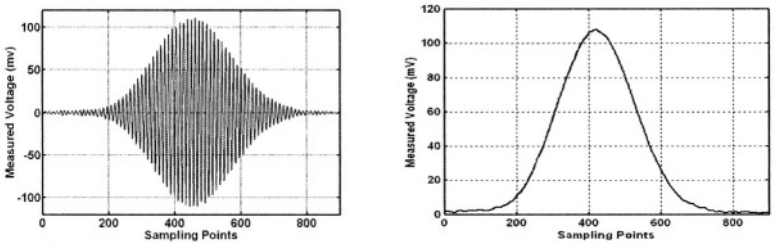

Figure 2. (a) time-modulated ac term of interference signal, (b) corresponding cross-correlation amplitude, i.e., envelope.

In addition to $1/f$ noise, there are several other noise sources such as quantum noise, shot noise, and electronic noise. The impact of these noise disturbances on the measurement can be described by signal-to-noise ratio (SNR), which is the ratio of the expected mean photocurrent power to its standard deviation. The dynamic range (DR) of an instrument is defined by the ratio of the maximum to the minimum measurable photocurrent power P of the interference signal:

$$DR = 10\log\frac{P_{\max}}{P_{\min}} = 10\log(SNR_{\max}) . \tag{12}$$

Photocurrent power P is proportional to the square of the light intensity impinging at the photodetector, hence

$$\frac{P_{\max}}{P_{\min}} = \frac{R_{\max}^2}{R_{\min}^2} = \frac{1}{R_{\min}^2} \quad \Rightarrow \quad DR = -20\log(R_{\min}) , \tag{13}$$

where R_{min} is the minimal reflectivity in the sample beam producing a photodetector signal power equal to the standard deviation of the photocurrent power generated by a reflectivity of R_{max}=1. In case of LCR and

OCT, the intensity at photodetector is caused by the interference of the sample beam with the reference beam. Hence according to the interference law, the signal intensity at the photodetector is proportional to the square root of the object intensity and we have in this case:

$$DR = -10\log(R_{\min}) . \tag{14}$$

The LCR and OCT has been designed near the shot noise limit by choosing a proper Doppler frequency to avoid low frequency $1/f$ noise [13], a proper balanced-detector scheme to reduce the excess photon noise [37], and a proper transimpedance amplifier resistance voltage to overcome thermal noise [38]. The simplest method for choosing a proper Doppler frequency is to mount the reference mirror on a linear translation stage moving at a chosen constant velocity. The other methods include the fiber stretching via a piezoelectric crystal [39], and frequency domain scanning by introduction of a grating-based phase control delay line [40].

13.2.4 Optical Coherence Tomography

Optical coherence tomography performs cross sectional imaging by measuring the time delay and magnitude of optical echoes at different transverse positions, essentially by the use of a low coherence interferometry. A cross sectional image is acquired by performing successive rapid axial measurements while transversely scanning the incident sample beam onto the sample (see Figure 3). The result is a two-dimensional data set, which represents the optical reflection or backscattering strength in a cross sectional plane through a material or biological tissue. OCT was first demonstrated in 1991 [7]. Imaging was performed *in vitro* in the human retina and in atherosclerotic plaque as examples of imaging in transparent, weakly scattering media as well as highly scattering media. The system implemented by the optic fiber couplers, matured in the telecommunication industry, offers the most advantage for the OCT imaging of biological tissues because it can be integrated into almost the all currently available medical imaging modalities, for example endoscope and microscope. Figure 4 gives an example of the optic-fiber versions of OCT [25,29]. In this type of optic-fiber version of interferometer, light from a low-coherence light source is coupled to a single-mode fiber coupler where half of light power is conducted through the single-mode fiber to the reference mirror. The remaining half enters the sample via proper focusing optics. The distal end of the fiber in the sample arm serves a dual role as a coherent light receiver and spatial filter analogous to a confocal pinhole. Because the dc signal and intensity noise generated by the light from the reference arm add to the interference signal, it makes the system prone to the photon excess noise. One way to reduce this type of noise is to use a balanced detection

configuration as shown in Figure 4 that would make the background noise components cancelled by subtracting the photocurrents generated by two photodetectors. The interference signals at the output of the detectors add because they vary out of phase [41].

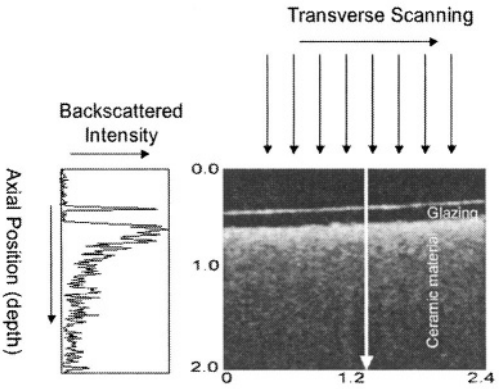

Figure 3. OCT images are generated by performing measurements of the echo time delay and magnitude of back-scattered light over a range of transverse positions. OCT are two or three-dimensional data sets which represents the optical backscattering in a cross-section or volume of the tissue (Courtesy of Cranfield Biophotonics Group).

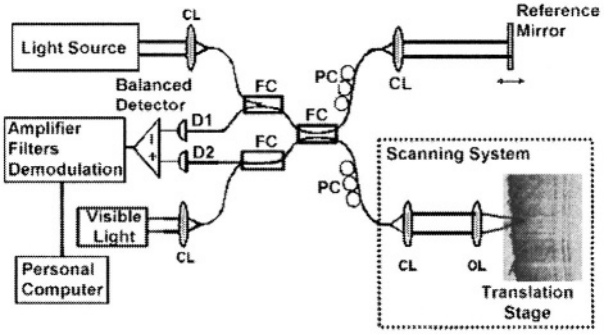

Figure 4. Example of the fiber-optic versions of OCT systems where CL is the collimating lens, FC the fiber coupler, PC the polarization controller, OL the objective lens, and D the detector.

OCT has the advantage that it can achieve extremely high axial image resolution independently of the transverse image resolution. The axial resolution is determined by the coherence length of light source used, i.e., equation 8, which is independent of the sampling beam focusing conditions. From equation 8, the axial resolution is inversely proportional to the spectral bandwidth of light source. Thus the higher axial resolution can be achieved by the use of a wider spectral bandwidth of light sources. Table 1 lists characteristics of a variety light sources suitable for use in OCT systems [6].

The most commonly used sources in the current OCT systems are the superluminescent diodes (SLD's) with peak emission wavelengths in either 820 nm or 1300 nm fiber-optic telecommunication bands because of their high irradiance and relatively low cost. However, the coherence lengths of SLDs are typically 10-30 microns that are not sufficient to achieve the resolution required for many medical and industrial applications. In the meantime, the moderate irradiance offered by the SLDs limits the real time applications for OCT system, which usually require a power with an order of at least 10 milliwatts. To meet the demands of the latest generation of OCT systems with scan rates that approach the television video rate, mode-locked $Ti:Al_2O_3$ and Cr^{4+}:forsterite lasers have been employed [42,43]. The high power and wide bandwidth of these lasers make them attractive sources for fast, high resolution OCT imaging of *in vivo* biological tissues. Recently the diode-pumped superfluorescent fiber sources [44, 45] also attract enormous attention in the current OCT developments because of their low cost and compactness.

Table 1. Low coherence sources suitable for use in OCT systems

Source	Central wavelength (nm)	Bandwidth (nm)	Emission Power	Reference
Edge-emitting LED	1300, 1550	50-100	20-300μW	[46]
SLD	800, 1300	20-50	1-10 mW	--------
Multiple QW	800	90	15 mW	[48]
LED/SLD	1480	90	5 mW	[49]
Laser-pumped fluorescent organic dye	590	40	9 mW	[47]
Mode locked $Ti:Al_2O_3$ laser	820	50-200	400 mW	[42]
Mode-locked Cr^{4+}forsterite laser	1280	75	30 mW	[43]
Superfluorescent optical fibers:				
Er-doped	1550	40-80	10-100mW	[45]
Tm-doped	1800	80	7mW	[45]
Nd-/Yb-doped	1060	65	108mW	[44]

The lateral or transverse resolution achieved with an OCT imaging system is determined by the focused spot size limited by the numerical aperture of the lens used to deliver the light onto the sample, and the optical frequency of incident light as in conventional microscopy [50]. The transverse resolution can be written

$$\Delta x = \frac{4\lambda f}{\pi d}\ , \tag{15}$$

where d is the spot size on the objective lens and f is its focal length. High transverse resolution can be achieved by the use of a large numerical aperture of lens and focusing the beam to a small spot size. In addition, the transverse resolution is also related to the depth of focus or confocal parameter, b. The confocal parameter is twice the Rayleigh range, $2z_R$. Its relationship to transverse resolution is described by the formula:

$$b = 2z_R = \pi\Delta x^2 / 2\lambda\ . \tag{16}$$

In addition to its high-resolution feature, advantages of OCT for medical imaging include its broad dynamic range, rapid data acquisition rate and compact portable structure. The frame rates for OCT systems are currently at four to eight frames per second [43]. At the beginning of OCT development, the path length in the reference arm was scanned via the use of a moving mirror or galvanometer [7]. However, such scanning would require approximately 40 seconds performing an image of non-transparent tissue [51]. A system similar to this is still in use for imaging the transparent tissue of the eye, and sometimes is sufficient for use as a research tool. Fiber-stretching with a piezoelectric crystal [39] in the reference arm offers a rapid scanning of the optical path length. However, there are disadvantages in the use of such technique, including polarization mode dispersion, hysteresis, crystal breakdown, and high voltage requirement. Presently, the most popular OCT systems employ a variable optical group delay in the reference arm through the introduction of a grating-based phase control delay line [40]. This configuration was originally designed for shaping femtosecond pulses that employs a grating-lens combination and an oscillating mirror to form an optical delay line [52]. It was reported to achieve high data acquisition rates up to 4-8 frames per second [43]. In addition to its high data acquisition rate, the system has two other advantages over the previous configurations. The optical group delay can be varied separately from the phase delay, and the group velocity dispersion can be varied without the introduction of a separate prism [53,54].

The OCT system described above is the main stream of current system developments, particularly for *in vivo* applications. This is usually called the time domain approach. There are varieties of other systems developed so far operating at different domains or revealing different functionalities of the tissue, but essentially the same mechanism, for example dual beam OCT [55,56], en-face OCT [57,58] (see also Chapter 16), Fourier domain OCT [59-61], whole field OCT [62,63], and functional OCT including polarization sensitive OCT [64-66] (see also Chapter 18), Doppler OCT [67-72] (see also Chapter 19), spectroscopic OCT [73] (see also Chapter 15), etc. For detailed information regarding to the different forms of OCT systems, please refer to a recent comprehensive review paper by Fercher *et al.* [74].

13.3 OCT IN IMAGING

13.3.1 Introduction

OCT was originally developed to image the transparent tissue of the eye at unprecedented resolution [7]. It has been used clinically to evaluate a wide range of retinal-macular diseases [75-77]. Recently, the technology has been advanced to image nontransparent tissue, where penetration of light is limited [78-82]. Non-transparent tissue has high light scattering in nature, which limits the light penetration depth for OCT imaging. To partially resolve this problem, most of OCT imaging of nontransparent tissues is implemented with light having an incident wavelength near 1300 nm, rather than 820 nm used in the relatively transparent tissues. At the wavelength of 1300 nm, light scattering is low relative to scattering of light in the visible region. Absorption is low because this wavelength is too long to result in large amounts of electron transitions but is too short to induce extensive vibrational transitions in water. Another method to enhance the OCT imaging depth for non-transparent tissue is to use the immersion technique to interrogate the tissue with biocompatible chemical agents. This will be described later in this chapter.

13.3.2 Ophthalmology

Due to the relatively transparent nature of human eye tissue to the near infrared light, its weakly scattering structures, including the retina, can be imaged by OCT to the full depth with a resolution at 20 μm without difficulty [18,20,83-85]. The diagnostic potential of OCT for non-contact biometry segment of abnormalities of the eye was first demonstrated by Izatt *et al.* [16]. Using the reflectometer technique at a central wavelength of 820 nm, structures such as cornea, sclera, iris, and lens anterior capsule can be clearly visualized. High resolution with high frequency sampling resulted in the visualization of the corneal epithelium, the stroma, and the endothelium, see Figure 5 for an example.

Many retinal diseases are accompanied by changes in retinal thickness. Hence high depth resolution is an important feature of any imaging techniques used to diagnose retinal pathology. Current diagnostic tools such as the confocal scanning ophthalmoscope are limited to a depth resolution no better than 300 microns [86]. Towards this, OCT offers a great potential to advance the diagnostic techniques because of its high resolution. Using a wavelength of 830 nm, it can easily differentiate the large-scale anatomical features, such as the fovea, optic disk, and retinal profiles. It can also

quantitatively assess the retinal thickening caused by macular edema and other diseases. Further studies have shown that the potential of OCT to quantify the amount of serous retinal detachments, macular holes, and mucular edema, [87, 88] and to assess the glaucoma [89].

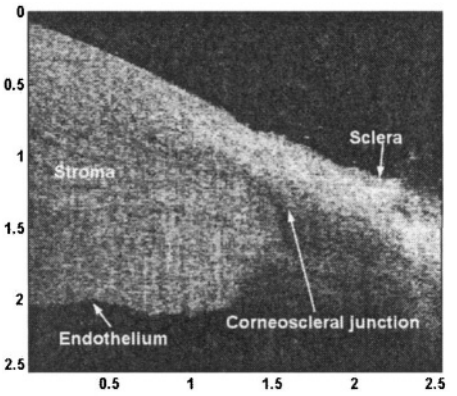

Figure 5. OCT image of human cornea-sclera tissue. Note the epithelium layer was stripped off before the experiments. The collagen fiber lining within stroma is seen. Unit: mm (Courtesy of Cranfield Biophotonics Group).

With the use of a laboratory based ultra-broadband femtosecond Titanium–sapphire laser light source, an axial resolution of OCT for ophthalmologic applications has been recently advanced to about 1-3 microns [90,91], enabling unprecedented *in vivo* imaging of intraretinal sub-cellular structures. The availability of this technology for clinical research and patient care will depend mainly on the availability of suitable sources for ultra-broad-bandwidth light, but it will no doubt have enormous impact on the future care of our vision.

13.3.3 Developmental Biology

Some of the most exciting applications of OCT have occurred in the basic science of developmental biology. Studies have shown the promises of OCT to real time monitor the developing neural and embryonic morphology [29,92-94] of *Xenopus laevis, Rana pipiens,* and *Brachydanio rerio.*

Figure 6 shows two *in vivo* OCT images obtained from a tadpole: a) dorsal scan across the eyes and b) longitudinal scan from ventral site. The images have resolutions of 8 μm (axial) and 20 μm (transversal) where the gray level corresponds to the logarithm of back-scattered light intensity collected by the optical system, with white representing the highest

backscattered signal. These images show high-resolution details of internal structures, including skin, eyes, brain, heart, and other features.

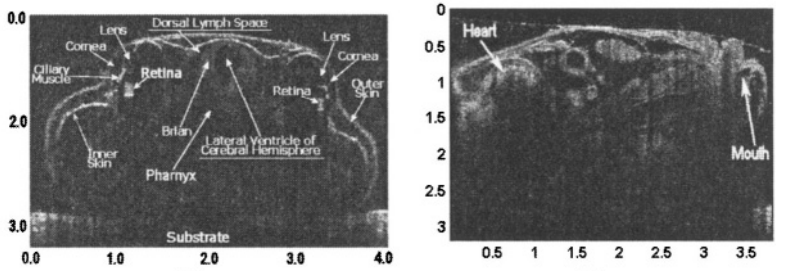

Figure 6. OCT images scanned from a tadpole: (a) dorsal scan across the eyes, (b) longitudinal scan at the ventral side [29].

Figure 7 illustrates a series of cross-sectional optical slices scanned perpendicular to the anteroposterior axis of the specimen. In each image, in addition to the other features, distinct regions of brain can be identified. Figure 7(a) shows the paired cerebral hemispheres and the two lateral ventricles. Figure 7(d) demarcates the narrowing of the aqueduct of Sylvius connecting the diocoel with the rhombocol. Although the current OCT system does not permit the imaging of individual cells due to its limited resolution, it performs well in imaging larger tissue and organ morphology, the structures that are too large to image *in vivo* with confocal microscopy. The above results demonstrate that OCT has applications to developmental biology because it can image biological species non-invasively and in real time. Such non-invasive cross-section imaging of the tadpole's internal organs could make OCT a powerful monitoring tool for developmental biology.

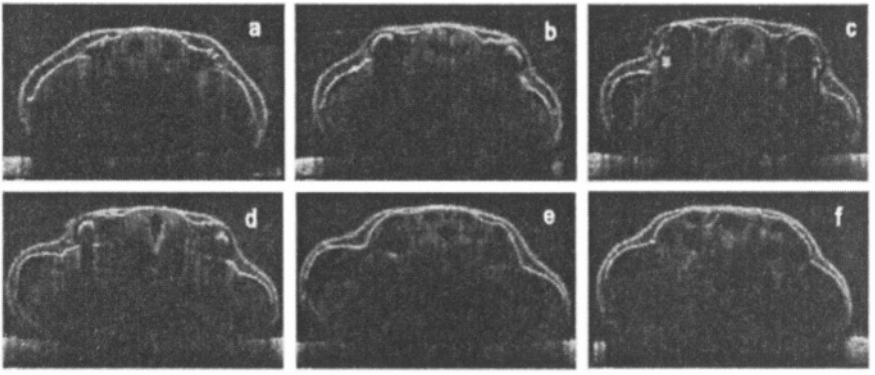

Figure 7. A series of OCT scans perpendicular to anteroposterior axis of a tadpole [29].

13.3.4 Dermatology

Dermatology also appeared to be a promising application field for OCT due to the obvious ease of access [95]. However, it turned out that skin is a much less favorable subject for OCT imaging than previously thought because of strong scattering of the probe light and poor optical contrast between structural components in clinically important areas. OCT penetration depth covers the stratum corneum, the living epidermis, and the dermis consisting mainly of a network of collagen and elastin fibers and fibroblasts. Nevertheless, it does offer potential for early detection of malignant melanoma [96,97]. However, the successful application to this problem will depend on establishing correlations with the standard histopathology through a vast amount of experimental studies. Whether sufficient optical contrast exists between normal and pathological tissue at a cellular scale is a critical question that needs to be addressed in the future.

Figure 8 illustrates the *ex vivo* OCT images from a five-day old rat at (a) the chest and (b) the abdomen. It clearly demonstrates that OCT has the capability of seeing through the skin of the species with high resolution. Different layers and features starting from skin surface are delineated sharply, including epidermis (E), dermis (D), hypodermis (H), muscle (M), fascia (F), bone (B), stomach, hair follicles and other features.

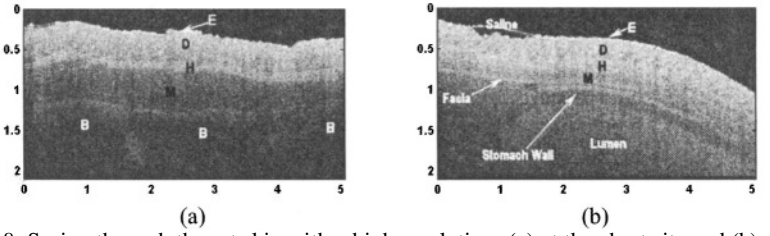

Figure 8. Seeing through the rat skin with a high resolution: (a) at the chest site and (b) at the abdomen site [29].

High-resolution delineation of the skin structures with OCT, have been demonstrated in Figure 9 where a whole body of an adult Wistar rat was used in the experiments. Skin imaging with OCT has traditional difficulties because of the skin has high scattering properties to the near infrared light which limit light penetration into deep skin. To reduce the light scattering in the skin, chemical agents were used in the experiments, including glycerol and propylene glycol, which agents has known to provide a bed for refractive index matching inside the superficial tissue [29]. After topical applications of the chemical agent solutions onto the skin surface, OCT imaging (Figure 9) allows us to visualize clearly the different layers and features in the skin including epidermis (E), epidermal basement (EB), papillary dermis (P), reticular dermis (R), hypodermis (HP), fascia (F), muscle and hair follicles, etc. Far more detailed structures are delineated in

dermis zone. Note that the experiments were done with topical applications of glycerol solution, Figure 9(a), and propylene glycol solution, Figure 9(b).

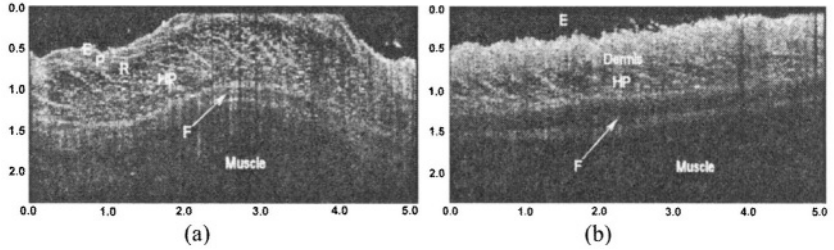

Figure 9. High resolution visualization of skin layers and features [29].

13.3.5 Gastroenterology

Gastrointestinal disorders, including cancer, represent a major international health problem. Conventional gastrointestinal endoscopic diagnosis is predicated on the gross morphological characteristics of mucosal and submucosal abnormalities [98]. However, endoscopic diagnosis is less successful in clinical situations where the underlying morphological or biochemical premalignant changes do not alter gross architecture. Due to its high resolution and in-depth imaging capability, OCT has the potential in the future routine clinical application in gastrointestinal endoscopy [99]. The depth range of OCT imaging, however limited, is sufficient to penetrate the mucosal lining of endoscopically accessible organs of the gastrointestinal tract to provide the in-depth images with a resolution superior to the currently available clinical imaging techniques [21-24].

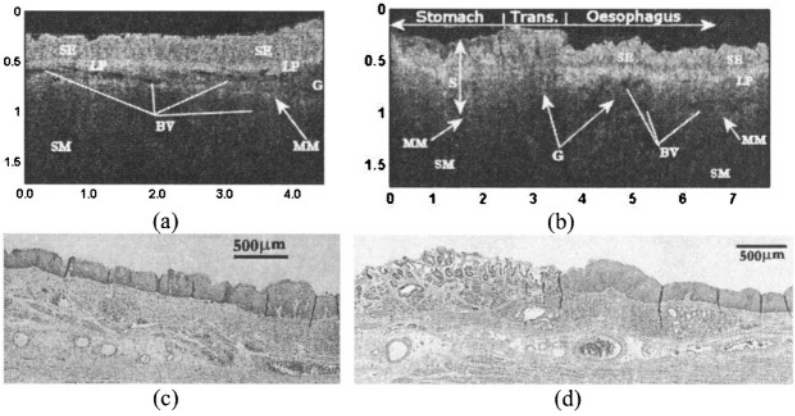

Figure 10. High resolution OCT images of normal (a) esophagus and (b) esophago-gastric junction, where S denotes the secretory glands, SE the stratified squamous epithelium, LP the lamina propria, MM the muscularis mucosae, ED the excretory ducts, BV the blood vessels, and SM the submucosa; and their corresponding histology (c) and (d) respectively (Courtesy of Cranfield Biophotonics Group).

OCT images of the normal esophagus, Figure 10(a), and esophago-gastric junction, Figure 10(b), allow the visualization of morphology of the mucosa, submucosa, and distinguishing the transitional features from esophagus to stomach. From Figure 10(a), the upper portion of the mucosa, including stratified squamous epithelial (SE) and lamina propria (LP), appears homogeneous in the OCT image. The muscularis mucosa (MM) is more highly reflective than the mucosa. Numerous blood vessels can be identified in the lamina propria zone.

The transition from the esophageal to the gastric tissues was clearly visualized by the OCT images as shown in Figure 10(b). It demonstrated that the mucosa of the tract undergoes an abrupt transition from a protective stratified squamous epithelium (SE) to a tightly packed glandular secretory mucosa (S). The lamina propria (LP) appears highly reflecting and homogeneous in the esophagus. The muscularis mucosae (MM) is continuous across the junction though it is less easily seen in the stomach where it lies immediately beneath the base of the gastric glands. Other architectural features such as the excretory ducts, blood vessels, and esophageal glands were also clearly delineated in the OCT images.

The OCT images of the normal colonic tissue allow visualization of the morphology of the mucosa (M), submucosa (SM), and muscle layers (ML). This is presented in Figure 11 (a). A distinct feature of mucosa for the large intestinal is its unbranched simple tubular glands (crypts of Lieberkühn) which extend through the lamina propria to the muscularis mucosae (MM). Such a feature is clearly delineated in the OCT images where they lie immediately above the muscularis mucosae while the latter is seen as a high reflecting layer [see upper portion of Figure 11(a)]. The muscle layer of the colon depicts as a dark layer because the muscle highly attenuates the incoming light. The regular horizontal lining seen in the muscle layer [see bottom of Figure 11 (a)] is probably demonstrating the fiber-bundle arrangement of muscularis externa.

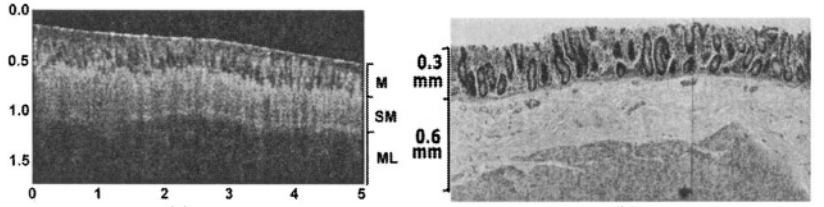

Figure 11. High resolution OCT image of (a) normal human colon and (b) its corresponding histology, where the mucosa (M), submucosa (SM), muscularis propria layer (ML), lymph nodule, crypts, etc can be visualized (Courtesy of Cranfield Biophotonics Group).

The eventual target for endoscopic OCT includes real time, *in situ* characterization of gastrointestinal pre-malignant changes such as dysplasia, as well as the identification and staging of small, superficial cancers.

Endoscopic implementations of OCT *in vivo* have been recently reported with some success [100,101]. As OCT technology matures, however, accurate primary diagnosis and staging by OCT could have a significant impact on clinical care because small, early stage malignancies would be amendable to immediate curative therapy at the time of endoscopy. This capability would enable physicians to make diagnostic and therapeutic decisions at the time of examination without referring to the histopathological diagnosis that normally requires a time frame of one week.

13.3.6 Other Biomedical Applications

The distinct features of optical coherence tomography, e.g., high resolution, relative high penetration depth and a potential for functional imaging, make OCT one of suitable candidates for optical biopsy. It offers a wide range of promising applications across all biomedical imaging disciplines. Apart from the applications stated above, we mention below briefly a few other examples of high resolution and functional OCT.

Due to optic-fiber implementation of system, OCT is predestinated as an endoscopic modality for high-resolution intraluminal imaging of organ systems, including intravascular walls. Preliminary studies have shown that OCT can detect intramural collections of lipid within the intimal vessel wall [102,103]. Compared to high frequency (30 MHz) ultrasound, OCT (1300 nm wavelength) yielded superior structural information [104,105].

Colston *et al.* presented a fiber-optics based dental OCT system operating at a central wavelength at 1300 nm [106]. Penetration depth varied from 3 mm in hard tissues to 1.5 mm in soft tissues. Hard tissue structures identified were enamel, dentin, and dento-enamel junction (see Figure 12 for example). In the early investigations, birefringence induced artifacts in the enamel OCT imaging [106,107]. These can be eliminated by measuring the polarization state of the returned light by using a polarization sensitive OCT (PSOCT). Birefringence detected by PSOCT, however, has been shown to be useful as a contrast mechanism indicating pre-carious or carious lesions in both enamel and dentin [108,109].

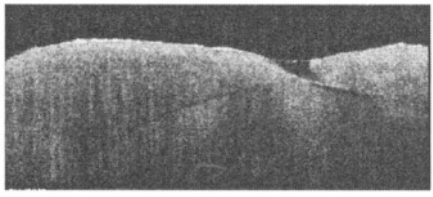

Figure 12. OCT imaging of human tooth near the gingiva (left). Image size is 1.8×4mm (Courtesy of Cranfield Biophotonics Group).

13.3.7 Industrial Applications

As stated previously, low coherence interferometry has already been used in optical production technology and metrology [32-34]. With the current development of OCT technique, Dunker *et al.* [110] analyzed the applicability of OCT for non-destructive evaluation of highly scattering polymer-matrix composites to estimate residual porosity, fiber architecture and structure integrity. OCT has also found its application to detect the subsurface extent of the Hertzian crack on the surface of a silicon nitride ball which has good agreement when compared with the predictions from crack propagation theories based on principal stresses and on maximum strain energy release [111]. Nondestructive evaluation of paints and coatings is another promising non-medical OCT application [112]. Operating in a confocal mode, OCT imaging though an 80-micron thick highly scattering polymeric two-component paint layer (corresponding to an equivalent thickness of ten mean free paths) has been demonstrated by a light source with central wavelength at 800 nm and bandwidth of 20 nm [112].

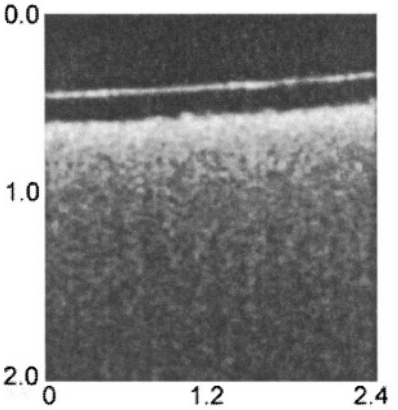

Figure 13. OCT image of ceramics of a dish plate [113]. The top is the glaze layer.

Figure 13 gives an example of OCT light penetration depth through a hard industrial material of a ceramic dish plate where the light source used is 820 nm central wavelength and 25 nm spectral bandwidth [113]. Despite the high scattering nature of ceramic materials, the imaging depth beyond 2.5 mm is possible.

13.4 EFFECTS OF LIGHT SCATTERING ON OCT

13.4.1 Introduction

Thus far, OCT has been seen to have the capability to delineate non-invasively sub-surface microstructures which has the potential to improve the diagnostic limits of currently available imaging techniques, allowing a wide range of clinical disorders to be addressed at an early stage. However, the reality is that OCT relies on the penetration and backscattering of light into tissue to construct cross-sectional, tomographic images. It collects the back-scattered photons that have experienced less scattering, i.e., ballistic or least-scattered photons. However, unlike the transparent ocular organs where OCT found its most successful applications [18], there is no evidence that an OCT imaging depth beyond 2 mm for opaque biological tissues is possible [81,82]. This is largely due to the multiple scattering inherent in the interactions between the probing light and the targeted tissue, which limits light penetration into the tissue, and therefore prevents the deep microstructures from imaging. Generally, multiple scattering could degrade signal attenuation and localization, leading to an image artifact that reduces the imaging depth, degrades the signal localization and affects the image contrast.

Smithies *et al.* [114] developed a Monte Carlo (MC) model according to their specific OCT system geometry to investigate how signal attenuation and localization are influenced by multiple scattering effects, where two specific media (intralipid and blood) are considered, representing moderately and highly anisotropic scattering respectively. The multiple scattering effects were clearly demonstrated in terms of the spreading of the point spread function (PSF). In the meantime, Yao and Wang [115] developed a MC model to simulate how multiple scattering degrades the OCT signal attenuation into the tissue, by separate considerations of least scattering and multiple scattered photons.

More recently, Wang [82] systematically investigated the multiple scattering effects on the OCT imaging performances including imaging depth, resolution degradation and signal localization. Generally from the results, it was found that signal localization and attenuation are dependent on the optical properties of tissue. The high scattering coefficient and the low degree of forward scattering are the primary causes for the degradation of signal localization and attenuation, leading to complication of interpretation of the measured OCT signals. More importantly, it was found that the imaging resolution is a function of the probing depth within the medium, as opposed to the claimed OCT system resolution. This fact has been overlooked recently in the OCT imaging applications. The imaging

resolution is greatly reduced with increasing depth; this case is even more severe for the highly scattering medium. Therefore, attention must be paid to this fact when applying the OCT to the human organs because of the high scattering nature of tissue.

Let's re-visit the OCT system by looking closely the backscattering light from the high scattering medium that has the possibility to contribute to the interference signal. A simple schematic of OCT system when probing the highly scattering medium is illustrated in Figure 14, where the sample beam progressively loses its spatial coherence as it penetrates a turbid biological tissue. This loss of coherence results from the scattering by a variety of cellular structures with sizes ranging from less than one wavelength (e.g., cellular organelles) to several hundreds of micrometers (e.g., the length of a collagen fiber).

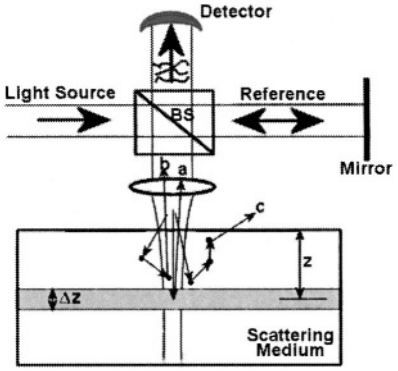

Figure 14. Simple schematic of OCT system showing scattering interactions between a probing beam and biological tissue. Three types of interactions are backscattered from within the tissue: single scatter **a,** small-angle scatter **b,** and wide-angle scatter **c.** A layer with a thickness Δz at the depth of z is the expected layer for OCT localization.

As illustrated in Figure 14, the dominant scattering interaction of the probing beam in the turbid medium can be categorized into three types [82,116] single backscatter **a,** 2) small angle forward scatter **b,** and 3) extinction by absorption or wide angle scatter **c** (i.e., light scattered out of the view of the interferometric receiver). The detector will only receive the first two categories of scatters because of the heterodyne detection characteristics of the OCT system. Furthermore, the low coherence light source used, as stated in the Section 13.2, provides a time gate to enable the detector only receive those photons that are traveled beneath the tissue surface with their optical path lengths matched the optical path length in reference arm to within coherence length of the light source. Consequently, the OCT system in reality plays a role to sieve all the backscattering photons

emerged at the detector according to their arrival times, or equivalently the optical path lengths that photons have traveled. For simplicity, we only consider the optical path length of the photon traveling beneath the tissue surface, i.e., the tissue surface is assumed to correspond with the zero position of reference mirror. Therefore, to enable the detector produce the signal, the following criteria must be fulfilled:

$$\left|L_p - 2nz\right| < \frac{L_c}{2}, \tag{17}$$

where L_p is the optical path length that the photon has traveled within the tissue, n is the refractive index of the medium, z is the depth of a layer whose distance from the tissue surface matches the scanning distance of mirror, nz, in the reference arm.

For the signal localization, we normally expect that the detected photons be backscattered from the layer whose thickness is determined by

$$2n\Delta z = L_c. \tag{18}$$

However, because of the multiple scattering there are possibilities for those photons contributing to the detected signal that are not backscattered from the expected layer, z, but fulfill the criteria of equation 17. As a consequence, this part of the photons degrades the signal attenuation, localization and resolution because they are not from the desired layer, leading to a signal artifact complicating the interpretation of OCT image. To gain insight into how single and multiple scattering effects would influence the signal attenuation and localization, it is therefore useful to classify the photons according to their localization information. We could classify the detected photons into those photons being backscattered from the desired layer, z, and those backscattered otherwise but fulfill the criterion of equation 17. Due to the requirement of matching the optical path lengths, the photons in the former must be undergoing less scattering events and very small-angle scattering including the single backscattering events, we therefore term this part of photons as the least scattered photons (LSP). While those photons satisfy equation 17 but are backscattered from a depth other than the desired layer are treated as the multiple scattered photons (MSP) that are experienced a wider-angle scattering. Clearly, the LSP signal is particularly useful as it provides the localized optical information about the targeted layer; while the MSP signal consists of multiply scattered photons which are not from the desired layer leading to the degradation of detected signal.

There is a clear relationship between the scattering interaction types described earlier in this section and the photon classifications that will be used in this study. The MSP comes solely from the interaction type **b,** while the LSP includes the interaction type **a** and part of type **b** because the photons backscattered from the desired layer might be subject to multiple scattering but with very small-angle scattering. A distinct difference

between them is that the LSP and MSP have been sorted according to their optical path lengths, thereby enabling the investigation of their influence on the OCT signal attenuation and localization.

With these conventions in mind, we now turn to looking at some results of how multiple scattering affects the OCT imaging performances by the use of the Monte Carlo simulation technique. For details, please refer to the reference [82].

13.4.2 The Effects of LSP and MSP on Attenuation

To investigate the influence of the photons coming back from the specific layer of interest, it is best to investigate separately the LSP and MSP signals on the backscattering profiles. Figure 15 illustrates such results for $\mu_s = 40$ mm^{-1} with $g = 0.7$, 0.9 and 0.98 respectively. It can be seen that the strength of the MSP signal increases with decreasing g in the medium at any optical depth of light penetration. This indicates that the photons that have reached a depth that does not correspond to the desired layer have a greater chance of emerging at the detector for the less anisotropic medium, leading to a greater degree of uncertainty in signal localization. The signal from LSP has an approximately logarithmic linear relationship with the probing depth for all cases but with different slopes.

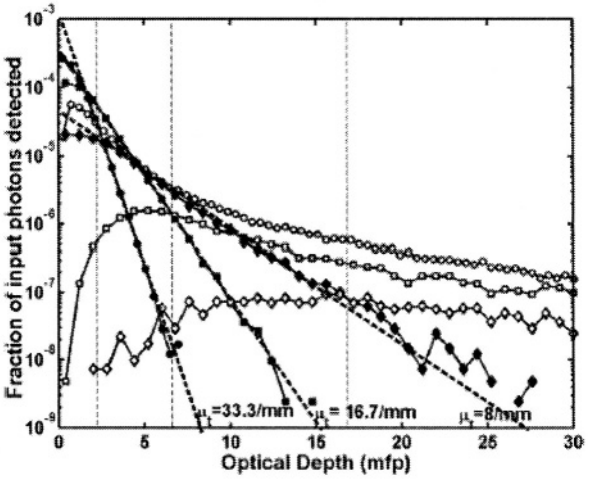

Figure 15. The profiles are shown as the backscattering intensities separately for the LSP and MSP photons for the media with optical properties of $g = 0.7$ (circle), 0.9 (square) and 0.98 (diamond), respectively, while $\mu_s = 40$ mm^{-1} is kept the same for all the media. The curves with solid symbols represent the LSP photons, and those with hollow symbols the MSP photons. The vertical dashed lines from left to right indicate the critical imaging depth for g = 0.7, 0.9 and 0.98, respectively. Thick dashed lines represent the least square fits of the LSP signals (Copyright @ Institute of Physics Publishing).

The slopes for the media investigated are calculated as 33.3 mm^{-1}, 16.7 mm^{-1} and 8.0 mm^{-1} for g = 0.7, 0.9 and 0.98 respectively. These values deviate significantly from the theoretical value of 40 mm^{-1}, with the worst case for the highest g. This is probably understandable because the higher the value of g, the greater the degree of forward scattering of photon in the medium, leading to a greater chance of the photon reaching the detector while satisfying the criterion of equation 17. Obviously such photons are able to survive more scattering events because of small-angle scattering.

Because the OCT signal is the summation of the MSP and LSP, it appears that the critical depth for optical imaging is the depth where signal from the LSP equals that from the MSP as the imaging contrast beyond this depth will be less than 1. These depths are illustrated in Figure 15 as vertical dashed lines from left to right for g = 0.7, 0.9 and 0.98, respectively, corresponding to 2 MFP, 6.65 MFP and 17 MFP, where MFP represents mean free path length measured as optical depth of $\mu_s d$. It should be noted that the critical depth, at which the MSP signal levels with the LSP signal, should actually be greater because the simulations do not take into account the polarization effects. The MSP photons undergo more scattering events than the LSP photons; the average scattering events increase much faster for the MSP photons with increasing depth. This is illustrated in Figure 16 where the detected photons are plotted as a function of the number of scattering events for the LSP and MSP signals backscattered from the depths of 50 μm and 100 μm respectively.

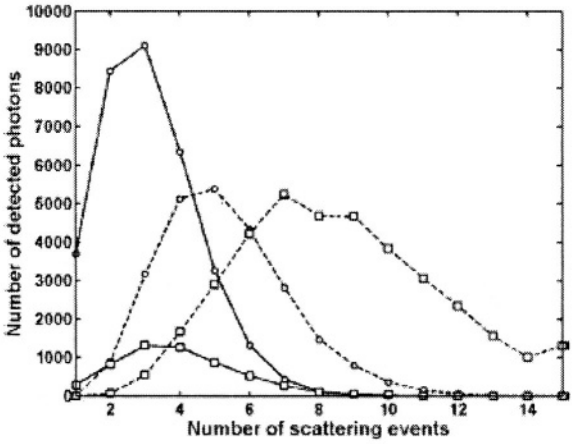

Figure 16. **Photons detected plotted as a function of the number of scattering events, backscattered from the specific depths at 50 μm (circle) and 100 μm (square), respectively. Solid curves are from LSP signals, while dashed curves are from MSP signals. Note that the number of detected photons backscattered from 100 μm is artificially magnified by five times to facilitate the comparisons (Copyright @ Institute of Physics Publishing).**

The optical parameters used for Figure 16 are $\mu_s = 67\ \text{mm}^{-1}$ and $g = 0.7$. Please note that the number of detected photons for the case of 100 μm has been artificially magnified by five times to facilitate the comparisons. All the curves are skewed towards the lesser number of scattering events. The average number of scatters from the LSP signal has only a slight increase from the depth of 50 μm to 100 μm, that is, from 2.5 to 2.8 scattering events respectively, while for the MSP signal, the average scattering increases much faster from 50 μm to 100 μm, that is, from 4.6 to 7.4 times. As multiple scattering depolarizes the light, the MSP photons are progressively and rapidly randomized with the increase in probing depth. As a consequence, the actual signal from MSP should be much lower than the calculated signals.

Despite the greater degree of degradation of signal attenuation, the probing critical depth increases dramatically with the increase of the anisotropic factor of the medium as illustrated in Figure 15. This is particularly useful in the optical clearing of blood by the use of biocompatible Dextrans where the Dextrans induce blood cell aggregation, an effect which might increase the forward direct scattering of the blood solution, leading to an enhanced optical imaging depth for OCT imaging through the blood [80,117].

13.4.3 Signal Localization

As a photon penetrates the turbid biological tissue, it progressively loses its spatial coherence due to the tendency of having a greater chance of being scattered by the tissue. In the meantime, the photons multiply backscatter from within the tissue at a greater depth, and those that are merged at the detector will have a greater chance of fulfilling the criterion of equation 17 for the photon categories of either MSP or LSP. It is the MSP that degrades signal localization because it is from a depth other than the expected layer, leading to reduced axial resolution of the OCT image. Signal localization was thus investigated systematically by means of the point-spread function (PSF) at the specific depth, for different optical properties to illustrate how the LSP and MSP contribute to signal localization.

Figure 17 gives examples of depth point spread function (zPSF) at different probing depths for the turbid media representing moderate scattering in the left column ($\mu_s = 10\ \text{mm}^{-1}$) and highly scattering in the right ($\mu_s = 67\ \text{mm}^{-1}$). The figures were obtained for $g = 0.7$, 0.9, and 0.98 from top to bottom respectively to allow us to scrutinize the influence of the anisotropic parameter of the medium on the signal localization. The depths monitored are indicated in each figure. The filled symbol curves are the actual PSFs that are the summation of LSP and MSP signals from a specific depth. However, to investigate the effects of LSP and MSP signals

separately on the PSFs, the signals from the LSP alone are plotted in each case, represented by the hollow symbol curves.

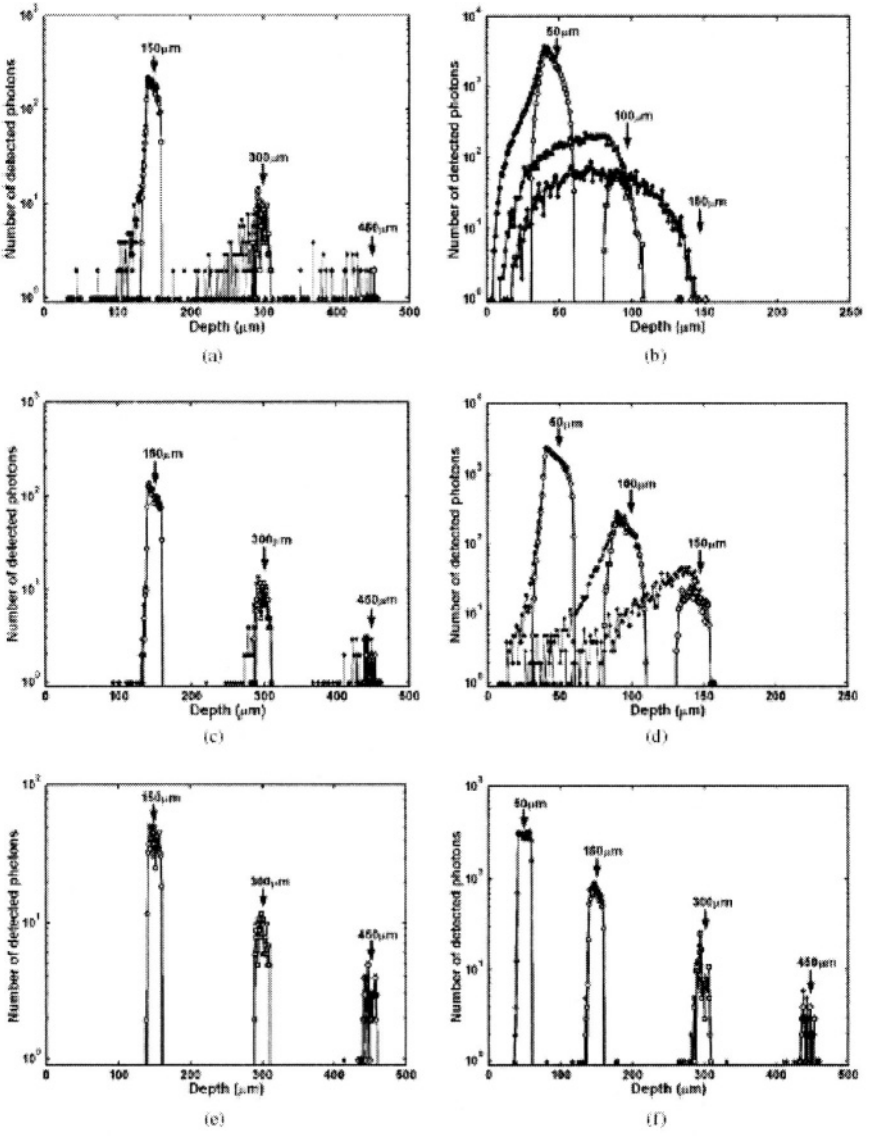

indicated, for the turbid media representing moderate scattering (μ_s = 10 mm^{-1}) in the left column and high scattering (μ_s = 67 mm^{-1}) in the right. From top to bottom, g = 0.7, 0.9 and 0.98 respectively. The LSP photons are plotted as the curves with hollow symbols (Copyright @ Institute of Physics Publishing).

Firstly, it is obvious that the worst case is from the medium with the highest scattering coefficient and lowest degree of forward scattering, i.e., μ_s = 67 mm^{-1} and g = 0.7 in this case (see the top right figure), where signal localization is merely discerned at a depth of 50 μm. Even at this depth, the contribution from an MSP signal is big enough to degrade the signal localization, where it can be seen that the PSF curve is skewed towards the nominal probing depth, indicating that the photons multiply scattered within the medium before this depth have more chances of surviving to reach the detector. Moreover, the photons backscattered from a very shallow depth at approximately 5 μm still survive the scattering to meet the criterion of equation 17 for depth localization at 50 μm. With an increase in probing depth to 150 μm, the PSF is overwhelmed by the MSP signal with only a few photons belonging to the LSP category. At this depth the signal localization is totally lost for OCT imaging. Furthermore, the axial resolution and imaging contrast are greatly reduced. The claim of high-resolution optical imaging of OCT is therefore questionable for highly scattering biological tissues. The axial resolution of OCT imaging is dependent on the optical properties of tissue and is a function of depth.

Figure 18 illustrates the measured axial resolution from the simulation results as a function of depth for the cases of (μ_s, g) = (67 mm^{-1}, 0.7), (67 mm^{-1}, 0.9) and (10 mm^{-1}, 0.9), respectively. The axial resolution of the OCT system is merely kept up to the depth of 50 μm for the case of (μ_s, g) = (67 mm^{-1}, 0.7). After this depth, the actual axial resolution degrades exponentially with the increase of depth, where it becomes approximately 220 μm at the depth of 200 μm as opposed to the system resolution of 40 μm. With the increase of g to 0.9, this performance has been improved, with system resolution retained up to a depth of 100 μm. If in the meantime, the scattering coefficient of the medium is reduced, for example, to μ_s = 10 mm^{-1} in this case, the probing depth at which imaging resolution is retained to the theoretical value would dramatically improve. This result is particularly welcome for the optical clearing of tissues with the purpose of enhancing the imaging depth of OCT which will be discussed in the next section.

With the reduction of the scattering coefficient (compare the left and right columns in Figure 17), signal localization improves with the lesser MSP signal contributing to the depth of PSFs. This indicates that the low scattering medium offers the more localized signal at any probing depth, which alternatively implies that the light penetration depth, i.e., optical imaging depth, is enhanced with less deterioration of the imaging resolution as stated above. On the other hand, it can be clearly seen from Figure 17 that with increasing g, the signal localization at any depth for the scattering medium improves dramatically, where the highly forward scattering medium, i.e., g = 0.98, offers the best signal localization for all the cases

investigated, see the bottom two figures for μ_s = 10 mm^{-1} and μ_s = 67 mm^{-1}, respectively. In these cases, only a few photons from the MSP category survive the scattering to contribute to final PSF at a depth of up to 600 μm.

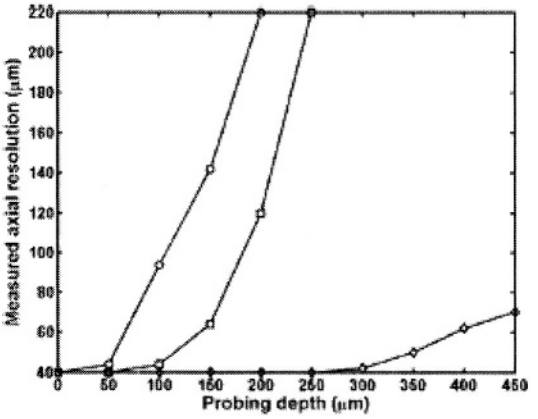

Figure 18. The measured axial resolution from the simulation results plotted as a function of the probing depth for (μ_s, g) = (67 mm^{-1}, 0.7) (circle), (67 mm^{-1}, 0.9) (square) and (10 mm^{-1}, 0.9) (diamond), respectively (Copyright @ Institute of Physics Publishing).

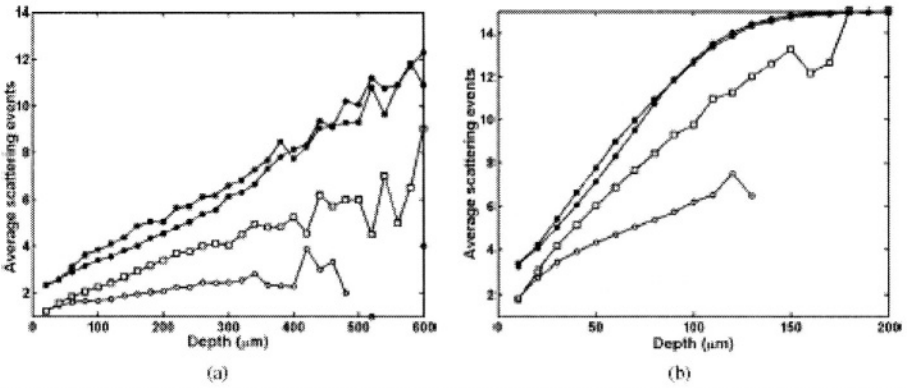

Figure 19. The average number of scattering events for the LSP (hollow symbols) and MSP (solid symbols), plotted as a function of probing depth for (a) μ_s = 10 mm^{-1} with g = 0.7 (circle) or 0.9 (square), and (b) μ_s = 67 mm^{-1} with g= 0.7 (circle) or 0.9 (square), respectively (Copyright @ Institute of Physics Publishing).

However, the results shown in Figure 17 do not give us the information as to how many times a photon has been scattered within the medium for both the LSP and the MSP signal before reaching the detector. Figure 19 gives such information of the average scattering event of the photons within

the medium as a function of the probing depth for the media with (μ_s, g) = (10 mm^{-1}, 0.7 or 0.9) and (67 mm^{-1}, 0.7 or 0.9), respectively. It is clear that the higher the scattering coefficient, the greater the number of scattering events of the photons at any depth before emerging at the detector in both LSP and MSP. For both the LSP and MSP photons, the average number of scattering events has an approximate linear relationship with the probing depth for all the cases investigated; but this relationship is stronger for the MSP.

For the high scattering medium, μ_s = 67 mm^{-1}, the average number of scattering events for MSP is close to 15 times at a depth of about 120 μm. Please note that after this depth, the curve looks like running into a flat region for MSP; this is an artifact due to the fact that the maximum scattering number of photons monitored in our MC program is set to 15 times in order to save the memory for computing. In the meantime, with the increase in g, the average number of scattering events increases with increasing probing depth for both the LSP and MSP; however, the pace for LSP is faster than that for MSP. For example, at a depth of 300 μm for μ_s = 10 mm^{-1} medium, the average number of scattering events for the LSP signal increases from 2.4 to 4.2, while for the MSP signal it only increases from 6.1 to 6.5. Bear in mind that the LSP photons have survived the criterion of equation 17 which alternatively means that they undergo a much smaller angle scattering than MSP photons.

Generally speaking, the average number of scattering events is much greater for MSP photons than for LSP photons. This is good in that the multiply scattered photons lose their polarization state progressively with an increase in scattering events, and thus actually contribute less to the final signal measured. The increased number of scattering events for increasing g accounts for the fewer slopes for LSP signals observed in Figure 15, and is the primary cause of the degradation of signal attenuation. To investigate how signal localization depends on the optical properties, for example, μ_s and g, Figure 20 gives such information for the determined PSF mean position from the simulations as a function of the probing depth for the media with g = 0.7, 0.9 and 0.98 and (a) μ_s = 10 mm^{-1} and (b) μ_s = 67 mm^{-1}, respectively. The broken lines in the figure represent the nominal depth positions for PSFs. It can be seen that for a less scattering medium with high g value, for example, μ_s = 10 mm^{-1} and g = 0.98 in Figure 20(a), the best accuracy of signal localization throughout the depth monitored is given; the opposite is true for the highest scattering medium and lowest g investigated. For μ_s = 67 mm^{-1} and g = 0.7, the accuracy of signal localization is only reliable up to a depth of 50 μm. With increasing probing depth the ability of OCT to provide signal localization is greatly reduced. This is because the MSP photons progressively overwhelm the LSP photons with increasing depth. This effect makes OCT lose its localization capability, while the

increase of g value dramatically improves signal localization, where it can be seen that for $\mu_s = 67\ \text{mm}^{-1}$ and $g = 0.98$ the signal localization is maintained up to about 600 μm. After this depth the accuracy starts to level off. Generally, the accuracy of signal localization is improved by either the reduction of the scattering coefficient or the increase of the degree of forward scattering of the medium.

Thus overall, it can be concluded that the signal localization or imaging depth can be improved by either reduction of the scattering coefficient or increasing the anisotropic value of the medium, or both. It can also be seen that the manipulation of g towards a high value is more efficient than that of the scattering coefficient. This conclusion is particularly useful for the optical clearing of tissues by the use of biocompatible chemical agents for the purpose of enhancing the optical imaging depth for high-resolution optical imaging techniques. A recent study indicated that the mechanisms for improving the light penetration depth for the Dextran-mediated blood is due to both the refractive matching and red blood cell (RBC) aggregation and disaggregation induced by the Dextrans [80,117]. The index-matching effect causes the reduction of the scattering coefficient of the medium, while RBC aggregation probably increases the anisotropic factor for the blood, leading to increased light penetration depth.

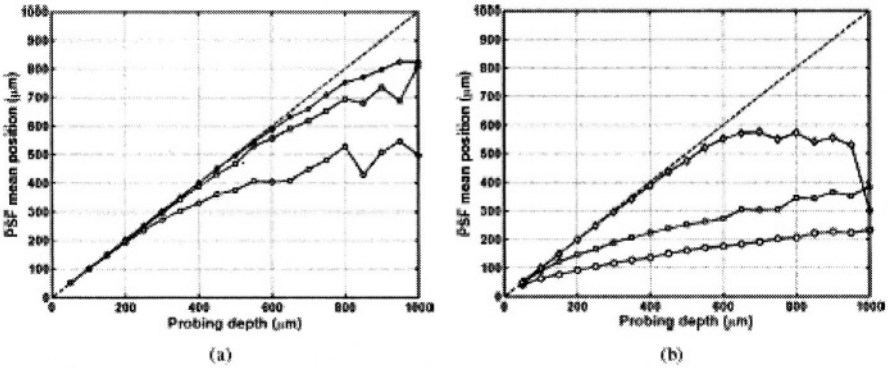

Figure 20. Measured PSF mean positions plotted against the probing depths for the media with $g = 0.7$ (circles), 0.9 (squares) and 0.98 (diamonds) and (a) $\mu_s = 10\ \text{mm}^{-1}$ and (b) $\mu_s = 67\ \text{mm}^{-1}$, respectively. The dashed lines represent the nominal depth positions for PSFs (Copyright @ Institute of Physics Publishing).

Above analysis has been used the Monte Carlo simulation technique as a tool to illustrate the multiple scattering effects on the OCT imaging performance. It is worth noting that there are analytical models developed for analyzing the multiple scattering effects as well. Schmitt and Knüttel described an OCT model by the use of a mutual coherence function based on

the extended Huygens–Fresnel principles of light propagation in homogeneous turbid media [118]. It was later extended by Thrane *et al.* by incorporating the so-called 'shower curtain' effect (see also Chapter 14). This model considers the OCT signal as the summation of singly back-scattered light (coherent) and multiply scattered light (partially coherent) [119]. Most recently, Feng *et al.* further simplified the Thrane's model through approximating the focusing optics in the sampling arm by an imaginary lens proximal to the tissue surface [120]. The advantage of the latter model is that it avoids the consideration of backscattering light from being traveling in the free space between the focusing lens and tissue surface before mixing with the reference beam, i.e., observing the object embedded in scattering medium at the mixing plane through a non-scattering distance. The detailed description of the analytical models for OCT will be covered in the next Chapter 14.

13.5 NEW TECHNIQUE TO ENHANCE OCT IMAGING CAPABILITIES

13.5.1 Introduction

From the last section, we have seen that multiple scattering is a detrimental factor that limits OCT imaging performances, for example imaging resolution, depth and localization. To improve the imaging capabilities, the multiple scattering of tissue must be reduced. Tissue as a scattering medium shows all optical effects that are characteristic to turbid physical system. It is well known that turbidity of a dispersive physical system can be effectively controlled using immersion effect matching of refractive indices of the scatters and the ground material [120-124]. The living tissue allows one to control its optical (scattering) properties using various physical and chemical actions such as compression, stretching, dehydration, coagulation, UV irradiation, exposure to low temperature, and impregnation by chemical solutions, gels, and oils [124-135], see also Chapter 5. Such methods of controlling optical properties of tissue have been explored to enhance the optical imaging capabilities of OCT [80,136-143]. The possible mechanisms of enhancing OCT imaging depth and contrast have been suggested [80,120, 124,136-146].

The depth of penetration for near-infrared light into a biological tissue depends on the scattering characteristics and absorptivity of the tissue. Optically, tissue can be described as a spatial distribution of refractive index on the microscopic scale that could be classified into those of the

extracellular and intracellular components [147,148]. Estimated from the dissolved fractions of proteins and carbohydrates, the intracellular and extracellular fluids have the approximate refractive index between 1.34 and 1.36 [149,150]. The results of earlier studies suggest that the tissue elements that contribute most to the local refractive index variations are the connective tissue fibers (bundles of elastin and collagen), cytoplasmic organelles (e.g., mitochondria), and cell nuclei [149,150]. The refractive index of the connective fiber is about 1.47, which corresponds to 55% hydration of collagen [151]. The nucleus and cytoplasmic organelles in mammalian cells that contain similar concentrations of proteins and nucleic acids, such as mitochondria and ribosome, have refractive indices that span within a relatively narrow range between 1.39 and 1.42 [152,153]. However, other cytoplasmic inclusions, particularly pigment granules, can have much higher refractive indices [149,150]. Therefore the local refractive index within the tissue can vary from anywhere within the background refractive index, i.e., 1.34, and 1.50 depending on what type of soft tissue is concerned. It is this variation of refractive index distribution within the tissue that causes a strong light scattering. Unfortunately, as stated in the last section, the light scattering limits light penetration depth and degrades the imaging contrast [81,82]. For non-interacting Mie scatterers, the reduced scattering coefficient of spheres is determined by the ratio of refractive indices of scattering center and ground matter [154,155]. If the mismatch between scattering centers and the ground substance decreases, it would result in less scattering at the interface between the ground substance and cellular components, leading to the decrease of reduced scattering coefficient of tissue [120,124,141].

To describe theoretically the optical scattering in tissues, attempts have been made using the particle model with some success [147, 148]. Based on the model, the biological tissue is treated as that consisting of the discrete scattering centers with different sizes, randomly distributed in the background media. According to the Rayleigh-Gans approximation, the reduced scattering, $\mu_s^{'}$, of turbid media is related to the reduced cross section, $\sigma_s^{'}$, and the total number of scattering particles per unit volume, i.e., number density, ρ:

$$\mu_s^{'} = \sum_{i=1}^{n} \rho_i \sigma_{si}^{'} = \sum_{i=1}^{n} \frac{3\varphi_i}{4\pi a_i^3} \sigma_{si}^{'}, \tag{19}$$

and

$$\sigma_{si}^{'} = \frac{9}{256\pi}\left|\frac{m_i^2-1}{m_i^2+2}\right|^2\left(\frac{\lambda}{n_0}\right)^2 \int_0^{\pi}(\sin u_i - u_i\cos u_i)^2\frac{(1+\cos^2\theta)\sin\theta(1-\cos\theta)}{\sin^6(\theta/2)}d\theta \tag{20}$$

where $u_i = 2(2\pi a_i n_0/\lambda)\sin(\theta/2)$, $m_i = n_{si}/n_0$ with n_{si} and n_0 being the refractive indices of the *i*-th scattering centers and background medium, φ_i the volume fraction of the *i*-th particles and a_i the radius of the *i*-th scatterer. It can be seen that the reduced scattering coefficient of scattering medium is dependent on both the refractive index ratio, m_i, and the size of the scattering centers.

The most popular method in enhancing OCT imaging performances is to use the biochemical and osmotically active chemical agents to interrogate the tissue. Below we give some examples to intuitively illustrate to what degree the multiple scattering can be reduced and how the imaging depth and contrast of OCT imaging can be improved by the use of impregnation of tissue with the biochemical agents. The agents used in these examples are glycerol and *dimethyl sulphoxide* (DMSO).

13.5.2 Enhancement of Light Transmittance

The light transmittance and scattering after the application of chemical agents can be assessed quantitatively by the use of near infrared spectroscopic method. With the use of Varian Cary 500 spectrophotometer with an internal integrating sphere (Varian UK Ltd), Figure 21 (a) and (b) illustrates the shift of transmittance and diffuse reflectance spectra, respectively, over the range of 800–2200 nm as a function of time when the native porcine stomach pyloric mucosa specimen was applied with 80% glycerol. The curves shown in the Figure were obtained at the time intervals of 0, 5, 10, 20 and 30 min, respectively, from bottom to top for transmittance [Figure 21 (a)] and from top to bottom for reflectance [Figure 21(b)]. It can be seen from Figure 21 that, over the whole wavelength range investigated, the transmittance was increased with time. Diffuse reflectance was decreased over the range of 800–1370 nm. The greatest increase in transmittance was at 1278 nm and the greatest decrease in reflectance was at 1066 nm.

Figures 22(a) and (b) show the similar results from the samples with the application of 50% DMSO respectively at the time intervals of 0, 5, 10, 20 and 30 min. Transmittance was enhanced and diffuse reflectance was reduced with the time course. From Figure 21, and 22, it is clear that both glycerol and DMSO has the ability to clear the tissue, thereby enhance the light transmittance through the tissue.

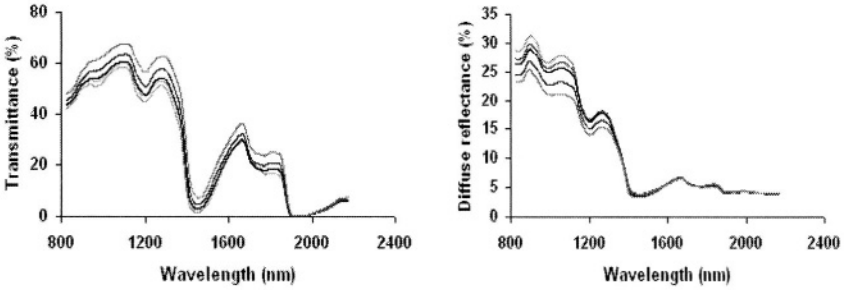

Figure 21 Optical changes for porcine stomach pyloric mucosa before and after application of 80% glycerol over the range from 800–2200 nm measured by spectrophotometer. (a) Transmittance after application of the agent at the time intervals of 0, 5, 10, 20 and 30 min (from bottom to top), respectively, (b) Diffuse reflectance at the time intervals the same as in (a) (from top to bottom) [143] (Copyright @ IEEE 2003).

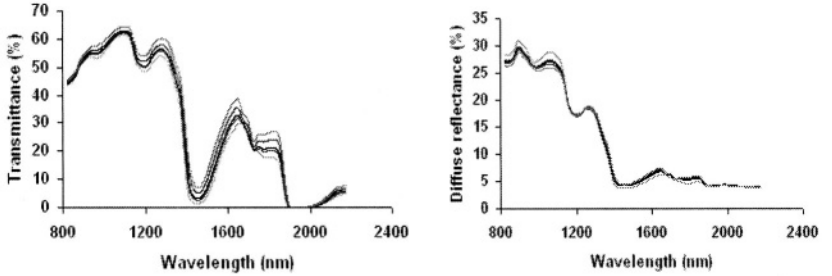

Figure 22. Optical changes for porcine stomach pyloric mucosa before and after application of 50% DMSO over the range from 800–2200 nm measured by spectrophotometer. (a) Transmittance after application of the agent at the time intervals of 0, 5, 10, 20 and 30 min (from bottom to top), respectively, (b) Diffuse reflectance at the time intervals the same as in (a) (from top to bottom) [143] (Copyright @ IEEE 2003).

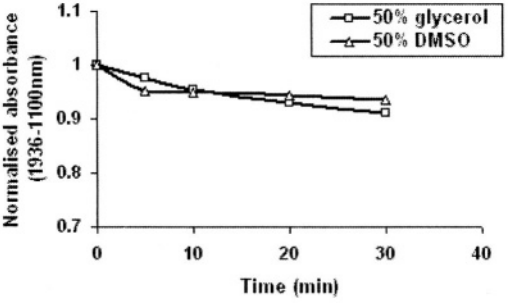

Figure 23. Correlation between the NIR absorbance (measured at 1936–1100 nm) and time of application of 50% glycerol and 50% DMSO, respectively [143] (Copyright @ IEEE 2003).

It is found that there is a strong correlation between optical clearing and water desorption [143-145]. The water activities for 80% glycerol and 50% DMSO measured with a water activity meter (Aqua Lab Model Series 3 TE, Labcell Ltd) give 0.486 and 0.936 respectively. Figure 23 gives the water content measurements at 30 min after the treatment, where 80% glycerol caused 15% water loss, whereas 50% glycerol and 50% DMSO caused 9% and 7%. The patterns of optical clearing are similar to those of water desorption.

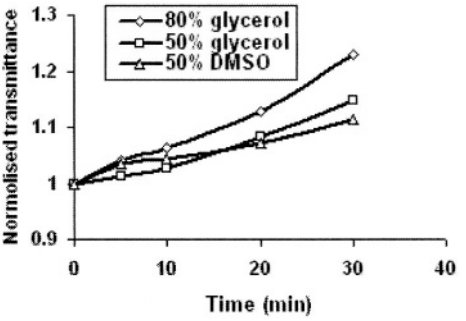

Figure 24. Changes in transmittance at 1278 nm against time for porcine stomach pyloric mucosa treated with 80%, 50% glycerol or 50% DMSO [143] (Copyright @ IEEE 2003).

Because most of OCT system uses the light source with a central wavelength at 1300 nm, Figure 24 gives experimental results of the transmittance enhancement at about 1300 nm after application of different chemical agent solutions, where it is seen that transmittance was increased by approximately 23% at 30 min after the application of 80%, while 15% and 11% were received after the treatment with 50% glycerol and 50% DMSO, respectively.

The optical clearing induced by the agents studied is a time dependent process [142,143,146]. This implies that the clearing effect occurs as a consequence of the diffusion of water out of the tissue, leading to dehydration [143,144], and the diffusion of chemical agents into the tissue [143,146], respectively. For tissue dehydration, the water will migrate from within tissue, where there is higher water potential and a lower osmotic potential, to the outside, where there is lower water potential and higher osmotic potential because the applied agents have the higher osmotic potential than that of tissue fluids. The migration of water will be terminated if the osmotic pressure is balanced inside and outside of the tissue if the agent is impermeable to the tissue.

However, the glycerol and DMSO are both permeable to tissue, indicating that the agents will diffuse into the tissue at the same time when

the water leaves the tissue. The mass transport of the chemical agents within tissue is a very complicated phenomenon that involves the bulk tissue and its constituent cells and fiber structures. Because tissue occupies the intracellular (and/or fibrillar) and extracellular (and/or extrafibrillar) spaces, we assume that the agent will first transport into the extracellular (and/or extrafibrillar - interstitial) space, and then into the intracellular (and/or fibrillar) space, leading to an activity for water in and out of the surrounding interstitial space (and/or cells). The general rule of water migration will apply, that is, the water will transport from an area with the higher water potential and lower osmotic pressure to an area with the lower water potential and higher osmotic pressure. When the agent transports from the inserted (topically or by injection) area into surrounding space, it induces a higher osmotic potential around and thus makes the water to migrate out from the surrounding interstitial space, and to leave the intrafibrillar (and/or intracellular) space, causing the fibers and/or cells to shrink, as a rule this is a second stage of the process. In the meantime, the glycerol and DMSO are membrane permeable, suggesting that the agent will diffuse into the intracellular space after it arrives at the extracellular space. The transmembrane permeability for glycerol and DMSO is much lower than that of water (water is on the order of 10^{-2} cm/minutes, whereas glycerol and DMSO are on the order of 10^{-5} cm/minutes [156,157]), which accounts for an initial decrease in cell volume as water leaves much faster than the agent migrates into it. Therefore, much of the intracellular water leaves the cell while the clearing agent continues to migrate into the cell, leading to a gradual increase in volume that stabilizes with the time course. Because both the anhydrous glycerol and DMSO have the refractive indices of about 1.47 [158], after the agent migrates into the extracellular and intracellular space, a refractive index matching environment is created by simply matching the chemical agents with the main scattering components within the tissue, leading to the enhanced light penetration together with the dehydration effect. It should be noted that this is different from the refractive index matching created by the dehydration where the matching is produced by the more closely packed scattering constituents.

On the other hand, the mass transport process is dependent on the permeability of water and the agents to the membrane, and the tissue as a whole. Among the glycerol and DMSO, the former has lower permeability than the latter. As a consequence, DMSO penetrates the membrane and tissue very rapidly [159], and even across the stratum corneum of skin [158] which glycerol is not able to do. The study on the hamster skin by Vargas et al [139] also showed that DMSO has a greater effect in enhancing the light transmittance than that of glycerol. However, the stomach tissue in the present study has different characteristics in allowing the agents diffusing into the tissue because it does not have a barrier of the stratum corneum for

the skin case. In addition, the mucosa layer of stomach is composed of loosely packed cells, and glands and ducts with narrow lumens are rich, which would facilitate the agents diffusing into the tissue. Thus, the mass transport process would be happened much quicker than that of the skin with the DMSO faster than the glycerol. As a consequence, with the progress of agent transport, a spatial gradient is created because water efflux will occur at the surface first and then deeper as the diffusion front moves [160]. The move of diffusion front for DMSO is much more rapid than that of the glycerol, indicating that the water efflux at the surface is occurring for much longer time with the glycerol than that of with the DMSO.

Accordingly, the changes in optical properties are observed almost linearly with time with the application of 50% glycerol (see Figures 23 and 24), probably because the solution diffuses into tissue at almost the same rate as the water efflux at the surface. It is also understandable that 80% glycerol has a greater slope for both the transmittance and reflectance because it has the stronger ability in dehydration. For the samples treated with 50% DMSO, at the first 5 min, DMSO permeates faster and replaces water faster (Figures 23 and 24), its optical clearing effect is greater than 50% glycerol. After 30 min treatment, dehydration caused by 50% glycerol is slightly higher than that by 50% DMSO. Consequently, the optical clearing effect induced by 50% glycerol is slightly greater than that by 50% DMSO within the time period investigated, although they both have the same refractive indices. The better effect caused by DMSO at the beginning stage results from the different mass transport process of DMSO and glycerol as stated above.

13.5.3 Enhancement of OCT Imaging Capabilities

In the last section, we clearly see that the chemical administration of tissue would increase light transmittance through the tissue, which effect would no doubt increase the imaging depth for OCT. Figure 25 shows dynamic OCT structural images of porcine stomach with the topical application of 50% glycerol solution, which was recorded at the time intervals of 0, 10, 20, 30, 40 and 50 minutes, respectively.

The OCT system used was working at wavelength of 1300 nm with axial and transverse resolutions at 15 μm and 20 μm, respectively. A metal needle was inserted into the tissue approximately 1 mm beneath the surface. The signals reflecting back from the needle surface were used to suggest improvement of back reflectance signal caused by the chemical clearing. The OCT image of the porcine stomach without the administration of glycerol has a visualization depth of approximately 1.0 mm as shown in Figure 25(a). It can be seen that a significant improvement of the imaging depth is clearly demonstrated after the topical application of glycerol. The penetration depth has increased to about 2.0 mm after 50 min application of glycerol as shown

in Figure 25(f). Tissue shrinkage occurs after the administration of the agents to tissue, see Figure 25(b)-(f). The needle embedded in the tissue become brighter and brighter with the increase of the time duration, see Figures from 25(b) to 25(f). It should be pointed out that the imaging contrast of Figure 25 (c) and (d) is also greatly improved. Such features as lamina propria (LP), muscularis mucusae (MM) are clearly visualized in Figure 25 (c) and (d). The neck, base, and MM layers of the tissue could be differentiated after 20-30 minutes application of glycerol. The reflection from needle surface is also sharp within this period of time. But it is interesting to find out that, with the increase of time, the imaging contrast improvement disappears gradually with the further increase of time course, as shown in Figure 25 (e) and (f).

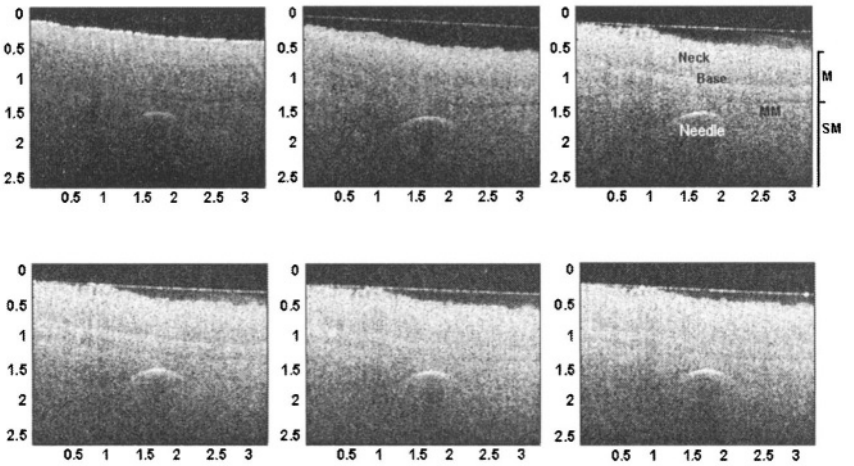

Figure 25. Dynamic OCT images obtained at the time (a) 0, (b) 10, (c) 20, (d) 30, (e) 40, and (f) 50 min after the topical application of 50% glycerol solution onto the porcine stomach tissue. All the units presented are in millimeters, and the vertical axis presents the imaging depth [142] (Copyright @ SPIE).

Figure 26 is the dynamic OCT structure images of porcine stomach with the topical application of 50% DMSO solution, which was again recorded at the time intervals of 0, 10, 20, 30, 40 and 50 minutes, respectively. Like the case with glycerol, it is also demonstrated that a significant improvement of the imaging depth is achieved in Figure 26(b)-(f) when comparing with Figure 26(a) after the application of DMSO. The penetration depth has increased to about 2.0 mm after 50 min application of DMSO as shown in Figure 26(f). However, image contrast enhancement was hardly observed during any period of time in the experiments. Tissue shrinkage due to the dehydration of the tissue is not clear as seen from Figure 26(b)-(f). The

reflection signal from needle surface is approximately the same level from (b) to (f).

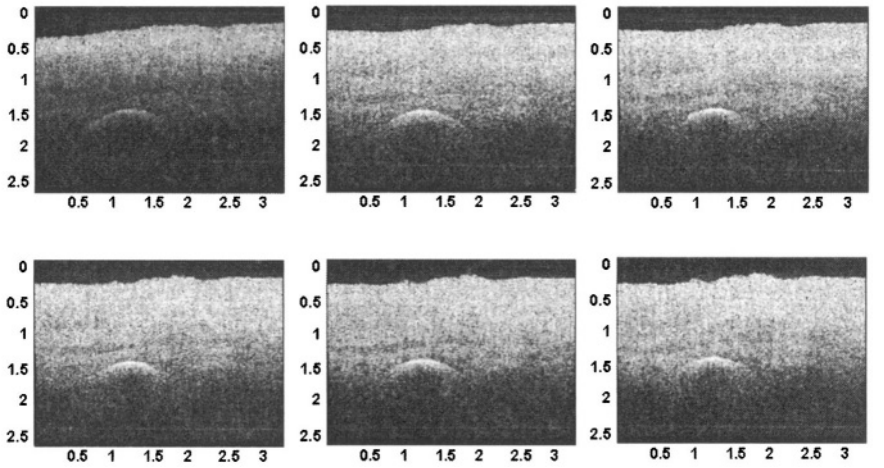

Figure 26. Dynamic OCT images obtained at the time (a) 0, (b) 10, (c) 20, (d) 30, (e) 40, and (f) 50 min after the topical application of 50% DMSO solution onto the porcine stomach tissue. All the units presented are in millimeters, and the vertical axis presents the imaging depth [142] (Copyright @ SP1E).

To further illustrate the different dynamics induced by the two agents, back-reflectance signals along with depth from the stomach tissue with glycerol and DMSO administrations are quantitatively plotted in Figure 27 and Figure 28, respectively. The signals were obtained at the different time intervals of 0, 10, 30, 50 minutes, respectively, at the same spatial point, but averaged over 10 repeated scans to minimize the random noise. It can be seen from Figure 27(a) that after application of glycerol the strength of the reflectance signal is reduced gradually starting from the superficial layers, while the signals coming from the needle surface are gradually raised from about 32 dB, 40 dB and 45 dB to 50 dB as shown in Figure 27(a) to (d). This suggests that the scattering property of tissue is reduced that is a function of the time duration. However, for the DMSO case as shown in Figure 28, the reflectance signal from the needle surface was increased from about 28 dB to 50 dB immediately after the application of agent, see Figure 28(b) and 28(a) for comparison. After about 1 minute, the signals from the tissue surface, deeper layer of tissue and the needle surface remain almost the same level; see Figure 28 (b) to 28 (d).

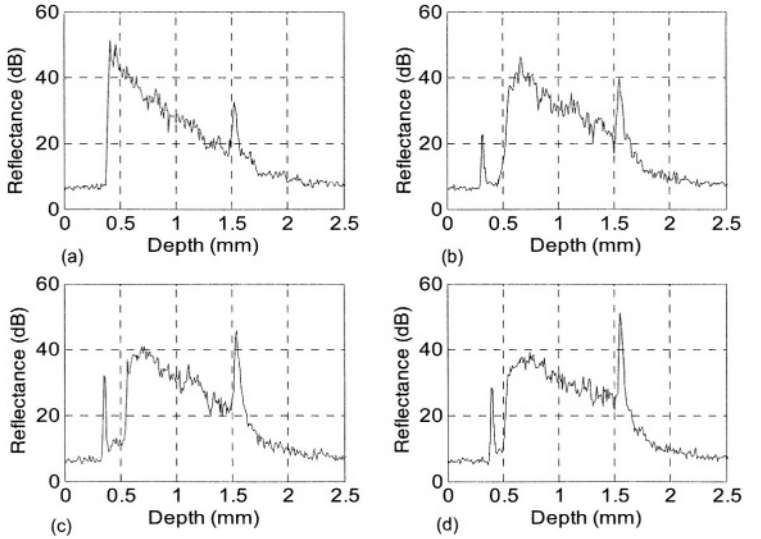

Figure 27. The measured OCT in-depth back-reflectance profiles at the time; (a) 0, (b) 10, (c) 30, and (d) 50 min after topical application of glycerol solution [142] (Copyright @ SPIE).

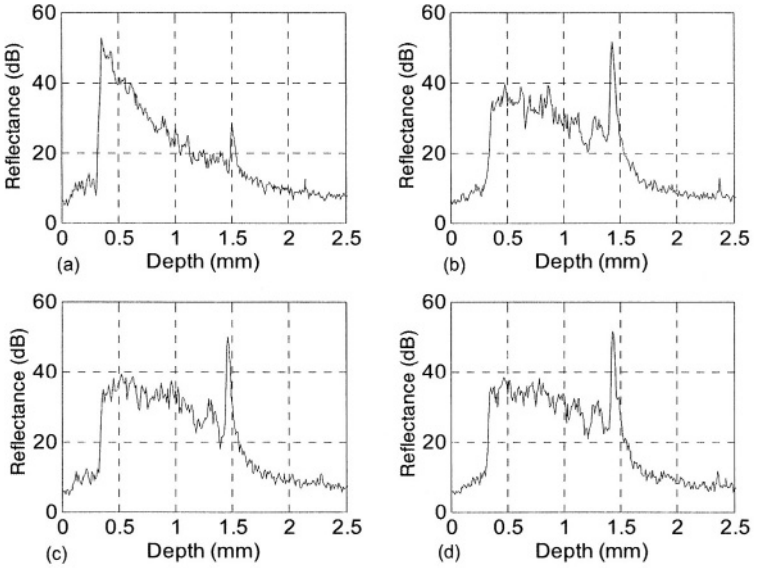

Figure 28. The measured OCT in-depth back-reflectance profiles at the time (a) 0, (b) 10, (c) 30, and (d) 50 minutes after topical application of DMSO solution [142] (Copyright @ SPIE).

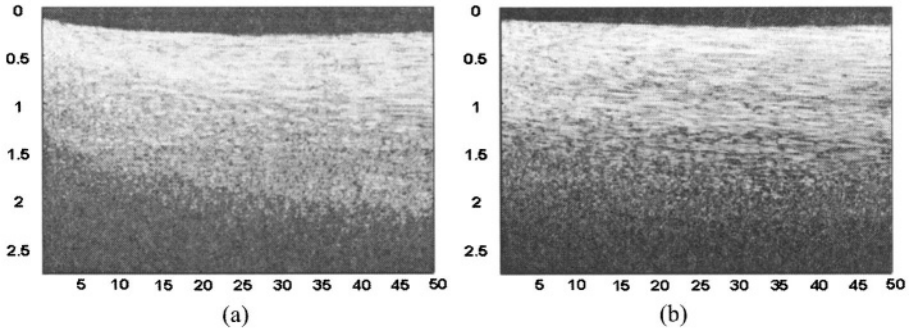

Figure 29. Comparison of the time course of repeated A-scans of the porcine stomach tissue with the application of (a) glycerol and (b) DMSO, respectively. The horizontal and vertical axes present the time (min) and the imaging depth (mm), respectively [142] (Copyright @ SPIE).

Figure 29 illustrates the M-mode OCT images obtained from the repeated A-scans of the porcine stomach with the application of (a) glycerol and (b) DMSO. Because the system used required to re-localize the tissue surface manually after topical application of agents, the registration of OCT signal starts at the time about 0.5 minute after the agent application. From the image obtained with glycerol application, it is clearly seen that the penetration depth increases gradually with the increase of time duration. However, from Figure 29(b), a significant depth improvement appears at the time immediately after the application of DMSO. This indicates that DMSO could fulfill tissue clearing within a very short time period. There is a slope of the surface of the tissue. The downward trend of the tissue surface is attributed to the tissue dehydration induced by the chemical agents.

Figure 30 shows the dynamics of dehydration effects after the application of the glycerol and DMSO solutions, respectively. It is shown that the application of glycerol causes a greater water loss of stomach tissue than that of DMSO does. During the time period between 0-30 min, dehydration induced by glycerol application increases with the time duration; and this reaches a maximum of approximately 12% at about 32 min. After this time, the curve goes down to 8% with the further increase of time to 50 min. It seems that the re-hydration occurs. Water re-enter into tissue to make it swollen. The application of DMSO only causes a small percentage (about 1%) of dehydration of tissue, and the re-hydration effect was not observed during the time period investigated. These results were consistent with the continuous A-scan experiments as shown in Figure 29.

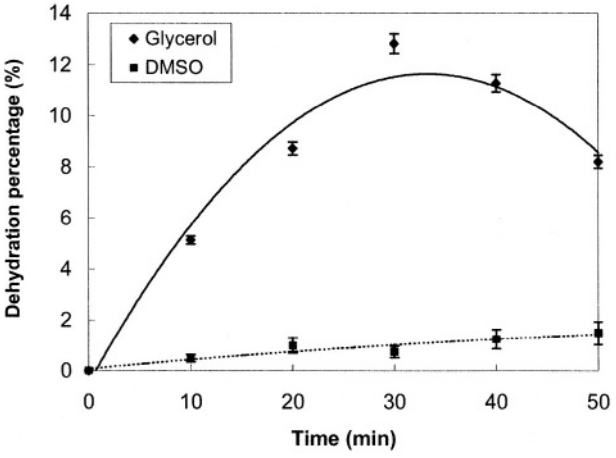

Figure 30. The dynamic dehydration effect of glycerol and DMSO. Data represent average ± SD from three independent experiments [142] (Copyright @ SPIE).

After glycerol was administrated on the surface of the tissue, it will come to the first diffusion stage mentioned in the last subsection. Note that the tissues used here were stomach tissues. The glycerol would diffuse into the intercellular space of the stomach tissue relatively fast because the epithelial layers of the internal organs is composed of loosely packed cells, and glands and ducts with narrow lumens are rich in the mucosa of gastrointestinal tract. However, it should be understood that this diffusion rate would still slower than that water migrates out from the tissue because of the high osmolarity of the solution and the large molecule of this agent. This causes the tissue dehydration as observed in Figures 25(a) to (d). After glycerol is being diffused into the tissue, it will play its role in not only drawing intercellular fluids out of tissue but also drawing the interstitial water further from cells and fibers. This would decrease microscopically the local volume fraction of the scattering centers, the subcellular structure within the cells; therefore increase the back reflective light signal. On the other hand, this diffusion increases the refractive index of the ground substances. Consequently, such dehydration effect would therefore increase the local reflectance signals leading to the increase of both imaging contrast and depth because OCT actually probes the refractive index difference between macroscopic structures limited by the OCT system resolution at least in the current study. The concurrent enhancement of imaging depth and contrast are evident from Figure 25(c) and (d).

Glycerol has been found to enter and exit cells by passive diffusion [156]. Therefore with the elapsing of time, glycerol will further diffuse into

the cells, i.e., the second diffusion stage mentioned above. This causes a full refractive index matching with the subcellular structure. After glycerol enters into cells, it could draw the water back into cells due to its water affinity property, leading to tissue re-hydration as observed in Figures 29(a) and Figure 30 respectively. During this period, the volume of scattering centers in cells could be enlarged by the re-hydration, and the increase of the local reflectance signals does not occur. However, light scattering still remains small because of the refractive index matching environment created between the chemical agents and the scattering centers within tissue. This explains that the OCT images of Figure 25(e) and (f), respectively where there is the improvement of imaging depth, but the imaging contrast is gradually reduced.

But for the DMSO, the first stage diffusion is much faster because its strong penetration ability, please also see the discussions in the last section. Employing (^{35}S) DMSO, Kolb *et al.,* [161] evaluated the absorption and distribution of DMSO in lower animals and man. It was reported [161] that ten minutes after the cutaneous application in the rat, radioactivity was measured in the blood. In man radioactivity was appeared in the blood 5 minutes after cutaneous application. One hour after application of DMSO to the skin, radioactivity could be detected in the bones. DMSO has also been found to be one of the most effective agents across cell membranes [162, 163], These indicate that the duration of the aforementioned second diffusion stage of DMSO is also happened within a very short time frame. The fast diffusion rate of DMSO could decrease the osmolarity of the solution rapidly although the original one is high. Therefore the application of DMSO will cause lighter dehydration of the tissue than glycerol does. This is confirmed by the experimental results as shown in Figure 29(b) and Figure 30. This also indicates that a little volume decrease of the scattering centers would occur, and the back reflective light signal would not increase once the agent diffuses into tissue. Consequently, no image contrast enhancement was observed with the OCT measurements as shown in Figure 26. In other words, the application of DMSO causes a rapid full refractive index matching with the subcellular scattering centers of turbid tissue, leading to the imaging depth but not contrast improvement.

Figure 31 shows an even more convincing case for the action of glycerol to the tissue where the OCT imaging depth and contrast are dramatically improved when comparing the images before and after the application of glycerol agent.

The experimental results by comparison of the tissue clearing dynamics of glycerol and DMSO not only allow us to understand its mechanism, but also are important in the selection of chemicals for the different applications. The above results indicate that DMSO may be more suitable for such applications as in that the high light energy penetration and fast process are desired, for example photodynamic therapy. Whilst glycerol may be more

suitable for the OCT imaging applications where the improvement of both the penetration depth and imaging contrast are required.

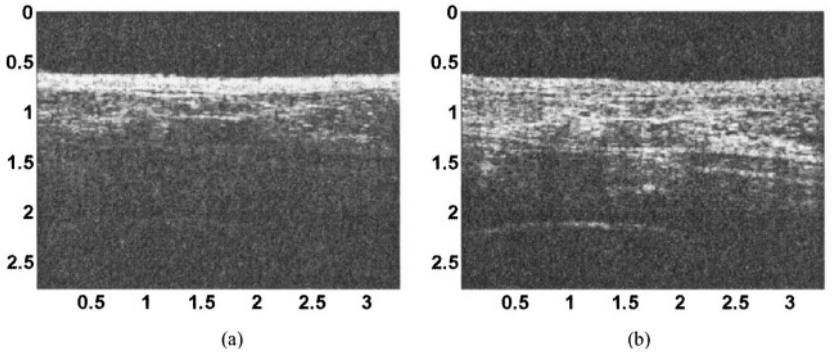

Figure 31. OCT images of chicken skin tissue (a) without and (b) with 20 min application of glycerol. Both the imaging depth and contrast were enhanced in (b) comparing with (a).

It should be pointed out that the above experiments were performed on the *in vitro* biological tissues. The dynamic optical clearing effect induced by the chemical agent would differ from that of *in vivo* case. Because of the cell self-regulation and blood circulation, the living tissues would have a less dehydration after the application of hyperosmotic chemical agent. However, a study conducted by Wang *et al.* [141] showed that the application of the propylene glycol agent solution on to the human tissue *in vivo* has the effect on enhancement of both the imaging depth and contrast. See Figure 32 for an example. Whether this is due to the simultaneous actions of dehydration and chemical diffusion as suggested in the current study is still currently unclear.

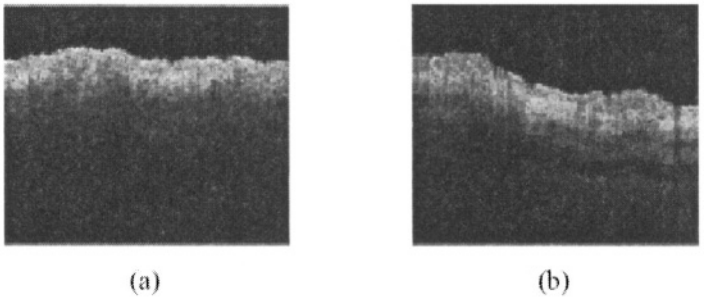

Figure 32. OCT images captured from human forearm *in vivo* (a) without and (b) with 50% topical application of propylene glycol solution. Image sizes: 1.8 × 1.6 mm [141] (Copyright @ Journal of X-ray Science).

Thus far, we have used the examples to illustrate that the impregnation of tissue with the biocompatible chemical can enhance OCT imaging capabilities through the optical clearing and chemical mass transport upon diffusion mechanisms. However, such imaging capability enhancement is agent selectable, particularly for the imaging contrast enhancement. The mechanisms for light penetration enhancement has been well established, i.e., in the framework of refractive index matching approach, which can improve the OCT imaging depth and resolution. The explanations for imaging contrast enhancement, thereby the improvement of OCT localization capability, are based on the dehydration induced by the chemicals and chemical mass transport characteristics. The exact mechanism behind the contrast enhancement still remains to be explored.

13.5.4 Imaging through Blood

As it follows from above discussion OCT is a powerful technique for study of structure and dynamics of highly scattering tissues and blood, including imaging of vascular system for the diagnosis of atherosclerotic lesions. *In vitro* studies performed on human aorta have shown that OCT is able to identify structural features such as lipid collections, thin intimal caps, and fissures characteristic of plaque vulnerability [103-105,164]. In *in vivo* OCT imaging of the rabbit aorta through a catheter a vascular structure was defined, but saline infusion was required during imaging since blood led to significant attenuation of the optical signal [105]. Eliminating the need of saline or minimization its concentration would represent a substantial advance for intravascular OCT imaging.

Refractive index mismatch between erythrocyte cytoplasm and blood plasma causes strong scattering of blood that prevents to get high quality images of intravascular structures through a whole blood. The refractive index of erythrocyte cytoplasm is mostly defined by hemoglobin concentration (blood hematocrit) [165]. The scattering properties of blood are also dependent on erythrocytes volume and shape, which are defined by blood plasma osmolarity [165,166], and aggregation or disaggregation ability [80,117,167]. Recently the feasibility of index matching as a method to overcome the limited penetration through blood for getting of OCT tissue images has been demonstrated [80,117,138]. Glucose, low and high molecular dextrans, *X*-ray contrasting, glycerol and some other biocompatible agents were used to increase the refractive index of blood plasma closer to that of the erythrocyte cytoplasm to improve penetration depth of OCT images.

The 1300 nm OCT system was used for taking images of the reflector through circulated blood *in vitro* [138]. The total intensity of the signal off the reflector was used to represent penetration. As immersion substances

dextran (group refractive index – 1.52) and IV contrast (group refractive index – 1.46) were taken. Both dextran and IV contrast were demonstrated to increase penetration through blood: 69±12% for dextran and 45±4% for IV contrast.

Studies of blood scattering reduction by the immersion technique using various osmotically active solutions, which are biocompatible with blood, like saline, glucose, glycerol, propylene glycol, trazograph (*X*-ray contrasting substance for intravenous injection), and dextran were also described [80, 117]. The 820 and 1310 nm OCX systems were applied for taking images of the reflector through a 1mm layer of un-circulating fresh whole blood. It was shown that for un-circulating blood the sedimentation plays an important role in blood clearing using immersion technique and OCT allows for precise monitoring of blood sedimentation and aggregation.

The result of the OCT study is the measurement of optical backscattering or reflectance, $R(z)$, from the RBCs versus axial ranging distance, or depth, z. The reflectance depends on the optical properties of blood, i.e., the absorption (μ_a) and scattering (μ_s) coefficients, or total attenuation coefficient (μ_t), $\mu_t = \mu_a + \mu_s$. For optical depths less than 4, reflected power can be approximately proportional to $-2\mu_t z$ in exponential scale according to the single scattering model [80,117], i.e.,

$$R(z) = I_0 \alpha(z) \exp(-2\mu_t z), \tag{21}$$

Here I_0 is the optical power launched into the blood sample and $\alpha(z)$ is the reflectivity of the blood sample at the depth of z. the factor of 2 in the exponential accounts for the light passing through the blood sample twice after it is backscattered.

Optical clearing (enhancement of transmittance) ΔT by an agent application can be estimated using the following expression

$$\Delta T = [(R_a - R_s)/R_s] \times 100\%, \tag{22}$$

where R_a is the reflectance from the backward surface of the vessel within a blood sample with an agent, and R_s is that with a control blood sample (whole blood with saline).

The OCT system used is described in Section 13.2, it yields 12 μm axial resolution in free space. This determines the imaging axial resolution which is comparable with the dimensions of red blood cells (RBCs) or small aggregates.

A few different glass vessels of 0.2 to 2 mm of thickness were used as blood sample holders. For some holders to enhance reflection from the bottom interface, a metal reflector was applied. The sample holder was mounted on a translation stage at the sample arm and was placed

perpendicular to the probing beam. The amplitude of reflected light as a function of depth at one spatial point within the sample was obtained. The result is the measurement of optical backscattering or reflectance, $R(z)$, from the RBCs versus axial ranging distance, or depth, z, described by equation 21. Optical clearing (enhancement of transmittance) ΔT by an agent application was estimated using equation 22. Averaging for a few tenths of z-scans were employed.

Venous blood was drawn from healthy volunteers and stabilized by K2E EDTA K2. For example, blood samples containing dextrans were prepared immediately after blood taking by gently mixing blood and dextran-saline solution with low rate manual rotating for 1 min before each OCT measurement. Four groups of the blood samples with various hematocrit values were investigated in this study [117]. The dextrans used in the experiments were D×10, D×70 and D×500 with the molecular weights (MW) at 10,500, 65,500 and 473,000, respectively.

Table 2 gives the results from 65% blood (from a 24 years old male volunteer) with 35% dextran saline solution. The concentration of dextrans used was $2.43\ \mathrm{gdl}^{-1}$. The measurement started immediately after the addition of dextran. It can be seen from Table 2 that D×500 and D×70 are effective agents to decrease the light attenuation of blood compared to the saline control, with the total attenuation coefficient decreased from $3.71\ \mathrm{mm}^{-1}$ for the saline control to $3.12\ \mathrm{mm}^{-1}$ and $2.97\ \mathrm{mm}^{-1}$, respectively. The optical clearing capability ΔT was approximately 90% and 100% for D×500 and D×70, respectively.

Table 2. Influence of dextrans ($2.43\ \mathrm{gdl}^{-1}$) on light attenuation property of the sample containing 65% blood and 35% saline [117].

Agent	$\mu_t\ (\mathrm{mm}^{-1})$	$\Delta T\ (\%)$
Saline	3.71	–
Dextran10	3.82	11.9
Dextran70	2.97	100.1
Dextran500	3.12	86.7

Interesting that D×500 providing a higher refraction had less effect than that of D×70 at the same concentration. Moreover, the increase in concentration (refraction power) cannot always achieve higher optical clearance. $0.5\ \mathrm{gdl}^{-1}$ D×500 had a stronger effect than $5\ \mathrm{gdl}^{-1}$ D×500 in 20% blood with 80% saline samples.

The changes in scattering property brought above by the addition of dextran solution may first be explained by the refractive index matching hypothesis [137,138]. It can be seen that scattering can be reduced when the refractive index of plasma is increased.

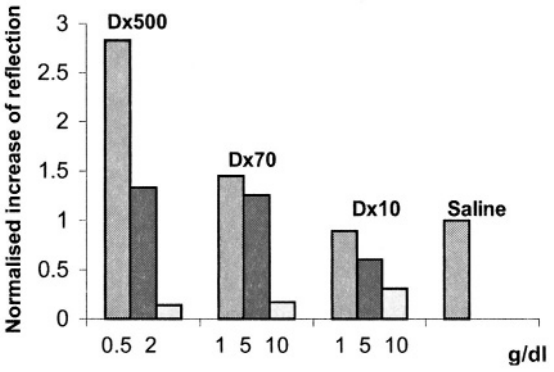

Figure 33. A summary of effects of dextrans compared to that of the saline control on light transmission after 10 min sedimentation. Lower concentration Dextran500 and Dextran70 had significant effects in enhancing light transmission. Efficiency of higher concentration dextrans was much lower than that of the saline control [117] (Copyright @ Institute of Physics Publishing).

The refractive index of dextran saline solution was increased with concentration in all molecular weight groups. The measured indices of blood samples with dextrans were in good agreement with the theoretical values calculated according to the equation $n = c_b n_b + (1 - c_b)n_s$, where c_b is the volume fraction (20%) of whole blood in the diluted sample and n_s is the index of saline with or without dextrans. As expected, the refractive index of blood with dextran increases as the concentration of the added dextran increases due to an increase of the index of the ground matter of the sample.

Blood optical property can be altered by dextrans-induced refractive index matching between RBCs and plasma. However, refractive index matching is not the only factor affecting blood optical properties. Obviously, this discrepancy resulted from the assumption of only refractive index influence. Thus other factors should be taken into account, particularly, the cellular aggregation effect induced by dextrans [117].

As the aggregation process is time-dependent, the blood sample was allowed 10 min sedimentation in this study after the measurement at the beginning stage of the addition of dextrans. Figure 33 shows the summary of the effect of dextrans compared to the saline control on light transmission for the sample with 20% blood and 80% saline after 10 min sedimentation. It can be seen from Figure 33 that the influence of dextran on the light transmission was different compared to that at the beginning of mixing dextrans in blood. The lower concentration ($0.5\ gdl^{-1}$) Dx500 still had the strongest effect on reducing the scattering of light in blood, with a 2.8 fold stronger effect than that of the saline control. However, enhancement by the

highest concentration of D×500 (5 gdl^{-1}) and D×70 (10 gdl^{-1}) was dramatically lower than that of the saline control. At the beginning, they both had a very high blood optical clearing capability with 67.5% and 76.8% ΔT, respectively. In addition, the effect was decreased with the increase of dextran in blood within all three groups, contrary to the expectation of the refractive index matching hypothesis.

The decreased aggregation capability of dextran with concentration explained well that light transmission decreased less with the increase of dextran for both types (mid-molecular and large-molecular). Over a range of concentrations, D×500 and D×70 induced RBC aggregation. However, dextrans have been known to exert a biphasic effect on RBC aggregation; they induce aggregation at low concentration, and disaggregation at high concentration [168]. For example, with D×70 the maximal aggregation size is obtained at approximately 3%, above which the size decreases. In our OCT measurements, 2 gdl^{-1} D×500 and 5 gdl^{-1} D×70 in 20% blood with 80% saline appeared to be the critical concentration to affect RBC aggregation. Their aggregation parameters became smaller than those of 0.5 gdl^{-1} D×500 and 1 gdl^{-1} D×70. When the concentration increased to 5 gdl^{-1} for D×500 and 10 gdl^{-1} for D×70, they played a role of disaggregation. That is the reason why the cells are much less packed than with the saline control, accounting for the reduced light transmission. Although refractive index matching suggested a higher light transmission, it can be seen that the aggregation-disaggregation effects are now dominant.

The behavior of red blood cells (RBC) in flow is dependent on the processes of aggregation-disaggregation, orientation and deformation. Increased RBC aggregability has been observed in various pathological states, such as diabetes and myocardial infarction, or following trauma. The aggregation and disaggregation properties of human blood can be used for the characterization of the hemorheological status of patients suffering different diseases [167]. Our work suggests that OCT may be a useful non-invasive technique to investigate rheology for diagnosis together with its additional advantage of monitoring blood sedimentation [80].

13.6 SUMMARY

To summary, we have discussed in this chapter the basic principles of optical coherence tomography system and shown briefly its applications, both medical and non-medical. The concentration was placed onto the low-coherence interferometry that consists of the building block for optical coherence tomography. OCT based on the time modulation of the interference signal, i.e., modulation of the time delay in order to increase the signal-to-noise ratio of the system, was discussed while other variations of

OCT systems were left for the readers to refer to the existing literatures. Several features of OCT suggest that it will be an important technique for both biomedical imaging and industrial applications. These features include: 1) high axial resolution of 1 to 15 μm, one to two orders of magnitude higher than conventional ultrasound; 2) non-invasive and non-contact which imply that the imaging can be performed without the contact with the sample and without the need to excise the specimen; 3) high speed, enabling real time imaging possible; 4) flexible that can be integrated into almost all medical imaging modalities; 5) cost-effective and portable because the system can be implemented by the optic-fibers commercially available in the telecommunication industrials.

The human tissue is highly scattering in nature to the near infrared light that is usually used to illuminate the OCT systems. In the second part of this chapter it was shown that multiple scattering of tissue is a detrimental factor that limits the OCT imaging performances, for example the imaging resolution, depth, localization and contrast. In order to improve the imaging capabilities for OCT systems, the multiple scattering of tissue must be reduced.

The last part of this chapter introduced a novel technique, i.e., using the biocompatible and osmotically active chemical agent to impregnate the tissue, to enhance the OCT imaging performances through the tissue. The mechanisms for such improvements, for example imaging depth and contrast were discussed, primary through the experimental examples. It is assumed that when chemical agents are applied onto the targeted sample, there are two approaches concurrently applied to the tissue. The imaging depth, or light penetration depth, is enhanced by the refractive index matching of the major scattering centers within the tissue with the ground material induced by the chemical agents, usually through the diffusions of the interstitial liquids of tissue and the chemical agents. Whereas, the imaging contrast enhancement is caused by the tissue dehydration due to the high osmotic characteristics of the chemical agents, which is also dependent on the mass transport of chemical agents within tissue.

ACKNOWLEDGEMENTS

Some of the results presented in this chapter were made possible with the fine financial supports received from the Engineering and Physical Science Research Council, UK, for the projects GR/N13715, GR/R06816 and GR/R52978; the North Staffordshire Medical Institute, UK; Keele University Incentive Scheme; Cranfield University Start-up fund; and the Royal Society for a joint project between Cranfield University and Saratov State University; as well as from grants N25.2003.2 of President of Russian

Federation "Supporting of Scientific Schools," N2.11.03 "Leading Research-Educational Teams," REC-006 of CRDF, and Contract No. 40.018.1.1.1314 of the Ministry of Industry, Science and Technologies of Russian Federation (Research-Technical Program "Biophotonics").

REFERENCES

1. A. Yodh and B. Chance, "Spectroscopy and imaging with diffusing light," *Physics Today* **48,** 34– 40(1995).
2. D. Delpy, "Optical spectroscopy for diagnosis," *Physics World* **7,** 34–39 (1994).
3. D.W. Piston, B.R. Masters, and W.W. Webb, "3-dimensionally resolved NAD(P)H cellular metabolic redox imaging of the *in-situ* cornea with 2-photon excitation laser-scanning microscopy," *J. Microsc.* **178**, 20–27 (1995).
4. M. Rajadhyaksha, M. Grossman, D. Esterowitz, R. Webb, and R. Anderson, *"In-vivo* confocal scanning laser microscopy of human skin - melanin provides strong contrast," *J. Invest. Dermatol.* **104**, 946–952 (1995).
5. A.F. Fercher, "Optical coherence tomography," *J. Biomed. Opt.* **1,** 157–173 (1996).
6. J.M. Schmitt, "Optical coherence tomography (OCT): A review," *IEEE J. Sel. Top. Quant. Electron.* **5**, 1205–1215 (1999).
7. D. Huang, E.A. Swanson, C.P. Lin, J.S. Schuman, W.G. Stinson, W. Chang, M.R. Hee, T. Flotte, K. Gregory, C.A. Puliafito, and J.G. Fujimoto, "Optical coherence tomography," *Science* **254**, 1178–1181 (1991).
8. A.F. Fercher, C.K. Hitzenberger, W. Drexler, G. Kamp, and H. Sattmann, *"In vivo* optical coherence tomography," *Amer. J. Ophthalmol.* **116**, 113–114 (1993).
9. J.M. Schmitt, A. Knüttel, M. Yadlowsky, and R.F. Bonner, "Optical coherence tomography of a dense tissue: statistics of attenuation and backscattering," *Phys. Med. Biol.* **42**, 1427–1439(1994).
10. J.G. Fujimoto, M.E. Brezinski, G.J. Tearney, S.A. Boppart, B.E. Bouma, M.R. Hee, J.F. Southern, and E.A. Swanson, "Optical biopsy and imaging using optical coherence tomography," *Nature Med.* **1**, 970–972 (1995).
11. G.J. Tearney, M.E. Brezinski, B.E. Bouma, S.A. Boppart, C. Pitris, J.F. Southern, and J.G. Fujimoto, *"In vivo* endoscopic optical biopsy with optical coherence tomography," *Science* **276,** 2037–2039 (1997).
12. R.C. Youngquist, S. Carr, and D.E.N. Davies, "Optical coherence domain reflectometry: A new optical evaluation technique," *Opt. Lett.* **12**, 158–160 (1987).
13. K. Takada, I. Yokohama, K. Chida, and J. Noda, "New measurement system for fault location in optical waveguide devices based on an interferometric technique," *Appl. Opt.* **26,** 1603–1606(1987).
14. A.F. Fercher, K. Mengedoht, and W. Werner, "Eye-length measurement by interferometry with partially coherent light," *Opt. Lett.* **13**, 1867–1869 (1988).
15. C.K. Hitzenberger, W. Drexler, and A.F. Fercher, "Measurement of corneal thickness by laser Doppler interferometry," *Invest. Ophthal. Vis. Sci.* **33**, 98–103 (1992).
16. J.A. Izatt, M.R. Hee, E.A. Swanson, C.P. Lin, D. Huang, J.S. Schuman, C.A. Puliafito and J.G. Fujimoto, "Micrometer-scale resolution imaging of the anterior eye with optical coherence tomography," *Arch. Ophthalmol.***112**, 1584–1589 (1994).
17. W. Clivaz, F. Marquis-Weible, R.P. Salathe, R.P. Novak, and H.H. Gilgen, "High-resolution reflectometry in biological tissue," *Opt. Lett.* **17**, 4–6 (1992).
18. M.R. Hee, J.A. Izatt, E.A. Swanson, D. Huang, C.P. Lin, J.S. Schuman, C.A. Puliafito, and J.G. Fujimoto, "Optical coherence tomography of the human retina," *Arch. Ophthalmol.* **113**, 326–332 (1995).

19. S.A. Boppart, M.E. Brezinsk, B.E. Boump, G.J. Tearney, and J.G. Fujimoto, "Investigation of developing embryonic morphology using optical coherence tomography," *Dev. Biol.* **177**, 54–64 (1996).
20. C.A Puliafito, M.R. Hee, C.P. Lin, and J.G. Fujimoto, "Imaging of macular disease with optical coherence tomography," *Ophthalmology* **102**, 217–229 (1995).
21. C. Pitris, C. Jesser, S.A. Boppart, D. Stamper, M.E. Brezinski, and J.G. Fujimoto, "Feasibility of optical coherence tomography for high resolution imaging of human gastrointestinal tract malignancies," *J. Gastroenterology* **35**, 87– 92 (2000).
22. S. Brand, J.M. Poneros, B.E. Bouma, G.J. Tearney, C.C. Compton, N.S. Nishioka, "Optical coherence tomography in the gastrointestinal tract," *Endoscopy* **32**, 796–803 (2000).
23. B.E. Bouma, G.J. Tearney, C.C. Compton, N.S. Nishioka, "High-resolution imaging of the human esophagus and stomach *in vivo* using optical coherence tomography," *Gastrointest. Endosc.* **51**, 467– 574 (2000).
24. S. Jackle, N. Gladkova, F. Feldchtein, A. Terentieva, B. Brand, G. Gelikonov, V. Gelikonov, A. Sergeev, A. Fritscher-Ravens, J. Freund, U. Seitz, S. Schroder, N. Soehendra, "*In vivo* endoscopic optical coherence tomography of the human gastrointestinal tract - toward optical biopsy," *Endoscopy* **32**, 743– 749 (2000).
25. R.K. Wang and J.B. Elder, "Propylene glycol as a contrasting agent for optical coherence tomography to image gastro-intestinal tissues," *Lasers Surg. Med.* **30**, 201–208 (2002).
26. B.W. Colston, M.J. Everett, L.B. Da Silva, L.L. Otis, P. Stroeve, and H. Nathel, "Imaging of hard- and soft- tissue structure in the oral cavity by optical coherence tomography," *Appl. Opt.* **37**, 3582–3585 (1998).
27. J.M. Schmitt, M. Yadlowsky, and R. Bonner, "Subsurface imaging of living skin with optical coherence tomography," *Dermatology* **191**, 93– 98 (1995).
28. N.D. Gladkova, G.A. Petrova, N.K. Nikulin, S.G. Radenska-Lopovok, L.B. Snopova, Y.P. Chumakov, V.A. Nasonova, V.M. Geilkonov, G.V. Geilkonov, R.V. Kuranov, A.M. Sergeev, and F.I. Feldchtein, *"In vivo* optical coherence tomography imaging of human skin: norm and pathology," *Skin Research and Technology* **6**, 6–16 (2000).
29. R.K. Wang and J.B. Elder, "High resolution optical tomographic imaging of soft biological tissues," *Laser Physics* **12**, 611– 616 (2002).
30. J.G. Fujimoto, B. Bouma, G.J. Tearney, S.A. Boppart, C. Pitris, J.F. Southern, M.E. Brezinski, "New technology for high speed and high resolution optical coherence tomography," *Annals New York Academy of Sciences* **838**, 95– 107 (1998).
31. C. Passmann and H. Ermert, "A 100 MHz ultrasound imaging system for dermatologic and ophthalmologic diagnostics," *IEEE Trans. Ultrason., Ferroelect., Freq. Contr.* **43**, 545–552 (1996).
32. P.A. Flournoy, "White light interferometric thickness gauge," *Appl. Opt.* **11**, 1907-1915 (1972).
33. T. Li, A. Wang, K. Murphy, and R. Claus, "White light scanning fibre Michelson interferometer for absolute position measurement," *Opt. Lett.* **20**, 785– 787 (1995).
34. Y.J. Rao, Y.N. Ning, and D.A. Jackson, "Synthesised source for white light sensing system," *Opt. Lett.* **18,** 462– 464 (1993).
35. J.W. Goodman, *Statistical Optics* (John Wiley and Sons, New York, 1985), 164–169.
36. R.K. Wang, "Resolution improved optical coherence-gated tomography for imaging through biological tissues," *J. Modern Optics* **46,** 1905–1913 (1999).
37. A. Podolenau and D.A. Jackson, "Noise analysis of a combined optical coherence tomograph and a confocal scanning ophthalmoscope," *Appl. Opt.* **38,** 2116–2127 (1999).
38. P.R. Gray and R.G. Meyer, *Analysis and Design of Integrated Circuits,* 2nd ed. (Wiley, New York, 1984).

39. A. Sergeev, V. Gelikonov, and A. Gelikonov, "High-spatial-resolution optical-coherence tomography of human skin and mucous membranes," presented at the Conf. Lasers and Electro Optics'95, Anaheim, Ca, May 21–26, 1995.
40. G.J. Tearney, B.E. Bouma, S.A. Boppart, B. Golubovic, E.A. Swanson, and J.G. Fujimoto, "Rapid acquisition of *in vivo* biological images by use of optical coherence tomography," *Opt. Lett.* **21,** 1408-1410 (1996).
41. K. Takada, H. Yamada, and M. Horiguchi, "Optical low coherence reflectometer using [3 × 3] fiber coupler," *IEEE Photon. Technol. Lett.* **6,** 1014–1016 (1994).
42. B.E. Bouma, G.J. Tearney, S.A. Boppart, M.R. Hee, M.E. Brezinski, and J.G. Fujimoto, "High-resolution optical coherence tomographic imaging using a mode-locked Ti :A12O3 laser source," *Opt. Lett.* **20,** 1486–1488 (1995).
43. G.J. Tearney, M. E. Brezinski, B. E. Bouma, S. A. Boppart, C. Pitris, J. F. Southern, and J. G. Fujimoto, "*In vivo* endoscopic optical biopsy with optical coherence tomography," *Science* **276,** 2037–2039 (1997).
44. R. Paschotta, J. Nilsson, A. C. Tropper, and D. C. Hanna, "Efficient superfluorescent light sources with broad bandwidth," *IEEE J. Select. Topics Quantum Electron.* **3,**1097–1099 (1997).
45. B.E. Bouma, L.E. Nelso, G. J. Tearney, D.J. Jones, M.E. Brezinski, and J.G. Fujimoto, "Optical coherence tomographic imaging of human tissue at 1.55 μm and 1.81 μm using Er- and Tm-doped fiber sources," *J. Biomed. Opt.* **3,** 76–79 (1998).
46. D.J. Derickson, P.A. Beck, T.L. Bagwell, D.M. Braun, J.E. Fouquet, F.G. Kellert, M.J. Ludowise, W.H. Perez, T.R. Ranganath, G.R. Trott, and S.R. Sloan, "High-power, low-internal-reflection, edge emitting light-emitting diodes," *Hewlett-Packard J.* **46,** 43–49 (1995).
47. H.H. Liu, P.H. Cheng, and J.P. Wang, "Spatially coherent white-light interferometer based on a point fluorescent source," *Opt. Lett.* **18,** 678–680 (1993).
48. C.F. Lin and B.L. Lee, "Extremely broadband AlGaAs/GaAs superluminescent diodes," *Appl. Phys. Lett.* **71,** 1598–1600 (1997).
49. P.J. Poole, M. Davies, M. Dion, Y. Feng, S. Charbonneau, R. D. Goldberg, and I.V. Mitchell, "The fabrication of a broad-spectrum light-emitting diode using high-energy ion implantation," *IEEE Photon. Technol. Lett.* **8,** 1145–1147 (1996).
50. T.R. Cole and G.S. Kino, *Confocal Scanning Optical Microscopy and Related Imaging Systems* (Academic, San Diego, CA, 1990).
51. J.M. Schmitt, A. Knüttel, M. Yadlowsky, and M.A. Eckhaus, "Optical coherence tomography of a dense tissue: Statistics of attenuation and backscattering," *Phys. Med. Biol.* **39,** 1705–1720 (1994).
52. C.B. Su, "Achieving variation of the optical path length by a few millimeters at millisecond rates for imaging of turbid media and optical interferometry: A new technique," *Opt. Lett.* **22,** 665–667 (1997).
53. G.J. Tearney, B.E. Bouma, and J.G. Fujimoto, "High speed phase and group-delay scanning with a grating-based phase control delay line," *Opt. Lett.* **22,** 1811–1813 (1997).
54. A.M. Rollins, M.D. Kulkarni, S. Yazdanfar, R. Ung-arunyawee, and J. A. Izatt, *"In vivo* video rate optical coherence tomography," *Opt. Express* **3,** 219–229 (1998).
55. A.F. Fercher, C.K. Hitzenberger, W. Drexler, G. Kamp, and H. Sattmann, *"In-vivo* optical coherence tomography," *Am. J. Ophthalmol.* **116,** 113–115 (1993).
56. W. Drexler, O. Findl, R. Menapace, A. Kruger, A. Wedrich, G. Rainer, A. Baumgartner, C.K. Hitzenberger, and A.F. Fercher, "Dual Beam Optical Coherence Tomography: Signal Identification for Ophthalmologic Diagnosis" *J. Biomed. Opt.* 3, 55-65 (1998)
57. J.A. Izatt, M.R. Hee, G.M. Owen, E.A. Swanson, and J.G. Fujimoto, "Optical coherence microscopy in scattering media," *Opt. Lett.* **19,** 590–592 (1994).

58. A.G. Podoleanu, "Unbalanced versus balanced operation in an optical coherence tomography system," *Appl. Opt.* **39,** 173–82 (2000).
59. A.F. Fercher, C.K. Hitzenberger, G. Kamp, and S.Y. El Zaiat, "Measurement of intraocular distances by backscattering spectral interferometry," *Opt. Commun.* **117,** 43–8(1995).
60. G. Hausler and M.W. Lindner, "Coherence Radar and Spectral Radar—New Tools for Dermatological Diagnosis" *J. Biomed. Opt.* **3**, 21–31 (1998).
61. Y. Yasuno, Y. Sutoh, M. Nakama, S. Makita, M. Itoh, T. Yatagai, and M. Mori, "Spectral interferometric optical coherence tomography with nonlinear beta-barium borate time gating," *Opt. Lett.* **27**, 403–405 (2002).
62. E. Beaurepaire, A.C. Boccara, M. Lebec, L. Blanchot, and H. Saint-Jalmes, "Full-field optical coherence microscopy," *Opt. Lett.* **23**, 244–2466 (1998).
63. L. Vabre, A. Dubois, and A.C. Boccara, "Thermal-light full-field optical coherence tomography," *Opt. Lett.* **27**, 530–532 (2002).
64. C.E. Saxer, J.F. de Boer, B. Hyle Park, Y. Zhao, Z. Chen, and J.S. Nelson, "High-speed fiber-based polarization-sensitive optical coherence tomography of *in vivo* human skin," *Opt. Lett.* **25**, 1257–355 (2000).
65. J.E. Roth, J.A. Kozak, S. Yazdanfar, A.M. Rollins, and J.A. Izatt, "Simplified method for polarization-sensitive optical coherence tomography," *Opt. Lett.* **26,** 1069–1071 (2001).
66. S. Jiao and L.V. Wang, "Two-dimensional depth-resolved Mueller matrix of biological tissue measured with double-beam polarization-sensitive optical coherence tomography," *Opt. Lett.* **27**, 101–103 (2002).
67. Z. Chen, T.E. Milner, D. Dave, and J.S. Nelson, "Optical Doppler tomographic imaging of fluid flow velocity in highly scattering media," *Opt. Lett.* **22,** 64–66 (1997).
68. J.A. Izatt, M.D. Kulkarni, S. Yazdanfar, J.K. Barton, and A.J. Welch, "*In vivo* bidirectional color Doppler flow imaging of picoliter blood volumes using optical coherence tomograghy," *Opt. Lett.* **22,** 1439–1441 (1997).
69. Y. Zhao, Z. Chen, C. Saxer, X. Shaohua, J.F. de Boer, and J.S. Nelson, "Phase-resolved optical coherence tomography and optical Doppler tomography for imaging blood flow in human skin with fast scanning speed and high velocity sensitivity," *Opt. Lett.* **25,** 114–116 (2000).
70. Y. Zhao, Z. Chen, Z. Ding, H. Ren, and J.S. Nelson, "Real-time phase-resolved functional optical coherence tomography by use of optical Hilbert transformation," *Opt. Lett.* **27**, 98–100 (2002).
71. S.G. Proskurin, Y. He, and R.K. Wang, "Determination of flow-velocity vector based on Doppler shift and spectrum broadening with optical coherence tomography," *Opt. Lett.* **28**, 1224-1226 (2003).
72. S.G. Proskurin, I.A. Sokolova, and R.K. Wang, "Imaging of non-parabolic velocity profiles in converging flow with optical coherence tomography" *Phy. Med. Biol.* **48**, 2907-2918 (2003).
73. U. Morgner, W. Drexler, F.X. Kartner, X.D. Li, C. Pitris, E.P. Ippen, and J.G. Fujimoto, "Spectroscopic optical coherence tomography," *Opt. Lett.* **25,** 111–113 (2000).
74. A.F. Fercher, W. Drexler, C.K. Hitzenberger, and T. Lasser, "Optical coherence tomography – principles and applications," *Rep. Prog. Phys.* **66**, 239–303 (2003).
75. M.R. Hee, J.A. Izatt, E.A. Swanson, D. Huang, J.S. Schuman, C.P. Lin, C.A. Puliafito, J.G. Fujimoto, "Optical coherence tomography of the human retina," *Arch. Opthalmol.* **113,** 325–332 (1995).
76. C.A. Puliafito, M.R. Hee, C.P. Lin, E. Reichel, J.S. Schuman, J.S. Duker, J.A. Izatt, E.A. Swanson, J.G. Fujimoto, "Imaging of macular diseases with optical coherence tomography," *Ophthalmol.* **120**, 217–229 (1995).

77. C.A. Puliafito, M.R. Hee, J.S. Schumann, and J.G. Fujimoto, *Optical Coherence Tomography of Ocular Diseases* (Slack, Thorofare, NJ, 1995).
78. M.E. Brezinski, G.J. Tearney, B.E. Bouma, J.A. Izatt, M.R. Hee, E.A. Swanson, J.F. Southern, and J.G. Fujimoto, "Optical coherence tomography for optical biopsy: Properties and demonstration of vascular pathology," *Circulation* **93**,1206–1213 (1996).
79. J.M. Schmitt, M. Yadlowsky, and R.F. Bonner, "Subsurface imaging of living skin with optical coherence microscopy," *Dermatol.* **191,** 93–98 (1995).
80. V.V. Tuchin, X. Xu, and R.K. Wang, "Dynamic optical coherence tomography in optical clearing, sedimentation and aggregation study of immersed blood," *Appl. Opt.* **41,** 258–271 (2002).
81. Special section on Coherence Domain Optical Methods in Biomedical Science and Clinics, V.V. Tuchin, H. Podbielska, and C.K. Hitzenberger eds., *J. Biomed. Opt.* **4,** 94–190 (1999).
82. R.K. Wang, "Signal degradation by multiple scattering in optical coherence tomography of dense tissue: A Monte Carlo study towards optical clearing of biotissues," *Phys. Med. Biol.* **47**, 2281–2299 (2002).
83. D. Huang, J. Wang, C.P. Lin, C.A Puliafito, and J.G Fujimoto, "Micron-resolution ranging of cornea anterior chamber by optical reflectometry," *Lasers Surg. Med.* **11,** 419–425 (1991).
84. A.F. Fercher, C.K. Hitzenberger, W. Drexler, G. Kamp, and H. Sattmann, *"In vivo* optical coherence tomography," *Am. J. Ophthalmol.* **116,** 113–114 (1993).
85. A.F. Fercher, C.K. Hitzenberger, G. Kemp, and S.Y. Elzaiat, "Measurement of intraocular distances by backscattering spectral interferometry," *Opt. Commun.* **117,** 43–48 (1995).
86. K. Rohrschneider, R.O. Burk, F.E. Kruse, and H.E. Volcker, "Reproducibility of the optic nerve head topography with a new laser tomographic scanning device," *Ophthalmol.* **101,** 1044–1049 (1994).
87. M.R. Hee, C.A. Puliafitom C. Wong, E. Reichel, J.S. Duker, J.S. Schuman, E.A. Swanson, and J.G. Fujimoto, "Optical coherence tomography of central serous chorioretinopathy," *Am. J. Ophthalmol.* **120**, 65–74 (1995).
88. M.R. Hee, C.A. Puliafitom C. Wong, E. Reichel, J.S. Duker, J.S. Schuman, E.A. Swanson, and J.G. Fujimoto, "Optical coherence tomography of macular holes," *Ophthalmol.* **102**, 748–756 (1995).
89. J.S. Schuman, M.R. Hee, C.A. Puliafito, C. Wong, T. Pedutkloizman, C.P. Lin, E. Hertzmark, J.A Izatt, E.A. Swanson, and J.G. Fujimoto, "Quantification of nerve fibre layer thickness in normal and glaucomatous eyes using optical coherence tomography," *Arch. Ophthalmol.* **113**, 586–596 (1995).
90. W. Drexler, U. Morgner, R.K. Ghanta, F.X. Kartner, J.S. Schuman, and J.G. Fujimoto, "Ultrahigh-resolution ophthalmic optical coherence tomography," *Nature Medicine* **7,** 502–507 (2001).
91. I. Hartl, T. Ko, R.K. Ghanta, W. Drexler, A. Clermont, S.E. Bursell, and J.G. Fujimoto, "*In vivo* ultrahigh resolution optical coherence tomography for the quantification of retinal structure in normal and transgenic mice," *Invest. Ophthal. Vis. Sci.* **42** (4), 4252 Suppl. (2001)
92. S.A. Boppart, M.E. Brezinski, B.E. Bouma, G.J. Tearney, and J.G. Fujimoto, "Investigation of developing embryonic morphology using optical coherence tomography," *Develop. Biol.* **177**, 54–63 (1996).
93. S.A. Boppart, B.E. Bouma, M.E. Brezinski, G.J. Tearney, and J.G. Fujimoto, "Imaging developing neural morphology using optical coherence tomography," *J. Neurosci. Methods,* **70**, 65–72 (1996).

94. S.A. Boppart, G.J. Tearney, B.E. Bouma, J.F. Southern, M.E. Brezinski, and J.G. Fujimoto, "Noninvasive assessment of the developing Xenopus cardiovascular system using optical coherence tomography," *PNAS* **94,** 4256–4261 (1997).
95. J.M. Schmitt, M.J. Yadlowsky, and R.F. Bonner, "Subsurface imaging of living skin with optical coherence microscopy," *Dermatology* **191**, 93–98 (1995).
96. N.D. Gladkova, G.A. Petrova, N.K. Nikulin, S.G. Radenska-Lopovok, L.B. Snopova, Y.P. Chumakov, V.A. Nasonova, V.M. Gelikonov, G.V. Gelikonov, R.V. Kuranov, A.M. Sergeev, and F.I. Feldchtein *"In vivo* optical coherence tomography imaging of human skin: norm and pathology," *Skin Res. Technol.* **6,** 6–16 (2000).
97. J. Welzel, "Optical coherence tomography in dermatology: a review," *Skin Res. Technol.* **7,** 1–9 (2001).
98. C.B. Williams, J.E. Whiteway, and J.R. Jass, "Practical aspects of endoscopic management of malignant polyps," *Endoscopy* **19**, 31–37 Suppl. 1 (1987).
99. K. Kobayashi, H.S. Wang, M.V. Sivak, and J.A. Izatt, "Micron-resolution sub-surface imaging of the gastrointestinal tract wall with optical coherence tomography," *Gastrointestinal Endoscopy* **43**, 29–29 (1996).
100. J.A. Izatt, "Micron scale *in vivo* imaging of gastrointestinal cancer using optical coherence tomography," *Radiology* **217**, 385 Suppl. S (2000).
101. A. Das, M.V. Sivak, A. Chak, R.C.K. Wong, V. Westphal, A.M. Rollins, J. Willis, G. Isenberg, and J.A. Izatt, "High-resolution endoscopic imaging of the GI tract: a comparative study of optical coherence tomography versus high-frequency catheter probe EUS," *Gastrointestinal Endoscopy* **54**, 219–224 (2001).
102. J.G. Fujimoto, M.E. Brezinski, G.J. Tearney, S.A. Boppart, B.E. Bouma, M.R. Hee, J.F. Southern, and E.A. Swanson, "Optical biopsy and imaging using optical coherence tomography," *Nature Med.* **1**, 970–972 (1995).
103. M.E. Brezinski, G.J. Tearney, B.E. Bouma, J.A. Izatt, M.R. Hee, E.A. Swanson, J.F. Southern, and J.G. Fujimoto, "Optical coherence tomography for optical biopsy - Properties and demonstration of vascular pathology," *Circulation* **93,** 1206–1213 (1996).
104. M.E. Brezinski, G.J. Tearney, N.J. Weissman, S.A. Boppart, B.E. Bouma, M.R. Hee, A.E. Weyman, E.A. Swanson, J.F. Southern, and J.G. Fujimoto, "Assessing atherosclerotic plaque morphology: Comparison of optical coherence tomography and high frequency intravascular ultrasound," *Heart* **77**, 397–403 (1997).
105. J.G. Fujimoto, S.A. Boppart, G.J. Tearney, B.E. Bouma, C. Pitris, and M.E. Brezinski, "High resolution *in vivo* intra-arterial imaging with optical coherence tomography," *Heart* **82**, 128–133 (1999).
106. B.W. Colston, U.S. Sathyam, L.B. DaSilva, M.J. Everett, P. Stroeve, and L.L. Otis, "Dental OCT," *Opt. Express* **3,** 230–238 (1998).
107. Y. Yang, L. Wu, Y. Feng, R.K. Wang, "Observations of birefringence in tissues from optic-fibre based optical coherence tomography," *Measur. Sci. Technol.* **14**, 41–46 (2003).
108. A. Baumgartner, C.K. Hitzenberger, H. Sattmann, W. Drexler, and A.F. Fercher, "Signal and resolution enhancements in dual beam optical coherence tomography of the human eye" *J. Biomed. Opt.* **3,** 45–54 (1998).
109. G. Yao and L.V. Wang, "Two-dimensional depth-resolved Mueller matrix characterization of biological tissue by optical coherence tomography," *Opt. Lett.* **24,** 537–539 (1999).
110. J.P. Dunkers, R.S. Parnas, C.G. Zimba, R.C. Peterson, K.M. Flynn, J.G. Fujimoto, and B.E. Bouma, "Optical coherence tomography of glass reinforced polymer composites," *Composites* **30A**, 139–145 (1999).
111. M. Bashkansky, D. Lewis III, V. Pujari, J. Reintjes, and H.Y. Yu, "Subsurface detection and characterization of Hertzian cracks in Si3N4 balls using optical coherence tomography," *NDT E-International* **34,** 547–555 (2001).

112. F. Xu, H.E. Pudavar, and P.N. Prasad, "Confocal enhanced optical coherence tomography for nondestructive evaluation of paints and coatings," *Opt. Lett.* **24** 1808–1810 (1999).
113. R.K. Wang and J.B. Elder, "Optical coherence tomography: a new approach to medical imaging with resolution at cellular level," *Proc. MBNT,* ISSBN 0951584235, 1–4 (1999).
114. D.J. Smithies, T. Lindmo, Z. Chen, J.S. Nelson, and T. Miller, "Signal attenuation and localisation in optical coherence tomography by Monte Carlo simulation," *Phys. Med. Biol.* **43,** 3025–3044 (1998).
115. G. Yao and L.V. Wang, "Monte Carlo simulation of an optical coherence tomography signal in homogeneous turbid media," *Phys. Med. Biol.* **44,** 2307–2320 (1999).
116. J.M. Schmitt, A. Knüttle, M.J. Yadlowsky, and M.A. Eckhaus, "Optical coherence tomography of a dense tissue: statistics of attenuation and backscattering," *Phys. Med. Biol.* **39**, 1705–1720 (1994).
117. X. Xu, R.K. Wang, J.B. Elder, and V.V. Tuchin, "Effect on dextran-induced changes in refractive index and aggregation on optical properties of whole blood," *Phys. Med. Biol.* **48,** 1205–1221 (2003).
118. J.M. Schmitt and A. Knüttel, "Model of optical coherence tomography of heterogeneous tissue," *J. Opt. Soc. Am.* **A 14**, 1231–1242 (1997).
119. L. Thrane, H.T. Yura, and P.E. Andersen, "Analysis of optical coherence tomography systems based on the extended Huygens-Fresenel principle," *J. Opt. Soc. Am.* **A 17**, 484–490 (2000).
120. Y. Feng, R.K. Wang, and J.B. Elder, "A theoretical model of optical coherence tomography for system optimization and characterization," *J. Opt. Soc. Am.* **A, 20,** 1792-1803 (2003).
121. V.V. Tuchin, *Tissue Optics: Light Scattering Methods and Instruments for Medical Diagnosis,* SPIE Tutorial Texts in Optical Engineering, **TT38** (SPIE Press, Bellingham, 2000).
122. V.V. Tuchin, "Light scattering study of tissue," *Physics-Uspekhi* **40**, 495–515 (1997).
123. V.V. Tuchin, I. L. Maksimova, D. A. Zimnyakov, I. L. Kon, A. H. Mavlutov, and A. A. Mishin, "Light propagation in tissues with controlled optical properties," *J. Biomed. Opt.* **2,**401–417 (1997).
124. V.V. Tuchin, "Coherent optical techniques for the analysis of tissue structure and dynamics," *J.Biomed. Opt.* **4,** 106–124 (1999).
125. *Handbook of Optical Biomedical Diagnostics,* **PM107**, V.V. Tuchin, ed. (SPIE Press, Bellingham, 2002).
126. B. Beauvoit, T. Kitai, and B. Chance, "Contribution of the mitochondrial compartment to the optical properties of rat liver: a theoretical and practical approach," *Biophys. J.* **67**, 2501–2510 (1994).
127. J.T. Bruulsema, J.E. Hayward, T.J. Farrell, M.S. Patterson, L. Heinemann, M. Berger, T. Koschinsky, J.S. Christiansen, H. Orskov, "Correlation between blood glucose concentration in diabetics and noninvasively measured tissue optical scattering coefficient," *Opt. Lett.* **22,** 190–192 (1997).
128. E.K. Chan, B. Sorg, D. Protsenko, M. O'Neil, M. Motamedi, and A.J. Welch, "Effects of compression on soft tissue optical properties," *IEEE J. Sel. Top. Quant. Electron.* **2,** 943–950 (1996).
129. B. Chance, H. Liu, T. Kitai, and Y. Zhang, "Effects of solutes on optical properties of biological materials: models, cells, and tissues," *Anal. Biochem.* **227**, 351–362 (1995).
130. I.F. Cilesiz and A. J. Welch, "Light dosimetry: effects of dehydration and thermal damage on the optical properties of the human aorta," *Appl. Opt.* **32,** 477–487 (1993).
131. M. Kohl, M. Esseupreis, and M. Cope, "The influence of glucose concentration upon the transport of light in tissue-simulating phantoms," *Phys. Med. Biol.* **40**, 1267–1287 (1995).

132. H. Liu, B. Beauvoit, M. Kimura, and B. Chance, "Dependence of tissue optical properties on solute-induced changes in refractive index and osmolarity," *J. Biomed. Opt.* **1,** 200–211 (1996).
133. J.S. Maier, S.A. Walker, S. Fantini, M.A. Franceschini, and E. Gratton, "Possible correlation between blood glucose concentration and the reduced scattering coefficient of tissues in the near infrared," *Opt. Lett.* **19**, 2062–2064 (1994).
134. X. Xu, R.K. Wang, and A. El Haj, "Investigation of changes in optical attenuation of bone and neuronal cells in organ culture or 3 dimensional constructs *in vitro* with optical coherence tomography: relevance to cytochrome-oxidase monitoring," *Europ. Biophys. J.* **32**, 355-362 (2003).
135. V.V. Tuchin, A.N. Bashkatov, E.A. Genina, Yu. P. Sinichkin, and N.A. Lakodina. "*In vivo* investigation of the immersion-liquid-induced human skin clearing dynamics," *Tech. Phys. Lett.* **27,** 489–490 (2001).
136. G. Vargas, E. K. Chan, J. K. Barton, H. G. Rylander III, and A. J. Welch, "Use of an agent to reduce scattering in skin," *Lasers Surg. Med.* **24,** 133–141 (1999).
137. R.K. Wang, X. Xu, V.V. Tuchin, and J. B. Elder, "Concurrent enhancement of imaging depth and contrast for optical coherence tomography by hyperosmotic agents," *J. Opt. Soc. Am.* **B18,** 948–953 (2001).
138. M. Brezinski, K. Saunders, C. Jesser, X. Li, and J. Fujimoto, "Index matching to improve OCT imaging through blood," *Circulation* **103**, 1999–2003 (2001).
139. G. Vargas, K.F. Chan, S. L. Thomsen, and A. J. Welch, "Use of osmotically active agents to alter optical properties of tissue: effects on the detected fluorescence signal measured through skin," *Lasers Surg. Med.* **29**, 213–220 (2001).
140. R.K. Wang and J.B. Elder, "Propylene glycol as a contrasting agent for optical coherence tomography to image gastro-intestinal tissues," *Lasers Surg. Med.* **30**, 201–208 (2002).
141. R.K. Wang and V.V. Tuchin, "Enhance light penetration in tissue for high resolution optical imaging techniques by use of biocompatible chemical agents," *J. X-Ray Sci. Tech.* **10,** 167–176 (2002).
142. Y. He, and R.K. Wang, "Dynamic optical clearing effect of tissue impregnated by hyperosmotic agents: studied with optical coherence tomography," *J. Biomed. Opt.* **9** (1) (2004).
143. R.K. Wang, X. Xu, Y. He, and J.B. Elder, "Investigation of optical clearing of gastric tissue immersed with the hyperosmotic agents," *IEEE J. Sel. Top. Quant. Electron.* (2003). In press
144. X. Xu and R.K. Wang, "The role of water desorption on optical clearing of biotissue: studied with near infrared reflectance spectroscopy," *Medical Physics,* **30,** 1246-1253 (2003).
145. X. Xu, R.K. Wang, and J.B. Elder, "Optical clearing effect on gastric tissues immersed with biocompatible chemical agents studied by near infrared reflectance spectroscopy," *J. Phys. D:Appl. Phys.* **36,** 1707-1713 (2003).
146. A.N. Bashkatov, E.A. Genina, Yu.P. Sinichkin, V.I. Kochubey, N.A. Lakodina, and V.V. Tuchin, "Glucose and mannitol diffusion in human *dura mater" Biophys. J.* **85** (5) (2003).
147. J.M. Schmitt and G. Kumar. "Optical scattering properties of soft tissue: a discrete particle model," *Appl. Opt.* **37**, 2788–2797 (1998).
148. R.K. Wang, "Modeling optical properties of soft tissue by fractal distribution of scatters, *J. Modern Opt.* **47**, 103–120 (2000).
149. A. Dunn and R. Richards-Kortum, "Three-dimensional computation of light scattering from cells," *IEEE J. Sel. Top. Quant. Electron.* **2,** 898–905 (1996).
150. R. Drezek, A. Dunn, and R. Richards-Kortum, "Light scattering from cells: finite-difference time-domain simulations and goniometric measurements," *Appl. Opt.* **38,** 3651–3661 (1999).

151. V. Twersky, "Transparency of pair-correlated, random distributions of small scatters, with applications to the cornea," *J. Opt. Soc. Am.* **65**, 524–530 (1975).
152. R. Barer, K.F. Ross, and S. Tkaczyk, "Refractometry of living cells," *Nature* **171,** 720–724 (1953).
153. P. Brunsting and P. Mullaney, "Differential light scattering from spherical mammalian cells," *Biophys. J.* **14**, 439–453 (1974).
154. C. F. Bohren and D. R. Huffman, *Absorption and Scattering of Light by Small Particles* (Wiley, New York, 1983).
155. R. Graaff, J. G. Aarnoudse, J. R. Zijp, P. M. A. Sloot, FF Demul, J Greve, MH Koelink, "Reduced light scattering properties for mixtures of the optical properties: A simple approximation derived from Mie calculation," *Appl. Opt.* **31,** 1370–1376 (1992).
156. J. Firm and P. Mazur, "Interactions of cooling rate, warming rate, glycerol concentration and dilution procedure on the viability of frozen-thawed human granulocytes," *Cryobiology* **20**, 657–676 (1983).
157. N. Songsasen, B.C. Bucknell, C. Plante, and S.P. Leibo, *"In vitro* and *in vivo* survival of cryopreserved sheep embryos," *Cryobiology* **32,** 78–91 (1995).
158. D. Martin and H. Hauthal, *Dimethyl Sulphoxide* (Wiley, New York, 1975).
159. W.M. Bourne, D.R. Shearer, and L.R. Nelson, "Human corneal endothelial tolerance to glycerol, dimethysulphoxide, 1,2-propanediol, and 2,3-butanediol," *Cryobiology* **31**,1–9 (1994).
160. J.O.M. Karlsson and M. Toner, "Long term storage of tissue by cryopreservation: Critical issues," *Biomaterials* **17**, 243–256 (1996).
161. K.H. Kolb, G. Janicke, M. Kramer, P.E. Schulze, and G. Raspe, "Absorption, distribution and elimination of labeled dimethyl sulfoxide in man and animals," *Ann. N.Y. Acad. Sci.* **141**, 85–95 (1967).
162. R. Herschler, S.W. Jacob, "The case of dimethyl sulfoxide," in *Controversies in Therapeutics,* L. Lasagna ed. (W.B. Saunders, Philadelphia, 1980).
163. A. Walter and J. Gutknecht. "Permeability of small nonelectrolytes through lipid bilayer membranes," *J. Membrane Biol.* **90**, 207–217 (1986).
164. P. Patwari, N. J. Weissman, S. A. Boppart, C. A. Jesser, D. Stamper, J. G. Fujimoto, and M.E. Brezinski, "Assessment of coronary plaque with optical coherence tomography and high frequency ultrasound," *Am. J. Card.* 85, 641–644 (2000).
165. A. Roggan, M. Friebel, K. Dorschel, A. Hahn, and G. Mueller, "Optical properties of circulating human blood in the wavelength range 400-2500 nm," *J. Biomed. Opt.* **4,** 36–46 (1999).
166. S.Yu. Shchyogolev, "Inverse problems of spectroturbidimetry of biological disperse systems: an overview,"*J. Biomed Opt.* **4,** 490–503 (1999).
167. A.V. Priezzhev, O.M. Ryaboshapka, N.N. Firsov, and I.V. Sirko, "Aggregation and disaggregation of erythrocytes in whole blood: study by backscattering technique," *J. Biomed. Opt.* **4,** 76–84 (1999).
168. S.M. Bertoluzzo, A. Bollini, M. Rsia, and A. Raynal, "Kinetic model for erythrocyte aggregation," *Blood Cells, Molecules, and Diseases* **25**(22), 339–349 (1999).

Chapter 14

OPTICAL COHERENCE TOMOGRAPHY: ADVANCED MODELING

Peter E. Andersen,[1] Lars Thrane,[1] Harold T. Yura,[2] Andreas Tycho,[1] and Thomas M. Jørgensen[1]

1. Risø National Laboratory, Optics and Fluid Dynamics Department, Roskilde, Denmark;

2. The Aerospace Corporation, Electronics and Photonics Laboratory, Los Angeles, CA USA

Abstract: Analytical and numerical models for describing and understanding the light propagation in samples imaged by optical coherence tomography (OCT) systems are presented. An analytical model for calculating the OCT signal based on the extended Huygens-Fresnel principle valid both for the single and multiple scattering regimes is derived. An advanced Monte Carlo model for calculating the OCT signal is also derived, and the validity of this model is shown through a mathematical proof based on the extended Huygens-Fresnel principle. From the analytical model, an algorithm for enhancing OCT images is developed; the so-called true-reflection algorithm in which the OCT signal may be corrected for the attenuation caused by scattering. The algorithm is verified experimentally and by using the Monte Carlo model as a numerical tissue phantom. It is argued that the algorithm may improve interpretation of OCT images. Finally, the Wigner phase-space distribution function is derived in a closed-form solution, and on this basis a novel method of OCT imaging is proposed.

Key words: multiple scattering, light propagation in tissue, optical coherence tomography, extended Huygens-Fresnel principle, Monte Carlo simulations, true-reflection algorithm, Wigner phase-space distribution

14.1 INTRODUCTION

Optical coherence tomography (OCT) has developed rapidly since its potential for applications in clinical medicine was first demonstrated in 1991 [1]. OCT performs high-resolution, cross-sectional tomographic imaging of

the internal microstructure in materials and biologic systems by measuring backscattered or backreflected light.

Mathematical models [2-9] have been developed to promote understanding of the OCT imaging process and thereby enable development of better imaging instrumentation and data processing algorithms. One of the most important issues in the modeling of OCT systems is the role of the multiple scattered photons, an issue, which only recently has become fully understood [10]. Hence, this model, capable of describing both the single and multiple scattering regimes simultaneously in heterogeneous media, is essential in order to completely describe the behavior of OCT systems.

Experimental validation of models on realistic sample structures, e.g., layered sample structures, would require manufacturing of complex tissue phantoms with well-controlled optical properties. However, a useful alternative to validate the analytical predictions on such geometries is to apply a Monte Carlo (MC) based simulation model [11], since there are few limitations on which geometries that may be modeled using MC simulations. MC models for analyzing light propagation are based on simulating the radiative equation of transfer by tracing a large number of energy packets each considered to represent a given fraction of the incident light energy [12,13]. Hence, as a numerical experiment one has full control of all parameters.

The scope of this chapter is the presentation of analytical and numerical models that are able to describe the performance of OCT systems including multiple scattering effects in heterogeneous media. Such models, where the contribution to the OCT signal from multiple scattering effects has been taken into account, are essential for the understanding and in turn optimization of OCT systems. Moreover, establishing a valid MC model of OCT systems is important, because such a model may serve as a numerical phantom providing data that are otherwise cumbersome to obtain experimentally. In general, these models, analytical as well as numerical, may serve as important tools for improving interpretation of OCT images.

14.1.1 Organization of This Chapter

The chapter is divided into four sections covering specific topics in modeling OCT systems. In section 14.2, an analytical model for the detected OCT signal is derived based on the extended Huygens-Fresnel principle. In the field of biomedical optics, Monte Carlo simulations have already proved their value. In section 14.3, an advanced Monte Carlo model for calculating the OCT signal is presented, and comparisons to the analytical model are made. The analytical model, in section 14.4 is then used to derive the optical properties of a scattering medium, which forms the basis of the so-called *true reflection algorithm.* The algorithm is verified using MC simulations as

well as experiments. The Wigner phase-space distribution function has been proposed as an alternative to OCT. In section 14.5, we demonstrate the applicability of using the extended Huygens-Fresnel principle to calculate the Wigner phase-space distribution function and to derive a novel method of OCT imagery.

14.2 ANALYTICAL OCT MODEL BASED ON THE EXTENDED HUYGENS-FRESNEL PRINCIPLE

Since the first paper describing the use of the OCT technique for noninvasive cross-sectional imaging in biological systems [1], various theoretical models of the OCT system have been developed. The primary motivation has been optimization of the OCT technique thereby improving the imaging capabilities. The first theoretical models were based on single-scattering theory [2,3]. These models are restricted to superficial layers of highly scattering tissue in which only single scattering occurs. Single scattering or single backscattering refers to photons which do not undergo scattering either to or from the backscattering plane of interest, i.e., ballistic photons. However, at larger probing depths, the light is also subject to multiple scattering. The effects of multiple scattering have been investigated on an experimental basis [4], and by using a hybrid Monte Carlo/analytical model [5], analysis methods of linear systems theory [6], on the basis of solving the radiative transfer equation in the small-angle approximation [7], a model based on the extended Huygens-Fresnel (EHF) principle [8], and MC simulations [9]. Note that modeling using MC simulations is treated in greater detail in subsection 14.3.3. As shown by these investigations, the primary effects of multiple scattering are a reduction of the imaging contrast and resolution of the OCT system, and a less steep slope of the signal intensity depth profile than the slope given by the single-backscatter model [4,6].

In the present section, a general theoretical description [10,14-16] of the OCT technique when used for imaging in highly scattering tissue is presented. The description is based on the EHF principle. It is shown that the theoretical model, based on this principle and the use of mutual coherence functions, simultaneously describes the performance of the OCT system in both the single and multiple scattering regimes. In a standard OCT system [1] with diffuse backscattering from the tissue discontinuity being probed, and a distance between the focusing lens and the tissue, the so-called shower curtain effect [17,18] is present. This effect has been omitted in previous theoretical models [8]. However, it is demonstrated in this section that inclusion of this effect is of utmost importance in the theoretical description of an OCT system.

14.2.1 The Extended Huygens-Fresnel Principle

When an optical wave propagates through a random medium, e.g., tissue, both the amplitude and phase of the electric field experience random fluctuations caused by small random changes in the index of refraction. Several different theoretical approaches have been developed for describing these random amplitude and phase fluctuations, based upon solving the wave equation for the electric field of the wave or for the various statistical moments of the field. By assuming a sinusoidal time variation in the electric field, it has been shown [19,20,21,22] that Maxwell's equations for the vector amplitude **E(R)** of a propagating electromagnetic wave through a non-absorbing refracting medium lead directly to

$$\nabla^2\mathbf{E} + k^2 n^2(\mathbf{R})\mathbf{E} + 2\nabla\left[\mathbf{E}\cdot\nabla \ln n(\mathbf{R})\right] = 0, \tag{1}$$

where **R** denotes a point in space, k is the wave number of the electromagnetic wave, and $n(\mathbf{R})$ is the index of refraction whose time variations have been suppressed. We now assume that the magnitude of the index of refraction fluctuations is small in comparison with unity. Hence, the index of refraction $n(\mathbf{R}) = \langle n(\mathbf{R})\rangle + n_f(\mathbf{R})$, where $n_f(\mathbf{R})$ is the small fluctuating part of the index of refraction with zero mean and a root-mean-square value much less than unity. This assumption is in general valid for tissue [23]. In this case it has been shown, that the last term on the left-hand side of equation 1, which is related to the change in polarization of the wave as it propagates, is negligible if the wavelength of the radiation $\lambda << 2\pi\, l_0$, where l_0 is a measure of the smallest random inhomogeneities in the medium [21,22]. The structures that dominate light propagation in tissue, for example cells, have a size of $2\ \mu m$ or more, which means that the criteria for neglecting the depolarization term is fulfilled in the case of interest where $\lambda \sim 1.0\ \mu m$. By dropping this term, equation 1 simplifies to

$$\nabla^2\mathbf{E} + k^2 n(\mathbf{R})\mathbf{E} = 0, \tag{2}$$

which is now easily decomposed into three scalar equations, one for each component of the field **E.** If we let $U(\mathbf{R})$ denote one of the scalar components transverse to the direction of propagation along the positive z-axis, then equation 2 may be replaced by the scalar stochastic equation

$$\nabla^2 U + k^2 n^2(\mathbf{R})U = 0. \tag{3}$$

Equation 3 cannot be solved exactly in closed form. Some early attempts to solve equation 3 were based on the geometric optics approximation [24], which ignores diffraction effects, and on perturbation theories widely known as the Born approximation and Rytov approximation [20]. One approach to solving equation 3 by other than perturbation methods was developed, independent of each other, by Lutomirski and Yura [25] and by Feizulin and Kravtsov [26]. This technique is called the extended Huygens-Fresnel (EHF) principle. As the name indicates, it is an extension of the Huygens-Fresnel principle to a medium that exhibits a random spatial variation in the index of refraction. That is, the field due to some arbitrary complex disturbance specified over an aperture can be computed, for propagation distances that are large compared with the size of the aperture, by superimposing spherical wavelets that radiate from all elements of the aperture. This principle follows directly from Green's theorem [27] and the Kirchhoff approximation [27] applied to the scalar wave equation together with a field reciprocity theorem between an observation point and a source point of spherical waves in the random medium. On the basis of this principle, the geometry of the problem, i.e., the aperture field distribution, can be separated from the propagation problem, which is determined by the way a spherical wave propagates through the medium. Furthermore, Yura and Hanson [28,29] have applied the EHF principle to paraxial wave propagation through an arbitrary ABCD system in the presence of random inhomogeneities. An arbitrary ABCD system refers to an optical system that can be described by an ABCD ray-transfer matrix [30]. In the cases of interest in this section, the ABCD ray-transfer matrix is real, and the field in the output plane is then given by [28]

$$U(\mathbf{r}) = \int U_0(\mathbf{p})\, G(\mathbf{p},\mathbf{r})\, d\mathbf{p}\,, \tag{4}$$

where $\mathbf{r}$ and $\mathbf{p}$ are two-dimensional vectors transverse to the optical axis in the output plane and input plane, respectively. Throughout this chapter it is understood that spatial integrals are to be carried out over the entire plane in question.

The quantity $U_0(\mathbf{p})$ is the field in the input plane, and $G(\mathbf{p},\mathbf{r})$ is the EHF Green's function response at $\mathbf{r}$ due to a point source at $\mathbf{p}$ given by [25, 28]

$$G(\mathbf{p},\mathbf{r}) = G_0(\mathbf{p},\mathbf{r}) \exp\left[i\varphi(\mathbf{p},\mathbf{r})\right], \tag{5}$$

where $G_0(\mathbf{p},\mathbf{r})$ is the Huygens-Fresnel Green's function for propagation through an ABCD system in the absence of random inhomogeneities, and $\varphi(\mathbf{p},\mathbf{r})$ is the random phase of a spherical wave propagating in the random

medium from the input plane to the output plane. The Huygens-Fresnel Green's function $G_0(\mathbf{p},\mathbf{r})$ is given by [28]

$$G_0(\mathbf{p},\mathbf{r}) = -\frac{ik}{2\pi B}\exp\left[-\frac{ik}{2B}\left(Ap^2 - 2\mathbf{p}\cdot\mathbf{r} + Dr^2\right)\right], \tag{6}$$

where A, B, and D are the ray-matrix elements for propagation from the input plane to the output plane. In the following, it is assumed that φ is a normally distributed zero-mean random process.

14.2.2 The OCT Signal

A conventional OCT system [1] consists of a superluminescent diode (SLD), a Michelson interferometer with movable reference mirror, and a photodetector. The rotationally symmetric sample arm geometry of the OCT system is shown in *Figure 1*. The tissue discontinuity being probed arises from a refractive index discontinuity between two tissue layers ($n \neq n_1$ in *Figure 1*). Therefore, the discontinuity, located at a depth z in the tissue, is characterized by a Fresnel reflection coefficient R_d. A lens with focal length f is placed at a distance d from the tissue surface. In the system of interest, the focal plane coincides with the tissue discontinuity. Furthermore, the reference arm optical path length in the Michelson interferometer is matched to the focal plane optical depth.

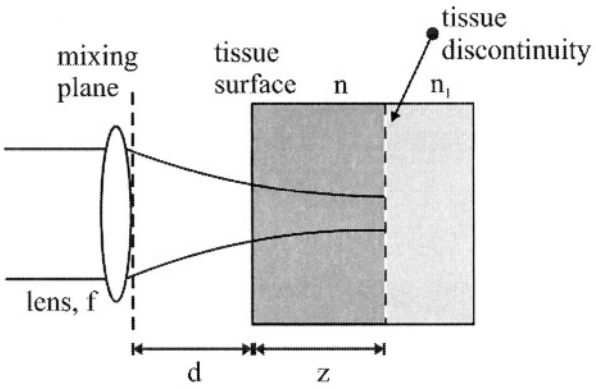

Figure 1. Sample arm geometry of the OCT system (from Ref. [10]).

In the case of human skin, light scattering in the bulk tissue is predominantly in the forward direction for the wavelengths of interest in the NIR region [31]. Hence, we neglect bulk backscattering, and use the EHF

principle [25,26] to describe the light propagation in the bulk tissue. This is justified by the fact that the EHF principle is based on the paraxial approximation and therefore valid for small-angle forward scattering. In particular, it can be shown that the paraxial approximation is valid up to 30°, i.e., 0.5 rad [30]. Because most tissues are characterized by *rms* scattering angles below this limit, the EHF principle may be used to describe light propagation in tissue retaining both amplitude and phase information. Also, the bulk tissue absorption is neglected [31]. Thus, the bulk tissue is characterized by a scattering coefficient μ_s, a root mean square scattering angle θ_{rms} or asymmetry parameter g [32], and a mean index of refraction n. Furthermore, the bulk tissue is modeled as a material with scatterers randomly distributed over the volume of interest. Note that in the present analysis polarization effects are excluded.

By mixing the sample field U_S reflected from the discontinuity in the tissue at depth z, with the reference field U_R on the photodetector of the OCT system, we obtain that the heterodyne signal current $i(z)$ can be expressed as [8]

$$i(z) \propto \mathrm{Re}\left[\int U_R(\mathbf{p},t) U_S^*(\mathbf{p},t+\tau)\, d\mathbf{p} \right], \tag{7}$$

where the integration is taken over the area of the photodetector, Re denotes the real part, and τ is the difference between the propagation times of the reference and sample beams. In practice, the heterodyne signal current $i(z)$ is measured over a time much longer than the source coherence time. In this case, it can be shown that [8]

$$i(z) \propto |g(\tau)| \mathrm{Re}\left[\int U_R(\mathbf{p}) U_S^*(\mathbf{p})\, d\mathbf{p} \right], \tag{8}$$

where $|g(\tau)|$ is the modulus of the normalized temporal coherence function of the source (notice that $g(\tau)$ is not related to the asymmetry parameter g).

Because the detailed structure of the tissue is unknown a priori, it is necessary and appropriate to treat the optical distortions as a random process and, as is commonly done in the literature, to specify certain measures of the average performance, e.g., the mean (i.e., ensemble average) square heterodyne signal current. It can be shown that the mean square heterodyne signal current $\langle i^2(z) \rangle$, which is proportional to the heterodyne signal power, is given by [8,17]

$$\left\langle i^2(z) \right\rangle = 2\alpha^2 |g(\tau)|^2 \mathrm{Re}\left[\iint \Gamma_S(\mathbf{p}_1,\mathbf{p}_2;z) \Gamma_R(\mathbf{p}_1,\mathbf{p}_2)\, d\mathbf{p}_1 d\mathbf{p}_2 \right], \tag{9}$$

where

$$\Gamma_R(\mathbf{p}_1,\mathbf{p}_2) = U_R(\mathbf{p}_1)U_R^*(\mathbf{p}_2), \tag{10}$$

$$\Gamma_S(\mathbf{p}_1,\mathbf{p}_2;z) = \left\langle U_S(\mathbf{p}_1;z)U_S^*(\mathbf{p}_2;z)\right\rangle \tag{11}$$

are the mutual coherence functions of the reference and the reflected sample optical fields in the mixing plane. The angular brackets denote an ensemble average both over the statistical properties of the tissue and the reflecting discontinuity. For simplicity, the heterodyne mixing process has been chosen to take place directly behind the lens at the side facing the tissue, and $\mathbf{p}_1$, $\mathbf{p}_2$ are two-dimensional vectors in this plane transverse to the optical axis. The quantity α is a conversion factor for power to current and equals $(q_e\eta/h\nu)$, where q_e is the electronic charge, η the detector quantum efficiency, ν the optical frequency, and h Planck's constant. In the case of interest, the reference arm optical path length in the Michelson interferometer is always matched to the sample arm optical path length, from which it follows that $|g(\tau)|=|g(0)|=1$ [8].

For the heterodyne detection scheme, the spatial coherence properties of the sample field contained in the mutual coherence function Γ_S are of utmost importance in the determination of the corresponding signal. In particular, if the spatial coherence of the sample field is degraded with respect to the reference field, one obtains a corresponding degradation in the signal-to-noise ratio.

The reference field and the input sample field U_{Si} in the lens plane impinging on the sample are assumed to be of Gaussian shape and given by

$$U_R(\mathbf{p},t) = \sqrt{\frac{P_R}{\pi w_0^2}}\exp\left[-\frac{p^2}{2}\left(\frac{1}{w_0^2}+\frac{ik}{f}\right)\right]\exp\left[i\omega_R t+\varphi_R(t)\right], \tag{12}$$

$$U_{Si}(\mathbf{p},t) = \sqrt{\frac{P_S}{\pi w_0^2}}\exp\left[-\frac{p^2}{2}\left(\frac{1}{w_0^2}+\frac{ik}{f}\right)\right]\exp\left[i\omega_S t\right], \tag{13}$$

where P_R and P_S are the powers of the reference and input sample beams, respectively, w_0 is the $1/e$ intensity radius of these beams in the lens plane, $k=2\pi/\lambda$, where λ is the center wavelength of the source in vacuum, ω_R and ω_S are the angular frequencies of the reference and input sample beams,

respectively, and φ_R is the phase of the reference field relative to the input sample field.

In the determination of the mutual coherence function Γ_S, we use the EHF principle to obtain a viable expression for $U_S(\mathbf{p};z)$, i.e., the reflected sample optical field in the mixing plane. Using equation 4, we have

$$U_S(\mathbf{p};z) = \int U_B(\mathbf{r};z)\, G(\mathbf{r},\mathbf{p};z)\, d\mathbf{r}, \tag{14}$$

where $U_B(\mathbf{r};z)$ is the reflected sample field in the plane of the tissue discontinuity, $\mathbf{r}$ is a two-dimensional vector in this plane transverse to the optical axis, and $G(\mathbf{r},\mathbf{p};z)$ is the EHF Green's function response at $\mathbf{p}$ due to a point source at $\mathbf{r}$, which includes the effects of scattering in the intervening medium. Combining equations 11and 14 yields

$$\Gamma_S(\mathbf{p}_1,\mathbf{p}_2;z) = \iint \left\langle U_B(\mathbf{r}_1;z)\, U_B(\mathbf{r}_2;z)\, G(\mathbf{r}_1,\mathbf{p}_1;z)\, G^*(\mathbf{r}_2,\mathbf{p}_2;z) \right\rangle d\mathbf{r}_1 d\mathbf{r}_2, \tag{15}$$

where $\mathbf{r}_1$, $\mathbf{r}_2$ are two-dimensional vectors in this plane transverse to the optical axis. For simplicity in notation, we omit in the following the explicit dependence of the various quantities on z.

We next assume that the statistical properties of the bulk tissue and the tissue discontinuity are independent, and that the propagation to the tissue discontinuity is statistically independent from the corresponding reflected propagation path. The former seems to be a reasonable assumption for a medium like tissue. The latter means that enhanced backscattering is neglected. Enhanced backscattering and the criterion for neglecting it are discussed in section 14.5. From these assumptions it follows that

$$\begin{aligned} &\left\langle U_B(\mathbf{r}_1)\, U_B^*(\mathbf{r}_2)\, G(\mathbf{r}_1,\mathbf{p}_1)\, G^*(\mathbf{r}_2,\mathbf{p}_2) \right\rangle = \\ &\left\langle U_B(\mathbf{r}_1)\, U_B^*(\mathbf{r}_2) \right\rangle \left\langle G(\mathbf{r}_1,\mathbf{p}_1)\, G^*(\mathbf{r}_2,\mathbf{p}_2) \right\rangle. \end{aligned} \tag{16}$$

The first term on the right hand side of equation 16 relates to both the mean value over statistics of the bulk tissue in propagating from the lens plane to the tissue discontinuity, and the reflection statistics of the discontinuity. The second term on the right hand side of equation 16 relates to the corresponding average over the statistics of the bulk tissue when propagating back from the discontinuity to the mixing plane. Assuming diffuse backscattering from the tissue discontinuity, we have [17,33]

$$\left\langle U_B(\mathbf{r}_1)U_B^*(\mathbf{r}_2)\right\rangle = \frac{4\pi}{k^2}\delta(\mathbf{r}_1-\mathbf{r}_2)\left\langle I_B(\mathbf{r}_1)\right\rangle, \tag{17}$$

where $\delta(\mathbf{r})$ is the two-dimensional Dirac delta function, and $I_B(\mathbf{r}_1)$ is the mean backscattered irradiance distribution in the plane of the discontinuity. An adequate analytic approximation for this mean backscattered irradiance distribution is obtained by multiplying the approximate expression for the mean irradiance distribution, derived in subsection 14.2.3, by the reflection coefficient R_d. The expression, which is valid for arbitrary values of the optical depth $\mu_s z$, is given by

$$\left\langle I_B(r)\right\rangle = \frac{R_d P_S}{\pi}\left[\frac{e^{-\mu_s z}\exp\left[-r^2/w_H^2\right]}{w_H^2} + \frac{\left(1-e^{-\mu_s z}\right)\exp\left[-r^2/w_S^2\right]}{w_S^2}\right]. \tag{18}$$

The first term in the brackets on the right hand side of equation 18 can be interpreted to represent the attenuated distribution obtained in the absence of the inhomogeneities, and the corresponding second term represents a broader halo resulting from scattering by the inhomogeneities. The quantities w_H and w_S are the $1/e$ irradiance radii or spot sizes in the discontinuity plane in the absence and presence of scattering, respectively, given by

$$w_H^2 = w_0^2\left(A-\frac{B}{f}\right)^2 + \left(\frac{B}{kw_0}\right)^2, \tag{19}$$

$$w_S^2 = w_0^2\left(A-\frac{B}{f}\right)^2 + \left(\frac{B}{kw_0}\right)^2 + \left(\frac{2B}{k\rho_0}\right)^2. \tag{20}$$

A and B are the ray-matrix elements for propagation from the lens plane to the discontinuity plane. For the geometry of interest, A and B are given by $A=1$ and $B=f=d+z/n$ [30]. The quantity ρ_0 appearing in equation 20 is the lateral coherence length of a spherical wave in the lens plane due to a point source in the discontinuity plane [17]. The lateral coherence length is discussed in detail in Ref. [10].

Combining equations 15-17 and simplifying yields

$$\Gamma_S(\mathbf{p}_1,\mathbf{p}_2) = \frac{4\pi}{k^2}\int\left\langle I_B(\mathbf{r})\right\rangle\left\langle G(\mathbf{r},\mathbf{p}_1)G^*(\mathbf{r},\mathbf{p}_2)\right\rangle d\mathbf{r}. \tag{21}$$

Using equation 5, the second term in the integral on the right-hand side of equation 21 may be written as

$$\left\langle G(\mathbf{r},\mathbf{p}_1)G^*(\mathbf{r},\mathbf{p}_2)\right\rangle = G_0(\mathbf{r},\mathbf{p}_1)G_0^*(\mathbf{r},\mathbf{p}_2)\Gamma_{pt}(\rho), \tag{22}$$

where $G_0(\mathbf{r},\mathbf{p})$ is the Huygens-Fresnel Green's function when propagating from the discontinuity plane to the lens plane, and Γ_{pt} is the mutual coherence function of a point source located in the discontinuity plane and observed in the lens plane given by

$$\Gamma_{pt} = \left\langle \exp\left[i\{\phi(\mathbf{p}_1)-\phi(\mathbf{p}_2)\}\right]\right\rangle. \tag{23}$$

The mutual coherence function Γ_{pt} contains the effects of the scattering inhomogeneities. Using equation 6, the Green's function $G_0(\mathbf{r},\mathbf{p})$ is given by

$$G_0(\mathbf{r},\mathbf{p}) = -\frac{ik}{2\pi B_b}\exp\left[-\frac{ik}{2B_b}\left(A_b r^2 - 2\mathbf{r}\cdot\mathbf{p} + D_b p^2\right)\right], \tag{24}$$

where A_b, B_b, and D_b are the ray-matrix elements for back-propagation to the lens plane. These quantities are given by: $A_b=D=1$, $B_b=B=d+z/n$, and $D_b=A=1$ [28]. In order to obtain an analytical solution, we have to use an approximate expression for the mutual coherence function Γ_{pt}. The expression, derived in subsection 14.2.3, is given by

$$\Gamma_{pt}(\rho) \cong e^{-\mu_s z} + \left(1-e^{-\mu_s z}\right)\exp\left[-\rho^2/\rho_0^2\right], \tag{25}$$

where $\rho=|\mathbf{p}_1-\mathbf{p}_2|$.

Substituting equations 10,12,18,21,22,24, and 25 into equation 9 and performing the indicated Gaussian integrations over $\mathbf{p}_1,\mathbf{p}_2$, and simplifying yields

$$\left\langle i^2(z)\right\rangle = \frac{2\alpha^2 P_R P_S \sigma_b}{\pi^2} \times \int\left[\frac{e^{-\mu_S z}\exp\left[-r^2/w_H^2\right]}{w_H^2} + \frac{\left(1-e^{-\mu_S z}\right)\exp\left[-r^2/w_S^2\right]}{w_S^2}\right]^2 d\mathbf{r}, \tag{26}$$

where the effective backscattering cross section of the tissue discontinuity $\sigma_b=4\pi R_d/k^2$. It is important to note that the algebraically simple result given

in equation 26 is, strictly speaking, valid only for propagation geometries where $A=D$, as is obtained in the case of interest. Performing the integration over the discontinuity plane in equation 26 and simplifying, we obtain the following expression for the mean square heterodyne signal current

$$\left\langle i^2(z)\right\rangle = \frac{\alpha^2 P_R P_S \sigma_b}{\pi w_H^2} \times \left[e^{-2\mu_s z} + \frac{2e^{-\mu_s z}\left(1-e^{-\mu_s z}\right)}{1+\frac{w_S^2}{w_H^2}} + \left(1-e^{-\mu_s z}\right)^2 \frac{w_H^2}{w_S^2} \right] \equiv \left\langle i^2 \right\rangle_0 \Psi(z). \tag{27}$$

The quantity $\langle i^2\rangle_0=\alpha^2 P_R P_S \sigma_b/\pi(w_H)^2$ is the mean square heterodyne signal current in the absence of scattering, and the terms contained in the brackets is the heterodyne efficiency factor $\Psi(z)$. A comparison between the analytic approximation of $\Psi(z)$, given in equation 27, and the exact numerical calculation is given in Ref. [34]. Physically, $\Psi(z)$ can be looked upon as the reduction in the heterodyne signal-to-noise ratio due to the scattering of the tissue. The first term in the brackets of equation 27 represents the contribution due to single scattering. The corresponding third term is the multiple scattering term, and the second term is the cross term. Physically, the cross term is the coherent mixing of the unscattered and the multiple scattered light.

14.2.2.1 Dynamic Focusing – Diffuse Reflectance

When the focal plane coincides with the tissue discontinuity, i.e., $fA=B$ with $A=1$, we obtain from equations 19 and 20

$$w_H^2 = \left(\frac{f}{kw_0}\right)^2; \qquad \frac{w_H^2}{w_S^2} = \frac{1}{1+\left(\frac{2w_0}{\rho_0(z)}\right)^2}. \tag{28}$$

The quantity $\rho_0(z)$ is the lateral coherence length of the reflected sample field in the mixing plane. For lateral separations much less (greater) than $\rho_0(z)$, the field can be considered to be mutually coherent (incoherent). Because of the diffuse backscattering from the tissue discontinuity, $\rho_0(z)$ is

determined only by the propagation back through the tissue from the tissue discontinuity to the mixing plane. As a consequence, $\rho_0(z)$ is the lateral coherence length of a point source located in the tissue discontinuity plane, as observed in the mixing plane. For the geometry of interest, it can be shown [34] that

$$\rho_0(z) = \sqrt{\frac{3}{\mu_s z}} \frac{\lambda}{\pi \theta_{rms}} \left(1 + \frac{nd(z)}{z}\right), \tag{29}$$

where $d(z)=f-(z/n)$, and $\theta_{rms} \approx [2(1-g)]^{1/2}$. The second term in the brackets of equation 29 indicates, that the lateral coherence length increases with increasing distance between the tissue surface and the mixing plane.

This well-known dependence of the lateral coherence length on the position of the scattering medium relative to the observation plane is the so-called shower curtain effect [17,18]. In general, the shower curtain effect implies that the lateral coherence length obtained for the case when the scattering medium is close to the radiation source is larger than for the case when the scattering medium is close to the observation plane. Physically, this is due to the fact that a distorted spherical wave approaches a plane wave as it further propagates through a non-scattering medium. As a consequence, e.g., from a distance one can see a person immediately behind a shower curtain, but the person cannot see you. The effect is well-known for light propagation through the atmosphere as discussed by Dror *et al.* [18], but has been omitted in previous theoretical OCT models [8]. However, due to the finite distance between the focusing lens and the tissue, the effect is inevitably present in practical OCT systems and could facilitate system optimization [34]. Finally, the reflection characteristics of the tissue discontinuity play a vital role for the shower curtain effect.

14.2.2.2 Dynamic Focusing – Specular Reflectance

If we, instead of diffuse backscattering, had a specular reflection at the tissue discontinuity, the corresponding mutual coherence function for plane waves would apply. Using this mutual coherence function, we have

$$\Psi(z) = \left[e^{-2\mu_s z} + \left(1 - e^{-2\mu_s z}\right) \frac{w_H^2}{w_S^2} \right] \tag{30}$$

and

$$\rho_0(z) = \sqrt{\frac{1}{2\mu_s z}}\frac{\lambda}{\pi\theta_{rms}}. \tag{31}$$

It is obvious from equation 31 that the shower curtain effect would not be present in the case of specular reflection at the tissue discontinuity, in contrast to the case of diffuse backscattering. However, it is important to note that it is diffuse backscattering which actually occurs in the case of (skin) tissue.

14.2.2.3 Collimated Sample Beam

In the case of a collimated sample beam the expressions for w_H and w_S in equations 19 and 20 need to be rewritten:

$$w_H^2 = \lim_{f\to\infty}\left[w_0^2\left(1-\frac{d+z/n}{f}\right)^2+\left(\frac{d+z/n}{kw_0}\right)^2\right] = w_0^2+\left(\frac{d+z/n}{kw_0}\right)^2 \tag{32}$$

$$w_S^2 = \lim_{f\to\infty}\left[w_H^2+\left(\frac{2\left(d+z/n\right)}{k\rho_0}\right)^2\right] = w_0^2+\left(\frac{d+z/n}{kw_0}\right)^2+\left(\frac{2\left(d+z/n\right)}{k\rho_0}\right)^2, \tag{33}$$

where it has been used that $A=1$ and $B=d+z/n$, and note that now $B\neq f$. In order to find the heterodyne efficiency factor these expressions must be inserted in equation 27 and, moreover, the expression for ρ_0 should be chosen in accordance with the reflection characteristics of the probed discontinuity.

14.2.2.4 Numerical Results

The heterodyne efficiency factor $\Psi(z)$ is shown as a function of depth z of the tissue discontinuity in *Figure 2* for typical parameters of human skin tissue with diffuse backscattering and the shower curtain effect included (dashed) and specular reflection (solid), respectively. For comparison, we show the case of diffuse backscattering with exclusion of the shower curtain effect (dash-dot) and the case of pure single scattering (dotted). At shallow depths single backscattering dominates. Due to multiple scattering, the slope is changed and $\Psi(z)$ becomes almost constant for three cases (curves 1–3). The important difference is, however, that the change of slope occurs at

different depths. This is due to the shower curtain effect leading to an appreciable enhancement of $\Psi(z)$, and with it the heterodyne signal, which is obtained by comparing curve 1 and 2 in *Figure 2.* Physically, this increase in the heterodyne signal is due to an enhanced spatial coherence of the multiple scattered light.

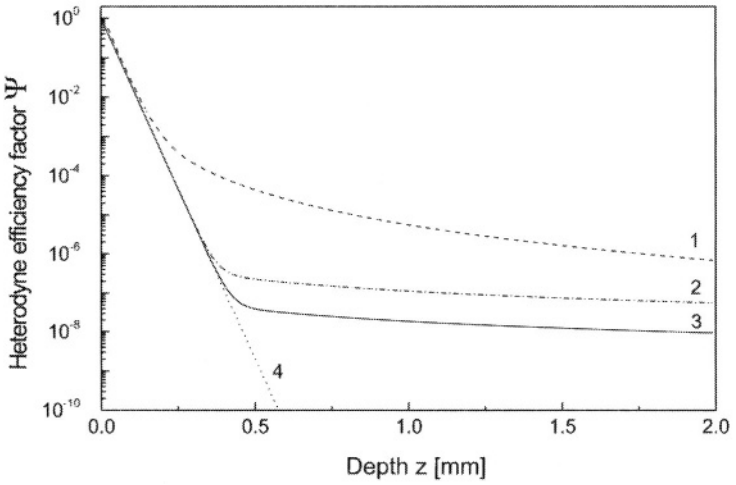

Figure 2. $\Psi(z)$ as a function of z for diffuse backscattering with the shower curtain effect included (curve 1), and for specular reflection (curve 3). Curve 2 is calculated for diffuse backscattering without the shower curtain effect, and curve 4 is the case of pure single backscattering; λ=814 nm, μ_s=20 mm^{-1}, g=0.955 (θ_{rms}=0.3 rad), n=1.4, f=5 mm, w_0=0.5 mm (from Ref. [10]).

In *Figure 3,* $\Psi(z)$ is shown as a function of depth z for μ_s=10 mm^{-1} and three values of g within the range of validity of the EHF principle. The curves are computed for the case of diffuse backscattering at the discontinuity, and inclusion of the shower curtain effect. This figure demonstrates the degree of sensitivity of the heterodyne efficiency factor with respect to changes in the asymmetry parameter. Moreover, in *Figure 4,* $\Psi(z)$ is shown as a function of depth z for g=0.95 and three values of μ_s within the range of interest with respect to tissue [31]. The curves are computed for the case of diffuse backscattering at the discontinuity, and inclusion of the shower curtain effect. This figure demonstrates the degree of sensitivity of the heterodyne efficiency factor with respect to changes in the scattering coefficient.

14.2.2.5 Choice of Scattering Function

In the present modeling of the OCT geometry, we use a Gaussian volume scattering function [35], as discussed in subsection 14.2.3 below. The

motivation for this choice of scattering function is the ability to obtain an accurate analytic engineering approximation, valid for all values of the optical depth. In the case of the Henyey-Greenstein scattering function [36], which is widely used in approximating the angular scattering dependence of single-scattering events in some biological media [31,37], the corresponding analytic approximation is not as accurate as for the case of a Gaussian scattering function. However, a numerical computation using the exact expressions may be carried out instead. Hence, both scattering functions may be used in the modeling of the OCT geometry presented in this chapter.

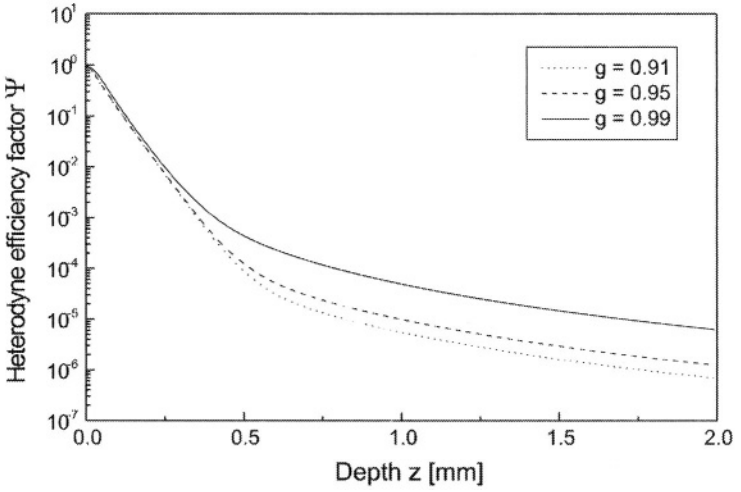

Figure 3. $\Psi(z)$ as a function of z for μ_s=10 mm^{-1} and three values of g. The curves are for the case of a diffuse backscattering at the discontinuity, and inclusion of the shower curtain effect (λ=814 nm, n=1.4, f=5 mm, w_0=0.5 mm).

14.2.2.6 Signal-to-Noise Ratio (SNR)

Without loss of generality, an OCT system with shot-noise limited operation is considered in a calculation of the signal-to-noise ratio (SNR). The only significant source of noise is the shot-noise caused by the reference beam. For a photoconductive detector the mean square noise power N_p can then be expressed as [38]

$$N_p = 2\alpha q_e G_{ca}^2 R_l B_w P_R, \tag{34}$$

where R_l is the resistance of the load, G_{ca} the gain associated with the current amplifier, and B_w the system bandwidth. The corresponding mean heterodyne signal power $S(z)$ is given by [39]

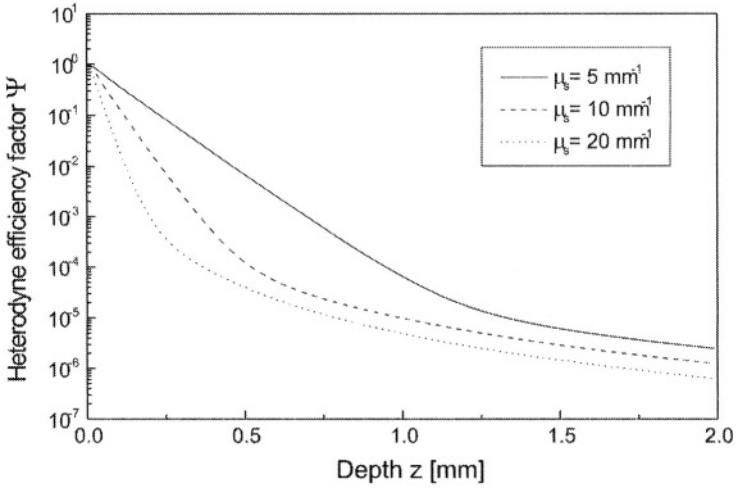

Figure 4. $\Psi(z)$ as a function of z for $g = 0.95$ and three values of μ_s within a range of interest with respect to tissue. The curves are for the case of a diffuse backscattering at the discontinuity, and inclusion of the shower curtain effect (λ=814 nm, n=1.4, f=5 mm, w_0=0.5 mm).

$$S(z) = \left\langle i^2(z) \right\rangle G_{ca}^2 R_l, \tag{35}$$

where $\langle i^2(z) \rangle$ is given by equation 27. Hence, the mean signal-to-noise ratio $SNR(z)$ is given by

$$SNR(z) = \frac{S(z)}{N_p} = (SNR)_0 \Psi(z), \tag{36}$$

where the signal-to-noise ratio in the absence of scattering $(SNR)_0$ is given by

$$(SNR)_0 = \frac{\eta P_S}{2h\nu B_w} \left(\frac{\sigma_b}{\pi w_H^2} \right). \tag{37}$$

In the case of interest where the focal plane coincides with the tissue discontinuity, we get the following expression for $(SNR)_0$

$$(SNR)_0 = \frac{2\eta P_S}{h\nu B_w}\left(\frac{w_0}{f}\right)^2 R_d, \tag{38}$$

where it has been used that $\sigma_b=4\pi R_d/k^2$.

Calculation of the Maximum Probing Depth

The maximum probing depth is of considerable interest in the characterization and optimization of an OCT system when used for imaging in highly scattering tissue. The maximum probing depth may be calculated by using the model presented above. Details of the calculation are found in Ref. [15], where the calculation of the maximum probing depth z_{max} is based on the minimum acceptable *SNR* in the case of shot-noise limited detection. In the calculations, a value of 3 is used as the minimum acceptable signal-to-noise ratio, i.e., $SNR(z_{max})=3$.

An important conclusion of Ref. [15] is that, in general, z_{max} depends on the focal length at small values of the scattering coefficient, but is independent of the focal length at larger values of the scattering coefficient. A similar behavior is observed for z_{max} as a function of μ_s and the $1/e$ intensity radius of the sample beam being focused. This behavior is due to multiple scattering of the light in the tissue. At scattering coefficients found in human skin tissue [31,40], for example, it is concluded that the maximum probing depth is independent of the focal length *f*. This is an important conclusion because the depth of focus and the lateral resolution of the OCT system may then be chosen independently of z_{max}. For example, if no scanning of the focal plane in the tissue is desirable and, therefore, a large depth of focus has been chosen, the same maximum probing depth is obtained as for a system with a short depth of focus where the focal plane is scanned to keep it matched to the reference arm. This conclusion is not surprising or contrary to assumptions already held in the field. However, the theoretical analysis in this section provides a theoretical foundation for such statements. Moreover, this agreement may also be taken as a further validation of the OCT model presented here.

14.2.3 The OCT Lateral Resolution

As already discussed, the lateral resolution of an OCT system is determined by the spot size at the depth being probed in the tissue. Therefore, we determine the mean irradiance distribution or the intensity pattern of the optical field as a function of the probing depth *z* in the tissue. In highly scattering tissue, the mean irradiance distribution, and with it the lateral resolution, are dependent on the scattering properties of the tissue.

The formalism presented in this chapter enables the calculation of the lateral resolution in highly scattering tissue, which is shown below.

For small-angle scattering, where the paraxial approximation is valid, the EHF principle yields that the mean irradiance distribution is given by [28]

$$\langle I(\mathbf{r})\rangle = \left(\frac{k}{2\pi B}\right)^2 \int K(\rho)\exp\left\{\frac{ik}{B}\boldsymbol{\rho}\cdot\mathbf{r}\right\}\Gamma_{pt}(\rho)\,d^2\rho, \tag{39}$$

where

$$K(\rho) = \int \exp\left\{-\frac{ikA}{B}\boldsymbol{\rho}\cdot\mathbf{P}\right\} U_{Si}(\mathbf{P}+\boldsymbol{\rho}/2)\,U_{Si}^{*}(\mathbf{P}-\boldsymbol{\rho}/2)\,d^2P, \tag{40}$$

and $\boldsymbol{\rho}=\mathbf{p}_1-\mathbf{p}_2$. For an OCT system focusing at a depth z in the tissue $A=1$, and $B=f$. The mutual coherence function Γ_{pt} can be expressed as [33]

$$\Gamma_{pt} = \left\langle \exp\left\{i\left[\phi(\mathbf{p}_1)-\phi(\mathbf{p}_2)\right]\right\}\right\rangle = \exp\left\{-s\left[1-b_\phi(\rho)\right]\right\}, \tag{41}$$

where we have assumed that the phase ϕ is a normally distributed zero-mean random process. The quantity s is the phase variance, and $b_\phi(\rho)$ is the normalized phase autocorrelation function for a point source whose origin is at the probing depth z. It can be shown [41] that the phase variance $s=\mu_s z$, which is equal to the optical depth. The normalized phase autocorrelation function $b_\phi(\rho)$ is given by [33]

$$b_\phi(\rho) = \frac{\int_0^L dz' \int_0^\infty \sigma(\theta;z')\,J_0(kp_s\theta)\,\theta\,d\theta}{\int_0^L dz' \int_0^\infty \sigma(\theta;z')\,\theta\,d\theta}, \tag{42}$$

J_0 is the Bessel function of the first kind, of order zero,

$$p_s = \frac{B_b(z')}{B_b}\rho, \tag{43}$$

where $B_b(z')$ is the B-matrix element for back propagation from the probing depth z to a distance z', and $\sigma(\theta, z')$ is the volume scattering or phase function with θ being the scattering angle. For the OCT geometry $B_b(z')=z'/n$

for $0 \le z' \le z$, $L=d+z$, and $\sigma(\theta, z')=\sigma(\theta)$ for $0 \le z' \le z$, and zero otherwise. In this model, we use a Gaussian volume scattering function, which in the small-angle approximation is given by

$$\sigma(\theta) = \exp\left[-\theta^2/\theta_0^2\right], \tag{44}$$

where $g = \langle \cos\theta \rangle \approx 1 - \langle \theta^2 \rangle / 2$, and $\theta_0 = \langle \theta^2 \rangle^{1/2} \approx [2(1-g)]^{1/2}$. Substituting equations 43 and 44 into equation 42 and performing the indicated integrations yields the following equation for the normalized phase autocorrelation function

$$b_\phi(\rho) = \frac{\sqrt{\pi}}{2} \frac{\rho_\phi}{\rho} \operatorname{erf}\left(\rho/\rho_\phi\right), \tag{45}$$

where $\operatorname{erf}(\rho/\rho_\phi)$ denotes the error function, and ρ_ϕ is the phase correlation length given by

$$\rho_\phi = \frac{\lambda}{\pi\sqrt{2(1-g)}} \left(1 + \frac{nd}{z}\right). \tag{46}$$

Hence, the mutual coherence function Γ_{pt} is given by equation 41 with $b_\phi(\rho)$ given by equation 45. Thus, for specific values of both s and g, the mutual coherence function is completely determined, and for a given value of the initial optical wave function U_{Si}, numerical results for the mean irradiance can be obtained directly from equation 39. Here U_{Si} is given by equation 13, and we get the following equation for the mean irradiance distribution at the probing depth z in the tissue

$$\langle I(\mathbf{r}) \rangle = \frac{P_S}{2\pi (f/kw_0)^2} \int_0^\infty \exp\left\{-\frac{x^2}{4}\right\} x J_0(ux) \Gamma_{pt}(xw_0)\, dx, \tag{47}$$

where J_0 is the Bessel function of the first kind of order zero, and

$$u = \frac{r}{f/kw_0} \tag{48}$$

is a normalized transverse coordinate.

As indicated above, numerical results can readily be obtained. However, it is useful to have an analytic approximation so that OCT system parameter studies can be performed. Examination of equation 41 reveals for large values of the optical depth, that Γ_{pt} is nonzero for $s\{1-b_\phi(\rho)\}$ less than the order unity, i.e., for $b_\phi(\rho)$ near unity. Expanding $b_\phi(\rho)$ in powers of ρ and retaining the first two nonzero terms yields from equation 45 that $b_\phi(\rho)\approx 1-\rho^2/3(\rho_\phi)^2$, from which it follows that

$$\Gamma_{pt} \approx \exp\left[-\rho^2/\rho_0^2\right], \quad s >> 1, \tag{49}$$

where $\rho_0=\rho_\phi(3/s)^{1/2}$. We expect that the ballistic, i.e., unscattered, component of the irradiance pattern is proportional to $e^{-\mu_s z}$. Thus, we approximate the mutual coherence function as

$$\Gamma_{pt} \approx e^{-\mu_s z} + \left(1-e^{-\mu_s z}\right)\exp\left\{-\rho^2/\rho_0^2\right\}. \tag{50}$$

Substituting equations 13 and 50 into equation 39, and performing the integration yields the following approximate expression for the mean irradiance distribution at the probing depth z in the tissue

$$\left\langle I(\mathbf{r})\right\rangle \approx \frac{P_S}{\pi}\left[\frac{e^{-\mu_s z}\exp\left\{-r^2/w_H^2\right\}}{w_H^2} + \frac{\left(1-e^{-\mu_s z}\right)\exp\left\{-r^2/w_S^2\right\}}{w_S^2}\right]. \tag{51}$$

The first term in the brackets on the right hand side of equation 5l can be interpreted to represent the attenuated distribution obtained in the absence of the inhomogeneities, and the corresponding second term represents a broader halo resulting from scattering by the inhomogeneities. The quantities w_H and w_S are the $1/e$ irradiance radii in the absence and presence of scattering, respectively, given by

$$w_H^2 = w_0^2\left(A-\frac{B}{f}\right)^2 + \left(\frac{B}{kw_0}\right)^2, \tag{52}$$

$$w_S^2 = w_0^2\left(A-\frac{B}{f}\right)^2 + \left(\frac{B}{kw_0}\right)^2 + \left(\frac{2B}{k\rho_0}\right)^2. \tag{53}$$

For the OCT system, we have

$$w_H = \frac{f}{kw_0}\,, \tag{54}$$

$$w_S = \sqrt{w_H^2 + \left(\frac{2f}{k\rho_0}\right)^2}\,. \tag{55}$$

It is only in the very superficial layers of highly scattering tissue that it is possible to achieve diffraction limited focusing. In this region, the lateral resolution is given by $2w_H$. At deeper probing depths the lateral resolution is dependent on the scattering properties and given by $2w_S$. It is seen from equations 55 and 29 that the lateral resolution is degraded due to multiple scattering when the probing depth is increased. This is illustrated in *Figure 5,* where the intensity pattern is shown as a function of the probing depth z in the tissue using equation 51. Finally, from equations 55 and 29 it is important to note that the shower curtain effect leads to an increased lateral resolution.

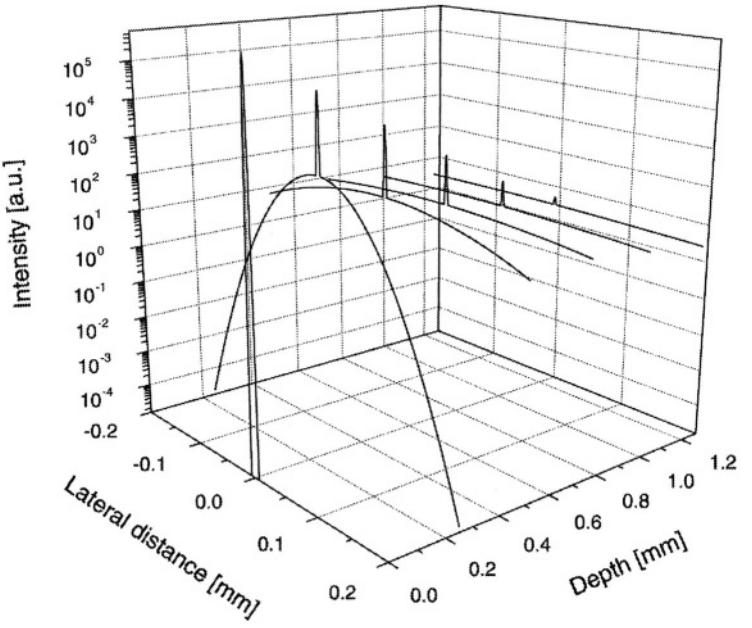

Figure 5. The intensity pattern as a function of the probing depth z in the tissue (λ=814 nm, μ_s=10 mm^{-1}, g=0.955 (θ_{rms}=0.3 rad), n= 1.4, f=5 mm, w_0=0.5 mm).

14.3 ADVANCED MONTE CARLO SIMULATION OF OCT SYSTEMS

In the previous section, the extended Huygens-Fresnel model was applied to model a generalized OCT setup, where the OCT signal from a diffusely reflecting discontinuity within the sample was found. In the following, we refer to this model as the EHF model. Also the so-called heterodyne efficiency factor Ψ was investigated, which describes the degradation of the OCT signal due to scattering. The predictions from the EHF model have been demonstrated to compare well with experiments carried out on aqueous suspensions of microspheres [10]. In the present section, we describe the derivation of a Monte Carlo (MC) model of the OCT signal. As stated in the introduction, our motivation for applying MC simulation is to develop a model which may serve as a numerical phantom for further theoretical studies.

It is important to note that the MC method only describes the transport of energy packets along straight lines and therefore the approach is incapable of describing coherent interactions of light. These energy packets are often referred to as photon packets or simply photons and this is adopted here. However, it should be emphasized that no underlying wave equation are guiding or governing these photons. Accordingly, any attempt to relate these to real quantum mechanical photons should be done with great care as argued in Ref. [42] regarding a suggested approach of including diffraction effects into MC simulations [43]. An MC photon packet represents a fraction of the total light energy and for some applications, especially continuous wave, it may be useful to think of the path traveled by a photon as one possible path in which a fraction of the power flows. A collection of photon packets may then be perceived as constituting an intensity distribution due to an underlying field and it can, accordingly, seem tempting to infer behavior known to apply to fields upon photon packets. Consider, as an example, that one wishes to determine whether the photon packets are able to enter an optical fiber. It can then seem intuitively correct to restrict the access of photons impinging on the fiber-end to those which fall within the numerical aperture of the fiber. However, such an angular restriction may not be correct, because the individual photon packet do not carry information of the entire field and its phase distribution. It is therefore not possible to determine whether a portion of the energy carried by a photon packet will enter the fiber due to a mode match between the fiber mode and the field underlying the collective intensity distribution of the photon packets. This discussion is treated in greater detail in Ref. [11].

With the above discussion of MC photons in mind, it may seem futile to investigate if MC simulation is applicable to estimate an OCT signal, which

is the result of heterodyne mixing, and thus depends upon the coherence properties of the light. However, the problem may be reformulated to investigate whether or not the effect of the lack of coherence information in a MC simulation may by circumvented, or at least minimized. Others [44, 45, 46, 47] have attempted to model similar optical geometries by interpreting the heterodyne process as a rejection process in which the detected photons must conform to a set of criteria on position and angle. We refer to such a set of criteria as a detection scheme. However, these criteria were found by *ad hoc* considerations of the optical system, which may easily lead to incorrect results as exemplified above. Instead a mathematical derivation of the true criteria of the detection scheme will be given in the present section.

In subsection 14.3.1, the EHF principle is used to derive an expression for the OCT signal depending on the intensity of the light only. This is obtained by calculating the mixing of the reference and sample beams in the plane conjugate to the discontinuity plane in the sample probed by the system. The result is surprising, because the expression for the signal given in equation 9 depends on the coherence properties of the light. However, it is shown that the formula used for calculating the OCT signal in this particular plane is mathematically identical to the result in equation 9. These results are valid for the, from a biomedical point of view, important case of a signal arising from a diffusely reflecting discontinuity embedded in a scattering sample. As a novelty, this proves the viability of MC simulation to model the OCT technique, because it is shown that only intensity, and not field and phase, is necessary for this case. In subsection 14.3.2 the necessary advanced method of simulating focused Gaussian beams in MC simulation is discussed. The results of subsections 14.3.1 and 14.3.2 are then combined in subsection 14.3.3 to form a MC model of the OCT signal. The results using this model are then compared to those of the EHF model in subsection 14.3.4.

14.3.1 Theoretical Considerations

The optical geometry of the sample arm is shown in *Figure 6,* and it should be noted that the enclosed section corresponds to the geometry used for the EHF calculation in subsection 14.2.2. An optical fiber end is positioned in the p-plane. The fiber emits a beam, which hits the collimating lens L1. The focusing lens L2 is positioned in the r-plane and in this plane the beam is a Gaussian beam with $1/e$-width, w_0, of the intensity. The beam is focused by L2 upon a diffusely reflecting discontinuity positioned at the depth z_f inside a scattering sample a distance d from L2. The sample is taken to be a slab infinite in the transverse direction. The part of the light that is reflected from the discontinuity propagates out through the sample, through

lenses L2 and L1 to the optical fiber, where it is collected. The lenses L1 and L2 have the focal length f and are taken to be identical, perfect and infinite in radius. This means that the q- and p-planes are conjugate planes with magnification one.

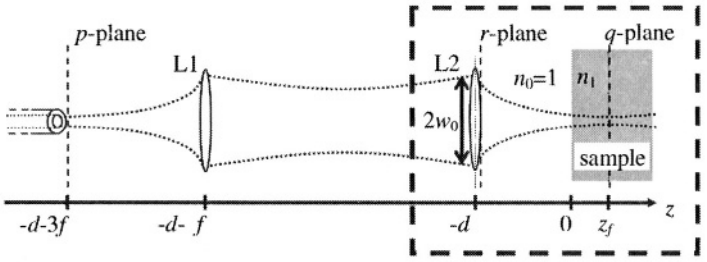

Figure 6. Sample arm setup of the OCT system. The lenses L1 and L2 are considered to be identical, perfect, and have infinite radius. The setup is essentially a 4F system (from Ref. [11]).

The OCT signal is produced by the mixing of the light from the reference and sample arms on the photodetector of the OCT system. Due to the symmetry of the system, in subsection 14.2.2 the EHF prediction of the mixing between signal and reference beam was conveniently calculated at the r-plane. The mean square of the signal current $\langle i^2 \rangle$ is given by equation 9 and rewritten according to the notation in *Figure 6* to yield

$$\left\langle i^2 \right\rangle = 2\alpha^2 \left| g(\tau) \right|^2 \mathrm{Re}\left[\iint \Gamma_R(\mathbf{r}_1, \mathbf{r}_2) \Gamma_S(\mathbf{r}_1, \mathbf{r}_2) \, d\mathbf{r}_1 d\mathbf{r}_2 \right] \equiv \Psi_r \left\langle i_0^2 \right\rangle, \qquad (56)$$

where $\Gamma_R(\mathbf{r}_1,\mathbf{r}_2)=U_R(\mathbf{r}_1)U_R^*(\mathbf{r}_2)$ is the cross correlation of the scalar reference field, $\Gamma_S(\mathbf{r}_1,\mathbf{r}_2)=\langle U_S(\mathbf{r}_1)U_S^*(\mathbf{r}_2)\rangle$ is the cross correlation of the sample field, and $\mathbf{r}_1$ and $\mathbf{r}_2$ are vectors in the r-plane, see *Figure 6*. Ψ_r is the heterodyne efficiency factor (defined in equation 27; subscript r refers to it being calculated in the r-plane), which quantifies the reduction in signal due to scattering, and $\langle i_0^2 \rangle$ is the OCT signal current in the absence of scattering. The angle brackets denotes an ensemble averaging over both the statistical properties of the scattering medium and the discontinuity and the function $g(\tau)$ is the normalized temporal coherence function of the field, where τ is the time difference of propagation between the two fields.

It is important to note that by using the EHF principle the investigation is limited to the paraxial regime as discussed above. In addition, most tissues are highly forward scattering in the near-infrared regime in which most OCT systems operate. It is assumed that the coherence length of the light source is short enough that signal powers from other reflections than the probed discontinuity are negligible. On the other hand, the coherence length is

assumed long enough so that the temporal distortion of the sample field, or the path length distribution of the reflected photons, is assumed negligible compared to the coherence length of the light source. Assuming that the optical path length of the reference beam and sample beam reflected from the discontinuity are perfectly matched then $g(\tau)\approx 1$. To obtain the best comparison with the EHF model, the MC model presented in this section adopts this approximation.

The approximation of $g(\tau)\approx 1$ is a justified approximation for highly forward scattering tissues [8]. However, it does render the EHF model unsuitable to investigate the effect of scattering on the axial resolution of an OCT system in general, because the coherence gate due to the limited coherence length of the light source is not incorporated. Others have suggested using MC simulation and the total optical path length traveled by a photon packet to determine the influence of the coherence gate [9,47,48]. While this may very well be a valid approach, it is clear from the above discussion of photon packets and coherence that, how intuitively correct it may seem, this may not be the case. However, no efforts have been published to establish the meaning of a photon packet in such a temporal mixing of fields, so future work is required to establish such a relation. It is the intention that the MC model of the OCT signal presented in this chapter may be instrumental in such studies.

The OCT signal depends upon the lateral cross correlation of the light from the scattering sample, see equation 27, and the lateral coherence length ρ_0 of the sample field in the r-plane for a single layer in front of the discontinuity is given by equation 29. With a non-zero lateral coherence length, ρ_0, it is seen that the OCT signal depends heavily upon the coherence properties of the field from the sample. As discussed above, an MC simulation does not describe the spatial coherence properties of light and thus a direct simulation of equation 56 is not possible. Like in subsection 14.2.2, we assume that the discontinuity is diffusely reflecting and this infers that the lateral coherence will be zero immediately after reflection. Our motivation for envisioning the system geometry considered in subsection 14.2.2 as part of a 4F setup is to obtain a conjugate plane to the q-plane, here the p-plane, see *Figure 6.* Through the conjugate relation it is given that, in the absence of scattering, the lateral coherence length in the p-plane will also be zero. Hence, the sample field will be delta-correlated [35] and the OCT signal will only depend upon the intensities of the reference and sample field. In Appendix A, we show that within the paraxial regime the sample field is delta-correlated even in the presence of scattering. We also show that the heterodyne efficiency factor calculated in the p-plane Ψ_p is mathematically identical to the heterodyne efficiency factor calculated in the r-plane, so that

$$\Psi_p = \frac{\langle i^2 \rangle}{\langle i_0^2 \rangle} = \frac{\int I_R(\mathbf{p}) \langle I_S(\mathbf{p}) \rangle d^2\mathbf{p}}{\int I_R(\mathbf{p}) \langle I_{S0}(\mathbf{p}) \rangle d^2\mathbf{p}} = \Psi_r , \tag{57}$$

where I_R is the intensity at the reference beam, and I_S, I_{S0} are the received intensities of the sample beam with and without scattering, respectively. The quantity $\mathbf{p}$ is a vector in the *p*-plane, see *Figure 6.* Equation 57 shows the viability of applying a MC simulation to an OCT system provided a good estimate of the intensity distribution of the sample field is achieved. This requires a method to simulate a focused Gaussian beam and a novel method for modeling such a beam using MC simulation is reviewed in subsection 14.3.2. Note that the identity proven in equation 57 is only strictly valid within the approximations of the EHF principle and thus also within the paraxial regime. However, for geometries with scattering that is not highly forward directed we expect coherence effects to be of even less importance and thus equation 57 should at least be a good first approximation even when the paraxial approximation is not strictly valid.

14.3.2 Modeling a Focused Gaussian Beam with Monte Carlo Simulation

Monte Carlo models have previously been applied to model the focusing of light beams in tissue. The motivations have been to study the distribution of absorbed power for photodynamic therapy (PDT) [49], the performance of confocal microscopy [44,45,48], the efficiency of 1- and 2-photon excitation microscopy [46,50], OCT [9], and the distribution within turbid media in general [49,51]. In the absence of scattering the focusing behavior of the beam is simply determined from the initial coordinates and propagation angles of the photons being launched. By carrying out MC simulations one may then determine the distortion caused by scattering and other structures. Previously, two different ways of modeling the focusing have been employed:

Geometric-focus method: The initial position of the photon launch is found stochastically according to the initial intensity distribution and the photon packets are simply directed towards the geometric focus of the beam [9, 49, 51, 52]. The geometric-focus method is obviously only a good approximation to a Gaussian beam for a very hard focus but even then, the infinite photon density of the unscattered photons at the geometric focus may pose a problem.

Spot-focus method: After the initial position has been found as in the geometric-focus method, the photon packets are then directed towards a random position within an area in the focal plane of the beam [44,45,46].

The position within the chosen spot in the focal plane may be chosen according to different probability distributions. If future applications of the proposed MC model involve the use of the path lengths of the received photon packets to study the effect temporal distortion of the light due to scattering, the stochastic nature of the photon paths may pose a problem.

We have developed a method of choosing initial coordinates and angles for the photons so that the full 3D spatial intensity distribution of a Gaussian beam, i.e., both the correct beam waist and finite spot size at focus, is obtained. This may be realized by utilizing the hyperbolic nature of a Gaussian beam, and we denote this approach the *hyperboloid method.* It is important to notice that this method does not require more simulation time than the two methods discussed above. Moreover, since the photons are still launched along straight lines the incorporation of the scheme into most MC simulation programs for light propagation will be straightforward. Details of the hyperboloid method may be found in Ref. [11].

As an illustration of the performance of the hyperboloid method the intensity distribution of a collimated beam has been found using three different methods: MC with the hyperboloid method, MC with the geometric-focus method (the most commonly used method in the literature), and an integral expression; see equation 39. The intensity distributions found using each method are shown in *Figure 7.* The modeled beam is a collimated beam with $1/e$-intensity radius w_0=0.4 mm, which is focused by a lens with f=4.0 mm at a depth of 1.0 mm into a scattering medium with μ_s=10mm^{-1} and g=0.92. The light propagation has been simulated using $50 \cdot 10^9$ photons for two sizes of the spatial discretisation grid, Δz=4 μm, Δq=0.5 nm, and Δz=2 μm, Δq=0.25 nm. The resulting intensity distributions have all been normalized to unity at (q,z)=(0,0).

In *Figure 7*(a) and *Figure 7*(b) the axial intensity distributions predicted by the geometric-focus and the hyperboloid method are shown, respectively. The dotted curves are the results of using the small grid size whereas the dashed curves are the results of using the larger grid size. The solid curve in *Figure* 7(b) is the result found by using integral expression in equation 39. For the large grid size, the geometric-focus method overestimates the peak height relative to the integral expression with a factor of 14, whereas the hyperboloid method underestimates the peak height with a factor of 0.5. We see that when the resolution is increased the hyperboloid method approaches the result of the integral expression in equation 39 to a factor of 0.95, whereas the peak height estimated by the geometric-focus method increases even further to a factor of 41. The latter is a result of the infinite photon density of the unscattered photons in the geometric-focus method. It is noted that the high-resolution curve for the hyperboloid method (dotted curve in *Figure 7*(b)) seems noisier than its counterpart from the geometric-focus

method (dotted curve in *Figure 7*(a)). In fact, the variance of the data used for the two curves is practically identical but less noticeable in *Figure 7*(a) due to the scale necessary to show the peak intensity estimated by the geometric-focus method. In *Figure 7*(c), the transverse intensity distribution in the focal plane estimated by the geometric-focus method (dotted), the hyperboloid method (dashed) and the integral expression (solid) are plotted, respectively. From *Figure 7*(a) and *Figure 7*(c), we see that the geometric-focus method is an inappropriate method for estimating the detailed intensity distribution around the focus. *Figure 7*(b) and *Figure 7*(c) show an excellent agreement between the hyperboloid method and the integral expression. Thus, for modeling applications, where spatial resolution is important, as in OCT, the hyperboloid method should be used when doing MC simulation of focused Gaussian beam.

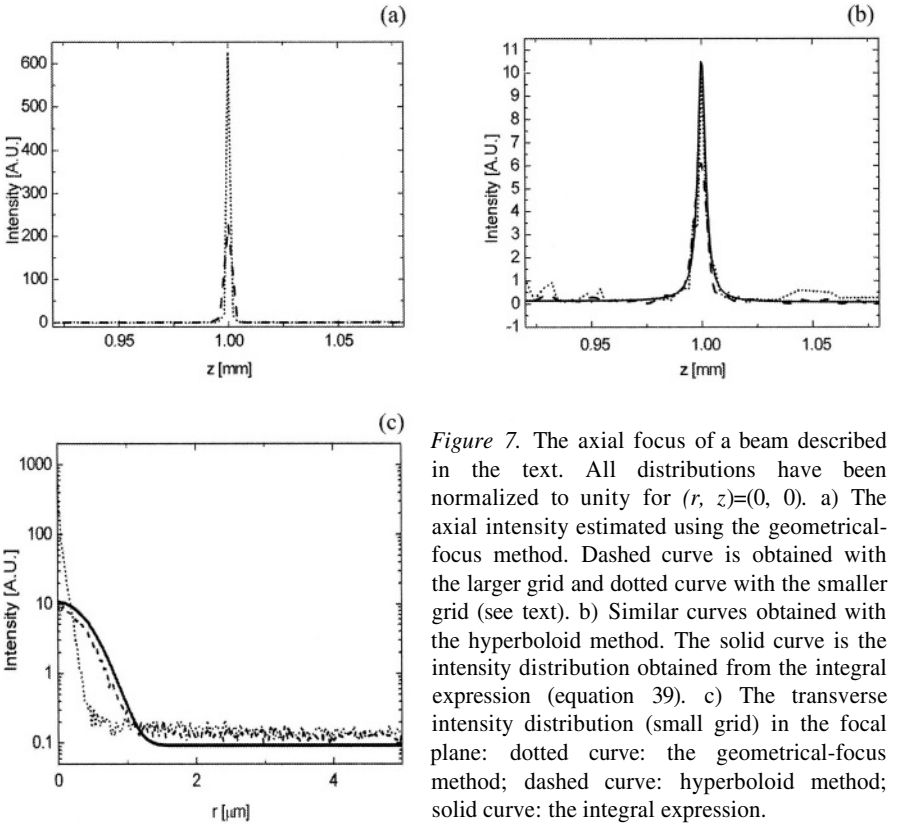

Figure 7. The axial focus of a beam described in the text. All distributions have been normalized to unity for $(r, z)=(0, 0)$. a) The axial intensity estimated using the geometrical-focus method. Dashed curve is obtained with the larger grid and dotted curve with the smaller grid (see text). b) Similar curves obtained with the hyperboloid method. The solid curve is the intensity distribution obtained from the integral expression (equation 39). c) The transverse intensity distribution (small grid) in the focal plane: dotted curve: the geometrical-focus method; dashed curve: hyperboloid method; solid curve: the integral expression.

14.3.3 Monte Carlo Simulation of the OCT Signal

In subsection 14.3.1 we found that the heterodyne efficiency factor of the OCT signal may be found using the knowledge of the intensity distributions of the sample and reference fields in the *p*-plane (see *Figure 6*), where the fiber end is situated:

$$\Psi_p = \frac{\int I_R(\mathbf{p})\langle I_S(\mathbf{p})\rangle d^2\mathbf{p}}{\int I_R(\mathbf{p})\langle I_{S0}(\mathbf{p})\rangle d^2\mathbf{p}}. \tag{58}$$

In the EHF principle the effect of a scattering medium is treated as a random phase distortion added to the deterministic phase of the light as it propagates through the medium. In the derivation of equation 58, see Appendix A, it is necessary to assume that the phase distortion added to the light propagating towards the discontinuity is statistically independent from the phase distortion added to the light propagating away from the discontinuity. It is important to note that this assumption is inherently fulfilled by MC methods such as that used by the MCML computer code [53]: A photon is traced through a dynamic medium in the sense that the distance to the next scattering event and scattering angle is a random variable independent upon the past of the photon. Hence, after each stochastic event the photon experiences a different realization of the sample. Therefore, an ensemble averaging over the stochastic sample in equation 58 is carried out through a single simulation. Moreover, to also obtain an averaging in the modeling of the diffusely reflecting discontinuity each reflected photon must experience a new realization of the discontinuity. Thus, we use the macroscopic intensity distribution of a Lambertian emitter [35] to sample the reflected angle:

$$I_r(\theta_r) = I_T \cos\theta_r. \tag{59}$$

Here I_T is reflected intensity at θ_r=0 and θ_r is the reflected angle. By following the method outlined by Prahl *et al.* [54] of sampling a physical quantity using a computer-generated pseudo random, we obtain the relations:

$$\theta_r = \arcsin(\xi), \tag{60}$$

$$\varphi_r = 2\pi\zeta, \tag{61}$$

where φ_r is the azimuthal angle of the reflected photon and ξ and ζ are both random numbers evenly distributed between 0 and 1.

Accordingly, the method of simulating the OCT signal is carried out as follows. The MC photon packet is launched from the focusing lens in the *r*-plane, see *Figure 6,* using the new hyperboloid method described in subsection 14.3.2. The interfacing with specular surfaces, such as the sample surface and the propagation through the scattering medium, is carried out using the MCML computer code. When a photon packet is reflected off the diffusely reflecting discontinuity equations 60 and 61 are used to determine the direction of the photon after reflection. As a photon exits the sample after interaction with the discontinuity its position and angle is used to calculate its position in the *p*-plane after propagation through the 4F system. To evaluate equation 58 numerically consider that the *m*'th photon packet exiting the medium, contributes to the intensity at the point p_m in the *p*-plane by the amount

$$I_{S,m} \propto \frac{w_m}{\Delta p^2}, \tag{62}$$

where w_m is the energy, or weight, carried by the photon packet and Δp^2 is a differential area around p_m. Using this and equation 58, the MC estimated heterodyne efficiency factor Ψ_{MC} is then given by

$$\Psi_{\mathrm{MC}} = \frac{\sum_m^M I_R(p_m) I_{S,m} \Delta p^2}{\langle i_0^2 \rangle} = \frac{\sum_m^M I_R(p_m) \mathrm{w}_m}{\langle i_0^2 \rangle}, \tag{63}$$

where $I_R(p)$ is the intensity distribution of the reference beam in the *p*-plane, and it is noted that the reference beam has a Gaussian intensity distribution of width w_f in the *p*-plane. The signal in the absence of scattering $\langle i_0^2 \rangle$ may be either simulated or calculated. The latter is straightforward, because with the conjugate relationship between the *p*- and *q*-plane, the intensity distribution of the sample beam will be identical to that of the reference beam in the absence of scattering.

Equation 63 reveals the important detection criterion of the MC simulation of the OCT signal: a photon must hit the *p*-plane within the extent of the reference beam. While detection schemes of previously published MC models of OCT also incorporate that photons must hit the detector, the novelty of this detection scheme is the analytically derived size and necessary position in the *p*-plane. Furthermore, contrary to these schemes the model does not incorporate an angular criterion that a photon packet must

fulfill in order to contribute to the signal. It may seem counter-intuitive that photon packets contribute to the desired signal without penalty regardless of angle of incidence upon the fiber in the *p*-plane. However, as demonstrated in Ref. [11] the inclusion of an angular criterion related to the angular extent of the incident beam, or equivalently the numerical aperture of the fiber, yields incorrect results.

14.3.4 Numerical Validation

14.3.4.1 Beam Geometries for Numerical Comparison

A set of beam geometries has been selected for numerical comparison between the EHF model and the MC model. These geometries are selected so that the two approaches are compared for different degrees of focusing and distances between the lens L2 and the sample. The selected cases are listed in Table 1 and are referred to as cases 1 through 4, respectively.

Table 1. Beam geometries for the four cases.

Case number	f [mm]	d [mm]	z [mm]	w_0 [mm]	w_0/f
1	16.0	15.5	0.5	0.125	0.008
2	8	7.5	0.5	0.4	0.05
3	0.5	0.0	0.5	0.125	0.25
4	16.0	15.0	1.0	4	0.25

For all cases the mean refractive index of the sample before the discontinuity and the surroundings are assumed to be matched so that $n_0=n_1=1$. We wish to investigate the effect of scattering on the OCT signal. A difference in the refractive index between the sample and the surrounding will impose a Snell's law refraction at the interface, which in turn imposes a focus distortion not treated in the paraxial approximation ($\sin\theta\approx\theta$) and thus not described by the EHF model. Such a distortion will be difficult to separate from the effects of scattering and is thus omitted here. As discussed in Ref. [51] there is only a severe distortion for very tightly focused beams.

In all cases discussed in the following, the wavelength of the light is chosen to be 814 nm, which is one relevant wavelength for biomedical applications of OCT. The sample is assumed to exhibit scattering described by a Gaussian scattering function (see, e.g., chapter 13 in Ref. [20]). The motivation for this choice is to enable comparison to analytical models of the propagation of Gaussian beams in random media [28] and the OCT signal, see subsection 14.2.2, which both applies the Gaussian scattering function. The comparisons presented here are carried out for different degrees of scattering and for two relevant values of the asymmetry parameter in tissue [31]:

very highly forward scattering (g=0.99) and highly forward scattering (g=0.92). The value g=0.92 was the value of the asymmetry factor in the experiments performed to validate the EHF model by Thrane *et al.* [10] With these two cases, the two approaches are compared for a sample geometry where the paraxial approximation is well satisfied and for a sample geometry, which is close to the limit of the paraxial approximation. Accordingly, it is expected that the best agreement will be found for g=0.99.

14.3.2.2 Comparison

In *Figure 8,* Ψ is plotted for cases 1 through 4 as a function of the scattering coefficient μ_s and for reference the case of single back-scattering, i.e., $\Psi_{single}=\exp(-2\mu_s z)$, has been included.

Three important observations may be made from *Figure 8.* Firstly, we observe fine agreement between the MC method and the EHF model for the four cases tested. Thus, we consider these plots as validation of the MC model. Secondly, it is inferred that the OCT signal for high optical depths is a result of multiple scattering effects in agreement with subsection 14.2.2. This is seen by comparing the single scattering curve to the plots of the MC and EHF. Finally, an important result of subsection 14.2.2 was the inclusion of the so-called shower curtain effect [17]. It is an effect caused by multiple scattering and thus plays an important role in calculating the OCT signal as the optical depth increases. Omitting this effect leads to an underestimation of the OCT signal of several orders of magnitude. Due to the fine agreement between the EHF model (with the shower-curtain effect included) and the MC model, we obtain the important result that the MC model inherently takes the effect into account.

For cases where the approximation of the EHF model is well satisfied we attribute the observed deviation between the EHF and MC models to be caused by coherence effects in the intensity distribution of the sample field. Apparently, from *Figure 8,* the lack of coherence information leads to an under-estimation of Ψ, but the specific cause for this has yet to be determined. Ψ is by definition unity in the absence of scattering, and for large optical depths coherence effects are expected to be negligible. Accordingly, we expect the two models to agree for small and large values of the optical depth of the discontinuity, whereas some deviation is to be expected in the intermediate region. As a highly forward scattering event perturbs the field only to a small degree, it is expected to distort coherence effects less than a more isotropic scattering case. In order to plot the relative deviation as a function of the effective distortion of the coherence, we plot the ratio Ψ_{EHF}/Ψ_{MC} as a function of the transport reduced optical depth of the discontinuity given by

$$s_{tr} = \mu_s z_f (1-g). \tag{64}$$

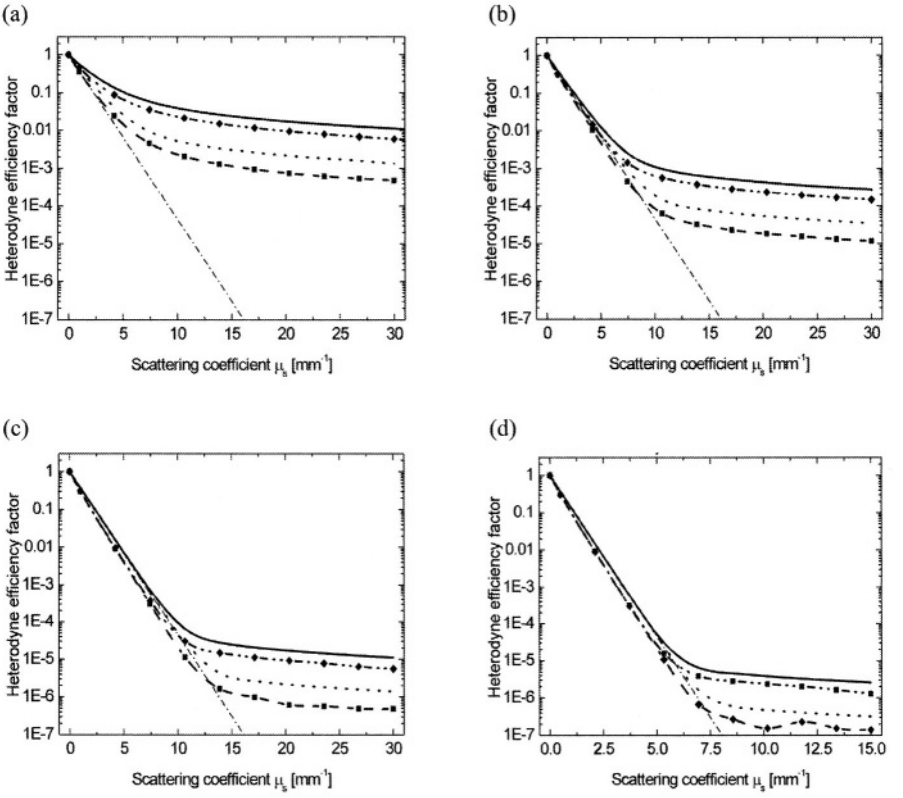

Figure 8. Heterodyne efficiency factors estimated using respectively the EHF model and the MC method for two cases of *g*. a), b), c) and d) show the estimated values for geometries 1, 2, 3, and 4 in *Table 1,* respectively. The solid line and dotted line curves are the results of the EHF model for g=0.99 and g=0.92, respectively. Dash-dot-dot and dashed curves are the results of the MC simulations for g=0.99 and g=0.92, respectively. Diamonds (♦) and squares (■) mark the actual data points obtained by the MC simulation method. For comparison, the exponential reduction in signal due to scattering obtained by a single-scatter model is shown as a dash-dot curve.

The relative difference between the EHF model and the MC method behaves, qualitatively, identical as a function of s_{tr} independent of beam geometry and *g*. This is illustrated in *Figure 9* for cases 2 (g=0.92 and 0.99), 3 (g=0.92), and 4 (g=0.92), respectively. The difference between the two approaches increases as a function of s_{tr} until $s_{tr} \approx 0.5$ after which it evens out. We mainly attribute this to the coherence effects in the intensity distribution discussed above. The more abrupt behavior of the curve for geometry 4 is

attributed to a higher numerical uncertainty in the case, caused by a more tightly focused beam. According to the new detection scheme, this implies that fewer photons will contribute to the signal resulting in an increased variance.

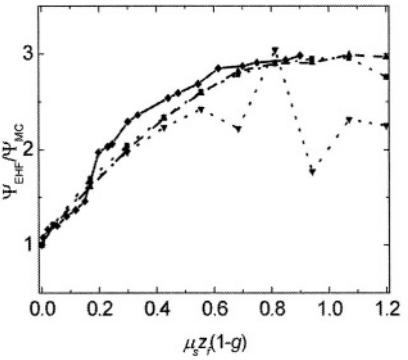

Figure 9. The relative numerical difference between the results of the EHF model and the MC model from *Figure 8* for a representative selection of the considered geometries. The ratio Ψ_{EHF}/Ψ_{MC} is plotted for case 2 and g=0.99 with symbols (♦) and solid curve, for case 2 and g=0.92 with symbols (■) and dash-dot-dot curve, for case 3 and g=0.92 with symbols (▼) and dashed curve, and for case 4 and g=0.92 with symbols (●) and dotted curve (from Ref. [11]).

In summary, due to the fine agreement between the results of the EHF model and MC simulations borne out in *Figure 8* and *Figure 9,* we conclude that the MC simulation presented in this section is a viable method of simulating the heterodyne efficiency factor of an OCT signal.

14.4 TRUE-REFLECTION OCT IMAGING

The interpretation of conventional OCT images may be a difficult task. One reason for this is the fact that an OCT signal, measured at a given position in a non-absorbing scattering medium, is a result of not only the amount of light reflected at the given position, but also the attenuation due to scattering when the light propagates through the scattering medium. Therefore, to make images, which give a direct measure of the amount of light reflected at a given position, thereby making interpretation of OCT images easier, it is necessary to be able to separate reflection and scattering effects.

In this section, we present the concept of a so-called *true-reflection OCT imaging algorithm* [34] based on the analytical model described in section 14.2. With this algorithm, it is possible to remove the effects of scattering

from conventional OCT images and create so-called *true-reflection OCT images.* This kind of post processing is similar to the correction for attenuation well-known in ultrasonic imaging. In that field, a mathematical model describing the relationship between the received signal and the two main acoustic parameters, backscatter and attenuation, has been considered [55]. The model has then been used to guide the derivation of a processing technique with the aim of obtaining ultrasonic images that faithfully represents one acoustic parameter, such as backscatter [55]. Due to the similarity between the ultrasonic case and the situation encountered in OCT, this forms a strong basis for introducing the concept of a true-reflection OCT imaging algorithm. The principle of the true-reflection OCT imaging algorithm is demonstrated experimentally by measurements on a solid scattering phantom in subsection 14.4.2 and in subsection 14.4.3 on a heterogeneous sample simulated by using the MC model presented in section 14.3.

14.4.1 True-Reflection OCT Imaging Algorithm

It was shown in subsection 14.2.2 that the mean square heterodyne signal current for light reflected at depth z in the tissue may be expressed as $\langle i^2(z)\rangle=\langle i^2(z)\rangle_0\Psi(z)$, where $\langle i^2(z)\rangle_0$ is the mean square heterodyne signal current in the absence of scattering, and $\Psi(z)$ is the heterodyne efficiency factor, which includes all of the scattering effects. The maximum of the envelope of the measured interference signal corresponds to $[\langle i^2(z)\rangle]^{1/2}$. Thus, by dividing the envelope of the measured interference signal with $[\Psi(z)]^{1/2}$, we are able to correct for the scattering effects, i.e., compensate for attenuation, and determine the envelope that would be obtained in the absence of scattering. It is important to note, that in addition to the system parameters λ, f, and w_0, knowledge about μ_s, θ_{rms}, and n of the scattering medium is necessary in order to enable calculation of $[\Psi(z)]^{1/2}$. However, in practice, μ_s and θ_{rms} may be obtained by fitting the expression for $[\langle i^2(z)\rangle]^{1/2}$ to a measured depth scan of the homogeneous backscattering tissue using an estimated value of n and the appropriate system parameters. Implementing this procedure as an option in the imaging program provides the opportunity to make what may be labeled *true-reflection OCT images.*

14.4.2 Experimental Demonstration of the True-Reflection OCT Imaging Algorithm

The principle of the true-reflection OCT imaging algorithm is demonstrated experimentally by measurements on a solid scattering phantom using a conventional OCT system comprised by a superluminescent diode with a center wavelength of 814 nm (22.8 nm spectral bandwidth (FWHM),

1.9 mW output power), a fiber-optic Michelson interferometer with moveable reference mirror, and a silicon photodetector. The two system parameters f and w_0 are 16 mm and 0.125 mm, respectively [56].

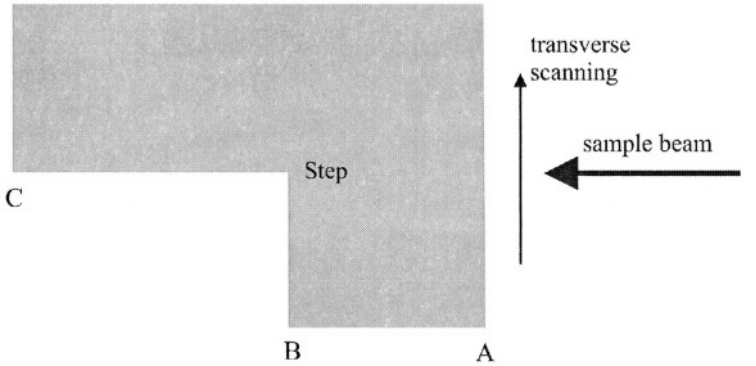

Figure 10. A schematic of the solid phantom used in the demonstration of the true-reflection OCT imaging algorithm.

The solid phantom having three discontinuities, A, B, and C, with identical reflection coefficients, is shown in *Figure 10.* It consists of scattering microspheres (approximate diameter size 10 μm) in a polymer. The optical parameters of the solid phantom, i.e., the asymmetry parameter, the scattering coefficient, and the absorption coefficient, were determined by carrying out integrating sphere and collimated transmission measurements, and using the inverse adding-doubling method [57]. It turned out that the phantom had negligible absorption.

In the experiment, 40 longitudinal (horizontal) scans are performed across the step as indicated in *Figure 10.* The distance between adjacent longitudinal scans is 10 μm, and only one longitudinal scan is taken in every lateral position. The light is reflected at the air-phantom discontinuity A (z=0.0 mm) and at the two phantom-air discontinuities at z=2.0 mm (B) and z=5.2 mm (C), respectively, which all give a diffuse backscattering. The backscattering from the bulk of the phantom is negligible and cannot be detected.

The original unprocessed envelopes of the 40 longitudinal scans are shown in *Figure 11* with the use of a linear palette. The orientation is similar to the orientation in *Figure 10.* For a better visualization of the effect of the true-reflection OCT imaging algorithm, the envelopes are shown as a 3D-plot. The first signal from the right is due to light reflected at the air-phantom discontinuity A, which will be denoted *the first discontinuity* in the following. The signal from the phantom-air discontinuity B at z=2.0 mm *(the second discontinuity),* and the signal from the phantom-air discontinuity C at

z=5.2 mm *(the third discontinuity)* cannot be distinguished in *Figure 11.* This is due to the scattering of the light in the phantom, which attenuates the signal.

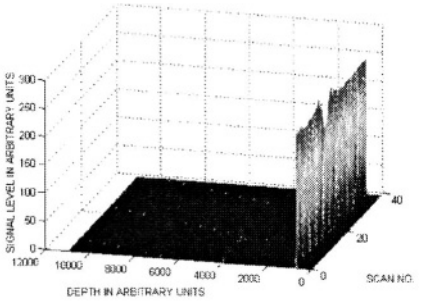

Figure 11. The original unprocessed envelopes of the 40 longitudinal scans (from Ref. [56]).

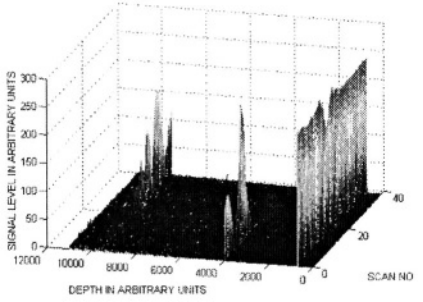

Figure 12. The result of using the true-reflection OCT imaging algorithm on an OCT image of a solid phantom having three discontinuities (pos. A, B, and C) with identical values of their reflection coefficients (from Ref. [56]).

By using the true-reflection OCT imaging algorithm described above to correct for the scattering effects, we get the envelopes shown in *Figure 12.* The optical parameters of the solid phantom, which were used in the algorithm, are μ_s=1.815 mm^{-1}, θ_{rms}=0.1096 rad (g=0.994), and n=1.5. As expected, the three signals from the discontinuities A, B, and C are nearly equal in strength after using the algorithm. A plausible explanation of the lateral variations of the signal is speckle [35], which is a well-known effect in OCT [58]. In addition, variation of the signal close to the step (see *Figure 10*) is likely due to a partly reflection of the beam.

The experimental errors of the measured values of μ_s and g of the solid phantom have been estimated to be ±5% and ±1%, respectively. Values of μ_s + 5% and -5% have been used in the algorithm, but the changes of the signal levels were very small. This is in contrast to the observation when a value of

g–1% was used in the algorithm, and the envelopes are shown in *Figure 13.* Note that the maximum signal of the second discontinuity is now slightly larger than the signal from the first discontinuity. However, the maximum signal levels of the second and third discontinuities seem to be closer to the signal level of the first discontinuity as compared to *Figure 12.*

Figure 14 shows, for comparison, the envelopes obtained if only the single scattering term is used in the expression for Ψ. Due to a large overestimate of the signal from the third discontinuity in this case, the signals from the first and second discontinuities are too small in amplitude to be observed in *Figure 14.* Thus, it is obvious that the single backscattering model is not sufficient, and, furthermore, it demonstrates the importance of taking multiple scattering effects into account.

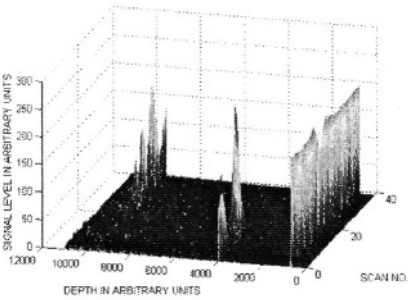

Figure 13. The envelopes of the 40 longitudinal scans when the true-reflection OCT imaging algorithm has been used together with a value of g–1% (from Ref. [56]).

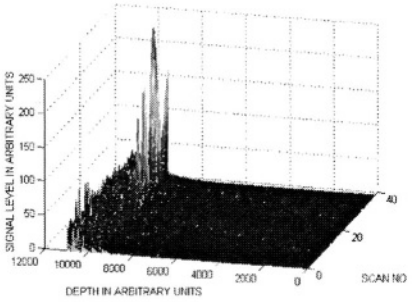

Figure 14. The envelopes obtained by using the true-reflection OCT imaging algorithm when only the single scattering term is used in the expression for Ψ (from Ref. [56]).

The experiment demonstrates the feasibility of the new algorithm for a homogeneously scattering medium. However, the algorithm may be extended to cover heterogeneously scattering media, e.g., skin tissue. *True-reflection OCT images* may be easier to interpret than conventional OCT

images, and improved diagnosis may be envisioned due to a better differentiation of different tissue types.

14.4.3 True-Reflection OCT Imaging on a MC-Simulated Heterogeneous Multi-Layered Sample

The MC model presented in section 14.3 may be used as a numerical phantom, which e.g. could be used to investigate the performance of the EHF model for sample geometries difficult to produce in the laboratory or for which one or more of the approximations made in the EHF model do not hold. It is important to note that the predictions from the EHF model have been demonstrated to compare well with experiments carried out on single-layered phantoms consisting of aqueous suspensions of microspheres [10]. In this section, we demonstrate the true-reflection OCT imaging algorithm on a heterogeneous multi-layered sample using the MC model.

Multi-layered structures are at best difficult to manufacture, and the simulation of such structures using the MCML computer code is well established. Thus, we use the MC model to simulate the OCT signal for a two-layer sample in order to demonstrate the true-reflection OCT imaging algorithm on a heterogeneous sample. Through the incorporation of the ABCD matrix formalism in the EHF theory, it is straightforward to model the OCT system applied to a multi-layered sample, see Appendix A of Ref. [10]. Thus, to demonstrate the true-reflection algorithm, we fit the two-layer EHF expression for the OCT signal to the MC simulation, extract the optical properties of the two layers, and use these values of the optical properties in the algorithm to correct for the attenuation caused by scattering.

As in the previous MC simulations in section 14.3, the refractive indices of the sample and the surroundings are matched and equal to unity. The system parameters in this case are λ=800 nm, w_0=0.4 mm, and f=8.0 mm. The first layer is 0.3 mm thick and has a constant scattering coefficient of μ_{s1}=5.0 mm^{-1} and g_1=0.99. The second layer is 0.9 mm thick and has a constant scattering coefficient of μ_{s2}=10.0 mm^{-1} and g_2=0.92. The MC simulation of the mean square heterodyne signal current is shown as squares in *Figure 15.* The fit of the two-layer EHF model to the MC simulation is shown as a solid line in *Figure 15,* and the hereby extracted optical properties μ_s and g (n is not a fitting parameter) of the two layers are shown in *Table 2* together with the input parameters of the MC simulation. The relatively large point separation of the MC simulation in the z-direction makes the gap between the last point of the first layer and the first point of the second layer rather distinct in this case.

The small percentage difference shown in *Table 2* between the MC input parameters and the extracted parameters demonstrate the capability of the

EHF model to extract optical properties from a heterogeneous multi-layered sample, e.g., human skin. The extracted optical properties of the two layers may now be used in the true-reflection algorithm. Thus, the MC simulation of the OCT signal after use of the true-reflection algorithm, i.e., after correction for the attenuation caused by scattering, is shown as triangles in *Figure 15* connected by a dashed line. The distinct signal levels obtained for the two different layers after using the true-reflection algorithm strongly indicate that a better differentiation of different tissue types may be obtained in OCT images of real tissue by using the true-reflection algorithm. This is expected to result in an improved diagnosis.

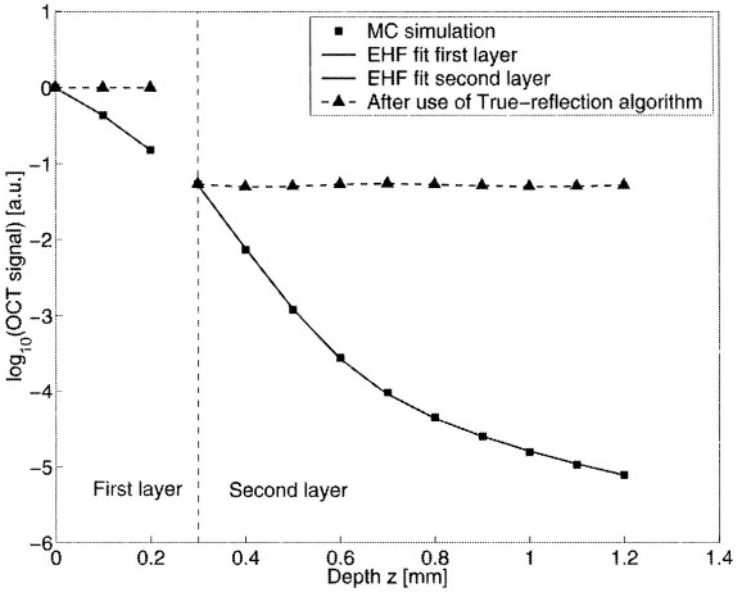

Figure 15. MC simulation of the OCT signal for a two-layer sample (squares); EHF fit to the first and second layers (solid line); the MC simulation of the OCT signal after use of the true-reflection algorithm (triangles connected with a dashed line).

Table 2. The input parameters of the MC simulation together with the extracted parameters obtained by using the EHF model, and the percentage difference.

Layer no.	Input μ_s [mm^{-1}]	Fitted μ_s [mm^{-1}]	Difference [%]	Input g	Fitted g	Difference [%]
1	5.00	4.92	-1.6	0.9900	0.9834	-0.67
2	10.00	10.22	2.2	0.9200	0.8586	-6.67

14.5 WIGNER PHASE-SPACE DISTRIBUTION FUNCTION FOR THE OCT GEOMETRY

Recently, the Wigner phase-space distribution [59] for multiple light scattering in biological media has received considerable attention. This is because, it has been suggested by numerous authors that new venues for medical imaging may be based on coherence tomography using measurements of Wigner phase-space distributions [60-65]. It has been suggested that the Wigner phase-space distribution is particularly useful for biomedical imaging because the phase-space approach provides maximum information, i.e., both space and momentum (angular) information, about the light being used. This section is devoted to the derivation of a closed form solution for the Wigner phase-space distribution function [65] obtained directly from the EHF [25] solution for the optical field.

In all cases considered in this section, as well as in Refs. [60–64], the Wigner phase-space distribution function is positive definite, and hence the Wigner function and the specific radiance may be used interchangeably. We are primarily concerned with a standard OCT propagation geometry shown in *Figure 1,* and, as such, we consider a sample beam reflected at a discontinuity giving rise to diffuse backscattering. The present section deals with the reflection geometry only; for the transmission geometry the reader is referred to Refs. [63, 65].

14.5.1 General Considerations

Consider a cw quasi-monochromatic optical wave propagating through a non-absorbing random small-angle scattering medium, reflecting off a discontinuity giving a diffuse reflection, and subsequently propagating back to the initial plane. Denote the resulting optical field in the initial plane, perpendicular to the optic axis, by $U(\mathbf{P})$, where $\mathbf{P}$ is a two-dimensional vector in this plane. For simplicity in notation, we omit the time dependence. The Wigner phase-space distribution, $W(\mathbf{P},\mathbf{q})$ may be written as [66]

$$W(\mathbf{P},\mathbf{q}) = \int \frac{d\mathbf{p}}{(2\pi)^2} \left\langle U(\mathbf{P}+\mathbf{p}/2)U^*(\mathbf{P}-\mathbf{p}/2)\right\rangle \exp[i\mathbf{q}\cdot\mathbf{p}], \qquad (65)$$

where angular brackets denote the ensemble average. That is, the Wigner phase-space distribution function is a two-dimensional Fourier transform of the indicated mutual coherence function $\langle U(\mathbf{P}+\mathbf{p}/2)\, U^*(\mathbf{P}-\mathbf{p}/2)\rangle$, and as such, contains the same information about the optical field as does the mutual coherence function. The quantity $\mathbf{q}$ is a transverse momentum, and in the small-angle approximation its magnitude q can be related directly to the

scattering angle simply as $q=2k\sin\theta/2\approx k\theta$, where k is the free space wave number. In addition, because in the small angle approximation the differential element of solid angle $d\Omega=2\pi\sin\theta d\theta\approx 2\pi\theta d\theta=2\pi q dq/k^2$, it is easily verified that the integral of $W(\mathbf{P},\mathbf{q})$ over all $\mathbf{q}$ (i.e., over solid angle) equals the intensity $I(\mathbf{P})$, i.e., $|U(\mathbf{P})|^2$, at the observation point $\mathbf{P}$. Hence, to within a multiplicative constant, the Wigner phase-space distribution is equal to the specific radiance distribution of the optical field at the observation point of interest for those cases where the Wigner phase-space distribution is positive definite. To be specific, the specific radiance distribution $N(\mathbf{P},\theta)=k^2W(\mathbf{P},k\theta)$ in those cases.

Here, we neglect polarization effects, bulk backscattering, and enhanced backscattering, which is obtained very close to the optical axis. In random media where the scattering particles are large compared to the wavelength and the index of refraction ratio is near unity, the bulk backscatter efficiency is much smaller than the scattering efficiency. Moreover, the scattering is primarily in the forward direction, which is the basis of using the paraxial approximation. Therefore, the bulk backscattering may be neglected when considering the light propagation problem, since its contribution is small. An example of this is skin tissue (cell sizes of 5-10 microns diameter and index of refraction ratio of 1.45/1.4=1.04).

It is well-known that a medium with random scattering inhomogeneities will produce an amplification effect of the mean intensity in the strictly backward direction, as compared to the corresponding intensity obtained in the homogeneous medium [67]. This so-called enhanced backscattering is due to multichannel coherence effects (i.e., interference at a source point between waves transmitted in the forward and backward directions by the same inhomogeneities in the medium). Additionally, because of conservation of energy, enhanced backscattering is accompanied by a corresponding reduction in intensity in directions close to the strictly backward direction. In general, as discussed in Ref. [67], the linear dimension of the region surrounding the strictly backward direction where enhanced backscattering is obtained is of the order or less than the transverse intensity correlation length, l. The corresponding reduction of intensity occurs near the surface of a cone of angle of the order l/Z, where Z is the (one way) propagation distance in the medium. Strictly speaking, enhanced backscattering effects are obtained in situations where the linear dimensions of the illuminated region, a, in the backscattering plane satisfies $a^2<<\lambda Z$, where λ is the wavelength. When the radiation at some point $\mathbf{P}$ in the observation plane results from illuminated regions that are large compared to $[\lambda Z]^{1/2}$, $\mathbf{P}$ will not be in the strictly backscattered direction with respect to the reflected light and, as a consequence, enhanced backscattering will not be

manifested. In all cases considered here $a>>[\lambda Z]^{1/2}$, and therefore enhanced backscattering effects are neglected.

As indicated in *Figure 1,* the signal of interest results from diffuse reflection at the discontinuity of interest only. As discussed above, the statistics of the forward and back propagating optical waves are assumed here to be independent. This case has been treated in section 14.2, and from equation 21 with $\mathbf{p}_{1,2}=\mathbf{P}\pm\mathbf{p}/2$, the EHF solution for the mutual coherence function for diffuse reflection in the discontinuity plane, and observation in the lens plane, is given by

$$\begin{aligned}&\left\langle U(\mathbf{P}+\mathbf{p}/2)U^{*}(\mathbf{P}-\mathbf{p}/2)\right\rangle = \\ &\frac{4\pi}{k^{2}}\int d\mathbf{r}\left\langle I_{B}(\mathbf{r})\right\rangle G_{0}(\mathbf{r},\mathbf{P}+\mathbf{p}/2)G_{0}^{*}(\mathbf{r},\mathbf{P}-\mathbf{p}/2)\Gamma_{pt}(\rho).\end{aligned} \tag{66}$$

$\langle I_B(r)\rangle$ is the mean backscattered irradiance distribution in the plane of the discontinuity, $\Gamma_{pt}(p)$ is the mutual coherence function of a point source located in the discontinuity plane and observed in the lens plane, where $p=|\mathbf{p}_1-\mathbf{p}_2|$, and $G_0(\mathbf{r},\mathbf{p})$ is the Huygens-Fresnel Green's function for homogeneous media given, in general, by [28]

$$G_{0}(\mathbf{r},\mathbf{p})=-\frac{ik}{2\pi B_{b}}\exp\left[-\frac{ik}{2B_{b}}\left(A_{b}r^{2}-2\mathbf{r}\cdot\mathbf{p}+D_{b}p^{2}\right)\right], \tag{67}$$

where A_b, B_b, and D_b are the (real) ABCD ray-matrix elements for back propagation through the optical system (because we are dealing with "real" ABCD optical systems, we tacitly assume that $B\neq 0$). To be as general as possible, we assume an arbitrary ABCD optical system between the lens and discontinuity planes, respectively. For the OCT geometry, we have $A_b=D_b=1$, and $B_b=d+z/n$, where d is the distance from the lens to the tissue surface, n is the mean index of refraction of the tissue, and z is the depth of the discontinuity. In equation 66, the positive definite quantity Γ_{pt} is the mutual coherence of a point source located in the discontinuity plane and observed in the initial lens plane, i.e., the mutual coherence function for backwards propagation through the medium. This quantity is given by [33]

$$\Gamma_{pt}(p)=\exp\left\{-s\left[1-b_{\phi}(p)\right]\right\}, \tag{68}$$

where the optical depth $s=\mu_s z$. The quantity μ_s is the bulk scattering coefficient, and $b_\phi(p)$ is the normalized phase autocorrelation function of a point source whose origin is in the discontinuity plane given by [33]

$$b_{\phi}(p) = \frac{\int_0^z dz' \int_0^{\infty} \sigma(\theta; z') J_0(kp_s\theta)\theta d\theta}{\int_0^z dz' \int_0^{\infty} \sigma(\theta; z')\theta d\theta}, \tag{69}$$

J_0 is the Bessel function of the first kind of order zero,

$$p_s = \frac{B_b(z')}{B_b} p, \tag{70}$$

where $B_b(z')$ is the B-matrix element for back propagation from the discontinuity plane to a distance z', and $\sigma(\theta,z')$ is interpreted as the volume scattering function as a function of position measured from the discontinuity plane in the optical system [28]. Strictly speaking, equation 68 applies to the case where the scattering is in the near-forward direction and all of the scattered light being contained within the collection solid angle of the optical system being used. For propagation in an inhomogeneous medium where appreciable light is scattered outside of the collection solid angle, the mutual coherence function of equation 68 becomes $\Gamma_{pt}(p)=\exp\{-s_W-s_N[1-b_\phi(p)]\}$, where the subscripts N and W refer to the near-forward and wide-angle contributions to the optical depth, respectively [61,64,68]. That is, the portion of the light scattered outside of the collection solid angle thus appears much like an effective absorption coefficient for propagation in the near-forward direction. We note that all correlation functions of interest here can be expressed directly in terms of the spectral densities via the relation $\sigma(\theta)=2\pi k^4\Phi_n(k\theta)$, where Φ_n is the three-dimensional spectrum of the index of refraction inhomogeneities, and we have omitted the functional dependence on path length for notational simplicity [41]. For the OCT geometry, we have $\sigma(\theta,z')=\sigma(\theta)$ for $0\le z'\le z$, and 0 otherwise; $B_b(z')=z'/n$ for $0\le z'\le z$, and $B_b(z')=z/n+z'-z$, for $z\le z'\le d+z$.

In the present section, it is tacitly assumed that we are dealing with a statistically stationary and isotropic random medium. Then, it is well known that all second-order spatial correlation functions of the optical field, such as $\Gamma_{pt}(p)$, are functions of the magnitude of the difference of the spatial coordinates and satisfies the identity $\Gamma_{pt}(-p)=\Gamma_{pt}^*(p)$ [41].

Because the point source mutual coherence function given in equation 68 is valid for arbitrary values of the optical depth s [41], the results given below for the Wigner phase-space distribution function are valid in both the single and multiple scattering regimes, i.e., arbitrary values of s.

Substituting equations 66 and 67 into equation 65 and simplifying yields

$$W(\mathbf{P},\mathbf{q}) = \frac{1}{\pi B^2}\int \frac{d\mathbf{p}}{(2\pi)^2}\exp\left[i\mathbf{p}\cdot\left(\mathbf{q}-\frac{kD}{B}\mathbf{P}\right)\right]\Gamma_{pt}(p)H(\mathbf{p}), \quad (71)$$

where

$$H(\mathbf{p}) = \int d\mathbf{r}\left\langle I_B(\mathbf{r})\right\rangle \exp\left[i\frac{k}{B_b}\mathbf{p}\cdot\mathbf{r}\right] \quad (72)$$

is related to the Fourier transform of $\langle I_B(\mathbf{r})\rangle$. In Ref. [65], it is shown that

$$H(\mathbf{p}) = R_d\Gamma_{pt}(-p)K(-\mathbf{p}) = R_d\Gamma^*_{pt}(p)K(-\mathbf{p}), \quad (73)$$

where R_d is the reflection coefficient of the discontinuity,

$$K(\mathbf{r}) = \int d\mathbf{R}U_{Si}(\mathbf{R}+\mathbf{r}/2)U^*_{Si}(\mathbf{R}-\mathbf{r}/2)\exp\left[-i\frac{kA}{B}\mathbf{r}\cdot\mathbf{R}\right], \quad (74)$$

and $U_{Si}(\mathbf{r})$ is the initial optical wave function. Substituting equation 73 into equation 71 yields

$$\begin{aligned} W(\mathbf{P},\mathbf{q}) &= \frac{R_d}{\pi B_b^2}\int \frac{d\mathbf{p}}{(2\pi)^2}\left|\Gamma_{pt}(p)\right|^2 K(-\mathbf{p})\exp\left[i\mathbf{p}\cdot\left(\mathbf{q}-\frac{kD_b}{B_b}\mathbf{P}\right)\right] \\ &= \frac{R_d}{2\pi^2 B_b^2}\int_0^\infty dpp\left|\Gamma_{pt}(p)\right|^2 K(p)J_0\left(\left|\mathbf{q}-\frac{kD_b}{B_b}\mathbf{P}\right|p\right) \\ &\quad \left(\text{for axially symmetric } U_{Si}\right). \end{aligned} \quad (75)$$

This is the required general solution for the Wigner phase-space distribution function for diffuse reflection in the paraxial approximation. That is, for a given initial optical wave function and a medium whose scattering function is known, equation 75 is the solution for the Wigner phase-space distribution function, i.e., specific radiance. Note, $I(\mathbf{P}) = \int W(\mathbf{P},\mathbf{q})d\mathbf{q} = R_d P_0/\pi B_b^2$, where P_0 is the transmitted power. As expected for diffuse reflection, the intensity in the observation plane is constant, independent of position.

14.5.1.1 Comments

For general scattering functions $\sigma(\theta)$, the integral indicated in equation 75 cannot be obtained analytically, although numerical results can be readily obtained. However, some general features of the Wigner phase-space distribution function can be obtained by direct examination of the general formula. First, examination of equation 75 reveals that, in general, the Wigner phase-space distribution attains its maximum along the line given by $\mathbf{P}=B_b\mathbf{q}/kD_b=B_b\boldsymbol{\theta}/D_b$. Additionally, because $\Gamma_{pt}(p)$ in equation 68 can be rewritten as

$$\Gamma_{pt}(p) = e^{-s} + e^{-s}\left(\exp\left[sb_{\phi}(p)\right]-1\right), \tag{76}$$

we can conclude, from equations 75 and 76, that in general, the Wigner phase-space distribution function consists of three terms. The square of the first term on the right hand side of equation 76, which corresponds to the ballistic photons, leads to an attenuated distribution of what would be obtained in the absence of the scattering inhomogeneities. The square of the corresponding second term represents a broader halo resulting from multiple scattering in the medium. The third term is a cross term between the ballistic and multiple scattering contributions, respectively. Physically, the cross term is the coherent mixing of the unscattered and multiple scattered light.

Next, for sufficiently large values of the optical depth *s,* examination of equation 68 reveals that Γ_{pt} is nonzero for $s[1-b_{\phi}(p)]$ less than the order unity, that is for $b_{\phi}(p)$ near unity. Expanding $b_{\phi}(p)$ in powers of p and retaining the first two non-zero terms allows one to obtain asymptotic results. In the limit $s>>1$, for all cases of practical concern, the resulting width of $|\Gamma_{pt}(p)|^2$ is much narrower than $K(p)$, and without loss of generality, we may replace $K(p)$ by its value at the origin $K(0)=P_0$, the transmitted power [see equation 74].

14.5.2 Applications to Optical Coherence Tomography

It follows from the analysis in section 14.2 that the signal-to-noise ratio (*SNR*) in a standard OCT system can be expressed as

$$SNR = \text{constant} \times \operatorname{Re}\left[\int\int \Gamma_R(\mathbf{P}+\mathbf{p}/2,\mathbf{P}-\mathbf{p}/2)\Gamma_S(\mathbf{P}+\mathbf{p}/2,\mathbf{P}-\mathbf{p}/2)\,d\mathbf{P}d\mathbf{p}\right], \tag{77}$$

where Re denotes the real part, Γ_R and Γ_S are the mutual coherence functions of the (deterministic) reference beam and sample beam in the mixing plane, respectively. Because the Wigner phase-space distribution function and the mutual coherence function are Fourier transform related, see equation 65, the *SNR* can be rewritten as

$$SNR = \text{constant} \times \text{Re}\left[\int\int W_R(\mathbf{P}, -\mathbf{q}) W_S(\mathbf{P}, \mathbf{q})\, d\mathbf{P} d\mathbf{q} \right], \tag{78}$$

where W_R and W_S are the corresponding Wigner phase-space distribution functions of the reference and sample beams, respectively. Equation 78 indicates, in particular, that the *SNR* of a standard OCT system is related globally to the Wigner phase-space distribution function of the sample beam. That is, images obtained from standard OCT systems contain global, rather than local, information of the Wigner phase-space distribution function of the sample beam. Improved OCT imagery can thus only be obtained from systems that make use of the local properties of the Wigner phase-space distribution function, rather than globally where information is inevitably lost. Below, we derive expressions for the Wigner phase-space distribution function of the sample beam for a standard OCT geometry for both classes of scattering functions discussed in Ref. [65].

Consider an OCT system where the initial optical wave function (i.e., immediately following the lens) is given by

$$U_{Si}(r) = \sqrt{\frac{P_0}{\pi w_0^2}} \exp\left[-\frac{r^2}{2}\left(\frac{1}{w_0^2} + \frac{ik}{f} \right) \right]. \tag{79}$$

For an OCT system, focusing at a tissue discontinuity at depth z, we then get the following equation for $K(r)$

$$K(r) = P_0 \exp\left[-\frac{r^2}{4w_0^2} \right], \tag{80}$$

and using equation 78 the heterodyne efficiency factor for the OCT signal for such a system may be written as

$$\Psi \equiv \frac{SNR}{SNR_0} = \frac{\int |K(\mathbf{p})|^2 \left| \Gamma_{pt}(\mathbf{p}) \right|^2 d\mathbf{p}}{\int |K(\mathbf{p})|^2 d\mathbf{p}}. \tag{81}$$

We now obtain analytic engineering approximations for the Wigner phase-space distribution function, valid for all values of *s,* for b_ϕ that are quadratic near the origin. Substituting equation 17 in Ref. [65] and equation 80 into equation 75 and simplifying yields

$$W(\mathbf{P},\mathbf{q}) \cong \frac{R_d P_0 4w_0^2}{(2\pi f)^2}\left[e^{-2s}\exp\left(-Q^2 w_0^2\right) + e^{-s}\left(1-e^{-s}\right)\frac{\tilde{\rho}_0^2}{4w_0^2}\exp\left(-\frac{Q^2\tilde{\rho}_0^2}{4}\right) + \left(1-e^{-s}\right)^2\frac{\tilde{\rho}_0^2}{8w_0^2}\exp\left(-\frac{Q^2\tilde{\rho}_0^2}{8}\right)\right], \quad (82)$$

where

$$\frac{1}{\tilde{\rho}_0^2} = \frac{1}{\rho_0^2} + \frac{1}{4w_0^2}, \quad (83)$$

$$\rho_0 = \sqrt{\frac{3}{s}}\frac{\lambda}{\pi\theta_{rms}}\left(\frac{nf}{z}\right). \quad (84)$$

Here $Q=|\mathbf{q}-(k/f)\mathbf{P}|$. The first, second, and third terms on the right hand side of equation 82 represent the ballistic, cross and multiple scattering contributions to the Wigner phase-space distribution function discussed below equation 76, respectively.

In the limit of $s<<1$, examination of equation 82 reveals that for **P=0,** the $1/e$ transverse momentum width, Δ_q, of the Wigner phase-space distribution is given by $\Delta_q=1/w_0$. Furthermore, in the limit $s>>1$, $\Delta_q=2\sqrt{2}\tilde{\rho}_0^{-1}$, where $\tilde{\rho}_0 \cong \rho_0$. In this case, $\Delta_q \propto z^{3/2}$ in the presence of the shower curtain effect, which manifests itself in the standard OCT geometry. For comparison, $\Delta_q \propto z^{1/2}$ in the absence of the shower curtain effect.

We have not been able to obtain a corresponding analytic approximation, valid for all values of *s,* for the Henyey-Greenstein type of scattering function [65]. For this case, we can only conclude that

$$W(\mathbf{P},\mathbf{q}) \cong \frac{R_d P_0}{(2\pi f)^2}(1-2s)\exp\left[-Q^2 w_0^2\right], \quad s<<1\ ; \quad (85)$$

and

$$W(\mathbf{P},\mathbf{q}) \cong \frac{R_d P_0}{\pi (2\pi f)^2}\left(\frac{r_0}{s}\right)^2 \frac{1}{\left(1+\left(\frac{r_0}{s}\right)^2\left|\mathbf{q}-\frac{k}{f}\mathbf{P}\right|^2\right)^{3/2}}, \quad s>>1, \qquad (86)$$

where $r_0=\{[\lambda g^{1/2}]/[2\pi(1-g)]\}[nf/z]$. In the limit of $s<<1$, examination of equation 85 reveals that for $\mathbf{P=0}$, the $1/e$ transverse momentum width, Δ_q, of the Wigner phase-space distribution is given by $\Delta_q=1/w_0$. Furthermore, in the limit $s>>1$, it is obtained from equation 86 that $\Delta_q=s/r_0$. In this case, $\Delta_q \propto z^2$ in the presence of the shower curtain effect. For comparison, $\Delta_q \propto z$ in the absence of the shower curtain effect.

It is important to note that for both types of scattering functions, the momentum width increases with increasing depth as z^{γ}, with considerably larger values of γ being obtained in the presence of the shower curtain effect. Furthermore, the actual value of γ is highly dependent on the details of the scattering function [65].

As shown above, it is possible to determine the lateral coherence length of the sample field from measurements of the Wigner phase-space distribution. As is evident from equation 84, the lateral coherence length depends on the optical parameters of the tissue, i.e., n, μ_s, and θ_{rms}. Therefore, it is feasible to create images based on measurements of the lateral coherence length as a function of position in the tissue. In contrast to OCT signals used to create conventional OCT images, the lateral coherence length is related only to the propagation of the light in the tissue, and its magnitude is independent of the amount of light backscattered or reflected at the probed depth.

In general, a discontinuity between two tissue layers is characterized by a change of the scattering coefficient, the backscattering coefficient, and the index of refraction. The relative change of the scattering coefficient and the backscattering coefficient is markedly greater than the corresponding relative change in the index of refraction [31]. In human skin tissue, for example, the scattering coefficients of epidermis and dermis are 50 mm^{-1} and 21.7 mm^{-1}, respectively, while the indices of refraction are lying in the range 1.37–1.5 [31]. On this basis, it can be shown from the analysis above, that an imaging system, based on measurements of the lateral coherence length, may have a higher sensitivity to changes in the scattering coefficient than the conventional OCT system probing the corresponding change in the backscattering coefficient. The higher sensitivity may lead to an improved contrast in the obtained image. This model and the above discussion gives more insight into the ideas presented recently that new venues for medical imaging may be based on coherence tomography using measurements of Wigner phase-space distributions [60–65].

APPENDIX A

The 4F system described in subsection 14.3.1 is inspected where we have designated three transverse coordinate planes (see *Figure 6*): the *p*-plane coinciding with the optical fiber, the *q*-plane coinciding with the diffusely reflecting discontinuity within the sample and the *r*-plane coinciding with the right side of the thin focusing lens at $z = -d$. By applying approximations identical to those used in Ref. [10] we now wish to show the following two statements. Firstly, that the heterodyne efficiency factor, defined by the cross-correlations of the sample and reference fields at the p-plane, may be written in terms of their respective intensities only, so that

$$\Psi_p = \frac{\langle i^2 \rangle}{\langle i_0^2 \rangle} = \frac{\int I_R(\mathbf{p}) \langle I_S(\mathbf{p}) \rangle d^2\mathbf{p}}{\int I_R(\mathbf{p}) \langle I_{S0}(\mathbf{p}) \rangle d^2\mathbf{p}}, \tag{A1}$$

where the integrals are taken over the *p*-plane and I_R, $\langle I_S(\mathbf{p}) \rangle$ and $\langle I_{S0}(\mathbf{p}) \rangle$ are the intensities of the reference, the ensemble average of the reflected light from the discontinuity and the ensemble average of the reflected light from the discontinuity in the absence of scattering, respectively. Secondly, that this calculation of the heterodyne efficiency factor Ψ in the *p*-plane, Ψ_p, is mathematically identical to calculating Ψ in the *r*-plane, Ψ_r, as given by equation (57), so that

$$\begin{aligned} \Psi_r &= \frac{\mathrm{Re}\left[\iint \Gamma_R(\mathbf{r}_1, \mathbf{r}_2) \langle \Gamma_S(\mathbf{r}_1, \mathbf{r}_2) \rangle d\mathbf{r}_1 d\mathbf{r}_2 \right]}{\mathrm{Re}\left[\iint \Gamma_R(\mathbf{r}_1, \mathbf{r}_2) \langle \Gamma_{S0}(\mathbf{r}_1, \mathbf{r}_2) \rangle d\mathbf{r}_1 d\mathbf{r}_2 \right]} \\ &= \frac{\mathrm{Re}\left[\iint \Gamma_R(\mathbf{p}_1, \mathbf{p}_2) \langle \Gamma_S(\mathbf{p}_1, \mathbf{p}_2) \rangle d\mathbf{p}_1 d\mathbf{p}_2 \right]}{\mathrm{Re}\left[\iint \Gamma_R(\mathbf{p}_1, \mathbf{p}_2) \langle \Gamma_{S0}(\mathbf{p}_1, \mathbf{p}_2) \rangle d\mathbf{p}_1 d\mathbf{p}_2 \right]} = \Psi_p. \end{aligned} \tag{A2}$$

To outline the derivation, the proof will be initiated by finding the field U_S due to an initial field propagating from the *r*-plane towards the sample and reflecting off the discontinuity. This field is then used to calculated the cross correlation $\langle \Gamma_S(\mathbf{p}_1, \mathbf{p}_2) \rangle = \langle U_S(\mathbf{p}_1) U_S^*(\mathbf{p}_2) \rangle$ and it is shown that U_S is delta-correlated [35] and thus the validity of equation A1 is demonstrated. It is then demonstrated that the obtained expression for Ψ_p is identical to equation 81. Because we are only concerned with the ratio Ψ any multiplicative constant not related to the properties of the scattering medium are omitted.

Using the Huygens-Fresnel principle the field at the *p*-plane, U_S, due to a field immediately to the right of the focusing lens in the *r*-plane, U_r, is given by

$$U_S(\mathbf{r},\mathbf{p}) = \int U_r(\mathbf{r}) G_{r-p}(\mathbf{r},\mathbf{p})\, d^2\mathbf{r}, \tag{A3}$$

where $G_{r\text{-}p}(\mathbf{r},\mathbf{p})$ is the Huygens-Fresnel Green's function for propagation from the *r*-plane to the *p*-plane. For a general ABCD matrix system this Green's function is given by [28]

$$G_0(\mathbf{r},\mathbf{p}) = -\frac{ik}{2\pi B}\exp\left[-\frac{ik}{2B}\left(Ar^2 - 2\mathbf{r}\cdot\mathbf{p} + Dp^2\right)\right], \tag{A4}$$

where *A, B,* and *D* are the matrix elements, and the notation *r* denotes the length of the vector **r**. For the propagation from *r* to *p; A*=–1, *B*=*f* and *D*=–1. The field at the *r*-plane due to a field, U_q, impinging upon the discontinuity is found using the EHF principle

$$U_r(\mathbf{r}) = \int \eta(\mathbf{q}) U_q(\mathbf{q}) G_f(\mathbf{q},\mathbf{r}) \exp\left[i\varphi(\mathbf{q},\mathbf{r})\right] d^2\mathbf{q}, \tag{A5}$$

where G_f is the Green's function for propagating the optical distance *f* given by equation A4 with the matrix elements *A*=1, *B*=*f* and *D*=1. $\varphi(\mathbf{q},\mathbf{r})$ is the stochastic phase added to the phase of a spherical wave propagating from **q** to **r** due to the scattering medium, and $\eta(\mathbf{q})$ is a complex reflection coefficient due to the discontinuity. Calculating the cross-correlation of the field U_S yields

$$\begin{aligned}\Gamma_S(\mathbf{p}_1,\mathbf{p}_2) = \iiiint & G_f(\mathbf{q},\mathbf{r}) G_f^*(\mathbf{q}',\mathbf{r}') G_{r-p}(\mathbf{r},\mathbf{p}_1) G_{r-p}^*(\mathbf{r}',\mathbf{p}_2) \\ & \times \left\langle U_q(\mathbf{q}) U_q^*(\mathbf{q}')\right\rangle \left\langle \eta(\mathbf{q})\eta(\mathbf{q}')\right\rangle \\ & \times \left\langle \exp\left[i\varphi(\mathbf{q},\mathbf{r}) - i\varphi(\mathbf{q}',\mathbf{r}')\right]\right\rangle d^2\mathbf{r} d^2\mathbf{r}' d^2\mathbf{q} d^2\mathbf{q}',\end{aligned} \tag{A6}$$

where primed variables are related to U_S^* and we have assumed that the scattering medium and the properties of the diffusely discontinuity are independent. It should also be noted that in writing $\langle U_q(\mathbf{q})U_q^*(\mathbf{q}')\exp[i\varphi(\mathbf{q},\mathbf{r})-i\varphi(\mathbf{q}',\mathbf{r}')]\rangle = \langle U_q(\mathbf{q})U_q^*(\mathbf{q}')\rangle \times \langle \exp[i\varphi(\mathbf{q},\mathbf{r})-i\varphi(\mathbf{q}',\mathbf{r}')]\rangle$ it has been assumed that the phase distortion due to the scattering medium added to the field propagating from L2 to the discontinuity is statistically independent of that added to the field propagating from the discontinuity to L2. The validity

of this assumption in MC simulations is discussed in subsection 14.3.3. Because the discontinuity is diffusely reflecting $\langle \eta(\mathbf{q})\eta(\mathbf{q}')\rangle=(4\pi/k^2)\delta(\mathbf{q}-\mathbf{q}')$, where $\delta(\mathbf{r})$ is the two-dimensional Dirac's delta function [27]. This yields

$$\Gamma_S(\mathbf{p}_1,\mathbf{p}_2)=\iiiint G_f(\mathbf{q},\mathbf{r})G_f^*(\mathbf{q},\mathbf{r}')G_{r-p}(\mathbf{r},\mathbf{p}_1)G_{r-p}^*(\mathbf{r}',\mathbf{p}_2) \times\left\langle I_q(\mathbf{q})\right\rangle\Gamma_{PT}(\mathbf{r}-\mathbf{r}')d^2\mathbf{r}d^2\mathbf{r}'d^2\mathbf{q}, \tag{A7}$$

where Γ_{PT} is given by equation 41 and I_q is the intensity of the field U_q. The average intensity $\langle I_q(\mathbf{q})\rangle$ can be found from equation 39 and it is noted that the difference vector, $\boldsymbol{\rho}$, in equation 39 is independent of $\mathbf{r}$ and $\mathbf{r}'$ in equation A7. Now, invoking the sum and difference coordinates $\mathbf{R}=\frac{1}{2}(\mathbf{r}+\mathbf{r}')$ and $\boldsymbol{\rho}=\mathbf{r}-\mathbf{r}'$ and performing the q-integration and the ρ-integration originating from equation 39 yields

$$\Gamma_S(\mathbf{p}_2,\mathbf{p}_2)=\iint\exp\left[-\frac{ik}{2f}\left\{p_2^2-p_1^2-\boldsymbol{\rho}\cdot(\mathbf{p}_1+\mathbf{p}_2)+2\mathbf{R}\cdot(\mathbf{p}-\mathbf{p}_1)\right\}\right], \times\left|\Gamma_{PT}(\boldsymbol{\rho})\right|^2K(-\boldsymbol{\rho})d^2\boldsymbol{\rho}d^2\mathbf{R}, \tag{A8}$$

where we have used the relation

$$\int\exp\left[i\mathbf{m}\cdot(\mathbf{u}+\mathbf{v})\right]d^2\mathbf{m}=(2\pi)^2\delta(\mathbf{u}+\mathbf{v}). \tag{A9}$$

Carrying out the $\mathbf{R}$-integration then yields

$$\Gamma_S(\mathbf{p}_2,\mathbf{p}_2)=\delta(\mathbf{p}_2-\mathbf{p}_1)\int\exp\left[-\frac{ik}{2f}\left\{p_2^2-p_1^2-\boldsymbol{\rho}\cdot(\mathbf{p}_1+\mathbf{p}_2)\right\}\right] \times\left|\Gamma_{PT}(\boldsymbol{\rho})\right|^2K(-\boldsymbol{\rho})d^2\boldsymbol{\rho} \tag{A10}$$

which shows the sample U_S to be delta-correlated and thus equation A1 is proven.

To calculate equation A1 we consider equation A8 for the case $\mathbf{p}_1=\mathbf{p}_2=\mathbf{p}$, which then yields the intensity

$$\left\langle I_S(\mathbf{p})\right\rangle=A_{lens}\int\exp\left[-\frac{ik}{f}\boldsymbol{\rho}\cdot\mathbf{p}\right]\left|\Gamma_{PT}(\boldsymbol{\rho})\right|^2K(-\boldsymbol{\rho})d^2\boldsymbol{\rho}, \tag{A11}$$

where A_{lens} is the area of the focusing lens.

To find the OCT signal $\langle i^2 \rangle$ we now insert equation A11 into the numerator of equation A1

$$\begin{aligned} \langle i^2 \rangle &= \iint \exp\left[-\frac{ik}{2f}(-2\boldsymbol{\rho}\cdot\mathbf{p}) \right] \left|\Gamma_{PT}(\boldsymbol{\rho})\right|^2 K(-\boldsymbol{\rho}) I_R(\mathbf{p}) d^2\boldsymbol{\rho} d^2\mathbf{p} \\ &= \int \left|\Gamma_{PT}(\boldsymbol{\rho})\right|^2 \left|K(\boldsymbol{\rho})\right|^2 d^2\boldsymbol{\rho}, \end{aligned} \tag{A12}$$

where we have used that the reference field impinging on the reference mirror may be calculated using equation 39 with $\Gamma_{PT}=1$, and $A=1$ and $B=f$. Because the p-plane is the conjugate plane to the plane of the reference mirror, the field here is identical to that impinging upon the reference mirror. Γ_{PT} is unity in the absence of scattering so it is now easy to see that Ψ may be calculated through

$$\Psi_p = \frac{\int \left|\Gamma_{PT}(\boldsymbol{\rho})\right|^2 \left|K(\boldsymbol{\rho})\right|^2 d^2\boldsymbol{\rho}}{\int \left|K(\boldsymbol{\rho})\right|^2 d^2\boldsymbol{\rho}}. \tag{A13}$$

Note that the integration is over the r-plane. It is seen that Ψ_p is identical to Ψ_r given by equation 81. It has thus been proven that within the approximation of the EHF principle the heterodyne efficiency factor of the OCT system depends solely upon the intensity distributions of the reference and sample fields in the p-plane. Furthermore, it is straightforward to prove that this will be true for any conjugate plane to a diffusely reflecting discontinuity plane within the sample.

One should note that there exists an ambiguity between obtaining a delta function in equation A10 and obtaining a finite area of the focusing lens in equation A11. Firstly, this area is irrelevant for the heterodyne efficiency factor and no assumption of a finite lens area is made in subsection 14.2.2. Furthermore, it is easy to show that equation A13 is just as well obtained by inserting equation A10 into equation A2. Secondly, a finite radius of the focusing lens would have yielded an Airy function in $R_A(\mathbf{p}_1-\mathbf{p}_2)$ instead of a delta function, where R_A is the radius of aperture. Thus, if the aperture is large the sample field will be essentially delta-correlated in the p-plane.

REFERENCES

1. D. Huang, E. A. Swanson, C. P. Lin, J. S. Schuman, W. G. Stinson, W. Chang, M. R. Hee, T. Flotte, K. Gregory, C. A. Puliafito, and J. G. Fujimoto, "Optical coherence tomography", *Science* **254**, 1178–1181 (1991).
2. J. M. Schmitt, A. Knüttel, and R. F. Bonner, "Measurement of optical properties of biological tissues by low-coherence reflectometry", *Appl. Opt.* **32**, 6032–6042 (1993).
3. J. M. Schmitt, A. Knüttel, A. S. Gandjbakhche, and R. F. Bonner, "Optical characterization of dense tissues using low-coherence interferometry", *Proc. SPIE* **1889,** 197–211(1993).
4. M. J. Yadlowsky, J. M. Schmitt, and R. F. Bonner, "Multiple scattering in optical coherence microscopy", *Appl. Opt.* **34,** 5699–5707 (1995).
5. M. J. Yadlowsky, J. M. Schmitt, and R. F. Bonner, "Contrast and resolution in the optical coherence microscopy of dense biological tissue", *Proc. SPIE* **2387**, 193–203 (1995).
6. Y. Pan, R. Birngruber, and R. Engelhardt, "Contrast limits of coherence-gated imaging in scattering media", *Appl. Opt.* **36**, 2979–2983 (1997).
7. L. S. Dolin, "A theory of optical coherence tomography", *Radiophys. and Quant. Electr.* **41,**850–873(1998).
8. J. M. Schmitt and A. Knüttel, "Model of optical coherence tomography of heterogeneous tissue", *J. Opt. Soc. Am. A* **14**, 1231–1242 (1997).
9. D. J. Smithies, T. Lindmo, Z. Chen, J. S. Nelson, and T. E. Milner, "Signal attenuation and localization in optical coherence tomography studied by Monte Carlo simulation", *Phys. Med. Biol.* **43**, 3025–3044 (1998).
10. L. Thrane, H. T. Yura, and P. E. Andersen, "Analysis of optical coherence tomography systems based on the extended Huygens-Fresnel principle", *J. Opt. Soc. Am. A* **17,** 484–490 (2000).
11. A. Tycho, T. M. Jørgensen, H. T. Yura, and P. E. Andersen, "Derivation of a Monte Carlo method for modeling heterodyne detection in optical coherence tomography systems", *Appl. Opt.* **41**, 6676–6691 (2002).
12. H. Kahn and T. E. Harris, "Estimation of particle transmission by random sampling", in *Monte Carlo Methods* (vol. 12 of National Bureau of Standards Applied Mathematics Series, U. S. Government Printing Office, 1951).
13. B. C. Wilson and G. Adam, "A Monte Carlo model for the absorption and flux distributions of light in tissue", *Med. Phys.* **10,** 824–830 (1983).
14. L. Thrane, H. T. Yura, and P. E. Andersen, "Optical coherence tomography: New analytical model and the shower curtain effect", *Proc. SPIE* **4001,** 202–208 (2000).
15. L. Thrane, H. T. Yura, and P. E. Andersen, "Calculation of the maximum obtainable probing depth of optical coherence tomography in tissue", *Proc. SPIE* **3915**, 2–11 (2000).
16. P. E. Andersen, L. Thrane, H. T. Yura, A. Tycho, and T. M. Jørgensen, "Modeling the optical coherence tomography geometry using the extended Huygens-Fresnel principle and Monte Carlo simulations", *Proc. SPIE* **3914,** 394–406 (2000).
17. H. T. Yura, "Signal-to-noise ratio of heterodyne lidar systems in the presence of atmospheric turbulence", *Optica Acta* **26,** 627–644 (1979).

18. I. Dror, A. Sandrov, and N. S. Kopeika, "Experimental investigation of the influence of the relative position of the scattering layer on image quality: the shower curtain effect", *Appl. Opt.* **37,** 6495–6499 (1998).
19. V. I. Tatarskii, *Wave Propagation in a Turbulent Medium* (McGraw-Hill, New York, 1961).
20. A. Ishimaru, *Wave Propagation and Scattering in Random Media* (IEEE Press, Piscataway, New Jersey, 1997).
21. *Laser Beam Propagation in the Atmosphere,* J. Strohbehn ed. (Springer, New York, 1978).
22. R. L. Fante, "Wave propagation in random media: A systems approach", in *Progress in Optics XXII,* E. Wolf ed. (Elsevier, New York, 1985).
23. J. M. Schmitt and G. Kumar, "Turbulent nature of refractive-index variations in biological tissue", *Opt. Lett.* **21,** 1310–1312 (1996).
24. S. M. Rytov, Y. A. Kravtsov, and V. I. Tatarskii, "Principles of statistical radiophysics" in *Wave Propagation Through Random Media* Vol. 4 (Springer, Berlin, 1989).
25. R. F. Lutomirski and H. T. Yura, "Propagation of a finite optical beam in an inhomogeneous medium", *Appl. Opt.* **10,** 1652–1658 (1971).
26. Z. I. Feizulin and Y. A. Kravtsov, "Expansion of a laser beam in a turbulent medium", *Izv. Vyssh. Uchebn. Zaved. Radiofiz.* **24,** 1351–1355 (1967).
27. J. W. Goodman, *Introduction to Fourier Optics* (McGraw-Hill, Singapore, second ed., 1996).
28. H. T. Yura and S. G. Hanson, "Optical beam wave propagation through complex optical systems", *J. Opt. Soc. Am. A* **4***,* 1931–1948 (1987).
29. H. T. Yura and S. G. Hanson, "Second-order statistics for wave propagation through complex optical systems", *J. Opt. Soc. Am. A* **6,** 564–575 (1989).
30. A. E. Siegman, *Lasers* (University Science Books, Mill Valley, California, 1986), 626–630.
31. M. J. C. Van Gemert, S. L. Jacques, H. J. C. M. Sterenborg, and W. M. Star, "Skin optics", *IEEE Trans. Biomed. Eng.* **36**, 1146–1154 (1989).
32. C. F. Bohren and D. R. Huffman, *Absorption and Scattering of Light by Small Particles* (J. Wiley & Sons, New York, 1983).
33. H. T. Yura and S. G. Hanson, "Effects of receiver optics contamination on the performance of laser velocimeter systems", *J. Opt. Soc. Am. A* **13**, 1891–1902 (1996).
34. L. Thrane, *Optical coherence tomography: Modeling and applications* (Risø National Laboratory, Denmark; PhD dissertation (2000), ISBN 87-550-2771-7).
35. J. W. Goodman, *Statistical Optics* (J. Wiley & Sons, New York, 1985).
36. L. G. Henyey and J. L. Greenstein, "Diffuse radiation in the galaxy", *Astro-Physical J.,* **93,** 70–83 (1941).
37. S. L. Jacques, C. A. Alter, and S. A. Prahl, "Angular dependence of He-Ne laser light scattering by human dermis", *Lasers Life Sci.* **1**, 309–333 (1987).
38. C. M. Sonnenschein and F. A. Horrigan, "Signal-to-noise relationships for coaxial systems that heterodyne backscatter from the atmosphere", *Appl. Opt.* **10,** 1600–1604 (1971).
39. D. L. Fried, "Optical heterodyne detection of an atmospherically distorted signal wave front", *Proc. IEEE* **55**, 57–67 (1967).
40. V. V. Tuchin, S. R. Utz, and I. V. Yaroslavsky, "Skin optics: Modeling of light transport and measuring of optical parameters", in *Medical Optical Tomography: Functional Imaging and Monitoring,* **IS11,** G. Mueller, B. Chance, R. Alfano *et al.* eds. (SPIE Press, Bellingham, Washington, 1993), 234–258.

41. V. I. Tatarskii, *The Effects of the Turbulent Atmosphere on Wave Propagation* (National Technical Information Service, Springfield, Va., 1971).
42. A. Tycho and T. M. Jørgensen, "Comment on 'Excitation with a focused, pulsed optical beam in scattering media: diffraction effects", *Appl. Opt.* **41,** 4709–4711 (2002).
43. V. R. Daria, C. Saloma, and S. Kawata, "Excitation with a focused, pulsed optical beam in scattering media: diffraction effects", *Appl. Opt.* **39**, 5244–5255 (2000).
44. J. Schmitt, A. Knüttel, and M. Yadlowski, "Confocal microscopy in turbid media", *J. Opt. Soc. A* **11**, 2226–2235 (1994).
45. J. M. Schmitt and K. Ben-Letaief, "Efficient Monte carlo simulation of confocal microscopy in biological tissue", *J. Opt. Soc. Am. A* **13**, 952–961 (1996).
46. C. M. Blanca and C. Saloma, "Monte Carlo analysis of two-photon fluorescence imaging through a scattering medium", *Appl. Opt.* **37**, 8092–8102 (1998).
47. Y. Pan, R. Birngruber, J. Rosperich, and R. Engelhardt, "Low-coherence optical tomography in turbid tissue – theoretical analysis", *Appl. Opt.* **34**, 6564–6574 (1995).
48. G. Yao and L.V. Wang, "Monte Carlo simulation of an optical coherence tomography signal in homogeneous turbid media", *Phys. Med. Biol.* **44,** 2307–2320 (1999).
49. Z. Song, K. Dong, "X.H. Hu, and J. Q. Lu, "Monte Carlo simulation of converging laser beams propagating in biological materials", *Appl. Opt.* **38**, 2944–2949 (1999).
50. C. M. Blanca and C. Saloma, "Efficient analysis of temporal broadening of a pulsed focused Gaussian beam in scattering media", *Appl. Opt.* **38**, 5433–5437 (1999).
51. L.V. Wang and G. Liang, "Absorption distribution of an optical beam focused into a turbid medium", *Appl. Opt.* **38**, 4951–4958 (1999).
52. A. K. Dunn, C. Smithpeter, A. J. Welch, and Rebecca Richards-Kortum, "Sources of contrast in confocal reflectance imaging", *Appl. Opt.* **35**, 3441–3446 (1996).
53. L.-H. Wang, S. L. Jacques, and L.-Q. Zheng, "MCML – Monte Carlo modeling of photon transport in multi-layered tissues", *Comput. Meth. Prog. Bio.* **47**, 131-146 (1995).
54. S. A. Prahl, M. Keijzer, S. L. Jacques, and A. J. Welch, "A Monte Carlo model for light propagation in tissue" in *Dosimetry of Laser Radiation in Medicine and Biology,* SPIE Institute Series **IS 5** (SPIE Press, Bellingham, Washington, 1998).
55. D. I. Hughes and F. A. Duck, "Automatic attenuation compensation for ultrasonic imaging", *Ultrasound in Med. & Biol.* **23***,* 651–664 (1997).
56. L. Thrane, T. M. Jørgensen, P. E. Andersen, and H. T. Yura, "True-reflection OCT imaging", *Proc. SPIE* **4619,** 36–42 (2002).
57. S. A. Prahl, M. J. C. van Gemert, and A. J. Welch, "Determining the optical properties of turbid media by using the adding-doubling method", *Appl. Opt.* **32**, 559–568 (1993).
58. J. M. Schmitt, S. H. Xiang, and K. M. Yung, "Speckle in optical coherence tomography", *J. Biomed. Opt.* **4***,* 95–105 (1999).
59. E. P. Wigner, "On the quantum correction for thermodynamic equilibrium", *Phys. Rev.* **40**, 749–759 (1932).
60. M. G. Raymer, C. Cheng, D. M. Toloudis, M. Anderson, and M. Beck, "Propagation of Wigner coherence functions in multiple scattering media" in *Advances in Optical Imaging and Photon Migration,* R. R. Alfano and J. G. Fujimoto eds. (Optical Society of America, Washington, D.C., 1996), 236–238.
61. C.-C. Cheng and M. G. Raymer, "Long-range saturation of spatial decoherence in wave-field transport in random multiple-scattering media", *Phys. Rev. Lett.* **82**, 4807–4810 (1999).
62. S. John, G. Pang, and Y. Yang, "Optical coherence propagation and imaging in a multiple scattering medium,"*J. Biomed. Opt.* **1**, 180–191 (1996).

63. A. Wax and J. E. Thomas, "Measurement of smoothed Wigner phase-space distributions for small-angle scattering in a turbid medium," *J. Opt. Soc. Am. A* **15**, 1896–1908 (1998).
64. C.-C. Cheng and M. G. Raymer, "Propagation of transverse optical coherence in random multiple-scattering media", *Phys. Rev. A* **62**, 023811-1–023811-12 (2000).
65. H. T. Yura, L. Thrane, and P. E. Andersen, "Closed-form solution for the Wigner phase-space distribution function for diffuse reflection and small-angle scattering in a random medium", *J. Opt. Soc. Am. A* **17**, 2464–2474 (2000).
66. M. Hillery, R. F. O'Connel, M. O. Scully, and E. P. Wigner, "Distribution functions in physics: fundamentals", *Phys. Rep.* **106,** 121–167 (1984).
67. V. A. Banakh and V. L. Mironov, *LIDAR in a Turbulent Atmosphere* (Artech House, Boston, MA, 1987).
68. M. G. Raymer and C.-C. Cheng, "Propagation of the optical Wigner function in random multiple-scattering media", *Proc. SPIE* **3914,** 372–380 (2000).

Chapter 15

ABSORPTION AND DISPERSION IN OCT

Christoph K. Hitzenberger
Department of Medical Physis, University of Vienna, Vienna A-1090, Austria

Abstract: Conventional optical coherence tomography (OCT) provides spatial information on intensity scattered back by the sample at a single wavelength. Advanced OCT techniques are developed to obtain additional information on the sample. Among these extensions are spectral OCT techniques. By measuring spectral intensity and spectral phase as a function of depth, information on sample absorption and dispersion can be obtained. On the other hand, dispersion can also cause problems, degrading OCT image quality. This chapter discusses spectral OCT techniques and their physical limits, dispersion induced image degradation and possible solutions, and provides a review of literature on absorption and dispersion related phenomena in OCT.

Key words: Optical coherence tomography, absorption, dispersion, spectral OCT

15.1 INTRODUCTION

Conventional optical coherence tomography (OCT), as first reported by D. Huang *et al.* [1], is based on a single probing beam of rather narrow bandwidth, centered at a single wavelength λ_0. This technology measures the distribution of backscattering sites and strength of backscattered signals in transparent and translucent samples with high axial and transversal resolution. Resolution figures on the order of 10 μm (within tissue samples) are typically achieved if a superluminescent diode (SLD) with a bandwidth of ~ 25 nm, centered at $\lambda_0 \cong 800$ nm is used [2,3,4]. The good resolution, which can further be improved by using state of the art $Ti:Al_2O_3$ femtosecond lasers [5], is the main advantage of OCT, as compared to other medical imaging techniques, e.g., ultrasound, CT, and MRI. However, conventional OCT also has some shortcomings: as is well known from

microscopy, many samples, especially biological tissues, show only poor contrast, if they are imaged on a pure intensity basis with only a single wavelength (or at a narrow bandwidth). Different extensions of OCT that employ other properties of light have been reported to improve image contrast and to generate new types of contrast. Among them are the polarization state [6,7,8,9,10] and frequency shifts caused by the Doppler effect of moving sample constituents, e.g., blood cells [11,12,13,14]. These methods are discussed in detail in other chapters of this book.

Other sample properties that change transmitted light beams and might be used for contrast improvement and measurement purposes are absorption [15,16], refractive index variations [17,18], and dispersion [19,20]. Absorption and dispersion in OCT are the topics of this chapter. These effects can be used for image contrast generation, for measurements, but can also have an adverse influence on OCT image quality.

The goal of using absorption properties as contrast generation mechanisms in OCT is to provide depth resolved quantitative tissue spectroscopy. One of the problems of conventional tissue spectroscopy is that Beer's law requires the penetration path length of light. In many cases, backscattering geometry has to be used, mainly because of low light penetration in tissue due to scattering. Because the backscattering geometry, in usual tissue spectroscopy, provides no information on the path length of the light in tissue, quantitative measurements are not possible. OCT provides depth information, therefore the penetration length in tissue becomes available, which offers a possible solution to the problem. Possible application fields cover the determination of location and concentration of absorbing substances like water, hemoglobin (including oxygenation state), cytochrome aa3, NADH, melanin, and other tissue chromophores. This might enable the application of OCT in functional studies.

Dispersion can also be used to obtain quantitative information on tissue constituents. Among the suggested applications are determination of DNA concentration by phase dispersion microscopy [19] and measurement of glucose concentration in aqueous solution [21]. These applications are, however, in a very early state of development. Presently, dispersion is regarded more as a problem for OCT since it can severely degrade OCT signals. Dispersion of optical elements in the two interferometer arms has to be carefully compensated. Furthermore, dispersion of the sample has to be compensated for, especially if measurements are to be performed through large sample depths [22] or if very broadband light sources are to be used in high-resolution OCT [23]. Otherwise, resolution and signal intensity can severely be degraded and image artifacts can arise [24].

The common feature of absorption and dispersion is that they are both wavelength dependent which was the reason for the decision to treat them in a single chapter. No comprehensive theory of these wavelength dependent phenomena in OCT has yet been published. Some basic theoretic

considerations can, however, be found in two recent review articles [3,4] and in original research papers [15,16,22,24,25]. It is the purpose of this chapter to provide a short overview of the theoretical aspects of absorption and dispersion in OCT, and to review the work published so far in these fields.

15.2 THEORETICAL ASPECTS

The principles of OCT have been discussed in detail in previous chapters of this book. Therefore, this chapter on theoretical aspects will be restricted to those basic concepts that are relevant to the understanding of wavelength dependent phenomena. More detailed considerations will be provided in the sub-chapters on absorption and dispersion related phenomena.

15.2.1 Low Coherence Interferometry

We consider a conventional time domain OCT device based on a Michelson interferometer setup, as depicted in Figure 1. As usual with this type of OCT device, the depth information is provided by a low coherence interferometry (LCI) scan (or A-scan), the transversal information is obtained by recording A-scans at several adjacent sample positions. In this section we discuss only the depth scans.

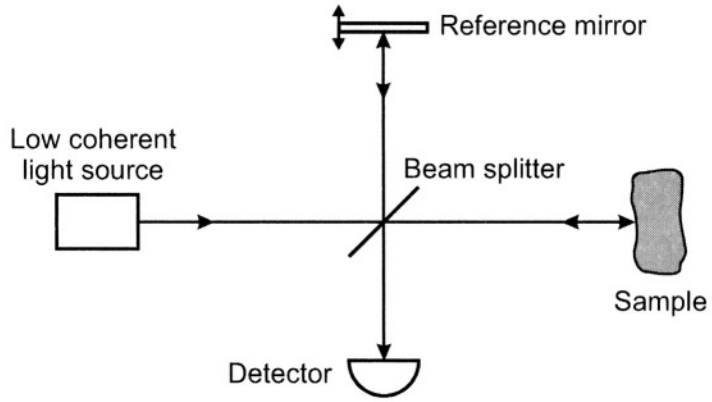

Figure 1. Low coherence Michelson interferometer.

A low coherent light source, e.g., an SLD, emits a light beam of short coherence length towards the Michelson interferometer. The beam is split into two components, the reference beam and the sample beam. After backreflection or – scattering at the reference mirror and the sample, the two beam components are recombined at the beamsplitter and superimposed on a

photodetector. According to the general interference law of partially coherent light beams, the (averaged) intensity at the photodetector is given by [26]:

$$\bar{I}(\tau) = I_s + I_r + 2\mathrm{Re}\{\Gamma_{sr}(\tau)\}, \tag{1}$$

where I_s, I_r are the intensities of sample and reference beam at the detector, respectively, Re means real part, Γ_{sr} is the mutual coherence function (or cross-correlation function) of sample and reference beams, and τ is the time delay between the two beams.

The term $G_{sr}(\tau) = 2\mathrm{Re}\{\Gamma_{sr}(\tau)\}$ is called "signature" of the interferometric signal, or "interferogram" [3,4]. It constitutes the oscillating interference term that depends on the time delay and is used to locate reflective sites in the sample:

$$G_{sr}(\tau) = 2\mathrm{Re}\{\Gamma_{sr}(\tau)\} = 2\sqrt{I_s I_r}\,|\gamma_{sr}(\tau)|\cos(\alpha_{sr} - \Delta_{sr}(\tau)). \tag{2}$$

$\gamma_{sr}(\tau)$ is the complex degree of coherence, α_{sr} is a constant phase, and $\Delta_{sr}(\tau) = 2\pi\bar{\nu}\tau$ is the phase delay between the two beams, with $\bar{\nu}$ the mean light frequency. The time delay τ is related to the path length difference Δz via the speed of light, c, by $\tau = \Delta z/c$. If the sample arm contains a dispersive medium, Δz has to be multiplied by the group refractive index of that medium.

If the sample consists of a single reflective interface (a mirror) located in air (refractive index = 1), the interferogram equals twice the real part of the coherence function (or autocorrelation) of the source light $\Gamma_{source}(\tau)$:

$$G_{sr}(\tau) = 2\mathrm{Re}\{\Gamma_{source}(\tau)\} = G_{source}(\tau). \tag{3}$$

$G_{source}(\tau)$ can be interpreted as the impulse response of an LCI depth scan.

In case of a sample with response function $h(\tau)$, the backscattered electric field is given by a convolution of incident field and response function, and the interferogram can be obtained by [27]:

$$G_{sr}(\tau) = 2\mathrm{Re}\{\Gamma_{sr}(\tau)\} = 2\mathrm{Re}\{\Gamma_{source}(\tau) \otimes h(\tau)\}, \tag{4}$$

where $\otimes$ is the convolution operation. The sample response function $h(\tau)$ resembles the local (amplitude) reflectivity.

15.2.2 Representation in Frequency Domain

We now switch to a representation in Fourier domain where the convolution operation is replaced by a simple multiplication. According to the Wiener-Khintchine theorem, the power spectrum $S_{source}(\nu)$ of a light source is obtained as the Fourier transform (FT) of the source self-coherence function:

$$S_{source}(\nu) = FT\{\Gamma_{source}(\tau)\}. \tag{5}$$

If a sample with response function $h(\tau)$ is in the sample arm, the interferogram in the spectral domain, or cross spectral density of sample and reference beams, $W_{sr}(\nu)$, is obtained by:

$$W_{sr}(\nu) = FT\{\Gamma_{sr}(\tau)\} = S_{source}(\nu) \cdot H(\nu), \tag{6}$$

where $H(\nu) = FT\{h(\tau)\}$ is the sample transfer function.

A real sample that shows absorption and dispersion introduces a frequency dependent phase $\Phi(\nu)$ and signal amplitude proportional to $\sqrt{R(\nu)}$ ($R(\nu)$, intensity reflection coefficient) to the sample transfer function H(ν). In a backscattering geometry, amplitude and phase changes of the transfer function depend on sample depth z:

$$H(\nu, z) = \sqrt{R(\nu, z)} \cdot \exp[i\Phi(\nu, z)]. \tag{7}$$

The amplitude spectrum $\sqrt{R(\nu, z)}$ can be expressed as [15]:

$$R(\nu, z) = \frac{\sigma_b(\nu, z)}{z^2} \cdot \exp\left[-2\int_0^z \mu_t(\nu, z')dz'\right], \tag{8}$$

where $\sigma_b(\nu,z)$ and $\mu_t(\nu,z)$ are the spectral backscatter cross-sections and the mean spectral attenuation coefficient (between the sample surface at z = 0 and the depth z in the sample), respectively. The phase spectrum is:

$$\Phi(\nu, z) = 2\frac{\omega}{c}\int_0^z [n(\nu, z') - 1]dz' = 2\int_0^z [k(\nu) - k_0]dz', \tag{9}$$

where ω is the angular frequency, $n(\nu,z')$ is the sample refractive index, $k(\nu) = 2\pi/\lambda(\nu)$ is the wave number, and k_0 is the mean wave number in air.

In principle, amplitude spectrum and phase spectrum can be obtained from a Fourier transform of the interferogram. This method has been used for simultaneous measurement of spectral absorption and dispersion in different liquid solutions [27]. So far, measurement of detailed spectral information of absorption and dispersion was limited to model substances in cuvettes; no application to depth resolved imaging in scattering media with simultaneous mapping of spectral absorption and/or dispersion curves were yet reported. There seems to be a fundamental limit to obtain spatial and spectral information simultaneously.

15.2.3 Limitations to Absorption and Dispersion Measurements

The amount to which spectral information can be obtained by LCI and OCT methods and the ability to localize the layer that causes a certain spectral change are limited by various factors.

One of the limiting factors is that OCT as a backscattering technique integrates absorption and dispersion effects in depth: If absorption and dispersion of the n-th layer of a layered sample are to be measured, the light has to penetrate the overlying n-1 layers twice. Absorption and dispersion within these superficial layers will influence the light beam and change its amplitude and phase. A differential technique could be used, in which information obtained from light backscattered at the superficial layers is used to subtract their influences. This method, however, requires appropriate layer boundaries that reflect sufficient light to provide the necessary information. Moreover, in scattering samples, speckle effects reduce the visibility of such boundaries and might lead to the necessity of gross signal averaging, thus reducing spatial resolution.

Another limitation are light sources. The most widely used light sources in OCT are SLDs and amplified spontaneous emission (ASE) sources. Both, the range of available center wavelengths λ_0, and bandwidths $\Delta\lambda$ are limited. SLDs are presently not available with λ_0<670 nm; typical SLD wavelengths (bandwidths) are 670 nm (10 nm), 800-850 nm (20-50 nm), 1300 nm (~40 nm), and 1550 nm (70 nm). ASE sources are available in the range 1300–1600 nm, with bandwidths in the range 50–100 nm. These limited wavelength ranges and bandwidths, especially the lack of such sources in the visible range below 670 nm, limit the amount of accessible spectral information. Recently, this situation has improved by the introduction of very broadband light sources to the field of OCT: Kerr-lens mode-locked Cr:forsterite [28] and Ti:sapphire [23] femtosecond pulse lasers operating at 1280 nm (120 nm) and 810 nm (260 nm), respectively, cover a much larger

bandwidth than SLDs or ASE sources, giving access to larger spectral regions. These sources also provide high output power, however, are still very expensive, large, and more difficult to operate. Photonic crystal fiber sources achieve even larger bandwidths; Hartl *et al.* reported a bandwidth of 370 nm centered at 1.3 μm [29], and Povazay *et al.* extended the spectral range farer into the visible, reporting a bandwidth of 370 nm at $\lambda_0 = 725$ nm [30]. While these sources seem promising for spectral OCT, they are still in an experimental state. They have to be pumped by femtosecond laser pulses and their emission spectrum is not very stable and far from a smooth Gaussian shape, causing unfavorable side lobes in the coherence signals.

Probably the most serious problem to spectral OCT techniques is the Fourier uncertainty relation. Since absorption and dispersion are to be determined by a Fourier transform of the interferogram, spectral resolution $\Delta\nu$ and depth resolution Δz are inversely proportional to each other [31]:

$$\Delta z \cdot \Delta \nu \geq \frac{c}{4\pi}. \tag{10}$$

If good spectral resolution is required, the spatial resolution will be poor and vice versa. The quantities used in equation 10 are defined as standard deviations of the signal distribution in z and frequency distribution in *v*. If, as common in OCT, full width at half maximum (FWHM) values are used, and the frequency resolution is converted into a wavelength resolution, equation 10 will become:

$$\delta z \cdot \delta \lambda \geq \frac{2\ln 2}{\pi} \cdot \lambda_0^2, \tag{11}$$

where δz and $\delta\lambda$ are now the FWHM widths of signal and wavelength distribution, and λ_0 is the center wavelength. If $\delta\lambda$ is equal to the source bandwidth, and if we assume a Gaussian shape of the emission spectrum, δz is equal or larger than the well-known round-trip coherence length l_c [32] which is commonly used as the definition of OCT depth resolution.

The consequence of equation 11 is that if the Fourier transform is taken over the width of the coherence length l_c, no additional spectral resolution is obtained. If the backscattered light shall be resolved into N spectral channels within the source emission spectrum $\Delta\lambda$, the spatial resolution will be degraded by the same factor N. As an example, if at $\lambda_0 = 830$ nm a spectral resolution of 10 nm is required, the spatial resolution δz will be ≥ 30 μm; a spectral resolution of 1 nm will degrade the spatial resolution to $\delta z \geq 300$ μm.

If measurements are to be performed in a non-scattering material with well-defined boundaries separated by at least the necessary distance δz (e.g., in liquids in a cuvette), high spectral resolution is possible. If, however, measurements are to be performed within highly scattering media with densely packed scattering sites, as is the case in most tissues, signals from adjacent sites (adjacent in depth) will overlap and Fourier transforms of undistorted signals over large distances might be impossible, imposing a limit to achievable spectral resolution. In highly scattering materials, the possible spectral resolution can be estimated by the speckle size. Fourier transforms should be taken over a distance not larger than the depth of a speckle. Since the speckle size is of the order of the coherence length, spectral resolution in scattering media by a direct Fourier transform method is probably very limited.

The situation might be improved by narrow band pass filtering of the signal into several separate spectral channels. This increases the coherence length and the speckle size. However, the generation of thus filtered OCT signals corresponding to the different wavelength regimes causes uncorrelated speckle fields in the different images [33]. To obtain quantitative absorption data from two such images corresponding to different wavelengths requires ratioing of data obtained at corresponding image points [15]. In case of uncorrelated speckle fields, such a ratioing requires a considerable amount of averaging over adjacent areas [34], thus further reducing spatial resolution.

Probably because of the problems mentioned above, only few results on spectral measurements by OCT have yet been published. Nevertheless, some interesting steps towards absorption and dispersion measurements by LCI and OCT have been reported. These methods and results will be presented in the following chapters.

15.3 ABSORPTION IN OCT

15.3.1 Time Domain Methods

Time domain methods are most commonly used in OCT at present. Time domain OCT is based on LCI and most of the presently used time domain OCT techniques are based on A-scans (cf. subsection 15.2.1) as a scanning scheme which simultaneously provides the carrier frequency by Doppler shift of the reference light. Applications to absorption measurement reported so far are based on this method. Two different approaches to obtain absorption information were reported so far: the two-wavelength method and the Fourier transform method.

15.3.1.1 Two-Wavelength Methods

The two-wavelength method, or differential absorption technique, avoids the above mentioned problem of Fourier transforming signals obtained with a broadband source over several speckles by using two separate light sources, one emitting within an absorption band of a chemical compound and the other emitting just outside that band. The two light sources give rise to two different interferometric signals that can be separated either by optical filtering (e.g., with an edge filter), diverting the two wavelengths to different detectors, or by electronic filtering based on their different Doppler frequencies. The two signals can be used to generate two separate OCT intensity images, each corresponding to one wavelength; from the differences of the signals, absorption based images can be derived.

J.M. Schmitt *et al.* used this method in connection with electronic filtering to generate images of local concentrations of water [15]. Since most tissues contain a considerable amount of water, the measurement of water concentration in tissue is of interest for many biomedical applications. Schmitt and coworkers used a pair of LEDs, one centered at $\lambda_{01} = 1.3\ \mu m$ (outside of an absorption band) and the other centered at $\lambda_{02} = 1.46\ \mu m$ (within the first vibrational overtone band of the OH bond). Starting from equation 8, the authors integrate over portions of the power spectrum to extract quantities proportional to the intensities I_{i1} and I_{i2} of the attenuated sample beams that are incident on the detector within the two frequency bands. After normalizing the ratio of incident intensities I_{i1}/I_{i2} to unity, assuming a homogenous medium within the target layer whose absorption is to be measured, and further assuming that the backscattering coefficients for the two bands are equal, the differential absorption coefficient $\Delta\mu_a$ can be expressed as:

$$\Delta\mu_a = \mu_{a2} - \mu_{a1} = \frac{1}{2(z - z_0)} \ln\left[\frac{I_1(z)}{I_2(z)}\right] - (\mu_{s2} - \mu_{s1}), \qquad (12)$$

where the attenuation coefficient $\mu_t = \mu_a + \mu_s$ has been resolved into its constituents: absorption coefficient μ_a and scattering coefficient μ_s, $z - z_0$ is the thickness of the layer to be measured, $I_{1,2}(z)$ are the light intensities measured at depth z, and the indices 1 and 2 refer to the two wavelength regimes. Because the scattering coefficients $\mu_{s1,2}$ are usually not known, a further assumption is necessary to calculated $\Delta\mu_a$ by equation 12. If the two wavelength regimes are chosen such that $|\mu_{s2} - \mu_{s1}| << \Delta\mu_a$, the differential absorption coefficient can be approximated by:

$$\Delta\mu_a \cong \frac{1}{2(z-z_0)} \ln\left[\frac{I_1(z)}{I_2(z)}\right]. \tag{13}$$

This method was used in two experiments to measure differential absorption in water. The first set of experiments measured $\Delta\mu_a$ of water (H_2O) and heavy water (D_2O) within a cuvette. D_2O has optical properties very similar to those of H_2O, except that D_2O does neither absorb at 1.3 μm nor at 1.46 μm. Excellent agreement between $\Delta\mu_a$ measured by LCI (2.88 mm^{-1} in H_2O) and by conventional transmission spectrophotometry (2.83 mm^{-1}) was found. The thinnest layer of water that could be measured by LCI was ~ 50 μm.

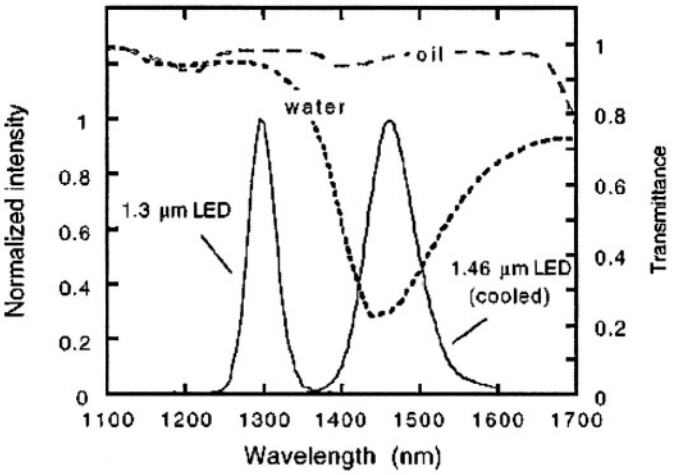

Figure 2. Transmission spectra of water and oil (dashed curves) and emission spectra of LEDs (solid curves) used in differential absorption OCX experiment. Reproduced from Schmitt *et al.* [15] by permission of the Optical Society of America.

In a second experiment the method was used for quantitative imaging of differential absorption of liquids embedded within a scattering phantom. The phantom consisted of two V-grooves milled into the surface of a diffusely reflecting plastic. One of the grooves was filled with weakly absorbing oil, the other with H_2O. The grooves were covered with a translucent plastic. Figure 2 shows transmission spectra of the oil and H_2O (path length 0.5 mm), overlaid with the emission spectra of the two LEDs. It is clearly seen that oil has transmittance ~ 1 over the spectral range of interest, while H_2O has an absorption band centered at 1.44 μm. Figure 3 shows results of the second experiment. Figure 3, top left, is a sketch of the phantom, Figure 3 bottom left and right show OCT intensity cross sectional images corresponding to 1.3 and 1.46 μm, respectively. It can clearly be observed

that the 1.46 μm radiation is stronger attenuated in the water-filled groove than in the oil-filled groove (the intensity of the posterior boundary of the liquid filled groove diminishes with depth only in the groove filled with water). Figure 3, top right, shows a conventional OCT image with an overlay of a map of differential absorption, $\Delta\mu_a$, whose magnitude is gray scale coded. The measured average of the difference between $\Delta\mu_a$ of water and oil is 2.4 mm^{-1}, slightly smaller than the expected value of 2.8 mm^{-1}. The reason for this difference might be attributed to speckle noise.

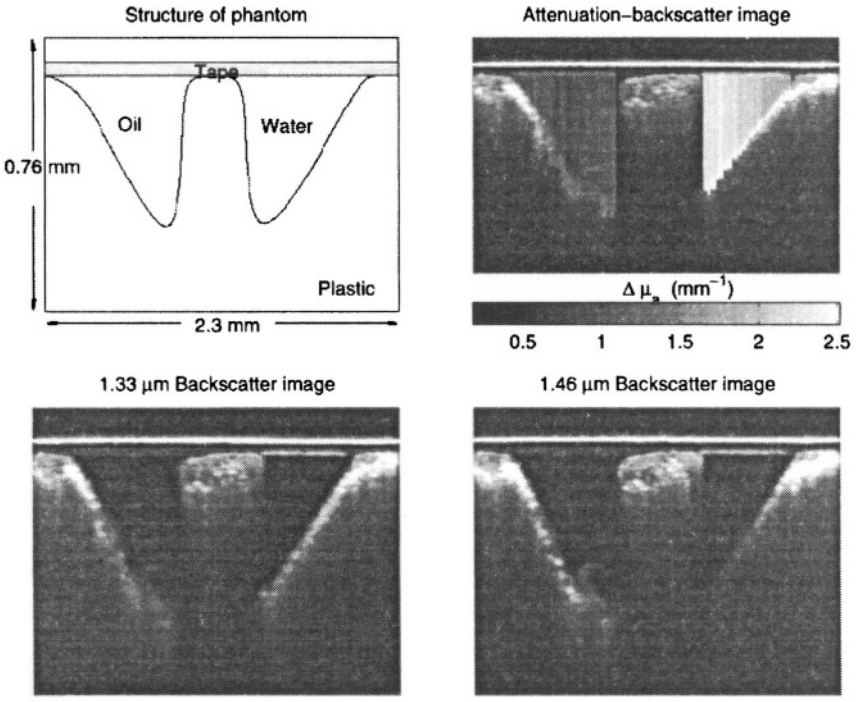

Figure 3. Top left, sketch of phantom used in differential absorption OCT experiment; bottom left and right, OCT intensity images recorded at 1.33 and 1.46 μm, respectively; top right, OCT intensity image overlaid with map of differential absorption. Reproduced from Schmitt *et al.*[15] by permission of the Optical Society of America.

In a careful analysis of the assumption that $\Delta\mu_s << \Delta\mu_a$, the authors come to the conclusion that this assumption is probably not true for the wavelength pair 1.3 / 1.46 μm in real tissue. Depending on estimated optical properties of tissue, the error of $\Delta\mu_a$ caused by scattering can lie between 11 and 84%. Therefore, the authors suggest to use the wavelength pair 1.8 / 1.93 μm for which scattering differences are expected to be much smaller. With this wavelength pair the error in $\Delta\mu_a$ caused by scattering should not exceed 7%.

Unfortunately, there are presently no suitable light sources available at these wavelengths.

While in the paper by Schmitt *et al.* differential absorption was measured in non-scattering liquids, U.S. Sathyam *et al.* used a similar technique to measure absorption in a scattering model substance [16]. They used two SLDs centered at $\lambda_{01} = 1.31$ μm and $\lambda_{02} = 1.53$ μm to measure absorption by LCI in intralipid solutions with variable scattering coefficient and variable water concentration. Water concentration, and therefore absorption, was varied by mixing with formic acid in various proportions.

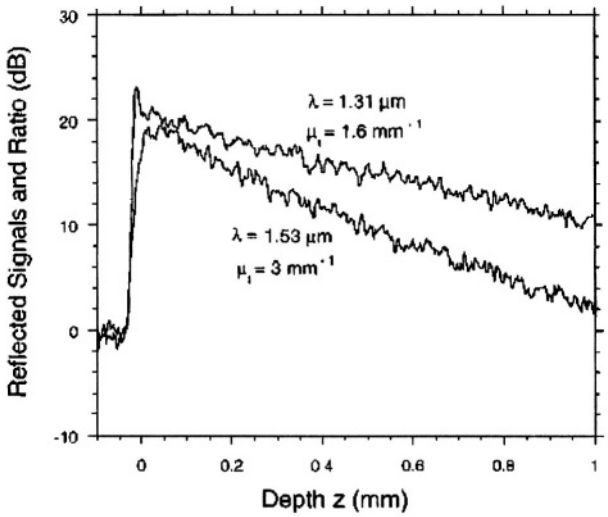

Figure 4. LCI scan signals from differential absorption experiment performed in a sample containing 99% water and 1% intralipid. Ordinate: logarithmic scale. Reproduced from Sathyam *et al.* [16] by permission of the Optical Society of America.

LCI signals were recorded at both wavelengths simultaneously, the two different wavelengths were separated by a combination of optical filtering (using a wavelength division multiplexer) and electronic band pass filtering. Figure 4 shows a plot of the logarithm of LCI signals obtained at the two wavelengths as a function of depth, in a solution of 99% water and 1% intralipid. From the slope of these curves, the total attenuation coefficient is determined: $\mu_t(1.31\ \mu m) = 1.6\ mm^{-1}$, $\mu_t(1.53\ \mu m) = 3\ mm^{-1}$. The attenuation at 1.31 μm, where water absorption is small, is attributed to scattering. By introducing a scaling factor equal to the ratio of scattering coefficients at 1.53 and 1.31 μm, the 1.31 μm signal can be used as a reference to correct for scattering and calculate the absorption coefficient of the solution at 1.53 μm. Figure 5 shows absorption coefficients thus obtained as a function of water content. While there is an approximately linear relation between μ_a

and water content, the slope of the curve is ~ 3 times larger than the theoretically expected value. The authors attribute this to a varying scattering coefficient of the sample caused by varying refractive index of the water – formic acid mixture (the refractive index of formic acid is larger than that of water). The authors also conclude by suggesting the use of wavelengths in the 1.8 μm regime, where water absorption is stronger and scattering effects are less pronounced.

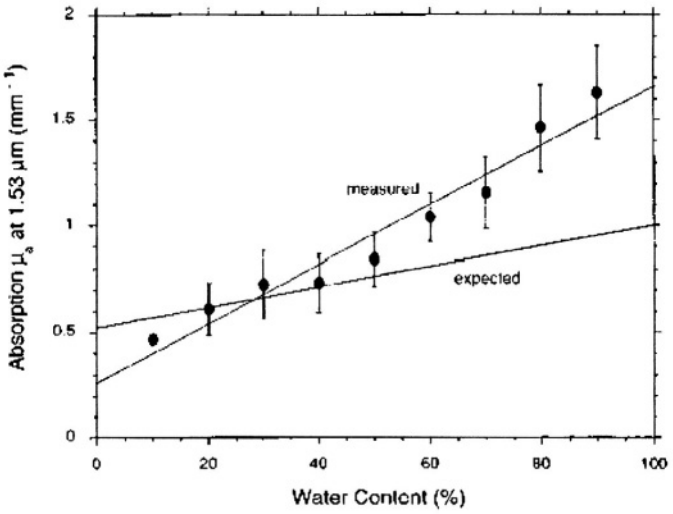

Figure 5. Differential absorption experiment. Measured and expected absorption as a function of water content. Reproduced from Sathyam *et al.* [16] by permission of the Optical Society of America.

Pircher *et al.* [34] were the first to apply this method to measure and image differential absorption in real tissue. Experiments were carried out in human cornea *in vitro.* Since scattering in corneal tissue is low, the above-mentioned problems of systematic errors introduced by a not precisely known scattering coefficient should be small. Two SLDs emitting at λ_{01} = 1312 nm and λ_{02} = 1488 nm were used; the signals corresponding to the two light sources were separated by a wavelength division multiplexer diverting the light to two separate detectors. Dynamic focusing [35] and interferometric control of reference delay were used to optimize the signals. Figure 6 shows a sketch of the instrument used.

Excised human corneas were stored in a nutrient solution that is routinely used to prevent them from dehydrating and taken from that solution immediately before OCT imaging. OCT tomograms were recorded at both wavelengths simultaneously. Figure 7 shows the results. Figures 7(a) and 7(b) show intensity images recorded at 1312 and 1488 nm, respectively. It

can clearly be observed that the backscattered intensity strongly decreases with depth in the case of 1488 nm which is absorbed by water, while the intensity decrease in the image recorded at 1312 nm (only weakly absorbed) is considerably lower. After normalizing to equal incident intensity and performing a floating average over an area of $50 \times 50\ \mu m^2$, an intensity difference image was calculated [Figure 7(c)] that clearly shows the effect of differential absorption with depth (false color image; black: small intensity difference, red: large intensity difference; areas shown in gray have a signal to noise ratio that is too low to produce reliable absorption data).

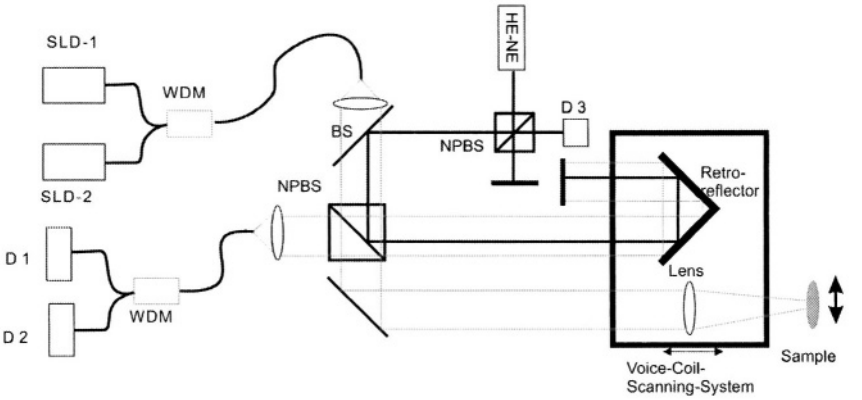

Figure 6. Sketch of differential absorption OCT system. SLD...superluminescent diodes; WDM...wavelength division multiplexer; NPBS...non polarizing beam splitter; BS...beam splitter; D1, D2, D3...detectors. Reproduced from Pircher *et al.* [34] by permission of the Optical Society of America.

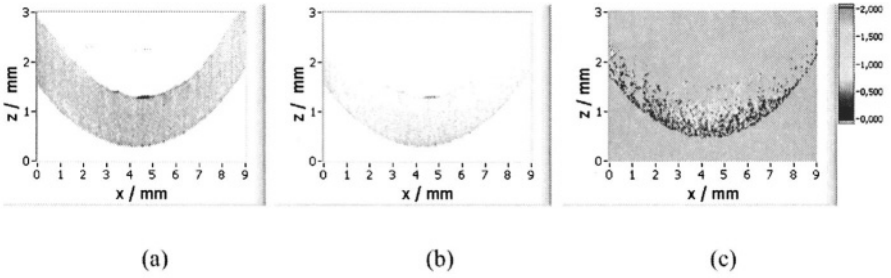

Figure 7. Differential absorption OCT. OCT images of a human cornea *in vitro.* a) intensity image recorded at 1312 nm; b) intensity image recorded at 1488 nm; c) differential intensity image. Reproduced from Pircher *et al.* [34] by permission of the Optical Society of America.

To demonstrate that the effect observed in Figure 7 was caused by absorption and not by scattering, the following experiment was made: the cornea was dehydrated and rehydrated with D_2O, which has similar optical properties as H_2O, with the exception of having no absorption band near

1488 nm. The OCT imaging was repeated with the D_2O hydrated cornea. The result is shown in Figure 8. Both, the 1312 and 1488 nm OCT intensity images show negligible attenuation with depth [Figures 8(a) and 8(b)] and the intensity difference image [Figure 8(c)], too, shows negligible difference between the two wavelengths, clearly indicating that a possible wavelength-dependent scattering factor does not disturb absorption measurements in the cornea.

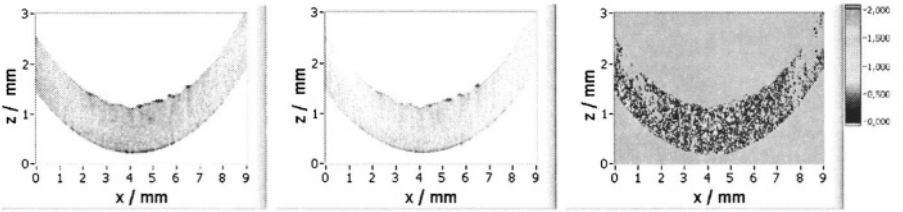

Figure 8. Differential absorption OCT. OCT images of a human cornea *in vitro* after re-hydration with D_2O. a) intensity image recorded at 1312nm; b) intensity image recorded at 1488nm; c) differential intensity image. Reproduced from Pircher *et al.* [34] by permission of the Optical Society of America.

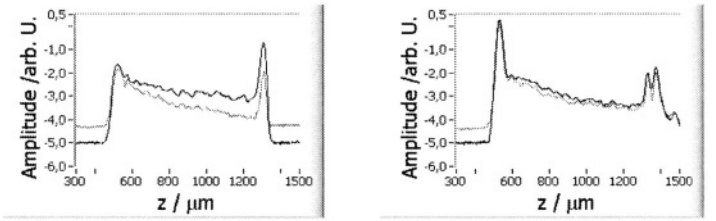

Figure 9. Results from differential absorption OCT. Plot of the averaged logarithmic intensities with depth: a) cornea containing H_2O; b) cornea containing D_2O.Black...1312nm, gray...1488nm. Reproduced from Pircher *et al.* [34] by permission of the Optical Society of America.

For a quantitative determination of the differential absorption coefficient, the A-scans covering the central part of the cornea of each experiment were averaged separately (for reduction of speckle noise), and the averaged logarithmic intensity is plotted as a function of depth in Figure 9. Figure 9(a) shows the results of the cornea containing H_2O, Figure 9(b) those of the cornea containing D_2O. It is clearly observed that the intensity at 1488 nm drops faster with depth than the intensity recorded at 1312 nm in the H_2O containing cornea, while the two slopes are equal in the cornea containing D_2O. A linear regression analysis of the central part of the A-scans (avoiding

the reflection peaks at the corneal surfaces) in Figure 9(a) shows a differential absorption coefficient $\Delta\mu_a = 1.7\ mm^{-1}$. With the known differential absorption coefficient of pure water [36] $\Delta\sigma_a = 2\ mm^{-1}$, and the known central corneal thickness (measured from the tomograms and assuming a group refractive index n = 1.385 [37]), the water concentration c of the cornea is calculated by:

$$c = \frac{\Delta\mu_a}{\Delta\sigma_a} \tag{14}$$

to be 85%. This is in excellent agreement with an independent method where water concentration of the cornea is estimated from its thickness [38], which yields c = 86%.

While this paper shows excellent agreement of water concentration measured via differential absorption OCT with that obtained by an independent method, it is also clear that a considerable amount of averaging is necessary to reduce speckle noise, thus degrading the spatial information on the water distribution.

15.3.1.2 Fourier Transform Methods

Due to the problems mentioned in subsection 15.2.3, the application of the Fourier transform method to obtain detailed absorption and dispersion spectra has so far been limited to measurements in simple model substances. In a preliminary study, Kulkarni and Izatt obtained spectral information of Fresnel reflections at a sample interface by use of the sample transfer function [39] (cf. equation 6).

In a more comprehensive study, T. Fuji *et al.* [27] measured absorption and dispersion spectra in different sample solutions in a cuvette by 1-dimensional LCI scans. As a light source, they used an incandescent lamp. The sample solution within a cuvette was placed in the sample arm and measured in transmission, the light being reflected by a movable corner cube prism. To cancel out the effects of the cuvette glass and the solvent, a similar cuvette filled with the pure solvent was placed in the reference arm. By measuring the autocorrelation (both, sample and reference arm cuvettes containing only the solvent) and the cross correlation (sample arm cuvette containing sample solution) signals, Fourier transforming them, and applying equation 6, the sample transfer function H(ν) was obtained and absorption spectrum and the spectrum of the refractive index were derived.

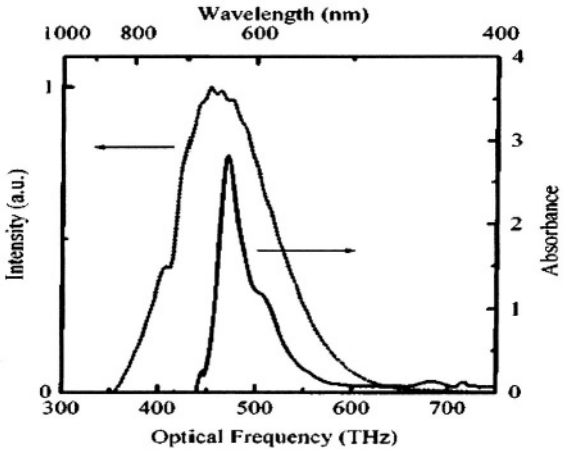

Figure 10. Fourier transform LCI experiment. Absorption spectrum of oxazine 1 in methanol and spectrum of incident light. Reproduced from Fuji *et al.* [27] by permission of the Optical Society of America.

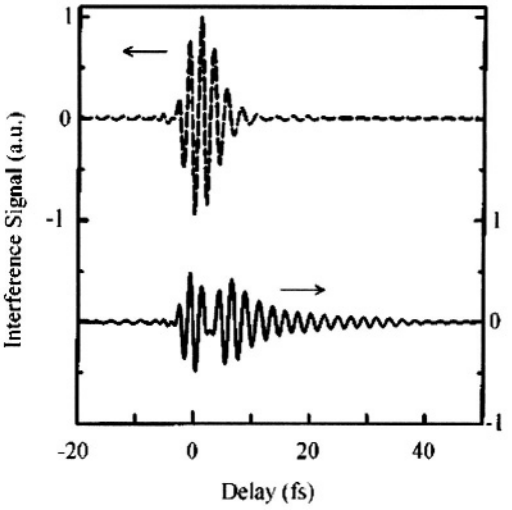

Figure 11. Fourier transform LCI experiment. Autocorrelation (dashed curve) and cross correlation (solid curve) of oxazine 1 in methanol. Reproduced from Fuji *et al.* [27] by permission of the Optical Society of America.

One of the sample solutions measured was oxazine 1 in methanol. The absorption spectrum of the solution used is shown in Figure 10, together with the spectrum of the incident light. The absorption band lies within the spectral region of the measurement. Figure 11 shows the interferometric autocorrelation and cross correlation signals. It is clearly observed that the

cross correlation is distorted, as compared to the autocorrelation signal, caused by absorption and dispersion effects. Figure 12 shows the absorption spectrum (solid curve) and the spectrum of the refractive index (dashed curve) derived from the measured interferometric signals by the Fourier transform method. An absorption spectrum measured by a conventional grating spectrometer (short-dashed curve) shows excellent agreement with that obtained by the interferometric technique.

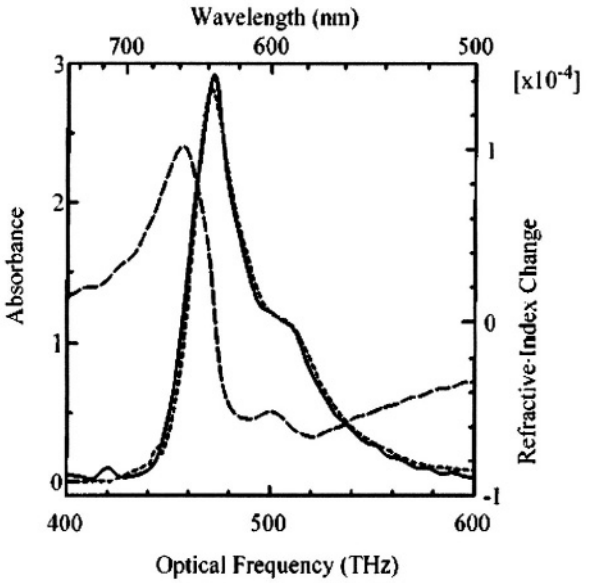

Figure 12. Fourier transform LCI experiment. Absorption spectrum (solid curve) and spectrum of refractive index (dashed curve) of oxazine 1 in methanol obtained from the measured interferograms (Figure 11). Absorption spectrum obtained with conventional grating spectrometer (short-dashed curve). Reproduced from Fuji *et al.* [27] by permission of the Optical Society of America.

B. Hermann *et al.* [40] used a related method to measure absorption spectra in a phantom consisting of a gel layer doped with Indocyanine Green (ICG) sandwiched between two thin cover glass plates. As a light source, they used a state of the art femtosecond Ti:sapphire laser (λ_0 = 800 nm, $\Delta\lambda$ = 125 nm), spectroscopic information was obtained by a Morlet wavelet transform instead of a conventional Fourier transform. The chosen wavelength region is of special interest since it covers the absorption peak of deoxy-hemoglobin at 760 nm as well as the hemoglobin isobestic point at around 800 nm, therefore possibly being useful for measuring blood oxygenation. The results of the study demonstrated that quantitative measurement of absorption in non-scattering phantoms is possible with a precision and repeatability of better than 10%. The authors conclude that for

measurements in scattering tissue additional strategies to extract the weak absorption profiles from highly scattering media remain to be developed.

First experiments towards measuring blood oxygenation by this technique were reported by D.J. Faber *et al.* [41]. These authors also used a Ti:sapphire laser at 800 nm and performed one-dimensional measurements in porcine blood within a cuvette. If light reflected at the posterior interface blood-glass was used to obtain spectral information, a slight spectral shift between oxygenated and deoxygenated blood was observed; the direction of the shift was in agreement with expectations from the corresponding blood spectral absorption curves. However, if the decay of signal intensity with depth was used, no clear relationship between decay of spectral amplitude with depth and oxygenation was found, indicating that the technology was not sensitive enough for blood oxygenation measurements within real tissue.

While the above mentioned studies obtained good spectral resolution, spatial resolution was not achieved since the measurements were performed in transmission on a single lateral location. Morgner *et al.* [42] reported on a variation of the Fourier transform method that obtains high spatial resolution in combination with qualitative spectral information. These authors used a broadband femtosecond Ti:sapphire laser emitting in a spectral range from 650-1000 nm, enabling a depth resolution of $\sim 1\ \mu m$.

The Fourier transform was replaced by a Morlet wavelet transform that reduces windowing artifacts associated with short-time Fourier transforms, however, cannot overcome the fundamental limits discussed in subsection 15.2.3. For each point in the OCT image, a spectrum was obtained and the center of mass of each spectrum was calculated. This allowed the spatially resolved determination of spectral shifts at each image point. To display the spectral data overlaid on the structural data, a hue-saturation-luminance color space was adopted instead of the RGB color space usually used in OCT false color-coded intensity images. While backscattered intensity was mapped into saturation, the spectral center of mass was mapped into hue, leaving luminance constant. A green hue indicates a spectral shift to shorter wavelengths, a red hue a shift towards longer wavelengths, while yellow is neutral.

This technique was used to image an anesthetized *Xenopus laevis* (African frog) tadpole *in vivo*. Figure 13 shows the result. Figure 13 (top) shows a conventional ultrahigh-resolution OCT intensity image of an area covering $\sim 0.54 \times 0.50\ mm^2$. Tissue morphology and cells (including membranes, nuclei, and melanocytes) are visible. Figure 13 (bottom) shows the corresponding spectroscopic image. It is consistent with the fact that longer wavelengths penetrate deeper than the shorter wavelengths. Shallower structures have a green hue while deeper structures have a red hue. Melanocytes appear bright red, indicating that they red-shift the light. While Figure 13 clearly shows that some spectral information can be achieved simultaneously with good spatial resolution, the authors also point out that

the image contrast results from a combination of scattering and absorption, and spectral modifications of light by deeper structures are convolved with the properties of the overlying structures, thus making it challenging to determine the exact optical properties of a given internal structure.

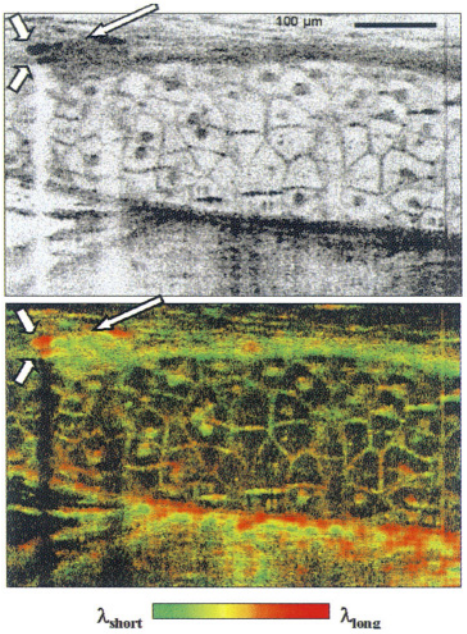

Figure 13. Ultrahigh resolution OCT images of *Xenopus laevis* tadpole *in vivo.* Mesanchymal cells are visualized. Top: OCT intensity image. Bottom: Spectroscopic OCT image. A green hue indicates a short-wavelength shift, a red hue a long-wavelength shift. Reproduced from Morgner *et al.* [42] by permission of the Optical Society of America.

15.3.2 Frequency Domain Methods

Frequency domain methods, though already discussed [43] and demonstrated [44,45] in the early times of LCI and OCT, have long played only a minor role in OCT, probably because sufficiently fast and sensitive CCD cameras were not available in these early times. However, recent work has shown that this technique had been underestimated and has a great potential, in terms of speed and sensitivity [46,47].

Frequency domain OCT is based on backscattering spectral interferometry. A detailed discussion of the fundamentals of this technology, based on Wolf's treatment of scattering by the first-order Born approximation [48], can be found in recent review articles [3,4]. Here is a short summary of the method: similar to time domain OCT, the object is

placed in the sample arm of an interferometer and illuminated by short-coherence light (cf. Figure 14). However, the reference mirror is kept in a fixed position. Instead of performing depth scans, the light exiting the interferometer is dispersed by a spectrometer, and the spectral distribution of the interference intensity is recorded by a detector array.

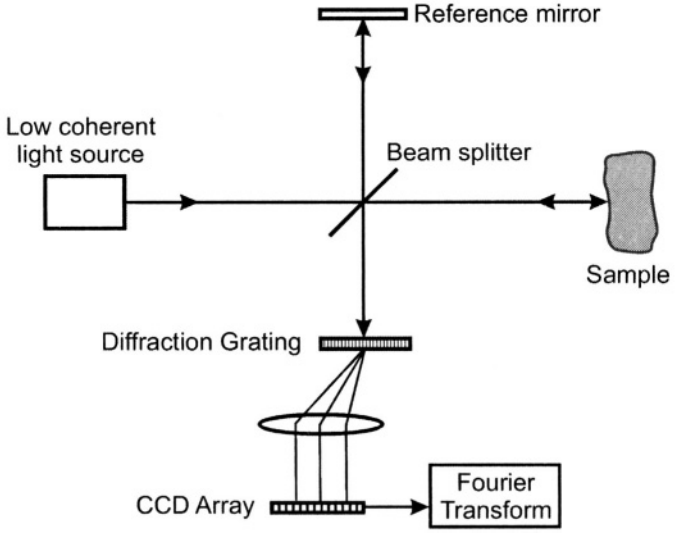

Figure 14. Frequency domain low coherence Michelson interferometer.

In a far field backscatter approximation, the electric field amplitude $A_o(K)$ of light scattered back in the z-direction is proportional to the inverse Fourier transform of the scattering potential $F_o(z)$ of the object [3]:

$$A_o(K) \propto FT^{-1}\{F_o(z)\}, \tag{15}$$

where $K = 2k = 4\pi/\lambda$ is the scattering vector (the factor 2 stems from the backscattering configuration), k the wavenumber, and the scattering potential of the object is given by:

$$F_o(z,k) = -k^2\left[m^2(z,k) - 1\right], \tag{16}$$

where $m(z,k) = n(z,k)(1+i\kappa(z,k))$ represents the complex index of refraction of the sample at depth z and wavenumber k, with n the refractive index and κ the attenuation index. Hence, $F_o(z)$, which equals (in backscattering geometry) the local amplitude reflectivity ($= \sqrt{R(z)}$) can be obtained by a Fourier transform of $A_o(K)$:

$$F_o(z) \propto FT\{A_o(K)\}. \tag{17}$$

If $A_o(K)$ where directly accessible, the depth distribution of the scattering potential (amplitude reflectivity) could be directly obtained by a Fourier transform of the backscattered field. However, $A_o(K)$ is the complex amplitude of the scattered field and thus not directly detectable. Instead, the intensity spectrum $I_o(K)$, which is proportional to the square of the inverse Fourier transform of the scattering potential of the object, is recorded. Taking the Fourier transform of $I_o(K)$ yields the autocorrelation function (ACF) of the scattering potential:

$$FT\{I_o(K)\} \propto ACF\{F_o(z)\}. \tag{18}$$

Autocorrelation is not reversible. If, however, the object is placed in one arm of an interferometer, and the other arm contains a reference mirror with amplitude reflectivity $\sqrt{R}$, as in the case of Figure 14, the autocorrelation contains one term that yields a reconstruction of the complex object structure, centered at the (negative) reference mirror position $z = -z_R$, i.e. $\sqrt{R}F_o(z + z_R)$ [44]. To avoid overlapping of the object structure with other terms of the autocorrelation, the reference mirror must be put in a position at least twice the object depth apart from the next object interface.

The advantage of frequency domain LCI and OCT is that the object structure along the complete depth is obtained by a single readout of the photodetector array, enabling short acquisition time without any movement of the reference mirror, thus reducing the number of moving components in the instrument. A further advantage, in the context of absorption measurements, is the direct access to spectral information.

R. Leitgeb *et al.* were the first to demonstrate the application of frequency domain OCT for obtaining absorption data [49]. They used a setup similar to that shown in Figure 14. The light source was an SLD (λ_0 = 830 nm, $\Delta\lambda$ = 25 nm), and the light at the interferometer exit was dispersed by a diffraction grating onto a CCD sensor of a digital camera (transverse resolution 1024 pixels).

To obtain spectral and structural information simultaneously, the Fourier transform was not calculated over the entire spectrum in one step; instead, a windowed Fourier transform was performed, with a frequency window of width ΔK, centered at wave number K_n, that was shifted along the spectrum step by step. The spectral data within the windows were Fourier transformed, obtaining a series of n scattering potentials $F_o(z,K_n)$ associated with each window centered at K_n and a point spread function (depth resolution) determined by ΔK. The n scattering potentials resemble n depth scans of the object structure at n different wavelengths, thus providing n object images

corresponding to the different spectral regions. The spectral resolution of this method is equal to the window width ΔK. By using small window widths, however, the depth resolution is poor, since the Fourier uncertainty relation (equations 10 and 11), of course, plays the same limiting role as in time domain OCT (cf. subsection 15.2.3).

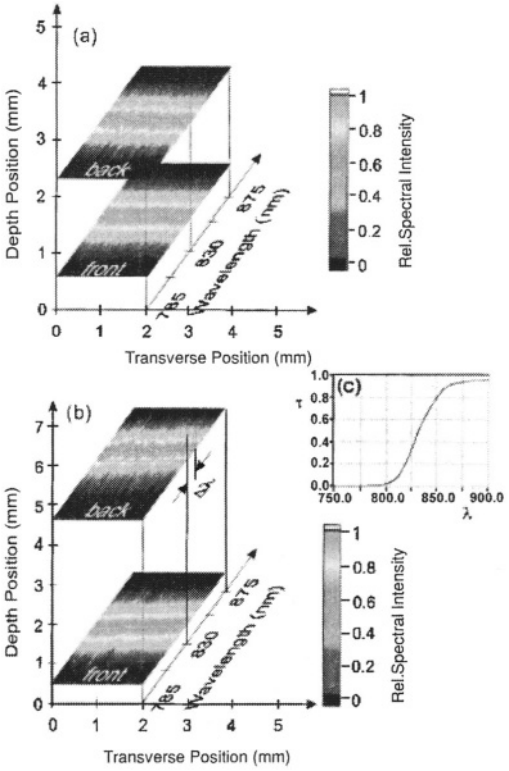

Figure 15. Absorption imaging by spectral OCT. Spectral OCT images of: a) a BK7 glass plate, and b) an IR filter glass plate (the spectra are normalized). (c) Transmission curve of IR filter glass plate. Reproduced from Leitgeb *et al.* [49] by permission of the Optical Society of America.

As a test sample, an IR filter glass plate with transmittance 0.5 at $\lambda = 830$ nm (absorbing at lower wavelengths and transmitting at higher wavelengths) was used. Several spectral interferometry scans were recorded at adjacent positions of the filter glass plate. For comparison, a similar experiment was carried out in a conventional BK7 glass plate. Windowed Fourier transforms were carried out on each scan and spectra of light reflected at the anterior and posterior interfaces of the glass plates were derived. Figure 15 shows the results. Figures 15(a) and (b) show spectral images corresponding to BK7 and the IR filter plate, respectively. Figure 15(c) shows the transmission

curve of the filter plate. In the BK7 plate, the spectra obtained at the anterior and posterior interfaces are both centered at 830 nm, the peak emission wavelength of the SLD. No spectral shift is observed. In the IR filter glass plate, however, the spectra derived at the posterior surface of the plate are shifted, as compared to those corresponding to the anterior surface, towards longer wavelengths by ~ 9 nm. This is in agreement with what is expected from a plate transmitting predominantly longer wavelengths.

Due to a lack of sufficiently fast and sensitive CCD cameras, absorption measurements by frequency domain OCT were not further pursued in the past. Since such cameras became available recently [46,47], research into and applications of this technology are likely to gain more attention in the next years.

15.4 DISPERSION IN OCT

Most papers on dispersion effects in OCT published so far regard dispersion as an unwanted effect that degrades image quality and has to be avoided or corrected for. However, recently some ideas to obtain additional information on a sample from dispersion phenomena were presented. Both, unwanted and wanted dispersion effects are treated in this chapter.

15.4.1 Signal and Image Degradation Caused by Dispersion

To discuss the origin of signal degradation by imaging within a dispersive medium we consider the case of placing a homogenous transparent (i.e., non-absorbing) sample of thickness d and refractive index $n(\omega)$ in the sample arm of a low coherence interferometer. For simplicity, we set the amplitude spectrum $\sqrt{R(\nu, z)} = 1$. The phase spectrum corresponding to a signal derived from a reflection at the posterior surface of that sample (i.e., in depth z = d) (cf. equation 9) becomes:

$$\Phi(\omega) = 2\frac{\omega}{c} d[n(\omega) - 1] = 2d[k(\omega) - k_0]. \tag{19}$$

The transfer function of this sample becomes:

$$H(\omega) = \exp[i2d(k(\omega) - k_0)]. \tag{20}$$

The impulse response function of an LCI depth scan by an interferometer containing a dispersive sample of thickness d is:

$$2\,\mathrm{Re}\left\{\mathrm{FT}^{-1}\left\{S_{\mathrm{source}}(\omega)\exp\left[i2d\left(k(\omega)-k_0\right)\right]\right\}\right\}. \tag{21}$$

The material dispersion $k(\omega) = n(\omega)\cdot\omega/c$ can be developed into a Taylor series to obtain the different orders of dispersion [50]:

$$\begin{aligned} k(\omega)-k_0 = {} & k^{(1)}(\omega_0)(\omega-\omega_0)+\tfrac{1}{2}k^{(2)}(\omega_0)(\omega-\omega_0)^2 \\ & +\tfrac{1}{6}k^{(3)}(\omega_0)(\omega-\omega_0)^3+\ldots \end{aligned} \tag{22}$$

where the j^{th} derivative $k^{(j)}(\omega_0) = d^j k/d\omega^j\big|_{\omega=\omega_0}$ of k is the j^{th} order dispersion.

The Fourier shift theorem implicates that a multiplication of a function by a phase factor in Fourier space shifts the Fourier transform of that function in direct space. To obtain the effect of the phase spectrum $\Phi(\omega)$ on the direct signal, we have to multiply the source spectrum $S_{\mathrm{source}}(\omega)$ by the transfer function $H(\omega)$ (equation 20) and calculate the inverse Fourier transform. If the additional phase in Fourier space is directly proportional to the frequency ω (i.e., only the first order dispersion $k^{(1)}$ is present), the Fourier shift theorem predicts a shift of the coherence function to a new position, the shape of the coherence function remains unchanged. This shift is known as the group delay (this is the reason why the optical path length is defined as product of the geometric sample length and the group index n_g instead of the phase index in case of dispersive samples). If higher order dispersions are present, the coherence function is distorted: non-zero second order dispersion $k^{(2)}$ causes a broadening of the coherence envelope (and a decrease of its amplitude), thus degrading the depth resolution [22,51], third order dispersion $k^{(3)}$ causes also a distortion of the shape of the coherence envelope [51].

If the width of the coherence envelope (or round trip coherence length) without dispersion l_c is given by [32]:

$$l_c = \frac{2\ln 2}{\pi}\frac{\lambda_0^2}{\Delta\lambda}, \tag{23}$$

(λ_0, center wavelength), and we define the group index by [52]:

$$n_g = n - \lambda\frac{dn}{d\lambda}, \tag{24}$$

and its derivative, the group dispersion GD, by [50]:

$$GD = \frac{dn_g}{d\lambda} = -\lambda \frac{d^2 n}{d\lambda^2} = -\frac{2\pi c^2}{\lambda^2} k^{(2)}, \tag{25}$$

the width of the coherence envelope, after double passing the dispersive medium with thickness d, can be calculated by [22]:

$$l_{c,m} = \sqrt{l_c^2 + (GD \cdot d \cdot \Delta\lambda)^2}, \tag{26}$$

where $\Delta\lambda$ is the FWHM of the (Gaussian) source spectrum. A constant GD within the range $\Delta\lambda$ and vanishing higher order derivatives of the refractive index have been assumed in the derivation of equation 26.

A direct consequence of the dispersion broadening of the interferogram is a reduction of the interference fringe contrast, and therefore of the amplitude of LCI and OCT signals. The effect of dispersion is to spread the signal over a larger depth, and by conservation of energy it can be shown [22,53] that the LCI and OCT signal amplitude $A_{OCT,m}$, after double passing the medium, is given by:

$$A_{OCT,m} = A_{OCT,0} \sqrt{\frac{l_c}{l_{c,m}}}, \tag{27}$$

where $A_{OCT,0} = 2\sqrt{I_r I_s}\,|\gamma_{sr}(\tau)|$ is the LCI and OCT signal amplitude without dispersive medium (cf. equation 2).

The physical reason for dispersion broadening of LCI and OCT signals is the different speed with which the different wavelengths of the broadband source travel through the dispersive medium. In case of normal dispersion, the refractive index for short wavelengths is higher (their speed in the medium is lower) and their traveling time (and path length) is therefore compensated at larger settings of the reference arm length, as compared to longer wavelengths. This causes a smearing out of the interference fringes, as compared to the non-dispersive case where all wavelengths travel with equal speed and are therefore compensated at a fixed reference arm length.

A further problem that can arise if dispersion is not compensated for are image artifacts caused by multiple signal peak splitting. The above mentioned effect of path length matching at different reference arm positions for different wavelengths causes a chirped LCI signal [24]. That means the length of the oscillation period (width of interference fringes) changes within an interferometric signal. If two interfaces that are closely spaced in depth are located behind a dispersive medium, and their separation is less than $l_{c,m}$, their signatures will overlap, giving rise to a beat signal. Figure 16 illustrates this effect. For simplicity, rectangular coherence envelopes and a linear

dependence of oscillation period with depth were assumed. The resulting signal shows four beat lengths. If, as frequently done in LCI and OCT, only the envelope of the rectified signal is recorded, four signal peaks would be observed though only two reflecting interfaces are present.

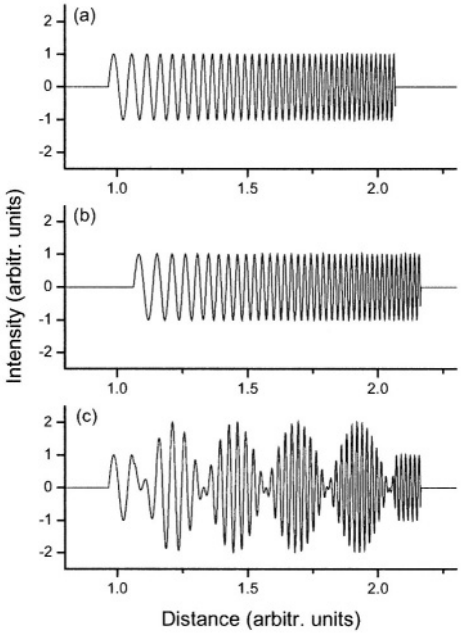

Figure 16. Dispersion induced beat effect giving rise to multiple signal peak splitting. a) and b) chirped interferograms shifted with respect to each other. c) resulting sum signal showing the beat effect. Reproduced from Hitzenberger *et al.* [24] by permission of Elsevier.

This effect was experimentally demonstrated by Hitzenberger *et al.* [24]. A thin foil of optical thickness 19 μm was placed behind a BK7 glass plate of thickness d = 25.7 mm. As a light source, a broadband SLD with $\Delta\lambda = 61$ nm was used. Figure 17 compares the measured LCI signal envelope [Figure 17(a)] obtained from the thin foil located behind the glass plate with a theoretically calculated signal. Although only two foil surfaces are present, four signal peaks are observed, in good agreement with the theoretically predicted signal [Figure 17(b)]. Further calculations showed that with the same sample illuminated by a broadband Ti:sapphire laser ($\Delta\lambda = 140$ nm) ~ 16 signal peaks would be generated by the beat effect.

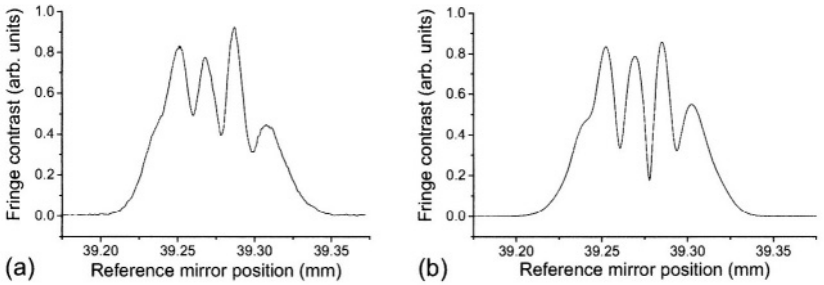

Figure 17. Dispersion induced multiple signal peak splitting. LCI signal envelope obtained from thin foil located behind dispersive glass plate. a) experimental LCI signal; b) calculated LCI signal. Reproduced from Hitzenberger *et al.* [24] by permission of Elsevier.

15.4.2 Dispersion Compensation

To obtain high quality OCT images, dispersion has to be compensated to avoid the image degradations discussed above. While compensation of dispersion within the interferometer is usually easy to achieve, by placing optical elements of similar dispersion in the two interferometer arms, this is not sufficient if either high resolution is to be achieved in dispersive samples or if measurements and imaging are to be performed through thicker layers of dispersive media. The latter case is frequently encountered in OCT imaging of the retina because the retina has to be imaged through ~ 24 mm of ocular media consisting mainly of (dispersive) water.

Different approaches to the problem of dispersion compensation have been reported, and they can be classified into hardware approaches where dispersion has to be compensated prior to the measurement, and software approaches where the compensation can be performed after data recording.

15.4.2.1 Dispersion Compensation by Hardware Methods

The simplest way to compensate the dispersion in case of measuring through a dispersive sample is to place a compensating element into the reference arm of the interferometer that has the same group dispersive effect as the layer through which the measurement is to be performed. The compensating element has to fulfill the condition:

$$GD_{el} \cdot d_{el} = GD_{ob} \cdot d_{ob}, \tag{28}$$

where the indices el and ob refer to the compensating element and the object layer to be compensated, respectively.

In case of retinal imaging through cornea, aqueous, lens, and vitreous, it has been shown that a compensating element made of BK7 glass, with d_{el} equal to approximately half the axial length of the eye is a good choice [22]. With this method, and employing a broadband SLD of $\Delta\lambda = 61$ nm, a depth resolution of ~ 5 μm (in tissue) has been obtained in a human retina *in vivo,* an improvement of about 2.5 as compared to the optimum case of ~ 12 μm without dispersion compensation. Even better resolutions of ~ 3 μm are obtained with broadband sources, if dispersion mismatch is kept small [5].

This method, though easy to apply, has some drawbacks: (i) the dispersive effect to be compensated has to be known prior to the measurement, (ii) only one fixed value of dispersion can be compensated (dynamic dispersion compensation matching increasing dispersion with depth would require mechanical movement of optical elements in the reference arm during an A-scan), and (iii) only second order dispersion can be compensated; to compensate higher orders, exact selection of compensating material would be necessary.

E.D.J. Smith *et al.* have recently presented an elegant method that allows real time dynamic dispersion compensation [54]. The method is based on the frequency domain rapid scanning optical delay line initially developed for laser pulse shaping [55] and later adapted as a versatile delay line for OCT [56,57]. This device uses a grating, a lens, and a tilting mirror to introduce a wavelength dependent shift to the phase of the reference light in Fourier space, which corresponds, via the Fourier shift theorem, to a time delay in real space. Small mirror tilts can produce rather long changes of delay length, enabling rapid scanning. Smith *et al.* have shown that a tilt of the grating away from normal to the optic axis by an angle θ_g introduces a path length dependent second order dispersion (or group dispersion). They derive the following expression for the dispersion parameter D_λ:

$$D_\lambda = \frac{n_g m \cdot \sin(\theta_g)}{p \cdot c \cdot \cos^2(\theta_g)}, \tag{29}$$

where D_λ is measured in seconds of relative delay per meter of wavelength difference per meter of geometric path; m is the diffraction order of the grating and p the grating period.

Figure 18 shows the result of applying this method to perform ranging in a highly dispersive $LiTaO_3$ waveguide of ~ 4 mm thickness. As a light source, an SLD with $\lambda_0 = 815$ nm and $\Delta\lambda = 22.5$ nm was used. Figure 18(a) shows the signals without dispersion compensation (grating tilt $\theta_g = 0°$). The signal corresponding to the anterior surface of the waveguide is undistorted, with a width of 13 μm, whereas the signal reflected at the posterior surface is broadened to 27 μm. Figure 18(b) shows a scan of the same sample recorded

with a slight tilt of the diffraction grating ($\theta_g = 7.5°$). This causes dispersion compensation, indicated by constant width of 13 μm of the coherence signals at both, the anterior and posterior interface.

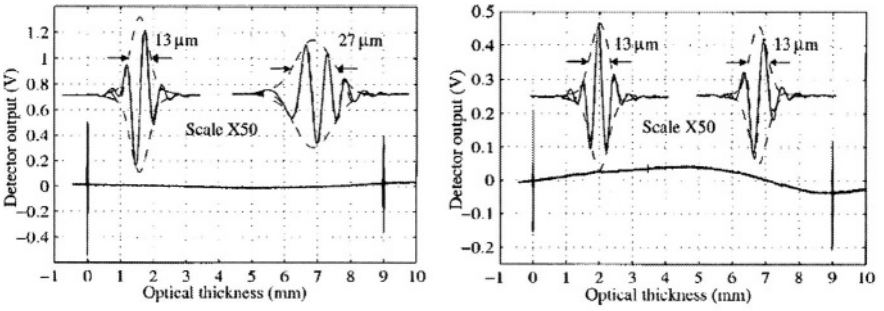

(a) (b)

Figure 18. Dispersion compensation by grating tilt in a Fourier domain rapid scanning optical delay line. LCI signals obtained at anterior and posterior surface of a $LiTaO_3$ waveguide, a) without, and b) with dispersion compensation. Reproduced from Smith *et al.* [54] by permission of the Optical Society of America.

The advantage of this method is that second order dispersion of arbitrary materials can be compensated simply by adjusting the grating tilt angle. However, variable dispersion (caused by varying sample composition in depth) and higher order dispersion can usually not be fully compensated.

15.4.2.2 Dispersion Compensation by Numeric Methods

As discussed above, second order dispersion $k^{(2)}$ adds a phase term non-linear in ω to the phase spectrum $\Phi(\omega)$, causing a broadening of the coherence envelope and therefore a degradation of depth resolution. The transfer function of a sample with first and second order dispersion is:

$$H_{disp;1,2} = \exp\left[i2d\left(k^{(1)}(\omega - \omega_0)\right) + \tfrac{1}{2}k^{(2)}(\omega - \omega_0)^2\right]. \qquad (30)$$

If $k^{(2)}$ is known, the effect of dispersion broadening can be numerically corrected by subtracting the non-linear phase term in Fourier space or by multiplying the cross spectral density $W_{sr,disp}(\omega)$ of the dispersive signal (obtained by Fourier transforming the time domain signal or by direct measurement by Fourier domain OCT) by the complex conjugate of the non-linear part of the transfer function, $H^*_{disp,2} = \exp[-idk^{(2)}(\omega - \omega_0)^2]$. This function can be either obtained numerically, e.g., from the Sellmeier formulas if measurements are performed in materials of known dispersion, or by measuring and Fourier transforming the interference signal generated

by a single reflective interface within the sample. To obtain variable dispersion compensation adapted to the increasing dispersive effect with sample depth, a windowed Fourier transform or a wavelet transform can be used.

A first application of numeric dispersion compensation to testing of integrated optical waveguides was reported by Brinkmeyer and Ulrich [58]. A deconvolution technique was used in that case. In deconvolution techniques, the recorded dispersive signal is divided by the (dispersive) impulse response (obtained from a single interface) in Fourier domain. This technique, however, has problems with noisy signals and in case of response functions containing zeros.

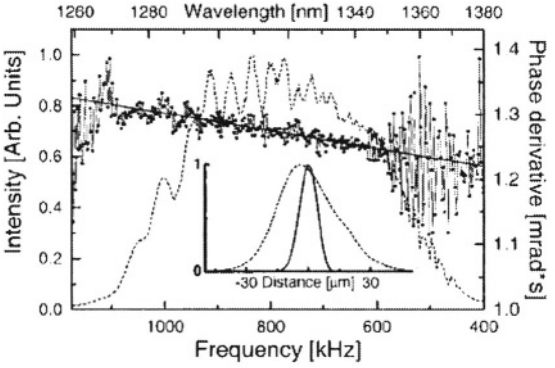

Figure 19. Dispersion compensation by numeric method. Spectrum (dashed curve, left y-axis) and phase derivative (connected squares, right y-axis) of the response to a single surface. Solid line: linear fit to phase derivative. Insert: coherence envelope before (dashed curve) and after (solid curve) numeric dispersion compensation. Reproduced from de Boer *et al.* [59] by permission of the Optical Society of America.

De Boer *et al.* were the first to apply the method of correcting quadratic phase shifts in the Fourier domain to dispersion compensation in OCT [59]. They used an amplified spontaneous emission (ASE) source (λ_0 = 1310 nm, $\Delta\lambda$ = 75 nm) and introduced artificial dispersion in the reference arm which was then numerically corrected to demonstrate the method. Figure 19 shows the spectrum of the light source, and the first derivative of the phase, determined by Fourier transform of the signal obtained from a single surface. A linear fit to the first derivative of the phase was used to obtain the quadratic phase shift and correct for it in Fourier domain. The insert in Figure 19 shows the broadened, uncorrected coherence envelope (dashed curve) and the coherence envelope after numerical dispersion compensation (solid curve). The reduction of envelope width and corresponding resolution improvement is clearly observed. Figure 20 shows an application of this method to tissue imaging. Figure 20(a) shows the uncorrected, and Figure

20(b) the dispersion compensated image of a human skin graft *ex vivo.* A fixed dispersion effect throughout tissue depth was assumed. The resolution improvement is clearly observed.

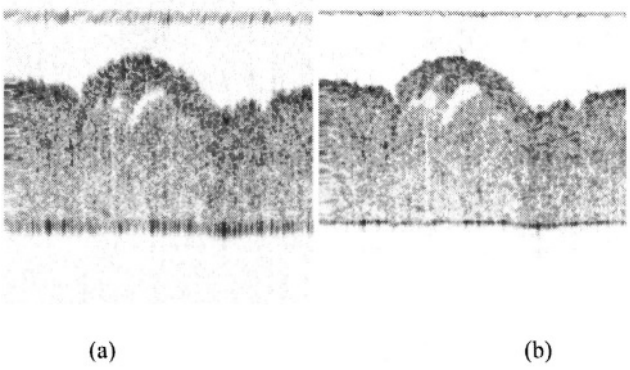

Figure 20. Dispersion compensation by numeric method. Images of *ex vivo* human skin graft. a) before, and b) after numeric dispersion compensation. Reproduced from de Boer *et al.* [59] by permission of the Optical Society of America.

A related numerical dispersion correction method based on a correlation approach has been presented by Fercher *et al.* [25,60]. Low coherence light can be considered as a random temporal distribution of ultra short Fourier transform limited light pulses. Second order dispersion induces chirping of these pulses. Chirped pulses are no more Fourier transform limited [52]; their width can be much larger than the inverse spectral width predicted by the Fourier uncertainty relationship (cf. equations 10 and 11). However, the autocorrelation width of a chirped light pulse is not broadened. Hence, the correlation of a dispersion-broadened signal with a similarly chirped signal can be used for numeric dispersion compensation.

The correlation technique is based on the fact that the autocorrelation of a quadratic phase term yields a δ – function [61]. The transfer function of a dispersive sample with first and second order dispersion is given by equation 30. If we omit the linear term caused by first order dispersion (it only shifts the signal by changing the speed of light), the response function $h_{disp,2}(\tau)$ of the sample (with just second order dispersion) can be obtained from the second order dispersion transfer function $H_{disp,2}(\omega)$ by inverse Fourier transform:

$$h_{disp,2}(\tau) = FT^{-1}\{H_{disp,2}(\omega)\} = FT^{-1}\left\{\exp\left[idk^{(2)}(\omega-\omega_0)^2\right]\right\}, \qquad (31)$$

The dispersion broadened interference signal in time domain can now be obtained by convolution of the coherence function of the light source with

$h_{disp,2}(\tau)$ (cf. equation 4). An autocorrelation of this dispersion broadened coherence function yields:

$$\begin{aligned} ACF\{\Gamma_{sr}(\tau)\} &= ACF\{\Gamma_s(\tau) \otimes h_{disp,2}(\tau)\} \\ &= ACF\{\Gamma_s(\tau)\} \otimes ACF\{h_{disp,2}(\tau)\} \\ &= ACF\{\Gamma_s(\tau)\} \otimes \delta(\tau) \\ &= ACF\{\Gamma_s(\tau)\} \end{aligned}, \qquad (32)$$

i.e., the width of the dispersive autocorrelation function is equal to the width of the undispersed autocorrelation function. The real part of this function resembles the dispersion compensated impulse response of the interferometer.

To apply the technique, the measured interferometric signal is numerically correlated with a kernel equal to the ideal dispersive interferometric signal. This kernel can be obtained by computation, if the dispersion of the sample is known (e.g., from a Sellmeier formula), or by a measurement at a single reflective interface at the required sample depth. If the sample's dispersion is known as a function of depth, a depth variant kernel can be used and dynamic, depth dependent dispersion compensation is possible.

Figure 21 shows an example of the application of this technique to compensate dispersion introduced by a microscopy cover glass of 144 μm thickness. A white light source of λ_0 = 710 nm and $\Delta\lambda$ = 210 nm was used. The oscillating signals show the interferograms obtained at the anterior and posterior glass surfaces. Dispersion increases the interferogram width from 1.03 to 3.23 μm. By using a correlation kernel obtained from a Sellmeier dispersion formula, the correlation technique reduced the width of the signal at the posterior interface from 3.23 to 1.32 μm (cf. correlation signals C(z) indicated by thick lines).

The advantage of the numerical dispersion compensation techniques is that dynamic dispersion compensation after signal recording is possible, without any change to the experimental setup. Of course, the sample dispersion has to be known (as with the hardware based techniques). Disadvantages are that the full interferometric signal has to be recorded (not just the envelope), and the larger computational effort.

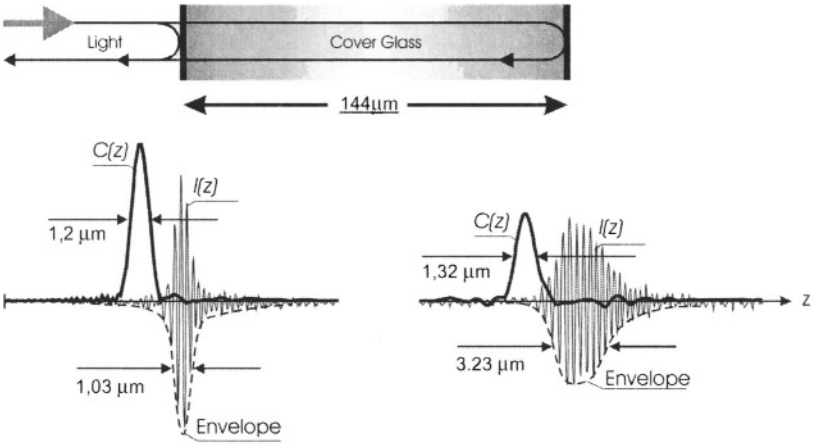

Figure 21. Numerical dispersion compensation by correlation. A depth variant correlation kernel is used. Top: sketch of sample. Bottom left: Signals at anterior sample surface; bottom right: signals at posterior sample surface. I(z)...interferometric LCI signals; C(z)...correlation signals. Reproduced from Fercher *et al.* [60] by permission of Elsevier.

15.4.3 Measurement of Dispersion by LCI and OCT

Similar to the case of absorption measurements, time domain and frequency domain methods can be used to measure dispersion. Frequency domain methods were reported in several applications to measure dispersion in transparent samples in transmission. E.g., D. Hammer *et al.* used this method to obtain dispersion in aqueous and vitreous humor in eyes of various animals *in vitro* [62]. That paper also reviews some related applications. However, since there seem to be no reports on OCT-near applications (depth resolved measurements and imaging applications) with this technology, it is not further discussed here. Time domain methods can be divided into two-wavelength methods and Fourier transform methods.

15.4.3.1 Two-Wavelength Methods

Two-wavelength methods probe the sample with two different wavelengths and measure the delay between the two signals. In general, direct phase measurements cannot be used because the different frequencies usually have non-integer relations and no fixed phase relation between two signals in different coherence envelopes or in case of vibration induced jitter can be established (the well known 2π ambiguity of interferometric methods prevents absolute phase measurements).

One way to overcome this problem is to measure the position of the coherence envelope peaks with very high precision. Drexler *et al.* [63] used

this method to measure group dispersion in ocular media. To avoid influences of axial ocular motions, they used the dual beam version of LCI [3,4,64,65,66], a technique that uses the anterior corneal surface as the reference surface. This technique matches unknown path differences within the eye with the known path difference of an external interferometer. Since not absolute positions but only path differences are measured, any influence of axial eye motions is eliminated. This method allows measurement of intraocular distances with a precision in the range of $0.5 - 3\ \mu m$ [66].

Measurements of intraocular distances were performed in healthy volunteers and in pseudophakic patients. As light sources two SLDs, centered at $\lambda_{0,1} = 814$ nm and $\lambda_{0,2} = 855$ nm, were used. Group dispersion causes a shift of the signal peak position between the two wavelengths. The shift is proportional to group dispersion GD and medium thickness d. The signal peak positions correspond to two different optical thickness values $d_{opt;1,2} = d \cdot n_{g;1,2}$ which are used to calculate $n_{g;1,2}$, if d is known (in fact an approximate value for the first group index $n_{g;1}$ is taken to calculate d, then $n_{g;2}$ is obtained). The group dispersion in the wavelength range between $\lambda_{0,1}$ and $\lambda_{0,2}$ is obtained by:

$$GD = \frac{n_{g;2} - n_{g;1}}{\lambda_{0,2} - \lambda_{0,1}}. \tag{33}$$

Figure 22 shows the result of such a measurement obtained in a human cornea *in vivo*. The coherence envelopes obtained from the posterior corneal surface are shifted slightly with respect to each other. Although the shift is only $1.9\ \mu m$ it is statistically significant (the precision of corneal thickness measurements achieved with this technique is better than $0.5\ \mu m$). This peak shift corresponds to a group index difference $\Delta n_g = 0.0037$. Similar measurements performed in 30 corneas of healthy subjects revealed a mean $GD = -(8.8 \pm 5.0) \cdot 10^{-5}\ nm^{-1}$, approximately 5 times larger than that of water (the method was tested with measurements of pure water; excellent agreement to literature values of water dispersion was found). Similar measurements were performed in the aqueous, lens, and for the total axial eye length. The results are summarized in Table 1.

Table 1. Group dispersion measured by two-wavelength LCI in human ocular media *in vivo*. Table adapted from Ref. [63].

Ocular medium	GD (nm^{-1})
Cornea	$-(8.8 \pm 5.0) \cdot 10^{-5}$
Aqueous humor	$-(1.43 \pm 1.05) \cdot 10^{-5}$
Crystalline lens	$-(3.08 \pm 0.46) \cdot 10^{-5}$
Axial eye length	$-(1.83 \pm 0.32) \cdot 10^{-5}$
Water	$-(1.62 \pm 0.06) \cdot 10^{-5}$

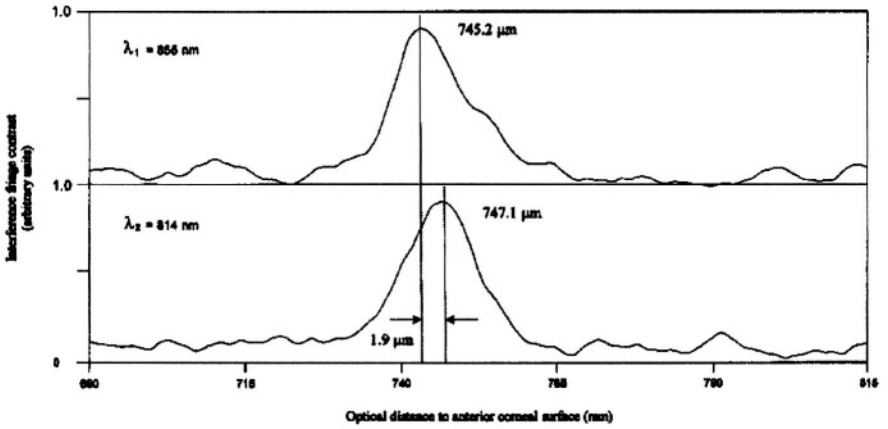

Figure 22. Measurement of group dispersion of *in vivo* cornea. Coherence envelopes of posterior corneal LCI signal. Dispersion causes a signal peak shift. Top: $\lambda_1 = 855$ nm; bottom: $\lambda_2 = 814$ nm. Abscissa: optical distance to anterior corneal surface (μm); ordinate: interference fringe contrast (arbitr. units). The peak is shifted by 1.9 μm. Reproduced from Drexler *et al.* [63] by permission of Academic Press.

C. Yang *et al.* [19] reported on a direct phase measurement technique that overcomes the problem of phase ambiguity encountered if two light sources of arbitrary frequency relationship are used. They used a composite light beam generated by a Ti:sapphire laser. The composite beam was generated by overlapping beams of the fundamental and the second harmonic frequencies (800 and 400 nm), the latter generated by a standard frequency doubler. This beam illuminates a Michelson interferometer where it is split in reference and sample beams. The sample beam is focused on the sample and makes a double pass through it (the beam is reflected at a mirror behind the sample). The reference beam double passes a compensator. The beams are recombined at the interferometer beam splitter and the wavelengths separated by a dichroic mirror and measured by two separate detectors.

The phases Φ_1 and Φ_2 of the two signals are extracted by a Hilbert transform method. A jitter of magnitude Δx in either reference or sample arm will vary the phases Φ_1 and Φ_2 by $k_1\Delta x$ and $k_2\Delta x$, respectively (k_1 and k_2 are the free-space wave numbers of fundamental and second harmonic light). As k_2 is exactly twice k_1, the effect of jitter can be completely eliminated by subtracting $2\Phi_1$ from Φ_2. This elimination requires that one wavelength is exactly an integer multiple of the other one. The optical path length difference experienced by the two wavelengths is given by:

$$\Delta OL = (\Phi_2 - 2\Phi_1)/k_2 \tag{34}$$

and can be measured with great sensitivity. If the thickness of the sample is known, the dispersion of the sample, relative to that of the compensator medium, can be determined.

Figure 23 demonstrates the application of this technique to generate dispersion contrast. A drop of water and a drop of DNA solution (1% vol. concentration), sandwiched between two cover slips, are imaged in transmission. The two drops can clearly be differentiated by different colors indicating different phase differences (Figures 23, bottom). A comparative image recorded with a conventional phase contrast microscope (Figure 23, top) is not able to differentiate between the two substances.

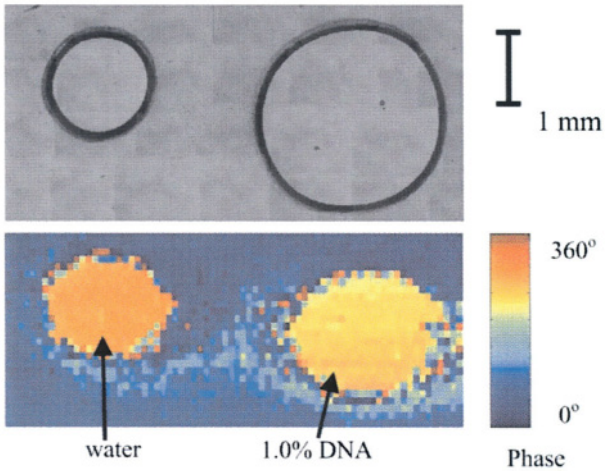

Figure 23. Dispersion contrast. The different dispersion of water and DNA solution in water is used to generate image contrast. Top: conventional phase contrast microscopy image. Bottom: phase-dispersion microscopy image. Reproduced from Yang *et al.* [19] by permission of the Optical Society of America.

The same authors extended their method to obtain 3D information on dispersion distribution by a reflection geometry [20]. The short coherence properties of the light source were used in that case to differentiate between layers of water and gelatin in a test sample. The advantage of this method, as compared to phase contrast microscopy, is that depth resolved information can be obtained even in non-scattering samples.

15.4.3.2 Fourier Transform Methods

As already mentioned in the chapter on absorption measurements (subsection 15.3.1.2), Fourier transform methods to obtain absorption and dispersion spectra are still in their infancies. Only one-dimensional measurements in simple model substances where yet reported. The study by

T. Fuji *et al.* [27] which measured absorption and dispersion by this technique has already been discussed in subsection 15.3.1.2.

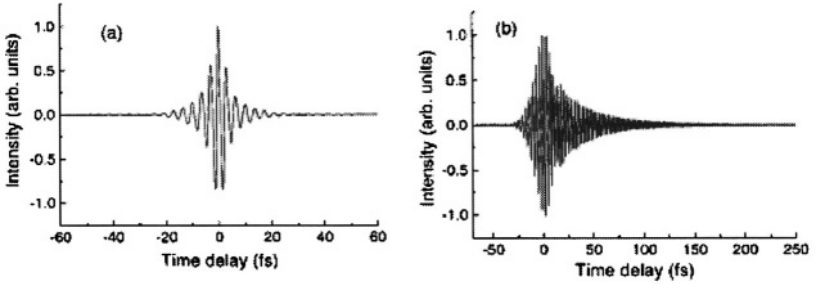

Figure 24. Measurement of water dispersion by LCI. Interferograms recorded a) without, and b) with dispersive water sample (note the different time scales in (a) and (b)). Reproduced from Van Engen *et al.* [50] by permission of the Optical Society of America.

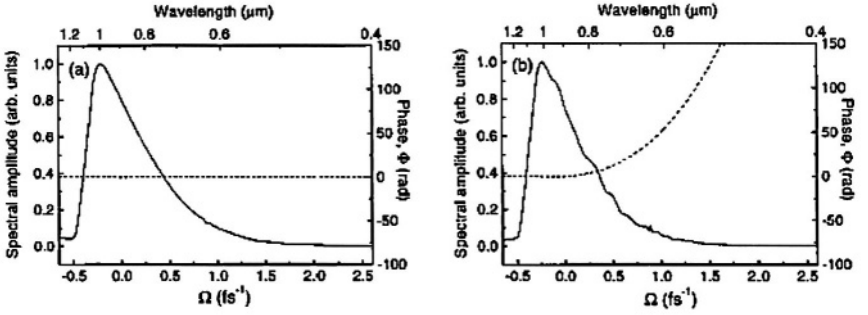

Figure 25. Measurement of water dispersion by LCI. Spectral amplitude (solid curve) and phase (dotted curve) obtained by Fourier transform of the interferograms of Figure 24. a) without, and b) with dispersive water sample. Reproduced from Van Engen *et al.* [50] by permission of the Optical Society of America.

In another study, A.G. Van Engen *et al.* [50] used a similar method to measure second and third order dispersion coefficients $k^{(2)}$ and $k^{(3)}$ of water. A water sample of thickness $d = 1050\ \mu m$ in a glass cell was placed in the sample arm of a Michelson interferometer. The white light source was a 20 W halogen lamp. Figure 24 shows an interferogram recorded without [Figure 24(a)] and with [Figure 24(b)] the dispersive water sample. The broadening and distortion of the interferogram recorded with the dispersive sample is clearly observed. A Fourier transform of the signals yields amplitude and phase spectra (Figure 25). While spectral amplitudes of non-dispersive [Figure 25(a)] and dispersive [Figure 25(b)] cases are similar (solid curves), the dispersion causes a pronounced curvature of the spectral phase (dashed lines) in Figure 25 (b), while the spectral phase remains flat in the dispersion

balanced case [Figure 25(a)]. By performing a polynomial fit to the spectral phase $\Phi(\omega - \omega_0)$, second and third order dispersion coefficients are obtained. Comparison with different water dispersion formulas found in literature showed good agreement with the experimental data over a large range of wavelengths.

The Fourier transform method was recently applied to a liquid solution of great medical relevance. J. Liu *et al.* measured second order dispersion in aqueous solutions of glucose [21]. A halogen lamp was used as the light source, and a cuvette of 20 mm length, filled with aqueous solutions of different glucose concentrations, was placed in the sample arm. A similar cuvette filled with pure water was placed in the reference arm to balance the dispersion of cuvette glass and water. Interferograms were recorded, Fourier transformed, and second order dispersion was obtained from a polynomial fit of the dispersion coefficients to the measured spectral phase.

Figure 26 shows the resulting second order dispersion as a function of wavelength (error bars indicate standard deviations). Three different glucose solutions were measured: 0.2 mg/ml (bottom curve, corresponding to hypoglycemia), 1 mg/ml (middle curve, normal glucose level), and 5 mg/ml (top curve, hyperglycemia). The best wavelength range to discriminate the different glucose levels is around 0.65 μm. While Figure 26 demonstrates that the method works in principle, it is also clear that this technology is still in its infancy. A possible application field might be a non-invasive measurement of glucose concentration in the aqueous humor of the eye.

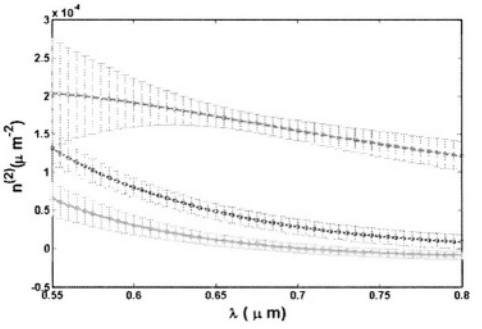

Figure 26. Second order dispersion of different glucose concentrations measured by LCI. Top line ... 5 mg/ml; middle line ... 1 mg/ml; bottom line ... 0.2 mg/ml. Error bars: standard deviation. Reproduced from Liu *et al.* [21] by permission of SPIE.

ACKNOWLEDGMENTS

The author thanks A.F. Fercher, R. Leitgeb, and M. Pircher for fruitful discussions. Parts of the work were financially supported by the Austrian

Fonds zur Förderung der Wissenschaftlichen Forschung (FWF grants P7300-MED, P9781-MED, P14103-MED).

REFERENCES

1. D. Huang, E.A. Swanson, C.P. Lin, J.S. Schuman, W.G. Stinson, W. Chang, M.R. Hee, T. Flotte, K. Gregory, C.A. Puliafito, and J.G. Fujimoto, "Optical coherence tomography," *Science* **254,** 1178-1181 (1991).
2. *Handbook of Optical Coherence Tomography,* B.E. Bouma and G.J. Tearney eds. (Marcel Dekker, New York, 2002).
3. A.F. Fercher and C.K. Hitzenberger, "Optical coherence tomography," *Progr. Opt.* **44,** 215-302(2002).
4. A.F. Fercher, W. Drexler, C.K. Hitzenberger, and T. Lasser, "Optical coherence tomography - principles and applications," *Rep. Progr. Phys.* **66,** 239-303 (2003).
5. W. Drexler, U. Morgner, R.K. Ghanta, F.X. Kärtner, J.S. Schuman, and J.G. Fujimoto, "Ultrahigh-resolution ophthalmic optical coherence tomography," *Nat. Med.* **7,** 502-507 (2001).
6. J.F. de Boer, T.E. Milner, M.J.C. van Gemert, and J.S. Nelson, "Two-dimensional birefringence imaging in biological tissue by polarization-sensitive optical coherence tomography," *Opt. Lett.* **22**, 934-936 (1997).
7. M.J. Everett, K. Schoenenberger, B.W. Colston Jr., and L.B. Da Silva, "Birefringence characterization of biological tissue by use of optical coherence tomography," *Opt. Lett.* **23,** 228-230 (1998).
8. C.E. Saxer, J.F. de Boer, B.H. Park, Y. Zhao, C. Chen, and J.S. Nelson, "High speed fiber based polarization-sensitive optical coherence tomography of in vivo human skin," *Opt. Lett.* **25,** 1355-1357 (2000).
9. S. Jiao and L.V. Wang, "Jones–matrix imaging of biological tissues with quadruple-channel optical coherence tomography," *J. Biomed. Opt.* **7,** 350-358 (2002).
10. C.K. Hitzenberger, E. Götzinger, M. Sticker, A.F. Fercher, "Measurement and imaging of birefringence and optic axis orientation by phase resolved polarization sensitive optical coherence tomography," *Opt. Express* **9,** 780-790 (2001).
11. Z. Chen, T.E. Milner, S. Srinivas, X. Wang, A. Malekafzali, M.J.C. van Gemert, and J.S. Nelson, "Noninvasive imaging of in vivo blood flow velocity using optical Doppler tomography," *Opt. Lett.* **22**, 1119-1121 (1997).
12. J.A. Izatt, M.D. Kulkarni, and S. Yazdanfar, "In vivo bidirectional color Doppler flow imaging of picoliter blood volumes using optical coherence tomography," *Opt. Lett.* **22,** 1439-1441 (1997).
13. Y. Zhao, Z. Chen, C. Saxer, S. Xiang, J.F. de Boer, and J.S. Nelson, "Phase-resolved optical coherence tomography and optical Doppler tomography for imaging blood flow in human skin with fast scanning speed and high velocity sensitivity," *Opt. Lett.* **25,** 114-116 (2000).
14. V. Westphal, S. Yazdanfar, A.M. Rollins, and J.A. Izatt, "Real-time, high velocity-resolution color Doppler optical coherence tomography," *Opt. Lett.* **27**, 34-36 (2002).
15. J.M. Schmitt, S.H. Xiang, and K.M. Yung, "Differential absorption imaging with optical coherence tomography," *J. Opt. Soc. Am. A* **15,** 2288-2296 (1998).

16. U.S. Sathyam, B.W. Colston Jr., L.B. Da Silva, and M.J. Everett, "Evaluation of optical coherence quantitation of analytes in turbid media by use of two wavelengths," *Appl.* Opf. **38,** 2097-2104 (1999).
17. C.K. Hitzenberger and A.F. Fercher, "Differential phase contrast in optical coherence tomography," *Opt. Lett.* **24,** 622-624 (1999).
18. M. Sticker, M. Pircher, E. Götzinger, H. Sattmann, A.F. Fercher, and C.K. Hitzenberger, "En face imaging of single cell layers by differential phase contrast optical coherence microscopy," *Opt. Lett.* **27,** 1126-1128 (2002).
19. C. Yang, A. Wax, I. Georgakoudi, E.B. Hanlon, K. Badizadegan, R.R. Dasari, and M.S. Feld, "Interferometric phase-dispersion microscopy", *Opt. Lett.* **25,** 1526-1528 (2000).
20. C. Yang, A. Wax, R.R. Dasari, and M.S. Feld, "Phase-dispersion optical tomography," *Opt. Lett.* **26,** 686-688 (2001).
21. J. Liu, M. Bagherzadeh, C.K. Hitzenberger, M. Pircher, R.J. Zawadzki, and A.F. Fercher, "Glucose dispersion measurement using white-light LCI" in *Coherence Domain Optical Methods and Optical Coherence Tomography in Biomedicine VII,* V.V. Tuchin, J.A. Izatt, J.G. Fujimoto eds. *Proc. SPIE* **4956,** 348-351 (2003).
22. C.K. Hitzenberger, A. Baumgartner, W. Drexler, and A.F. Fercher, "Dispersion effects in partial coherence interferometry: implications for intraocular ranging," *J. Biomed. Opt.* **4,** 144-151 (1999).
23. W. Drexler, U. Morgner, F.X. Kärtner, C. Pitris, S.A. Boppart, X.D. Li, E.P. Ippen, and J.G. Fujimoto, "In vivo ultrahigh-resolution optical coherence tomography," *Opt. Lett.* **24,** 1221-1223 (1999).
24. C.K. Hitzenberger, A. Baumgartner, and A.F. Fercher, "Dispersion induced multiple signal peak splitting in partial coherence interferometry," *Opt. Commun.* **154,** 179-185 (1998).
25. A.F. Fercher, C.K. Hitzenberger, M. Sticker, R. Zawadzki, B. Karamata, and T. Lasser, "Numerical dispersion compensation for partial coherence interferometry and optical coherence tomography," *Opt. Express* **9,** 610-615 (2001).
26. M. Born and E. Wolf, *Principles of Optics,* **6th** ed. (Pergamon Press, Oxford, 1986).
27. T. Fuji, M. Miyata, S. Kawato, T. Hattori, and H. Nakatsuka, "Linear propagation of light investigated with a white-light Michelson interferometer," *J. Opt. Soc. Am. B* **14,** 1074-1078 (1997).
28. B.E. Bouma, G.J. Tearney, I.P. Bilinsky, B. Golubovic, and J.G. Fujimoto, "Self-phase-modulated Kerr-lens mode-locked Cr:forsterite laser source for optical coherence tomography," *Opt. Lett.* **21,** 1839-1841 (1996).
29. I. Hartl, X.D. Li, C. Chudoba, R.K. Ghanta, T.H. Ko, J.G. Fujimoto, J.K. Ranka, and R.S. Windeler, "Ultrahigh-resolution optical coherence tomography using continuum generation in an air silica microstructure optical fiber," *Opt. Lett.* **26,** 608-610 (2001).
30. B. Povazay, K. Bizheva, A. Unterhuber, B. Hermann, H. Sattmann, A. F. Fercher, W. Drexler, A. Apolonski, W. J. Wadsworth, J. C. Knight, P. St. J. Russell, M. Vetterlein, and E. Scherzer, "Submicrometer axial resolution optical coherence tomography," *Opt. Lett.* **27,** 1800-1802 (2002).
31. R.N. Bracewell, *The Fourier Transform and its Application,* **3rd** ed. (McGraw-Hill, Boston, 2000).
32. E.A. Swanson, D. Huang, M.R. Hee, J.G. Fujimoto, C.P. Lin, and C.A. Puliafito, "High-speed optical coherence domain reflectometry," *Opt. Lett.* **17,** 151-153 (1992).
33. M. Pircher, E. Götzinger, R. Leitgeb, A.F. Fercher, and C.K. Hitzenberger, "Speckle reduction in optical coherence tomography by frequency compounding," *J. Biomed. Opt.* **8**, 565-569 (2003).

34. M. Pircher, E. Götzinger, R. Leitgeb, A.F. Fercher, and C.K. Hitzenberger, "Measurement and imaging of water concentration in human cornea with differential absorption optical coherence tomography," *Opt. Express,* submitted: July 2003
35. J.M. Schmitt, S.L. Lee, and K.M. Yung, "An optical coherence microscope with enhanced resolving power in thick tissue," *Opt. Commun.* **142,** 203-207 (1997).
36. G.M. Hale and M.R. Querry, "Optical constants of water in the 200 nm to 200 μm wavelength region," *Appl. Opt.* **12,** 555-563 (1973).
37. C.K. Hitzenberger, A. Baumgartner, W. Drexler, and A.F. Fercher, "Interferometric measurement of corneal thickness with micrometer precision," *Am. J. Opthalmol.* **118,** 468-476 (1994).
38. H.E. Kaufmann, B.A. Barron, M.B. McDonald, *The Cornea* (Butterworth-Heinemann, 1998).
39. M.D. Kulkarni and J.A. Izatt, "Spectroscopic optical coherence tomography," *OSA Technical Digest* **9,** 59-60 (1996).
40. B. Hermann, K. Bizheva, H. Sattmann, A. Unterhuber, B. Povazay, A.F. Fercher, and W. Drexler, "Quantitative measurement of absorption with spectroscopic optical coherence tomography," *Proc. SPIE* **4956,** 375 (2003).
41. D.J. Faber, E.G. Mik, M.C.G. Aalders, F.J. van der Meer, and T.G. van Leeuwen, "Blood oxygenation measurement with optical coherence tomography," *Proc. SPIE* **4251,** 128-135 (2001).
42. U. Morgner, W. Drexler, F.X. Kärtner, X.D. Li, C. Pitris, E.P. Ippen, and J.G. Fujimoto, "Spectroscopic optical coherence tomography," *Opt. Lett.* **25,** 111-113 (2000).
43. A.F. Fercher, C.K. Hitzenberger, and M. Juchem, "Measurement of intraocular optical distances using partially coherent laser light," *J. Mod. Optics* **38,** 1327-1333 (1991).
44. A.F. Fercher, C.K. Hitzenberger, G. Kamp and S.Y. El-Zaiat, "Measurement of intraocular distances by backscattering spectral interferometry," *Opt. Commun.* **117,** 43-48 (1995).
45. G. Häusler and M.W. Lindner, ""Coherence radar" and "spectral radar" – new tools for dermatological diagnosis,"*J. Biomed. Opt.* **3,** 21-31 (1998).
46. M. Wojtkowski, R. Leitgeb, A. Kowalczyk, T. Bajraszewski, and A.F. Fercher, *"In vivo* human retinal imaging by Fourier domain optical coherence tomography," *J. Biomed. Opt.* **7,** 457-463 (2002).
47. R. Leitgeb, C.K. Hitzenberger, and A.F. Fercher, "Performance of fourier domain vs. time domain optical coherence tomography," *Opt. Express* **8,** 889-894 (2003).
48. E. Wolf, "Three-dimensional structure determination of semi-transparent objects from holographic data," *Opt. Commun.* **1,** 153-156 (1969).
49. R. Leitgeb, M. Wojtkowski, A. Kowalczyk, C.K. Hitzenberger, M. Sticker, A.F. Fercher, "Spectral measurement of absorption by spectroscopic frequency-domain optical coherence tomography," *Opt. Lett.* **25,** 820-822 (2000).
50. A.G. Van Engen, S.A. Diddams, and T.S. Clement, "Dispersion measurements of water with white-light interferometry," *Appl. Opt.* **37,** 5679-5686 (1998).
51. B.L. Danielson and C.Y. Boisrobert, "Absolute optical ranging using low coherence interferometry," *Appl Opt.* **30,** 2975-2979 (1991).
52. A. Ghatak and K. Thyagarajan, *Introduction to Fiber Optics* (Cambridge University Press, Cambridge 1998).
53. W.J. Tango, "Dispersion in stellar interferometry," *Appl. Opt.* **29,** 516-521 (1990).
54. E.D.J. Smith, A.V. Zvyagin, and D.D. Sampson, "Real time dispersion compensation in scanning interferometry," *Opt. Lett.* **27,** 1998-2000 (2002).

55. K.F. Kwong, D. Yankelevich, K.C. Chu, J.P. Heritage, and A. Dienes, "400-Hz mechanical scanning optical delay line," *Opt. Lett.* **18,** 558-560 (1993).
56. G.J. Tearney, B.E. Bouma, and J.G. Fujimoto, "High-speed phase- and group-delay scanning with a grating-based phase control delay line," *Opt. Lett.* **22,** 1811-1813 (1997).
57. A.M. Rollins, M.D. Kulkarni, S. Yazdanfar, R. Ung-arunyawee, and J.A. Izatt, *"In vivo* video rate optical coherence tomography," *Opt. Express* **3**, 219-229 (1998).
58. E. Brinkmeyer and R. Ulrich, "High-resolution OCDR in dispersive waveguides," *Electron. Lett.* **26**, 413-414 (1990).
59. J.F. de Boer, C.E. Saxer, and J.S. Nelson, "Stable carrier generation and phase-resolved digital data processing in optical coherence tomography," *Appl. Opt.* **40**, 5787-5790 (2001).
60. A.F. Fercher, C.K. Hitzenberger, M. Sticker, R. Zawadzki, B. Karamata, and T. Lasser, "Dispersion compensation for optical coherence tomography depth-scan signals by a numerical technique," *Opt. Commun.* **204**, 67-74 (2002).
61. J.D. Gaskill, *Linear Systems, Fourier Transforms, and Optics,* chapter 8 (John Wiley & Sons, New York , 1978).
62. D.X. Hammer, A.J. Welch, G.D. Noojin, R.J. Thomas, D.J. Stolarski, and B.A. Rockwell, "Spectrally resolved white-light interferometry for measurement of ocular dispersion", *J. Opt. Soc. Am. A* **16**, 2092-2102 (1999).
63. W. Drexler, C.K. Hitzenberger, A. Baumgartner, O. Findl, H. Sattmann, and A.F. Fercher, "Investigation of dispersion effects in ocular media by multiple wavelength partial coherence Interferometry," *Exp. Eye Res.* **66**, 25-33 (1998).
64. A.F. Fercher, K. Mengedoht, W. Werner, "Eye-length measurement by interferometry with partially coherent light," *Opt. Lett.* **13**, 186-188 (1988).
65. C.K.Hitzenberger, "Optical measurement of the axial eye length by laser Doppler interferometry," *Invest. Ophthalmol. Vis. Sci.* **32**, 616-624 (1991).
66. W. Drexler, A. Baumgartner, O. Findl, C.K. Hitzenberger, H. Sattmann, and A.F. Fercher, "Submicrometer precision biometry of the anterior segment of the human eye," *Invest. Opthalmol. Vis. Sci.* **38**, 1304-1313 (1997).

This page intentionally left blank

Chapter 16

EN-FACE OCT IMAGING

Adrian Podoleanu
School of Physical Sciences, University of Kent at Canterbury, Canterbury CT2 7NR, UK

Abstract: *En-face* OCT imaging delivers slices in the tissue of coherence length thickness with an orientation similar to that of confocal microscopy. In the flying spot implementation, the phase modulation introduced by the transverse scanners may be exploited to generate *en-face* OCT images. New avenues opened by the *en-face* OCT are presented, such as the versatile operation in A, B, C scanning regimes, simultaneous OCT and confocal imaging and simultaneous OCT imaging at different depths. B-scan and C-scan images from different types of tissue are presented.

Key words: white light interferometry, simultaneous confocal and OCT imaging, multiple interferometer configurations

16.1 DIFFERENT SCANNING PROCEDURES

To obtain 3D information about the object, any imaging system, operating on the flying spot concept, is equipped with three scanning means, one to scan the object in depth and two others to scan the object transversally. Depending on the order these scanners are operated and on the scanning direction associated with the line displayed in the raster of the final image delivered, different possibilities exist.

16.1.1 A-scan

Low coherence interferometry has evolved as an absolute measurement technique which allows high resolution ranging [1] and characterisation of optoelectronic components [2,3]. The first application in the biomedical optics field was for the measurement of the eye length [4]. A reflectivity

profile in depth is obtained, called A-scan, as shown in Figure 1. A low coherence interferometry system is generally based on a two-beam interferometer. A-scan technique was facilitated by a technical advantage: when moving the mirror in the reference path of the interferometer, not only is the depth scanned, but a carrier is also generated. The carrier frequency is the Doppler shift produced by the longitudinal scanner itself (moving along the axis of the system, Z, to explore the tissue in depth). Due to the high potential of the technique for high resolution imaging of the tissue, it is often referred to as optical coherence tomography (OCT) [5].

16.1.2 A-scan Based B-scan

B-scan images, analogous to ultrasound B-scan are generated by collecting many A-scans for different and adjacent transverse positions. The lines in the raster generated correspond to A-scans, i.e., the lines are oriented along the depth coordinate. The transverse scanner (operating along X or Y, or along the polar angle θ in polar coordinates in Figure 1, with X shown in Figure 2 top) advances at a slower pace to build a B-scan image. The image bandwidth, given by the speed the depth pixel size is scanned, appears in the spectrum of the photodetected signal as an enlargement of the Doppler frequency component, and is practical identical with the bandwidth required to process an individual A-scan (as the lateral movement of the beam is at a much slower speed than the scanning in depth). The majority of reports in literature [6-8] refer to this way of operation. A commercial OCT instrument [9] exists which can produce a B-scan image of the retina in ~ 1 second.

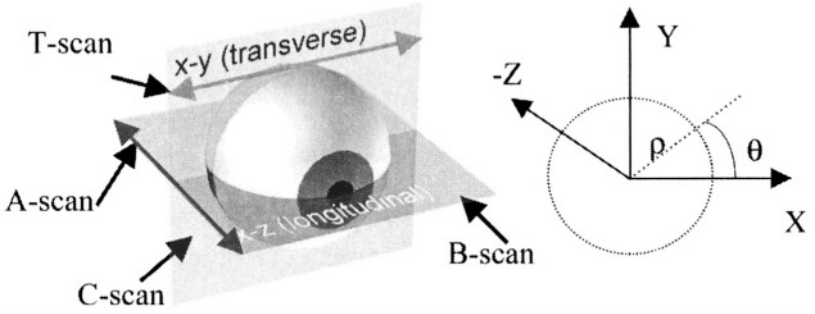

Figure 1. Relative orientation of the axial scan (A-scan), longitudinal slice (B-scan), x-y (transverse) scan (T-scan), and *en-face* or transverse slice (C-scan).

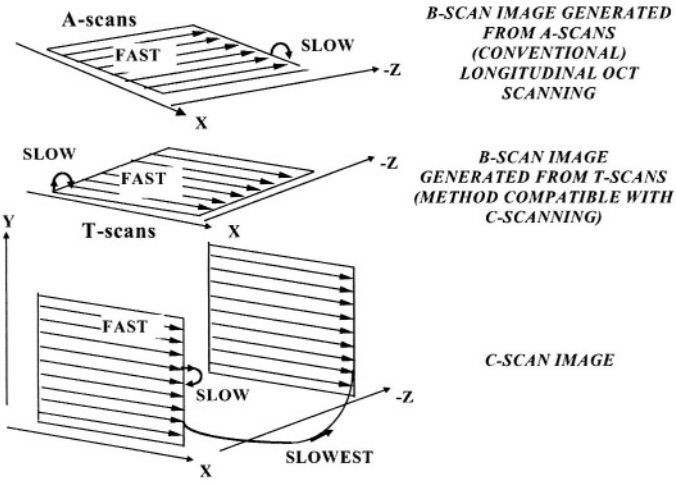

Figure 2. Different modes of operation of the three scanners in a flying spot OCT system.

16.1.3 T-scan Based B-scan

In this case, the transversal scanner produces the fast lines in the image [10-12]. We call each such image line as a T-scan. This can be produced by controlling either the transverse scanner along the X-coordinate, or along the Y-coordinate or along the polar angle θ, with the other two scanners fixed. The example in the middle of Figure 2 illustrates the generation of a T-scan based B-scan, where the X-scanner produces the T-scans and the axial scanner advances slower in depth, along the Z-coordinate. As shown below, this procedure has a net advantage in comparison with the A-scan based B-scan procedure as it allows production of OCT transverse (or *en-face*) images for a fixed reference path, images called C-scans.

16.1.4 C-scan

C-scans are made from many T-scans along either of X, Y, ρ or θ coordinates, repeated for different values of the other transverse coordinate, Y, X, θ or ρ respectively in the transverse plane. The repetition of T-scans along the other transverse coordinate is performed at a slower rate than that of the T-scans (Figure 2 bottom), called the frame rate. In this way, a complete raster is generated. Different transversal slices are collected for different depths Z, either by advancing the optical path difference in the OCT in steps after each complete transverse (XY) or (ρ,θ) scan, or continuously at a much slower speed than the frame rate. For correct

sampling in depth of the tissue volume, the speed of advancing in depth should be such that on the duration of the frame, the depth variation should be no more than half the depth resolution.

16.1.5 Collecting 3D Data

3D complete information could be collected in different ways, either acquiring many longitudinal OCT images (B-scans) at different *en-face* positions [13,14] or many *en-face* OCT images (C-scans) at different depth positions [15-18]. In principle, the volume rendered by either procedure from the tissue should be equivalent. However, the devices used to scan the object in the three directions are not identical. They are chosen or designed according to the scanning method used: either (i) *en-face,* where a fast galvanometer scanner, a resonant scanner or a polygon mirror to generate T-scans is paired to a slower scanning device for scanning the depth along depth, such as a translation stage or (ii) longitudinal OCT, where a fast scanner to generate A-scans such as a turbine driven mirror [19] or a spectral scanning line, using a diffraction grating [20] and a fast galvanometer mirror or a resonant scanner, is paired with a slower scanning device to perform the advance in the transverse plane, using a piezo or a galvanometer scanner. This dedicated design determines the way the 3D information is collected using the flying spot concept.

16.1.6 Sampling Function in *En-Face* OCT

In order to generate C-scan images at a fixed depth, a path imbalance modulator is needed in order to create a carrier for the image bandwidth. This will obviously require the introduction of a phase modulator in one of the arms of the interferometer, which would complicate the design and introduce dispersion [21]. Research has shown that the X or Y-scanning device itself introduces a path modulation which plays a similar role to the path modulation created by the longitudinal scanner employed to produce A-scans or A-scan based B-scans. Theoretical analysis has shown that the generation of a C-scan OCT image can be interpreted as interrogating the object with a specific sampling function. Depending on the position of the incident beam on the scanner mirror and on the interface optics used, the sampling function could look either as Newton rings or as a regular grid of lines. The sampling function is in fact a fringe pattern in transversal section. Consequently, when the beam scans the target, the OCT signal is modulated by this fringe pattern. As the pattern is not regular, the transverse resolution varies across the target and different frequencies result in contrast to the generation of A-scans, where the carrier frequency is constant. However, for

sufficiently large image size, the errors introduced in the image by the variable sampling pattern can be neglected.

16.1.6.1 Newton rings

Figure 3 shows the beam being deflected from point O on the galvanometer mirror MX by tilting this mirror at different angles β. In this simplified approach, the distance between galvanometer mirrors MX and MY is neglected in comparison with the distance z_1 to lens L1, i.e., as regards to scanning along Y, the beam may also be considered as originating from O. The conjugate point of O is O' and therefore the optical path lengths of all the reflected rays measured between mirror MX and O' are equal. Let us consider a flat surface S as the object under test, perpendicularly oriented to the system axis and intersected by the scanned beam at N.

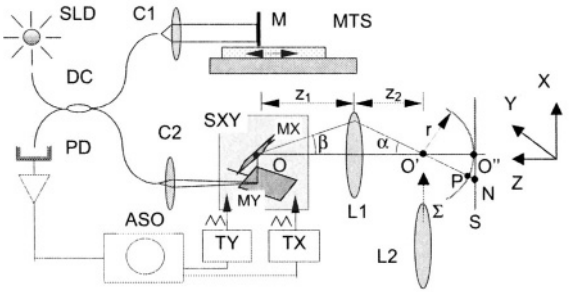

Figure 3. SLD: Superluminescent diode; DC: directional coupler; C1, C2: microscope objectives; M: mirror; MTS: micrometer translation stage; SXY: galvanometer scanning mirror system; MX, MY: scanner mirrors; L1: lens; PD: photodetector; ASO: analogue storage oscilloscope; TX, TY: triangle waveform generators.

The coherence surface Σ, defined by the length of the reference arm, is given by the spherical surface of radius r centered in O'. For each scanning angle β, two beams are superposed on the photodetector, one being reflected from the point N and the second reflected by mirror M, which may be equivalently considered as originating from point P on surface Σ. The optical path difference (OPD) between the reference and the sensing arm is:

$$OPD = 2(O'N - O'P) = 2\left[\frac{r}{\cos\alpha} - r\right] . \qquad (1)$$

Maxima are obtained when

$$OPD = 2M\frac{\lambda}{2}, \tag{2}$$

where λ is the central wavelength and M an integer. The variation in the angle β measured about the point O between adjacent rays corresponding to two maxima is connected to the variation in angle α measured about the point O' and is given by:

$$\delta\beta = \frac{z_2}{z_1}\delta\alpha = \frac{z_2}{z_1}\frac{\lambda\cos^2\alpha}{2r\sin\alpha} \approx \frac{z_2}{z_1}\frac{\lambda}{2r\alpha}, \tag{3}$$

where we have taken into account the distances z_1 and z_2 in Figure 3 and assumed small angles in equation 3. If mirror MX is driven by a triangular voltage signal of amplitude U and frequency F_x then:

$$\beta(t)=4kUtF_x, \tag{4}$$

where k is measured in rad/V and represents the scanner angular efficiency. Using equations 1- 4, the frequency ν at which maximums are encountered in the signal can be obtained as:

$$\nu = \frac{8kUz_1F_x}{z_2}\frac{r\alpha}{\lambda}. \tag{5}$$

A similar expression can be obtained by considering the speed of OPD variation when performing A-scanning, in which case the reference mirror is moved at a constant speed, v, and the frequency of the Doppler beat signal amounts to: $\nu = 2v/\lambda$. Comparing this with equation 5 leads to an equivalent depth scanning speed:

$$v = \frac{4kUx_1F_x}{z_2}r\alpha. \tag{6}$$

The geometrical locus of the points on the surface S of maximum interference according to equation 2 is described by rings of radius RM = O"N. For small angles and low order M, the radius of such rings is given by:

$$R_M \approx \sqrt{Mr\lambda}\,, \tag{7}$$

which shows that the locus of maximum interference is given by a similar relation to that describing Newton rings. However, the configuration in Figure 3 differs from the Newton rings configuration presented in classical Optics textbooks based on a spherical element in contact with a planar element [22]. Here, the interfering rays producing Newton rings are coming from two different arms of the interferometer.

Given the coherence length l_c of the source, the target area sampled by these Newton rings is limited to:

$$A \approx \frac{\pi}{2} l_c r\,. \tag{8}$$

The analysis shows that the object is being interrogated with a sampling function which in the particular case of the set-up in Figure 3 looks like concentric circles centered on the system axis. When the object is a mirror, the T-scan maps the sampling function and the returned signal is modulated in intensity at the frequency ν given by equation 5.

In order to improve the transversal resolution, another lens L2, is placed in O'. The previously obtained relations are still valid with r replaced by f_2, the focal length of lens L2.

An image from a mirror displays the sampling function pattern described by Newton rings, as shown in Figure 4. Such an image was obtained by using a lens L2 of 2.5 cm focal length, and by driving the horizontal and vertical scanners with signals at F_x = 20 Hz (signal generator GX) and 0.25 Hz (signal generator GY) respectively. The amplitude of both signals was 0.25 V and scanners with k = 69.81 rad/V were used.

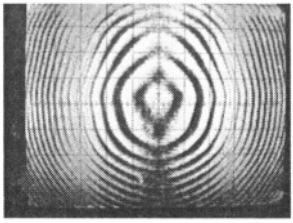

Figure 4. Newton rings sampling function; 50 mV/div (185 μm/div).

The main advantages of the method are its simplicity and quick display capability.

16.1.6.2 Grid Sampling Function

The incident beam direction is shifted by δ away from the rotation center of the line scanner, chosen to be the X-scanner in Figure 5. To obtain this, the scanner is displaced towards the objective C2 by a distance δ and then the support holding the fiber and collimator C2 (Figure 3) is moved towards lens L1 by another distance δ. In this way, for $\beta = 0$, the incoming ray is incident on the galvanometer mirror in a point B on the optical axis (of the lens), situated at z_1 - δ away from lens L1. Shown in Figure 5 is a ray undergoing reflection at mirror MX when MX is at the angular position β = 0 (impact point B) and $\beta \neq 0$ (impact point C). The ray deflected from C intersects the optical axis in A.

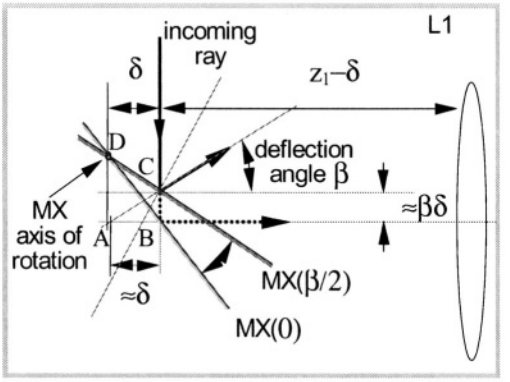

Figure 5. The object beam in Figure 3 is incident on the galvanometer scanner at a distance δ away from the center of rotation. Axes X and Z are in the plane of the drawing.

For small scanning angles β, the segment AB $\approx \delta$. In these circumstances it can be shown that the path imbalance OPD introduced between the central ray (deflected from B along the optic axis) and the ray deflected from C at an angle β from the optic axis is given by the equation:

$$\mathrm{OPD} \approx -2\delta\beta + f_2 \frac{z_1^2}{z_2^2}\beta^2 . \qquad (9)$$

The first term in Figure 9 can be intuitively thought of as arising from the double pass of light along segment BC (to and from the object), although the exact calculations are more elaborated. The second term gives the path imbalance responsible for Newton rings imaging in which case the ray geometry and formula were presented in subsection 16.1.6.1. Point A at a distance z_1 in front of L1 and point O' at a distance z_2 behind L1 (Figure 3) are conjugate by virtue of L1. The frequency of the photodetected signal due to scanning a mirror placed in the focal plane of lens L2, perpendicular to the optic axis, is given by:

$$\nu = \frac{8kF_x U}{\lambda}[\delta - 4kUf_2 \frac{z_1^2}{z_2^2} F_x t], \tag{10}$$

where the same notations as those in Figure 5 were used. During a scan, the frequency ν varies between:

$$\nu_{min,max} = \nu_c \pm \nu_n = \frac{8kF_x U}{\lambda}[\delta \pm f_2 \frac{z_1^2}{z_2^2} \beta_m], \tag{11}$$

where ν_c is the central frequency and ν_n the frequency spread owing to the nonlinear OPD dependence on β in (10) (this is also the maximum component in the spectrum in the centered beam case in Figure 3, Newton rings sampling function case.

Interference occurs for $|OPD| < l_c$, where l_c is the coherence length of the source, and the maximum angle $|\beta|$ for which $|OPD| = l_c$ is β_c. For $|\beta| > \beta_c$, $\beta_m = \beta_c$, and for $|\beta| < \beta_c$, $\beta_m = kU$. Based on the Airy disk size of a pixel defined on a target situated in the focal plane of lens L2 (focal length f_2), for a beam diameter D the image bandwidth is:

$$B_i = 0.82 \frac{F_x D}{\lambda} \frac{\Delta X}{f_2}, \tag{12}$$

where ΔX is the width of the T-scan on the target.

The linear term in equation 10 becomes dominant when the shift δ is high enough, giving a first limiting condition for the minimum value of δ. A second condition results from $\nu_c - \nu_n > B_i$. It can be shown that the second condition prevails, resulting in:

$$\delta > \frac{z_1}{z_2}\sqrt{f_2 l_c + 0.04D^2} \,. \tag{13}$$

During scanning, the carrier frequency ν varies and the bandwidth of the bandpass filter preceding the rectifier has to be large enough to accommodate frequency values between a minimum ν_{min} - B_i and a maximum $\nu_{max} + B_i$, i.e., a bandwidth $2(B_i + \nu_n)$ (this is only an approximate evaluation). In terms of noise, therefore, the method presented here is inferior to the A-scan based OCT conventional technique, especially for large scan angles.

A "carrier" is distinguishable as shown in Figure 6 bottom (beam displaced by $\delta = 3$ mm), in comparison with the non-displaced beam spectrum shown in Figure 6 top. For example, values of $\nu_c = 6.86$ kHz and $\nu_n = 1.6$ kHz are obtained from equation 10, in agreement with Figure 6 bottom left, when $F_x = 20$ Hz, $\lambda = 0.83$ μm, D = 2 mm, $f_2 = 3$ cm, and $\Delta X = 2$ mm. Equation 12 gives $B_i = 5.27$ kHz. To produce a lateral scan $\Delta X = 2$ mm for $z_1 = 14.5$ cm and $z_2 = 10.2$ cm, the value of the applied voltage is U = 0.34 V. Using equation 13 with $l_c = 31.89$ μm, δ should be higher than 2.1 mm.

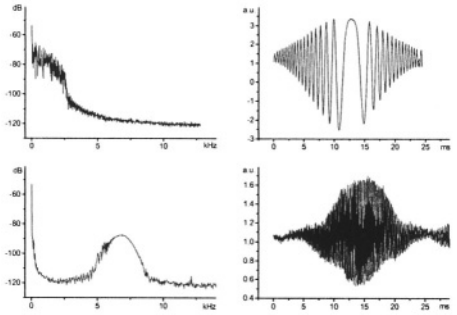

Figure 6. Spectra (left) and the temporal evolution (right) for optical beam centered (top) and shifted by $\delta = 3$ mm (bottom). $z_1 = 14.5$ cm, $z_2 = 10.2$ cm, X-scanner triangular drive signal of amplitude U = 0.17 V and frequency $F_x = 20$ Hz, Y-scanner not driven.

The sampling function takes the form of a grid of regular lines, as shown in Figure 7. This was obtained by driving the X and Y scanners with ramp signals of amplitude 0.17 V, $F_x = 20$ Hz and $F_y = 0.2$ Hz, for $\delta = 3$ mm and using the same scanner head as that used to generate the sampling function in Figure 4. Using the conversion factor of 29 μm/mV, the period on the

target is found to be about 6 μm which indicates that the minimum feature size which can be imaged using this sampling function is 12 μm. In comparison with the Newton rings case, the spatial sampling rate is constant across the area displayed.

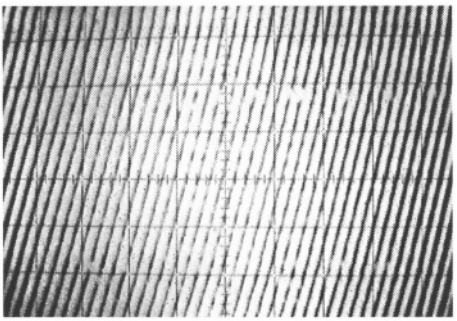

Figure 7. Grid sampling function. Horizontal and vertical scale: 10 mV/div.

To reduce the contribution of 1/f noise, a high modulation frequency is desirable. By driving the X galvo-scanner with a ramp signal at a frequency 300 Hz, amplitude 2 V and $\delta = 3$ mm (maximum permissible by the size of the scanning mirror), a value of ν_c in excess of 200 kHz was obtained.

Compared to the case of the non-displaced beam Newton rings sampling function, the coherence surface now changes from spherical to conical. For small angles β, the conical surface can be approximated with a plane forming an angle $90^o - \varphi$ with the plane of the diagram in Figure 3 and intersecting it in O, with $\tan\varphi \approx \delta / f_2$.

By generating a carrier, the features of the object in the centre of the image are now sampled at the same rate as those at the periphery of the image, in opposition to the $\delta = 0$ case (Newton rings). This method has similarities with topographical methods such as Moiré fringe pattern imaging. The sampling function acts as a selective topographic function, with only those features of the object sampled for which $|OPD| < l_c$.

16.1.6.3 Using a phase modulator

Ideally, to insure constant sampling rate within the C-scan image, a phase modulator should be introduced in the interferometer. This is especially required for imaging small size features, less than the sampling spatial period (determined by the distance between Newton rings in Figure 4 or the lines in the grid in Figure 7). However, for sufficiently large size images, a phase modulator may not be required. To illustrate the role each modulation has in the creation of the C-scan image, depending on the image size, a

phase modulator PM based on a piezo-cylinder was introduced in an OCT interferometer [12] and driven at 30 kHz. The X-galvo-scanner was driven by ramp signals of frequency Fx = 600 Hz and different amplitudes U. The Y-galvo-scanner was not driven. Figure 8 shows the ratio between the amplitudes of the components in the spectrum of the photodetected current in a bandwidth of 5 kHz centered about 60 (90) kHz obtained with and without the sinusoidal modulation of PM at 30 kHz. The amplitudes were averaged over 100 measurements. These graphs show that for voltages over U_c = 0.6 V, corresponding to a lateral image size of 1.6 mm, the external phase modulation does not add any noticeable contribution to the demodulated signal. Consequently, for an image size larger than 1.6 mm, the phase modulation created by the X-galvo-scanner is sufficient. Little enhancement is brought about by the PM in the range 0.3-0.6 V. For voltage less than U_3 = 0.32 V, the modulation introduced by PM becomes more important, as proved by the graphs in Figure 8. This corresponds to a lateral image size of less than 0.8 mm for the configuration used in Figure 3, where L1 has a focal length of 12 cm and a lens L2 of 2 cm.

The carrier frequency needs to be larger than the bandwidth. Therefore, for video rate OCT, only fast modulators can be used, which work at over few MHz, such as electro-optic modulators. However, such modulators introduce dispersion [21]. Non-dispersive modulation methods rely on piezo-vibration of tiny mirrors or on stretching fiber. Such methods cannot however approach 1 MHz required for fast OCT imaging. Utilization of such modulators limits the acquisition time. For instance, in reference [18], microscopic size C-scan images of 0.6 x 0.35 mm of a frog embrio were obtained with piezo - modulation at 120 kHz. The external phase modulation was essential in this case, as the scanners were moved relatively slow (acquisition of a 10^6 voxel in 5 minutes).

Transillumination tomography [23] has been demonstrated using the same principle, where the phase modulator was implemented in fiber. Utilization of a low frequency phase modulator was made possible by the slow transverse scanning (8 minutes for a 200 x 50 pixels images), so the carrier frequency generated by the external phase modulator was much larger than the image bandwidth. The small band required allowed a high dynamic range, 130 dB.

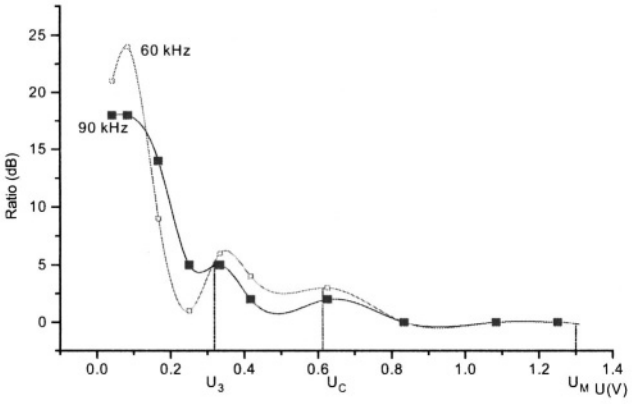

Figure 8. Ratio of the amplitudes of the 60 kHz (and 90 kHz) components in the spectrum with and without the sinusoidal PM modulation, versus the amplitude of the ramp driving signal, U. Fx = 600 Hz, the Y-galvo-scanner not driven.

16.1.6.4 Profilometry

The images in Figure 5 and 7 above display the sampling function when the object is a flat mirror. When imaging scattering elements of a rough surface, or a tilted surface, the sampling function is distorted. However, a C-scan image could still be generated. Four C-scan images at 20 μm depth intervals are shown in Figure 9, obtained from the rough surface of a 5 pence coin.

Similar images could be obtained irrespective if the beam was incident on the center of the mirror scanner or off-axis. With the off-axis configuration, a band-pass filter could be used for better signal to noise ratio.

What is important for imaging is the generation of fringe cycles when the features are at coherence. The amplitudes of these cycles are rectified and presented as proportional brightness on the screen. If the features are rough, even if they happen to be in the centre of the Newton rings sampling function, they may be sampled with a transverse resolution better than that determined by the distance between successive Newton rings (in Figure 4) or the lines in the grid (in Figure 7). The roughness itself, compounded with the aberrations of the interface optics, introduces phase changes which lead to the modulation of interference under the form of spikes. The variations in the signal due to roughness may be denser when reported to the transverse coordinate than that due to the sampling function. If such variation exists,

then it is presented as an ac voltage to the rectifier. The amplitude of the spikes bear resemblance to the reflectivity of the local profile and a high detailed image can be produced.

When imaging very small features, it is expected to "see" the sampling function superposed on the image [11]. The sampling function is noticeable in Figure 9, especially in the image in the top raw right.

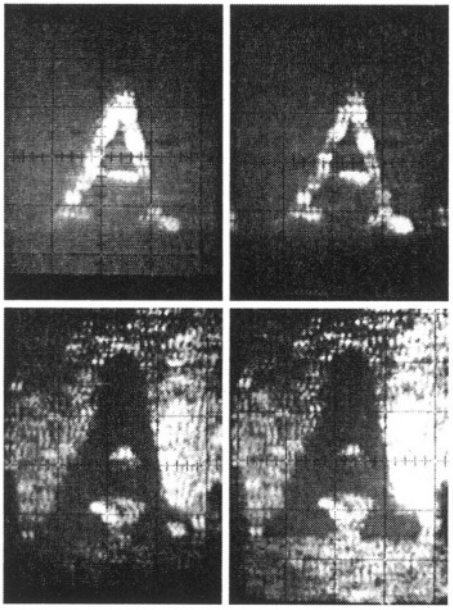

Figure 9. Images obtained from a 5 pence coin. The reference path was increased in steps of 20 μm between top left and bottom right image; 370 μm/div both horizontally and vertically.

For profilometry, the technique has the disadvantage that no modulation arises when the surface coincides with the coherence surface (Σ in Figure 3). A very smooth surface with curved profile matching the curvature of the rays emerging from O' may be missed. However, this is a relatively unlikely case, excluded in practice when dealing with rough surfaces.

In practice, the result of scanning the beam over tiny scattering features reduces to the effect encountered in anemometry. In that case the beam is stationary and particles are intersecting the beams. The interference pattern is modulated by fluctuations due to the intersecting particles.

Using the same principle, images from the tissue are generated, as demonstrated below.

16.1.6.5 B-scan Images

Figures 10 and 11 present T-scan based B-scan OCT images using an SLD as a source, which determines 12 μm depth resolution in the tissue. The image in Figure 10, collected from the retina in the right eye of a volunteer displays the optic nerve up to the fovea. Figure 11 shows with high resolution the nerves in the cornea structure.

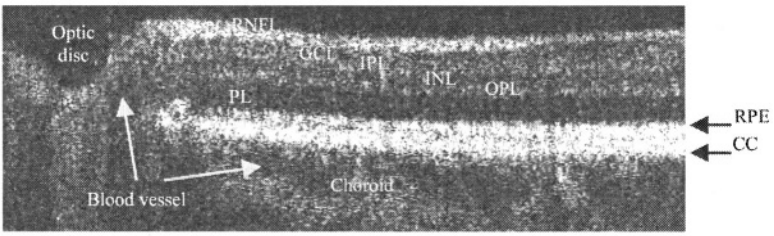

Figure 10. 20° B-scan OCT image constructed from T-scans showing the parafovea and the optic nerve. 1 mm depth (vertical axis, measured in air). RNFL (bright): retinal nerve fiber layer; GCL (dark): ganglion cell layer; IPL (bright): inner plexiform layer; INL (dark): inner nuclear layer; OPL (bright): outer plexiform layer; PL (dark): photoreceptor layer; RPE (bright): retinal pigment epithelium; CC (bright): choriocapillaris. Transversal pixel size: 15 μm, depth pixel size: 12 μm in tissue.

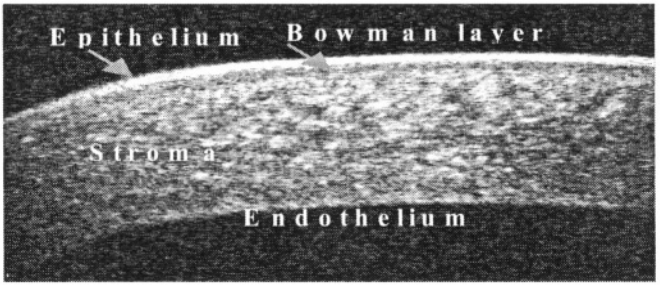

Figure 11. B-scan OCT image (2 mm lateral, 1.25 mm depth in air) constructed from T-scans.

Images in Figure 9, 10 and 11 demonstrate the capability of the T-scanning procedure in building images from rough structures and tissue, without recurring to a phase modulator.

16.2 SIMULTANEOUS *EN-FACE* OCT AND CONFOCAL IMAGING

(i) It is simply to note that once the OCT image is oriented *en-face,* as described in Figure 1, it has the same aspect with that of images generated by using confocal microscopy (CM) [24,25]. In both imaging technologies, the *en-face* OCT and CM, the fast scanning is *en-face* and the depth scanning (optical path change in the OCT case and focus change in the CM case) is much slower (performed at the frame rate);

(ii) The better the depth resolution, the more fragmented the C-scan image looks like. A single C-scan image from the tissue may contain only a few fragments and may be challenging to interpret;

(iii) In order to produce a B-scan OCT image, adjacent imaging instruments are required to guide the OCT system in directions perpendicular to the optical axis, towards the part of the tissue to be imaged.

The three reasons above have led to a new imaging instrument [26] which blends together the two principles, OCT and CM. Making the most of the components used to generate the OCT image, a confocal channel is added to the system. The two C-scan images produced by the two channels are naturally pixel to pixel correspondent [27]. This helps with the guidance, especially in imaging the eye. When imaging the retina, the confocal channel provides an image similar to that of a confocal scanning laser ophthalmoscope (CSLO) [28].

Owing to such a narrow sectioning depth interval, the OCT images show only fragments of the retina and are difficult to interpret. The smaller the coherence length, the more fragmented the image appears. The usefulness of these images for the ophthalmologists can be greatly improved if the fragments sampled by OCT of the fundus are uniquely in correspondence with fundus images produced by a CSLO. In addition, the ophthalmologists have built large data bases of CSLO images for diseased eyes. In order to exploit this knowledge in the interpretation of the OCT transversal images, it is useful to produce simultaneously a transverse OCT and a CSLO image. Having a witness image, with sufficient contrast could lead to an improvement in the overall OCT imaging procedure for retinal assessment.

The combination of confocal imaging and interferometry has already been discussed in microscopy [29] and a comparison between confocal and OCT imaging through scattering media also reported [30]. However, (i) the object here is the tissue, which imposes a safety power limit and requires a special interface optics and (ii) the same low coherence source is used for both confocal and interferometer channels with implications in terms of the obtainable signal to noise ratio.

A possible configuration is shown in Figure 12. Light from a pigtailed superluminescent diode, SLD, is injected into a single mode directional coupler, DC1. Light in the object arm propagates via the microscope objective C3 and plate beam-splitter PB and then enters the orthogonal scanning mirror pair, MX, MY. The converging lens L1 sends the beam towards the object under investigation, typically the retina, HR, of the human eye, HE. Lens L1 brings the fan of rays to convergence at the eye lens, EL. The reference beam is directed via microscope objectives C1 and C2 and the corner cube CC to coupler DC2. The corner cube CC is mounted on a computer controlled translation stage, TS used to alter the reference path length. The light backreflected from the object and transferred via DC1 to DC2, interferes with the reference signal in the coupler DC2. Two photodetectors, PD1 and PD2, collect the signal and their outputs are applied to the two inputs of a differential amplifier, DA, in a balanced detection configuration. The OCT signal is then demodulated in the demodulator block, DMOD which drives the OCT input of a dual variable scan frame-grabber, VSG, under control of a personal computer, PC.

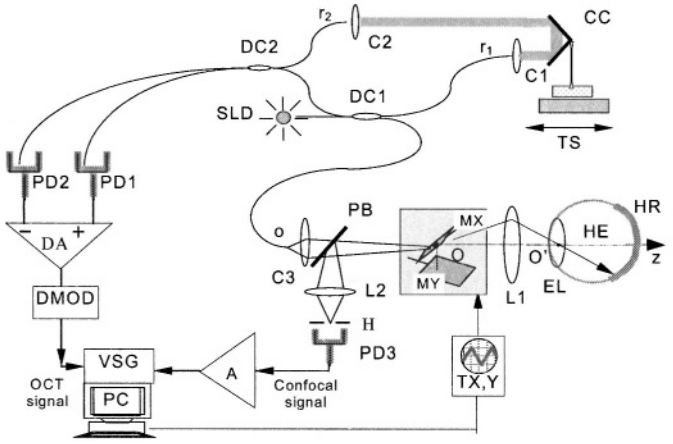

Figure 12. Detailed schematic diagram of the apparatus using a plate beam-splitter to divert light to the confocal receiver. SLD: Superluminescent diode; C1, C2, C3: microscope objectives; DC1, DC2: directional couplers; TS: computer controlled translation stage; CC: corner cube; M1, M2: mirrors; MX, MY: orthogonal galvanometer mirrors; TX(Y): ramp generators; DMOD: demodulation block; L1: convergent lens; PD1, PD2: photodetectors; DA: differential amplifier; PD3 and A: photodetector and amplifier respectively for the confocal receiver; H: pinhole; PB: plate beam-splitter; HE: patient's eye; EL: eye lens; HR: human retina; PC: personal computer; VSG: dual input variable scan frame grabber for displaying and manipulating two images simultaneously.

Ramp generators TX,Y drive the transverse scanners equipped with the mirrors MX and MY respectively, and also trigger signal acquisition by the frame grabber.

OCT configuration with balance detection is chosen here in order to attenuate: (a) the intensity modulation resulting from vibrations in the translation stage, TS, moving the corner cube, CC; (b) the excess photon noise, not possible with an unbalanced configuration when the OCT acquires data fast [31]. As an additional bonus, recirculation of the reference power avoids a large power beam being sent back to the SLD, known being that these devices are prone to oscillations.

A separate confocal receiver is used based on a plate beamsplitter PB (or a directional coupler), which reflects a percentage χ of the returned light from the object to a photodetector PD3 via a lens L2 and a pinhole H. The confocal signal is subsequently amplified in A and applied to the other input of the variable frame grabber VSG.

Two types of photodetectors are employed, Silicon pin diodes for the photodetecors PD1 and PD2 in the OCT and an avalanche photodiode (APD) for the photodetector PD3 in the separate confocal receiver.

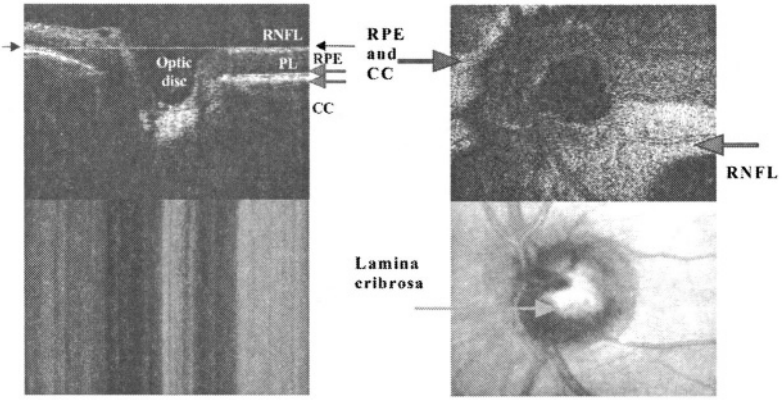

Figure 13. Pair of images from the optic nerve acquired with the standalone OCT/confocal system. Left: B-scan regime at y = 0; Right: C-scan regime. Top images: OCX; Bottom images: confocal. The C-scan OCT image on the right is collected from the depth shown by the double arrow in the B-scan OCT image in the left. RNFL (bright): retinal nerve fiber layer; PL (dark): photoreceptor layer; RPE (bright): retinal pigment epithelium; CC (bright): choriocapillaris. 3 mm horizontal size in all images, Left: vertical coordinate in the OCT image is 2 mm depth measured in air while in the confocal image it corresponds to the acquisition time of the B-scan OCT image, 0.5 s. The lateral variations of the shades indicate lateral movements of the eye during the acquisition. Right: vertical coordinate is 3 mm.

The system can operate in different regimes. In the B-scan OCT regime only one galvo-mirror of the galvanometer scanning pair is driven with a ramp at 500 - 1000 Hz and the translation stage is moved for the depth range

required in 0.2 - 1 s. In this case, an OCT B-scan image is produced either in the plane (x, z) or (y, z). A B-scan OCT image from the optic nerve in the plane (x, z) is shown at the top of the left pair of images in Figure 13. The multi-layer structure is clearly visible.

In the C-scan OCT regime, one galvo-scanner is driven with a ramp at 500 - 1000 Hz and the other galvo-scanner with a ramp at 1 - 5 Hz. In this way, a C-scan image, in the plane (x, y) is generated, at constant depth. Then the depth is changed by moving the translation stage in the reference arm of the interferometer and a new C-scan image is collected. An example of such *en-face* OCT image is shown at the top of the right pair of images in Figure 13. The bottom images in Figure 12 are confocal and they do not bear any depth significance. The brightness of each pixel in the confocal image is an integration of the signal received over the depth of focus determined by the interface optics and the pinhole in the confocal channel. Because the focus is not changed when altering the path imbalance in the OCT, the linear variation of the intensity received along the axis X in Figure 13 bottom-left and the (x, y) map of the intensity in Figure 13 bottom-right do not change with the depth z.

Choosing the Beamsplitter Ratio

Different criteria can be devised to find the most suitable value for the percentage of light, χ, diverted by the beam-splitter towards the confocal receiver. However, due to the fact that the two systems employ different principles, comparisons of parameters to be balanced is difficult. An optimum design should address the trade-off between χ and the confocal channel depth resolution. The larger χ, the higher the intensity of the signal collected by the confocal photodetector, PD3 and smaller size for the pinhole H could be achieved before reaching the noise floor. The smaller the pinhole size, the better the depth resolution in the confocal channel [24]. However, at the same time with the increase in χ, the signal to noise ratio in the OCT image worsens, as quantitatively described in reference [27].

16.3 PARALLEL OCT

The time to investigate the tissue in volume using *en-face* OCT could be reduced using a multiple optical paths configuration. Two possible configurations are presented.

16.3.1 Unbalanced Multi-Interferometer OCT Configuration

The method is illustrated by acquiring and simultaneously displaying two *en-face* images from the retina of a post mortem human eye, collected from different depths [32]. Such a set-up is shown in Figure 14. Light from a pigtailed superluminescent diode, SLD, is injected into a single mode directional coupler, DC2. The transmitted light from one of the output ports is injected into a second single mode coupler, DC1, whilst the light from the other port is directed to mirror M2. The elements in the object arm following DC1 up to the tissue are similar to those used in Figure 3. Two Michelson interferometers are formed using this arrangement. The reference arm in each interferometer consists of a microscope objective, C1 (C2) and a mirror, M1 (M2). Mirrors M1 and M2 are vibrated by two electrostrictive elements, EE, driven by sinusoidal generators G1 and G2, at f1 = 30 kHz and f2 = 22.5 kHz respectively. Both mirrors are mounted on the same computer controlled translation stage, TS. The tissue required a range of exploration in depth of 1 mm. Therefore, to generate distinct images, the difference between the depths of the two interferometers was chosen 1/4 from the range, i.e., 250 μm. This was adjusted by shifting the supports of the fiber ends and collimators C1, C2 relative to mirrors M1 and M2. Two photodetectors, PD1 and PD2, collect the returned optical signals. After photodetection, the signals in the two channels are band pass filtered (BPF), at 2f1 (2f2) in order to avoid the residual intensity modulation on the fundamental frequency.

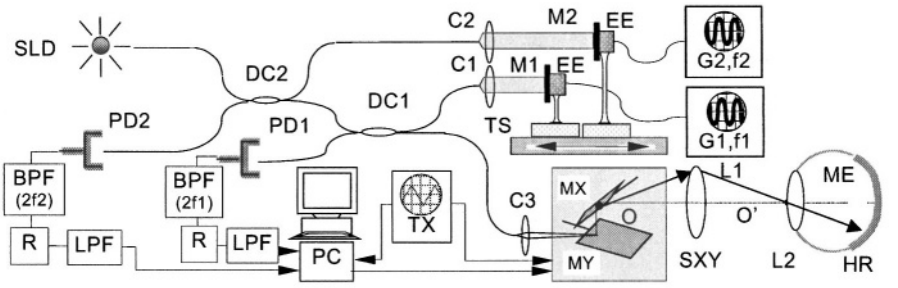

Figure 14. SLD: Superluminescent diode (850 nm); C1, C2, C3: microscope objectives; DC1, DC2: directional couplers; M1, M2: mirrors; PD1, PD2: photodetectors; SXY: orthogonal galvo scanners; MX(MY): mirror of the X(Y) scanner; ME: model eye consisting of a lens, L2 and HR, human post mortem retina; BPF: bandpass filter; R: rectifier; LPF: low pass filters; TS: computer controlled translation stage; EE: electrostrictive element; G1, G2; sinusoidal generators.

The signals are then rectified (R) and low pass filtered (LPF). The amplitude of the driving signals was adjusted to maximize the modulation at 2f1 and 2f2.

The triangle generator TX drives the horizontal line scanner, MX, and triggers the acquisition of the two analog signals via an A/D interface. Data acquisition and hardware commands are synchronized under the control of a LabView™ Virtual Instrument (VI). This VI also produces incremental voltage steps via a D/A interface to drive the vertical scanner, MY. With MX driven at 20 Hz, peak-to-peak amplitude 1 V, and MY driven over 100 steps from -0.5 V to 0.5 V, the images in Figure15 were obtained. It can be noticed that the upper image in the set for $z = 250\ \mu m$ becomes similar to the lower image in the set for $z = 0\ \mu m$. Due to the low frequency phase modulation and scanning rate used, the display of the pairs of images required 3 seconds.

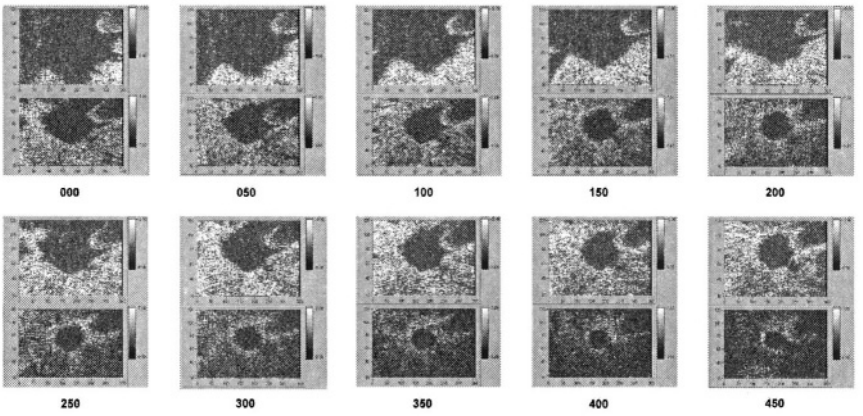

Figure 15. 12 pairs of 4 mm x 4 mm *en-face* images taken at 50 μm intervals from an *in-vitro* retina tissue.

The production of two images is not done at the expense of speed or signal to noise ratio in the first interferometer. The addition of a second coupler (and interferometer) is compensated for by a corresponding increase in optical power, so there is no penalty for adding a second interferometer (if one neglects the increase in Rayleigh scattering due to longer fiber lengths).

However, the image quality obtained in the second interferometer may not be as good as in the first interferometer, as shown in the following.

This method could be extended to display more than two layers in depth. Considering the power from the SLD launched into the fiber to be P_0, the photodetectors to have sensitivity η, the directional couplers DC to have zero loss, the reflectivity of mirrors M_j to be R_j, and the eye to return a

fraction O of the incident power (both R_j and O adjusted to include coupling losses in and out of fiber) the power at the last photodetector, PDn, is given by:

$$i_n = \eta P_0 \left[\frac{O}{2^{2n}} + \frac{1}{4} \sum_{j=1}^{n} \frac{R_j}{2^{2(n-j)}} + \frac{(-1)^{n-1}}{2^n} \sqrt{OR_n}\,\gamma(d_{On}) \cos\left(\frac{2\pi}{\lambda} d_{On}\right) + \sum_{j=1}^{n-1} c_j(n) \sqrt{OR_j}\,\gamma(d_{Oj}) \cos\left(\frac{2\pi}{\lambda} d_{Oj}\right) + \sum_{j,p=1}^{n} e_{jp}(n) \sqrt{R_p R_j}\,\gamma(d_{pj}) \cos\left(\frac{2\pi}{\lambda} d_{pj}\right) \right], \quad (14)$$

where γ stands for the modulus of the optical field correlation function, d_{Oj} is the OPD in interferometer j, d_{pj} is the OPD between mirrors Mj and Mp, c_j and e_{jp} numerical coefficients and λ is the central wavelength of the SLD. The first two terms represent the bias, the third one is the useful signal, periodic with components at multiples of f_n. The fourth term represents interference events between the object and the previous reference mirrors, j=1,...n-1. These are periodic terms at multiples of frequencies f_j which can be sufficiently attenuated by the band pass filter tuned to f_n, if the frequency values f_j are correctly selected. The last term represents interference events between the signals reflected by the mirrors M_j and M_p with p = j. These are very small when the OPD increment from mirror to mirror exceeds the coherence length (due to the small value of $\gamma(d_{pj})$ in equation 14). In the configuration shown in Figure 14, d_{12} = 250 μm, which is much longer than the 25 μm coherence length of the source.

It can be shown that from one interferometer to the next, the object power decreases with the reference power increasing by the same factor. Consequently, a similar amplitude for the useful interference signal given by the third term in equation 14 results for all photodetectors.

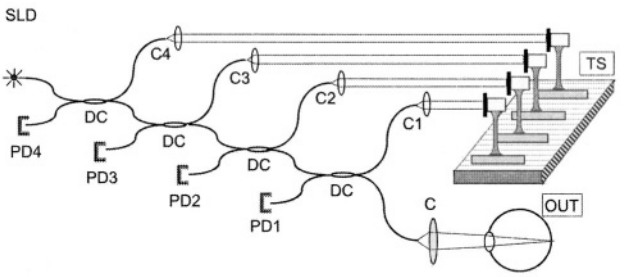

Figure 16. System with 4 couplers (interferometers) for the simultaneous display of 4 *en-face* layers. SLD: superluminiscent diode; DC:50:50 single mode directional couplers; PD1-4: photodetectors; M1-4: mirrors; TS: computer controllable translation stage; C1-5: microscope objectives; OUT: object under test.

An increase in the number of layers should be accompanied by a corresponding increase in the optical source power. For safety reasons, the power of the beam should be limited to a safety value P_s, with $P_0/2^n = P_s$ in the third term in equation 14. It is clearly seen that the useful term is maintained constant as n increases if the source power is correspondingly increased. This increase in power is feasible with existing large bandwidth optical sources. The images in Figure 15 were obtained with an SLD of 0.7 mW optical power. In principle, up to P_s = 1 mW CW power could be injected in the eye at 800 nm [33] when the beam is scanned. Given that the average power of solid state large bandwidth lasers [34], such as a Kerr lens mode-locked $Ti:Al_2O_3$ laser can exceed 400 mW, a very large number of interferometers may in principle be operated simultaneously. The diagram in Figure 16 shows the concept extended to 4 interferometers.

Another important constraint on increasing the number of layers (and accordingly of interferometers) derives from the fact that the interferometers are not physically independent. The interference signal from the first interferometer is present on the photodetector in the second interferometer, the interference signal from the second is present in the third interferometer and so on. The electronics in the n^{th} interferometer has to filter out n-1 interference signals, as shown by the fourth term in equation 14.

In addition, the higher the number n, the higher the bias in equation 14 and the shot noise. These two contributions act as a noise source. The noise given by the fourth term in equation 14 can be reduced by a correct selection of frequencies f_j. Electrostrictive and tiny piezo-elements can vibrate millimeter size mirrors slightly over 100 kHz. For a 20 Hz period of the signal applied to the horizontal scanner, a bandwidth enlargement of up to 0.5 kHz was measured. With Q = 20 for the bandpass filter, a minimum carrier frequency of at least 20 kHz is needed. In the range 20 - 100 kHz, 4 carriers could be placed safely, in such a way that no multiples of any one carrier fit inside the bandwidth of any other channel and the nearest component is at least 4 kHz away from the tuned frequency. Higher modulation frequencies could be achieved by using electrooptic crystals, in which case another unmodulated crystal should be placed in the sensing arm to compensate for dispersion.

The contribution to noise of the constant power on the detector, represented by the first two terms in equation 14, could be kept low only by reducing the bandwidth, i.e., increasing the image acquisition time. Considering that all BPFs have the same bandwidth, that all the unwanted interference signals (the 4^{th} term in equation 14) are largely attenuated, and assuming $0 << R_j \cong 1$, a calculation in the shot noise limited case based on the shot noise value given by the second term in equation 14 reveals that compared to the first interferometer, the signal to noise ratio decreases by

about 4 dB in the second interferometer, by 7 dB in the 3rd interferometer and 10 dB in the 4th interferometer.

The diagrams in Figure 14 and 16 have an important disadvantage in terms of excess photon noise. To reduce such noise, a balance configuration is required. A possible solution is described in the next paragraph.

16.3.2 Simultaneous C-scan Imaging Using Balanced OCT Configuration

Simultaneous *en-face* OCT imaging at multiple depths and rejection of excess photon noise are possible using an integrated modulator. A configuration with two channels [35] is shown in Figure 17. The scheme employs only one interferometer with RF multiplexing-demultiplexing.

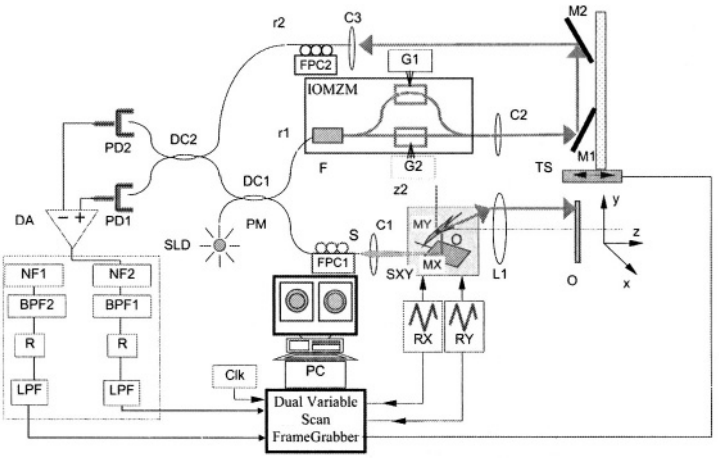

Figure 17. Experimental set up for *en-face* OCT imaging at two depths.

The configuration is based on a single mode coupler array [12]. Light from a pigtailed superluminescent diode, SLD is injected into a single mode coupler, DC1. The SLD delivers 120 μW to the object, has a central wavelength at 860 nm and a spectral FWHM of 18 nm. Assuming a Gaussian spectral profile, the coherence length, l_c = 32 μm gives a depth sampling interval of 16 μm in air. In the object arm, the light propagates from the port S via a microscope objective, C1, the galvanometer scanner head, SXY, and then, passes through lens L1, focal length 6 cm to the object, O. Two saw-tooth generators, RX and RY drive mirrors MX and MY of the SXY. The transmitted light from the other port of DC1 (the reference beam), which is of much higher power than the signal beam, is transferred via ferrule, F, to the integrated optic Mach - Zehnder modulator, IOMZM. The

ferrule F is in direct contact with the input guide of the IOMZM. The light at its output is collected via a microscope objective, C2, and then re-routed by mirrors M1 and M2 to the second coupler DC2. The two IOMZM electrodes are driven by sinusoidal signals from two generators G1 and G2 at $f_1 = 1.5$ MHz and $f_2 = 5$ MHz respectively. The mirrors serving to re-circulate the light in the reference arm are mounted on a computer controlled translation stage TS to enable coherence matching of the reference and the object arm. Polarization controllers, FPC1,2 are mounted in the sensing and in the reference arms. Two photodetectors, PD1 and PD2 collect the returned optical signals from the coupler DC2. The photodetected signals are applied to the two inputs of a differential amplifier, DA, in a balanced detection configuration. After DA, the signal is split into two electronic channels, each equipped with a notch filter, NF1 and NF2 and band pass filters, BPF1 and BPF2, a rectifier, R and a low pass filter, LPF. The system has consequently two channels, providing two OCT images. Two variable-scan-rate frame grabbers are used to simultaneously display the two images.

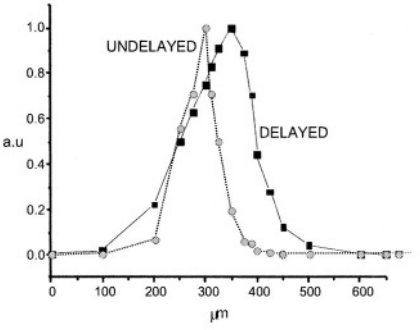

Figure 18. Depth sectioning interval of the two channels measured using a mirror as object, normally oriented to the system axis Z.

Saw-tooth signals, of 700 Hz and of 2 Hz are applied to the X-and Y-galvanometer scanners respectively. For an image size of 150x150 pixels, the image bandwidth required is ≈ 100 kHz .

Modulating only one electrode at a time and processing the signal received from a mirror used as a target on the corresponding frequency, the correlation profile shown in Figure 18 was obtained. Channel 2 uses the straight guide (undelayed) and exhibits a FWHM sectioning interval of 40 μm. Channel 1 uses the bent waveguide (delayed) and exhibits 120 μm. The sectioning intervals in both channels larger than the value of 16 μm (given

by half of the coherence length l_c) shows dispersion in the system with a larger dispersion component in the bent waveguide channel.

The simultaneous *en-face* OCT imaging at two depths is illustrated using a 5 p coin as object, O (the coin has a diameter of 18 mm). The amplitude on the two galvanometer scanners was such as to cover an area of 3 mm x 3 mm at the back of the lens L1. Both BPFs were set at pass bands of $\approx 100\ kHz$ and the low pass filter cut-off was adjusted to $\approx 150\ kHz$. The coin is an example of a two-layer object in depth separated by $\approx 60\ \mu m$, one layer, the plane of the coin background and the second layer, the top of the embossed letters. In channel 1 (Figure 19 bottom), the background around the letter R is displayed while in channel 2 (Figure 19 top), the peaks of the letter R and some of the areas surrounding the letter G, showing that the coin is inclined with respect to the 0Z axis.

The first implementation of such modulator and its coupling to the configuration was such that it could not be applied successfully to obtain images from tissue. Especially the presence of dispersion in the curved waveguide affected the achievable performances of the system. Progress in the technology of integrated optic modulators and more efficient coupling into fiber are envisaged in the near future. This will allow such a configuration to be applied to imaging of tissue.

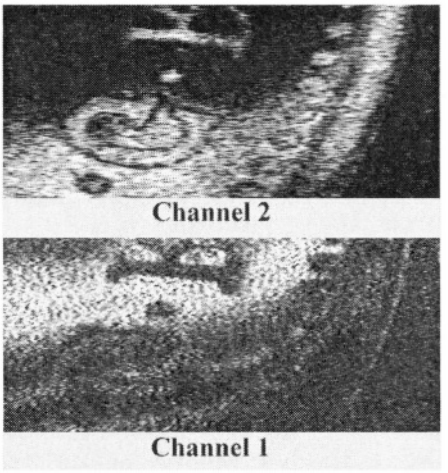

Figure 19. Simultaneous *en-face* OCT imaging at two depths from a 5 pence coin. Transversal size: 3 mm x 3 mm.

16.4 *EN-FACE* OCT IMAGING WITH ADJUSTABLE DEPTH RESOLUTION

Interest on imaging the tissue with adjustable depth resolution is required by *en-face* OCT only. While B-scan imaging demands the highest achievable depth resolution, and 2 μm depth resolution was reported from the cornea and 3 μm from the retina [36], a resolution of 50 to 200 μm has applications in the *en-face* imaging of the retina. Such applications are for guidance, topography and faster operation of *en-face* OCT imaging.

Penalties are incurred using *en-face* OCT imaging when attempting to improve the depth resolution by reducing the coherence length of the source, namely: fragmentation of the image, increased difficulty in bringing the object to coherence and increased sensitivity to movements and vibrations. A wider sectioning depth interval may alleviate these problems.

Different possibilities [37,38] exist to implement a source with adjustable coherence length. Generally, if by different means, the spectral width of the spectrum is narrowed, longer coherence length is obtained.

Simple spectral filters or gratings with limited aperture can be used in the front of broadband sources, with the disadvantage of lowering the power, so only a limited extension of the coherence length could be achieved before the power is too small to ensure a minimum signal to noise ratio.

Another possibility consists of changing the laser diode current just below the threshold. However, such an adjustment is highly nonlinear and very good stability is required for the power supply and eventually for the device temperature.

Combination of two sources has also been tested, one broadband (one or several lamps, SLDs or mode-locked lasers) and the other coherent, with a large coherence length (single mode laser diode or another type of laser with a coherent length larger than the coherence length of the broadband source). The optical powers are added via a directional coupler with a suitable coupling ratio depending on the powers of the two sources. The two sources need to have the same central wavelength, otherwise, the system dispersion may result in a relative shift in path imbalance of the correlation function peaks for the two wavelengths.

Multiple electrode semiconductor devices are also known, which under suitable electrical drive, can produce a controlled spectral width within a certain range. Such a source with adjustable coherence length [39], in combination with an SLD was suggested as a versatile choice. Figure 20 shows how the coherence length varies with the current for such a device, a three electrode laser (3EL) produced by Superlum Ltd., Moscow. The power also varies with the current, and therefore only a limited range could be

exploited, for instance that corresponding to 50% power variation, between 450 and 750 μm coherence length.

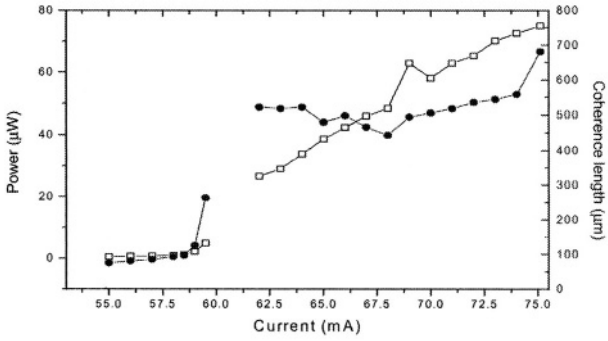

Figure 20. Power (open rectangles) and coherence length (filled circles) versus the current through the three-electrode source. The coherence length was obtained from measurements of the FWHM spectrum.

The images in Figure 21 show the difference in fragmentation between images collected with the 3EL and with the SLD from the optic nerve *in vivo*. The power to the eye was 120 μW from SLD and 75 μW from the 3EL

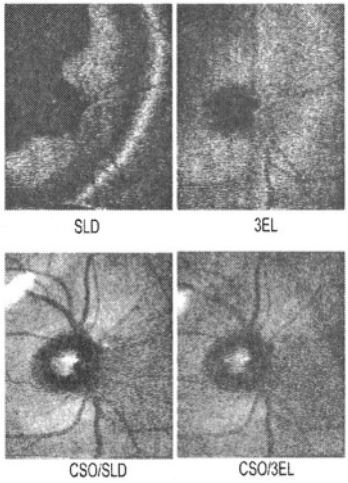

Figure 21. Comparison between OCT (top raw) and confocal images (bottom raw) obtained using the confocal channel (CSO) of the standalone OCT/confocal (Figure 12) of the optic nerve in the living eye. The images in the left column are obtained with the SLD only, driven at 120 mA, 120 μW. The images in the right column are obtained with the 3EL only, driven at 75 mA. Transversal size: 3 mm x 3 mm.

The SLD has a central wavelength of 860 nm and the 3EL of 858 nm and their FWHM were 18 nm and 0.95 nm respectively. The OCT image produced with the 3EL is less fragmented and shows better the eye tissue morphology than the OCT image acquired with the SLD. For comparison, images of larger than 1 mm depth resolution, collected with the confocal scanning laser ophthalmoscope (CSLO) channel, of a dual OCT/confocal system (section 16.2) using either source are presented in Figure 21.

16.5 *EN-FACE* OCT AND 3D IMAGING OF TISSUE

16.5.1 Images from the Retina

The combination of the C-scan OCT and confocal imaging was tested on eyes with pathology, such as: exudative ARMD, macular hole, central serous choroidopathy, RPE detachment, polypoidal choroidal vasculopathy and macular pucker [40]. A case of diabetic retinopathy is shown in Figure 22.

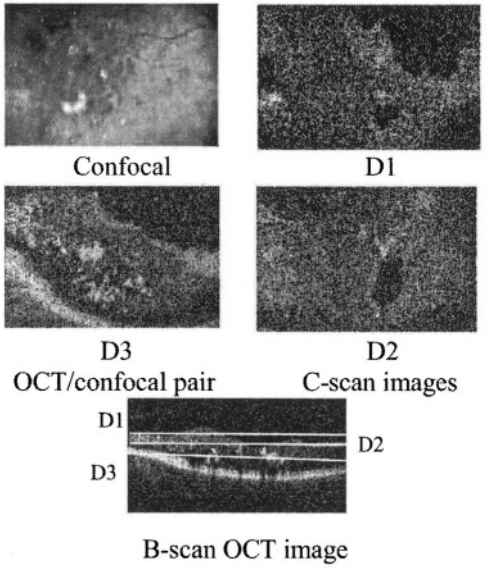

Figure 22. Diabetic retinopathy. The lines, 1, 2, 3 in the B-scan OCT image show the depths where the C-scan OCT images have been collected from. Lateral size: 15° x 15°.

The confocal image along with three other C-scan OCT images and a B-scan OCT image are shown. Here, the C-scan OCT image, at the depth D3 shows the RPE due to the curvature of the retina. The images in Figure 13

and 22 show the two challenging features of the high resolution C-scan imaging: patchy fragments and display of depth structure for the tilted parts of the tissue (please see subsection 16.6.4 below). However, the combined display of sections in the eye is extremely useful. Following the cuts along the straight lines indicated in the B-scan image, the brightness level in the corresponding part of the C-scan OCT image can be inferred.

Similar aspect looking images with those produced by CSLO are obtained in real time using C-scan OCT. The confocal image in the dual channel OCT/confocal system (section 16.2) was found very helpful in orientating the eye. It was much more difficult to align the eye using the OCT, as an image is displayed only when at coherence.

16.5.1.1 3D Imaging of the Retina

3D imaging of the retina is already common with CSLO technology [41]. Proceeding with *en-face* sections in depth is already accepted and understood by ophthalmologists. The standalone OCT/confocal system (section 16.3) can proceed in the same way, however with *en-face* slices as thin as allowed by the OCT technology [17]. To collect the reflectivity distribution from the volume of the retina, the standalone OCT/confocal system is operated in the C-scan mode collecting *en-face* images at different depths.

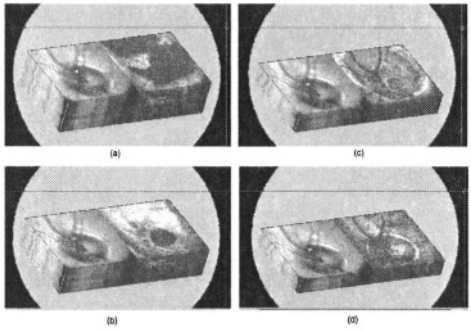

Figure 23. 3D presentation of pairs of C-scan OCT images (right) and confocal images (left) from the optic nerve. 3 mm x 3 mm (transversal) and 1.5 mm (depth in air).

Ideally, the depth interval between successive frames should be much smaller than the system resolution in depth and the depth change applied only after the entire C-scan image was collected. However, in practice, to speed up the acquisition, the translation stage in the reference arm was moved continuously. For a 2 Hz frame rate, with 20 μm between frames, 60 frame-pairs from a volume in depth of 1.2 mm in air (sufficient to cover the

volume of the retina around the optic nerve) can be acquired in 30 s. After acquisition, the images can be aligned transversally using the first confocal image and then the stack of OCT images or the stack of the pairs of OCT and confocal images are used to construct a 3D profile of the volume of the retina (Figure 23).

The confocal image is displayed sideways, along with the *en-face* OCT image at each depth. Then, by software means, the 3D profile can be reconstructed.

Alternatively, the confocal image can be superposed on the stack of C-scan OCT images to guide the exploration in depth, as shown in Figure 24.

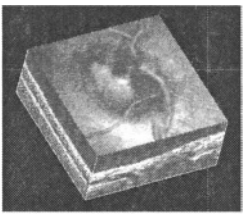

Figure 24. Confocal image superposed on the 3D volume generated from a stack of *en-face* OCT images. Longitudinal OCT cuts can be seen laterally. 3 mm x 3 mm (transversal) and 1.5 mm (depth in air).

Different longitudinal cuts can be inferred on the sides of the reconstructed volume from the stack of *en-face* images in Figure 23 and 24.

16.5.1.2 Anterior Chamber

Continuous examination from the cornea to the lens is not possible using the same optical design confocal microscope [42]. The reflection from the tear film in front of the epithelium is 2%. If a confocal instrument is built to image the lens, then it can be used for imaging the cornea with limited success. The low numerical aperture of the interface optics precludes separation of the different layers in the cornea from the strong reflection at the air-tear film interface. Additionally, by changing the numerical aperture means that the depth resolution at the lens depth is less than that achievable at the cornea. Thirdly, due to the low reflectivity of the transparent tissue in the anterior eye structure, there is a lack of contrast.

OCT addresses all these disadvantages and insures the same depth resolution from the cornea level up to very deep in the anterior chamber [43].

An OCT/confocal instrument was reported for collecting images from the cornea and the anterior chamber [44]. An SLD at 850 nm which delivers 300 μW to the eye was used, depth resolution in air slightly below 20 μm.

To visualize the cornea only, a numerical aperture of the interface optics of 0.1 was used. This gave a transversal resolution of better than 20 μm and a depth of focus of 0.25 mm in both the OCT and confocal channel (the values are larger than those theoretically expected due to aberrations). The C-scan images in Figure 25 show the multi-layer structure of the cornea. The top raw shows sections from the epithelium.

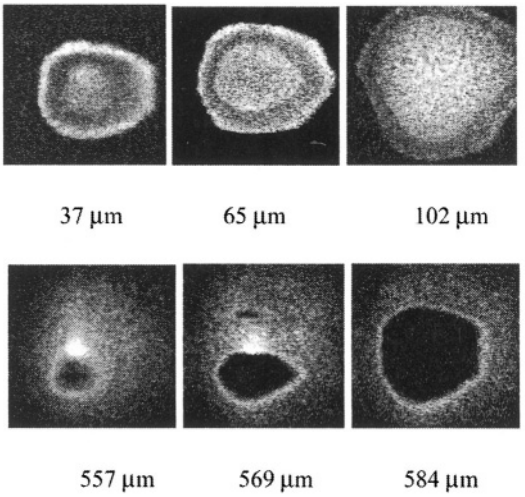

Figure 25. En-face OCT images of the cornea, 3 mm x 3 mm. All the depths are measured in air relative to the top of the cornea.

The Bowman layer is visible in transverse section, its separation from the epithelium is transferred to the distance between the two external and internal circles. The bottom raw displays C-scan images from the endothelium.

In order to collect images in the anterior chamber as deep as from the lens, a low NA aperture interface optics was used. This gives a long depth of focus with the disadvantage that the signal strength is just sufficient to allow visualization of the most important features in the anterior chamber. Figure 26 shows a couple of pairs of C-scan images, confocal and OCT, deep in the anterior chamber, with a low NA=0.02. The iris and the lens are visible. The images have been collected at a rate of 1 frame of pair images per second. The images at the top are the confocal images. Scanning deep in the anterior chamber, the iris appears at a depth of 3.5 mm. The irregularities of the iris rim are clearly visible at this magnification and the meshwork-like structure of the iris stroma. Then, at 4 mm depth, the lens becomes visible. The OCT images underneath show the *en-face* sections around the first Purkinje reflected spot. The offset of the lens from the center of the image indicates how sensitive C-scan imaging is at off-axis orientation in comparison with

the B-scan OCT imaging. The Purkinje reflections may be useful in aligning the eye axially, information difficult to handle when generating B-scan OCT images. The first two Purkinje images are visible in the confocal channel in Figure 26.

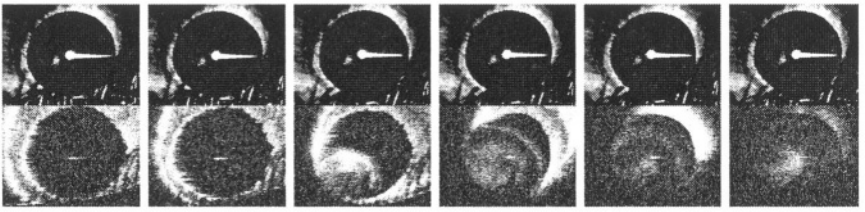

Figure 26. Pairs of confocal (top) and OCT (bottom) images deep in the anterior chamber. Confocal images show the Purkinje reflections and the iris. Deeper, the lens is seen, offset from the optic axis, around the 3rd Purkinje image (0.12 mm in air between the pairs; 6 mm x 6 mm transverse size).

16.5.2 3D Imaging for Dermatology

A-scan based B-scan OCT imaging proved capable of differentiating coetaneous structures in skin [45,46]. Similar capability was demonstrated using T-scan based B-scan imaging. Below, C-scan images and 3D reconstruction are shown for images collected from the fingertip of a volunteer [17]. The fingertip was placed at 3.5 cm away from the last lens of the interface optics. In order to increase the penetration depth, the scanning rate was reduced to 200 Hz a line and 1.75 s for a frame and power to the skin was 0.27 mW. A glass window was used as support for the fingertip. 40 OCT transversal images were collected by moving the glass plate support along with the finger towards the OCT system in steps of 25 μm measured in air.

The finger tip ridges are visible touching the glass plate interface at the top of the 3D volume in Figure 27 left, in the plane A. Not all ridges are visible, which indicates that the finger was slightly off the centre, towards the lower part of the voxel. This obviously eases the interpretation of OCT B-scan images seen on the sides of the voxel. Without the transversal information the B-scan OCT images would have been more difficult to interpret. The longitudinal cuts show the stratum corneum, epidermis and dermis. The thickness of different layers can be easily determined. The longitudinal cut in the face B in Figure 27 right shows the spiraled structure of the sweat ducts.

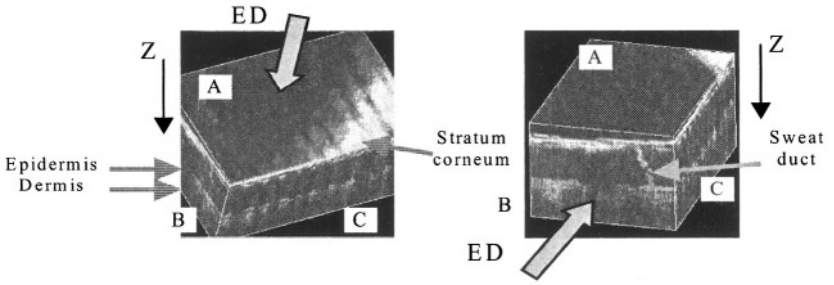

Figure 27. 3D display of *in vivo* OCT image of normal human skin from a volunteer's fingertip, produced with 0.27 mW, 850 nm. Volume size: 5 mm x 4 mm x 1 mm (depth measured in air). The arrow ED shows the direction of exploration of the 3D reconstructed volume made from 40 *en-face* images collected at 25 μm depth interval (measured in air).

16.5.3 Teeth

Several reports [47,48] proved the ability of OCT to provide high resolution images of dental tissues including caries lesion in enamel. However, all previous reports refer to longitudinal OCT imaging only. The information which can be collected cutting the object axially is obviously limited. It would be more natural to generate *en-face* slices in the tooth in the way we are used to see them when looking through a microscope. Therefore, *en-face* OCT was extended to the imaging of dental tissue structures.

Work to evaluate the demineralization of bovine teeth [49] employed a dual imaging OCT/confocal system (section 16.2). The teeth were painted with two coats of a non-fluorescent acid-resistant colorless nail varnish, except for an exposed window (2 mm x 2 mm) on the labial surface of the teeth. Caries-like lesions were then produced on each window by 3-day demineralization of the teeth in acidic buffer solution, as described in reference [50]. A pair of *en-face* OCT image and confocal image is displayed in Figure 28. Both the C-scan and B-scan OCT images showed the caries lesion as volumes of reduced reflectivity. The caries appears bright in the confocal image. The confocal image displays an integral of the reflectivity over a large depth, 1 mm and therefore the high reflectivity of the superficial layer is expected to dominate any confocal variations in depth.

Again, the confocal channel was instrumental in guiding the investigation.

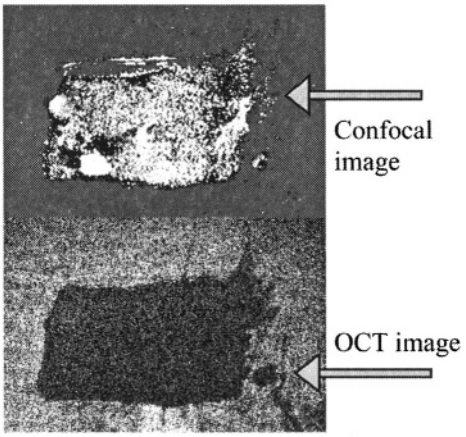

Figure 28. Single frame of OCT and confocal images from a bovine tooth showing the demineralized part. Lateral size: 5 mm x 5 mm. Depth in the OCT image, 0.25 mm from the top of the tooth.

16.5.4 3D Imaging of Teeth

42 frames containing both the OCT and confocal images have been collected at 2 Hz. Then a stack of images was constructed. Figure 29 shows sections in the stack at different depths.

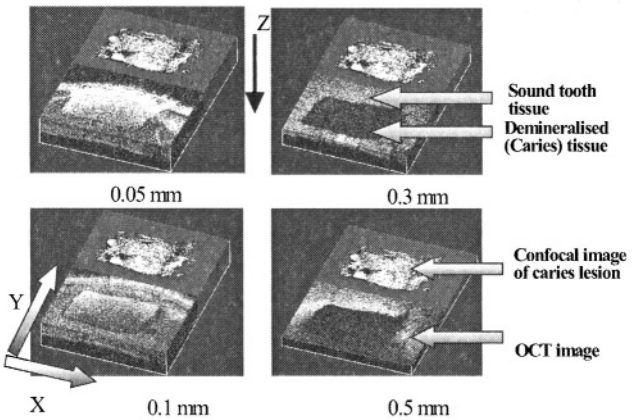

Figure 29. Stack of 42 pairs of OCT and confocal images viewed at different depths, as indicated below each frame. Transversal size: 5 mm x 5 mm each image in the pair.

The 3D display shows the transversal appearance as well as longitudinal OCT images. Clicking on any of the faces of the stack, an exploration

perpendicular on that face could be displayed. The top of the stack shows the *en-face* slices of the tooth tissue (including both sound and carious areas) from the tooth surface up to the maximum penetration depth.

On examination of a tooth, the compounding information in rectangular directions, transversal and axial, allows better diagnosis than when using longitudinal OCT imaging only. Successive displays of transversal and longitudinal cuts at different positions in the 3D stack of *en-face* OCT images gives a direct view of the caries volume. A-scan remains the best mode for quantitative analysis of demineralization or remineralization of the caries lesion over time, and therefore could be exploited in the determination of the effect of caries therapeutic agents (e.g., fluoride mouth rinse, fluoride dentifrice) or laboratory testing of a new oral healthcare product. However, the 3D imaging mode was helpful in choosing the best position of the A-scan in transversal section.

It was concluded that by versatile use of C-scans and B-scans, OCT could detect early caries lesions and show the depth of the lesion into the tissue.

16.6 PARTICULARITIES OF *EN-FACE* OCT

16.6.1 *En-face* Scanning Allows High Transversal Resolution

Due to transverse scanning, the T-scan based B-scan OCT image is continuous along the line in the raster, as opposed to A-scan based B-scan OCT images generated using fast axial scanning, where the lateral scanning is discrete. This improves the quality of the images along the lateral coordinate and allows a good distinction of scatterers and layers in depth as demonstrated in Figure 10 and 11. Although an SLD was used to obtain these images, which determined a depth resolution of only 12 μm in tissue, similar layers to those identified in the highest depth resolution, 3 μm, reported to date from the retina [36], are very well resolved. The continuity of layers in the transverse section allows visualization of small protuberances in the tissue. This has been proven in imaging the retina, on several cases of pathology, such as macular hole, central serous choroidopathy, RPE detachment, polypoidal choroidal vasculopathy, and macular pucker [40].

16.6.2 Synergy between the Channels

When a confocal channel is added to the imaging instrument, further versatility is gained. This can be added only to an *en-face* OCT system. The design described in section 16.2 insures a strict pixel-to-pixel correspondence between the two C-scan images (OCT and confocal). This helps in two respects: for small movements of the tissue, the confocal image can be used to track the movements between frames and for subsequent transversal alignment of the OCT image stacks; for large movements, like blinks when imaging the eye, the confocal image gives a clear indication of the OCT frames which need to be eliminated from the collected stack. As a reference for the aligning procedure, the first artifact-free confocal image in the set is used. For example in Figure 13 bottom left, movements of the eye are indicated by distortions of the sequence of confocal traces. Each horizontal line in the confocal image corresponds to a depth position. The relative eye movement, proven by the slight deviation of shadows to the right, can easily be transferred to the B-scan OCT image in Figure 13 top left for correction.

16.6.3 Topography

As another advantage, *en-face* OCT is ideal for topography. Procedures using A-scans or B-scans, by repeating a number of radial cuts around the nerve [51] are cumbersome, as they require interpolation in the *en-face* plane. Obviously, it is more natural to construct the topography (which refers to an *en-face* image) from collected *en-face* images as demonstrated in reference [52].

Software A-scans, called A'-scans are inferred from a stack of C-scan images spanning the volume of the optic nerve. A'-scans from 6x6 adjacent transversal positions were superposed. This provided an averaging over both transversal and axial directions. Transversally, this results in an increase in the lateral pixel size while axially this leads to a smoothing of the A'-scans which provide an average A'-scan more tolerant to discontinuities due to artifacts. Topography is provided in a matrix of 36 x 36 elements out of the area of 210 x 210 pixels of the aligned images, of 60 μm x 60 μm. Topography means in fact finding the depth position of a single layer surface. When the object is multi-layer, the problem is complex and a choice has to be made. Either the depth of the first scatterer or the depth of the scatterer with the highest backreflected signal is "sought" by a searching procedure. A simple thresholding method was applied. The optimum value of the threshold was adjusted until the position of the first peak in depth was consistent with the frame number in the collection, 1 to 60, which started to

show a bright pixel. The topography of the first layer and of the deepest layer are shown in Figure 30.

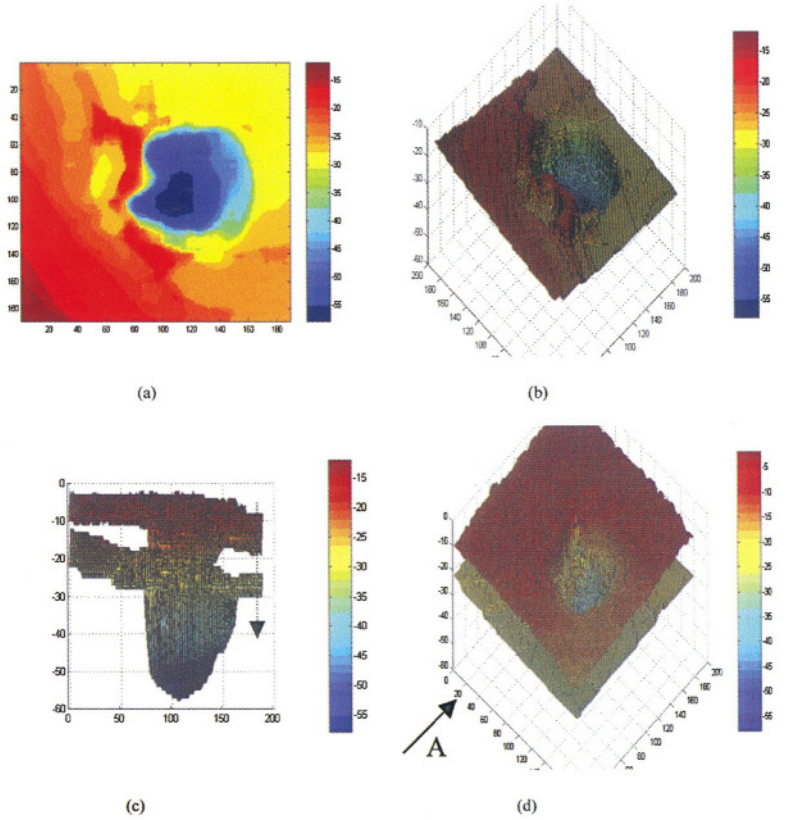

Figure 30. Topography of the deepest surface, 186 x 186 pixels transversal (1.9 mm x 1.9 mm). Depth map (the value in the bar represents the frame number and the depth could be inferred by multiplying the frame number by 20 μm); (a): as seen from the top; (b): 3D view; (c): first and the deepest surfaces seen from the direction A in (d); (d): 3D views of the first and the deepest surfaces superposed. [52].

Topography of the deepest layer is obtained by "seeking" for features starting from the end of the A'-scans. Due to the high depth resolution of the OCT, the two surfaces, corresponding to the top and the bottom layer are clearly discernible. These layers can be approximated with the retinal fiber layer and the choriocapillaris

16.6.4 New Challenge

New imaging technology brings not only new information to the clinician, but with it, the requirement of interpretation. *En-face* OCT is no

exception in this respect. The OCT images shown so far illustrate the challenges in interpreting and using the C-scan images.

First, the C-scan OCT image looks fragmented, and on its own, such an image cannot be interpreted. The higher the resolution of the OCT system, the more fragmented the *en-face* OCT image looks like [12,15-17]. As the imaging proceeds at a few frames a second, the inherent eye movements may result in significant changes in the size of fragments sampled out from the tissue. The fragmentation (Figure 13 top right, Figure 15, 19, 21 top left, 22, 25, and 26) is especially visible when imaging very inclined layers.

Second, variations in tissue inclination with respect to the coherence wave surface alters the sampling of structures within the depth in the tissue, producing novel slice orientations [53] which are often challenging to interpret. The bright patches in the OCT image represent the intersection of the surface of optical path difference (OPD) = 0 with the tissue.

Additional complication is brought about the particular way the tissue is scanned. The retina is scanned, with a fan of rays converging on the eye pupil, so the surface of OPD = 0 is an arc circle with the center in the eye pupil. When the depth is explored, the radius of the arc is altered. If the arc has a small radius, it may just only intersect the top of the optic nerve with the rest of the arc in the aqueous. The radius of the arc is changed by changing the length of one of the arms of the interferometer in the OCT channel to explore the retina up to the RPE and choroid.

When scanning the cornea and the skin, the scanning ray is moved parallel to itself and with a normal to the tissue. Any curvatures in the tissue will alter the curvature of the C-scan image. When imaging the cornea for instance, the pixels in the C-scan images in Figure 25 do not belong to a plane perpendicular to the cornea, but to a curved surface with elevation towards the top of the corneal epithelium. Normally, the curvature of deep C-scan surfaces follows the curvature of the external surface of the tissue, while deep layers are curved against the external surface curvature of the tissue in B-scan images.

The layers at the back of the eye are also not planar and this complicates the interpretation of the image even further.

Consequently, despite cutting images *en-face,* along the T-scan direction, C-scan images may display the structure in depth like in any B-scan OCT image. For instance, the C-scan images in Figure 25 top raw display the Bohman layer, shown in the B-scan OCT image in Figure 11.

As far as the fragmentation problem is concerned, this can be addressed by providing a confocal image which guides the user (section 16.2) and by collecting many C-scan images at different depths and subsequently building the 3D profile. However, the display of structures in depth in the *en-face* OCT images requires education of the interpretation process.

16.6.5 Safety

When performing T-based B-scan in comparison to A-scan based B-scan, higher values are tolerated for the incident power to the tissue. Let us consider a depth and transverse pixel size of 15 μm and a B-scan image size of 200 x 200 pixels. This corresponds to a 3 mm x 3 mm image and let us consider that it is acquired in 1 second by collecting 200 A-scans. This means that on each pixel in transverse section, the beam spends 1/200 s and a new irradiation event is repeated at 1s. In opposition, when performing T-scans prior to building a B-scan, the beam spends on each transverse pixel $1/200^2$ s only every 1/200 s. When building a C-scan image, a new T-scan line of pixels is irradiated, so each pixel is irradiated for only $1/200^2$ with a 1 s repetition. Consequently, in both B-scan and C-scan image, each transverse pixel is irradiated for shorter time than in a A-scan based B-scan OCT image which leads to a higher power level tolerated. In imaging the retina, due to an $1/e^2$ beam diameter to the eye of 2.5 mm, the transversal resolution is expected to be ~ 15 μm, the same in both channels as reported elsewhere when using either confocal [28] instruments or OCT [54]. Using this value as an approximation for the lateral pixel size, the maximum exposure time can be evaluated. For a line of 3 mm covering the retina (as a minimum to scan the optic disk), this gives 200 pixels. With the example above, the T-scan will perform at 400 Hz. In these conditions, investigation with 1 mW is allowed [32] for many hours at 850 nm.

16.6.6 Compatibility with Adaptive Optics

As another advantage, the *en-face* orientation allows further improvements in the resolution of imaging the eye. The transverse resolution in OCT imaging is governed by the optics of the eye and its aberrations. Adaptive optics (AO) was employed to demonstrate in a flood illuminated eye that transverse resolution could be improved to the point where it was possible to distinguish the cones in the fovea [55]. AO utilizes two devices operating in closed loop. In the AO system a wavefront sensor (WS) [56] measures the aberrations of the eye by comparing the image reflected from the fundus with the image of a reference point. This information is used to actuate a wavefront corrector (WC), in the form of an electrostatic or piezo-electrically driven deformable mirror [57].

Recently, a flying spot ophthalmoscope incorporating AO elements [58] was reported with an estimated resolution of 2.5 μm transversal and 100 μm axial.

A system like that described in section 16.2 could benefit from such developments, by using a WC for both channels. Further research remains to

assess this exciting potential. If compatibility can be established, then an instrument incorporating both techniques could provide images with much improved depth and transversal resolution than the existing instruments. It should be stressed that implementing AO in OCT raises a number of issues not present in the simpler cases of the scanning laser ophthalmoscope or the fundus camera.

16.7 *EN-FACE* NON-SCANNING SYSTEMS

The presentation so far referred to the flying spot concept. This paragraph mentions in brief other developments on the front of *en-face* OCT imaging.

Using parallel collection of rays within the scene and interfering them with a bunch of reference rays, allows the generation of B-scan and C-scan images with no mechanical scanner. Such a method was denoted as Coherence Radar [59]. For each pixel in the transverse coordinates of the object, a pair of object beam and reference beam can be identified, using telecentric optics. The simplest implementation set-up employs a CCD array. In this case, the processing can be performed only after the information for all pixels arranged along the line in the image is collected (equivalent to a T-scan image as discussed in subsection 16.1.3). This means that real time processing is not possible. Therefore, the amplitude of the interference signal is recovered using phase stepping algorithms. Phase shifts are introduced by exact steps which in total add up to a wavelength, or by continuous change of the OPD and comparing the sequences obtained.

The detection of reflective interfaces in a multilayer object using the original Coherence Radar method (one CCD camera and Michelson interferometer) is limited by the dynamic range of the analogue to digital (A/D) converter of the frame grabber. This is especially detrimental when there are variations of object reflectivity in the transversal section of the object. Also, the OPD change by mechanical means introduces noise in the system. Therefore, a differential detection method for Coherence Radar which reduces the required dynamic range of the A/D converter and attenuates the vibration noise was implemented [60] (Figure 31). The system employs two line-scan CCD cameras and a Mach-Zehnder interferometer. A collimated illumination beam is reflected by a beam splitter onto the object of interest (which is mounted on a translation stage) and is transmitted to reference mirror 1. Light returned from the object is imaged by a telecentric telescope in the object arm (lens 1 and 2) onto two CCD line-scan cameras (Thomson, TH 7811 A) via an additional beam splitter. Light travelling in the reference arm (via mirror 1 and 2) is subject to identical magnification due to a telecentric telescope in the reference arm (lens 3 and 4) and is also incident

on both cameras via the second beam splitter. Both mirrors 1 and 2 as well as the second telecentric telescope (lens 3 and 4) are mounted on a translation stage to allow the optical path length to be equalized initially. The electrical signals generated by the CCD line-scan cameras are balanced and differentially amplified before being digitized by the A/D converter in the frame grabber.

The amplitude of the interference signal is recovered using a phase stepping algorithm. Phase shifts are induced by the continuous displacement of the object (or reference mirrors 1 and 2). Coherence radar systems were initially applied for profilometry, due to the low dynamic range of the first experiments, using 8-bits CCD cameras. The surface topography of a crater [61,62] created by fast impact of a hypervelocity object is shown in Figure 32. Later on, with the development of higher dynamic range CCD cameras, coherence radar has been extended to OCT of the tissue [63].

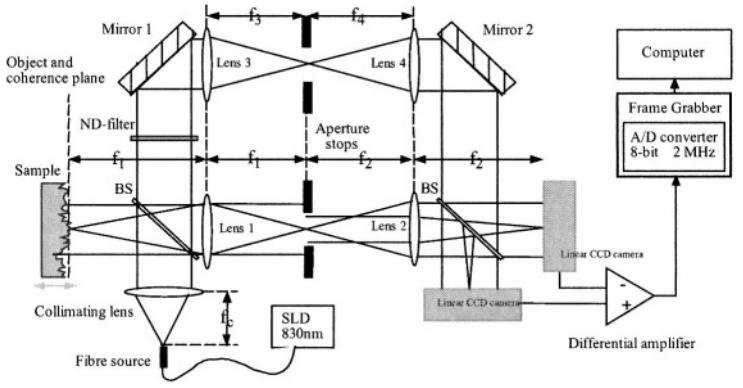

Figure 31. Differential coherence radar set-up.

A system based on a Linnik interference microscope with high-numerical-aperture objectives has been reported [64,65]. Lock-in detection of the interference signal is achieved in parallel on a CCD by use of a phase modulator (such as a photoelastic birefringence modulator) and full-field stroboscopic illumination. C-scan images are obtained in real time with better than 80 dB at a 1-image/s acquisition rate, which allows tomography in scattering media such as biological tissues. Local defects inside multidielectric optical components are detected using a similar set-up [66].

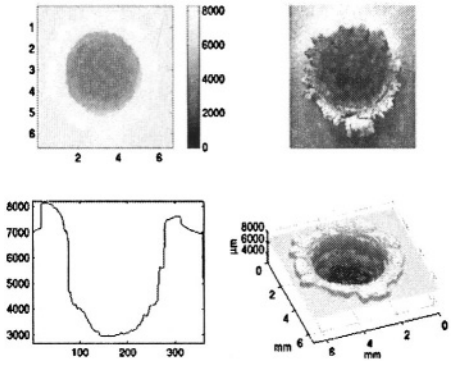

Figure 32. Surface topography of a hypervelocity impact crater [62].

A parallel faster processing method uses an array of photodetectors. A photodetector is employed for each pixel in the *en-face* image, followed by a processing electronics channel (demodulation, rectifier, amplifier, conditioning). Such a configuration was proved possible by implementing a smart chip [67,68]. One pixel consists of a 35 x 35 μm^2 silicon photodiode coupled to a CMOS electronic circuit. The smart chip is composed of 58 x 58 smart pixels. The smart pixel approach has two major advantages: elimination of the transverse scanners and no excess photon noise. The optical power on each photodetector is small, less than 0.2 μW, and the excess photon noise is consequently negligible. Because there is no transverse scanning to alter the OPD, a phase modulator is used. The reading is sequential, similar to the reading of a CCD camera in the classical case of a coherence radar system. However, the reading is not that of a photodetector signal but of a demodulated OCT signal. The amplitude of the signal provided by each channel is proportional to the envelope of the OCT interference signal. C-scan and B-scan images of onion [69] were obtained demonstrating the capability of the method to image scattering tissue.

ACKNOWLEDGEMENTS

The author acknowledges the support of the UK Engineering and Physical Sciences Research Council; of European Commission, INCO Copernicus, of the New York Eye and Ear Infirmary; Ophthalmic Technologies Inc., Toronto, Canada; Superlum, Moscow; and Pfizer, UK.

REFERENCES

1. S.A. Al-Chalabi, B. Culshaw and D.E.N. Davies, "Partially coherent sources in interferometric sensors," Book of Abstracts, First International Conference on Optical Fibre Sensors, 26-28 April 1983, I.E.E. London, 132-135 (1983).
2. R.C. Youngquist, S. Carr, and D.E.N. Davies, "Optical coherence-domain reflectometry: A new optical evaluation technique," *Opt. Lett.* **12,** 158-160 (1987).
3. H.H. Gilgen, R.P. Novak, R.P. Salathe, W. Hodel, P. Beaud, "Submillimeter optical reflectometry," *Lightwave Technol.* **7,** 1225-1233 (1989).
4. A.F. Fercher and E. Roth, "Ophthalmic laser interferometry," *Proc. SPIE* **658,** 48-51, 1986.
5. D. Huang, E.A. Swanson, C.P. Lin, J.S. Schuman, W.G. Stinson, W. Chang, M.R. Hee, T. Flotte, K. Gregory, C. A. Puliafito, and J. G. Fujimoto, "Optical coherence tomography," Science **254**, 1178-1181 (1991).
6. J.A. Izatt, M.R. Hee, D. Huang, J.G. Fujimoto, E.A. Swanson, C.P. Lin, J.S. Shuman, and C. Puliafito, "Ophthalmic diagnostics using optical coherence tomography," *Proc. SPIE* **1877**, 136-144 (1993).
7. J.A. Izaat, M.R. Hee, G.M. Owen, E.A. Swanson, and J. G. Fujimoto "Optical coherence microscopy in scattering media," *Opt. Lett.* **19,** 590-592 (1994).
8. A.M. Rollins, M.D. Kulkarni, S. Yazdanfar, R. Ungarunyawee, and J.A. Izatt "*In vivo* video rate optical coherence tomography," *Opt. Express* **3**, 219-229 (1998); http://www.opticsexpress.org/abstract.cfm?URI=OPEX-3-6-219.
9. Data sheets of Humphrey Instruments, Optical Coherence Tomography (Humphrey Instruments, San Leandro CA 94577 1996).
10. A.Gh. Podoleanu, G.M. Dobre, D.J. Webb, and D.A. Jackson, "Coherence imaging by use of a Newton rings sampling function," *Opt. Lett.* **21,** 1789-1791 (1996).
11. A.Gh. Podoleanu, G.M. Dobre, and D.A. Jackson, *"En-face* coherence imaging using galvanometer scanner modulation," *Opt. Lett.* **23**, 147-149 (1998).
12. A.Gh. Podoleanu, M. Seeger, G.M. Dobre, D.J. Webb, D.A. Jackson, and F. Fitzke "Transversal and longitudinal images from the retina of the living eye using low coherence reflectometry," *J. Biomed Opt.* **3**, 12-20 (1998).
13. Y. Pan and D. Farkas, "Non-invasive imaging of living human skin with dual-wavelength optical coherence tomography in two and three dimensions," *J. Biomed Opt.* **3**, 446-455 (1998).
14. S.A. Boppart, G.J. Tearney, B.E. Bouma, J.F. Southern, M.E. Brezinski, and J.G. Fujimoto, "Noninvasive assessment of the developing Xenopus cardiovascular system using optical coherence tomography," *Proc. Natl. Acad. Sci. USA* **94**, 4256-4261 (1997).
15. A.Gh. Podoleanu, G.M. Dobre H.M. Seeger, D.J. Webb, D.A. Jackson, F.W. Fitzke, and G.A.S. Halfyard, "Low Coherence interferometry for *En-face* Imaging of the Retina," *Lasers Light Ophthalmol* **8**, 188-192 (1998).
16. A.Gh. Podoleanu, J.A. Rogers, S. Dunne, and D.A. Jackson, "3 D OCT Images from retina and skin," *Proc. SPIE* **Vl. 4087,** 1043-1053 (2000).
17. A.Gh. Podoleanu, J.A. Rogers, D.A. Jackson, S. Dunne, "Three dimensional OCT images from retina and skin," *Opt. Express,* **7**, 292-298 2000; http://www.opticsexpress.org/abstract.cfm? URI=OPEX-7 -9-292.
18. B. Hoeling, A. Fernandez, R. Haskell, E. Huang, W. Myers, D. Petersen, S. Ungersma, R. Wang, M. Williams, and S. Fraser, "An optical coherence microscope for 3-dimensional imaging in developmental biology," *Opt. Express* **6**, 136-145 (2000); http://epubs.osa.org/oearchive/source/19250.htm.

19. L. Giniunas, R. Danielius, Karkockas, "Scanning delay line with a rotating-parallelogram prism for low- coherence interferometry," *Appl. Opt.* **38**, 7076-7079 (1999).
20. A.V. Zvyagin, E.D.J. Smith, D.D. Sampson, "Delay and dispersion characteristics of a frequency-domain optical delay line for scanning interferometry," *JOSA A,* **20** 333-341 (2003).
21. C.K. Hitzenberger, A. Baumgartner, and A.F. Fercher, "Dispersion induced multiple signal peak splitting in partial coherence interferometry," *Opt. Commun.* **154**, 179-185, (1998).
22. A.F. Leung and J.E. Lee, "Newton's rings: A classroom demonstration with a He-Ne laser," *Am. J. Phys.* **59**, 663-664 (1991).
23. M.R. Hee, J.A. Izatt, E.A. Swanson, and J.G. Fujimoto, "Femtosecond transillumination tomography in thick tissues," *Opt. Lett.* **18**(13), 1107-110 (1993).
24. T. Wilson, *Confocal Microscopy,*(Academic Press, London, 1990).
25. R. Rajadhyaksha, R. Anderson, and R. Webb, "Video-rate confocal scanning laser microscope for imaging human tissues in vivo," *Appl. Opt.* **38**, 2105-2115 (1999).
26. A.Gh. Podoleanu and D.A. Jackson, "Combined optical coherence tomograph and scanning laser ophthalmoscope," *Electron. Lett.* **34**, 1088-1090 (1998).
27. A.Gh. Podoleanu and D.A. Jackson, "Noise Analysis of a combined optical coherence tomography and confocal scanning ophthalmoscope," *Appl. Opt.* **38**, 2116-2127 (1999).
28. R.H. Webb, "Scanning laser ophthalmoscope," in *Noninvasive Diagnostic Techniques in Ophthalmology,* B. R. Masters ed. (Springer-Verlag, New York, 1990), 438-450.
29. R. Juskaitis and T. Wilson, "Scanning interference and confocal microscopy," *J. Microscopy,* **176**, 188-194 (1994).
30. M. Kempe, W. Rudolph, and E. Welsch, "Comaparative study of confocal and heterodyne microscopy for imaging through scattering media," *J. Opt. Soc. Am. A* **13**, 46-52 (1996).
31. A.Gh. Podoleanu, "Unbalanced versus balanced operation in an OCT system," *Appl. Opt.* **39**, 173-182 (2000).
32. A.Gh. Podoleanu, G.M. Dobre, D.J. Webb, and D.A. Jackson, "Simultaneous *en-face* imaging of two layers in human retina," *Opt. Lett.* **22**, 1039-1041 (1997).
33. *American National Standard for the Safe Use of Lasers: ANSI Z 136.1* (Laser Institute of America, New York, NY, 1993).
34. B. Bouma, D.J. Tearney, S.A. Boppart, M.R. Hee, M.E. Brezinski, and J.G. Fujimoto, "High-resolution optical coherence tomographic imaging using a mode-locked Ti:A12O3 laser source," *Opt. Lett.* **20**, 1486-1488 (1995).
35. A.Gh. Podoleanu, J.A. Rogers, R.C. Cucu, D.A. Jackson, B. Wacogne, H. Porte, and T. Gharbi, "Simultaneous low coherence interferometry imaging at two depths using an integrated optic modulator," *Opt. Commun.* **191**, 21-30 (2001).
36. W. Drexler, U. Morgner, R.K. Ghanta, F.X. Kartner, J.S. Schuman, and J.G. Fujimoto, "Ultrahigh-resolution ophthalmic optical coherence tomography," *Nature Medicine* **7**, 502-507 (2001).
37. A.Gh. Podoleanu, R.G. Cucu, G.I. Suruceanu, and D.A. Jackson, "Covering the gap in depth resolution between OCT and SLO in imaging the retina," *Proc. SPIE* **4251**, 220–227 (2001).
38. A.Gh. Podoleanu, R. Rosen, J.A. Rogers, R.G. Cucu, D.A. Jackson, and V.R. Shidlovski, "Adjustable coherence length sources for low coherence interferometry," *Proc. SPIE* **4648**, 116-224 (2002).

39. A.Gh. Podoleanu, J.A. Rogers, D.A. Jackson, "OCT En-face Images from the Retina with Adjustable Depth Resolution in Real Time," *IEEE J. Select. Tops Quant. Electr.* **5**, 1176-1184 (1999).
40. R. Rosen, A.Gh. Podoleanu, J.A. Rogers, *et al.,* "Multiplanar OCT/confocal ophthalmoscope in the clinic," *Proc. SPIE* **4956,** 59-64 (2003).
41. R.H. Webb, G.W. Hughes, and F.C. Delori, "Confocal scanning laser ophthalmoscope," *Appl. Opt.* **26**, 1492-1499 (1987).
42. P. Furrer, J.M. Mayer, and R. Gurny, "Confocal microscopy as a tool for the investigation of the anterior part of the eye," *J. Ocular Pharmacol. Therap.* **13**, 559-578 (1997).
43. S. Radhakrishnan, A.M. Rollins, J.E. Roth *et al.,*"Real-time optical coherence tomography of the anterior segment at 1310 nm," *Arch. Ophthalmol-Chic* **119**, 1179-1185 (2001).
44. A.Gh. Podoleanu, J.A. Rogers, G.M. Dobre, R.G. Cucu, and D.A. Jackson, *"En-face* OCT imaging of the anterior chamber," *Proc. SPIE* **4619**, 240-243 (2002).
45. J.M. Schmitt, M.J. Yadlowsky, and R.F. Bonner, "Subsurface imaging of living skin with optical coherence microscopy," *Dermatology,* **191**, 93-98 (1995).
46. A. Pagnoni, A. Knuettel, P. Welker, M. Rist, T. Stoudemayer, L. Kolbe, I. Sadiq, and A. M. Kligman, "Optical coherence tomography in dermatology," *Skin Res. Technol.* **5**, 83-87 (1995).
47. B.W. Colston, Jr., M.J. Everett, L.B. DaSilva L.L. Otis, P. Stroeve, and H. Nathel, "Imaging of hard - and soft - tissue structure in the oral cavity by optical coherence tomography," *Appl. Opt.* **37,** 3582-3585 (1998).
48. F.I. Feldchtein, G.V. Gelikonov, V.M. Gelikonov, R.R. Iksanov, R.V. Kuranov, A.M. Sergeev, N.D. Gladkova, M.N. Ourutina, J.A. Warren, Jr., and D.H. Reitze, *"In vivo* OCT imaging of hard and soft tissue of the oral cavity," *Opt. Express* **3**, 239-250 (1998).
49. B. Amaechi, A. Podoleanu, G. Komarov, J. Rogers, S. Higham, and D. Jackson, "Application of optical coherence tomography for imaging and assessment of early dental caries lesions," *Laser Meth. Med. Biol.* **13** (5), 703-710 (2003).
50. B.T. Amaechi, S.M. Higham, and W.M. Edgar, "Factors affecting the development of carious lesions in bovine teeth *in vitro," Arch. Oral Biol.* **43**, 619-628 (1998).
51. J.S. Schuman, T. Pedut-Kloizman, E. Hertzmark, M.R. Hee, J.R. Walkins, J.G. Cooker, C.A. Puliafito, J.G. Fujimoto, and E.A. Swanson, "Reproducibility of nerve fiber layer thickness measurements using optical coherence tomography," *Ophthalmology* **103,** 1889-1898 (1996).
52. J.A. Rogers, A.Gh. Podoleanu, G.M. Dobre, D.A. Jackson, and F.W. Fitzke, "Topography and volume measurements of the optic nerve using en-face optical coherence tomography," *Opt. Express* **9**, 476 – 545 (2001); http://www.opticsexpress.org/abstract.cfm?URI=OPEX-9-10-533.
53. M. Ohmi, K. Yoden, and M. Haruna, "Optical reflection tomography along the geometrical thickness," *Proc. SPIE* **4251,** 76-80 (2001).
54. J.S. Schuman, T. Pedut-Kloizman, E. Hertzmark, M.R. Hee, J.R. Walkins, J.G. Cooker, C.A. Puliafito, J.G. Fujimoto, and E.A. Swanson, "Reproducibility of nerve fiber layer thickness measurements using optical coherence tomography," *Ophthalmology* **103,** 1889-1898 (1996).
55. J. Liang and D.R. Williams, "Aberrations and retinal image quality of the normal human eye," *J. Opt. Soc. Am. A* **14** (11), 2873-2883 (1997).
56. J. Fernandez, I. Iglesias, and P. Artal, "Closed-loop adaptive optics in the human eye," *Opt. Lett.* **26**, 746-748 (2001).

57. J.C. Dainty, A.V. Koryabin, and A.V. Kudryashov, "Low-order adaptive deformable mirror," *Appl. Opt.* **37** (21), 4663-4668 (1998).
58. A. Roorda, F. Romero-Borja, W.J. Donnelly III, H. Queener, T.J. Herbert, and M.C.W. Campbell, "Adaptive optics scanning laser ophthalmoscopy," *Opt. Express* **10,** 405-412 (2002).
59. T. Dresel, G. Hausler, and H. Venzke. "Three-dimensional sensing of rough surfaces by Coherence Radar," *Appl. Opt.* **31,** 919-925 (1992).
60. A.Gh. Podoleanu, M. Seeger, and D.A. Jackson, "CCD based low-coherence interferometry using balanced detection," Book of Abstracts, CLEO-Europe, 14-18 Sept., Glasgow 1998, CWF80, 73.
61. L. Kay, A.Gh. Podoleanu, M. Seeger, and C.J. Solomon, "A new approach to the measurement and analysis of impact craters," *Intern. J. Impact Eng.* **19** 793-753 (1997).
62. M. Seeger, *3-D Imaging Using Optical Coherence Radar,* PhD Thesis (University of Kent, Canterbury, UK, 1977).
63. G. Hausler and M.W. Lindner, "Coherence radar and spectral radar – new tools for dermatological diagnosis," *J. Biomed. Opt.* **3,** 21-31 (1998).
64. A. Dubois, L. Vabre, A.C. Boccara, *et al.,* "High-resolution full-field optical coherence tomography with a Linnik microscope," *Appl. Opt.* **41** (4), 805-812 (2002).
65. H. Saint-James, M. Lebec, E. Beaurepaire, A. Dubois, and A.C. Boccara, "Full field optical coherence microscopy" in *Handbook of Optical Coherence Tomography,* B.E. Bouma, G.J. Tearney eds. (Marcel Dekker Inc, New York-Basel, 2002), 299-333.
66. L. Vabre, V. Loriette, A. Dubois, *et al.,* "Imagery of local defects in multilayer components by short coherence length interferometry," *Opt. Lett.* **27,** 1899-1901 (2002).
67. S. Bourquin, P. Seitz, and R.P. Salathe, "Optical coherence topography based on a two-dimensional smart detector array," *Opt. Lett.* **26**, 512-514 (2001).
68. S. Bourquin, V. Monterosso, P. Seitz, *et al.,* "Video-rate optical low-coherence reflectometry based on a linear smart detector array," *Opt. Lett.* **25**, 102-104 (2000).
69. S. Bourquin, P. Seitz, and R.P. Salathe, "Parallel optical coherence tomography in scattering samples using a two-dimensional smart-pixel detector array," *Opt. Commun.* **202,** 29-35 (2002).

This page intentionally left blank

Chapter 17

FUNDAMENTALS OF OCT AND CLINICAL APPLICATIONS OF ENDOSCOPIC OCT

Lev S. Dolin,[1] Felix I. Feldchtein,[2] Grigory V. Gelikonov,[1]
Valentin M. Gelikonov,[1] Natalia D. Gladkova,[3] Rashid R. Iksanov,[1]
Vladislav A. Kamensky,[1] Roman V. Kuranov,[1] Alexander M. Sergeev,[1]
Natalia M. Shakhova,[1] and Ilya V. Turchin[1]

1. Institute of Applied Physics of the Russian Academy of Sciences, Nizhny Novgorod, 603950 Russian Federation; 2. Imalux Corporation, Cleveland, OH 44114 USA; 3. Medical Academy, Nizhny Novgorod, 603005Russian Federation

Abstract: This chapter is devoted to different aspects of optical coherence tomography. First, the theoretical issues of OCT image formation are discussed from the standpoint of the wave and energy approaches. The next section discusses the development and creation of optical elements based on polarization maintaining fiber for the "heart" of the OCT scheme - Michelson interferometer. Then, various modifications of OCT such as "two-color", 3D, cross-polarized and endoscopic OCT modalities are discussed briefly. Following the theoretical and technical issues of OCT the chapter overviews clinical applications of OCT. OCT criteria of norm and pathology, diagnostic value of OCT and clinical indications for OCT are discussed. Influence of tissue compression and various chemical agents on OCT images are also shown. Finally, a mathematical algorithm for postprocessing of OCT images is demonstrated and results of recovering of tissue scattering properties are discussed.

Key words: theoretical model of OCT, endoscopic OCT, PM fiber interferometer, cross-polarization OCT, clearing, gynecology, gastroenterology, urology, image processing

17.1 INTRODUCTION

In the past decade, an increasing interest to new optical bioimaging modalities and rapid development of relevant optical technologies have stimulated elaboration of a number of OCT schemes which resulted in

various laboratory setups. A wide range of optical components such as femtosecond lasers, superluminescent and thermal light sources, fiber optical and air interferometers, mechanical and piezo-optical scanning systems, highly sensitive detectors of interference signals with a large dynamic range were mastered for applications in OCT for the entire infra-red frequency band.

Selection of a scheme and creation of a specific OCT setup is guided primarily by the problem OCT is intended to solve. The main purpose of the study which results are presented in this chapter was creation of an endoscopic OCT device and application of this device for multi-disciplinary clinical studies. Obviously, in order to comply with the above requirements this OCT device is to be compact, reliable, easy to use in clinical environment, and potentially be compatible with majority of modern standard endoscopic equipment. These requirements determined the choice of fiber optical interferometry based on polarization maintaining (PM) fiber and superluminescent light sources as main components of an endoscopic OCT setup. Use of PM fibers allows implementing a flexible sample arm of an interferometer, which facilitates access to internal organs; superluminescent light sources are apparently preferable to femtosecond lasers primarily due to the excessive size of the latter.

Creation of the proposed OCT scheme was accompanied by solving several optical engineering problems. First, a new system for fast piezo-optical scanning of the path-length difference between the interferometer arms was devised which allowed to get rid of mechanically moving parts in the interferometer and to create an all optical fiber OCT device. Second, a miniature optical probe performing lateral scanning of a probing beam was invented and constructed; the size of the optical probe is sufficiently small to fit standard channels of endoscopic equipment. Third, fiber optical elements with unique characteristics allowed creation of ultra broadband and multicolor OCT schemes. All these inventions were put together and lead to development of the whole range of compact OCT devices, which were successfully introduced into research clinical practice. This chapter discusses theoretical issues of OCT image formation, experimental and technical aspects of the OCT scheme used and also presents some clinical results obtained by means of created OCT devices.

17.2 THEORETICAL MODELS FOR OCT IMAGING

From the standpoint of optical theory, the problem of detecting a foreign object embedded in a turbid medium and that of imaging separate elements of the medium (i.e., its tomography) are very closely related. In each case, the ability to perform remote sensing is limited by three factors. First, light

that propagates from the source to the object (or a specific element of the medium) and from the object to the detector can be either absorbed or scattered out of the propagation path, resulting in signal attenuation. Second, due to scattering, photons coming from the object change their direction of propagation and contribute to "strange" elements in the image. It results in the so-called multiplicative noise. Finally, light which has scattered out of the propagation path can re-scatter back into the path and be detected, but with a different phase. This is an additive noise source resulting from multiple light scattering events in the volume of the turbid medium. The first limitation can be overcome by choosing an appropriate operating wavelength that suffers the least losses and employing a source that delivers a sufficiently large number of photons to the detector. The influence of the other two factors can be attacked using special methods of control of the illumination field and selective detection of the received signals. Such methods were developed for radar and hydroacoustic sensing [1,2]; their application in optics became possible with the advent of lasers. In particular, the technique of optical sounding was developed and used for observation of light scattering layers in the ocean and atmosphere with depth resolution of about a meter. With the advent of femtosecond lasers it became tempting to apply the lidar technique to imaging of biological tissue with micrometer-scale resolution. However, unlike nanosecond oceanic optical ranging experiments, direct time-of-flight measurements are difficult in the femtosecond temporal regime, and usually require cumbersome nonlinear-optical-gating techniques. This problem does not arise in optical coherence tomography [3-10] that realizes the sounding technique based on coherent reception of a broadband continuous signal.

An OCT image is formed by a continuous optical signal radiated and received by the tip of a single-mode optical fiber (Figure 1). The radiation is transmitted to the medium as a narrow focused beam. Separate observation of reflections from tissue elements that are located at different depths (z) is performed by measuring the cross-correlation function of the reflected optical signal and the reference signal. The reference signal is a copy of probing signal and is formed by branching the source light to the reference arm of the optical fiber Michelson interferometer. The received and reference waves are recombined on a photodetector. The tomographic signal is obtained as a result of detection of Doppler beats which emerge in the photodetector current in response to variation of the length of the interferometer reference arm. The image in the $z = const$ plane is formed due to the shift of the OCT system aperture along the tissue surface.

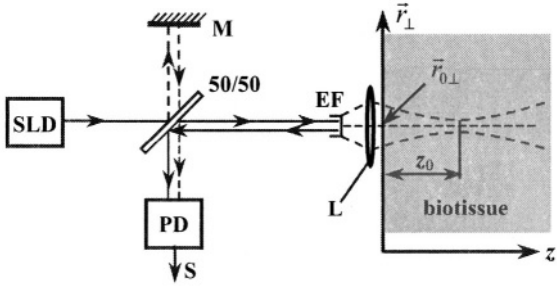

Figure 1. A principal scheme of OCT setup. SLD (superluminescent diode), M (reference mirror), EF (optical fiber end), L (lens), PD (photodetector), S (OCT signal).

Although OCT and pulsed methods use different ways of forming the image versus depth, this difference has no impact on the informative properties of the image. Therefore, models of OCT images are constructed by analogy with lidar signal models. Solutions of radiative transfer equation (RTF) or results of modeling of photon migration in a scattering medium by the Monte-Carlo method are usually used for this purpose.

It should be noted that energy (or corpuscular) description of a light field does not take into consideration two factors affecting characteristics of OCT images; namely, (i) high coherence (regularity) of a signal formed at the input of the OCT system during observation of a point object and (ii) identity of spatial structures of the wave fields radiated and received by the OCT system because the OCT optical system selectively detects a phase conjugated wave only. These factors are taken into account by the wave model of a backscattered signal [11].

17.2.1 Similarity Relations for the Signals of Coherence and Pulsed Sounding

Let the emitted wave inside the optical fiber be

$$u_e = M(\vec{r}')S_e(t - z'/c'),$$

where $\vec{r}'$ is the radius vector of a point in the fiber cross section Σ, z' is the coordinate along the fiber axis. Function $M(\vec{r}')$ characterizes the transverse structure of the fiber mode and satisfies the normalization condition

$$\int_{\Sigma} M^2 d^2\vec{r}' = 1,$$

c' is the phase velocity of the mode. Emitted signal $S_e(t)$ is a random stationary process with zero mean $\overline{S}_e = 0$, center frequency ω_0, bandwidth $\Delta\omega_0 << \omega_0$, power spectrum $W(\omega)$ and autocorrelation function

$$B(\tau) = \overline{S_e(t+\tau) \cdot S_e(t)} = \int_{-\infty}^{\infty} W(\omega)\cos(\omega\tau)d\omega = P_e \cdot b(\tau) \cdot \cos(\omega_0\tau), \quad (1)$$

P_e is the average emitted power, and $b(0) = 1$. The received wave inside the optical fiber is

$$u_r = M(\vec{r}')S_r(\vec{r}_{0\perp}, t + z'/c'),$$

where $S_r(\vec{r}_{0\perp}, t)$ is the received signal as a function of the transverse coordinate ($\vec{r}_{0\perp}$) where the light-beam axis crosses the medium surface (see Figure 1).

According to similarity relations for the signals of coherence and pulsed sounding [11] the "useful" current at the output of OCT heterodyne detector

$$i(\vec{r}_{0\perp}, t_0) = \eta\sqrt{2P_{ref}/P_e} \cdot \overline{S_r(\vec{r}_{0\perp}, t)S_e(t - t_0)}, \quad (2)$$

can be expressed as

$$i(\vec{r}_{0\perp}, t_0) = \eta\sqrt{\tau_0 P_e P_{ref}}\, \hat{S}_r(\vec{r}_{0\perp}, t_0), \quad \tau_0 = \int_{-\infty}^{\infty} b^2(\tau)d\tau, \quad (3)$$

where t_0 is the delay time of the reference signal with respect to the probing signal, η is the photodetector sensitivity [A/W], P_e, P_{ref} stand for the power of emitted and reference signals, respectively, $\hat{S}_r(\vec{r}_{0\perp}, t)$ is the received signal inside the optical fiber in the case of a pulsed probing signal

$$\hat{S}_e(t) = \sqrt{(2/\tau_0)}\, b(t)\cos(\omega_0 t) \quad (4)$$

with spectrum

$$f_e(\omega) = \frac{1}{2\pi}\int_{-\infty}^{\infty}\hat{S}_e(t)\exp(-i\omega t)dt = \sqrt{(2/\tau_0)}\cdot P_e^{-1}\cdot W(\omega),$$

power

$$\hat{P}_e(t) = \overline{\overline{(\hat{S}_e)^2}} = \frac{1}{\tau_0}b^2(t), \qquad (5)$$

and energy $\hat{W}_e = \int_{-\infty}^{\infty}\hat{P}_e\,dt = 1$ (the double bar in equation 5 means averaging over a time interval $2\pi/\omega_0$). If the coherence time (τ_c) of the signal $S_e(t)$ and duration (d_e) of the pulse (see equation 4) are determined from the following relations $\tau_c^2 = \tau_0^{-1}\int_{-\infty}^{\infty}\tau^2 b^2(\tau)d\tau$, $d_e^2 = \int_{-\infty}^{\infty}t^2\hat{P}_e dt$, then $d_e = \tau_c$.

17.2.2 Model of Random Realization of a Backscattered Signal

The biological tissue is considered as a medium with random distribution of dielectric permittivity

$$\varepsilon(\vec{r}) = \langle\varepsilon\rangle\left[1+\varepsilon_1(\vec{r})+\varepsilon_2(\vec{r})\right], \quad <\varepsilon_{1,2}>=0$$

(angle brackets <> denote statistical averaging). The term ε_1 describes the fluctuations of ε with spatial scale $l_1 >> \lambda_0$, and ε_2 are the fluctuations with scale $l_2 < \lambda_0$, where $\lambda_0 = 2\pi c/\omega_0$, c is the light velocity in a medium. The fields $\varepsilon_{1,2}(\vec{r})$ are characterized by correlation functions

$$B_{1,2}(\vec{r},\rho) = <\varepsilon_{1,2}(\vec{r}+\vec{\rho}/2)\varepsilon^*_{1,2}(\vec{r}-\vec{\rho}/2)>,$$

and spatial spectra

$$\Phi_{1,2}(\vec{r},\kappa) = (2\pi)^{-3}\iiint_{\infty} B_{1,2}(\vec{r},\rho)\exp(-i\vec{\kappa}\vec{\rho})d^3\vec{\rho}\,, \qquad \kappa = |\vec{\kappa}|.$$

The model of a pulsed signal reflected by the medium, $\hat{S}_r(\vec{r}_{0\perp},t)$, is constructed under certain assumptions. It is assumed that backscattering of a probing pulse $\hat{S}_e(t)$ occurs on small-scale heterogeneities (ε_2), and large-scale heterogeneities (ε_1) do not reflect light but rather work as a source of multiplicative noise. We denote by $U_\omega(\vec{r}_{0\perp},\vec{r})\cdot\exp(i\omega t)$ the field formed in the medium with permittivity $\varepsilon(\vec{r}) = \langle\varepsilon\rangle\left[1+\varepsilon_1(\vec{r})\right]$ when the emitted wave inside the optical fiber is $M(\vec{r}')\exp\left[i\omega(t-z'/c)\right]$. Then, in the single backward scattering approximation one can write

$$\hat{S}_r(\vec{r}_{0\perp},t) = -(2c)^{-1}\iiint_{z>0}\varepsilon_2(\vec{r})\left[\int_{-\infty}^{\infty} i\omega f_e(\omega)\cdot U_\omega^2(\vec{r}_{0\perp},\vec{r})\cdot e^{i\omega t}d\omega\right]d^3\vec{r}\,.$$

Based on the equation

$$U_\omega(\vec{r}_{0\perp},\vec{r}) = A(\vec{r}_{0\perp},\vec{r})\exp\left(-ik\varphi(\vec{r}_{0\perp},\vec{r})\right),$$

where A, φ are the wave amplitude and eikonal, $k=\omega/c$, the pulsed response of medium will be

$$\hat{S}_r(\vec{r}_{0\perp},t) = -(2c)^{-1}\iiint_{z>0}\varepsilon_2(\vec{r})A^2(\vec{r}_{0\perp},\vec{r})\frac{d}{dt}\hat{S}_e\left(t-2\varphi(\vec{r}_{0\perp},\vec{r})/c\right)d^3\vec{r} \approx$$

$$\approx \frac{k_0}{\sqrt{2\tau_c}}\iiint_{z>0}\varepsilon_2(\vec{r})\sin[\omega_0(t-2\varphi/c)]A^2(\vec{r}_{0\perp},\vec{r})\,b(t-2\varphi/c)\,d^3\vec{r}\,, \quad (6)$$

where $k_0=\omega_0/c$. Assuming $\varphi = z+\Delta\varphi,\ \Delta\varphi << z$ one can see that backscattering of the probing signal occurs in the sinusoidal component of ε_2 with spatial period of about $\lambda_0/2$. Factor A^2 in equation 6 describes a distribution of field intensity in a continuous illumination beam with allowance for focusing medium parameters and light scattering on large-scale heterogeneities. Factor *b* determines the position and longitudinal size of the medium element from which the signal originates at a given moment

of time. This signal is noise-like due to the random nature of ε_2 and of functions A, φ; the correlation time of the signal is equal to τ_c, $< \hat{S}_r >= 0$.

17.2.3 Model of a Statistically Average Backscattered Signal

The scales of spatial fluctuations of A and φ are assumed to be large compared to l_2, and the fields ε_1 and ε_2 are assumed to be statistically independent. Then power of the signal $\hat{S}_r$ averaged over an ensemble of spatial series of ε_1 and ε_2 yields

$$\hat{P}_r = < \overline{\overline{\hat{S}_r^2}} >= 2\pi^3 k_0^2 \iiint_{z>0} \Phi_2(\vec{r},\, 2k_0) < A^4 \hat{P}_e(t - 2\varphi / c) > d^3\vec{r}\,. \qquad (7)$$

Under some additional assumptions we can express the integrand factor $< A^4 \hat{P}_e >$ through energy characteristics of illumination field, which can be found from a radiative transfer equation (RTE). Let us represent U_ω as a sum of nonscattered and scattered fields and assume that fluctuations of the scattered field amplitude and phase are not cross-correlated; the amplitude is distributed according to the Rayleigh law and the phase is distributed uniformly in the interval from 0 to 2π.

Then taking into consideration that the backscattering coefficient (the effective area of backscattering of a unit medium volume) is $\sigma_0(\vec{r}) = 2\pi^2 k_0^4 \Phi_2(\vec{r}, 2k_0)$, we can write equation 7 in the form

$$\hat{P}_r(\vec{r}_{0\perp}, t) = (\lambda_0^2 / 4\pi) \iiint_{z>0} \sigma_0(\vec{r}) \mathrm{K}(\vec{r}_{0\perp}, \vec{r}, t)\, d^3\vec{r}\,, \qquad (8)$$

$$\mathrm{K}(\vec{r}_{0\perp}, \vec{r}, t) = \left[2E^2(\vec{r}_{0\perp}, \vec{r}) - E_{ns}^2(\vec{r}_{0\perp}, \vec{r})\right] \int_{-\infty}^{\infty} \hat{P}_e(t - t') T\left(\vec{r}_{0\perp}, \vec{r}, \frac{t'}{2}\right) \frac{dt'}{2}, \qquad (9)$$

$$T(\vec{r}_{0\perp}, \vec{r}, t) = \hat{E}_\delta(\vec{r}_{0\perp}, \vec{r}, t) / E(\vec{r}_{0\perp}, \vec{r})\,, \qquad (10)$$

where E, E_{ns} are the total irradiance and irradiance by nonscattered light from the stationary illumination beam with power $P_e = 1$, $\hat{E}_\delta$ is the irradiance in the medium from a pulsed source with power $\hat{P}_e(t) = \delta(t)$, T denotes photon distribution in the time of flight from point $\vec{r}_{0\perp}$ to point $\vec{r}$.

Note for comparison that calculations on the basis of RTE of received signal power give a different expression for K

$$\mathrm{K}(\vec{r}_{0\perp},\vec{r},t) = E^2 \int_{-\infty}^{\infty} \hat{P}_e(t-t')T_1(\vec{r}_{0\perp},\vec{r},t')dt', \tag{11}$$

$$T_1(\vec{r}_{0\perp},\vec{r},t) = \int_{-\infty}^{\infty} T(\vec{r}_{0\perp},\vec{r},t')T(\vec{r}_{0\perp},\vec{r},t-t')dt'. \tag{12}$$

17.2.4 Comparison of Wave and Energy Models of an OCT Signal

The OCT optical fiber detects only the scattered field component whose spatial structure is similar to that of the probing beam, i.e., a phase conjugated wave. Therefore, OCT images feature the phenomena of backscattering amplification and dispersion doubling of received wave's phase fluctuations [12] which is caused by passage of the probing and reflected wave through the same large-scale heterogeneities (ε_1). The wave model of a statistically average backscattered signal (equations 8-10) takes these effects into account and the energy model (equations 8, 11, and 12) neglects them. We can illustrate this on an example of a signal from a "point" object with effective area of scattering Σ located at point $\vec{r}_1$ of a medium containing large-scale heterogeneities. This signal is calculated according to the formulas

$$\hat{P}_r(\vec{r}_{0\perp},t) = \alpha K(\vec{r}_{0\perp},\vec{r}_1,t), \quad \alpha = \lambda_0^2(\Sigma/4\pi), \tag{13}$$

which are obtained from equation 8 with assumption of $\sigma_0(\vec{r}) = \Sigma\delta(\vec{r}-\vec{r}_1)$.

When an object is illuminated primarily by ballistic photons (the light scattered "forward" does not make any significant contribution to irradiance E), we can make use of the relations $E \approx E_{ns}$, $T(\vec{r}_{0\perp},\vec{r},t) \approx \delta(t-z/c)$. In this case, two sets of equations 9, 10, 13 and 11-13 yield the same result: power and energy of the received signal are expressed as

$$\hat{P}_r(\vec{r}_{0\perp},t) = \alpha E_{ns}^2(\vec{r}_{0\perp},\vec{r}_1)\hat{P}_e(t-2z_1/c), \quad \hat{W}_r = \int_{-\infty}^{\infty} \hat{P}_r dt = \alpha E_{ns}^2(\vec{r}_{0\perp},\vec{r}_1),$$

where arrival time of a signal "center of gravity" is given by $t_r = (\hat{W}_r)^{-1} \int_{-\infty}^{\infty} t\hat{P}_r dt = 2z_1 / c$, and characteristic duration of the signal is

$$d_r = \left[(\hat{W}_r)^{-1} \int_{-\infty}^{\infty} (t - \bar{t})^2 \hat{P}_r dt \right]^{1/2} = d_e .$$

However, these models are not equivalent in a general case. According to the wave model

$$\hat{W}_r = \alpha \left[2E^2(\vec{r}_{0\perp}, \vec{r}_1) - E_{ns}^2 \right], \quad t_r = 2\bar{t}, \quad d_r = \sqrt{d_e^2 + 4d^2},$$

where

$$\bar{t} = \int_{-\infty}^{\infty} tT(\vec{r}_{0\perp}, \vec{r}_1, t)dt, \qquad d^2 = \int_{-\infty}^{\infty} (t - \bar{t})^2 T(\vec{r}_{0\perp}, \vec{r}_1, t)dt$$

are average value and dispersion of photon propagation time from point $\vec{r}_{0\perp}$ to point $\vec{r}_1$, whereas the energy model gives $\hat{W}_r = \alpha E^2(\vec{r}_0, \vec{r}_1)$, $t_r = 2\bar{t}$, $d_r = \sqrt{d_e^2 + 2d^2}$. Comparison of the wave and energy models shows that for $E_{ns} << E$, $d_e << d$ the energy model gives underestimated values for energy of the received signal (by a factor of two) and yields axial blurring of the image (by a factor of $\sqrt{2}$ times). Such error will also manifest in modeling of images by the Monte-Carlo method.

17.2.5 Formulas for Calculating OCT Image

As follows from equation 3, mean-square current at the input of heterodyne receiver of an OCT system is expressed through a pulsed response of a medium in the following form

$$< \overline{\overline{i^2(\vec{r}_0, t_0)}} >= \eta^2 \tau_0 P_e P_{ref} \hat{P}_r(\vec{r}_0, t_0) \qquad (14)$$

(double bar in the left-hand side of equation 14 denotes averaging over time interval π / ω_1, where $\omega_1 = \omega_0 \left[dt_0(t) / dt \right]$ is an intermediate frequency). Consequently, the equations 8-10 can be used straightforwardly for

calculation of images formed by an OCT system with quadratic video signal detector.

If we suppose that a signal with delay t_0 comes from depth $z_0 = ct_0/2$, then the structure of three-dimensional image of the medium can be described by a dimensionless function $P(\vec{r}_{0\perp}, z_0) = \tau_0 \hat{P}_r(\vec{r}_{0\perp}, 2z_0/c)$ related to current i by $<\overline{\overline{i^2(\vec{r}_{0\perp}, t_0)}}>=\eta^2 P_e P_{ref} P(\vec{r}_{0\perp}, ct_0/2)$. Given statistical homogeneity of field ε_1 in the z = *const* plane, we have

$$P(\vec{r}_{0\perp}, z_0) = (\lambda_0^2/4\pi)\iiint_{z>0} \sigma_0(\vec{r}_\perp, z) Q(\vec{r}_{0\perp} - \vec{r}_\perp, z_0, z)\, d^2\vec{r}_\perp dz\,, \qquad (15)$$

$$Q(\vec{r}_\perp, z_0, z) = \left[2\overline{E}^2(\vec{r}_\perp, z) - \overline{E}_{ns}^2(\vec{r}_\perp, z)\right]\int_{-\infty}^{\infty} b^2(2t - 2z_0/c)\overline{T}(\vec{r}_\perp, z, t)dt\,, \qquad (16)$$

where $\vec{r}_\perp$ is the component of $\vec{r}$ in the z = 0 plane,

$$\overline{E}(\vec{r}_\perp, z) = E(0, \vec{r}),\ \overline{E}_{ns}(\vec{r}_\perp, z) = E_{ns}(0, \vec{r}),\ \overline{T}(\vec{r}_\perp, z, t) = T(0, \vec{r}, t)\,.$$

Employing the relationships $\overline{E} = \int_{-\infty}^{\infty} \hat{E}_\delta(0, \vec{r}, t)dt$, $\overline{T} = \hat{E}_\delta(0, \vec{r}, t)/\overline{E}$ we can express function Q through irradiance $\hat{E}_\delta$ from a supplementary δ-pulse source in . a medium with volume scattering function $\beta_1(z, \theta) = 0.5\pi k_0^4 \Phi_1\left(z, 2k_0 \sin(\theta/2)\right)$. Therefore, calculation of OCT images based on equations 15 and 16 may be made using the energy models of light pulse propagation in a medium with strongly anisotropic scattering [13-15]. In the case when duration of a δ-pulse signal at depth z_0 is short compared to d_e, we obtain a simpler expression for Q: $Q = \left[2\overline{E}^2 - \overline{E}_{ns}^2\right] b^2\left(2(z - z_0)/c\right)$. It contains only characteristics of a continuous illumination beam that are described well by analytical solutions of RTE in the small-angle approximation [13,14].

Note that statistically average current at the output of a linear video signal detector is $<\overline{\overline{|i(\vec{r}_0, t_0)|}}>\approx\sqrt{<\overline{\overline{i^2(\vec{r}_0, t_0)}}>}$. Hence, equations 15 and 16 can be used for calculation of images formed by an OCT system with linear video signal detector too.

The model of a random realization of an OCT signal (equations 3 and 6) also allows evaluating its fluctuations which generate speckle noise in the

image. In particular, if the amount of small-scale heterogeneities in the resolution element is large, then, according to this model, coefficients of variation of a video signal for linear and quadratic detectors are 0.523 and 1, respectively.

17.3 METHODS AND ELEMENT BASIS FOR PM FIBER OPTICAL INTERFEROMETRY

As was shown in the previous section information about optical heterogeneities of a turbid medium may be recovered from a nonscattered (or weakly scattered) coherent component, which usually a few orders of magnitude smaller than background formed by a noninformative strongly scattered component of probing radiation. Discrimination of such a weakly scattered component is effectively accomplished by means of optical interferometry with broadband light sources in the visible and near infrared (IR) frequency ranges. An interference signal is detected only when the optical path length difference between the sample and reference arms of the interferometer are matched within the coherence length that is determined by the bandwidth of the probing radiation. Therefore, by changing the reference arm length once can perform in-depth scanning. The interference signal is contributed mostly by backscattering on tissue heterogeneities. Since the informative signal decreases exponentially with depth of the medium, thus, its detection with an acceptable dynamic range is extremely challenging and demands new engineering ideas and their experimental realizations.

Imaging modalities are to meet a number of technical requirements, i.e., adequate imaging depth, appropriate image contrast, high acquisition rate, etc. The main requirements for the optical coherence tomography (OCT) device were dictated by the planned object of study, namely, soft mucosal tissues of human organs. The requirements were the following: spatial resolution of about 10 μm, imaging depth of several millimeters, low non-invasive probing power, and combined acquisition and visualization time for an image with 200 × 200 pixels of about 1 s. Since the OCT device was intended primarily for clinical use, therefore, additional requirements were simplicity of using the device in clinical environment and in particular its compactness.

Since the “heart” of OCT is an optical interferometer, consequently, the main challenge was to devise an interferometer that would satisfy all the requirements listed above and to fabricate necessary fiber optical parts. We chose the Michelson scheme for the interferometer and decided to build it using polarization-maintaining (PM) fibers. PM fiber allowed constructing of the interferometer with a flexible sample arm and provided stable detection of the interference signal. Flexibility of a sample arm facilitates

access to the examined site of biological tissue, which is vital for diagnosis of, for instance, internal organs. The interferometer comprised several fiber optical elements with unique characteristics, which were developed and fabricated by our research team. Another important part of the OCT device is a light source. The commercially available quantum sources of broadband optical radiation in the near IR range with short coherence duration and high cross-sectional spatial coherence were employed as light sources.

All the ideas and expertise of the research team resulted in creation of the compact OCT device based on PM fiber, commercially available low-coherent light source and unique fiber optical elements. The device featured wide dynamic range and high-speed lateral and longitudinal scanning. The miniaturized OCT optical probe was optimized and suited for a variety of clinical applications.

17.3.1 Optical Interferometers Based on PM Fiber

Low-coherence fiber interferometry proved to be a convenient tool for image acquisition in turbid media. It is highly effective for rejecting non-informative multiply scattered light and for detecting the informative component formed by nonscattered or weakly scattered light propagating at almost rectilinear trajectories ("snake-photons"). Calculations and model experiments in media similar to biological tissue verify that the effect of multiple scattering blur the image generated by the informative component at the depth of 6 to 8 of mean free path of a photon. Due to low reflectivity of biological tissue structures it is necessary to detect backscattered light, which is attenuated to the level of 90-100 dB as compared to the incident light. High signal-to-noise ratio for detecting such weak signals in the developed OCT setups was attained by minimizing power losses in the optics, heterodyning of the detected signal at the shot noise level, and reducing the influence of various parasitic effects leading to appearance of false "spurious" signals. In order to eliminate the latter we investigated the dynamic characteristics, fluctuations, and parasitic phenomena in anisotropic fiber interferometers with broadband light sources. This allowed us to formulate technical requirements and as a result develop all interferometer components with improved qualitative and quantitative characteristics.

The dynamic range of a signal is a basic characteristic determining the maximum imaging depth. It depends on the used interferometer scheme. The quality of the optical elements, their alignment, and the level of noise induced during fiber splicing are the parameters determining quality of the interferometer. It was found out that the major limitation of a dynamic range in a Michelson interferometer used in our experimental OCT device is primarily caused by interaction of fiber waveguide modes during their

propagation in anisotropic fiber. Technically, there are four single mode waveguides for light waves in a two-arm interferometer. Two waves oriented along the «fast» and «slow» anisotropy axes of fiber can propagate in each arm, respectively. When orthogonal modes are launched into an interferometer, the fiber waveguide modes with orthogonal polarizations interfere in pairs independently. Practically, parameters of anisotropic fiber vary over length and, thus, cause large-scale fluctuations of group velocities modes propagating along then slow and fast axes. Consequently, zero path-length difference for different modes occurs at slightly different arm lengths. As a result when a mirror is placed into a sample arm which is a standard procedure for adjusting the interferometer and checking its quality, there appear two cross-correlation functions (CCF) with a time delay, i.e., the real image and a parasitic copy of the real image. Besides, additional parasitic signals may arise in CCF due to undesired coupling of modes in fiber elements such as couplers, polarizers, etc at the sites of fiber splicing. This obviously leads to reduce in the dynamic range of the interferometer.

Due to low coherence nature of radiation employed in OCT it is more convenient to speak about different speed of delays for different waveguide modes of fiber rather than about modulation of a polarization state by means of a phase modulator. This leads to different values of the Doppler frequency for orthogonal polarizations. In case of SLDs emitting partially polarized light and a linearly varying path length difference between the interferometer arms, two independent CCF are observed at close Doppler frequencies. Presence of two close frequencies in the signal results in beating. This parasitic effect is removed by polarization filtering of one of the orthogonal modes.

Parasitic coupling of orthogonal fiber modes may also manifest in OCT images when only one linearly polarized mode is excited initially. Experiments demonstrated that such mode coupling was induced at the sites of anisotropic fiber splicing and in the regions of mechanical stresses, etc. This type of coupling excites a weak wave with orthogonal polarization and a group velocity different from that of a primary wave. Due to the secondary parasitic coupling of orthogonal modes, part of the parasitic wave power may return to the initial wave down the propagation path, thus, producing another coherent component with a time delay. Secondary coupling may have the same origin as the primary one and may be formed in a polarizer and coupler [16, 17]. In this case the appearance of the echo-like parasitic spikes in the interferometric signal is caused by the defects of anisotropy of the optical tract which limits the dynamic range of an interferometer [18].

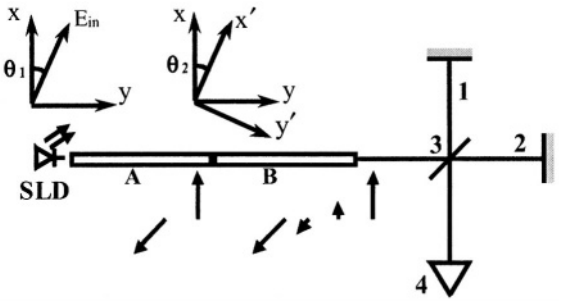

Figure 2. Illustration of the spikes appearance on the two PM (A, B) fiber joint: interferometer arms (1, 2), 3 dB splitter (3), photoreceiver (4).

The appearance of such spikes can be illustrated on the example of two spliced anisotropic fibers (Figure 2) using the time correlation approach. This approach in the general case considers propagation of individual coherent pulse trains; each of these trains is considered to be a source of secondary coherent pulse trains. A Michelson interferometer is employed here to estimate the quality of the mutual orientation of axes of spliced fibers.

Let the radiation from a superluminescent diode $\vec{E}(t) = \vec{E}_{in} E_0(t)$ be linearly polarized at an angle of θ_1 to the eigen axes x', y' of the first fiber A, while the axes of the second fiber B are directed at an angle of θ_2 with respect to the axes of the first fiber. Here, $E_0(t)$ is the time dependence of the electric field at the input of the first fiber and $\vec{E}_{in}$ is the dimensionless vector describing the polarization state and the field amplitude $\vec{E}(t)$ at the input of the first fiber. In this case, one coherent pulse train will propagate with delays τ_{1x} and τ_{1y} along each of the axes x' and y', respectively, at the output from the first fiber (further we will omit primes in x and y for brevity). The amplitudes of the trains propagating along axes x and y are $A_x = E_{in} \cos\theta_1$ and $A_y = E_{in} \sin\theta_1$, respectively. Because the axes of the first and second fibers do not coincide, each of the trains gives the projections on both the x and y axes, so these two pulse trains will propagate along each of the axes in the second fiber.

Therefore, two trains with delays $\tau_{1x} + \tau_{2x}$ and $\tau_{1y} + \tau_{2x}$ and amplitudes $B_{1x} = \cos\theta_1 \cos\theta_2 E_{in}$ and $B_{2x} = \sin\theta_1 \sin\theta_2 E_{in}$; will propagate along the x axis of the second fiber, and two trains with delays $\tau_{1y} + \tau_{2y}$ and $\tau_{1x} + \tau_{2y}$ and amplitudes $B_{1y} = \sin\theta_1 \cos\theta_2 E_{in}$ and $B_{2y} = -\cos\theta_1 \sin\theta_2 E_{in}$ will

propagate along the y axis. The parameters of secondary coherent pulse trains are analyzed with a Michelson interferometer, whose axes are made coincident with the axes of the second fiber. Assuming that a beamsplitter shown in Figure 2 is isotropic, i.e., the power division coefficients for radiation with x and y polarizations are equal ($\kappa_x = \kappa_y = \kappa$), we can express the components of the autocorrelation function along x and y axes in the form:

$$G_x(\tau \pm \Delta\tau) = 2 \cdot \kappa(1-\kappa) \cdot \left\{ (\cos^2\theta_1 \cos^2\theta_2 + \sin^2\theta_1 \sin^2\theta_2) \cdot E_{in}^2 G_0(\tau) + \sin\theta_1 \cos\theta_1 \sin\theta_2 \cos\theta_2 E_{in}^2 G_1(\tau \pm \Delta\tau) \right\}, \quad (17)$$

$$G_y(\tau \pm \Delta\tau) = 2 \cdot \kappa(1-\kappa) \cdot \left\{ (\sin^2\theta_1 \cos^2\theta_2 + \cos^2\theta_1 \sin^2\theta_2) \cdot E_{in}^2 G_0(\tau) - \sin\theta_1 \cos\theta_1 \sin\theta_2 \cos\theta_2 E_{in}^2 G_1(\tau \pm \Delta\tau) \right\}, \quad (18)$$

where $G_0(\tau) = \langle E_0(t) \cdot E_0(t+\tau) \rangle$ is the initial autocorrelation function of the light source (the random process $E_0(t)$ is assumed to be stationary); the angle brackets denote time averaging; $G_1(\tau \pm \Delta\tau)$ is the cross-correlation function; $\Delta\tau = \tau_{1x} - \tau_{1y}$ is the difference of delays for radiations with x and y polarizations in the first fiber. The sign ± reflects the symmetry of the autocorrelation function, which physically means that the situation when the first arm of the interferometer is shorter than the second one is equivalent to the situation when the second arm is shorter than the first one (Figure 2).

One can see from equations 17 and 18 that, in the absence of dichroism of the optical tract or anisotropy of the division coefficient, for each of the trains propagating along the *x* axis with the nonzero delay (the condition $\tau = 0$ means the equality of the interferometer arms), there will be a pulse train that propagates along the y axis with the same delay and the same amplitude but with an opposite sign. Such trains will cancel each other out (see equation 19). Therefore, the term $G_1(\tau \pm \Delta\tau)$ in equations 17 and 18 corresponding to the propagation of trains with different polarizations in the first fiber will disappear from the total autocorrelation function

$$G(\tau) = G^x(\tau) + G^y(\tau) = 2 \cdot k(1-k) \cdot \left|\vec{E}_{ax}\right|^2 G_0(\tau) = 2 \cdot k(1-k) \cdot I_0 \cdot G_0(\tau), \quad (19)$$

where I_0 is the initial radiation intensity entering the interferometer. In the absence of dichroism or anisotropy of the division coefficient the mutual

orientation of the spliced fibers cannot be determined. In the presence of anisotropy of the division coefficient in the interferometer ($\kappa_x \neq \kappa_y$), the subtraction of the trains will be incomplete. The subtraction depth is defined by the coefficient:

$$\eta = \frac{\left|\sqrt{\kappa_x \cdot (1-\kappa_x)} - \sqrt{\kappa_y \cdot (1-\kappa_y)}\right|}{\sqrt{\kappa_x \cdot (1-\kappa_x)} + \sqrt{\kappa_y \cdot (1-\kappa_y)}}, \tag{20}$$

where $\eta = 0$ corresponds to the complete subtraction and $\eta = 1$ to the absence of subtraction.

Let us assume that the first fiber is longer than the depolarization length $L_d = \lambda_0^2 / (\Delta\lambda \Delta n_a)$, where λ_0 is the central wavelength of the light source in vacuum; $\Delta\lambda$ is the spectral width of the light source; Δn_a - the difference of the refractive indices of polarization axes of fibers. In the presence of dichroism or anisotropy of the division coefficient the interference pattern will have a separate interference region (hereafter, the correlation or interference peak) with a delay $\Delta\tau$. Two trains propagating with different initial polarizations and the same time delay will separate when the propagation length will exceed the depolarization length which will result in appearance of an additional interference peak. For a light source with spectral width of 20 nm, the central wavelength of 0.8 mm, and the birefringent refractive index of $\Delta n_a = 1.5 \cdot 10^{-4}$, the corresponding depolarization length is 21 cm.

Therefore, a separate correlation peak can be already induced by splicing two relatively short pieces of PM fibers. As one can see from equations 17 and 18 the best condition for the observation of this peak (when the peak amplitude is maximal for given θ_2) is attained when the polarization modes of the first fiber are excited at the same rate, and radiation with one of the polarizations is not sent to a photodetector. In this case, the subtraction is completely absent.

The wave with one of the polarizations can be suppressed by placing a polarizer between the second fiber and a photodetector whose axis is oriented to coincide with one of the axes of the second fiber [18]. The amplitude of the correlation peak depends on the angle between the axes of spliced fibers and changes from zero (when the axes are coincident or orthogonal) to the maximum equal to the half amplitude of the main peak (when the angle between the axes of the fibers is 45°). The correlation peak amplitude also depends on the angle between the transmission axis of the polarizer and the axis of the output fiber and varies from the maximum

(when the axes are coincident or orthogonal) to zero (when the angle between axes is 45°). The appearance of new components with given polarization from components with orthogonal polarization (energy transfer) upon splicing two PM fibers can be described with a rotational matrix $O(\theta_2)$ where θ_2 is the angle between the intrinsic axes of spliced fibers.

$$O(\theta_2) = \begin{pmatrix} \cos\theta_2 & \sin\theta_2 \\ -\sin\theta_2 & \cos\theta_2 \end{pmatrix}. \tag{21}$$

In this case, the fields along the axes x and y at the output of the second fiber can be written as:

$$\begin{aligned} E_x &= E_{in} \cdot \left(E_1(t+\tau_{1x})\cos\theta_1\cos\theta_2 + E_2(t+\tau_{1y})\sin\theta_1\sin\theta_2\right) \\ E_y &= E_{in} \cdot \left(-E_1(t+\tau_{1x})\cos\theta_1\sin\theta_2 + E_2(t+\tau_{1y})\sin\theta_1\cos\theta_2\right) \end{aligned}. \tag{22}$$

Such a representation of the output field components is convenient for analysis of more complicated systems, for example, systems with distributed heterogeneities, multiple defects of anisotropy, etc.

It can be shown that distributed defects of anisotropy induce transferring of the part of the power from initial polarization into orthogonal polarization [18]. The amplitude of the power with orthogonal polarization is determined by the two basic parameters: maximum angle between intrinsic polarization axis and induced axis and ratio of the defect length (L_i) to the beat length of fiber $L_b=2\pi/\Delta\beta$, where $\Delta\beta$ – is the difference between propagation constants of fiber for orthogonal polarizations.

The appearance of new pulse trains in orthogonal polarizations can be described by the time correlation analysis. In this case propagation of low-coherence radiation can be mathematically represented by transformation of a pair of complex vectors with dimension $2n$

$$\boldsymbol{V}_{2n} = \begin{pmatrix} \mathrm{a}^{nx} \\ \mathrm{a}^{ny} \end{pmatrix}, \quad \begin{aligned} \mathrm{a}^{nx} &= \left(a_1^{nx}, a_2^{nx}, \ldots, a_n^{nx}\right) \\ \mathrm{a}^{ny} &= \left(a_1^{ny}, a_2^{ny}, \ldots, a_n^{ny}\right) \end{aligned}. \tag{23}$$

Each of n elements of the vector a^{nx} - $a_j^{nx} = A_j^{nx} e^{i\varphi_j^{nx}}$ corresponds to the single random process (pulse train) with a certain time delay $\Delta\tau_j^{nx} = \varphi_j^{nx}(\omega_0)/\omega_0$ and amplitude A_j^{nx} with polarization along the x axis; the same relations are held for each element of vector a^{ny} but for the y axis.

Transformation of radiation with polarization along *x* and *y* axes on the *m+1* defect of anisotropy yields a pair of vectors $\boldsymbol{V}_{2nx}^{u} = \hat{U}_{m+1}\boldsymbol{V}_{2nx}$ and $\boldsymbol{V}_{2ny}^{u} = \hat{U}_{m+1}\boldsymbol{V}_{2ny}$, where $\hat{U}_{m+1}$ is the Jones matrix of the defect of anisotropy and $\boldsymbol{V}_{2nx} = \begin{pmatrix} \mathrm{a}^{nx} \\ 0 \end{pmatrix}$; $\boldsymbol{V}_{2ny} = \begin{pmatrix} 0 \\ \mathrm{a}^{ny} \end{pmatrix}$. It should be noted that when defects of anisotropy are short compared to the depolarization length the dependence of the Jones matrix elements could be neglected. It should be noted that when the length of a piece of a fiber with anisotropy defects is short compared to the depolarization length the frequency dependence of the Jones matrix elements could be neglected [18].

Total transformation on the defect of anisotropy for x and y polarizations is given by a pair of vectors $\boldsymbol{V}_{4n}$

$$\boldsymbol{V}_{4n} = \boldsymbol{V}_{2nx}^{u} + \boldsymbol{V}_{2ny}^{u} = \begin{pmatrix} u_{11}^{m+1}\mathrm{a}^{nx}, u_{12}^{m+1}\mathrm{a}^{ny} \\ u_{21}^{m+1}\mathrm{a}^{nx}, u_{22}^{m+1}\mathrm{a}^{ny} \end{pmatrix} = \begin{pmatrix} \mathrm{a}^{2nx} \\ \mathrm{a}^{2ny} \end{pmatrix}, \tag{24}$$

the pair of vectors $\boldsymbol{V}_{4n}$ is twice as long the initial pair of vectors $\boldsymbol{V}_{2n}$.

While propagating between two defects of anisotropy each pulse train acquires different time delays for x and y polarizations:

$$\boldsymbol{V}_{4n}^{/} = \begin{pmatrix} e^{0.5i\Delta\beta L} & 0 \\ 0 & e^{-0.5i\Delta\beta L} \end{pmatrix} \begin{pmatrix} \mathrm{a}^{2nx} \\ \mathrm{a}^{2ny} \end{pmatrix}, \tag{25}$$

where *L* is the distance between two defects of anisotropy. The dimension of the pair of vectors is not changed by this operation.

Using this approach one can describe the propagation of low coherence radiation in the arms of an interferometer independently. A pair of vectors $\boldsymbol{V1}_{4n1}$ and $\boldsymbol{V2}_{4n2}$ with dimensions of *4n1* and *4n2* are needed for description of the interferometric signal on the input of a photodetector. The above pair of vectors will contain the final set of delays and amplitudes in the first and second arms of the interferometer, respectively.

The final correlation function of the system can be written using the following formula:

$$G_{x,y}(\tau) = \sum_{j1=1}^{n1}\sum_{j2=1}^{n2} A1_{j1}^{x,y} \cdot A2_{j2}^{x,y} \cdot N1_{j1j2}^{x,y}\left(\tau - \Delta\tau_{j1j2}^{x,y}\right), \tag{26}$$

where

$$N1_{j1j2}^{x,y}(\tau-\Delta\tau_{j1j2}^{x,y})=\int_{-\infty}^{\infty}S(\omega)\cdot e^{i\cdot\Delta\varphi_{j1j2}^{x,y}(\omega)}\cdot e^{i\cdot\omega\cdot\tau}d\omega. \qquad (27)$$

$A1_{j1}^{x,y}$ and $A2_{j2}^{x,y}$ are the modules of a pair of vectors $\boldsymbol{V1}_{4n1}=\begin{pmatrix}\mathrm{a1}^{2n1x}\\ \mathrm{a1}^{2n1y}\end{pmatrix}$ and $\boldsymbol{V2}_{4m}=\begin{pmatrix}\mathrm{a2}^{2n2x}\\ \mathrm{a2}^{2n2y}\end{pmatrix}$ correspondingly. All possible variations of phase differences between $a1_{j1}^{2n1x,y}$ and $a2_{j2}^{2n2x,y}$ are normalized on the central frequency of a light source ω_0 and used as delays $\Delta\tau_{j1j2}^{x,y}$.

The number of elements required for calculations increases as 2^m, where m is the number of defects of anisotropy. For instance, 50 defects of anisotropy in the optical tract would require a pair of vectors with $1.1*10^{15}$ elements. The number of elements can be reduces by applying the perturbation theory. This theory is valid when power transferred to the orthogonal polarization on the defect of anisotropy is much smaller than power in the initial polarization. Mathematically this can be expressed by the following inequality:

$$|u_{12}|<<1,|u_{21}|<<1, \qquad (28)$$

where $|u_{12}|$ and $|u_{21}|$ are non-diagonal elements of the Jones matrix. The theory of perturbations of the s-order considers series terms from zero to s-th order inclusively. For example, if the initial pulse train is of the 0-order; then, on the defect of anisotropy it generates the pulse train of the 1-order with orthogonal polarization.

In this case it is convenient to split the Jones matrix describing appearance of the new field components on the next defect of anisotropy into two matrices:

$$\hat{U}_{m+1}=\hat{U}1_{m+1}+\hat{U}2_{m+1}=\begin{pmatrix}u_{11}^{m+1}&0\\0&u_{22}^{m+1}\end{pmatrix}+\begin{pmatrix}0&u_{12}^{m+1}\\u_{21}^{m+1}&0\end{pmatrix}. \qquad (29)$$

When the first term in equation 29 is multiplied on the pair of vectors, the order of the perturbation series does nor change, conversely, the second term

in equation 29 being multiplied on the pair of vectors cause an increase in the order by 1. Therefore, application of the perturbation theory decreases the number of elements required for calculations to m^s. For instance, for 50 defects of anisotropy and pulse trains up to the second order inclusively the required number of elements is 2.5×10^3.

In addition to the primary mode coupling can occurs before entering the interferometer, the OCT image tomogram features symmetrical stripes parallel to the object surface following the bright structures of the image. Such parasitic stripes generated by excitation of orthogonal modes at the site of splicing of the isotropic fiber output of the light source and the anisotropic fiber input of the polarizer were removed by compensating the delay difference according to the method described in [19]. The idea of the method is to splice the input fiber of a polarizer with a piece of same type of fiber of the same length, but with the anisotropy axis turned by 90 degrees. Such a compensator makes the total delays for the orthogonally polarized modes equal prior to entering the polarizer, thus effectively decreasing the parasitic signal by 20-25 dB.

An alternative method of compensating optical birefringence in single mode optical waveguides was proposed and investigated in [20, 21]. In this approach 45-degree Faraday cells are placed at the end of each interferometer arm through which light passes twice. As a result, both regular and parasitic fiber anisotropies are compensated completely and the initial polarization state of light is restored with its axis turned by 90 degrees. This approach was investigated theoretically by means of the apparatus of the Jones matrices. This method can provide a handy tool for fabricating the OCT interferometer partially or completely based on isotropic single mode fiber.

The principal limitation of the compensation method described above is dispersion of light in a Faraday cell. However, our experiments using light source with a central wavelength of 1.3 μm and bandwidth of 50 nm and a Faraday cell based on YIG crystal in oversaturated magnetic field demonstrated that regular and parasitic anisotropy can be compensated, at least, up to level of 40 dB.

A 45-degree Faraday cell was also used for creation of an interferometer in the setup for polarization OCT described in subsection 17.4.4. The Faraday cell was placed in one, for example, reference arm, thus, linearly polarized light returning to the coupler had orthogonal polarization. Therefore, interference occurred only with a part of the backscattered wave in the sample arm which also had polarization orthogonal to the initial one. The orthogonal polarization appeared in backscattered light due to reflection from of the sample with a change in polarization. This approach introduces additional suppression of non-informative component which is a limiting

factor for OCT imaging, Moreover, simultaneous acquisition of images in initial and orthogonal polarizations provided a basis for development of the method of cross-polarization OCT [22, 23].

Another original interferometer scheme was elaborated for «color» optical coherence tomography, i.e., for imaging of the same sample regions at several wavelengths simultaneously. This is of great interest, because optical properties of biological tissues noticeably vary in the short and long wavelength regions of the «therapeutic transparency window» (e.g., at wavelengths of about 0.8 μm and 1.3 μm). We fabricated a fiber optical interferometer which was built using a single-mode fiber and optimized for wavelengths of 0.8 μm and 1.3 μm simultaneously [24]. Group delays and dispersion in both interferometer arms were simultaneously compensated at the both wavelengths even though the material and waveguide dispersion of fiber were quite different at these wavelengths. The idea was to insert into both arms of the interferometer two sections of additional optical fiber whose optical properties differ strongly from those of the primary fiber. Thus, the interferometer scheme was artificially extended to include additional degrees of freedom provided by optical parameters of the additional fiber sections. By optimizing the latter optical paths were made equal and the duration of cross-correlation functions for signals at both wavelength were minimized. The setup for "color" OCT is described in detail in subsection 17.4.2.

17.3.2 Fabrication of Fiber Optical Elements Based on PM Fiber

A polished 3 dB coupler based on single mode isotropic fiber and a polarizer based on the half of a coupler were developed for low-coherent interferometry. The 3 dB coupler was optimized to yield stable coupling of waveguide modes in a wide temperature range with good orthogonal mode decoupling and losses less than 0.1 dB.

The couplers and polarizers for OCT based on PM fiber were fabricated employing the technologies developed earlier [25, 26]. The most challenging problem was to increase accuracy of orienting anisotropy axes of fibers relative to the symmetry axes of the optical elements. Among a variety of anisotropic fibers we chose PANDA anisotropic fiber because its structure allows the most precise optical control of alignment of fiber axes. The fiber axes were aligned relative to the axes of the optical element with accuracy of 1 degree. Custom designed equipment for accurate angular orientation of fibers allowed aligning without twisting; the quality of alignment was optically controlled using the CCD array. The results of subsequent computer data analysis were further used for correction of alignment. The

specially designed correlometer described in [18] controlled appearance of local coupling of fiber modes in fiber during its installation and fixing in a profiled groove of the basic optical element of the polarizer or coupler. Each individual basic optical element was then grinded and polished. Then these basic elements were used as halves of the assembled coupler. The basic elements employed for polarizers were preliminary processed by depositing dielectric and metal layers. The parameters of deposited structures were simulated numerically and further tested experimentally. The polarizer extinction, whose maximum value depended on parasitic mode mixing, was measured by a correlometer. As a result, for wavelengths of 0.83 μm and 1.3 μm we obtained the following unique parameters of a polarizer based on anisotropic fiber: extinction coefficient of about 35-40 dB and the level of induced losses less than 0.2 dB.

Analogous anisotropic fiber elements were used to fabricate 3 dB couplers with crosstalk less than -40 dB and the level of induced losses less than 0.1 dB. We also developed a unique technique and fabricated a 3 dB coupler working on two distant wavelengths of 0.83 μm and 1.3 μm simultaneously.

In-depth OCT scanning was realized by changing the optical path length difference between the sample and reference arms according to a linear law. This was attained by elastically stretching the fibers of the interferometer arms in counter phase. Optical fibers were glued to piezoceramic actuators which provided fiber stretching with relative elongation of up to 10^{-4}. Given a sufficient fiber length, the absolute path length difference between the interferometer arms could achieve several thousand wavelengths.

17.4 EXPERIMENTAL OCT SYSTEMS

Successful creation of experimental OCT setups became possible due to a combination of several factors, namely, promising results of the theory of vision in turbid media described in Section 1, development of methods for precision fiber optical interferometry, and fabrication of unique fiber optical elements.

17.4.1. Compact OCT Device Based on Michelson Fiber Optical Interferometer

The schematic of the optical coherence tomography device is depicted in Figure 3. The setup features a broadband light source in the near IR frequency range, the Michelson interferometer based on PM fiber, the electron-mechanical system performing in-depth scanning by means of modulation of lengths of interferometer arms, the electro-mechanical system

for lateral scanning of the sample (optical probe), the system for photodetection of the interference signal, the electron system for analog signal processing, and a personal computer for digital signal processing, image visualization and storage, and for general control of the OCT device.

In different OCT designs we used light sources superluminescent diodes (SLD) with central wavelengths ranging from 0.83 μm to 1.28 μm, bandwidths ranging from 25 nm to 50 nm, and power in a single mode fiber output from 1 mW to 10 mW. For experimental purposes we also employed femtosecond lasers (a titanium-sapphire (Ti:Sa) laser with a central wavelength of 0.8 μm, bandwidth up to 70 nm and output power up to 200 mW; a chromium-forsterite laser with a central wavelength of 1.3 μm, bandwidth up to 30 nm and power up to 100 mW). Novel semiconductor superluminescent sources operating in the IR frequency range with bandwidth up to 100 nm are expected to appear in the near future. These sources [27] would be competitive with femtosecond Ti:Sa lasers that are currently the sources of coherent radiation with the widest broadband.

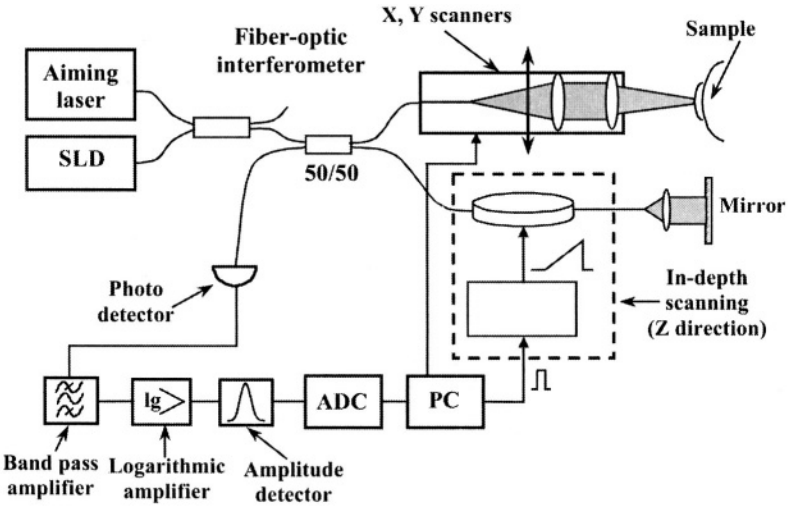

Figure 3. OCT functional scheme.

The heterodyne detection is attained by modulating the path length difference between interferometer arm lengths, ΔL, according to a linear law $\Delta L = \Delta \dot{L} \cdot t$. The general principle of low-coherence interferometry states that the depth h within the sample from which the OCT signal is detected changes with velocity $\dot{h} = \Delta \dot{L} \dfrac{n_{fgr}}{n_{mgr}}$, where n_{fgr} and n_{mgr} are the group

refractive indices of the fiber material and of the sample, respectively. The detector discriminates from the total measured signal an interference component at the Doppler frequency $F = \frac{2\Delta \dot{L} n_f}{\lambda_0} = 2n_{mgr}\frac{\dot{h}}{\lambda_0}\frac{n_f}{n_{fgr}}$, where n_f is the phase refractive index of the fiber material and λ_0 is the vacuum wavelength of probing light. For example, for the wavelength of 1.3 μm, the scanning velocity of 65 cm/s corresponds to the Doppler frequency of 1 MHz.

The modulation speed of the arm path length difference and its stability are critical OCT parameters. The scanning velocity of 50 cm/s is required to acquire images with a size of 2.5×4 mm^2 (axial size × lateral size), resolution of 20×20 μm^2 and acquisition rate of 1 image/second. The scanning velocity should be maintained constant with an accuracy of at least of 1 percent to confine the Doppler frequency signal within the detection band. Resonance properties of currently available mechanical systems cannot guarantee constant velocity with required accuracy throughout the modulation period. For our OCT setups we developed and fabricated a scanning system based on the original fiber optical piezoelectric converter [28] This converter is capable of scanning the path length difference between the interferometer arms at the rate of 50 cm/s up to 4 mm in depth. Another advantage of our scanning system is almost inertia-free response within the working amplitude and modulation frequency range that simplifies detection of the informative signal at the Doppler frequency substantially.

The probing beam is moved along the sample surface by means of a custom designed one- or two-coordinate scanner embedded inside of the optical at the distal end of the sample arm. The probing light is focused by a system of lenses with fixed magnification into a 10-20 μm spot at the certain sample depth that can be adjusted mechanically. The fiber tip is swung transversally in the focal plane of the lens system, thus, causing transversal movement of a probing beam within the sample. The scanning process is fully automated and computer controlled.

The interference signal is detected by a photodiode with an optical fiber input which is characterized by high quantum yield (>0.8) and low noise level. The photodiode is coupled with a circuit filtering the electrical signal and extracting the Doppler component with a central frequency of about 1 MHz. The signal consequently passes a linear pre-amplifier characterized by the intrinsic noise level lower than the shot noise of detected light, then a system of filters, a multicascade logarithmic amplifier, and finally an amplitude detector. The logarithmic amplifier with the dynamic range exceeding 70 dB was necessary for detection of extremely low signals because backscattered light intensity decreases exponentially with depth.

After analog processing the signal is fed to a computer through the analog-digital converter for further processing, data recording, and displaying of OCT images.

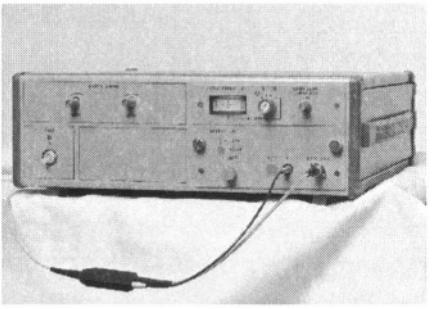

Figure 4. General view of the portable optical coherence OCT device.

As it was shown in section 17.1, the measured signal is proportional to the logarithm of tissue backscattering. The two-dimensional map of tissue backscattering obtained by scanning in depth (by varying the optical path-length difference between the interferometer arms) and by scanning along the sample surface (by moving the probing beam transversally) is displayed on a computer monitor and stored for further use and processing. Such 2D OCT images are called tomograms.

A general view of the compact OCT device is shown in Figure 4. The device is portable (15"×14"×5.5"; weight 18 lbs.); the data acquisition board is internal and is connected via an interface cable to a standard PC printer port. The image acquisition is automated and controlled by a computer. Developed software controls the instrument, processes the data and displays the images.

17.4.2 "Two-color" OCT System

The scattering and absorbing properties of samples generally depend on the probing wavelength. Back in the days of early OCT experiments there appeared an idea of "color" low-coherence imaging in turbid media. The idea was to measure OCT images of the same sample regions at two or more wavelengths simultaneously and then superimpose these images using different colors and relative amplitudes for different wavelengths. We were pioneers in developing and fabricating a setup for two-color optical coherence tomography [24] that could acquire OCT images at two wavelengths simultaneously using only one interferometer and focusing system.

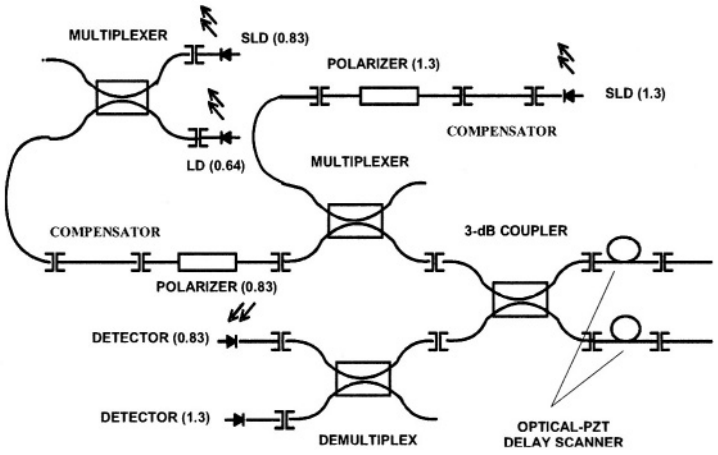

Figure 5. The schematic for two-color OCT setup.

The schematic of the setup is shown in Figure 5. The light source consisted of two SLDs with central wavelengths of 0.83 μm and 1.3 μm, spectral bandwidths of 25 nm and 50 nm (corresponding axial coherence lengths of 13 μm and 19 μm) and power of 1.5 mW and 0.5 mW, respectively. The light from both SLDs was coupled to same Michelson interferometer. The incident radiation was split into two equal parts between the sample and reference arms by a fiber coupler with 3 dB light separation at both wavelengths. The path length difference between the interferometer arms was modulated by means of the piezoceramic converter (see subsection 15.2.2.) providing in-depth scanning as deep as 3 mm. The most challenging problem was compensation of wave dispersion in interferometer arms for two different wavelengths simultaneously. This problem was solved by inserting an additional piece of fiber whose dispersion properties were quite different from those of the principal fiber into one of the arms of the interferometer. Durations of cross-correlation functions in the reference and sample arms were minimized by changing the lengths of the principal and compensating fibers for both probing wavelengths. The corresponding attained in-depth spatial resolution for wavelengths of 0.83 μm and 1.3 μm was 15 μm and 34 μm, respectively.

17.4.3 3D OCT Imaging

In the optical probe for two-dimensional OCT imaging, the trajectory of a probing beam is linear. For 3D imaging the electromechanical system of beam deflection was improved to allow an arbitrary trajectory of a probing beam. This type of the optical probe permits recording of three-dimensional

OCT images with an arbitrary shape of regions within the scattering medium. The simplest way to obtain three-dimensional images is to record a series of two-dimensional images of parallel sections of a sample and then fuse them together. For better visualization we developed software for animation and presentation of 3D OCT images in the form of semitransparent three-dimensional structures, which greatly simplified perception of large data amount of tomographic information [22].

17.4.4 Cross-Polarization OCT Setup

Multiple experiments conducted by different research groups have shown that OCT is sensitive to structural alterations in biological objects that occur at the level of cell groups and tissue layers [29-32]. Nevertheless using standard OCT imaging, it is very difficult to differentiate inflammatory processes, papillomatosis, cancer, and scar changes [23].

In many pathologies structural violations are preceded by biochemical and initial morphological changes. It is known that some structural components of biotissue, e.g., stromal collagen fibers that constitute the basis of healthy mucosa, can strongly depolarize incident radiation. Also fibrous tissues such as collagens are linear birefringent, i.e., they change the polarization state of light, depending on the value of birefringence and penetrated tissue depth. Both these processes lead to the appearance of cross-polarized component in backscattered light. Pathological processes with different origin are characterized by the difference in both the amount of collagen fibers and their spatial organization. Therefore, a comparative analysis of cross-polarization backscattering properties of biological objects may be taken as an underlying point of the technique for early diagnosis of neoplastic processes.

The specificity of standard OCT can be improved by studying polarization properties of probing radiation when it propagates through a biological object. This approach was implemented in the polarization-sensitive OCT technique (PS OCT), which is described in details in Chapter 18 by J.F. de Boer. At present, in the majority of studies on PS OCT, the criterion of pathological changes in tissue is a sharp decrease in its macroscopic birefringence. For early diagnostics of neoplastic processes, a reliable signal reception at depths 400-700 μm is required. To correctly determine phase characteristics, such as birefringence, the signal-to-noise ratio should be not less than 10-15 dB, which is difficult to achieve when studying layers at depths more than 300-500 μm. For deeper layers (up to 1.5 mm) a variant of PS OCT – the cross-polarization OCT (CP OCT) can be employed. OCT setups may be equipped with a means for recording images with polarization orthogonal to that of incident probing light. It is a new

realm of tomographic information because only regions of the medium that depolarize backscattered light contribute to the interference signal. In order to detect the OCT signal in the orthogonal polarization a 45-degree YIG Faraday cell was inserted into the reference arm of the interferometer. The CP OCT technique is based on the detection of a backscattered component that is orthogonal to linearly polarized probing radiation [22, 33].

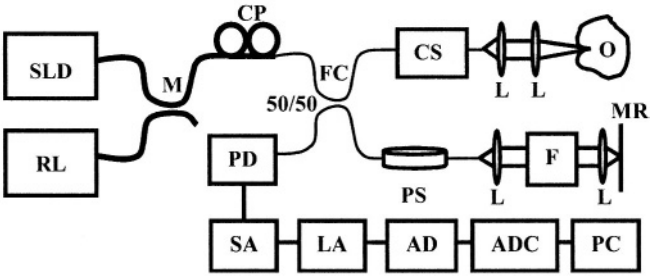

Figure 6. The experimental setup for the cross-polarization OCT: crossectional scanner (CS), investigated object (O), longitudinal piezo-scanner (PS), lenses (L), photodiode (PD), selective amplifier (SA), logarithmic amplifier (LA), amplitude detector (AD), analog to digital converter (ADC), personal computer (PC). Bold line corresponds to single-mode fiber; thin line illustrates polarization maintaining fiber.

A sketch of the experimental setup used for measuring OCT and cross-polarized OCT images is shown in Figure 6. Using a multiplexer low-coherence IR radiation from a superluminescent diode (SLD) with wavelength of 1.3 μm and coherence length of 21 μm is combined with radiation from a semiconductor red laser (RL) used for alignment purposes. Then one of polarization eigen modes of a PM 3dB fiber coupler is selected by means of a Lefevre polarization controller (CP). PM fiber is used to transport radiation with a certain polarization state in both the signal and reference arms of the interferometer. When there is no Faraday rotator (F) in the reference arm, a co-polarized component of backscattered radiation is recorded. The Faraday rotator performs rotation of an arbitrary polarization state by a specified angle and the direction of the rotation depends only on the direction of the magnetic field inside the rotator and does not depend on the propagation direction of the radiation [20]. Therefore, in the case of the 45° Faraday rotator the radiation passes through it, gets reflected by a mirror, goes back through the rotator and becomes orthogonally polarized in the reference arm. As a result, only cross-polarized component of light backscattered by a biological object would interfere with light from the reference arm. In [33] a quarter wave plate oriented at 45° to the incident polarization was used for this purpose. We use a Faraday rotator instead

because it does not require the angular alignment, therefore, minimizing the realignment time for the whole system. The readjustment of the system takes approximately 30 s. The acquisition time of one OCT image is 1 s. For all OCT images the logarithmic intensity scale is used. Lateral resolution of the system determined by the diameter of the probing beam in the focus is chosen close to axial (in–depth) resolution which is determined by coherence length and in our case is 21 μm. It should be noted that when the system is readjusted to obtain images in the orthogonal polarization the probe is held still. Therefore, both types of images (OCT and CP OCT) are obtained from the same tissue site.

Since this design is based on PM fiber, a portable setup with a flexible probe can be created, thus, making it easy to use in clinical applications, e.g., endoscopically.

17.4.5 Miniature Probe for Endoscopic OCT

The main problem to be solved for endoscopic implementation of OCT is to provide a reliable and convenient access of low-coherence probing radiation to the surface of internal organs. This problem includes several optical, engineering and biomedical aspects such as creation of an OCT interferometer with a flexible arm, development of a remotely controlled miniaturized optical probe, acquisition of OCT data in parallel with standard endoscopic imaging. The implementation of the endoscopic OCT (EOCT) system required integration of a sample arm of an all-optical-fiber interferometer into a standard endoscope using the biopsy channel to deliver probing light to investigated tissue. As a result a whole family of diagnostic EOCT devices suitable for studying different internal organs has been created [34].

To probe the surface of an internal organ we have developed a miniaturized electromechanical unit (optical probe) controlling and performing lateral scanning (Figure 7). This probe is located at the distal end of the sample arm and its size allows fitting the diameter and the curvature radius of standard biopsy channels of endoscopes. Figure 8(a) demonstrates the head of an endoscope for GI investigations with the integrated OCT scanner. A schematic diagram of the optical scanning probe and how it is positioned against a studied object is shown in Figure 8(b). The probing beam is swung along the tissue surface with amplitude of 2 mm. The beam deviation system embodies the galvanometric principle, and the voltage with the maximum of 5V is supplied to the distal end of the endoscope. The distance between the output lens and a sample varies from 5 to 7 mm; the focal spot diameter is 20 μm. The optical scanning probe and the part of the flexible sample arm which is inserted in the endoscope are both sealed,

therefore, the conventional cleaning procedure and sterilization can be performed before applying the setup clinically.

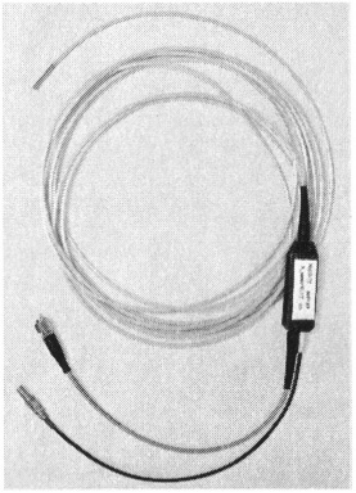

Figure 7. Miniature probe for endoscopic OCT.

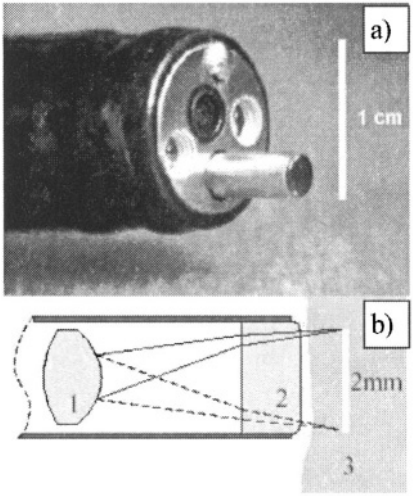

Figure 8. (a) distal end of gastroscope with OCT probe introduced through biopsy channel; (b) schematic diagram of scanning unit: 1 – output lens, 2 - output glass window, 3 – sample.

Implementation of an extended flexible arm of the OCT interferometer became feasible due to use of polarization maintaining fibers as a means for transportation of the low-coherence probing light. This allows eliminating polarization fading caused by polarization distortions at the sites of bending of the endoscope arm. The device features high-quality fiber polarizers and couplers. The "single-frame" dynamic range of our OCT scheme determined as the maximum variation of the reflected signal power within a single image frame attains 35-40 dB. With the scanning rate of 45 cm/s and the image depth of 3 mm (in free space units), an OCT picture with 200x200 pixels is acquired for approximately 1 s. This acquisition rate is sufficient to eliminate influence of moving of internal organs (moving artefact) on the image quality.

The combination of the OCT device with the standard endoscopic equipment has proven to be convenient for clinical studies. A clinician can perform standard observation of internal organs and in the case of interest can also extend the analysis by noninvasive optical biopsy simultaneously of as many tissue sites as desired.

17.5 CLINICAL APPLICATIONS OF OCT

17.5.1 Motivation for OCT Use in Clinical Practice

Majority of pathological processes are accompanied by structural alterations of tissue. Information on these tissue changes is decisive for diagnosis and choosing a treatment strategy. The conventional method for obtaining such information is histological study of biopsy specimens of tissue. Biopsy is considered to be the "golden" standard. A tissue site to be biopsied is typically chosen using additional modalities such as microscopy, endoscopy, etc. These methods however can provide information only about the surface of the studied object. Meanwhile, it is known that neoplastic and inflammatory processes primarily involve parabasal and basal layers, the basement membrane and components of the *lamina propria* of mucosa and rarely affect the surface layers of the epithelium. Structural alterations in these portions of the epithelium cannot be detected by surface imaging methods. Therefore, a clinician is to rely on indirect subtle superficial manifestations of pathological processes in order to perform a guided biopsy that eventually leads to a high rate of false-negative results of biopsy [35].

Information on the internal structure of biological tissues is essential not only for diagnosis of disease, but also for planning of the extent of treatment, control of treatment adequacy and follow-up. In these situations, application of an invasive method such as biopsy is impractical and sometimes contraindicated.

Optical coherence tomography (OCT) is a very promising imaging modality characterized by high spatial resolution, noninvasiveness, and high rate of image acquisition. An OCT device developed at IAP RAS (Nizhny Novgorod, Russia) is compact, portable, and easy to operate; the device is equipped with miniature optical probes compatible with working channels of standard endoscopes, which provides an additional advantage for clinical applications.

Our experience of clinical studies using OCT can be divided into three stages: determination of OCT criteria for norm and pathology for various human tissues, evaluation of diagnostic efficiency of the method, and development of OCT procedures for different clinical situations.

17.5.2 OCT Criteria of Normal and Pathological Tissue

At the first stage, we performed *ex vivo* and *in vivo* OCT studies of various human organs. OCT images were compared with the results of standard histology and based on this comparative analysis the optical criteria

of the states of human tissues were determined. It was established that due to different scattering properties of different tissue layers, OCT images reveal the stratified structure. Mucosa of different organs, skin of various localization and hard dental tissues have a specific structure with distinctive optical patterns, which makes these objects favorable for OCT.

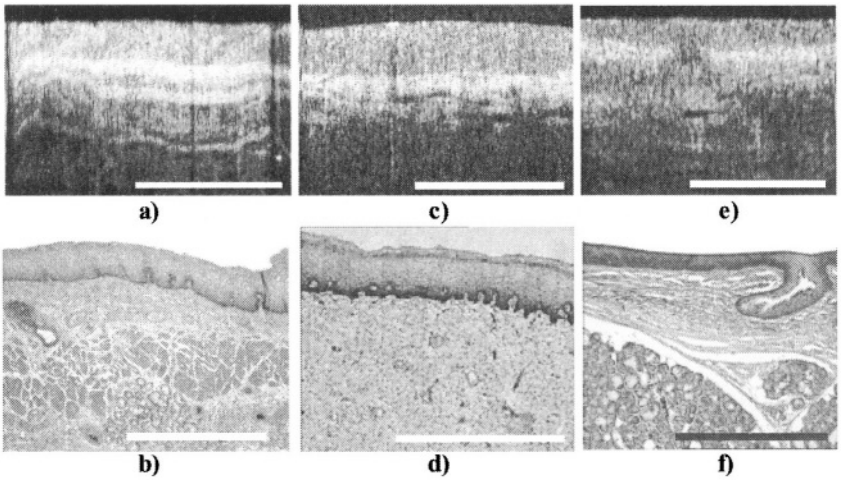

Figure 9. OCT images and histology of healthy mucosa of esophagus (a, b), uterine cervix (c, d), and larynx (e, f) covered by stratified squamous epithelium.

Figures 9 and 10 illustrate examples of parallel OCT and histological study of healthy mucosa of the esophagus [Figures 9(a) and (b)], uterine cervix [Figures 9(c) and (d)] and larynx [Figures 9(e) and (f)], which are covered by the stratified squamous epithelium; of the urinary bladder whose internal layer is represented by the transitional epithelium [Figures 10(a) and (b)], and of the colon [Figures 10(c) and (d)] which is covered by the simple single-layer epithelium atop irregular basement membrane forming glands or crypts. All histological layers inherent to mucosa are evident in these OCT images. It is known that the stratified (transitional) epithelium is separated from the underlying stroma by a smooth basement membrane. Due to different scattering properties of the epithelium and stroma, the location of the basement membrane is clearly seen on these tomograms. In the case of the colon the basement membrane is irregular and its form is difficult to define accurately. However, the intestinal crypts and the structure of subepithelial layers are well visualized. Blood vessels, whose backscattering is much lower than that of the fibrous connective tissue, appear in the images as poorly scattering oval shadows with distinct borders. Mucous glands are also visualized as poorly scattering shadows but their borders are much less distinct [Figure 9(e)].

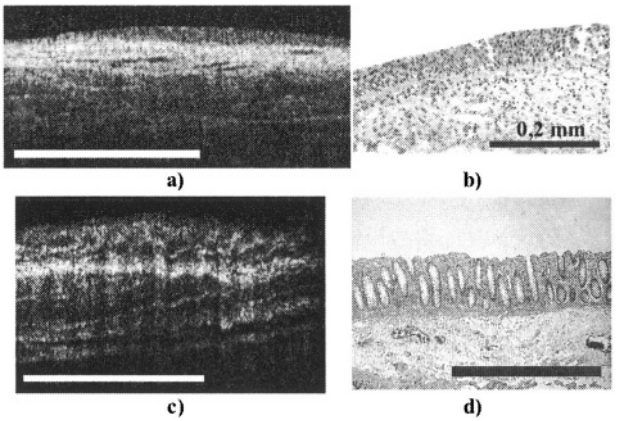

Figure 10. OCT images and histology of urinary bladder covered by transitional epithelium (a, b) and colon covered by the simple single-layer epithelium (c, d).

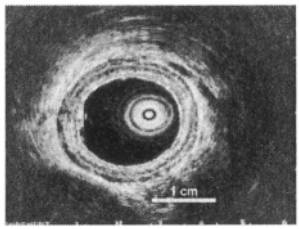

Figure 11. Typical endosonographic image of healthy esophagus.

A typical endosonographic image of healthy esophagus is shown in Figure 11. The zone of OCT imaging is also depicted in the same figure. Obviously spatial resolution of endoscopic ultrasound is not sufficient for revealing details of the mucosal structure, OCT though easily visualizes the layered optical pattern [Figure 9(a)].

OCT images of the skin [Figures 12(a) and (b)] differ from those of mucosa in the relatively weak optical contrast between structural components. This is likely caused by strong reflection of probing light from the tissue surface due to keratinization. Nevertheless, the tomograms clearly demonstrate the morphological features of thick and thin skin.

In vivo OCT imaging of dental tissues showed that the effective penetration depth of probing radiation in teeth was 2-2.5 mm. The structure and content of dentin is known to be considerably different from those of enamel, thus, allowing differentiation between dentin and enamel and estimation of the state of the dentino-enamel junction [Figures 13(a) and (b)].

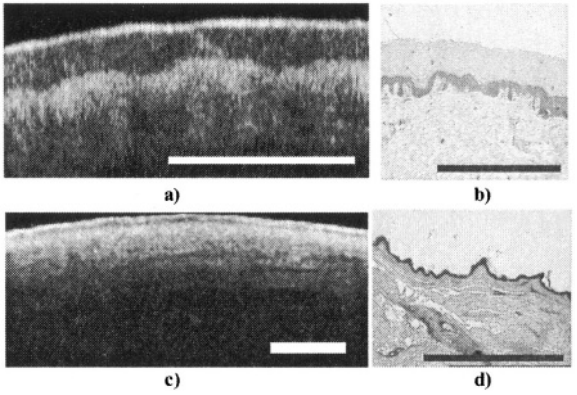

Figure 12. OCT images and histology of thick (a, b) and thin skin (c, d).

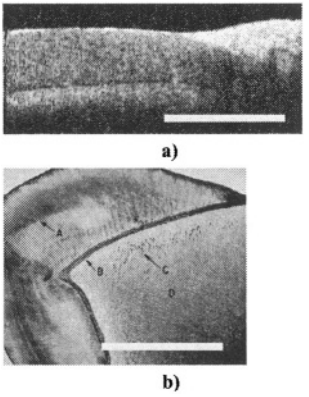

Figure 13. OCT image and histology of hard dental tissues (a, b).

Therefore, due to different optical properties, OCT can differentiate tectorial and hard dental tissues revealing their regular layered structure. The type of the epithelium, keratinization processes, and the architecture of the basement membrane affect the OCT pattern of tectorial tissues. Since optical properties of blood vessels and mucous glands are considerable different from those of the stroma, therefore, OCT can both reliably identify and quantify them throughout the entire range of sizes limited only by spatial resolution of the OCT method. Interestingly, healthy human tissues, which do not have the layered structure, appear in OCT images unstructured. A good example of such tissue is cartilage covering articulating surfaces of bones [Figures 14(a) and (b)].

We performed clinical studies using OCT involving in various fields of medicine such as gastroenterology, urology, laryngology, gynecology, dermatology, dentistry, etc. Total of about 2000 patients was involved. These studies show that there is a number of universal OCT patterns corresponding to different structural alterations which are in turn caused by different pathological processes [22,32,36-39]. Figure 15 a demonstrates a typical OCT image of a chronic inflammatory process in the uterine cervix accompanied by atrophy of the epithelium. The OCT manifestations of the above processes are a decrease in the height of the upper moderately bright layer down to 50 μm (in comparison to 300-350 μm in norm, see Figure 15(b) and an excessive amount of blood vessels with large (up to 80 μm) diameter in the subepithelial layer. The blood vessels are visualized in tomograms as dark areas. The identical optical signs of epithelial atrophy are found also in other localizations.

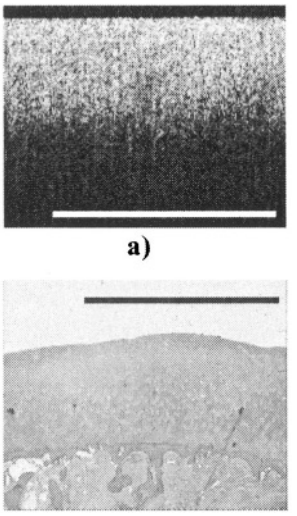

Figure 14. OCT image and histology of cartilage covering articulating surfaces of bones (a, b).

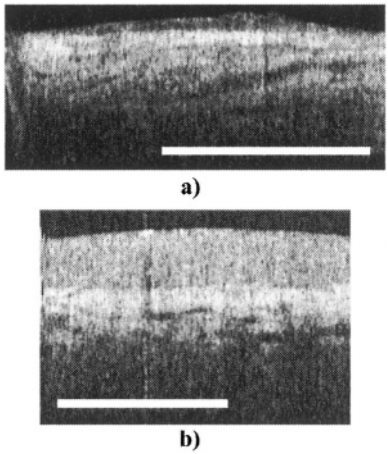

Figure 15. OCT image of chronic inflammatory process in the uterine cervix (a) as compared to the norm (b).

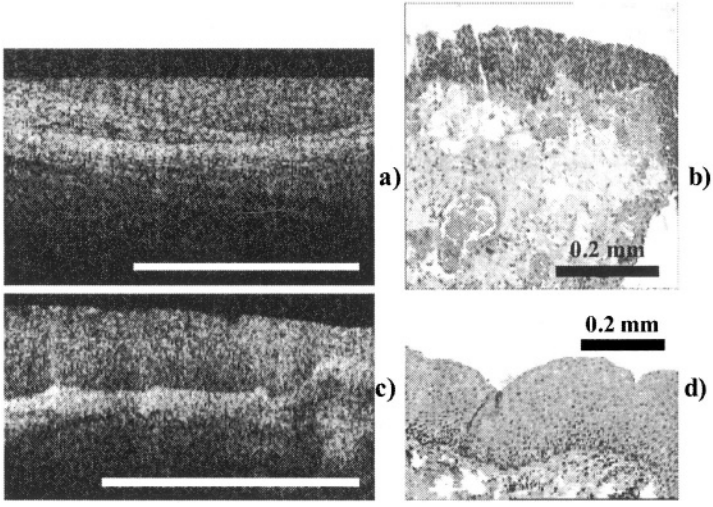

Figure 16. OCT image and histology of epithelial hyperplasia. Transitional epithelium in the urinary bladder (a, b); stratified squamous epithelium in the vocal fold (c, d).

Hyperplasia (hypertrophy) of the epithelium manifests in OCT images as an increase in the height of the epithelial layer (corresponding examples of the transitional epithelium of the urinary bladder are shown in Figures 16(a)

and (b); the stratified squamous epithelium of a vocal fold – Figures 16(c) and (d). In these cases of epithelial hypertrophy the basement membrane is not affected and, hence, the two-layered optical pattern with high contrast is preserved.

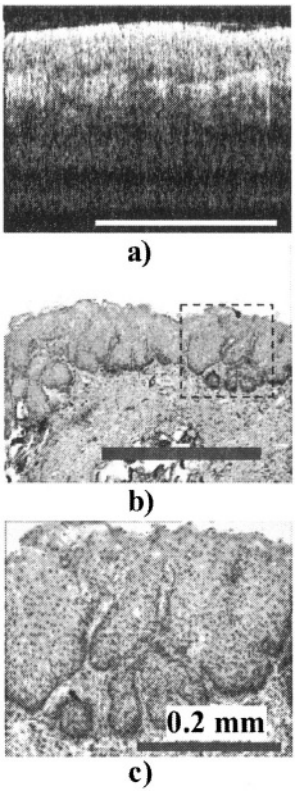

Figure 17. OCT image (a) and parallel histology (b and c) of acanthosis and papillomatosis of uterine cervix mucosa.

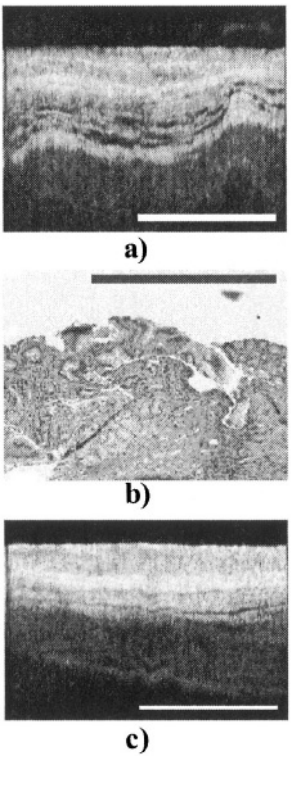

Figure 18. OCT images of metaplasia of stratified squamous epithelium of esophagus (c) into columnar specialized epithelium in Barrett's esophagitis (a), parallel histology (b).

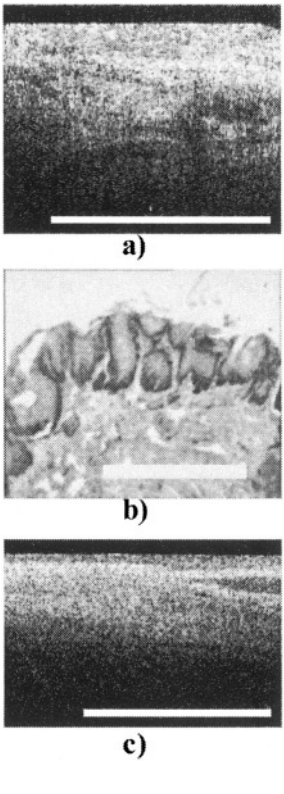

Figure 19. OCT image and histology of squamous metaplasia of urinary bladder mucosa (a, b), OCT image of normal urothelium (c).

Hypertrophy with acanthosis and papillomatosis alters not only the height but also the optical properties of the epithelium (increasing the level of epithelial backscattering) and the course of the basement membrane (making it winding). All these phenomena lead to a decrease in the contrast of the characteristic two-layer pattern of mucosae. Figure 17 presents a tomogram (a) and parallel histology (b) and (c) of acanthosis and papillomatosis of mucosa in the uterine cervix where stromal papillae come up to the epithelial

surface. Each papilla contains an enlarged terminal vessel, which is visualized in the image as a dark area. Note that these alterations of the epithelium are benign the two-layer architecture of tectorial tissue is preserved.

OCT can be also used for imaging of the metaplastic processes. Figure 18 demonstrates an OCT image and parallel histology of metaplasia of the stratified squamous epithelium of the esophagus into the columnar specialized epithelium in Barrett's esophagitis [Figures 18(a) and (b)]. An OCT image of healthy esophagus is shown in Figure 18(c) for comparison. The tomogram of benign Barrett's esophagitis indicates the layered architecture of esophageal mucosa; only at the sites of the uniform moderately scattering squamous epithelium a so-called glandular mucosa is visualized by alternating dark (corresponding to the glandular epithelium) and light (corresponding to connective tissue layers of *Lamina Propria*) horizontal stripes. The OCT image of squamous metaplasia of urinary bladder mucosa [Figures 19(a) and (b)] is characterized by an increase in the height of the epithelium, as compared to urothelium inherent to this mucosa in norm [Figure 19(c)], and a higher brightness of the epithelial layer due to hyperkeratosis.

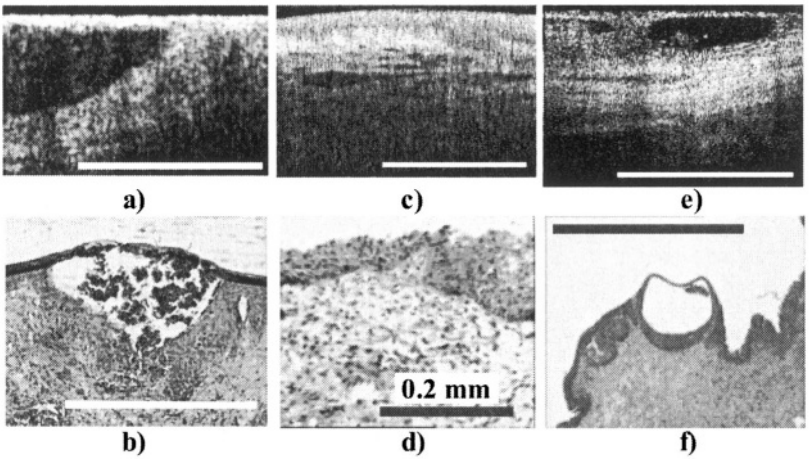

Figure 20. OCT images and histology of different types of liquid accumulation: subcorneal blister (a, b), uterine cervix at pregnancy (c, d), Brunn's nests in cystitis cystica (e, f).

Thus, various benign processes occurring in the epithelium manifest in OCT images as changes in the epithelial height, scattering properties and the course of the basement membrane.

OCT can detect changes that occur not only in the epithelium but in the stromal component of mucosa as well. Pathological processes of different

origin can be accompanied by either stromal edema or accumulation of liquid with formation of cavities and cystic structures. Different types of liquid accumulation are presented in Figure 20. Figure Figure 20(a) shows an OCT image of the skin from a shoulder with a subcorneal blister in a patient with paraneoplastic skin eruption. An OCT image of the uterine cervix in pregnancy [Figure 20(b)] shows accumulation of liquid inside of tissue and disconnection of connective tissue fibers (so-called physiological edema) and indicates that the well-organized structure of the connective-tissue layer is destroyed which results in appearance of dark irregular areas. OCT can clearly visualize various glandular structures: enlarged glands of esophageal mucosa in Barrett's metaplasia [Figure 20(c)] and Brunn's nests in cystitis cystica [Figure 20(d)]. These examples demonstrate the capability of OCT not only to visualize hollow structures but also to detect their form and localization precisely.

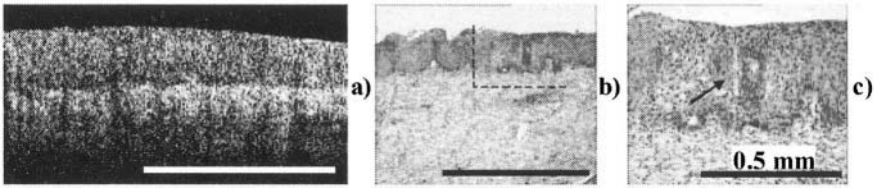

Figure 21. OCT image of low-grade dysplasia accompanied by hyperplastic stratified squamous epithelium of uterine cervix with signs of acanthosis and papillomatosis (a), parallel histology (b, c).

The information on the structure of objects provided by OCT can be used for tumor detection. Although our OCT device has spatial resolution of about 10-20 μm and, thus, cannot detect neoplastic changes at the cellular level, but its spatial resolution is sufficient to reveal certain specific features of the tissue architecture accompanying the malignization process such as abnormal accumulation of cells, penetration of the epithelium into the stroma and, conversely, of the stroma into the epithelium without disruption of the basal membrane (leading to changes in optical properties of the epithelium and loss of the optical contrast between the epithelium and stroma), and an increase in the amount of blood vessels.

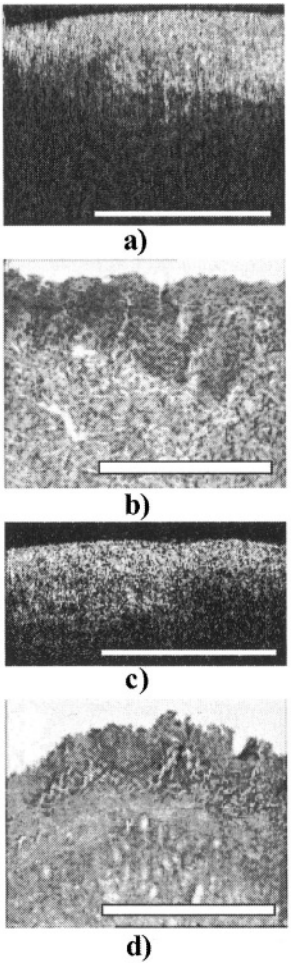

Figure 22. OCT image of high-grade dysplasia of uterine cervix (a), parallel histology (b); OCT image of microinvasive cancer of uterine cervix (c), parallel histology (d).

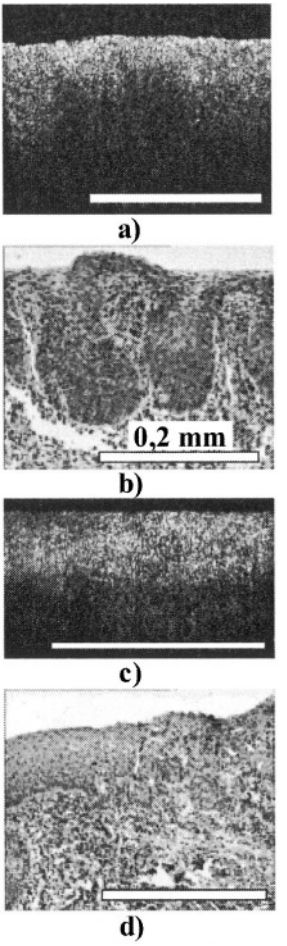

Figure 23. OCT image of high-grade dysplasia of the epithelium of a vocal fold (a), parallel histology (b); OCT image of microinvasive cancer of a vocal fold (c), parallel histology (d).

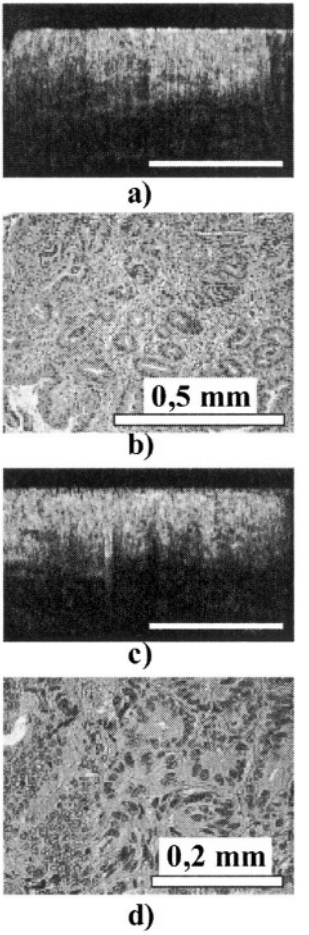

Figure 24. OCT image of high-grade dysplasia of metaplastic epithelium in Barrett's esophagus (a), parallel histology (b); OCT image of microinvasive adenocarcinoma of the esophagus (c), parallel histology (d).

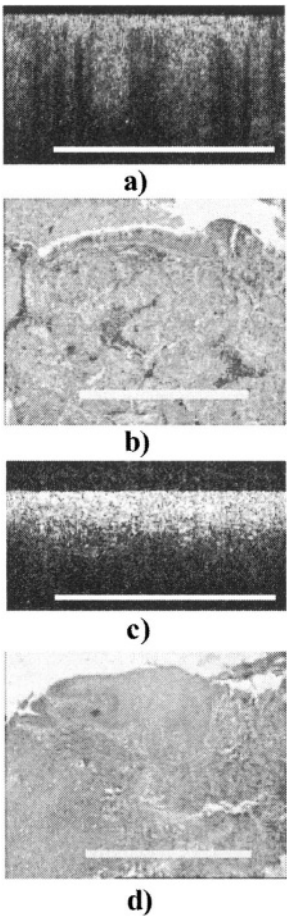

Figure 25. OCT image of invasive squamous cell carcinoma of segmented bronchus (a), parallel histology (b); OCT image of invasive squamous cell carcinoma of vocal fold (c), parallel histology (d).

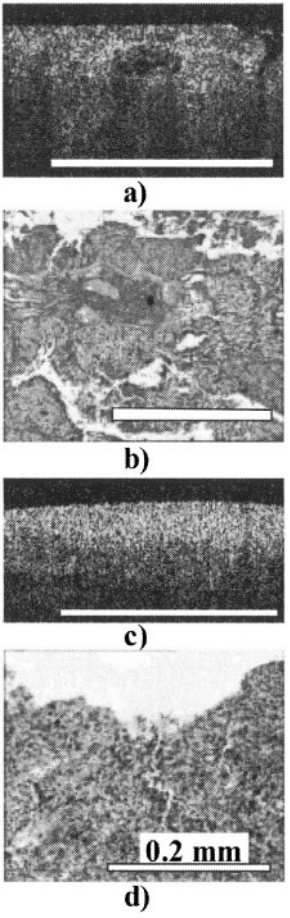

Figure 26. OCT image of invasive transitional cell carcinoma of urinary bladder (a), parallel histology (b); OCT image of invasive squamous cell carcinoma of uterine cervix (c), parallel histology (d).

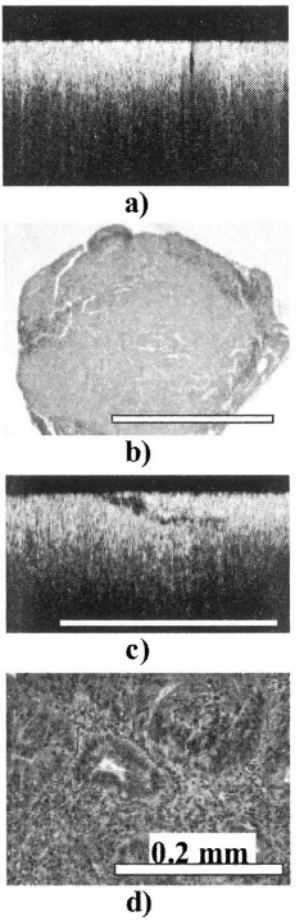

Figure 27. OCT image of invasive adenocarcinoma of esophagus (a), parallel histology (b); OCT image of invasive adenocarcinoma of rectum (c), parallel histology (d).

Result of our OCT demonstrate:

1) Low grade dysplasia almost does not change optical properties of the epithelium and, thus, preserves the layered optical pattern with good contrast, which is typical for benign mucosa (Figure 21);

2) High grade dysplasia changes optical properties of the epithelium and underlying connective tissue and, therefore, considerably reduces contrast between the epithelium and the stroma in OCT images [Figures 22(a) and (b); Figures 23(a) and (b); Figures 24(a) and (b)];

3) Microinvasive cancer is characterized by local disappearance of the basement membrane and leads to further changes of optical properties of the epithelium and stroma; as a result, OCT images of microinvasive cancer appear weakly structured [Figures 22(c) and (d); Figures 23(c) and (d); Figures 24(c) and (d)];

4) Invasive cancer is an extreme stage of malignization; it is visualized by OCT as a bright homogeneous pattern. The effective imaging depth in this case is sufficiently smaller (Figure 25, Figure 26, and Figure 27).

17.5.3 OCT Diagnostic Value

To evaluate the efficiency of the OCT method for detection of different stages of malignization, three independent blind tests were performed using OCT images of the uterine cervix, urinary bladder and larynx. The studies showed that OCT is highly efficient for diagnosing of mucosal neoplasia of the uterine cervix, urinary bladder and larynx: OCT sensitivity was 82, 98, 77%, respectively, specificity – 78, 71, 96%, diagnostic accuracy – 81, 85, 87% with significantly good agreement index of clinicians kappa – 0.65, 0.79, 0.83 (confidence intervals: 0.57-0.73; 0.71-0.88; 0.74-0.91). Error in detection of high grade dysplasia and microinvasive cancer was 21.4% in average.

17.5.4 Clinical Indications for OCT

OCT can provide information on the internal structure of biological tissues in real time with high resolution noninvasively. These capabilities of OCT can be used to improve current diagnostic methods. First of all, this would benefit oncology where exact knowledge of morphological alterations is essential for choosing treatment strategy.

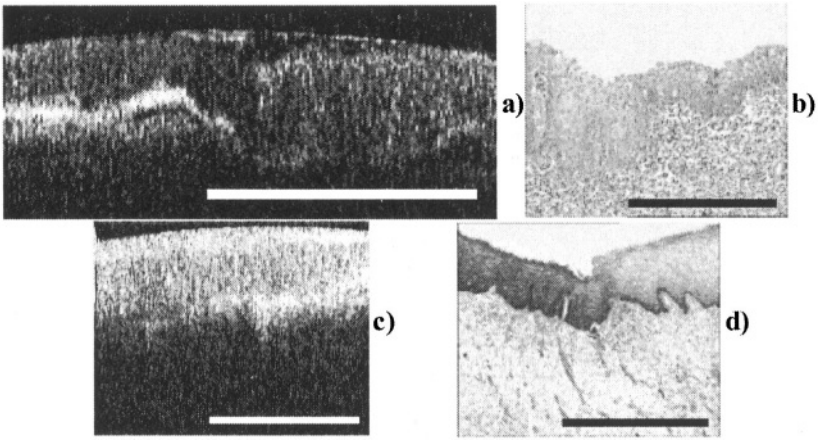

Figure 28. OCT images (a, c) and parallel histology (b, d) of carcinoma of larynx (a,b); benign mucosae (to the left), high grade dysplasia (to the right). Uterine cervix (c,d); benign mucosae (to the right), high grade dysplasia (to the left).

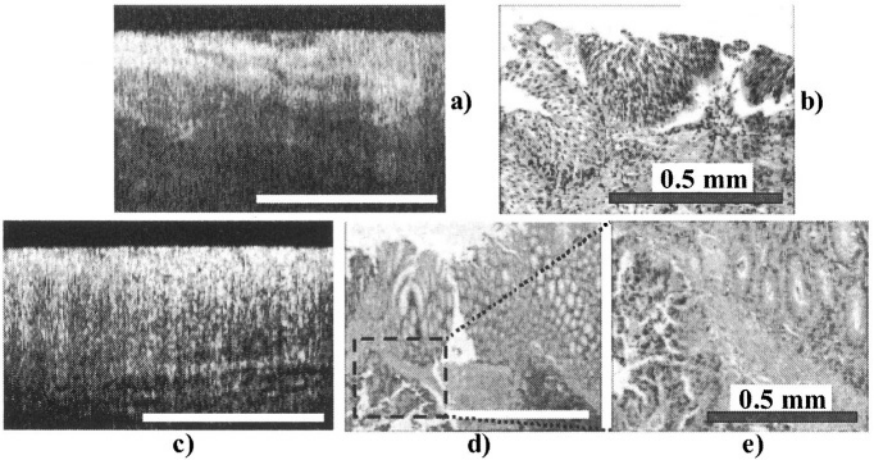

Figure 29. OCT images (a,c) and parallel histology (b,d) urinary bladder (a,b, to the left – benign mucosae, to the right – high grade dysplasia) and rectum (c,d,e, to the right–benign mucosae, to the left – invasive carcinoma).

Nonaltered tissues with different internal structure have specific optical patterns determined by certain features of their structure. Loss of tissue specificity accompanying neoplastic changes makes tissues look similar without any architectural and optically structure. Figure 28 and Figure 29 present tomograms and histological sections of patients with carcinoma of the larynx, uterine cervix, urinary bladder and rectum. Results of histology

show the presence of a distinct border between malignant tumor and benign mucosa [Figures 28(b) and (d); Figures 29(b), (d), and (e)]. The transition from a structureless optical pattern with high backscattering from subsurface layers typical of malignant tumors into a structured optical pattern with a clearly detectable, layered organization is clearly seen in the OCT images [Figures 28(a) and (c); Figures 29(a) and (c)]. Therefore, OCT is capable not only to detect tissue regions suspicious for neoplasia but also to accurately and reliable determine their borders.

This fact is very important clinically. First, OCT data may be critical for choosing a tissue site for excisional biopsy when conventional methods are inadequate. For instance, biopsy sampling from the areas of the uterine cervix suspicions for cancer is routinely guided colposcopy. So-called abnormal colposcopic findings are indicative of malignization. However, these abnormal colposcopic findings are not pathognomic signs of malignant growth and can be found in benign lesions as well [40]. In our opinion, additional information on the tissue structure provided by OCT can improve the specificity of colposcopy and optimize target biopsy of uterine cervix pathology. In laryngology OCT imaging proves to as helpful as in gynecology. Currently, even when the state-of-the-art microlaryngoscopy is used, from 7% to 20% of patients need to come back to have biopsy repeated in order to confirm the laryngeal carcinoma diagnosis [41, 42]. This may cause serious complications, especially for such a vulnerable organ as the larynx.

Second, the capability of OCT to detect tumor borders and their linear dimensions can be employed for staging of the malignant process in clinical situations for which the linear extent of tumor is essential.

Third, information provided by OCT can be used to plan a resection line in the course of organ-preserving operations and to control adequacy of resection. The main requirements for successful organ-preserving surgeries are adequacy of resection of a pathological region and minimal damage of healthy surrounding tissues. Necessity for such surgeries is dictated by the need to preserve the organ function. For example, at the initial stage of uterine bladder cancer, it is still possible to perform transurethral resection (TUR), when the organ is totally preserved, or partial resection followed by plastic surgery of the bladder, the latter is feasible only if the sphincter is preserved. According to existing rules, the resection line should be 2 cm away from the visual tumor border at TUR and not less than 3 cm from the urinary bladder cervix at partial resection. Such stringent requirements limit the number of patients in whom the organ-preserving surgery can be performed. However, notwithstanding such a strict approach, the recurrence rate for partial resection is as high as 40 – 80 % [43]. The same situation takes place with rectal tumors where the recurrence rate attains 78 %. It was

shown that the high recurrence rate is caused by deficient resection of tumors [44]. Reported data proves that existing methods for monitoring of organ-preserving operations in most of the cases are inadequate. The OCT technology can definitely be helpful and aid conventional method in solving this problem. The method provides high spatial resolution images in real-time, thus, allowing using OCT intraoperatively. OCT is noninvasive (no tissue damage, no side effects), therefore, one can perform monitoring of surgeries. Compatibility of OCT probes with working channels of standard endoscopes permits applying OCT endoscopically.

Fourth, since information on the tissue structure is obtained *in vivo,* OCT imaging can be used during both surgery and conservative treatment to monitor whether reparative processes are timely and adequate, and to detect early recurrence during follow-up.

17.5.5 Development of Clinical Procedures for OCT

At the present stage of its development, OCT has a number of disadvantages and limitations. Most prominent of them are the following. First, spatial resolution of 15-20-μm is sufficient to identify cellular layers but too low to visualize single cells. Consequently, in situations where detection of changes occurring at the cellular level is critical, OCT cannot provide adequate specificity. Second, the informative imaging depth of OCT is limited to 2 mm, which is a serious limitation especially for oncology where estimation of the depth of tumor invasion into underlying tissue is of high importance.

These disadvantages and limitations are rather technical. At the same time, the diagnostic value of OCT can also be decreased by drawbacks of the imaging procedure, which affect the quality of images, namely, lower brightness and contrast and introduce movement artifacts, etc. On the one hand, these factors to some extent impede extensive application of OCT in clinical practice, but on the other hand, it is a strong reason for further improvement of the OCT technology.

There are several ways of improving OCT imaging which can be grouped as follows:

development of OCT procedures taking into account both specific features of objects being studied and particular clinical tasks;

modification of standard OCT;

additional processing of OCT images

17.5.5.1 Effects of Biotissue Compression

One of the most important practical problems in the development of OCT technology is creation of OCT procedures taking into account both clinical

tasks and specific features of objects being studied. One of requirements for obtaining of high-quality images is the absence of movement artifacts. For this, an OCT probe must be fixed relative to the object. The latter can be eliminated by keeping the OCT probe still and by slightly pressing it against the tissue region being studied. However, soft biological tissues are very elastic and, consequently, even slight pressure leads to compression of the object, which affects measured OCT information. Figure 29 shows *ex vivo* tomograms of the sigmoid colon clearly demonstrating that OCT images depend on the degree of object's compression. As pressure increases, the contrast between layers improves, which is most likely caused by the induced increase in the tissue density. Moreover, at the maximum compression [Figure 30(c)] all layers of the intestinal wall were visible in the OCT image. The thickness of the wall surely exceeds 2 mm, therefore, compression technically allowed to image tissue layers below the effective OCT imaging depth.

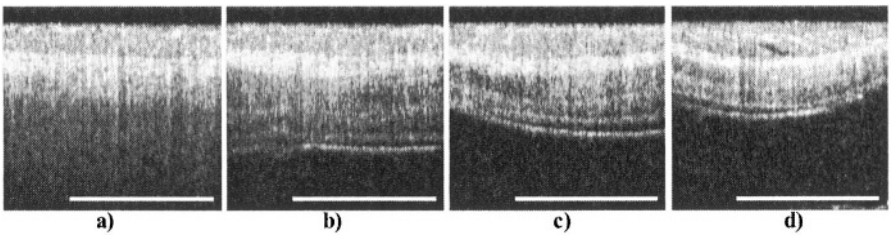

Figure 30. Ex vivo OCT images of sigmoid colon, demonstrating the dependence of image character on the degree of compression of the object (a,b,c,d).

17.5.5.2 Effects of Chemical Agents

One of the approaches to improve OCT penetration depth is based on biological tissue clearing using biocompatible chemical agents [45, 46]. Hyperosmolar chemical agents such as glycerol, propylene glycol, and concentrated glucose solutions reduce the refractive index mismatch on the air-tissue boundary and upon penetration into tissue also facilitate matching of refractive indices of tissue constituents which leads to a decrease in scattering of tissue components. For instance, refractive indices of glycerol (1.47) and propylene glycol (1.43) are slightly different that of the skin (1.47) [45, 46]. Application of these agents allows to increase the effective depth of OCT imaging and to improve image contrast. The effect of clearing is shown in Figure 31. The OCT image of skin with psoriatic erythrodermia acquired in 60 min after application of glycerol [Figure 31(b)] differs from the initial image [Figure 31(a)] in greater penetration depth and better contrast. These image improvements facilitate identifying of important

morphological phenomenon of acanthosis [Figure 31(c)]. It is known that tissue clearing depends on time and the type of tissue. Development of a clinical procedure for various pathological processes and types of biological tissue requires accurate choice of chemical agents and optimal exposure times.

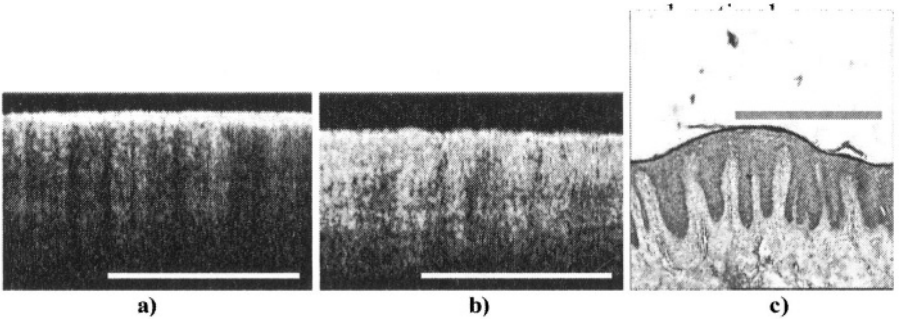

Figure 31. OCT images of skin with psoriatic erythrodermia a) before application of glycerin b) 60 min after application of glycerin c) parallel histology.

17.5.5.3 Cross-Polarization OCT

The specificity of standard OCT can be improved by studying collected light reflected back from a biological object with respect to polarization. In many pathologies severe structural alterations are preceded by biochemical and initial mild morphological changes. It is known that several structural components of biological tissue, e.g., stromal collagen fibers constituting the basis of healthy mucosa, can strongly scatter and also depolarize incident radiation [47]. Both these phenomena can lead to the appearance of the cross-polarized component in backscattered light. Pathological processes of different origin are characterized by various spatial organization and density of collagen fibers that would affect the OCT signal intensity detected in orthogonal polarization. Therefore, analysis of cross-polarization backscattering properties of biological objects may provide a new way for diagnosis of different pathological processes.

OCT images in initial and orthogonal polarizations were acquired *ex vivo* on the resected esophagus (no later than 60 min after extirpation) and *in vivo* during esophagoscopy. It should be noted that when the system was readjusted to measure images in the different polarizations while probe was kept still for 30 s. OCT and cross-polarization (CP) OCT images were verified by comparing with results of parallel analysis of biopsy H&E and Van Gieson stained samples. The Van Gieson staining is specific for collagen fibers of connective tissue [48].

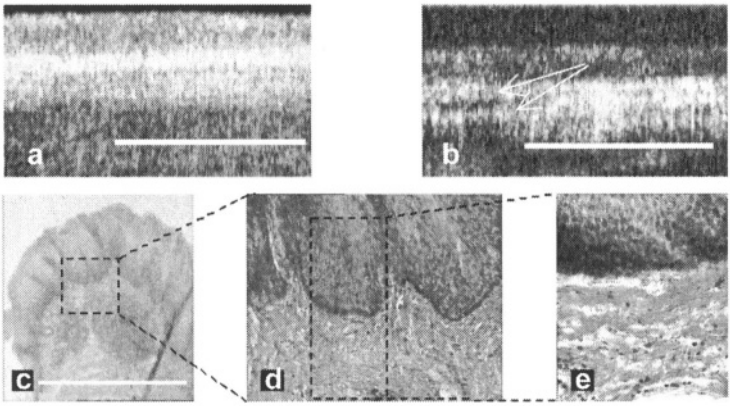

Figure 32. a) Standard OCT image, b) CP OCT image c) H&E histology d), e) Van Gieson histology at different magnification of health esophagus. White bar corresponds to 1 mm.

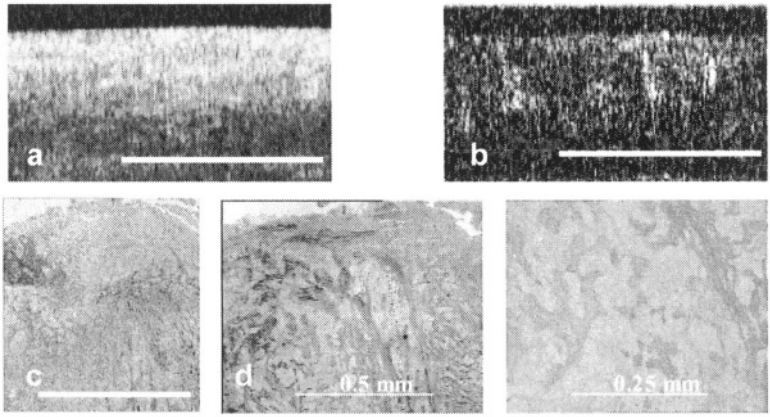

Figure 33. a) Standard OCT image, b) CP OCT image c) H&E histology d), e) Van Gieson histology at different magnification of cancerous esophagus. White bar corresponds to 1 mm where not specially marked.

The results of the OCT study of the healthy esophagus are presented in Figure 32. Tomograms of unaltered esophageal mucosa obtained in both polarizations have a layered horizontally organized pattern. In the initial polarization [Figure 32(a)] the epithelium appears as a moderately scattering layer with a distinct boundary atop the bright underlying stroma characterized by higher backscattering. In the orthogonal polarization [Figure 32(b)] the epithelium conversely appears as a very poorly scattering layer. The main fibrous component of the stroma is collagen fibers [red staining in Figures 32(d) and (e)], which are responsible for efficient depolarization and birefringence of the tissue [47, 49]. Depolarizing collagen

fibers explain presence of an intense signal in the CP OCT images; horizontally oriented stripes on the OCT images may be explained by birefringence nature of collagen. These structures correlate well with collagen fiber bundles [Figure 32(e)]. The transversal size of these collagen bundles shown in Figure 32(e) and of the striped structures in Figure 32(b) is approximately 70-80 μm.

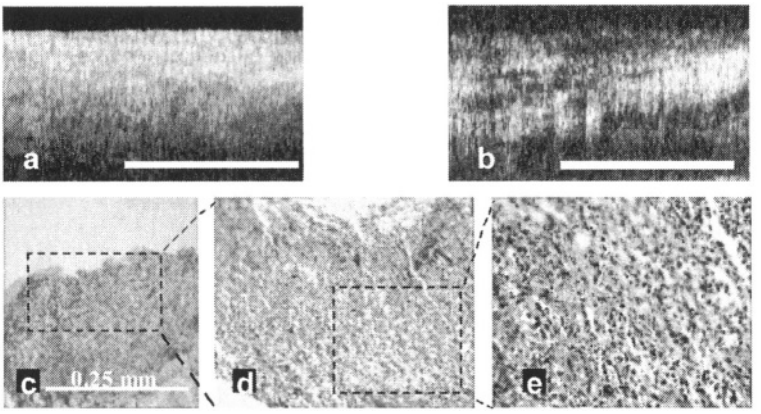

Figure 34. a) Standard OCT image, b) CP OCT image c) H&E histology d), e) Van Gieson histology at different magnification of scar esophagus. White bar corresponds to 1 mm where not specially marked.

OCT and CP OCT images of carcinoma and scar tissue of the esophagus are shown in Figure 33 and Figure 34, respectively. Standard OCT images of carcinoma and scar tissue [Figure 33(a) and Figure 34(a)] are barely distinguishable; both images are structureless. Therefore, it is very difficult to differentiate neoplastic and scar changes using standard OCT. Meanwhile, CP OCT images of these pathologies [Figure 33(b) and Figure 34(b)] are considerably different. Cancer cells almost do not change polarization of the probing light and the signal level on the average is substantially (about 10dB) lower than that of CP OCT images of healthy tissue. In the CP OCT images vertically-oriented regions of a stronger signal are visible against the weak background [Figure 32(b)]. These images correlate well with single vertically-oriented collagen fibers shown in Figure 32(d), where they are visualized as red elongated individual structures. CP OCT images of scar tissue of the esophagus demonstrate levels of the signal comparable to those of healthy tissue [Figure 33(b)]. At the same time, in the CP OCT image one can note a large number of chaotically oriented regions of both intense and weak signal. This is due to the nature of scar tissue whose organization is different than that of cancer. As is can be seen from Figure 34(d) collagen fibers are one of the main components of immature scar tissue (pink regions

in the image correspond to maturing collagen). In Figure 34(d) the collagen regions are alternating with regions of accumulation of cells forming granular tissue, which correlates well with the signal behavior in the CP OCT image of scar. The difference in structural features of collagen fibers in cancer and scar tissue provide the basis for differentiation of these pathologies because their cross-polarization backscattering properties are determined, in a considerable degree, by anisotropic structures, i.e., by collagen fibers.

Presented results demonstrate that CP OCT providing additional information on cross-polarization backscattering properties of biological tissues, thereby can improve the diagnostic value of standard OCT.

17.5.6 OCT Image Processing

Numerous experiments carried out independently by different research groups proved that the method of OCT was sufficiently sensitive to detect abnormality of biological tissue at the level of cell groups and tissue layers [6, 34]. Generally, only visual analysis of OCT images is performed in order to detect the type of pathology. The transformations of biological tissue, such as the alternation of the number of tissue layers or the emergence of contrast inclusions in OCT images can be revealed visually [22, 34]. However, some pathological processes develop without disruption of the layered structure of tissue, but proceed inducing changes in scattering properties. In some cases in spite of a tremendous change in optical characteristics of tissue layers pathological processes can hardly be detected by visual analysis [50]. Nevertheless, it was observed that additional numerical processing of OCT images facilitated detection of such processes [29,51].

In this chapter we propose an OCT image processing algorithm based on the theoretical model of the OCT signal versus depth [11]. Biological tissue is considered to be a stratified scattering medium described by a set of parameters specified for each layer, namely, total scattering coefficient and backscattering coefficient. These parameters are varied in order to fit the measured OCT curve with a theoretical OCT signal. The best-fit values are assumed to be true biological tissue properties.

17.5.6.1 Theoretical Model of the OCT Signal

The major requirements for an OCT theoretical model are the following: 1) it should be universal and valid for different types of biological tissue (healthy tissue and different stages of various pathologies), 2) it should be based on an adequate model of scattering properties of tissue and take into account the characteristics of a probing light beam, 3) it should use as few

parameters to describe the medium as possible, 4) the analytical expressions for the signal should be simple in order to decrease computational time of fitting. The last requirement is necessary if one wants to include numerical processing of OCT images as a part of a real-time medicine procedure.

As far as optical scattering is concerned, biological tissue contains variety of scatterers with sizes smaller, comparable and larger than the wavelength and in a general scatterer size distribution is given by a complicated function [52]. Majority of soft biological tissues is characterized by strong forward scattering. Correct description of light propagation within tissue should take into account the effects of multiple small-angle scattering, which start contributing significantly for depth larger than one mean free path. In contrast to previous publications [6, 51, 53] where OCT signal attenuation with the probing depth is described using only total and diffusion scattering, we do not neglect the changes in the beam structure caused by small-angle scattering at small depths and by light diffusion at large depths. This problem is solved based on the stationary radiance-transfer equation in small-angle approximation. Since light is scattered mainly in a forward direction, then, the probability of backscattering is a small parameter and it is reasonable to use single backscattering approximation to calculate the OCT signal. According to this approximation, the scattering phase function can then be presented as a sum of a small-angle scattering phase function $x_1(z,\theta)$ that tends to zero for $\theta > \pi/2$, and a constant that corresponds to isotropic scattering [11]:

$$x(z,\theta) = (1-2p_b(z))x_1(z,\theta) + 2p_b(z). \tag{30}$$

Backscattering probability, p_b, is determined by the part of the light energy scattered into the backward semisphere:

$$p_b(z) = \frac{1}{2}\int_{\pi/2}^{\pi} x(z,\theta)\sin\theta d\theta. \tag{31}$$

As a result, the expression for the OCT signal was derived in a simple single-integral form [11]. Thereby, the developed theoretical model appeared to take tissue properties into account adequately and, at the same time, it is not too time consuming and computationally demanding in comparison with Monte-Carlo modeling [6, 54].

The theoretical OCT signal formed by single backscattered photons is given by average intensity $I_{th}(z)$ versus depth z. The signal undergoes squared detection, and is normalized on its value at the tissue boundary [11, 51]

$$I_{th}(z)/I_{th}(0)=2A^2(0)\frac{\mu_{bs}(z)}{\mu_{bs}(0)}\exp\left(-2\int_0^z\mu_s(z')dz'\right)\times$$
$$\times\left[\int_0^\infty\exp\left(-\frac{A^2(z)h^2}{2}+2\int_0^z\mu_{fs}(z-z')\tilde{x}_1(z',hz')dz'\right)hdh-\frac{1}{2A^2(z)}\right], \quad (32)$$

where $\mu_s(z)$ is the total scattering coefficient; $\mu_{bs}(z)=\mu_s(z)p_b(z)$ - backscattering coefficient; $\mu_{fs}=\mu_s-2\mu_{bs}$ - forward scattering coefficient; $\tilde{x}_1(z,p)=\frac{1}{2}\int_0^\pi x_1(z,\theta)J_0(p\theta)\sin\theta\,d\theta$ - spectrum of the small-angle scattering phase-function $x_1(z,\theta)$, which was defined by equation 30; $A^2(z)=A_0^2+(z-f)^2\lambda^2/(2\pi nA_0)^2$ - radius of a Gaussian probing beam with focusing depth f minimum beam waist A_0 and wavenumber $k=2\pi n/\lambda$ in a non-scattering medium with a refractive index n. Along with the initial beam shape and the attenuation of the OCT signal due to total scattering on the way to the reflection side and back, the equation 32 accounts for the effects of multiple small-angle scattering, expressed by the convolution integral $\int_0^z\mu_{fs}(z-z')\tilde{x}_1(z',hz')dz'$.

17.5.6.2 Biological Tissue Scattering Properties

Equation 32 contains the following scattering characteristics of a stratified scattering medium: distributions of a total scattering coefficient $\mu_s(z)$, a backscattering coefficient $\mu_{bs}(z)$ and a small-angle phase function $x_1(z,\theta)$. Generally the inverse problem of reconstructing these distributions from an OCT image does not have a unique solution. Nevertheless, in the case when the phase function is described by a few parameters and tissue consists of a limited number of homogeneous layers the solution is unique and can be found numerically. The numerical algorithm implemented the Henyey-Greenstein phase-function [8]. This function is characterized by a single parameter, the anisotropy factor, and represents well experimental scattering for a wide range of tissue types. The anisotropy factor for each *i*-th biotissue layer can be expressed via total scattering coefficient $\mu_{s,i}$ and a backscattering one $\mu_{bs,i}$, therefore each layer is described by two parameters, $\mu_{s,i}$ and $\mu_{bs,i}$.

17.5.6.3 Algorithm for Reconstruction of Tissue Scattering Properties

In the current algorithm, the total scattering coefficient of *i-th* tissue layer $\mu_{s,i}$, its backscattering coefficient $\mu_{bs,i}$ and the position of the layer boundary

l_i are recovered via fitting of the experimental OCT signal versus depth $I_{ex}(z)$ by the theoretical curve $I_{th}\left(z, \vec{\mu}_s, \vec{\mu}_{bs}, \vec{l}\right)$; $\vec{\mu}_s = \left(\mu_{s,1},..., \mu_{s,N}\right)$, $\vec{\mu}_{bs} = \left(\mu_{bs,1},..., \mu_{bs,N}\right)$, $\vec{l} = \left(l_1,..., l_N\right)$, where N is the total number of tissue layers. A mean-square deviation of the logarithms of the experimental and fitting theoretical curves yields the discrepancy for the varying set of tissue parameters. In this case, the "true" medium parameters are obtained as a result of minimizing the integral within the given range of values

$$\left(\vec{\mu}_s, \vec{\mu}_{bs}, \vec{l}\right) = \arg \min_{\left(\vec{\mu}_s, \vec{\mu}_{bs}, \vec{l}\right)} \int_0^L \log^2\left(I_{th}\left(z, \vec{\mu}_s, \vec{\mu}_{bs}, \vec{l}\right) / I_{ex}(z)\right) dz, \qquad (33)$$

where L is the maximum depth of the OCT signal. Finding the global minimum of equation 33 with I_{th} defined in equation 32, is time consuming and computationally intensive. We applied the genetic algorithm [55] to minimize integral (equation 33), which allowed reducing time essentially in comparison with conventional methods.

Figure 35 shows an example of fitting an experimental OCT signal with a theoretical curve in the case of a relatively homogeneous tissue. Before the fitting procedure is applied a certain region of the tomogram, where the parameters of the medium are to be estimated, is selected. Within this window, the in-depth OCT profiles are added together in order to reduce the noise level and yield an average OCT signal, which is used for fitting. Both the noise dispersion in the experimental curve I_{ex} and the covariance of the recovered tissue parameters decrease as the width of the window is increased. Let us consider an example of the window composed of 20 adjacent OCT scans spaced with a 10 μm lateral step [Figure 35(a)]. Reconstruction of tissue parameters using the theoretical model described in equation 32 takes about 1 minute for each OCT experimental curve.

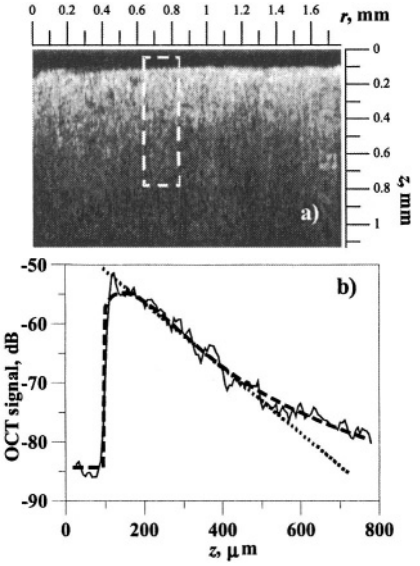

Figure 35. An example of fitting of an OCT signal from single layered tissue; (a) a typical *in vivo* OCT image of cervical cancer; (b) an OCT signal averaged out over the selected window (solid line), a theoretical fitting curve (dashed line); Beer's law approximation of the fast attenuating part of the experimental curve (dotted line). Recovered tissue parameters are: μ_s = 223 1/cm, μ_{bs} = 1.3 1/cm.

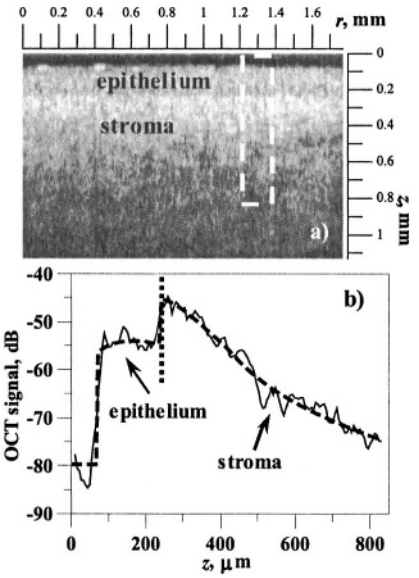

Figure 36. An example of fitting of an OCT signal from two-layered tissue; (a) a typical *in vivo* OCT image of healthy cervical mucosa; (b) an OCT signal averaged out over the selected window (dashed line), a theoretical fitting curve (thick line). Recovered parameters are: *(epithelium)* μ_s = 75 1/cm, μ_{bs} = 0.28 1/cm; (*stroma*) μ_s = 284 1/cm, μ_{bs} = 3.3 1/cm.

It is clearly seen in the Figure 35 that the theoretical dependence describes well the main features of the experimental OCT signal. According to the theoretical model, the fast decrease of the OCT signal at small depth is mainly caused by attenuation of the probing light beam due to small-angle scattering. This "fast" attenuation obeys the Beer's law (the dotted line in the figure), and the slope of the curve corresponds to the doubled coefficient of small-angle scattering $2\mu_{fs} = 2(\mu_s - 2\mu_{bs})$. At larger depth, the regular beam structure collapses due to diffusion and backscattering, which, in fact, is weaker than small-angle scattering, and the rate of OCT signal attenuation slows down. Both regions of fast and slow attenuation are observed in the experimental OCT images obtained from homogeneous tissue [Figure 35(b)].

Figure 36 demonstrates an example of fitting of the experimental OCT signal and recovering scattering parameters of the two-layered tissue

(epithelium and *stroma).* The jump in the OCT signal at the depth of 250 microns is caused by the mismatch of backscatering coefficients between the first layer *(epithelium)* and the second layer *(stroma).*

17.5.6.4 Algorithm Testing

To test the performance of the algorithm an experimental OCT setup with the following technical characteristics was used: wavelength of 1.3 μm, the same axial and transversal resolution of 15 μm, scanning depth of 1-2 mm, acquisition time for a 2-D image of 1.5 second.

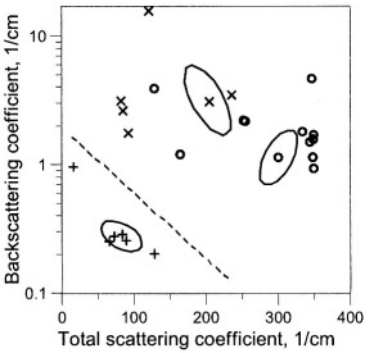

Figure 37. Result of processing of OCT images obtained from a patient with cervical cancer (one clinical example). Both healthy and neoplastic areas of tissue were included in analysis. Points on the plane correspond to recovered scattering parameters for the epithelium and the stroma in the case of healthy mucosa and one parameter in the case of cancer. Scattering parameters of healthy areas: + - *epithelium* and ×– *stroma*; parameters of cervical cancer: O. Ellipses are the confidence areas of the estimated parameters. The dashed line separates scattering parameters corresponding to the healthy epithelium and cancer.

The OCT images of healthy and neoplastic areas in a patient with cervical cancer were obtained *in vivo* using a flexible probe with diameter of 2.5 mm. The results of reconstruction of scattering parameters are given in Figure 37. Each layer of each processed tomogram is characterized by a point at the scattering parameter plane. In the reconstruction algorithm, the two-layered model of the OCT signal is used for OCT images of healthy areas *(epithelium* and *stroma)* and one-layered model for neoplastic areas. Results of processing of the obtained data show that the estimated values of the total scattering coefficient are in a good agreement with the reported data for these types of tissue [8]. For all processed images recovered scattering parameters of healthy epithelium and neoplastic tissue are localized in two separate non-overlapping regions on the scattering parameter plane. The boundary between these regions is marked with the dashed line (Figure 37). We believe that during progression of a neoplastic process the scattering parameters

of the epithelium gradually increase from low values of total and backscattering coefficients to higher values, thus, crossing the boundary between domains of scattering parameters. This fact can provide a basis for identification of the abnormal changes in tissue structure.

17.6 DISCUSSION AND FUTURE DIRECTIONS

The described algorithm can aid visual analysis of OCT images by providing an additional tool for quantitative assessment of biological tissue optical properties and, thus, improving capabilities of OCT in identification of pathological processes. Since a one-dimensional model of the OCT signal is employed in the algorithm, the processed region of a tomogram is to be stratified. The speckle noise of the average OCT signal and the covariance of estimated parameters can be reduced significantly by choosing a wider region of an OCT image for averaging out. Tomograms of mucosa of the uterine cervix, larynx, esophagus, etc. are the most appropriate for such processing, because the architecture of these types of biological tissue is close to plane stratified. Reliable differentiation of pathologies using reconstructed scattering parameters can be attained only when the confidence areas of these parameters do not overlap (see the confidence areas marked with ellipses in Figure 37). As it can be seen from Figure 37, the dispersion of the estimated parameters is determined not only by speckle noise but also by patient-to-patent variations of optical properties within the same state of tissue. This problem has not been enough studied yet, and this will be addressed in future investigations. The increase of dispersion can also be caused by the imperfection of the theoretical model applied in the algorithm. For example, the scattering phase function needs to be studied more carefully for different states of tissue. Additional parameters may be required in scattering phase function to provide more adequate description for light scattering in tissue. These characteristics can be then included in the fitting procedure using equation 33 together with the total scattering coefficient and backscattering coefficient. On the other hand, additional fitting parameters would increase computational time and make interpretation of the obtained results more difficult. The theoretical model of the OCT signal is based on some approximations described above, which also need to be verified. Moreover, the radiative transfer theory does not take into account wave phenomena such as interference of light fields.

In summary, an improved phase function to describe tissue scattering and an advanced model for an OCT signal are needed and will be developed in future.

ACKNOWLEDGEMENTS

The authors are grateful to Yakov Khanin and Irina Andronova for valuable scientific discussions and advises, Alexander Turkin, Yuri Potapov, Andrey Morozov, Pavel Morozov and Marina Kucheva for assistance in creating optical elements and radioelectronics; medical stuff of Nizhny Novgorod Regional Hospital and Nizhny Novgorod Regional Oncological Clinic for assistance in clinical research, Nadezhda Krivatkina and Lidia Kozina for providing translation and Marina Chernobrovtzeva for editing. This work was partly supported by the Russian Foundation for Basic Research under the grants #01-02-17721, #03-02-17253 and by the Civilian Research & Development Foundation under the grants RB2-2389-NN-02 and RB2-542.

REFERENCES

1. *Radar Handbook,* M. I. Skolnik ed. (Mc Craw-Hill Book Company, NY, 1970).
2. *Principles of Underwater Soundfor Engineers,* 2nd ed, R. J. Urick ed. (McGraw - Hill Book Company, NY, 1975).
3. D. Huang, E.A. Swanson, C.P. Lin, J.S. Schuman, W.G. Stinson, W. Chang, M.R. Hee, T. Flotte, K. Gregory, C.A. Puliafito, and J.G. Fujimoto, "Optical coherence tomography," *Science* **254,** 1178-1181 (1991).
4. V.M. Gelikonov, G.V. Gelikonov, R.V. Kuranov, K.I. Pravdenko, A.M. Sergeev, F.I. Feldchtein, Ya.I. Khanin, D.V. Shabanov, N.D. Gladkova, N.K. Nikulin, G.A. Petrova, and V.V. Pochinko, "Coherent optical tomography of microscopic inhomogeneties in biological tissues," *JETP Lett.* **61**, 158-162 (1995).
5. A.F. Fercher, "Optical coherence tomography," *J. Biomed. Opt.* **1** (2), 157-173 (1996).
6. J.M. Schmitt, "Optical coherence tomography (OCT): A review," *IEEE J. Select. Tops Quant. Electr.* **5** (4), 1205-1215 (1999).
7. J.G. Fujimoto, W. Drexler, U. Morgner, F. Kartner, and E. Ippen, "Optical coherence tomography: high resolution imaging using echoes of light," *Optics & Photonics News* January, 24–31 (2000).
8. V.V. Tuchin, *Tissue Optics: Light Scattering Methods and Instruments for Medical Diagnosis* (SPIE Press, Bellingham, 2000).
9. A.M.Sergeev, L.S. Dolin, and D.H. Reitze, "Optical tomography of biotissues: past, present, and future," *Optics & Photonics News* July, 28-35 (2001).
10. *Handbook of Optical Coherence Tomography,* B.E. Bouma and G.J. Tearney eds. (Marcel Dekker, NY, 2002).
11. L.S. Dolin, "A theory of optical coherence tomography," *Radiophys. Quant. Electr.* **41** (10), 850-873 (1998).
12. Yu.A. Kravtsov and A.I. Saichev, "Effects of double transition of waves in random-inhomogeneous media," *Uspekhi Fizicheskikh Nauk* **137**, 501-527 (1982).
13. A. Ishimaru, *Wave Propagation and Scattering in Random Media* (Academic, NY, 1978).
14. L.S. Dolin and I.M. Levin, "Optics underwater," in *Encyclopedia of Applied Physics* **12**,571-601 (1995).

15. J.W. McLean, J.D. Freeman, and R.E. Walker, "Beam spread function with time dispersion,"*Appl. Opt.* **37** (21), 4701-4711(1998).
16. I.A. Andronova, D.D. Gusovskii, V. M. Gelikonov, V.I. Leonov, Y.A. Mamaev, A.A. Turkin, and A.S. Yakhnov, "Fluctuation characteristics of an all-fiber Sagnac interferometer at a wavelength of 0.85 mcm," *Sov. Phys. Tech. Phys.* **35,** 270-272 (1990).
17. I.A. Andronova, V.M. Gelikonov, Y.A. Mamaev, and A.A. Turkin, "Performance of a Sagnac fiber interferometer as a phasemeter," *Radiophys. Quant. Electr.* **34**, 346-50 (1991).
18. V.M. Gelikonov, R.V. Kuranov, and A.N. Morozov, "Time correlation analysis of the propagation of low-coherence radiation in an optical channel with imperfections anisotropy," *Quant. Electr.* **32**, 59-65 (2002).
19. V.M. Gelikonov, M.N. Kucheva, and G.B. Malykin, "Measurement of optical fiber birefringence with a wide-band radiation source," *Radiophys. Quant. Electr.* **34**, 598-599(1991).
20. V.M. Gelikonov, D.D. Gusovskii, V.I. Leonov, and M.A. Novikov, "Birefringence compensation in single-mode optical fibers," *Sov. Tech. Phys. Lett.* **13**, 322-223 (1987).
21. V.M. Gelikonov, V.I. Leonov, and M.A. Novikov, "Optical anisotropy induced in a round trip through single-mode optical waveguides and methods for suppression of this anisotropy,' *Sov. J. Quant. Electr.* **19,** 1227-1230 (1989).
22. F.I. Feldchtein, G.V. Gelikonov, V.M. Gelikonov, R.R. Iksanov, R.V. Kuranov, A.M. Sergeev, N.D. Gladkova, M.N. Ourutina, J.A. Warren, Jr., and D.H. Reitze, "*In vivo* OCT imaging of hard and soft tissue of the oral cavity," *Opt. Express* **3**, 239-250 (1998).
23. R.V. Kuranov, V.V. Sapozhnikova, I.V. Turchin, E.V. Zagainova, V.M. Gelikonov, V.A. Kamensky, L.B. Snopova, and N.N. Prodanetz, "Complementary use of cross-polarization and standard OCT for differential diagnosis of pathological tissues," *Opt. Express* **10,** 707-713 (2002).
24. S.N. Roper, M.D. Moores, G.V. Gelikonov, F.I. Feldchtein, N.M. Beach, M.A. King, V.M. Gelikonov, A.M. Sergeev, and D.H. Reitze, *"In vivo* detection of experimentally induced cortical dysgenesis in the adult rat neocortex using optical coherence tomography," J. *Neurosci. Meth.* **80**, 91- 98 (1998).
25. V.M. Gelikonov, D.D. Gusovskii, Y.N. Konoplev, V.I. Leonov, Y.A. Mamaev, and A.A. Turkin, "Investigation of a fiber-optic polarizer with a metal film and a dielectric buffer layer," *Sov. J. Quant. Electr.* **20**, 76-78 (1990).
26. V.M. Gelikonov, Y.N. Konoplev, M.N. Kucheva, Y.A. Mamaev, and A.A. Turkin, "Effect of buffer layer on extinction coefficient of fiber-optic polarizer with metallic coating," *Opt. Spectrosc.* **71**, 397-398 (1991).
27. V.K. Batovrin, I.A. Garmash, V.M. Gelikonov, G.V. Gelikonov, A.V. Lyubarskii, A.G. Plyavenek, S.A. Safin, A.T. Semenov, V. R. Shidlovskii, M.V. Shramenko, and S.D. Yakubovich, "Superluminescent diodes based on single-quantum-well (GaA1)As heterostructures," *Quant. Electr.* **26**, 109-114 (1996).
28. V.M. Gelikonov, G.V. Gelikonov, N.D. Gladkova, V I. Leonov, F.I. Feldchtein, A.M. Sergeev, and Y.I. Khanin, "Optical fiber interferometer and piezoelectric modulator," USA, Patent #5835642 (1998).
29. N.M. Shakhova, V.M. Gelikonov, V.A. Kamensky, R.V. Kuranov, and I.V. Turchin, "Clinical aspects of the endoscopic optical coherence tomography and the ways for improving its diagnostic value," *Laser Phys.* **12**, 617-626 (2002).

30. M.E. Brezinski and J.G. Fujimoto, "Optical coherence tomography: high resolution imaging in nontransparent tissue," *IEEE J. Select. Tops Quant. Electr.* **5,** 1185-92 (1999).
31. C. Pitris, C. Jesser, S.A. Boppart, D. Stamper, M.E. Brezinski, and J.G. Fujimoto, "Feasibility of optical coherence tomography for high-resolution imaging of human gastrointestinal tract malignancies," *J. Gastroenterol.* **35,** 87-92 (2000).
32. N.D. Gladkova, G.A. Petrova, N.K. Nikulin, S.G. Radenska-Lopovok, L.B. Snopova, Yu.P. Chumakov, V.A. Nasonova, V.M. Gelikonov, G.V. Gelikonov, R.V. Kuranov, A.M. Sergeev, and F.I. Feldchtein, *"In vivo* optical coherence tomography imaging of human skin: norm and pathology," *Skin Res. Technol.* **6,** 6-16 (2000).
33. J.M. Schmitt and S.H. Xiang, "Cross-polarized backscatter in optical coherence tomography of biological tissue," *Opt. Lett.* **23,** 1060-1062 (1998).
34. A.M. Sergeev, V.M. Gelikonov, G.V. Gelikonov, F.I. Feldchtein, R.V. Kuranov, N.D. Gladkova, N.M. Shakhova, L.B. Snopova, A.V. Shakhov, I.A. Kuznetzova, A.N. Denisenko, V.V. Pochinko, Yu. P. Chumakov, and O.S. Streltzova, *"In vivo* endoscopic OCT imaging of precancer and cancer states of human mucosa," *Opt. Express* **1,** 432-440 (1997).
35. E.H. Hopman, P. Kenemans, and T.J. Helmerhorst, "Positive predictive rate of colposcopic examination of the cervix uteri: an overview of literature," *Obstet. Gynecol. Surv.* **53,** 97-106 (1998).
36. S. Jackie, N.D. Gladkova, F.I. Feldchtein, A.B. Terentieva, B. Brand, G.V. Gelikonov, V.M. Gelikonov, A.M. Sergeev, A. Fritscher-Ravens, J. Freund, U. Seitz, S. Schruder, and N. Soehendra, *"In vivo* endoscopic optical coherence tomography of the human gastrointestinal tract - toward optical biopsy," *Endoscopy* **32,** 743-749 (2000).
37. E.V. Zagainova, O.S. Strelzova, N.D. Gladkova, L.B. Snopova, G.V. Gelikonov, F.I. Feldchtein, and A.N. Morozov, *"In vivo* optical coherence tomography feasibility for bladder disease," *J. Urology* **167,** 1492-1497 (2002).
38. N.D. Gladkova, A.V. Shakhov, and F.I. Feldchtein, "Capabilities of optical coherence tomography in laryngology" in *Handbook of Optical Coherence Tomography,* B.E. Bouma and G.J. Tearney eds. (Marcel Dekker, NY, 2002), 705-724.
39. N.M. Shakhova, F.I. Feldchtein, and A.M. Sergeev, "Applications of optical coherence tomography in gynecology" in *Handbook of Optical Coherence Tomography,* B.E. Bouma and G. J. Tearney eds. (Marcel Dekker, NY, 2002), 649-672.
40. *Colposcopy, Cervical Pathology: Textbook and Atlas,* E. Burghardt, H. Pickel, and F. Girardi eds. (Thieme, NY, 1998).
41. *Head and Neck Tumors,* A.I. Panches ed. (De-Yure, Moscow, 1996)
42. A. Welge-Luessen, H. Glanz, C. Arens, P. Oberholzer, R. Probst, "Die mehrmalige Biopsie bei der Diagnosestellung von Kehlkopfkarzinomen," *Laryngo-Rhino-Otologie* **75,** 611-615, (1996).
43. N.P. Dandekar, H.B. Tongaonkar, A.V. Dalai, *et al,* "Partial cystectomy for invasive bladder cancer," *J. Surg. Oncol.* **60,** 24-29 (1995).
44. L. Blomqvist, "Rectal adenocarcinoma: assessment of tumor involvement of the lateral resection margin by MRI of resected specimen," *Brit. J. Radiol.* **72,** 18-23 (1999).
45. V.V. Tuchin, X. Xu, and R.K. Wang, "Dynamic optical coherence tomography in studies of optical clearing, sedimentation, and aggregation of immersed blood," *Appl. Opt.* **41,**258-271(2002).
46. R.K. Wang and J.B. Elder, "Propylene glycol as a contrasting agent for optical coherence tomography to image gastrointestinal tissues," *Lasers Surg. Med.* **30,** 201-208 (2002).

47. S. L. Jacques, J. R. Roman, and K. Lee, "Imaging superficial tissues with polarized light," *Lasers Sur. Med.* **26**, 119-129, (2000).
48. *Histopathologic Technique and Practical Histochemistry,* R.D. Lillie ed. (McGraw – Hill Book Com., New York-Toronto-Sydney-London, 1965), Chap. 15; http://www.ebsciences.com/staining/van_gies.htm.
49. D.J. Maitland and J.T. Walsh, "Quantitative measurements of linear birefringence during heating of native collagen," *Lasers Sur. Med.* **20**, 310-318 (1997).
50. G. Zuccaro, N.D. Gladkova, J. Vargo, F.I. Feldchtein, J. Dumot, E.V. Zagaynova, D. Conwell, G.W. Falk, J.R. Goldblum, J. Ponsky, G.V. Gelikonov, and J.E. Richter, "Optical coherence tomography (OCT) in the diagnosis of Barrett's esophagus (BE), high grade dysplasia (HGD), intramucosal adenocarcinoma (ImAC) and invasive adenocarcinoma (InvAC)," *Gastrointestinal Endoscopy* **53**, 330 (2001).
51. J.M. Schmitt and A. Knüttel, "Measurement of optical-properties of biological tissues by low-coherence reflectometry," *Appl. Opt.* **32**, 6032-6042 (1993).
52. J.M. Schmitt and G. Kumar, "Optical scattering properties of soft tissue: a discrete particle model," *Appl. Opt.* **37,** 2788-2797 (1998).
53. L. Thrane and H.T. Yura, "Analysis of optical coherence tomography systems based on the extended Huygens-Fresnel principle," *J. Opt. Soc. Am. A* **17,** 484-490 (2000).
54. G. Yao, L. Wang, "Monte Carlo simulation of an optical coherence tomography signal in homogeneous turbid media," *Phys. Med. Biol.* **44,** 2307-2320 (1999).
55. *Handbook of Genetic Algorithms,* L. Davis ed. (Van Nostrand Reinhoed, NY, 1991).

Chapter 18

POLARIZATION SENSITIVE OPTICAL COHERENCE TOMOGRAPHY

Phase Sensitive Interferometry for Multi-Functional Imaging

Johannes F. de Boer
Wellman Center of Photomedicine, Massachusetts General Hospital, Harvard Medical School, Boston, MA 02114 USA

Abstract: The principle of the determination of Stokes parameters in OCT by the coherent detection of interference fringes is explored. The implementation of a real time fiber based PS-OCT system, the associated behavior of polarization states in single mode fibers, and optimal polarization modulation schemes will be described. Processing of PS-OCT signals to extract polarization properties of tissue, such as birefringence, optical axis orientation, and diattenuation will be explained. In vivo determination of skin birefringence, and birefringence of the retinal nerve fiber layer for glaucoma detection will be demonstrated.

Keywords: Optical Coherence Tomography, imaging, elipsometry, polarimetry

18.1 INTRODUCTION

Optical Coherence Tomography (OCT) is an emerging technology for minimally invasive high resolution imaging (1-10 μm) of tissue in two- or three-dimensions up to a depth of 2-3 mm [1]. OCT images tissue reflectivity by measuring the spatially resolved backscattered intensity in turbid media. In contrast to ultrasound, the velocity of light prohibits time resolved measurement of the time delay of short temporal pulses backscattered from tissue. OCT measures the time delay by means of interferometry. OCT instrumentation uses a spectrally broadband light source and a two-beam interferometer (e.g., Michelson) with the reflector in one path (i.e., sample arm) replaced by a turbid medium. Depth ranging in the turbid medium is possible because interference fringes are observed only for light in sample and reference arms that has traveled equal optical path lengths to within the source coherence length. By scanning optical path length in the reference arm and amplitude detection of the interference fringes, a depth scan (A-scan) can be recorded that maps sample reflectivity.

Temporal coherence length of the source light determines axial resolution of a system, while numerical aperture of the focusing optics determines lateral resolution. The availability of sources with shorter coherence length over the past decade has increased the axial (depth) resolution of OCT from 15 μm to approximately 1 μm. Lateral scanning mechanisms allow two- and three-dimensional recording of images from consecutive A-scans. Although light is frequently treated as a scalar wave many applications require a description using transverse electro-magnetic waves. The transverse nature of light is distinguished from longitudinal waves (e.g., sound), by the extra degree of freedom, which is described by the polarization state of light. Polarization sensitive OCT (PS-OCT) uses the information encoded in the polarization state of the recorded interference fringe intensity to provide additional contrast in images of the sample under study. PS-OCT provides high resolution spatial information on the polarization state of light reflected from tissue that is not discernible using existing diagnostic optical methods. In this chapter a review will be presented of PS-OCT, the theory of calculation of the Stokes vectors, implementation of PS-OCT in fiber-based systems for clinical applications, and recent results in the field of dermatology and ophthalmology.

18.1.1 Optical Properties of Tissue that Influence Polarization

Scattering is the principle mechanism that modifies the polarization state of light propagating through biological tissue. The polarization state of light after a single scattering event depends on the scatterer, direction of scatter and incident polarization state. In many turbid media such as tissue, scattering structures have a large variance in size and are distributed/oriented in a complex and sometimes apparently random manner. Because each scattering event can modify the incident polarization state differently, the scrambling effect of single scattering events accumulates, until finally the polarization state is completely random (i.e. uncorrelated with the incident polarization state).

An important exception is when the media consists of organized linear structures, such as fibrous tissues that can exhibit form birefringence. Many biological tissues exhibit form birefringence, such as tendons, muscle, nerve, bone, cartilage and teeth. Form birefringence arises when the relative optical phase between orthogonal polarization components is non-zero for forward scattered light. After multiple forward scattering events, relative phase difference accumulates and a delay (δ) similar to that observed in birefringent crystalline materials (e.g., calcite) is introduced between orthogonal polarization components. For organized linear structures, the increase in phase delay may be characterized by a difference (Δn) in the

effective refractive index for light polarized along, and perpendicular to, the long axis of the linear structures. The phase retardation, δ, between orthogonal polarization components is proportional to the distance x traveled through the birefringent medium,

$$\delta = \frac{2\pi\Delta n x}{\lambda}. \tag{1}$$

The advantage in using PS-OCT is the enhanced contrast and specificity in identifying structures in OCT images by detecting induced changes in the polarization state of light reflected from the sample. Moreover, changes in birefringence may, for instance, indicate changes in functionality, structure, or viability of tissues.

18.2 THEORY

18.2.1 Historical Overview

Application of laser interferometry to characterize the polarization state of light reflected from optical components was reported by Hazebroek and Holscher in 1973 [2]. More recently, bright broadband light sources that emit in a single spatial mode have provided the basis for novel applications in testing of optical components and biomedical imaging. For example, Newson *et al.*[3] constructed a combined Mach-Zehnder/Michelson interferometer (configured in tandem) that used a low coherence semiconductor light source and polarization sensitive detection to measure temperature changes in a birefringent fiber. Kobayashi *et al.* [4] reported an early demonstration of a polarization-sensitive fiber Michelson interferometer using a low coherence light source for testing optical components.

The emphasis in Optical Coherence Tomography (OCT) has been on the reconstruction of two-dimensional maps of tissue reflectivity while neglecting the polarization state of light. In 1992, Hee *et al.*[5] reported an optical coherence ranging system able to measure the changes in the polarization state of light reflected from a sample. Using an incoherent detection technique, they demonstrated birefringence sensitive ranging in a wave plate, an electro-optic modulator, and calf coronary artery. In 1997, the first two-dimensional images of birefringence in bovine tendon were presented, and the effect of laser induced thermal damage on tissue birefringence was demonstrated,[6] followed in 1998 by a demonstration of the birefringence in porcine myocardium [7]. To date, polarization sensitive OCT measurements have attracted active interest from several research

groups. Potential biomedical applications that are being explored include determination of thermal injury for burn depth assessment[8] and retinal nerve fiber layer birefringence determination for early detection of glaucoma [9, 10]. For an overview of the earlier developments in PS-OCT and a discussion of the theory in the context of bulk optical interferometers we refer to de Boer and Milner [11].

18.2.2 Stokes Vector and Poincaré Sphere

The Stokes vector is composed of four elements, I, Q, U and V (sometimes denoted S_0, S_1, S_2 and S_3) and provides a complete description of the light polarization state. Historically, Stokes vectors were developed because they describe observable quantities of light. I, Q, U and V can be measured with a photodetector and linear and circular polarizers. Lets call I_t the total light irradiance incident on the detector, I_0^o, I_{90}^o, I_{+45}^o and I_{-45}^o the irradiances transmitted by a linear polarizer oriented at an angle of, respectively, 0°, 90°, +45° and -45° to the horizontal. Lets define also I_{rc} and I_{lc} as the irradiances transmitted by a circular polarizer opaque to, respectively, left and right circularly polarized light. Then, the Stokes parameters are defined by,

$$\begin{aligned} I &= I_t, \\ Q &= \left(I_{0^\circ} - I_{90^\circ}\right), \\ U &= \left(I_{+45^\circ} - I_{-45^\circ}\right), \\ V &= \left(I_{rc} - I_{lc}\right). \end{aligned} \tag{2}$$

After normalizing the Stokes parameters by the irradiance I, Q describes the amount of light polarized along the horizontal (Q=+1) or vertical (Q=-1) axes, U describes the amount of light polarized along the +45° (U=+1) or –45° (U=-1) directions, and V describes the amount of right (V=+1) or left (V=-1) circularly polarized light. Figure 1 shows the definition of the normalized Stokes parameters with respect to a right handed coordinate system, where we have adopted the definition of a right-handed vibration ellipse (positive V parameter) for a clockwise rotation as viewed by an observer who is looking toward the light source. Positive rotation angles are defined as counter clockwise rotations.

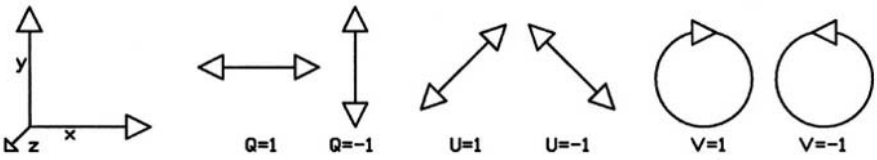

Figure 1. Definition of the Stokes parameters with respect to a right-handed coordinate system. The light is propagation along the positive z-axis, i.e. towards the viewer. *Q* and *U* describe linear polarizations in frames rotated by 45° with respect to each other. The *V* parameter describes circular polarized light.

For practical reasons the Stokes vector is sometimes represented in the Poincaré sphere system [12], where it is defined as the vector between the origin of an x-,y-,z- coordinate system and the point defined by *(Q, U, V).* The ensemble of normalized Stokes vectors with the same degree of polarization ($0<P<1$) defines a sphere with radius that varies between 0 for natural light and 1 for totally polarized light.

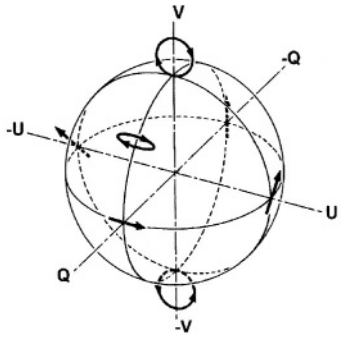

Figure 2. Poincaré sphere representation of the Stokes parameters (Adapted from [12]).

The Poincaré sphere is a convenient geometrical tool to analyze change in polarization state due to linear, circular or elliptical birefringence. The transformation by a linear retarder of a Stokes vector representing the incident polarization state is given by a rotation around an axis in the *Q-U* plane of the Poincaré sphere. The orientation of the rotation axis corresponds to the orientation of the optic axis with respect to the horizontal. For example, when the optic axis of the linear retarder is at 45° with respect to the horizontal, the rotation axis on the Poincaré sphere is coincident with the positive *U*- axis. The angle of rotation about the axis on the Poincaré sphere equals the amount of phase retardation. From the Poincaré sphere it is clear that a circular polarization state (V= +/- 1) is always perpendicular to a rotation axis in the Q-U plane, and thus will always be modified by a linear

retarder, regardless of the orientation of the optic axis. When a linear polarization state is incident parallel to the optic axis of a linear retarder, the state is unchanged. The retardation and orientation of the optic axis of a linear retarder can be determined from the transformation of the Stokes vector in the Poincaré sphere by finding the three dimensional rotation matrix with a rotation axis in the Q-U plane that describes the transformation. Circular birefringence (optical activity) is a rotation around the V-axis. Linear dichroism, i.e., the differences in the absorption and scattering coefficients for linearly polarized light, is described by an evolution of the Stokes vector over an arc in the Poincaré sphere towards the equator (Q-U plane). Circular dichroism, i.e., the differences in the absorption and scattering coefficients for circularly polarized light, is described by an evolution of the Stokes vector over an arc in the Poincaré sphere towards the poles ($V = 1$ or $V = -1$). A more detailed description of these transformations in the Poincaré sphere is given in subsection 18.4.4.

18.2.3 Calculating the Stokes Parameters of Reflected Light

Combining the principles of interferometric ellipsometry and OCT, the depth resolved Stokes parameters of reflected light can be determined. Polarimetry requires in general 4 measurements of the intensity in pre-selected polarization states to determine the Stokes vector of light. An interferometric technique however allows recovery of not only the intensity, but also the relative phase between the electromagnetic fields in orthogonal polarization states. Preserving this phase information allows determination of the Stokes vector of the reflected light as a function of depth in the sample with a single measurement. The amplitude and relative phase of the interference fringes in each orthogonal polarization channel will be used to derive the depth resolved Stokes vector of reflected light. The use of interferometry to characterize the polarization state of laser light specularly reflected from a sample was first demonstrated by Hazebroek and Holscher [2]. In their work, coherent detection of the interference fringe intensity in orthogonal polarization states formed by He:Ne laser light in a Michelson interferometer was used to determine the Stokes parameters of light reflected from a sample. Using a source with short temporal coherence adds path length discrimination to the technique, since only light reflected from the sample with an optical path length equal to that in the reference arm within the coherence length of the source will produce interference fringes. When using incoherent detection techniques, only two of the four Stokes parameters can be determined simultaneously. In the present analysis, we demonstrate that coherent detection of the interference fringes in two orthogonal polarization states allows determination of all four Stokes parameters simultaneously. Before giving a mathematical description, the principles underlying calculation of the Stokes vector will be discussed. We

assume that the polarization state of light reflected from the reference arm is perfectly linear, at an angle of 45° with the horizontal axis. After the polarizing beam splitter in the detection arm, the horizontal and vertical field components of light in the reference arm will have equal amplitude *and* phase. Light reflected from the sample will interfere with that from the reference, and the amplitude and *relative phase difference* of the interference fringes in each polarization channel will be proportional to the amplitude and *relative phase difference* between horizontal and vertical electric field components of light in the sample arm. The electric field vector of light reflected from the sample arm can be reconstructed by plotting the interference term of the signals on the horizontal and vertical detectors along the x and y axes, respectively.

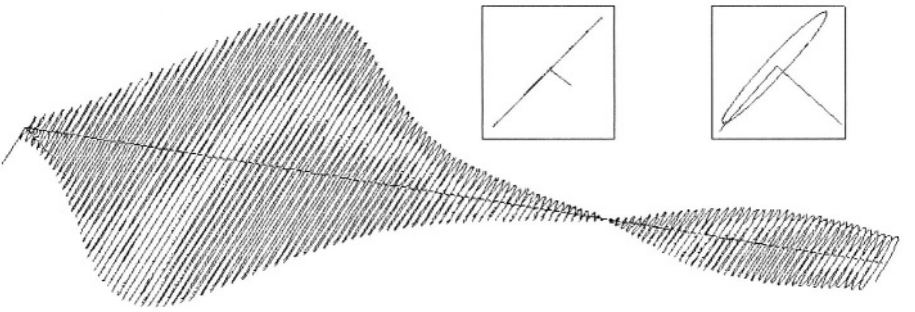

Figure 3. Evolution of the electric component of the electro-magnetic wave of the reflected light propagating through birefringent mouse muscle. The electric field is reconstructed from the horizontal A_H and vertical A_V polarized components and relative phase of the interference fringes. The displayed section is a small part of a longitudinal scan. Length of the section is 38 μm in a sample with refractive index n=1.4. The beginning of the section shows the reflection from the sample surface modulated by the coherence envelope. The inserts show cross sections of the electric field over a full cycle perpendicular to the propagation direction taken at, respectively, 5.7 μm and 35.7 μm from the beginning of the section. As can be seen from the inserts the initial polarization state of reflected light is linear along one of the displayed axes, changing to an elliptical polarization state for reflection deeper in the tissue. Reprinted from [13] with permission of the Optical Society of America.

Figure 3 shows a reconstruction of the electric field vector over a trace of 38 μm. The plot does not reflect the actual polarization state reflected from the sample, since the light has made a return pass through the quarter wave plate in the sample arm before being detected. The plot indicates change in polarization state from a linear to an elliptic state as a consequence of tissue birefringence.

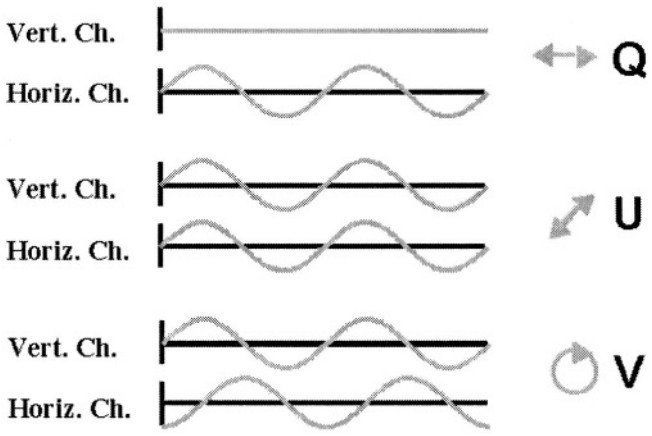

Figure 4. Determination of the Stokes vector from the detected interference fringe amplitude and phase in the horizontal and vertical polarized detection channel. From top to bottom, examples of fringe amplitude and phase are given for three Stokes vectors, Q=1, U=1 and V=1, respectively.

The Stokes parameters can be determined from the detected interference fringe intensity signals. Figure 4 shows three examples interference fringes detected in the orthogonal polarization channels that correspond to Stokes parametes $Q = 1$, $U = 1$, and $V = 1$, respectively. For instance, if the interference fringes are maximized on one detector, and minimal on the other, the polarization state is linear in either the horizontal or vertical plane, which corresponds to the Stokes parameter Q being one or minus one. If the interference fringes on both detectors are of equal amplitude and in phase, or π out of phase, the polarization state is linear, at 45° degrees with the horizontal or vertical, corresponding to the Stokes parameter U being one or minus one. If the interference fringes on both detectors are of equal amplitude and are exactly $\pi/2$ or $-\pi/2$ out of phase, the polarization state is circular, corresponding to the Stokes parameter V being one or minus one.

In the more mathematical description given in Refs. 11, 14 and 15, the Stokes vector was calculated by Fourier transforming the interference fringes in each channel over a length of approximately the coherence length, and computing the relative phase difference and amplitude of the Fourier components at each wave number.

In conclusion, determination of the ampltude and relative phase of interference fringes in orthogonal polarized detection channels gives acces to all four Stokes parameters, while applying an incoherent detection technique that does not compute the relative phase between fringes in orthogonal detection channels, allows determination of only two of the four Stokes parameters from a single A-line scan.

18.2.4 The Degree of Polarization

The complete characterization of the polarization state of reflected light by means of the Stokes parameters permits the calculation of the degree of polarization P, defined as,

$$P = \frac{\sqrt{Q^2 + U^2 + V^2}}{I}. \tag{3}$$

For purely polarized light, the degree of polarization is unity, and the Stokes parameters obey the equality $I^2 = Q^2 + U^2 + V^2$, while for partially polarized light, the degree of polarization is smaller than unity, leading to $I^2 > Q^2 + U^2 + V^2$. Natural light, characterized by its incoherent nature, has (by definition) a degree of polarization of zero. An interferometric gating technique such as OCT measures only the light reflected from the sample arm that does interfere with the reference arm light. On first inspection, this suggests that the degree of polarization will always be unity, since only the coherent part of the reflected light is detected. We will demonstrate however, that the degree of polarization can be smaller than unity, and is a function of the interval Δz over which the degree of polarization is calculated.

An input beam with P<1 can be decomposed into purely polarized beams (P=1). After propagation through an optical system, the Stokes parameters of the purely polarized beam components are added to give the Stokes parameters for the original input beam. In Bohren and Huffman's words: "If two or more quasi-monochromatic beams propagating in the same direction are superposed *incoherently,* that is to say there is no fixed relationship between the phases of the separate beams, the total irradiance is merely the sum of individual beam irradiances. Because the definition of the Stokes parameters involves only irradiances, it follows that the Stokes parameters of a collection of incoherent sources are additive" (see Ref. [16], p.53).

Implicit in our analysis is that a broadband OCT source may be viewed as an incoherent superposition of beams with different wavenumbers or wavelenghts and the observation that scattering and polarization properties of samples have a spectral dependence.

If the source were monochromatic, the degree of polarization of reflected light as measured in a PS-OCT system would always be 1. However, an OCT source ideally is broad band to obtain high axial resolution. In addition the polarizarion properties of the sample will have a spectral dependence, meaning that different wavelength will be reflected from the sample in different polarization states. As an example, consider an OCT source emitting two monochromatic beams in the same polarizaton state at different wavelenght, and assume that the light reflected from the sample at these two

wavelengths are in orthogonal polarization states. Using the above quoted description by Bohren and Huffman, Stokes parameters of incoherently superposed beams are summed, and the light source has a degree of polarization of unity, while the light reflected from the sample has a degree of polarization of zero, i.e., the reflected light is completely unpolarized. For a broad band source, the degree of polarization of reflected light is determined by the vector sum of Stokes vectors at independent wavelenghts, divided by the sum of intensities over the independent wavelengths. Using the Poincare sphere representation, one can visualize that the magnitude of a sum of Stokes vectors will be greatest if the direction of all components are colinear. For instance, directly after a polarizer, all wavelength components are in the same polarization state, and the Stokes vectors add colinearly, resulting in a degree of polarization of unity. For the reflected light, the Stokes vectors for different ave lenghts are not necessarily colinear, leading to a degreee of polarization that can be smaller than unity.

As stated above, the degree of polarization for light reflected from a particular depth in the sample depends on the length of the interval Δz over which the degree of polarization is calculted. This can be understood by considering that the wavelength resolution in Fourier transform spectrometry is proportional to the scan range. For instance, two wavelengths can only be discriminated if the number of oscillations within a scan range Δz differs by an integral number. Thus, the number of independent wavelengths that contribute to the vector sum of Stokes vectors depends on the length of the interval Δz. The longer the interval, the more independent wavelenghts contribute to the vector sum, increasing the probability that the length of the vetor sum is smaller than the sum of intensities, which leads to a degree of polarization less than unity. When the interval Δz is so small that the wavelenght resolution is coarser than the spectral width of the source there will be only one independent wavelenght, and the degree of polarization is necessarily unity.

An alternative argument will lead to the same conclusion. The reconstruction of the electric field vector in Figure 3 shows that the Stokes parameters can be determined over a single cycle of the field, where at each cycle the degree of polarization will be (very close to) unity. The Stokes parameters over an interval Δz are the sum of the Stokes parameters of single cycles of the electric field vector within the interval. The degree of polarization P of the depth resolved Stokes vector will be a function of the interval length Δz, since Stokes parameters can vary from cycle to cycle.

The reduction of the degree of polarization with increasing depth, that is demonstrated in Figure 6, can be attibuted to several factors. First, spectral components that may have travelled over different paths with equal lengths through the sample. Second, spectral dependence of the Stokes parameters of light forward or backscattered by (irregularly shaped) particles. Third,

presence of multiple scattered light and speckle in the pupil of the sample arm. Fourth, a decrease in the signal to noise ratio. Note that elastic (multiple) scattering does not destroy the coherence of the light in the sense of its ability to interfere with the source light (or the reference arm light). However, spectral phase variations within or between polarization channels may reduce the coherence envelope in a manner similar to the effect of dispersion. Inelastic interactions, such as incoherent Raman scattering or fluorescence, do destroy the coherence and interference with source light is lost.

18.3 DETERMINATION OF THE SAMPLE POLARIZATION PROPERTIES

From the Stokes parameters, the birefringence and optic axis of the sample can be determined, assuming that the orientation is constant with depth. The values of Q and U depend on the choice of the reference frame (i.e., the orientation of the polarizing beam splitter in the detection arm). The reference frame, or laboratory frame, is determined by the orientation of orthogonal polarization states exiting the polarizing beam splitter, which in our case is along the horizontal and vertical axes. The Mueller matrix for an ideal retarder is given by,

$$\begin{pmatrix} 1 & 0 & 0 & 0 \\ 0 & C^2 + S^2\cos\delta & SC(1-\cos\delta) & -S\sin\delta \\ 0 & SC(1-\cos\delta) & S^2 + C^2\cos\delta & C\sin\delta \\ 0 & S\sin\delta & -C\sin\delta & \cos\delta \end{pmatrix}, \tag{4}$$

where $C = \cos 2\alpha$, $S = \sin 2\alpha$, with α the angle of the optic axis with the horizontal, and δ the retardance. Equation 4 is the Mueller matrix representation of a linear retarder, with $\delta = k_0 z \Delta n$, k_0 the wave vector, z the distance traveled through the birefringent material, and Δn the birefringence. Upon specular reflection inside the sample, the Stokes parameters U and V change sign. The angle α of the optic axis of the Mueller matrix for the linear retarder on the return pass changes sign because the coordinate handedness is changed (the propagation direction of the light is reversed). After the return pass through the retarder, the combined Mueller matrix of propagation, reflection, and return pass is given by,

$$\begin{pmatrix} 1 & 0 & 0 & 0 \\ 0 & C^2 + S^2 \cos\delta & SC(1-\cos\delta) & -S\sin\delta \\ 0 & -SC(1-\cos\delta) & -S^2 - C^2\cos\delta & -C\sin\delta \\ 0 & -S\sin\delta & C\sin\delta & -\cos\delta \end{pmatrix}, \tag{5}$$

with $\delta = 2k_0 z\Delta n$. For example, when right circularly polarized light is incident onto a sample with linear retardance, the reflected light polarization state can be defined by the product of the Stokes vector (1,0,0,1) and the above matrix. The reflected light Stokes vector is:

$$\begin{pmatrix} I \\ Q \\ U \\ V \end{pmatrix} = \begin{pmatrix} 1 \\ -\sin 2\alpha \sin 2k_0 z\Delta n \\ -\cos 2\alpha \sin 2k_0 z\Delta n \\ -\cos(2k_0 z\Delta n) \end{pmatrix} \tag{6}$$

From equation 6 it is immediately clear that the birefringence can be determined from the Stokes parameter V and the optic axis orientation α can be determined from the Q and U parameters, $\tan\alpha = Q/U$.

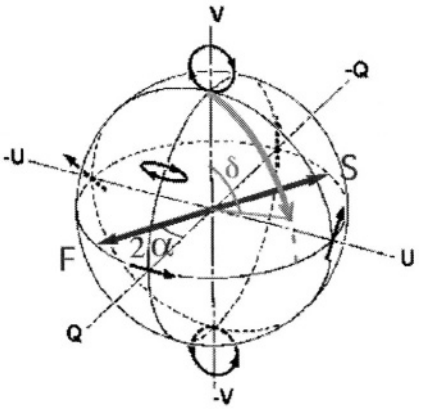

Figure 5. Rotation of the Stokes vector for a circular polarization state (1,0,0,1) by a birefringent medium with retardation δ and optic axis at an angle α with respect to the horizontal plane. F and S denote fast and slow optic axis orientation, respectively.

Figure 5 shows a graphical depiction of the transformation of a Stokes vector due to a birefringent medium as described in equation 6. An incident

circular polarization state is shown that is transformed by a rotation over an angle (δ) around an optical axis in the *Q-U* plane oriented at angle 2α.

18.3.1 Depth Resolved Imaging of Stokes Parameters

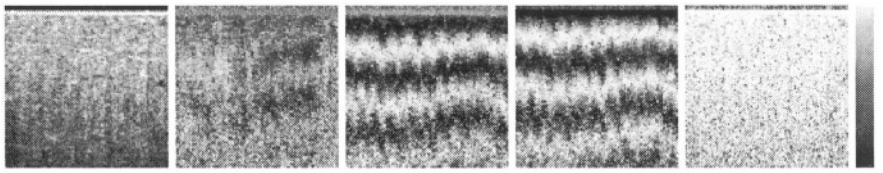

Figure 6. PS-OCT images of *ex vivo* rodent muscle, 1 mm ×1 mm, pixel size 10 μm ×10 μm. From left to right, the Stokes parameter *I*, normalized parameters *Q, U* and *V* in the sample frame for right circularly polarized incident light, and the degree of polarization *P*. The gray scale to the right gives the magnitude of signals, 35 dB range for *I*, from 1 (white) to -1 (black) for *Q, U* and *V,* and from 1 (white) to 0 (black) for *P*. Reprinted from [14] with permission of the Optical Society of America.

As an example, two dimensional images of the spatially resolved Stokes parameters of light reflected from ex vivo rodent muscle are shown in Figure 6. Rodent muscle was mounted in a chamber filled with saline and covered with a thin glass cover slip to avoid dehydration during measurement. Figure 6 shows images of Stokes parameters for right circularly polarized incident light. Several periods of normalized *U* and *V,* cycling back and forth between 1 and -1, are observed in muscle indicating that the sample is birefringent, further demonstrated by the averages of the Stokes parameters over all depth profiles in Figure 7a.

To verify experimentally the orientation of the optical axis, light incident on the sample was prepared in three linear polarization states with electric fields parallel, perpendicular, and at an angle of 45° to the experimentally determined optical axis of the birefringent muscle. Figure 7b shows the average of the normalized Stokes parameter *Q* over all depth profiles at the same sample location. The negligible amplitude of oscillation in *Q* for light polarized parallel and perpendicular to the optical axis verified the experimentally determined orientation. When light is incident at an angle of 45° to the optical axis of the sample, *Q* oscillates with increasing sample depth as expected for a birefringent sample. The similarity of the reflected intensity for circular, parallel and perpendicular light (shown in Figure 7c) indicates that the polarization state changes are not due to dichroism of the muscle fibers. The birefringence Δn was determined by measuring the distance of a full *V* period, which corresponds to a phase retardation of $\pi = k_0 z \Delta n$, giving Δn=1.4×10^{-3}.

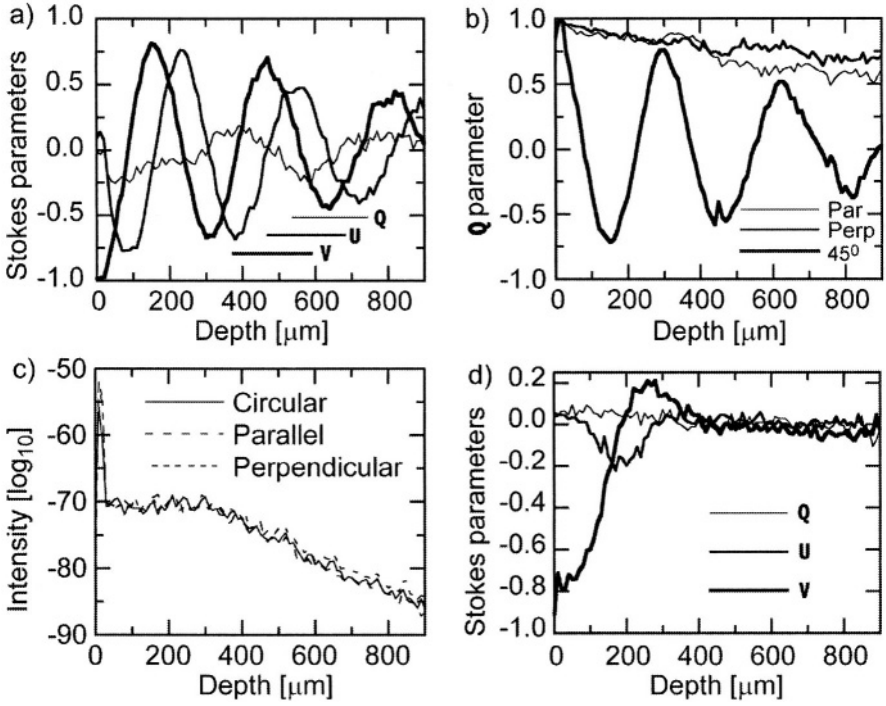

Figure 7. Averages of Stokes parameter *I*, and normalized parameters *Q, U* and *V* in the sample frame over all depth profiles of, respectively, a) rodent muscle, right circular incident polarization, b) rodent muscle, linear incident polarization, parallel, perpendicular, and at 45° with the optical axis, c) rodent muscle, right circular, parallel and perpendicular incident polarization, d) *in vivo* rodent skin, right circular incident polarization. Reprinted from [14] with permission of the Optical Society of America.

18.3.2 Polarization Diversity Detection

To summarize, PS-OCT is important not only to measure birefringence, but also for accurate interpretation of OCT images. Most fibrous structures in tissue (e.g. muscle, nerve fibers) are form birefringent due to their structural anisotropy. Single detector OCT systems can generate images that show structural properties by a reduction in tissue reflectivity, solely due to polarization effects. Polarization diversity detection is defined as the depth resolved measurement of the *I* component of the Stokes vector of light reflected from the sample. Intuitively, one might expect that use of unpolarized sources may be advantageous for polarization diversity detection.

Although a polarized light source was assumed, the presented analysis is easily extended to include unpolarized sources. An unpolarized source can

be described by the addition of two orthogonally polarized sources that are mutually incoherent. The interference fringes at the detector(s) need to be analyzed separately for the two pure polarization states and the total interference fringe pattern at the detector(s) is given by the sum of the fringe patterns generated by each pure polarization state.

An OCT system with an unpolarized source and a single detector does not necessarily provide polarization diversity detection. On the contrary, this system is even more sensitive to polarization effects than a system with a polarized source.

Consider polarized source light incident on a birefringent sample acting as linear retarder with optic axis at 45° with respect to the incident light polarization axis. The polarization state of reflected light from some depth has undergone a π phase retardation and is orthogonal to the incident polarization state. Since orthogonally polarized states can not interfere, light from the sample and reference arms do not produce interference fringes. The same holds for each of the orthogonally polarized states in the decomposition of an unpolarized source into linear states at 45° and -45°with the optic axis. Therefore, for the unpolarized source no interference fringes will be detected. Suppose now that the decomposition of the unpolarized source is chosen differently for the above mentioned birefringent sample, such that the two orthogonal linearly polarized mutually incoherent states are along and perpendicular to the optic axis. Both orthogonal polarization states reflected from the sample are unaltered by the birefringence, and will produce interference fringes with the reference arm light. However, at the same depth as above the interference fringes for orthogonal polarization states are exactly π out of phase and cancel after summation on the single detector, and no interference fringe pattern is observed. Thus, in this example, the unpolarized source will not produce interference fringes at one depth regardless of the orientation of the optic axis (as is expected from symmetry arguments). In contrast, a polarized source would produce interference fringes if the state is polarized (partially) along the optic axis.

18.3.3 Summary

PS-OCT systems can be constructed with bulk optical components. These systems are too cumbersome to work with for practical application of this technique in a clinical setting. For portable, robust systems, implementation of the technique in optical fiber is necessary. In addition, probing with a single polarization state results in incomplete polarization properties information of the sample. As an example, consider a circular polarization state incident on a birefringent sample. At some point in depth, this circular state will be converted to a linear state. If at this depth the optical axis of the sample changes to one collinear with the linear

polarization state, the polarization will remain unchanged, i.e., no change in polarization state will be detected. To remedy this erroneous result, the sample needs to be interrogated with more than one polarization state. In the next section, implementation of PS-OCT systems in optical fiber will be described, and optimal polarization modulation schemes will be discussed to accurately determine the polarization properties of samples under study.

18.4 FIBER BASED PS-OCT SYSTEMS

Previous PS-OCT systems were air spaced interferometers using bulk optical components that allowed precise control over the polarization state of light in the sample and reference arms [5-7,14,17]. Fiber based interferometers offer distinct advantages in terms of system alignment and handling, but pose design problems due to polarization changes induced in optical fibers. Polarization Maintaining (PM) fibers have a large birefringence with a beat length of 2-3 mm. The energy of wave components along the primary axes of the fiber is preserved, but the relative phase is lost due to the difference in experienced optical path length. In order to determine the Stokes parameters, such phase information is needed [14]. Recently an OCT system was demonstrated where the difference in optical path length in PM fiber was compensated for by splicing two matching sections with orthogonal orientation of the optic axis [18].

18.4.1 Polarization Mode Dispersion and Differential Group Delay

Single Mode (SM) fibers (and the above described compensated PM fibers) have Polarization Mode Dispersion (PMD). Due to random birefringence, induced by core ellipticity, non circularly symmetric stresses and fiber bends, SM fibers propagate two nearly degenerate orthogonal polarization states. Differential Phase Delay (DPD) and Differential Group Delay (DGD) between these two states cause, respectively, an evolution of the polarization states along the fiber, and a broadening of the interferogram in an OCT system. With respect to DPD, which describes fiber birefringence, and thus the polarization state change while the light propagates through the fiber, the spectral dependence should be kept minimal to minimize the effect of spectral components transforming to different polarization states. DGD, which describes the difference in group delay between orthogonal polarization states, should at least result in an optical path length difference less than the source coherence length. The mode coupling length h describes the distance in the fiber with a constant orientation of the optic axis. It can be interpreted similarly to the mean free path (the distance between scattering events) in a random walk model of

light diffusion. For fiber length L shorter than the mode coupling length h, DPD and DGD are directly proportional to fiber length. This relationship changes to a square root dependence for $L >> h$, indicating the underlying one dimensional random walk nature of PMD [19]. We used a single mode fiber (Corning SMF-28) with a PMD $\leq 0.1[ps/\sqrt{km}]$ if $L > h$ and $\leq 0.1\sqrt{km}/\sqrt{h}\,[ps/km]$ if $L < h$, resulting in an optical path length difference between orthogonal polarization states that is in either case less than $2\ \mu m$ for 4.4 m of fiber.

18.4.2 Fiber Based PS-OCT Instrument

In Figure 8 a single mode fiber based PS-OCT system is presented, which was described earlier [20]. A low coherence source (AFC Technologies) with a FWHM bandwidth of 80 nm centered at 1310 nm was polarized by a bulk polarizer and coupled back into the fiber. Quarter and half wave plates before the polarizer were used to select the polarization state of the source with the highest power (8 mW). Quarter and half wave plates after the polarizer prepared the polarization such that after a short fiber length (15 cm) the light emerged with equal magnitude wave components parallel and perpendicular to the optic axis of a bulk electro-optic polarization modulator (New Focus 4104). The modulator allows control of the polarization state over a grand circle on Poincaré's sphere.

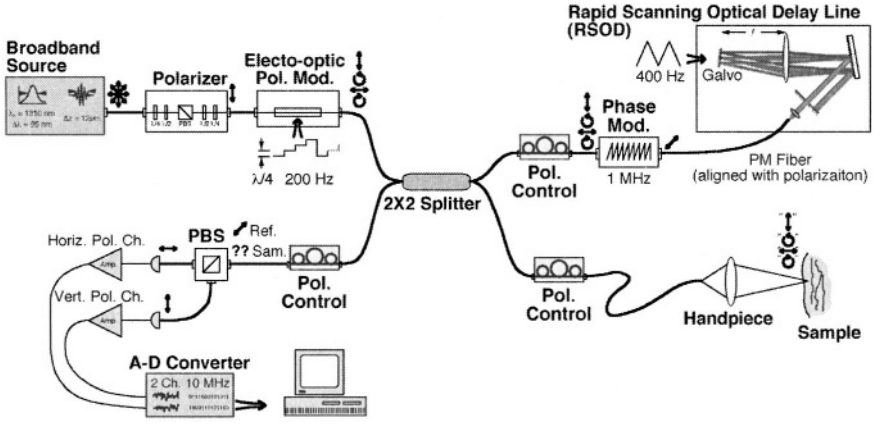

Figure 8. Schematic of the fiber-based PS-OCT system.

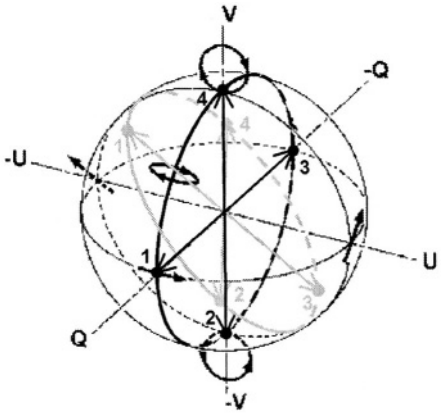

Figure 9. The black dots numbered 1 through 4 on the black grand circle and axes show the four polarization states with 90 degrees retardance increments after the polarization modulator. The gray dots numbered 1 through 4 on the gray grant circle show a possible realization of the polarization states at the sample arm fiber tip. In the absence of polarization dependent loss, the 90° angle between the Stokes vectors after the polarization modulator is maintained at the sample arm fiber tip. The random orientation of circular and linear birefringence in the fiber transforms the light after the polarization modulator by a rotation in the Poincaré sphere.

A four step driving function, where each step introduces a $\pi/2$ phase shift, cycles the light over four Stokes vectors. In Figure 9, the numbered black dots on the black grand circle indicate the polarization states immediately after the modulator, before a fiber 2x2 coupler. Due to the sample arm fiber circular and linear birefringence (or equivalently the DPD), the polarization state at the tip of the sample arm fiber is unknown. However, in a lossless fiber (with a total DGD smaller than the coherence time of the light), the transformations in Poincaré's sphere are orthonormal, preserving the angles between the four Stokes vectors. The numbered gray dots on the gray grand circle in Figure 9 indicate a possible realization of the four polarization states at the fiber tip. The sample arm consists of a fiber with a collimator and focusing lens, mounted on a motorized linear translation stage.

In the reference arm, a static polarization controller is aligned such that for all four polarization states half of the light is transmitted through a PM fiber pigtailed phase modulator (JDS Uniphase) which by its structure polarizes the light. The PM fiber is also used to couple the light into a Rapid Scanning Optical Delay line (RSOD) [21, 22], which was operated with the spectrum centered on the galvo mirror. The RSOD thus only generates a group delay and no phase delay; the carrier of the interferometric signal at the detector is only generated by the phase modulator. The phase modulator

is driven by a sawtooth waveform at 1 MHz, generating a maximum 2π phase shift after double passage.

In the detection arm a static polarization controller before the polarizing beam splitter is aligned such that the reference arm light is split equally over both detectors. Electronic signals were high pass filtered, amplified and digitized by a 12 bit dual channel 10 Msamples/s per channel A/D board (Gage Applied Sciences Inc.).

18.4.3 Fiber Based PS-OCT Data Processing

Data processing consists of lock-in detection in software of the sine and cosine components at the reference frequency of 1 MHz. The sine and cosine components of 5 μm segments in each A-line (depth profile) of 2 mm length are processed to obtain the Stokes parameters as described earlier [14, 23].

$$\begin{aligned} I &= \sin_H^2 + \cos_H^2 + \sin_V^2 + \cos_V^2, \\ Q &= \sin_H^2 + \cos_H^2 - \sin_V^2 - \cos_V^2, \\ U &= 2\sin_H * \sin_V + 2\cos_H * \cos_V, \\ V &= 2\sin_H * \cos_V - 2\cos_H * \sin_V . \end{aligned} \tag{7}$$

Figure 10 shows 16 images of the four Stokes parameters for each of the four input states. A close look at these images reveals that the Stokes parameter images Q, U and V for input polarization state 1 and 3 form an (nearly) identical pair that only differ in sign. In the images this is apparent by an opposite gray scale color. Input polarization states and 2 and 4 form a similar pair. The four input states form two pairs of orthogonal polarizations. In the Poincaré's sphere representation two orthogonal states are collinear vectors pointing to opposite points on the sphere. In a purely birefringent medium, two orthogonal states will undergo the exact same transformation and one Stokes vector can be obtained from the corresponding orthogonally polarized vector by a mirror operation in the origin. The pairs 1,3 and 2,4 carry independent information and are necessary to determine tissue birefringence properties. The lack of control over the polarization state incident on the sample due to the unknown polarization state change in the sample arm fiber could lead to the undesirable situation that the polarization state for pair 1,3 is linear, and aligned with the optic axis of the medium. In this case, the polarization state will remain unchanged while propagating through the birefringent medium. In the Poincaré's sphere representation the incident Stokes state is collinear with the rotation. However Stokes vector pair 2,4 is oriented at an angle of 90 degrees with pair 1,3, which was

collinear with the axis of rotation. Thus, pair 2,4 makes a right angle with the rotation axis, and thus will be transformed over a grand circle.

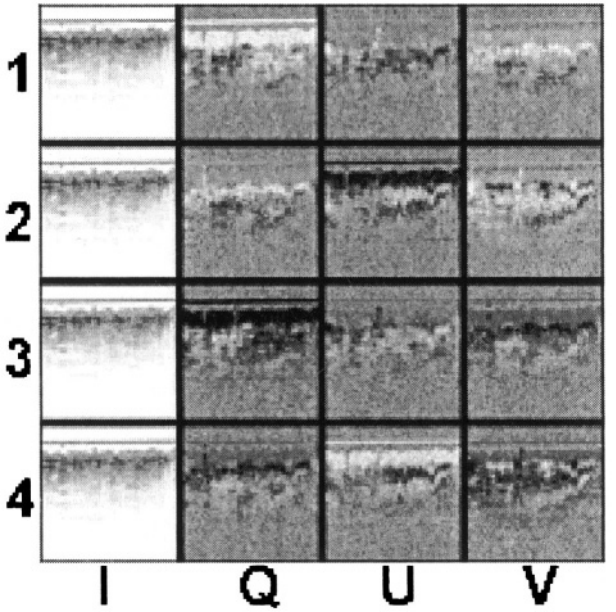

Figure 10. Stokes parameter images *I*, *Q*, *U* and *V* for each of the four input polarization states for *in vivo* human skin. Image size is 2 x 2 mm, gray scale coded on a logarithmic scale for the I parameter, and linearly gray scale coded from black to white for *Q*, *U* and *V* values between 1 and -1.

In conclusion, any set of two polarization states that make an angle of 90 degrees in the Poincaré sphere will necessarily be transformed by sample birefringence. In contrast, a colinear set (180 degrees angle in the Poincare sphere) is not necessarily transformed by sample birefringence. By calculating a single rotation matrix that transforms both pairs simultaneously, the birefringence of the sample can be determined, regardless of the actual realization of the polarization states at the fiber tip or the orientation of the sample optic axis. Pure diattenuation in the sample will lead to different transformations for orthogonally polarized Stokes vector pairs; the Stokes vectors of a pair do not remain colinear.

The effect of of diattenuation in the measurement can be eliminated by averaging these 16 images as follows: for each pair of orthogonal incident polarizations, the *I* images are averaged by addition and the *Q*, *U* and *V* images are averaged by subtraction since they have opposite signs. Any diattenuation contribution to the transformation of the remaining 2 Stokes vectors is eliminated. The resulting eight images (one set of I, Q, U and V images per input pair) define two Stokes vectors that are described by

lengths I_1 and I_2 and three component (Q, U, and V) vectors $\mathbf{I_1}$ and $\mathbf{I_2}$ with unit length.

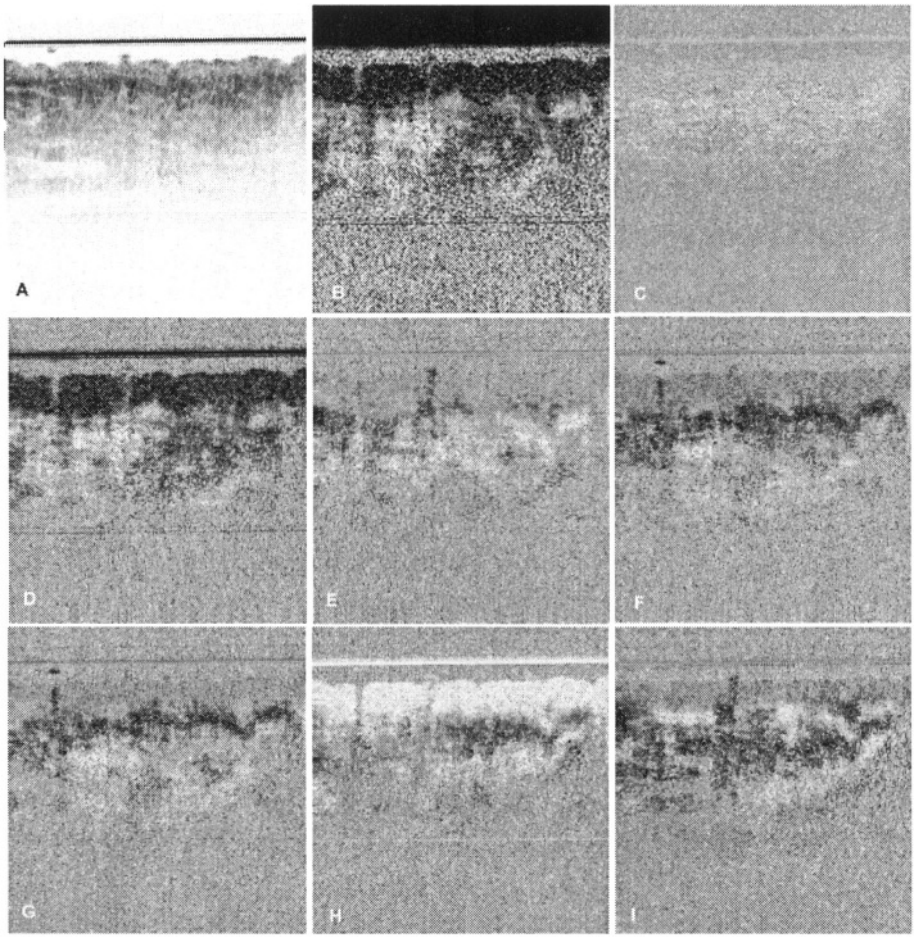

Figure 11. Polarization sensitive OCT images of *in vivo* human skin of the (inside) ventral forearm. (a) Conventional intensity image averaged from four scans with different incident polarizations. (b) Retardation phase map indicating the minimum amount of retardation to shift the incident polarization vector to the polarization state reflected back from a given depth, (c) Orthogonality image depicting the value of the cross product of the Stokes vectors. The remaining six images depict the polarization components of the Stokes vectors of the backscattered light for the pairs of polarizations that have been averaged: polarization 1 (d) Q, (e) U, (f) V, polarization 2 (g) Q, (h) U, (i) V.

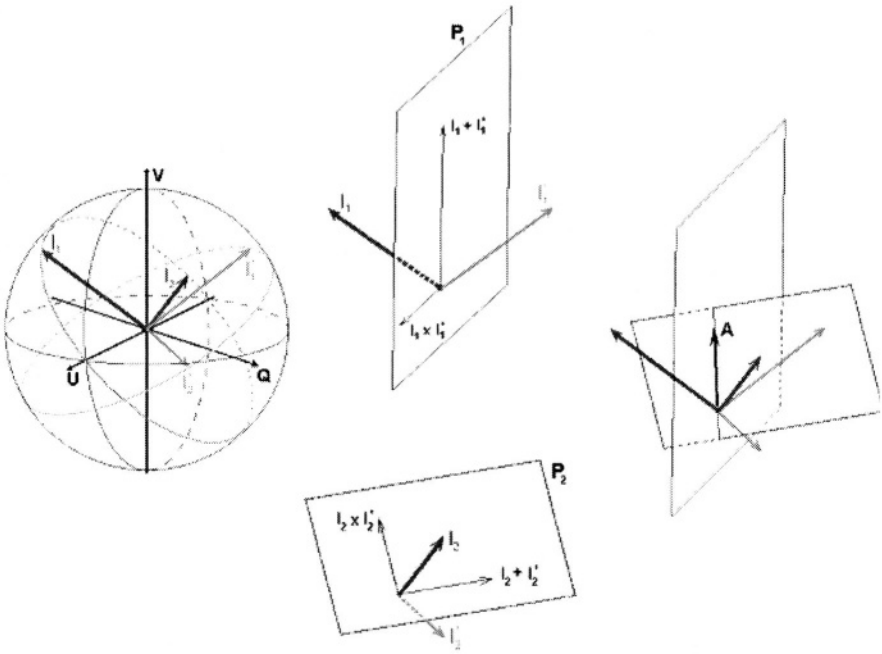

Figure 12. These figures illustrate an example of a birefringence calculation. The polarization states at the surface, I_1 and I_2, are depicted on Poincaré's sphere along with the polarization states reflected from a particular point in the sample, I_1' and I_2'. Plane P_1 is determined from I_1 and I_1'. Plane P_2 is determined from I_2 and I_2'. The intersections of planes P_1 and P_2 are taken as the combined optic axis A. Reprinted from [8] with permission of the Society of Photo-Optical Instrumentation Engineers.

The incident polarization states $\mathbf{I_1}$ and $\mathbf{I_2}$ are now determined by the polarization state of light returning from the surface of the sample. $\mathbf{I_1}$ and $\mathbf{I_2}$ are compared to Stokes vectors returning from deeper in the sample, denoted by states $\mathbf{I_1'}$ and $\mathbf{I_2'}$. The calculation involves first determining an optic axis and then a degree of phase retardation about that axis. A single rotation, for example, from $\mathbf{I_1}$ to $\mathbf{I_1'}$, determines a plane of possible optic axes spanned by the sum and cross product of the two states. The intersection of the two planes, one determined by $\mathbf{I_1}$ and $\mathbf{I_1'}$ (Figure 12b), the other determined from $\mathbf{I_2}$ and $\mathbf{I_2'}$ (Figure 12c), is taken as the overall optic axis, **A** (Figure 12d). The final step in the analysis is determining the degree of phase retardation over this optic axis. θ_1 may be defined as the degree of rotation about **A** that takes $\mathbf{I_1}$ to $\mathbf{I_1'}$, and θ_2 is defined analogously. The expectation is that the two rotation angles are equal, however, in practice they differ slightly due to noise. The overall phase retardation is taken as the intensity weighted average of the angles,

$$\theta = \frac{\left|\vec{I}_1'\right|\theta_1 + \left|\vec{I}_2'\right|\theta_2}{\left|\vec{I}_1'\right| + \left|\vec{I}_2'\right|}. \tag{8}$$

These values are encoded on a gray scale with black and white representing rotation of 0 and π radians, respectively. A more elaborate expression for equation 8 was given in B.H Park *et al.* [24].

Currently, a single rotation matrix is calculated at each depth in the sample, which assumes that the optical axis is constant. In a more advanced approach, the rotation matrix could be calculated between consecutive Stokes vectors along a depth profile, which would take into account variations in the orientation of the optic axis with depth. The total encountered birefringence would be the sum of the absolute values of the consecutive rotation angles. However, the presence of speckle noise would likely lead to a significant over estimation of the total phase retardation.

18.4.4 Polarization Modulation Schemes

In order to evaluate the optimal choice of polarization states with which to interrogate the sample to determine the polarization properties, the possible polarization changes in the sample will be analyzed in the framework of Jones matrices and transformations in the Poincaré sphere. In the description discussed so far, the amplitude and the electric field components in orthogonal polarization channels were used to calculate the Stokes vector, and the polarization properties of tissue were analyzed by transformations in the Poincaré sphere. Equivalently, the amplitude and the electric field components can be used to perform an analysis using Jones matrix formalism [25, 26]. A Jones matrix is a complex 2x2 transfer matrix describing the transformation of the electric field components propagating through matter. Since a common phase factor can be extracted, a Jones matrix has 7 independent variables. The polarization properties can be separated into four fundamental effects: Linear birefringence (LB), circular birefringence (CB), linear diattenuation (LD) and circular diattenuation (CD). A sample that acts as a polarizer can be described by diattenuation. The transmission Jones matrices for the above described effects are given by, respectively,

$$\text{LB: } \begin{pmatrix} Cos\alpha & -Sin\alpha \\ Sin\alpha & Cos\alpha \end{pmatrix} \begin{pmatrix} e^{-i\delta/2} & 0 \\ 0 & e^{i\delta/2} \end{pmatrix} \begin{pmatrix} Cos\alpha & Sin\alpha \\ -Sin\alpha & Cos\alpha \end{pmatrix} \tag{9}$$

$$\text{CB: } \begin{pmatrix} Cos\gamma & Sin\gamma \\ -Sin\gamma & Cos\gamma \end{pmatrix} \tag{10}$$

$$\text{LD: } \begin{pmatrix} Cos\alpha & -Sin\alpha \\ Sin\alpha & Cos\alpha \end{pmatrix} \begin{pmatrix} P_1 & 0 \\ 0 & P_2 \end{pmatrix} \begin{pmatrix} Cos\alpha & Sin\alpha \\ -Sin\alpha & Cos\alpha \end{pmatrix} \tag{11}$$

$$\text{CD: } \begin{pmatrix} e^{i\pi/4} & -e^{i\pi/4} \\ e^{-i\pi/4} & e^{-i\pi/4} \end{pmatrix} \begin{pmatrix} P_1 & 0 \\ 0 & P_2 \end{pmatrix} \begin{pmatrix} e^{-i\pi/4} & e^{i\pi/4} \\ -e^{-i\pi/4} & e^{i\pi/4} \end{pmatrix} \tag{12}$$

with α the orientation of the birefringence or diattenuation optic axis with the horizontal, δ and γ the linear and circular phase retardance, respectively, and P_1 and P_2 the diattenuation coefficients with a value between 0 and 1.

A sample can be described by the matrix product of these Jones matrices. Since these matrices do not commute, the order does matter. The corresponding transformations in the Poincaré sphere for these four effects are depicted in Figure 13. The transformation in the Poincaré sphere for a product of Jones matrices is given by a subsequent application to the Stokes vector of the corresponding transformations in the Poincaré sphere.

As discussed previously, a single polarization state will not suffice to determine uniquely the polarization properties, since the incident state could coincide with the optic axis for birefringence, or the convergence point for diattenuation. For birefringent tissue and a circular input polarization state, the polarization state will be converted to a linear state at some depth in the tissue. If at that depth the orientation of the optic axis changes to be co-linear with the linear polarization state, no additional change in the polarization state will be detected from that depth on.

The minimal number of polarizaton states needed to uniquely determine the polarization properties in reflection is two. Due to the Jones reversibility theorem the Jones matrix for light propagating forth and back through the same optical element is transpose symmetric [27]. Because of this symmetry, the number of independent parameters in the Jones matrix is reduced from seven to five [26]. A single measurement results in three known quantities: The electric field amplitudes in orthogonal polarization channels and their relative phase. Two measurements with different polarization states yield six known quantities, more than sufficient to determine the 5 independent parameters in the Jones matrix [26]. The elimination of 2 independent parameters in the Jones matrix is a consequence of the cancellation of circular birefringence and circular diattenuation upon forth and back

propagation through the same optical element. This can be verified by taking the matrix product of the Jones matrix for reflection sandwiched between the Jones matrix for circular birefringence or diattenuation, respectively. The resulting matrix is a diagonal matrix with opposite sign of the diagonal elements, representative of the Jones matrix for reflection. The effects of circular birefringence and diattenuation are eliminated from the resulting matrix.

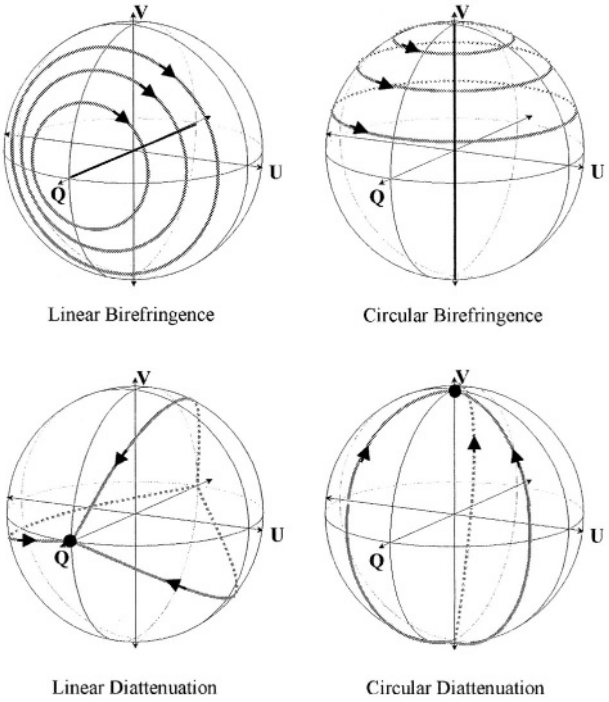

Figure 13. Representation of the transformations in the Poincaré spehere for linear, and circular birefringence (top panel) and linear and circular diattenuation (bottom panel). Linear birefringence is described by a rotation around an axis in the *Q*-*U* plane (in this example the *Q*-axis). Circular birefringence is described by a rotation around the *V*-axis. Linear diattenuation is described by a transformation of the Stokes vector over trajectories converging towards a point on a grant circle in the *Q*-*U* plane (in this example the *Q*=1 point). Circular diattenuation is described by a transformation of the Stokes vector over trajectories converging towards the poles on the *V*-axis. Diattenuation is associated with loss. In these examples, the Stokes vectors were normalized on the intensity to obtain length unity.

The optimal choice for the two polarization states with which to probe the sample is given by to states that make a right angle in the Poincaré sphere representation [8, 10, 20, 28], e.g. a *V*=1 and a *Q*=1 pair, or a *Q*=1 and a *U*=1 pair. As is evident from the transformations associated with birefringence as depicted in Figure 13, if one state is an eigenvector of the

transformation, the other state of the pair will trace out the longest arc on the sphere under the transformation. The worst choice of pairs is two orthogonal states, as used by Jiao and Wang,[25, 26] since both states can be simultaneously eigenstates of the transformation in the Poincaré sphere.

18.5 MULTI-FUNCTIONAL OCT

Various extensions have been shown to provide more information on tissue properties than standard OCT imaging alone. Polarization sensitive OCT (PS-OCT) is sensitive to light polarization changing properties of the sample [6, 7, 14, 17, 29, 30]. Simultaneous detection of interference fringes in two orthogonal polarization channels allows determination of the Stokes parameters of light [14]. Comparison of the Stokes parameters of the incident state to that reflected from the sample can yield a depth-resolved map of optical properties such as birefringence. PS-OCT can even be incorporated in fiber-based systems without the need for polarization-maintaining fibers [20,31]. Another extension, optical Doppler tomography (ODT), is capable of depth-resolved imaging of flow [28,32-38]. Flow sensitivity can be achieved by measuring the shift in carrier frequency of the interference fringe pattern due to backscattering of light from moving particles or by comparing the phase of the interference fringe pattern from one A-line to the next. Both methods have been implemented in real-time systems, either with dedicated hardware [36,37] or by use of an optical Hilbert transform [38]. A multi-functional OCT system capable of simultaneously measuring all three images (intensity, birefringence, and flow) requires acquisition of the full interference fringe patterns. Due to the processing time necessary to analyze this large amount of data, displaying all three images simultaneously and in real-time requires efficient data collection and processing. Measurements were usually taken and saved with data processing and display occurring separately afterwards.

18.5.1 Multi-Functional OCT Instrument

We describe here a fiber-based OCT system, which provides real-time simultaneous imaging of tissue structure, birefringence and flow. Only two polarization states are used that make a right angle in the Poincaré sphere representation, one state in forward and the other state in reverse depth scans [28]. This arrangement permits comparison of the phase between points in successive forward (or reverse) axial scans with incident light in the same polarization state for flow imaging. Birefringence and optic axis orientation are determined using data from successive axial scans, in this case, A-lines with incident light in different polarization states [8, 20].

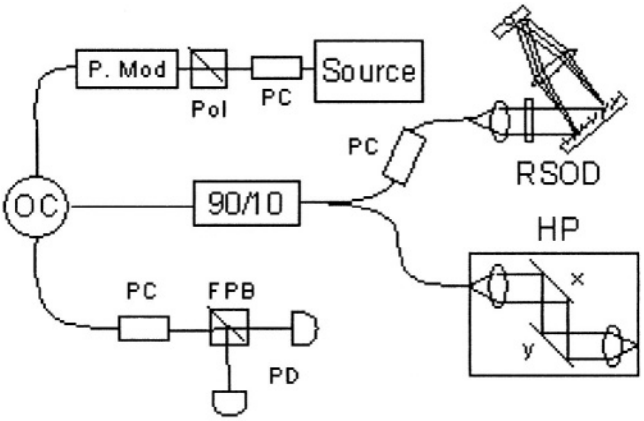

Figure 14. Schematic diagram of the fiber-based OCT system. Pol: Polarizer, PC: passive polarization controller, P. Mod: electro-optic polarization modulator, OC: optical circulator, FPB: all-fiber polarizing beamsplitter, HP: scanning handpiece, PD: fiber-pigtailed photodiodes. Reprinted from [28] with permission of the Optical Society of America.

The fiber-based system, a slight modification of the system presented earlier, is shown in Figure 14. Light was coupled through standard single-mode fiber to a polarization-independent optical circulator, then divided in a 90:10 ratio using a fiber optic splitter into sample and reference arms, respectively. 2.5 mW of source light was incident on the sample surface in a focused spot of 30 μm diameter. A grating-based rapid scanning optical delay line (RSOD) was used with the source spectrum offset on the scanning mirror to provide both group and phase delay scanning [21, 22], generating a carrier frequency at 800 kHz. The two-step voltage function used to drive the polarization modulator was synchronized with the 1 kHz triangular scanning waveform of the RSOD, such that the polarization states incident on the sample during inward and outward A-line scans were orthogonal in the Poincaré sphere representation. A polarizing cube was inserted in the reference arm to ensure that light in the RSOD was always in the same linear state, regardless of the polarization state at the sample. Static polarization controllers in the detection and reference arms were aligned for equal distribution of reference arm light over both horizontal and vertical detection channels for both input polarization states. Electronic signals from each detector were amplified, filtered and digitized with a 12-bit 5 MS/s A-D board (National Instruments NI 6110).

18.5.2 Signal Processing

Sine and cosine components of the interference fringe signals at each detector are obtained over sections Δz, in each A-line, by multiplying the measured signal $f(z)$ by a sine and cosine term at the carrier frequency ω_0,

and averaging over a few cycles of the oscillation corresponding to the coherence length of the source. Both cosine and sine terms can be extracted conveniently by determining the real and imaginary parts of the single function, $f(z)\exp(i\omega_0 z)$ and averaging over Δz. Using the convolution theorem, we can express our function of interest in the following manner,

$$f(z)\exp(i\omega_0 z) = \vec{F}\left[\int f(q-\omega)\delta(\omega_0+\omega)d\omega\right] = \vec{F}\left[f(q-\omega_0)\right], \qquad (13)$$

where we have also used $f(z)g(z) = \vec{F}\left[\vec{F}\left[f(z)g(z)\right]\right] = \vec{F}\left[f(\omega)\otimes g(\omega)\right]$, with $\vec{F}\left[\exp(i\omega_0 z)\right] = \delta(\omega_0+\omega)$, and $\vec{F}$ and $\vec{F}$ representing forward and reverse Fourier transformations respectively. Equation 13 demonstrates that the sine and cosine components of interest may be obtained by taking the inverse Fourier transform of the shifted Fourier spectrum $f(q-\omega_0)$, from the original interference fringe signal, $f(z)$. The implementation of this efficient algorithm is discussed in detail in Refs. [24, 28].

The Stokes parameters *I*, *Q*, *U* and *V* are then determined as described previously [14, 20], using the calculated sine and cosine components. Structural OCT images are formed by displaying values of the Stokes parameter $I(z)$ mapped onto a logarithmic grayscale range, for all A-lines in an image. Birefringent regions in tissue are visualized by mapping the accumulated phase retardation from the sample surface. Stokes parameters are calculated for light in each of the two input polarization states, defining vectors of length *I* with components *Q*, *U*, and *V*, at all points in each A-line. The tissue optic axis and accumulated phase retardation are found as described earlier [8, 20].

Phase-resolved imaging of blood flow is achieved by comparing the phase at each point in A-line *i* with the phase at the same point in A-line *i*+2, therefore comparing consecutive A-lines with incident light in the same polarization state. $\phi(z)$ describes the phase in an A-line at position *z* and is calculated not by the Hilbert transform, but by using the same sine and cosine components of the interference fringe signals obtained previously;

$$\phi_{H,V}(z) = \arctan\left(\frac{\sin_{H,V}(z)}{\cos_{H,V}(z)}\right). \qquad (14)$$

Subscripts *H* and *V* indicate horizontal and vertical polarization channels respectively. The phase difference between points in successive A-lines $\Delta\phi(z)$, is used to calculate the Doppler frequency shift ω, due to scattering of light from moving particles, and is given by $\omega = \Delta\phi(z)/T$, where *T* is the

time interval between consecutive A-line scans with light in the same polarization state (1 ms). Knowledge of the imaging geometry then enables the bi-directional flow velocity to be determined. We calculated a value of 24 μm/s for the minimum detectable flow velocity of the system used here at an axial scan rate of 1 kHz, based on an average phase standard deviation in the absence of flow of 0.24 rad, as described later in this section. This velocity sensitivity is equivalent to the value of 10 μm/s at 400 Hz reported in Ref [34], indicating no increase in the noise floor in this system where polarization information is additionally obtained.

$\Delta\phi_{H,V}(z)$ are also used to calculate the phase variance *Var(z),* defined as

$$Var(z) = \Delta\phi_H^2(z) + \Delta\phi_V^2(z), \tag{15}$$

with values of *Var(z)* obtained from eight sequential pairs of A-lines averaged to improve signal-to-noise. Displaying these values in a variance map provides a semi-quantitative measure of flow in a sample, with higher contrast than that provided by mapping only the Doppler shift [35].

Imaging regions of flow with this phase-resolved technique relies on consistently sampling data at the same points within each A-line, to ensure that measured phase shifts are due purely to the presence of flow. Carrier generation by offsetting the source spectrum on the scanning mirror in an RSOD results in greater phase instability than when operating with the spectrum centered on the RSOD [39], however, we successfully counter this accompanying reduction in phase stability by using a correction algorithm in software. The corrected phase difference between A-lines *i* and *i*+2 is given by $\Delta\phi_i'(z) = \Delta\phi_i(z) + \alpha + \beta z$, where parameters α and β are determined by an intensity-weighted linear least squares fit to the originally calculated phase difference, $\Delta\phi_i(z)$.

Phase variance images taken at the inside surface of a human finger are presented in Figure 15, with and without making these corrections. Values of phase variance ranging from 0 to 2.5 rad^2 are mapped onto the grayscale range. In the left (uncorrected) image, a blood vessel is identified as the large structure at a depth of approximately 1 mm, but with phase differences between A-lines appearing as vertical white lines, finer detail is difficult to resolve. The average phase variance over the image is 0.64 rad^2. In the right (corrected) image, the same large vessel is again apparent, but now two smaller capillaries may also be identified at lesser depths. Removing contributions to phase variance due to scanning instability reduces the average phase variance over the image, in this case to a value of 0.058 rad^2, representing a lowering of the noise floor to less than 3% of the image dynamic range.

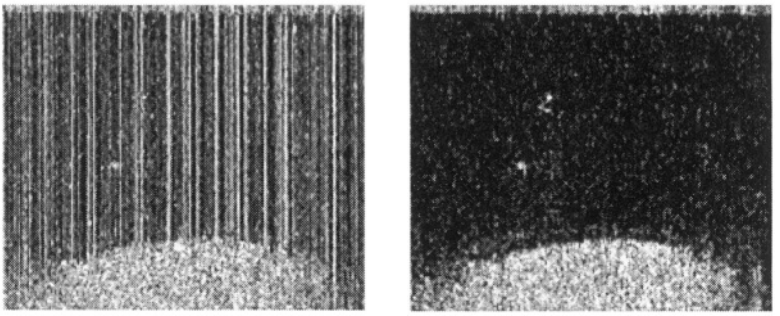

Figure 15. Phase-resolved flow image from the inside surface of a human finger, demonstrating the effect of correction in data processing for phase instability. The image is 1.2 x 1.2 mm, uncorrected on the left, corrected on the right. For details of these corrections, see text. Reprinted from [28] with permission of the Optical Society of America.

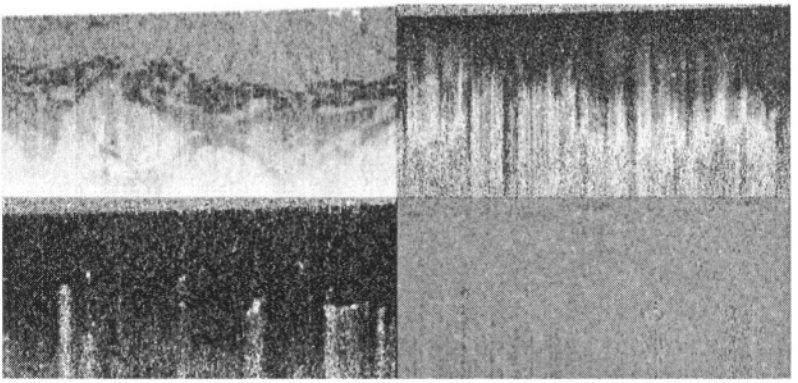

Figure 16. Single frame from a movie sequence demonstrating simultaneous *in vivo* imaging of structure, birefringence and flow at the inner surface of a human lip. Upper left; structural image. Upper right; phase map. Lower left; phase variance. Lower right; Doppler shift. Each image is 2.5 mm x 1.2 mm, with all data acquired in 1 second. Reprinted from [28] with permission of the Optical Society of America.

Figure 16 presents images taken at the inner surface of the lip of a human volunteer. The uppermost layer in the structural image is the squamous epithelium, ranging between 200 and 400 μm in thickness. The lamina propria appears below as a darker and more uneven layer, 100 to 200 μm thick, with submucosal tissue extending to the lower boundary of the image. The transition from black to white in the phase map indicates the presence of birefringent tissue, approximately following the epithelium – lamina propria boundary. Blood vessels ranging in diameter from 25 to 100 μm are evident in the Doppler shift and phase variance maps, located in the lower two structural layers at depths between 400 and 600 μm. Blood flow is visualized

with high contrast in the phase variance map, while the Doppler map indicates the directionality of flow as positive Doppler shifts are mapped towards white and negative shifts towards black, as illustrated by the opposite gray scale mapping of two small vessels circled at the left side of the image.

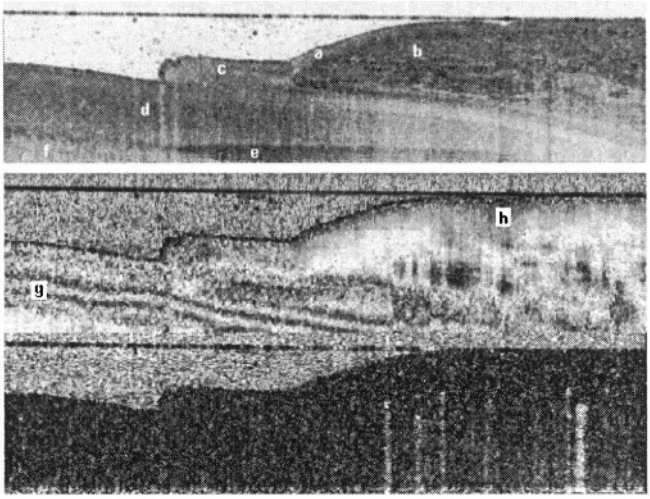

Figure 17. Intensity, birefringence, and flow (phase variance) images of the proximal nail fold of a human volunteer (upper, middle, and lower images respectively). The epidermal (a) and dermal (b) areas of the nail fold, cuticle (c), nail plate (d), nail bed (e), and nail matrix (f) are all identifiable in the intensity image. The birefringence image shows the phase retardation of the epidermal-dermal boundary (g) as well as the lower half of the nail plate (h). Small transverse blood vessels in the nail fold are distinguishable in the flow image by their lighter color. Each image is 5 mm × 1.2 mm, with all data acquired in 1 s. Reprinted from [24] with permission of the Optical Society of America.

Figure 17 shows a single frame of a movie acquired at the nail fold of a human volunteer *in vivo.* An MPEG movie demonstrating the real-time MF-OCT system can be found in Ref. [24] at: http://www.opticsexpress.org/abstract.cfm?URI=OPEX-11-7-782

18.6 PS-OCT IN OPHTHALMOLOGY

In this subsection, *in vivo* depth-resolved birefringence measurements of the human retinal nerve fiber layer (RNFL) are presented. Glaucoma causes nerve fiber layer damage, which may cause loss of retinal birefringence. Therefore, PS-OCT is a potentially useful technique for the early detection of glaucoma. The presented PS-OCT instrument allows for real-time imaging of the human retina *in vivo,* co-registered with retinal video images of the location of PS-OCT scans.

Glaucoma is the world's second leading cause of blindness. Glaucoma causes damage to the retinal ganglion cells and thinning of the retinal nerve fiber layer (RNFL). When glaucoma is detected at an early stage, further loss of vision can be prevented by medication or surgery. Currently, there is no direct method that can measure the health and function of the RNFL. The visual field test is the current standard method of subjectively detecting loss of peripheral vision from glaucoma. However, up to 40% of the nerves can be irreversibly damaged before a clinically detectable loss of peripheral vision occurs [40]. Therefore, there is a need for objective instruments that can detect nerve fiber layer thinning prior to loss of vision. Two of such instruments that are in development are optical coherence tomography (OCT) and scanning laser polarimetry (SLP). With OCT, cross-sectional structural images of the retina can be made *in vivo,* allowing determination of the RNFL thickness [41,42]. From light reflected back from the retina, SLP measures polarization state changes, which are attributed to the birefringence of the RNFL [43]. Polarization Sensitive Optical Coherence Tomography (PS-OCT) combines the depth resolution of OCT with the polarization sensitivity of SLP to obtain depth resolved images of the optical birefringence of biological tissue [6,8,10,14,20,28,44]. *Ex vivo* measurements of primate and enucleated rabbit eyes demonstrated birefringence in the retinal nerve fiber layer and showed good correlation between the thickness determined with PS-OCT and histology [9, 45]. Huang and Knighton measured the single pass phase retardation of isolated rat RNFL [46]. Measurement of RNFL optical birefringence will enhance specificity in determining its thickness in structural OCT images. Although speculative, a decrease in birefringence could be an early sign of glaucomatous atrophy of the RNFL. Measurements at six different locations around the optic nerve head (ONH) will be presented.

18.6.1 Ophthalmic PS-OCT Instrument

The experimental configuration to measure the RNFL birefringence in human subjects *in vivo* is shown in Figure 18. A high power superluminescent diode (Superlum, Russia) generated a broadband spectrum with a power of 4.6 mW (after polarization) and with a full width half maximum (FWHM) bandwidth of 50 nm centered at 839 nm. As shown in Figure 18, a fiber coupler divided the light between sample and reference arms. The beam splitter ratio in the interferometer was chosen as 70/30, since the power that can be sent into the eye has to be below the ANSI standard limit of 610 μW [47].

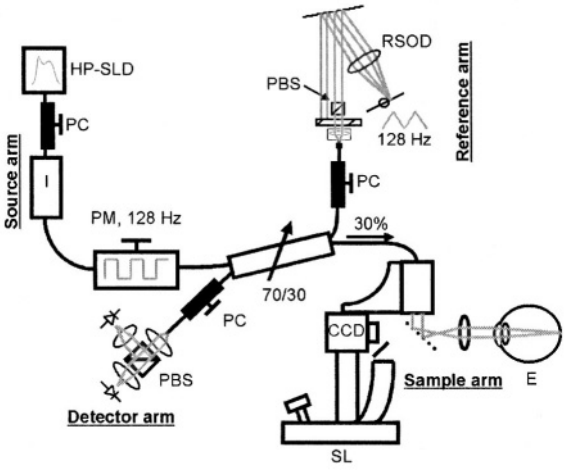

Figure 18. Schematic overview of the fiber-based PS-OCT setup. Near infra red light from a high power super luminescent diode (HP-SLD) is sent through an isolator (I), after which it is polarization modulated (PM) and split by means of a 70/30 fiber coupler. 70% of the light is injected into the RSOD, where a polarizer (PBS) ensures that light is always in the same linear state, regardless of changes in the polarization state in the fiber before the RSOD. 30% of the power is directed towards the slit lamp in the sample arm. Light reflected back from the sample arm and delay line interfere in the detection arm and are split by a polarizing beam splitter (PBS), after which both orthogonal states are detected by means of two silicon detectors. Reprinted from [44] with permission of the Society of Photo-Optical Instrumentation Engineers.

As shown in Figure 19 the sample arm consisted of a telecentric XY retina scanner and a headrest from a standard slit lamp, with the sample beam pivoting about the center of the entrance pupil of the eye. Because aberrations are incurred in the cornea and lens, optimal spot size (and therefore maximum retinal reflection) is obtained when the beam has a width of about 2 to 3 mm at the pupil plane [48]. A dichroic beam splitter was used to reflect the sample beam towards a D40 ophthalmic Volk lens positioned 25 mm in front of the cornea. Incident power on the eye was 500 ± 5 μW, well below the maximum level specified in the ANSI standards. The retina was illuminated with an incandescent source of a slit lamp through the dichroic beam splitter. Both PS-OCT beam and illumination beam traveled off-axis through the Volk lens to avoid the strong surface reflections from this lens and the cornea. A charged coupled device (CCD) camera was available for visual inspection of the retina and localization of PS-OCT scans in the retina.

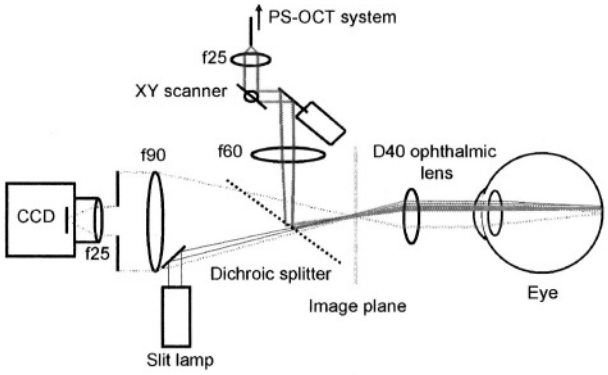

Figure 19. Schematic overview of the optical paths in the slit lamp. A single mode fiber guides the OCT beam into an XY galvanometer scanner. The f60 lens (f = 60 mm), positioned 60 mm from the XY galvanometer scanner in the pupil plane, focuses the PS-OCT beam in the image plane. The ophthalmic D40 lens images the PS-OCT spot of the image plane onto the retina. During scanning, the sample beam pivots in the pupil plane positioned near the corneal surface. The retina is illuminated by the incoherent source of the slit lamp. The ophthalmic lens forms an image of the retina in the image plane, which is projected on the CCD chip through a dichroic splitter, transparent for visible light and highly reflective for near infra red light. To avoid specular reflections that decrease quality of recorded video images, the OCT beam, the illumination beam and the fixation light propagate off-axis through the D40 ophthalmic lens. Reprinted from [44] with permission of the Society of Photo-Optical Instrumentation Engineers.

During a PS-OCT B-scan, which took 2 seconds, eight CCD images were acquired subsequently and stored to hard disk. While thirty percent of the power was sent to the sample, the remaining seventy percent of the power was directed towards the reference arm, consisting of a rapid scanning optical delay line (RSOD) [21, 22]. A polarizing beam splitter was used as a polarizer in order to ensure that light in the RSOD was always in the same linear state, regardless of changes in the polarization state in the fiber before the RSOD. A polarization controller prior to the RSOD was aligned such that the power reflected from the RSOD was constant for both input polarization states. The dispersion in sample and reference arms was matched by adjusting the grating to lens distance in the delay line. The delay line's scanning mirror was positioned off-axis and driven by a triangular waveform with a frequency of 128 Hz, synchronized with the polarization modulator, which was driven by a block wave of the same frequency. The carrier signal was at approximately 330 kHz and signals were digitally bandpass filtered with a bandwidth of 120 kHz centered at the carrier frequency. Due to the enhanced splitter ratio, seventy percent of the returned light from the sample arm goes to the detection arm, while thirty percent of the light returning from the RSOD reaches the detectors. The detection arm consisted of a polarization controller and a polarizing beam splitter that split

the light into two orthogonal components before detection by two silicon detectors. Signal detection was shot noise limited. The two signals were digitized with a 12-bit 2.5 MHz A/D board and immediately stored to hard disk. During one B-scan, 512 A-lines of 8192 samples over a depth of 1 mm in tissue were acquired in 2 seconds. The accuracy of the phase retardation measurement was determined by measuring a calibrated mica waveplate with 58.6° single pass retardance. Since the setup was designed to measure samples in a human eye through a cornea and lens, the set-up had to be adapted for this calibration. An image of the waveplate was created in the image plane (see Figure 19) by shifting the ophthalmic lens and increasing the length of the delay line. The waveplate was slightly tilted such that a small amount of light was reflected back into the PS-OCT system. Data was taken at two different optic axis orientations of the wave plate that were 90° apart. Data analysis on the waveplate measurements showed that the birefringence measurement was accurate within 3%, independent of the orientation of the optic axis of the waveplate.

18.6.2 Structural OCT imaging

All human experiments were performed under a protocol approved by the institutional review boards of both the Massachusetts Eye and Ear Infirmary and the Massachusetts General Hospital. Experiments were performed on a healthy 38 year-old-adult who had given informed consent. Prior to the measurements, the volunteer's right eye was dilated with a solution of phenylephrine hydrochloride 5.0% and tropicamide 0.8%. Images were taken superior, inferior, temporal and nasal to the optic nerve head.

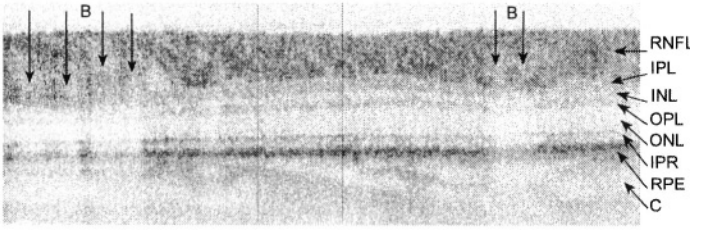

Figure 20. Realigned intensity image of an area superior to the optic nerve head. The image is 2.1 mm wide by 0.7 mm deep. The dark top layer is the RNFL, followed by the inner plexiform layer (IPL), the inner nuclear layer (INL), the outer plexiform layer (OPL) and the outer nuclear layer (ONL). The two dark bands at the bottom of the image are the interface between inner and outer segments of the photoreceptor layer (IPR) and the retinal pigmented epithelium (RPE). The structure below the RPE consists of choriocapillaris and choroid (C). The position of blood vessels can be recognized by a lower reflection signal below the vessels, due to absorption in the blood. The blood vessels (B) are marked with vertical arrows. Double pass phase retardation calculations were performed on regions of 64 averaged A-lines. An example of such a region is indicated by the two vertical lines. Reprinted from [44] with permission of the Society of Photo-Optical Instrumentation Engineers.

By processing the interference fringe data as described earlier [8, 14, 20], the 8192 samples within one A-line were converted to 1024 Stokes parameters I, Q, U and V. An intensity image therefore consisted of 512 A-lines of 1024 pixels each, showing the intensity I gray-scale encoded on a logarithmic scale over a dynamic range of 37 dB. White pixels represent areas with low reflection, while highly reflective areas are represented by black pixels. Figure 20 presents an intensity image, recorded in an area superior to the optic nerve head. The image was realigned to remove axial motion artifacts. Structural features of the different layers in the retina are evident. Based on the work done by Drexler *et al,* subsequent layers can be identified as follows [42]: the dark top layer is the highly scattering RNFL. At this retinal location, the thin ganglion cell layer located below the RNFL is difficult to identify. Below the RNFL we find the less scattering inner plexiform layer (IPL), the nearly transparent inner nuclear layer (INL), the scattering outer plexiform layer (OPL) and the nearly transparent outer nuclear layer (ONL). Both nuclear layers can be identified by a low reflectivity. The two dark bands below the ONL are the interface between inner (IPR) and outer segments of the photoreceptor layer (OPR) and the retinal pigmented epithelium (RPE). The structure below the RPE consists of blood vessels in choriocapillaris and choroid (C). The presence of blood vessels in the RNFL at the left and right side of the image is indicated by a reduced intensity reflected from the RPE below these structures, which is attributed to signal attenuation by blood absorption. The blood vessels are marked with arrows.

18.6.3 Birefringence of the RNFL

For double-pass phase retardation (DPPR) calculations, two adjacent A-lines, created with two different input polarization states are necessary to calculate one DPPR A-line. In the phase retardation calculation, a considerable reduction of speckle noise was achieved by averaging the Stokes parameters of 32 adjacent A-lines with the same input polarization state. The surface Stokes vector was calculated 10 μm below the surface edge, which was determined from the I Stokes parameter in an A-line by a threshold function, preceded by a 3 x 3 median filter. Stokes vectors at the RNFL's surface were compared with Stokes vectors at lower depths to determine DPPR and optic axis orientation [8, 14, 20]. Figure 21 shows the evolution of the two incident Stokes states over the surface of the Poincaré sphere with increasing depth of tissue for the delineated region of 64 A-lines in Figure 20. The rotation of both states over an arc around a single axis explicitly demonstrates birefringence with a single optic axis, as expected for the regularly oriented fibers in the RNFL. The angle between two equidistant Stokes vectors was approximately 90° on the Poincaré sphere.

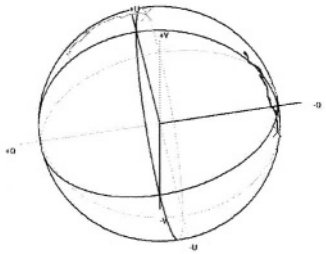

Figure 21. Evolution of the two incident polarization states over the Poincaré sphere as a function of depth, using data averaged over 64 A-lines. The Poincaré sphere is oriented such that the axis of rotation is pointing out of the plane of the drawing. Thick lines on the sphere's surface show the change in Stokes vectors over a distance of 140 μm in the RNFL and crosses indicate the surface Stokes states. The DPPR is derived from the angle of rotation about the optic axis, starting with the Stokes vector that belongs to the surface and finishing with the vector that belongs to a certain depth. Reprinted from [44] with permission of the Society of Photo-Optical Instrumentation Engineers.

Corneal birefringence changes the incident polarization state unpredictably [49]. Since the RNFL surface is used as a reference in the phase retardation calculation, our method is not influenced by corneal birefringence.

Images taken with the slit lamp's near infra red sensitive CCD camera were used to determine the location of a B-scan in the retina. PS-OCT data was analyzed in order to quantify the birefringence of the RNFL and to determine a relationship between location in the RNFL and birefringence. In an image, the RNFL was divided into 8 regions, each with 64 A-lines. The DPPR per unit depth (DPPR/UD) of each region was calculated. Data points that were considered to originate from the RNFL were fitted with a linear least squares fit, with the slope yielding the reported DPPR/UD. The corresponding intensity graph was used to determine the boundaries of the RNFL. Regions with visible blood vessels were excluded, because the absence of birefringence in blood vessels distorted the birefringence measurement in nerve tissue.

As an example, Figure 22 shows the DPPR, the reflected intensity, and a linear fit to the DPPR, which corresponds to the delineated area in Figure 20 and data in Figure 21. Both the intensity and phase retardation graphs were used to determine the position of the RNFL boundary, represented by the vertical dash-dot line. In the intensity graph, a sharp drop in intensity indicates the border between RNFL and ganglion cell layer. In the DPPR graph, birefringence of RNFL tissue linearly increases the DPPR as a function of depth. Between the RNFL and the choroid, the DPPR is constant

and indicates and absence of birefringence in inner and outer plexiform layer, inner and outer nuclear layer, inner and outer segments of the photoreceptor layer, RPE and choroid. The strong reflection from the RPE renders values, which are equal to the values measured at the bottom of the RNFL, strongly supporting an absence of birefringence in between the RNFL and the RPE. Therefore, the transition from a linearly increasing value to a constant value in the DPPR graph indicates the RNFL boundary. Below the RPE, the intensity drops further while the double pass phase retardation increases. This could indicate the presence of a highly birefringent medium like collagen in the sclera.

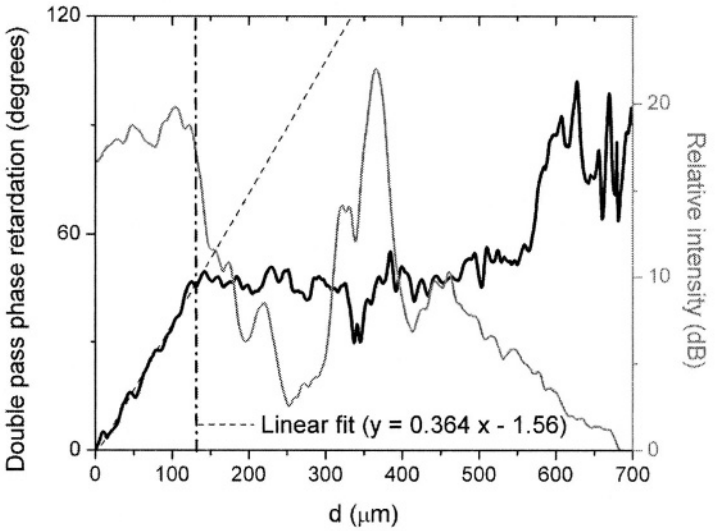

Figure 22. Double pass phase retardation as a function of depth, using the data from Figures. 20 and 21. Black line: double pass phase retardation; gray: reflected intensity; dashed: least square linear fit to double pass phase retardation data over a region considered to belong to the RNFL. The vertical dash-dot line represents the estimated RNFL boundary. Reprinted from [44] with permission of the Society of Photo-Optical Instrumentation Engineers.

An alternative explanation for the rise in DPPR values is that when the reflected signal at this depth is low, as can be seen in the intensity graph of Figure 22, the DPPR increases to 115° [8, 10]. This lower reflected signal is possibly caused by the attenuation of light in the blood vessels of the choroid above this layer. In order to show the relationship between birefringence and the position in the retina, data was taken from six different regions and analyzed. These six regions were temporal, nasal, inferior and superior to the optic nerve head, with locations close and far away from the optic nerve

head in the inferior and superior regions. Only one area close to the optic nerve head was selected in the temporal and nasal regions. In the inferior and superior parts, the RNFL is relatively thick and changes in thickness as a function of the distance from the center of the optic nerve head.

In Figure 23, the relationship between RNFL averaged thickness, retinal location and measured DPPR/UD is shown. The horizontal and vertical error bars indicate the standard deviations of RNFL thickness and DPPR/UD within an averaged area, respectively. The following trend is observed: thicker nerve fiber layer tissue located in inferior and superior regions exhibits stronger birefringence than the thinner tissue located in the temporal and nasal regions. This observed difference might be caused by a difference in nerve tissue birefringence as a function of location or by a difference in birefringence as a function of thickness. DPPR/UD values are not constant, but vary in between 0.18 and 0.37°/μm.

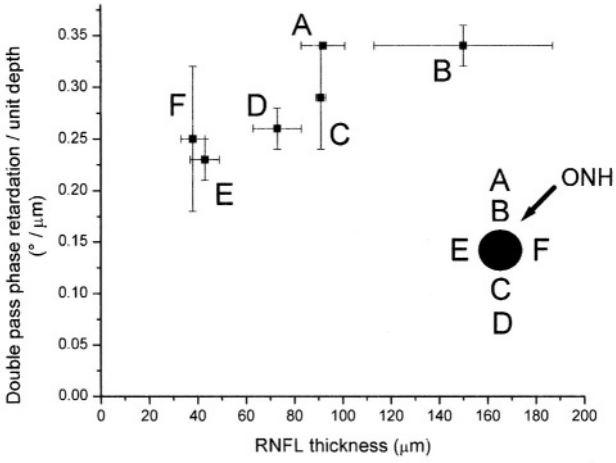

Figure 23. The relationship between the nerve fiber layer thickness, the retinal location and the measured DPPR. The letters in the drawing indicate the locations of averaged measurements around the ONH and correspond to the labeled values in the graph. The number of averaged points per area was as follows: A [n= 15]; B [n = 13]; C [n = 15]; D [n = 16]; E [n = 16]; F [n = 16]. The error bars indicate the standard deviation of the averaged thickness and DPPR/UD values. The DPPR/UD values of this volunteer's RNFL vary in between 0.18 and 0.37 ° / μm. Reprinted from [44] with permission of the Society of Photo-Optical Instrumentation Engineers.

18.6.4 Conclusion

Ducros *et al.* measured the DPPR/UD at a wavelength of 859 nm in the RNFLs of primates [45]. They found a typical value of $0.29°/\mu m$. Huang and Knighton measured the single pass phase retardation of isolated rat RNFL [46]. At 830 nm and converting to double pass, they found average DPPR/UD values of $0.20°/\mu m$. Both results are in good agreement with values reported here.

PS-OCT is a modality suitable for *in vivo* depth resolved birefringence measurements in the human retina. Preliminary measurements on one volunteer show that the double pass phase retardation in the RNFL near the optic nerve head is not constant, but varies in between 0.18 and $0.37°/\mu m$. The following trend was observed: thicker nerve fiber layer tissue located in inferior and superior regions exhibits stronger birefringence than the thinner tissue located in the temporal and nasal regions.

18.7 FUTURE DIRECTIONS IN PS-OCT

The potential biological and medical applications of PS-OCT are just beginning to be explored. Much work remains for further development of PS-OCT. We anticipate progress will proceed in three major areas, these include: instrumentation, biological and medical applications, and data interpretation/image processing. Many clinical applications of PS-OCT will require a fiber based instrument that can record images at frame rates comparable to current OCT systems (~5 frames/s). Recently, we reported on fiber based high speed polarization sensitive systems at 1.3 micron.[20, 28] Because many components in biological materials contain intrinsic and/or form birefringence, PS-OCT is an attractive technique for providing an additional contrast mechanism that can be used to image/identify structural components. Moreover, because functional information in some biological systems is associated with transient changes in birefringence, the possibility of functional PS-OCT imaging should be explored. PS-OCT may hold considerable potential for monitoring, in real-time, laser surgical procedures involving birefringent biological materials. Because many laser surgical procedures rely on a photothermal injury mechanism, birefringence changes in subsurface tissue components measured using PS-OCT may be used as a feedback signal to control laser dosimetry in real-time. The loss of birefringence in thermally denatured collagen might provide a means for *in vivo* burn depth assessment [6, 8, 29]. Changes in birefringence of the retinal nerve fiber layer might provide an early indication of the onset of glaucoma. Finally, many features of PS-OCT interference fringe data require additional interpretation and study. Because polarization changes in light propagating in the sample may be used as an additional contrast mechanism, the relative

contribution of light scattering and birefringence-induced changes requires further study and clarification. In principle, one would like to distinguish polarization changes due to scattering and birefringence at each position in the sample and utilize each as a potential contrast mechanism. In conclusion, we anticipate PS-OCT will continue to advance rapidly and be applied to novel problems in clinical medicine and biological research.

ACKNOWLEDGEMENT

A number of people have made invaluable contributions to the work presented in this chapter. First and foremost Thomas Milner, who introduced me to the field of the optical polarization properties of tissue. Furthermore the post-docs and graduate students Christoper Saxer, Boris Hyle Park, Nader Nassif, Renu Tripathi, Mark Pierce and Barry Cense, whose published and unpublished work forms the basis of the presented results.

Research grants from the National Eye Institute (1R 24 EY 12877), Whitaker Foundation (26083), Department of Defense (F4 9620-01-1-0014), and a generous gift from Dr. and Mrs. J.S. Chen to the Optical Diagnostics Program of the Wellman Center of Photomedicine are gratefully acknowledged for the support of this research.

REFERENCES

1. D. Huang, E.A. Swanson, C.P. Lin, J.S. Schuman, W.G. Stinson, W. Chang, M.R. Hee, T. Flotte, K. Gregory, and C.A. Puliafito, "Optical coherence tomography," *Science* **254**, 1178-1181 (1991).
2. H.F. Hazebroek and A.A. Holscher, "Interferometric ellipsometry," *J. Physics E-Scientific Instr.* **6**, 822-826 (1973).
3. T.P. Newson, F. Farahi, J.D.C. Jones, and D.A. Jackson, "Combined interferometric and polarimetric fiber optic temperature sensor with a short coherence length source," *Opt. Communs.* **68**, 161-165 (1988).
4. M. Kobayashi, H. Hanafusa, K. Takada, and J. Noda, "Polarization-independent interferometric optical-time-domain reflectometer," *J. Lightwave Technol.* **9**, 623-628 (1991).
5. M.R. Hee, D. Huang, E.A. Swanson, and J.G. Fujimoto, "Polarization-sensitive low-coherence reflectometer for birefringence characterization and ranging," *J. Opt. Soc. Am. B* **9**, 903-908 (1992).
6. J.F. de Boer, T.E. Milner, M.J.C. van Gemert, and J.S. Nelson, "Two-dimensional birefringence imaging in biological tissue by polarization-sensitive optical coherence tomography," *Opt. Lett.* **22**, (1997).
7. M.J. Everett, K. Schoenenberger, B.W. Colston, and L.B. Da Silva, "Birefringence characterization of biological tissue by use of optical coherence tomography," *Opt. Lett.* **23**, 228-230(1998).

8. B.H. Park, C. Saxer, S.M. Srinivas, J.S. Nelson, and J.F. de Boer, *"In vivo* burn depth determination by high-speed fiber-based polarization sensitive optical coherence tomography," *J. Biomed Opt.* **6**, 474-479 (2001).
9. M.G. Ducros, J.F. de Boer, H.E. Huang, L.C. Chao, Z.P. Chen, J.S. Nelson, T.E. Milner, and H.G. Rylander, "Polarization sensitive optical coherence tomography of the rabbit eye," *IEEE J. Select. Top. Quant. Electr.* **5**, 1159-1167 (1999).
10. B. Cense, T.C. Chen, B.H. Park, M.C. Pierce, and J.F. de Boer, *"In vivo* depth-resolved birefringence measurements of the human retinal nerve fiber layer by polarization-sensitive optical coherence tomography," *Opt. Lett.* **27**, 1610-1612 (2002).
11. J.F. de Boer and T.E. Milner, "Review of polarization sensitive optical coherence tomography and Stokes vector determination," *J. Biomed. Opt.* **7**, 359-371 (2002).
12. W.A. Shurcliff and S.S. Ballard, *Polarized Light* (Van Nostrand, New York, 1964).
13. J.F. de Boer, T.E. Milner, and J.S. Nelson, "Two dimensional birefringence imaging in biological tissue using phase and polarization sensitive optical coherence tomography" in *Trends in Optics and Photonics (TOPS): Advances in Optical Imaging and Photon Migration* (OSA, Washington, DC, 1998).
14. J.F. de Boer, T.E. Milner, and J.S. Nelson, "Determination of the depth-resolved Stokes parameters of light backscattered from turbid media by use of polarization-sensitive optical coherence tomography," *Opt. Lett.* **24**, 300-302 (1999).
15. J.F. de Boer, T.E. Milner, M.G. Ducros, S.M. Srinivas, and J.S. Nelson, *Polarization-sensitive optical coherence tomography,* in *Handbook of Optical Coherence Tomography,* B.E. Bouma and G.J. Tearney, eds. (Marcel Dekker, Inc., New York, 2002), 237-274.
16. C.F. Bohren and D.R. Huffman, *Absorption and Scattering of Light by Small Particles* (Wiley, New York, 1983).
17. G. Yao and L.V. Wang, "Two-dimensional depth-resolved Mueller matrix characterization of biological tissue by optical coherence tomography," *Opt. Lett.* **24**, 537-539 (1999).
18. D.P. Davé, T. Akkin, and T.E. Milner, "Polarization-maintaining fiber-based optical low coherence reflectometer for birefringence characterization and ranging," *Opt. Lett.* (2003).
19. C.D. Poole, "Statistical treatment of polarization dispersion in single-mode fiber," *Opt. Lett.* **13**, 687-689 (1988).
20. C.E. Saxer, J.F. de Boer, B.H. Park, Y.H. Zhao, Z.P. Chen, and J.S. Nelson, "High-speed fiber-based polarization-sensitive optical coherence tomography of *in vivo* human skin," *Opt. Lett.* **25**, 1355-1357 (2000).
21. G.J. Tearney, B.E. Bouma, and J.G. Fujimoto, "High-speed phase- and group-delay scanning with a grating-based phase control delay line," *Opt. Lett.* **22**, 1811-1813 (1997).
22. A.M. Rollins, M.D. Kulkarni, S. Yazdanfar, R. Ung-arunyawee, and J.A. Izatt, *"In vivo* video rate optical coherence tomography," *Opt. Express* **3**, 219-229 (1998).
23. J.F. de Boer, S.M. Srinivas, B.H. Park, T.H. Pham, Z.P. Chen, T.E. Milner, and J.S. Nelson, "Polarization effects in optical coherence tomography of various biological tissues," *IEEE J. Select. Top. Quant. Electr.* **5**, 1200-1204 (1999).
24. B.H. Park, M.C. Pierce, B. Cense, and J.F. de Boer, "Real-time multi-functional optical coherence tomography," *Opt. Express* **11,** 782-793 (2003).
25. S.L. Jiao and L.H.V. Wang, "Two-dimensional depth-resolved Mueller matrix of biological tissue measured with double-beam polarization-sensitive optical coherence tomography," *Opt. Lett.* **27**, 101-103 (2002).
26. S.L. Jiao and L.H.V. Wang, "Jones-matrix imaging of biological tissues with quadruple- channel optical coherence tomography," *J. Biomed. Opt.* **7**, 350-358 (2002).

27. N. Vansteenkiste, P. Vignolo, and A. Aspect, "Optical reversibility theorems for polarization - application to remote-control of polarization," *J. Opt. Soc. Am. A* **10**, 2240-2245 (1993).
28. M.C. Pierce, B.H. Park, B. Cense, and J.F. de Boer, "Simultaneous intensity, birefringence, and flow measurements with high speed fiber-based optical coherence tomography," *Opt. Lett.* **27**, 1534-1536 (2002).
29. J.F. de Boer, S.M. Srinivas, A. Malekafzali, Z. Chen, and J.S. Nelson, "Imaging thermally damaged tissue by polarization sensitive optical coherence tomography," *Opt. Express* **3**, (1998).
30. J.M. Schmitt and S.H. Xiang, "Cross-polarized backscatter in optical coherence tomography of biological tissue," *Opt. Lett.* **23**, 1060-1062 (1998).
31. J.E. Roth, J.A. Kozak, S. Yazdanfar, A.M. Rollins, and J.A. Izatt, "Simplified method for polarization-sensitive optical coherence tomography," *Opt. Lett.* **26**, 1069-1071 (2001).
32. Z.P. Chen, I.E. Milner, S. Srinivas, X.J. Wang, A. Malekafzali, M.J.C. van Gemert, and J.S. Nelson, "Noninvasive imaging of *in vivo* blood flow velocity using optical Doppler tomography," *Opt. Lett. 22,* 1119-1121 (1997).
33. J.A. Izatt, M.D. Kulkami, S. Yazdanfar, J.K. Barton, and A.J. Welch, *"In vivo* bidirectional color Doppler flow imaging of picoliter blood volumes using optical coherence tomography," *Opt. Lett.* **22**, (1997).
34. Y.H. Zhao, Z.P. Chen, C. Saxer, S.H. Xiang, J.F. de Boer, and J.S. Nelson, "Phase-resolved optical coherence tomography and optical Doppler tomography for imaging blood flow in human skin with fast scanning speed and high velocity sensitivity," *Opt. Lett.* **25**, 114-116 (2000).
35. Y.H. Zhao, Z.P. Chen, C. Saxer, Q.M. Shen, S.H. Xiang, J.F. de Boer, and J.S. Nelson, "Doppler standard deviation imaging for clinical monitoring of *in vivo* human skin blood flow," *Opt. Lett.* **25**, 1358-1360 (2000).
36. V. Westphal, S. Yazdanfar, A.M. Rollins, and J.A. Izatt, "Real-time, high velocity-resolution color Doppler optical coherence tomography," *Opt. Lett.* **27**, (2002).
37. A.M. Rollins, S. Yazdanfar, J.K. Barton, and J.A. Izatt, "Real-time *in vivo* colors Doppler optical coherence tomography," *J. Biomed. Opt.* **7**, 123-129 (2002).
38. Y.H. Zhao, Z.P. Chen, Z.H. Ding, H.W. Ren, and J.S. Nelson, "Real-time phase-resolved functional optical coherence tomography by use of optical Hilbert transformation," *Opt. Lett.* **27**, 98-100 (2002).
39. J.F. de Boer, C.E. Saxer, and J.S. Nelson, "Stable carrier generation and phase-resolved digital data processing in optical coherence tomography," *Appl. Opt.* **40**, (2001).
40. H.A. Quigley, E.M. Addicks, and W.R. Green, "Optic nerve damage in human glaucoma. III. Quantitative correlation of nerve fiber loss and visual field defect in glaucoma, ischemic neuropathy, papilledema, and toxic neuropathy," *Arch. Ophthal.* **100**, 135-146(1982).
41. J.S. Schuman, M.R. Hee, C.A. Puliafito, C. Wong, T. Pedut-Kloizman, C.P. Lin, E. Hertzmark, J.A. Izatt, E.A. Swanson, and J.G. Fujimoto, "Quantification of nerve fiber layer thickness in normal and glaucomatous eyes using optical coherence tomography," *Arch. Ophthal.* **113**, 586-596 (1995).
42. W. Drexler, H. Sattmann, B. Hermann, T.H. Ko, M. Stur, A. Unterhuber, C. Scholda, O. Findl, M. Wirtitsch, J.G. Fujimoto, and A.F. Fercher, "Enhanced visualization of macular pathology with the use of ultrahigh-resolution optical coherence tomography," *Arch. Ophthal.* **121**, 695-706 (2003).
43. R.N. Weinreb, A.W. Dreher, A. Coleman, H. Quigley, B. Shaw, and K. Reiter, "Histopathalogic validation of Fourier-ellipsometry measurements of retinal nerve fiber layer thickness," *Arch. Ophthal.* **108**, 557-560 (1990).

44. B. Cense, T.C. Chen, B.H. Park, M.C. Pierce, and J.F. de Boer, "*In vivo* birefringence and thickness measurements of the human retinal nerve fiber layer using polarization-sensitive optical coherence tomography," *J. Biomed. Opt.* (2004).
45. M.G. Ducros, J.D. Marsack, H.G. Rylander, S.L. Thomsen, and T.E. Milner, "Primate retina imaging with polarization-sensitive optical coherence tomography," *J. Opt. Soc. Am. A* **18**, 2945-2956 (2001).
46. X.R. Huang and R.W. Knighton, "Linear birefringence of the retinal nerve fiber layer measured *in vitro* with a multispectral imaging micropolarimeter," *J. Biomed. Opt.* **7**, 199-204 (2002).
47. American National Standards Institute, "American National Standard for Safe Use of Lasers Z136.1." 2000: Orlando.
48. F.W. Campbell and D.G. Green, "Optical and retinal factors affecting visual resolution," *J. Physiology (London)* **181,** 576-& (1965).
49. D.S. Greenfield, R.W. Knighton, and X.R. Huang, "Effect of corneal polarization axis on assessment of retinal nerve fiber layer thickness by scanning laser polarimetry," *Am. J. Ophthal.* **129,** 715-722 (2000).

Chapter 19

OPTICAL DOPPLER TOMOGRAPHY

Zhongping Chen
Department of Biomedical Engineering, Beckman Laser Institute, University of California, Irvine, Irvine, CA 92612

Abstract: This chapter describes optical Doppler tomography (ODT). This is an imaging modality that combines Doppler principles with optical coherence tomography to image tissue structure and blood flow velocity simultaneously. We will review the principle and technology of ODT, and illustrate a few examples of its applications.

Key words: Optical Doppler tomography, Doppler OCT, biomedical imaging

19.1 INTRODUCTION

Noninvasive techniques for imaging *in vivo* blood flow are of great value for biomedical research and clinical diagnostics [1] where many diseases have a vascular etiology or component. In dermatology, for example, the superficial dermal plexus alone is particularly affected by the presence of disease (e.g., psoriasis, eczema, scleroderma), malformation (e.g., port-wine stain, hemangioma, telangiectasia), or trauma (e.g., irritation, wound, burn). In these situations, it would be most advantageous to the clinician if blood flow and structural features could be isolated and probed at user-specified discrete spatial locations in either the superficial or deep dermis. In ophthalmology, many ophthalmic diseases may involve disturbances in ocular blood flow, including diabetic retinopathy, low tension glaucoma, anterior ischemic optic neuritis, and macular degeneration. For example, in diabetic retinopathy, retinal blood flow is reduced and the normal autoregulatory capacity is deficient. Ocular hemodynamics is altered in patients with glaucoma, and severe loss of visual function has been associated with reduced macular blood flow. Simultaneous imaging of tissue

structure and blood flow can provide critical information for early diagnosis of ocular disease. Finally, three-dimensional mapping of microcirculation may also provide important information for the diagnosis and management of cancers. It is known that the microvasculature of mammary tumors has several distinct differences from normal tissues. Tumor vasculature provides significant additional information for the differentiation of benign and malignant tumors [2]. The mapping of *in vivo* blood changes following pharmacological intervention is also important for the development of antiangiogenic drugs for cancer treatment.

Currently, techniques, such as Doppler ultrasound (DUS) and laser Doppler flowmetry (LDF), are used for blood flow velocity determination. DUS is based on the principle that the frequency of ultrasonic waves backscattered by moving particles is Doppler shifted. However, the relatively long acoustic wavelengths required for deep tissue penetration limit the spatial resolution of DUS to approximately 200 μm. Although LDF has been used to measure mean blood perfusion in the peripheral microcirculation, high optical scattering in biological tissue prevents its application for tomographic imaging.

Optical coherence tomography (OCT) is a noninvasive imaging modality for cross-sectional imaging of biological tissue with micrometer scale resolution [3]. OCT uses coherence gating of backscattered light for tomographic imaging of tissue structure. Variations in tissue scattering due to inhomogeneities in the optical index of refraction provide imaging contrast. However, in many instances and especially in the early stages of disease, the change in tissue scattering properties between normal and diseased tissue is small and difficult to measure. One of the great challenges for extending the clinical applications of OCT is to find more contrast mechanisms that can provide physiological information in addition to morphological structure.

Optical Doppler tomography (ODT) (also named Doppler OCT) combines the Doppler principle with OCT to obtain high-resolution tomographic images of static and moving constituents simultaneously in highly scattering biological tissues [5-7]. The first use of coherence gating to measure localized flow velocity was reported in 1991, where the one-dimensional velocity profile of the flow of particles in a duct was measured [4]. In 1997, the first two-dimensional *in vivo* ODT imaging was reported using the spectrogram method [5, 6]. The spectrogram method uses a short time fast Fourier transformation (STFFT) or wavelet transformation to determine the power spectrum of the measured fringe signal [5-10]. Inasmuch as detection of the Doppler shift using STFFT requires sampling the interference fringe intensity over at least one oscillation cycle, the minimum detectable Doppler frequency shift, f_D, varies inversely with the STFFT window size [8-11]. Therefore, velocity sensitivity, spatial

resolution, and imaging speed are coupled. This coupling prevents the spectrogram method from achieving simultaneously both high imaging speed and high velocity sensitivity, which are essential for measuring flow in small blood vessels where flow velocity is low [5-7].

Phase-resolved ODT was developed to overcome these limitations [11, 12]. This method uses the phase change between sequential line scans for velocity image reconstruction [11-14]. Phase-resolved ODT decouples spatial resolution and velocity sensitivity in flow images and increases imaging speed by more than two orders of magnitude without compromising spatial resolution and velocity sensitivity [11, 12]. The minimum flow velocity that can be detected using an A-line scanning speed of 1000 Hz is as low as 10 μm/s while maintaining a spatial resolution of 10 μm. The significant increases in scanning speed and velocity sensitivity make it possible to image *in vivo* tissue microcirculation in human skin [11, 12, 15]. A real-time phase-resolved ODT system that uses polarization optics to perform Hilbert transformation was demonstrated [14]. A number of real-time, phase-resolved ODT systems using hardware and software implementations of a high-speed processor have also been reported [16, 17].

One of the limitations of using the Doppler shift to study the blood flow is that the Doppler shift is only sensitive to the flow velocity parallel to the probing beam. However, in many biological cases where flow direction is not known, Doppler shift measurement alone is not enough to fully quantify the flow. Furthermore, there are many clinical applications, such as ocular blood flow, in which vessels are in the plane perpendicular to the probing beam.

Several methods have been reported to measure the vector flow, including multiple angle measurements. However, sequential measurements with different angles of incident beam will only be useful for measuring steady state flow. A dual-channel, optical low-coherence reflectometer has been demonstrated that performs simultaneous measurements from two incident beams with different angles from two polarization channels [18]. The advantage of the dual channel method is that two incident angle measurements are performed simultaneously. The disadvantage is that probing beams involve polarization optics and may not be suitable for endoscopic applications. A method to measure transverse flow velocity using the bandwidth (standard deviation) of the Doppler spectrum was reported in 2002 [19]. The advantage of this technique is that a single measurement of the Doppler spectrum will provide both transverse and longitudinal flow velocity.

Due to its exceptionally high spatial resolution and velocity sensitivity, ODT has a number of applications in biomedical research and clinical medicine. Several clinical applications of ODT have been demonstrated in our laboratory, including screening vasoactive drugs, monitoring changes in image tissue morphology and hemodynamics following pharmacological

intervention and photodynamic therapy, evaluating the efficacy of laser treatment in port wine stain patients, assessing the depth of burn wounds, and the mapping cortical hemodynamics for brain research [8, 9, 11-13, 15]. Application of ODT in ophthalmology was demonstrated [20]. Recently, endoscopoic applications of ODT for imaging blood flow in the gastrointestinal tracts was also reported [21].

In this chapter, I will review the principle and technology of ODT, and describe a few examples of potential applications of ODT.

19.2 PRINCIPLE AND TECHNOLOGY OF ODT

19.2.1 Doppler Principle

ODT combines the Doppler principle with OCT to obtain high resolution tomographic images of static and moving constituents in highly scattering biological tissues. When light backscattered from a moving particle interferes with the reference beam, a Doppler frequency shift (f_D) occurs in the interference fringe:

$$f_D = \frac{1}{2\pi}(\mathbf{k}_s - \mathbf{k}_i) \bullet \mathrm{v} \ , \tag{1}$$

where $\mathbf{k}_i$ and $\mathbf{k}_s$ are wave vectors of incoming and scattered light, respectively, and $\mathbf{v}$ is the velocity of the moving particle (Figure 1). Since ODT measures the backscattered light, assuming the angle between flow and sampling beam is θ, the Doppler shift equation is simplified to:

$$f_D = \frac{2V\cos\theta}{\lambda_0} \ , \tag{2}$$

where λ_0 is the vacuum center wavelength of the light source. Longitudinal flow velocity (velocity parallel to the probing beam) can be determined at discrete user-specified locations in a turbid sample by measurement of the Doppler shift. Transverse flow velocity can also be determined from the broadening of the spectral bandwidth due to the finite numeric aperture of the probing beam [19].

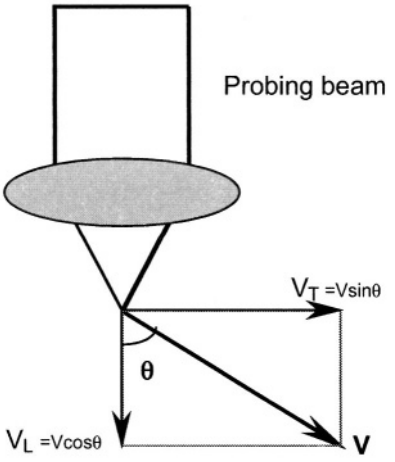

Figure 1. Schematic of flow direction and probe beam angle.

19.2.2 Spectrogram Method

The optical system of ODT is similar to that of OCT. The primary difference is in signal processing. Figure 2 shows an ODT instrument that uses a fiber optic Michelson interferometer with a broadband light as a source [5, 7-9]. Light from a broadband partial coherence source is coupled into a fiber interferometer by a 2x2 fiber coupler and then split equally into reference and target arms of the interferometer. Light backscattered from the turbid sample is coupled back into the fiber and forms interference fringes with the light reflected from the reference arm. High longitudinal (axial) spatial resolution is possible because interference fringes are observed only when the path length differences between the light from the sample arm and reference arm are within the coherence length of the source. A rapid-scanning optical delay (RSOD) line is used for group phase delay and axial scanning. Because RSOD can decouple the group delay from the phase [22], an electro-optical phase modulator is introduced to produce a stable carrier frequency. Temporal interference fringe intensity ($\Gamma_{ODT}(\tau)$) is measured by a single element silicon photovoltaic detector, where τ is the time delay between light from the reference and sample arms, and is related to the optical path length difference (Δ) by $\tau = \Delta/c$. The interference fringe intensity signal is amplified, band pass filtered, and digitized with a high-speed analog-to-digital (A/D) converter. The signal processing is carried out at the same time as data is transferred to the computer, and real-time display can be accomplished with the use of a digital signal processing board.

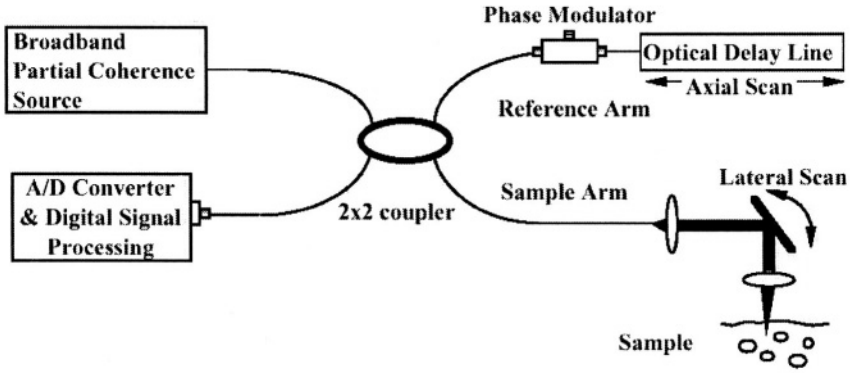

Figure 2. Schematic of the prototype ODT instrument.

Time-frequency analysis can be used to calculate the Doppler shift. Signal processing algorithms to obtain structural and velocity images from recorded temporal interference fringe intensities using the spectrogram method are illustrated in Figure 3.

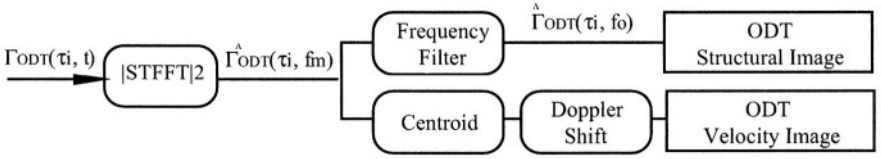

Figure 3. Signal processing algorithms for ODT structural and velocity images.

The spectrogram is an estimate of the power spectrum of the temporal interference fringe intensity ($\hat{\Gamma}_{ODT}(\tau_i, f_j)$) in the i'th time delay window [23]. The power spectrum of the temporal interference fringe at the i'th pixel corresponding to time delay τ_i in the structural and velocity images is calculated by a short-time fast Fourier transformation (STFFT) or a wavelet transformation:

$$\hat{\Gamma}_{ODT}(\tau_i, f_m) = \left| STFT\left(f_m; \Gamma_{ODT}(\tau)\right) \right|^2 , \tag{3}$$

where f_m is the discrete frequency value. A tomographic structural image is obtained by calculating the value of the power spectrum at the phase modulation frequency (f_0). Because the magnitude of the temporal interference fringe intensity decreases exponentially with increasing depth in the turbid sample, a logarithmic scale (equation 4) is used to display the ODT structural images:

$$S_{ODT}(i) = 10 \cdot \log\left(\hat{\Gamma}_{ODT}(\tau_i, f_o)\right). \quad (4)$$

Fluid flow velocity is determined from the Doppler frequency shift (f_D), which is the difference between the carrier frequency established by the optical phase modulation (f_0) and the centroid (f_c) of the measured power spectrum at the i'th pixel:

$$v_{ODT}(i) = \frac{\lambda_o f_D}{2\bar{n}\cos(\theta)} = \frac{\lambda_o (f_c - f_o)}{2\bar{n}\cos(\theta)}, \quad (5)$$

where we have assumed, $\mathbf{k}_s = -\mathbf{k}_i$ and θ is the angle between $\mathbf{k}_i$ and $\mathbf{v}$ (equation 2). The centroid of the measured power spectrum is determined by:

$$f_c = \sum_m f_m \hat{\Gamma}_{ODT}(\tau_i, f_m) / \sum_m \hat{\Gamma}_{ODT}(\tau_i, f_m). \quad (6)$$

Lateral and axial spatial resolutions are limited by the beam spot size and source coherence length (L_C). Velocity resolution is dependent on pixel acquisition time (Δt_p) and the angle (θ) between flow velocity ($\mathbf{v}$) and the incoming light direction ($\mathbf{k}_i$) in the turbid sample; velocity resolution may be improved with a smaller angle (θ) or longer pixel acquisition time (Δt_p).

Figure 4 shows the first *in vivo* structural and blood flow images from a chick chorioallantoic membrane (CAM), which is a well-established model for studying the microvasculature and the effects of vasoactive drugs on blood vessels [5]. In the structural image (Figure 4A), the lumen wall, chorion membrane, and yolk sac membrane are observed. In the velocity image (Figure 4B), static regions (v=0) in the CAM appear dark, while blood flowing at different velocities appears as different brightnesses on the gray scale. The velocity profile taken from a horizontal cross-section passing through the center of the vessel is shown in Figure 4C.

19.2.3 Phase-Resolved ODT Method

Although spectrogram methods allow simultaneous imaging of *in vivo* tissue structure and flow velocity, the velocity sensitivity is limited for high speed imaging. When STFFT or a wavelet is used to calculate flow velocity, the resolution is determined by the window size of the Fourier transformation for each pixel [5-7]. The minimum detectable Doppler frequency shift, f_D, varies inversely with the STFFT window size (i.e., Δf_D

$\approx 1/\Delta t_p$). With a given STFFT window size, velocity resolution ($v_{ODT}(\min)$) is given by:

$$v_{ODT}(\min) = \frac{\Delta f_D(\min)\ \lambda_o}{2\bar{n}\cos(\theta)} \quad . \tag{7}$$

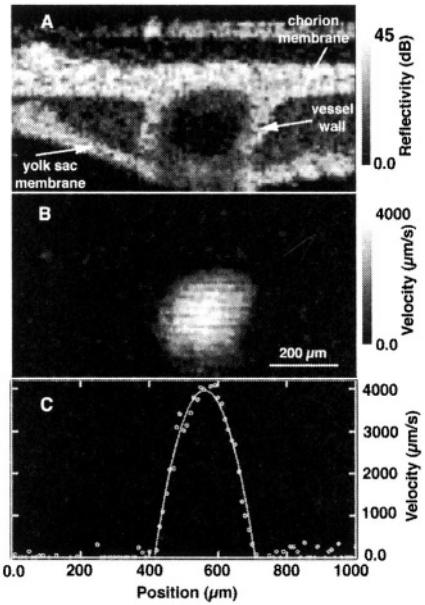

Figure 4. ODT images of in vivo blood flow in a CAM vein. A: structural image; B: velocity image; and C: velocity profile taken from a horizontal cross-section passing through the center of the vein, where the open circles are experimental data and the solid line is a parabolic fit (from Ref. [5]).

Because pixel acquisition time is proportional to the STFFT window size, the image frame rate is limited by velocity resolution. Furthermore, spatial resolution, Δx_p, is also proportional to the STFFT window size. Therefore, a large STFFT window size increases velocity resolution while decreasing spatial resolution. This coupling between velocity sensitivity, spatial resolution, and imaging speed prevents the spectrogram method from achieving simultaneously both high imaging speed and high velocity sensitivity, which are essential for measuring flow in small blood vessels where flow velocity is low [5-7].

Phase-resolved ODT overcomes the compromise between velocity sensitivity and imaging speed by using the phase change between sequential scans to construct flow velocity images (Figure 5) [11, 12, 14, 15].

The phase information of the fringe signal can be determined from the complex analytical signal $\tilde{\Gamma}(t)$, which is determined through analytic

continuation of the measured interference fringe function, $\Gamma(t)$, using a Hilbert transformation [11, 14]:

$$\tilde{\Gamma}(t) = \Gamma(t) + \frac{i}{\pi} P \int_{-\infty}^{\infty} \frac{\Gamma(\tau)}{\tau - t} d\tau = A(t) e^{i\phi(t)} \quad , \tag{8}$$

where P denotes the Cauchy principle value, i is the complex number, and $A(t)$ and $\phi(t)$ are amplitude and phase of $\tilde{\Gamma}(t)$, respectively. Because the interference signal $\Gamma(t)$ is quasi-monochromatic, the complex analytical signal can be determined by [14]:

$$\tilde{\Gamma}(t) = 2 \int_{0}^{+\infty} \int_{0}^{+\tau} \Gamma(t') \exp(-2\pi i v t') dt' \exp(2\pi i v t) dv \quad , \tag{9}$$

where τ is the time duration of the fringe signal in each axial scan.

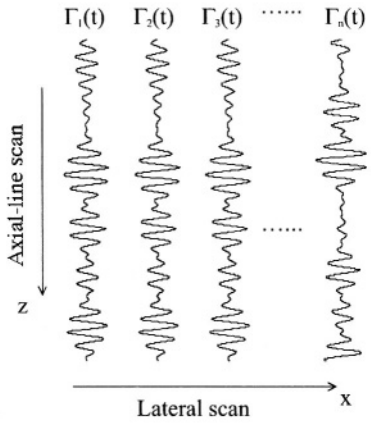

Figure 5. Schematic signal processing diagram for the phase-resolved ODT system.

A digital approach to determine the complex analytical signal using Hilbert transformation is shown in Figure 6, where FFT denotes the fast Fourier transformation and $H(v)$ is the Heaviside function given by:

$$H(v) = \begin{cases} 0 & v < 0 \\ 1 & v \geq 0 \end{cases} \quad , \tag{10}$$

and FFT $^{-1}$ denotes the inverse fast Fourier transformation. Multiplication of the Heaviside function is equivalent to performing an operation that discards the spectrum in the negative frequency region.

Figure 6. Block diagram for calculating complex analytical signal using Hilbert transformation.

The Doppler frequency shift (f_n) at n'th pixel in the axial direction is determined from the average phase shift between sequential A-scans. This can be accomplished by calculating the phase change of sequential scans from the individual analytical fringe signal [11, 12]:

$$f_n = \frac{\Delta\phi}{2\pi T} = \frac{1}{2\pi T} \sum_{m=(n-1)M}^{nM} \sum_{j=1}^{N} \left[\tan^{-1}\left(\frac{\mathrm{Im}\tilde{\Gamma}_{j+1}(t_m)}{\mathrm{Re}\tilde{\Gamma}_{j+1}(t_m)} \right) - \tan^{-1}\left(\frac{\mathrm{Im}\tilde{\Gamma}_{j}(t_m)}{\mathrm{Re}\tilde{\Gamma}_{j}(t_m)} \right) \right]. \quad (11)$$

Alternatively, the phase change can also be calculated by the cross-correlation method [11, 12]:

$$f_n = \frac{1}{2\pi T} \tan^{-1}\left(\frac{\mathrm{Im}\left[\sum_{m=(n-1)M}^{nM} \sum_{j=1}^{N} \tilde{\Gamma}_j(t_m) \cdot \tilde{\Gamma}^*_{j+1}(t_m) \right]}{\mathrm{Re}\left[\sum_{m=(n-1)M}^{nM} \sum_{j=1}^{N} \tilde{\Gamma}_j(t_m) \cdot \tilde{\Gamma}^*_{j+1}(t_m) \right]} \right), \quad (12)$$

where $\tilde{\Gamma}_j(t_m)$ and $\tilde{\Gamma}^*_j(t_m)$ are the complex signals at axial time t_m corresponding to the jth A-scan and its respective conjugate; $\tilde{\Gamma}_{j+1}(t_m)$ and $\tilde{\Gamma}^*_{j+1}(t_m)$ are the complex signals at axial time t_m corresponding to the next A-scan and its respective conjugate; M is an even number that denotes the window size in the axial direction for each pixel; N is the number of sequential scans used to calculate the cross correlation; and T is the time duration between A-scans. Because T is much longer than the pixel time window within each scan used in spectrogram method, high velocity sensitivity can be achieved.

Phase-resolved ODT decouples spatial resolution and velocity sensitivity in flow images and increases imaging speed by more than two orders of magnitude without compromising spatial resolution and velocity sensitivity. In addition, because two sequential A-line scans are compared at the same location, speckle modulations in the fringe signal cancel each other and, therefore, will not affect the phase difference calculation. Consequently, the phase-resolved method reduces speckle noise in the velocity image. Furthermore, if the phase difference between sequential frames is used, then

the velocity sensitivity can be further increased. Real-time imaging with velocity sensitivity on the order of 10 μm/s has been demonstrated.

A Doppler flow image is very sensitive to environmental disturbances, such as sample motions. However, because we are interested in the relative motion of blood flow with respect to the tissue, motion artifacts can be minimized by choosing the tissue as a stable reference point for phase measurement in each axial scan [13].

In addition to digital processing of the fringe signal using Hilbert transformation, the complex analytical signal can also be achieved through hardware implementation. Optical Hilbert transformation using polarization optics has been implemented for real-time phase-resolved ODT imaging [14]. Real-time ODT imaging using hardware demodulation of the ODT signal has also been demonstrated by several groups [16, 17, 24].

19.2.4 Phase-Resolved Spectral Domain ODT

Spectral domain OCT (also named Fourier domain OCT) uses the spectral information from the interference signal for tomographic image reconstruction. It was first developed by Fercher *et al.* in 1995 [25]. It has the advantage that no optical delay line is required. Recently, it has also been demonstrated that spectral domain OCT can achieve high signal to noise ratio over time domain OCT [26-28]. Because parallel data acquisition can be implemented in spectral domain OCT, high speed imaging is possible [29]. Spectral domain ODT combines Doppler principle with the spectral domain OCT [30-32]. A schematic diagram of a spectral domain ODT system is shown in Figure 7. The signal from the Michelson interferometer is directly coupled to a spectrometer that records the spectral fringe pattern. The temporal interference fringe can be calculated by a Fourier transform of the spectral fringe pattern. The Doppler shift can then be determined from the phase shift between sequential scans using the phase resolved ODT algorithm described in previous sections.

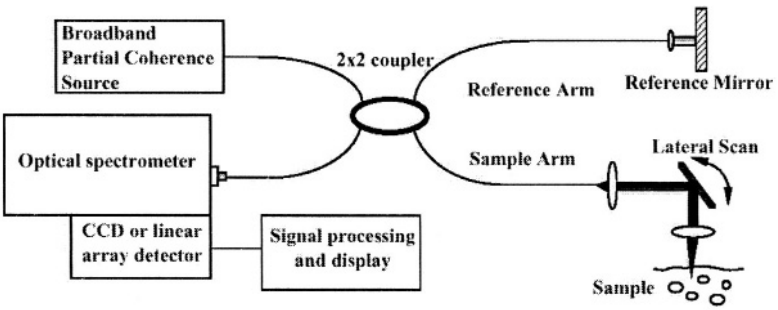

Figure 7. Schematic diagram of a spectral domain ODT instrument.

To understand spectral domain ODT, we first look at the relation between time and spectral domain fringe signals. Let us denote $U(t)$ as a complex-valued analytical signal of a stochastic process representing the field amplitude emitted by a low coherent light source, and $\overline{U}(\nu)$ as the corresponding spectral amplitude at optical frequency ν. The amplitude of a partially coherent source light coupled into the interferometer at time t is written as a harmonic superposition

$$U(t) = \int_0^\infty \overline{U}(\nu) e^{2\pi i \nu t} d\nu . \tag{13}$$

Because the stochastic process of a partially coherent light source is stationary, cross spectral density of $\overline{U}(\nu)$ satisfies

$$\left\langle \overline{U}^*(\nu)\overline{U}(\nu') \right\rangle = S_o(\nu)\delta(\nu - \nu'), \tag{14}$$

where $S_o(\nu)$ is the source power spectral density, and $\delta(\nu - \nu')$ is the Dirac delta function. Assuming that light couples equally into the reference arm and sample arm with spectral amplitude of $\overline{U}_0(\nu)$, the light coupled back to the detectors from the reference, $\overline{U}_r(\nu)$, and sample, $\overline{U}_s(\nu)$, is given by equations 15 and 16 respectively:

$$\overline{\mathrm{U}}_\mathrm{r}(\nu) = \mathrm{e}^{2\pi i \nu (2L_\mathrm{r} + L_\mathrm{d})/\mathrm{c}} \mathrm{K}_\mathrm{r}(\nu) \mathrm{e}^{\mathrm{i}\alpha_\mathrm{r}} \overline{\mathrm{U}}_\mathrm{o}(\nu), \tag{15}$$

$$\overline{\mathrm{U}}_\mathrm{s}(\nu) = \mathrm{e}^{2\pi i \nu (2L_\mathrm{s} + L_\mathrm{d})/\mathrm{c}} \mathrm{K}_\mathrm{s}(\nu) \mathrm{e}^{\mathrm{i}\alpha_\mathrm{s}} \overline{\mathrm{U}}_\mathrm{o}(\nu), \tag{16}$$

where L_r and L_s are the optical path lengths from the beam splitter to the reference mirror and sample, respectively, L_d is the optical path from the beam splitter to the detector, $K_r(\nu)e^{i\alpha_r(\nu)}$ and $K_s(\nu)e^{i\alpha_s(\nu)}$ is the amplitude reflection coefficient of light backscattered from the reference mirror and turbid sample, respectively.

The total power detected at the interferometer output is given by a time-average of the squared light amplitude

$$P_d = \left\langle \left| U_s(t) + U_r(t) \right|^2 \right\rangle . \tag{17}$$

Combining harmonic expansions for $U_s(t)$ and $U_r(t)$ and applying equation 14 when computing a time-average, total power detected is a sum

of three terms representing reference (I_r), sample (I_s), and the interference fringe intensity ($\Gamma_{ODT}(\Delta_0)$),

$$\begin{aligned} P_d &= \int_0^\infty \left(P_r(\nu) + P_s(\nu) + P_{ODT}(\nu)\right) d\nu \\ &= I_r + I_s + \Gamma_{ODT}(\Delta_d) \end{aligned} \tag{18}$$

with

$$P_r(\nu) = S_o(\nu)\left|K_r(\nu)\right|^2 \quad , \tag{19}$$

$$P_s(\nu) = S_o(\nu)\left|K_s(\nu)\right|^2, \tag{20}$$

$$P_{ODT}(\nu) = 2S_o(\nu)K_r(\nu)K_s(\nu)\cos\left[2\pi\nu\Delta_d / c + \alpha_s(\nu) - \alpha_r(\nu)\right], \tag{21}$$

and

$$I_r = \int_0^\infty P_r(\nu)d\nu \ , \tag{22}$$

$$I_s = \int_0^\infty P_s(\nu)d\nu \ , \tag{23}$$

$$\Gamma_{ODT}(\Delta_d) = \int_0^\infty P_{ODT}(\nu)d\nu d\nu \ , \tag{24}$$

where Δ_d determines the optical phase delay between light traveled in sample and reference arms. Light scattered from a moving particle is equivalent to a moving phase front; therefore, Δ_d can be written as:

$$\Delta_d = \Delta + 2\bar{n}v_z t \ , \tag{25}$$

where Δ is the optical path length difference between light in the sampling and reference arms, v_z is the velocity of a moving particle parallel to the probe beam, $\bar{n}$ is the refractive index of flow media. To simplify the

computation, we assume $\alpha_{S,}$ and α_r are constant over the source spectrum and can be neglected. The spectral domain fringe signal, $P_{ODT}(\nu)$, is simplified to:

$$P_{ODT}(\nu) = 2S_o(\nu)K(\nu)_r K_s(\nu)\cos\left[2\pi\nu(\Delta + 2\bar{n}v_z t)/c\right]. \qquad (26)$$

The corresponding time domain signal, $\Gamma_{ODT}(\Delta)$, is given by:

$$\Gamma_{ODT}(\Delta) = 2\int_0^\infty S_o(\nu)K(\nu)_r K_s(\nu)\cos\left[2\pi\nu(\Delta + 2\bar{n}v_z t)/c\right]d\nu. \qquad (27)$$

Equation 26 shows that $P_{ODT}(\nu)$ contains information on both location and velocity of moving particles. Spectral interference fringe intensity of single backscattered light from the static particle (v_z=0) is a sinusoidal modulation of the power spectral density. A moving particle in the sample path results in a phase shift in the spectral domain signal. A comparison of equations 26 and 27 shows that there is a Fourier transformation relation between spectral domain and time domain signal. The phase shift due to the moving particle can be determined from the Fourier transformations of two sequential spectral fringe signals. The Doppler frequency can then be calculated using equation 11 or 12 of the phase-resolved method.

Figure 8 shows the structural and velocity images of an intralipid solution flowing in a plastic tube obtained by spectral domain phase-resolved ODT with a 1.3 μm fiber system [32]. The spectrometer used to measure the spectral data has a spectral acquisition speed at 800 Hz. Spectral domain ODT with 10 kHz depth scanning rate has also been demonstrated [31]. Since the dynamic range of the phase-resolved ODT depends on the speed of the line scans, spectral domain ODT has the advantage in terms of imaging speed and velocity dynamic range.

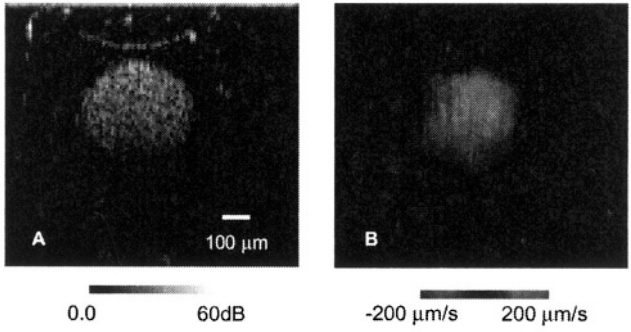

Figure 8. Phase-resolved spectral domain ODT images. A: structure image; B: flow velocity image (from Ref. [33]).

19.2.5 Transverse Flow Velocity Determination

One of the limitations of using Doppler shift to determine the flow is that the technique is only sensitive to longitudinal flow velocity (flow velocity along the probing beam direction, V_L). If one knows the flow direction, Doppler shift measurement can fully quantify the flow. However, in many biological cases where flow direction is not known, Doppler shift measurement alone is not enough to fully quantify the flow. Furthermore, there are many clinical cases, such as ocular blood flow, where vessels are in the plane perpendicular to the probing beam. When flow direction is perpendicular to the probing beam (V_T), the Doppler shift is not sensitive to transverse blood flow. Therefore, a method to measure transverse flow velocity is essential to clinical applications of ODT.

We have developed a method that uses standard deviation of the Doppler spectra to determine the transverse flow [19]. The technique is based on the fact that ODT imaging uses a relatively large numeric aperture lens in the sampling arm. The beam from different sides of the edges will produce different Doppler shifts f_1 and f_2 as indicated in Figure 9 [19]. Consequently, the Doppler spectra will be broadened by the transverse flow. In a simple geometrical consideration, the broadening can be calculated as:

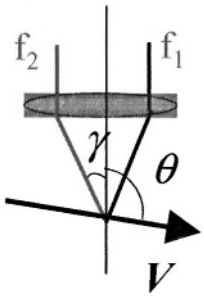

Figure 9. Effect of numerical aperture and transverse flow velocity on Doppler bandwidth.

$$f_1 = 2V\cos(\theta-\gamma)/\lambda\ , \tag{28}$$

$$f_2 = 2V\cos(\theta+\gamma)/\lambda\ , \tag{29}$$

$$B = f_1 - f_2 = \frac{4V\sin\theta NA_{eff}}{\lambda}\ . \tag{30}$$

If we assume that the incident beam has a Gaussian spectral profile and contributions from Brownian motion and other sources that are independent of the macroscopic flow velocity are included, we can find a linear relation between standard deviation of the Doppler spectra and transverse flow velocity, $V_T = V\sin\theta$.

$$\sigma = \frac{\pi V \sin\theta NA_{eff}}{8\lambda} + b, \tag{31}$$

where b is a constant, and NA_{eff} is the effective numeric aperture. The standard deviation can be determined from the measured analytical fringe signal:

$$\sigma^2 = \frac{1}{2\pi^2 T^2}\left(1 - \frac{\left|\sum_{m=(n-1)M}^{nM}\sum_{j=1}^{N}\tilde{\Gamma}_j(t_m)\cdot\tilde{\Gamma}^*_{j+1}(t_m)\right|}{\frac{1}{2}\sum_{m=(n-1)M}^{nM}\sum_{j=1}^{N}[\tilde{\Gamma}_j(t_m)\cdot\tilde{\Gamma}^*_j(t_m)+\tilde{\Gamma}_{j+1}(t_m)\cdot\tilde{\Gamma}^*_{j+1}(t_m)]}\right), \tag{32}$$

where $\tilde{\Gamma}_j(t_m)$ and $\tilde{\Gamma}^*_j(t_m)$ are the complex signals at axial time, t_m, corresponding to the jth A-scan and its respective conjugate; $\tilde{\Gamma}_{j+1}(t_m)$ and $\tilde{\Gamma}^*_{j+1}(t_m)$ are the complex signals at axial time, t_m, corresponding to the next A-scan and its respective conjugate; M is an even number that denotes the window size in the axial direction for each pixel; N is the number of sequential scans used to calculate the cross correlation, and T is the time duration between A-scans.

The measured standard deviation as a function of transverse flow velocity is shown in Figure 10. It is found that above a certain threshold level the Doppler bandwidth is a linear function of flow velocity and the effective numerical aperture of the optical objective in the sample arm determines the slope of this dependence. This result indicates that standard deviation can be used to determine the transverse flow velocity.

Since both longitudinal, V_L, and transverse flow velocity, V_T, can be measured by the Doppler shift and standard deviation, respectively, flow direction can be determined from a single measurement of the Doppler fringe signal [19, 34, 35,36]. Figure 11 shows the angle of the flow direction measured by the Doppler shift and standard deviation. The result indicates that the angle determined by the Doppler shift and standard deviation of the Doppler spectrum fits with the predicted value very well.

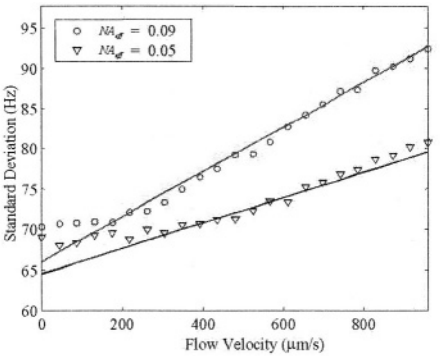

Figure 10. Standard deviations as a function of flow velocity for two different numeric apertures at a Doppler angle of 77° (from Ref. [19]).

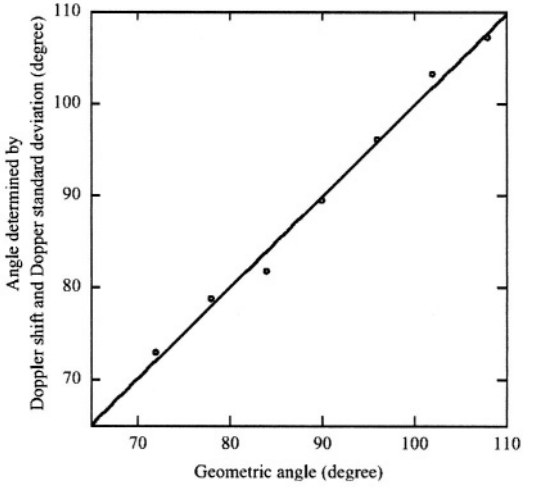

Figure 11. Relationship between the measured Doppler angle by ODT and predicted Doppler angle. The solid line is a linear fit of the measured data (from Ref. [36]).

19.3 APPLICATIONS OF ODT

The high velocity sensitivity and high imaging speed of phase-resolved ODT have made it possible to image *in vivo* tissue microcirculation. We describe in the following sections a few examples of applications.

19.3.1 Drug Screening

Noninvasive drug screening is essential for the rapid development of new drugs. To demonstrate the potential applications of ODT for *in vivo* blood flow monitoring after pharmacological intervention, the effects of

nitroglycerin (NTG) on the CAM artery and vein are investigated [8]. Changes in arterial vascular structure and blood flow dynamics are shown in Figure 12-I, where Figures A and B are structural and velocity images, respectively, before, and Figures A' and B' are after, topical application of NTG. The arterial wall can be clearly identified and dilation of the vessel after nitroglycerin application is observed in the structural images. Although velocity images appear discontinuous due to arterial pulsation (Figures B and B'), enlargement of the cross-sectional area of blood flow is evident. Peak blood flow velocity at the center of the vessel increased from 3000 to 4000 μm/s after NTG application.

The effects of NTG on CAM venous blood flow are shown in Figures 12-II, where A and B are structural and velocity images, respectively, before, and A' and B' are corresponding images after, topical application. Dilation of the vein due to nitroglycerin is observed in both structural and velocity images. In contrast to the artery, the peak velocity at the center of the vein decreased from 2000 to 1000 μm/s after NTG application.

NTG is a vasodilator used in the treatment of ischemic and congestive heart disease. Figure 12 indicates that the degree of CAM arterial dilation is greater than the venous in response to NTG. This is probably due to the reversal of oxygenation in the CAM vasculature where arteries and veins are oxygen poor and rich, respectively, because the embryo oxygenates itself from the surrounding air through the shell. The reversal of oxygenation could result in a reversal in selectivity, making NTG arterioselective in the CAM.

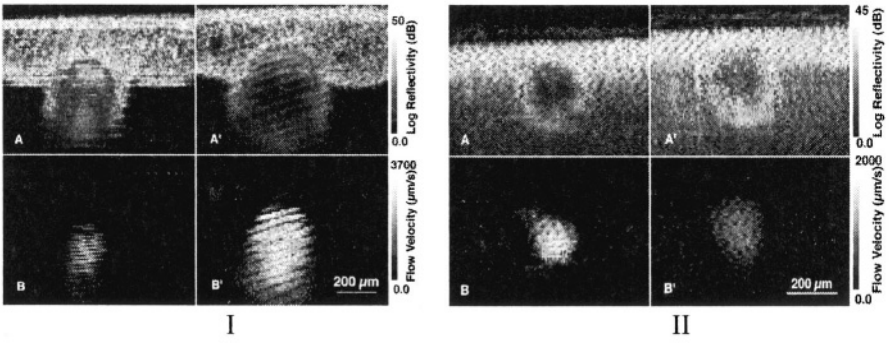

Figure 12. Effects of topical NTG on blood flows in CAM artery (I) and vein (II), respectively. OCT/ODT structural2 and velocity images, respectively, before (A, B) and after (A', B'), drug application (from Ref. [8]).

19.3.2 *In vivo* Blood Flow Monitoring During Photodynamics Therapy (PDT)

The potential application of ODT for *in vivo* blood flow monitoring during PDT was investigated in rodent mesentery after benzoporphyrin derivative (BPD) injection and laser irradiation (Figure 13) [8]. ODT structural and velocity images, respectively, were recorded before laser irradiation (Figures A and A'), 16 (Figures B and B') and 71 minutes after laser irradiation (Figures C and C'). The results indicate that the artery goes into vaso-spasm after laser exposures and compensatory vasodilatation occurs in response to PDT induced tissue hypoxia.

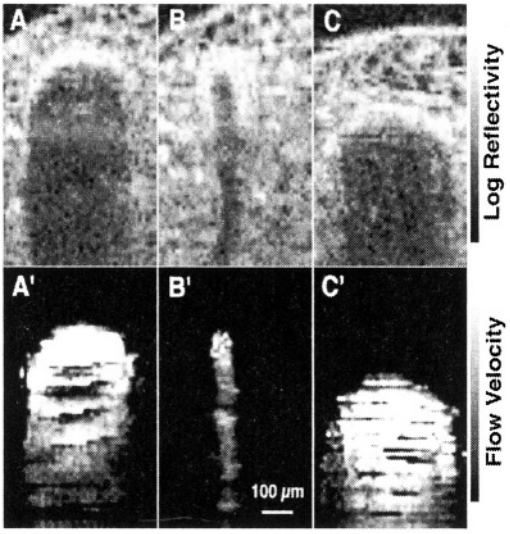

Figure 13. Vessel structure and blood flow dynamics in rodent mesenteric artery after PDT. ODT structural and velocity images, respectively, prior to laser irradiation (A, A'), 16 minutes (B, B'), and 71 minutes (C, C') after laser irradiation (from Ref. [8]).

The pharmacokinetics of the PDT drug can also be studied with ODT. ODT images were taken at different intervals between photosensitizer injection and laser irradiation. Rodents were given a PDT sensitizing drug 20 minutes, 4 hours, and 7 hours before mesenteric laser irradiation, and the changes in arterial diameter and flow were calculated from ODT images (Figure 14). The results indicate that the effects of PDT are strongly dependent on the time interval between drug injection and light irradiation. For a drug-light time interval of 20 minutes, the arterial diameter (Figure 14A) decreased by 80% after light irradiation followed by a rebound with vasodilative overshoot. Mesenteric arterial flow (Figure 14B) mirrored changes in diameter with an initial reduction with a subsequent rebound.

These effects are significantly reduced with longer post injection times due to progressive diffusion of the photosensitizer out of the vasculature. These results suggest that characterizing intratumoral hemodynamics by ODT not only provides insight into understanding the mechanism(s) of PDT, but could also be used to monitor the progress of treatment in real-time.

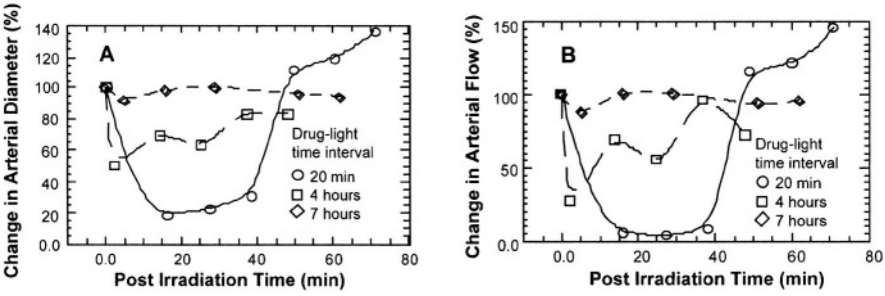

Figure 14. Changes in relative arterial diameter (A) and flow rate (B) in rodent mesentery following PDT as a function of post-irradiation time (from Ref. [37]).

19.3.3 ODT Images of Brain Hemodynamics

ODT has also been used to image brain hemodynamics in the cerebral cortex of the brain. The cerebral cortex is generally believed to be composed of functional units, called "columns," that are arranged in clusters perpendicular to the surface of the cortex [38]. Alterations in the brain's blood flow are known to be coupled to regions of neuronal activity [38]. A number of techniques such as positron emission tomography (PET), functional magnetic resonance imaging (fMRI), and diffuse reflectance spectra, have been used to study brain hemodynamics. However, the resolution of PET and fMRI is too low to resolve the columns. Although optical spectral reflectance techniques can map out *en face* cortex hemodynamics, it does not provide depth resolution. Currently, the two-photon microscopy has been used for mapping cortex activity. However, this technique requires the injection of a fluorescent dye and has limited penetration depth. The noninvasive and tomographic capability of ODT makes it an ideal technique for mapping depth resolved blood flow in the cortex. Figure 15 shows an ODT image of *in vivo* blood flow in the rat cerebral cortex. The parietal cortex of an anesthetized rat was imaged through a dural incision. This preliminary investigation demonstrated that ODT can map blood flow in the cortex with high axial resolution. ODT shows great promise in brain research for imaging the entire depth of the cortex and it can be used to measure stimulus-induced changes in blood flow [9].

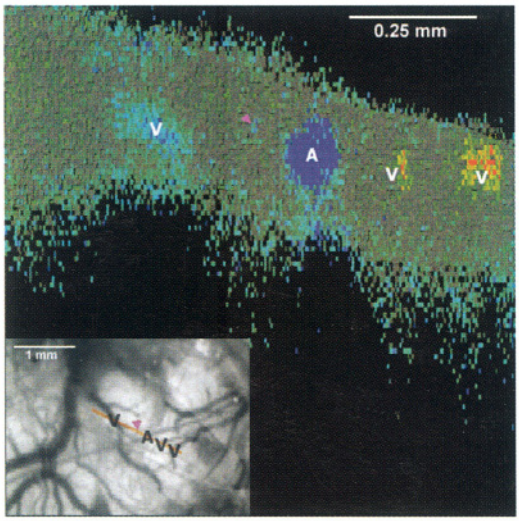

Figure 15. ODT image of in vivo blood flow in the rat cerebral cortex. The colored pixels denote regions of flow, either out of the page (blue) or into the page (red/yellow). The red line in the inset depicts the surface projection of the region of cortex imaged. Note the corresponding arteries (A) and veins (V) in the inset with the blue and red pixels in the image (from Ref. [9]).

19.3.4 *In Vivo* Monitoring of the Efficacy of Laser Treatment of Port Wine Stains

The high spatial resolution and high velocity sensitivity of ODT has many potential clinical applications. The first clinical application of ODT is the *in vivo* monitoring of the efficacy of laser treatment of port wine stains (PWS) [11, 12, 15]. PWS is a congenital, progressive vascular malformation of capillaries in the dermis of human skin that occurs in approximately 0.7% of children. Histopathological studies of PWS show an abnormal plexus of layers of dilated blood vessels located 150-750 μm below the skin surface in the dermis, having diameters varying on an individual patient basis, and even from site to site on the same patient, over a range of 10-150 μm. The pulsed dye laser can coagulate selectively PWS vessels by inducing microthrombus formation within the targeted blood vessels. However, currently there is no technique to evaluate efficacy of therapy immediately after the laser treatment. Phase-resolved Doppler OCT provides a means to evaluate the efficacy of laser therapy in real-time.

Figure 16 shows ODT structural and flow velocity images of a patient with PWS before and after laser treatment, respectively. For comparison, we also include a histology picture taken at the same site. The vessel location from the ODT measurement and histology agree very well. Furthermore, the destruction of the vessel by laser can be identified since no flow appears on

the Doppler flow image after laser treatment. This result indicates that ODT can provide a fast semi-quantitative evaluation of the efficacy of PWS laser therapy *in situ* and in real-time.

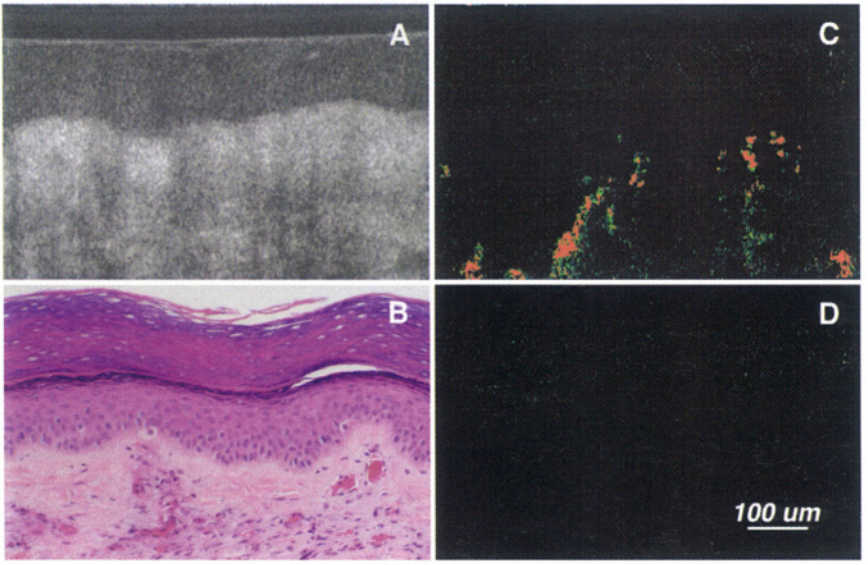

Figure 16. Phase resolved Doppler OCT images taken in situ from PWS human skin. A: structural image; B: histological section from the imaged site; C: Doppler standard deviation image before laser treatment; and D: Doppler standard deviation image after laser treatment (fromRef. [15]).

19.3.5 Three-Dimensional Images of a Microvascular Network

It is known that the microvasculature of mammary tumors has several distinct differences from normal tissues. Three-dimensional images of a microvascular network may provide additional information for cancer diagnosis. This can be accomplished in ODT by stacking the 2-D scans together [13]. Figure 17 shows multiple blood vessels imaged in human skin from a patient with a PWS birthmark. Different colors represent different signs of the Doppler shift, which depends on the angle between the direction of flow and probing beam. The convoluted nature of the blood vessels is consistent with the typical vasculature observed in PWS patients.

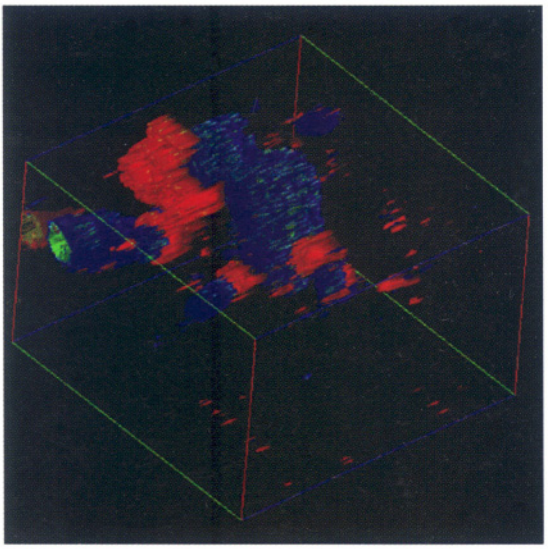

Figure 17. Three-dimensional ODT images of multiple blood vessels in human skin from a patient with a PWS birthmark (from Ref. [13]).

19.3.6 Imaging and Quantification of Flow Dynamics in MEMS Microchannel

Currently, there is great interest in miniaturizing biochemical analysis instruments on a small chip using the micro-electro-mechanic-system (MEMS) technology. One of the most important components in BioMEMS is microfluidic flow handling, including microfluidic channel, vale, and mixing chamber. However, currently there is no technology that can measure and quantify the structure and flow dynamics of BioMEMS devices simultaneously. Conventional metrology and imaging techniques, such as scanning transmission electronic microsopy, has been widely used in the semiconductor industry. However, it is not versatile enough to image BioMEMS devices consisting of different materials. In addition, it is also a destructive technique that requires coating. More importantly, these techniques cannot image and measure flow dynamics in microfluidic devices. Particle imaging velocimetry can produce velocity field maps over a large region within the focal plane of the imaging system. However, it cannot provide a cross-sectional structure and velocity imaging for complex geometries. For many BioMEMS devices for biomedical diagnosis, the structural dimension is on the order of 10 ~ 500 μm, and flow dynamics depend strongly on the surface characteristics of the microfluidic channel. A nondestructive imaging and metrology technique that can image both structure and flow velocity of a microfluidic device simultaneously is

essential for the development of integrated system technologies for BioMEMS applications [32, 39].

ODT can provide cross-sectional imaging of channel geometry and flow velocity within a microfluidic channel with a spatial resolution on the order of a micrometer and a velocity sensitivity of 10 μm/s. Figure 18A shows an S-shaped polymer microchannel with a cross-sectional dimension of 30×150 μm. ODT structural and velocity images are shown in Figure 18B and C, respectively. The scan is perpendicularly through three parallel channels. The structure of three channels is clearly visible in Figure 18B. The upper surface of the PDMS channel layer and the interface between the PDMS layer and glass substrate can also be observed. The velocity image provides a background-free picture of the velocity of the moving intralipid. The velocity profile along the horizontal direction near the center of the channel is shown in Figure 18D. The velocity profile in each channel is close to a parabolic shape, which agrees with the predicted profile of a pressure driven laminar flow. The direction of the flow velocity is also shown.

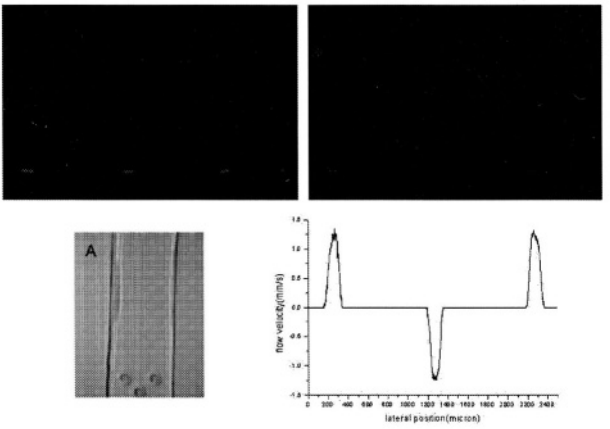

Figure 18. Imaging and quantification of geometry and flow velocity of an S-shaped microchannel with cross-section dimension of 30×150 μm. A: Polymer chip with an S-shaped channel; B: structural image; C: velocity image; and D: velocity profile (from Ref. [40]).

Figure 19 shows a velocity profile of electrokinetic driven flow in a microchannel. The polymer microchannel with a cross-sectional dimension of 100 x 30 μm was treated with oxygen plasma. The applied voltage was 1000 V, producing an electric field of 333V/cm, and the profile clearly shows a flat plateau flow front and very steep slope of velocity near the channel wall. This is in contrast to the parabolic profile observed in pressure driven flow.

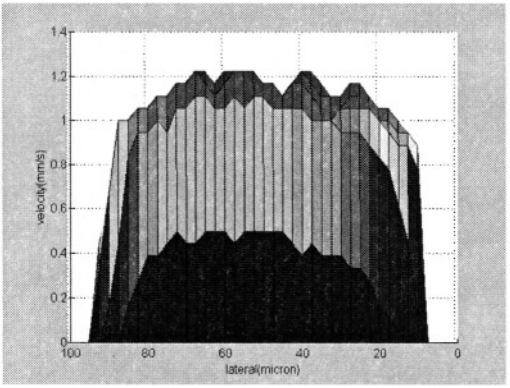

Figure 19. Cross section velocity profile of electrokinetic driven flow using ODT. The cross-sectional dimension is 30×100 μm, and the PDMS layer and glass substrate are pre-treated by oxygen plasma (from Ref. [40]).

In addition to imaging, ODT can also be used to measure osmotic mobility, quantify size of the scattering particle, and study flow dynamics of microfluid in microchannel of different materials, geometry, and surface treatment [33].

19.4 CONCLUSIONS

ODT is a rapidly developing imaging technology with many potential applications. New developments in all components of a OCT system can be integrated to a ODT system, including new light sources for high resolution OCT, new scanning probes for endoscopic imaging, and new processing algorithms. Integration of the ODT with other functional OCT, such as polarization sensitive OCT, spectroscopic OCT, and second harmonic OCT, can greatly enhance the potential applications of this technology. Given the noninvasive nature and exceptionally high spatial resolution and velocity sensitivity, functional OCT that can simultaneously provide tissue structure, blood perfusion, birefringence, and other physiological information has great potential for basic biomedical research and clinical medicine.

ACKNOWLEDGMENTS

I would like to thank many of my colleagues who have contributed to the functional OCT project at Beckman Laser Institute and Center for Biomedical Engineering at UCI, particularly to the students and postdoctoral fellows whose hard work made it possible for me to review many of the

excitation results in this chapter. I also want to acknowledge the research grants awarded from the National Institutes of Health (EB-00293, NCI-91717, RR-01192 and EB-00255), the National Science Foundation (BES-86924), the Whitaker Foundation (WF-23281) and the Defense Advanced Research Program Agency (Bioflip program). Institutional supports from the Air Force Office of Scientific Research (F49620-00-1-0371), and the Beckman Laser Institute Endowment are also gratefully acknowledged. Dr. Chen's e-mail address is zchen@bli.uci.edu.

REFERENCES

1. E. Yamada, M. Matsumura, S. Kyo, and R. Omoto, "Usefulness of a prototype intravascular ultrasound imaging in evaluation of aortic dissection and comparison with angiographic study, transesophageal echocardiography, computed tomography, and magnetic resonance imaging," *Am. J. Cardiol.* **75,** 161-165 (1995).
2. P. L. Carson, D. D. Adler, and J. B. Fowlkes, "Enhanced color flow imaging of breast cancer vasculature: continuous wave Doppler and three-dimensional display," *J. Ultrasound Med.* **11,** 77 (1992).
3. D. Huang, E. A. Swanson, C. P. Lin, J. S. Schuman, W. G. Stinson, W. Chang, M. R. Hee, T. Flotte, K. Gregory, C. A. Puliafito, and J. G. Fujimoto, "Optical Coherence Tomography," *Science* **254**(5035), 1178-1181 (1991).
4. V. Gusmeroli and M. Martnelli, "Distributed laser Doppler velocimeter," *Opt. Lett.* **16,** 1358-1360(1991).
5. Z. Chen, T. E. Milner, S. Srinivas, X. J. Wang, A. Malekafzali, M. J. C. van Gemert, and J. S. Nelson, "Noninvasive Imaging of in vivo blood flow velocity using optical Doppler tomography," *Opt. Lett.* **22,** 1119-1121 (1997).
6. J. A. Izatt, M. D. Kulkarni, S. Yazdanfar, J. K. Barton, and A. J. Welch, "In vivo bidirectional color Doppler flow imaging of picoliter blood volumes using optical coherence tomography," *Opt. Lett.* **22,** 1439-1441 (1997).
7. Z. Chen, T. E. Milner, D. Dave, and J. S. Nelson, "Optical Doppler tomographic imaging of fluid flow velocity in highly scattering media," *Opt. Lett.* **22,** 64-66 (1997).
8. Z. Chen, T. E. Milner, X. J. Wang, S. Srinivas, and J. S. Nelson, "Optical Doppler tomography: imaging in vivo blood flow dynamics following pharmacological intervention and photodynamic therapy," *Photochem. Photobiol.* **67**, 56-60 (1998).
9. Z. Chen, Y. Zhao, S. M. Srinivas, J. S. Nelson, N. Prakash, and R. D. Frostig, "Optical Doppler Tomography," *IEEE J. Select. Tops Quant. Electr.* **5**(4), 1134-1141 (1999).
10. M. D. Kulkarni, T. G. van Leeuwen, S. Yazdanfar, and J. A. Izatt, "Velocity-estimation accuracy and frame-rate limitations in color Doppler optical coherence tomography.," *Opt. Lett.* 23, 1057-1059 (1998).
11. Y. Zhao, Z. Chen, C. Saxer, S. Xiang, J. F. de Boer, and J. S. Nelson, "Phase-resolved optical coherence tomography and optical Doppler tomography for imaging blood flow in human skin with fast scanning speed and high veocity sensitivity," *Opt. Lett.* **25**(2), 114 (2000).
12. Y. Zhao, Z. Chen, C. Saxer, Q. Shen, S. Xiang, J. F. de Boer, and J. S. Nelson, "Doppler standard deviation imaging for clinical monitoring of in vivo human skin blood flow," *Opt. Lett.* **25**, 1358-1360 (2000).
13. Y. Zhao, Z. Chen, Z. Ding, H. Ren, and J. S. Nelson, "Three-dimensional reconstruction of in vivo blood vessels in human skin using phase-resolved optical Doppler tomography," *IEEE J. Select. Tops Quant. Electr.* **7**, 931-935 (2001).

14. Z. Ding, Y. Zhao, H. Ren, S. J. Nelson, and Z. Chen, "Real-time phase resolved optical coherence tomography and optical Doppler tomography," *Opt. Express* **10,** 236-245 (2002).
15. J. S. Nelson, K. M. Kelly, Y. Zhao, and Z. Chen, "Imaging blood flow in human port-wine stain in situ and in real time using optical Doppler tomography," *Arch. Dermatol.* **137**(6), 741-744(2001).
16. V. X. Yang, M. L. Gordon, A. Mok, Y. Zhao, Z. Chen, R. S. C. Cobbold, B. C. Wilson, and I. A. Vitkin, "Improved phase-resolved optical Doppler tomography using the Kasai velocity estimator and histogram segmentation," *Opt. Commun.* **208,** 209-214 (2002).
17. V. Westphal, S. Yazdanfar, A. M. Rollins, and J. A. Izatt, "Real-time, high velocity-resolution color Doppler optical coherence tomography," *Opt. Lett.* **27**, 34-36 (2002).
18. D. P. Dave and T. E. Milner, "Doppler-angle measurement in highly scattering media," *Opt. Lett.* **25**(20), 1523-1525 (2000).
19. H. Ren, M. K. Breke, Z. Ding, Y. Zhao, J. S. Nelson, and Z. Chen, "Imaging and quantifying transverse flow velocity with the Doppler bandwidth in a phase-resolved functional optical coherence tomography," *Opt. Lett.* **27**, 409-411 (2002).
20. S. Yazdanfar, A. M. Rollins, and J. A. Izatt, "Imaging and velocimetry of the human retinal circulation with color Doppler optical coherence tomography," *Opt. Lett.* **25**, 1448-1450 (2000).
21. V. X. Yang, M. L. Gordon, S. Tang, N. E. Marcon, G. Gardiner, B. Qi, S. Bisland, E. Seng-Yue, S. Lo, J. Pekar, B. C. Wilson, and I. A. Vitkin, "High speed, wide velocity dyhamic range Doppler optical coherence tomography (part III): *in vivo* endoscopic imaging of blood flow in the rat and human gastrointestinal tracts," *Opt. Express* **11,** 2416–2424 (2003).
22. G. J. Tearney, B. E. Bouma, and J. G. Fujimoto, "High-speed phase- and group-delay scanning with a grating-based phase control delay line," *Opt. Lett.* **22**(23), 1811-1813 (1997).
23. F. Hlawatsch and G. F. Boudreaux-Bartels, "Linear and Quadratic Time-Frequency Signal Representations," *IEEE Spectrum* **4**, 21-67 (1992).
24. S. Yazdanfar, A. M. Rollins, and J. A. Izatt, "ultrahigh velocity resolution imaging of the microcirculation *in vivo* using colar Doppler optical coherence tomography," *Proc. SPIE* **4251**, 156(2001).
25. A. F. Fercher, C. K. Kitzenberger, G. Kamp, and S. Y. El-Zaiat, "Measurement of intraocular distances by backscattering spectral interferometry," *Opt. Commun.* 117, 43-48 (1995).
26. R. Leitgeb, C. K. Hitzenberger, A. F. Fercher, and M. Kulhavy, "Performance of Fourier domain vs. time domain optical coherence tomography," *Opt. Express* **11,** 889-894 (2003).
27. M. A. Choma, M. V. Sarunic, C. Yang, and J. A. Izatt, "Sensitvity advantage of swept source and Fourier domain optical coherence tomography," *Opt. Express* **11,** 2183-2189 (2003).
28. J. F. de Boer, B. Cense, B. H. Park, M. C. Pierce, G. J. Tearney, and B. E. Bouma, "Improved signal-to-noise ratio in spectral-domain compared with time-domain optical coherence tomography," *Opt. Lett.* **28**, 2067-2069 (2003).
29. S. H. Yun, G. J. Tearney, J. F. de Boer, N. Iftimia, and B. E. Bouma, "High speed optical frequency domain imaging," *Opt. Express* **11,** 2593-2563 (2003).
30. Z. Chen, "Optical Doppler tomography for high resolution imaging of *in vivo* microcirculation," Whitaker Foundation Investigator Abstract, 1997.
31. R. Leitgeb, L. Schmetterer, M. Wojtkowski, M. Sticker, C. K. Hitzenberger, and A. F. Fercher, "Flow velocity measurement by frequency domain short cohrence interferometry," *Proc. SPIE* **4619,** 16 (2002).
32. L. Wang, Y. Wang, M. Bachaman, G. P. Li, and Z. Chen, "Phase-resolved frequency domain optical Doppler tomography," *Proc. SPIE* 5345, to be published (2004).

33. L. Wang, X. Wei, Y. Wang, M. Bachaman, G. P. Li, and Z. Chen, "Imaging and quantifying of microflow by phase-resolved optical Doppler tomography," *Opt. Commun.* in press (2004).
34. D. Piao, L. L. Otis, and Q. Zhu, "Doppler angle and flow velocity mapping by combine Doppler shift and Doppler bandwidth measurements in optical Doppler tomography," *Opt. Lett.* **28**, 1120(2003).
35. S. Proskurin, Y. He, and R. Wang, "Determination of flow velocity vector based on Doppler shift and spectrum boradening with optical coherence tomography," *Opt. Lett.* **28**, 1227(2003).
36. L. Wang, Y. Wang, M. Bachaman, G. P. Li, and Z. Chen, "Quantify flow vector using phase resolved optical Doppler tomography," *Proc. SPIE* **5316**, to be published (2004).
37. A. Major, S. Kimel, S. Mee, T. E. Milner, D. J. Smithies, S. M. Srinivas, Z. Chen, and J. S. Nelson, "Microvascular photodynamic effects determined in vivo using optical Doppler tomography," *IEEE J. Select. Tops Quant. Electr.* **5**, 1168-1175 (1999).
38. R. D. Frostig, E. E. Lieke, D. Y. Ts'o, and A. Grinvald, "Cortical functional architechture and local coupling between neuronal activity and the microcirculation revealed by in vivo high-resolution optical imaging of intrinsic signals," *Proc. Natl. Acad. Sci. USA* **87**, 6082-6086 (1990).
39. Y. Chen, Z. Chen, Y. Zhao, J. S. Nelson, M. Bachman, Y. Chiang, C. Chu, and G. P. Li, "Test channels for flow characterization of processed plastic microchannels," Materials Science of Microelectromechanical Systems (MEMS) Devices II, M.P. deBoer, A.H. Heuer, S.J. Jacobs, E. Peeters, Eds., MRS, December (1999).
40. Y. Chen, "*In vivo* measurement and characterization of fluid flow in microchannels using OCT/ODT system," M. S. Thesis, University of California, Irvine, Irvine, CA, (2001).

Part V:
MICROSCOPY

This page intentionally left blank

Chapter 20

COMPACT OPTICAL COHERENCE MICROSCOPE

Grigory V. Gelikonov,[1] Valentin M. Gelikonov,[1] Sergey U. Ksenofontov,[1] Andrey N. Morosov,[1] Alexey V. Myakov,[1] Yury P. Potapov,[1] Veronika V. Saposhnikova,[1] Ekaterina A. Sergeeva,[1] Dmitry V. Shabanov,[1] Natalia M. Shakhova,[1] and Elena V. Zagainova[2]

1. Institute of Applied Physics of the Russian Academy of Sciences, Nizhny Novgorod, 603950; 2. Medical Academy, Nizhny Novgorod, 603005 Russian Federation

Abstract: This chapter discusses development and creation of a compact OCM device for imaging internal structures of biological tissue at the cellular level. Ultrahigh axial resolution of 3.4 μm and lateral resolution of 3.9 μm within tissue was attained by combining broadband radiations of two spectrally shifted SLDs and implementing the dynamic focus concept which allows in-depth scanning of a coherence gate and beam waist synchronously. The created OCM prototype is portable and easy to operate; creation of a remote optical probe was feasible due to use of PM fiber. The chapter also discusses results of theoretical investigation of OCM axial and lateral resolution degradation caused by light scattering in biological tissue. We demonstrate the first OCM images of biological objects on the example of plant and human tissue *ex vivo.*

Key words: Optical coherence microscopy, ultrahigh resolution, dynamic focus, low coherence interferometer based on PM fiber

20.1 OVERVIEW OF MAIN APPROACHES TO OCM DESIGN

Optical coherence microscopy (OCM) is a new biomedical modality for cross-sectional subsurface imaging of biological tissue combining ultimate sectioning abilities of optical coherence tomography (OCT) and confocal microscopy (CM). In OCM spatial sectioning due to tight focusing of the probing beam and pinhole rejection provided by CM is enhanced by

additional longitudinal sectioning provided by OCT coherence gating. For the first time, the OCT technique was used to enhance optical resolution of confocal microscopy by Izatt *et al.* [1]. Later, the OCM method and its potential for clinical application were studied and discussed in Ref. [2]. In that study OCM images of a 5-μm layer located at the depth of 500 μm of the normal human colon specimen were acquired. The OCM images clearly demonstrated structures with resolution at the cellular level.

One of the main challenges of OCM is to provide high axial resolution by means of ultrabroad band light sources. As in OCT, the longitudinal resolution in OCM depends on bandwidth of a light source. Axial OCM resolution at a subcellular level was reported in Ref. [3], where a Kerr-lens mode-locked Ti:sapphire laser with double-chirped mirrors with a bandwidth up to 350 nm was used. At the wavelength of 0.8 μm, authors attained 1-μm longitudinal resolution and 3-μm transverse resolution in biotissue. In Ref. [4] a superluminescent $Ti:Al_2O_3$ crystal was demonstrated as a possible light source for ultrahigh-resolution OCT. This new source yielded light with power of 40 μW and bandwidth of 138 nm which provided longitudinal resolution of 2.2 μm in air and 1.7 μm in tissue.

The feasibility of ultrahigh axial resolution using supercontinuum generation was demonstrated by Hartl *et al.* [5]. Authors developed a broadband OCT imaging system with bandwidth of 370 nm and central wavelength of 1.3 μm. The longitudinal resolution of 2.5 μm in air and 2 μm in tissue was attained. An unprecedented axial resolution using supercontinuum generation was reported in Ref. [6]. The optical spectrum of generated light extended from 550 nm to 950 nm (λ=725 nm, P_{out}=27 mW); the corresponding axial resolution in air was 0.75 μm and 0.5 μm in biological tissue.

Nowadays, semiconductor diodes are the most compact broadband IR light sources. In [7] authors combined radiations of several broadband luminescent diodes (LEDs) in order to improve longitudinal resolution of OCM by broadening the probing light spectrum. As a result resolution was sufficient to successfully image microspheres with a diameter of 6 μm up to the depth of 500 μm in a scattering medium containing suspension of 0.2-μm particles. For the same purpose of improving axial resolution radiations of two superluminescent diodes (SLDs) with central wavelengths separated by 25 nm (830 nm and 855 nm, respectively) were combined [8]. The effective bandwidth of 50 nm was achieved, which corresponded to axial resolution of 6-7 μm in tissue. Although, the semiconductor sources cannot yet provide axial resolution attainable by other sources; nevertheless, the field of IR optics is rapidly evolving.

A second major challenge in OCM is to perform synchronous axial scanning of a sharply focused focal spot and the coherence gate while keeping their spatial alignment constant. For this purpose, in Refs. [1] and

[2] the object itself was moved through a high-aperture lens and OCM images of a thin layer of the object near the focal area were acquired. In Refs. [3] and [4] several individual images obtained with the focus at different depths were fused to yield a composite image. The problem of synchronous scanning was partially solved when the dynamic focus method was proposed [7,6]. In this method the coherence gate and the sharply focusing focused area of the probing beam are spatially aligned and moved in the axial direction simultaneously. In some designs the dynamic focus was attained by mounting an output objective of the signal arm and a retroreflector in the reference arm on the same scanning platform. However, this schematic provides satisfactory results only for relatively short scanning distances, because the mismatch between the coherence gate and sharply focused area is compensated only partially. In the alternative approach of dynamic coherence focus described in Ref. [9] the optical length of the sample arm does not change during scanning. As a result, the coherence gate remains in the beam focus, requiring no additional adjustment of the reference arm. In Ref. [10] authors describe another realization of the method for precise alignment of the focal area and coherence gate. Synchronous scanning is attained by moving the tip of the output fiber and a lens inside of the objective. This approach was successfully applied to determine refractive indices of different subsurface layers of biological tissue *in vivo.*

In our study we developed and fabricated a prototype of compact optical coherence microscope (OCM) with a flexible sample arm and a remote optical probe for laboratory and clinical environment. To achieve axial resolution at the cellular level, a light source with effective bandwidth of 100 nm was developed. It comprised two semiconductor SLDs based on one-layer quantum-dimensional (GaAl)As-heterostructures with shifted spectra. Radiations from both SLDs were coupled into polarization-maintaining (PM) fiber by means of a specially designed multiplexer. The multiplexer was spectrally adjusted in order to achieve the minimum width of auto-correlation function (ACF). To broaden the bandwidth of a Michelson interferometer the polished coupler based on anisotropic fiber with broadband of 3 dB was developed.

We also solved the problem of the dynamic focus by scanning the output lens of the objective located at the very end of the sample arm. The lens movement was controlled by the electronic system, thus, allowing to align the sharply focused focal spot with the coherence gate spatially during their simultaneous scanning up depth of 0.5-0.8 mm in biological tissue.

A method for suppression of spectral sidelobes caused by non-uniformity of the light source spectrum was developed and successfully applied; the suppression efficiency was also estimated.

In addition, the problem of light propagation in a scattering medium was solved numerically. The dependence of axial resolution on the probing depth

was studied for different parameters of the scattering and absorbing medium and the incident spectrum of probing radiation.

20.2 INTERFEROMETER FOR COMPACT OCM

A diagram of a compact OCM interferometer based on the traditional OCT scheme using PM-fiber is shown in Figure 1. The fiber optical Michelson interferometer employed for OCM comprises sample and reference arms. The use of anisotropic fiber allows the signal arm to be flexible, which is important for clinical applications. A light source consisted of two SLDs based on one-layer quantum-dimensional (GaAl)As-heterostructures with central wavelengths of 907 nm and 948 nm, bandwidths of approximately 53.4 nm and 72 nm, and initial power of 0.9 mW and 3 mW, respectively.

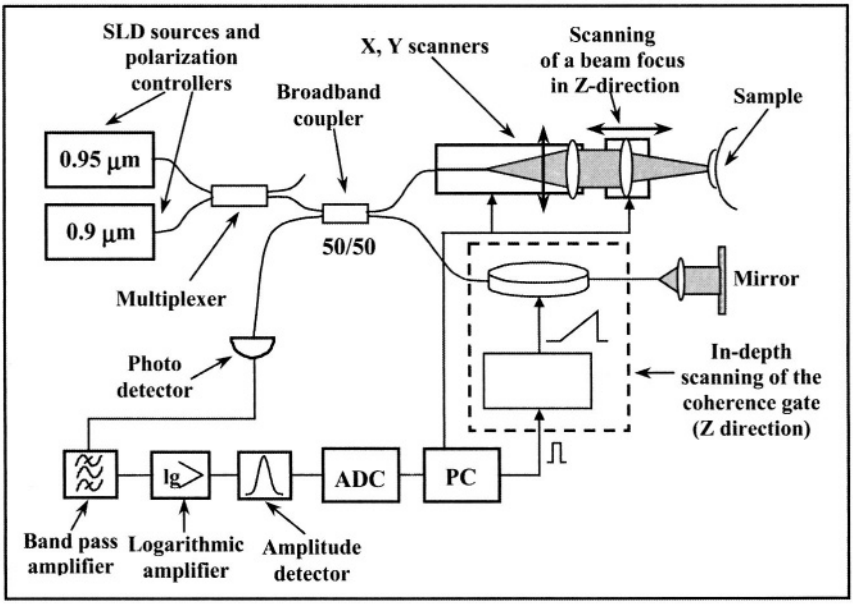

Figure 1. OCM functional scheme.

The probing light produced by the light source is passed through the sample arm to the optical probe. The probe comprises the optical and mechanical systems that perform focusing of the beam and also axial and lateral scanning. At the same time, the probe collects light backscattered by the object. The reference arm delivers light onto a reference mirror and transports it back to the beamsplitter. At the beamsplitter the light from both arms of the interferometer is combined. The light backscattered by the object would produce interference fringes with light reflected from the reference

mirror only if the path-length difference between the arms does not exceed the coherence length of the source. The interference fringes are detected by the photo diode. The path-length difference between the arms of the interferometer (ΔL) was modulated by a linear law $\Delta L = \Delta \dot{L} \cdot t$ to perform heterodyne detection of the interference signal. This was attained by elastically stretching and contracting in antiphase the fibers using modulators based on piezoelectric converters [11]. In this case, the probing depth h inside of the object, from which the signal is measured, varies at a rate $\dot{h} = \Delta \dot{L} \frac{n_{fgr}}{n_{mgr}}$, where n_{fgr} and n_{mgr} are group refractive indices of a fiber material and the object, respectively. When the path-length difference between the arms is changed linearly at the rate of $\Delta \dot{L}$, optical frequencies in the interferometer arms differ by a value of the Doppler shift. Therefore, the interference signal contains the component at a Doppler frequency $F = \frac{2\Delta \dot{L} n_f}{\lambda_0} = 2 n_{mgr} \frac{\dot{h}}{\lambda_0} \frac{n_f}{n_{fgr}}$, where n_f is the fiber phase refractive index, and λ_0 is the vacuum wavelength of probing radiation. For instance, at the wavelength of $0.94\ \mu m$ and the Doppler frequency of 0.4 MHz the optical path-length difference between the interferometer arms is changed at the rate of $\Delta \dot{L} n_f \sim 0.13$ m/s.

The optical probe comprises a scanner that provides the "dynamic focus" by longitudinally scanning an output lens of the objective in the axial direction. The scanner also moves the probing beam in the lateral directions, thus, generating both 2D and 3D images. The optical layout of a scanner consists of a two-lens objective; therefore, allowing to use maximum numerical aperture of the output lens. The objective magnification is equal to unity; the diameter of the focal spot is less than $4\ \mu m$. In the current design the effective "dynamic focus" is implemented up to the depths at which sharp beam focusing starts to degrade due to multiple scattering of light.

Movement of an optical beam along the object surface is attained by moving an additional lens of the objective transversely. Scanning is performed by an electromechanical system which is incorporated into an optical probe at the end of the sample arm of the interferometer. The scanning process is fully automated and computer controlled.

The interference signal was detected using a photo diode with a fiber optical input characterized by a high quantum yield (>0.8) and low noise level. After analog processing, the signal is fed to a computer through an analog-digital converter. The computer is further utilized for digital signal processing, recording and displaying of images.

According to the scheme of signal detection and analog processing, the resulting signal comprises a component that is proportional to the logarithm of the coefficient of tissue backscartering. The two-dimensional field of tissue backscattering coefficient obtained by scanning in depth (by changing the optical path-length difference between the interferometer arms) and along the object surface (by moving the probing beam laterally) is displayed on a computer monitor and stored for further processing. In contrast to many other indirect modalities of imaging of turbid media reconstruction of both OCT and OCM images from the measured signal does not require solution of the complex inverse problem. Each in-depth element of an image corresponds to the certain time of light propagation to this element and back, i.e., the certain path-length difference between the interferometer arms. Therefore, the obtained images are relatively easy to interpret because they do not require any post processing and can be displayed in real time during scanning.

20.3 DEVELOPMENT OF BROADBAND LIGHT SOURCE AND INTERFEROMETER ELEMENTS

Miniature superluminescent emitters and fiber elements of the interferometer are the basis for creation of compact portable devices which are suitable for clinical and industrial environment. The superluminescent semiconductor diodes based on one-layer quantum-dimensional (GaAl)As-heterostructures with central wavelengths of 907 nm and 948 nm, spectral widths of about 53.4 nm and 72 nm, and initial radiation power in the output of the single-mode fibers of 0.9 and 3 mW were employed as a light source. Spectra and corresponding ACFs of SLDs used and are shown in Figure 2.

The spectra of the both SLDs have complicated shapes which are inherent for quantum-dimensional heterostructures [12]. When the radiations of two SLDs are mixed the spectrum of resulting radiation considerably depends on the ratio of initial powers of each SLD. Figure 3(a) illustrates several resulting spectra obtained at the fixed power (0.9 mW) of a 907 nm SLD and varying power of a 948 nm SLD (relative attenuation α of the initial power of the 948 nm SLD is attained by lowering the pumping current). Corresponding ACFs are shown in Figure 3(b). The resulting optimal spectrum was of a complex shape; bandwidth of generated light was slightly wider than 100 nm and corresponding minimum width of the central ACF lobe was 4.9 μm (free space). The sidelobes of ACF were suppressed to the level of 17.5 dB as compared to the central main peak.

Spectral tuning of the fiber optic multiplexer combining optical radiations from two SLDs in one fiber was found to be critical. By controlling the parameters of the multiplexer during assembly, the multiplexer output was optimized to provide the narrowest ACF, which

automatically provided the widest bandwidth of the resulting spectrum. The multiplexer was made of halves of a polished coupler using anisotropic fiber. The final assembly of the multiplexer was performed with light introduced into both halves; the output ACF of the resulting radiation was controlled with a correlometer and optimized as described above till the minimum width of the resulting ACF was attained.

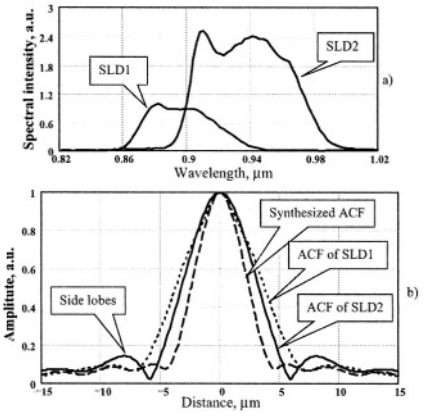

Figure 2. (a): spectral characteristicsof superluminescent diodes (b): autocorrelation functions.

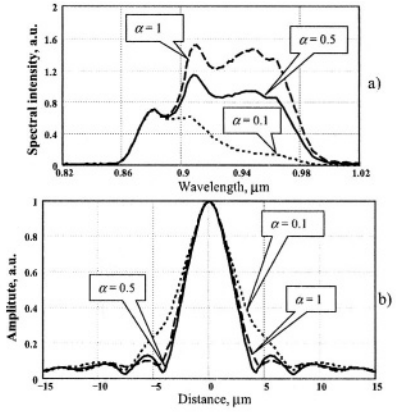

Figure 3. Synthesis of broadband signal at different values of attenuation factor α of the second source (SLD2). (a): synthesized spectrum, (b): corresponding autocorrelation function.

Figure 4 shows several curves of the resulting ACF width versus total output power of the multiplexer. Parameter α was a ratio of current power of 948 nm SLD to the initial power of 3 mW. The narrowest achieved ACF width corresponded to 4.75 μm in air.

The interferometer comprised a fiber optical 3dB coupler built of polished elements. There was observed optical coupling of modes in the polished elements due to interaction of exponentially decreasing fields occurring mostly in fiber coating. Polished couplers in contrast to welded ones usually provide a higher degree of isolation of polarization modes with the extinction coefficient of at least 35 dB. However, typical couplers of this type have bandwidths that are insufficiently wide for use in interferometers with bandwidths of light sources at the order of 100 nm. In our study, we analyzed the possibility of increasing the broadband of the 3dB coupler by optimizing its parameters. As a result, we determined a more optimal domain of parameters and developed a 3dB coupler with improved broadband. Figure 5 presents experimental curves of the transfer coefficient during

successive propagation and coupling in conventional and novel couplers. As it can be seen from the graph the novel design provides broadband approximately twice as large as that of a conventional design. The parameters of the novel 3dB fiber optical coupler are listed below: spectral bandwidth of 150 nm with central wavelength of 0.94 μm, insertion losses less than 0.2 dB, and the level of cross-talk between the polarization modes less than 35 dB.

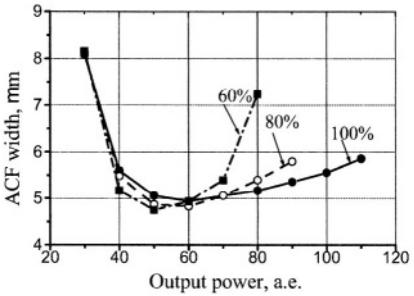

Figure 4. Dependence of resulting ACF width versus output power of the multiplexer.

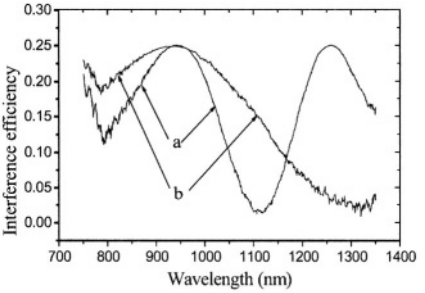

Figure 5. Coupling efficiency, forward and backward pass, (a) with conventional broadbandness, and (b) enhanced broadbandness.

20.4 INFLUENCE OF LIGHT SCATTERING ON OCM SPATIAL RESOLUTION

Multiple small-angle scattering affects spatial resolution of the OCM method significantly. In the transparent non-scattering medium in-depth spatial resolution of the method is defined by a longitudinal coherence length (l_c) that is related to a coherence time (τ_c) and the velocity of light in the medium (v_n): $l_c = \frac{v_n \tau_c}{2}$. OCM sub-micron lateral resolution is determined by the waist size of the probing beam and is attained by using large numerical apertures. However at typical imaging depths within biological tissue multiple small-angle scattering becomes the dominant reason responsible for reducing the quality of obtained OCM images. Owing to multiple small-angle scattering the radius of the focal spot increases thus resulting in degradation of OCM lateral resolution. Moreover, the phenomenon of small-angle scattering also decreases OCM axial resolution due to multipass of photons.

However the analysis of OCM resolution performed on the basis of the discussed above theoretical model allows us to conclude that loss of spatial

resolution due to scattering can be reduced by strong focusing of the probing beam, and in this way both lateral and axial resolution can be improved.

Figure 6 shows a dependence of OCM lateral resolution versus imaging depth for various waist sizes of the probing beam waist. It is assumed that an OCM image is reconstructed by synchronous in-depth scanning of the beam focal spot and the length of the reference arm while keeping the beam waist size constant. The lateral resolution was estimated by the FWHM of an OCM image of a point object obtained from the theoretical OCT model described in Chapter 17 (section 17.2) [13,14]. (All presented dependences are calculated for a medium with scattering coefficient μ_s = 10 mm^{-1}, anisotropy factor g = 0.9 and initial longitudinal coherence length l_c = 5 μm.) As it is seen from the Figure 6 OCM lateral resolution is preserved for larger imaging depths for probing beams with smaller initial sizes of beam waists. Starting from 10 mean free paths (mfp), a considerable loss of lateral resolution occurs due to diffuse widening of the probing beam at the focal depth. Under these conditions the focusing effect also disappears and the behavior of lateral resolution versus depth becomes asymptotic and universal for all initial sizes of beam waists.

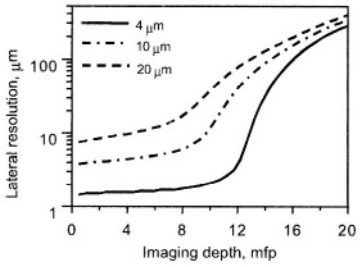

Figure 6. Dependence of OCM lateral resolution versus depth for different initial waist sizes of probing beam.

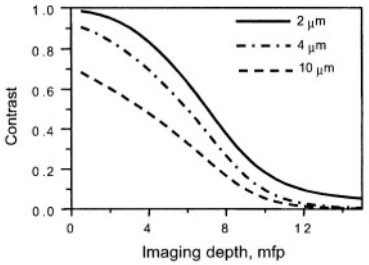

Figure 7. The contrast of the layer with spatially modulated backscattering coefficient for various initial beam waist sizes.

The idea of how OCM lateral resolution is lost can be deducted from imaging the layer with sinusoidal spatial modulation of the backscattering coefficient. Figure 7 demonstrates contrast of such a structure, i.e., the relative modulation amplitude of detected intensity versus the layer depth within scattering medium. The contrast depends on the structure scale significantly. At shallow depth the structures which scale is comparable to the size of the beam waist have far less contrast than those with the scale at the order of 10 diameters of the beam waist. Contrast degradation with the imaging depth can be explained by beam widening at the focal volume, the beam waist first becomes comparable with the structure scale and then exceeds it.

It is important to point out that axial resolution of the method of OCM benefits from tight focusing of the probing beam due to retaining of the

longitudinal coherence length for larger imaging depth in comparison to non-focused or weakly focused beams. OCM axial resolution is defined as the width of an OCM image of a thin backscattering layer. Figure 8 shows the dependence of OCM axial resolution on the imaging depth for different sizes of beam waists. At shallow depth strong focusing provides better axial resolution because ballistic photons of a highly focused beam contribute greater to the total light distribution at the focal volume. However at larger depths one can notice a sharper decrease of axial resolution for beams with smaller widths. This effect can originate from the fact that for a the beam focused deep inside of a scattering medium, the backscattered OCM signal is registered not from the focal volume precisely but from a closer distance due to group retardation of photons. In the case of tight focusing, the beam volume that contributes to the detected signal is larger than that of a weakly focused beam. Therefore OCM image is formed by photons undergoing more scattering events, which results in a significant loss of axial resolution. Figure 9 shows the behavior of OCM axial resolution for various imaging depths as the beam waist increases.

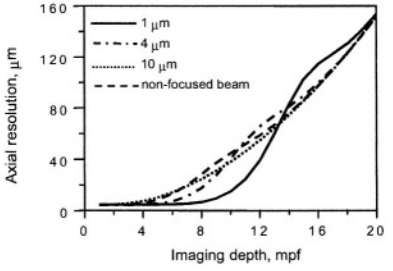

Figure 8. OCM axial resolution versus the imaging depth for different waist sizes of probing beam.

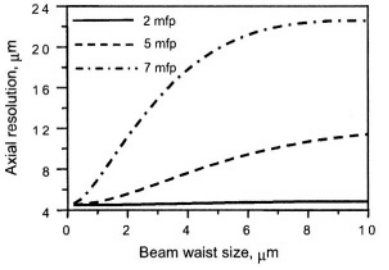

Figure 9. OCM resolution degradation versus beam waist size at various imaging depths.

In summary the analysis of OCM spatial resolution shows that tight focusing of the probing beam allows to preserve both lateral and axial resolution up to the depth of 10 mfp due to increased contribution of ballistic photons to an OCM signal.

20.5 ELECTRO-MECHANICAL SYSTEM FOR DYNAMIC FOCUS

The optical probe comprising the focusing system and the means for transversal beam scanning is located at the distal end of the sample arm of the interferometer. The optical layout of the focusing system consists of two lenses with effective magnification of unity. The lateral focal spot size was

equal to 3.9 μm, i.e., to the diameter of fiber mode of the sample arm. The second lens allows using the objective aperture with maximum efficiency. The dynamic focus is attained in this OCM prototype by moving the output lens axially and thus providing longitudinal movement of the focal spot through the object [Figure 10(a)]. The relationship between the axial displacement of the focal spot in a medium and the coherence gate while they are simultaneously scanned and the path-length difference between the arms of the interferometer is established below. If the focal spot during lens scanning is placed inside of a uniform medium with a refractive index n, then, as shown in Ref. [9], the lens displacement Δz_L will correspond to the increase in the optical path-length of the sample arm by $nn_g\Delta z_L$. Here n_g is the group refractive index of the medium. Therefore, when the lens is moved, the distance between centers of the focal and coherence zones gets shifted by $nn_g\Delta z_L$. In our interferometer, an additional modulator is used to scan the optical path-length difference between the interferometer arms [11]. The path length difference of Δz in free space corresponds to the displacement of the coherence zone in the medium of $\Delta z/n_g$. Obviously, the initially aligned focal spot and coherence gate centers will not diverge during scanning only if the following condition is satisfied $nn_g\Delta z_L = \Delta z$. At the fixed rate of the path length difference scanning which determines a Doppler frequency, the rate of the axial movement of the output lens should be

$$\Delta \dot{z}_L = \Delta \dot{z} / \left(n \cdot n_g\right).$$

The typical length of the focal area (Rayleigh waist), say, for a focal spot diameter of 3.9 μm is 26 μm. Therefore, spatial alignment of the coherence gate and the focal spot should be quite accurate. The output lens was hanged in flexible suspension and scanned according to the triangular law by an electromagnetic controller with frequency of 100 Hz [Figure 10(c)]. The amplitude-frequency characteristic of the mechanical system was typical for resonance mechanical systems with a resonance frequency of ~40 Hz and a Q factor of ~4 [Figure 10(b)]. Since the frequency of lens scanning was close to the resonance frequency of the system, the control triangular signal was pre-distorted to compensate for the resonance response. As a result, it was measured that for the amplitude of lens oscillations of 0.6 mm, the difference between the real motion and the theoretical one did not exceed 2% for approximately 80% of the movement range [Figure 10(d)]. The lateral resolution of OCM was analyzed using a grating with a step of 10-μm. The OCM images of the periodic pattern were recorded for several longitudinal positions of the sample. In a typical image is shown in Figure 11, the contrast of the image is about 30 dB. This corresponds well with the computational results for a Gaussian beam with a waist of 3.9 μm in diameter.

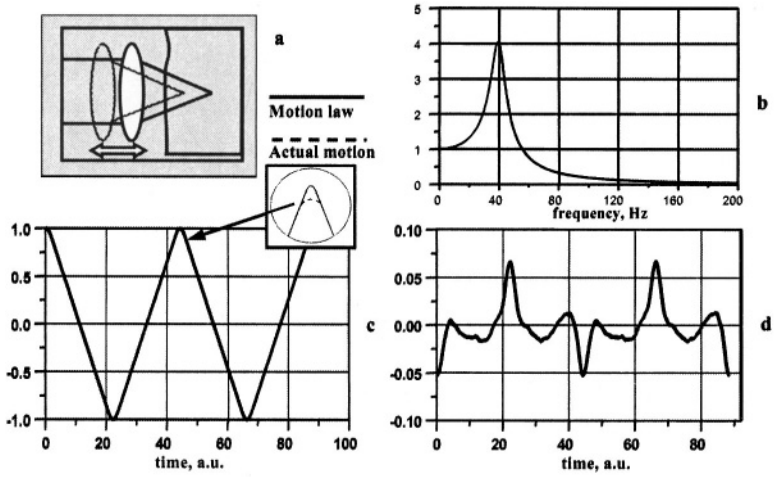

Figure 10. Dynamic focusing in OCM.

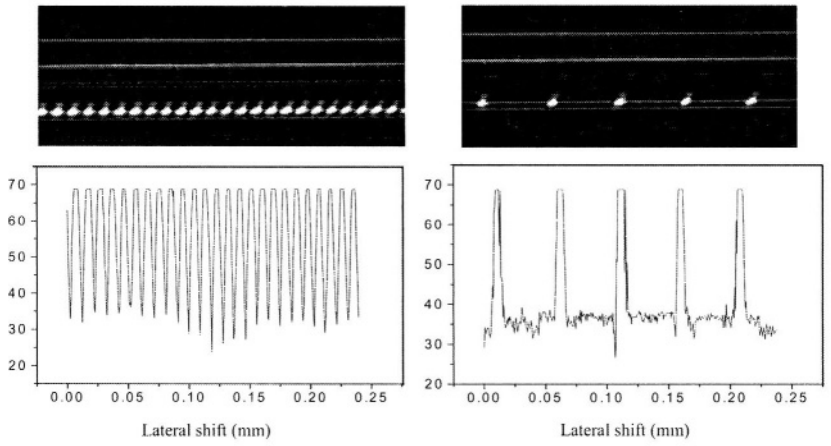

Figure 11. OCM images of periodic patterns.

Of course, it is not always possible to precisely align the coherence gate and focal zone in real biotissue. This can be caused by deviations of refraction index from its mean, which are typical for biotissue layers [10]. In fairly thick layers of biological tissue, the misalignment can exceed the size of the focal zone. However, this misalignment can be eliminated in a single layer by correcting the lens movement law. To obtain an image with

maximum resolution over the whole scanning range, it is necessary to acquire several 2D images with corrected focusing for particular layers of biological tissue and then fuse these 2D images.

20.6 DIGITAL SIGNAL PROCESSING AS A TOOL TO IMPROVE OCM RESOLUTION

As it was described in section 20.3 the radiation from two spectrally separated SLDs was combined in one fiber. It was observed that the resulting radiation had a spectrum of a non-Gaussian shape. This phenomenon led to the appearance of sidelobes in ACF at the distance of ±10 μm from the main center peak with amplitude of -18 dB. To suppress the sidelobes we developed a method of regularization of the spectrum of the Doppler signal by means of digital signal processing. The idea of the method is to devise a regularization function which could be used to multiply the original ACF with sidelobes and the product would yield ACF with nearly Gaussian shape with suppressed sidelobes. Using this function, the recorded radio-frequency (RF) signal was converted and an OCM image was reconstructed.

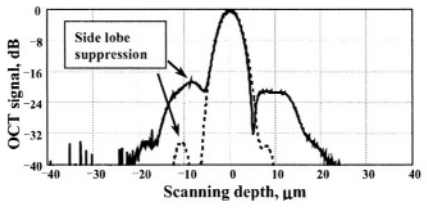

Figure 12. Autocorrelation function before (bold line) and after (dotted line) regularization procedure.

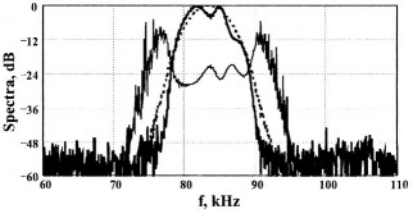

Figure 13. Spectra of the Doppler signal before (bold solid line) and after regularization (bold dotted line) and the spectrum of the regularizing function (solid thin line).

Figure 12 shows the ACF shape before and after spectrum regularization. It can be seen that the sidelobes were suppressed approximately by 17 dB. Figure 13 presents spectra of the Doppler signal before and after regularization and the spectrum of the regularizing function. Note that along with the correction of the spectrum, the regularization procedure eliminated noise outside of the Doppler detection band. Figure 14 illustrates an example of an OCM signal from two thin scattering boundaries separated from each other by 18 μm, before and after regularization.

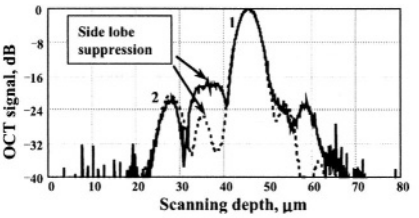

Figure 14. Bold line: OCT signal obtained from two reflectors, peaks 1 and 2, correspondingly; dotted line: OCT signal after spectra regularization procedure. The amplitude of a side lobe between peaks 1 and 2 is larger than the amplitude of peaks 2 and thus produces a false target on a tomogram. Regularization method allows one to suppress side lobes significantly.

It can be seen from this figure that the sidelobes of responses from two boundaries overlap. Obviously, the resulting sidelobes in the OCM signal in between the central peaks of boundary responses depend on the phase difference between the latter. As a result, the suppression of these combined sidelobes by means of regularization would also depend on a distance between responses. In this particular case the sidelobes were suppressed by 8 dB. If the distance between neighboring imaging elements exceeds the coherence length, the degree of sidelobe suppression by regularization will be the same as for ACF and will be equal to 17 dB.

20.7 EXPERIMENTAL OCM PROTOTYPE

All the ideas and approaches described above were implemented in our experimental compact OCM prototype. The OCM setup features a flexible signal arm and a remote optical probe at the distal end. The probe is equipped with a three-coordinate scanning device that controls a focal zone position. The size of the optical probe in the largest dimension does not exceed 5 cm. The studied object is placed atop the output window with immersion. Figure 15 presents a general view of the compact optical coherence microscope and the remote optical probe connected to the main body by flexible optical and electrical cables. The dimensions of the OCM device in this configuration do not exceed $12\times30\times40$ cm^2, weight is about 7 kg. The OCM requires standard AC power network, device power consumption is no more than 25 W. The OCM device can be operated and images can be recorded and stored using a personal desktop or portable computer with a processor 486DX-33 or higher. The OCM device in the current design may be applied for intraoperative express analysis of human tissues *ex vivo.*

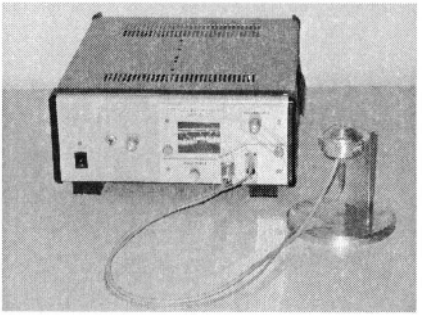

Figure 15. General view of OCM.

20.8 BIOMEDICAL APPLICATIONS

Preliminary biomedical experiments using OCM were carried out on model media and on biological materials *ex vivo,* namely, plant leaves and excised human tissues were studied. Plant leaves were observed immediately after separation from the stem in order to minimize influence of a decrease in cellular turgor on the quality of images. Postoperative samples of human tissue were placed into physiological solution right after excision and were studied during next 40 minutes to avoid postmortal tissue alterations.

Figure 16 shows OCM and OCT images of tomato and tradescantia leaves. Images clearly demonstrate morphological features of studied objects. Advantages of OCM over OCT are obvious: while OCT allows to differentiate mostly cellular layers, and rarely large cells with a size of 50-100 μm, OCM easily visualize both cellular layers and single cells with a size of 10-20 μm constituting these layers.

Quality of visualization of intracellular structures is determined not only by spatial resolution of the method but also by the chosen plane of scanning because sometime 2D scans miss cellular nuclei. 3D scanning of the object with a step of several microns between the 2D planes allowed reconstructing the true 3D structure of the object, detecting cellular nuclei and accurate estimating of cellular shapes and sizes.

Based on our experience with OCT where the most informative were tissues with a stratified internal structure for the OCM study we chose organs covered with the squamous epithelium. The idea of the study was to compare OCM and OCT performances. Results of the study are shown in Figure 17. Comparative analysis revealed that while standard OCT could visualize the tissue layers, namely, the epithelium and underlying stroma, OCM could distinguish single cells constituting the epithelium up to depth of 500 μm.

Therefore, clinical and biological experiments clearly demonstrate that spatial resolution of OCM is sufficient for visualizing single cells. High spatial resolution of OCM advances us to realization of the idea of absolutely non-invasive "optical" biopsy. We believe that another promising applications of OCM is monitoring of plants *in vivo* with a purpose of dynamic control of structural alterations. Non-invasive investigation of internal structures of plants would allow studying the influence of various environmental factors (external and internal). Such studies would definitely benefit selections, ecology and cosmic biology.

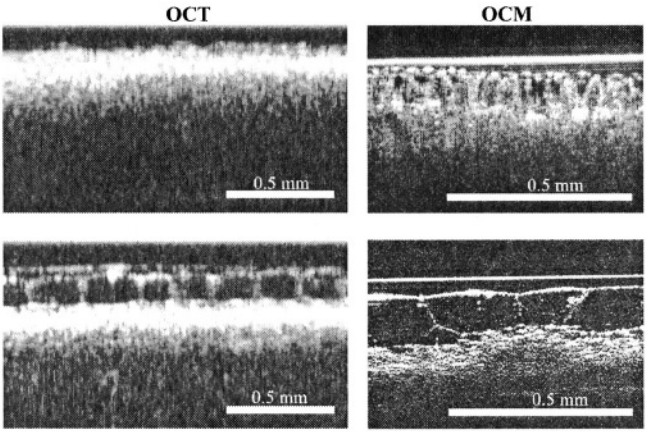

Figure 16. OCT and OCM images of tomato and tradescantia leaves.

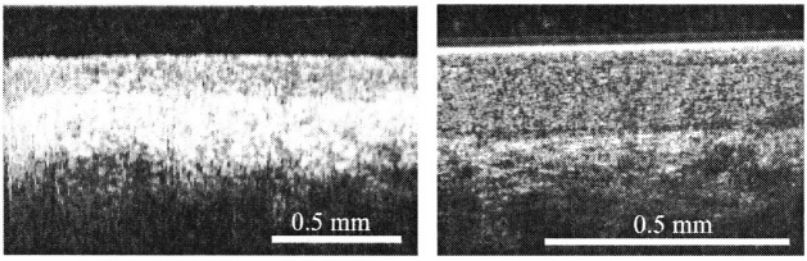

Figure 17. OCT and OCM images of uterine cervix *ex vivo.*

20.9 SUMMARY

In this chapter we report about development and fabrication of a compact optical coherence microscope (OCM) based on broadband PM fiber

elements. OCM combines advantages of ultra broadband OCT and high numerical aperture confocal microscopy. An ultra broadband light source was devised and constructed using two SLDs with spectra covering the wavelength range of 0.88 – 0.98 μm. The light source provided axial resolution of 4.75 μm in air. The optical layout of the OCM probe comprised two micro lenses transposing the fiber tip with magnification of 0.8 – 1 and provided lateral resolution of about 3.9 μm. The focal volume of the probing beam and the coherence gate were spatially matched and scanned in-depth synchronously using the principle of the dynamic focus. For this purpose we developed and created a three-coordinate electro-mechanical system. We also proposed and investigated a method for correction of distortion of the ACF form caused by the non-Gaussian shape of the light source spectrum. This method corrects the envelope shape and suppresses the spectral sidelobes by regularizing the spectrum of the Doppler signal at the stage of digital signal processing. The dependences of axial and lateral spatial resolutions of the optical coherence microscope on imaging depth in media with scattering parameters typical for tissue were investigated theoretically. OCM images of model media and biological objects *ex vivo* were acquired.

ACKNOWLEDGEMENTS

The authors thank Alexander Turkin and Pavel Morozov for assistance in creating optical elements, Irina Andronova for valuable scientific discussion, Nadezhda Krivatkina and Lidia Kozina for providing translation and Marina Chernobrovtzeva for editing. This work was partly supported by the Russian Foundation for Basic Research under the grants #01-02-17721, #03-02-17253, #03-02-06420 and by the Civilian Research & Development Foundation under the grant RB2-2389-NN-02.

REFERENCES

1. J.A. Izatt, M.R. Hee, G.M. Owen, E.A. Swanson, and J.G. Fujimoto, "Optical coherence microscopy in scattering media," *Opt. Lett.* **19,** 590-592 (1994).
2. J.A. Izatt, M.D. Kulkarni, H.-W. Wang, K. Kobayashi, and M.V. Sivak, Jr., "Optical coherence tomography and microscopy in gastrointestinal tissues," *IEEE J. Select. Tops Quant. Electr.* **2**, 1017-1028 (1996).
3. W. Drexler, U. Morgner, F.X. Kartner, C. Pitris, S.A. Boppart, X.D. Li, E.P. Ippen, and J.G. Fujimoto, *"In Vivo* ultrahigh-resolution optical coherence tomography," *Opt. Lett.* **24**, 1221-1223(1999).
4. A.M. Kovalevicz, T. Ko, I. Hartl, J.G. Fujimoto, M. Pollnau, and R.P. Salathe, "Ultrahigh resolution optical coherence tomography using a superluminescent light source," *Opt. Express* **10,** 349-353 (2002).

5. I. Hartl, X.D. Li, C. Chudoba, R. K. Ghanta, T.H. Ko, J.G. Fujimoto, J.K. Ranka, and R.S. Windeler, "Ultrahigh-resolution optical coherence tomography using continuum generation in an air-silica microstructure optical fiber," *Opt. Lett.* **26,** 608-610 (2001).
6. B. Povazay, K. Bizheva, A. Unterhuber, B. Hermann, H. Sattmann, A.F. Fercher, W.Drexler, A. Apolonski, W.J. Wadsworth, J.C. Knight, P.S.J. Russel, M. Vetterlein, and E. Scherzer, "Submicrometer axial resolution optical coherence tomography," *Opt. Lett.* **27**, 1800-1802(2002).
7. J.M. Schmitt, S.L. Lee, and K.M. Yung, "An optical coherence microscope with enhanced resolving power in thick tissue," *Opt. Communs.* **142,** 203-207 (1997).
8. A. Baumgartner, C.K. Hitzenberger, H. Sattmann, W. Dresler, and A.F. Fercher, "Signal and resolution enhancements in dual beam optical coherence tomography of the human eye," *J. Biomed Opt.* **3**, 45-54 (1998).
9. F. Lexer, C.K. Hitzenberger, W. Drexler, S. Molebny, H. Sattmann, M. Sticker, and A.F. Fercher, "Dynamic coherent focus OCT with depth-independent transversal resolution,"*J. Mod. Opt.* **46,** 541-553 (1999).
10. A. Knüttel and M. Boehlau-Godau, "Spatially confined and temporally resolved refractive index and scattering evaluation in human skin performed with optical coherence tomography," *J. Biomed. Opt.* **5**, 83-92 (2000).
11. V.M. Gelikonov, G.V. Gelikonov, N.D. Gladkova, V.I. Leonov, F.I. Feldchtein, A.M. Sergeev, and Ya.I. Khanin, "Optical fiber interferometer and piezoelectric modulator." USA, Patent #5835642, 1998.
12. V.K. Batovrin, I.A. Garmash, V.M. Gelikonov, G.V. Gelikonov, A.V. Lyubarskii, A.G. Plyavenek, S.A. Safin, A.T. Semenov, V.R. Shidlovskii, M.V. Shramenko, and S.D. Yakubovich, "Superluminescent diodes based on single-quantum-well (GaA1)As heterostructures," *Quant. Electr.* **26,** 109-114 (1996).
13. L.S. Dolin, "A theory of optical coherence tomography," *Radiophys. Quant. Electr.* **41**, 850-873(1998).
14. L.S. Dolin, "On the passage of a pulsed light signal through an absorbing medium with strong anisotropic scattering," *Radiofizika* **26,** 300-309 (1983).

Chapter 21

CONFOCAL LASER SCANNING MICROSCOPY

Barry R. Masters
Fellow of OSA, Fellow of SPIE, Formerly Gast Professor, Department of Ophthalmology, University of Bern, Bern, Switzerland

Abstract: Principles and instrumentation of laser scanning confocal microscopy are described. Applications to materials inspection are discussed. Current results on *in vivo* imaging of skin, eye tissues, and cells are demonstrated. The principles of optical sectioning in confocal and multiphoton excitation microscopies are compared.

Key words: confocal microscopy, cornea, slit scanning confocal microscopy, three-dimensional imaging, tandem scanning confocal microscope, laser scanning confocal microscope, multiphoton excitation microscopy

21.1 INTRODUCTION

Confocal microscopy is a revolutionary development in optical microscopy. Its use has resulted in spectacular advances in cell biology, developmental biology, and neurobiology as well as in clinical medicine; specifically in ophthalmology and dermatology. *In vivo* confocal microscopy is routinely used in the clinic and has become an important diagnostic and research tool. Confocal microscopy has also provided an invaluable tool for the qualitative and quantitative observation of materials, microstructures and composites; it is extensively used for quality control during the manufacture of microelectronics. The development of confocal microscopy has caused a revolution in optical microscopy by providing the researcher and clinician with increased axial resolution and contrast; thus presenting the capability of optical sectioning and three-dimensional microscopy. It is in the area of live cell and tissue imaging that many advances are being made. The development of new fluorescent probes permits three-dimensional microscopy of cells and tissues to be observed over extended periods of time. The use of nonlinear microscopy such as multiphoton excitation

microscopy has extended the depth and the duration for live cell and tissue imaging.

21.2 OPTICAL PRINCIPLES OF CONFOCAL MICROSCOPY

21.2.1 Introduction

A great advance in the understanding of light microscopy was the seminal work of the physicist Abbe in Jena, Germany on the analysis of image formation and resolution of a lens based on wave diffraction theory [1,2]. Geometrical optics is not suitable to solve this problem. Abbe's theory of image formation can be summarized as follows: interference between the zero-order and higher-order diffracted rays in the diffraction plane (back focal plane of the lens) forms image contrast and limits the spatial resolution of an objective lens. Abbe showed that image formation in the image plane is the result of interference between the zero-order (undeviated rays) and at least one if the first-order deviated rays. The angular aperture of the microscope objective must be sufficiently large enough to collect the zero-order and the first-order beams. Abbe also made several other major contributions to the field of microscopy: the first planachromatic objective, the first apochromatic objective, lens designs based on his sine-squared condition, and an interference test to determine lens curvature.

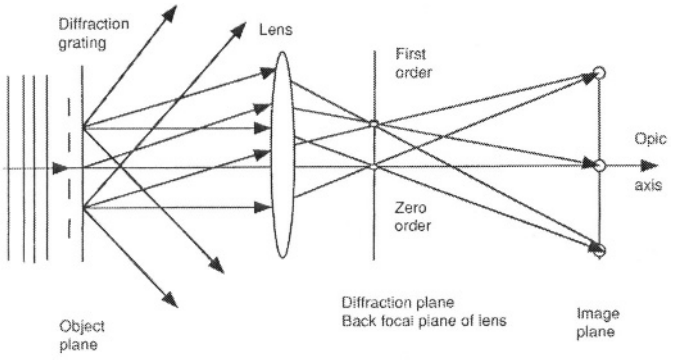

Figure 1. Diagram to illustrate Abbe's theory of image formation. A plane wave is diffracted by a grating in the object plane. The lens produces a magnified real image in the image plane. In the back focal plane of the lens (the diffraction plane) the diffracted rays are separated, but they are combined in the image plane. Note that some diffracted rays do not enter the lens. Only those components corresponding to ray angles which pass through the lens form the image of the object.

The interference in the image plane results in image contrast. At least two different orders of diffracted rays must enter the lens for interference to occur in the image plane. The coherent light beams coming from the various parts of the diffraction pattern mutually interfere and produce the image in the front focal plane of the microscope eye piece. A result of his analysis is the importance of the use of high numerical aperture microscope objectives (high NA). The Abbe analysis gives the following result for the smallest detail that can be resolved with a microscope as a function of wavelength, λ, and numerical aperture (NA) of the microscope objective as:

$$\Delta x \equiv \frac{\lambda}{2\mathrm{NA}} \quad . \tag{1}$$

This result is based on the Abbe analysis which considered the object with an amplitude that varied sinusoidally in space. Abbe suggested that the light from the object could be considered as the superposition of two plane waves that move towards the lens and are inclined at an angle (θ) to the optical axis. The object must diffract light and this diffracted light must enter the lens in order for image formation to occur. If the microscope objective is not able to collect the plane waves, then they cannot contribute to the image formation. Thus, the resolution of the microscope is limited by both the wavelength of the illumination light and the numerical aperture of the microscope objective. The above relation is the diffraction limited resolution of the microscope [2].

The experimental verification of the theoretical wave analysis of microscopic image formation was shown by Abbe. He used a diffraction grating for the specimen and observed its image in the microscope when the condenser aperture was closed down. Abbe showed that there is a reciprocal relationship between the line spacing of the grating and the separation of the diffraction spots at the aperture plane. He observed the diffraction pattern of the grating, or the image of the condenser iris diffracted by the periodic spacing of the grating. Each diffracted-order ray including the zero-order ray is focused in the back focal plane of the objective lens. His most important experimental finding was that when the first-order pattern was blocked at the back aperture of the objective, the zero and the second-order patterns were transmitted. Then he found that the image (orthoscopic image) appeared with twice the spatial frequency due to the interference between zero order and second order diffraction patterns. This remarkable result proved that the waves that form the diffraction pattern at the aperture plane converge and interfere with each other and form the image in the back focal plane of the objective. Abbe was able to further demonstrate that for the image of the diffraction grating to be resolved it was required for at least the zero-order and the first-order diffraction patterns to be accepted by the numerical aperture of the objective lens.

Another approach is based on the Fourier approach to wave optics and leads to the same result and equation given above. What limits the resolution of the image is the number of spatial frequencies that can enter the microscope objective. Thus, the Fourier series representing the image is truncated due to the numerical aperture of the microscope objective and this limits the spatial resolution of the image. Therefore, there is an upper limit to the ability of an optical system to resolve the spatial features in an object.

A second important consideration in microscopic image formation is the signal-to-noise ration of the image which is a consequence of the quantum nature of light. Shot noise or Poisson noise is caused by the quantum nature of light. Photons interact with the detector at random time intervals. This random distribution can be approximated by the Poisson distribution. The Poisson contribution to the signal-to-noise ratio is given by the number of photons detected per unit time, N, divided by the square root of N.

$$\mathrm{SNR} = \frac{\mathrm{N}}{\sqrt{\mathrm{N}}} \ . \tag{2}$$

The higher the signal-to-noise ratio of the image results in an improved image quality with higher information content.

21.2.2 Resolution in Confocal Microscopy

21.2.2.1 Optical Sectioning

In a simple lens microscope the lateral resolution and the axial resolution are not independent. The great advantage of a confocal microscope is that the axial resolution is enhanced, and this enhancement applies for any object, not only a point object. It is this increase in the axial resolution that results in the "optical sectioning" capability of confocal microscopes. And this wonderful property of "optical sectioning" has led to the revolution in biological imaging and also widespread utility in material imaging and clinical imaging in ophthalmology and dermatology as well as plant biology and neurobiology and developmental biology.

21.2.2.2 Lateral and Axial Resolution

Lateral or transverse resolution is in the plane of the specimen or the x-y plane. Axial resolution is along the z-axis or the optical axis of the microscope. The lateral resolution of a confocal microscope is proportional to the numerical aperture (NA) of the microscope objective. However, the axial resolution is more sensitive to the numerical aperture of the microscope objective. Therefore, to obtain the maximum axial resolution, and hence the

best degree of optical sectioning, it is preferred to use microscope objectives with the largest numerical aperture. For an oil immersion microscope objective with a numerical aperture of 1.4, and blue light wavelength 442 nm, the lateral resolution is 0.14 μm, and the axial or depth resolution is 0.23 μm.

The lateral resolution of a conventional and a confocal microscope are now compared following the analysis of Wilson [3,4]. We examine the case of a conventional microscope with the pinhole removed, or a confocal microscope with the pinhole in place in front of a detector. The image of a single point specimen is viewed in reflected light. The image intensity is given by equation 3.

$$I_{CONV}(v) = \left(\frac{2J_1(v)}{v}\right)^2 \quad , \tag{3}$$

where I_{conv} is the intensity of light from the object, J_1 is the first-order Bessel function, and v is a coordinate which is related to the lateral distance in the focal plane *r,* by equation 4.

$$v = \frac{2\pi}{\lambda} r \sin\alpha \ . \tag{4}$$

The symbol λ is the wavelength, and the numerical aperture of the objective is $\sin\alpha$. For the confocal case in the presence of the pinhole, the image is now given by equation 5.

$$I_{CONF}(v) = \left(\frac{2J_1(v)}{v}\right)^4 \ . \tag{5}$$

For the confocal case the image is sharpened by a factor of 1.4 relative to the conventional microscope. With a confocal microscope the resolution is about 40% better than in a conventional microscope. An experimental method to measure the axial resolution of a given microscope objective in a confocal microscope is to measure the variation of the intensity of the light reflected from a front surface mirror as it is scanned through the focal plane. One measure of this resolution is the width of the curve at one half maximum intensity [5]. A non-confocal or standard microscope would not show any variation in the intensity as the mirror is scanned through the focal plane.

Wilson has shown the following treatment for the axial resolution in a confocal microscope for imaging both points and planes. A confocal

microscope is scanned axially so that the intensity of light reflected from a plane mirror is detected as a function of the distance that the mirror moves towards the focal plane. At the focal plane the intensity of the reflected signal is maximum. The intensity of the reflected light is given by simple paraxial theory as equation 6.

$$\mathrm{I}(\upsilon) = \left[\frac{\sin\left(\frac{\upsilon}{2}\right)}{\frac{\upsilon}{2}} \right]^2 . \tag{6}$$

The symbol υ is a normalized axial coordinate which is related to the real axial distance z by equation 7,

$$\upsilon = \frac{8\pi}{\lambda} z \sin^2\left(\alpha/2\right) . \tag{7}$$

These equations are for plane reflectors. For point or line reflectors the equation 6 becomes:

$$I(\upsilon) = \left[\frac{\sin(\upsilon/2)}{\upsilon/2} \right]^4 . \tag{8}$$

The optical sectioning is weaker for a point or a line than for a plane. All of these equations refer only to brightfield imaging in the reflection mode. For fluorescence imaging which is incoherent light imaging all of the equations are different. Image quality is not only dependent on resolution, but also is very dependent on the contrast of the image.

The principle of the out of focal plane rejection in a confocal microscope is shown in Figure 2.

Note that the reflected light from the focal plane passes through the pinhole and reaches the detector. In the case for the unfocused system the reflected light is spread out over a region larger than the pinhole; only a very small amount of the light from the out of focal plane passes the pinhole and is detected.

An important problem in confocal microscopy is the optical aberrations that are introduced by the specimen and or the instrument itself. A recent paper by the Wilson group at University of Oxford presents a solution to this problem: a wave-front sensor that is capable of restoring diffraction-limited optical performance in confocal microscopy [6].

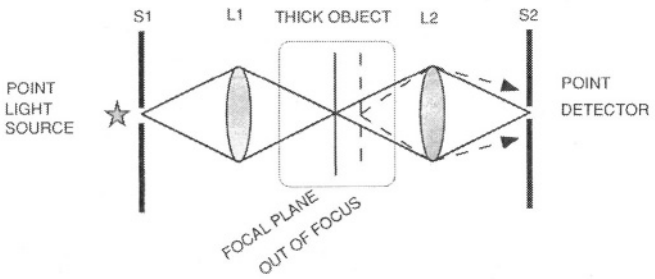

Figure 2. Schematic diagram illustrating the principle of a confocal microscope. S1 and S2 are confocal apertures. L1 and L2 are focusing lens for illumination and detection respectively. The focal volume that is illuminated with the point source of light from S1 and focused with lens L1. This illuminated focal volume is imaged by lens L2 to form an image at the aperture S2.

Several generic types of confocal light microscope are now described [7]. Minsky described in his patent two methods of point scanning. The image is build up of a number of points which correspond to the illumination and detection volumes. These volumes may be scanned sequentially as in a raster scan, or in parallel as in a line scan.

21.2.3 Development of Confocal Microscopy

The reader may find the following concise annotated biography useful. There is great value in reading the original reprinted papers that document the development of a field. A recent reprint collection of selected papers on confocal microscopy contains numerous early papers on the development of confocal microscopy as well as key papers and patents on instrument design, applications and further resources [8], A similar volume the offers a comprehensive coverage of multiphoton excitation microscopy from theory to applications and patents is also available [9]. *Theory and Practice of Scanning Optical Microscopy* is the best comprehensive book on confocal microscopy [3]. Another book, *Confocal Scanning Optical Microscopy and Related Imaging Systems* presents a detailed development of the optical theory of various scanning optical microscopes and includes many examples of application to materials sciences and microelectronics [5]. The application of the transfer-function to three-dimensional imaging in confocal microscopes is the subject of *Principles of Three-Dimensional Imaging in Confocal Microscopes* [10]. Finally, two recent books cover many applications of confocal and multiphoton excitation microscopy: *Methods in Cellular Imaging* [11] and *Confocal and Two-Photon Microscopy* [12]. A very clear and comprehensive book that develops the field of nonlinear

optics including the topic of multiphoton absorption is *Nonlinear Optics,* second edition [13]. The book *Fundamentals of Light Microscopy and Electronic Imaging* is a wonderful introduction to the field of confocal microscopy and electronic imaging [14].

There is a wealth of information relating to the topics in this chapter on the world wide web. The terms confocal microscopy and multiphoton microscopy typed into the google web site (www.google.com) will provide the reader with the web sites of many university and research optical imaging centers. I list three specific sites that contain tutorials on the theory, technical notes, and application notes of confocal microscopy. Molecular Probes, Inc. (www.probes.com) is the publisher of the *Handbook of Fluorescent Probes and Research Products,* by Richard Haugland. The Handbook contains an introduction to fluorescence techniques and many images from cell and molecular biology as well as detailed technical information. Two other recommended sites are (www.zeiss.com) from Zeiss, and (www.bio-rad.com) from Bio-Rad. Both of these sites contain tutorials on theory and application as well as many examples from biology, pathology, and materials.

This chapter contains several references to the online, OSA journal *Optics Express* (www.opticsexpress.org) for multimedia peer-reviewed papers that cover the application of confocal microscopy and multiphoton excitation microscopy to ophthalmology and dermatology [15-18].

The history of the confocal microscope clearly illustrates the linkage between the development of new types of optical microscopes and the need to image thick, highly scattering tissues and organs. The modern confocal microscope provides the capability to image thick samples and provide thin optical sections with high resolution and high contrast. The ability to optically section thick specimens and then perform volume visualizations in a computer has resulted in three-dimensional microscopy.

It is instructive to follow the developments in optical microscopy as applied to imaging the cornea, the lens, and the retina. Subsequent instrumental developments that resulted in real-time confocal microscopy were motivated by the need to optical section the surface of the brain. Three groups of scientists working in three different countries developed three different types of confocal microscopes: Minsky in the United States, Petran and Hadravsky in Czechoslovakia, and Svishchev in Russia. All of these developments solved several problems involved with imaging thick tissues and they were subsequently incorporated into the designs of confocal imaging microscopes. Although Leeuwenhoek observed extremely thin sections of ocular tissues with his single lens microscope about 300 years ago, the problems of imaging their full thickness in the living eye have persisted until their solution in this decade.

We now review the development of the slit lamp, the specular microscope, and finally the confocal microscope; their common design

principles will become apparent. The emphasis is on the optical principles that are incorporated into modern confocal microscopes. The design goal of these inventors was to develop an optical microscope that could image a thin optical section within a thick, highly scattering tissue. In a confocal microscope both fluorescence and light scattered from outside of the focal plane is minimal; however, in classical microscopes this is the leading cause of loss of contrast within the focal plane.

The development of the slit lamp, a microscope that uses oblique illumination and microscopic observation, provided oblique sectioned views of the cornea and the ocular lens in the living eye. The light scattered from the tissue is detected without the interfering bright light of the illumination beam. The slit lamp is a long working distance microscope for observation of the living eye. A slit of light from a lamp, hence the name, is projected onto the cornea or the lens. A viewing microscope with a long working distance objective is focused on the same focal region as the image of the illuminated slit. Therefore, both the slit illumination and the detection system are focused on the same small volume. The key design principle is the following: a slit illumination system that transfers a slit of light across the thick tissue is coupled with an oblique light detection system; both use the same volume of the tissue. The slit lamp suffers from the fact that there is a shallow depth of field and that the reflectivity of the interior cornea is very weak. In contrast, the reflection from the anterior and posterior surfaces are much larger than the internal reflections. Now that we stated the problem let us look at the solution.

Goldmann offered a clever solution to this problem [19-20]. His modification of the Gullstrand slit lamp used a photographic system which moved on the optic axis. This clever technique permitted an integrating system that could integrate the images from the various thin optical sections into a composite image of larger area. This concept of moving the focal plane and integrating the small fields of view into a composite image of narrow depth of field is the basis of the future works of Maurice (wide-field specular microscope), and Koester (wide-field specular microscope for *in vivo* use).

The next major development was the specular microscope. A light source and the observer can be arranged to view this specular reflection from large differences in refractive index that occurs in biological tissues. The conditions for specular reflection are that the angle of incidence as measured from the normal and the angle of reflection are equal. An important problem solved by David Maurice was how to obtain en face images of the cellular layers of the cornea of living eyes [21,22]. Maurice coined the term "specular microscopy" and developed a working instrument. The microscope aperture was divided; one side used for illumination of the cornea with the projected image of a thin slit, and the other side was used for observation. The principle of using one half of the microscope objective for illumination,

and the other half of the objective to collect the light from the specimen results in a definite separation of the illumination and collection beams of light; however, the resolution of the optical system is reduced due to the smaller numerical aperture (one-half of the numerical aperture of the full microscope objective). The use half of the numerical aperture for illumination in the divided aperture microscope objective is common in several types of confocal microscopes that are designed for ophthalmology.

Following the instrument development of Goldmann, Maurice developed new type of specular microscope that used very narrow slits. While the use of narrow slits resulted in thin optical sections of the corneal endothelial cells the field of view was very narrow and therefore only a small number of endothelial cells were observed at a time. Maurice conceived the following solution to this problem. The eye and the film in the camera were moved in tandem. Therefore the narrow image of the corneal endothelium was integrated into a set of adjacent narrow images which formed an integrated image of high contrast and a large field of view. The disadvantage of this instrument was that it could only be used on *ex vivo* eyes. It was not suitable for *in vivo* observation of the corneal endothelium. It is important to note that the work of Maurice in the early development of the specular microscope formed the foundation of all modern developments in specular microscopy of the endothelium-optically sectioning the cornea and other thick tissues. To review, we restate the problem of using narrow slits. In order to separate the strong reflection from the tear/cornea interface from over whelming the weak specular reflection from the endothelium it was necessary to use very narrow slits. Only a few endothelium cells could be observed. If the slits were widened, then the optical sectioning of the specular microscope was degraded.

The next step in instrument development was devised by Koester [23,24]. He modified the principle of Maurice to produce a wide field specular microscope suitable for *in vivo* examination of the cornea. The slits were again made narrow. The divided aperture was used for the microscope objective. An applanating cone was used to flatten the cornea. The use of an applanating microscope objective helped to reduce the motion of the cornea due to cardiac pulse; however, it also induced folds in the stroma of the cornea and thus artifacts into corneal imaging [25]. What was new, and provided a solution to the problem of narrow slits, was the use of an oscillating, three-sided mirror. The mirror scanned and synchronously descanned a narrow beam of light across the corneal endothelium. This clever solution solved the long lasting experimental problems the designs of specular microscopes. Koester was later involved with further developments and refinements of his wide field specular microscope. The improvements involved increasing the numerical aperture of the applanating microscope objective. The Koester wide field specular used two conjugate slits and was a true confocal microscope. It suffered from poor optical sectioning

capability due to the low numerical aperture of the original applanating cone objective (0.33 NA). This resulted in poor efficiency of light collection. To observe images the slits had to be opened and the resulting images had large depth of focus. While the corneal epithelium and the corneal endothelium could be easily observed, the wing, basal and stromal details were very difficult to image. Following the work of Koester there were several applications of confocal microscopes to thick tissues.

We now describe a unique confocal microscope which has been developed to image the *in vivo* retina. In 1949 Ridley pioneered the development of the television ophthalmoscope, and point scanning of the retina using a cathode ray tube as a scanning point source of light for retinal illumination [26]. The spot of light on the screen of a cathode ray tube was raster scanned and imaged into the retina of a subject's eye. The spot of light scattered from the retina was imaged onto a photomultiplier tube and the two dimensional image of the retina was displayed in real-time on a television monitor. Ridley correctly pointed out that the use of point scanning, in which each spot on the retina is sequentially illuminated and the reflected and scatted light from that point imaged onto a detector, greatly improved the contrast of the image. This is a general principle which is valid for all confocal microscopes-the concept of point scanning of the illumination. Ridley's invention of a scanning spot ophthalmoscope is based on a cathode ray tube which served as a scanning point source of light for retinal illumination. This concept was implemented in the modern development of the scanning laser ophthalmoscope [27,28].

21.2.4 Developments of Confocal Imaging Systems in Biology

The field of biology and medicine traditionally generated many technological innovations in microscope development. The developments in confocal microscope were driven by the need to obtain thin optical sections from thick specimens, and to improve the contrast of fluorescent images from cells and tissues.

An early design of a confocal microscope was developed by Naora in 1951 to analyze nucleic acids in cell nuclei [8]. The microscope used two microscope objectives, one for illumination and one for light collection. Naora's development in optical microscope may perhaps be the first confocal microscope; however, it only worked in the transmission mode. The confocal microscope used one microscope objective above and another identical microscope objective below the specimen.

The innovation of beam scanning derived from the work on flying spot microscopes. An important innovation was the use of electromagnetic drivers to scan the microscope objective in the *x-y* plane. Roberts and Young

elucidated the principles of the flying spot microscope with their design of a flying-spot microscope [29].

Several approaches were used to provide beam scanning. In the early years mechanical devices were used for beam scanning. The work of Caspersson is noteworthy for the development of fluorescent microscopy of chromosomes, and cell nuclei.

Marvin Minsky is credited with the experimental realization of a stage scanning confocal microscope [30]. He clearly stated the advantages of stage or specimen scanning in his 1961 patent on the confocal microscope [8]. This idea decoupled the magnifications of the objective from the resolution. The magnification could be changed by changing the number of pixels in the image. His patent also clearly showed the folded mode (reflected mode) of modern confocal microscopes.

In Moscow, Russia a physicist with the name Svishchev developed and built a scanning slit, divided aperture confocal microscope for the study of transparent objects in incident light [31,32]. The Svishchev confocal microscope used two confocal adjustable slits. Changing the slit heights would vary the thickness of the optical sections. A double-sided oscillating mirror was used to scan and descan the image and was in the back focal place of the microscope objective. Many years later the Svischev design which consisted of an oscillating two-sided mirror was reinvented in the Netherlands as a confocal microscope with "bilateral scanning."

The modern development of the real-time tandem scanning confocal microscope is credited to Petran and co-workers [33]. They were interested in optical imaging structure of brain and neural tissue *in vivo.* This was the driving force for the development of their Nipkow disk confocal microscope. Petran later brought his microscope to the U.S. and collaborated with Egger at Yale University. Their 1967 paper published in *Science* included a composite pen hand drawing of the three-dimensional structure of ganglion [34]. In the time that they did the work there were not the small computers with three-dimensional volume rendering software that we have today. Therefore, there was not much interest in the technological development for the next 20 years.

In parallel with the development of the Nipkow disk beam scanning confocal microscope a variety of new confocal designs evolved. Baer developed several types of tandem scanning slit microscopes [35]. These developments influenced Maurice and also Koester in their work in the development of specular microscopes for observation of the cornea.

At the same time there were new developments in laser scanning confocal microscopes. The availability of the laser provided a new, bright light source which resulted in several new laser scanning microscopes [8]. In the last decade there were many technological innovations in beam scanning confocal microscopes. Wilson in Oxford, UK and Sheppard in Sidney, Australia developed various types of confocal microscopes. Brakenhoff

demonstrated the importance of high aperture immersion microscope objectives for optical sectioning. Aslund and his group in Sweden demonstrated the use of optically sections for the three-dimensional reconstruction of thick specimens.

21.3 TYPES OF CONFOCAL MICROSCOPES

21.3.1 Introduction

This section discusses a new paradigm to visualize living cells and tissues: the real-time confocal microscope. The observer will notice two improvements in the imaging characteristics of a confocal microscope: (1) enhanced transverse resolution, and (2) enhanced axial resolution as compared to a standard microscope. The former improvement results in higher resolution in the plane of the specimen. The latter effect results in the superb capability of a confocal microscope to optical section a thick, highly scattering specimen. This is the main advantage of a confocal microscope.

The confocal microscope provides "en face" images of the specimen; the plane of the image is orthogonal to the thickness of the specimen. These images are very different, and are oriented perpendicular, from the typical sections obtained in histopathology in which the tissue is cut along the thickness of the tissue.

In contrast to the conventional light microscope, which images all of the points in the specimen in parallel, a confocal optical microscope optimizes illumination and detection for only a single spot on the specimen. In order to form a two-dimensional image with a confocal microscope, it is necessary to scan the illumination spot over the area of the specimen. Several generic types of confocal light microscope are now described.

21.3.2 Tandem Scanning Nipkow Disk Based Confocal Microscope

In 1884 Paul Nipkow invented the electrical telescope, a forerunner of our modern television. The key component is the so-called Nipkow disk, a rotating disk with holes arranged in a spiral or interleaved set of spirals. The Nipkow disk, was later to be used as the basis of beam scanning real-time confocal microscopes.

A real-time tandem scanning confocal microscope, in which the image could be observed with the naked eye, was developed by Petran and Hadravsky [33,34]. They acknowledged the contribution of Nipkow who

invented the Nipkow disk in 1884 to provide real-time, point illumination and point detection.

The principle of the tandem scanning confocal microscope is as follows. Sets of conjugate pinholes (40-60 microns in diameter) are arranged in several sets of Archimedes spirals. Each pinhole on one side of the disk has an equivalent and conjugate pinhole on the other side of the disk. The illumination light passes through a set of pinholes (about 100 at a time) and is imaged by the microscope objective to form a diffraction limited spot on the specimen. The reflected light from the specimen passes through a conjugate set (about 100 at a time) of pinholes on the other side of the disk and can be observed in the eye piece of the microscope. Both the illumination and the reflected light are scanned in parallel over the specimen to generate the two-dimensional image of the focal plane by spinning the Nipkow disk. This microscope is called a tandem scanning reflected light microscope.

Since the ratio of the area of the holes to the area of the disk is usually only about 1-2 percent, only a small fraction of the illumination reaches the sample, and a similar small fraction of the light reflected from the sample passes the disk and reaches the detector. Therefore, the illumination must be very bright (a xenon or mercury arc lamp is usually required).

These systems are best suited for reflected light confocal imaging. However, even in the reflected light mode, confocal microscopes based on a Nipkow disk containing pinholes have a very poor light throughput. The reason for this is that the sets of conjugate pinholes occupy only a small percent of the area of the spinning Nipkow disk. In order to minimize the cross-talk between adjacent pinholes on the Nipkow disk it is usually designed so that the separation between adjacent pinholes is about 10 times the pinhole diameter.

The tandem scanning Nipkow disk based confocal microscope is a poor choice for weakly reflecting specimens such as living cells, tissues, and organs. The low intensity of light that reaches the detector (the eye of the observer, the film plane of a camera, or the CCD camera) results in an image with marginal image quality. However, for strongly reflecting objects such as hard tissue, composites, and microelectronics the use of a tandem scanning Nipkow disk based confocal microscope may be a reasonable choice. The advantages of the Nipkow disk type confocal microscope include the following: real-time viewing, true color of the specimen is observed, color can be used to map the depth of the features in the specimen, and direct view observation of the specimen.

21.3.3 One-Sided Nipkow Disk Confocal Microscope

It is possible to use the set of pinholes on the same side of the Nipkow disk for both the illumination and the detection. Xiao, Corle and Kino invented a real-time, one sided, Nipkow disk based confocal microscope [36, 37]. This design has several advantages over the tandem scanning confocal microscope: it is less sensitive to vibration of disk, it has a simplified optical design, and it is easier to align the microscope. A one sided real-time confocal microscope based on the Nipkow disk was developed at Stanford University by Kino and his co-workers. The driving force was the need to improve the metrology of semiconductor devices using simple optical confocal microscopes. Their confocal microscope used a rotating Nipkow disk in which the illumination and the reflected light passed through the same holes in the Nipkow disk. In order to reduce the light reflection from the disk a quarter wave place and a set of analyzers and polarizers were employed. The beam scanning was provided by a Nipkow disk confirms the contribution of Paul Nipkow.

In order to reduce the reflected light from the surface of the Nipkow disk three techniques were implemented. The disk is tilted so that the light reflected from the surface of the disk is reflected into a beam stop. The surface of the disk is blackened to reduce the surface reflections. A polarizer is placed between the light source and the disk, which illuminates the disk with polarized light. A quarter wave plate is placed between the Nipkow disk and the microscope objective, and an analyzer is placed between the Nipkow disk and the detector. The combination of polarizer, quarter wave plate and analyzer effectively separates the light from the specimen and the light reflected from the surface of the disk. This optical arrangement sharply discriminates light reflected from the surface of the disk; however, it also slightly reduces the light reflected from the object that reaches the detector.

An advantage of the one-sided Nipkow disk confocal microscope is a simpler optical design as compared to the tandem scanning Nipkow disk confocal microscope. A disadvantage is that since the illumination and reflected light follow the same optical path it is not easy to correct for chromatic aberrations in the microscope. This design, as with the tandem scanning Nipkow disk based microscope, has the disadvantage of the low transmission of the disk which also makes the microscope a poor choice for weakly reflecting specimens such as living cells, tissues, and organs.

The following is the analysis for a Nipkow type confocal microscope with sets of conjugate pinholes on a disk [36]. It is based on the Rayleigh-Sommerfeld scalar diffraction theory, using the Fraunhoffer approximation, that at a distance h_1 (the tube length of the objective) from a circular pinhole, the field Ψ_1 at the pupil plane of the objective at radius r_1 from the axis varies as:

$$\Psi_1 = A\Psi_0 \frac{J_1(kr_1/h_1)}{kr_1/h_1}, \tag{9}$$

where Ψ_0 is the field at the pinhole, $k=2\pi/\lambda$, A is a constant, λ is the optical wavelength in free space, and $J_1(x)$ is a Bessel function of the first kind and first order.

When the size of the pinhole is infinitesimal, the normalized intensity of the signal reflected from a perfect mirror a distance z from the focal plane is given by the approximate formula:

$$I(z) = \left[\frac{\sin k_2 z(1-\cos\theta_0)}{k_2 z(1-\cos\theta_0)}\right]^2, \tag{10}$$

where $k_2=nk$, n is the refractive index of the medium, and the numerical aperture of the objective is equal to $n\sin\theta_0$.

We may derive from equation 11 a very useful formula for the spacing d_z of the half power points of the response:

$$d_z = \frac{0.45\lambda}{n(1-\cos\theta_0)}. \tag{11}$$

The definition of resolution depends to a large extent on what type of object is imaged and what criteria are important to the observer. For integrated circuits, we are often interested in measuring profiles of stepped surfaces. For biological applications of confocal microscopy, we are often more interested in distinguishing two neighboring point reflectors. When a confocal microscope images a point reflector, the intensity I(z) of the optical signal at the detector varies with distance z from the focus as follows:

$$I(z) = \left\{\frac{\sin\left[\frac{k_2 z(1-\cos\theta_0)}{2}\right]}{\frac{k_2 z(1-\cos\theta_0)}{2}}\right\}^4. \tag{12}$$

It should be noted that this formula is different from that for the reflection from a plane mirror and gives an axial resolution approximately 1.4 times greater than that given by equation 10 for the reflection from a plane mirror. The intensity of the signal due to small scatterers falls off far more rapidly with increasing distance than does the reflection from a mirror. Consequently, a large number of scatterers some distance from the focus give very little glare.

It is apparent that in all confocal microscopes, the size of the pinhole is of critical importance. If the pinhole is too large, the transverse and axial resolution is impaired. If the pinholes are too small, the amount of light passing through the disk is decreased and the light budget becomes critical.

There is also a major source of light loss due to the relatively small fraction a of pinhole area to total illuminated area of the disk. As this fractional area is increased the light efficiency increases, but the rejection of glare from out-of-focus layers in the object gets worse, for a fraction of the defocused light will pass back to the detector through the pinholes. Thus the fractional area of the pinholes relative to that of the disk is normally kept in the 1-2% range.

21.3.4 Microlens Nipkow Disk Confocal Microscope

However, there is a new design of a real-time Nipkow disk confocal microscope that mitigates this problem of low light throughput. A group of researchers of the Yokogawa Institute Corporation in Tokyo, Japan has solved this problem with an interesting solution [38-40]. In the Yokogawa confocal microscope a laser illuminates the upper spinning disk which contains about 20,000 microlenses over the pinholes on the disk. The lower disk contains pinholes that are arranged in the same pattern as the microlens on the upper disk. Both disks rotate on a common axis. Figure 3 shows the principle of the microlens confocal microscope. With the presence of the microlenses, the pinholes pass 40% of the light incident on the upper disk.

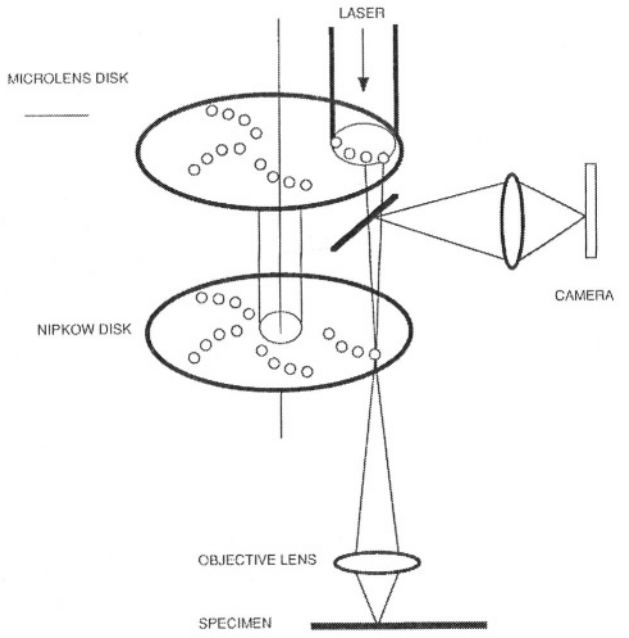

Figure 3. The principle of the microlens-Nipkow disk confocal microscope.

The design containing the microlenses achieves high light throughput and its high sensitivity even in the presence of weakly reflecting specimens. The small pinholes in the Nipkow disk give high resolution in the transverse and axial axes. Another advantage of this confocal microscope design is the high frame rate: 1 frame/ms. This clever microscope design has no optical relays between the pinhole and the objective lens. This is a great advantage in minimizing optical aberrations and distortions which are present in other Nipkow disk confocal microscope designs. With a microscope objective having a numerical aperture of 0.9 and a laser with a wavelength of 488 nm the measured resolution on the optical axis is 0.6 μm (FWHM).

21.3.5 Scanning Slit Confocal Microscope

An alternative to point scanning, as exemplified in the designs of confocal microscopes based on the Nipkow disk, is to use a slit of illumination which is scanned over the back focal plane of the microscope objective [41]. The advantage of this optical arrangement is that since many points on the axis of the slit are scanned in parallel, the scanning time is markedly decreased. Another very important advantage is that scanning slit confocal microscopes have superior light throughput as compared to point scanning Nipkow disk systems. The disadvantage is that the microscope is truly confocal only in the axis perpendicular to the slit height. In comparison to a pinhole based confocal microscope, a slit based confocal microscope provides lower transverse and axial resolution. This comparison is for the same wavelength of illumination and reflected light and the same microscope objective in each case. However, for confocal imaging of weakly reflecting living biological specimens, the trade off between lower resolution and higher light throughput is acceptable.

Several arrangements have been developed to provide the scanning of the slit of illumination over the specimen, and the synchronous descanning of the reflected light from the object. The simplest design is a two sided mirror mounted on a single oscillating shaft. The Svishchev design of a two-sided mirror is the technique used in several modern designs of real-time confocal microscopes with bilateral scanning [31-32].

The optical design of the real-time scanning slit *in vivo* confocal microscope developed by Dr. A. Thaer [41]. The design consists of two adjustable slits placed in conjugate planes of the confocal microscope. Both scanning of the illumination slit over the back focal plane of the microscope objective and descanning of the reflected light from the object is accomplished with an oscillating two-sided mirror.

There are several advantages to scanning slit confocal microscopes. The slit height can be adjusted which allows the user to vary the thickness of the optical section. A more important feature is that the user can vary the slit

height, and therefore control the amount of light that reaches the sample as well as the amount of reflected light that reaches the detector. This is important for samples that are very transparent and therefore can be imaged with the slit height very small; more opaque samples require that the slit height is increased. The microscope can operate in real time; that is at video rates. The light throughput is much greater for a slit scanning confocal microscope than for a confocal microscope based on the Nipkow disk containing sets of conjugate pinholes.

The advantage of slit scanning confocal microscope over those based on Nipkow disks containing pinholes is shown in the following example. For cases of weakly reflecting specimens, such as living, unstained, cells and tissues, the advantage of the much higher light throughput from the slit scanning systems is crucial for observation. The basal epithelial cells of the normal, *in vivo,* human cornea cannot be observed with a tandem scanning confocal microscope. However, corneal basal epithelial cells are always observed *in vivo,* in normal, human subjects when they are examined with a real-time, slit scanning, *in vivo* confocal microscope [42]. The reason for this discrepancy is that although the tandem scanning confocal microscope has higher axial and transverse resolution the very low light throughput of the disk does not pass enough reflected light from the specimen to form an image on the detector (in a single video frame) which has sufficient signal-to-noise and, therefore, contrast to show an image of the cells.

21.3.6 Laser Scanning Confocal Microscope

The original patent of Minsky contained the concepts that are implemented in the commercial laser scanning confocal microscopes that are used for both laboratory investigations, and also in the scanning laser ophthalmoscope [29,43,44].

A laser is used as a high intensity light source and the laser beam is scanned over the back focal plane of the microscope objective by a set of galvanometer scanning mirrors. Figure 4 shows the design of the laser scanning confocal microscope.

Several developments in ocular instruments have resulted in superior images of the retina *in vivo.* The human eye has several monochromatic aberrations that severely degrade the retinal image quality. These effects are maximal when the pupil is dilated. A major advance in retinal imaging is the use of adaptive optics to correct these aberrations [45]. The authors constructed a fundus camera with adaptive optics that provides a resolution that was not previously obtainable. Earlier, Dreher working in the laboratory of Bille used a deformable mirror to correct the aberrations in the human eye [46]. Liang *et al.* have combined a Hartmann-Shack wave-front sensor with

a deformable mirror to correct the aberrations of the human eye and have used this device to image photoreceptors in the living human retina [45].

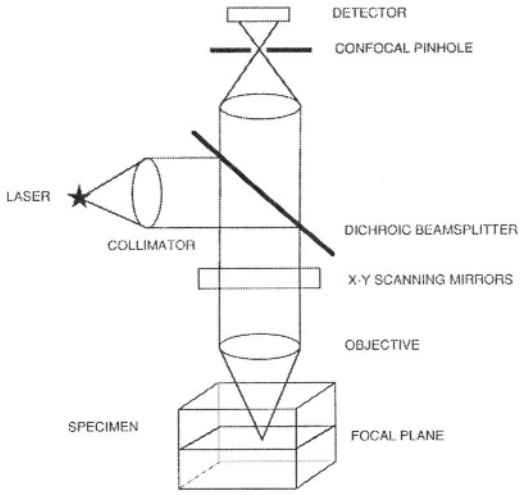

Figure 4. The principle of the laser scanning confocal microscope.

An important advance was the use of adaptive optics for the scanning laser ophthalmoscope [47]. The use of adaptive optics increased both the lateral and the axial resolution and thus permits axial optical sectioning of the retinal *in vivo*. This instrument can be used to visualize photoreceptors, nerve fibers and the flow of white blood cells in retinal capillaries.

Another instrumental advance for confocal microscope of the living retina is the use of image stabilization [48]. The integration of a retinal eye tracker with a scanning laser ophthalmoscope has several advantages: it enhances clinical imaging in cases where fixation is difficult, and for diagnostic procedures which require long duration exposures to collect the data.

21.3.6 The Development of the Clinical Confocal Microscope

Petran and co-workers developed a real-time, direct view confocal microscope which was based on a spinning Nipkow disk [33]. They were able to observe and photograph thin optical sections of the *ex vivo* animal cornea [34]. Corneal epithelial cells, nuclei of stromal keratocytes and endothelial cells were observed and photographed in *ex vivo* eyes.

The Petran tandem scanning Nipkow disk confocal microscope was used to observe the *ex vivo* cornea by Lemp, Dilly and Boyde [49]. Lemp subsequently arranged to have a Petran tandem scanning microscope mounted on a head rest and applied it to observations of the *in vivo* human cornea. Lemp working together with Jester and Cavanagh produced a series of studies on the rabbit eye and the *in vivo* human cornea. They used a low numerical aperture applanating microscope objective developed for specular microscopy. The *in vivo* cornea was flattened by the applanating microscope objective. The disadvantages of the system are high noise in the intensified video camera and scan lines on the single images.

A clinical confocal microscope based on a Nipkow disk with an intensified video camera as a detector was developed by the Tandem Scanning Corporation, Inc. in the U.S.A. It used a higher numerical objective than was used in the first system that Lemp used at Georgetown University. Their later version of the instrument contained an internal focusing lens which varied the depth of focus while the applanating microscope objective was held stationary on the surface of the deformed cornea. This design was first proposed by Masters [50].

At the same time Masters and Kino coupled the real-time one sided Nipkow disk confocal microscope with a new detector, a cooled, slow scan CCD camera, to obtain images of the *ex vivo* rabbit eye [37]. There were no scan lines, the dynamic range was 14 bits, and the confocal system was suitable for both *ex vivo* eyes and *in vivo* animal studies.

The use of a clinical confocal microscope based on the Nipkow disk has severe inherent problems. The transmission of the typical Nipkow disk is less than 1%. This means that only 1% of the incident light is transmitted through the disk on the illumination side. The cornea has a very low reflectivity and of the small amount of light that is reflected from the cornea only about 1 % of this light passes through the disk from the microscope objective to the ocular or detector.

Masters developed a confocal line scan system for obtaining intensity profiles throughout the depth of the cornea of *in vivo* rabbits [51]. Both reflectance and fluorescence [NAD(P)H redox fluorometry] were obtained *in vivo.* The microscope objective was mounted on a piezoelectric driver, and computer controlled the position of the focal plane as it was scanned on the optic axis. The main part of the confocal system was a modified specular microscope. Two sets of slits were used; on the illumination side and one on the detection side in the eye-piece the system used the divided aperture in the objective first used by Maurice [22].

The main unsolved problem was how to deal with eye motion. The solution of Masters was to use a rapid line scan. This was provided by a piezoelectric driver rapidly scanning the microscope objective along the optic axis of the eye. The instrument produced line scans of reflected light or fluorescence light from the different depths in the cornea [51].

A new, real-time, scanning slit confocal microscope was developed by Thaer for the observation of the *in vivo* human cornea [41]. The image of a slit is scanned over the back focal plane of the microscope objective. The slit width can be varied in order to optimize the balance of optical-section thickness and image brightness. The instrument is based on the double-sided mirror which is used for scanning and descanning. This confocal microscope used a halogen lamp for illuminating the slit. The detector is a video camera that acquires images at video rates. This confocal microscope can image basal epithelial cells and the adjacent wing cells in the living human cornea due to its high light throughput. This design was first developed into a real-time confocal microscope over twenty years ago by Svishchev, in Moscow. Svishchev designed and constructed a real-time confocal microscope based on a oscillating two-sided mirror (bilateral scanning) and used this microscope to observe living neural tissue in the reflected light mode [31,32].

The following design parameters were incorporated into the real-time, scanning slit confocal microscope:

- The use of nonapplanating, high numerical aperture, water immersion microscope objectives, 50X and 100X microscope objectives.
- The microscope objective would use a methylcellulose gel to optically couple the tip of the microscope objective to the cornea. There was no applanation or direct physical contact, which deforms the cornea, between the objective and the surface of the cornea.
- One half of the numerical aperture was used for illumination, and one half of the numerical aperture was used for collection of the reflected and fluorescence light.
- Optical sectioning in the plane of the cornea was obtained with two sets of conjugate slits. The slit heights are variable and adjustable.
- An oscillating, two sided mirror (bilateral scanning) was used for scanning the image of the slit over the back focal plane of the microscope objective, and for descanning the reflected and back scattered light collected by the microscope objective from the focal plane in the specimen.
- The light source is a 12 volt halogen lamp. For fluorescence studies a mercury arc lamp or a xenon arc lamp can be used.
- The scanning was synchronized with the read-out of an interline CCD camera in order that the full vertical resolution of the intensified CCD camera could be utilized.

The real-time, scanning slit *in vivo* confocal microscope is based on two sets of adjustable conjugate slits. An oscillating two-sided mirror is used for both scanning and descanning. This is similar to the design and construction of the Svishchev microscope.

The microscope used standard nonapplanating microscope objectives with RMS threads that are interchangeable. Several different microscope objectives can be used which permits the use of various magnifications and

fields of view. Typically a Leitz 50X, 1.0 NA, water immersion objective is used. When a larger field of view is required a Leitz 25X, 0.6-NA water immersion microscope objective is used.

An intensified video camera with video output to a Sony U-matic tape recorder is used. In parallel with the video recording, there is a video monitor in addition, so the operator can observe the confocal images of the subject's eye in real time. This real-time, scanning slit confocal microscope does not require any frame averaging for producing the image quality and contrast shown in this chapter.

Another type of scanning slit confocal microscope was developed by Koester who modified his original design of the wide-field specular microscope. The Koester wide field specular used two conjugate slits and was a true confocal microscope. It suffered from poor optical sectioning capability due to the low numerical aperture of the original applanating cone objective (0.33 NA). This resulted in poor efficiency of light collection. To observe images the slits had to be opened and the resulting images had large depth of focus. While the corneal epithelium and the corneal endothelium could be easily observed, the wing, basal and stromal details were very difficult to image.

Recent development of a new applanating objective with an effective numerical aperture of 0.75 resulted in an improved wide-field specular microscope for clinical observation of the human cornea. This new instrument uses a divided aperture, applanating microscope objective with an improved numerical aperture. The divided aperture objective design uses one half of the objective for illumination, and the other half of the objective for light detection. This scheme results in the effective numerical aperture of 0.38 in the meridian perpendicular to the obscuration divider in the center of the objective, and an effective numerical aperture of 0.75 in the meridian parallel to the obscuration divider. The transverse resolution differs in the two perpendicular meridians, reflecting these two different numerical apertures. This instrument can image basal epithelial cells in the normal *in vivo* human eye. In the initial design, a photographic camera was used as the detector; therefore images are not obtained in real-time and require negative development and printing after image acquisition. A more recent design uses a CCD camera. The microscope has an optical section thickness of about 40 μm. This new modification of the previous Koester wide-field specular microscope can image the normal basal epithelial cells of the *in vivo* human cornea. However, it requires an applanating microscope objective which in addition to helping to stabilize the *in vivo* cornea induces artificial deformation induced ridges in the stroma and in Descemet's membrane.

What are the advantages of using a scanning slit confocal microscope such as is described and demonstrated in this chapter? Slit scanning confocal microscopes have a much higher light throughput than confocal microscopes based on Nipkow disk. This has two consequences. First, the illumination

incident on the patient's eye can be much less. This allows for a much longer duration of the use of the confocal microscope on the patient's eye without the severe patient discomfort and high light intensity that is necessary with the use of the confocal microscope based on the Nipkow disk. Second, it is possible to image the low reflecting layer of wing cells that are immediately adjacent to the basal epithelial cells in the normal human cornea. This layer of wing cells has been imaged, in real-time, as single video frames without the need for any analog or digital image processing using the real-time scanning slit confocal microscope. No other real-time confocal microscope has been able to image these wing cells in the normal, *in vivo* human cornea. It is extremely difficult to image in real-time the basal epithelial cells of the normal *in vivo* human cornea. Only one group in Kyoto, using a Nipkow disk based confocal microscope, has succeeded in imaging the normal basal epithelial cells. The modified wide field specular microscope of Koester based on slits can image basal epithelial cells in the normal *in vivo* human cornea; however this is not in real-time since it is a photographic system.

Confocal microscopes based on slit systems have other advantages. The slit height can be varied to change the depth of the optical section and the amount of light throughput. If the cornea is very clear the slits can be closed down to yield a thinner optical section. However, if the cornea is cloudy, one can open the slits to pass more light.

What are the disadvantages of slit scanning confocal microscope as compared to confocal microscope based on a Nipkow disk containing pinholes? The resolution of a pinhole based confocal microscope is higher than that based on slits. This does not seem to be an important factor for *in vivo* confocal microscope of the human cornea. The transverse resolution of a slit scanning confocal microscope varies in the *x-y* plane according to the direction of the slits. A confocal microscope based on pinholes would not have this directional variation in transverse resolution.

The most important design features of the real-time scanning slit *in vivo* confocal microscope described in this article is the use of non-applanating, long working distance, high numerical aperture water immersion microscope objectives. This high numerical aperture microscope objective is very efficient in collecting the light from the weakly reflecting corneal structures.

21.3.7 Light Sources

Light sources for confocal microscopes can be divided into either spatially coherent or spatially incoherent. Laser scanning confocal microscopes are spatially coherent. However, many of the clinical confocal microscopes used in the clinic, for example, the scanning slit confocal microscope used in the ophthalmology clinic use halogen lamps as a spatially incoherent light

source. With spatially incoherent illumination the phase relations between fields at nearby points are statistically random.

Spatially coherent light sources have the important property that the phase difference between any two points is constant with time. Examples of spatially coherent light sources are lasers and arc lamps with a small aperture which acts as a spatial filter. There is another important term: temporal coherence. A laser with a single frequency would have a high temporal coherence. That term implies that there exists a definite phase relationship between the fields at a given point after a time delay of *T*. Usually practical lasers show this definite phase relationship for a fixed time which is called the coherence time.

A wide variety of light sources are used with confocal microscopes. Halogen lamps, arc lamps and many different lasers sources are employed to provide a variety of wavelengths.

The Helium-Cadmium laser is useful for the production of several lines in the ultraviolet region. The emission at 442 nm is useful for the excitation of flavins and other fluorescent molecules. It is suggested that a laser stabilization device based on an acousto-optic device be employed to improve the laser stability. Argon-ion lasers are commonly used to excite fluorescent probes with confocal microscopes. Another useful light source is the mixed gas Argon-Krypton laser. This laser can produce several laser line across a wide range of the spectrum and offers a cost reduction compared to the purchase of two individual lasers. The combination of red, green, and blue lasers can be used to produce true color confocal microscopy.

While one may think that increasing the power of the illumination will result in more intense images with an increase signal-to-noise there are two important processes to be considered: light-saturation and photobleaching. When the rate of absorption of a fluorescent molecule exceeds the rate at which the energy from the excited state can be released by either radiative processes such as fluorescence or nonradiative processes such as singlet-triplet transfer or heat production then we have the phenomena of light-saturation. Further increases in the intensity of illumination will not increase the intensity of fluorescence.

The second process is called photobleaching of fluorescent molecules. The excited state of the fluorescent molecule reacts with oxygen to produce a photochemical reaction in which the fluorescent molecule is transformed into a nonfluorescent molecule. Thus, over a period of time with constant illumination of a volume in the specimen it will be observed that the intensity of fluorescence is reduced. Therefore, a high intensity of illumination may be damaging to the fluorescent molecules. Lowering the intensity of the illumination will only lower the rate of photo-destruction of the fluorescence, it will not completely eliminate the process.

21.3.8 Scanning Systems

In principle we can either mechanically scan the specimen relative to a diffraction limited spot of illumination light or we can mechanically scan the diffraction limited spot of light over a region of the specimen. These two methods are not equivalent. For the case in which the specimen is raster scanned relative to a diffraction limited spot of light there are distinct advantages. The optical system is simple and it must only produce an axial diffraction-limited spot of light. Since we only use the axial region of the lens many off-axis aberrations are eliminated or minimized. Another advantage is that the resolution and contrast are identical across every region of the specimen. Finally, the resolution and contrast are independent from the magnification; there is space invariant imaging. In principle, this system could obtain a continuously variable magnification with a single microscope objective. A possible disadvantage of this system is the relatively slow speed of image acquisition, on the order of a few seconds. Some imaging situations in which rapid image acquisition, for example in calcium imaging in excitable tissues would not work with this type of scanning. A similar method of scanning is to scan the microscope objective over the specimen. In principle this technique of microscope objective scanning is similar to object scanning. Both techniques are space invariant and both scanning techniques are not real time.

Many of the commercial confocal microscopes use a beam scanning system. Various scanning systems are used to scan the light beam over the back-focal plane of the microscope objective. Either a diffraction limited spot or a slit of light can be scanned over the back-focal plane of the objective. Several methods can be used to achieve beam scanning: vibrating galvanometer-type mirrors, rotating polygon mirrors and acousto-optic beam deflectors. Very high frame rates can be achieved by combining a scanning mirror on one axis (relatively slow) with a rotating polygon mirror on the orthogonal axis (very fast). For the case of beam scanning the magnification is now coupled to the resolution; that is the imaging is not space invariant. Several different microscope objectives are normally required to cover a range of magnifications. Beam scanning confocal microscope can easily be constructed around a conventional microscope.

21.3.9 Detectors

The important rule in detectors is that every photon counts. It is important to maximize the collection and detection of all photon from the specimen. In the reflection mode of confocal microscope the image is formed from the reflected and the scattered light. The use of various wavelengths could alter the penetration depth of thick specimens and also the contrast of the images.

In the fluorescence mode of confocal microscopy it is important to use barrier filters or dichroic mirrors to isolate the fluorescence light of the specimen from the excitation light. The use of coatings on the optical elements and the careful design of the optical system to reduce stray light is critical. Since each optical element contributes to the flare and stray light it is an important design consideration to minimize the number of optical elements in the microscope.

Confocal microscopes use several types of detectors: photomultiplier tubes (PMT), avalanche photodiodes (APD), and charge-coupled device cameras (CCD). The most common detector used in confocal microscopy is the photomultiplier since it is relatively inexpensive, very sensitive and stable. An excellent review of solid-state detectors and cameras is chapter 7 in the book, *Video Microscopy,* second edition, by S. Inoué and K. Spring [52].

An important consideration is the role of noise in the detector and its associated amplifier. The signal-to-noise ratio is the number that will determine the quality of the image derived from the confocal microscope. There are several sources of noise including the quantum nature of the light. In general, as the number of detected photons (N) increases the signal-to-noise ratio will be enhanced by the square-root of (N).

21.3.10 Microscope Objectives

The selection, care, cleaning, and use of a microscope objective may be considered the most important part of the confocal microscope. It is suggested that the user of a confocal microscope study the web sites of the major manufactures of microscope objectives: Zeiss, Nikon, Olympus, and Leica for the latest information on the available microscope objectives and their information sheets.

While the choice of a specific microscope objective depends on the use and the sample it is critical that it be carefully cleaned and kept free of dust and dirt. The use of tissue paper to clean a microscope objective will result in permanent damage to the optical surface!

The selection of an appropriate microscope objective will depend on the following: the magnification required, the use of a cover slip of the correct thickness for the particular microscope objective, the numerical aperture of the microscope objective, and the free-working distance required. Other factors to be considered are the various types of aberrations. Often there is a large refractive index mismatch between the specimen and the optical system consisting of a layer of index matching oil, a cover slip and the microscope objective. This index mismatch can result in large aberrations of the optical system and a loss of image fidelity between the specimen and the resulting image.

Many modern confocal microscopes use infinity-corrected microscope objectives. An important advantage of infinity-corrected optics is that the focal plane can be changed by moving the position of the objective rather that having to displace the microscope stage.

In recent years several manufacturers have produced high quality microscope water-immersion microscope objectives with long working distances, high numerical aperture, and high magnification.

For the optical observation of thick living specimen an optimal solution may be the use of long-working distance water-immersion microscope objectives without the use of a cover slip.

21.4 APPLICATIONS TO MATERIAL SCIENCES

The development of optical inspection devices for the microelectronics industry has resulted in the production of several types of confocal microscopes [53-58]. Semiconductor metrology refers to the visual inspection of wafers containing many individual microscopic electronic components and their connections is an important aspect in their production. The basic problem is to visually inspect the line widths, and the heights of trenches and their angles within the many thin layers. The Helium-Neon laser is a good like source for the inspection of multilayered semiconductors since its wavelength is capable of penetration into the deeper layers. Another very important area is the confocal microscopy of photoresists. The enhanced axial and transverse resolution of the optical confocal microscope is used to perform these measurements.

Another important optical mode is the photoluminescent mode of the confocal microscope. Photolumnescence of semiconductors can yield important information about the electronic states and their spatial positions in the sample, binding energies, band structures, defects in the structures and the concentration of various atomic and molecular species.

Other optical techniques include laser Raman microscopy and the optical beam induced current technique (OBIC). Laser confocal Raman imaging are commercially available and provide additional tools for material identification and inspection. The OBIC technique is important for the evaluation and testing of photoconductors, photodiodes, laser diodes, and integrated circuits.

The confocal microscope has found many other uses for visual measurement and inspection outside the field of microelectronics. For example in the testing of fibers, hair, bone, teeth, and ceramics devices. The enhanced axial and transverse resolution of the confocal microscope has proved useful in the forensic analysis of samples of fibers, hair, bone, and teeth [59]. In addition, confocal microscopy has proved its utility in the analysis of composites, coatings, foams, and emulsions.

21.5 BIOMEDICAL APPLICATIONS

It is in the field of biomedical and basic biological science that confocal microscopy has made many advances [60]. The enhanced axial resolution of confocal microscopy provides the capability for *in vivo* imaging of the living eye and *in vivo* human skin. Another area of active research is the study of living cells in thick tissue. Prior to the development of confocal microscopy these types of imaging applications were not possible.

21.5.1 Ophthalmology

It is in the field of ophthalmology that the development of clinical confocal microscopy has had a great impact. In previous sections we have developed the historical thread from the early slit lamp, to the specular microscope and finally to the development of a real-time confocal microscope for imaging the human eye *in vivo.* It is important to point out that while many types of confocal microscope use a laser (coherent light) as the source of illumination, this is not a rigid requirement. For example, the scanning slit confocal microscope used for clinical studies and diagnosis in the ophthalmology clinic uses a halogen lamp (non-coherent light) as the light source.

Böhnke and Masters have recently published a short handbook on the use of the clinical confocal microscope in the ophthalmology clinic [61]. It contains section on the historical development of optical instruments for biomicroscopy of the living eye, technical information on the scanning slit clinical confocal microscope, a detailed review of how to perform a complete examination of the cornea in patients, and several sections on both the normal and the pathological cornea.

The normal cornea is semitransparent and an ideal structure to be imaged with a clinical confocal microscope. As previously described the scanning slit confocal microscope developed by Thaer produced images of thin optical sections of the *in vivo* cornea that are devoid of motion artifacts. This type of clinical microscope is unique in its capability to image all of the layers of the cornea, specifically the basal cell layer which is so important for the maintenance of the corneal epithelium through the processes of cell proliferation and differentiation. The tandem scanning Nipkow disk confocal does not have sufficient sensitivity to image the basal epithelial cells.

Another very important instrument development is the scanning laser ophthalmoscope [27,28]. The scanning laser ophthalmoscope follows the early work of Ridley on the point scanning of the retina [26]. With modern instruments it is possible to follow blood flow in the retina, study the normal and pathological structure of the retina and map out the pigments of the photoreceptors. A recent major development is the use of adaptive optics to

correct for the optical aberrations of the eye [45-47]. The use of a scanning laser ophthalmoscope with corrections of ocular aberrations with adaptive optics results in improved resolution and the ability to image individual photoreceptors.

Below is a brief review of the key studies of the *in vivo* cornea that were performed with the clinical confocal microscope in the last decade. Many of the published studies reviewed on the topic of clinical confocal microscopy of the eye were based on various designs of confocal imaging microscopes. Various investigators used different microscope objectives as well as different techniques of image processing, e.g. image averaging. The conclusions presented in each paper are therefore dependent on at least four considerations: (1) the experience and skill of the observer, (2) the type of confocal microscope used, (3) the magnification and numerical aperture of the microscope objective, and (4) the type of image averaging, image processing, and enhancement employed. Finally, it has been our experience that even with a newly installed commercial confocal microscope the image quality is highly dependent on the optical alignment of the components.

21.5.1.1 Corneal Alterations Due to Long Term Contact Lens Wear

This investigation shows how the use of a real-time, scanning-slit confocal microscope with a high numerical aperture water immersion objective and single frame review led to the discovery of a new corneal degeneration [62]. The absence of frame averaging or other digital image processing (usually required with a Nipkow disk based confocal microscope) was critical to the observation, since frame averaging would preclude the detection of the microdots that led to the discovery. A new type of chronic, stromal aberration has been observed in subjects with long-term contact lens wear. A real-time, scanning slit confocal microscope with a 50X/1.0 NA water immersion objective was used to observe the corneas. The corneal optical sections from the superficial epithelium to the endothelium were recorded in real time without any further image processing and were reviewed frame by frame. This study confirmed the presence of epithelial microcystic changes and alterations of endothelial cell morphology which was previously described by others. The new and important finding of this study was the presence of highly reflective panstromal microdot deposits in the corneal stroma. The dots were highly reflective and had a size of 0.3 to 0.6 microns with a round-to-polygonal shape. The density and the size of the microdot deposits scales with the duration of contact lens wear. In patients wearing soft contact lenses for longer than 6 years, the microdots were observed in all cases investigated. The microdots may be lipofuscin or some other high reflective matter. This stromal microdot degeneration may be the early state of a significant corneal disease, which eventually may affect large

numbers of patients after decades of contact lens wear. A quantitative analysis of the density distribution of the microdots has been reported [63].

21.5.1.2 Cell Morphology and Movement in the Normal Cornea

In vivo confocal microscopy was used to investigate the hypothesis that cells in the epithelial layer of the normal cornea migrate centripetally. In order to make sequential time dependent observations of the living human cornea it is necessary to return to the same microscopic fields. In specular microscopy of the cornea the observer can use the posterior rings that are formed in the cornea by the applanating specular microscope objective, or use unique pigment aggregates as specific site markers. A new technique was described to obtain time-lapse reflected light confocal images in the basal epithelium and adjacent wing cell layer from the *in vivo* human cornea [64]. The technique is based on the sequential relocation of the unique patterns of the subepithelial nerve plexuses. The patterns of individual subepithelial nerve plexuses, as well as perforation points where the nerves traverse Bowman's layer, serve as fixed landmarks. A potential example of this technique would be the investigation the dynamics of basal cell proliferation and differentiation in the living eye with the *in vivo* confocal microscope.

21.5.1.3 Corneal Alterations Following Photorefractive Keratectomy

A frequent and very legitimate question is: what new clinical observations and discoveries have been directly linked to the use of the clinical confocal microscope? The work of Böhnke *et al.* provides an interesting illustration of how confocal microscopy led to the observation of persistent stromal changes after myopic photorefractive keratectomy (PRK) in zero haze corneas [65]. In photo-refractive keratectomy treated patients and contact lens wearers, the basal epithelial cells sporadically showed enhanced reflectivity. However, rods and needles were observed in all photorefractive keratectomy treated patients, irrespective of previous contact lens wear. In contact lens wearing controls, there were highly reflective granules which were scattered throughout the thickness of the stroma; however, rods and needles were never observed [62]. The authors conclude that after 8 to 43 months post photorefractive keratectomy there are abnormal reflective bodies that persist beyond the time that acute wound healing would be expected to be complete. The clinical significance of these findings in the context of visual acuity and long-term status of the cornea is unknown.

A slit-scanning *in vivo* confocal microscope was used to assess human corneal morphological characteristics after photorefractive keratectomy [66]. Each layer of the cornea was studied. The minimum follow-up time

was 12 months. Fine linear structures were observed in the anterior stroma and in the midstroma, and a thin hyperreflective scar was noted after one-month post PRK. These structures were more marked at 4 months, but were still present up to 26 months. The extension of these structures to the midstroma indicated that permanent corneal changes caused by PRK affect deeper stromal layers than the immediate subepithelial region. Anterior stromal keratocyte density increased significantly 1 and 4 months after PRK. The midstromal and posterior keratocyte densities and endothelial cell densities were not affected. The significance of this investigation is that long-term alterations of the cornea in the midstroma could be observed over time with an *in vivo* confocal microscope.

The persistent corneal haze following PRK reduces visual function. *In vivo* confocal microscopy was used to study morphological changes following PRK for a 12-month period [67]. Computer analysis of the images quantified the keratocytes and the subepithelial deposits. This study found that epithelial and keratocyte alterations only transiently affect visual function; however, the subepithelial deposits can have a lasting effect on visual performance. The authors provide a caution to the reader by pointing out two limitations of histological analysis with confocal microscopy: the potential for introducing artifacts with digital image processing of the images, and the difficulty to interpret complex, irregular images associated with cellular and extracellular changes during wound healing [67]. Therefore, it is of great benefit to perform correlative microscopy whenever possible; for example, the combination of confocal microscopy and light or electron microscopy.

21.5.1.4 Clinical Confocal Microscopy in the Diagnosis of Corneal Disease

Corneal infection by *Acanthamoeba* is becoming more widespread and the *in vivo* confocal microscope may provide a useful diagnostic instrument in the clinic. An important case study is a diagnosis of *Acanthamoeba* keratitis based on clinical confocal microscopy and confirmed with subsequent corneal biopsy [68]. Scanning slit confocal microscopy showed a 26-micron diameter object which resembled an *Acanthamoeba* cyst in the cornea of a 29-year-old woman who showed clinical signs and symptoms of *Acanthamoeba* keratitis. This study is an important example of a clinical observation made with an *in vivo* confocal microscope that was confirmed with direct biopsy.

The use of confocal microscope for the identification of *Acanthamoeba* organisms *in vivo* within the corneal epithelium and anterior stroma is demonstrated in eight case reports [69]. These cases of *Acanthamoeba* keratitis were studied with the clinical confocal microscope which was used

to observe the *Acanthamoeba* cysts. The organisms were highly reflective, ovoid, and were 10-25 microns in diameter. The authors also used the same confocal microscope to observe *Acanthamoeba* organisms on an agar plate. The organisms on the agar plate were identical in size and shape to those observed in the corneas of the patients. The authors followed the course of treatment with the clinical confocal microscope which has potential as a noninvasive optical biopsy.

The life cycle of these eukaryotes has two stages; an active trophozoite and an inactive cyst. The cysts are round, highly reflective and easily identified with the confocal microscope. The noncystic organisms are very difficult to discern from the myriad shapes and forms of the keratocytes that have been observed with the confocal microscope in the *in vivo* cornea.

21.5.1.5 Alterations of the Human Cornea During Examination with an Applanating Confocal Microscope

The use of confocal microscope for the examination of the human eye *in vivo* is not without alterations of the eye. The study by Auran *et al.* illustrates the flattening-induced effects of an applanating microscope objective. They reported corneal bands and ridges throughout the cornea following the contact with an applanating microscope objective [70].

In addition to the previously discussed mechanical flattening with the use of an applanating microscope objective there are several other sources of morphological and physiological alteration with the use of confocal microscopy. First, the use of anesthetic drops which contain preservatives affects the cell junctions in the corneal epithelium. Second, the index matching gel used between the tip of the microscope objective and the tear film of the cornea may dehydrate the surface cell layers of the cornea. Third, if microscope objective is not sterilized between patient examinations, there is a risk of bacterial and viral transmission. Finally, repeated daily examinations may lead to a low-grade cellular reaction to the combined insults of anesthetic drops and the index matching gel. We mention these possibilities as a matter of caution.

One way to mitigate these alterations of the cornea is to use a noncontact confocal microscope [71]. For example, a long working distance air microscope objective could be designed for in vivo observation of the cornea. The use of a noncontact microscope objective has many potential benefits for clinical observation of patients. There is not need for an index matching fluid; therefore, there is no physical contact with the ocular surface. There is no need for the use of anesthetic drops in the patient's eye. There is minimal chance of bacterial and viral transmission from patient to patient. For these reasons we suggest and promote the development and use of noncontact confocal microscopy for the observation of the living eye.

This brief summary of some key clinical findings supports the thesis that they could only have been observed with a real-time clinical confocal microscope with sufficient resolution and contrast. To this date the observation of contact lens induced microdots in the corneal stroma cannot be confirmed with the tandem scanning Nipkow disk based confocal microscope due to its poor resolving power.

21.5.1.6 Three-Dimensional Imaging of Human Cataracts *In Vivo*

Another important development in ophthalmic imaging is the three-dimensional imaging of human cataracts *in vivo* [72-76]. Cataract (opacities in the ocular lens) is a major cause of visual disability in the world. The next section demonstrates a new technique to visualize the human ocular lens *in vivo* with three-dimensional microscopy.

A Scheimpflug slit camera acquires two-dimensional optical slices across the full thickness of the lens. Each image represents the spatial distribution of the intensity of light scatter in the optical section. If the Scheimpflug slit camera is mounted on a rotating gimbal, then slit images can be acquired from any meridian on the eye. In order to visualize the three-dimensional spatial distribution of light scatter intensity in the human lens it is necessary to reconstruct the three-dimensional lens from the acquired set of rotated slices. A set of 60 Scheimpflug images were acquired with the Anterior Eye Segment Analysis System (Nidek, EAS-1000). The slit beam of light of the Scheimpflug camera was rotated about the optic axis of the patients eye in three-degree increments. A transformation technique was developed to convert the original rotated data set into a new data set which consists of a set of images aligned on the Z-axis. The resulting three-dimensional lens is shown in Figure 5 and is a major development in ocular imaging.

21.5.2 Dermatology

21.5.2.1 Anatomy of Skin

The structure of skin presents many challenges for the researcher. It is composed of layered structures and contains vascular elements, glands, nerves, and various forms of connective tissue. In addition, the skin is subject to movement and therefore makes it difficult to use an optical microscope for imaging.

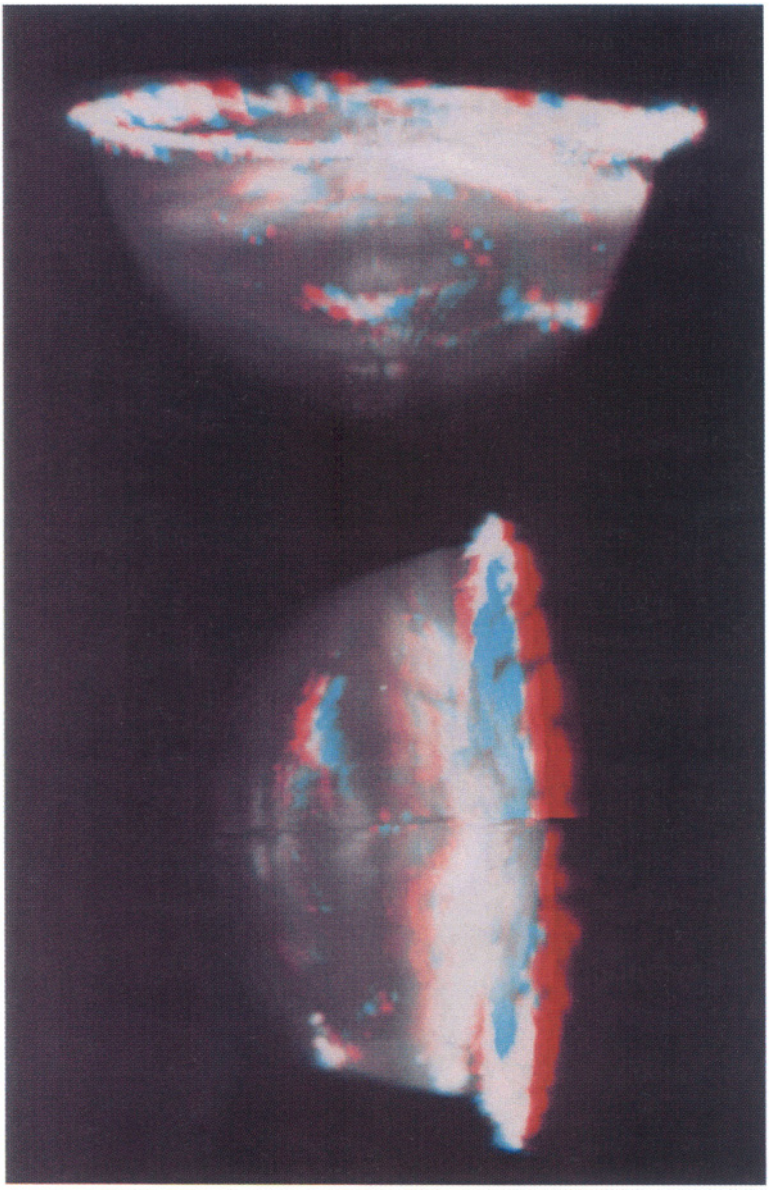

Figure 5. Two views of the three-dimensional visualization of the human lens *in vivo*. For this example a human lens *in vivo* with anterior and posterior opacities has been imaged in three dimensions and visualized as two red/blue anaglyphs that are rotated and tilted with respect to each other.

The skin being the largest tissue in the human body provides several protective function for the body. The epidermis is a continuously renewing multilayered tissue which continuously differentiates to produce stratified

layers of resultant dead cells, the corneocytes, whose function is to protect the body against external insults (barrier function). Except for the palms and soles, thin epidermis which covers the body comprises from the surface to the dermis: a stratum corneum which contains 15-20 layers of flat, anucleate, pentagonal shaped dead cells (corneocytes). The stratum lucidum contains 1-2 layers of corneocytes and marks the transition with the living cellular domain. The stratum granulosum contains about 2 layers of flattened cells with flat nuclei. The stratum spinosum contains several layers of polyhedral keratinocytes with spherical nuclei. The stratum basale (germinative layer) consists of a single layer of cuboidal cells-with ellipsoidal nuclei-adhering to the basement membrane of the dermis.

Four types of cells are located within the living epidermis: keratinocytes, and a few percent of dendritic cells: Langerhans cells, melanocytes, and rare Merkel cells. Keratinocytes are located in all strata. Melanocytes are located within the stratum basale Langerhans cells are mostly located in the stratum spinosum and Merkel cells are in or adjacent to stratum basale.

The dermoepidermal junction is comprised of structures at the interface between the epidermis and the dermis. As viewed with the light microscope, we observe this boundary as a undulating pattern of rete ridges (downward projections of the epidermis) and dermal papillae (upward projection of the dermis into the epidermis). The single layer of basal cells located at the dermoepidermal junction is the source of new keratinocytes (by their differentiation and migration to the surface) in the renewal of the epidermis.

The development of optical methods to investigate the structure of normal and pathological human skin has occurred over a forty years period [77]. However, it is only recently that the confocal microscope has been developed as a tool for *in vivo* microscopy.

A tandem scanning confocal microscope was developed by Petran and co-workers to optically section thick, highly scattering tissues in real-time [33]. The tandem scanning confocal microscope has been adapted for the in vivo examination of skin by several researchers. In particular, Corcuff and co-workers have advanced the development of a real-time confocal microscope for skin imaging [78-82]. In their adaptation of the tandem scanning confocal microscope, a contact system responsible for vertical movement was driven along the Z-axis by a stepping motor-driven position controller [83]. This permitted precise control of the position of the focal plane which forms the optical section within the thick specimen. The key feature of this microscope is a movable annular ring which both stabilize the skin and changes the focal plane for the microscope. The microscope acquires a series of optical sections as the annular ring which contacts the surface of the skin, is displaced. The microscope objective is fixed to the microscope; only the annular ring is moved and this caused the skin to be displaced; hence the capability to image human skin *in vivo* at different focal

depths. This study demonstrated that three-dimensional *in vivo* confocal microscopy is feasible on thick, highly scattering specimens.

The real-time tandem scanning confocal microscope based on a Nipkow disk is now described in more detail. The key feature of this microscope is a microscope objective which is fixed in position, and a annular ring which makes contact with the skin and moves under computer control along the Z-axis. This device stabilizes the skin during image acquisition and displaces the skin with respect to the focal plane of the microscope. A 50X/0.85 NA Nikon oil immersion objective lens was used. A drop of microscope immersion oil (n=1.518) was placed between the skin surface and the tip of the microscope objective. The light source was a 250 W halogen lamp, transmitted via a fiber optic light guide to the microscope. Real-time video frames were captured with a low-light-video camera (Dage MTI SIT68) coupled to a Sony Hi8 video recorder (PAL). Rapid video recording of the Z-series through the ventral aspect of the forearm avoided shifts caused by subject movement and blood flow pulsations. Two video frames were averaged, and the average was digitized, providing a stack of 64 optical sections in one micron vertical steps. The field of view of each image was 240 microns at the skin. The images were digitized in a format of 512 x 512 pixels (8 bits) and stored in the TIFF format. Masters and his coworkers have shown the feasibility of three-dimensional visualization of in vivo human skin [84-86]. Figure 6 shows the three-dimensional image of *in vivo* human skin.

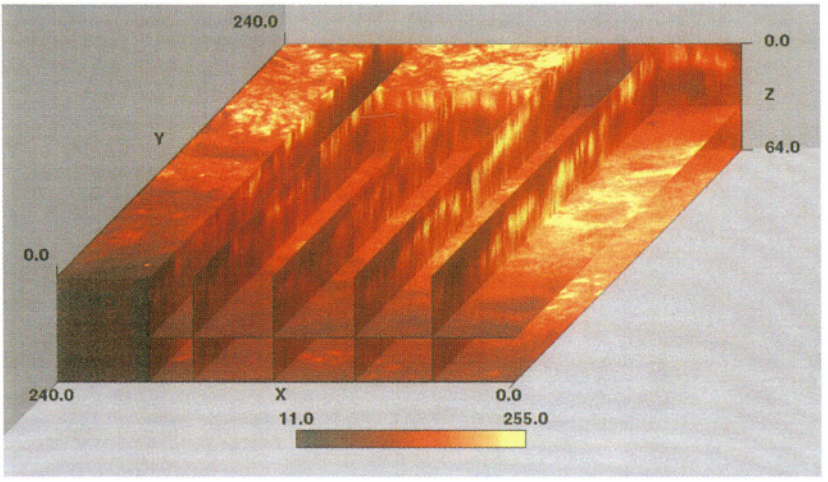

Figure 6. The three-dimensional image of *in vivo* human skin. A reflected light confocal microscope was used to acquire a stack of optical sections of in vivo human skin. A computer was used to prepare the three-dimensional visualization with the intensities of the reflected light presented in false color.

A video-rate laser scanning confocal microscope has been developed for imaging *in vivo* human skin [87]. These authors demonstrated that there is a good correlation between real-time confocal microscopy of *in vivo* human skin and conventional histology of fixed, stained sections obtained from punch biopsies.

21.5.2.2 Laser Scanning Confocal Microscope

The use of reflected light confocal microscopy has been proposed to rapidly observe unfixed, unstained biopsy specimens of human skin. Reflected light laser scanning confocal microscopy was used to compare a freshly excised, unfixed, unstained biopsy specimen, and human skin *in vivo.* Image contrast was derived from the intrinsic differences in the scattering properties of the organelles and cells within the tissue. The combination of reflected light confocal microscopy and three-dimensional visualization techniques provides a rapid technique for observing fresh biopsies of human skin without the necessity for fixing, cutting and histological staining.

21.5.2.3 Video-Rate Scanning Laser Confocal Microscope

A confocal scanning laser microscope was developed for video-rate imaging of human skin *in vivo* [87]. The fast rotating polygon mirror and a slower oscillating galvanometer mirror is used to achieve video rates. This design is similar to the video rate scanning system in the scanning laser ophthalmoscope. This instrument used for skin imaging, which operates at video rates, has the capacity of reflected light imaging with wavelengths of 488 nm, 514 nm, 647 nm, and 800 nm. These light sources are coherent light lasers. This microscope also incorporates a microscope objective which can be scanned in the z-axis in order to change the focal plane of the microscope objective within the skin. An annular ring is fixed to the skin to provide some position stability of the skin during microscopic observation.

21.5.2.4 Skin Autofluorescence Images by Scanning Laser Confocal Microscopy

Autofluorescence of human skin *in vivo* with excitation at 488 nm and with emission detected at wavelengths longer than 515 nm was studied with a scanning laser confocal microscope [84]. A major component of this autofluorescece is the fluorescence from the reduced pyridine nucleotides [88-92]. Optical sections of the stratum corneum were obtained from the anterior surface of the index finger and the lower surface of the human forearm. Pseudocolor depth-coded projections were formed from stacks of optical sections to a depth of about 100 μm. Individual cells could only be

observed at the top surface of the skin. With ultraviolet excitation at 365 nm the penetration depth was limited to the 20 μm of the stratum corneum at the skin surface. This paper demonstrated the use of autofluorescence as a source of natural contrast for confocal microscopy of human skin *in vivo.* It was possible to image the squames, or dead cells that are in the process of sloughing fro the surface. The linear arrangements of the openings of the sweat pores were imaged on the fingers. These preliminary studies indicate that skin autofluorescence with confocal excitation of 488 nm may be useful to observe the skin surface for bacteria, alterations of surface morphology due to the aging process or disease.

21.5.3 Cell Biology

21.5.3.1 Cell Lineage and the Differentiation of Corneal Epithelial Cells

This investigation, performed on the rat cornea, was designed to determine whether epithelial cell division and cell differentiation are linked [93]. The methods included immunocytochemical staining and three-dimensional confocal microscopy of the whole mounts with quantification of proliferating and differentiated cells in the full thickness of the cornea (central, mid-peripheral, and limbal regions. Rats were injected with 5-bromo-deoxyuridine (BrdU), and killed after various periods. Corneas were fixed and permeabilized, and the BrdU labeled nuclei were observed with a monoclonal antibody to BrdU and a fluorescent-labeled secondary antibody. The results were confirmed with ^{3}H-thymidine-autoradiography of corneal epithelia sectioned parallel to the corneal surface. This study concluded that cell division and differentiation are not directly linked in the corneal epithelium. Following cell division, daughter cells either remain in the basal epithelial layer, and undergo additional cycles of cell division, or both cells differentiate synchronously. An important methodological point is contained in this paper: why were these finding not observed previously in the many studies performed with ^{3}H-thymidine autoradiography? Previous studies were based on protocols that sectioned the corneas with vertical sections; hence, the sampling problem precluded observing pairs of synchronously differentiating cells. The three-dimensional observation of the full thickness of the cornea in immunocytochemical labeled fluorescent whole mounts with the confocal microscope avoided the errors and false conclusions obtained with autoradiography of vertically sectioned sampled. This is a good example of how an inappropriate sampling technique in the experimental design can results in misleading observations and therefore false conclusions. It also illustrated how an independent technique,

autoradiography, confirmed the studies performed with confocal microscopy.

21.5.3.2 Correlative Microscopy

The most important consideration in microscopy is the correct interpretation of the image. The strength of correlative microscopy, that is the use of different microscopic techniques to image the same specimens, is that instrument and specimen preparation artifacts are unlikely to occur in identical fashion in the disparate techniques. For example, the same specimen can be investigated both with confocal light microscopy and with scanning electron microscopy. While this principle may be more difficult to implement with the living human eye a variation should be exploited. That is to use different types of confocal microscopes, e.g. tandem scanning confocal microscopes, scanning laser confocal microscopes, and scanning slit confocal microscope to image similar ocular structures in the normal and pathological eye. As an example of correlative microscopy to interpret ocular structures an *in vitro* study of human ocular lenses was performed with both confocal light microscopy and scanning electron microscopy [76, 94]. *In vitro* confocal light microscopy showed high resolution images of the lens epithelium and superficial lens fibers were well visualized with their vacuolar elements. These light microscopic observations were fully confirmed with the scanning electron microscopy studies on the same lenses.

21.5.3.3 Redox Confocal Imaging: Intrinsic Fluorescent Probes of Cellular Metabolism

Redox fluorometry is a noninvasive optical method to monitor the metabolic oxidation-reduction (redox) states of cells, tissues and organs. It is based on measuring the intrinsic fluorescence of the reduced pyridine nucleotides, NAD(P)H and the oxidized flavoproteins of cells and tissues [88, 89]. Both the reduced nicotinamide adenine dinucleotide, NADH, and the reduced nicotinamide adenine dinucleotide phosphate, NADPH, are denoted as NAD(P)H. Redox fluorometry is based on the fact that the quantum yield of the fluorescence, and hence the intensity is greater for the reduced form of NAD(P)H, and lower for the oxidized form. For the flavoproteins, the quantum yield and hence the intensity, is higher for the oxidized form and lower for the reduced form. The reduced pyridine nucleotides are located in both the mitochondria and in the cytoplasm. The flavoproteins are uniquely localized in the mitochondria. The fluorescence from the reduced pyridine nucleotides is usually measured in tissue investigations since the measured fluorescence is higher than for the case of the flavoprotein fluorescence. Redox fluorometry has been applied to many

physiological studies of cells, tissues and organs [90]. Functional imaging of cellular metabolism and oxygen utilization using the intrinsic fluorescence has been extensively studied in cells. Specific studies based on redox fluorometry include the following: redox measurements of *in vivo* rabbit cornea based on flavoprotein fluorescence [91]; chemical analysis of nucleotides and high energy phosphorous compounds in the various layers of the rabbit cornea [92]; and redox fluorescence imaging of the *in vitro* cornea with ultraviolet confocal fluorescence microscopy.

21.6 COMPARISON BETWEEN CONFOCAL MICROSCOPY AND MUTIPHOTON EXCITATION MICROSCOPY

While the advent of confocal microscopy and its subsequent developments and application resulted in numerous studies on thick highly scattering tissues and materials there were still unsolved problems. Confocal microscopy can be used in both the reflection mode and in the fluorescence mode. The advantage of working with confocal fluorescence microscopy is specificity; cell components can be selectively labeled with fluorescent probe molecules, or the intrinsic fluorescence of cells and tissues can be used. First, it was noted that during the observation period the tissue fluorescence would fade or decrease. This phenomena is called photobleaching and is the destruction of the fluorescent molecule by the interaction of light and oxygen. Photopbleaching occurs in the total volume of the inverse cone of illumination light from the microscope objective. It can be reduced by reducing the intensity of the illumination. Second, many of the fluorescent dyes of interest have absorption band in the ultraviolet region. There are problems to design an optical system that uses ultraviolet light in a confocal microscope. Third, it was observed that the short wavelength ultraviolet illumination is damaging to live cell and tissue studies. These limitations can be mitigated by the use of a new type of nonlinear microscopy-multiphoton excitation microscopy.

The 1931 Doctoral Thesis publication of Maria Göppert-Mayer (Ann. Phys., Leipzig), developed the early theory of two photon processes. Multiphoton absorption processes are shown in Figure 7.

Between 1931 and 1990 there were many important papers on the theory and the practice of multiphoton excitation spectroscopy and microscopy [95]. The first experimental demonstration of two-photon absorption was shown in 1961 by Kaiser and Garrett. Franken *et al.* (1961) is the first observation of second harmonic generation (SHG) in a quartz crystal irradiated with ruby laser. In the book, *Theory and Practice of Scanning Optical Microscopy,* by Wilson and Sheppard we read: "The depth of focus

is of great importance in harmonic microscopy. Detail outside the focal plane does not interfere with the image as much as in conventional microscopy since the harmonic generated is proportional to the intensity squared and this results in the main contribution only coming from the region of focus where the intensity is very large." The authors illustrated this point with second harmonic images of three focal planes in a crystal. Sheppard and Kompfner made the first proposal of two-photon fluorescence microscopy, pulsed laser sources and heating effects.

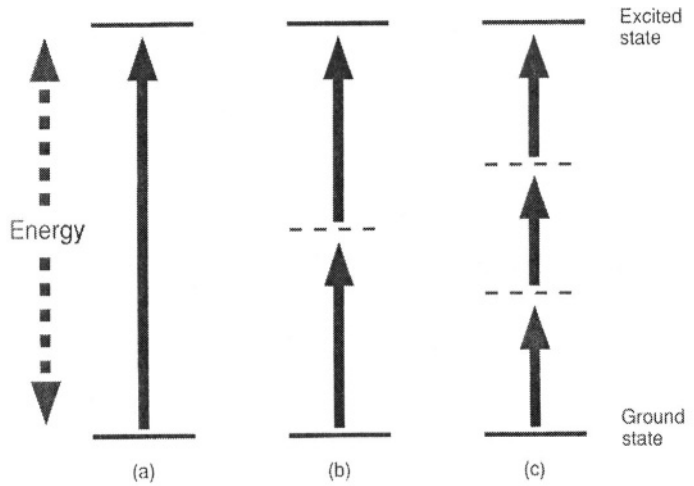

Figure 7. Diagram showing the absorption processes for a two-level molecule with (a) one-photon absorption, (b) two-photon absorption, and (c) three-photon absorption. The dashed lines represent virtual states.

It was the seminal publication of Winfried Denk, James H. Strickler, Watt W. Webb (Science, 1990) on "Two-photon laser scanning fluorescence microscopy" that provided the key experiments to convince the biological community of the utility of the methodology [96].

21.6.1 Experimental Processes

In order to experimentally demonstrate that a multiphoton excitation process is occurring it is necessary to demonstrate the nonlinear nature of the process in the following manner [97]. The intensity of the fluorescence is measured as a function of the intensity of the excitation light. These two measured quantities are plotted on a log-log plot and the slopes of the linear regions of the plot are determined. A two-photon excitation process is characterized by a slope of two; a three-photon excitation process is characterized by a slope of three. This experimental verification of multiphoton excitation processes follows from the physical analysis of the processes which is described below.

It is instructive to compare the expressions for the rates of one photon and two-photon absorption processes for a single fluorophore. For a one-photon absorption process, the rate of absorption is the product of the one photon absorption cross-section and the average of the photon flux density. For a two-photon absorption process, in which two photons are simultaneously absorbed by the fluorophore, the rate of absorption is given by the product of the two-photon absorption cross-section and the average squared photon flux density. In respect for the work of Maria Göppert-Mayer, who predicted the existence of two-photon absorption processes, the units of two-photon absorption cross-section are measured in GM (Göppert-Mayer) units. One GM unit is equal to 10^{-50} cm^4 s / photon.

The rate of two-photon excitation can be described analytically as shown in equation 13. This rate is expressed as the number of photons absorbed per fluorophore per pulse and is a function of the pulse duration, the repulse repetition rate, the photon absorption cross section and the numerical aperture of the microscope objective which focuses the light [98-100]. The derivation of this equation assumes negligible saturation of the fluorophore and that the paraxial approximation is valid. Note that n_a, the number of photons absorbed per fluorophore per pulse is inversely related to τ_p, the pulse duration. Shortly, we shall review the detrimental effect of pulse dispersion on the intensity of the fluorescence, and show how to compensate for pulse dispersion.

$$n_a \approx \frac{p_0^2 \delta}{\tau_p f_p^2} \left(\frac{\pi (NA)^2}{hc\lambda} \right)^2 , \qquad (13)$$

where τ_p is the pulse duration, f_p is the repetition rate, p_0 is the average incident power, δ is the photon absorption cross-section, h is Planck's constant, c is the speed of light, NA is the numerical aperture of the focusing lens, λ is the wavelength.

21.6.1.1 Optical Sectioning

In a two-photon excitation process the rate of excitation is proportional to the average squared photon density. This quadratic dependence follows from the requirement the fluorophore must simultaneously absorb two photons per excitation process. The laser light in a two-photon excitation microscope is focused by the microscope objective to a focal volume. Only in this focused volume is there sufficient intensity to generate appreciable excitation. The low photon flux outside the focal volume results in a negligible amount of fluorescence signal. In summary, the origin of the optical sectioning

capability of a two-photon excitation microscope is due to the nonlinear quadratic dependence of the excitation process and the strong focusing capability of the microscope objective. Most specimens are relatively transparent to near infrared light. The focusing of the microscope objective results in two-photon excitation of ultraviolet absorbing fluorochromes in a small focal volume. It is possible to move the focused volume through the thickness of the sample and thus achieve optical sectioning in three-dimensions.

It is important to stress that the optical sectioning in a two-photon excitation microscope occurs during the excitation process. The emitted fluorescence can then be detected, without the requirement of descanning, by placing an external photon detection device as close as possible to the sample. There is no valid reason to descan the fluorescence, as this results in the loss of signal due to the mirrors and other optical components associated with the descanning system. It is strongly recommended that an external photon detector, one with high quantum efficiency in the range of the fluorescence, be situated near to the sample with a minimum number of optical components in the light path.

21.6.1.2 Laser Pulse Spreading due to Dispersion

The laser pulses have a pulse width of 10^{-13} seconds as they emerge from the mode-locked laser. As the short laser pulses propagate through the glass and multilayer dielectric coatings in the microscope and in the microscope objective, they are spread out in time. This effect is due to a phenomenon called group velocity dispersion. Since each individual laser pulse consists of a distribution of optical frequencies, the wave packets will propagate at different velocities as determined by their group velocities.

Why is this dispersive laser pulse spreading important? From equation 13, we observe that n_a, the number of photons absorbed per fluorophore per pulse is inversely related to τ_p, the pulse duration. Therefore, an increase in the laser pulse duration, due to group velocity dispersion, results in a decrease in the number of photons absorbed per fluorophore per pulse. The net effect is a decrease in the fluorescence due to multiphoton excitation. There are pulse compression techniques, also called ‘prechirping,” that can be used to compensate for group velocity dispersion.

21.6.2 Multiphoton Excitation Microscopy and Confocal Microscopy

21.6.2.1 Spatial Resolution and Optical Sectioning

The three-dimensional imaging properties between two-photon and single-photon fluorescence microscopes has been compared [98]. A two-photon excitation microscope does not require a spatial filter in front of the photon detector in order to achieve optical sectioning. The optical sectioning is strictly a consequence of the physics of the two-photon excitation process. In contrast to a confocal microscope, in a two-photon excitation microscope the fluorescence is predominately limited to the focus of the microscope objective. This is shown in Figure 8.

In the z-direction of a two-photon excitation microscope, the excitation probability falls off with the fourth power of the distance on the optic axis. This can be compared single-photon excitation probability which falls off with the square of the distance on the optical axis. The depth discrimination of a multiphoton excitation microscope is similar to an ideal confocal laser scanning microscope with conjugate pinholes for spatial filtering.

The resolution of a microscope depends on the wavelength of the illumination light and the numerical aperture of the microscope objective. The resolution of a two-photon excitation microscope is limited by the size of the excitation volume of the focused light in the specimen. As previously explained, the emitted fluorescence need not be focused in order to be detected, and therefore it is less affected by scattering and chromatic aberration. A confocal microscope with ultraviolet illumination will have superior spatial resolution, increased by a factor of two, as compared to a two-photon excitation microscope with red or near infrared illumination [99, 100].

21.6.2.2 Depth of Penetration

One advantage of two-photon excitation microscopy is that the longer wavelengths of the red and near-infrared laser illumination afford deeper penetration into thick, highly scattering tissues, e.g., human skin *in vivo* [101, 102]. A reduction of penetration depth can be caused by light scattering and light absorption. In order to excite ultraviolet absorption fluorophores a confocal laser scanning microscope usually uses an ultraviolet laser. The tissue scattering coefficient for ultraviolet light is higher than for near-infrared light, and therefore the intensity is rapidly diminished as a function of depth. In many cells and tissues the absorption of the illumination light is much less for near infrared light than for ultraviolet

or blue light that is used with confocal microscopes. In summary, the wavelengths used in multiphoton excitation microscopy are usually twice the wavelength used for single photon excitation confocal microscopy. These wavelengths have deeper penetration into the specimen. This advantage is useful for fluorophores which absorb in the ultraviolet region; i.e. Indo-1, Fura-2, DAPI and the Hoechst 33342 dyes.

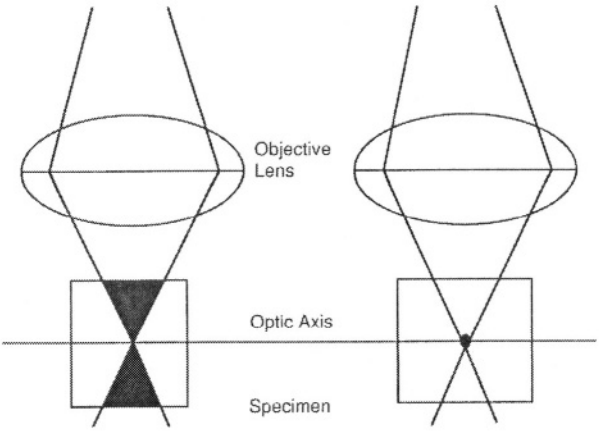

Figure 8. Diagram illustrating the difference between confocal microscopy and multiphoton excitation microscopy. In the confocal microscope photobleaching and fluorescence occurs in the double inverted cone shown in the left diagram. In the multiphoton excitation microscope the fluorescence only occurs in the focal volume shown in the diagram on the right. Photobleaching is limited to the focal volume. In the case of multiphoton excitation microscope the optical sectioning is a consequence of the physics of the two-photon absorption process and pinholes are not required.

In a confocal microscope there is a spatial filter or pinhole in front of the photon detector. Photons that are scattered within the specimen will not pass through the pinhole and therefore will not be detected by the photon detector. For a highly scattering sample such as skin, more photons can be detected in the absence of an emission pinhole as in confocal microscopy. With an external photon detector, both scattered and unscattered photons derived from the fluorescence can be detected.

Near-infrared light was able to penetrate the full thickness (400 μm thickness) of an *ex vivo* rabbit cornea. Potter *et al.* reported that for a variety of living and fixed specimens they were able to image two or three times deeper with two-photon excitation microscopy as compared to laser scanning confocal microscopy.

21.6.2.3 Photobleaching

In a confocal microscope there is fluorescence in the focal volume and also in both lobes of the right circular cone of illumination light. Consequently the process of photobleaching occurs in the entire illuminated volume within the specimen. In two-photon excitation microscopy the fluorescence, and therefore the photobleaching is predominately restricted to the focal volume. Therefore, in the out-of-focus regions there is almost no photobleaching and photodamage.

In summary, the use of multiphoton excitation microscopy has the following advantages: near infrared illumination results in less tissue damage, less scatter, and therefore deeper penetration into tissue; photobleaching is limited to the focal plane, and no confocal pinhole is required [103]. Multiphoton absorption is of great interest to the field of spectroscopy because it can be used to investigate both high-lying electronic states and electronic states that are not accessible from the ground state because of selection rules. Biologists are rapidly discovering the capability of multiphoton absorption processes in their quest to image thick, highly scattering specimens. Both the reduced scatter at the longer wavelengths and the high sensitivity provided by the small focal volume are exploited in studies based on multiphoton excitation processes.

21.6.3 Multiphoton Excitation Microscopy and Spectroscopy of *In Vivo* Human Skin: Functional NAD(P)H Imaging

Multiphoton excitation microscopy at 730 nm was used to image *in vivo* human skin autofluorescence [18,101,102]. This is an example of cellular functional imaging based on the which the naturally occurring fluorophore NAD(P)H. The concentration of NAD(P)H, and therefore its fluorescence intensity, is strongly linked to cellular oxidative metabolism. Cellular NAD(P)H provides both the contrast for cellular imaging, and also is an indicator of cellular metabolism.

The lower surface of the right forearm (of one of the authors) was placed on the microscope stage where an aluminum plate with a 1 cm hole is mounted. The hole is covered by a standard cover glass. The skin was in contact with the cover glass to maintain a mechanically stable surface. The upper portion of the arm rested on a stable platform prevented motion of the arm during the measurements. The measurement time was always less than 10 minutes. The estimated power incident on the skin was 10-15 mW. The photon flux incident upon a diffraction-limited spot on the skin is on the order of 10 MW/cm^2. We observed individual cells within the thickness of the skin at depths from 25 to 75 μm below the skin surface. No cells were

observed in the stratum corneum. These results are consistent with studies using reflected light confocal microscopy. In order to show the three-dimensional distribution of the autofluorescence we acquired optical sections with the two-photon excitation microscope and formed a three-dimensional visualization across the thickness of the *in vivo* human skin. It is important to characterize the source of the fluorescence that is imaged with multiphoton excitation microscopy. Two types of measurements are useful in the characterization of the fluorophore; emission spectroscopy and lifetime measurements. We measured these characteristics at selected points on the skin. Fluorescent spectra were obtained close to the stratum corneum (0-50 μm) and deep inside the dermis (100-150 μm). Measurements were made for 730 nm excitation wavelength which corresponds to a one-photon excitation wavelengths of about 365 nm. The fluorescent lifetimes were measured at selected points on the skin to compliment the fluorescent spectral data obtained. The lifetime results support NAD(P)H as the primary source of the autofluorescence at 730 nm excitation. Multiphoton excitation microscopy, coupled with emission spectroscopy and lifetime measurements, is a useful tool for the functional and morphological microscopic imaging of human skin in vivo [101,103-105].

ACKNOWLEDGMENTS

The author is thankful that he shared with Professor M. Böhnke, the 1999 Alfred Vogt-Prize for Ophthalmology (the highest award in Switzerland for scientific research in ophthalmology) from the Alfred Vogt-Stiftung zur Förderung der Augenheilkunde Zürich, for their work - "Confocal Microscopy of the Cornea." The authors thank Dr. Andreas A. Thaer for his collaboration in the development of the clinical confocal microscope. This work was supported by NIH grant EY-06958 (BRM). Professor Peter So is thanked for his help in the multiphoton excitation microscopy investigations. Dr. József Czégé of the Biomedical Instrumentation Center at the Uniformed Services University of the Health Sciences is thanked for technical assistance.

REFERENCES

1. S. Inoué and K.R. Spring, "Microscope image formation" in *Video Microscopy, The Fundamentals,* Second Edition (Plenum Press, New York, 1997), 13-117.
2. R.H. Webb, "Confocal optical microscopy," *Rep. Prog. Phys.* **59**, 427-471 (1996).
3. T. Wilson and C. Sheppard, "Image formation in scanning microscopes," in *Theory and Practice of Scanning Optical Microscopes* (Academic Press, London, 1984), 37-78.

4. T. Wilson, "Confocal Microscopy," in *Confocal Microscopy,* T. Wilson, ed. (Academic Press, London, 1990), 1-64.
5. T. R. Corle and G. S. Kino, "Depth and transverse resolution" in *Confocal Scanning Optical Microscopy and Related Imaging Systems* (Academic Press, San Diego, 1996), 147-223.
6. M. J. Booth, M. A. A. Neil, and T. Wilson, "New modal wave-front sensor: application to adaptive confocal fluorescence microscopy and two-photon excitation fluorescence microscopy," *J. Opt. Soc. Am. A* **19** (10), 2112-2120 (2002).
7. B.R. Masters, "Confocal microscopy: history, principles, instruments, and some applications to the living eye," *Comm. Molec. Cell. Biophys.* **8**, 243-271 (1995).
8. B.R. Masters, *Selected Papers on Confocal Microscopy,* Milestone Series **MS 131** (SPIE Optical Engineering Press, Bellingham, WA. 1996).
9. B.R. Masters, *Selected Papers on Multiphoton Excitation Microscopy,* Milestone Series **MS 175** (SPIE Optical Engineering Press, Bellingham, WA. 2003).
10. M. Gu, *Principles of Three-Dimensional Imaging in Confocal Microscopes* (World Scientific, Singapore, 1996).
11. *Methods in Cellular Imaging,* A. Periasamy ed. (Oxford University Press, New York, 2001).
12. *Confocal and Two-Photon Microscopy: Foundations, Applications, and Advances,* A. Diaspro ed. (Wiley-Liss, New York, 2002).
13. R.W. Boyd, *Nonlinear Optics,* second edition (Academic Press, New York, 2003).
14. D. B. Murphy, *Fundamentals of Light Microscopy and Electronic Imaging* (Wiley-Liss, New York, 2001).
15. B.R. Masters, "Three-dimensional microscopic tomographic imaging of the cataract in a human lens *in vivo,*" *Opt. Express* **3**, 332-338 (1998). http://www.opticsexpress.org
16. B.R. Masters, "Three-dimensional confocal microscopy of the living in situ rabbit cornea," *Opt. Express* **3,** 351-355 (1998). http://www.opticsexpress.org
17. B.R. Masters, "Three-dimensional confocal microscopy of the human optic nerve *in vivo*" *Opt. Express* **3,** 356-359 (1998). http://www.opticsexpress.org
18. B.R. Masters, P.T.C. So, "Confocal microscopy and multi-photon excitation microscopy of human skin *in vivo,*" *Optics Express* **8**, 2-10 (2001). http://www.opticsexpress.org
19. H. Goldmann, "Zur Technik der Spaltlampenmikroskopie," *Ophthal.* **96**, 90-96 (1938).
20. H. Goldmann, "Spaltlampenphotographie und photometrie," *Ophthal.* **98**, 257-270 (1940).
21. D.M. Maurice, "Cellular membrane activity in the corneal endothelium of the intact eye," *Experientia* **24**,1094-1095 (1968).
22. D.M. Maurice, "A scanning slit optical microscope," *Invest. Ophthal.* **13**, 1033-1037 (1974).
23. C.J. Koester, "Scanning mirror microscope with optical sectioning characteristics: applications to ophthalmology," *Appl. Opt.* **19** 1749-1757 (1980).
24. C.J. Koester, J.D. Auran, H.D. Rosskothen, G.J. Florakis, and R.B. Tackaberry, "Clinical microscopy of the cornea utilizing optical sectioning and a high-numerical-aperture objective," *J. Opt. Soc. Am. A* **10**, 1670-1679 (1993).
25. J.D. Auran, C.J. Koester, R. Rapaport, and G.J. Florakis, "Wide field scanning slit *in vivo* confocal microscopy of flattening induced corneal bands and ridges," *Scanning* 16, 182-186 (1994).
26. H. Ridley, "Recent methods of fundus examination including electronic ophthalmoscopy," *Trans. Ophthalmol. Soc. UK.* **72**, 497-509 (1952).
27. R.H. Webb, G. W. Hughes, and F. C. Delori, "Confocal scanning laser ophthalmoscope," *Appl. Opt*. **26***,* 1492-1499 (1987).
28. R.H. Webb, "Scanning laser ophthalmoscope," in *Noninvasive Diagnostic Techniques in Ophthalmology,* B. R. Masters ed. (Springer-Verlag, New York, 1990).

29. F. Roberts, J. Z. Young, "The flying-spot microscope," *Proc. IEEE* **99**, 747-757 (1952).
30. M. Minsky, "Memoir on inventing the confocal scanning microscope," *Scanning* **10**, 128-38(1988).
31. G.M. Svishchev, "Microscope for the study of transparent light-scattering objects in incident light," *Opt. Spectrosc.* **26**, 171-172 (1969).
32. G.M. Svishchev, "Image contrast in a microscope with synchronous object scanning by slit field diagrams," *Opt. Spectrosc.* **30**, 188-191 (1971).
33. M. Petran and M. Hadravsky, M. D. Egger, R. Galambos, "Tandem-scanning reflected-light microscopy," *J. Opt. Soc. Am. A* **58**, 661-664 (1968).
34. M.D. Egger and M. Petran, "New reflected-light microscope for viewing unstained brain and ganglion cells," *Science* **157**, 305-307 (1967).
35. S.C. Baer, "Microscopy Apparatus," United States Patent, 3,705,755, December 12, 1972.
36. T.R. Corle and G.S. Kino, *Confocal Scanning Optical Microscopy and Related Imaging Systems* (Academic Press, San Diego 1996).
37. G.Q. Xiao, G.S. Kino, and B.R. Masters, "Observation of the rabbit cornea and lens with a new real-time confocal scanning optical microscope," *Scanning* **12**, 161-166 (1990).
38. T. Tanaami, S. Otsuki, N. Tomosada, Y. Kosugi, M. Shimizu, and H. Ishida, "High-speed 1-frame/ms scanning confocal microscope with a microlens and Nipkow disks," *Appl. Opt.* **41**(22), 4704-4708 (2002).
39. H.J. Tiziani and H-M. Uhde, "Three-dimensional analysis by a microlens-array confocal arrangement," *Appl. Opt.* **33**, 567-572 (1994).
40. H.J. Tiziani, R. Achi, R.N. Krämer, and L. Wiegers, "Theoretical analysis of confocal microscopy with microlenses," *Appl. Opt.* **35**, 120-125 (1996).
41. B.R. Masters and A.A. Thaer, "Real-time scanning slit confocal microscopy of the *in vivo* human cornea," *Appl. Opt.* **33**, 695-701 (1994).
42. B.R. Masters and M. Böhnke, "Video-rate, scanning slit, confocal microscopy of the living human cornea *in vivo:* Three-dimensional confocal microscopy of the eye" in *Methods in Enzymology, Confocal Microscopy* **307**, P.M. Conn ed. (Academic Press, New York, 1999), 536-563.
43. P. Davidovits and M.D. Egger, "Scanning laser microscope for biological investigations," *Appl. Opt.* **10**, 1615-1619 (1971).
44. P. Davidovits and M.D. Egger, "Photomicrography of corneal endothelial cells *in vivo,*" *Nature* **244**, 366-367 (1973).
45. J. Liang, D.R. Williams, and D.T. Miller, "Supernormal vision and high-resolutin retinal imaging through adaptive optics," *J. Opt. Soc. Am. A* **14**, 2884-2892 (1997).
46. A.W. Dreher, J.F. Bille, and R.N. Weinreb, "Active optical depth resolution improvement of the laser tomographic scanner," *Appl. Opt.* **24**, 804-808 (1989).
47. A. Roorda, F. Romero-Borja, W.J. Donnelly III, H. Queener, T.J. Hebert, and M.C.W. Campball, "Adaptive optics scanning laser ophthalmoscopy," *Opt. Express* **10**(9), 405-412(2002).
48. D.X. Hammer, R.D. Ferguson, J.C. Magill, M.A. White, A. Elsner, and R.H. Webb, "Image stabilization for scanning laser ophthalmoscopy," *Opt. Express* **10**(26), 1542-1549 (2002).
49. M.A. Lemp, P.N. Dilly, and A. Boyde, "Tandem scanning (confocal) microscopy of the full thickness cornea," *Cornea* **4**, 205-209 (1986).
50. B.R. Masters, "Confocal microscopy of ocular tissue" in *Confocal Microscopy* (Academic Press, London, 1990), 305-324.
51. B.R. Masters, "Effects of contact lenses on the oxygen concentration and epithelial redox state of rabbit cornea measured noninvasively with an optically sectioning redox

fluorometer microscope" in *Transactions of the World Congress on the Cornea III,* H.D. Cavanagh ed. (Raven Press, New York, 1988), 281-286.
52. *Video Microscopy: the Fundamentals,* second edition, S. Inoué and K.R. Spring eds. (Plenum Press, New York, 1997).
53. T.R. Corle, L.C. Mantalas, T.R. Kaack, and L.J. LaComb, Jr., "Polarization-enhanced imaging of photoresist gratings in the real-time scanning optical microscope," *Appl. Opt.* **33**, 670-677, (1994).
54. S.S.C. Chim and G. S. Kino, "Optical pattern recognition measurements of trench arrays with submicrometer dimensions," *Appl. Opt.* **33**, 678-685 (1994).
55. T. Wilson and C. Sheppard, "The scanning optical microscopy of semiconductors and semiconducting devices," in *Theory and Practice of Scanning Optical Microscopy,* (Academic Press, London, 1984), 79-195.
56. R.W. Wijnaendts-van-Resandt, "Semiconductor Metrology," in *Confocal Microscopy,* (Academic Press, London, 1990), 339-360.
57. T.R. Corle and G.S. Kino, "Differential interference contrast imaging on a real time confocal scanning optical microscope," *Appl. Opt.* **29**, 3769-3774 (1990).
58. T.R. Corle and G.S. Kino, "Applications" in *Confocal Scanning Optical Microscopy and Related Imaging Systems* (Academic Press, San Diego, 1996), 277-322.
59. A. Boyde, C.E. Dillon, and S.J. Jones, "Measurement of osteoclastic resorption pits with a tandem scanning microscope," *J. Microscopy* **158,** 261-265 (1989).
60. *Biomedical Optical Biopsy and Optical Imaging: Classic Reprints on CD-ROM Series,* R.R. Alfano and B.R. Masters eds. (Optical Society of America, Washington, DC, 2004).
61. M. Böhnke and B.R. Masters, "Confocal microscopy of the cornea," *Prog. Retinal Eye Res.* **18,** 553-628 (1999).
62. M. Böhnke and B.R. Masters, "Long term contact lens wear induces a corneal degeneration with micro-dot deposits in the corneal stroma," *Ophthalmol.* **104,** 1887-1896(1997).
63. R. Cadez, B. Frueh, and M. Böhnke, "Quantifizierung intrastromaler Mikroablagerungen bei Langzeitträgern von Kontaktlinsen," *Klin Mbl Augenhlk* **212,** 257-258(1998).
64. B.R. Masters and A.A. Thaer, *"In vivo* human corneal confocal microscopy of identical fields of subepithelial nerve plexus, basal epithelial, and wing cells at different times," *Microsc. Res. Tech.* **29,** 350-356 (1994).
65. M. Böhnke, A. Thaer, and I. Shipper, "Confocal microscopy reveals persisting stromal changes after myopic photo refractive keratectomy in zero haze cornea," *Br. J. Ophthalmol.* **82**, 1393-1400(1998).
66. B.E. Frueh, R. Cadez, and M. Böhnke," *In vivo* confocal microscopy after photorefractive keratectomy in humans," *Arch. Ophthalmol.* **116,** 1425-1431 (1998).
67. M.C. Corbett, J.I. Prydal, S. Verma, K.M. Oliver, M. Pande, and J. Marshall, "An *in vivo* investigation of the structures responsible for corneal haze after photorefractive keratectomy and their effect on visual function," *Ophthalmol.* **103**, 1366-1380 (1996).
68. J.D. Auran, M.B. Starr, C.J. Koester, and V.J. LaBombardi, *"In vivo* scanning slit confocal microscopy of *Acanthamoeba* keratitis," *Cornea* **13**, 183-185 (1994).
69. K. Winchester, W.D. Mathers, J.E. Sutphin, and T.E. Daley, "Diagnosis of *Acanthamoeba* keratitis *in vivo* with confocal microscopy," *Cornea* **14**, 10-17 (1995).
70. J.D. Auran, C.J. Koester, R. Rapaport, and G.J. Fkorakis, "Wide field scanning slit *in vivo* confocal microscopy of flattening induced corneal bands and ridges," *Scanning* **16,** 182-186 (1994).
71. J.H. Massig, M. Preissler, A.R. Wegener, and G. Gaida, "Real-time confocal laser scan microscope for examination and diagnosis of the eye *in vivo,*" *Appl. Opt.* **33**, 690-694 (1994).

72. B.R. Masters, K. Sasaki, Y. Sakamoto, M. Kojima, Y. Emori, S. Senft, and M. Foster, "Three-dimensional volume visualization of the *in vivo* human ocular lens showing localization of the cataract," *Ophthal. Res.* **28**, 120-126 (1996).
73. B.R. Masters, "Three-dimensional confocal microscopy of the lens," *Ophthal. Res.* **28**, 115-119(1996).
74. B.R. Masters and S.L. Senft, "Transformation of a set of slices rotated on a common axis to a set of z-slices: application to three-dimensional visualization of the *in vivo* human lens," *Comp. Med. Imag. Graph.* **2**, 145-151 (1997).
75. B.R. Masters, "Optical tomography of the *in vivo* human lens: three-dimensional visualization of cataracts," *J. Biomed. Opt.* **3**, 289-295 (1996).
76. B.R. Masters, G.F.J.M. Vrensen, B. Willekens, and J. Van Marie, "Confocal light microscopy and scanning electron microscopy of the human eye lens," *Exp. Eye Res.* **64**, 371-377 (1997).
77. L. Goldman, "Some investigative studies of pigmented nevi with cutaneous microscopy," *J. Invest. Dermatol.* **16**, 407-427 (1951).
78. P. Corcuff, C. Bertrand, and J.-L. Lévêque, "Morphology of human epidermis *in vivo* by real-time confocal microscopy," *Arch. Dermatol. Res.* **285**, 475-481 (1993).
79. P. Corcuff and J.-L. Lévêque, "*In vivo* vision of the human skin with the tandem scanning microscope," *Dermatology* **186**, 50-54 (1993).
80. C. Bertrand, "Développement d'une nouvelle méthode d'imagerie cutanée *in vivo* par microscopie confocale tandem," These de doctoral de l'Universite de Saint-Etienne, (1994).
81. P. Corcuff, C. Hadjur, C. Chaussepied, and R. Toledo-Crow, "Confocal laser microscopy of the *in vivo* skin revisited," in *Three-Dimensinal and Multidimensional Microscopy: Image Acquisition and Processing,* D. Cabib, C J. Cogswell, J. Conchello, J. M. Lerner, and T. Wilson eds., *Proc. SPIE* **3605**, 73-81 (1999).
82. C. Bertrand and P. Corcuff, "*In vivo* spatio-temporal visualization of the human skin by real-time confocal microscopy," *Scanning* **16**, 150-154 (1994).
83. P. Corcuff, G. Gonnord, G.E. Pierard, and J.-L. Lévêque, "*In vivo* confocal microscopy of human skin: a new design for cosmetology and dermatology," *Scanning* **18**, 351-355 (1996).
84. B.R. Masters, "Three-dimensional confocal microscopy of human skin *in vivo:* autofluorescence of normal skin," *Bioimages* **4**, 1-7, (1996).
85. B.R. Masters, G. Gonnord, and P. Corcuff, "Three-dimensional microscopic biopsy of *in vivo* human skin: a new technique based on a flexible confocal microscope," *J. Microsc.* **185**, 329-338, (1997).
86. B.R. Masters, D. Aziz, A. Gmitro, J. Kerr, B. O'Grady, and L. Goldman, "Rapid observation of unfixed, unstained, human skin biopsy specimens with confocal microscopy and visualization," *J. Biomed. Opt.* **2,** 437-445, (1997).
87. M. Rajadhyaksha, M. Grossman, D. Esterowitz, R.H. Webb, and R. Anderson, "*In vivo* confocal scanning laser microscopy of human skin: melanin provides strong contrast," *J. Invest. Dermatol.* **104**, 946-952 (1995).
88. B. Chance, "Pyridine nucleotide as an indicator of the oxygen requirements for energy-linked functions of mitochondria," *Circ. Res. Suppl.*1, **38**, I-31-I-38 (1976).
89. B.R. Masters and B. Chance, "Redox confocal imaging: Intrinsic fluorescent probes of cellular metabolism" in *Fluorescent and Luminescent Probes for Biological Activity,* second edtion, W.T. Mason ed. (Academic Press, London, 1999), 361-374.
90. B.R. Masters, "Functional imaging of cells and tissues: NAD(P)H and flavoprotein redox imaging" in *Medical Optical Tomography: Functional Imaging and Monitoring,* G. Müller, B. Chance, R. Alfano, S. Arridge, J. Beuthan, E. Gratton, M. Kaschke, B.R. Masters, S. Svanberg, P. van der Zee eds. (SPIE Press, Bellingham, Washington, 1993), 555-575.

91. B.R. Masters, A.K. Ghosh, J.Wilson, and F.M. Matschinsky, "Pyridine nucleotides and phosphorylation potential of rabbit corneal epithelium and endothelium," *Invest. Ophthal. Vis. Sci.* **30,** 861-868 (1989).
92. B.R. Masters, A. Kriete, and J. Kukulies, "Ultraviolet confocal fluorescence microscopy of the in vitro cornea: redox metabolic imaging," *Appl. Opt.* **34**, 592-596 (1993).
93. D.C. Beebe and B. R. Masters, "Cell lineage and the differentiation of corneal epithelial cells," *Invest. Ophthal Vis. Sci.* **37**, 1815-1825 (1996).
94. B.R. Masters, "Specimen preparation and chamber for confocal microscopy of the *ex vivo* eye," *Scanning Microsc.* **7,** 645-651 (1993).
95. T. Wilson, C. Sheppard, "Nonlinear Scanning Microscopy" in *Theory and Practice of Scanning Optical Microscopy* (Academic Press, London, 1984), 196-209.
96. W. Denk, J.H. Strickler, and W.W. Webb, "Two-photon laser scanning fluorescence microscopy," *Science* **248**, 73-76 (1990).
97. C. Buehler, K-H Kim, C.Y. Dong, B.R. Masters, and P.T.C. So, "Innovations in two-photon deep tissue microscopy," *IEEE Eng. Med. Biol.* **18**, 23-30, (1999).
98. P.T.C. So, C.Y. Dong, B.R. Masters, and K.M. Berland, "Two-photon excitation fluorescence microscopy" in *Annual Review of Biomedical Engineering* (Annual Reviews, Palo Alto, CA. 2000).
99. P.T.C. So, C. Y. Dong, and B.R. Masters, "Two-photon excitation fluorescence microscopy," in *Biomedical Photonics Handbook,* T. Vo-Dinh ed. (CRC Press, Boca Rotan, Florida, 2003).
100. P.T.C. So, Ki-H Kim, C. Buehler, B.R. Masters, L. Hsu, and C.Y. Dong, "Basic principles of multi-photon excitation microscopy" in *Methods in Cellular Imaging,* A. Periasamy ed. (Oxford University Press, New York, 2001).
101. B.R. Masters, P.T.C. So, E. Gratton, "Multiphoton excitation microscopy and spectroscopy of cells, tissues and human skin *in vivo*" in *Fluorescent and Luminescent Probes for Biological Activity,* second edition, W.T. Mason ed. (Academic Press, London, 1999).
102. B.R. Masters, P.T.C. So, and E. Gratton, "Multi-photon excitation fluorescence microscopy and spectroscopy of *in vivo* human skin," *Biophys. J.* **72**, 2405-2412 (1997).
103. B.R. Masters and P.T.C. So, "Multi-photon excitation microscopy and confocal microscopy imaging of *in vivo* human skin: a comparison," *Microsc. Microanalys.* **5,** 282-289(1999).
104. D.W. Piston, B.R. Masters, and W.W. Webb, "Three-dimensionally resolved NAD(P)H cellular metabolic redox imaging of the *in situ* cornea with two-photon excitation laser scanning microscopy," *J. Micros.* **178**, 20-27 (1995).
105. B.R. Masters and T.P.C. So, *Handbook of Multiphoton Excitation Microscopy and other Nonlinear Microscopies* (Oxford University Press, New York, 2004).

This page intentionally left blank

Chapter 22

COMPARISON OF CONFOCAL LASER SCANNING MICROSCOPY AND OPTICAL COHERENCE TOMOGRAPHY

Sieglinde Neerken, Gerald W. Lucassen, Tom (A.M.) Nuijs, Egbert Lenderink and Rob F.M. Hendriks

Philips Research, Personal Care Institute and Optics and Mechanics, Professor Holstlaan 4, (WB 32), 5656 AA Eindhoven, the Netherlands. Corresponding author: Sieglinde Neerken, e-mail: Sieglinde.Neerken@philips.com, fax: +31-40-27 44 288; phone: +31-40-27 43 764

Abstract: This chapter deals with a comparison of two optical techniques to study human skin *in vivo.* The two methods, Optical Coherence Tomography (OCT) and Confocal Laser Scanning Microscopy (CLSM), deliver different information on the skin structure, mainly due to differences in penetration depth into the skin, resolution and field of view. On the one hand, our OCT system produces images of 2 x 2 mm^2 perpendicular to the skin surface, at one frame per second, with 14 µm axial resolution and 1 to 2 mm penetration depth. On the other hand, video rate CLSM with a modified Vivascope1000 (Lucid Inc., USA) provides images of 0.5 x 0.5 mm^2 parallel to the skin surface with 1 x 5 µm (lateral x axial) resolution, but with a limited penetration depth into the skin of 0.25 mm. In this chapter, some examples are presented on the application of the OCT and CLSM systems to study changes in skin due to UV irradiation and ageing. The image analysis, applied to the OCT and CLSM data, is described and a comparison of the results obtained by the two measurement techniques and the interpretation of the images is discussed.

Key words: confocal microscopy, dermis, epidermis, human skin, *in vivo,* optical coherence tomography

22.1 INTRODUCTION

During recent years, various optical techniques have become available that allow to study *in vivo* human tissue at a high resolution and contrast. Series of optical sections of intact living tissue are obtained and three-dimensional images can be generated of turbid media. The possibility of

taking non-invasive, "optical biopsies" allows to study tissue without artifacts by dehydration, fixation and staining, that is required for histological sectioning.

Confocal laser scanning microscopy (CLSM) has become a frequently used technique to study *in-vivo* and non-invasively the upper human skin layers [1-6]. In the lateral images cellular structure in the epidermis and fibrous tissue of the superficial dermis can be visualized and good similarity of the confocal images with histology has been reported [4,5]. The optical sectioning ability in confocal microscopy is based on the detection of singly scattered photons. Due to multiple scattering especially from deeper layers the signal-to-noise ratio diminishes with depth and the technique is therefore restricted to the upper layers of the skin. Optical coherence tomography (OCT) is a technique that more effectively reduces the effects of multiple scattering and therefore enables imaging of highly scattering skin layers as deep as 1 to 2 mm [7-15]. The principle is based on low-coherence interferometry [16] For reviews we refer to Schmitt [17], Fujimoto *et al.* [18], Welzel [19] and the book edited by Bouma and Tearney dealing with several application fields of OCT [20]. Very recently, large progress has been achieved in ultrahigh resolution OCT imaging [21,22] and optical coherence microscopy (OCM) [23]. *Ex-vivo* images with even sub-cellular resolution were obtained.

This chapter deals with a comparison of OCT and CLSM applied to human skin *in vivo* in a number of human volunteer studies. In contrast to CLSM, the resolution in the present OCT system is not high enough to visualize individual cells. OCT rather reveals images of optical structural inhomogeneities in tissue. The penetration depth and field of view of OCT, however, is much larger as compared to CLSM. OCT provides cross-sectional images, whereas CLSM measures images parallel to the skin surface. In this chapter, a general analysis of the OCT and CLSM data is explained and some examples are given on the application of the two systems to determine the thickness and location of different skin layers. In some cases, due to the lower resolution, interpretation of the OCT signals is not straightforward and the results appear not always to be consistent with those obtained with confocal laser scanning microscopy and histology [19,24]. As will be discussed below, a comparison of the results obtained with OCT and CLSM enables, however, a consisted interpretation of the images.

22.2 TECHNIQUES

22.2.1 Optical Coherence Tomography Set-up

OCT is the optical analog of ultrasound imaging, where infrared light is used instead of ultrasonic sound waves and low-coherence interferometry is used for depth discrimination. The principle of OCT is extensively described elsewhere [16,17]. The specially designed OCT system as used in our laboratory is displayed schematically in Figure 1. A fiber-optic interferometer forms the basis of the system, where one of the arms is terminated by a rapid scanning optical delay line and the other by a hand-held probe (see Figure 1) containing two lateral scanning mirrors and an objective lens. A broadband semiconductor amplifier source (BBS 1310, AFC Technologies) is used to provide low-coherence light at a central wavelength of 1310nm with a spectral width of 50 nm. Part of the light going back to the light source is coupled out by a second fiber coupler and used as the reference signal in an auto-balanced detector (Nirvana IR, New Focus). One frame (200×200 pixels) covering a slice of $2\times2\ mm^2$ is acquired in 1 second by driving the delay line scanner with a 100 Hz triangle wave and one of the scanning mirrors of the measuring head with a 1 Hz saw tooth. One "measurement" consists of taking ten of these slices at ~0.25 mm lateral intervals. During this measurement, the measuring head remained in the same position, and the slices were selected using the second lateral scanning mirror.

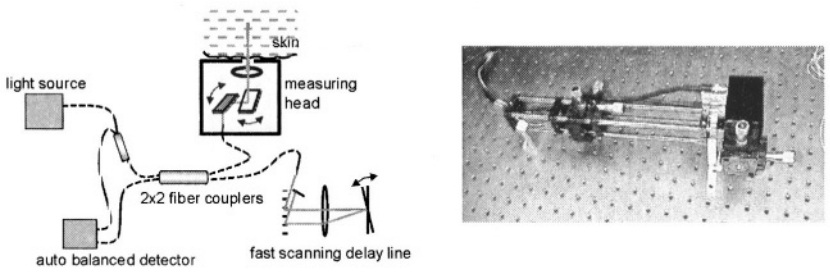

Figure 1. Schematic drawing of the OCT system (left) and photograph of hand-held probe (right) (This figure has been reproduced with permission from Ref. [24]. Copyright 2002 SPIE).

22.2.2 Confocal Laser Scanning Microscopy Set-up

Confocal laser scanning reflectance microscopy is performed with a modified Vivascope 1000 (Lucid Inc.), using a laser diode with a wavelength

of 834 nm. The Vivascope 1000 is equipped with a piezo mechanical positioner (Physik Instrumente E-500) on the objective assembly. A photograph of the microscope is shown in Figure 2. Together with proprietary software for control and data acquisition, automated accurate axial stepping is possible. Images are taken *en face* to the skin surface. A region of interest of approximately 0.5×0.4 mm^2 is scanned at various depths up to 200 μm. Usually the step size for axial scanning is 1 or 2 μm. The three-dimensional scans are saved on disk for further analysis. During an axial scan the applied laser power at each depth is adjusted for optimum brightness. Before scanning the laser power was adjusted at each 25 μm depth interval; i.e., near the surface we used 4 % of the maximum laser power, while for imaging the deepest layers the maximum laser power of 15 mW was applied. A 0.8 NA, 40 x water immersion microscope objective (Leica) was used. To achieve good optical contact between the skin and the optical system we applied water to the skin. The resolution of the microscope is 1 μm in lateral and about 5 μm in axial direction. One measurement (of, e.g., 100 steps of 2 μm) takes approximately 20 s.

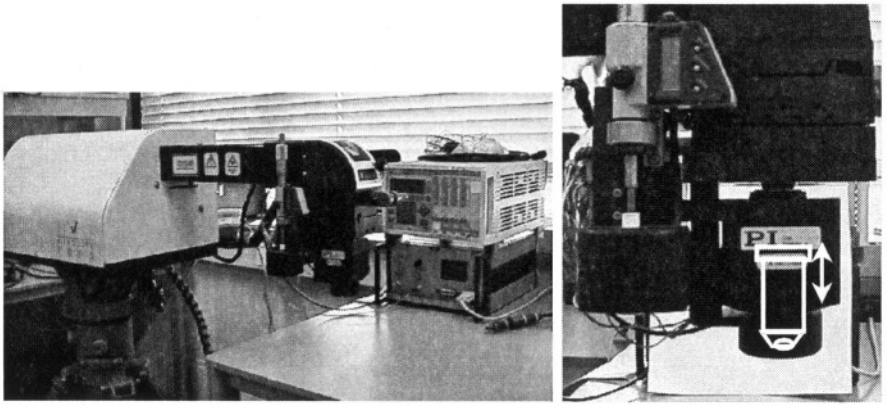

Figure 2. Confocal Laser Scanning Microscope, Viavascope 1000, Lucid Inc. (left) equipped with a piezo mechanical positioner on the objective assembly for fast axial scanning (right).

22.2.3 Data Analysis – OCT

A two dimensional, cross-sectional OCT image of human skin shows a number of bright bands, depending on the body site. In images obtained at the back of the hand three different bands can be distinguished whereas images of forearm, temple and back show two bands only. At all body sites, the first bright band is due to scattering of light at the skin surface, the other layers are located deeper in the skin. To determine the location of the deeper located layers relative to the surface, each image is flattened such that the

maximum intensity, caused by the reflection at the skin surface, is located at a fixed depth. An intensity profile is calculated from integration of the signal in the image along the lateral position x as a function of depth z. From the ten images obtained in a single measurement an average intensity profile is determined. The skin surface is defined at the depth at which the intensity of the first peak has reached half of its maximum, set to a depth of 0 μm. The locations of the deeper located layers at *Doct* are determined relative the skin surface by calculating the positions at which the bands have climbed half of their maximum intensity on the ascending slopes.

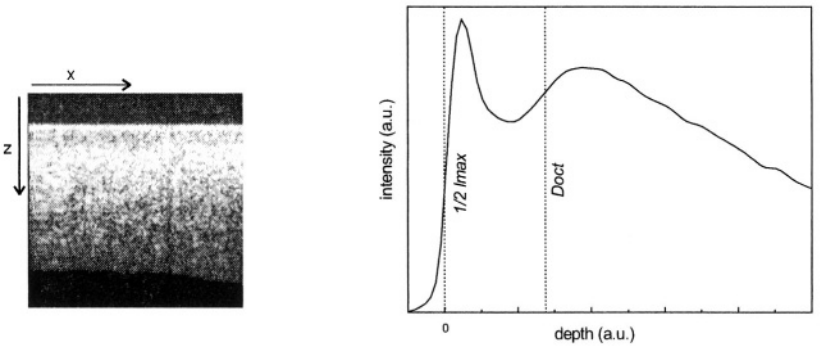

Figure 3. Cross-sectional OCT image of the volar forearm (flattened surface) and corresponding intensity profile. The intensity profile is constructed by averaging profiles along the lateral direction x after flattening the surface. The profile shows two peaks caused by the two bright bands in the image. The determination of the location of the second band at *Doct* relative the surface at ½ I_{max} is indicated by the dashed line.

As example, Figure 3 shows an image (flattened surfaces) measured at the volar forearm together with the corresponding intensity profile. The profile shows two peaks, caused by the two bright reflecting bands and the location of the second layer, *Doct,* is indicated in the graph. Usually, at each site three individual measurements are performed and the average locations of the different layers are calculated. The measured optical depth *d'*(*OCT*) is corrected for the refractive index to obtain the real physical depth *d*(*OCT*)

$$d(OCT) = \frac{d'(OCT)}{n},$$

where *n* is the average refractive index of the tissue. We assume a constant refractive index for all skin layers of $n = 1.4$ [25].

22.2.4 Data Analysis – CLSM

The thickness and location of different skin layers in the epidermis and upper part of the dermis can also be derived from the CLSM measurements. Boundaries of different skin layers are determined from visual inspection of the structural information in the images (see Figure 4) in combination with analysis of the average reflected intensity profile (Figure 5). The 3D stacks of bitmap images are visualized with the software package Alice (version 3.0, Perspective Systems Inc.). The profile of the reflected intensity can be derived from the stack of images: at each depth the reflected intensity in the whole image is averaged, divided by the applied laser intensity and plotted as a function of depth. An example of a typical profile on a logarithmic scale is shown in Figure 5. The CLSM images corresponding to certain boundaries are presented in Figure 4.

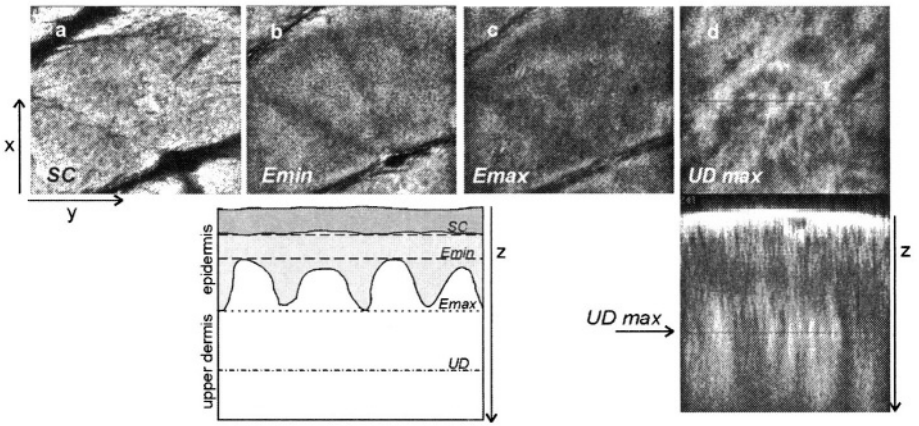

Figure 4. CLSM images of the volar forearm at different depth in the skin and schematic drawing of the upper skin layers in cross-section illustrating the definition of the markers: image a) measured at lower border of the stratum corneum; image b) upper border of epidermis at top of papillae; image c) lower border of epidermis; image d) fibrous structure in upper dermis. The location of this layer is also visible in the cross-sectional reconstruction.

At the glass-skin interface we determined the location of the skin surface from the depth at which the reflected intensity has reached half its maximum (1/2 I_{max}); this depth is set to 0 μm. The thickness and locations of various skin layers are determined relative to this plane. The measured depth *d'(CLSM)* has been corrected for the refractive-index mismatch to obtain the real physical depth *d(CLSM)*

$$d(CLSM) = \frac{n}{n_0} d'(CLSM) \quad ,$$

where n is the average refractive index of the tissue (n = 1.4) and n_0 is the refractive index of the immersion medium, in our case water (n_0 = 1.33). From the CLSM data several skin layer parameters in the upper layers of the skin can be determined. For an overview of the derived parameters we refer to the schematic drawing in Figure 4 representing in a schematic way the different layers and markers of the upper skin layers. Figure 4 also presents a selection from the stack of CLSM images obtained at different depths below the skin surface. The images show the typical structure at the different markers in the skin:

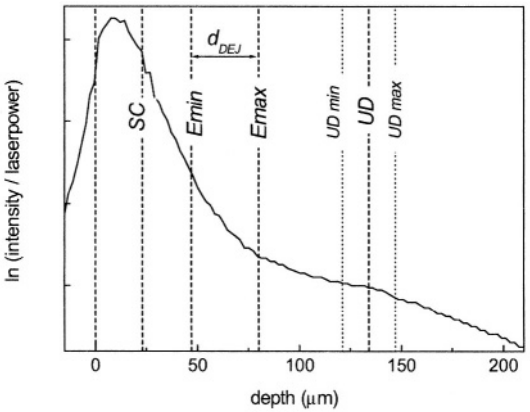

Figure 5. CLSM intensity profile at the volar forearm on a logarithmic scale derived from stack of images (see Figure 4) with boundaries of different skin layers indicated.

Stratum Corneum: The thickness of the stratum corneum d_{SC} is determined as the depth at which at first a regular structure of cells is visible in the image (Figure 4, image a).

Epidermis *(Emin* and *Emax):* (i) The minimum thickness of the epidermis d_{Emin} is determined by the depth at the top of the uppermost papillae (at *Emin*). If no papillae were visible in the image, *Emin* is defined as the

maximum depth at which only the cellular structure of the epidermis contributes to the signal; no contribution of the dermis (Figure 4, image b). At this depth the epidermal cells are much smaller in size compared to the image at the border of the stratum corneum (image a) (ii) The maximum thickness of the epidermis d_{Emax} is defined by the valleys of the papillae. The different optical properties of cellular structure in the epidermis and fibrous structure in the dermis cause a change in slope in the reflected intensity profile. The onset of this change in slope (at *Emax*) corresponds to the depth at which for the first time no cellular structure is observed anymore in the stack of images in going from the surface to deeper positions. The signal in the image is determined by the dermis only (Figure 4, image c).

Dermo-epidermal junction: The determination of d_{Emin} and d_{Emax} allows to calculate the thickness of the dermo-epidermal junction $d_{DEJ} = d_{Emax} - d_{Emin}$.

Upper dermis: At a certain depth a reflecting layer of fibrous structure in the dermis is observed in the stack of three-dimensional CLSM images (Figure 4, image d). The location *UD* of this layer is defined as *(UD min + UD max)*/2, where *UD min* is the location of the onset of this layer and *UD max* the location of its maximum intensity. The boundary can also be derived from the intensity profile, appearing as a second change in slope around *UD* (Figure 5, intensity profile).

22.2.5 Measurements and Statistics

For all studies described below, the volunteers gave informed consent. Measurements were carried out in climate controlled test rooms at 22°C, 50 % relative humidity. With OCT and CLSM three measurements at slightly different positions were performed and the skin parameters were derived per measurement. The results of the three individual measurements per volunteer were averaged and the mean values and standard deviations for the whole group of volunteers were calculated. In order to find relations between measured parameters scatter plots, Pearson correlations and principal components analysis were employed. To compare parameters between different groups or measurements at different time points independent samples t-tests have been used, with a significance level of $p = 0.05$.

22.3 APPLICATION OF OCT AND CLSM

We have applied OCT and CLSM in a number of human volunteer studies to determine the layer thickness and location of different skin layers and to compare the results obtained by the two techniques. Three different human volunteer studies are discussed below. In the very first test the effect of ultraviolet irradiation on the skin layer thickness was studied. The second

study focused on the evaluation of difference in skin due to ageing. Finally, the third study delivered additional data to deriving a more complete understanding of the comparison between CLSM and OCT.

22.3.1 Changes due to Ultraviolet Irradiation

The thickness of the epidermis is recognized nowadays as an important factor in determining a person's sensitivity to ultraviolet (UV) exposure [26]. However, hard data concerning this effect are lacking, because of the difficulties associated with measuring this thickness. Histology has previously been the only technique that could give the answer, and even in histology large uncertainties arise due to deformation of the skin during processing. Apart from this uncertainty, histology is invasive; any technique that would not involve inflicting damage to healthy skin would be preferable. Over the last decade, non-invasive optical techniques, like OCT and CLSM, have become available to image *in vivo* without the need for sample preparation. We have applied OCT and CLSM in a study with 15 volunteers that were exposed to UV in a three week tanning schedule, to see if we could detect changes in the thickness over this period and over a two-week period after the exposures. For a more extensive description we refer to Lenderink *et al.* [24].

Exposure and measurement protocol

CLSM and OCT were applied in a study into the effects of exposure to UV on the thickness of the epidermis. 15 volunteers (3 male, 12 female; ages ranging from 37-63 years, 51 years mean) were exposed on their backs in seven sessions during a period of three weeks, with a progressive dose schedule beginning at one personal minimal erythema dose (MED_p; established for each subject before the study by a dermatologist using a standard protocol for MED determination), leading to a cumulative dose of ~16 MED_p. The lamps emit partly in the UV-B range of the spectrum, which is thought to stimulate epidermal thickening [27].

The volunteers were measured on six regions with OCT and with CLSM. Measurements were performed four times during the study: at the beginning of the exposure schedule (day 1), halfway (day 14), and at the end (day 26), and again two weeks after the end of the exposure schedule (day 43).

Results and Discussion

With CLSM individual cells can be visualized and therefore a relatively easy assignment of tissue to the various layers in the skin is possible. In this study the CLSM data were analyzed to determine the following two parameters: the thickness of the stratum corneum d_{SC} and the minimum thickness of the epidermis d_{Emin} that is determined by the top of the papillae.

The OCT images reveal less detailed structural information and consequently the assignment of the signals is less straightforward. An OCT image of the back, as it is measured in this study, shows two bright layers. The upper layer is caused by the surface and the second layer is located deeper in the skin. In this very first human volunteer study various points in the OCT data were tested as a criterion to define a boundary between the different layers. The location of the second bright band in the image was determined as the distance between the location of the maximum reflected intensity (due to surface reflection) and the point where the signal intensity caused by the second layer had reached half of its maximum intensity. (In the subsequent studies we have defined the location of the skin surface at the depth at which the intensity of the first band has reached half of its maximum intensity (see subsection 22.2.3)).

In this tanning study, the average value of all measurements for the location of the second bright layer in OCT was 92 ± 11 μm. When corrected for a putative refractive index of 1.4 (ignoring refractive index variations in the tissue), real thicknesses in the order of 65 μm are obtained. With OCT no consistent response in thickness as a result of UV exposure was found.

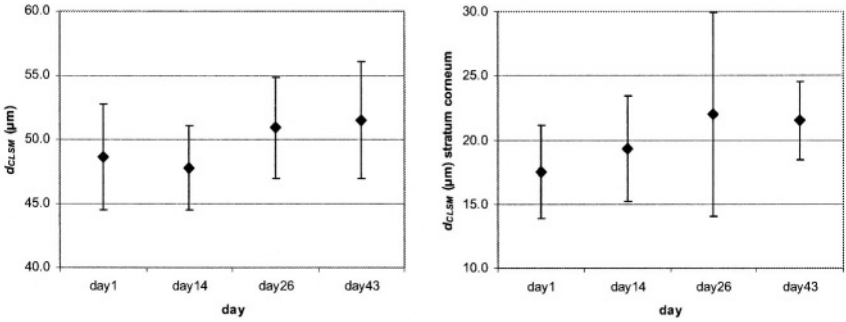

Figure 6. Minimum epidermal thickness (left) and thickness of the stratum corneum (right) at the back upon UV irradiation determined with CLSM as a function of time (values are not corrected for the refractive index mismatch) (This figure has been reproduced with permission from Ref. [24]. Copyright 2002 SPIE).

The results for the CLSM measurements of the minimum epidermal thickness are displayed in Figure 6 (left panel). A small, but statistically significant increase was consistently observed both at the end of the exposure schedule (day 26) and two weeks afterwards (day 43). By analyzing the stratum corneum thickness from the CLSM data (Figure 6, right panel), we found roughly the same change in thickness over the days. *p*-Values were 0.002 for the (day 26 – day 1) difference and <0.001 for the

(day 43 – day 1) difference. Here it seems that a small increase is just discernible on day 14 ($p = 0.03$) as well.

OCT and CLSM yield different values for the thickness of the skin layers. In the analysis, the values obtained with OCT are larger than those obtained for the minimum thickness of the epidermis derived from CLSM. With OCT an average value of about 65 µm was measured for the location of the second layer relative to the surface, whereas with CLSM values between 51 and 54 µm were obtained for the skin layer up to the top of the papillae. It appears that the values of the two techniques cannot be directly compared with each other, due to their sensitivity to different markers and their different spatial resolutions. For further investigation of the comparison of CLSM and OCT signals and the identification of the markers visible in the OCT images we have performed additional studies that are described in the subsections 22.3.2 and 22.3.3.

In this study, the high spatial resolution of CLSM allowed the detection of a very small increase in thickness that remained obscure to OCT due to the relatively lower spatial resolution of 14 µm of the OCT system. The skin thickness changes in a tanning schedule of ~16 MED_p are too small to be detected by OCT. CLSM was found to be able to detect a small change of 3 µm ($p = 0.011$), which could be attributed entirely to stratum corneum thickening.

The thickening effects of the exposure protocol used in the current test are very minor, much smaller than previously thought on the basis of histology [27]. The epidermis increases in thickness by at most a few micrometers. Our results are consistent with the picture where the entire thickness change is attributed to a thickening of the stratum corneum. The source of the discrepancy with histology is not clear to us. The difficulties associated with the preparation of skin biopsies while retaining layer morphology are well known. Especially the stratum corneum tends to disrupt and blow up. It is however premature to state that this caused the discrepancy. More experience with *in vivo* measurements is needed to resolve this matter.

22.3.2 Changes due to Ageing

This section describes a study into the age-related changes in human skin *in vivo* by applying the two imaging techniques, CLSM and OCT. In the past, age-related changes in skin have extensively been studied by histological sectioning [28-33]; data obtained with *in vivo* imaging are, however, rare [34]. Our *in vivo* characterization of the various human skin layers of the epidermis and upper dermis has been performed in two groups of volunteers differing in age (younger and older group). A direct comparison of the results obtained by CLSM and OCT allows a better and

more consistent interpretation of the images. A more extensive description of this study can be found in Neerken *et al.*[35].

Study design

In order to investigate age-related changes in healthy human skin *in vivo,* we have studied two groups of 15 volunteers each, with Caucasian skin type. One group comprised of volunteers with an age of 19 up to 24 years, referred to as "younger group", (mean age: 22.5 years; 8 female, 7 male) and the other group with an age of 54 up to 57 years, referred to as "older group", (mean age: 55.3 years; 5 female, 10 male). Measurements were performed on the volar aspect of the forearm and on the temple.

Results and Discussion

CLSM and OCT were used to characterize non-invasively age-related changes in human skin *in vivo* in two groups of volunteers, differing in age. From the stack of CLSM images the following five skin parameters were obtained as described above (see Figure 4) for the two groups at the forearm and at the temple: (i) the thickness of the stratum corneum d_{SC}, (ii) the minimum thickness of the epidermis, d_{Emin}, that is determined by the top of the papillae and (iii) the maximum thickness of the epidermis, d_{Emax}, defined by the bottom line of the papillae. (iv) The determination of d_{Emin} and d_{Emax} allows the calculation of the thickness of interface between the epidermis and dermis, d_{DEJ}. (v) Finally, the location of a fibrous layer in the upper dermis relative to the skin surface, *UD,* is derived from the images and the intensity profile. The OCT data deliver one parameter, *Doct.* In the OCT images of the temple and of the volar forearm two bright layers could be distinguished. The first one is caused by the skin surface and the location of the second layer, *Doct,* is determined relative the surface. Figure 7 summarizes the mean values per group and site for the thickness and location of the different skin layers. At both sites, forearm and temple, the parameters show a similar trend. The overall effect of ageing skin was found to be a statistically significant decrease in d_{Emax}, d_{DEJ}, *UD* and *Doct,* whereas d_{SC} and d_{Emin} changed only slightly with age.

In general, our data are in fair agreement with those of earlier studies [36] and good correspondence is obtained between *in vivo* data and histological sectioning. As already found by histology [30], the thickness of the very upper layer of the skin, the stratum corneum, does not change with age. The epidermis up to the top of the papillae (at *Emin*) increases slightly with age, whereas the bottom line of the papillae (at *Emax*) is shifted considerably towards the surface as the skin ages. The findings agree with the observation from histological sectioning [28,31,32,37]. The decrease of d_{Emax} together with a slight increase of d_{Emin} results in a significantly flatter interface between the epidermis and dermis in aged skin, confirming histological data of earlier studies [31-33]. Besides the decrease in thickness of the dermo-

epidermal junction, the number of the papillae per area decreases as well, especially at the temple. This aspect has been studied in a more quantitative manner by Huzaira *et al.* [38] and Sauermann *et al.* [36] and the results are consistent with histology.

In the upper dermis, just below the bottom line of the epidermis a low scattering, "optically dark" area is entered. Only little contrast is obtained in the CLSM images of this layer. Images recorded from this first layer of the dermis show some fine fibrous structure, presumably due to collagen and elastin. At a certain depth a strongly light reflecting layer of larger, more tightly packed collagen bundles is observed. The location of the collagen layer at *UD* in the upper dermis decrease significantly with increasing age at both sites Figure 7.

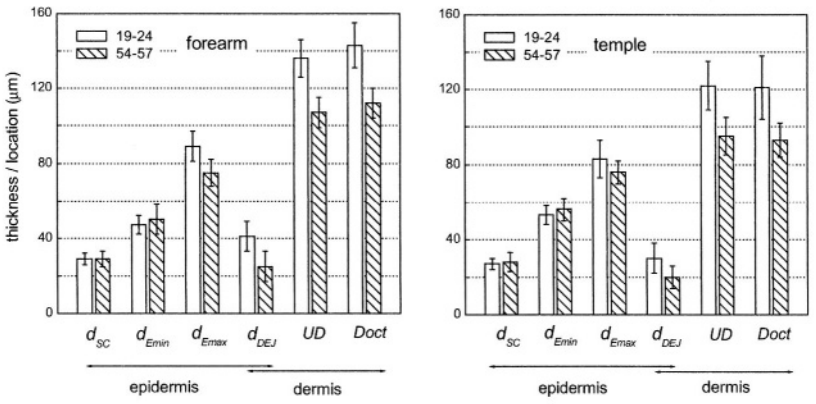

Figure 7. Mean values and standard deviations of all skin parameters determined with CLSM and OCT for the two age groups, 19-24 years open bars and 54-57 years striped bars, at forearm (left) and temple (right).

Not only the position of the fibrous layer changes with age, large changes were also observed in the structure of the collagen fibers and bundles. Figure 8 shows CLSM images of the fibrous structure in the upper dermis parallel to the skin surface (x-y view). The left CLSM image represents a measurement on the temple of a younger volunteer and the right one on an older volunteer. The structure of the bundles in younger skin consists of relatively large bundles, whereas older skin shows a network of thinner and smaller fibers.

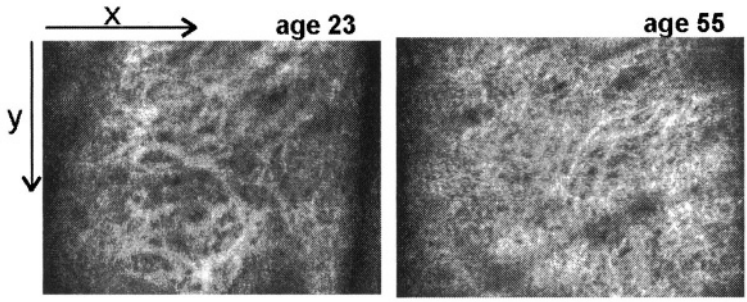

Figure 8. CLSM images of fibrous structure in upper dermis at a depth *UD* of a younger (left) and an older (right) volunteer measured at the temple. Structural changes upon ageing of the collagen fibers are visible.

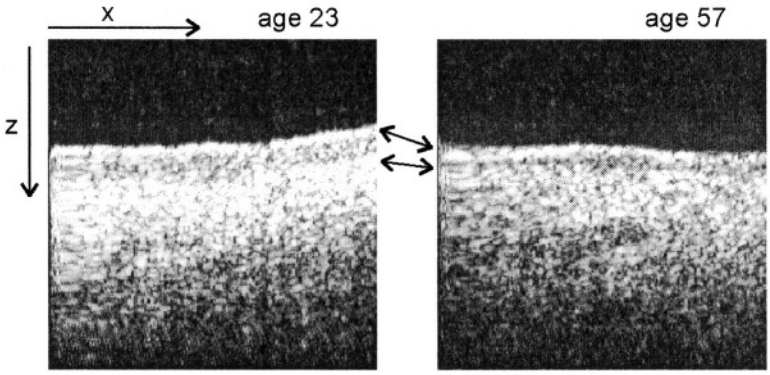

Figure 9. OCT images of a younger volunteer (left image) and older volunteer (right image). The positions of the surface reflection and of the second reflecting layer are roughly indicated (arrows). The images indicate that the value of *Doct* is relatively small for the older volunteer.

Like the CLSM results the data obtained with OCT show significant differences between the skin of the younger and of the older group at the volar forearm and at the temple. Figure 9 shows two OCT images of skin from a younger and an older volunteer, respectively. In the images two bright reflecting layers are visible. The first bright band is due to the reflectance from the stratum corneum. Just below this layer, in the viable epidermis, the signal intensity diminishes and a second reflecting layer is located deeper in the skin. In the younger volunteer this reflecting layer is located much deeper below the surface as compared to the situation in the elderly volunteer. The images clearly show smaller values of *Doct* for elderly skin. The differences in the mean values of *Doct* between the younger and older group (Figure 7) are statistically highly significant at both sites.

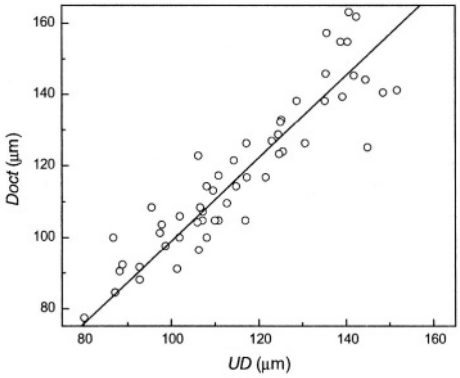

Figure 10. Comparison of values *Doct* and *UD* determined with OCT and CLSM, respectively. Pearson correlation coefficient: 0.91. The regression line derived from a principal component analysis revealed: $Doct = 1.16 \cdot UD - 17$ µm, indicating a reasonably strong association between the two variables.

For the interpretation of the signals measured with OCT a direct comparison is performed between the two measurement techniques. Figure 7 indicates that the mean values of the parameters *UD* and *Doct* are of the same order of magnitude, suggesting that the signals might be due to the same layer in the skin. We have tested the agreement of the two measurement parameters by plotting all values obtained for *Doct* with OCT against the corresponding values *UD* determined with CLSM (Figure 10). The association between the two parameters was tested by a principal components analysis. The resulting regression line suggests a reasonably strong association between *Doct* and *UD* measured by the different techniques. Our analysis indicates that the marker, *Doct,* measured with OCT corresponds with *UD* obtained by CLSM. In other words, the second light-reflecting layer in the OCT images of the forearm and temple is due to scattering at fibrous structures in the upper dermis, of which the structure and location can also be observed with CLSM (Figure 11). In earlier studies [19,24], the second layer was in the first place thought to be caused by the fibrous structure immediately below the basal cell layer, the interface between epidermis and dermis. The direct comparison described in the current study of the OCT images with the corresponding CLSM data, however, shows that the second bright reflecting band is located much deeper below the epidermal basal layer and can be ascribed to scattering of light at fibrous structure in the dermis. Possibly, the signal is caused by the interface between the papillary and reticular dermis.

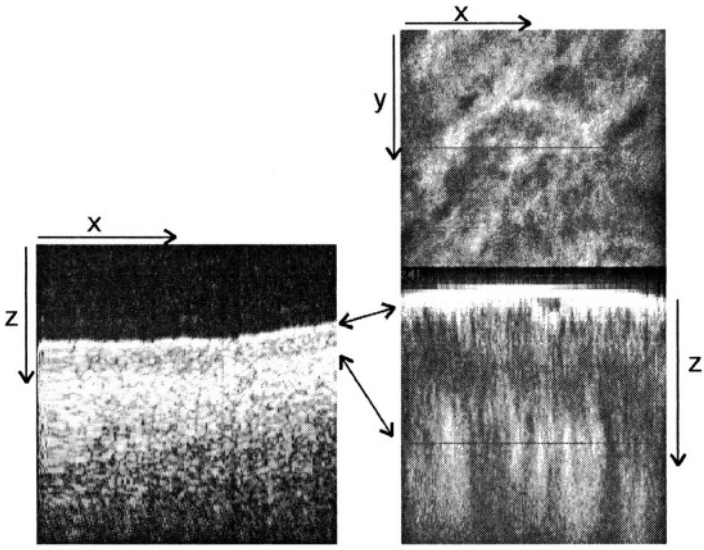

Figure 11. Comparison of OCT image (left) with CLSM image in plane (xy-view) and in cross section measured at volar forearm. With OCT and CLSM two bright layers can be distinguished (see arrows) in cross-sectional view. The fibrous structure of the second layer is imaged in lateral direction with CLSM.

22.3.3 Skin Layer Thickness at the Back of the Hand

In the previous sections the characterization of the upper skin layers with CLSM and OCT is described. A careful definition of markers and a comparison of the results obtained with CLSM and OCT enabled to derive a consistent interpretation of the measured signals. The data presented in the previous sections were collected from different body sites: the forearm, the temple and the back. In general, no large differences were obtained in the images from the different sites. The properties of human skin are, however, very much dependent on the body site. This section reports on an *in-vivo* study by CLSM and OCT performed at the back of the hand. It appears that images from this body site deliver a quite pronounced contrast caused by the basal layer that is not resolved in the studies at the forearm, temple and back. By comparing the results obtained by the two techniques the interpretation of the images is possible. A more detailed discussion of these measurements can be found in Neerken *et al.* [39].

Study design

We have studied *in vivo* human skin at the dorsal aspect of the right hand with OCT and CLSM. Sixteen volunteers with healthy skin and Caucasian skin type, age: 25-42 years, participated in the study.

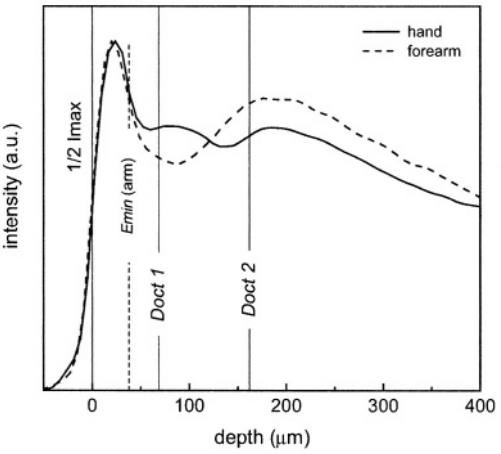

Figure 12. OCT intensity profile measured on the back of the hand (solid line) and at the volar forearm (dashed line). For the measurement at the back of the hand the locations of the parameters, *Doct 1* and *Doct 2,* are indicated. In the profile of the forearm the location of *Emin* determined with CLSM is indicated.

Results and Discussion

From the OCT data obtained at the back of the hand three different layers can be distinguished, whereas at the forearm, temple and back only two layers were observed. An intensity profile derived from the measurements at the back of the hand is shown in Figure 12 (solid line). For comparison a profile obtained at the forearm with its two peaks is plotted too (dashed line). At the back of the hand the first peak is due to the surface reflection, the second one is located directly below the surface while the third one is located deeper in the skin. The locations of the latter two layers, at *Doct 1* and *Doct 2,* relative to the surface was determined for all volunteers and the mean values with the standard deviations are shown in Figure 13.

Measurements were also performed with CLSM. Again, the values for the thickness of the stratum corneum d_{SC}, the minimum and maximum thickness of the epidermis, d_{Emin} and d_{Emax}, and the location of the fibrous structure in the upper dermis, *UD,* were derived from the images in combination with the intensity profiles. Figure 14 represents a cross-sectional reconstruction that has been derived from a stack of lateral images. The locations of the above described markers are also indicated by the lines. In cross-section three areas of increased reflection can be distinguished. The uppermost reflecting signal is caused by the stratum corneum with the marker *SC* as lower border, the second one is located around the border

Emin at the basal layer and the third one is located in the upper dermis. In the cross-sectional image the undulation of the dermo-epidermal junction, between the markers *Emin* and *Emax,* is resolved and as is visible in the xy-image too (Figure 14, right image), the density per area of papillae at the back of the hand is very high. In the very upper part of the dermis, just below *Emax* the reflected intensity is diminished. The third, higher reflecting layer starts at a depth *UD min* and reaches its maximum intensity at *UD max.* The mean values and standard deviations for all volunteers of the different skin parameters are depicted in Figure 13.

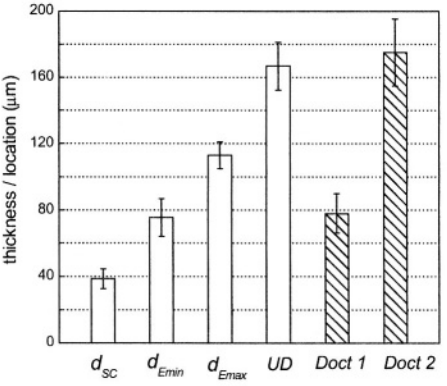

Figure 13. Mean values and standard deviations of skin parameters at the back of the hand derived from CLSM (open bars) and OCT (striped bars).

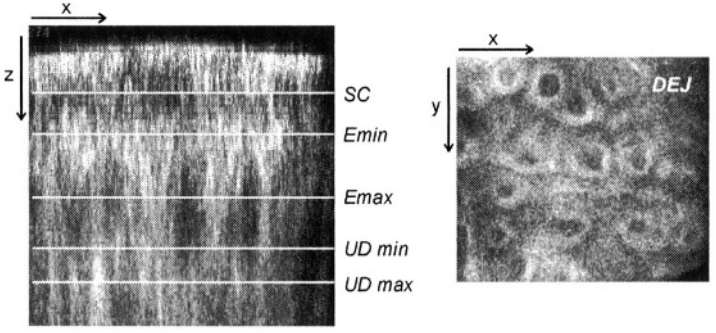

Figure 14. Cross-sectional reconstruction from a stack of CLSM images with markers indicated. Right: Lateral image at the depth of the dermo-epidermal junction, with a high density of papillae visible.

The mean values in Figure 13 of d_{Emin} obtained with CLSM and *Doct 1* derived from OCT and the values of d_{Emax} and *Doct 2* are of the same order of magnitude. Like in the previous section (Figure 10), the relation between the variables obtained with the two measurement techniques was checked by applying a principal components analysis to the data sets. For the first set of parameters, d_{Emin} and *Doct 1,* the analysis revealed good agreement between the two variables, indicating that the same layer in the skin is imaged by OCT and CLSM: the second layer in OCT, directly below the skin surface at *Doct 1,* is caused by scattering of light at the basal layer of the epidermis. This layer is observed in the cross-sectional CLSM image as a bright layer around *Emin* too, Figure 14. For the second pair of parameters, *UD* and *Doct 2,* it was concluded that the third layer measured with OCT at *Doct 2* is caused by the fibrous layer in the dermis of which the structure can be visualized in plane by CLSM and its location can also be obtained in the cross-sectional representation (Figure 14).

The OCT measurements on forearm, temple and back resolved only two bright reflecting layers. The first layer is due to the reflection of light at the skin surface and the second layer was ascribed to fibrous structure in the upper dermis. A transition between epidermis and dermis was not observed. OCT images of the back of the hand, however, do resolve the interface between epidermis and dermis. A close inspection of the mean values obtained at the back of the hand compared to values obtained at other body sites indicates that the values at the hand of the all skin layers are much larger. The stratum corneum is about 10 μm thicker at the hand than at the forearm. If we take the average values for the epidermal thickness at the forearm of the two age groups, the values at the hand are in average 28 μm larger for d_{Emin} and 31 μm for d_{Emax}. The fibrous layer in the upper dermis at *UD* is located 46 μm deeper in the skin at the hand than at the forearm. This indicates that the distance between the different layers is much larger at the hand than at the forearm. Consequently, the different layers can better be resolved in the images. The additional signal obtained with OCT at the back of the hand is due to the basal epidermal layer. Since the epidermal thickness is relatively small at the forearm the signal from the basal layer in OCT is hidden by scattering from the surface. The location of *Emin* at the forearm determined with CLSM is indicated in the OCT intensity profile in Figure 12. Moreover, the CLSM images of the hand show a very high density of papillae and a strong undulation of the dermo-epidermal junction (Figure 14). As a consequence, the number of basal cells per area is higher at the hand than at a body site with a lower density of papillae, such as the forearm, temple and back. This may also increase scattering at the basal layer and lead to the fact that this layer is resolved in the OCT images at the hand but not at the forearm.

The signals obtained by CLSM and OCT strongly depend on the site of measurement. This may hamper an easy interpretation of the signals. Applying a combination of techniques that give complementary information, however, enables a better assignment of the different skin layers.

22.4 DISCUSSION

During recent years, the upper skin layers, especially of the epidermis, have been studied extensively and good correspondence between *in vivo* measurements and histology is reported [1,4,36,40,41]. This chapter reports on the characterization of the upper skin layers *in vivo* by two optical techniques, OCT and CLSM. The results demonstrate that OCT and CLSM are feasible tools for non-invasive and *in vivo* analysis of skin morphology. The data allow the determination of the thickness and location of various skin layers in the epidermis and upper part of the dermis. CLSM and OCT are capable of detecting significant differences in the thickness, location and structure of various skin layers upon UV-irradiation and upon ageing. A careful definition of markers and a comparison of the results obtained with OCT and CLSM deliver a consistent interpretation of the measured signals.

Due to differences in spatial resolution and penetration depth of these methods, OCT and CLSM give complementary information on the composition and structure of skin. The interpretation of our OCT signals, however, is not always straightforward, since the resolution of our system at present is too low to resolve structural detail in the upper layers of the skin. The cross-sectional images rather show different layers of varying intensity. On the other hand, CLSM images, measured parallel to the skin surface, are obtained with higher resolution and give more detailed information on the structural composition of the various layers. A direct comparison of the skin parameters obtained with CLSM and OCT enables the assignment of the layers and allows a consistent interpretation of the images.

A disadvantage of CLSM compared to OCT is its higher sensitivity to motion artifacts. This is mainly due to its comparatively slow depth scan. On the other hand, OCT turns out to be an attractive measuring technique, since it is easy to use, very comfortable for the subjects and the measurements in depth direction are very fast (5 ms per individual axial scan). This strongly reduces the effect of subject motion on the images. Moreover, it is easier to sample a large surface area with OCT to average out small-scale variations.

To increase its usefulness, the resolution of OCT has to be improved. Recently, several groups made great progress in the field of ultrahigh resolution OCT. The axial resolution in OCT is inherently connected to the probe-light bandwidth. Ultra-broad spectra can be generated by short laser pulses that are focused onto small core diameter specialty fibers. Highly

non-linear effects within a long interaction region lead to the generation of extremely broadband continuum. The group of Fujimoto demonstrated ultrahigh resolution OCT imaging with 5-6 μm axial resolution at a central wavelength at 1064 nm [21]. Very recently, the group of Drexler has even demonstrated ultrahigh resolution OCT *ex vivo* with an axial resolution of 0.5 μm and 2.5 μm in lateral direction around 725 nm and around 1350 nm with an axial resolution of 1.4 μm lateral 3 μm [22]. In the images even intracellular structure was resolved. Large progress is also achieved in optical coherence microscopy (OCM) [23]. Images parallel to the skin surface, like with CLSM, can be obtained in real time with an axial resolution better than 1 μm and 0.5 μm lateral resolution.

Applying OCM or OCT with a resolution that is comparable to that of CLSM to human skin or in general to human tissue would be a great step towards *in vivo* characterization on a cellular level. It combines the advantage described in this chapter of OCT and CLSM of fast and comfortable scanning of a large tissue area and imaging at the cellular level for easy identification of tissue.

REFERENCES

1. M. Rajadhyaksha, M. Grossman, D. Esterowitz, R. H. Webb, and R. R. Anderson, *"In vivo* confocal scanning laser microscopy of human skin: melanin provides strong contrast," *J. Invest Dermatol.* **104,** 946-952 (1995).
2. B.R. Masters, G. Gonnord, and P. Corcuff, "Three-dimensional microscopic biopsy of *in vivo* human skin: a new technique based on a flexible confocal microscope," *J. Microsc.* **185 (Pt 3),** 329-338 (1997).
3. F. Koenig, S. Gonzalez, W.M. White, M. Lein, and M. Rajadhyaksha, "Near-infrared confocal laser scanning microscopy of bladder tissue *in vivo,*" *Urology* **53,** 853-857 (1999).
4. M. Rajadhyaksha, R.R. Anderson, and R.H. Webb, "Video-rate confocal scanning laser microscope for imaging human tissue," *Appl. Opt.* **38,** 2105-2115 (1999).
5. M. Rajadhyaksha, S. Gonzalez, J. M. Zavislan, R. R. Anderson, and R. H. Webb, "*In vivo* confocal scanning laser microscopy of human skin II: advances in instrumentation and comparison with histology," *J. Invest. Dermatol.* **113,** 293-303 (1999).
6. P. Corcuff, C. Chaussepied, G. Madry, and C. Hadjur, "Skin optics revisited by *in vivo* confocal microscopy: melanin and sun exposure," *J. Cosmet. Sci.* **52,** 91-102 (2001).
7. J.M. Schmitt, A. Knüttel, and R.F. Bonner, "Measurement of optical properties of biological tissue by low-coherence reflectometry," *Appl. Opt.* **32,** 6032-6042 (1993).
8. J.M. Schmitt, M.J. Yadlowsky, and R.F. Bonner, "Subsurface imaging of living skin with optical coherence microscopy," *Dermatol.* **191,** 93-98 (1995).
9. J.A. Izatt, M.R. Hee, G.M. Owen, E.A. Swanson, and J.G. Fujimoto, "Optical coherence microscopy in scattering media," *Opt. Lett.* **19,** 590-592 (1994).
10. J.A. Izatt, M.D. Kulkarni, K. Kobayashi, A.V. Sivak, J.K. Barton, and A.J. Welsh, "Optical coherence tomography for biodiagnostics," *Opt. Photon. News* **8,** 41-47 (1997).

11. J.G. Fujimoto, M.E. Brezinski, G.J. Tearney, S.A. Boppart, B. Bouma, M.R. Hee, J.F. Southern, and E.A. Swanson, "Optical biopsy and imaging using optical coherence tomography," *Nat. Med.* **1,** 970-972 (1995).
12. Y. Pan, E. Lankenau, J. Welzel, R. Birngruber, and R. Engelhardt, "Optical coherence-gated imaging of biological tissues," *IEEE J. Select. Tops Quant. Electr.* **2**, 1029-1034(1996).
13. A.F. Fercher, "Optical coherence tomography," *J. Biomed. Opt.* **1,** 157-173 (1996).
14. J. Welzel, E. Lankenau, R. Birngruber, and R. Engelhardt, "Optical coherence tomography of the human skin," *J. Am. Acad. Dermatol.* **37,** 958-963 (1997).
15. N.D. Gladkova, G.A. Petrova, N.K. Nikulin, S.G. Radenska-Lopovok, L.B. Snopova, Y.P. Chumakov, V.A. Nasonova, V.M. Gelikonov, G.V. Gelikonov, R.V. Kuranov, A.M. Sergeev, and F.I. Feldchtein, "*In vivo* optical coherence tomography imaging of human skin: norm and pathology," *Skin Res. Technol.* **6,** 6-16 (2000).
16. D. Huang, E.A. Swanson, C.P. Lin, J.S. Schuman, W.G. Stinson, W. Chang, M.R. Hee, T. Flotte, K. Gregory, C.A. Puliafito, and J.G. Fujimoto, "Optical coherence tomography," *Science* **254,** 1178-1181 (1991).
17. J.M. Schmitt, "Optical coherence tomography (OCT): a review," *IEEE J. Select. Tops Quant. Electr.* **5,** 1205-1215 (1999).
18. J.G. Fujimoto, C. Pitris, S.A. Boppart, and M.E. Brezinski, "Optical coherence tomography: an emerging technology for biomedical imaging and optical biopsy," *Neoplasia.* **2**, 9-25 (2000).
19. J. Welzel, "Optical coherence tomography in dermatology: a review," *Skin Res. Technol.* **7,** 1-9(2001).
20. *Handbook of Optical Coherence Tomography,* B.E. Bouma and G.J. Tearney eds. (Marc Dekker, New York, 2002).
21. S. Bourquin, I. Hartl, A. D. Aguirre, P.-L. Hsiung, T.H. Ko, T.A. Birks, W.J. Wadsworth, U. Bünting, D. Kopf, and J.G. Fujimoto "Portable broadband light source using a fs Nd:glass laser and non linear fiber for ultrahigh resolution OCT imaging," *Proc. SPIE* **4956,** 4-8 (2003).
22. B. Povazay, K. Bizheva, A. Unterhuber, H. Sattmann, A. F. Fercher, W. Drexler, A. Apolonski, W. J. Wadsworth, J. C. Knight, P. S. J. Russell, M. Vetterlein, and E. Scherzer, "Submicrometer axial resolution optical coherence tomography," *Opt. Lett.* **27,** 1800-1802(2002).
23. A. Dubois, L. Vabre, A.C. Boccara, and E. Beaurepaire, "High-resolution full-field optical coherence tomography with a Linnik microscope," *Appl. Opt.* **41,** 805-812 (2002).
24. E. Lenderink, G.W. Lucassen, P.M. van Kemenade, M.J.S.T. Steenwinkel, and A. A. Vink, "*In vivo* measurements of epidermal thickness with optical coherence tomography and confocal laser scanning microscopy: a comparison of methods," *Proc. SPIE* **4619**, 194-201 (2002).
25. G.J. Tearney, M.E. Brezinski, J.F. Southern, B.E. Bouma, M.R. Hee, and J.G. Fujimoto, "Determination of the refractive index of highly scattering human tissue by optical coherence tomography," *Opt. Lett.* **20,** 2258-2260 (1995).
26. J. Lock-Andersen, P. Therkildsen, O.F. de Fine, M. Gniadecka, K. Dahlstrom, T. Poulsen, and H.C. Wulf, "Epidermal thickness, skin pigmentation and constitutive photosensitivity," *Photodermatol. Photoimmunol. Photomed.* **13,** 153-158 (1997).
27. S. de Winter, A. A. Vink, L. Roza, and S. Pavel, "Solar-simulated skin adaptation and its effect on subsequent UV-induced epidermal DNA damage," *J. Invest. Dermatol.* **117,** 678-682 (2001).
28. R. Marks, "Measurement of biological ageing in human epidermis," *Br. J. Dermatol.* **104,** 627-633 (1981).

29. L.T. Smith, K.A. Holbrook, and P.H. Byers, "Structure of the dermal matrix during development and in the adult," *J. Invest. Dermatol.* **79, Supplement 1,** 93s-104s (1982).
30. G.L. Grove and A.M. Kligman, "Age-associated changes in human epidermal cell renewal," *J. Gerontol.* **38,** 137-142 (1983).
31. R.M. Lavker, P.S. Zheng, and G. Dong, "Aged skin: a study by light, transmission electron, and scanning electron microscopy," *J. Invest. Dermatol.* **88,** 44s-51s (1987).
32. M.C. Branchet, S. Boisnic, C. Frances, and A.M. Robert, "Skin thickness changes in normal aging skin," *Gerontology* **36,** 28-35 (1990).
33. R.S. Kurban and J. Bhawan, "Histologic changes in skin associated with aging," *J. Dermatol. Surg. Oncol.* **16,** 908-914 (1990).
34. K. Sauermann, S. Clemann, S. Jaspers, T. Gambichler, P. Altmeyer, K. Hoffmann, and J. Ennen, "Age related changes of human skin investigated with histometric measurements by confocal laser scanning microscopy in vivo," *Skin Res. Technol*. **8,** 52-56 (2002).
35. S. Neerken, G.W. Lucassen, M.A. Bisschop, E. Lenderink, and A.M. Nuijs, "Characterization of age-related effects in human skin: A comparative study applying confocal laser scanning microscopy and optical coherence tomography," *J. Biomed. Opt.* (2003).
36. K. Sauermann, S. Clemann, S. Jaspers, T. Gambichler, P. Altmeyer, K. Hoffmann, and J. Ennen, "Age related changes of human skin investigated with histometric measurements by confocal laser scanning microscopy *in vivo*" *Skin Res. Technol.* **8,** 52-56 (2002).
37. J. L. Leveque, P. Corcuff, J. de Rigal, and P. Agache, "*In vivo* studies of the evolution of physical properties of the human skin with age," *Int. J. Dermatol.* **23,** 322-329 (1984).
38. M. Huzaira, F. Rius, M. Rajadhyaksha, R.R. Anderson, and S. Gonzalez, "Topographic variations in normal skin, as viewed by *in vivo* reflectance confocal microscopy," *J. Invest Dermatol.* **116,** 846-852 (2001).
39. S. Neerken, G.W. Lucassen, E. Lenderink, and A.M. Nuijs, "*In vivo* imaging of human skin: A comparison of optical coherence tomography and confocal laser scanning microscopy," *Proc. SPIE* **4956,** 299-306 (2003).
40. P. Corcuff and J.L. Leveque, "*In vivo* vision of the human skin with the tandem scanning microscope," *Dermatology* **186,** 50-54 (1993).
41. P. Corcuff, C. Bertrand, and J. L. Leveque, "Morphometry of human epidermis *in vivo* by real-time confocal microscopy," *Arch. Dermatol. Res.* **285,** 475-481 (1993).

This page intentionally left blank

Index

A

Abbe's theory of image formation, 364
ABCD
  ray-transfer matrix, 65
  system, 65
Abdomen, 16
Aberrations, 175
Absorbance, 35
Absorption, 120
  coefficient, 97; 127; 276
    differential, 127
  spectral, 124
  water, 130
Acid
  formic, 130
Acquisition time, 140
Adaptive optics (AO), 202; 382
Adenocarcinoma, 250
Airy disk, 171
Algorithm
  phase stability correction, 299
  true reflection, 62
American National Safety Institute (ANSI), 302
Amplitude
  vector, 64
Anemometry, 176
Angular frequency, 123
Anisotropy defects, 229
Artery
  calf coronary, 273
Atherosclerotic
  lesions (lipid collections, thin intimal caps, and fissures), 46
  plague, 9
Atmosphere, 213
Attenuation, 96
  coefficient, 127
Autocorrelation function, 215
  phase, 79
Avalanche photodiode (APD), 180;389

B

Backscattered light, 223
Backscattering, 9; 63
  amplification, 219
  coefficient, 127; 218
  cross section, 71
  diffuse, 69
  enhanced, 103
  geometry, 123

probability, 261
spectral interferometry, 138
Balanced detector, 9; 179
Bandwidth
full-width-half-maximum (FWHM), 7
Beer's law, 264
Benzoporphyrin derivative (BPD), 333
Biocompatible chemical agents, 13
Biological tissue (biotissue), 3; 61;119; 163; 211; 271; 315;345; 363
Biology
developmental, 366
neuro-, 366
plant, 366
Biopsy, 242
Birefringence, 19
form, 272
circular, 275
corneal, 307
elliptical, 275
linear, 275
retinal nerve fiber layer, 274
tissue, 305
Bladder
urinary, 243
Blood, 21
aggregation, 46
disaggregation, 46
flow, 315
macular, 315
ocular, 315
retinal, 315
hematocrit, 46
microcirculation, 316
oxygenation, 136
perfusion, 316
plasma, 46
osmolarity, 46
rheology, 50
scattering, 47
sedimentation, 47
vessels, 17; 243
whole, 47
Born approximation, 65; 138
Brain, 15
hemodynamics, 334
Brownian
motion, 330

C

Cancer
diagnostics, 17; 336
invasive, 252
laryngeal, 254
microinvasive, 252
superficial, 18
Carcinoma, 251
invasive, 253
squamous cell, 251
transitional cell, 251
Carious (pre-carious), 19
Cataract, 396
CCD
array, 203
camera, 138; 303; 389
line-scan, 203
Cell
membrane, 137
mesanchymal, 138
nucleus, 137
organelles, 22
Ceramic materials, 20; 390
Chest, 16
Clinical
environment, 222
Coatings, 20; 390
Coherence
effects, 93
envelope, 143
width, 144
function, 7
complex
degree, 122

temporal, 6
gating, 246
length, 6; 125; 169, 272
lateral, 70
mutual, 107; 122
temporal, 85; 272
mutual, 68
radar, 203
signal, 125
spatial, 21; 75; 86
temporal, 67
Coherent
mixing, 72
Colposcopy, 254
Collagen, 308
bundle, 429
fiber, 14; 238
Complex analytical signal, 323
Composites, 390
Confocal
microscopy (CM), 87; 178
parameter, 12
Convolution
integral, 262
theorem, 298
Correlation
function
optical field, 184
length
phase, 80
transverse intensity, 103
Correlometer, 233
Cross-correlation, 85
function, 122
amplitude, 6
Crypts, 18
Lieberkühn's, 18

D

Deconvolution technique, 149
Dehydration, 36
Dental, 4
OCT system, 19
Dentistry, 245
Depolarization, 258
length, 227
Dermatology, 4; 245
Detector
linear, 222
quadratic, 222
Developmental biology, 14
Dextrans, 26; 47
Diabetes, 50
Diabetic retinopathy, 191; 315
Diagnostic
accuracy, 252
sensitivity, 252
specificity, 252
Diattenuation, 290
circular (CD), 293
linear (LD), 293
Dichroic mirror, 154
Dichroism, 227
linear, 276
circular, 276
Dielectric permittivity, 216
Diffraction
grating, 140
Diffusion
water, 36
Dimethyl sulphoxide (DMSO), 34
Dirac delta function, 70
Dispersion, 120; 166; 188
broadening, 144
compensation, 146
hardware methods, 146
numerical, 148
contrast, 155
doubling, 219
group (GD), 143
velocity, 12
material, 143
orders, 143
photon propagation time, 220
Dispersive
autocorrelation function, 151
medium, 122

DNA, 120
Doppler
beat signal, 168; 213
effect, 7; 120
frequency shift, 5; 126; 164; 234; 298; 316
spectrum, 297
ultrasound (DUS), 316
Drug
vasoactive, 321
Duct
excretory, 17
Dynamic
focusing, 131; 347
range (DR), 8; 174
Dysplasia, 18;
high grade, 250
low grade, 249

E

Ecology, 360
Edema
physiological, 249
Eikonal, 217
Elastin fiber, 16; 429
Emulsions, 390
Endoscopic diagnosis, 17
Ensemble averaging, 85
Environmental
factors, 360
Epithelial
hyperplasia, 246
metaplasia, 247
Epithelium
atrophy, 245
columnar, 248
glandular, 248
squamous, 300; 359
stratified, 17; 243
transitional, 243
Erythrocyte (red blood cell), 46
cytoplasm, 46
Esophagus, 17; 243
Esophago-gastric junction, 17
Esophagoscopy, 257
Eye
anterior chamber, 193
aqueous, 147
cornea, 13; 131; 147; 176; 303
dehydrated, 132
retrydrated, 132
corneal
Acanthamoeba keratitis, 394
Bowman layer, 177; 194; 392
endothelium, 13; 177; 194; 372
epithelium, 13; 177; 194; 384
cells
basal, 384
wing, 384
infection, 394
stroma, 13; 177; 385
stromal
aberration, 392
keratocyte, 394
subepithelial nerve plexuses, 392
disease
central serous choroidopathy, 191
exudative ARMD, 191
macular
edema, 14
hole, 191
pucker, 191
polypoidal choroidal vasculopathy, 191
RPE detachment, 191
fovea, 13; 176
fundus, 178
ganglion cell layer (GCL),177
iris, 13; 194
rim, 194
stroma, 194
lens, 147; 193
anterior capsule, 13
optic
disk, 13

nerve, 176
head, 305
outer plexiform layer (OPL), 177
photoreceptor layer (PL), 177
pseudophakic, 153
pupil, 201
Purkinje reflected spot, 194
retina, 146; 164; 176
retinal
choriocapillaris (CC), 177; 305
choroid, 201; 305
ganglion cells, 302
nerve fiber layer (RNFL), 177; 305
nuclear layer
inner (INL), 177; 305
outer (ONL), 305
photoreceptor layer
inner (IPR), 305
outer (OPR), 305
pigment epithelium (RPE), 177; 305
plexiform layer,
inner (IPL), 177; 305
outer (OPL), 305
sclera, 13; 308
tear film, 193
tissue, 13
vitreous, 147

F

Faraday cell (rotator), 231; 239
Far field (Fraunhofer zone)
backscatter approximation, 139
Fiber
birefringent, 273
coupler cross-talk, 233
coupling
length, 287
losses, 184
mode, 214
multiplexer, 350
polarization
maintaining (PM), 212; 286; 348
mode, 227
cross-talk, 352
dispersion (PMD), 286
single mode
anisotropic, 224; 287
PANDA, 232
coupler array, 186
isotropic, 231
stretching, 9
Fibroblast, 16
Field
amplitude fluctuations, 64
delta-correlated, 86
phase fluctuations, 64
statistical moments, 64
Filter
bandpass, 8; 126; 172; 304
edge optical, 127
low-pass (LPF), 8; 183
spatial, 9
Filtering
electronic, 127
optical, 127
polarization, 224
Finger, 300
Fingertip, 195
Flavins, 387
Flow
transverse, 328
velocity, 328
Fluctuations
amplitude, 218
index of refraction, 64
phase, 218
Flying spot concept, 163
Foams, 390
Fourier
approach, 366
domain, 123
shift theorem, 143
shifted spectrum, 298
transform (FT), 106; 123

forward, 298
inverse, 139
reverse, 298
short time fast (STFFT), 316
uncertainty relation, 125
Frame
grabber, 187
rate, 165
Fraunhoffer approximation, 377
Frequency
carrier, 167
domain
method
LCI, 138
OCT, 138
scanning, 9
Fresnel
reflection, 134
coefficient, 66

G

Gastroenterology, 245
Gastrointestinal
disorders, 16
endoscopy, 17
tract, 4
Gaussian
beam, 84; 262
focused, 84
waist, 88
function, 7
shape, 68; 125
volume scattering (phase)
function, 75
Geometric optics approximation, 65
Gingiva, 19
Glaucoma, 274
low tension, 315
Gland
esophageal, 18
gastric, 18
secretory, 17
tubular, 18
Glycerol, 16; 34; 47; 256
Glucose, 47; 256
detection, 120
dispersion, 157
Grating-based phase control delay line, 9
Green's
function, 65
theorem, 65
Group delay, 143
differential, 286
Gynecology, 245

H

Hair follicles, 16
Halo, 70
Heart, 15
Heaviside function, 323
Hemoglobin
deoxy-, 136
isobestic point, 136
Hertzian crack, 20
Heterodyne
detection, 5; 215
efficiency factor, 74
mixing, 68; 84
signal, 67
Heterogeneities
large-scale, 217
small-scale, 217
Hilbert transform, 296; 323
Histopathology, 16
Histology, 243
Huygens-Fresnel
Green's function, 66
principle, 62
extended (EHF), 63
Hyperkeratosis, 248

I

Image

acquisition rate, 222
artifacts, 120
bandwidth, 166
degradation, 142
contrast, 120; 222
endosonographic, 244
false color, 132
resolution
axial (depth), 10, 189
spatial, 137
transverse, 10
OCT, 127; 221
B-scan, 164
conventional, 95; 129
3-D,238;336
dispersion compensated, 150
dynamic structural, 38
en-face, 163
intensity
cross sectional, 128
difference, 132
M-mode, 42
processing algorithm, 260
spectroscopic, 137
glass plate
BK7, 141
IR filter, 141
orthoscopic, 365
Imaging
biomedical, 19; 119
blood flow, 298
confocal, 191
contrast, 27; 44; 63
cross sectional, 9; 63
CT (computer tomography), 119
3D, 192
depth, 21; 32; 44
enhanced, 26
intraluminal, 19
localization, 32
Moiré fringe pattern, 173
MRI (magnetic resonance), 119
OCT, 16; 61; 221
algorithm,
data processing, 62
true-reflection, 95
intravascular, 46
phase-resolved, 298
resolution, 32
degradation, 21; 142
through
blood, 26; 46
vascular system, 46
tissue, 315
ultrasound, 119
Immersion
technique, 13
medium, 423
Impulse response function, 142
Indocyanine Green (ICG), 136
Inflammatory process, 242
Integrating sphere measurements, 97
Intensity
averaged, 122
reflection coefficient, 123
Interference
fringe
contrast, 144
fringes, 276
Fourier transforming, 278
law, 9
pattern, 166
time-modulated signal, 8
two-beam, 6
Interferometric
control, 131
receiver, 22
signal (or "interferogram"), 122
Interferometer
anisotropic fiber, 223
dynamic range, 224
external, 153
low-coherence (LCI), 130
Mach-Zehnder, 5; 203
Mach-Zehnder/Michelson, 273
Michelson, 5; 66; 121; 155; 182; 237; 276; 348

optical fiber, 213; 319
polarization-sensitive, 273
multiplexing-demultiplexing, 186
polarization, 273
Interferometric
ellipsometry, 276
Interferometry
backscattering spectral, 138
low-coherence (LCI), 7; 121; 163
chirped signal, 144
white light, 163
Intimal vessel wall, 19
Intoxication, 397
Intralipid, 21; 130
Intraocular
distances, 153
Intravascular wall, 19
Inverse
adding-doubling method, 97
problem, 262
Irradiance, 70

J

Jones reversibility theorem, 294

K

Keratinization process, 245
Kirchhoff approximation, 65

L

LabView™ Virtual Instrument (VI), 183
Lambertian emitter, 90
Lamina propria, 17
Laryngology, 245
Laser
Argon
-ion, 387
-Krypton, 387
Cr^{4+}: forsterite, 11; 234
Doppler
flowmetry (LDF), 315
femtosecond, 119
Helium-Cadmium, 387
Helium-Neon, 390
mode-locked, 11
-pumped fluorescent organic dye, 11
Ti: sapphire ($Ti:Al_2O_3$), 11; 119; 136; 234
Lidar technique, 213
Light
back-scattered, 14
beam
partially coherent, 122
emitting diode (LED), 11
edge-emitting, 11
emission spectrum, 128
multiple QW, 11
intensity, 8
penetration depth, 27
scattering, 3; 61; 119;
sources
broadband, 124; 223
amplified spontaneous emission (ASE), 124
halogen lamp, 156
incandescent lamp, 134
Kerr-lens mode-locked laser
Cr:forsterite, 124
Ti:sapphire, 124; 185
multiple electrode semiconductor device, 189
photonic crystal fiber, 125
superluminescent, 212
superluminescent diode (SLD), 121; 167
transmittance, 34
enhanced, 34
Lip, 300
Lipids, 19
Low-coherence
interferometry, 7

light source, 5
optical reflectometry (LCR), 5
Lymph,
nodule, 18

M

Malignant
melanoma, 16
tumor, 254
Malignization process, 249
Mass transport, 37
Matrix
Jones, 229; 293
Mueller, 281
rotation, 276
Maxwell's equations, 64
Mean free path (MFP), 20
Melanocytes, 137
Methylcellulose gel, 384
Metrology, 20
Microchannel, 339
Micro-electro-mechanic-system (MEMS), 337
bioMEMS, 337
Microscope
applanating objective, 372
confocal, 363
laser scanning, 381
microlens, 379
Nipkow disk, 374
real-time, 375
scanning slit, 380
tandem scanning, 375
Linnik interference, 204
phase contrast, 155
slit lamp, 371
specular, 371
wide-field, 385
Microscopy
confocal, 363
laser scanning (CLSM), 418
fluorescent, 374
laser Raman, 390
multiphoton excitation, 363
phase dispersion, 120
three-dimensional, 363
two-photon
excitation, 87
laser scanning fluorescence, 404
Minimal erythema dose (MED), 425
Model,
random walk, 286
Modulation
optical phase, 321
Modulator
electro-optic, 174; 273
fiber pigtailed phase, 288
integrated optic Mach - Zehnder (IOMZM), 186
non-dispersive, 174
path imbalance, 166
phase, 166; 204; 288
photoelastic birefringence, 204
Monte Carlo
MCML computer code, 90
model (method), 214
advanced, 62
geometric-focus, 87
hybrid, 63
hyperboloid, 88
spot-focus, 87
simulation, 21; 62
Morphology
embryonic, 14
neural, 14
Mucosa, 238
benign, 252
basement membrane, 242
glands, 243
glandular, 248
lamina propria, 242; 300
layer
basal, 242
parabasal, 242
stomach pyloric, 34

Mucosal
abnormalities, 17
neoplasia, 252
Muscle, 16
Muscularis mucosae, 17
Myocardium infarction, 50

N

NADH, 375
Nail fold, 301
Neoplastic
process, 242
Newton rings, 166
Nitroglycerin (NTG), 330
Noise, 7
additive, 213
background, 10
dispersion, 263
electronic, 8
excess photon, 9; 186
intensity, 9
mechanical 1*/f,* 7
multiplicative, 213
quantum, 8
Poisson, 366
shot, 7; 76; 185; 223; 305; 366
speckle, 129; 221; 293; 324
Numerical aperture, 11; 194; 272; 365
fiber, 92

O

Object
depth, 140
interface, 140
structure, 140
Ocean, 213
Oncology, 252
Ophthalmic
slit-lamp, 303
Volk lens, 303
Ophthalmology, 4; 391
Ophthalmoscope
confocal scanning laser (CSLO), 13; 178; 382
Optical
beam induced current technique (OBIC), 390
biopsy, 19; 360;418
clearing of
blood, 26
tissue, 27
coherence
-domain reflectometry (OCDR), 4
microscopy (OCM), 345; 418
tomography (OCT), 3; 61; 119; 163;211;271;316;345;418
"color", 232
Doppler, 316
conventional, 103; 119
cross-polarization (CPOCT), 232
dispersion, 142
dual beam, 12
endoscopic (EOCT), 18; 212; 240
en-face, 12
Fourier domain, 12
frequency domain, 138
functional, 12
high-resolution, 120
miniaturized optical probe, 222
multi-functional, 296
parallel, 181
polarization sensitive (PS OCT), 12; 19; 272
resolution
axial, 86; 272
lateral, 78; 272
scan
A, 42; 121; 163; 271; 324
B,163; 304
C, 163
T, 165

spectral, 12; 125; 325
time domain, 121
two-color, 236
video rate, 12; 174
whole field, 12
depth, 66
Doppler tomography (ODT), 316
phase-resolved, 317
echoe, 9
fiber, 83
coupler, 9
single-mode, 9
superfluorescent
Er-doped, 11
Nd-/Yb-doped, 11
Tm-doped, 11
path
length, 6; 66; 154
difference (OPD), 165; 201
production technology, 20
"sectioning", 366
time delay, 6
wave
quasi-monochromatic, 101
Osmotic
mobility, 339
potential, 36
pressure, 36
Osmotically active chemical agents, 34

P

Paints, 20
Paraxial
approximation, 87
wave propagation, 65
Particle
volume fraction, 34
Path length difference, 224
Pearson correlations, 424
Penetration length, 120
Peripheral vision, 302
Phantom, 136
Phase
delay, 288
differential (DPD), 286
retardation, 275
Photobleaching, 387
Photochemical reaction, 387
Photodynamic therapy (PDT), 87; 333
Photon
ballistic, 21; 63; 219; 354
density, 88
least-scattered (LSP), 21
mean free path (mfp), 223; 353
multiple scattered (MSP), 22
packets, 83
"snake", 223
Photorefractive keratectomy (PRK), 393
Photoresists, 390
Piezoceramic actuator, 233
Pinhole, 181
Pixel depth size, 164
Plants, 360
Poincaré sphere, 275
Point-spread function (PSF), 21; 140
depth (zPSF), 26
Polarimetry, 276
Polarization, 238; 273
circular, 274
controller (CP), 239
cross-, 238
degree, 279
linear, 274
Polarizer, 377
circular, 274
linear, 274
Polarizing beam splitter, 277
Polymer-matrix composite, 20
Porosity, 20
Power spectral density, 7
Premalignant changes, 17
Probing depth, 78

Profilometry, 176
Propylene glycol, 16; 45; 256
Psoriatic erythrodermia, 256
Pulsed response of medium, 217

R

Radiative transfer
  equation (RTE), 62; 214
    small-angle approximation, 63
Random
  inhomogeneities, 65
  medium, 64; 92
    small-angle scattering, 102
  phase, 65
  process
    stationary, 215
    zero-mean, 79
Raster, 165
Rayleigh-Gans approximation, 33
Rayleigh
  law, 218
  range, 12
Redox fluorometry, 402
Reflection,
  specular, 281
Refractive index, 6; 33; 64; 120
  birefringent, 227
  complex, 139
  connective tissue fiber
  (elastin and collagen), 33
  cytoplasmic organelles and
inclusions (mitochondria, nuclei,
ribosome, pigment granules), 33
  formic acid, 131
  group, 122; 143; 234
  matching, 16; 33; 50
  mismatch, 33
  random spatial variation, 65
  spectrum, 134
    oxazine 1 in methanol, 136
  water, 131
Remote sensing, 212
Resolution
  depth (axial), 125; 166; 240;
353;366
  degradation, 148
  of the microscope, 365
  spatial, 125; 222
  spectral, 125
  sub-cellular, 418
  transverse (lateral), 166; 202;
353; 366
  velocity, 322
  wavelength, 125
Retardance
  phase
    circular, 294
    linear, 294
Retardation
  double-pass phase (DPPR), 306
Retarder
  linear, 281
Retina, 9
Retinal-macular diseases, 13
Retinal nerve fiber layer (RNFL),
301
  glaucomatous atrophy, 302
Rough surface, 176
Roughness, 175
Rytov approximation, 65

S

Sample
  multi-layered, 100
  transfer function, 123
Sampling
  function, 166
  in depth, 166
  rate, 173
Scalar stochastic equation, 64
Scanner
  angular efficiency, 168
  electrostrictive, 185
  diffraction grating, 166
  fast galvanometer, 166
  piezo, 166
  polygon mirror, 166

resonant, 166
telecentric XY retina scanner, 303
translation stage, 166
turbine driven mirror, 166
Scanning
bilateral, 374
group delay, 297
laser polarimetry (SLP), 302
lateral, 198; 272
lens, 354
phase delay, 297
rapid optical delay line (RSOD), 288; 319
speed, 168
synchronous, 347
systems, 388
Scattering
angle,
root mean square, 67
anisotropic, 21; 221
anisotropy factor (asymmetry parameter), 24; 67; 262
centers, 34
coefficient, 24; 67; 78; 97; 127; 276
back-, 262
forward, 262
reduced, 34
forward, 93; 272
function (phase or volume)
Gaussian, 75; 80
Henyey-Greenstein, 76; 262
small-angle, 261
medium, 9; 62; 126
multiple, 21; 62; 213; 352
particle, 33
potential (amplitude reflectivity), 139
autocorrelation function (ACF), 140
single, 22; 62; 217
small-angle, 22; 352
total, 262
vector, 139
wider-angle, 22
Scheimpflug slit camera, 396
Sellmeier formulas, 148
Semiconductor metrology, 390
Sensing
hydroacoustic, 213
radar, 213
remote, 212
Shower curtain effect, 63; 73
Shrink
cell, 37
fiber, 37
Signal
attenuation, 21
autocorrelation, 134
backscattered, 214
beat, 144
cross correlation, 134
degradation, 142
full width at half maximum (FWHM), 125
interferometric, 229
localization, 21
pulsed probing, 215
sounding
coherence, 215
pulsed, 215
-to-noise ratio (SNR), 8; 67; 76; 175; 181; 223; 366
video, 221
Skin, 15; 74; 244; 291; 391; 418
ageing, 427
derma (dermis), 16; 195; 422
papillary, 16; 431
reticular, 16; 431
dermo-epidermal junction, 424
disease
psoriasis, 315
eczema, 315
scleroderma, 315
epidermal basement, 16
epidermal-dermal boundary, 301
epidermis, 16; 195; 418; 423

fascia, 16
graft, 150
hypodermis, 16
malformation
hemangioma, 315
port-wine stain, 315
telangiectasia, 315
stratum corneum, 16; 37; 195; 400; 423
structure, 16
sweat ducts, 195
tanning, 426
trauma
burn, 315
irritation, 315
wound, 315
Small-angle
approximation, 221; 261
forward scattering, 67
Snell's law refraction, 92
Space
fibrillar, 37
extracellular, 37
extrafibrillar - interstitial, 37
hue-saturation-luminance color, 137
intracellular, 37
RGB color, 137
Speckle, 98
effects, 124
field (s)
uncorrelated, 126
noise, 128
reduction, 133
size, 126
Spectral
absorption, 124
backscatter cross-section, 123
dispersion, 124
mean attenuation coefficient, 123
resolution, 125
shifts
spatially resolved
width, 7
Spectrophotometer with integrating sphere, 34
Spectrophotometry
transmission, 128
Spectroscopy
near infrared, 34
Spectrum
absorption, 134
oxazine 1 in methanol, 136
amplitude, 123
diffuse reflectance, 34
dispersion, 134
phase, 123
transmittance, 34
oil, 128
water, 128
Specular
reflection, 7
surface, 91
Spot size, 70
Statistical average, 219
Stokes vector, 274
Stomach, 18
Subcorneal blister, 249
Submucosa, 17
Superluminescent diode (SLD), 11; 66; 119; 121; 167; 237;302; 350

T

Tadpole, 15
African frog, 137
Telecentric telescope, 203
Telecommunication industry, 9
Theory
linear system, 63
perturbation, 231
single-scattering, 63
Time gate, 22
Tissue
aorta, 46
birefringence, 238

bone, 244; 272
bronchus, 251
burn, 274
cartilage, 245; 272
cervical, 250
chemical administration, 38
chromophores (water, hemoglobin, cytochrome aa3, NADH, melanin), 120
colonic, 18; 243
sigmoid, 256
connective, 32; 252
dental, 195; 272
dentin, 19; 244
dento-enamel junction, 19; 244
enamel, 19; 195; 244
caries lesion, 195
demineralization, 195
remineralization, 198
epithelium, 243
esophageal, 18; 243
fibrous, 418
fluids, 36
functionality, 273
gastric, 18
hard, 19
immersion, 33
lamina propria, 243
larynx, 243
morphology, 137; 191
myocardium, 273
muscle, 272
nerve, 272
optical
clearing, 32; 256
properties control, 32
coagulation, 32
compression, 32; 256
dehydration, 32; 36
exposure to low temperature, 32
impregnation by chemical agents, 32; 256
stretching, 32
UV irradiation, 32; 424
phantom, 62; 128
solid scattering, 96
rectal, 251
refractive index, 33
re-hydration, 44
scar, 259
immature, 259
stomach, 37
stroma, 14; 234
structure, 273
submucosal, 300
superficial, 16
surface curvature, 201
tectorial, 245
tendon, 272
thermal damage, 273
turbid, 22
viability, 273
Tomographic imaging, 21; 38
Tomography, 296
Topical application, 16; 38
Topography, 189
Tooth, 19
Transmembrane permeability, 37
Transmission
collimated, 97
Turbid medium, 22; 212

U

Urology, 245
Uterine cervix, 243
mucosa
acanthosis, 247
papillomatosis, 247

V

Vocal fold, 246

W

Water

desorption, 36
dispersion, 156
concentration, 127; 134
heavy, 128
vibrational overtone band, 127
Wave
equation, 64
number, 64
phase conjugated, 214
plate, 273
half, 287
quarter, 287; 377
Wavefront
corrector (WC), 202
sensor, 368
Waveguide
$LiTaO_3$, 147
Wavelet transform
Morlett, 136
Wavelets
spherical, 65
Wiener-Khintchine theorem, 7; 123
Wigner phase-space distribution, 102
function, 63; 109
transverse momentum width, 109

X

X-ray contrasting agent, 46